Settimio Mobilio · Federico Boscherini
Carlo Meneghini *Editors*

Synchrotron Radiation

Basics, Methods and Applications

Springer

Synchrotron Radiation

Settimio Mobilio · Federico Boscherini
Carlo Meneghini
Editors

Synchrotron Radiation

Basics, Methods and Applications

Springer

Editors
Settimio Mobilio
Carlo Meneghini
Department of Science
University "Roma Tre"
Rome
Italy

Federico Boscherini
Department of Physics and Astronomy
University of Bologna
Bologna
Italy

ISBN 978-3-642-55314-1 ISBN 978-3-642-55315-8 (eBook)
DOI 10.1007/978-3-642-55315-8
Springer Heidelberg New York Dordrecht London

Library of Congress Control Number: 2014942061

© Springer-Verlag Berlin Heidelberg 2015
This work is subject to copyright. All rights are reserved by the Publisher, whether the whole or part of the material is concerned, specifically the rights of translation, reprinting, reuse of illustrations, recitation, broadcasting, reproduction on microfilms or in any other physical way, and transmission or information storage and retrieval, electronic adaptation, computer software, or by similar or dissimilar methodology now known or hereafter developed. Exempted from this legal reservation are brief excerpts in connection with reviews or scholarly analysis or material supplied specifically for the purpose of being entered and executed on a computer system, for exclusive use by the purchaser of the work. Duplication of this publication or parts thereof is permitted only under the provisions of the Copyright Law of the Publisher's location, in its current version, and permission for use must always be obtained from Springer. Permissions for use may be obtained through RightsLink at the Copyright Clearance Center. Violations are liable to prosecution under the respective Copyright Law.
The use of general descriptive names, registered names, trademarks, service marks, etc. in this publication does not imply, even in the absence of a specific statement, that such names are exempt from the relevant protective laws and regulations and therefore free for general use.
While the advice and information in this book are believed to be true and accurate at the date of publication, neither the authors nor the editors nor the publisher can accept any legal responsibility for any errors or omissions that may be made. The publisher makes no warranty, express or implied, with respect to the material contained herein.

Printed on acid-free paper

Springer is part of Springer Science+Business Media (www.springer.com)

Preface

Since the first observation of synchrotron radiation in 1947, progress in the generation of electromagnetic radiation using particle accelerators and in experimental methods has allowed enormous progress in the fine analysis of matter. This progress has not been incremental but rather truly innovative and in some cases revolutionary. Thanks to advances in accelerator physics and technology the improvement in the characteristics of synchrotron radiation and free electron laser sources, especially brilliance, coherence and time structure, has spanned many orders of magnitude. At the same time, new methods to investigate matter have been developed which have led to original approaches for its characterization in the domains of real and reciprocal space, energy and time. Progress in these two aspects—sources and experimental methods—has been truly synergic.

While the first applications of synchrotron radiation were in the field of solid-state physics, its use now is ubiquitous in all the physical and natural sciences, with also significant medical applications. 'Samples' studied at beamlines range from man-made inorganic materials and devices, natural minerals and rocks, environmentally significant specimens, cultural heritage materials, biologically relevant molecules, tissues and in some cases even live human patients.

The importance and societal relevance of synchrotron radiation has been recognized by the scientific community and by policy makers worldwide. Due to the investment and operation costs required to operate a synchrotron radiation or free electron laser source, centralized large-scale infrastructure user facilities have been developed. In recent decades, there has been an evolution from the parasitic use of synchrotron radiation emitted by accelerators designed for particle physics experiments to facilities specially designed exclusively for photon science-based experiments. The scientific goal of numerous important national laboratories in the world has changed from particle physics to photon science.

Most industrialized and some developing countries now have a national synchrotron radiation facility; there are also important examples of international cooperation for the construction and operation of facilities, ranging from the European Synchrotron Radiation Facility in Grenoble, a major laboratory funded by a wide European collaboration, to SESAME—a UNESCO sponsored project intended also as a means to encourage collaboration and peace in the Middle East. Access to these facilities is commonly regulated by an open access policy based exclusively on merit: whoever has a good idea to use synchrotron radiation has

free access to the instruments; this is a key aspect which contributes very significantly to maintain a competitive, curiosity-driven and young intellectual community all over the world. In parallel, synchrotron radiation and free electron laser sources are a key tool to meet important societal challenges in the near future, including providing essential tools to characterize nanostructures and advanced materials used in key areas of future technologies in the inorganic and bio areas; refined methods to characterized new materials and devices are essential to provide key answers in challenging areas such as, for example, those defined by the Horizon 2020 programme of the European Union, including health and wellbeing, sustainable agriculture, secure, clean and safe and efficient energy and a clean environment.

This is the context within which we are proud to present this book, which reports the lecture notes of lessons held at the 12th edition of the School on Synchrotron Radiation, organized by the Italian Synchrotron Radiation Society (Società Italiana di Luce di Sincrotrone, SILS, www.synchrotron-radiation.it) in collaboration with Elettra—Sincrotrone Trieste (www.elettra.eu). SILS is one of the oldest independent scientific societies, the objective of which is to promote synchrotron radiation in Italy in the European context.

The School took place in the town of Grado (near Trieste) in September 2013 and benefited from partial financial support from COST Action MP1103—Nanostructured materials for solid-state hydrogen storage. The directors of the school were Settimio Mobilio and Gilberto Vlaic. The SILS school has become one of the most important educational events in the field of synchrotron radiation in Europe. Its important role is testified by the high number of applications (over 100 for 45 places) and the strongly international character, with participants coming from as far away as Canada, China and Iran. In the course of the two weeks' duration, which included a full day devoted to a practical session at Elettra, including hands on experience at selected beamlines and data analysis, the lectures covered the fundamentals of synchrotron radiation and free electron laser emission, the interaction between electromagnetic radiation and matter, the main experimental methods and the most important and recent applications.

All these aspects are included in this volume, which is organized as follows. Part I describes the emission of synchrotron and free electron laser sources and the basic aspects of beamline instrumentation; Part II illustrates the fundamentals of the interaction between electromagnetic radiation and matter; Part III describes the most important experimental methods, ranging from spectroscopies, diffraction and scattering, to imaging; finally, Part IV reports a range of applications of current topical interest.

Rome
Bologna

Settimio Mobilio
Federico Boscherini
Carlo Meneghini

Contents

Part I Basics of Synchrotron Radiation

1 Introduction to Synchrotron Radiation 3
Antonella Balerna and Settimio Mobilio
1.1 Introduction 3
1.2 Storage Rings and Synchrotron Radiation Sources 4
1.3 Synchrotron Radiation Properties 8
1.4 Radiated Power and Time Structure 9
1.5 Angular, Spectral and Intensity Distribution. 12
1.6 Polarization 17
1.7 Spectral Brightness and Emittance 19
1.8 Insertion Devices 20
References 28

2 Characteristics and Properties of Synchrotron Radiation 29
Giorgio Margaritondo
2.1 Introduction: Broad Picture of a Synchrotron Light Source . . . 29
2.2 Relativistic Effects in a Nutshell 31
2.3 Definition of the Main Parameters 34
2.3.1 Spectral Distribution Features 34
2.3.2 Total Emission 34
2.3.3 Brightness 35
2.3.4 Polarization 37
2.3.5 Time Features 38
2.3.6 Coherence Parameters 38
2.4 Bending Magnets 42
2.5 Wigglers 44
2.6 Undulators 44
2.7 Free Electron Lasers 50
2.7.1 The Gain Length 52
2.7.2 Infrared FELs Versus X-FELs 53
2.7.3 The Subtle Effects of Relativity 54
2.7.4 Saturation 55
2.7.5 Seeding 57

2.8 Why Are Synchrotron and X-FELs Sources Important? 57
2.9 New Types of Synchrotron-Related Sources 60
2.10 A Few Practical Equations 61
References 61

3 Instrumentation at Synchrotron Radiation Beamlines 65
Giuliana Aquilanti, Lisa Vaccari, Jasper Rikkert Plaisier and Andrea Goldoni
3.1 Introduction 65
3.2 Beamlines in the Hard X-Ray Range (2000–50000 eV) 69
3.2.1 Hard X-Ray Optics 70
3.2.2 X-Ray Detectors 77
3.2.3 Diffraction Beamlines: MCX at Elettra 79
3.2.4 Absorption Beamlines: the XAFS Beamline at Elettra 80
3.3 Soft X-Ray and Vacuum Ultraviolet Beamlines 81
3.3.1 Soft X-Ray Energy Optics 83
3.3.2 Layout for a Soft X-Ray Energy Beamline 85
3.3.3 Low Energy VUV (4–40 eV) and Visible-Infrared Beamlines 87
3.3.4 Experimental Examples to Test the Beamline Performance 91
3.4 Cooling of Optics and Other Beamline Parts 94
3.5 X-Ray Optics for Microscopy 95
3.5.1 X-Ray Focusing Optics 96
References 102

Part II Fundamental Interactions

4 Introduction to Matter Radiation Interaction 107
Settimio Mobilio
4.1 Introduction 107
4.2 Classical Description of Electromagnetic Waves and Their Interaction with the Matter 109
4.2.1 Electromagnetic Waves in the Vacuum 109
4.2.2 Electromagnetic Waves in Matter 111
4.2.3 Classical Microscopic Description of the Complex Index of Refraction 114
4.2.4 The Scattering and its Classical Description 118
4.2.5 Elastic Scattering at High Energy 119
4.2.6 Anomalous Scattering 122
4.3 Semiclassical Description of the Interaction Between Matter and Radiation 124

4.3.1 Quantum Description of the Matter. 124
4.3.2 Semiclassical Description of the Interaction. 125
4.3.3 Absorption Coefficient in the Semiclassical Approach. 125
4.3.4 The Scattering in the Semi-classical Approach. 127
4.4 Quantum Description of the Absorption and Scattering. 130
4.4.1 Quantum Description of the Electromagnetic Field. . . 130
4.4.2 Quantum Description of the Interaction of Electromagnetic Fields and Matter 131
4.4.3 Absorption Cross Section 132
4.4.4 First Order Scattering 132
4.4.5 Second Order Scattering: Anomalous and Resonant Scattering 135
4.4.6 High Energy Behaviour of the Second Order Scattering 137
4.5 Relativistic Scattering 137
4.5.1 First Order Relativistic Contribution to the Scattering 138
4.5.2 Second Order Relativistic Scattering. 139
4.5.3 Total Scattering Cross Section at High Energy. 140
References 143

5 Quantum Description of the Matter-Radiation Interaction 145
Carlo Maria Bertoni
5.1 The Classical Description of the Free Electromagnetic Field 145
5.2 The Quantized Free Electromagnetic Field 148
5.3 Moving Charges in Interaction with the Electromagnetic Field 153
5.4 The Expansion of the Amplitude of Transition. 155
5.5 Elementary Processes 157
5.6 The Matrix Element 158
5.7 Beyond the Dipole Approximation 160
5.8 Absorption. 161
5.9 Photoemission 163
5.10 Thomson Scattering 170
5.11 Second Order Processes. 171
5.12 Resonant Raman Scattering 172
5.13 Conclusions 174
5.14 Appendix. 174
References 177

Part III Experimental Methods

6 Introduction to X-Ray Absorption Spectroscopy 181
Paolo Fornasini
6.1 A Phenomenological Introduction to XAFS 181
6.2 Photoelectric Absorption of X-Rays 184
6.2.1 Golden Rule and Further Approximations 185
6.2.2 De-excitation Mechanisms 187
6.3 Basic EXAFS Theory 188
6.3.1 The EXAFS Function 188
6.3.2 Approximate Derivation of EXAFS 190
6.3.3 Disorder Effects on EXAFS 194
6.3.4 Summary 197
6.4 Interpretation of EXAFS Parameters 197
6.4.1 EXAFS Distance and Crystallographic Distance 198
6.4.2 Parallel and Perpendicular MSRDs 199
6.4.3 Structural Disorder 201
6.5 Experimental Techniques 201
6.5.1 Optical Apparatus 202
6.5.2 Measurement Apparatus 203
6.6 EXAFS Analysis 205
6.6.1 Extraction of the EXAFS signal 205
6.6.2 Fourier Transform and Back-Transform 207
6.6.3 Quantitative Determination of Structural Parameters 209
References 210

7 A Close Look into the Low Energy Region of the XAS Spectra: The XANES Region 213
Maurizio Benfatto and Carlo Meneghini
7.1 Introduction 213
7.2 The Origin of Near Edge Features 215
7.3 Semi-quantitative Understanding of XANES Features 218
7.4 Theoretical Background and the Fit of the XANES Energy Region 220
7.5 Conclusions 237
References 238

8 X-Ray Diffraction by Crystalline Materials 241
Davide Viterbo and Giuseppe Zanotti
8.1 Introduction 241
8.1.1 The Crystal 242
8.1.2 Crystal Symmetries 243

8.1.3 The X-Rays . . . 245
8.1.4 Some Useful Mathematical Concepts . . . 245
8.2 X-Ray Diffraction . . . 252
8.2.1 X-Ray Scattering . . . 253
8.2.2 Interference of Scattered Waves . . . 255
8.2.3 Scattering by Matter . . . 256
8.2.4 Diffraction by a Crystal . . . 257
8.2.5 Other Useful Relations and Concepts . . . 261
8.3 The Phase Problem . . . 263
8.3.1 Patterson Methods . . . 264
8.3.2 Direct Methods . . . 265
8.3.3 Other Methods Used to Solve the Phase Problem . . . 265
8.4 Refinement of the Crystal Structure . . . 266
8.5 Diffraction by Polycrystalline Samples . . . 267
8.5.1 Experimental Techniques for Obtaining Powder Diffraction Patterns . . . 268
8.5.2 Analysis of Powder Diffraction Patterns . . . 271
References . . . 272

9 Photoemission Spectroscopy: Fundamental Aspects . . . 275
Carlo Mariani and Giovanni Stefani
9.1 Introduction . . . 275
9.2 Basic Concepts . . . 276
9.3 Energy Conservation, Binding Energy and Photoelectron Energy . . . 278
9.4 Satellite Structures . . . 281
9.4.1 Spin-Orbit Splitting . . . 284
9.4.2 Multiplet Splitting . . . 284
9.4.3 Chemical Shift . . . 286
9.5 Molecular Photoelectron Spectroscopy . . . 287
9.5.1 Vibrational Overtones . . . 287
9.6 Photoelectron Angular Distributions . . . 291
9.7 Core Hole State Relaxation . . . 294
9.7.1 The Auger Decay . . . 295
9.7.2 Resonant Auger and Photoemission . . . 298
9.8 Photoemission from Solids: The Three-Step Model . . . 300
9.9 Spectral Function of Interacting Electrons in a Solid . . . 303
9.10 Energy Distribution Curves . . . 305
9.10.1 Valence Band Examples (Cross-Section Exploitation and Cooper Minima) . . . 305
9.10.2 Core Level Examples . . . 307
9.11 Angular Resolved PhotoElectron Spectroscopy . . . 309
9.11.1 Band Structures . . . 309
9.11.2 Adsorbates . . . 309

9.11.3 Graphite and Graphene as Exemplary 2D System 311
9.12 Final Considerations and Perspectives 314
References 315

10 Powder Diffraction and Synchrotron Radiation 319
Gilberto Artioli
10.1 Powder Diffraction 319
10.2 Flat Plate Sample (Bragg-Brentano Geometry) 322
10.3 Cylindrical Sample (Debye Geometry) 324
10.4 The Implementation of Capillary Geometry at Synchrotron Sources, Case Examples 325
10.5 Basics of Instrumental Strategies 327
10.6 Time Resolved Experiments, Kinetics, Non-ambient Conditions 328
10.7 Simultaneous and Combined Studies 331
References 333

11 Small Angle X-Ray Scattering (SAXS) with Synchrotron Radiation Sources 337
Stefano Polizzi and Francesco Spinozzi
11.1 The Physical Phenomenon 337
11.1.1 Why Small Angles? 338
11.1.2 How Small Is "Small"? 338
11.1.3 What Is an "Object" for SAXS? 339
11.2 Data Analysis 343
11.2.1 Guinier's Approximation 344
11.2.2 Porod's Law 345
11.2.3 The Scattering Power 346
11.2.4 Debye's Approximation and Kratky Plot 347
11.2.5 Distance Distribution Function 347
11.2.6 Fractality 348
11.3 Experimental 349
11.4 Case Studies 351
References 358

12 Resonant and Magnetic X-Ray Diffraction 361
Luigi Paolasini
12.1 Introduction 361
12.1.1 Theoretical Aspects of Magnetic and Resonant X-Ray Scattering 362
12.1.2 X-Rays Scattering Amplitudes 363
12.2 Experimental Methods 366
12.2.1 Polarization Analysis and Azimuthal Scans 366
12.2.2 Circular Polarisation 367

12.3 Magnetic Diffraction 369
12.3.1 Linear Polarisation Analysis of a Simple Antiferromagnetic Structure 370
12.3.2 Exemple II: Circular Polarisation Analysis in Multiferroics 372
12.4 Resonant X-Rays Scattering 375
12.4.1 Interplay Between Magnetic and Orbital Ordering in $KCuF_3$ 378
12.4.2 High Order Multipoles in V_2O_3 380
12.5 Conclusions 383
References 384

13 Hard X-Ray Synchrotron Imaging Techniques and Applications 389
Jean-Yves Buffiere and José Baruchel
13.1 Introduction 389
13.2 Imaging Techniques 391
13.2.1 Absorption Radiography 391
13.2.2 Microtomography 393
13.2.3 Phase Imaging 394
13.2.4 Microbeam Based X-Ray Imaging Techniques/Nano Imaging 398
13.2.5 X-Ray Bragg Diffraction Imaging 400
13.3 Selected Examples of the Application of Synchrotron Radiation Imaging Techniques 403
13.4 Conclusion 406
References 407

14 X-Ray Microscopy 409
Diane Eichert
14.1 Introduction 409
14.2 Fundamentals of X-Ray Microscopy 411
14.2.1 X-Ray Sources 411
14.2.2 X-Ray Optics 412
14.2.3 Detectors 412
14.3 Imaging Modes 413
14.3.1 Interactions of X-Rays with Matter 413
14.3.2 Contrast Mechanisms 414
14.4 Imaging Methods 417
14.4.1 Projection Microscopy 418
14.4.2 Transmission X-Ray Microscope 419
14.4.3 Scanning Transmission X-Ray Microscope 420
14.4.4 Complementary Techniques and Methodological Developments 421

14.5 Experimental Conditions 423
14.5.1 Experimental Conditions 424
14.5.2 Conditions of Analysis 424
14.6 Applications. 426
14.6.1 Materials Science 427
14.6.2 Environmental Science 428
14.6.3 Life Science. 429
14.7 Conclusions 431
References 432

15 Infrared Synchrotron Radiation: From the Production to the Scientific Applications 437
Andrea Perucchi, Lisa Vaccari and Stefano Lupi
15.1 Introduction 437
15.2 IRSR Figures of Merits 438
15.2.1 Definitions. 438
15.2.2 Emitted Power 441
15.2.3 Brilliance. 442
15.3 Unconventional SR Sources 444
15.3.1 Edge Radiation. 444
15.3.2 Superradiance Phenomena and Terahertz Coherent Radiation 445
15.4 Application of IRSR 446
15.4.1 Applications of IRSR at High Pressure 446
15.4.2 Terahertz Spectroscopy 449
15.4.3 Synchrotron Radiation Infrared Microspectroscopy for Biology and Medicine 453
15.4.4 Synchrotron Radiation Infrared Microspectroscopy for Cultural Heritage. 457
References 458

16 The High-Frequency Atomic Dynamics of Disordered Systems Studied by High-Resolution Inelastic X-Ray Scattering 461
Giulio Monaco
16.1 Introduction 461
16.2 The High-Resolution Inelastic X-Ray Scattering Experiment 464
16.3 Models to Describe the IXS Spectra 466
16.4 Selected Results 470
16.4.1 High-Frequency Sound Waves in Glasses 470
16.4.2 Relaxation Processes in Liquids 474
16.4.3 The Non-Ergodicity Factor 477
16.5 Conclusions 480
References 480

Part IV Applications

17 Applications of XAFS to Nanostructures and Materials Science . . 485
Federico Boscherini
17.1 XAFS in Materials and Nanoscience 485
17.2 Dopants 486
17.2.1 Arsenic Dopants in Silicon Ultra-Shallow Junctions 486
17.2.2 Solar Grade Silicon 487
17.2.3 Silicon in Gallium Arsenide 489
17.3 Defect Complexes 490
17.4 Bulk and Heterostructure Semiconductor Alloys 491
17.5 Phase Transitions 492
17.6 Correlated Oxides 494
17.7 Thin Films 495
17.8 Semiconductor Dots 496
17.9 Metallic Clusters 497
References 497

18 Diffraction from Nanocrystalline Materials 499
Paolo Scardi and Luca Gelisio
18.1 Introduction 499
18.2 From Single Crystal to Powder Diffraction 501
18.3 Powder Diffraction Line Profiles 503
18.4 Atomistic Modeling of Powder Diffraction from Nanocrystals 511
18.5 Conclusions 516
References 517

19 High-Energy Resolution Core Level Photoelectron Spectroscopy and Diffraction: Powerful Tools to Probe Physical and Chemical Properties of Solid Surfaces 519
Alessandro Baraldi
19.1 Introduction 519
19.2 Single-Element Clean Metal Surfaces 521
19.2.1 Surface Core Level Shifts 521
19.2.2 Surface Reconstruction 523
19.2.3 From Surface Structure to Chemical Identity 525
19.3 Atoms and Molecules on Solid Surfaces 526
19.3.1 Adsorption and Co-Adsorption: The Adsorbate Core-Levels 526
19.3.2 Adsorption on Stepped Surfaces 529
19.3.3 Vibrational Excitations in Chemisorbed Molecules . . . 530
19.3.4 Adsorbate-Induced Surface Core Level Shifts 531

19.4 New Opportunities for Core Level Photoelectron Spectroscopy from Epitaxial Graphene 534
References 537

20 Spin Polarization of the Photoelectrons and Photon Polarization of X-Ray Absorption: Spectroscopy and Magnetometry 539
Giorgio Rossi
20.1 Introduction 539
20.2 Definition and Measure of the Spin Polarization of the Photoelectrons 541
20.2.1 Detecting the Electron Spin 542
20.2.2 LS Mott Scattering 543
20.2.3 Exchange Scattering 546
20.3 Towards the Complete Electron Spectroscopy 547
20.3.1 Spin Polarized ARPES 547
20.3.2 Spin Polarization of the Quantum Yield 548
20.3.3 Matrix Element Effects 550
20.3.4 Core Levels 550
20.3.5 Band States 553
20.4 Symmetry Breaking Mechanisms 556
20.5 Time Resolved Experiments and High Excitation Density 559
20.6 X-Ray Absorption Dichroism 559
20.6.1 The XMCD as Diagnostic of Magnetization 562
20.6.2 The XMCD as a Magnetometer 564
20.6.3 The XLD 567
20.6.4 The X-Ray Measurement of Ferromagnetic Resonance 568
20.7 Conclusions 569
References 569

21 Chemical and Magnetic Imaging with X-Ray Photoemission Electron Microscopy 571
Andrea Locatelli and Tevfik Onur Menteş
21.1 Introduction 571
21.2 Photoemission Electron Microscopy 572
21.2.1 Instrumental Aspects 573
21.2.2 Combination with Low Energy Electron Microscopy 575
21.2.3 PEEM Methods 576
21.3 Applications and Examples 578
21.3.1 Chemical Imaging of Nano-Structured Surfaces and Interfaces 578
21.3.2 Graphene 580

21.3.3 Biominerals . . . 581
21.3.4 Magnetic Imaging . . . 584
21.4 Conclusions and Outlook . . . 587
References . . . 588

22 Medical Imaging with Synchrotron Radiation . . . 593
Giuliana Tromba
22.1 Introduction . . . 593
22.2 Advantages of Synchrotron Radiation for Medical Imaging . . . 594
22.3 Current Research Status at SR Beamlines . . . 595
22.3.1 Angiography . . . 595
22.3.2 Microangiography . . . 596
22.3.3 Bronchography . . . 597
22.3.4 Breast Imaging . . . 597
22.3.5 Imaging of Cartilages . . . 601
22.3.6 Lungs Imaging . . . 603
22.3.7 Microvascularization and Imaging of Soft Tissues . . . 606
22.3.8 Brain Imaging . . . 608
22.4 Conclusions . . . 609
References . . . 611

23 Synchrotron Radiation and Bio-crystallography . . . 615
Marco Nardini and Martino Bolognesi
23.1 Macromolecular Crystals . . . 615
23.1.1 Physical and Chemical Properties . . . 616
23.1.2 Crystal Growth . . . 616
23.1.3 Crystal Handling and Radiation Damage . . . 618
23.2 X-Ray Diffraction and Phasing Problem . . . 620
23.2.1 Fundamentals of Crystallography . . . 620
23.2.2 Solution of the Phase Problem . . . 623
23.2.3 The MIR Method . . . 624
23.2.4 The SIRAS Method . . . 626
23.2.5 The MAD Method . . . 628
23.2.6 The Molecular Replacement Method . . . 629
23.3 Density Modification . . . 631
23.4 Crystallographic Refinement . . . 632
23.4.1 Least Squares Refinement . . . 632
23.4.2 Maximum-Likelihood Refinement . . . 634
23.4.3 Quality of the Model . . . 636
23.5 The Protein Data Bank . . . 637
23.6 Structural Genomics . . . 638
References . . . 639

24 Synchrotron Radiation in the Earth Sciences 641
Simona Quartieri
24.1 Introduction 641
24.2 X-Ray Diffraction 644
24.2.1 X-Ray Powder Diffraction 644
24.2.2 Single-Crystal X-Ray Diffraction 644
24.3 X-Ray Absorption Spectroscopy 646
24.4 X-Ray Fluorescence Microanalysis 648
24.5 Materials Under Extreme Conditions 649
24.5.1 Single-Crystal and Powder X-Ray Diffraction 653
24.5.2 Single-Crystal and Powder IR Spectroscopy 653
24.5.3 X-Ray Absorption Spectroscopy 654
24.5.4 HP Synchrotron Mössbauer 655
24.6 X-Ray Tomography and Topography 655
24.7 Future Prospects 656
References 656

25 Synchrotron Radiation and Environmental Sciences 661
Giovanni De Giudici, Piero Lattanzi and Daniela Medas
25.1 Introduction: What Is Environmental Science? 661
25.2 Overview of the Most Common Techniques 663
25.2.1 Synchrotron-Based X-Ray Diffraction 664
25.2.2 X-Ray Absorption Spectroscopy 664
25.2.3 Microbeam Techniques 666
25.2.4 Surface Techniques 669
25.3 Case History: Zinc Biomineralization at Naracauli, Sardinia 671
25.4 Concluding Remarks 673
References 674

26 Synchrotron Radiation in Art, Archaelogy and Cultural Heritage 677
Simona Quartieri
26.1 Introduction 677
26.2 Examples of SR-X-Ray Diffraction Studies of Cultural Heritage 678
26.3 Archaeometric Applications of X-Ray Absorption Spectroscopy 682
26.4 SR-Based FT-Infrared Micro-Spectroscopy Applied to Cultural Heritage 688
26.5 SR-Based Techniques for Non-Destructive Sub-surface Analysis of Painted Cultural Heritage Artifacts 688
26.6 X-Ray Computed Tomography in Cultural Heritage Studies 689

26.7 Application of SR-Based Techniques to the Study of Paleontological Findings . . . 691
26.8 Recent and Future Trends . . . 693
References . . . 693

27 Synchrotron Radiation and Chemistry: Studies of Materials for Renewable Energy Sources . . . 697
Antonino Martorana, Francesco Giannici and Alessandro Longo
27.1 Introduction . . . 697
27.2 Metal-Organic Frameworks . . . 699
27.3 Hydrides for Hydrogen Storage . . . 701
27.4 Dye-Sensitized Solar Cells . . . 704
27.5 Oxide-Ion and Proton Conductors . . . 706
27.6 Electrodes for Fuel Cells . . . 710
27.7 Conclusions . . . 713
References . . . 713

28 Catalyst Characterization by XAS and XES Spectroscopies: In Situ and Operando Experiments . . . 717
Francesca Bonino, Elena Groppo, Carmelo Prestipino, Giovanni Agostini, Andrea Piovano, Diego Gianolio, Lorenzo Mino, Erik Gallo and Carlo Lamberti
28.1 Introduction . . . 718
28.2 Methods and Instrumentation . . . 719
28.3 Understanding the Structure of the Ti Active Site in TS-1 Catalyst: A XAS/XES Study . . . 721
28.4 Understanding the Chemistry of the Oxychlorination Catalysis by In Situ and Operando Experiments . . . 727
28.5 Conclusions and Perspectives . . . 731
References . . . 733

29 Studies of Matter at Extreme Conditions . . . 737
Sakura Pascarelli
29.1 High Pressure Research . . . 737
29.1.1 Introduction . . . 738
29.1.2 Matter Under "Extreme Conditions" . . . 738
29.1.3 High Pressure to Study Earth's Interior, Understand Climate Change, Explore New Sources of Energy . . . 739
29.1.4 Tools and Experimental Methods . . . 741
29.2 Physics . . . 744
29.2.1 Collapse of Ferromagnetism in the 3d Metals . . . 744
29.2.2 Examples of Recent Work on Fe, Co and Ni . . . 746

29.3 Earth Science . . . 750
29.3.1 Fe Partitioning in the Earth Mantle . . . 750
29.3.2 Fe Partitioning at and Beyond the Core-Mantle Boundary . . . 753
29.4 Energy, Environment, Climate . . . 755
29.4.1 The Deep Carbon Cycle . . . 755
29.4.2 Stability of Hydrocarbons in the Deep Earth . . . 756
29.4.3 Exploring the Nature of C-bearing Minerals . . . 757
References . . . 759

30 Science Frontiers with X-Ray Free Electron Laser Sources . . . 761
Flavio Capotondi, Martina Dell'Angela, Marco Malvestuto and Fulvio Parmigiani
30.1 Introduction . . . 762
30.2 Coherent Free Electron Laser Sources . . . 763
30.3 Coherent Diffraction Imaging with Free Electron Lasers . . . 765
30.4 Spectroscopy on Solids at FELs . . . 768
30.4.1 Photoelectron Spectroscopy . . . 770
30.4.2 X-Ray Absorption Spectroscopy . . . 773
30.4.3 Resonant X-Ray Emission Spectroscopy . . . 774
30.5 Magneto-Dynamical Studies . . . 778
30.5.1 Ultra Fast X-Ray Experiments . . . 781
30.5.2 Ferromagnetism and Superconductivity: A Background Starting Point . . . 782
30.5.3 Physics of FM/SC Heterostructures . . . 783
30.5.4 New and Promising Fields of Research and Innovation . . . 783
References . . . 784

Index . . . 787

Contributors

Giovanni Agostini Department of Chemistry, NIS Centre of Excellence and INSTM Reference Center, University of Turin, Torino, Italy; European Synchrotron Radiation Facility (ESRF), Grenoble, France

Giuliana Aquilanti Elettra-Sincrotrone Trieste S.C.p.A, Basovizza, Trieste, Italy

Gilberto Artioli Dipartimento di Geoscienze, Università degli Studi di Padova, Padova, Italy

Antonella Balerna Laboratori Nazionali di Frascati, INFN, Frascati, RM, Italy

Alessandro Baraldi Physics Department, University of Trieste, Trieste, Italy; Surface Science Laboratory, Elettra-Sincrotrone Trieste, Trieste, Italy; Laboratorio TASC, IOM-CNR, Trieste, Italy

José Baruchel European Synchrotron Radiation Facility, Grenoble Cedex, France

Maurizio Benfatto Laboratori Nazionali di Frascati, INFN, Frascati, Italy

Carlo Maria Bertoni Dipartimento di Scienze Fisiche, Informatiche e Matematiche, University of Modena and Reggio Emilia, and CNR-Istituto Nanoscienze S3, and CNISM, Modena, Italy

Martino Bolognesi Department of Biosciences, University of Milano, Milan, Italy

Francesca Bonino Department of Chemistry, NIS Centre of Excellence and INSTM Reference Center, University of Turin, Torino, Italy

Federico Boscherini Department of Physics and Astronomy, University of Bologna, Bologna, Italy

Jean-Yves Buffiere INSA Lyon, Villeurbanne, France

Flavio Capotondi Elettra-Sincrotrone Trieste S.C.p.A., Basovizza, Trieste, Italy

Giovanni De Giudici Department of Chemical and Geological Science, University of Cagliari, Cagliari, Italy

Martina Dell'Angela Elettra-Sincrotrone Trieste S.C.p.A., Basovizza, Trieste, Italy

Diane Eichert Elettra-Sincrotrone Trieste S.C.p.A., Basovizza, TS, Italy

Paolo Fornasini Department of Physics, University of Trento, Trento, Italy

Erik Gallo European Synchrotron Radiation Facility (ESRF), Grenoble, France

Luca Gelisio Department of Civil, Environmental and Mechanical Engineering, University of Trento, Trento, Italy

Francesco Giannici Dipartimento di Fisica e Chimica, Università di Palermo, Palermo, Italy

Diego Gianolio Diamond Light Source Ltd, Harwell Science and Innovation Campus, Didcot, UK

Andrea Goldoni Elettra-Sincrotrone Trieste S.C.p.A, Basovizza, Trieste, Italy

Elena Groppo Department of Chemistry, NIS Centre of Excellence and INSTM Reference Center, University of Turin, Torino, Italy

Carlo Lamberti Department of Chemistry, CrisDi Interdepartmental Centre for Crystallography and INSTM Reference Center, University of Turin, Torino, Italy; Southern Federal University, Rostov-on-Don, Russia

Piero Lattanzi Department of Chemical and Geological Science, University of Cagliari, Cagliari, Italy

Andrea Locatelli Elettra-Sincrotrone Trieste S.C.p.A., Basovizza, Trieste, Italy

Alessandro Longo ISMN-CNR, Palermo, Italy

Stefano Lupi INFN and Department of Physics, Sapienza University of Rome, Rome, Italy

Marco Malvestuto Elettra-Sincrotrone Trieste S.C.p.A., Basovizza, Trieste, Italy

Giorgio Margaritondo Faculté des Sciences de Base, Ecole Polytechnique Fédérale de Lausanne (EPFL), Lausanne, Switzerland

Carlo Mariani Dipartimento di Fisica, CNISM, Università di Roma "La Sapienza", Roma, Italy

Antonino Martorana Dipartimento di Fisica e Chimica, Università di Palermo, Palermo, Italy

Daniela Medas Department of Chemical and Geological Science, University of Cagliari, Cagliari, Italy

Carlo Meneghini Dipartimento di Scienze, Università Roma Tre, Roma, Italy

Tevfik Onur Menteş Elettra-Sincrotrone Trieste S.C.p.A., Basovizza, Trieste, Italy

Lorenzo Mino Department of Chemistry, NIS Centre of Excellence and INSTM Reference Center, University of Turin, Torino, Italy

Settimio Mobilio Dipartimento di Scienze, Universita' Roma Tre, Roma, Italy

Giulio Monaco Dipartimento di Fisica, Universitá di Trento, Povo, TN, Italy

Marco Nardini Department of Biosciences, University of Milano, Milan, Italy

Luigi Paolasini European Synchrotron Radiation Facility, Grenoble Cedex, France

Fulvio Parmigiani Elettra-Sincrotrone Trieste S.C.p.A., Basovizza, Trieste, Italy; Department of Physics, University of Trieste, Trieste, Italy

Sakura Pascarelli European Synchrotron Radiation Facility, Grenoble Cedex, France

Andrea Perucchi Elettra Sincrotrone Trieste, Basovizza, TS, Italy

Andrea Piovano Institut Laue-Langevin (ILL), Grenoble Cedex, France

Jasper Rikkert Plaisier Elettra-Sincrotrone Trieste S.C.p.A, Basovizza, Trieste, Italy

Stefano Polizzi Dipartimento di Scienze Molecolari e Nanosistemi, Università Ca' Foscari, Venezia, Italy

Carmelo Prestipino Institut des Sciences Chimiques de Rennes, Université de Rennes 1, Rennes Cedex, France

Simona Quartieri Dipartimento di Fisica e di Scienze della Terra, Università di Messina, Messina, Italy

Giorgio Rossi Dipartimento di Fisica dell'Università degli studi di Milano, Milan, Italy; Advanced Photoelectric-Effect Experiments (APE) and Nano Foundries and Fine Analysis (NFFA) collaborations, Istituto Officina dei Materiali-CNR, Basovizza, TS, Italy

Paolo Scardi Department of Civil, Environmental and Mechanical Engineering, University of Trento, Trento, Italy

Francesco Spinozzi Dipartimento di Scienze della Vita e dell'Ambiente, Università Politecnica delle Marche, Ancona, Italy

Giovanni Stefani Dipartimento di Scienze, Università Roma Tre and CNISM Unità Roma 3, Roma, Italy

Giuliana Tromba Elettra-Sincrotrone Trieste S.C.p.A., Basovizza, Trieste, Italy

Lisa Vaccari Elettra-Sincrotrone Trieste S.C.p.A, Basovizza, Trieste, Italy

Davide Viterbo Torino, Italy

Giuseppe Zanotti Dipartimento di Scienze Biomediche, Università di Padova, Padova, Italy

Part I
Basics of Synchrotron Radiation

Chapter 1
Introduction to Synchrotron Radiation

Antonella Balerna and Settimio Mobilio

Abstract Relativistic charged particles forced to move along curved trajectories by applied magnetic fields emit electromagnetic radiation called Synchrotron Radiation; today electron storage rings are routinely used to provide synchrotron radiation to users in a wide spectral range from infrared to hard X-rays. Thanks to its peculiar characteristics, synchrotron radiation is one of the more powerful tools for investigating the properties of matter in many different fields like molecular and atomic physics, cell biology, medical applications, nanotechnology, catalysis and cultural heritage. Up to now three generations of synchrotron radiation sources emitting radiation with increasing quality have been developed; the fourth generation, based on free-electron lasers, already produces high power and ultrafast pulses of highly coherent radiation. In the present contribution, the main characteristics and properties of the synchrotron radiation sources and of the produced radiation are introduced and explained using a simple approach.

1.1 Introduction

When electrons or other charged particles moving at relativistic speeds are forced by magnetic fields to follow curved trajectories they emit electromagnetic radiation in the direction of their motion, known as synchrotron radiation. Synchrotron radiation is emitted, for example, by cosmic sources. The blue light visible in Fig. 1.1, that shows a mosaic image of the Crab Nebula, the remnant of a supernova explosion seen on earth by many astronomers in 1054, comes from high energy electrons whirling

A. Balerna (✉)
Laboratori Nazionali di Frascati, INFN, via E. Fermi 40, 00044 Frascati, RM, Italy
e-mail: balerna@lnf.infn.it

S. Mobilio
Dipartimento di Scienze, Universita' Roma Tre, via della Vasca Navale 84, 00146 Rome, Italy
e-mail: settimio.mobilio@uniroma3.it

S. Mobilio et al. (eds.), *Synchrotron Radiation*,
DOI: 10.1007/978-3-642-55315-8_1, © Springer-Verlag Berlin Heidelberg 2015

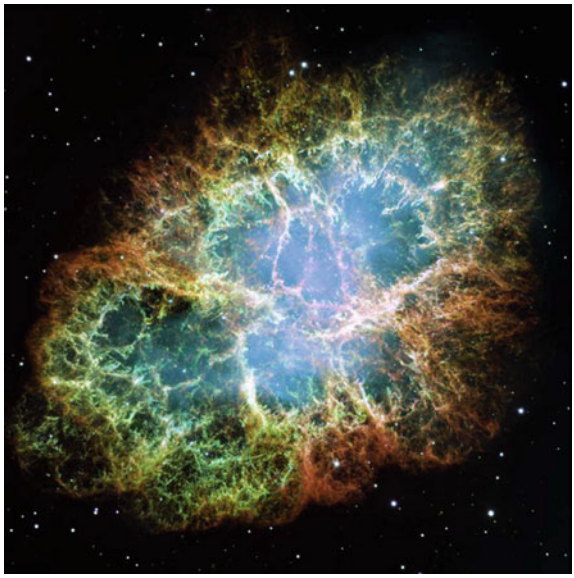


Fig. 1.1 NASA Hubble Space Telescope image of the Crab Nebula (*NASA, ESA and Allison Loll/Jeff Hester* (*Arizona State University*). *Acknowledgement*: *Davide De Martin* (*ESA/Hubble*))

around magnetic field lines due to the presence of a pulsar (pulsating radio source). In this lecture we present the properties and characteristics of the synchrotron radiation produced in particle accelerators by electrons or positrons; such radiation is extremely intense and extends over a broad energy range from the infrared through the visible and ultraviolet, into the soft and hard x-ray regions of the electromagnetic spectrum. It was observed for the first time in 1947 at the General Electric synchrotron in the USA; for a long time it was considered only as a problem for particle physics since represents the major source of energy loss in high energy particle accelerators. Only in the late sixties it was realized that synchrotron radiation was very useful for condensed matter research. Since then, there was an explosive growth in its use and dedicated synchrotron radiation facilities were built, making this radiation a unique tool in many research fields. Nowadays synchrotron radiation is being used to study many aspects of the structure of matter at the atomic and molecular scale, from surface properties of solids to the structure of protein molecules.

1.2 Storage Rings and Synchrotron Radiation Sources

Electrons traveling at a speed close to c, the speed of light, and forced to change the direction of their motion under the effect of magnetic fields (perpendicular to the direction of their motion), emit light, with peculiar characteristics, known as synchrotron radiation. The 'natural' man-made sources of this radiation [1] are high energy, electron or positron circular accelerators, like storage rings. They consist

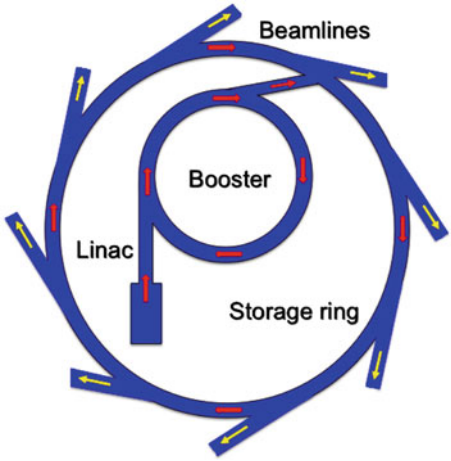


Fig. 1.2 Schematic planar view of a synchrotron radiation facility

of circular evacuated pipes where the electrons are forced to follow circular paths under the action of magnets placed along the circumference (bending magnets). The electrons enter the storage ring only after they have been accelerated by a linear accelerator or 'linac' until their energy reaches several millions of electron volts (MeV) and then by a booster ring that gives them a boost in energy from millions to billions or giga electron volts (GeV); at that point they are transferred to the final circular accelerator as shown in Fig. 1.2.

Here the electrons, if needed, may be further accelerated to higher energies by the radio frequency (RF) electric fields. When the electrons reach the expected energy they are in a quasi-stationary situation; forced to follow circular paths by the magnetic field of the bending magnets, they loose, during each turn, part of their energy, emitting synchrotron radiation. The energy lost in this way is fully regained in passing through the RF cavities. More precisely, storage rings consist of an array of magnets for focusing and bending the beam, connected by straight linear sections (see Fig. 1.3). In one or more of these linear sections, RF cavities are installed in order to accelerate the particles.

After its discovery in 1947, during the 1960s and early 70s pioneering use of the light was made in the so called *first generation synchrotron radiation facilities*; these machines were not dedicated to synchrotron radiation studies, but were used in a parasitic way, during high energy physics experiments. In the mid-70s facilities totally dedicated to synchrotron light, were built. These early-dedicated facilities, in which synchrotron light was mainly produced by bending magnets, are called *second generation sources*; also the use of high magnetic field devices, known as wigglers, started in this period. Afterwards, the optimization of magnetic structures, like wigglers and undulators, placed in straight sections made possible the realization of new synchrotron radiation sources the so called *third generation sources* like the European Synchrotron Radiation Facility (E.S.R.F. Grenoble France) and many other [2].

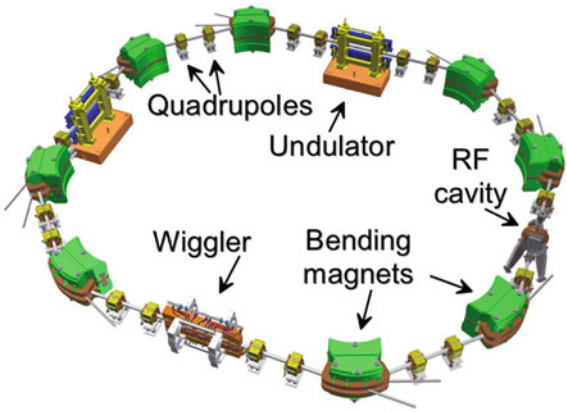


Fig. 1.3 Schematic view of a storage ring where some main elements like bending magnets, focusing and de-focusing magnets (quadrupoles), insertion devices (undulator, wigglers) and the RF (radio frequency) cavity are visible; the injection system is not shown (*courtesy of S. Tomassini INFN-LNF*)

Due to the advanced designs and beam control of third generation light sources, source size and divergence have been greatly improved. Nowadays for many experiments, like the ones involving imaging or microscopy, the beam has to be focused down to very small spots and so a relevant synchrotron radiation property becomes its spectral brightness[1] or flux per unit source area and per unit solid angle [3].

Undulators are excellent sources of high brightness radiation. This is shown in Fig. 1.4, where the gain in brightness achieved by the new synchrotron radiation sources, as a function of time, is shown; its increase of many orders of magnitude gives an idea of the spectacular progress obtained in beam quality by *third generation sources*.

While improvements in third generation synchrotron radiation sources are still possible, *fourth generation sources* are being developed, based on free electron lasers (FELs) able to produce very short coherent light pulses of very high peak intensity and brightness (FEL sources characteristics and applications are described in Chaps. 2 and 30).

[1] Brightness or brilliance? Several authors give different definitions while other authors use both terms to define the same quantity. The best thing to do, is to look to units to be sure of what you are dealing with. In any case in this lecture we will use the conclusions of [3] and define the spectral brightness as photons per second, per unit source size and divergence in a given bandwidth.

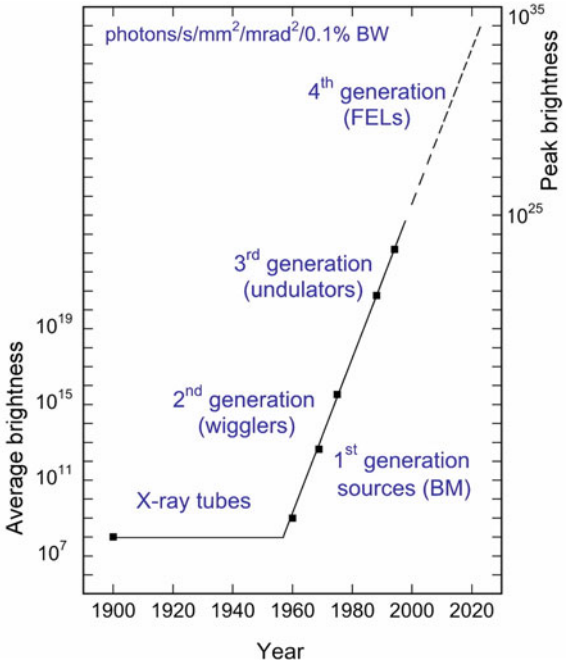


Fig. 1.4 Comparison between the average brightness of storage rings of different generations. As a comparison also the average brightness of x-ray tubes and of X-ray FELs (Free Electron Lasers) are reported (the figure was redrawn: it is based on data of Figs. 1.1 and 1.2 of [4])

Comparison of the brightness of different radiation sources at a given wavelength.

- 60 W light bulb

$$Brightness = 10^6 \frac{Photons}{\mathrm{s} \cdot \mathrm{mm}^2 \cdot \mathrm{mr}^2 \cdot (0.1\,\%\,\mathrm{BW})}$$

- Sun

$$Brightness = 10^{10} \frac{Photons}{\mathrm{s} \cdot \mathrm{mm}^2 \cdot \mathrm{mr}^2 \cdot (0.1\,\%\,\mathrm{BW})}$$

- Third generation synchrotron radiation source: bending magnet

$$Brightness = 10^{16} \frac{Photons}{\mathrm{s} \cdot \mathrm{mm}^2 \cdot \mathrm{mr}^2 \cdot (0.1\,\%\,\mathrm{BW})}$$

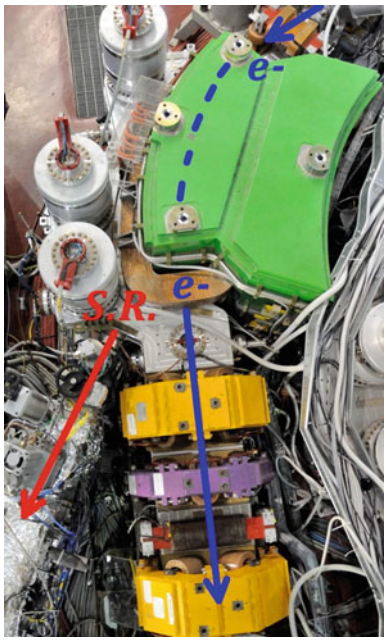


Fig. 1.5 One of the bending magnets of the INFN-LNF DAΦFNE storage ring and the initial part of a beamline collecting synchrotron radiation (*courtesy of V. Tullio*)

1.3 Synchrotron Radiation Properties

The main properties of the synchrotron radiation are the following

1. high intensity;
2. very broad and continuous spectral range from infrared up to the hard x-ray region;
3. natural narrow angular collimation;
4. high degree of polarization;
5. pulsed time structure;
6. high brightness of the source due to small cross section of the electron beam (see Fig. 1.4) and high degree of collimation of the radiation;
7. ultra-high vacuum environment and high beam stability;
8. all properties quantitatively evaluable.

All these properties depend on the characteristics of the storage ring and can be calculated by applying classical electrodynamics to the motion of relativistic charged particles. Some details on these important properties will be now introduced starting from the radiation emitted by bending magnets (BM) known as 'dipole radiation'. (see Fig. 1.5). In Chap. 2 these properties will be explained in more detail, in particular it will be shown that they have a relativistic origin.

1.4 Radiated Power and Time Structure

Accelerated charged particles emit electromagnetic radiation. In a storage ring, bending magnets keep electrons moving in a closed trajectory applying a magnetic field of fractions or few Tesla perpendicular to their velocity [5]. The acceleration of such particles is given by the Lorentz equation:

$$\frac{d\mathbf{p}}{dt} = e\left(\mathbf{E} + \frac{\mathbf{v} \times \mathbf{B}}{c}\right)$$

where **p**, e and **v** are respectively the particle momentum, charge and velocity and **E** and **B** are the electric and magnetic fields.

The power radiated [1] by a relativistic electron forced to move along a circular orbit, with a radius of curvature, R, is given by the Schwinger's formula [5]:

$$P_e = \int\int P(\lambda, \psi) d\lambda d\psi = \frac{2}{3}\frac{e^2 c}{R^2}\left[\frac{E}{mc^2}\right]^4 \tag{1.1}$$

where λ is the wavelength of the emitted radiation, ψ is the azimuthal or vertical half-opening angle perpendicular to the orbital plane. $P(\lambda, \psi)$, the power radiated by an electron in a unit wavelength interval centered at λ and in a unit vertical angular aperture centered at ψ. E is the electron energy, m its mass, c is the speed of light and mc^2 is the electron rest mass energy (0.511 MeV). In (1.1), the dependence of the radiated power on E^4 must be noted; this implies that, to keep the radiated power at reasonable values, in order to increase the energy of the storage rings, it is necessary to increase also their radius. In the same equation it must be noted that, due to the dependence on m^{-4}, the radiation produced by proton accelerators is negligible.

The energy lost per turn by the charged particle, taking into account a revolution time, $2\pi R/c$, is given by:

$$\Delta E_e = \frac{4\pi}{3}\frac{e^2}{R}\left[\frac{E}{mc^2}\right]^4$$

In order to replenish the energy lost with the emission of radiation and keep the electrons at a constant energy, radio frequency (RF) cavities are used. In a RF cavity a longitudinal electric field accelerate the electrons. The RF fields have an accelerating effect only during one half of their period and a decelerating action during the other half; so the RF is effective in restoring the electron energy only for one half of the time. Additional considerations have to be performed, regarding the stability of the electron orbit. Let us suppose that at the time t_0 an electron passing through the RF finds exactly the electric field he needs to fully restore the energy lost during a turn. We will call this electron a "synchronous" electron (Fig. 1.6).

Synchronous electrons continue their motion along the ring returning in the RF again in time to regain the exact amount of energy lost along the circular path. So

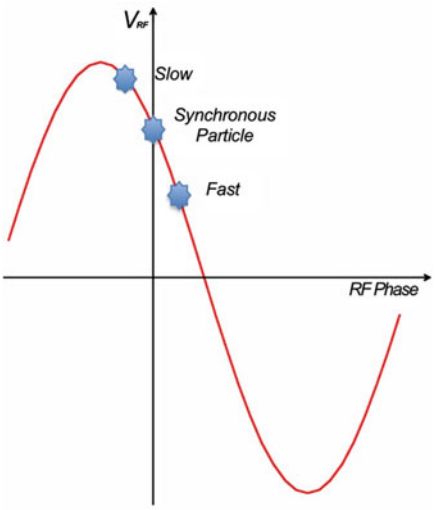


Fig. 1.6 Sinusoidal time dependence of the RF cavity voltage that effects energy restoration

the synchronous electrons are in a stable condition. Let us now consider electrons arriving in the RF a little bit later than the synchronous electrons. They are slower than the first ones, i.e. they have a lower energy. In order to restore the energy, they have to find an electric field higher than that found by the synchronous electrons otherwise they will continue to lose energy with respect to them. In the next turn they will arrive later, and after some turns they will enter the RF during the decelerating semi-period and will be lost. Vice versa electrons arriving before the synchronous ones must find a lower electric field, otherwise their energy will increase with respect to the synchronous electrons. These considerations show that only one half of the accelerating semi-period (i.e. one fourth of the period) is effective in maintaining the electrons on the orbit (Fig. 1.6).

The stability condition is effectively more strict, and only 5–10 % of the RF period is effective in restoring the electron energy. All the electrons, passing through the RF, not in phase with this 5–10 % effective time, do not follow the ideal circular orbit of the ring and therefore are lost. As a consequence the electrons in the storage ring are grouped in bunches with time lengths that are typically 5–10 % of the RF period. Also the radiation appears in pulses with the same time duration and separation (Fig. 1.7).

Along the storage ring many bunches can be distributed. The time interval between them is an integer multiple of the RF period (called harmonic number of the ring). The maximum separation between two pulses is obtained in the single bunch mode, i.e. when only one bunch in the full ring is present. In this case the time interval is equal to the period of revolution, typically of the order of microseconds. When more bunches are present the time interval is lower; the minimum possible time interval between bunches is equal to the RF period. The filling of bunches in a machine is a parameter that can be completely controlled; it is possible to choose how many and which bunches have in the ring. This flexibility is often used to relate to the photon

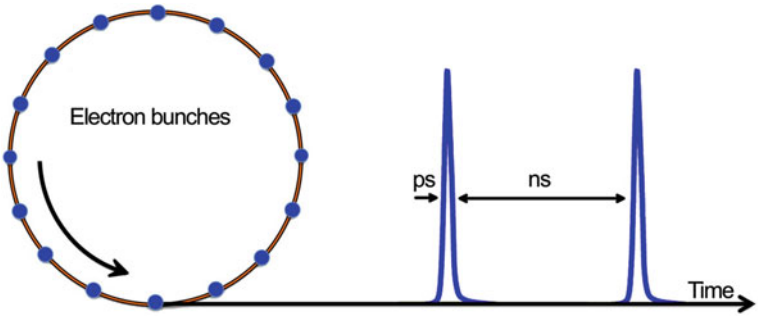


Fig. 1.7 Electron bunches moving in the storage ring produce radiation peaks having the same bunch length (ps) and separation (ns)

source different time dependence characteristics. The total current depends on the number of filled bunches. The current is lower when few bunches are filled, because the total amount of current that can be stored in a single bunch is limited.

Application to a third generation electron storage ring like the European Synchrotron Radiation Facillity (*ESRF, Grenoble -FR*).

- The energy of the electrons at ESRF is E = 6 GeV, it has a circumference (C) of 844 m, the frequency of the RF cavity is ν_{RF} = 355 MHz (8 MV RF accelerating voltage) and I_{max} = 200 mA is the maximum current.
- Single bunch mode: I = 20 mA

$$T_0 = \mathrm{C/c} = 2.81\,\mu\mathrm{s}$$

where T_0 represents the maximum time separation between bunches achievable only in single bunch mode.

- Uniform bunch mode: $I_{max} = 200\,\text{mA}$

$$T_{RF} = 1/\nu_{RF} = 2.82\,\text{ns}$$

where T_{RF} represents the minimum time separation between bunches achievable only in uniform bunch mode (corresponding to a separation of about 86 cm between them). The maximum number of bunches that can be stored depends on ν_{RF} and on $\nu_0 = (1/T_0)$:

$$N_{max} = \nu_{RF}/\nu_0 = 992.$$

The bunch lengths are normally of the order of *mm* corresponding to tens of *picoseconds*. At ESRF in uniform bunch mode the bunch length is of the order of 20 ps while in single bunch mode it is of the order of 73 ps.

1.5 Angular, Spectral and Intensity Distribution

In order to understand the angular and spectral distribution of the emitted radiation let us first remind the emission from a classical electron moving at a speed, v, much lower than the speed of light, c ($v \ll c$)(see Fig. 1.8).

In this case the emitted pattern is similar to that of an oscillating dipole with its maximum of intensity in the direction perpendicular to the acceleration and does not depend on the electron speed.

For a relativistic effect, when the speed of the emitting electrons increases to relativistic values ($v \approx c$) the radiation pattern is compressed into a narrow cone in the direction of motion, resulting into an emission tangential to the particle orbit. The vertical half-opening angle, ψ, is given by:

$$\psi \approx mc^2/E \approx \gamma^{-1}.$$

For electrons and positrons, in practical units:

$$\gamma = 1957E(\text{GeV})$$

so for a storage ring of energy $E = 1\,\text{GeV}$ it follows that $\psi \approx 0.5$ mrad $\approx 0.029°$: synchrotron radiation is highly collimated. This characteristic provides extremely high fluxes on very small areas also at distances of tens of meters from the storage ring.

In a bending magnet the horizontal collimation is lost because the electrons move along a circular orbit emitting the radiation along the tangent. The radiation is

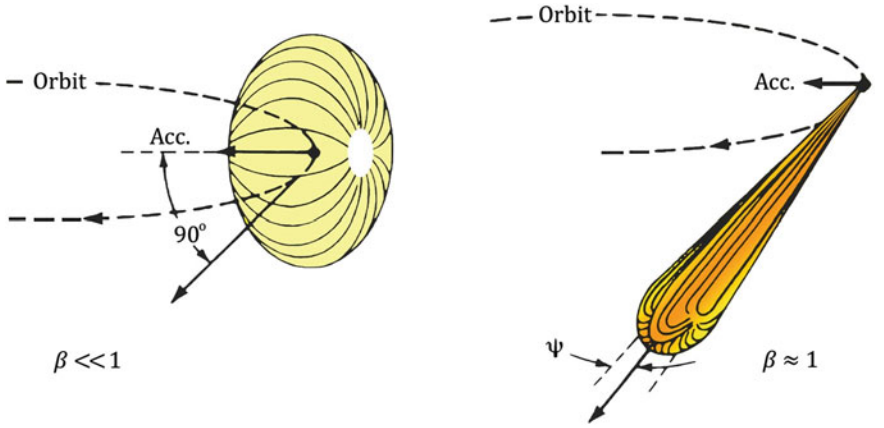


Fig. 1.8 Qualitative radiation patterns related to charged particles moving in a circular orbit. The dipole pattern achieved for slow particles (*left*) ($\beta = v/c << 1$) is distorted into a narrow cone when $\beta \approx 1$ (*right*) (the figure was redrawn: it is based on Fig. 1.1 of [6])

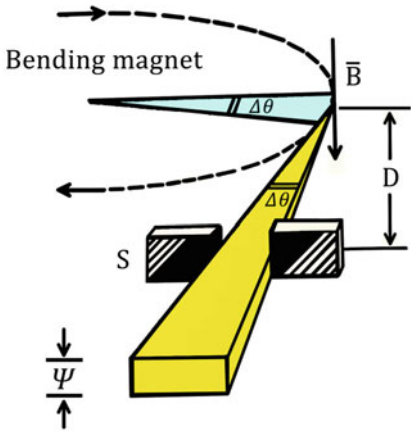


Fig. 1.9 Synchrotron radiation emitted by a relativistic electron travelling along a curved trajectory. The magnetic field is perpendicular to the electron orbit plane, Ψ is twice the natural opening angle in the vertical plane while $\Delta\theta$ is horizontal angular distribution, normally much bigger than Ψ limited in the figure by the horizontal slits, S

collected, for experiments, through a horizontal slit (S) of width, w, at a distance, D, from the electron orbit (see Fig. 1.9); this corresponds to an angular collection angle, $\Delta\theta = w/D >> \psi$.

It means that all the radiation emitted along an orbital arc, $\Delta\theta$, is collected and summed incoherently. For this reason the natural narrow collimation, ψ, is preserved only in the vertical direction, the direction perpendicular to the plane of the orbit as shown in Fig. 1.9. We anticipate here that using undulators as insertion devices the collimation can be kept in both directions.

The spectral distribution of the BM synchrotron radiation flux, is a continuous function, that extends from the x-ray to the infrared region (see Fig. 1.10) and is characterized by a critical wavelength, λ_c, given by:

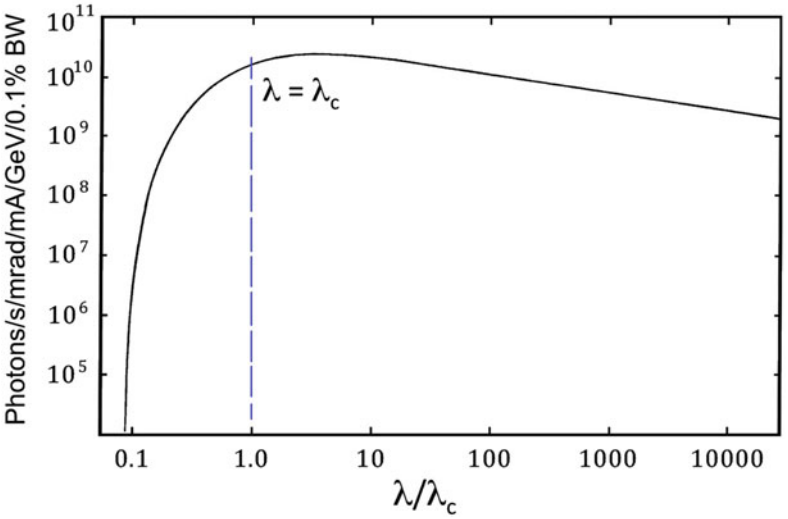


Fig. 1.10 Universal curve function of the spectral distribution of BM synchrotron radiation drawn as a function of λ_c/λ

$$\lambda_c = (4/3)\pi R\gamma^{-3} \text{ or in practical units } \lambda_c(\text{Å}) = 5.59\text{R(m)}\,\text{E}^{-3}\ \text{(GeV)}.$$

that depends only on the machine parameters γ and R. The critical wavelength, λ_c, represented by the discontinuous line in Fig. 1.10), divides the spectrum into two parts of equal radiated power: 50 % of the total power is radiated at wavelengths shorter than λ_c and 50 % at wavelengths longer than λ_c.

The physical origin of such broad distribution can be qualitatively understood. Let us consider to have a single electron moving in the storage ring and to record the emitted radiation using a point detector which looks tangentially at a specific point of the orbit (see Fig. 1.11). The detector will receive a short pulse of radiation every time the electron passes through that point of the orbit, i.e. at a frequency equal to the frequency of the period of motion $\omega = v/2\pi R$.

In the frequency domain the spectral distribution will be composed of the fundamental frequency and of its harmonics. At high frequency a cutoff will be present because the detector will receive the radiation emitted by the electron along the arc $2/\gamma$ and this originates a pulse of non zero duration, $\Delta\tau$, given by the difference between the time for the electron to travel along the arc and the time for the light to travel along the chord subtended by this arc (see Fig. 1.11):

$$\Delta\tau = \frac{R}{c}\left[\frac{1}{\gamma\beta} - 2sin\left(\frac{1}{2\gamma}\right)\right] \simeq \frac{R}{c\gamma^3}.$$

A light pulse of this duration has frequency components up to about:

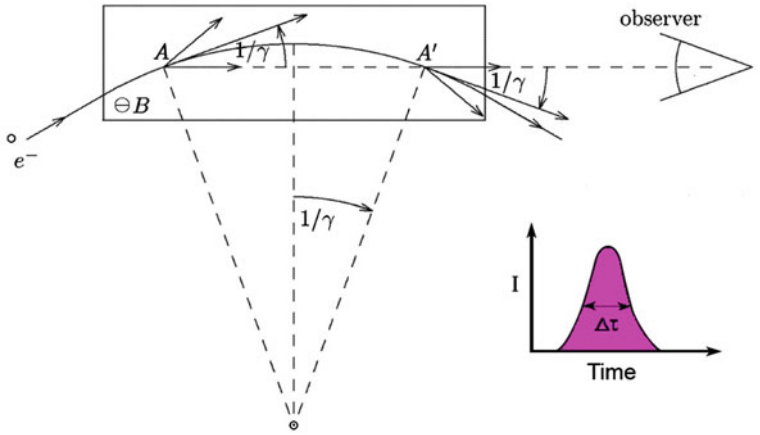


Fig. 1.11 Graphical view of the origin of the duration of the light pulse emitted by a bending magnet. The detector records the radiation emitted by the electron along the path from A to B (the figure was redrawn: it is based on Fig. II.2 of [7])

$$\omega_{cutoff} \approx \Delta\tau^{-1} = \mathrm{c}\gamma^3/\mathrm{R}$$

corresponding to a cutoff wavelength, $\lambda_{cutoff} = 2\pi R/\gamma^3 = 3/2\lambda_c$. Therefore, in principle, synchrotron radiation from one electron consists of a discrete spectrum of closely spaced lines up to ω_{cutoff}.

In practice, the spectral distribution coming from many electrons is continuous due to the statistical oscillations of the electrons around the main orbit, to the fluctuations in their kinetic energy and to the statistical nature of the emission itself: all effects that lead to a line broadening of each harmonic. This results in the continuous broad spectrum with the cutoff at $\lambda < \lambda_c$.

Quantitatively, the number of photons, $N(\lambda)$, emitted by a single electron in all the vertical angles, in a wavelength band of width $\Delta\lambda/\lambda$ centered at λ, while moving along an arc of length $\mathrm{R}\Delta\theta$ is given by:

$$N(\lambda) = \frac{3^{1/2}}{2\pi}\frac{e^2}{hR}\gamma\, G_1\frac{\Delta\lambda}{\lambda}\Delta\theta \tag{1.2}$$

where all quantities are expressed in CGS units. G_1, known as the *universal synchrotron radiation function* is the function plotted in Fig. 1.10.

In order to calculate the emission from a storage ring, it is necessary to multiply (1.2) by N_e the number of electrons in the storage ring given by:

$$N_e = I\,(2\pi R)/ec$$

where I is the electron current. This gives for $N\,(\lambda)$ the following equation:

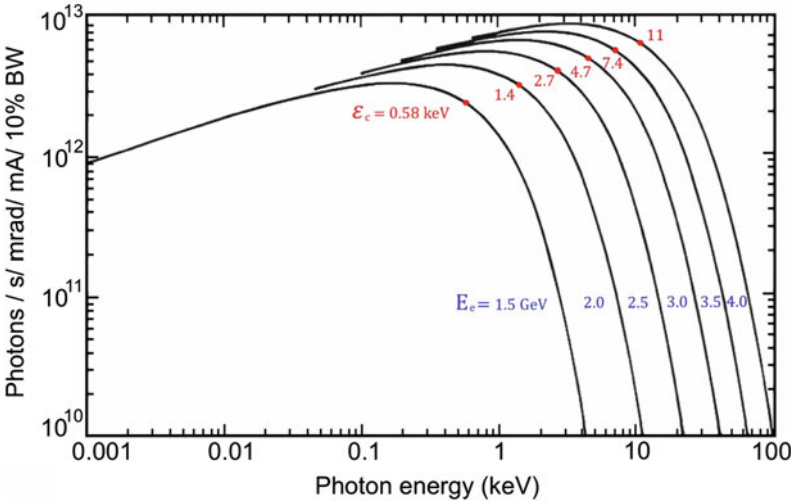


Fig. 1.12 Spectral distribution of synchrotron radiation as a function of the value of critical energy, ε_c, of the storage ring

$$N(\lambda) = 3^{1/2} \frac{e}{hc} \gamma I G_1 \frac{\Delta\lambda}{\lambda} \Delta\theta$$

that in practical units [8], assuming $\Delta\lambda/\lambda = 10^{-3}$ and $\Delta\theta = 1$ mrad can be written as:

$$N(\lambda) = 2.457 \times 10^{13} E[GeV] I[A] G_1 \left[\frac{photons}{\mathrm{s} \cdot 0.1\,\% \,\mathrm{BW} \cdot mrad\,\theta} \right]. \qquad (1.3)$$

The spectral distribution of the emitted photons, given by (1.3), is that shown in Fig. 1.10. For $\lambda \ll \lambda_c$ the spectral distribution falls off exponentially while for $\lambda \gg \lambda_c$ it decreases slowly, it is practically independent of the energy of the electrons and it is mainly determined by the current of the machine.

The photon flux is frequently expressed as a function of energy (Fig. 1.12); in order to do this, $y = \lambda_c/\lambda$ must be replaced by $y = \varepsilon/\varepsilon_c$ where $\varepsilon_c = hc/\lambda_c$ represents the critical energy given by:

$$\varepsilon_c = 3hc\gamma^3/(4\pi R)$$

or in practical units

$$\varepsilon_c(\mathrm{keV}) = 2.218 E^3(\mathrm{GeV})/R(m). \qquad (1.4)$$

As shown in Fig. 1.12, the maximum photon energy achievable with a storage ring is few times its critical energy, ε_c.

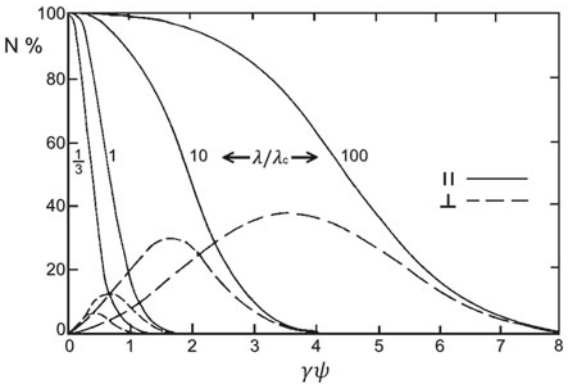


Fig. 1.13 Intensity of the parallel and perpendicular components of the photon flux as a function of $\gamma\psi$. The curves are reported for $\lambda/\lambda_c = 1/3$, 1, 10 and 100 and are normalized to the intensity at $\psi = 0$ (the figure is based on data of [9])

1.6 Polarization

The radiation emitted by a bending magnet is mostly linearly polarized. When observed in the horizontal plane, the electric field is parallel to the plane of the electron orbit (horizontal). Observing the radiation above and below this plane at finite vertical angles, a polarization component perpendicular to the plane of the electron orbit is present. In Fig. 1.13, the behavior of these two components as a function of $\gamma\psi$, is shown: it is clearly visible that the vertical opening angle, $\Delta\psi$, is approximately given by γ^{-1} ($\gamma\psi = 1$) when $\lambda \approx \lambda_c$. For $\lambda < \lambda_c$ the radiation fan is more collimated, while for $\lambda > \lambda_c$ it becomes wider.

The horizontal componnt has its maximum roughly at angles at which the intensity of the vertical component is 1/2 of its maximum.

Because of the presence of a horizontal and a vertical component, it is useful to define the degree of linear polarization, P_{Linear}, as [1]:

$$P_{Linear} = \frac{I_{//} - I_{\perp}}{I_{//} + I_{\perp}}.$$

In the orbital plane, ($\psi = 0$), P is equal to 1, i.e. the light is 100 % linearly polarized. When the observation is off axis the linear polarisation decreases as a function of $\gamma\psi$. The integration over all wavelengths gives:

$$I_{//} = (7/8)I_{total} \qquad I_{\perp} = (1/8)I_{total}$$

that means a linear polarisation degree of about 75 %.

Above and below the plane there is a constant phase difference of $+\pi/2$ and $-\pi/2$ between the parallel and perpendicular components of the electric field. Therefore the radiation is respectively elliptically right and left polarized. The degree of circular polarisation, P_C, defined as:

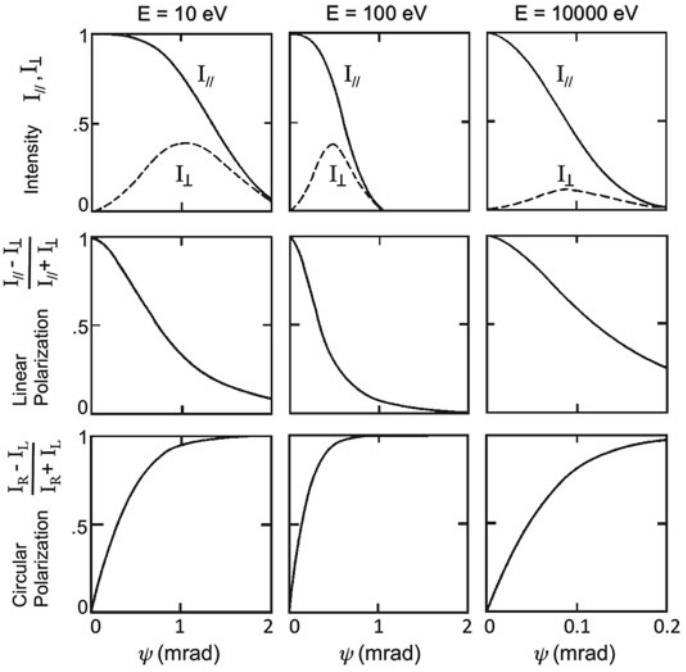


Fig. 1.14 Intensity distribution of the parallel and perpendicular components of the radiation as a function of ψ at three different photon energies, for a storage ring with $E = 3.5$ GeV, $R = 12.12$ m; the critical energy is 7.8 keV and $1/\gamma$ is 0.146. The behaviour of the *linear* and *circular* degrees of polarisation are also shown (the figure was redrawn: it is based on Fig. 1.8 of [1])

$$P_C = \frac{I_R - I_L}{I_R + I_L} = \frac{\pm 2\sqrt{(I_{//} I_{\perp})}}{I_{//} + I_{\perp}}$$

where I_R and I_L are the intensities of the right and left polarized light and the sign, $\pm$, corresponds to positive or negative values of ψ, is shown in Fig. 1.14, and compared with the degree of linear polarisation.

The vertical angular dependence of the SR beam on the vertical angle ψ can be well approximated by a Gaussian function $1/(2\pi\sigma_R^2)^{0.5} \exp(-\psi^2/2\sigma_R^2)$ [9]; σ_R, in the range $0.2 < \lambda/\lambda_c) < 100$, is approximately given by:

$$\sigma_R = \frac{0.565}{\gamma}\left[\frac{\lambda}{\lambda_c}\right]^{0.425}$$

where σ_R is expressed in radians. The FWHM ($2.35\sigma_R$) of the angular distribution in practical units is given by:

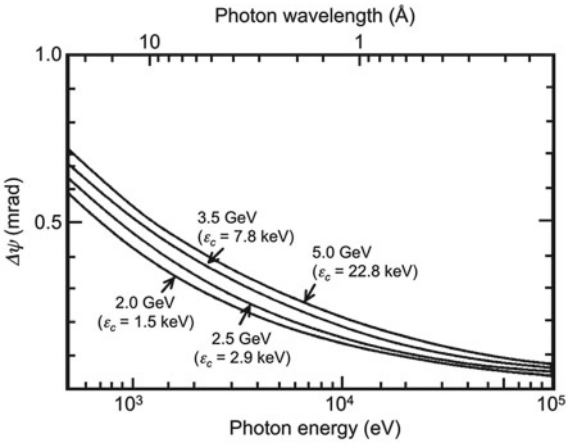


Fig. 1.15 Values of the angular width $\Delta\psi$ plotted a function of photon energy for different values of the electron energy and of the critical energy (the figure was redrawn from Fig. 1.5 of [10])

$$\Delta\psi(FWHM) = 2.35 \cdot \sigma_R = \frac{0.682}{E(GeV)}\left[\frac{\lambda}{\lambda_c}\right]^{0.425}$$

In Fig. 1.15, $\Delta\psi$ is shown as a function of the photon wavelength/energy and of the energy of the storage ring.

Normally, σ_R, that represents the standard deviation of the vertical angular distribution of the SR beam, includes also a contribution due to the divergence of the electron beam negligible for storage rings having small electron beam divergence and dimension.

1.7 Spectral Brightness and Emittance

An useful quantity for experiments which do not use focussing optics, is the photon flux per solid angle, because from it the flux on the sample can be easily evaluated using simple geometrical considerations. This quantity, defined as the number of photons emitted per second, in a spectral bandwidth $\Delta E/E = 0.1\,\%$, into a unit solid angle, is given by:

$$N = 1.327 \times 10^{13} E^2[\mathrm{GeV}]\, I\,[\mathrm{A}] H_2(\mathrm{y})$$

where H_2 is (like G_1) a dimensionless function of $y = \varepsilon/\varepsilon_c$, whose behaviour is reported in Fig. 1.17. It has a broad maximum around ε_c, decreases as $(\varepsilon/\varepsilon_c)^{2/3}$ for $\varepsilon/\varepsilon_c \ll 1$ and as $[\varepsilon/\varepsilon_c \exp(-\varepsilon/\varepsilon_c)]$ for $\varepsilon/\varepsilon_c \gg 1$ (Fig. 1.16).

When focussing optics are used, the relevant quantity is the photon intensity that can be focused into a specific area; at this purpose the *spectral brightness* of the source must be calculated. It is defined as the number of photons emitted per

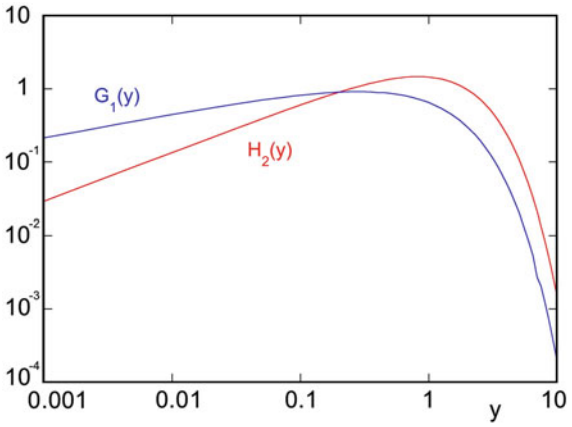


Fig. 1.16 Comparison of the spectral dependence of the $G_1(y)$ and of the $H_2(y)$ functions

second, in a spectral bandwidth $\Delta E/E = 0.1\,\%$ in an unit source area and per unit of solid angle. As well known due to the Liouville's theorem, focussing preserves the brightness, i.e. the brightness of the source is equal to the brightness of the beam when focussed on the sample. The brightness is determined by the size of the source, that is given by the size of the electron beam and by the angular spread of the radiation, given by the convolution of the angular distribution of synchrotron radiation, $\Delta\psi$, with the angular divergence of the electron beam. Therefore the characteristics of the electron beam source are essential in order to determine the brightness of the photon source. In a storage ring the product of the electron beam transverse size and angular divergence is a constant along the ring and is called emittance. Although the electron beam transverse size and angular divergence vary around the ring, their product or emittance is a constant. There is a horizontal and a vertical emittance. The horizontal emittance is measured in nanometer-radians (nm-rad).The vertical emittance is normally a few percent of the horizontal one. In order to get high brightness, small emittance machines must be used.

Brightness is the main figure of merit of synchrotron radiation sources and its huge increase, shown in Fig. 1.4, was obtained thanks to the designing of low emittance machines, like the European Synchrotron Radiation Facility (ESRF), that minimize the source size and the beam divergence.

1.8 Insertion Devices

Insertion devices (ID) are periodic magnetic structures installed in the straight sections of storage rings. Passing through such alternating magnetic field structures, electrons oscillate perpendicularly to the direction of their motion and therefore emit synchrotron radiation during each individual wiggle. The primary effects of the IDs are:

(1) the shift of the critical energy to higher values due to the smaller bending radius with respect to the bending magnets;

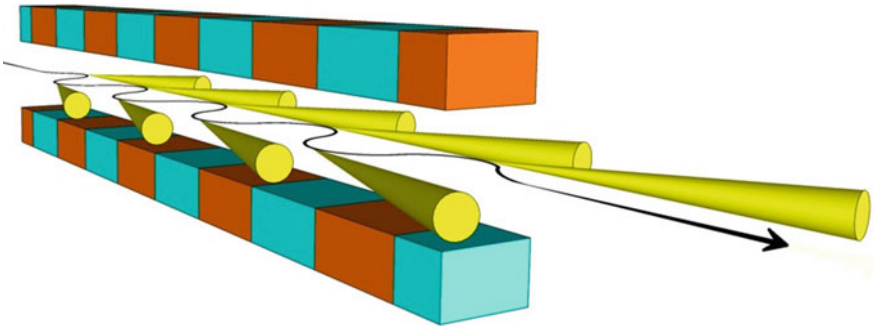


Fig. 1.17 Artistic view of the radiation beam emission from a multipole wiggler magnetic structure *(courtesy of V. Tullio INFN-LNF)*

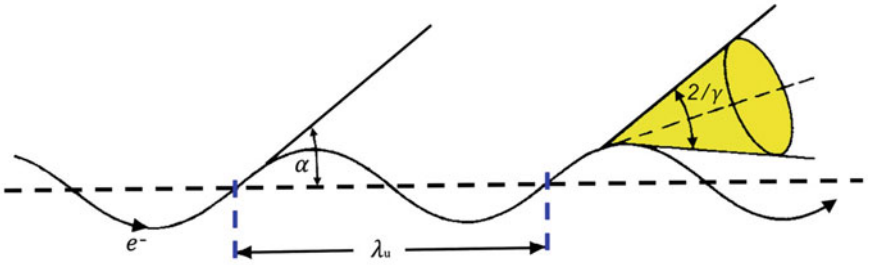


Fig. 1.18 Schematic view of the 'wiggler' regime, where λ_u represents the period of the oscillations

(2) the increase of the intensity of the radiation by a factor related to the number of wiggles induced by the many poles of the magnetic structure;
(3) the relevant increase of the spectral brightness.

Insertion devices are of two kinds: wigglers and undulators. Inside both these devices the electron beam is periodically deflected but outside no deflection or displacement of the electron beam occurs (Fig. 1.17).

A wiggler is a multipole magnet made up of a periodic series of magnets (N periods of length λ_u, the overall length being $L = N\lambda_u$), whose magnetic field forces the electrons to wiggle around the straight path (Fig. 1.18).

The alternating magnetic field is normally applied in the vertical direction so the sinusoidal trajectory of the electron beam lies in the horizontal plane. Electrons follow in this way a curved trajectory with a smaller local radius of curvature with respect to the one of the dipole-bending magnet, because in a wiggler, magnetic fields, higher than in a bending magnet can be used.

Using the value of the instantaneous radius of curvature of the electron trajectory, R(m):

$$R(\mathrm{m}) = 3.34E(\mathrm{GeV})/B(\mathrm{T})$$

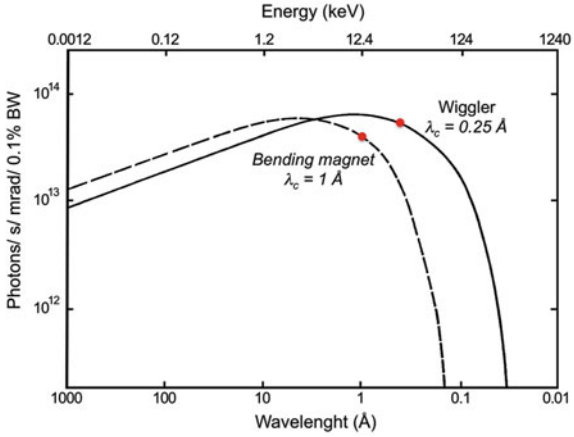


Fig. 1.19 Comparison between the spectral flux from a bending magnet (—) (B = 0.74 T) and from a wiggler (wavelength shifter: N = 1, B = 3.0 T))

where B is the magnetic field strength given in Tesla and using (1.4) the critical energy, ε_c, can be expressed as:

$$\varepsilon_c(\text{keV}) = 0.665\, E^2(\text{GeV})B(\text{T}).$$

The use of higher magnetic fields increases the critical energy with respect to the values achievable with bending magnets and extends the spectral range of a storage ring towards higher energies (Fig. 1.19).

The radiation observed is the incoherent sum of the radiation emitted by each individual pole. Therefore the overall characteristics of the beam are the same as those of a bending magnet with the same magnetic field but with an intensity enhanced by the factor N, the number of poles.

The total power generated by a wiggler is given, in practical units, by the equation:

$$P_T[\text{kW}] = 0.633E^2[\text{GeV}]B^2[\text{T}]L[\text{m}]I[\text{A}]$$

where B and L are the maximum magnetic field and length of the device.

In order to introduce undulators and clarify their difference with respect to wigglers, we make use of the dimensionless parameter K. It is given by the ratio between the wiggling angle of the trajectory, α, and the natural angular aperture of synchrotron radiation, $1/\gamma$, (Fig. 1.18) i.e.

$$K = \alpha\gamma.$$

For an electron moving in a sinusoidal magnetic field, it is easy to show that K is given by:

$$K = \frac{e}{2\pi mc}\lambda_u B = 0.934\,\lambda_u\,[\text{cm}]B[T]$$

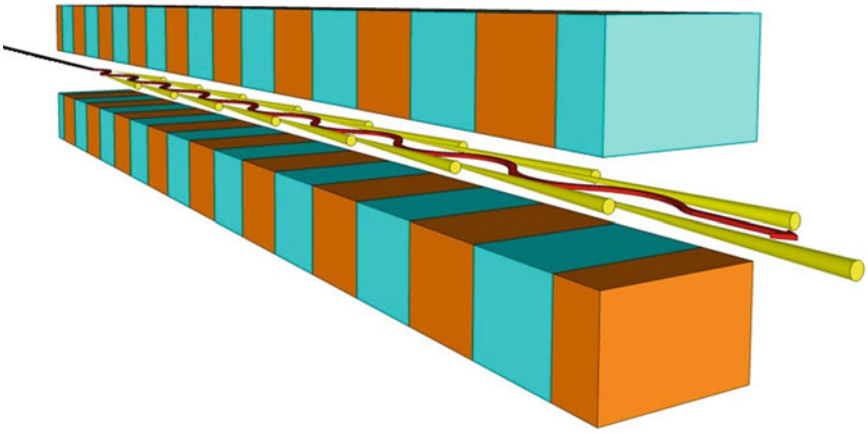


Fig. 1.20 Artistic view of the radiation beam emission from a multipole undulator magnetic structure (*courtesy of V. Tullio INFN-LNF*)

where, λ_u , is the period of the device. In a wiggler the transverse oscillations of the electrons are very large and the angular deviations, α, (Fig. 1.18) much wider than the natural opening angle $\psi = \gamma^{-1}$, therefore K >> 1. In these large K devices, the interference effects between the emission from the different poles can be neglected and the overall intensity is obtained by summing the contribution of the individual poles.

An undulator is very similar to a wiggler, but its K value is less than 1, that means, that the wiggling angle α is smaller than, or close to, the photon natural emission angle γ^{-1} (Fig. 1.20).

In this case interference occurs between the radiation emitted by electrons at different points along the trajectory. Considering the phase differences between the photons emitted at different points along the sinusoidal orbit, it is easy to show that observing the radiation in a direction forming an angle θ with the axis of the undulator, constructive interference occurs at the wavelength, λ:

$$\lambda = \frac{\lambda_u}{2\gamma^2}\left(1 + \frac{K^2}{2} + \gamma^2\theta^2\right). \tag{1.5}$$

In addition to the fundamental wavelength, also higher harmonics of shorter wavelength, $\lambda_n = \lambda/n$, are emitted (1.21). Their number and intensity increases with K; on the axis ($\theta = 0$) only odd harmonics are emitted.

The dependence of λ on K^2 that is on B^2 (1.5) is of extreme importance, because allows to vary the energy of photon emission. In the insertion devices the magnetic gap is the distance between the upper and lower arrays of magnets (Fig. 1.22) and in some ID it is fixed while in other it can change. The widening or shortening of the

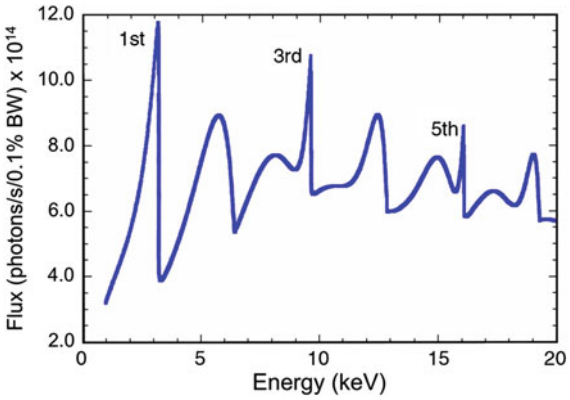


Fig. 1.21 Calculated flux spectrum of the APS (Advanced Photon Source (7 GeV)- Argonne (Illinois)) undulator A, a planar device (L = 2.4 m, N = 72) optimized to generate x-ray photons in a wide energy range, using the first, third and fifth radiation harmonics (*sharp peaks*), with I = 100 mA, K = 2.6 giving $E_1 = 3.21$ keV and no slits (the figure was redrawn: it is based on data of [11])

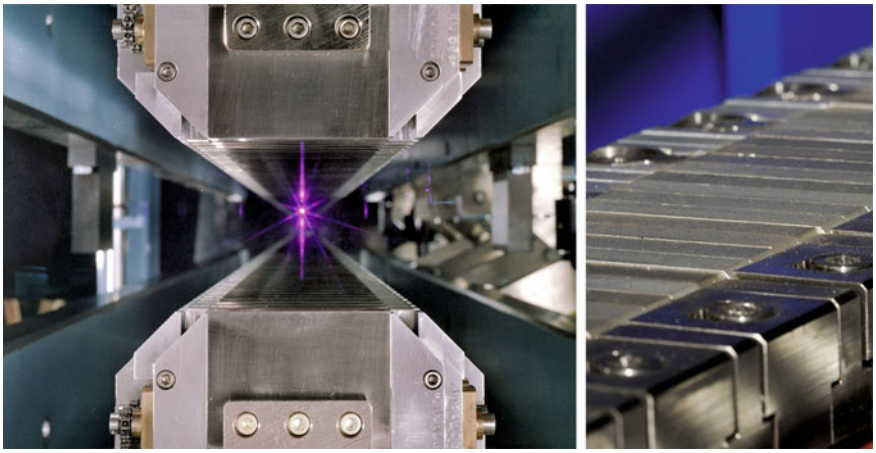


Fig. 1.22 *Left panel* Looking head on into the upper and lower rows of magnets (*jaws*) in an undulator. The adjustable vertical distance (*gap*) between the jaws determines the emitted wavelength. A laser was used to simulate the burst of light produced (*courtesy of Advanced Light Source*). *Right panel* Lower row of magnets of one of the SPARC undulators (*courtesy of SPARC_ LAB group INFN-LNF*)

gap distance in an undulator has an inverse effect on the amplitude of the magnetic field and is routinely used to change λ.

In an undulator, the amplitudes of the fields radiated by each individual period of the undulator add up coherently, so the intensity increases with N^2 while it increases only as 2N in a wiggler.

Each harmonic has a limited wavelength bandwidth approximately given by:

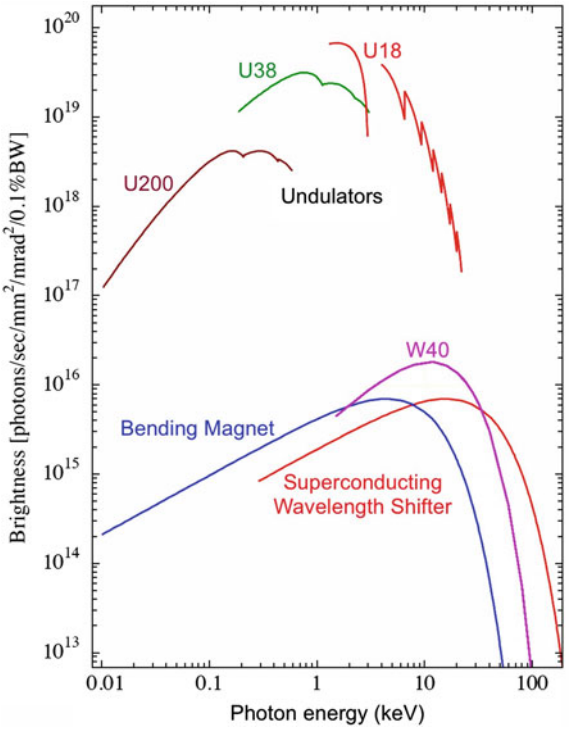


Fig. 1.23 Calculated brightness of beams emitted by undulators (200 mm (L = 10 m), 38 mm (L = 4 m) and 18 mm (L = 2 m) periods), wigglers (wavelength shifter and 40 mm (L = 2 m) period) and bending magnets for a 2.4 GeV storage ring with 400 mA circulating current (the figure was redrawn: it is based on data of [12])

$$\Delta\lambda/\lambda = 1/(nN)$$

Values of 10^{-2} can be easily achieved on the fundamental. Note that the bandwidth decreases with the number, N, of periods of the undulator and with the harmonic number, n.

The angular distribution, of the n-th harmonic is concentrated in a narrow cone in both the horizontal and vertical directions (Fig. 1.20) whose half width is given by:

$$\sigma = \sqrt{\frac{3}{4\pi}\frac{1+(K^2/2)}{\gamma^2 nN}} \approx \frac{1}{\gamma}\frac{1}{\sqrt{nN}}$$

so it is always lower than the natural emission cone, $1/\gamma$ of a bending magnet and decreases as the square root of the number of poles and of the harmonic number.

This very narrow angular distribution together with the N^2 dependence of the intensity radiated in the 'undulator' regime explain why the spectral brightness achievable with undulators exceeds by several order of magnitude that of bending magnets and of wigglers (Fig. 1.23).

We underline here that the observed properties of the photon beam are determined also by the electron beam emittance; while first and second-generation rings have an horizontal emittance of the order of 100–200 nm-rad, third generation ones are

in the 3–25 nm-rad range. Such low emittance values made possible to achieve the incredible brightness of the third generation synchrotron radiation facilities. However the increase in photon beam brightness as a function of the emittance decrease has a limit given by diffraction effects. The diffraction limited emittance or lowest useful emittance to produce high brightness photons of a given wavelength is $\lambda/4\pi$: for a photon energy of 1 keV the diffraction limited electron beam emittance is of the order of 0.1 nm-rad.

IDs are normally classified also as a function of the different technologies used to generate the magnetic fields, that include the use of electromagnets at room temperature (conventional iron and coil magnets) or superconducting (superconducting coils with or without iron) and the use of permanent magnets (NdFeB and SmCo). At room temperature if high photon energies are required, the highest magnetic field at the shortest possible period is necessary and for this reason normally permanent magnets are used (B_{max} = 3–4 T): electromagnets are an economical choice but produce smaller magnetic fields (factor 2–5). To overcome the problem related to the maximum achievable magnetic field, superconducting electromagnets can be used (B_{max} = 10–12 T). Operating at the liquid He temperature (4 K) superconducting IDs are more expensive to build and operate than permanent magnets but represent the most important and cheap solution to achieve high critical energies with a high magnetic field rather than increasing the whole storage ring energy. Nowadays most of the IDs, operating with a periodic vertical field, are realized using permanent magnets. In order to perform very specific studies like the ones needing circular polarization, complex IDs, like helical undulators can be also designed and built. Helical undulators generate helical magnetic fields that force electrons to move along spirals and emit circularly polarized radiation. In practice the use of the insertion devices in the third generation facilities has opened also the possibility to perform a quite large number of experiments that were quite impossible or difficult to realize in the past.

Acknowledgments The authors are very grateful to Mr. Vinicio Tullio for his help in the realization of many figures of this lecture.

Appendix: Basic Synchrotron Radiation Equations

Synoptic overview of some basic synchrotron radiation equations:

- Power radiated by a relativistic electron along a circular orbit (radius R):

$$P_e = \frac{2}{3}\frac{e^2 c}{R^2}\left[\frac{E}{mc^2}\right]^4$$

or in practical units:

$$P_e(kW) = 6.76\times 10^{-10} E^4(GeV) R^{-2}(m).$$

and in practical units the power radiated in a storage ring:

$$P(kW) = 88.47 E^4(GeV) I(A) R^{-1}(m).$$

- Vertical half-opening angle, ψ:

$$\psi \approx mc^2/E \approx \gamma^{-1}$$

where for electrons and positrons, in practical units:

$$\gamma = 1957\, E\ (\mathrm{GeV}).$$

- The critical wavelength, λ_c:

$$\lambda_c = (4/3)\pi R \gamma^{-3}$$

or in practical units:

$$\lambda_c(\text{Å}) = 5.59\mathrm{R(m)E}^{-3}(\mathrm{GeV}).$$

- Critical energy, ε_c in practical units:

$$\varepsilon_c(\mathrm{keV}) \ = \ 2.218\mathrm{E}^3(\mathrm{GeV})\mathrm{R}^{-1}(\mathrm{m}).$$

- Bending radius, R:

$$R(\mathrm{m}) \ = \ 3.34\mathrm{E(GeV)B}^{-1}(\mathrm{T}).$$

References

1. E.E. Koch, D.E. Eastman, Y. Farges, Synchrotron radiation—a powerful tool in science, in *Handbook of Synchrotron Radiation*, ed. by E.E. Koch (North-Holland Publishing Company, Amsterdam, 1983), pp. 1–63
2. Lightsources of the World. http://www.lightsources.org/regions
3. D.M. Mills et al., Report of the Working Group on Synchrotron Radiation Nomenclature brightness, spectral brightness or brilliance? J. Synchrotron Rad. **12**, 385 (2005)
4. H. Winick, Synchrotron radiation sources—present capabilities and future directions. J. Synchrotron Rad. **5**, 168–175 (1998)
5. J. Schwinger, On the classical radiation of accelerated electrons. Phys. Rev. **75**, 1912–1925 (1949)
6. D.H. Tomboulian, P.L. Hartman, Spectral and angular distribution of ultraviolet radiation from the 300-mev cornell synchrotron. Phys. Rev. **102**, 1423–1447 (1956)
7. D. Raoux, in *Introduction to Synchrotron Radiation and to the Physics of Storage Rings*, ed. by J. Baruchel et al. Neutron and Synchrotron Radiation for Condensed Matter Studies (Les Editions de Physique, Springer, 1993), pp. 37–78
8. P.J. Duke, *Synchrotron Radiation Sources*, ed. by A.G. Michette, C.J. Buckley. X- Ray Science and Technology (Institute of Physics Publishing, London, 1993), pp. 64–109
9. G.K. Green, *Spectra and Optics of Synchrotron Radiation, Report BNL 50522: Particle Accelerators and High-Voltage Machine-TID 4500* (Brookhaven National Lab, Upton, 1976), pp. 1–63
10. G. Materlik, in *Properties of Synchrotron Radiation*, ed. by H.B. Stuhrmann. Uses of Synchrotron Radiation in Biology (Academic Press Inc., London, 1982), pp. 1–21
11. W.-K. Lee, P. Fernandez, D.M. Mills, in *X-Ray Crystal Optics*, ed. by H. Onuki, P. Elleaume. Undulators, Wigglers and Their Applications (Taylor & Francis, London, 2003), pp. 369–420
12. M. Boge et al., The Swiss Light Source Accelerator Complex: An Overview. http://accelconf.web.cern.ch/Accelconf/e98/PAPERS/MOP28G.PDF

Chapter 2
Characteristics and Properties of Synchrotron Radiation

Giorgio Margaritondo

Abstract The properties of synchrotron radiation are primarily explained by classical electromagnetism and special relativity. The formal derivation based on relativistic electrodynamics is rather complex, but the underlying physics is quite simple and can lead to the essential properties in an intuitive way. Many of such properties are directly related to the combination of relativistic effects such as the Lorentz contraction and the Doppler shift. Based on this philosophy, we treat with minimum formalism essential features such as the intensity, brightness and spectral distribution of the emission from bending magnets, wigglers and undulators, the time structure and the space and time coherence. Then we extend the same strategy to the essential features of free electron lasers.

2.1 Introduction: Broad Picture of a Synchrotron Light Source

The characteristics of electron "storage rings" as photon sources are exceptional but not universally understood. Rigorous theories are indeed mathematically complex and not easily accessible for non-specialists. However, the underlying physical facts are quite simple, and their impact on the source performances can be understood with elementary, semi-qualitative arguments [1–6]. This is the purpose of our discussion.

Electrons circulating in the vacuum chamber of a storage ring emit the light. After being generated and accelerated in the injection system, the electrons are inserted in the main ring where they circulate for many hours or days, at a speed close to c, the speed of light (see Fig. 2.1). In some facilities, the injection takes place continuously so that a constant electron beam can circulate indefinitely [7].

G. Margaritondo (✉)
Faculté des Sciences de Base, Ecole Polytechnique Fédérale de Lausanne (EPFL),
1015 Lausanne, Switzerland
e-mail: giorgio.margaritondo@epfl.ch

S. Mobilio et al. (eds.), *Synchrotron Radiation*,
DOI: 10.1007/978-3-642-55315-8_2, © Springer-Verlag Berlin Heidelberg 2015

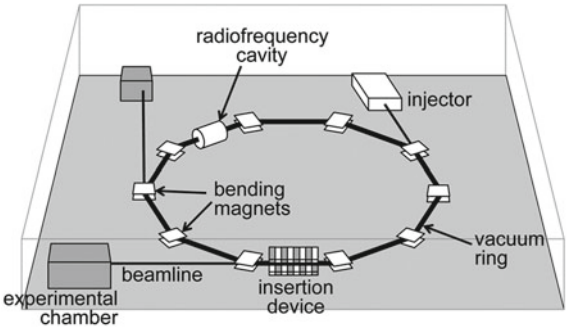


Fig. 2.1 Schematic picture of a synchrotron radiation facility with its main components. In reality, a facility includes many more insertion devices (undulators and wigglers), and beamlines

As shown in Fig. 2.1, what keeps the electrons in a closed trajectory is a system of (dipole) bending magnets. In addition, the facility includes other magnet systems (not shown in Fig. 2.1 and not discussed here), to control the characteristics of the electron beam. The bending magnets apply to each electron a Lorentz force perpendicular to its vector velocity. The force does not do any work and cannot change the energy of the electrons, but it does cause a centripetal acceleration that changes the direction of the velocity.

Classical electromagnetism shows that a point-like electric charge like an electron, when accelerated, emits electromagnetic waves. This is the cause of synchrotron light. The consequence is the loss of energy by the electrons. Without a correction, this loss would make it impossible for the electrons to keep circulating in a stable trajectory around the ring. Thus, the energy loss must be compensated: this is done by the radiofrequency cavity, which applies an electric field in phase with the passage of the electrons and accelerates them in the longitudinal direction.

Each bending magnet is a source of synchrotron light. This emission is collected by a beamline, optically processed along it and finally sent into an experimental chamber to be utilized.

In modern facilities, besides the bending magnets, other magnetic systems—called "insertion devices"—also act as synchrotron light sources. They increase the flexibility in producing light with the desired characteristics and in reaching an extremely high source quality.

An insertion device consists of a periodic series of magnets that force the electrons to slightly undulate in the transverse direction. There exist two broad classes of insertion devices: "wigglers" and "undulators". A wiggler has a stronger magnetic field and larger transversal undulations than an undulator. We shall see later how this impacts the characteristics of the emitted light.

Note in Fig. 2.1 that the beamlines are very narrow and aligned to the velocity of the electrons moving around the ring. The reason is that synchrotron light is only emitted in a very narrow longitudinal cone [2, 6], like an extremely collimated flashlight. This geometrical property is a direct consequence of the relativistic speed

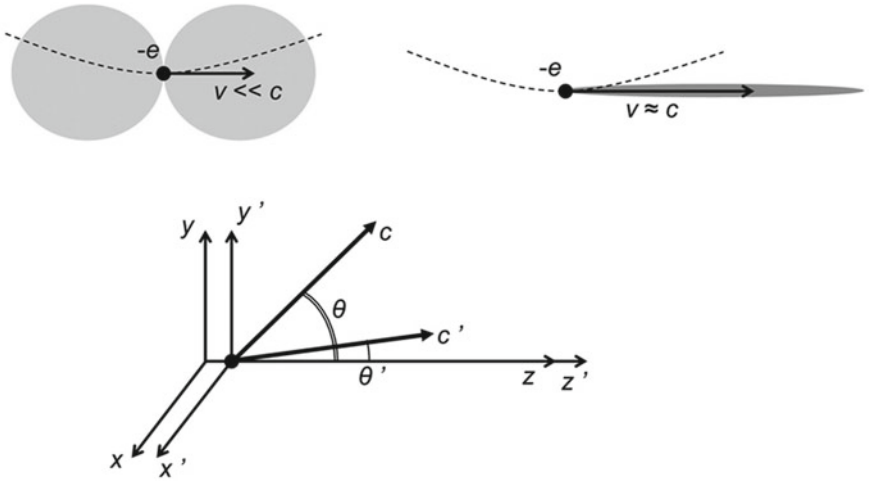


Fig. 2.2 Angular collimation of synchrotron light. *Top left* an electron moving at nonrelativistic speed $v \ll c$ emits radiation, when accelerated by a bending magnet, in a broad angular range. *Top right* this emission pattern becomes instead a narrow beam (angular spread $\approx 1/\gamma$) for relativistic speed. *Bottom* a simple use of the Lorentz transforms from the "electron frame" R(x, y, z) to the "laboratory frame" R$'(x', y', z')$ explains the collimation

of the emitting electrons, as many other characteristics of synchrotron light. We shall thus begin our discussion by discovering some important links between synchrotron light and relativity.

2.2 Relativistic Effects in a Nutshell

Why is the electron emission so strongly collimated in the forward longitudinal direction? This does not happen at low speed: the emission covers instead a broad angular range, as shown in Fig. 2.2, top left.

To understand the effects of relativity, we shall work with two different reference frames (Fig. 2.2, bottom): the "laboratory frame" R$'(x', y', z')$ where an electron moves at speed v, and the "electron frame" R(x, y, z). This latter is actually the inertial frame moving with speed v, with respect to R$'$, where the electron has (instantaneously) zero speed and nonzero (transverse) acceleration.

The emission in R roughly exhibits the typical $\cos^2\theta$ pattern of antenna emitters, extending to large angles. To find the angular pattern in R$'$, we must Lorentz-transform the velocity vector of the light from $\boldsymbol{c}$ to $\boldsymbol{c}'$:

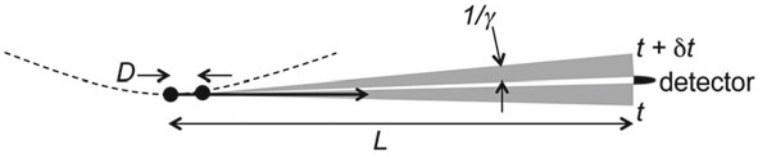


Fig. 2.3 Schematic explanation of how the angular collimation justifies the high photon energy of synchrotron radiation

$$c'_x = (c_x/\gamma)(1 + vc_z/c^2); \tag{2.1}$$

$$c'_y = (c_y/\gamma)(1 + vc_z/c^2); \tag{2.2}$$

$$c'_z = (c_z + v)(1 + vc_z/c^2); \tag{2.3}$$

where γ is the relativistic factor, $\gamma = 1(1 - v^2/c^2)^{1/2} = m/m_o$, the ratio between the electron mass in R and its rest mass—and therefore the ratio between the electron energy and its rest energy, $mc^2/(m_o c^2)$.

For $c_y = c_y{}' = 0$, we have $tg\theta = c_x/c_z$ and $\text{tg}\theta' = c'_x/c'_z$. Equations (2.1) and (2.3) show that in this last ratio there is a γ-factor in the denominator that does not appear in c_x/c_z. Roughly speaking, this means that the emission angles in R, when seen in R′, are squeezed by the same factor, and the emission is confined to an angular range of the order of $1/\gamma$.

For a typical electron storage ring energy with $mc^2 = 2\,\text{GeV}$, the γ-factor is $\approx$3,900. Thus, the angular collimation confines the emission within a fraction of a milliradians.

This collimation conserves energy: the emission found in the R-frame over a broad angular range is now concentrated in a small cone. This directly affects a fundamental merit figure for light sources: the "brightness" or "brilliance". As discussed later, this parameter is proportional to the emitted flux divided by the angular spread and by the source size. By decreasing the angular spread, relativity boosts the brightness. The advantages can be easily understood: as for a common flashlight, a collimated beam is easier to use when one wants to concentrate a strong intensity in a small area.

The extreme collimation is one of the factors explaining why the spectral distribution of synchrotron light emission occurs primarily at high energies, in the X-ray range. Let us see how.

Consider (Fig. 2.3) an electron emitting a narrow cone of synchrotron light, captured by a point-like detector at a distance L. At each passage of an electron in the corresponding bending magnet, the detector "sees" a flash of light. Each flash begins when the emitted beam enters the detector, at the time $t = L/c$ after the corresponding emission by the electron. What is the duration of the light pulse, δt?

To exit the detector, the emission cone must rotate by an angle $\approx 1/\gamma$. If r is the curvature radius of the trajectory, this corresponds for the electron to the distance

$r(1/\gamma) = D$, requiring a traveling time $D/v = r/(\gamma v)$. The pulse-end emission thus starts at this time and reaches the detector at:

$$t + \delta t = r/(\gamma v) + (L - r/\gamma)/c = L/c + (r/\gamma)(1/v - 1/c) = t + (r/\gamma)(1/v - 1/c).$$

Thus, the pulse duration is $\delta t = (r/\gamma)(1/v - 1/c) = [r/(\gamma v)](1 - v/c)$. For $v \approx c$, we have $(1 - v/c) = (1 - v^2/c^2)/(1 + v/c) \approx 1/(2\gamma^2)$, and $\delta t \approx r/(2c\gamma^3)$.

The Fourier theorem relates this pulse duration to a typical frequency $\nu_c \approx 1/(2\pi\delta t) \approx c\gamma^3/(\pi r)$. The corresponding photon energy $h\nu_c = hc\gamma^3/(\pi r)$ is high, in the X-ray range, primarily due to the large γ-factor.

We can express this result in terms of the bending magnet field strength B. The motion induced by the dipole bending magnet is a cyclotron phenomenon: the trajectory is part of a circle of radius r. Using the transverse relativistic mass γm_o, the relation between force and acceleration is $\gamma m_o v^2/r = evB$, hence $r = \gamma m_o v/(eB)$, and:

$$h\nu_c \approx hc\gamma^2 eB/(\pi m_o v) \approx h\gamma^2 eB/(\pi m_o). \tag{2.4}$$

The same result can be derived in a different way, revealing other facets of the relativistic effects. In the electron reference frame R, the B-field of the bending magnet is Lorentz-transformed into a transverse electric field of strength $E = \gamma vB$. The relation between force and acceleration in R is, therefore: $m_o v^2/r = \gamma evB$, giving an angular velocity $\omega = \gamma eB/m_o$.

This is also the cyclotron frequency. In the electron frame, the spectral peak of the emission is $(h/2\pi)\omega = h\gamma eB/(2\pi m_o)$. However, when seen in the *laboratory* frame this photon energy is shifted by the (relativistic) Doppler effect, becoming larger. The Doppler factor in the longitudinal direction is close to 2γ. Therefore, the emission peak in the laboratory frame is:

$$h\nu_c \approx h\gamma^2 eB/(\pi m_o), \tag{2.5}$$

the same results of (2.4). This second derivation reveals that the factor γ^2—that brings the emission peak to the X-ray range—is caused by the Doppler shift combined with another relativistic effect, in this case the Lorentz transformation of the fields.

The electrons, accelerated by the magnets, continuously emit synchrotron radiation. We have seen that the lost energy is restored by the radiofrequency cavity. However, this only works for electrons entering the cavity when its field is in the "accelerating" phase, and not before or after. Thus, the circulating electrons form longitudinal bunches of finite length Δz_B.

Each electron in a bunch follows its own trajectory around the ring, slightly different with respect to the others. This is notably due to the fact that the emission of synchrotron radiation photons is a stochastic effect, causing different energy losses for different electrons. All together, the different electron trajectories determine the finite transverse cross section of the electron bunch.

When an electron bunch passes a bending magnet feeding photons to its beamline, a burst of light is sent to the experimental chamber. The light pulse for each

bunch—not to be confused with that of a single electron—has a duration given by the passage time of the bunch in front of the beamline, $\Delta t_B = \Delta z_B/v \approx \Delta z_B/c$. The emitted light pulse is spectrally centred at the X-ray photon energy defined by (2.4) or (2.5).

2.3 Definition of the Main Parameters

To continue our analysis, we must first define our objectives: this means deciding what parameters we will use to describe the source properties, and discuss in semi-quantitative terms. We will target six types of parameters: spectral distribution features (photon energy peak and bandwidth), emitted intensity, brightness, polarization, time features (pulse duration, pulse shape) and coherence features. There exist links between some of these parameters, for example—see later—between spectral bandwidth and longitudinal coherence.

2.3.1 Spectral Distribution Features

We already treated the peak photon energy of the bending magnet emission, $h\nu_c$. This parameter can be actually used for all types of synchrotron sources: bending magnets, wigglers and undulators.

As already shown, the spectral distribution of a bending magnet is not an infinitely narrow peak, but a band of finite width with its maximum at $h\nu_c$. A full characterization would require the exact shape of the band. In first approximation, we will use, besides $h\nu_c$, the distribution bandwidth $\Delta h\nu_c$.

Another spectral parameter is often used for bending magnets, primarily because of historical reasons: the so-called critical photon energy $\Delta h\nu_{cr}$. This is defined by saying that equal amounts of synchrotron radiation energy are emitted at photon energies lower and higher than $\Delta h\nu_{cr}$. We shall see later that a simple relation exists between $h\nu_{cr}$ and $h\nu_c$.

In many cases, the spectral distribution and the corresponding parameters are defined not in terms of photon energy but of wavelength λ. The conversions are straightforward and based on the relation $\lambda = c/\nu$.

2.3.2 Total Emission

The overall synchrotron light emission is extremely high and can be characterized by several parameters. The most popular are the total emitted power and the spectral flux $F(h\nu, \theta)$, defined for a bending magnet as the power emitted as a function of the photon energy and of the vertical angle θ, within a certain horizontal angle and within a certain bandwidth. The spectral flux for a zero vertical angle, i.e., emitted in the horizontal plane, is called the "central spectral flux". So, for example, the

central spectral flux $F(h\nu, 0)$ can be measured in photons per second, per 0.1 spectral bandwidth, per (vertical) milliradiant.

The total emitted power is extremely high mostly because of two facts. First, the emission process is intrinsically very efficient. The power emitted by an accelerated charge is proportional to the square of the acceleration. For bending magnets, we have seen that in the R-frame $m_o v^2/r = \gamma e v B$. Thus, the acceleration is proportional to γB and:

$$\text{Total emitted power} = \text{constant x}\gamma^2 B^2. \tag{2.6}$$

The squared γ-factor brings the overall emission to very high levels. In terms of the curvature radius of the bending magnet, $r = \gamma m_o v/(eB)$, we have:

$$\text{Total emitted power} = \text{constant x}\gamma^4/r^2, \tag{2.7}$$

so for a constant radius the synchrotron emission increases as the fourth power of the electron energy, i.e., very rapidly.

The second factor leading to high emission levels is the physical nature of the source. If the emitting electrons were part of a solid, the host medium could be damaged by the high emitted power. In a storage ring, the electrons are "free", i.e., externally controlled by the magnet systems. This eliminates the host medium and the risk of damage—until the radiation reaches the first optical component of each beamline.

The combined effect of the above two factors is quite impressive. For a single electron, the constant in (2.7) is $\approx 4.6 \times 10^{-20}\,\mathrm{W\,m^2}$. In a storage ring with 2 GeV energy, corresponding to $\gamma \approx 3.9 \times 10^3$, each electron passing through a bending magnet with radius $r = 5\,\mathrm{m}$ emits $\approx 0.42\,\mu\mathrm{W}$. Since in a modern storage ring there are typically 10^{12} circulating electrons, the total emitted power is very high indeed!

2.3.3 Brightness

The quality of a photon source must be assessed based on how effective it is for practical applications. A high flux is certainly important: most experiments profit from the consequently high signal-to-noise ratio. But flux alone is not sufficient to describe all aspects of a "good" source.

In many applications, one must concentrate as many photons as possible in a small area. This is accomplished with a suitable focusing system. A lossless optical system obeys one of the many versions of the Liouville (phase space conservation) theorem: along it, the "brightness", *b,* remains constant.

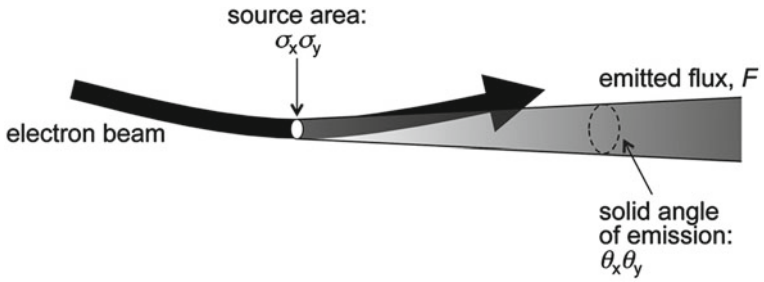


Fig. 2.4 Rough definition of the brightness

What is this quantity? As shown in Fig. 2.4: the brightness is proportional to the flux divided by the area of the source as well as by the solid angular divergence of the emission:

$$b = \text{constant x} F/(\sigma_x \sigma_y \theta_x \theta_y). \tag{2.8}$$

The conservation of b along an optical system implies that the final focusing is easier if the source has a high b-value. For example, a source with a small angular divergence is preferable since a high angular divergence requires large optical components that are technically difficult to fabricate and expensive.

Synchrotron sources possess high brightness not only because of their high flux but also because of their excellent geometric characteristics, corresponding to the σ_x, σ_y, θ_x, and θ_y parameters in (2.8). In this context, "excellence" means of course that these parameters have small values.

Note that the source area $\sigma_x\sigma_y$ is not the transverse cross section of a single electron. We have seen, indeed, that the different trajectories of different electrons cause a finite transverse cross section of the electron bunches. This effect contributes to the source size.

Likewise, the angular divergence of a single-electron emission is not the only factor in the overall angular divergence $\theta_x\theta_y$ of the source. In this case too the different electron trajectories play an important role.

When considering geometric factors in brightness one must distinguish between the vertical and horizontal directions. For a bending magnet, the horizontal source size and angular dependence are not only determined by the electron beam geometry: they also depend on the portion of the curved trajectory from which emission can reach the beamline. Similar factors can affect the geometric parameters of other kinds of sources.

As previously shown, progress was made over four decades in improving the denominator of (2.8) and boosting the brightness. Accelerator science has become very sophisticated and capable to control the electron beam with extremely high accuracy.

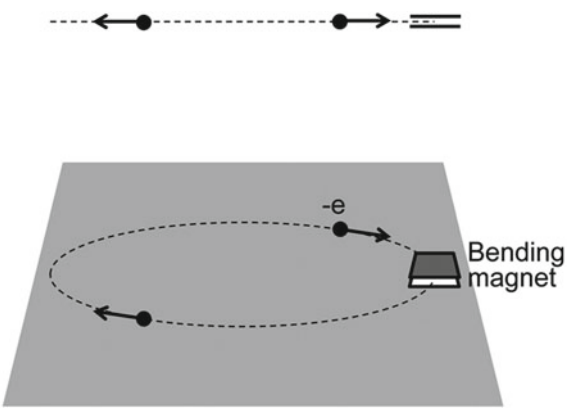


Fig. 2.5 Polarization of bending magnet emission. *Bottom* two electrons moving around the vacuum ring, seen from a point of view tilted with respect to the (horizontal) ring plane, together with a bending magnet. The motion appears elliptical and leads to elliptical polarization. *Top* seen from a point of view in the ring plane, the motion occurs in a straight line and leads to linear polarization

2.3.4 Polarization

This is an important and very useful feature of synchrotron light. Why is synchrotron light polarized? We can qualitatively understand this property from Fig. 2.5.

The bottom part schematically shows two electrons circulating in a storage ring and one of the bending magnets, seen from a given angle with respect to the horizontal plane. The top part corresponds instead to a point of view in the horizontal plane. This second point of view suggests that the motion in the bending magnet can be considered as a fraction of a linear oscillation, like charges in a radio-emitter antenna. The electric field perturbation that creates the waves is in the horizontal direction, thus the emission is linearly polarized when observed in the plane of the storage ring.

The bottom part of Fig. 2.5 suggests instead that, seen from a non-horizontal direction, the emission is elliptically polarized. This is indeed true.

An elliptically polarized wave can be considered as the combination of two linearly polarized waves in perpendicular directions. Quantitatively speaking, one can characterize the degree of elliptical polarization by comparing the intensities of these two components. Considering the electric fields, one could wrongly believe that the vertical component intensity is proportional to $\sin^2\theta$, where θ is the angle between the line of sight and the horizontal direction. But this is not true since the emitted intensity rapidly decreases outside the horizontal plane due to the angular collimation.

The emission is indeed confined to an angular range $\approx 1/\gamma$, thus elliptically polarized emission only occurs with a few milliradians of the horizontal plane. This emission is nevertheless quite useful, in particular for specialized spectroscopy techniques. However, the best way to obtain intense elliptically polarized synchrotron light is to use elliptical wiggler or undulator sources [8].

2.3.5 Time Features

Synchrotron light is not continuously emitted but has a pulsed time structure. Before discussing it, we should note that this time structure is very useful for many experimental techniques. For example, it can set the "start" time for dynamic spectroscopic studies of time-dependent properties [9].

The first factor in the time structure is the emission by individual electrons. Indeed, light is sent into a beamline only when an electron passes through the source point. The other important factor, however, is the already discussed effect of electron bunches: the micropulses of individual electrons occur within macropulses of duration $\Delta t_B \approx \Delta z_B/c$. There are several equally-spaced electron bunches circulating around the ring, thus the overall time structure consists of macropulses of duration Δt_B spaces by time intervals ΔT.

These two parameters, macropulse duration and separation, are commonly used to characterize the time structure of a synchrotron facility. For quantitative values, consider that a typical bunch length is several mm, a storage ring circumference several hundred meters, and the number of electron bunches from 1 to several hundred. Dividing the bunch length and separation by the speed of light, we obtain pulse durations below 0.1 ns and pulse separations from nanoseconds to microseconds.

2.3.6 Coherence Parameters

Coherence is a characteristic of synchrotron light whose practical importance is continuously increasing [2, 10] and therefore deserves particular attention. Roughly speaking, "coherence" is the property of a wave that enables us to observe physical-optics phenomena like diffraction and interference (as opposed to geometrical-optics effects like refraction and reflection).

To understand the difference between coherent and incoherent waves, consider the pinhole diffraction phenomenon of Fig. 2.6. In the ideal case (top) the wave source is point-like and emits only one photon energy: such a source always produces a visible diffraction pattern on the fluorescent screen. Imagine, however, that the source area becomes gradually bigger. Each point produces a pattern like that of the top figure and one sees their superposition. If the source area is too big (Fig. 2.6, middle), diffraction features are no longer visible in the superposition.

Likewise, if the point source does not emit a single photon energy but a band with finite bandwidth, each energy within the band produces its own pattern. If the bandwidth is too large, diffraction features are not visible in the superposition (Fig. 2.6, bottom).

The above arguments show that we must consider two kinds of coherence: "longitudinal" or "time" coherence linked to the spectral bandwidth, and "lateral" or "space" coherence linked to the source geometry. We shall consider longitudinal coherence first.

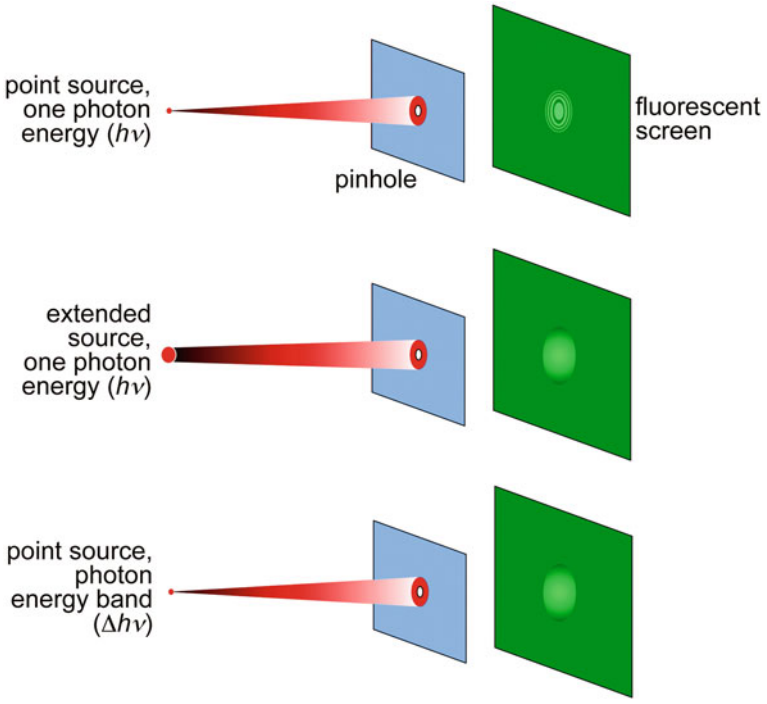


Fig. 2.6 Pinhole diffraction can be used to discuss longitudinal and lateral coherence

Using Fig. 2.7, the optical path difference between the rays passing through the center and the edge of the pinhole (of size $2d$) and reaching a point at a distance y from the center of the pattern is $\approx d \sin(y/D) \approx dy/D$. The constructive interference condition for the wavelength $\lambda = hc/(h\nu)$ is:

$$dy/D \approx nhc/(h\nu), \text{ with } n = 0, 1, 2, \ldots; \tag{2.9}$$

the distance between the central and $n = 1$ features of the diffraction pattern is, therefore, $y_1 - y_0 \approx (D/d)hc/(h\nu)$. Assume now that the source has a finite bandwidth $\Delta h\nu$. The y-broadening derived from (2.9) for $n = 1$ is

$$\Delta y \approx (D/d)hc[\Delta h\nu/(h\nu)^2] \tag{2.10}$$

Roughly speaking, the diffraction pattern features are still visible if Δy is smaller than $y_1 - y_0$, i.e., from (2.9) and (2.10):

$$\Delta h\nu/(h\nu) < 1. \tag{2.11}$$

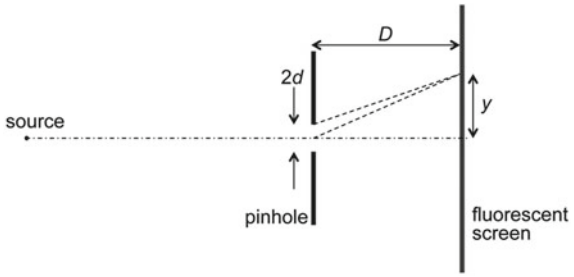


Fig. 2.7 Discussion of longitudinal coherence based on diffraction by a pinhole of size $2d$

We can use (2.11) as a criterion for minimal longitudinal coherence. This is not a stringent requirement in terms of monochromaticity: applied to sunlight, it explains why we see diffraction and interference effects in everyday life.

In more general terms, (2.11) suggests that we can measure the degree of longitudinal coherence using the relative spectral bandwidth $\Delta h\nu/(h\nu)$ of the emission. Synchrotron light can reach a low $\Delta h\nu/(h\nu)$ value and high longitudinal coherence for different reasons. In the case of broadband emission (e.g., from bending magnets or wigglers, as discussed later), the high source brightness makes it possible to filter it with a monochromator and still send many photons on the sample. We shall also see that undulators are not broadband sources and therefore automatically possess a good level of longitudinal coherence.

The longitudinal coherence can also be characterized using the "coherence length" L_c. Assume that a monochromatic wave of photon energy $h\nu$ and wavelength $\lambda = ch/(h\nu)$ starts with a given phase. After a distance L, the phase changes by $2\pi L/\lambda$ but it is still the same for the entire wave. If, however, the wave has finite photon energy bandwidth and therefore a finite wavelength bandwidth $\Delta\lambda$, different wavelengths will have different phases. The maximum phase difference is:

$$|[d(2\pi L/\lambda)/d\lambda]|\Delta\lambda = (2\pi L/\lambda^2)\Delta\lambda$$

This difference can be considered small if $(2\pi L/\lambda^2)\Delta\lambda \ll 2\pi$, which is true as long as:

$$L \ll L_c = \lambda^2/(\Delta\lambda), \tag{2.12}$$

which defines the "coherence length". A large coherence length corresponds to high longitudinal coherence, once again due to a small relative bandwidth.

Consider now the effects of a finite source size σ_y in Fig. 2.6, middle. Referring to Fig. 2.8, the emission from the lower edge of the source would not reach the upper pinhole edge with the same phase as the emission from the upper edge of the source. The optical path difference is $\approx\sigma_y\eta_y$ and the phase difference $\approx 2\pi(\sigma_y\eta_y)h\nu/(hc)$. Considering also the emission from the other points of the source, this would be the overall phase spread. If the spread is too big, a diffraction pattern is no longer visible.

Assume as a criterion that the phase spread is small if $\ll\pi$, the phase difference between constructive and destructive interference. This gives:

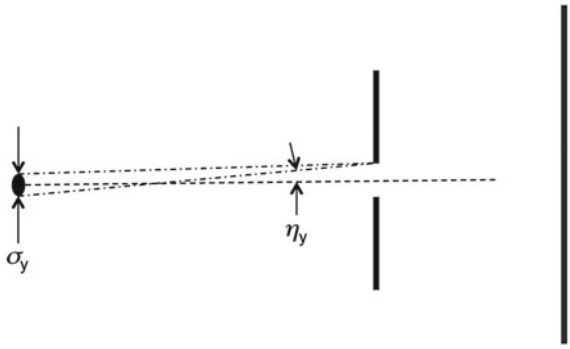


Fig. 2.8 Discussion of lateral coherence

$$(\sigma_y \eta_y) h\nu/(hc) \ll 1/2. \tag{2.13}$$

This conclusion can be interpreted in a slightly different way: only emission angles $\eta_y \ll hc/(2h\nu\sigma_y)$ can contribute to a visible diffraction pattern. Suppose that the overall angular spread of the emission is θ_y: only a fraction $\approx hc/(2h\nu\sigma_y\,\theta_y)$ contributes to a visible diffraction pattern. Taking into account similar arguments for the x-direction, we reach the notion of "fraction of lateral coherent power":

$$C = [hc/(2h\nu)]^2 [1/(\sigma_x \sigma_y \theta_x \theta_y)], \tag{2.14}$$

that characterizes the level of lateral coherence of the source.

Equation (2.14) has two noteworthy aspects. First, the coherent power decreases as the reciprocal square of the photon energy; likewise, (2.12) shows that the longitudinal coherence length decreases as the square of the wavelength. So, all types of coherence are more difficult to achieve at high photon energies, e.g., X-rays, than at lower photon energies like visible or infrared radiation. This explains why coherence and its applications started only nine decades after the discovery of X-rays, whereas for visible light they have been around for centuries.

The second noteworthy aspect is that the geometric factors in the denominator of (2.14) are exactly the same found in the denominator of (2.8), the definition of brightness/brilliance. Thus, the efforts dedicated to the increase of the brightness by improving the geometry also produced, as a second but not secondary result, a boost in lateral coherence.

There exists a natural limitation in the achievable lateral coherence. Figure 2.9 illustrates this point. One could imagine (top) boosting the lateral coherence of a source by using a pinhole. The pinhole becomes the new small-size source, with high lateral coherence although at the expense of a loss of flux.

However, if the pinhole becomes too small (Fig. 2.9, bottom), diffraction effects increase the angular spread. The rule is that the pinhole size times the angular spread cannot be smaller than the wavelength, $\lambda = hc/(h\nu)$; in particular:

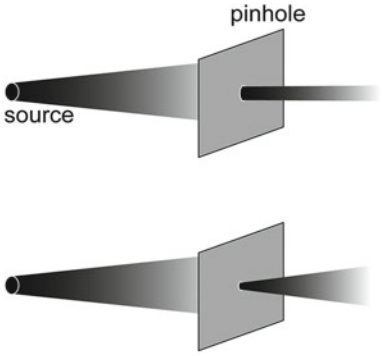


Fig. 2.9 Discussion of the "diffraction limit"

$$\sigma_x \theta_x > hc/(h\nu). \tag{2.15}$$

Equation (2.15) expresses the so-called Abbe's "diffraction limit" [11] and sets a maximum level for lateral coherence. When this limit is reached, the source has full (lateral) coherence. No simple technical improvement can beat the diffraction limit, which is a fundamental optical property.

2.4 Bending Magnets

We will now further analyse the spectral properties of bending magnet emission. The emission spectrum is peaked at the photon energy given by (2.4) and (2.5). We can reconsider the discussion leading to (2.4) from a different point of view. The pulse duration for a single electron, $\delta t \approx r/(2c\gamma^3)$, is also related by the uncertainty principle to the photon energy bandwidth $\Delta h\nu$, so that:

$$\Delta h\nu \approx h\gamma^2 eB/(\pi m_o), \tag{2.16}$$

and therefore the ratio between bandwidth and peak energy equals to unity:

$$\Delta h\nu / h\nu_c \approx 1. \tag{2.17}$$

This reveals that synchrotron radiation from a bending magnet is a broadband emission, including many different photon energies and wavelengths. From it, the desired individual photon energies can be filtered with suitable monochromators.

Without performing a full calculation of the spectral distribution, we can assume as a first approximation (Fig. 2.10, top) a bell-shaped Gaussian-like peak. This approximated lineshape may not be immediately recognizable as similar to the real distribution, for a trivial reason. Traditionally, the bending magnet spectrum is plot-

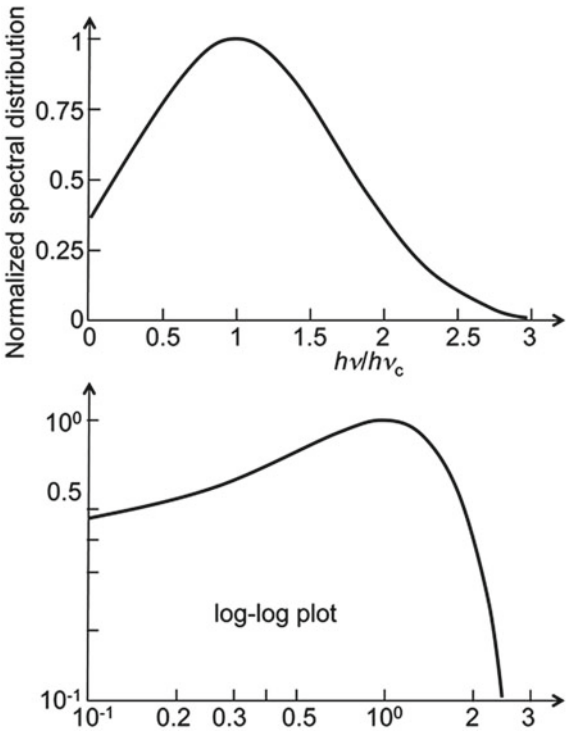


Fig. 2.10 *Top* linear-linear plot of a Gaussian peak, assumed as the approximate lineshape for broadband bending magnet emission. *Bottom* the same curve in a log-log plot is more easily recognizable as similar to the real emitted lineshape

ted not with linear-linear scales but with log-log scales. When plotted in this way (Fig. 2.10, bottom), the similarity between the approximated curve and the real lineshape becomes quite evident.

We already mentioned a parameter that is traditionally used to characterize the bending magnet emission: the critical photon energy $h\nu_{\mathrm{CR}}$. The rigorous theories of the emission demonstrate a direct link between $h\nu_{\mathrm{CR}}$ and the peak photon energy of (2.4) and (2.5):

$$h\nu_{\mathrm{CR}} = (3/4)h\nu_{\mathrm{c}} \approx 3h\gamma^2 eB/(4\pi m_{\mathrm{o}}), \tag{2.18}$$

so that the two parameters are qualitatively equivalent.

2.5 Wigglers

Bending magnets played a major role in the development of synchrotron light research, and are still widely used sources. The reason, of course, is they are automatically available in all storage rings. However, their double function—keeping the electrons in their trajectory and emitting light—limits the flexibility: for example, the peak emitted photon energy is determined by the magnet lattice characteristics rather than by the synchrotron radiation applications.

This stimulated the development of sources entirely dedicated to the emission of light [1], wigglers and undulators. A wiggler, with its periodic series of magnets, is inserted in one of the straight sections of the storage ring. We have already seen that their Lorentz force causes the electrons to "wiggle" in the transverse direction. The motion is thus accelerated and stimulates the emission of synchrotron light.

Each wiggle is practically equivalent to a bending magnet. But, unlike the bending magnets of the storage ring lattice, the magnetic field strength and therefore (2.4, 2.5) the emission peak can be selected to fit the needs of the experiments, e.g., to provide photons of very high energy.

Due to the large amplitude of the "wiggles", the narrow emission cone periodically enters and exists the detector. Thus, the emitted light is observed as a series of short pulses, in contrast to the single pulse from a bending magnet.

Figure 2.11 shows the spectral consequences, related to the Fourier theorem: a single, short bending-magnet pulse (top) corresponds to a broad photon energy bandwidth. The pulses emitted by a wiggler (middle) are also short, and their bandwidth is likewise broad. What changes, therefore, is not the spectral distribution but the overall intensity (and brightness): the wiggler acts indeed as a combination of several bending magnets.

The bottom part of Fig. 2.11 illustrates the case of undulators, with a narrow bandwidth. Let us see its causes.

2.6 Undulators

For wigglers, we assumed that each "wiggle" emits radiation independent of the other wiggles. This is justified by the fact that the wiggles have large amplitude and brings the narrow emission cone in and out of the detector, producing individual light pulses.

Suppose instead that the "wiggles" are weak, specifically that their transverse oscillations keep the emission cone (of amplitude $1/\gamma$) within the detector. The consequence (Fig. 2.11, bottom) is that a single, long pulse replaces the pulse series. The spectral consequence is that the bandwidth narrows and the emission is almost monochromatic: the wiggler becomes an "undulator".

There are other important effects of having weak wiggles. The waves emitted during each "wiggle" can interfere with those emitted during the other wiggles.

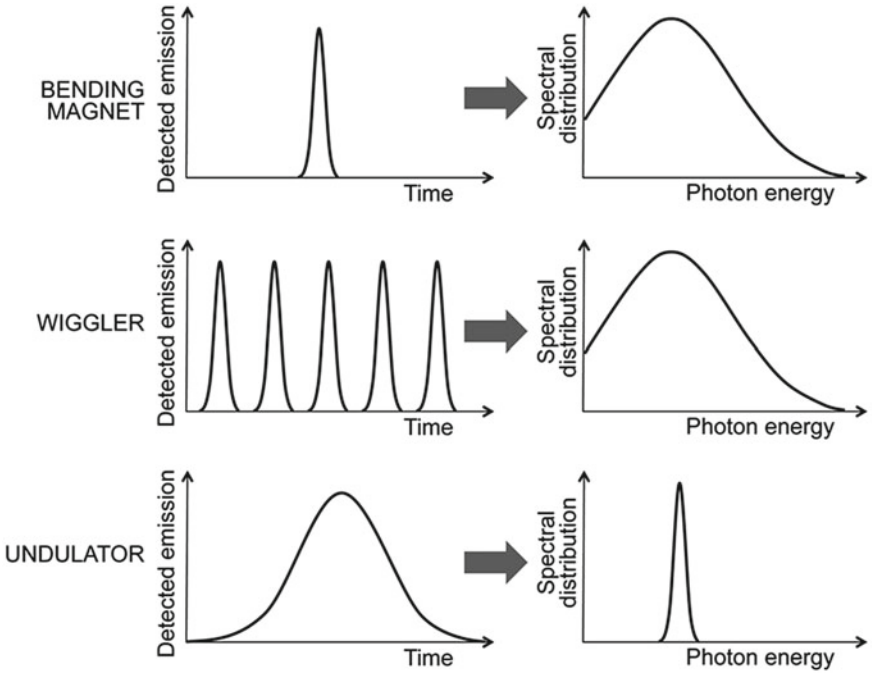


Fig. 2.11 Time structure and its emission spectrum counterpart for different types of sources. *Top* short pulse and broad emission band from a bending magnet. *Middle* series of short pulses from a wiggler, again corresponding to a broad emission band. *Bottom* longer pulse from an undulator and narrower bandwidth

This filters out the wavelengths—and photon energies—for which the interference is not constructive. The emission becomes a narrow band around the peak photon energy $h\nu_c$.

The value of $h\nu_c$ can be easily derived. Assume that the period of the undulator magnets, in the reference frame R of the electron, is P. Constructive interference occurs if P equals an integer number n of wavelengths: the emitted wavelengths in R are given by P/n .

Let us consider only, for the moment, the intense first-order emission of wavelength P. Note that P is *not* the period of the undulator, L_u, as seen in the laboratory reference frame R′. Indeed, the undulator and its period, when observed by the moving electron, are affected by the relativistic Lorentz contraction.

Along the longitudinal direction, the contraction factor is γ. Therefore, the first-order wavelength is L_u/γ in the R reference frame. In the laboratory frame R′, this value is changed by the Doppler effect. Also in the longitudinal direction, the Doppler factor is:

$$[(c+v)/(c-v)]^{1/2} = [(c+v)^2/(c^2-v^2)]^{1/2} = (1+v/c)[1/(1-v^2/c^2)]^{1/2} \approx 2\gamma,$$

and therefore:

$$\text{First-order emitted wavelength} \approx L_u/(2\gamma^2). \tag{2.19}$$

In terms of photon energy, the first-order peak is:

$$h\nu_c \approx 2\gamma^2 hc/L_u. \tag{2.20}$$

Note that the large photon energy is again caused by the γ^2 factor, which in turn is the result of two relativistic effects: here, the Doppler shift and the Lorentz contraction.

The peak photon energy of (2.20) can be also derived with a slightly different approach that reveals additional facets of the undulator mechanism. Referring to Fig. 2.12, when going from the R′-frame to the R-frame the undulator is affected by two important changes. First, as already seen, the Lorentz contraction, from L_u to L_u/γ. Second, the transverse periodic B-field is Lorentz-transformed into the combination of a transverse B-field plus a transverse electric E-field. The two fields have the same period and are perpendicular to each other.

Thus, the moving electron "sees" the undulator as the combination of electric and magnetic fields, both transverse, periodic and in perpendicular directions, traveling at a speed close to the speed of light. This is essentially the description of an electromagnetic wave. This "wave" is backscattered by the electron, producing waves in the opposite direction and with the same wavelength: synchrotron radiation.

The backscattered wave, when seen in the R′-frame (Fig. 2.12, bottom), is subject to the Doppler effect. This produces the wavelength and photon energy of (2.19) and (2.20).

Having derived the emitted peak with a good understanding of the physical mechanisms, we can now deal with other spectral aspects. First, our analysis was so far limited to the first order radiation. But the emission also includes higher harmonics:

$$n\text{th-order emitted wavelength} \approx L_u/(2\gamma^2 n); \tag{2.21}$$

$$h\nu_c \approx 2\gamma^2 hnc/L_u. \tag{2.22}$$

with $n =$ integer. Actually, one can demonstrate that in the longitudinal direction only odd harmonics are emitted, $n = 1, 3, 5, \ldots$.

Let us now consider the spectral distribution around the peak of (2.19) and (2.20). The constructive interference producing the emission peak is similar to that of a diffraction grating. Thus, the emitted peak has a finite bandwidth $\Delta h\nu$, determined by the number of periods in the undulator, N_u:

$$\Delta h\nu/h\nu_c \approx 1/(nN_u). \tag{2.23}$$

Next, we must note that the analysis leading to (2.19)–(2.23) is only valid in the longitudinal direction. Specifically, these equations were derived using the longitudi-

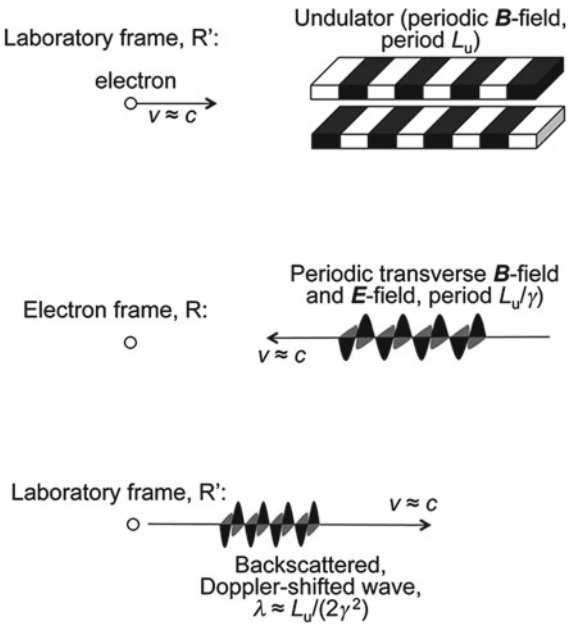


Fig. 2.12 Relativity determines the peak of the undulator emission. *Top* an electron approaches the undulator in the laboratory R′-frame. *Middle* seen in the R-frame of the electron, the undulator period is Lorentz-contracted, and its magnetic field becomes a combination of transverse electric and magnetic field perpendicular to each other, like an electromagnetic wave. *Bottom* the scattering of this "wave" produces synchrotron radiation with a wavelength that is Doppler-shifted in the R′-frame

nal Doppler shift factor 2γ. Suppose instead that the emission is observed at a (small) angle from the longitudinal direction, θ' in the (laboratory) R′-frame (Fig. 2.13, top).

The Doppler factor is not 2γ but $1/[\gamma(1-v\cos\theta'/c)]$. For small angles, $\cos\theta' \approx 1-\theta'^2/2$, and:

$$\begin{aligned}1/[\gamma(1-v\cos\theta'/c)] &\approx 1/[\gamma(1-v/c+(v/c)\theta'^2/2)]\\ &= 1/\{\gamma(1-v/c)[1+(v/c)(\theta'^2/2)/(1-v/c)]\}\\ &= (1+v/c)/\\ &\quad \{\gamma(1-v^2/c^2)[1+(v/c)(1+v/c)(\theta'^2/2)/(1-v^2/c^2)]\}\\ &\approx 2\gamma/(1+\gamma^2\theta'^2)\end{aligned}$$

so that the first-order peak photon energy becomes:

$$h\nu_c \approx 2\gamma^2 hc/[L_u(1+\gamma^2\theta'^2)]. \tag{2.24}$$

This result has an interesting implication: one could harvest different photon energies from an undulator by changing the collection angle. However, the usefulness of this strategy is limited by the sharp decrease in emitted intensity as the angle increases.

In fact, the angular spread of an undulator is even smaller than that of a bending magnet. Let us see why: from (2.24), we realize that the angle between zero and θ' contains photon energies in the bandwidth:

$$\begin{aligned}\Delta h\nu &= 2\gamma^2 hc/L_\mathrm{u} - 2\gamma^2 hc/[L_\mathrm{u}(1+\gamma^2\theta'^2)] \\ &= (2\gamma^2 hc/L_\mathrm{u})[1 - 1/(1+\gamma^2\theta'^2)] \approx (2\gamma^2 hc/L_\mathrm{u})\gamma^2\theta'^2,\end{aligned}$$

corresponding to the relative bandwidth: $\Delta h\nu/(h\nu) \approx \gamma^2\theta'^2$; now, this relative bandwidth cannot exceed the value derived from (2.23), $1/(N_\mathrm{u})$ for $n = 1$. Therefore, $\gamma^2\theta'^2 < 1/(N_\mathrm{u})$, and:

$$\theta' < 1/(\gamma N_\mathrm{u}^{1/2}), \tag{2.25}$$

a value typically much smaller than the standard $1/\gamma$ angular divergence of bending magnet emission.

Finally, we must analyze the dependence of the undulator peak emission on the magnetic field strength. The cause of this dependence, not described by (2.19)–(2.22), is quite simple. The transverse periodic B-field forces the electrons to undulate, i.e., to acquire a transverse component of the velocity. The corresponding Lorentz force, however, cannot do any work—it cannot change the kinetic energy nor the square of the vector velocity. The onset of transverse velocity thus requires a decrease of the longitudinal velocity.

The factor $2\gamma^2$ in (2.19)–(2.22) was derived assuming a longitudinal motion with speed $v \approx c$. The transverse oscillations decrease this factor and the peak photon energy: let us see by how much.

The transverse Newton equation in its relativistic form, assuming z as the longitudinal direction and y as the B-field direction, is:

$$\gamma m_\mathrm{o} \mathrm{d}v_\mathrm{x}/\mathrm{d}t = \text{force} = -eBv_\mathrm{z}; \tag{2.26}$$

for the periodic undulator field strength, we can assume the form $B = B_\mathrm{o}\sin(2\pi z/L_\mathrm{u})$, so that (2.26) becomes:

$$\gamma m_\mathrm{o} \mathrm{d}v_\mathrm{x}/\mathrm{d}t = -eB_\mathrm{o}\sin(2\pi z/L_\mathrm{u})v_\mathrm{z}; \tag{2.27}$$

the solution is $v_\mathrm{x} = v_\mathrm{ox}\cos(2\pi z/L_\mathrm{u})$; inserted in (2.27), this gives:

$$-\gamma m_\mathrm{o} v_\mathrm{ox}\sin(2\pi z/L_\mathrm{u})2\pi v_\mathrm{z}/L_\mathrm{u} = -eB_\mathrm{o}\sin(2\pi z/L_\mathrm{u})v_\mathrm{z}$$

and therefore:

$$v_\mathrm{ox} = eB_\mathrm{o}L_\mathrm{u}/(2\pi\gamma m_\mathrm{o}). \tag{2.28}$$

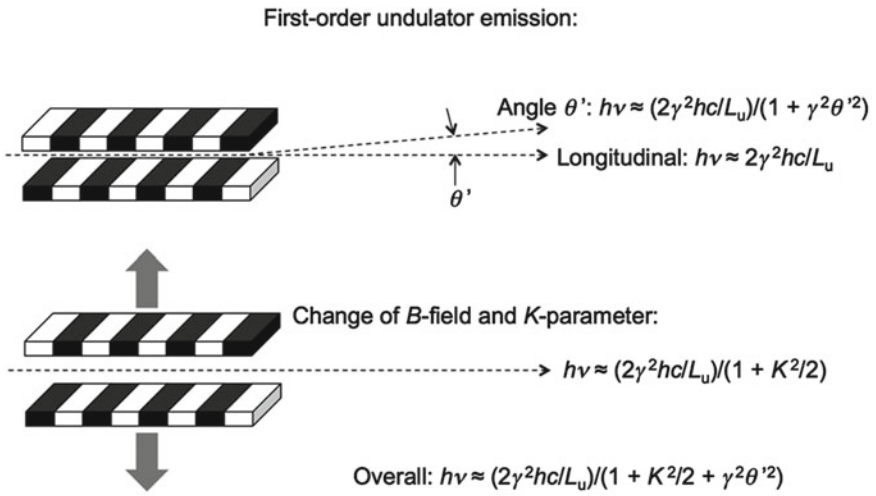


Fig. 2.13 Change in the undulator peak emission with the emission angle (*top*) and with the magnetic field strength, proportional to the undulator parameter. The overall corrected equation is shown at the *bottom*

The average magnitude of $v_x^2 = v_{ox}^2 \cos^2(2\pi z/L_u)$ is $v_{ox}^2/2 = [eB_o L_u/(2\pi\gamma m_o)]^2/2$. We can express this result using the so called "undulator parameter":

$$K = eB_o L_u/(2\pi m_o c), \tag{2.29}$$

so that the average value of $v_x{}^2$ is $c^2K^2/(2\gamma^2)$. We can use this result to calculate the corrected longitudinal $2\gamma^2$ factor, by replacing v^2 with $v^2 - v_x^2$:

$$\begin{aligned}\text{Corrected } 2\gamma^2 \text{ factor} &= 2/[1 - (v^2 - v_x^2)/c^2] \\ &= 2/\{(1 - v^2/c^2)[1 + (v_x^2/c^2)/(1 - v^2/c^2)]\} \\ &= 2\gamma^2/(1 + \gamma^2 v_x^2/c^2),\end{aligned}$$

which is, on the average, $2\gamma^2/(1 + K^2/2)$. Thus, we must correct (2.19)–(2.22) obtaining (Fig. 2.13, bottom):

$$\text{first order: } h\nu_c \approx 2\gamma^2(hc/L_u)/(1 + K^2/2). \tag{2.30}$$

$$n\text{th-order: } h\nu_c \approx 2\gamma^2(hnc/L_u)/(1 + K^2/2). \tag{2.31}$$

These results offer the opportunity to control the peak emission in a way much more interesting than (2.24). Indeed, the K-factor (2.29) is proportional to the B-field strength, and can be modified, for example, by changing the gap of the undulator magnets.

Lastly, one can demonstrate that (2.24), (2.30) and (2.31) can be combined together giving:

$$\text{first order: } h\nu_c \approx 2\gamma^2(hc/L_u)/(1 + K^2/2 + \gamma^2\theta'^2). \tag{2.32}$$

$$n\text{th-order: } h\nu_c \approx 2\gamma^2(hnc/L_u)/(1 + K^2/2 + \gamma^2\theta'^2). \tag{2.33}$$

2.7 Free Electron Lasers

Many properties of synchrotron sources are reminiscent of lasers: high angular collimation, high brightness and monochromaticity (for undulators). We must emphasize, however, that such sources are *not* lasers: their emission mechanism is classical spontaneous emission and their operation does not involve optical amplification.

There exist, however, a laser-like counterpart of synchrotron sources: the "free electron laser" or FEL [12–33]. It has several aspects similar to other types of lasers, but also some unique characteristics. FELs have been developed over a broad spectral range, and infrared FELs have been in operation for decades [20]. Quite recently, the first X-ray FELs or X-FELs were commissioned [34], opening up tremendous new research opportunities in many domains.

The basic ingredient in any kind of laser is optical amplification, the intensity increase with distance of a photon beam. In a standard laser, the mechanism for optical amplification is quantum stimulated emission. The FEL mechanism, instead, is classical but with a relativistic background.

Imagine a bunch of electrons entering an undulator. The electrons start oscillating and emit electromagnetic waves. In addition, a phenomenon occurs that was not previously taken into account: the emitted waves start interacting with the electrons.

This interaction is caused by the transverse *B*-field of the wave and by the transverse electron velocity: together, they produce a longitudinal Lorentz force that slightly shifts the electrons within the bunch. The force is zero only at the nodes of the wave. Therefore, the electrons tend to accumulate at the nodes—actually, at every other node as show in Fig. 2.14 (top).

The electron bunch (macrobunch) becomes in this way a structure consisting of equally spaced microbunches, with a periodicity equal to the wavelength (Fig. 2.14, bottom). Electrons in different microbunches (Fig. 2.15, bottom) emit with the same phase: their waves combine together in a correlated fashion. In this way, the initial wave that triggered the phenomenon is progressively enhanced, i.e., optically amplified.

Note one important difference between standard undulator emission and FEL emission: the dependence on the total number of emitting electrons, *N*. In the first case, the intensities of the waves emitted by individual electrons are combined together (Fig. 2.15, top), and the total intensity is proportional to *N*. For an FEL, as shown Fig. 2.15 (bottom), the wave themselves are combined together. The electric

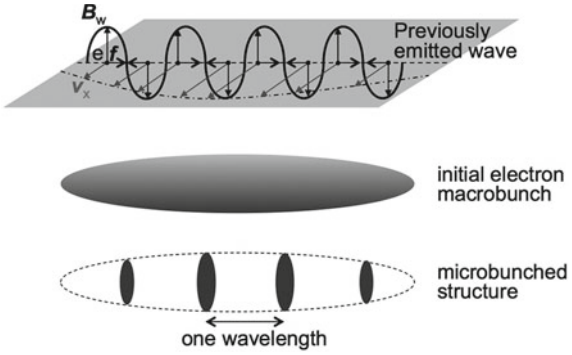


Fig. 2.14 Microbunching mechanism. *Top* the Lorentz force due to the interaction between the transverse *B*-field of previously emitted waves and the transverse velocity of electrons oscillating in an undulator pushes the electrons towards every other node in the wave. In this way, an initially unstructured macrobunch (*middle*) develops a structure (*bottom*) consisting of microbunches with the period of one wavelength

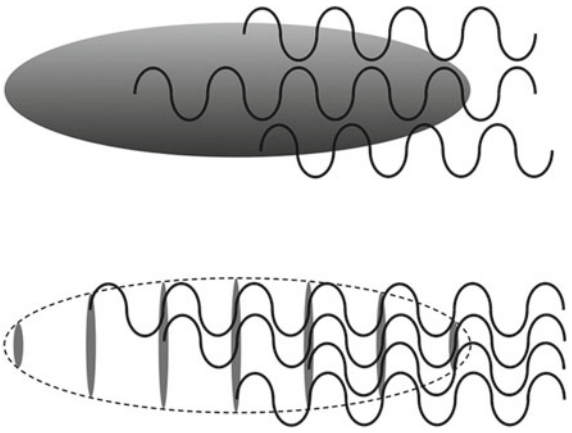


Fig. 2.15 *Top* electrons in an unstructured macrobunch emit radiation in an uncoordinated wave. *Bottom* on the contrary, the emission of electrons in microbunches is correlated

(and magnetic) wave field strength is proportional to N, so the total intensity is proportional to N^2.

One can also realize with semi-qualitative arguments that the optical amplification caused by microbunching leads to an exponential increase of the wave intensity I along the longitudinal direction. First, the Lorentz force cannot do any work and therefore cannot cause the electron-to-wave energy transfer. Therefore, the transfer is caused by the (transverse) wave electric field, of strength E_W. The energy transfer rate is the (negative) work per unit time, $v_x E_W$. Since I is proportional to ${E_W}^2$, this rate is proportional to $I^{1/2}$.

With microbunching, the fraction of electrons that are microbunched increases the wave intensity in a coordinated way as shown in Fig. 2.15 (bottom). Therefore, the rate of energy increase is proportional both to the energy rate transfer for a single electron $v_x E_W$ and to the fraction of microbunched electrons.

Microbunching requires the electrons, on the average, to shift longitudinally by one-half wavelength. We can thus assume that the fraction of microbunched electrons is roughly proportional to the longitudinal displacement Δz divided by the wavelength. We shall see later that Δz is proportional to the longitudinal Doppler force strength, and so is the fraction of microbunched electrons. The Lorentz force strength is given by $eB_W v_x$, where B_W is the wave B-field strength. Since I is proportional to ${B_W}^2$, the fraction of microbunched electrons is proportional to $I^{1/2}$.

Thus, the overall rate of energy increase for the wave is proportional to $I^{1/2} I^{1/2} = I$:

$$dI/dz = AI, \tag{2.34}$$

(A = constant). The solution of (2.34) is an exponential intensity increase, $I = I_o \exp(Az)$. This result is normally expressed in terms of the so-called "gain length" L_G:

$$I = I_o exp(z/L_G). \tag{2.35}$$

2.7.1 The Gain Length

In order to understand the main properties of L_G, we must further analyze the longitudinal shift of electrons that leads to microbunching. The approach can be semi-empirical: since the exponential increase of (2.35) was experimentally verified [34], we can use it as a given fact. This implies that the B-field B_W of the wave at the position z is proportional to $I^{1/2} = {I_o}^{1/2} exp[z/(2L_G)]$.

The longitudinal Lorentz force is proportional to the same factor and to the trasverse electron velocity v_x. Equation (2.28) shows that v_x is proportional to $B_o L_u/\gamma$; thus:

$$\text{Longitudinal force} = \text{constant x} I_o^{1/2}\, exp[z/(2L_G)](B_o L_u/\gamma). \tag{2.36}$$

The small longitudinal displacements Δz that causes microbunching is linked to this force by the relativistic form of Newton's law. This requires the use of the *longitudinal* relativistic mass $\gamma^3 m_o$:

$$\begin{aligned} &\gamma^3 m_o(d^2\Delta z/dt^2) = \text{constant x} I_o^{1/2} exp[z/(2L_G)](B_o L_u/\gamma), \text{ or} \\ &\gamma^3 m_o(d^2\Delta z/dt^2) = \text{constant x} I_o^{1/2}\, exp[vt/(2L_G)](B_o L_u/\gamma). \end{aligned} \tag{2.37}$$

The solution is: Δz = constant x $(1/\gamma^3)(4{L_G}^2/v^2){I_o}^{1/2} exp[vt/(2L_G)](B_o L_u/\gamma)$, which can be written:

$$\Delta z = \text{constant x}(B_o L_u {L_G}^2/\gamma^4) I^{1/2}, \tag{2.38}$$

so that the fraction of microbunched electrons is roughly proportional to: $\Delta z/\lambda =$ constant x $[B_o L_u {L_G}^2/(\gamma^4\,\lambda)]I^{1/2} \approx$ constant x $\{B_o L_u {L_G}^2/[\gamma^4 L_u/(2\gamma^2)]\}I^{1/2}$, thus:

$$\text{fraction of microbunched electrons} \approx \text{constant x}(B_o L_G^2/\gamma^2) I^{1/2}. \tag{2.39}$$

If i is the electron current in the undulator and Σ the electron beam cross section, the contribution of these microbunched electrons to the wave intensity increase is proportional to $(i/\,\Sigma)(B_o {L_G}^2/\gamma^2)I^{1/2}$.

In order to find the electron-to-wave energy transfer rate, we must multiply this result by the energy transfer rate for one electron, $v_x E_W$. Using again (2.28) and the fact that the wave E-field is proportional to $I^{1/2}$, this rate is a constant multiplied by $(B_o L_u/\gamma)I^{1/2}$. The overall energy transfer rate is, therefore: constant x $(i/\Sigma)(B_o {L_G}^2/\gamma^2)I^{1/2}(B_o L_u/\gamma)I^{1/2}$ = constant x $(i/\Sigma)({B_o}^2 {L_G}^2 L_u/\gamma^3)I$, a result consistent with (2.34) and (2.35) if one assumes: L_G = constant x $[(i/\Sigma)({B_o}^2 {L_G}^2 L_u/\gamma^3)]^{-1}$, or ${L_G}^3$ = constant x $(i/\Sigma)^{-1}{B_o}^{-2}{L_u}^{-1}\gamma^3$, which finally gives:

$$L_G = \text{constant x}(i/\Sigma)^{-1/3} B_o^{-2/3} L_u^{-1/3} \gamma. \tag{2.40}$$

Quite often, this result is expressed not in terms of the gain length but of the so-called "Pierce parameter":

$$\rho = L_u/(4\pi 3^{1/2} L_G), \tag{2.41}$$

so that:

$$\rho = \text{constant x}(i/\Sigma)^{1/3} B_o^{2/3} L_u^{4/3} \gamma^{-1}. \tag{2.42}$$

Equations (2.40) and (2.42) constitute one of the central results of FEL theory [12–33]. Although derived here with many approximations, they are consistent with rigorous treatments. Our empirical approach thus enabled us to reveal the physics background of fundamental FEL features.

Specifically, a strong optical amplification requires a short gain length. In turn, we see from (2.40) and (2.42) that this requires large values for the undulator parameters B_o and L_u, a large electron beam current and a small cross section, and a large γ-factor. There is not, however, complete flexibility in tuning these parameters: for example, γ and L_u also determine the emitted photon energy.

2.7.2 Infrared FELs Versus X-FELs

The previous discussion can also clarify the differences between infrared FELs and those working at low wavelengths. Why were these last developed decades after the first? Consider a conventional laser: the medium where optical amplification takes

place is placed in an optical cavity consisting of two mirrors. The photons thus travel back-and-forth and are amplified over several passages.

This same approach is used for infrared FELs, boosting optical amplifications. But not for X-FELs, since the normal-incidence reflectivity at low wavelengths is extremely low. Optical cavities cannot assist optical amplification in X-FELs, and lasing must occur in one passage, with strong enough optical amplification to offset all losses.

This is already a considerable technical challenge, but not the only one: difficulty of microbunching further complicates the situation. This might be puzzling: microbunching requires a longitudinal electron shift of the order of the wavelength, which is much smaller for X-rays than for infrared radiation. Why, then, is microbunching much more difficult for X-FELs?

Equation (2.37) provides the answer: X-FELs require a large γ-factor since the emitted photon energy is proportional to it. But a large γ-factor boosts the longitudinal relativistic mass $\gamma^3 m_o$. The electrons become "heavy", and even a small longitudinal shift is difficult—complicating the realization of X-FELs.

These technical problems required efforts over decades, for example to achieve an excellent electron beam control to decrease the cross section Σ while increasing the beam current i. Such efforts were finally successful and the first X-FELs are operating realities [33], open to real experiments. They notably produce ultrashort (down to a few femtoseconds) X-ray pulses with unprecedented levels of peak brightness. The first experimental results confirm the impact of these sources on many research fields.

2.7.3 The Subtle Effects of Relativity

Our discussion of FEL optical amplification did not yet deal with an important detail. Consider Fig. 2.14, top: this is a snapshot of the situation at a specific time, in which the directions of the transverse velocities and those of the wave B-field are just right to push the electrons towards one-half of the nodes.

However, as the electrons travel along the undulator, their undulation changes the direction of the transverse velocity. Does this reverse the longitudinal Lorentz forces (Fig. 2.16a, b), pushing electrons away from the existing microbunches and towards the other half of the nodes? This would nullify the microbunching mechanism!

Fortunately, the force reversal does not happen. The reason is the small difference between the wave speed, c, and the longitudinal speed of the electrons, v. The microbunching reversal would happen (Fig. 2.16a, b) if the electrons and the waves travelled at the same speed. But they do not: the electrons are slower.

Figure 2.16c and d illustrate this point. Here, Δt is the time necessary for an electron to travel along a distance corresponding to one-half of the undulator period, $L_u/2$—experiencing a reversal of the transverse velocity. Therefore, $\Delta t = L_u/(2v)$. During the same time, the wave travels over a distance $[L_u/(2v)]c$.

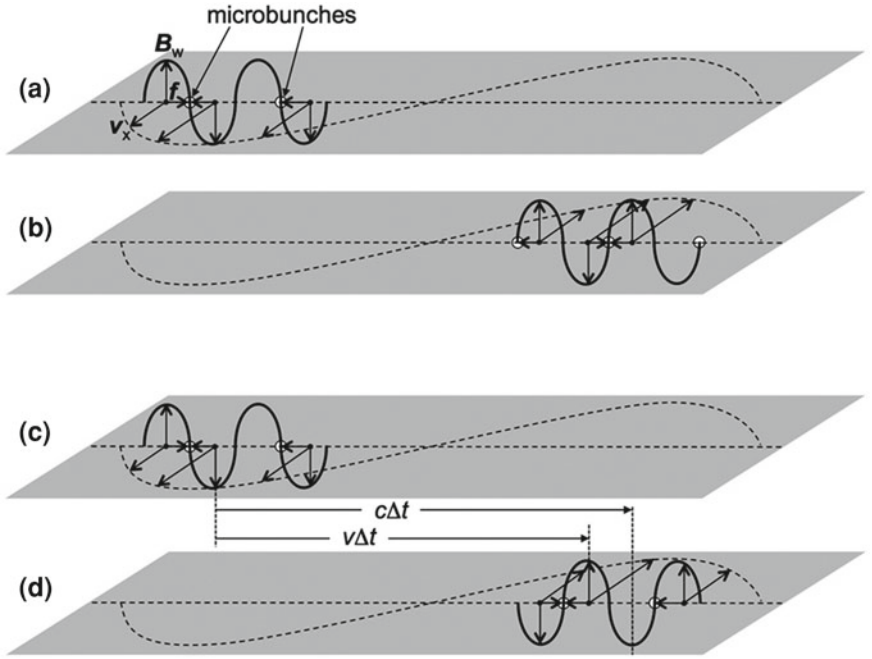


Fig. 2.16 **a** and **b** hypothetic situation in which the transverse undulations of the electrons reverse the directions of the Lorentz forces and change the nodes of the microbunches. This would occur if the electrons traveled at the same speed as the waves. However, **c** and **d**, the two speed are not equal and the shift between electrons and waves is just right, over one transverse oscillation, to keep the Lorentz forces in the same direction ad continue microbunching at the same nodes

The difference between the distances traveled by the wave and by the electron is:

$$\begin{aligned}\delta z &= [L_\mathrm{u}/(2v)]c - L_\mathrm{u}/2 = (L_u/2)(c/v - 1) = (L_\mathrm{u}/2)(c/v)(1 - v/c) \\ &= (L_\mathrm{u}/2)(c/v)(1 - v/c)(1 + v/c)/(1 + v/c) \approx [L_\mathrm{u}/(4\gamma^2)], \text{ thus} \\ \delta z &\approx [L_\mathrm{u}/(4\gamma^2)], \end{aligned} \tag{2.43}$$

i.e., one-half of the peak wavelength of (2.19). Thus, the wave shifts with respect to the electrons precisely as required to reverse the direction of its B-field. As both the transverse velocity and the wave B-field are reversed, the Lorentz forces stays in the same directions—and keep pushing the electrons towards the same microbunches.

2.7.4 Saturation

The previous section illustrates the importance of the phase of the wave with respect to the electron transverse velocity. With the wrong phase, one would have wave-to-electron energy transfer instead of electron-to-wave! We can thus imagine the FEL

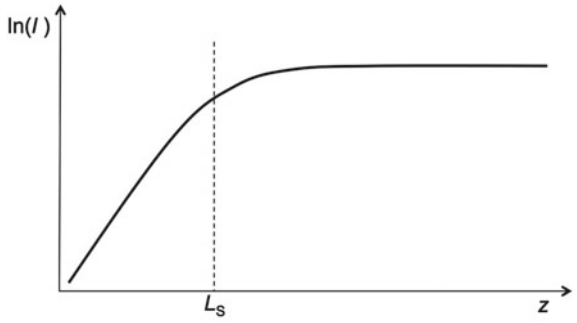


Fig. 2.17 The optical amplification des not continue forever in the undulator, but saturates after a characteristic distance L_s, the "saturation length"

mechanism in the following way. As the electron macrobunch enters the undulator, the first waves are emitted at random. Some of them have the right phase for microbunching and optical amplification, others do not. Those with the right phase are subsequently amplified and dominate the emission.

The optical amplification, however, cannot continue forever along the undulator. As illustrated in Fig. 2.17, after a characteristic distance—the so-called "saturation length" L_s—the amplification saturates: let us see why.

Consider a wave emitted at the beginning of the undulator with the right phase to be amplified. The wave thereafter takes energy from the electrons. This slows down the electrons, so the conditions for the electron-to-wave energy transfer are progressively deteriorated. At a certain point, they are reversed and energy is transferred from the wave to the electrons: this is linked to saturation. The electrons are then accelerated and go back to the conditions for electron-to-wave energy transfer. Then the cycle is repeated: the energy transfer should oscillate from one direction to the opposite and vice-versa.

By how much should the electrons slow down to reverse the energy transfer? In essence, over the path L_s they must longitudinally shift by an additional δz equal to one-half wavelength, $L_u/(4\gamma^2)$. If the longitudinal speed loss over L_s is δv, then δz is of the order of $(\delta v/2)(L_s/v)$, and:

$$(\delta v/v)(L_s/2) \approx L_u/(4\gamma^2); \tag{2.44}$$

on the other hand, since $\gamma(1 - v^2/c^2)^{-1/2}$ and $v = (1 - 1/\gamma^2)^{1/2}c$, $\delta v = [c^2/(v\gamma^3)]\delta\gamma$, which, inserted in (2.44), gives $(c^2/v^2)(L_s/2)(\delta\gamma/\gamma^3) \approx L_u/(4\gamma^2)$, or: $(\delta\gamma/\gamma) \approx L_u/(2L_s)$.

Thus, L_s is proportional to the average percentage loss of relativistic energy γmc^2 by the electron between the arrival in the undulator and saturation; this result is close to that of rigorous theories:

$$(\delta\gamma/\gamma) \approx L_u/L_s. \tag{2.45}$$

Note that the average energy loss per electron, and therefore $\delta\gamma$, are proportional to the total energy taken by the wave until saturation. Therefore, (2.45) also sets this amount of energy. According to (2.35), the same energy is proportional to $\exp(L_s/L_G) - 1 \approx exp(L_s/L_G)$. Thus, (2.35) and (2.45) imply $L_s/L_G =$ constant, or:

$L_s =$ constant x L_G.

A complete and rigorous treatment [13, 14] actually shows that:

$$L_s = 4\pi(3)^{1/2} L_G. \tag{2.46}$$

2.7.5 Seeding

So far, in our qualitative description, the FEL mechanism was activated by the first emitted waves—see Fig. 2.18 (top). The FEL acts as an oscillator and the mechanism is called "self-amplified spontaneous emission" or SASE [17–20].

This approach, however, is affected by major problems. The time structure of the emitted pulse is determined by the random emission of the initial photons that gives the right conditions for amplification. This means that the time structure changes from pulse to pulse. The Fourier transform shows that these fluctuations impact the monochromaticity of the emission and therefore its time coherence.

The middle part of Fig. 2.18 shows an alternate approach: a photon pulse emitted by another source triggers the FEL mechanism. The FEL becomes an "amplifier" rather than a SASE "oscillator". Alternatively, the "seeding" pulse could be obtained by the first part of the FEL itself, after filtering with a monochromator (Fig. 2.18, bottom). After solving many challenging technical problems, X-FELs based on seeding recently became a reality [35].

2.8 Why Are Synchrotron and X-FELs Sources Important?

Synchrotron light research can be traced as far back as a pioneering work of Lienard [36] who conceived the phenomenon the year after the 1897 discovery of the electron by Thompson. Much theoretical work was done in the 1940s, primarily stimulated by the development of accelerators for elementary particle research [37, 38]. And synchrotron light was first detected [39] on April 24, 1947, when this author was an eight months old baby!

Pioneering efforts to use the emission initiated in the two subsequent decades. However, only in 1968 a ground-breaking event really started this domain: Ednor M. Rowe conceived and implemented [40] the revolutionary idea of a storage ring (Tantalus in Wisconsin) entirely dedicated to the use of synchrotron light. Afterwards, the field evolved into a major scientific instrumentation enterprise, with more than

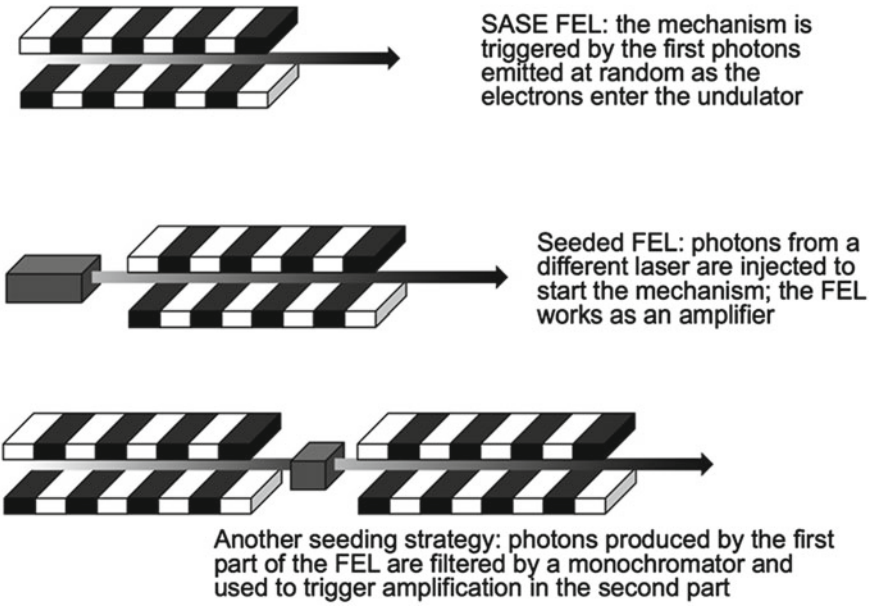


Fig. 2.18 *Top* X-FEL scheme based on the optical amplification of the waves initially emitted by the electrons after they enter the undulator. *Middle* X-FEL based on seeding by an external photon source. *Bottom* Seeding by the first part of the X-FEL

sixty facilities worldwide, one hundred billion dollars of cumulated investments, and more than 10,000 users only in Europe.

What justifies this very broad interest? We can use very general arguments—see Fig. 2.19. In experimental research, one must use "probes". When dealing with atomic-scale objects, such probes can be, for example, electrons, photons or neutrons. As a general rule, the "size" of a probe must be not far from that of the investigated object.

Here, "size" does not only mean the physical size but also the energy and the wavelength. Synchrotron and FEL facilities can provide photons over a very broad spectrum, from hard-X-rays (sub-angstrom wavelengths) to terahertz radiation (sub-millimeter wavelengths). For most of the spectral range, they are the best—and sometimes the only—sources.

So, their importance can be understood by looking at things and properties whose energy or physical sizes are similar to the photons in this broad spectral range. As seen in Fig. 2.19, we find very many important features, from chemical bond lengths to atomic vibrations in solids and molecules.

Many of such features are directly or indirectly related to chemical bonds. For example, valence electrons are directly engaged in bond formation, and core electrons, although not directly participating, have energies affected by bonding. We can

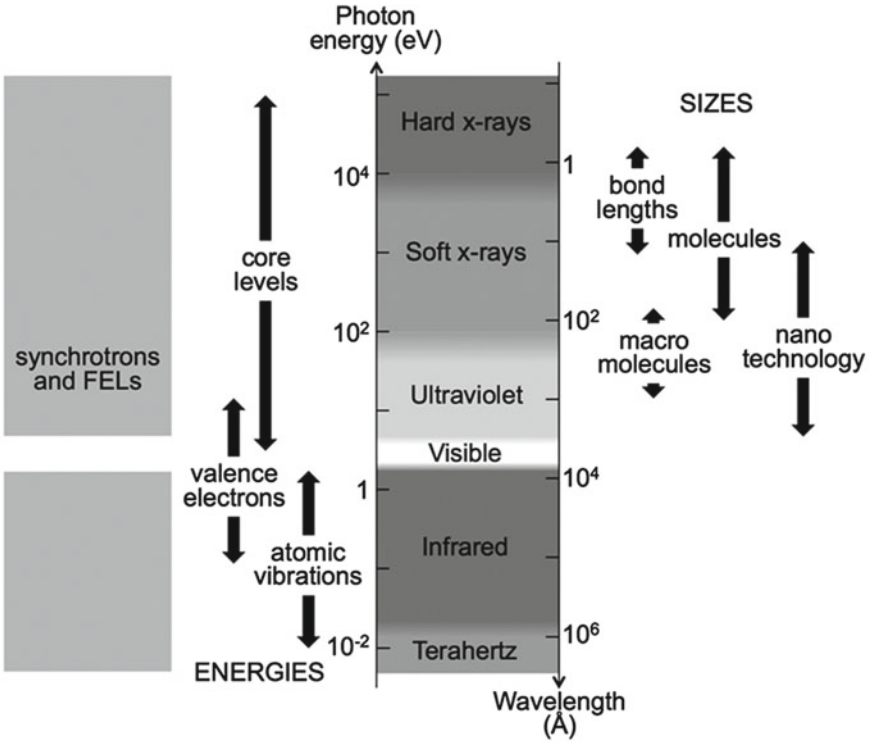


Fig. 2.19 The general interest of synchrotron sources can be understood by looking at the things and properties in nature that have a spatial or energy "size" comparable to the photon energy or wavelength of the emission. One sees many important objects and phenomena, mostly related to chemical bonds

thus conclude that synchrotrons and FELs are excellent tools to investigate properties related to chemical bonds.

In turn, such properties underlie the vast majority of the current and future scientific and technological issues. With the exception of specialized areas like elementary particle physics, most of the research is indeed related to chemical bonds, in diverse areas from chemistry and materials science to biology, environmental research and forensic medicine.

Synchrotron sources are not specialized instruments only serving a focused community, but very versatile facilities useful for most research domains. And the many beamlines of each facility can support in parallel tens of user groups, spreading the operation costs. On the contrary, FELs cannot serve a large number of users in parallel. But like synchrotrons they are very versatile machines, whose usefulness we are currently discovering.

2.9 New Types of Synchrotron-Related Sources

In addition to X-FELs, many efforts are currently dedicated to other novel types of photon sources based on accelerators. These efforts are governed by some general principles, such as the following.

The emitted synchrotron power depends on the square of the particle acceleration and therefore (2.27 and 2.28) strongly decreases as the particle mass increases. The mechanisms work much better for accelerators of light particles like electrons or positrons than for hadron accelerators. That is why all new types of sources are, like the current ones, based on electrons or positrons.

Technical improvements cannot beat the diffraction limit [11], which is now reached by several facilities in a broad spectral range. Further improvements in the brightness/brilliance (2.8) can only come from the flux increase. FELs attack this problem by increasing the peak emitted power by orders of magnitude with respect to standard synchrotron sources.

The electron beam size and angular deviations—that contribute negatively to the brightess/brilliance (2.8)—are to a good extent caused by the emission of synchrotron radiation. The electrons circulating in a storage ring emit photons at random and change their trajectories with respect to one another—increasing the beam cross section. This phenomenon cannot be avoided for storage rings since countermeasures similar to the "stochastic cooling" [41] of hadron accelerators were not developed for electron accelerators. One can solve the problem, however, by using a linear accelerator (LINAC) instead of a closed-loop machine with circulating electrons. Indeed, electrons in a LINAC do not have a previous history of photon emission that impacts the electron beam geometry. But this solution has a very high price, literally: the investment in accelerating an electron beam—for example the cost of the electric power—is used only once instead of feeding continuously the beamlines for days, as in a storage ring. Still, LINACs are the best solution for facilities requiring excellent electron beam characteristics, like the X-FELs.

The new sources developed under these general principles can be analyzed with simple arguments as we did for storage rings and FELs. Consider, for example, the so-called "energy recovery" sources [42]. These are synchrotron facilities based on LINACs that counter the high-cost problem by recovering most of the energy of the accelerated electrons and re-using it. The general features of such machines, for example the emission spectrum, can be understood with simple arguments like those of storage rings.

Inverse Compton scattering facilities [43] are another class of new sources, under development for specialized applications. They rival the brightness of storage rings, but are compact, inexpensive and in principle easy to operate. Such advantages could offset, for many applications, the limited performances.

These sources are based on the inverse Compton scattering of a seeding laser beam by a high-energy electron beam. As illustrated in Fig. 2.20, the incoming photon energy is $h\nu$. This is the value in the R′-frame of the laboratory. Seen in the R-frame of the electrons, it is Doppler-shifted to $\approx 2\gamma h\nu$ in the longitudinal direction.



Fig. 2.20 Scheme of an inverse compton scattering source

The backscattered photon energy does not change in the R-frame. But in the laboratory R′ frame it is again Doppler-shifted by $\approx 2\gamma$, so that:

$$h\nu' \approx 4\gamma^2 h\nu; \tag{2.47}$$

thus, the mechanism increases the photon energy by a very large factor . It can in fact convert a visible or infrared laser beam into an X-ray beam.

2.10 A Few Practical Equations

Before concluding our discussion, we would like to present a few useful equations in practical numerical forms that can be directly used for concrete calculations.

- Equation (2.18) (bending magnet): $h\nu_{CR} = 3h\gamma^2 eB/(4\pi m_o) \approx 0.665 \times$ (electron energy in GeV)$^2 \times$ (B in tesla) [result in keV]
- Equation (2.19) (undulator): First-order emitted wavelength $\approx L_u/(2\gamma^2) \approx 13.06 \times$ (L_u in cm)/ (electron energy in GeV)^2[result in Å]
- Equation (2.20) (undulator): $h\nu_c \approx 2\gamma^2 hc/L_u \approx 0.9496\times$ (electron energy in GeV)^2/(L_u in cm) [result in keV]
- Equation (2.41) (FEL): $\rho = L_u/(4\pi 3^{1/2} L_G) \approx 0.0459\ (L_u/L_G)$
- Equation (2.46) (FEL): $L_s = 4\pi(3)^{1/2}\ L_G \approx 21.8\ L_G$.

We trust that these concrete formulae, as well as the practically oriented spirit of our discussion, coached the reader into a better understanding and effective use of these wonderful facilities.

References

1. G. Margaritondo, *Introduction to Synchrotron Radiation* (Oxford University Press, New York, 1988)
2. G. Margaritondo, *Elements of Synchrotron Light for Biology, Chemistry and Medical Research* (Oxford University Press, New York, 2002)
3. P. Wilmott, *An Introduction to Synchrotron Radiation: Techniques and Applications* (Wiley, New York, 2011)

4. O. Duke, *Synchrotron Radiation: Production and Properties* (Oxford University Press, New York, 2009)
5. A. Hofmann, *The Physics of Synchrotron Radiation* (Cambridge University Press, Cambridge, 2007)
6. G. Margaritondo, A primer in synchrotron radiation: everything you wanted to know about SEX (Synchrotron Emission of X-rays) but were afraid to ask. J. Synchrotron Rad. **2**, 148–154 (1995)
7. E. Karantzoulis, A. Carniel, K. Casarin, S. Ferry, S. Krecic, G. Gaio, F. Giacuzzo, E. Quai, C. Scafuri, G. Tromba, A. Vascotto, L. Zambon, Top-up implementation and operation at ELETTRA, in *Proceedings of IPAC'10*, Kyoto (2010), pp. 2543–2545
8. R.P. Walker, D. Bulfone, B. Diviacco, W. Jark, P. Michelini, L. Tosi, R. Visintini, G. Ingold, F. Schafers, M. Scheer, G. Wustefeld, M. Eriksson, S. Werin, Design of an electromagnetic elliptical wiggler for ELETTRA, in *Proceedings of the 1997 Particle Accelerator Conference*, vol. 3 (1997), pp. 3527–3529
9. C. Bressler, M. Chergui, Molecular structural dynamics probed by ultrafast X-ray absorption spectroscopy. Annual Rev. **61**, 263–282 (2010)
10. G. Margaritondo, Y. Hwu, J.H. Je, Nondestructive characterization by advanced synchrotron light techniques: spectromicroscopy and coherent radiology. Sensors **2008**, 8378–8400 (2008)
11. M. Born, E. Wolf, *Principles of Optics* (Cambridge University Press, Cambridge, 1997)
12. J. Madey, Stimulated emission of bremsstrahlung in a periodic magnetic field. J. Appl. Phys. **42**, 1906–1913 (1971)
13. G. Dattoli, A. Renieri, Free-electron generators of coherent radiation, in *Laser Handbook*, vol. 4, ed. by M.L. Stich, M.S. Bass (North Holland, Amsterdam 1984), p. 2
14. G. Dattoli, A. Renieri, A. Torre, *Lectures in Free-Electron Laser Theory and Related Topics* (World Scientific, Singapore, 1995)
15. B.D. Patterson, R. Abela, H.H. Braun, U. Flechsig, R. Ganter, Y. Kim, E. Kirk, A. Oppelt, M. Pedrozzi, S. Reiche, L. Rivkin, T. Schmidt, B. Shmitt, V.N. Strocov, S. Tsujino, A.F. Wrulich, Coherent science at the SwissFEL X-ray laser. New J. Phys. **12**, 035012 (2010)
16. R. Bonifacio, S. Casagrande, Classical and quantum treatment of amplifier and superradiant free-electron laser dynamics. J. Opt. Soc. Am. B **2**, 250–258 (1985)
17. R. Bonifacio, L. De Salvo, P. Pierini, N. Piovella, C. Pellegrini, Spectrum, temporal structure, and fluctuations in a high-gain free-electron laser starting from noise. Phys. Rev. Lett. **73**, 70–73 (1994)
18. R. Bonifacio, C. Pellegrini, L.M. Narducci, Collective instabilities and high-gain regime in a free electron laser. Opt. Commun. **50**, 373–378 (1984)
19. C. Pellegrini, High power femtosecond pulses from an X-ray SASE-FEL. Nucl. Instrum. Methods Phys. Res. A **445**, 124–127 (2000)
20. P. Rebernik Ribic, G. Margaritondo, Status and prospects of X-ray free-electron lasers (X-FELs): a simple presentation. J. Phys. D **45**, 213001 (2012)
21. G. Margaritondo, P. Rebernik Ribic, A simplified description of X-ray free-electron lasers. J. Synchrotron Radiat **18**, 101–108 (2010)
22. P. Rebernik Ribic, G. Margaritondo, The physics behind free electron lasers (FELs) based on magnetoscatic and optical undulators. Phys. Stat. Sol B **249**, 1210–1217 (2012)
23. C.A. Brau, *Free-Electron Lasers* (Academic Press, Oxford, 1990)
24. K.J. Kim, An analysis of self-amplifield spontaneous emission. Nucl. Instrum. Methods A **250**, 396–403 (1986)
25. K.J. Kim, M. Xie, Self-amplified spontaneous emission for short wavelength coherent radiation. Nucl. Instrum. Methods A **331**, 359–364 (1993)
26. K. Kondratenko, E. Saldin, Generation of coherent radiation by a relativistic electron beam in an ondulator. Part. Accel. **10**, 207–216 (1980)
27. S.V. Milton et al., Exponential gain and saturation of a self-amplified spontaneous emission free-electron laser. Science **292**, 1059955 (2001)
28. P. Schmueser, M. Dohlus, J. Rossbach, *Ultraviolet and Soft-X-ray Free-Electron Lasers* (Springer, Berlin, 2008)

29. J. Feldhaus, J. Arthur, J.B. Hastings, X-ray free-electron lasers. J. Phys. B **38**, S799 (2005)
30. Z. Huang, K.J. Kim, Review of X-ray free-electron laser theory. Phys. Rev. Spec. Top. Accel. Beams **10**, 034801 (2007)
31. T. Shintake, H. Tanaka, T. Hara, K. Togawa, T. Inagaki, Y.J. Kim, T. Ishikawa, H. Kitamura, H. Baba, H. Matsumoto, S. Takeda, M. Yoshida, Y. Takasu, Status of spring-8 compact SASE source FEL project. Nucl. Instrum. Methods A **507**, 382–387 (2003)
32. C.W. Roberson, P. Sprangle, A review of free-electron lasers. Phys. Fluids **B1**, 3–42 (1989)
33. E. Saldin, E. Schneidmiller, M. Yurkov, *The Physics of the Free Electron Laser* (Springer, Berlin, 2000)
34. P. Emma et al., First lasing and operation of an angstrom-wavelength free-electron laser. Nature Photon. **4**, 641–647 (2010)
35. E. Allaria et al., Highly coherent and stable pulses from the FERMI seeded free-electron laser in the extreme ultraviolet. Nature Photon. **6**, 699–704 (2012)
36. J.P. Blewett, Synchrotron radiation: early history. J. Synchrotron Radiat. **5**, 135–139 (1998)
37. D. Ivanenko, I. Pomeranchuk, On the maximum energy attainable in a betatron. Phys. Rev. **65**, 343–343 (1944) (and the references therein)
38. J. Schwinger, On the classical radiation of accelerated electrons. Phys. Rev. **75**, 1912–1925 (1949)
39. F.R. Elder, A.M. Gurewitsch, R.V. Langmuir, H.C. Pollock, Radiation from electrons in a synchrotron. Phys. Rev. **71**, 829–830 (1947)
40. E.M. Rowe, F.E. Mills, Tantalus I: a dedicated storage ring synchrotron radiation source. Part. Accel. **4**, 211–227 (1973)
41. J. Marriner, Stochastic cooling overview. Nucl. Instrum. Methods A **532**, 11–18 (2003)
42. D.H. Bilderback, P. Elleaume, E. Weckert, Review third and next generation synchrotron light sources. J. Phys. B At. Mol. Opt. Phys. **38**, S773–S798 (2005)
43. F.E. Carroll, M.H. Mendenhall, R.H. Traeger, C. Brau, J.W. Waters, Pulsed tunable monochromatic X-ray beams from a compact source: new opportunities. Am. J. Roentgenol. **181**, 1197–1202 (2003)

Chapter 3
Instrumentation at Synchrotron Radiation Beamlines

Giuliana Aquilanti, Lisa Vaccari, Jasper Rikkert Plaisier and Andrea Goldoni

Abstract Today there are a number of third-generation synchrotron facilities around the world, which are dedicated to the production of extremely intense radiation, ranging from infrared to hard X-rays. The wavelength tunability and the very high brightness of these sources have opened a wide range of new characterization procedures for research purposes. This paragraph is intended to describe various facets of both technological and analytical methods using synchrotron radiation, in order to help researchers and students who are interested in the study of materials. First, a concise introduction to synchrotron facilities and an overview of the main characteristics of the existing third-generation sources are presented. Then a basic line-up of beamlines for different energy ranges as well as the problems associated to beamline constructions and choices are described. Finally, for each energy range, a brief description of some techniques available in third-generation synchrotron facilities is given.

3.1 Introduction

When synchrotrons were first developed, their primary purpose was to accelerate particles to study the atomic nucleus, and not specifically designed to generate light. Nowadays only a few of them still used as colliders for high-energy physics

G. Aquilanti · L. Vaccari · J. R. Plaisier · A. Goldoni (✉)
Elettra-Sincrotrone Trieste S.C.p.A, Strada Statale 14-km 163, AREA Science Park 5, 34149 Basovizza, Trieste, Italy
e-mail: Andrea.Goldoni@elettra.eu

G. Aquilanti
e-mail: giuliana.aquilanti@elettra.eu

L. Vaccari
e-mail: lisa.vaccari@elettra.eu

J. R. Plaisier
e-mail: jasper.plaisier@elettra.eu

S. Mobilio et al. (eds.), *Synchrotron Radiation*,
DOI: 10.1007/978-3-642-55315-8_3, © Springer-Verlag Berlin Heidelberg 2015

experiments such as the Large Hadron Collider at CERN, but there are many more synchrotrons dedicated to exploit the special characteristics of the generated light. From the early 1990s machines were designed with insertion devices from scratch. The first such third-generation source, the European Synchrotron Radiation Facility (ESRF) in Grenoble, France, started operating in 1994. Insertion devices (undulators and wigglers) are arrays of magnets placed into the straight sections of the storage ring. They help to create a very bright beam with intensity peaks with a wavelength that can be varied by adjusting the field strength (often the gap between two magnet arrays). The demand for synchrotron light led to the construction of 3rd-generation machines around the world and to constant upgrades of existing ones to provide brighter light, increased user hours and more flexible experimental stations. The modular nature of modern synchrotrons allows new technologies to be incorporated into existing machines. By using powerful linear accelerator technology, fourth-generation sources—known as free-electron lasers (FELs)—can generate shorter, femtosecond pulses with a peak intensity comparable to the one emitted by synchrotron sources in one second, therefore producing X-rays that are millions of times brighter in each pulse. FELs are complementary to third-generation machines, enabling studies requiring very high peak brightness.

There are now more than 50 dedicated light sources in the world, both of second- and third-generation. They cover a wide spectral (frequency) range from infrared to the hard X-rays. The emitted light is characterized by high brightness, many orders of magnitude brighter than conventional sources. The light is highly polarized, tunable, collimated (consisting of almost parallel rays). These machines support a huge range of applications, from condensed matter physics to structural biology, environmental science and cultural heritage.

As shown in Table 3.1 the majority of 3rd generation sources operate with electron beam in the medium-energy range (2–4 GeV). Only a few of 3rd generation synchrotrons are optimized to work in the high-energy range of electron beams (6–8 GeV) in order to produce high intensity X-rays in 10–50 keV range (ESRF, PETRA III, Spring8, APS). Since many X-ray diffraction studies are performed in the range up to 20 keV, the medium-energy machines may be competitive with the high-energy ones in many areas of science, against a fraction of their costs. On the other hand, at a photon energy of 10 keV, medium-energy sources typically have an order of magnitude smaller brilliance than, e.g., ESRF. In the soft X-ray range, however, they are of course superior in performance.

Nowadays, many 3rd generation synchrotrons operate in top-up mode. Small injections at relatively short intervals compensate for the loss of electron current. A constant current in the storage ring gives rise to a constant heat load on the ring chamber including the electron optical elements along its circumference. This in turn has been shown to lead to an exceptionally high position stability of the beam. A constant temperature in the ring tunnel within 0.1 °C and a stable mounting of the magnets of the ring lattice onto girders with a positioning accuracy of ca 30 mm are also essential for obtaining high level of stability. Important for beam stability and essential for top-up injection is the use of a full-energy injector. At the Elettra synchrotron, full-energy injection is achieved through the use of a booster that is

Table 3.1 Third generation sources in operation and under construction

Light sources	Energy (GeV)	Current (mA)	Emittance (μm rad)	Ring (m)	Linear sections	Web site www.
ESRF	6.0	200	4.0	844.4	32	www.esrf.eu
APS	7.0	100	3.0	1104	40	www.aps.anl.gov
SPring-8	8.0	100	3.4	1436	48	www.spring8.or.jp
ALS	1.9	400	6.3	196.8	12	www.als.lbl.gov
TLS	1.5	240	25	120	6	www.nsrrc.org.tw
Elettra	2–2.4	300–170	7.0	259	12	www.elettra.eu
PLS	2.5	200	12.0	280.6	12	www.paleng.postech.ac.kr
LNLS	1.37	250	100	93.2	6	www.lnls.cnpem.br
MAX-II	1.5	280	9.0	90	10	www.maxlab.lu.se
BESSY-II	1.7	200	6.1	240	16	www.helmholtz-berlin.de/zentrum/grossgeraete/elektronenspeicherring
Siberia-II	2.5	200	98	124	12	www.ssrc.inp.nsk.su
New SUBARU	1.5	500	38	119	6	www.lasti.u-hyogo.ac.jp
SLS	2.4	400	5	288	12	www.psi.ch/sls
ANKA	2.5	200	50	110.4	8	www.anka.kit.edu
CLS	2.9	300	22.7	171	12	www.lightsource.ca
SPEAR-3	3.0	500	18	234	18	www.ssrl.slac.stanford.edu/spear3
SAGA-LS	1.4	300	7.5	75.6	8	www.saga-ls.jp
SOLEIL	2.75	500	3.75	354	24	www.synchrotron-soleil.fr
Diamond	3.0	300	2.7	561.6	24	www.diamond.ac.uk
ASP	3.0	200	10	216	14	www.synchrotron.org.au

(continued)

Table 3.1 (Continued)

Light sources	Energy (GeV)	Current (mA)	Emittance (μm rad)	Ring (m)	Linear sections	Web site www.
Indus II	2.5	300	58.1	172.5	8	www.cat.ernet.in/technology/accel/indus
SSRF	3.5	300	3.9	432	20	www.ssrf.sinap.ac.cn
ALBA	3.0	400	4.3	269	24	www.cells.es
PETRA III	6.0	100	1.0	2304	20	www.petra3.desy.de
PLS-II	3.0	400	5.8	280	24	www.paleng.postech.ac.kr
TPS	3.0	400	1.7	518	24	www.nsrrc.org.tw
NSLS-II	3.0	500	1.5	792	30	www.bnl.gov/ps/nsls2
SESAME	2.5	400	26	133	16	www.sesame.org.jo
CANDLE	3.0	350	8.1	216	16	www.candle.am
MAX IV Two rings	1.5–3	500	5.6/0.24	96/528	12/20	www.maxlab.lu.se/maxiv

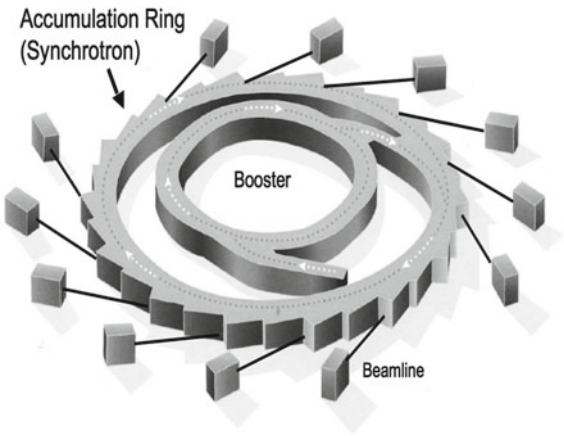


Fig. 3.1 General scheme of a 3rd generation synchrotron, with booster and beamlines tangent to the circumference

installed in the same tunnel of and concentric to the storage ring. The booster provides a low emittance, resulting in a good matching to the ring acceptance and hence a high injection efficiency in the top-up mode.

Considering the insertion devices, there is a trend toward the use of undulators instead of wigglers. Anyway, for certain techniques, like X-ray absorption spectroscopy, the use of sources with a large energy range emission may be preferred.

The experimental configurations of different synchrotron facilities are quite similar (see Fig. 3.1). The storage rings where the light is generated have many ports, each of them opening onto a beamline. Here scientists set up their experiments and collect data. Beamlines are built tangentially to the electron beam orbit of the storage ring and capture the radiation emitted from bending magnets, wigglers or undulators. The beamlines, however, have optical schemes that depend on the experimental methods they are used for.

It has to be highlighted that the precise missions of the beamlines are likely to evolve accordingly to their scientific goals and their capabilities will be continuously improved by the synergic interactions with the user community. The following pages offer a brief description of instruments available in different beamlines depending on the working energy and techniques. In general, standard beamline components that are addressed in this section consist of filters, slits, photon shutters, monochromators, and mirrors. Of these components, the monochromators and mirrors have the greatest importance, complexity, and cost, so more effort will be dedicated in describing these latter components.

3.2 Beamlines in the Hard X-Ray Range (2000–50000 eV)

A synchrotron beamline can be divided in two main parts: the optical section and the experimental station. In the next paragraphs the typical optical instrumentation for a beamline designed to work in the hard X-ray range will be discussed. We will

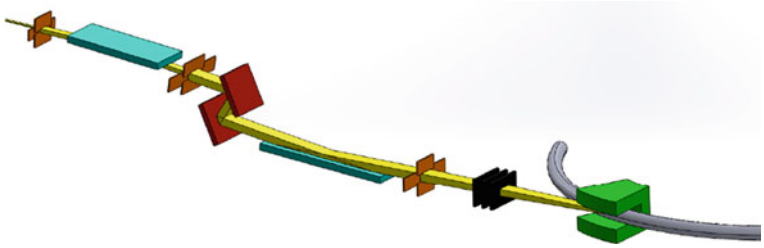


Fig. 3.2 Schematic overview of the optics of a typical beamline operating in the hard X-ray range

briefly show the most common systems to detect hard X-rays, and finally we will give the description of two beamlines operating at the Elettra synchrotron dedicated to X-ray diffraction and X-ray absorption spectroscopy respectively.

3.2.1 Hard X-Ray Optics

A typical optical scheme for a beamline working in the hard X-ray range is shown in Fig. 3.2.

Low absorbing windows (typically beryllium or polymeric windows) along a beamline are used to separate different vacuum sections. Very often a window is installed just after the front end to separate the beamline vacuum from the machine vacuum. Windows are also used to absorb a significant fraction of the unused low-energy radiation, therefore reducing the overall power delivered to the downstream components. The windows can be protected to prevent thermal failures and additional attenuator packages may be used to further manage the power load on the optical components. Filters and windows effectively establish the lower limit of the energy range of a beamline. Slits are also present along the beamline. These are used to define the size of the beam. They are set to accept the beam horizontally and vertically according to the specification of the optics. Slits are also used also to eliminate spurious beam scattered from the optics.

X-ray mirrors are used both as high-energy cut-off filters to remove unwanted higher order harmonics delivered by the monochromators and as focusing devices. In addition, they reduce the power load on the more delicate single crystal monochromators present along the beamline.

When used as high-energy cut-off, specular reflection must be taken into account. This is related to the index of refraction n, given in the X-ray regime, by Parrat [1]:

$$n = (1 - \delta) - i\beta$$

where the quantities δ and β are related to dispersive and absorptive nature of the materials. As the index of refraction is less than unity, X-rays incident on a material

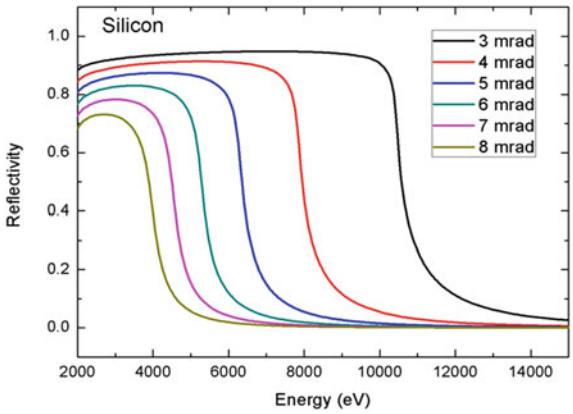


Fig. 3.3 Reflectivity of Silicon as a function of energy for different glancing angles

are totally reflected if the glancing angle θ is less than the critical angle θ_c. Otherwise, they are absorbed by the material. From Snell's law:

$$\theta_c = \sqrt{2\delta}$$

in the absence of absorption edges. θ_c, for usual mirror materials, is in the order of milliradiants, e.g. $\theta_c = 5.1$ mrad for α-quartz silica and $\theta_c = 10$ mrad for gold at $\lambda = 1.54$ Å. The mirror reflectivity ρ as a function of angle (or energy) is a step-like function, the step occurring at the critical angle (or energy). Figure 3.3 shows the reflectivity of Si (density: 2.33 mg/cm^3) at different glancing angles. Typical substrate materials are Si and/or SiO_2. Coating materials are Pt, Rh, Ni, Au depending on the energy, reflectivity and absorption edges.

Because of such small glancing angles, the X-ray mirrors may be connected to a feedback system with a beam position monitor close to the experiment. In this way small variations in the beam position can automatically be adjusted by repositioning the mirror.

The second application of X-ray mirrors is to collimate or to focus the beam onto the following optical element or the sample. The efficiency of collimation/focusing is determined by aberrations and by the mirror imperfections such as micro-roughness and slope errors. The best conditions are obtained with an elliptical or parabolic shape of the mirror surface although, very often, these shapes are approximated by spheres or cylinders. Mirrors can also be bent dynamically in meridional direction for adjusting the curvature when changing the glancing angle, for correcting deformation arising from gravitation and thermal load and to obtain a parallel, focused or divergent beam on the sample depending on the nature of the experiment. A dynamical sagittal focusing is also possible. Figure 3.4 shows a drawing of a toroidal mirror, which is curved in both meridional and sagittal directions.

When the mirror is used as the first optical element in the beamline, problems related to radiation damage and thermal gradients arise. These create strains, which

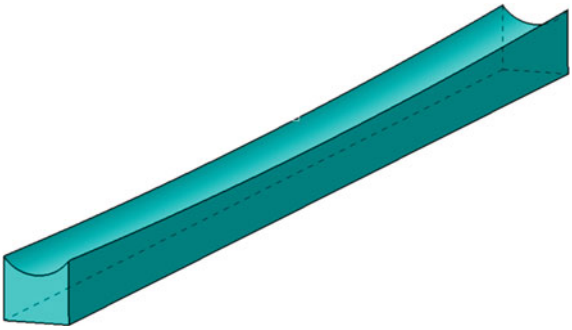


Fig. 3.4 Drawing of a toroidal X-ray mirror. Both meridional and sagittal curvatures are visible

deform the surface and degrade mirror performances. Nonetheless, the X-ray mirrors have the advantage that the heat and the radiation are spread over a large surface because the reflection angle is very small. Typical length for X-ray mirrors is 1 m with radius of curvature of the order of kilometers and centimeters in the meridional and sagittal directions respectively.

Contrary to laboratory X-ray sources, synchrotron sources as bending magnets and wigglers produce a broad spectrum of wavelengths. In the hard X-ray regime single crystal monochromators are employed to monochromatize the X-ray beam. The role of the monochromators is to deliver an X-ray beam with a high monochromaticity with an energy resolution $\Delta E/E \leq 10^{-4}$ for the most common applications and high intensity of reflection. In X-ray monochromators, diffraction from perfect crystals (typically silicon, germanium, diamond) is used to monochromatize the beam. The condition for X-ray diffraction is expressed by Bragg's law:

$$2d \sin \theta = n\lambda$$

where d is the spacing of crystal lattice planes, λ is the wavelength and θ is the incident angle. The integer n denotes the reflection order, and thus wavelengths λ, $\lambda/2$, $\lambda/3$, …, λ/n are diffracted simultaneously as far as the reflections are not forbidden by the crystal structure. For instance, in the case of Si, the structure factor of the second order reflection is zero, but the third-order reflection might be present. In practice, this means that when selecting, for instance a photon energy of 7 keV, photons with an energy of 21 keV will be present as well. Since $\sin \theta$ is less than one, a set of Bragg planes does not reflect wavelengths longer than $2d$. Therefore long wavelengths require large interplanar spacing. On the other hand, excessively large d spacing causes the Bragg angle to be inconveniently small, leading to degraded separation of the reflected beam from the scattered radiation. In the ideal case, the d spacing of the crystal of the monochromator must match the wavelength to be selected.

As mentioned above, an important property of a monochromator is the energy resolution. In the differential form of the Bragg equation

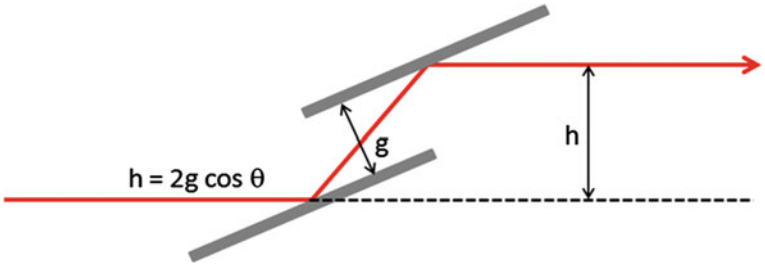


Fig. 3.5 Principle of a double crystal monochromator

$$\frac{\Delta E}{E} = \frac{\Delta\lambda}{\lambda} = \Delta\theta \cot\theta_B$$

the energy resolution is determined by the angular spread $\Delta\theta$ and the Bragg angle θ_B. In fact, within the dynamical diffraction theory [2] that describes the diffraction processes inside a perfect crystal, the intrinsic angular width of diffraction ω (Darwin width) must be taken into account, and therefore the energy resolution becomes

$$\frac{\Delta E}{E} = \cot\theta_B \sqrt{\omega^2 + \Delta\theta^2}$$

where ω is proportional to $\tan\theta_B$.$\Delta\theta$ depends on the geometry of the experiment. It is determined by the angular width of the beam upstream the monochomator and therefore by the angular width of the source to tan coupled with the preceding optics and distance to the source and on the perfection of the crystal. Crystals with imperfections have reflection widths much larger than perfect crystals. Assuming a perfect crystal such as, for instance Si(111) and a perfectly parallel beam, $\omega = 2.66 \times 10^{-5}$ rad at 10 keV and $\frac{\Delta E}{E} = \omega \cot\theta_B = 2.66 \times 10^{-5} \cot(11.4°) = 1.32 \times 10^{-4}$. Another important property of a monochromator is the intensity of reflection. There are two relevant quantities that must be distinguished: the reflectivity, i.e. the height of the Darwin width, and the integral reflecting power, i.e. the area under the Darwin width. The intensity of the reflected beam is determined by the latter when the angular spread of the incident beam is much larger than the Darwin width. Both the quantities are affected by crystal quality.

The standard method to obtain monochromatic X-rays of desired properties is to use multiple Bragg reflections. A double crystal monochromator with two parallel crystals produces a monochromatic beam running parallel to incident white X-ray beam. The scheme of a double crystal monochromator is shown in Fig. 3.5.

The whole system is mechanically designed in order to rotate the pair of crystals to change the incident angle corresponding to a given energy. While the direction of the incident and exit beam is the same, the vertical offset $\boldsymbol{h}$ between the incident and the exit beam changes with energy according to the relation

$$\boldsymbol{h} = 2g\cos\theta$$

where g is the distance between the two crystals and θ is the Bragg angle. The obvious way to minimize the changes of $\boldsymbol{h}$ with θ is to make the width of the channel g as small as possible. In order to make the position of the exit beam independent of θ, it is necessary that

$$g \sim \frac{1}{\cos\theta}$$

Energy variation is obtained by rotating the whole two-crystal assembly around a common axis. In such geometry, the reflectivity of the system is given by the convolution of the Darwin widths of the two crystals leading to a rapid falling off the tail intensity. In order to obtain monochromatic radiation with the maximum possible intensity an accurate parallelism between the two crystals is necessary. The constraints on the parallelism of the first and second crystals are determined by the angular emittance of the source and acceptance of the crystal used and is typically of the order of sub-μ rad. Generally a fine mechanical adjustment of the parallelism of one crystal with respect to the other is possible through a piezoelectrically controlled feedback circuit. Other conditions for the alignment of a double crystal monochromator are the parallelism normal to the scattering plane and to the rotating axis, which should be both better than 10^{-3}–10^{-4} rad. A kind of double crystal monochoromators are monolithic or grooved channel cut monochromators [3], having the additional advantage that both diffracting parts of the monochromator are naturally aligned. Double crystal monochromators in which rotation is the only movement, coupled with opportune mechanics and data acquisition strategies, can be successfully used for QEXAFS application i.e. EXAFS measurements in the subsecond regime implying an oscillation of the Bragg angle with up to 100 Hz in the EXAFS range [4–7].

A particular case of double crystal monochromators are the fixed exit double crystal monochromators, where not only the output direction is constant and parallel to the incident beam direction, but also the vertical beam position (offset) as the energy is varied [8–11]. To obtain the fixed exit monochromatic beam, the spacing between the two crystals is made dependent upon the Bragg incidence angle through a translation of one of the two crystals. A number of different schemes have been developed to realize fixed exit double crystal monochromators, such as those based on single or double cams. Figure 3.6 shows the double cam fixed exit double crystal monochromator from Kohzu (Japan) installed at the XAFS beamline at Elettra synchrotron source.

A different way to achieve the fixed exit of the monochromatic beam is given by the four bounce monochromators [12–16].

Moving one of the crystals slightly away from perfect parallelism can be used to reduce higher order energies that obey Bragg's law. As the Darwin width for higher energies is narrower, the lower energy selected by the first crystal is still within the Darwin width of the detuned crystal and therefore gets diffracted. For the higher order energies, on the other hand, the angle is now just outside the Darwin width, and therefore the photons are absorbed. For instance, in the case of silicon a misalignement of $\Delta\theta = 12\,\mu$rad produces 70 % of peak intensity for fundamental

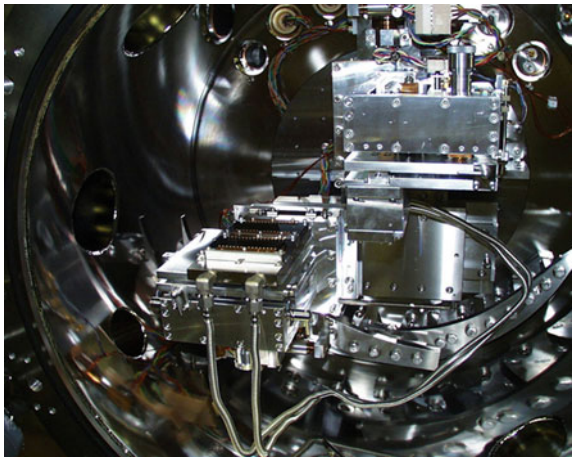


Fig. 3.6 Picture of the interior of the monochromator installed at the XAFS beamline at Elettra

reflection 111 at 10 keV and 0.3 % of peak for 3rd harmonic 333 reflection at 30 keV. A more efficient way to eliminate this issue is to use X-ray mirrors as high energy cut–off filters as discussed above.

In addition, the crystals of the monochromator can also be used to provide sagittal focusing. For this purpose bendable crystals have been developed. The crystal is mounted on a bending device in order to change the curvature of the crystal. As the angle of diffraction depends on the selected energy, also the curvature of the second crystal depends on the wavelength of the X-rays. A second bendable crystal, as the one installed on the MCX beamline at Elettra, has many degrees of freedom and as a consequence many remotely controlled movements. The number of degrees of freedom and the quality of the bending mechanism and the crystal results in a procedure for changing the energy that is not always straightforward [17].

As opposed to X-ray mirrors, crystals deflect at large angles, therefore they may be used to construct branchlines allowing photons to arrive at an alternative experimental station. Figure 3.7 shows a scheme of the SAXS beamline at Elettra [18]. The beamline uses the same source, a 57-pole wiggler, as the XRD1 beamline. The first crystal of the monochromator of SAXS intercepts a part of the beam. The remaining part of the beam continues its path indicated by the dotted line in Fig. 3.7 and goes to the optical and experimental sections of the XRD1 beamline. The part that is diffracted by the crystal finds a second parallel crystal one floor higher. After diffraction at the second crystal the beam continues a path that is parallel to the incoming beam, but several meters higher. As the difference in height between the first and second crystal is large, it is not practical to have a translating second crystal. In the case of the SAXS beamline, three different second crystals are installed, each at a specific position and at a specific angle. In this way three different energies can be selected for the experiment by changing the angle of the first crystal.

In general branch lines are often constructed with one crystal that partially intercepts the beam. When the beam is diffracted in the horizontal plane, usually a second

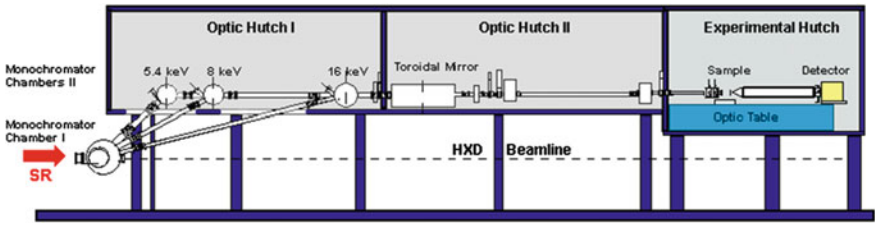


Fig. 3.7 Schematic representation of the SAXS beamline at Elettra

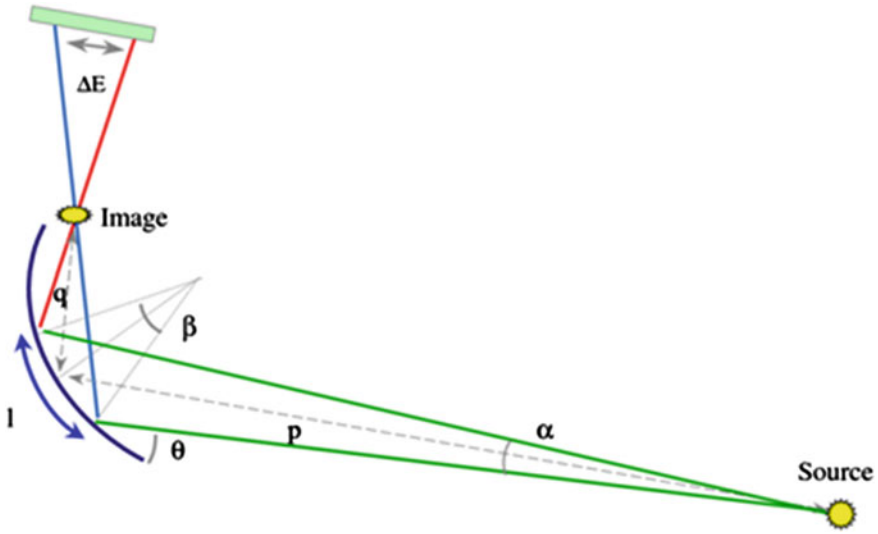


Fig. 3.8 Geometrical arrangement of the energy dispersive optics

crystal is omitted. The consequence of this is that the branch line has to work at a fixed energy, as changing the energy would imply having to move the branchline.

Besides double-crystal monochromators selecting one specific wavelength according to the incident angle, a single crystal polychromator can be used for X-ray to disperse different energies at different directions similarly to prisms for visible light. The geometrical arrangement of the energy dispersive optics is given in Fig. 3.8.

A quasi-parallel and polychromatic beam, supplied by a synchrotron radiation source, is energy dispersed and focused by an elliptically curved crystal. Because the incident X-rays strike the crystal at slightly different angles along its length, the bent crystal acts as a polychromator diffracting a different energy at each point. This energy-dispersed beam converges to a focus at the sample position. The beam, transmitted through the sample position, then diverges towards a position sensitive detector. The position of the beam, incident in the detector, can be directly correlated to energy. Considering a cylindrically bent crystal, which is a good approximation for an ellipse, the source to crystal distance p is large compared to the radius of

curvature R of the crystal. R is related to the source to crystal distance p, crystal to focal point q, and bragg angle θ for the central X-ray beam, through the equation of cylindrical optics:

$$\frac{1}{q} + \frac{1}{p} = \frac{2}{R \sin \theta_B}$$

The angular dispersion $\Delta\theta$ is:

$$\Delta\theta = \beta - \alpha = \frac{l}{R} - \frac{l \sin \theta_B}{p}$$

where l is the illuminated length of the crystal. The diffracted energy range is given by

$$\Delta E = E_H - E_L = E_0 \cot\theta \, \Delta\theta = E_0 \cot\theta \left(\frac{l}{R} - \frac{l \sin \theta_B}{p} \right)$$

where E_H and E_L are the highest and the lowest energies respectively, E_0 is the energy of the central beam.

Examples of dispersive EXAFS spectrometer are ID24 at the ESRF [19] and ODE beamline at SOLEIL [20].

3.2.2 X-Ray Detectors

One of the fundamental elements of the experimental station is the X-ray detector. Various types of X-ray detectors exist and the best choice is a trade-off between the nature of the experiment and the merits of different technological approaches. X-ray detectors can be either photon counting or integrating. Photon-counting detectors measure each individual X-ray photon separately, while integrating detectors measure the total amount of energy deposited in the active region of the detector. In general the detectors can be divided into three classes: (i) 1D detectors (or point detectors), (ii) position sensitive detectors, and (iii) energy dispersive detectors. The latter provide information on the energies of the detected X-rays. The position sensitive detectors give spatial information and the 1D detectors only give information on the X-ray flux. The field of X-ray detection is large and merits a chapter of its own. Here we will discuss the most important characteristics of detectors and give just one example of each type.

The parameters that are of universal applicability and permit the comparison of different detection systems are:

1. *Wavelength range*. The long wavelength limit is set by the minimum photon energy required to produce an event, while the short wavelength limit is typically set by the transmission of the window or protective coating of the detector.
2. *Detective Quantum efficiency (DQE)* defined as

$$(\text{signal}_{\text{out}}/\text{noise}_{\text{out}})^2/(\text{signal}_{\text{in}}/\text{noise}_{\text{in}})^2.$$

3. *Noise*. Fluctuations of the detected signal by different elements within the detector system limit the minimum-detectable signal level. Some of the more important sources of noise are:
    a. *Photon noise*. The number of photons arriving at a detector in a given time interval is subject to statistical fluctuations. If the number is N, then the standard deviation will be $\sqrt{N}$.
    b. *Dark noise.* It is given by the signal in absence of incident radiation. The dark noise is subject to the same statistical fluctuations as the signal from the incident photons. The *dark* si*gnal fluct*uations contribute to the overall noise of the system and may be a serious limitation at very low signal levels.
4. *Dynamic range*. It is expressed as the ratio of the maximum signal that can be measured before the onset of saturation effects, to the root mean square value of the intrinsic noise of the detector. The intrinsic detector noise is that corresponding to noise events which are registered as true signal events. A certain 'dead time' is associated with the detection of each event, and at high count rate, lost events results in non-linearity of response. In this case the detector is said to have reached saturation.
5. *Spatial resolution*. The ability of the detector to identify the position of arrival of the detected photons.
6. *Temporal resolution*. The ability of the detector to determine the time-of-arrival of the detected photons.
7. *Environmental requirements*. Special requirements needed for the correct operation of the detector (e.g. cooling, high vacuum, shielding from external magnetic fields).

One example of point detector is the ionization chamber in which a photon with energy greater than the ionization threshold is absorbed in the gas, producing an electron-ion pair. The overall detection efficiency will be a function of the quantum yield of the gas at a given photon energy, the number of photons absorbed in the total path length of the gas chamber, and the transmittance of the window material. The number of photons absorbed is defined by the Lambert-Beer law as:

$$N = I(1 - e^{-\sigma \varrho L})$$

where I is the intensity of radiation in the chamber (photons/s); L is the length of the chamber (cm); ρ is the density of atoms and molecules (cm^{-3}): and σ is the absorption cross section of the gas (cm^2). The number of electron-ion pair n produced is:

$$n = I_0 T \gamma (1 - e^{-\sigma \varrho L})$$

where I_0 is the intensity of the incident radiation, T is the transmittance of the window material, and γ is the photoionization yield of the gas. If a high voltage is applied to

the ionization chamber, than the primary electron gains sufficient energy during its transit through the gas to cause a secondary ionization. Under these conditions, the output current is amplified.

In diffraction and scattering experiments spatial information (the angle at which the X-rays are scattered) is very important. Position sensitive detectors are therefore commonly used as they provide a large amount of spatial- and intensity data in a relatively short time. An example of a position sensitive detector is the direct-detection pixel-based solid-state detector. In these detectors the X-rays (or electrons) directly hit a semiconductor, creating free electrons and holes that are detected by electronics. Read-out electronics are designed to have a low noise, a high dynamic range and a fast readout. X-ray pixel detectors built in hybrid design consist of a radiation sensor, a reverse biased pn-diode (usually silicon) with a segmented contact structure on the p-side, and a readout ASIC-chip, with the same pixel structure. Sensor and read-out chips are connected via tiny conducting indium balls, called bump-bonds. X-rays are detected in the sensor and the resulting signal is amplified in the pixel chip. When the detected charge reaches a certain threshold, a photon is counted. By adjusting the threshold value one can also exclude lower energy photons. In this way background resulting from fluorescence may be removed. Due to the direct detection of the X-rays with a silicon sensor, the spatial resolution of such detectors is excellent. The DQE is given by the absorption of the X-rays by the silicon, which is 80 % at 12 keV and even 100 % at 8 keV.

Other type of experiments may require detections of the various energies of the X-ray photons, e.g. fluorescence measurements. In this case energy dispersive detectors may be preferred. A silicon drift detector (SDD) is an example of such an energy dispersive detector. Silicon Drift Detectors are basically discs of n-type silicon. On the opposite side of the part that is exposed to the X-rays a transverse electric field is generated by means of a series of ring-electrodes. Electrons are generated in the silicon when X-ray radiation is absorbed. The electric field forces the electrons to drift in a sideways direction towards a small anode. The amount of electrons that reach the anode is proportional to the energy of the absorbed photon. The small size of the anode and the integration of the first FET of the amplifier electronics in the anode greatly minimize the capacitance of the detector giving a higher energy resolution and a higher photon count rate. The energy resolution is expressed in full width at half maximum (FWHM) and is typically 125–150 eV for Mn Kα wavelength ($\sim$2.1 Å).

3.2.3 Diffraction Beamlines: MCX at Elettra

The MCX (Material Characterization by X-rays) beamline at Elettra [21] allows to perform a wide range of non-single crystal diffraction experiments: grazing angle diffraction and reflectivity, residual stress and texture analysis, phase identification, structural and kinetic studies. Systems that can be investigated vary from organic and inorganic thin films, to thermally and/or mechanically modified surfaces of mechanic

components, to polymers, catalysts and highly disordered materials in the form of powders and fibers.

In order to fulfill the required flexibility in terms of beam characteristics at the experiment, ranging from spot focus to line focus and to parallel beam, the optics of the beamline consist of two mirrors and a monochromator: a first Pt-coated cylindrical mirror collimates the beam on the sagitally focusing Si(111) double crystal monochomator in 1:1 configuration. The second—meridional focusing—platinum coated mirror is flat and bendable, with a radius adjustable from 6 km to flat.

The fixed-exit double crystal monochromator (DCM) consists of two Si(111) crystals, which can be precisely positioned and oriented in the X-ray beam. The energy resolution is that inherent to Si(111). This fixed exit operation is obtained by placing the crystals on two independent rotation stages, and translating the second crystal along the beam direction. This crystal provides sagittal focusing; it is a ribbed crystal, cylindrically bent to a variable curvature radius.

The station has been designed to provide the maximum flexibility and easy use with reasonable precision and performance and is based on a 4-circle Huber goniometer in full circle configuration with a flat sample-holder plate (Ø 100 mm) controlled by a precision x-y-z motor system, 360° phi-rotation and $-90 \div +90°$ chi-tilting. The 2θ rotation is provided with an encoding system for accurate control and real-time feedback on the actual angular positions. The diffracted arm carries, as a default, a crystal analyzer/scintillation detector system.

3.2.4 Absorption Beamlines: the XAFS Beamline at Elettra

The Elettra synchrotron source hosts a spectrometer dedicated to XAS, the "XAFS" beamline [22], installed on a bending magnet source. It was designed to cover a wide energy range: from 2.4 to 27 keV meeting the needs of a large number of researchers in the area of conventional XAS. The optical layout is shown in Fig. 3.9.

The mask defines the size of the beam accepted by the collimating mirror. The mirror, placed at 16.5 m from the source provides vertical collimation and consists of a silicon ingot with platinum coating. It has an optically active length of 1,000 mm and width of 60 mm respectively and it is positioned at 3 mrad with respect to the direct beam. The mirror is water cooled and is operated under ultra high vacuum conditions. Two pairs of entrance tungsten alloy slits define the shape of the beam impinging on the monochromator. The monochromator, placed at 21.7 m from the source is a fixed exit double flat crystal double cam Kohzu apparatus. The energy range 2.4–27 keV can be covered using interchangeable under vacuum pairs of Si(111) and Si(311) crystals. The energy resolution is that inherent to Si(111) and Si(311). The fixed exit is achieved by the rotation and translation of the first crystal along the two cams. The detuning of the second crystal provides harmonic rejection at working energies below 9 keV. Downstream the monochromator a second set of tungsten alloy slits are used to define the beam on the sample. Any specialized sample environment set-up is mounted on a wide motorized table. The standard set-up allowed transmission mode

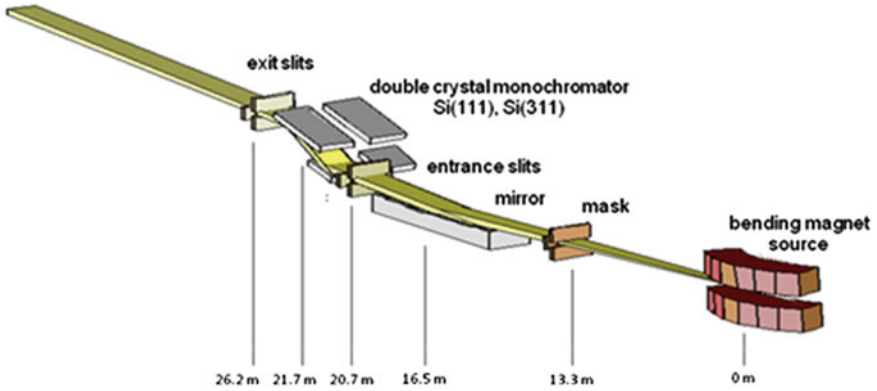


Fig. 3.9 Scheme of the optical layout of the XAFS beamline at Elettra

with ionization chambers for beam intensity measurements. These are filled with optimal He, Ne_2, Ar, Kr gas mixtures at a total pressure of 2 bars and are operated at a field of 2 kV per 30 cm of length. The ionization chambers signals are amplified and digitalized by a voltage to frequency converters before being finally read by the counters of the data collection PC. The typical photon flux at the sample for standard beam size and ring current is in the 10^{10} photon/s range. The noise level contribution due to the photon statistics in the normal transmission geometry can be therefore limited below the 10^{-4} level. A large-area Si drift detector is the standard device for fluorescence measurements.

3.3 Soft X-Ray and Vacuum Ultraviolet Beamlines

The absorption coefficient of optical materials makes the VUV and soft X-ray part of the spectrum very different from the visible and hard X-ray photons. In this energy range there are no windows, no optical lenses, no prisms, etc…, but only poorly reflecting mirrors. Even air is opaque to radiation in the 6–1,000 eV range. Thus, the entire optical system for a beamline must be kept under vacuum. Only at very small angles of incidence the reflectivity increases at a given photon energy (i.e. as the photon beam tends to become more parallel to the optical element surface).

Conversely, for the same reason, light in this spectral region is particularly sensitive to the electronic properties of matter. This is due to its strong coupling to valence electrons in the solid and to resonant processes at accessible core levels that can enhance the scattering amplitudes by orders of magnitude. Such phenomena lie at the core of the renewed interest in the exploitation of VUV and soft X-rays for the investigation of wide classes of materials including technologically relevant compounds, alloys, and advanced nanoscale materials.

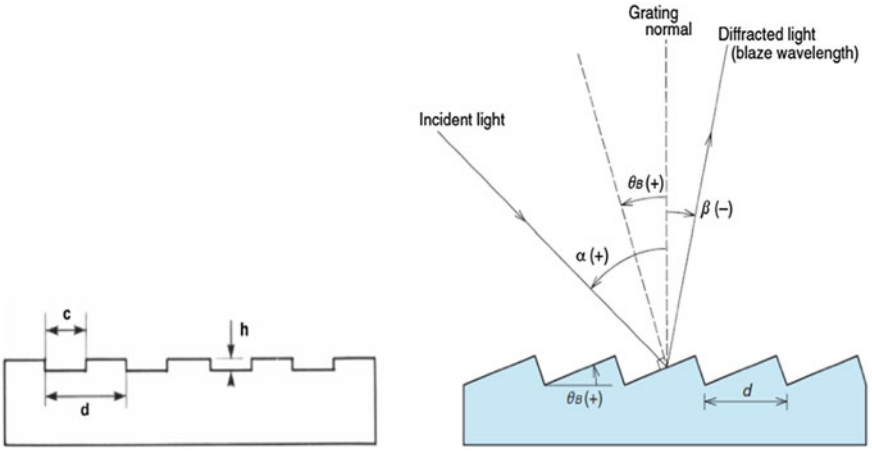


Fig. 3.10 Laminar (*left*) and blazed (*right*) gratings. The incidence α and diffracted β angles are defined

Furthermore, the wavelength of soft X-rays, from ~ 0.5 nm to a few nanometers, well matches with many interesting and useful length scales occurring in several materials either natural or engineered. However, those wavelengths do not allow the use of single crystals as monochromators, as done in the hard X-ray region. We need, therefore, to engineer gratings with well-defined line spacing and size using mechanical systems or holography in order to utilize the Bragg diffraction for monochromatization [23, 24]. Usually there are two kinds of grooves for gratings: blazed or laminar tooth profile as shown in Fig. 3.10. The notation adopted in Fig. 3.10 uses opposite sign of the angles α and β if they are on opposite sides of the normal. The Bragg grating equation may be written as $m\lambda = d\,(\sin\alpha + \sin\beta)$.

The distance d is the separation between lines, m is the order of diffraction. The angles α and β are both arbitrary, so it is possible to impose various conditions relating them. If this is done, then for each λ, there will be a unique α and β. The following conditions are typically used [25]:

- On-blaze condition:

$$\alpha + \beta = 2\theta_B$$

where θ_B is the blaze angle (the angle of the sawtooth).
The grating equation is then $m\lambda = 2d \sin\theta_B \cos(\beta + \theta_B)$

Fixed in and out directions (entrance and exit slits):
$\alpha - \beta = 2\theta$, where 2θ is the (constant) included angle.

The grating equation becomes $m\lambda = 2d\cos\theta_B \sin(\theta + \beta)$
In this case, the wavelength scan ends when α or β reaches 90°, which occurs at the horizon wavelength $\lambda_H = 2d\cos^2\theta$.

- Constant focal distance:

$\frac{\cos\beta}{\cos\alpha}$ a constant C, leading to a grating equation

$$1 - \left(\frac{m\lambda}{d} - \sin\boldsymbol{\beta}\right)^2 = \cos^2\frac{\beta}{c^2}$$

The typical experimental techniques in this energy range can be summarized as near-edge X-ray absorption fine structure (NEXAFS) spectroscopy, soft X-ray emission spectroscopy (SXES), resonant inelastic X-ray scattering (RIXS), X-ray magnetic circular dichroism (XMCD), X-ray photoemission spectroscopy, in all of its aspects (XPS, ARPES, Resonant XPS etc…), and Auger spectroscopy.

These types of spectroscopies exploit the excitation of electrons in relatively shallow core levels and valence band to probe the electronic structure of various kinds of matter. They are extremely demanding techniques because they require all the characteristics of a modern X-ray beamline at the same time, such as:

- Brilliance. The illuminated spot on the sample must be very small. The flux must be as high as possible because the cross sections of the processes are small. State of the art focusing and optics that transmit as much as possible the brilliance of the light emitted by the insertion devices are required.
- Resolving power. A total resolving power greater than 10^4 requires that the monochromator must work at least at 20,000 resolving power over the whole energy range in order to have photon energy resolutions of ten's of millielettronvolts.
- Stability. These experiments are intrinsically slow and long acquisitions are needed. The stability needs to be maintained when varying energy and polarization. Gains in the thermal stability of the beamline optics, as well as in the machine stability, will be directly reflected in the data quality.
- Polarization tunability. The source must be capable of delivering linearly and circularly polarized radiation with any orientation over the whole spectral range.

3.3.1 Soft X-Ray Energy Optics

In order to design a beamline featuring all these characteristics we must analyze the focusing effect of the optical elements (mirrors and monochromators).

Toroidal (spherical) mirrors [26] and gratings [27] are commonly used in beamlines working in the soft X-ray range, primarily because they are commercially available at low cost and because the number of optical element present in a beamline can be reduced, since in this case both mirrors and gratings can focalize the

beam. However, the beam image produced is poor having the dropping arc form due to astigmatism.

Parabolic mirrors [26, 28] can be used to collimate the synchrotron radiation in front of a plane grating and then to re-focus the scattered radiation on the exit slits of the monochromator. However it is difficult to manufacture these aspheric surfaces. Therefore, these optical elements have larger tangent errors and higher costs. Moreover, the fact that two of such mirrors are required for a monochromators is a further disadvantage for the use of parabolic mirrors.

Elliptical mirrors [26, 28] are also difficult to manufacture with small tangent errors, but the possibility to use two of them or one elliptical and one toroidal mirror in a Kirkpatrick-Baez (KB) design [28] (see the paragraph 5) allows one to have a system almost free of aberrations. In this geometry two mirrors are used before the monochromator, which independently focus the beam in the two orthogonal planes on the monochromator exit slit.

For the monochromator we can choose between spherical (toroidal) gratings, that have the intrinsic advantage to reduce the number of optical elements in the monochromator, or plain gratings that, instead, have the advantage to cover a larger energy range and to have typically higher resolution [29]. The resolution and flux (as well as the presence of high order diffraction lines) also depend on the blazed or laminar groove profiles. Blazed profiles typically have high-flux, but lower resolution and important high order diffraction lines. Laminar profiles shrink the flux but increase the resolution and have negligible high order diffraction lines [29]. The choice of blazed *vs* lamellar gratings and the optimization of their profile parameters determines the characteristics of a beamline. Due to glancing angles on the mirrors as well as optimized groove densities and profiles of the gratings, high photon flux can be achieved reaching up to 10^{13} photons/s/0.01%BW at 1 keV.

In the case of spherical or toroidal grating monochromator (SGM or TGM), a very simple solution is just to have the grating (or more gratings) as the only optical element between the entrance and exit slits. This solution is very cheap and in some cases may be a very good solution for photon energy in the VUV range (see the next paragraph). However, in many cases, the typical optics for SGM (TGM) are formed by a plane mirror and a spherical (toroidal) grating between the entrance and exit slits. These types of monochromators are severely limited by the fact that the gratings must also focus the entrance slit beam to the exit slit. This implies that the focus on the exit slits will change by moving the grating and this change may become too large in the soft X-ray range for practical purposes. Moreover, the energy resolution ΔE is proportional to the energy E, so at high energy it may be unfavorable.

For plain grating monochromators (PGM) typically one grating can be enough to cover a wide range of energy (50–1,500 eV). However, the optical design of the monochromator is more complicated than a SGM since it requires a plane mirror to send the beam on the plain grating and a refocusing mirror (usually elliptical mirror) after the grating to focus the beam on the exit slits. This conceptual design is called SX700 [30–32]. The resolving power $E/\Delta E$ decreases in a slower way with the increasing energy with respect to the SGM, given that it is proportional to $E^{1/2}$.

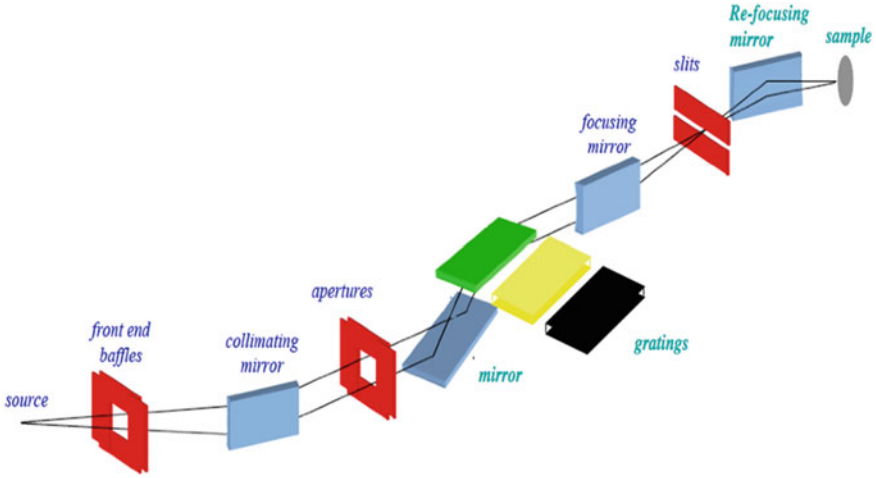


Fig. 3.11 Optical layout of a soft X-ray beamline based on the collimated-light PGM

3.3.2 Layout for a Soft X-Ray Energy Beamline

The conceptual layout of the optics of a soft X-ray beamline optimized for spectroscopy studies is shown in Fig. 3.11. This scheme is based mainly on the design of high-resolution soft-X-ray spectroscopy beamlines present in 3rd generation synchrotrons, like ADRESS [33] at SLS, SuperESCA at Elettra [34] or the beamline 4.0.2 at ALS [35].

In this case the optics is based on the proven scheme of plane grating monochromator operating in collimated light [36]. The frontend pinhole (baffles) selects the coherent cone of radiation coming from the insertion device. The collimating mirror (CM) is a toroid, which converts the divergent beam from the pinhole into a photon beam parallel in the vertical (dispersive) plane. This deflecting toroidal mirror is designed to collimate along the vertical direction and to focus the beam horizontally at the exit slit. The mirror is typically made of Si, glass, SiC or zerodur ® substrates coated with about 30 nm of some coinage metals. In Fig. 3.12 the reflectivity of some metals at different grazing incidence angles are shown. They show a good reflectivity up to 2.2 keV. We note that at the reported incidence angles (88–89°) the *s* and *p* reflectivity are almost identical. Therefore, the beamline will not distort circular polarized radiation.

The monochromator situated downstream consists of a plane mirror (PM) and selectable gratings, dispersing the beam in photon energies. The vertically collimated beam is deflected by the plane mirror illuminating the plane grating, at an angle of incidence α necessary to select the energy. This second optical element, the plane mirror PM, like the CM, is made of Si, SiC, etc… substrates coated by Au or Pt. Since the incidence angle of the monochromator must be moved to select different energies, the typical angular resolutions for the gratings are 0.03 and 0.05 μ rad for

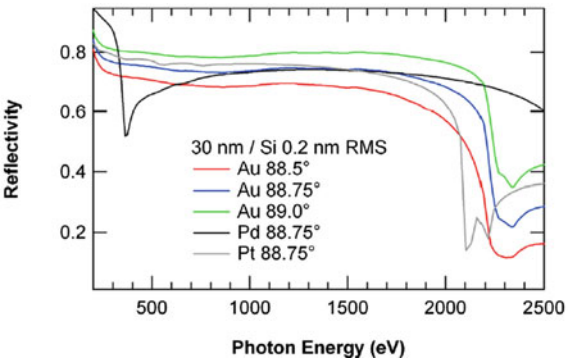


Fig. 3.12 Reflectivity of possible coatings for s polarized light as a function of the photon energy. The substrate is Si and the coating is 30 nm thick. The RMS surface roughness is 0.2 nm

the plane mirror. Since the angle of incidence on the mirror for a given grating is determined by the focusing condition and the grating equation at that energy, it is advantageous to have at least three gratings that allow exchanging resolution for flux, keeping a fixed exit slit width. In the proposed scheme three gratings with constant groove densities N in the possible ranges $300 < N < 1{,}000$, $1{,}100 < N < 3{,}000$ and $3{,}100 < N < 5{,}000$ l/mm are used to provide even coverage of the beamline resolution and transmission parameters.

However, the collimated light PGM [37] in general benefits from high resolution, high flux, due to absence of the entrance slit allowing the beamline to accept the whole coherent cone of undulator radiation, and wide energy range already covered with one single grating. In fact, large $\cos\beta/\cos\alpha$ values are used to improve resolution at the expenses of flux.

After the grating there is the focusing mirror (FM). FM is an elliptical cylinder mirror, which focuses the dispersed collimated beam on the exit slit of the monochromator, producing monochromatic light. In the horizontal (non-dispersive) plane, the FM has no focusing properties and, as explained above, the beam from the source is directly focused by the CM on the exit slit, producing a stigmatic focus. This collimated PGM design is almost free of aberrations.

Finally, the refocusing mirror (RM), that can have a toroidal or elliptical shape, refocuses the beam on the sample in the endstation. The angle of incidence on both mirrors is close to 88–89°. Examples of parameters of all optical elements can be found in [33, 34].

Typically these beamlines will achieve a resolving power $E/\Delta E$ between 5×10^3 to 10^5 in the photon energy range 100–1,000 eV with a 10 μm exit slit width and with RMS slope errors of 0.1 μ rad over ~100 mm on the plane optical elements. A spot size (vertical × horizontal) with FWHM of less than 10×100 μm^2 requires RMS slope errors of approximately 0.5 μ rad along the meridional direction. The photon flux at the sample (depending on resolution and gratings) is in general between 10^{11} to 10^{13} photons/s/0.01%BW.

Other possible optical layouts are reported in many books [29, 38] and are present in several synchrotron beamlines [39–42]. Since a beamline is intended for a

particular set of techniques, the knowledge of the requirements of the experimental methods used is necessary before building a beamline. In addition the available space is also an important point for choosing the optical elements.

In order to match the high resolving power asked for the soft X-ray beamlines, state-of-the-art optical elements are required and some unavoidable constraints must be respected. The horizontal source size is much larger than the vertical one and, therefore, is not used in the dispersion direction in high-resolution systems. The vertical source size in 3rd generation synchrotrons is about 40-200 μm at the pinhole, and since this size limits the resolution, the optics of the beamline should reduce this size to less than 10 μm at the exit slits of the monochromator. The mirrors can demagnify the source by a maximum of 8, so in many cases the monochromator should also contribute to the demagnification.

Spherical gratings typically have 1:1 demagnification or slightly magnify the source. Therefore, demagnification by mirrors is required and a vertical entrance slit must be used to cut the beam. A typical example of a beamline based on a spherical (toroidal) grating monochromator is shown in Fig. 3.13, where the demagnification and astigmatic corrections are made by the KB mirror before the monochromator and the refocusing mirror after the exit slit.

PGM monochromators typically demagnify the source by a factor of 6, therefore an entrance slit is not required (although it may be advantageous) and there are even less requirements on the demagnification of the mirrors. If long energy scans without a grating change and with high-energy resolution is required for the experiments, an optical configuration based on a PGM monochromator is preferable, as shown in Fig. 3.11.

3.3.3 Low Energy VUV (4–40 eV) and Visible-Infrared Beamlines

Probes that use this region of the spectrum are very well suited to elucidate bonding in solids, surfaces, and molecules and to investigate electron–electron correlations and velocities in solids, atoms, and ions. At the lowest end of this energy range (below 3 eV), visible, infrared, and terahertz spectroscopies can be successfully used to study vibrational modes and optical excitations. Below 40 eV a myriad of techniques exists such as angle-resolved photoelectron spectroscopy (ARPES), photon-ion spectroscopy, inelastic ultraviolet scattering spectroscopy (IUVS), Fourier transform infrared (FTIR) spectroscopy and microscopy, terahertz (THz) spectroscopy, photoelectron-photoion coincidence spectroscopy. Since THz and IR beamlines are described in Chap. 15 of this volume, here we will focus on the VUV beamlines.

For wavelengths above 30 nm normal incidence optical configuration can still be used as some materials present a reflectivity close to 30 %, which is not the case below 30 nm. Nevertheless, a reflectivity of 30 % does not allow a beamline configuration with numerous optical elements, if relatively high monochromator throughput has to be conserved. Therefore, single optics normal incidence monochromators (NIM) based on a slightly modified Rowland circle principle (off-plane) are chosen [43, 44].

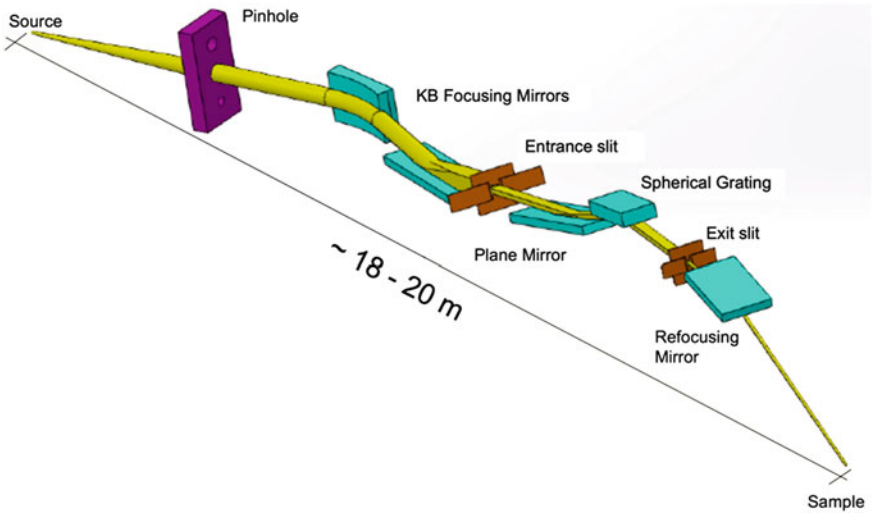


Fig. 3.13 Optical layout for a beamline based on a spherical grating monochromator and a KB focusing system. The total length is the typical distance from the source to the sample reported in m

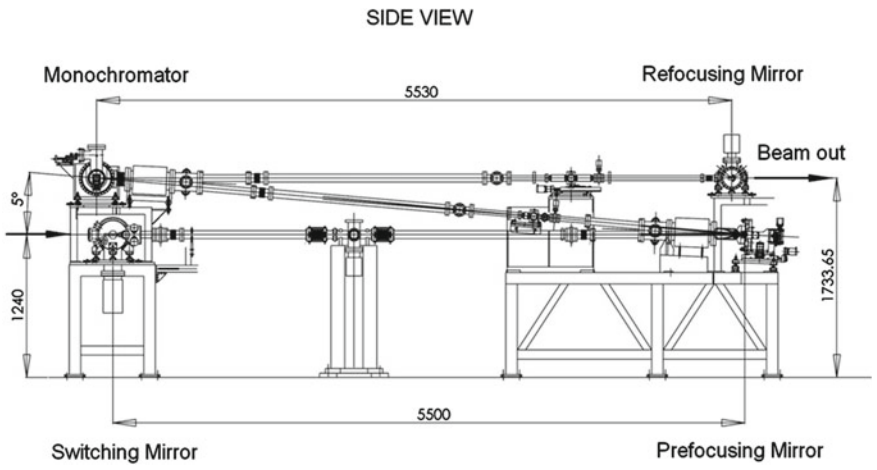


Fig. 3.14 Layout of the BaD ElPh beamline at Elettra. The distances are in mm

In this design a spherical grating is the only optical elements for the dispersion and focalization of light. The main difficulty in Rowland circle design is the non-constant position of the spherical grating focal point, which moves during the wavelength scanning.

The layout for a beamline based on a normal incidence monochromator, with 4-m-long focal length and constant included angle of 5°, is shown in Fig. 3.14 and

illustrates the BaD ElPh beamline at Elettra [45]. NIMs in this energy range offer the highest resolving power, but the photon energy range is restricted to a maximum of about 40 eV.

In this particular case, the light from the undulator is deflected towards the BaD ElPh beamline by a plane switching mirror, since this undulator serves two branchlines, BaD ElPh and IUVS (Inelastic Ultra Violet Scattering) [46]. The spherical prefocusing mirror upstream of the monochromator focuses the light onto the entrance slit. Due to the normal incidence, the demagnification factor of this mirror is about 14. The bare silicon portion of the surface of the mirror is used for photon energies up to about 11 eV, while the reflectivity of the Pt coated part is suitable for higher photon energies.

The monochromator is equipped with three exchangeable spherical gratings with efficiencies that are optimized for the photon energy ranges of about 4.6–13 eV (1,500 l/mm, laminar profile, Al/MgF_2 coated), 13–19 eV (3,000 l/mm, laminar profile, SiC), and 19–40 eV (3,000 l/mm, blazed profile, Pt coated). The groove profiles of the two laminar gratings (Al/MgF_2 coated and SiC) were designed to suppress the higher order diffraction efficiency. The Pt coated grating, designed to maximize the first order diffraction efficiency, has a blazed groove profile with a blaze angle of 3°. The exit slit distance from the gratings varies from 4,070 to 4,190 mm. This variation corresponds to the change in the vertical focal distance of the gratings moving from lower to higher photon energies. The last optical element of the beamline, namely the toroidal refocusing mirror, focuses the light onto the sample inside the experimental chamber. The parameters of the optical elements are given in Table 3.2.

The calculated resolving power ($\frac{E}{\Delta E}$) of the monochromator is shown in Fig. 3.15. The separate contributions from the slits, grating tangent slope error, and diffraction limit are presented for the 1,500 l/mm grating and for the 3,000 l/mm grating. The entrance slit is completely open while the exit slit is 10 μm. For each grating, the tangent slope error used for the calculations was 0.5 μ rad rms.

The photon flux of the BaD ElPh beamline (see Fig. 3.16) has been measured using a removable photodiode, located between the refocusing mirror and the endstation. With a pinhole of $4.5 \times 6.1\,mm^2$, slits width of 300 μm, and with 200 mA accumulated in the storage ring, the maximum photon flux, reached at 9 eV in first harmonic, is more than 5×10^{12} photons/s, while at 6.5 and 11 eV it decreases to about 1×10^{12} photons/s. For the SiC grating the maximum flux of more than 3×10^{11} photon/s is reached at about 20 eV. For the Pt grating the maximum photon flux, reached at 23 eV, is more than 1×10^{12} photons/s, while at 19 and 35 eV it decreases to about 3×10^{11} photons/s.

Other undulator-based NIM beamlines optimized for low-energy high-resolution ARPES with comparable resolving power and/or flux are present in other facilities like SSRL, SRC, NSLS, HiSOR, and BESSY [39, 47–53].

Table 3.2 Components of the BaD ElPh beamline [45]

Optical element	Distance from source center(mm)	Optical parameters	Incident angle to surface	Material	Coating
Source	0	Figure-8 undulator		NdFeB	
Pin hole	11,490			CuOFHC	
Heat loader	15,800	Plane	6°	GlidCop	Au
mirrors	16,400	Plane	6°	Si	None
Switching mirror	21,000	Plane	8°	Si	None
Prefocusing mirrors	26,500	Sphericeal R = 3,444 mm	87.5°	Si	None&Pt
Entrance slit	28,340			Strainless steel	
Three Gratings	32,160	Spherical			
Deviation angle = 175°		R = 4,038 mm 1,500 l/mm 3,000 l/mm Laminar		Silica SiC	Al/MgF_2 None
		R = 4,007 mm 3,000 l/mm Blazed		Silica	Pt
Exit slit	36,230–36,350			Stainless steel	
Refocusing mirror	37,690	Toroidal R = 13,000 mm ρ = 150.1mm	6.17°	Silica	Au
Sample	39,090				

Because of the use of a particular undulator and the presence of cooled heat load mirrors before the switching mirror, the power on the optics is strongly reduced and the monochromator is not cooled

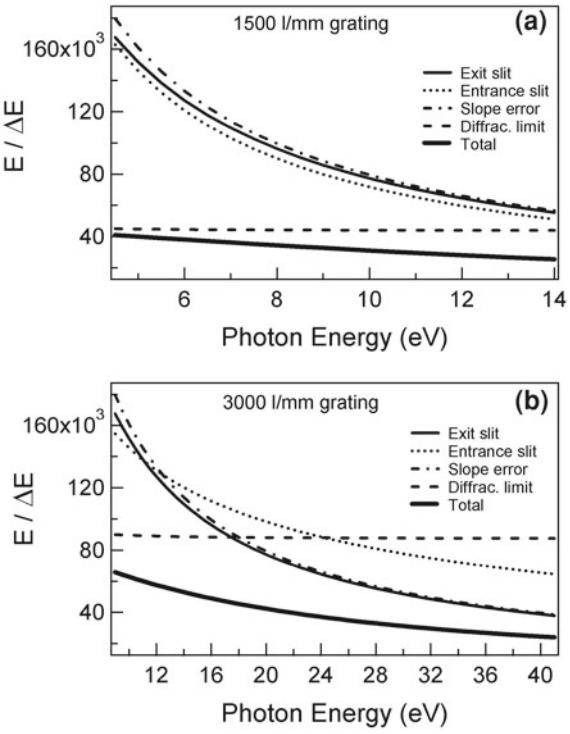


Fig. 3.15 Calculated partial and total resolving power, in first diffraction order, of the BaD ElPh NIM for the 1,500 l/mm (**a**) and 3,000 l/mm (**b**) gratings

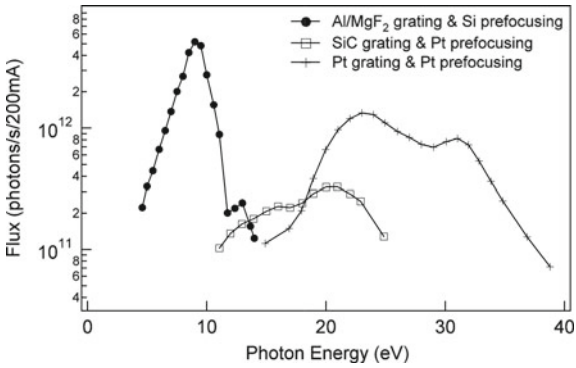


Fig. 3.16 Photon flux of the BaD ElPh beamline [45] measured with a photodiode using entrance and exit slit widths of 300 μm, and with 200 mA of electron current accumulated in the storage ring. In these experimental conditions the typical resolving power was around 2,500

3.3.4 Experimental Examples to Test the Beamline Performance

Absorption spectra of noble gases are typically considered to test the maximum energy resolution of the soft X-ray beamlines. Here we show the measurements made on the BaD ElPh beamline where the spin-orbit autoionization spectra of Ne gas between the $^2P_{3/2}$ and $^2P_{1/2}$ thresholds have been recorded via gas phase ion

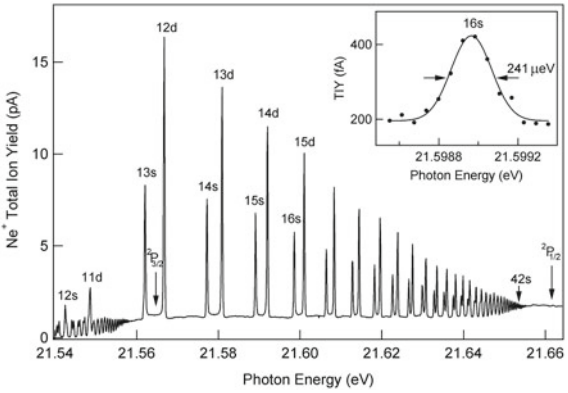


Fig. 3.17 Ne autoionization spectrum, measured with the 3,000 l/mm SiC grating in second order and with 20 μm exit slit width, showing an energy resolution of 310 μeV. *Inset* (*dots*) 16 s resonance spectrum recorded with 10 μm exit slit and (*solid line*) Gaussian fitting curve showing a FWHM of 241 μeV. The ionization energies for the formation of Ne^+ in the $^2P_{3/2}$ and $^2P_{1/2}$ states are also indicated

yield measurements. Above the ionization potential $Ne^+ {}^2P_{3/2}$, two Rydberg series 2p5ns and 2p5nd converge to the spin-orbit-excited $Ne^+ {}^2P_{1/2}$ ionization limit [54]. These Rydberg states are long-living with a very narrow natural line widths. As a result, using the neon spectrum the resolution of the monochromator can be observed directly from the line shapes of the Rydberg resonances [55].

The total ion yield measurements were performed with a gas cell, which is an integral part of BaD ElPh end-station.

In Fig. 3.17 we present a selected Ne^+ autoionization spectrum between the two 2p thresholds, showing the s and d Rydberg series, that has been calibrated on an absolute energy scale according to [56]. This spectrum has been recorded with the 3,000 l/mm SiC grating, operating in second diffraction order, with 20 μm of exit slit width and a completely open entrance slit (spot size at the entrance slit of about 7 μm). The observed FWHM of the neon 16 s resonance is 310 μeV, providing a resolving power $\frac{E}{\Delta E}$ of 69,000 at 21.6 eV in second order. This high resolution, together with the long-term stability of the entire beamline and of the electron beam in the storage ring, allows the observation of Rydberg states up to the 42 s level. The sharp and strong peaks below the $^2P_{3/2}$ threshold are due to collision-induced ionization in the neon gas. The inset of Fig. 3.17 shows the 16s spectrum, recorded with 10 μm of exit slit. The corresponding FWHM is 241 μeV, providing a resolving power of 89,000. In the above condition, with the grating operating in first diffraction order at 21.6 eV, the resolving power is 40,000.

Because the BaD ElPh beamline is connected to an end-station primarily devoted to ARPES [57, 58] from solids, which is common to many beamlines in the VUV and soft X-ray range, we briefly describe the main characteristics and some results of the corresponding end station in particular for the low photon energy regime. With respect

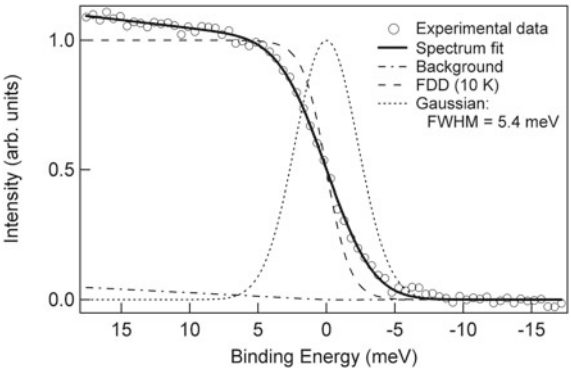


Fig. 3.18 Raw Fermi-edge photoemission spectrum from polycrystalline silver (*open circles*) and the fit of the data (*solid line*). The spectrum was measured at 10 K with a photon energy of 7.8 eV

to high-energy ARPES, the low energy counterpart offers great advantages in terms of energy and momentum resolution. Moreover, low photon energies provide enhanced bulk sensitivity, since the inelastic mean free path is expected to increase drastically for the electrons with kinetic energies below 10 eV [59], and are useful for tuning matrix elements, which vary rapidly at low energy. The universal demand in this area is for a high signal rate with very high resolving power. The high brightness and small spot size achievable with synchrotron radiation, particularly at third-generation sources and operation of very advanced monochromators, permits the design of new spectrometers, and electron energy analyzers with very high resolution.

In fact, the main part of the analysis chamber is the hemispherical 150 mm electron energy analyzer with a 2D-CCD detector system. This commercial 150 mm mean-radius hemispherical analyzer is mounted in a fixed geometry with an angle of 50° relative to the synchrotron radiation direction. The angular dispersive plane of the analyzer coincides with the polarization plane of the synchrotron light in first harmonic. The use of a 2D-CCD detector offers the possibility of simultaneous acquisition of the energy as well as the angular distributions of the photoelectrons. The span of $k_{||}$-vectors simultaneously probed by the analyzer is defined by the angular acceptance of the particular lens mode and by the photon energy. The maximum angular acceptance is about $\pm 17°$; moreover, an ultimate angular resolution of about 0.05° could be achieved.

The energy resolution in photoemission experiments is defined by the energy spread of the photon beam and the transfer function of the electron analyzer. For solids, it can be conveniently determined by measuring Fermi edges of polycrystalline noble metals at low temperature. Figure 3.18 shows a photoemission spectrum of the Fermi-edge of polycrystalline silver at 10 K acquired at the photon energy of 7.8 eV together with the fit of the data and its components. The exit slit of the beamline was set to 300 μm, while the entrance slit and the pass energy of the analyzer were set to 0.5 mm and 1 eV, respectively. The fitting function was the product of a linear background with the Fermi-Dirac distribution at the experimental temperature convoluted with a Gaussian. As a result of the fit the FWHM of the Gaussian, i.e. the combined experimental resolution of the beamline and analyzer, was found to be

5.4 meV. Under the above conditions, the calculated energy resolution of the BaD ElPh NIM is 2.4 meV. Therefore, an energy resolution of 4.8 meV can be estimated for the electron analyzer.

Finally, we note that on the experimental chamber of the soft X-ray and VUV beamlines, the sample must be mounted on a manipulator that typically has six degrees of freedom (three translations and three rotational axis). The sample holder, capable of accommodating transferable samples, is mounted on a cryostat that reaches, with liquid helium, temperatures lower than 10 K.

3.4 Cooling of Optics and Other Beamline Parts

Thermal considerations dominate the design aspects of modern optics and monochromators in view of the extremely high power and power densities of the insertion device beams of third-generation synchrotron sources. Typically the total power emitted from sources is in the order of 2–3 kW, while on the first optics after the pinhole it is reduced by one order of magnitude (about 150 W on an area of $2 \times 1.5\text{mm}^2$), but with the new superconducting and *in-vacuum* undulator a power density of >300 W can be reached.

It is clear that thermal issues are associated not only with the first optic that is impacted by the direct beam, but also with all the optics up to the monochromators and eventually slits, filters and shutter before the monochromator. To properly handle the incident heat load on these optics and beamline parts requires special measures, usually internal cryogenic cooling or the use of external water or liquid nitrogen cooling.

Filters can be used in the hard X-ray regime to attenuate the low-energy portion of the spectra, thereby reducing the power load on the following beamline components. Most existing filters are based on very thin layers of pyrolytic graphite, arranged in a stack in such a way that each filter absorbs a particular amount of power. The power is predominantly thermally radiated away by each graphite layer. Such filters can reduce the incident power by as much as 60–70 %. An alternative choice of filter material is CVD diamond, which can also be used as a vacuum window material.

Slits, used to define the beam dimension, are now very standard components of beamlines and are available either as independently adjusted jaws or as apertures of fixed widths (horizontally or vertically) that can be positioned anywhere in the beamline. It is prudent to place slits between successive optical components, as well as near the downstream end of the beamline. Commercial versions are available and the slits positioned before the monochromator (pinhole, entrance slit etc…) must be cooled.

Every beamline will have at least one pneumatically actuated photon shutter placed downstream the source. Shutter designs, material and shielding will vary to meet the needs of individual beam sources and to handle the radiation spectrum that the shutter will confront. Whereas copper might be acceptable as a shutter material

if only synchrotron radiation must be stopped, heavier materials such as tungsten alloy would have to be considered if bremsstrahlung radiation must also be stopped.

The implications that thermal issues have on the brightness of the diffracted beam can be treated individually for each component factor of the brightness. Flux, relative wavelength spread and angular spread are impacted in a negligible way by thermal distortion and slope error variation (less than 2 %), but careful attention must be paid to the position spread of the diffracted beam. Thermal slope errors of monochromator planes have the same blurring impact on the beam dimension in the vertical plane as mirror figure errors would. It is determined by twice the RMS slope error multiplied by the distance from the monochromator. The effect of a 6 μ rad RMS thermal slope error is a blurring of the beam dimension by 240 μm at a distance of 20 m downstream of the monochromator. These effects might be significant, given that existing state of the art focusing mirrors (with figure errors of 2 μ rad or less) will attain vertical focus sizes less than 50 μm. Thus, cooling of monochromators is important to preserve most, but not all, of the aspects of the beam brightness. In some cases, to compensate the impact of the monotonic thermal distortion variation on the position spread of the diffracted beam in the vertical direction, it should be feasible to mechanically adjust, only slightly, the curvature of the vertical focusing mirror that would typically be used downstream of the monochromator. Considerable cooling must be provided to the mirrors before the monochromator to avoid deformations of the ideal mirror shape. The cooling needs to ensure that the heat-induced meridional RMS slope errors are below 0.5 μ rad.

In the case of high-energy X-ray beamlines that use a double crystal monochromator, the heat load on the first crystal must be taken into account, as more than 99.9 % of the photon flux from the source is being absorbed. The power deposited by the synchrotron radiation sources must be efficiently removed. The head load produces a temperature rise ΔT leading to a crystal d-spacing change $\Delta d = \alpha \Delta T$ where α is the thermal expansion coefficient. If a miss-matching between the first and the second crystal is produced, thermal drifts, loss of intensity and brightness and broadening of the beam may occur. Solutions for crystal cooling should take into account (i) the thermal expansion of the crystal α, (ii) the thermal conductivity in the crystal κ, and (iii) the heat transfer to coolant and crystal holder. Good cooling strategies are obtained for large $\frac{\kappa}{\alpha}$ ratios, large contact area between crystal and coolant/holder and of course if small power density is distributed over a large area. Typically this is achieved using water or liquid nitrogen circulation. Sometimes also closed-cycle circulating gaseous helium is used. This last option is employed, for example, on four existing NSLS insertion device beamlines.

3.5 X-Ray Optics for Microscopy

Visible and electron microscopies dominated for a long time the microscopy field. The former allows imaging thick samples with sub-micrometer lateral resolution in their natural aqueous environment, an appealing feature especially for the analysis of

biological specimens. Conversely, electron microscopes can provide sub-nanometric lateral resolution but they are limited to the imaging of thin samples in vacuum environment. X-ray microscopy covers the gap between visible and electron microscopy. The short wavelength and high penetration depth of X-rays offer the chance to image thicker samples, at few nanometer lateral resolutions, and even better. Despite X-ray imaging potentialities are known from almost one century, X-ray microscopes are among the latest developed in the microscopy field but nowadays they are becoming more and more popular in many 3rd generation synchrotron facilities. Indeed, they benefit from high brilliance, low emittance and coherence properties of X-ray synchrotron emission, but also from the technical advances achieved in the fabrication of X-ray optics, in detector performances and imaging modalities.

An X-ray microscope basically provides morphological and chemical information on the sample, and the image contrast is given by the specific interaction of the analyzed specimen with X-rays, a topic extensively detailed in Chaps. 13, 14 and 22 of this volume (for more details see also [60–62]).

3.5.1 X-Ray Focusing Optics

Generally speaking, there are three different geometries of X-ray microscopes: X-ray projection microscopes, Transmission X-ray Microscopes (TXM), also known as full-field transmission X-ray microscopes, and Scanning Transmission X-ray Microscopes (STXM). Here we focus on X-ray optics, on their working principle and on the technological progress toward nanoscale X-ray imaging.

Each focusing optical element is characterized by several parameters, which could be helpful to briefly remember at this stage: Magnification (M), Numerical aperture (NA), Resolution (Res), Depth Of Focus (DOF) and chromatic aberration. The optical magnification is a dimensionless number given by the ratio of the image size of the objected on its real size. For the Thin-Lens Equation, defined as p and q the source and image distance from the lens respectively, $M = \frac{q}{p}$. This implies that linear demagnification capabilities of X-ray microscopes can be improved by reducing q, and therefore, the optical focal length *f*, or increasing p, that is building longer beamlines. For synchrotron radiation, micro- and nano-probes are characterized by M$\sim 10^{-2}$–10^{-4} [63]. The numerical aperture of a focusing lens is a dimensionless number that measures the light gathered power. In air/vacuum $NA \sim \frac{r}{f}$, where r is the lens radius. NA is closely related to the photon flux at the focal spot, F, to the diffraction limited Res as well as to DOF. As a matter of fact, for the Liouville's theorem, $F \sim B \cdot \sigma^2 \cdot NA^2$, where B is the source brightness and σ the spot size. It clearly pops up that bright sources and large NA optics enhance the signal to noise ratio (S/N), lowering the detection limits. Lateral resolution, that defines the smallest resolvable sample feature, and depth of focus, that determines the maximum sample thickness in 2D imaging and sampled volume in tomography, are both inversely proportional to NA:

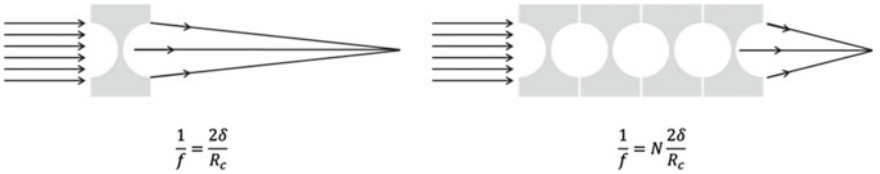


Fig. 3.19 Layout of refractive X-ray optics. **a** Single concave X-ray lens with focal length *f*. Rc is the lens curvature radius and δ the phase shifting part of the refractive index of the lens material. **b** Compound concave lens made of N single lenses having the same characteristic of (**a**)

$$Res = 0.61\frac{\lambda}{NA} \; for \; the \; Rayleigh' \; criterion$$

$$DOF = \pm\frac{\lambda}{2NA^2}$$

Chromatic aberrations introduced by a focusing element depend on the type of optics employed, that can be refractive, reflective of diffractive for X-rays.

Refractive optics were considered not particularly useful and quite impractical for X-ray focusing for long time. Since the real part of the refractive index for X-rays for all materials is slightly less than one in air or vacuum, X-ray focusing lenses must have a double concave shape and outstanding curvature radius. Indeed, for the Lensmaker's equation, the focal length would be of several hundreds of meters considering lens curvature radius in the range of few centimeters. Nowadays, compound refractive lenses (CRLs) are used. These are a series of concave lenses (see Fig. 3.19), first proposed in the 1996 by Snigirev and coworkers [64]. In order to increase CRLs' efficiency by limiting X-ray absorption, CRLs should be made as this as possible and fabricated with high density, low Z number materials, such as aluminum, beryllium, carbon (diamond or graphite), silicon, boron or lithium.

In 2002, CRLs made by N = 120 parabolic single lenses of polycrystalline aluminum (f = 1048 mm) were proposed and tested at the beamline ID22 of ESRF [65]. The tomogram of a microprocessor test sample has been obtained with a resolution slightly above 400 nm from the 3D rendering. In 2003, planar silicon parabolic CRLs with focal distances of few millimeters have been proposed and fabricated by using e-beam lithography and deep trench reactive ion etching, techniques that permitted to achieve the micrometric radius of curvature needed for shortening the focal length [66]. By exploiting a cross geometry for producing a 2D focus, two CRLs were used to generate at 25 keV at a distance of 42 m from the source (ID22 beamline at ESRF) a microbeam having a FWHM beam size of 210 ± 50 nm and 380 ± 90 nm in the horizontal and vertical plane respectively. By using planar silicon CRLs with similar design, a monochromatic hard X-ray beam (E = 21 keV) has been focused in a 47 × 55 nm^2 nanospot at the beamline ID13 at ESRF [67].

The major advantages offered by CRLs are the manufactory simplicity, with respect to reflective and diffractive X-ray optics, the low cost, the small size and

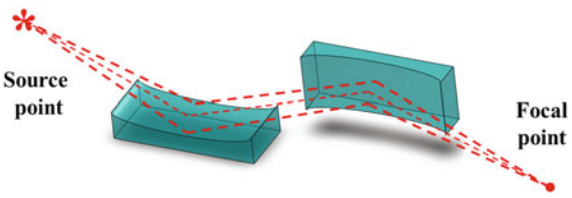


Fig. 3.20 Sketch of Kirkpatrick-Beaz mirror layout

alignment simplicity, the focal length tunability by simply adding or removing individual lenses and the low sensitivity to heat loading. Therefore, despite the absorption-limited efficiency, that makes them not useful in the soft X-ray regime, and the strong chromatic aberrations that affect them, CRLs are quite promising hard X-ray focusing elements and they have been recently used for imaging purposes [68].

With respect to reflective optics, it is well known that X-ray reflection efficiency is enhanced when working at grazing angle incidence, lower than the critical angle Θ_c, typically lower than 5° for soft X-rays. Grazing incidence reflective mirrors have been largely employed for hard X-ray focusing in SR facilities and still they are. In order to decrease the focal spot size, the reflector geometry mostly employed nowadays is indeed based on the use of two orthogonal elliptical grazing mirrors, which allow the successive focusing of the X-ray beam in the vertical and horizontal plane. This configuration, shown in Fig. 3.20, is known as Kirkpatrick-Baez system, first proposed in the 1948 [28]. Despite the relative simplicity of the working principle, efficient KB mirrors impose tight manufacturing constraints for both mirror shape and finishing. Shape errors introduce image aberrations worsening the achievable resolution while surface roughness affects mirror contrast and throughput due to scattering effects [69]. The shorter the X-ray wavelength being focused, the more precise the mirror surface must be. Technological advances over the years allowed improving both the precision of the figure shape and the surface smoothing.

The KB system can be either static or dynamic. In the static configuration, an elliptical shape can be obtained from a spherical mirror by differential polishing or differential profile coating [70, 71]. The mode of operation of static KBs is relatively simple and well suited for short radius ellipses. However, the fabrication technology is very expensive and KBs are optimized for a single set of working conditions, i.e. angle of incidence and focusing distance. Dynamic KBs are obtained bending flat mirrors by mechanical or piezoelectric actuation [72]. Dynamic KBs are less expensive than static KBs. They can be produced with a lower roughness and they allow the easy and fast tuning of focusing parameters, but they are not suitable for achieving very short curvature radius.

First KB mirrors were manufactured on glass or quartz substrates and coated with a reflective metal film. Nowadays, they are typically made from silicon crystals polished to near-atomic smoothness (micro-roughness lower than 3 Å) and then coated with ultra-thin layers of hard silicon carbide or dense metals. Multilayer coatings make possible to cover a wide spectral range, from 2 to 90 keV [73]. The improved manufacture capabilities came with advances in mirror cooling system and

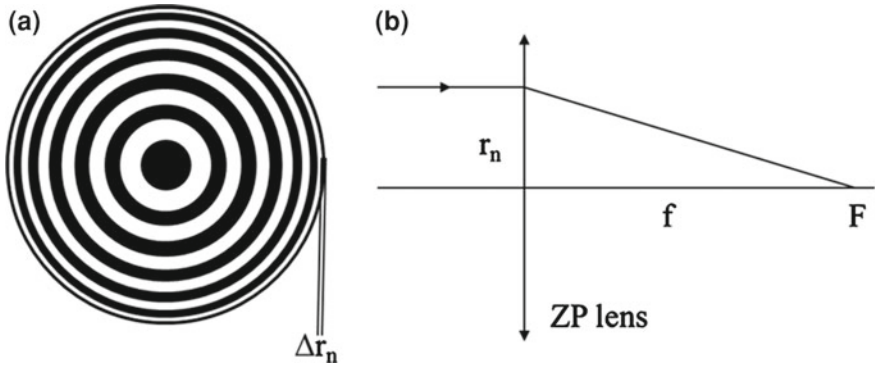


Fig. 3.21 Sketch of a Fresnel Zone Plate (FZP) **a** Zone plates are circular diffraction gratings with radially increasing line density. $\Delta\, r_n$ is the width of the outermost n zone. The central absorbing region, known as stopper, suppresses the strong zero-order diffraction. **b** Geometry for calculating the radius of the *n*th zone, r_n; n is the zone number; f is the focal length and F the focal point

positioning control. Actually, mirror deformation/degradation induced by heat load and tiny errors in axis adjustment would vanish any shape/finish upgrade.

KB mirrors have low chromaticity, which makes them particularly useful for spectroscopy purposes since the incident beam energy can be tuned without the need to adjust the focus on the sample. Resolution of several tens of nanometers has been achieved by exploiting KB systems [74] while the 10 nm resolution barrier has been overcome in more recent years operating an upstream deformable mirror and a multilayer coated KB mirror pair at 20 keV, a system installed at BL29XUL, the 1-km-long beamline of SPring-8 [75].

If KB geometry is the one mostly employed for hard X-ray focusing, the majority of soft X-ray microscopes exploit the focusing capabilities of diffraction optics, in particular the Fresnel Zone Plate (FZP). For this reason, we will devote more attention to their working principle, design, and performances. It has to be highlighted that a complete treatment of ZP theory if far beyond the purpose of this short section, and the reader is refereed to [76].

Figure 3.21 shows the geometry of a FZP. It is made by an alternate sequence of absorbing (black) and transmitting (white) regions, the width of which progressively decreases from the ZP center to the outermost region. The basic idea behind the ZP design can be explained retrieving the constructive interference conditions for a plane wave that illuminates a FZP made by n zones, having radius r_n and outer zone width Δr_n. For a given wavelength λ, in order to have constructive interference for the beams coming from the open zones of the ZP, the optical path difference between two adjacent open zones must be an integer multiple of λ. Being f the first-order focal length, considering the sketch in Fig. 3.21b, it follows:

$$f^2 + r_n^2 = \left(f + \frac{n\lambda}{2}\right)^2 \tag{3.1}$$

$$r_n^2 = n\lambda f + \frac{n^2\lambda^2}{4} \tag{3.2}$$

Neglecting the quadratic term of the expansion, which correspond to spherical aberrations [76], (3.2) can be approximated as:

$$r_n \approx \sqrt{n\lambda f} \tag{3.3}$$

Equation (3.3) defines the focusing condition for a ZP, and shows that a single ZP can focus well for a range of wavelengths, while the focal length increases with decreasing λ. Therefore, ZP lenses have very high chromaticity and incoming beam monochromaticity is mandatory for achieving diffraction-limited resolution. From (3.1) to (3.3), the fundamental parameter describing a zone plate can be retrieved. Defined as Δr_n the width of the nth zone, it is

$$\Delta r_n = \frac{r_n}{2n} = \frac{\lambda f}{2r_n} \tag{3.4}$$

From (3.4) it derives that the surface area of each ZP's zone is the same (i.e. $\pi\lambda f$), once the wavelength and the focal length are fixed. Therefore, each zone contributes equally to the focus intensity.

A ZP has m diffraction orders (being m an odd integer) that lead to multiple focusing points at distances f/m with respect to the optical element. When a zone plate is used as focusing lens, usually the first diffraction order is exploited and all other orders are blocked by a stopper for zero order and suitable Order Sorting Apertures (OSA) for higher ones. Negative diffractive orders also exist, so that a ZP can be operated also as a disperse lens.

The numerical aperture of a ZP can be estimated as in the following:

$$NA = n_{mat}\sin\theta \approx n_{mat}\frac{r_n}{f} = \frac{m\lambda}{2\Delta r_n} \tag{3.5}$$

where n_{mat} is the real part of the refractive index of the medium where the ZP is, Θ is the entrance acceptance angle of the zone plate and m the diffraction order considered, assumed n_{mat} close to 1 and small acceptance angles. Both conditions hold true under standard FZP working condition for X-ray microscopy. On the basis of the Rayleigh-criterion, the ZP spatial resolution δ_{ZP} can be calculated as

$$\delta_{ZP} = 1.22\frac{\lambda}{2NA} = 1.22\frac{\Delta r_n}{m} \tag{3.6}$$

From (3.6) the focal spot dimension decreases with decreasing the width of the outermost absorbing ring and at diffraction orders higher than 1. Conversely, FZP efficiency (i.e. the fraction of the incoming radiation diffracted into a focal spot) decreases by increasing m. A qualitative explanation of the ZP efficiency can be easily understood. First it has to be considered that opaque zones absorb part of the incoming

radiation. Since the fraction of the opaque zones is almost 50 %, it is possible to demonstrate that ∼50 % of the incoming radiation is lost by absorption. Moreover, 25 % of the incoming radiation is just transmitted by the FZP, or better focused at infinite distance for $m = 0$. The remaining 25 % of the focused power is divided among odd focusing order with efficiency inversely proportional to the diffraction order. Actually at the first order the efficiency is about 10 %. By "replacing" the absorbing rings with phase-reversing zones, the thickness of which introduces a phase change of π while minimizing absorption, theoretical ZP efficiency may be improved up to 40 %, since there is no more zero-order focusing at infinite distance. These are the so called phase-reversal zone plates.

The theoretical ZP efficiency is achieved for opaque zones completely absorbing the incoming light or introducing a phase shift of π and transparent zones virtually 100% transparent for the incoming beam. The choice of both absorbing and transparent materials is therefore critical for achieving real ZP efficiency as close as possible to the theoretical one. In addition, absorption efficiency and phase shifting capabilities are also determined by the thickness t of the opaque zones, and therefore related to ZP fabrication strategies. As the lateral resolution of a ZP is inversely proportional to the width of the outermost zone, the best parameter that describes both resolution and efficiency of a ZP is the so called *aspect ratio*, defined as the ratio of outermost region thickness to its width.

For soft X-rays, ZP efficiency at first diffraction order approaches the theoretical value for a thickness of the optical element in the range of few hundreds of nanometers while the phase shift allows to further reduce the absorbing zone thickness [77]. Advances in e-beam lithography, reactive ion etching, electroplating techniques as well as in thin film technologies have guaranteed in recent years significant improvements both in resolution and in efficiency of FZP, allowing to overcome the 10 nm resolution limit for soft X-ray microscopy [78] and to produce structures with aspect ratios greater than 20:1 and an outer zone width of 25 nm [79]. For improving FZP efficiency for higher photon energies, thicker optical focusing elements have to be fabricated, therefore made by very high aspect ratio structures in order to preserve nanometer focusing. Sub-micrometer hard X-ray imaging can be routinely performed using ZP focusing elements, and several examples hard X-ray focusing down to 50 nm have been already published [80–82].

For improving both lateral resolution and efficiency of hard X-ray optics, Multilayer Laue lenses (MLLs) can be used. MLL is a one-dimensional ZP-like optic element [83] made of thousands of alternating layers fabricated by magnetron sputtering, the thickness of which obeys the zone plate law in the direction normal to the surface [84]. Magnetron sputtering is a thin-film deposition technique that enables the accurate deposition of a large number of alternating thin layers [85] and it allows overcoming the aspect ratio limitations in fabricating a ZP imposed by the conventional lithography methods. MLLs have been fabricated that produce 20 nm line focus with an efficiency of ∼30 % at 20 keV [86, 87]. Focusing capabilities below 1 nm have been postulated for MLLs [88] and outer zones having width down to 0.7 nm have been deposited by sputtering with an almost limitless aspect ratio [89]. In order to obtain a 2D focus, two MLLs focusing in orthogonal directions

have been recently assembled, similarly to KB mirrors [90]. Focusing capabilities to 25×40 nm FWHM spot with an efficiency of 17 % at 19.5 keV have been achieved, demonstrating the great potential of MLL optics for scientific applications.

References

1. L.G. Parratt, Phys. Rev. B **95**, 359–369 (1954)
2. W.H. Zachariasen, *Theory of X-ray Diffraction in Crystals* (Dover, New York, 1945)
3. J. Hrdý, Czech. J. Phys. B **39**, 261–265 (1989)
4. R. Frahm, Rev. Sci. Instrum. **60**, 2515–2518 (1989)
5. S. Narayanan, A.R. Sandy, M. Sprung, J. Sullivan, C. Preissner, D. Shu, AIP Conf. Proc. **879**, 911–914 (2007)
6. J. Als-Nielsen, G. Grübel, B.S. Clausen, Nucl. Inst. Methods Phys. Res. B **97**, 522–525 (1995)
7. E. Fonda, A. Rochet, M. Ribbens, L. Barthe, S. Belin, V. Briois, J. Synchrotron Rad. **19**, 417–424 (2012)
8. M. Lemonnier, R. Fourme, F. Rousseaux, R. Kahn, Nucl. Inst. Methods Phys. Res. A **152**, 109–111 (1977)
9. J.A. Golovchenko, R.A. Levesque, P.L. Cowan, Rev. Sci. Instr. **52**, 509–516 (1981)
10. D.M. Mills, M.T. King, Nucl. Inst. Methods Phys. Res. A **208**, 341–347 (1983)
11. J. Goulon, M. Lemonnier, R. Cortes, A. Retournard, D. Raoux, Nucl. Inst. Methods Phys. Res. A **208**, 625–630 (1983)
12. J.W.M. DuMond, Phys. Rev. **52**, 872–883 (1937)
13. G. Faigel, D.P. Siddons, J.B. Hastings, P.E. Haustein, J.R. Grover, J.P. Remeika, A.S. Cooper, Phys. Rev. Lett. **58**, 2699–2701 (1987)
14. H. Tolentino, A.R.D. Rodrigues, Rev. Sci. Instrum. **63**, 946–949 (1992)
15. K. Nakayama, H. Hashizume, A. Miyoshi, S. Kikuta, K. Kohra, Z. Naturforsch. Teil A **28**, 632–635 (1971)
16. S. Díaz-Moreno, J. Synchrotron Rad. **19**, 863–868 (2012)
17. T. Matsushita, T. Ishikawa, H. Oyanagi, Nucl. Inst. Methods Phys. Res. A **246**, 377–379 (1986)
18. H. Amenitsch, S. Bernstorff, M. Rappolt, H. Kriechbaum, H. Mio, P. Laggner, J. Synchrotron Rad. **5**, 506–508 (1998). See also www.elettra.eu/lightsources/elettra/elettra-beamlines/saxs.html
19. G. Aquilanti, O. Mathon, S. Pascarelli, J. Synchrotron Rad. **16**, 699–706 (2009)
20. F. Baudelet, Q. Kong, L. Nataf, J.D. Cafun, A. Congeduti, A. Monza, S. Chagnot, J.P. Itié, High Press. Res. **31**, 136–139 (2011)
21. www.elettra.eu/lightsources/elettra/elettra-beamlines/mcx.html
22. A. Di Cicco, G. Aquilanti, M. Minicucci, E. Principi, N. Novello, A. Cognigni, L. Olivi, J. Phys. Conf. Ser. **190**, 012043 (2009)
23. M. Born, E. Wolf, *Principles of Optics* (Pergamon Press, Oxford 1980)
24. M.C. Hutley, *Diffraction Grating* (Academic Press, London, 1982)
25. M.R. Howells, Section 4.3 in *X-Ray Data Booklet*, ed. by A.C. Thompson, D. Vaughan (Lawrence Berkeley National Laboratory, California, 2001)
26. E. Spiller, Chapter 12 in *Handbook on Synchrotron Radiation*, vol.1, ed. by E.E. Koch (North-Holland, Amsterdam, 1983), pp. 1093–1130
27. H. Haber, J. Opt. Soc. Am. **40**, 153–165 (1950)
28. P. Kirkpatrick, A.V. Baez, J. Opt. Soc. Am. **38**, 766–774 (1948)
29. W.B. Peatman, *Gratings, Mirrors and Slits—Beamline Design for Soft-X-ray Synchrotron Radiation Sources* (Gordon and Breach Science Publishers, Amsterdam, 1997)
30. H. Petersen, Opt. Commun. **40**, 402–406 (1982)
31. H. Petersen, SPIE **733**, 262–264 (1986)

32. W. Jark, Rev. Sci. Instrum. **63**, 1241–1246 (1992)
33. V.N. Strocov, T. Schmitt, U. Flechsig, T. Schmidt, A. Imhof, Q. Chen, J. Raabe, R. Betemps, D. Zimoch, J. Krempasky, X. Wang, M. Grioni, A. Piazzalunga, L. Patthey, J. Synchrotron Rad. **17**, 631–643 (2010)
34. www.elettra.eu/lightsources/elettra/elettra-beamlines/superesca.html
35. http://ssg.als.lbl.gov/ssgdirectory/arenholz/BL402.html
36. R. Follath, F. Senf, Nucl. Inst. Methods Phys. Res. A **390**, 388–394 (1997)
37. H. Petersen, C. Jung, C. Hellwig, W.B. Peatman, W. Gudat, Rev. Sci. Instr. **66**, 1–14 (1995)
38. R.L. Johnson, Chapter 3 in *Handbook on Synchrotron Radiation*, vol.1, ed. by E.E. Koch (NorthHolland, Amsterdam, 1983), pp. 173–260
39. C.T. Chen, F. Sette, Rev. Sci. Instrum. **60**, 1616 (1989)
40. R. Reininger, V. Saile, Nucl. Inst. Methods Phys. Res. A **288**, 343–345 (1990)
41. E. Dietz, W. Braun, A.M. Bradshaw, R.L. Johnson, Nucl. Inst. Methods Phys. Res. A **239**, 359–366 (1985)
42. R. Reininger, J. Bozek, Y. Chuang, M. Howells, N. Kelez, S. Prestemon, S. Marks, T. Warwick, C. Jozwiak, A. Lanzara, Hasan,M.Z., Hussain, Z. AIP Conf. Proc. **879**, 509–512 (2007)
43. H.A. Rowland, Philos. Mag. **13**, 469–474 (1882)
44. A. Rowland, Philos. Mag.**16**, 197–202 (1883)
45. L. Petaccia, P. Vilmercati, S. Gorovikov, M. Barnaba, A. Bianco, D. Cocco, C. Masciovecchio, A. Goldoni, Nucl. Inst. Methods Phys. Res. A **606**, 780–784 (2009). www.elettra.eu/lightsources/elettra/elettra-beamlines/badelph.html
46. www.elettra.eu/lightsources/elettra/elettra-beamlines/iuvs.html
47. http://www-ssrl.slac.stanford.edu/beamlines/bl5-4/
48. T. Kubala, M. Bissen, M. Severson, G. Rogers, D. Wallace, M. Thikim, M.V. Fisher, AIP Conf. Proc. **417**, 91–94 (2000)
49. http://www.src.wisc.edu/facility/list/Port_011.pdf
50. http://www.nsls.bnl.gov/beamlines/beamline.asp?blid=U13UB
51. T. Yamasaki, K. Yamazaki, A. Ino, M. Arita, H. Namatame, M. Taniguchi, A. Fujimori, Z.-X. Shen, M. Ishikado, S. Uchida, Phys. Rev. B **75**, 140513(R) (2007)
52. http://www.hsrc.hiroshima-u.ac.jp/
53. G. Reichardt, J. Bahrdt, J.-S. Schmidt, W. Gudat, A. Ehresmann, R. Müller-Albrecht, H. Molter, H. Schmoranzer, M. Martins, N. Schwentner, S. Sasaki, Nucl. Inst. Methods Phys. Res. A **467–468**, 462–465 (2001)
54. K. Radler, J. Berkowitz, J. Chem. Phys. **70**, 216–220 (1979)
55. P.A. Heimann, M. Koike, C.W. Hsu, D. Blank, X.M. Yang, A.G. Suits, Y.T. Lee, M. Evans, C.Y. Ng, C. Flaim, H.A. Padmore, Rev. Sci. Instrum. **68**, 1945–1951 (1997)
56. K. Ito, T. Sasaki, T. Namioka, K. Ueda, Y. Morioka, Nucl. Inst. Methods Phys. Res. A **246**, 290–293 (1986)
57. S. Hufner, *Photoelectron Spectroscopy* (Springer-Verlag, Berlin, 1995)
58. F. Reinert, S. Hufner, New, J. Phys. **7**, 97 (2005)
59. M.P. Seah, W.A. Dench, Surf. Interface Anal. **1**, 2–11 (1979)
60. B. Kaulich, P. Thibault, A. Gianoncelli, M. Kiskinova, J. Phys.: Condens. Matter **23**, 083002 (2011)
61. R. Falcone, C. Jacobsen, J. Kirz, S. Marchesini, D. Shapiro, J. Spence, Contemporary Physics **52**, 293–318 (2011)
62. A. Sakdinawat, D. Attwood, Nature Photonics 4, 840–848 (2010)
63. http://cheiron2007.spring8.or.jp/pdf/Lai.pdf
64. A. Snigirev, V. Kohn, I. Snigireva, B. Lengeler, Nature **384**, 49–51 (1996)
65. C.G. Schroer, J. Meyer, M. Kuhlmann, B. Benner, T.F. Günzler, B. Lengeler, C. Rau, T. Weitkamp, A. Snigirev, I. Snigireva, Appl. Phys. Lett. **81**, 1527–1529 (2002)
66. C.G. Schroer, M. Kuhlmann, U.T. Hunger, T.F. Günzler, O. Kurapova, S. Feste, F. Frehse, B. Lengeler, M. Drakopoulos, A. Somogyi, A.S. Simionovici, A. Snigirev, I. Snigireva, C. Schug, W.H. Schröder, Appl. Phys. Lett. **82**, 1485–1487 (2003)

67. C.G. Schroer, O. Kurapova, J. Patommel, P. Boye, J. Feldkamp, B. Lengeler, M. Burghammer, C. Riekel, L. Vincze, A. van der Hart, M. Küchler, Appl. Phys. Lett. **87**, 124103 (2005)
68. A. Bosak, I. Snigireva, K.S. Napolskii, A. Snigirev, Adv. Mater. **22**, 3256–3259 (2010)
69. E.L. Church, P.Z. Takacs, Opt. Eng. **34**, 353–360 (1995)
70. G.E. Ice, J.S. Chung, J. Tischler, A. Lunt, L. Assoufid, Rev. Sci. Instrum. **71**, 2635–2639 (2000)
71. K. Yamauchi, K. Yamamura, H. Mimura, Y. Sano, A. Saito, K. Endo, A. Souvorov, M. Yabashi, K. Tamasaku, T. Ishikawa, Y. Mori, Jpn. J. Appl. Phys. **42**, 7129–7134 (2003)
72. Y. Dabin, G. Rostaing, A. Rommeveaux, A.K. Freund, Proc. SPIE **4782**, 235–245 (2002)
73. C. Morawe, P. Pecci, J.C. Peffern, E. Ziegler, Rev. Sci. Instrum. **70**, 3227–3232 (1999)
74. S. Matsuyama, H. Mimura, H. Yumoto, Y. Sano, K. Yamamura, M. Yabashi, Y. Nishino, K. Tamasaku, T. Ishikawa, K. Yamauchi, Rev. Sci. Instrum. **77**, 103102–103106 (2006)
75. H. Mimura, S. Handa, T. Kimura, H. Yumoto, D. Yamakawa, H. Yokoyama, S. Matsuyama, K. Inagaki, K. Yamamura, Y. Sano, K. Tamasaku, Y. Nishino, M. Yabashi, T. Ishikawa, K. Yamauchi, Nat. Phys. **6**, 122–125 (2010)
76. M. Howells, C. Jacobsen, T. Warwick, A. van den Bos, in *Science of Microscopy*, ed. by P.W. Hawkes, J.C.H. Spence (Springer, New York, 2007), pp. 835–926
77. S.-R. Wu, Y. Hwu, G. Margaritondo, Materials **5**, 1752–1773 (2012)
78. J. Vila-Comamala, K. Jefimovs, J. Raabe, T. Pilvi, R.H. Fink, M. Senoner, A. Maassdorf, M. Ritala, C. David, Ultramicroscopy **109**, 1360–1364 (2009); W. Chao, J. Kim, S. Rekawa, P. Fischer, E.H. Anderson, Opt Express **17**, 17669–17677 (2009)
79. J. Vila-Comamala, S. Gorelick, V.A. Guzenko, E. Färm, M. Ritala, C. David, Nanotechnology **21**, 285305 (2010)
80. T. Koyama, H. Takano, S. Konishi, T. Tsuji, H. Takenaka, S. Ichimaru, T. Ohchi, Y. Kagoshima, Rev. Sci. Instrum. **83**, 013705 (2012)
81. G.C. Yin, Y.F. Song, M.T. Tang, F.R. Chen, K.S. Liang, F.W. Duewer, M. Feser, W.B. Yun, H.P.D. Shieh, Appl. Phys. Lett. **89**, 221122 (2006)
82. S. Gorelick, J. Vila-Comamala, V.A. Guzenko, R. Barrett, M. Salome, C.J. David, Synchrotron Radiat. **18**, 442–446 (2011)
83. H.C. Kang, J. Maser, G.B. Stephenson, C. Liu, R. Conley, A.T. Macrander, S. Vogt, Phys. Rev. Lett. **96**, 127401–127405 (2006)
84. C. Liu, R. Conley, A.T. MacRander, J. Maser, H.C. Kang, M.A. Zurbuchen, G.B. Stephenson, J. Appl. Phys. **98**, 113519 (2005)
85. H. Yan, Y.S. Chu, J. Synchrotron Rad. **20**, 89–97 (2013)
86. H.C. Kang, H.F. Yan, R.P. Winarski, M.V. Holt, J. Maser, C.A. Liu, R. Conley, S. Vogt, A.T. Macrander, G.B. Stephenson, Appl. Phys. Lett. **92**, 221114 (2008)
87. T. Koyama, H. Takenaka, S. Ichimaru, T. Ohchi, T. Tsuji, H. Takano, Y. Kagoshima, AIP Conf. Proc. **1365**, 24–27 (2011)
88. H.F. Yan, J. Maser, A. Macrander, Q. Shen, S. Vogt, G.B. Stephenson, H.C. Kang, Phys. Rev. B. **76**, 115438 (2007)
89. R. Conley, C. Liu, C.M. Kewish, A.T. Macrander, C. Morawe, Proc. SPIE **6705**, 670505 (2007)
90. H. Yan, V. Rose, D. Shu, E. Lima, H.C. Kang, R. Conley, C. Liu, N. Jahedi, A.T. Macrander, G.B. Stephenson, M. Holt, Y.S. Chu, M. Lu, J. Maser, Opt. Express **19**, 15069–15076 (2011)

Part II
Fundamental Interactions

Chapter 4
Introduction to Matter Radiation Interaction

Settimio Mobilio

Abstract The main phenomena associated to the interaction between radiation and matter relevant for synchrotron radiation studies, i.e. absorption and scattering, are introduced and described. First a classical approach is used in which the radiation is described as an electromagnetic wave and the matter as a macroscopic system characterized by its optical constants; then the optical constants are calculated using the microscopic classical Lorentz model, describing the matter as a set of damped oscillators. A more accurate description is achieved using the semiclassical approach, describing the matter as a quantum system and the radiation as a perturbation which induces transition between the quantum state of the matter. Then, using the full quantum approach in which the radiation field is described as a set of photons, the complete expressions of the absorption and scattering cross section are calculated. In particular for the scattering cross section, relativistic effects associated with the spin are also taken into accounts.

4.1 Introduction

The interaction between matter and radiation is a fundamental topic of large interest and with strong implications for many field of physics; because there exists an extensive literature on the argument this lecture do not aim to give a complete overview of the field, but only to remaind those aspects relevant for this book in order to describe and understand the experimental methods used in synchrotron radiation research (for a full description of the interaction between matter and radiation, see the books [1, 2]). In the energy range of interest for synchrotron radiation mainly two processes play a role, namely the absorption and the scattering (Fig. 4.1). Absorption measures the ability of a sample to attenuate a photon beam, providing information on the dis-

S. Mobilio (✉)
Dipartimento di Scienze, Universita' Roma Tre, via della Vasca Navale 84, 00146 Rome, Italy
e-mail: settimio.mobilio@uniroma3.it

S. Mobilio et al. (eds.), *Synchrotron Radiation*,
DOI: 10.1007/978-3-642-55315-8_4, © Springer-Verlag Berlin Heidelberg 2015

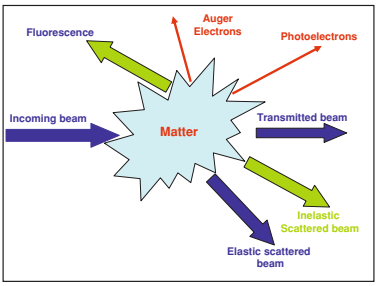


Fig. 4.1 Basic interactions between matter and radiation

tribution of the energy levels of a sample and giving a picture mainly of its electronic and vibrational properties. It relies on the absorption of a photon that brings the system under study into an excited state; when the excited state is above the vacuum level, one or more photoelectrons can be emitted; the study of the properties of these photoelectrons give rise to photoemission spectroscopy. In the ultraviolet and X-ray range the system may also undergo decay processes with emission of fluorescence photons or Auger electrons or with the fragmentation into neutral/ionized fragments.

Quantitatively absorption is described by the absorption coefficient that can be measured in a direct way by measuring the attenuation of the beam in passing through the sample as a function of the incoming photon energy (transmission spectroscopy) or in an undirect way, by measuring the yield of the photoemitted electrons or of a decay process (fluorescence photons, Auger electrons, charged or neutral fragments), whose intensities are linked to the absorption coefficient.

The second interaction mechanism is the scattering: there is a finite probability that incoming photons are diffused by the matter changing their direction of propagation. The diffusion can be elastic, with no exchange of energy between the photons and matter resulting in diffused photons with the same energy than the incoming ones; but it may be also inelastic, resulting in outcoming photons whose energy is different from that of the incoming ones. Diffraction techniques are based on the elastic scattering and the main information they bring are on the structural properties of a sample. In inelastic scattering the exchange of energy equals the energy of an excited state of the sample; therefore using inelastic scattering, the excitation spectrum of the sample can be studied.

Imaging methods are mainly based on absorption, photoemission and scattering processes; they achieve extreme sensitivity when synchrotron radiation is used, thanks to the intensity and brilliance of the source that allows to focus the beam to sub-micrometer sizes and to reach extremely high spatial resolution and dilution sensitivity.

In this lecture the absorption and scattering interaction processes are described in some details.

In Sect. 4.2 the interaction between the radiation and matter is described using a classical approach, in which the radiation is considered as an electromagnetic

wave interacting with a medium that is characterized by its macroscopical optical constants (refraction index and absorption coefficient or dielectric function). In order to have an analytical formulation of the optical constants, the matter is microscopically described as composed by an ensemble of independent classical oscillators. The same model is used also to describe the main aspects of the scattering of the radiation from electrons and from atoms.

In Sect. 4.3 the so called semiclassical approximation is introduced, in which the radiation field is described in a classical way and the matter as a quantum system. First the probability of transitions between quantum states under the influence of the electromagnetic radiation is calculated. Then the absorption coefficient is calculated and its relationships with the simple classical model are underlined. Finally it is shown how the elastic and Compton scattering can be calculated using this approach.

In Sect. 4.4 the interaction between radiation and matter is presented in the full quantum approach in which the electromagnetic field is described by an ensemble of photons. First it is shown how using such an approach the absorption cross section comes out; then the scattering process is carefully analysed, calculating the cross section for elastic, inelastic, anomalous and resonant scattering. Finally, it is shown that at high energy the anomalous scattering cross section becomes proportional to the magnetic orbital moment of the system, so introducing the ability of X-ray scattering to measure magnetic properties.

In Sect. 4.5 relativistic effects are considered, showing how they give rise to additional scattering effect associated with the spin of the electrons.

4.2 Classical Description of Electromagnetic Waves and Their Interaction with the Matter

4.2.1 Electromagnetic Waves in the Vacuum

In vacuum the Maxwell equations give rise to the wave equations for the electric **E** and magnetic field **B**:

$$\nabla^2\mathbf{E} - \varepsilon_0\mu_0\frac{\partial^2\mathbf{E}}{\partial t^2} = 0 \qquad \nabla^2\mathbf{B} - \varepsilon_0\mu_0\frac{\partial^2\mathbf{B}}{\partial t^2} = 0 \tag{4.1}$$

The solutions of these wave equations foresee that the electric and the magnetic fields propagate as waves with a speed $c = 1/\sqrt{\varepsilon_0\mu_0} = 2.99792456\ 10^8$ m/s. The electric and magnetic fields are not independent, because for the Maxwell equations they are perpendicular one to other, oscillates in phase and the ratio between their amplitude has a well define value. In the particular case of a plane wave, the fields can be written as:

$$\mathbf{E} = \mathbf{E}_0 e^{j(\mathbf{kr}-\omega t)} \text{ and } \mathbf{B} = \mathbf{B}_0 e^{j(\mathbf{kr}-\omega t)} \tag{4.2}$$

where the vector **k** is the wave-vector of the radiation field; its direction gives the direction of propagation of the plane wave, while its modulus gives the wavelength λ_0 through the relation: $|\mathbf{k}| = 2\pi/\lambda_0$. ω is the angular frequency of the radiation, equal to: $\omega = 2\pi\nu$, with ν the frequency of the radiation. An important relationship between these quantities is the dispersion relation obtained by substituting the plane wave expressions into the wave equations:

$$k^2 - \varepsilon_0\mu_0\omega^2 = 0 \tag{4.3}$$

This expression connect the wave-vector and the wavelength to the frequency; other forms of the dispersion relation in vacuum are $\omega = ck$ and $\lambda_0\nu = \mathrm{c}$.

The vectors $\mathbf{E}_0$ and $\mathbf{B}_0$ are the amplitude of the oscillations of the electric and magnetic fields; their directions give the direction of the oscillations, while their modulus the amplitude of the oscillations. The modulus of the two vectors are not independent, because their ratio is always equal to c, that is $|\mathbf{E}|/|\mathbf{B}| = c$. This relation implies that the energy density w_E associated to the electric field is equal to the energy density associated to the magnetic field w_B; in fact:

$$w_E = \frac{1}{2}\varepsilon_0|\mathbf{E}|^2 = \frac{1}{2}\varepsilon_0 c^2|\mathbf{B}|^2 = \frac{1}{2\mu_0}|\mathbf{B}|^2 = w_B \tag{4.4}$$

The energy density of the electric and magnetic field are both function of time; it is useful to calculate their mean value, that for a plane wave is: $\bar{w}_E = \frac{1}{2}\varepsilon_0|\bar{\mathbf{E}}|^2 = \frac{1}{4}\varepsilon_0|\mathbf{E}_0|^2$.

The total energy density w associated with the wave is $\mathrm{w} = w_E + \mathrm{w}_B = \varepsilon_0|\mathbf{E}|^2$; the total mean energy density is: $\bar{w} = \frac{1}{2}\varepsilon_0|\mathbf{E}_0|^2$.

The directions of $\mathbf{E}_0$ and $\mathbf{B}_0$ are those in which the electric and magnetic field oscillate. These two fields are mutually perpendicular and are also perpendicular to the wavevector **k**. A synthetic way to write these properties is $\mathbf{E} = c\mathbf{B} \times \mathbf{k}$.

The intensity of the radiation I is the mean power carried per unit area by the beam and is given by: $\mathrm{I} = \bar{w}\mathrm{c}$; it propagates into the direction of the wave that is into the direction of the wave-vector **k**. It can be also written as the mean flux of the so-called Poynting **S**.

$$\mathbf{S} = \frac{\mathbf{E} \times \mathbf{B}}{\mu_0} = \varepsilon_0|\mathbf{E}|^2 c\hat{k} \;\rightarrow \bar{\mathbf{S}} = \frac{1}{2}\varepsilon_0|\mathbf{E}_0|^2 c\hat{k} \tag{4.5}$$

We see that the Poynting vector points into the propagation direction of the radiation.

From the above reported properties of the electric and magnetic field, it is clear that it is enough to know one of the two fields to determine the other one. This allows in advanced electromagnetism and in electrodynamics to introduce an additional vector **A**, called the vector potential and to deduce the properties of **E** and **B** from

those of **A**.[1] In classical electromagnetism **A** has no specific physical meaning, it is only a powerful way to synthesize the overall properties of **E** and **B**, which are the physical measurable quantities. This is no more true in quantum electrodynamics, when the vector potential **A** assume a crucial role in describing electromagnetic fields. Without entering into the details, we recall here only the main relationships between the vector potential **A** and the electric and magnetic fields, which are:

$$\mathbf{E} = -\frac{\partial \mathbf{A}}{\partial t} \qquad \mathbf{B} = \nabla \times \mathbf{A} \tag{4.6}$$

In the case of a plane wave **A** is written as: $\mathbf{A} = \mathbf{A}_0 e^{j(\mathbf{kr}-\omega t)}$, so we get:

$$\mathbf{E} = \omega \mathbf{A}_0 e^{j(\mathbf{kr}-\omega t)} \qquad \mathbf{B} = \mathbf{k} \times \mathbf{A}_0 e^{j(\mathbf{kr}-\omega t)} \tag{4.7}$$

The mean energy density is written as $\bar{w} = \frac{1}{2}\varepsilon_0 \omega^2 |\mathbf{A}_0|^2$ and the Poynting vector as: $\mathbf{S} = \frac{1}{2}\varepsilon_0 \omega^2 |\mathbf{A}_0|^2 c\hat{k}$

4.2.2 Electromagnetic Waves in Matter

In the matter the wave equations of the radiation are modified by the interaction of the electric and magnetic fields with the charges through the Lorentz force: $\mathbf{F} = q(\mathbf{E} + \mathbf{v} \times \mathbf{B})$ and become:

$$\nabla^2 \mathbf{E} - \varepsilon\mu \frac{\partial^2 \mathbf{E}}{\partial t^2} = 0 \qquad \nabla^2 \mathbf{B} - \varepsilon\mu \frac{\partial^2 \mathbf{B}}{\partial t^2} = 0 \tag{4.8}$$

ε and μ are the dielectric constant and the magnetic permeability of the material. Three new phenomena occur:

1. the speed of light changes, becoming $\mathrm{v} = 1/\sqrt{\varepsilon\mu}$; introducing the relative dielectric constant ε_r and the relative magnetic permeability μ_r through the relationships:
$$\varepsilon = \varepsilon_r \varepsilon_0 \qquad \mu = \mu_r \mu_0 \tag{4.9}$$
we get $\mathrm{v} = c/\sqrt{\varepsilon_r \mu_r} = c/n$, where $\mathrm{n} = \sqrt{\varepsilon_r \mu_r}$ is the index of refraction of the material. [2]
2. The intensity of the wave is no more constant during the propagation, but decreases according to the Lambert equation: $I = I_0 e^{-\mu x}$ where μ is the absorption coefficient of the material.

[1] This is true in the Coulomb Gauge and in absence of external electric charges; see Chap. 5 for a detailed description.

[2] Hereafter we assume that the wave propagates into a non magnetic medium in which $\mu_r = 1$, therefore $\mathrm{n} = \sqrt{\varepsilon_r}$.

3. The wave is partially deviated into directions different from the propagation one; these additional waves, called scattered waves, may have the same frequency (elastic scattering) or different frequency (inelastic scattering) with respect to the incoming radiation; the decrease of intensity of the beam due to the scattering is one of the phenomena determining the absorption coefficient μ.

The index of refraction n introduced above is the physical quantity entering the low of refraction that occurs at the interfaces between different media, where an incoming wave is partially reflected and partially refracted.

In matter the dispersion relation for a plane wave becomes:

$$k^2 - \varepsilon\mu\omega^2 = 0 \quad \text{or} \quad k^2 - \frac{\omega^2 n^2}{c^2} = 0 \tag{4.10}$$

This relation implies that $\lambda = \lambda_0/\mathrm{n}$: the wavelength is reduced with respect to the vacuum case by the factor n. The expression of the plane wave becomes:

$$\mathbf{E} = \mathbf{E}_0 e^{j(\mathbf{kr}-\omega t)} = \mathbf{E}_0 e^{j(\frac{n\omega}{c}\hat{\mathbf{k}}\mathbf{r}-\omega t)} \qquad \mathbf{B} = \mathbf{B}_0 e^{j(\mathbf{kr}-\omega t)} = \mathbf{B}_0 e^{j(\frac{n\omega}{c}\hat{\mathbf{k}}\mathbf{r}-\omega t)} \tag{4.11}$$

They show how the index of refraction modifies the spatial dependence of the wave.

In general the index of refraction is a complex quantity $\mathrm{n} = \mathrm{n}_r + \mathrm{j}\beta$ with a real n_r and a imaginary part β.[3] A plane wave propagating in a medium with a complex index of refraction behaves as:

$$\mathbf{E} = \mathbf{E}_0 e^{j(\frac{n\omega}{c}\hat{\mathbf{k}}\mathbf{r}-\omega t)} = \mathbf{E}_0 e^{j(\frac{n_r\omega}{c}\hat{\mathbf{k}}\mathbf{r}-\omega t)} e^{-\frac{\beta\omega}{c}r} \tag{4.12}$$

We see that the amplitude of the wave decreases exponentially during propagation and the intensity I decreases as:

$$I = I_0 e^{-\frac{2\beta\omega}{c}r} = I_0 e^{-\mu r} \tag{4.13}$$

This expression shows that the absorption coefficient μ of a material is determined by the imaginary part of the index of refraction β:

$$\mu = 2\beta\omega/c = 4\pi\beta/\lambda \tag{4.14}$$

The index of refraction n_r and the absorption coefficient μ fully describe the propagation of a beam in a medium; some aspects are to be underlined:

[3] Often in literature (and also in this chapter when not misleading) "index of refraction" means the real part of the index of refraction n_r and "complex index of refraction" means n.

- generally their values depend on the frequency of the wave;
- they are not independent, the knowledge of one of them in all the frequency range allows to determine the other one through the so called Kramers-Kronig relationships;
- to characterize the propagation of electromagnetic wave in the matter, their use is not unique but other physical quantities can be chosen.

The physical origin of the index of refraction is in the interaction of the electromagnetic field **E** with the charge of the matter, which, under the action of the electric force, start to oscillate; the positive and the negative charges move in opposite directions, giving rise to an electric dipole moment. Macroscopically the phenomenon is described by the vector **P**, the induced electric dipole moment per unit volume. Without entering now into the microscopic description of this phenomenon we can say that the oscillations of the vector P are characterized by an amplitude $\mathbf{P}_0$ and a phase shift δ with respect to the electric field, that is: $\mathbf{P} = \mathbf{P}_0 e^{j(kr-\omega t+\delta)}$; in the simplest approximation, the linear one, the vector **P** is proportional to the electric field through the susceptibility coefficient χ:

$$\mathbf{P} = \mathbf{P}_0 e^{j(\mathbf{kr}-\omega t+\delta)} = \varepsilon_0 \chi \mathbf{E} = \varepsilon_0 \chi \mathbf{E}_0 e^{j(\mathbf{kr}-\omega t)} \Rightarrow \chi = \frac{|P_0|}{\varepsilon_0 |E_0|} e^{j\delta} = \chi_0 e^{j\delta} \tag{4.15}$$

Remembering that the dielectric constant is: $\varepsilon = \varepsilon_0(1+\chi)$ we get $\varepsilon_r = 1 + \chi_0 e^{j\delta} = \varepsilon' + j\varepsilon''$: in general the dielectric constant is a complex quantity, with a real and an imaginary part. As a consequence also the index of refraction is in general a complex quantity; in fact from its definition $\mathrm{n} = \mathrm{n}_r + \mathrm{j}\beta = \sqrt{\varepsilon_r}$ we get:

$$n_r = \sqrt{\frac{\varepsilon' + \sqrt{\varepsilon'^2 + \varepsilon''^2}}{2}} \cong \sqrt{\varepsilon'} \qquad \beta = \sqrt{\frac{-\varepsilon' + \sqrt{\varepsilon'^2 + \varepsilon''^2}}{2}} \cong \frac{\varepsilon''}{2} \tag{4.16}$$

As already said, the two optical constant n_r and β as well as n_r and μ are not independent one from the other one, because they are related by the well known Kramers Kronig transformations (KK relationships):

$$n_r(\omega) = 1 + \frac{c}{\pi} \int_0^\infty \frac{\mu(\omega')}{\omega'^2 - \omega^2} \tag{4.17}$$

$$\mu(\omega) = -\frac{4\omega^2}{\pi c} \int_0^\infty \frac{n_r(\omega') - 1}{\omega'^2 - \omega^2} \tag{4.18}$$

The measurement of μ in all the frequency domain allows to calculate n_r and viceversa. The Kramers-Kronig relationships originate from very general considerations on the cause-effect relation between the electric field and the polarization; as a matter of fact a polarization **P**(t) can be caused only by the values of the electric

field at time $t' < t$; this implies the existence of a specific mathematical relationship between the optical constants, expressed by the KK transformations.

4.2.3 Classical Microscopic Description of the Complex Index of Refraction

In order to study the microscopic characteristics of a material from its refraction index a microscopic model is needed in order to calculate the electric dipole moment vector P and the index of refraction and to compare the calculations with experimental measurements. A very simple and incredibly powerful model is the Lorentz one, according to which the matter is performed by independent classical charged damped electron oscillators of charge e, mass m and frequency ω_i. In presence of an external electric field the electrons move according to the equation:

$$\frac{d^2\mathbf{r}}{dt^2} - \gamma\frac{d\mathbf{r}}{dt} + \omega_i^2\mathbf{r} = \frac{-e}{m}\mathbf{E}_0 e^{j\omega t} \tag{4.19}$$

whose solution is:

$$\mathbf{r}(t) = \frac{-e}{m}\frac{\mathbf{E}_0 e^{j\omega t}}{\omega_i^2 - \omega^2 - j\gamma\omega} \tag{4.20}$$

Each oscillator give rise to an electric dipole moment:

$$\mathbf{p}(t) = -e\mathbf{r}(t) = \frac{e^2}{m}\frac{\mathbf{E}_0 e^{j\omega t}}{\omega_i^2 - \omega^2 - j\gamma\omega} \tag{4.21}$$

Assuming the presence of N_i electrons of frequency i per unit volume we get for the polarization vector per unit volume P

$$\mathbf{P} = \sum_i N_i \frac{e^2}{m}\frac{\mathbf{E}_0 e^{j\omega t}}{\omega_i^2 - \omega^2 - j\gamma\omega} \Rightarrow \chi = \frac{1}{\varepsilon_0}\sum_i N_i \frac{e^2}{m}\frac{1}{\omega_i^2 - \omega^2 - j\gamma\omega} \tag{4.22}$$

The relative dielectric constant becomes:

$$\varepsilon_r = 1 + \chi = 1 + \frac{1}{\varepsilon_0}\sum_i N_i \frac{e^2}{m}\frac{1}{\omega_i^2 - \omega^2 - j\gamma\omega} \tag{4.23}$$

whose real and imaginary parts are:

$$\varepsilon' = 1 + \frac{1}{\varepsilon_0}\sum_i \frac{N_i e^2}{m}\frac{\omega_i^2 - \omega^2}{(\omega_i^2 - \omega^2)^2 + \gamma^2\omega^2} \qquad \varepsilon'' = \frac{1}{\varepsilon_0}\sum_i \frac{N_i e^2}{m}\frac{\gamma\omega}{(\omega_i^2 - \omega^2)^2 + \gamma^2\omega^2} \tag{4.24}$$

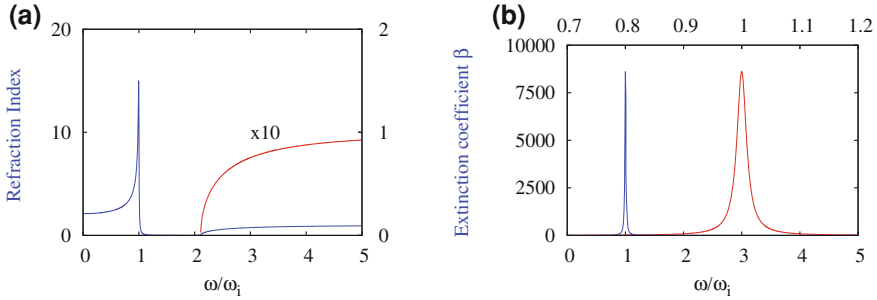


Fig. 4.2 Typical behaviour of the refraction index associated with a single oscillator frequency; simulation is based on SiO_2 data. In *panel a* the *red curve* (upper curve on the *right*) was multiplied by a factor 10 and shows how the refraction index goes to 1 at high energy; *panel b* shows how the imaginary part is negligible, apart in a small region around ω_i of the order of $1/\gamma$; the *red curve* (on the *right*) refers to the upper x-scale.

The index of refraction n is then calculated according to (4.16).

Figure 4.2a reports the behaviour of the real part of the refraction index, for a single electron oscillator. At low frequency (i.e. for frequency considerably lower than the oscillator frequency ω_i) the real part is higher than 1 and increases smoothly with energy; near the resonance it increases sharply, reaches the maximum value near the resonance and then decreases rapidly assuming negligible values in a rather large range above the resonance; in this range an electromagnetic wave cannot propagate into the material because ε' is negative; at higher energy, ε' becomes again positive, the index of refraction starts to increase towards the asymptotic value of 1 reached at very high energy; however its value is always lower than 1. This characteristic is of extreme importance in many experimental techniques as we shall see in a moment. The imaginary part, called also extinction coefficient, shows a sharp peak in correspondence of the resonance with a width of the order of $1/\gamma$ (Fig. 4.2b). Apart this sharp region, it is negligible in all the spectral range; because according to (4.14) the absorption coefficient μ is proportional to the extinction coefficient β, this behaviour implies that the absorption of the radiation occurs only in a small region around the resonance whose width is of the order of $1/\gamma$.

In a real material many different electron oscillators contribute to the index of refraction and to the absorption coefficient, therefore they show a much more complex behaviour that can also differ significantly from those of a single resonance case (see Figs. 4.3 and 4.4).

It is interesting to look at the behaviour of the refraction index at high frequency, in the X-ray region, where the radiation frequency ω is much higher than the resonance frequencies ω_i of all electrons; in this region the real part of the index of refraction n_r becomes:

$$n_r \cong \sqrt{1 - \frac{1}{\varepsilon_0} \sum_i N_i \frac{e^2}{m\omega^2}} \cong 1 \tag{4.25}$$

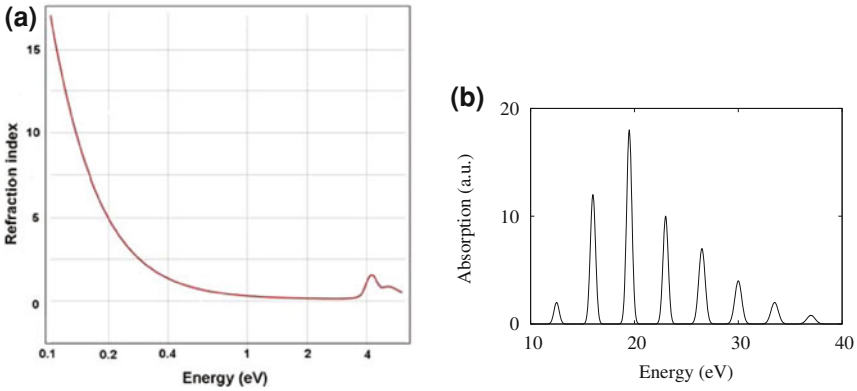


Fig. 4.3 Index of refraction in real materials. *Panel a*: refraction index of Ag (data from [3]) the decrease of the refraction index with energy in apparent contrast with Fig. 4.2a is due to the presence of a continuous distribution of resonances: increasing the energy, the number of resonances whose contribution drops to a negligible value increase, resulting in a continuous decrease of n_r; the step increase around 4 eV is due to a plasma resonance. *Panel b* typical behaviour of an absorption spectrum in presence of more well separated resonances; a quantitative analysis of these peaks allows to determine the physical parameters of each resonance ω_i, N_i and γ_i.

$\sum_i N_i$ is the number of electrons per unit volume of the material, that is the electron density in electron units ρ_e; it can be written also as $\rho_e = \sum_k N_k Z_k$ where N_k is the number of atoms of kind k and atomic number Z_k per unit volume.

The above expression can be expanded in series around the value 1:

$$n_r \cong 1 - \frac{1}{2\varepsilon_0} \sum_k N_k \frac{Z_k e^2}{m\omega^2} = 1 - \delta \tag{4.26}$$

In the X-ray region the index of refraction is a little bit lower than 1 for the small quantity $\delta \sim 10^{-5}$–10^{-6}; in the same energy region the imaginary part is $\beta = 4\pi\mu/\lambda \sim 10^{-9}$–$10^{-10}$.

The small deviation from one of the real part and the smallness of β with respect to δ, are of extreme importance in several experimental methodologies, like grazing incidence methods (see Chaps. 3, 6, 11 and 29) and phase contrast imaging (see Chaps. 13, 14 and 22).

Let us examine briefly the case of grazing incidence. It is well known that when an electromagnetic wave reach a surface separating two media with different index of refraction, the wave is partially reflected and partially transmitted as shown in Fig. 4.5. The angles θ and ϕ are connected by the law of refraction: $n_{r1}\cos\theta = n_{r2}\cos\phi$, that reduces to $\cos\theta = n_r\cos\phi$ in the case the first medium is the vacuum. Because in the X-ray region $n_r < 1$, we have: $\cos\theta < n_r\cos\phi \Rightarrow \theta > \phi$, as shown in the figure. It is clear that there exist a critical angle θ_c for which $\phi = 0$, given by

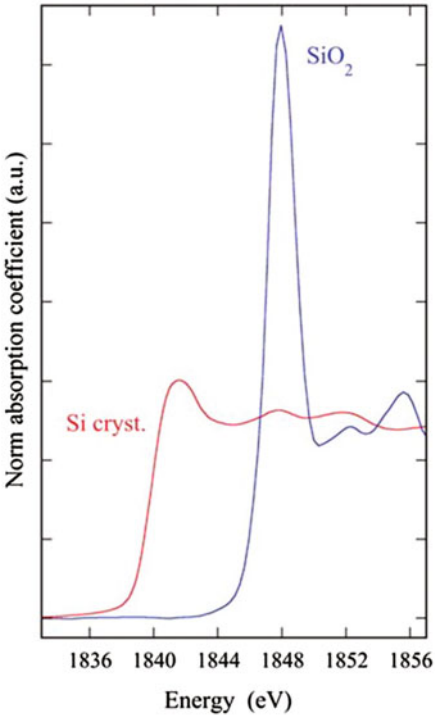


Fig. 4.4 Absorption spectrum of Si and SiO_2 in the X-ray region measured at DAFNE-Light source; in this region the width of resonances is not negligible with respect to their energy difference, therefore the absorption peaks merge, resulting into a continuum increase of the absorption, called absorption edge. In the case of SiO_2 a resonance is clearly visible superimposed to the edge increase; in the case of Si the resonance is much less evident (courtesy of A. Balerna)

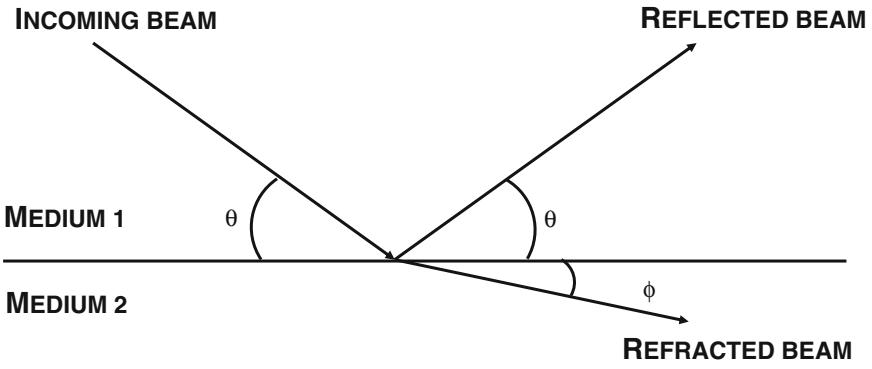


Fig. 4.5 Reflection and refraction phenomena occurring at the interface between two media

the relation: $\cos\theta_c = n_r$: for a grazing incidence angle lower or equal to the critical value θ_c the wave does not enter into the material and is only and totally reflected. Because θ_c is a small angle, it results that:

$$\cos\theta_c = 1 - \frac{\theta_c^2}{2} = 1 - \delta \Rightarrow \theta_c = \sqrt{2\delta} = \sqrt{\frac{1}{\varepsilon_0}\sum_k N_k \frac{Z_k e^2}{m\omega^2}} \sim 1 - 10\,\text{mrad} \quad (4.27)$$

Total reflection is the physical principle on which mirrors working in the X-ray range are based (see Chap. 3).

Grazing incidence spectroscopies methods profit of the penetration of the radiation into the medium, which is not zero but is limited to a small region called penetration depth (pd), whose value is given by the relation[4]:

$$pd = \frac{\lambda}{2\pi\theta_c} \simeq 5\ \text{Å for Au and } 15\ \text{Å for Si.} \quad (4.28)$$

The presence of an electric field inside the material limited to a small region near the interface gives the possibility to isolate and measure the response of the atoms which are near the surface suppressing the response of the atoms which are inside the bulk, so giving surface sensitivity to grazing incidence methods.

4.2.4 The Scattering and its Classical Description

The other phenomenon occurring during the propagation of an electromagnetic wave in a medium is the scattering: additional waves are originated into any direction with the same frequency or different frequency with respect the original wave. To characterize the scattering we will use the double differential scattering cross section $d^2\sigma/d\Omega dE$ that gives the power scattered into a solid angle $d\Omega$ and in a energy region dE normalized to the incoming intensity; when dealing with elastic scattering, we will use the single differential cross section $d\sigma/d\Omega$ i.e. the normalized power scattered in a solid angle $d\Omega$. The origin of the scattering is very simple: in the presence of the incoming wave the charges constituting the matter start to oscillate and, according to the classical electromagnetic theory, they emit electromagnetic radiation. The main driving force of these oscillations is the electric field of the incoming radiation that force the electrons to oscillate[5]; also other mechanisms associated to the magnetic field of the radiation and to the magnetic moment of the electrons give rise to a smaller but not negligible scattering, as we shall see later on. Maxwell equations foresees that an electron at position R_k oscillating at frequency ω irradiates electromagnetic waves; into the direction of observation forming an angle θ with that of the incoming electric field, the scattered electric field $\mathbf{E}_\theta$ is:

[4] This value gives the depth at which the amplitude of the wave is 1/e of that at the surface.

[5] In principle also the positively charged nuclei oscillate and emit electromagnetic waves; but their contribution can be completely neglected, for the extremely higher mass, that limit their acceleration.

$$\mathbf{E}_\theta = \frac{er_0}{4\pi\varepsilon_0}\frac{\omega^2}{c^2}e^{j\mathbf{k}_{in}\mathbf{R}_\mathbf{k}}\sin\theta\frac{e^{j(\mathbf{k}_{out}(\mathbf{r}-\mathbf{R}_\mathbf{k})-\omega t)}}{|\mathbf{r}-\mathbf{R}_\mathbf{k}|} \simeq \frac{er_0}{4\pi\varepsilon_0}\frac{\omega^2}{c^2}e^{j(\mathbf{k}_{in}-\mathbf{k}_{out})\mathbf{R}_\mathbf{k}}\sin\theta\frac{e^{j(\mathbf{k}_{out}\mathbf{r}-\omega t)}}{r} \tag{4.29}$$

In this equation r_0 is the amplitude of the oscillations, $e^{j\mathbf{k}_{in}\mathbf{R}_k}$ the phase of the incoming wave at $\mathbf{R}_k$, $\mathbf{k}_{out}$ the wave-vector of the scattered wave and we have approximated $|\mathbf{r}-\mathbf{R}_k|$ with $|\mathbf{r}|$. In the Lorentz classical model of damped electron oscillators, the amplitude of the electron oscillation is given by:

$$r_0 = -\frac{e}{m}\frac{E_0}{\omega_i^2-\omega^2+j\gamma\omega} \tag{4.30}$$

so, introducing the exchanged wave-vector $\mathbf{q} = \mathbf{k}_{out} - \mathbf{k}_{in}$ we get:

$$\mathbf{E}_\theta = -\frac{1}{4\pi\varepsilon_0}\frac{e^2}{mc^2}\frac{\omega^2}{\omega_i^2-\omega^2+j\gamma\omega}E_0\sin\theta e^{-j\mathbf{q}\mathbf{R}_\mathbf{k}}\frac{e^{j(\mathbf{k}_{out}\mathbf{r}-\omega t)}}{r} \tag{4.31}$$

In general the amplitude of the scattered wave depends on the frequency of the incoming one.

4.2.5 Elastic Scattering at High Energy

Let us now consider the very important case of free electrons; this situation is achieved at high frequency i.e. when the frequency of the incoming wave ω is much higher than the resonance frequency ω_i of all electrons. In this case the amplitude r_0 becomes:

$$r_0 = \frac{eE_0}{m\omega^2} \tag{4.32}$$

and the scattered amplitude

$$\mathbf{E}_\theta = \frac{1}{4\pi\varepsilon_0}\frac{e^2}{mc^2}E_0\sin\theta e^{-j\mathbf{q}\mathbf{R}_\mathbf{k}}\frac{e^{j(\mathbf{k}_{out}\mathbf{r}-\omega t)}}{r} \tag{4.33}$$

does not depend on the frequency. The mean power dW scattered in the solid angle $d\Omega$ at the point P of Fig. 4.6 is given by:

$$dW = \varepsilon_0 c\langle|\mathbf{E}_\theta|^2\rangle r^2 d\Omega = \frac{\varepsilon_0 c}{2}\left(\frac{1}{4\pi\varepsilon_0}\right)^2\left(\frac{e^2}{mc^2}\right)^2\langle|\mathbf{E}_0|^2\rangle\sin^2\theta \tag{4.34}$$

We get the cross section normalizing to the incoming intensity:

$$\frac{d\sigma}{d\Omega} = \left(\frac{1}{4\pi\varepsilon_0}\right)^2\left(\frac{e^2}{mc^2}\right)^2\sin^2\theta = r_e^2\sin^2\theta \tag{4.35}$$

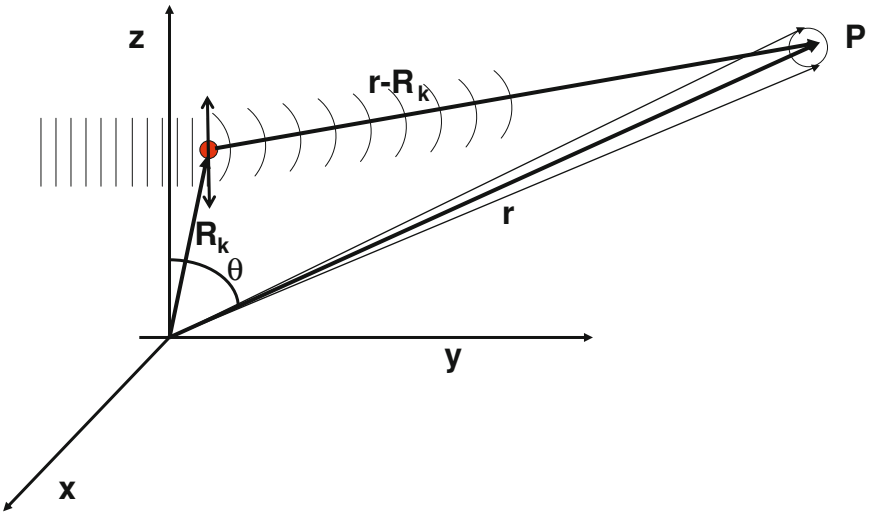


Fig. 4.6 Scattering of a plane wave polarized along z from a point charge at R_k

The quantity r_e

$$r_e = \frac{1}{4\pi\varepsilon_0}\frac{e^2}{mc^2} = 2.818\ \ 10^{-15}\ \text{m} \tag{4.36}$$

is called the electron classical radius.[6]

The total cross section σ is obtained by integrating over all the solid angle; it results:

$$\sigma = \int \frac{d\sigma}{d\Omega} = \int_0^{\pi} r_e^2 \sin^2\theta 2\pi d\theta = \frac{8}{3}\pi r_e^2 = 6.7\ 10^{-29}\ \text{m}^2/\text{electron} \tag{4.37}$$

This formula is known as the Thompson cross section; we derived it for a linear polarized incoming wave, however it is easy to show that it holds whenever the polarization of the incoming wave is: a single electron has always a total scattering cross section equal to the Thompson cross section.

Suppose now to have more electrons contributing to the scattering; indicating with $\rho_e(R)$ the electron density at point R, to get the total scattering power we have first to sum the electric field contribution arising at the point P from each electron and then to calculate the power as shown in Fig. 4.7; in doing this we have to take into account

[6] In the Gauss Unit System, the classical radius of the electron is

$$r_e = \frac{e^2}{mc^2} = 2.818\ \ 10^{-13}\ \text{cm}.$$

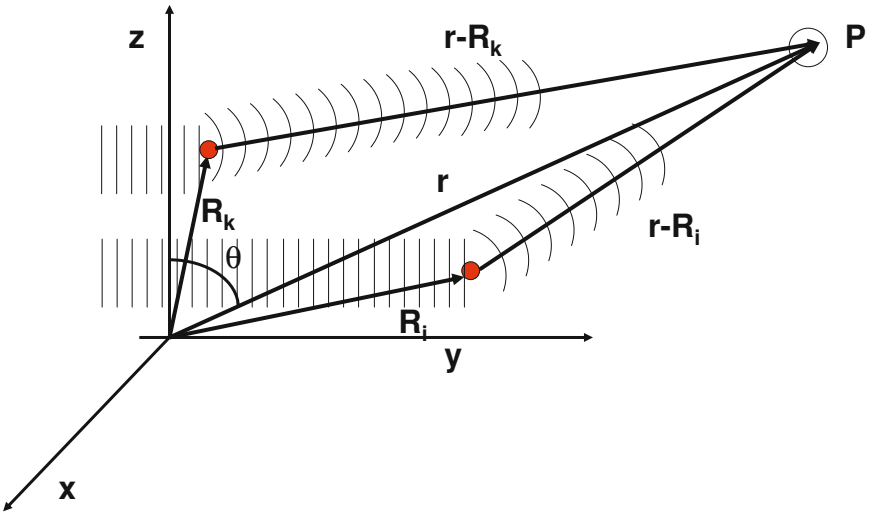


Fig. 4.7 The total electric field at P is the sum of the contributions coming from all the charges; each contribution has a well defined phase e^{-jqR}, where R is the position of the scattering charge, and an amplitude proportional to ρ_e(R)dV, the number of electrons in the volume dV at R

the phase difference between contributions due to the different positions occupied by the electrons. After a simple calculation we get:

$$\mathbf{E}_\theta = \frac{1}{4\pi\varepsilon_0}\frac{e^2}{mc^2}E_0 \sin\theta \frac{e^{j(\mathbf{k}_{out}\mathbf{r}-\omega t)}}{r}\int \rho_e dV e^{-j\mathbf{qR}} = \mathbf{E}_\theta^{free}\int \rho_e e^{-j\mathbf{qR}} dV \tag{4.38}$$

where $\mathbf{E}_\theta^{free}$ is the amplitude of the wave scattered by a single free electron at the origin; the vector $\mathbf{q}$ is the exchanged wavevector equal to [7]

$$\mathbf{q} = \mathbf{k}_{out} - \mathbf{k}_{in}$$

Equation (4.38) shows that the amplitude of the wave scattered by an electron distribution is equal to the amplitude of the scattering of a single electron located at the origin multiplied by the Fourier transform of the electron distribution ρ_e. It is often written as:

[7] In Chaps. 8 and 18, as usual in crystallography, unit vector $\hat{\mathbf{s}}$ and vector $\mathbf{S}$ are used instead of vectors $\mathbf{k}$ and $\mathbf{q}$. The relation between these quantities are:

$$\hat{\mathbf{s}} = \frac{\mathbf{k}}{k} = \frac{\lambda}{2\pi}\mathbf{k}$$

$$\mathbf{S} = \frac{\hat{\mathbf{s}}_{out} - \hat{\mathbf{s}}_{in}}{\lambda} = \frac{\mathbf{q}}{2\pi}.$$

$$\mathbf{E}_\theta = \mathbf{E}_\theta^{free} \int \rho_e e^{-j\mathbf{qR}} dV = \mathbf{E}_\theta^{free} f(\mathbf{q}, \omega) \tag{4.39}$$

where:

$$f(\mathbf{q}, \omega) = \int \rho_e e^{-j\mathbf{qR}} dV \tag{4.40}$$

From these equation we get the cross section:

$$\frac{d\sigma}{d\Omega} = r_e^2 \sin^2\theta |f(\mathbf{q}, \omega)|^2 \tag{4.41}$$

f($\mathbf{q}$, ω), known as scattering function, is a complex quantity; in general it depends on the frequency but in the specific case we are dealing with (elastic scattering at high energy) it depends only on the exchanged wave-vector $\mathbf{q}$, as evident from (4.40). All the structural information obtainable from elastic scattering are in this relationship: a scattering experiment gives the Fourier transform of the electron distribution of a medium.[8]

However, there are strong limitation and difficulties in using this very important and simple relationship because in experiments we measure only the intensity of the scattered beam that give us the cross section; this means that we measure only the modulus of the scattering function: it is necessary to determine also its phase in order to invert (4.40) and obtain the electron density; this problem is known as the Phase Problem of diffraction. Methods used to solve such problem will be addressed in Chaps. 8 and 23; they are partially based also on the properties of synchrotron radiation.

4.2.6 Anomalous Scattering

Anomalous scattering is the frequency dependence of the scattering function f($\mathbf{q}$, ω) that arise when the approximation of high energy does not hold.

In this case the amplitude of the scattered electric field and the cross section are:

$$\mathbf{E}_\theta = -\mathbf{E}_\theta^{free} \frac{\omega^2}{\omega_i^2 - \omega^2 + j\gamma\omega} e^{-j\mathbf{qR}_k} \tag{4.42}$$

$$\frac{d\sigma}{d\Omega} = \frac{\omega^4}{(\omega_i^2 - \omega^2)^2 + (\gamma\omega)^2} r_e^2 \sin^2\theta \tag{4.43}$$

[8] At small scattering angle $\mathbf{q} \simeq 0$ and f(q = 0) = $\int \rho_e$dV is the total charge, that for a single atom is equal to the atomic number Z; so the cross section at small angle is proportional to Z^2.

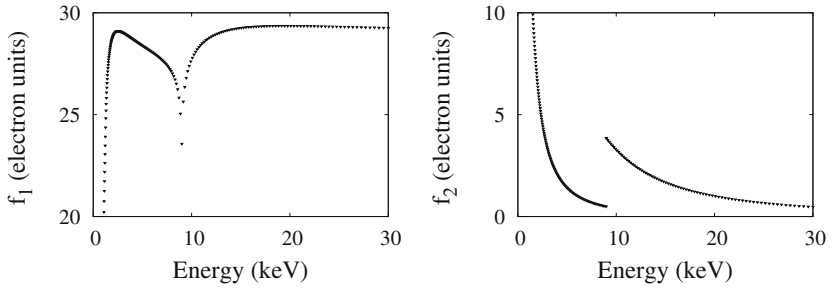


Fig. 4.8 Real and imaginary part of anomalous scattering of Copper (from [4]); the tip in the real part and the discontinuity in the imaginary part at about 8.9 keV are associated with the 1 s electrons binding energy. At high energy the real part of the scattering factor in electron units is equal to 29 i.e. to the atomic number of Cu; at low energy it goes to zero because bound electrons do not contribute to the scattering

We note that at low frequency the scattering cross section goes to zero: bounds electrons do not contribute to the scattering when the frequency of the incoming wave is much smaller than the resonance frequency. At high frequency the cross section becomes that of a free electrons: so the atomic cross section becomes proportional Z^2, the squared number of electrons.

In presence of an electronic distribution, if $\rho_i(\mathbf{R})dV$ is the number of electron with frequency resonance ω_i in the volume dV, we have for the amplitude of the scattered electric field, for the scattering function and for the cross section the expressions:

$$\mathbf{E}_\theta = -\frac{1}{4\pi\varepsilon_0}\frac{e^2}{mc^2}E_0 \sin\theta \frac{e^{j(\mathbf{k}_{out}\mathbf{r}-\omega t)}}{r}\sum_i \frac{\omega^2}{\omega_i^2-\omega^2+j\gamma\omega}\int dV\rho_i(R)e^{j\mathbf{qR}} \tag{4.44}$$

$$f(\mathbf{q},\omega) = \sum_i \frac{\omega^2}{\omega_i^2-\omega^2+j\gamma\omega}\int dV\rho_i(R)e^{j\mathbf{qR}} \tag{4.45}$$

$$\frac{d\sigma}{d\Omega} = r_e^2\sin^2\theta|f(\mathbf{q},\omega)|^2 = r_e^2\sin^2\theta|\sum_i \frac{\omega^2}{\omega_i^2-\omega^2+j\gamma\omega}\int dV\rho_i(R)e^{j\mathbf{qR}}|^2 \tag{4.46}$$

We underline that in presence of anomalous scattering, the scattering function depends on the energy; the behaviours of its real and imaginary part are reported in Fig. 4.8 for the copper.[9]

The frequency dependence of the scattering function arising from the anomalous scattering is of extreme importance in many experimental methods and in particular in finding solutions to the phase problem of diffraction as described in Chaps. 8 and 23.

[9] In general the anomalous corrections to the scattering cross section (4.46) do not depend on **q** because they are associated to inner shell electrons, which have a sharp distribution in space and, consequently, a flat distribution in q.

4.3 Semiclassical Description of the Interaction Between Matter and Radiation

In the semi-classical approach the matter is treated as a quantum mechanical system and the radiation as a classical field described by its electrical and magnetic fields, through the potential vector A.[10]

4.3.1 Quantum Description of the Matter

The microscopic description of the matter requires the use of quantum mechanics, according to which the matter is described by a wavefunction Ψ solution of the Schrodinger equation

$$\hat{H}\Psi = E\Psi \tag{4.47}$$

The wavefunction Ψ depends on the coordinates of all the particles constituting the matter, i.e. of the electrons (r_i) and of the nuclei (R_k): $\Psi(r_1, r_2 \ldots r_n; R_1, R_2, \ldots R_N)$. Many approximations are needed in order to simplify the problem and find solutions that describe the system in an acceptable way.

The first step consists in decoupling the motion of the nuclei from that of the electrons (Born-Oppenheimer approximation): the nuclei are assumed at rest at their equilibrium positions R_j^0. In this approximation, the real Hamiltonian is substituted by an effective Hamiltonian, with the ions at rest originating an attractive potential on the electrons.

The second approximation is the mean field approximation, according to which correlation effects between electrons are averaged and the electrons are assumed to move in a mean field created by the others electrons. Mathematically it implies that the electron wavefunction depends only on the coordinates of the electrons $\mathbf{r}_j$ and not on their relative positions. To take into account for the exclusion principle the electron wavefunction is generally written as a Slater determinant; the well know Hartee-Fock approximation is a way to determine the wavefunctions of each electron in this scheme.

The third approximation is the so called one electron approximation, according to which the wave-function of a specific electron is singled out from the other N−1 electrons and the N-electron wavefunction is approximated as:

$$\Psi(r_1, r_2 \ldots r_n; R_1^0, R_2^0, \ldots R_N^0) \simeq \Psi(r_1, r_2 \ldots r_{n-1}; R_1^0, R_2^0, \ldots R_N^0)\psi(r_n) \tag{4.48}$$

In this approximation the wavefunction of electron n is given by an effective Hamiltonian, which depends only on the coordinates of the electron n:

[10] In the following the CGS unit system will be used, as usual in most textbooks in Quantum Mechanics; in appendix it is shown how to change previous formula in order to get CGS expressions.

$$\hat{H}_{eff}(\mathbf{r}_n)\psi(r_n) = E_n\psi(r_n) \tag{4.49}$$

4.3.2 Semiclassical Description of the Interaction

The electromagnetic radiation interacts mainly with the charges of the electrons and nuclei inducing transitions between eigenstates of the system; we will assume hereafter that the interaction occurs mainly with the electrons, because most of the experimental techniques used with synchrotron radiation involve only electronic states. We will assume that our system is composed of N identical microscopic entities per unit volume (molecules, atoms, clusters. . .) and that we know the eigenstates and the eigenfunctions of electrons of the microscopic entities in absence of the electromagnetic wave. The electromagnetic wave acts as a time dependent perturbation, modifying the wave-function of the electrons and inducing transitions between eigenstates. The transition rate per unit volume w_{fi} between an initial and a final unperturbed eigenstate is given by the Fermi Golden Rule[11], according to which up to the second order:

$$w_{fi} = \frac{2\pi}{\hbar}|\langle\Psi_f|H_{int}|\Psi_i\rangle + \sum_k \frac{\langle\Psi_f|H_{int}|\Psi_k\rangle\langle\Psi_k|H_{int}|\Psi_i\rangle}{E_i - E_k - \hbar\omega}|^2\delta(E_f - E_i - \hbar\omega) \tag{4.50}$$

Here H_{int} is the interaction Hamiltonian, which for electromagnetic waves is:

$$H_{int} = \sum_j \left(-\frac{e}{mc}A(r_j)\cdot p_j + \frac{e^2}{2mc^2}A^2(r_j)\right) \tag{4.51}$$

In this expression the sum is over all the electrons of the system; this interaction Hamiltonian is obtained as the classical limit of the Dirac equation, that describes the relativistic behaviour of electrons in an electromagnetic field.

4.3.3 Absorption Coefficient in the Semiclassical Approach

Absorption is described by the first order term in the potential vector A of the Fermi Golden Rule; assuming an incoming plane wave we have:

$$w_{fi} = \frac{2\pi}{\hbar}|\langle\Psi_f| - \frac{e}{mc}\sum_j \mathbf{A}_k(r_j)e^{j\mathbf{k}\mathbf{r}_j}\cdot\mathbf{p}_j|\Psi_i\rangle|^2\delta(E_f - E_i - \hbar\omega) \tag{4.52}$$

[11] The demonstration of the Fermi Golden Rule is given in Chap. 5.

To get the absorption coefficient consider that[12]

$$\mu = -\frac{1}{I}\frac{dI}{dx} = \sum_f \frac{2\pi c}{\omega^2 A_k^2} N\hbar\omega\, w_{fi} \tag{4.53}$$

where N is the number of microscopic absorbing elements per unit volume and the sum runs over the different possible final states. Therefore:

$$\begin{aligned}\mu &= \sum_f \frac{2\pi c}{\omega^2 A_0^2} N\hbar\omega \frac{2\pi}{\hbar} |\langle\Psi_f| - \frac{e}{mc}\sum_j \mathbf{A}_0(r_j) e^{j\mathbf{k}\mathbf{r}_j}\cdot\mathbf{p}_j|\Psi_i\rangle|^2 \delta(E_f - E_i - \hbar\omega) \\ &= 4\pi^2\alpha\,\hbar\omega\,\frac{1}{m^2\omega^2}\sum_f |\langle\Psi_f|\sum_j \hat{\varepsilon}_k e^{j\mathbf{k}\mathbf{r}_j}\cdot\mathbf{p}_j|\Psi_i\rangle|^2\, N\,\delta(E_f - E_i - \hbar\omega)\end{aligned} \tag{4.54}$$

where $\hat{\varepsilon}_k$ is the polarization vector of the incoming electromagnetic wave. α is the so called fine structure constant, an a-dimensional constant equal to:

$$\alpha = \frac{e^2}{\hbar c} = \frac{1}{137} \tag{4.55}$$

The above formula is the basic one describing the absorption in the non relativistic quantum description of the matter.

Few additional steps simplify and clarify the meaning of this formula; the first one consists in the transformation of the impulse operator $\mathbf{p}_j$ into the electric dipole operator $e\mathbf{r}_j$; in fact according to quantum mechanics:

$$\langle\Psi_f|\mathbf{p}_j|\Psi_i\rangle = \langle\Psi_f|m\frac{d\mathbf{r}_j}{dt}|\Psi_i\rangle = \frac{m}{j\hbar}\langle\Psi_f|\mathbf{r}_j\hat{H} - \hat{H}\mathbf{r}_j|\Psi_i\rangle = -jm\omega\langle\Psi_f|\mathbf{r}_j|\Psi_i\rangle \tag{4.56}$$

where we used the relation: $E_f - E_i = \hbar\omega$ for the delta function present in (4.54); so the absorption coefficient becomes:

$$\mu = 4\pi^2\alpha\,\hbar\omega\sum_f |\langle\Psi_f|e^{j\mathbf{k}\mathbf{r}_j}\sum_j \hat{\varepsilon}_k\cdot\mathbf{r}_j|\Psi_i\rangle|^2\, N\,\delta(E_f - E_i - \hbar\omega) \tag{4.57}$$

---

[12] The expression of the Fermi Golden Rule given above is valid for a perturbation of the form

$$A_k(e^{j(kr-\omega t)} + e^{-j(kr-\omega t)}) \propto 2A_k$$

whose intensity I is given by:

$$I = 4\times\frac{1}{8\pi c}\omega^2 A_k^2.$$

A second step is the dipole approximation: the extension of the wave-functions involved in the matrix element of the above expression is in general small compared with the wavelength of the radiation, so we can assume the factor $e^{j\mathbf{k}\mathbf{r}_j}$ as a constant bringing it out of the integral; for the presence of the square modulus, this is equivalent to approximate it as 1. So we get the dipole approximation formula:

$$\mu = 4\pi^2\alpha\ \hbar\omega\ \sum_f |\langle\Psi_f| \sum_j \hat{\varepsilon}_k \cdot \mathbf{r}_j |\Psi_i\rangle|^2\ N\ \delta(E_f - E_i - \hbar\omega) \tag{4.58}$$

A more compact way to write the term $\mathrm{N}\delta(\mathrm{E}_f - \mathrm{E}_i + \hbar\omega)$ is introducing the density of states per unit volume ρ_{fi} i.e. the number of final state per unit volume of energy $\mathrm{E}_f = \mathrm{E}_i + \hbar\omega$; in this way the absorption coefficient becomes:

$$\mu = 4\pi^2\alpha\ \hbar\omega\ |\langle\Psi_f| \sum_j \hat{\varepsilon}_k \cdot \mathbf{r}_j |\Psi_i\rangle|^2\ \rho_{fi}(E_f) \tag{4.59}$$

We stress that in the above formula the initial and final state wave-functions are many electrons wave-functions, depending on the coordinates $\mathbf{r}_j$ of all the electrons of the system and the matrix element involves an integral over all the coordinates. A further very important step is the one electron approximation; according to this approximations, electrons move independently one from the other one in the mean field created by the charge distribution of the others; we can therefore concentrate our attention on the particular electron (active electron) which makes the transition. The other electrons are spectators during the transition, modifying their state only slightly (passive electrons). In this way we can write the many electron wave-function as

$$|\Psi_{i,f}\rangle = |\Phi_{i,f}^{N-1}\rangle |\psi_{i,f}\rangle \tag{4.60}$$

where $|\Phi_{i,f}^{N-1}\rangle$ is the many electron wave-function of the N-1 passive electrons, generally written as a Slater determinant. $|\psi_{i,f}\rangle$ is the initial (final) state wave-function of the active electron. In this way we obtain:

$$\mu = 4\pi^2\alpha\ \hbar\omega\ |\langle\Phi_f^{N-1}|\Phi_i^{N-1}\rangle|^2 \langle\psi_f|\hat{\varepsilon}_k \cdot \mathbf{r}|\Psi_i\rangle|^2\ \rho_{fi}(E_f) \tag{4.61}$$

This is the starting formula to study absorption coefficient in the one electron approximation, as we will see in Chap. 6 for X-ray absorption spectroscopy and in Chap. 9 for photoemission spectroscopy.

4.3.4 The Scattering in the Semi-classical Approach

In the semi-classical approach, the scattering originates from the currents associated to the electron wave-functions and velocity; according to quantum mechanics an

electron in a quantum state $\Psi_n(\mathbf{r}, t)$ gives rise to a local current density $\mathbf{j}_{nm}(\mathbf{r}, t)$ given by:

$$\mathbf{j}_{nm} = \frac{1}{2m} \sum_j (\Psi_n^* \hat{p}_j \Psi_m - \Psi_n \hat{p}_j \Psi_m^*) \tag{4.62}$$

In presence of a external electromagnetic field, this equation becomes:

$$\mathbf{j}_{nm} = \frac{1}{2m} \sum_j (\Psi_n^* \hat{p}_j \Psi_m - \Psi_n \hat{p}_j \Psi_m^*) - \sum_j \frac{eA(r_j, t)}{2m} (\Psi_n^* \Psi_m + \Psi_n \Psi_m^*) \tag{4.63}$$

where the second term arises from the modification to the electron momentum due to the presence of an external electromagnetic field (minimal substitution). When the external electromagnetic field changes with time, also the wavefunction Ψ and the current density matrix elements are time dependent; according to classical electromagnetism these time dependent currents emit electromagnetic waves. This is the origin of the scattering in the semi-classical approach; the elastic scattering arises from the diagonal elements of the current operator, the inelastic scattering from the non-diagonal ones.

It is useless to deduce all formulas of scattering using this approach, because the full quantum approach gives the same results in a much more simple way. We will limit to show only the origin of the basic scattering effects, i.e. the first order elastic scattering and the inelastic one. The reader interested to the origin of all the scattering mechanisms can refer to [5, 6].

In fact, at first order in the perturbation A, the current density becomes:

$$\mathbf{j}_{nm} = -\sum_j \frac{eA(r_j, t)}{2m} (\Psi_n^* \Psi_m + \Psi_n \Psi_m^*) \tag{4.64}$$

Assuming a plane wave perturbation we get:

$$\mathbf{j}_{nm}(t) = -\sum_j \frac{eA_k}{2m} e^{jkr_j} (\psi_n^* \psi_m e^{j(\omega_n - \omega_m - \omega)t} + \psi_n \psi_m^* e^{j(\omega_m - \omega_n - \omega)t}) \tag{4.65}$$

The diagonal term

$$\mathbf{j}_{nn} = -\sum_j \frac{eA_k}{m} e^{jkr_j} \psi_n^* e^{jkr_j} \psi_n e^{-j\omega t} \tag{4.66}$$

oscillates at the same frequency of the incoming wave, so it gives rise to the elastic scattering; the cross section is obtained by substituting into (4.40) and (4.41) the charge density distribution $\rho = \Psi_n^* \sum_j e^{-jkr_j} \Psi_n$[13]; it results:

[13] Equation (4.41) was obtained from a classical charge distribution $\rho(r)$ oscillating as

$$\left(\frac{d\sigma}{d\Omega}\right)_{el.} = r_e^2 \sin^2\theta |\langle\Psi_n| \sum_j e^{-jqr_j} |\Psi_n\rangle|^2 \tag{4.67}$$

This formula is identical to the classical one of the elastic scattering from a charge distribution, showing how at first order the elastic scattering cross section is proportional to the square modulus of the Fourier transform of the charge density of the system. The difference with respect to the classical approach is that it holds whenever the system is i.e. also for a single electron, that does not scatters as a classical point charge, but as a charge distribution of density $\Psi_n^* \Psi_n$.

The non diagonal first order term is:

$$\mathbf{j}_{nm}(t) = -\sum_j \frac{eA_k}{2m} e^{jkr_j} (\psi_n^* \psi_m e^{j(\omega_n - \omega_m - \omega)t} + \psi_n \psi_m^* e^{j(\omega_m - \omega_n - \omega)t}) \tag{4.68}$$

which oscillates at a frequency $\omega' = \omega \pm (\omega_m - \omega_n)$ different from that of the incoming wave and produces scattering at these frequencies. Assuming the system in the fundamental state Ψ_n, only the frequency $\omega' = \omega - (\omega_m - \omega_n)$ is compatible with the energy conservation. The cross section results to be:

$$\left(\frac{d\sigma}{d\Omega}\right)_{inel.} = r_e^2 \sin^2\theta \sum_{m \neq n} \frac{\omega'}{\omega} |\langle\Psi_m| \sum_j e^{-jqr_j} |\Psi_n\rangle|^2 \tag{4.69}$$

This is the Compton scattering cross section. At high energy $\omega' \simeq \omega$ and the scattering cross section becomes:

$$\left(\frac{d\sigma}{d\Omega}\right)_{inel.}^{high\ energy} = r_e^2 \sin^2\theta \sum_{m \neq n} |\langle\Psi_m| \sum_j e^{-jqr_j} |\Psi_n\rangle|^2 \tag{4.70}$$

A very peculiar property links the elastic and inelastic scattering cross sections with the classical one, at high energy; in fact:

(Footnote 13 continued)

$$\frac{eE_k}{m\omega^2} e^{-j\omega t}$$

that correspond to a current density j

$$j = \rho \frac{-j\omega e E_k}{m\omega^2} e^{-j\omega t} = -\rho \frac{eA_k}{m} e^{-j\omega t}.$$

Comparing this last expression with (4.66) we see that for the present case $\rho = \Psi_n^* \sum_j e^{-jkr_j} \Psi_n$

$$\begin{aligned}\sum_{m\neq n}|\langle\Psi_m|\sum_j e^{-qr_j}|\Psi_n\rangle|^2 &= \sum_{m\neq n}\langle\Psi_n|\sum_j e^{qr_j}|\Psi_m\rangle\langle\Psi_m|\sum_j e^{-qr_j}|\Psi_n\rangle \\ &= \sum_{all\ m}\langle\Psi_n|\sum_j e^{qr_j}|\Psi_m\rangle\langle\Psi_m|\sum_j e^{-qr_j}|\Psi_n\rangle - \langle\Psi_n| \\ &\quad \sum_j e^{qr_j}|\Psi_n\rangle\langle\Psi_n|\sum_j e^{-qr_j}|\Psi_n\rangle \qquad (4.71) \\ &= Z - |\langle\Psi_n|\sum_j e^{-qr_j}|\Psi_n\rangle|^2\end{aligned}$$

where Z is the total number of electrons of the systems. So we get for the inelastic cross section:

$$\left(\frac{d\sigma}{d\Omega}\right)_{inel.} = r_e^2\sin^2\theta\left(Z - |\langle\Psi_n|\sum_j e^{-qr_j}|\Psi_n\rangle|^2\right) \qquad (4.72)$$

Summing the elastic and inelastic cross section we get:

$$\left(\frac{d\sigma}{d\Omega}\right)_{el.} + \left(\frac{d\sigma}{d\Omega}\right)_{inel.} = Zr_e^2\sin^2\theta \qquad (4.73)$$

In the limit of very high energy the sum of the elastic and inelastic cross section is equal to the classical Thompson cross section of Z point free electrons.

4.4 Quantum Description of the Absorption and Scattering

4.4.1 Quantum Description of the Electromagnetic Field

In the quantum theory a quantum state of the electromagnetic field is described by the occupation number n of the different photon states of wavevector **k** and polarization s $|n_{k_1,s_1};\ldots n_{k,s};\ldots;n_{k_t,s_t}\rangle$.[14] On such state act the so called creation and annihilation operators $a^\dagger_{k,s}$ and $a_{k,s}$, whose effect is to increase or decrease of one unit the occupation number of a specific photon state, according to the rules:

$$a^\dagger_{k,s}|n_{k_1,s_1};\ldots n_{k,s};\ldots;n_{k_t,s_t}\rangle = \sqrt{n_{k,s}+1}|n_{k_1,s_1};\ldots n_{k,s}+1;\ldots;n_{k_t,s_t}\rangle \qquad (4.74)$$

$$a_{k,s}|n_{k_1,s_1};\ldots n_{k,s};\ldots;n_{k_t,s_t}\rangle = \sqrt{n_{k,s}}|n_{k_1,s_1};\ldots n_{k,s}-1;\ldots;n_{k_t,s_t}\rangle \qquad (4.75)$$

[14] A full description of the quantum theory of electromagnetic field is given in Chap. 5.

It is clear that the matrix elements of the creation and annihilation operators are different from zero only between states with an unitary difference in the number of photons of a specific kind [15]:

$$\langle n_{k,s}+1|a^{\dagger}_{k,s}|n_{k,s}\rangle=\sqrt{n_{k,s}+1} \qquad \langle n_{k,s}-1|a_{k,s}|n_{k,s}\rangle=\sqrt{n_{k,s}} \tag{4.76}$$

All other matrix elements in which the occupancy between the initial and final state appears differently, are zero.

Classically the electromagnetic field is described by the potential vector **A**; it can be expanded in a series of harmonic components, i.e. of plane waves of well defined frequency and wavevector. In the quantum description, each harmonic component is treated as an oscillator and is quantized; as a consequence, the vector potential **A** becomes an operator, whose expression is:

$$\mathbf{A}(\mathbf{r},t)=\sum_{k,s}\sqrt{\frac{4\pi\hbar c^2}{2V\omega_k}}\left(a_{k,s}\hat{\varepsilon}_{k,s}e^{j\mathbf{kr}-\omega t}+a^{\dagger}_{k,s}\hat{\varepsilon}^{*}_{k,s}e^{-j\mathbf{kr}-\omega t}\right) \tag{4.77}$$

This operator field acts on photon states changing their occupancy of one unit.

The system is now composed of electrons states and photons, and their quantum states are specified when the wavefunction of the electrons and the occupancy numbers of the photon states are known i.e.:

$$|\Psi\rangle=|\Psi(r_1,\ldots r_n);n_{k,s}\rangle \tag{4.78}$$

4.4.2 Quantum Description of the Interaction of Electromagnetic Fields and Matter

In Sect. 3.2 we have seen that the interaction Hamiltonian that describe the perturbation on a system of electrons due to the presence of a electromagnetic field is:

$$\hat{H}_{int}=\sum_{j}\left(-\frac{e}{mc}\mathbf{A}(\mathbf{r}_j)\cdot\hat{p}_j+\frac{e^2}{2mc^2}\mathbf{A}^2(\mathbf{r}_j)\right) \tag{4.79}$$

In the quantum approach, the interaction Hamiltonian is obtained by substituting (4.77) in (4.79); this interaction Hamiltonian induces transitions between unperturbed states, whose probability is given by the Fermi Golden Rule. We do not report now its whole expression, but we underline that from the term proportional to **A** we

[15] Generally we will indicate a photon state specifying only the photon numbers of the specific kind we are interested in i.e. $|n_{k,s}\rangle$.

will get terms proportional to $a_{k,s}$ and $a^{\dagger}_{k,s}$, while from the term in $\mathbf{A}^2$ we will get terms proportional to $a_{k,s}a^{\dagger}_{k',s'}$, to $a^{\dagger}_{k,s}a_{k',s'}$, to $a^{\dagger}_{k,s}a^{\dagger}_{k',s'}$ and to $a_{k,s}a_{k',s'}$.

4.4.3 Absorption Cross Section

In the simplest case the absorption process consist in a transition of an electron system from a initial state Ψ_i of energy E_i to a final state Ψ_f of energy E_f with a simultaneous annihilation of a photon of energy $\hbar\omega = \mathrm{E}_f - \mathrm{E}_i$. The process need the action of only $a_{k,s}$ operator so we have to consider only the linear term in $\mathbf{A}$, i.e the term:

$$\sum_j -\frac{e}{mc}\mathbf{A}(\mathbf{r}_j)\cdot\hat{p}_j = \sum_j -\frac{e}{mc}\sum_{k,s}\sqrt{\frac{4\pi\hbar c^2}{2V\omega_k}}\left(a_{k,s}e^{j\mathbf{kr}_j}\hat{\varepsilon}_{k,s}\cdot\hat{p}_j + a^{\dagger}_{k,s}e^{-j\mathbf{kr}_j}\hat{\varepsilon}^{*}_{k,s}\cdot\hat{p}_j\right) \tag{4.80}$$

The matrix element $\langle F|\hat{H}_{int}|I\rangle$ between an initial state $|I\rangle = |\Psi_i; n_{k,s}\rangle$ and a final state $|F\rangle = |\Psi_f; n_{k,s}-1\rangle$ is:

$$\langle F|\hat{H}_{int}|I\rangle = -\frac{e}{mc}\sqrt{\frac{4\pi\hbar c^2}{2V\omega_k}}\sqrt{n_{k,s}}\sum_j\langle\Psi_f|e^{j\mathbf{kr}_j}\hat{\varepsilon}_{k,s}\cdot\hat{p}_j|\Psi_i\rangle \tag{4.81}$$

The transition rate w_{fi} becomes:

$$w_{fi} = \frac{2\pi}{\hbar}\left(\frac{e}{mc}\right)^2\frac{4\pi\hbar c^2}{2V\omega_k}n_{k,s}|\sum_j\langle\Psi_f|e^{j\mathbf{kr}_j}\hat{\varepsilon}_{k,s}\cdot\hat{p}_j|\Psi_i\rangle|^2\delta(E_f - E_i - \hbar\omega) \tag{4.82}$$

The transition rate gives the number of photon absorbed per unit time and unit volume. To get the cross section $\sigma_{abs.}$ we have to sum over all the final states, to multiply by the density of the absorbing objects and to divide by the incoming photon flux $\left(n_{k,s}\ c/V\right)$:

$$\sigma_{abs.} = 4\pi^2\alpha\hbar\omega\frac{1}{m^2\omega^2}\sum_f|\sum_j\langle\Psi_f|e^{j\mathbf{kr}_j}\hat{\varepsilon}_{k,s}\cdot\hat{p}_j|\Psi_i\rangle|^2N\delta(E_f - E_i - \hbar\omega) \tag{4.83}$$

in agreement with (4.54).

4.4.4 First Order Scattering

In general in a scattering process a photon is removed from the incoming beam and a second one is produced in the final state with a different propagation vector,

frequency and polarization; so the initial and final state eigenvectors are:

$$|I\rangle = |\Psi_i; n_{k_{in},s_{in}}; 0_{k_{out},s_{out}}\rangle \qquad |F\rangle = |\Psi_f; n_{k_{in},s_{in}} - 1; 1_{k_{out},s_{out}}\rangle \tag{4.84}$$

Transitions from such initial and final states involve two photons operators, an annihilation one $a_{k_{in},s_{in}}$ and a creation one $a^{\dagger}_{k_{out},s_{out}}$. At first order, in the Fermi Golden rule such combination of operators comes out from the term

$$\sum_j \frac{e^2}{2mc^2}\mathbf{A}^2(\mathbf{r}_j)$$

of the interaction Hamiltonian. Explicitly we have:

$$\sum_j \frac{e^2}{2mc^2}\mathbf{A}^2(\mathbf{r}_j) = \sum_j \frac{e^2}{2mc^2}\sum_{k,s}\sqrt{\frac{4\pi\hbar c^2}{2V\omega_k}}\left(a_{k,s}\hat{\varepsilon}_{k,s}e^{j\mathbf{kr}} + a^{\dagger}_{k,s}\hat{\varepsilon}^*_{k,s}e^{-j\mathbf{kr}}\right) \tag{4.85}$$

$$\cdot\sum_{k',s'}\sqrt{\frac{4\pi\hbar c^2}{2V\omega_{k'}}}\left(a_{k',s'}\hat{\varepsilon}_{k',s'}e^{j\mathbf{k'r}} + a^{\dagger}_{k',s'}\hat{\varepsilon}^*_{k',s'}e^{-j\mathbf{k'r}}\right)$$

Considering in the double sum only terms that contribute to the process of interest, we get:

$$\sum_j \frac{e^2}{2mc^2}\mathbf{A}^2(\mathbf{r}_j) = \sum_j \frac{e^2}{2mc^2}\frac{4\pi\hbar c^2}{2V\sqrt{\omega_{k_{in}}\omega_{k_{out}}}}\hat{\varepsilon}_{k_{in},s_{in}}\cdot\hat{\varepsilon}^*_{k_{out},s_{out}}e^{j(k_{in}-k_{out})r_j}2a_{k_{in},s_{in}}a^{\dagger}_{k_{out},s_{out}} \tag{4.86}$$

The matrix element between the initial and final state is:

$$\langle F|H_{int}|I\rangle = \frac{e^2}{2mc^2}\frac{4\pi\hbar c^2}{2V\sqrt{\omega_{k_{in}}\omega_{k_{out}}}}\sqrt{n_{k_{in},s_{in}}}(\hat{\varepsilon}_{k_{in},s_{in}}\cdot\hat{\varepsilon}^*_{k_{out},s_{out}})\sum_j\langle\Psi_f|e^{j(k_{in}-k_{out})r_j}|\Psi_i\rangle \tag{4.87}$$

and the transition rate:

$$w_{fi} = \frac{2\pi}{\hbar}\left(\frac{e^2}{2mc^2}\right)^2\left(\frac{4\pi\hbar c^2}{2V\sqrt{\omega_{k_{in}}\omega_{k_{out}}}}\right)^2 n_{k_{in},s_{in}}|\langle\Psi_f|\sum_j e^{j(k_{in}-k_{out})r_j}|\Psi_i\rangle\ \hat{\varepsilon}_{k_{in},s_{in}}\cdot$$
$$\hat{\varepsilon}^*_{k_{out},s_{out}}|^2\delta(E_f - E_{in} + \hbar\omega_{out} - \hbar\omega_{in}) \tag{4.88}$$

The transition rate gives the number of photons scattered in the direction $\mathbf{k}_{out}$ per unit time and unit volume; to calculate the double differential cross section we need the number of photons emitted in a solid angle $d\Omega$ and energy interval $d\mathrm{E} = \hbar d\omega$; at this purpose we multiply w_{fi} by the number of independent final states that are in the volume $d^3k_{out} = k^2_{out}dk_{out}d\Omega$ i.e. by:

$$\frac{V}{8\pi^3}d^3k_{out} = \frac{V}{8\pi^3}k_{out}^2 dk_{out}d\Omega = \frac{V}{8\pi^3}\frac{1}{c^3}\omega_{out}^2 d\omega_{out}d\Omega \tag{4.89}$$

where we have used the relation k = ω/c. Multiplying the transition rate by this factor, dividing by the incoming photon flux and summing over all the possible electronic final states we get the double differential cross section:

$$\frac{d^2\sigma}{d\omega d\Omega} = r_e^2\left(\frac{\omega_{out}}{\omega_{in}}\right)(\hat{\varepsilon}_{k_{in},s_{in}}\cdot\hat{\varepsilon}^*_{k_{out},s_{out}})^2\sum_f|\langle\Psi_f|\sum_j e^{-\mathbf{qr}_j}|\Psi_i\rangle|^2 \tag{4.90}$$

where $\mathbf{q} = \mathbf{k}_{in} - \mathbf{k}_{out}$ is the exchanged wave-vector; the conservation of the energy requires that: $E_f + \hbar\omega_{out} = E_{in} + \hbar\omega_{in}$. This formula gives the cross section of the elastic and inelastic scattering at the first order in the perturbation.

In order to compare this formula with those previously found, we stress here that, for a linear polarized electromagnetic wave,

$$\hat{\varepsilon}_{k_{in},s_{in}}\cdot\hat{\varepsilon}^*_{k_{out},s_{out}} = \sin\theta \tag{4.91}$$

where θ is the angle between the electric field and the direction of propagation. it appears now how the above formula is identical with (4.69)

4.4.4.1 Elastic Scattering

When the electronic state do not change, the energy conservation ensure that the scattering is elastic i.e. $\omega_{out} = \omega_{in}$ and the double differential cross section reduces to:

$$\left(\frac{d\sigma}{d\Omega}\right)_{el.} = r_e^2(\hat{\varepsilon}_{k_{in},s_{in}}\cdot\hat{\varepsilon}^*_{k_{out},s_{out}})^2|\langle\Psi_{in}|\sum_j e^{-qr_j}|\Psi_i\rangle|^2 \tag{4.92}$$

This results confirm and generalise the results previously shown (4.41) and (4.67): the elastic cross section for an electron distribution is proportional to the square modulus of the Fourier Transform of the electron density; as already underlined this holds whenever the distribution is, i.e. for a molecule, a solid and even for a single electron in a orbital, which does not scatter according to the classic Thompson point charge but like a classical charge distribution.

4.4.4.2 High Energy Inelastic Scattering

When the final electronic state is different from the initial one, the scattering becomes inelastic with an exchange of energy between the photons and the electron system. At very high energy, when the energy lost by the scattered photon is negligible with respect to the energy of the incoming photon we can neglect the energy differ-

ence between the incoming and outcoming photons and the inelastic cross section becomes:

$$\left(\frac{d\sigma}{d\Omega}\right)_{inel.} = r_e^2(\hat{\varepsilon}_{k_{in},s_{in}} \cdot \hat{\varepsilon}^*_{k_{out},s_{out}})^2 \sum_{fin \neq in} |\langle \Psi_{fin}| \sum_j e^{-qr_j} |\Psi_{in}\rangle|^2 \tag{4.93}$$

This formula is identical with that previously found with the semiclassical approach at high energy (4.70) and confirms that at high energy the sum of the elastic and inelastic cross section is equal to the Thompson cross section of Z point free electrons:

$$\left(\frac{d\sigma}{d\Omega}\right)_{el.} + \left(\frac{d\sigma}{d\Omega}\right)_{inel.} = Zr_e^2(\hat{\varepsilon}_{k_{in},s_{in}} \cdot \hat{\varepsilon}^*_{k_{out},s_{out}})^2 = Zr_e^2 \sin^2\theta \tag{4.94}$$

4.4.5 Second Order Scattering: Anomalous and Resonant Scattering

In the second order of the Fermi Golden rule, the term proportional to $\mathbf{A} \cdot \mathbf{p}$ in the interaction Hamiltonian gives rise to additional frequency dependent contributions to the scattering cross section that are the quantum description of the anomalous correction to the scattering factors. There contributions are composed of two terms, one of which is resonant: when the incoming photon energy is equal to one of the excitation energies of the electronic system it diverges giving rise to the Resonant Scattering (see Chap. 12). Moreover at high energy these contributions have a very peculiar behaviour becoming proportional to the orbital magnetic moment of the scattering atoms: it is this characteristics, together with the scattering originating from the spin of the electrons, that makes X-ray scattering a powerful tool to investigate the magnetic properties of the matter (see Chap. 12 for a complete discussion of the magnetic scattering).

In this case we have to calculate the matrix elements:

$$\langle F| - \frac{e}{mc}\mathbf{A} \cdot \mathbf{p}|N\rangle\langle N| - \frac{e}{mc}\mathbf{A} \cdot \mathbf{p}|I\rangle \tag{4.95}$$

where N is an intermediate unoccupied state. In principle such matrix elements are to be calculated for all possible intermediate states; however there are only two possible intermediate states $|N_1\rangle$ and $|N_2\rangle$ that give a non zero contribution for a specific intermediate electronic state Ψ_n, namely:

$$|N_1\rangle = |\Psi_n; n_{k_{in},s_{in}}; 1_{k_{out},s_{out}}\rangle \quad \text{of energy} \quad E_{N_1} = E_n - E_i + \hbar\omega_{out} \tag{4.96}$$

$$|N_2\rangle = |\Psi_n; n_{k_{in}-1,s_{in}}; 0_{k_{out},s_{out}}\rangle \quad \text{of energy} \quad E_{N_2} = E_n - E_i - \hbar\omega_{in} \tag{4.97}$$

For these two intermediate states we have:

$$\begin{aligned}
&\langle F|-\frac{e}{mc}\mathbf{A}\cdot\mathbf{p}|N_1\rangle\langle N_1|-\frac{e}{mc}\mathbf{A}\cdot\mathbf{p}|I\rangle \\
&=\left(\frac{e}{mc}\right)^2\sqrt{\frac{4\pi\hbar c^2}{2V\omega_{k_{in}}}}\sqrt{\frac{4\pi\hbar c^2}{2V\omega_{k_{out}}}}\langle F|a_{k_{in},s}e^{j\mathbf{kr}_j}\hat{\varepsilon}_{k_{in},s}\cdot\hat{p}_j|N_1\rangle\langle N_1|a^{\dagger}_{k_{out},s}e^{-j\mathbf{kr}_j}\hat{\varepsilon}^{*}_{k_{out},s}\cdot\hat{p}_j|I\rangle \\
&=\left(\frac{e}{mc}\right)^2\frac{4\pi\hbar c^2}{2V\sqrt{\omega_{k_{in}}\omega_{k_{out}}}}\sqrt{n(k_{in})}\langle\Psi_f|e^{j\mathbf{kr}_j}\hat{\varepsilon}_{k_{in},s}\cdot\hat{p}_j|\Psi_n\rangle\langle\Psi_n|e^{-j\mathbf{kr}_j}\hat{\varepsilon}^{*}_{k_{out},s}\cdot\hat{p}_j|\Psi_i\rangle \qquad (4.98)
\end{aligned}$$

and

$$\begin{aligned}
&\langle F|-\frac{e}{mc}\mathbf{A}\cdot\mathbf{p}|N_2\rangle\langle N_2|-\frac{e}{mc}\mathbf{A}\cdot\mathbf{p}|I\rangle \\
&=\left(\frac{e}{mc}\right)^2\sqrt{\frac{4\pi\hbar c^2}{2V\omega_{k_{in}}}}\sqrt{\frac{4\pi\hbar c^2}{2V\omega_{k_{out}}}}\langle F|a^{\dagger}_{k_{out},s}e^{-j\mathbf{kr}_j}\hat{\varepsilon}^{*}_{k_{out},s}\cdot\hat{p}_j|N_2\rangle\langle N_2|a_{k_{in},s}e^{j\mathbf{kr}_j}\hat{\varepsilon}_{k_{in},s}\cdot\hat{p}_j|I\rangle \\
&=\left(\frac{e}{mc}\right)^2\frac{4\pi\hbar c^2}{2V\sqrt{\omega_{k_{in}}\omega_{k_{out}}}}\sqrt{n(k_{in})}\langle\Psi_f|e^{-j\mathbf{kr}_j}\hat{\varepsilon}^{*}_{k_{out},s}\cdot\hat{p}_j|\Psi_n\rangle\langle\Psi_n|e^{j\mathbf{kr}_j}\hat{\varepsilon}_{k_{in},s}\cdot\hat{p}_j|\Psi_i\rangle \qquad (4.99)
\end{aligned}$$

The transition probability is:

$$\begin{aligned}
w^n_{fi}=\frac{2\pi}{\hbar}\left(\frac{e}{mc}\right)^4\left(\frac{4\pi\hbar c^2}{2V\sqrt{\omega_{k_{in}}\omega_{k_{out}}}}\right)^2 n(k_{in})|&\frac{\langle\Psi_f|e^{-j\mathbf{kr}_j}\hat{\varepsilon}^{*}_{k_{out},s}\cdot\hat{p}_j|\Psi_n\rangle\langle\Psi_n|e^{j\mathbf{kr}_j}\hat{\varepsilon}_{k_{in},s}\cdot\hat{p}_j|\Psi_i\rangle}{E^{el.}_i-E^{el.}_n-\hbar\omega_{out}} \\
&+\frac{\langle\Psi_f|e^{-j\mathbf{kr}_j}\hat{\varepsilon}^{*}_{k_{out},s}\cdot\hat{p}_j|\Psi_n\rangle\langle\Psi_n|e^{j\mathbf{kr}_j}\hat{\varepsilon}_{k_{in},s}\cdot\hat{p}_j|\Psi_i\rangle}{E^{el.}_i-E^{el.}_n+\hbar\omega_{in}}|^2 \qquad (4.100)
\end{aligned}$$

In these expressions $E^{el.}$ is the energy of the electronic states. Limiting to the elastic case: (i.e. $\hbar\omega_{in}=\hbar\omega_{out}$), we get the differential cross section by multiplying the transition rate by the number of final photon states, summing over all possible intermediate electronic states and normalizing to the incoming photon flux:

$$\begin{aligned}
\left(\frac{d\sigma}{d\omega}\right)_{II\ order}=r_e^2\left(\frac{1}{m}\right)^2|&\frac{\langle\Psi_f|e^{-j\mathbf{kr}_j}\hat{\varepsilon}^{*}_{k_{out},s}\cdot\hat{p}_j|\Psi_n\rangle\langle\Psi_n|e^{j\mathbf{kr}_j}\hat{\varepsilon}_{k_{in},s}\cdot\hat{p}_j|\Psi_i\rangle}{E^{el.}_i-E^{el.}_n-\hbar\omega_{in}} \\
&+\frac{\langle\Psi_f|e^{-j\mathbf{kr}_j}\hat{\varepsilon}^{*}_{k_{out},s}\cdot\hat{p}_j|\Psi_n\rangle\langle\Psi_n|e^{j\mathbf{kr}_j}\hat{\varepsilon}_{k_{in},s}\cdot\hat{p}_j|\Psi_i\rangle}{E^{el.}_i-E^{el.}_n+\hbar\omega_{in}}|^2 \qquad (4.101)
\end{aligned}$$

This contribution is frequency dependent: its accounts for the frequency dependance of the scattering factors and in particular it is the quantum description of the anomalous scattering.

We underline that the second term is resonant when the incoming photon energy is equal to the excitation energy of the intermediate electronic state, i.e. when:

$$\hbar\omega_{in}=E^{el.}_n-E^{el.}_i \qquad (4.102)$$

4.4.6 High Energy Behaviour of the Second Order Scattering

An important limiting case of such cross section is the high frequency case, i.e. when the energy of the photon $\hbar\omega_{in}$ is much higher than all electronic excitation energies. In such case we can approximate the denominators with $\pm\hbar\omega_{in}$; with this approximation the cross section becomes [7–9]:

$$\left(\frac{d\sigma}{d\omega}\right)^{high\ energy}_{II\ order} = r_e^2 | - i\frac{\hbar\omega_{in}}{mc^2}\langle\Psi_{in}\sum_l e^{jqr_l}\frac{i\mathbf{q}\times\mathbf{p}_l}{\hbar k^2}\Psi_{in}\rangle\cdot\mathbf{P}_L|^2 \tag{4.103}$$

where the sum is over all the electrons and $\mathbf{P}_L$ is a polarization factor given by:

$$\mathbf{P}_L = \hat{\varepsilon^*}_{out,s}\times\hat{\varepsilon}_{in,s} \tag{4.104}$$

It can be shown that the matrix element present in the above equation is proportional to the atomic orbital magnetic momentum [16] [7–9], therefore by a careful analysis of such contribution to the scattering cross section, we can get information on the value of the orbital magnetic momentum.

Including the scattering due to the charges and to the orbital magnetic moment, the elastic scattering cross section at high energy is given by[17]:

$$\begin{aligned}\left(\frac{d\sigma}{d\omega}\right)^{High\ energy}_{el.} &= r_e^2\langle\Psi_{in}|\sum_l e^{-qr_l}|\Psi_{in}\rangle\hat{\varepsilon}_{k_{in},s_{in}}\cdot\hat{\varepsilon}^*_{k_{out},s_{out}} \\ &- i\frac{\hbar\omega_{in}}{mc^2}\langle\Psi_{in}\sum_l e^{jqr_l}\frac{i\mathbf{q}\times\mathbf{p}_l}{\hbar k^2}\Psi_{in}\rangle\cdot\mathbf{P}_L|^2\end{aligned} \tag{4.105}$$

We underline that the second contribution is reduced with respect to the first one by a factor $\hbar\omega/mc^2 \cong 10^{-2}$ at the typical energy of a scattering experiment; this reduces the intensity of the magnetic term of many order of magnitude with respect to charge one making the experiments quite difficult.

4.5 Relativistic Scattering

The interaction Hamiltonian (4.79) does not take into consideration relativistic effects; these are obtained starting from the Dirac equation of a relativistic electron in an electromagnetic field, making the limit to low velocity and taking only

[16] Remember that classically the angular momentum is proportional to $\mathbf{r}\times\mathbf{p}$ whose Fourier Transform is proportional to $\mathbf{q}\times\mathbf{p}$.

[17] We remind here that according to quantum mechanics rules we have first to add the amplitude of the transition matrix elements and than to square to the get the probability.

terms that the go to zero as v/c. In this way it is shown that the full interaction Hamiltonian between an electron and an electromagnetic field is:

$$\hat{H}_{int} = \sum_j \left(-\frac{e}{mc}\mathbf{A}(\mathbf{r}_j)\cdot\hat{p}_j + \frac{e^2}{2mc^2}\mathbf{A}^2(\mathbf{r}_j) - \frac{e\hbar}{mc}\mathbf{s}_j\cdot\nabla\times\mathbf{A} + \frac{e\hbar}{2m^2c^3}\mathbf{s}_j\cdot\frac{\partial\mathbf{A}}{\partial t} \times(p-\frac{e}{c}\mathbf{A})\right) \tag{4.106}$$

The physical meaning of the two additional terms is quite simple; the first one is due to the interaction of the spin of the electrons with the magnetic field $\mathbf{B} = \nabla\times\mathbf{A}$ of the radiation. The second one is the so-called spin-orbit interaction; for this second term it can be shown that, in the energy range of interest:

$$\frac{e\hbar}{2m^2c^3}\mathbf{s}_j\cdot\frac{\partial\mathbf{A}}{\partial t}\times(p-\frac{e}{c}\mathbf{A}) \cong -\frac{e\hbar}{2m^2c^3}\mathbf{s}_j\cdot\frac{\partial\mathbf{A}}{\partial t}\times\frac{e}{c}\mathbf{A} \tag{4.107}$$

Therefore the relativistic interaction Hamiltonian is well approximated as:

$$\hat{H}_{int} = \sum_j \left(-\frac{e}{mc}\mathbf{A}(\mathbf{r}_j)\cdot\hat{p}_j + \frac{e^2}{2mc^2}\mathbf{A}^2(\mathbf{r}_j) - \frac{e\hbar}{mc}\mathbf{s}_j\cdot\nabla\times\mathbf{A} - \frac{e\hbar}{2m^2c^3}\mathbf{s}_j\cdot\frac{\partial\mathbf{A}}{\partial t}\times\frac{e}{c}\mathbf{A}\right) \tag{4.108}$$

The third term is proportional to $\mathbf{A}$, so it give rise to scattering only in the second order perturbation theory, as the first term; the fourth term is proportional to $\mathbf{A}^2 = \mathbf{A}\cdot\mathbf{A}$ so it gives rise to scattering in the first order perturbation theory as the second term.

4.5.1 First Order Relativistic Contribution to the Scattering

Let us start considering the fourth term; comparing it with the second term, it is clear that we can determine its contribution to the scattering from that of the second terms with the following substitutions:

$$\frac{e^2}{2mc^2} \rightarrow -\frac{e\hbar}{2m^2c^3}\,\frac{e}{c} \tag{4.109}$$

$$\mathbf{A}^2 = \mathbf{A}\cdot\mathbf{A} \rightarrow \mathbf{s}_j\cdot\frac{\partial\mathbf{A}}{\partial t}\times\mathbf{A} \tag{4.110}$$

From (4.77) we get:

$$\frac{\partial\mathbf{A}}{\partial t} = \sum_{k,s}\sqrt{\frac{4\pi\hbar c^2}{2V\omega_k}}\left(-i\omega_k a_{k,s}\hat{\varepsilon}_{k,s}e^{j\mathbf{kr}-\omega t} + i\omega_k a^{\dagger}_{k,s}\hat{\varepsilon}^{*}_{k,s}e^{-j\mathbf{kr}-\omega t}\right) \tag{4.111}$$

Therefore:

$$\mathbf{s}_j \cdot \frac{\partial \mathbf{A}}{\partial t} \times \mathbf{A} = \sum_{k,s} \sum_{k',s'} \frac{4\pi\hbar c^2}{2V\omega_k} \left(-i\omega_k a_{k,s} a^{\dagger}_{k',s'} \mathbf{s}_j \cdot \hat{\varepsilon}_{k,s} \times \hat{\varepsilon}^*_{k',s'} + i\omega_k a^{\dagger}_{k,s} a_{k',s'} \mathbf{s}_j \cdot \hat{\varepsilon}^*_{k,s} \times \varepsilon_{k',s'} \right) \tag{4.112}$$

$$\mathbf{A}^2 = \sum_{k,s} \sum_{k',s'} \frac{4\pi\hbar c^2}{2V\omega_k} \left(a_{k,s} a^{\dagger}_{k',s'} \hat{\varepsilon}_{k,s} \cdot \hat{\varepsilon}^*_{k',s'} + a^{\dagger}_{k,s} a_{k',s'} \hat{\varepsilon}^*_{k,s} \cdot \varepsilon_{k',s'} \right) \tag{4.113}$$

where we have considered only the terms relevant for the scattering, i.e. the term in which an annihilation and a creation operator are present. Now in the sums we consider only the terms that contribute to our specific case, i.e. a incoming photon k_{in} is annihilated and a outcoming photon k_{out} is created; so we have only:

$$\mathbf{s}_j \cdot \frac{\partial \mathbf{A}}{\partial t} \times \mathbf{A} = \frac{4\pi\hbar c^2}{2V\omega_k} \, 2\, i\omega_k \, a^{\dagger}_{k_{out},s_{out}} a_{k_{in},s_{in}} \mathbf{s}_j \cdot \hat{\varepsilon}^*_{k_{out},s_{out}} \times \varepsilon_{k_{in},s_{in}} \tag{4.114}$$

$$\mathbf{A}^2 = \frac{4\pi\hbar c^2}{2V\omega_k} \, 2 \, a^{\dagger}_{k_{out},s_{out}} a_{k_{in},s_{in}} \hat{\varepsilon}^*_{k_{out},s_{out}} \cdot \varepsilon_{k_{in},\mathrm{sin}} \tag{4.115}$$

Now, starting from (4.87), making the substitution according to (4.109), (4.110), (4.114) and (4.115), we get:

$$\left(\frac{d\sigma}{d\Omega} \right)^{rel.}_{I\ order} = r_e^2 \, | -i \frac{\hbar\omega_k}{mc^2} \langle \Psi_{in} | \sum_j e^{-qr_j} \mathbf{s}_j | \Psi_{in} \rangle \cdot \hat{\varepsilon}^*_{k_{out},s_{out}} \times \hat{\varepsilon}_{k_{in},s_{in}} |^2 \tag{4.116}$$

4.5.2 Second Order Relativistic Scattering

In a similar way, the contribution of the third term in (4.106) can be obtained from that of the first term with the substitution[18]:

$$\mathbf{p}_j \cdot \mathbf{A} \Rightarrow \hbar \mathbf{s}_j \cdot \nabla \times \mathbf{A} \tag{4.117}$$

The cross section is easily obtained by making this substitution into (4.101)

[18] Note that $\mathbf{p}_j \cdot \mathbf{A}$ is proportional to the interaction energy between the electric dipole moment of the electron and the electric field, while the term $\hbar \mathbf{s}_j \cdot \nabla \times \mathbf{A}$ is proportional to the interaction energy between the magnetic spin moment of the electron and the magnetic field.

$$\left(\frac{d\sigma}{d\omega}\right)^{rel.}_{II\ order} = r_e^2 \left(\frac{1}{m}\right)^2 |\frac{\langle\Psi_f|e^{-j\mathbf{kr}_j}\,\hbar\mathbf{s}_j\cdot\mathbf{k}_{out}\times\hat{\varepsilon}^*_{k_{out},s}|\Psi_n\rangle\langle\Psi_n|e^{j\mathbf{kr}_j}\,\hbar\mathbf{s}_j\cdot\mathbf{k}_{in}\times\hat{\varepsilon}_{k_{in},s}|\Psi_i\rangle}{E_i^{el.}-E_n^{el.}-\hbar\omega_{in}} \tag{4.118}$$

$$+\frac{\langle\Psi_f|e^{-j\mathbf{kr}_j}\,\hbar\mathbf{s}_j\cdot\mathbf{k}_{out}\times\hat{\varepsilon}^*_{k_{out},s}|\Psi_n\rangle\langle\Psi_n|e^{j\mathbf{kr}_j}\,\hbar\mathbf{s}_j\cdot\mathbf{k}_{in}\times\hat{\varepsilon}_{k_{in},s}|\Psi_i\rangle}{E_i^{el.}-E_n^{el.}+\hbar\omega_{in}}|^2$$

We recognize that the second term is resonant when the incoming photon energy equals one of the excitations energies of the electronic system; this resonant term, together with the analogous term of (4.101) give rise to the magnetic resonant scattering effects, that will be considered in Chap. 12.

We now consider the high energy approximation of this expression; in [9] it is shown that:

$$\left(\frac{d\sigma}{d\Omega}\right)^{rel.,\ highenergy}_{II\ order} = r_e^2\,|-i\frac{\hbar\omega_k}{mc^2}\langle\Psi_{in}|\sum_j e^{-qr_j}\mathbf{s}_j|\Psi_{in}\rangle\cdot[(k_{out}\times\hat{\varepsilon}^*_{k_{out},s_{out}})(k_{out}\cdot\hat{\varepsilon}_{k_{in},s_{in}})$$

$$-(k_{in}\times\hat{\varepsilon}_{k_{in},s_{in}})(k_{in}\cdot\hat{\varepsilon}^*_{k_{out},s_{out}})-(k_{out}\times\hat{\varepsilon}^*_{k_{out},s_{out}})\times(k_{in}\times\hat{\varepsilon}_{k_{in},s_{in}})]|^2 \tag{4.119}$$

We note that this contribution has an amplitude similar to the orbital momentum one but with a very different polarization dependence; moreover the matrix element involved is the same of (4.116).

4.5.3 Total Scattering Cross Section at High Energy

We now can collect all the contributions to the high energy scattering cross section coming from the A^2 term (4.92), from the high energy behaviour of the A·p term (4.103), from the first order relativistic scattering (4.116) and from the high energy behaviour of the second order relativistic scattering (4.119), obtaining the complete expression of elastic cross section at high energy:

$$\left(\frac{d\sigma}{d\Omega}\right)^{High\ energy}_{el.,\ total} = r_e^2\,|\langle\Psi_{in}|\sum_j e^{-qr_j}|\Psi_{in}\rangle\hat{\varepsilon}_{k_{in},s_{in}}\cdot\hat{\varepsilon}^*_{k_{out},s_{out}} - i\frac{\hbar\omega_{in}}{mc^2} \tag{4.120}$$

$$\times[\langle\Psi_{in}|\sum_l e^{jqr_l}\frac{i\mathbf{q}\times\mathbf{p}_l}{\hbar k^2}|\Psi_{in}\rangle\cdot\mathbf{P}_L+\langle\Psi_{in}|\sum_j e^{-qr_j}\mathbf{s}_j|\Psi_{in}\rangle\cdot\mathbf{P}_S]|^2$$

where the two polarization vectors $\mathbf{P}_L$ and $\mathbf{P}_S$ are:

$$\mathbf{P}_L = \hat{\varepsilon^*}_{out,s}\times\hat{\varepsilon}_{in,s} \tag{4.121}$$

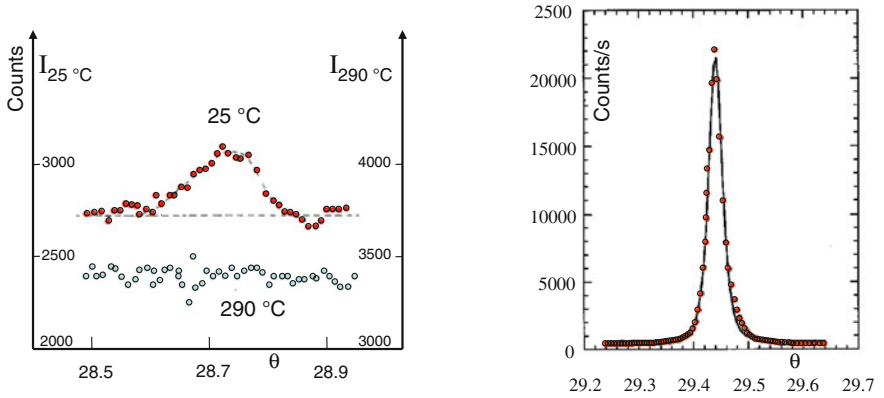


Fig. 4.9 Comparison between the pioneering measurements of De Bergevin and Brunel [10] (*left panel*) and those today routinely performed at third generation synchrotron radiation facilities [11] (*right panel*) on the (3/2, 3/2, 3/2) magnetic peak of NiO in the antiferromagnetic phase. Pictures are redrawn from the original papers

$$\begin{aligned}\mathbf{P}_S = &\hat{\varepsilon}^*_{k_{out},s_{out}} \times \hat{\varepsilon}_{k_{in},s_{in}} + (k_{out} \times \hat{\varepsilon}^*_{k_{out},s_{out}})(k_{out} \cdot \hat{\varepsilon}_{k_{in},s_{in}}) \\ &- (k_{in} \times \hat{\varepsilon}_{k_{in},s_{in}})(k_{in} \cdot \hat{\varepsilon}^*_{k_{out},s_{out}}) - (k_{out} \times \hat{\varepsilon}^*_{k_{out},s_{out}}) \times (k_{in} \times \hat{\varepsilon}_{k_{in},s_{in}})\end{aligned} \tag{4.122}$$

The first term is the charge scattering factor, the second and third are the magnetic scattering factors; the second term originates from the orbital momentum, the third one from the spin momentum. The magnetic terms are multiplied by the factor $\hbar\omega/mc^2 \cong 10^{-2}$ at the typical energy of a scattering experiment, that reduces their intensity with respect to charge one of $\approx 10^{-4}$; in addition while all the electrons contribute to the charge scattering, only uncoupled electrons contribute to the magnetic scattering, so an additional factor of the order of 10^{-2} reduces the magnetic contribution to the scattering intensity with respect to the charge contribution to $\approx 10^{-6}$. This reduction makes the experiments very difficult and only the extreme high brilliance and intensity today achievable at the third generation synchrotron radiation facilities allow measurements with signal to noise ratio high enough for a quantitative determination of the magnetic order and of the magnetic atomic moments (see Fig. 4.9).

We underline also that the two magnetic contributions to the cross section have a very different polarization dependence; this gives the possibility to discriminate between them, making profit of the polarization control today achievable at the third generation synchrotron radiation facilities.

The third term of (4.120) is the Fourier Transform of the spin density $\mathbf{S}(\mathbf{q})$:

$$\mathbf{S}(\mathbf{q}) = \langle \Psi_{in} | \sum_j e^{-qr_j} \mathbf{s}_j | \Psi_{in} \rangle \tag{4.123}$$

The second term of (4.120) can be expressed in term of the Fourier Transform of the orbital moment density $\mathbf{L}(\mathbf{q})$:

$$\mathbf{L}(\mathbf{q}) = \langle \Psi_{in} | \sum_j e^{-\mathbf{q}\mathbf{r}_j} \mathbf{l}_j | \Psi_{in} \rangle \tag{4.124}$$

Because [12]:

$$\sum_l e^{jqr_l} \frac{i\mathbf{q} \times \mathbf{p}_l}{\hbar k^2} = -4\sin^2\theta_B \, [\hat{\mathbf{q}} \times \frac{\mathbf{L}(\mathbf{q})}{2} \times \hat{\mathbf{q}}] \tag{4.125}$$

the total cross section (4.120) is usually written also as:

$$\left(\frac{d\sigma}{d\Omega}\right)^{High\ energy}_{el.,\ total} = r_e^2 \, |\langle \Psi_{in} | \sum_j e^{-qr_j} | \Psi_{in} \rangle \hat{\varepsilon}_{k_{in},s_{in}} \cdot \hat{\varepsilon}^*_{k_{out},s_{out}} - i \frac{\hbar\omega_{in}}{mc^2} \, [\hat{\mathbf{q}} \times \frac{\mathbf{L}(\mathbf{q})}{2} \times \hat{\mathbf{q}} \cdot \mathbf{P}'_L + \mathbf{S}(\mathbf{q}) \cdot \mathbf{P}_S]|^2 \tag{4.126}$$

where:

$$\mathbf{P}'_L = -4\sin^2\theta_B \, \hat{\varepsilon^*}_{out,s} \times \hat{\varepsilon}_{in,s} \tag{4.127}$$

And also as:

$$\left(\frac{d\sigma}{d\Omega}\right)^{High\ energy}_{el.,\ total} = r_e^2 \, |\langle \Psi_{in} | \sum_j e^{-qr_j} | \Psi_{in} \rangle \hat{\varepsilon}_{k_{in},s_{in}} \cdot \hat{\varepsilon}^*_{k_{out},s_{out}} - i \frac{\hbar\omega_{in}}{mc^2} \, [\frac{1}{2}\mathbf{L}(\mathbf{q}) \cdot \mathbf{P}''_L + \mathbf{S}(\mathbf{q}) \cdot \mathbf{P}_S]|^2 \tag{4.128}$$

where:

$$\mathbf{P}''_L = -4\sin^2\theta_B \, [\hat{\mathbf{q}} \times (\hat{\varepsilon^*}_{out,s} \times \hat{\varepsilon}_{in,s} \times \hat{\mathbf{q}})] \tag{4.129}$$

These equations will be the starting point in Chap. 12 for the study of non resonant magnetic scattering.

Appendix

In the non rationalized CGS unit system the unit charge (esu) is defined from Coulomb force equation assuming $4\pi\varepsilon_0 = 1$ and the magnetic field B is defined assuming in the Biot-Savart $\mu_0 = 4\pi/c$. These assumptions imply that all formula in CGS units system can be derived from those in SI system with the substitutions:

$$\varepsilon_0 \to \frac{1}{4\pi} \qquad \mu_0 \to \frac{4\pi}{c^2} \qquad B \to \frac{B}{c} \qquad A \to \frac{A}{c}$$

In particular, it is easy to show that in CGS system:

$$E = B \qquad w_E = \frac{1}{8\pi}E^2 = w_B = \frac{1}{8\pi}B^2 \qquad I = \frac{1}{4\pi}cE^2 = \frac{1}{4\pi c}\omega^2 A^2$$

References

1. S.H. Chen, M. Kotlarchyk, *Interaction of Photons and Neutrons With Matter: An Introduction* (World Scientific, Singapore, 1997)
2. R. Loudon, *Quantum Theory of Light* (Oxford Science Publications, Oxford, 2003)
3. A.D. Rakic, A.B. Djuriic, J.M. Elazar, M.L. Majewski, Appl. Opt. **37**(22), 5271–5283 (1998)
4. C.T. Chantler, K. Olsen, R.A. Dragoset, J. Chang, A.R. Kishore, S.A. Kotochigova, D.S. Zucker, Detailed tabulation of atomic form factors, photoelectric absorption and scattering cross section, and mass attenuation coefficients for Z = 1–92 from E = 1–10 eV to E = 0.4–1.0 MeV. NIST web site. http://www.nist.gov/pml/data/ffast/index.cfm. Accessed 5 Jan 2014
5. S. Mobilio, Interaction between radiation and matter: an introduction, in *Synchrotron Radiation: Fundamentals, Methodologies and Applications*, ed. by S. Mobilio, G. Vlaic (Societa' Italiana di Fisica, Bologna, 2003), pp. 55–94
6. R.W. James, *The Optical Principles of The Diffraction of X Rays*, vol. II (G. Bell And Sons Limited, Osmania University, London, 1962)
7. M. Blume, J. Appl. Phys. **57**, 3615–3618 (1985)
8. M. Blume, in *Resonant Anomalous X-Ray Scattering*, ed. by G. Materlik, J. Sparks, K. Fisher (Elsevier Science B.V., Amsterdam, 1994)
9. M. Altarelli, X-Ray magnetic scattering: Theoretical introduction, in *Synchrotron Radiation: Fundamentals, Methodologies and Applications*, ed. by S. Mobilio, G. Vlaic (Societa' Italiana di Fisica, Bologna, 2003), pp. 581–605
10. F. De Bergevin, M. Brunel, Phys. Lett. **A39**, 141–142 (1972)
11. V. Fernandez, C. Vettier, F. De Bergevin, C. Giles, W. Neubeck, Phys. Rev. B **57**, 7870–7876 (1998)
12. M. Blume, D. Gibbs, Phys. Rev. B **37**, 1779–1789 (1988)

Chapter 5
Quantum Description of the Matter-Radiation Interaction

Carlo Maria Bertoni

Abstract Quantum physics describes the radiation field, matter systems (like atoms, molecules and solids) and their interactions. The processes of interaction consist of absorption, emission and diffusion of *photons*, the basis of many experimental techniques to study materials and their electronic properties. The states of the electron systems can be studied in a single-particle picture or in a many-electron scheme; the two approaches will be compared in the study of the elementary processes of interaction with light at different levels of approximation for the initial, final and intermediate states of the matter system.

5.1 The Classical Description of the Free Electromagnetic Field

In classical electrodynamics the real vector fields $\mathbf{E}(\mathbf{r}, t)$ and $\mathbf{B}(\mathbf{r}, t)$ are solutions of Maxwell equations:

$$\nabla \cdot \mathbf{E} = 4\pi\rho \qquad \nabla \times \mathbf{B} - \frac{1}{c}\frac{\partial \mathbf{E}}{\partial t} = \frac{4\pi \mathbf{J}}{c} \tag{5.1}$$

$$\nabla \cdot \mathbf{B} = 0 \qquad \nabla \times \mathbf{E} + \frac{1}{c}\frac{\partial \mathbf{B}}{\partial t} = 0 \tag{5.2}$$

where c is the speed of light in vacuum.

In the first pair of inhomogeneous equations the source terms are present: the charge density $\rho(\mathbf{r}, t)$ and the current density $\mathbf{J}(\mathbf{r}, t)$. The units used here are the non-rationalized c.g.s. units and the four equations can be derived by their

C. M. Bertoni (✉)
Dipartimento di Scienze Fisiche, Informatiche e Matematiche, University of Modena and Reggio Emilia, and CNR-Istituto Nanoscienze S3, and CNISM, via Campi 213/A, 41100 Modena, Italy
e-mail: bertoni@unimore.it

S. Mobilio et al. (eds.), *Synchrotron Radiation*,
DOI: 10.1007/978-3-642-55315-8_5, © Springer-Verlag Berlin Heidelberg 2015

more familiar expression in S.I. units by putting $4\pi\boldsymbol{\varepsilon}_0 = 1$ and $\mu_0 = 1/(\boldsymbol{\varepsilon}_0 c^2)$ and replacing $\mathbf{B}$ with $\mathbf{B}/c$.

The two fields $\mathbf{E}$ and $\mathbf{B}$ can be derived by a scalar potential $\varphi(\mathbf{r}, t)$ and a vector potential $\mathbf{A}(\mathbf{r}, t)$ through the relations

$$\mathbf{E}(\mathbf{r}, t) = -\nabla\varphi(\mathbf{r}, t) - \frac{1}{c}\frac{\partial \mathbf{A}(\mathbf{r}, t)}{\partial t} \tag{5.3}$$

$$\mathbf{B}(\mathbf{r}, t) = \nabla \times \mathbf{A}(\mathbf{r}, t) \tag{5.4}$$

While the vector field $\mathbf{E}(\mathbf{r}, t)$ and $\mathbf{B}(\mathbf{r}, t)$ are completely determined by the knowledge of $\varphi(\mathbf{r}, t)$ and $\mathbf{A}(\mathbf{r}, t)$, the inverse is not true. A transformation on $\varphi(\mathbf{r}, t)$ and $\mathbf{A}(\mathbf{r}, t)$ of the type

$$\varphi(\mathbf{r}, t) \to \varphi(\mathbf{r}, t) + \frac{1}{c}\frac{\partial f(\mathbf{r}, t)}{\partial t} \qquad \mathbf{A}(\mathbf{r}, t) \to \mathbf{A}(\mathbf{r}, t) - \nabla f(\mathbf{r}, t) \tag{5.5}$$

(*gauge transformation*) leaves unchanged the values of $\mathbf{E}(\mathbf{r}, t)$ and $\mathbf{B}(\mathbf{r}, t)$, with an arbitrary choice of the differentiable function $f(\mathbf{r}, t)$. The *gauge invariance* offers a wide choice of scalar ans vector potentials. By inserting (5.3) and (5.4) into (5.1) one gets two equations for the potentials:

$$\nabla(\nabla \cdot \mathbf{A}) - \nabla^2\mathbf{A} + \frac{1}{c^2}\frac{\partial}{\partial t}\nabla\varphi + \frac{1}{c^2}\frac{\partial^2 \mathbf{A}}{\partial^2 t} = \frac{4\pi}{c}\mathbf{J} \tag{5.6}$$

$$-\nabla^2\varphi - \nabla\cdot\left(\frac{1}{c}\frac{\partial \mathbf{A}}{\partial t}\right) = 4\pi\rho \tag{5.7}$$

The vectors fields like $\mathbf{J}(\mathbf{r}, t)$ can be splitted into two parts, i.e.

$$\mathbf{J}(\mathbf{r}, t) = \mathbf{J}_T(\mathbf{r}, t) + \mathbf{J}_L(\mathbf{r}, t) \tag{5.8}$$

where

$$\nabla \cdot \mathbf{J}_T = 0 \quad \text{and} \quad \nabla \times \mathbf{J}_L = \mathbf{0} \tag{5.9}$$

The subscript T indicates the *transverse* or solenoidal part and L the *longitudinal* or irrotational part of the field. Thus only $\mathbf{J}_L$ appears in the continuity equation

$$\nabla \cdot \mathbf{J}_L = -\frac{\partial \rho}{\partial t}. \tag{5.10}$$

The separation into a transverse and a longitudinal part can be done for other vector fields, $\mathbf{A}$ in parti cular.

A possible choice of the gauge is represented by the *Coulomb gauge* [1]. In this gauge one has

$$\nabla \cdot \mathbf{A} = 0 \tag{5.11}$$

and $\mathbf{A}_L = 0$ or constant.

From (5.7) and the condition (5.11) one obtains the Poisson equation with a particular solution of the form:

$$\varphi(\mathbf{r}, t) = \int d\mathbf{r}' \frac{\rho(\mathbf{r}', t)}{| \mathbf{r} - \mathbf{r}' |} \tag{5.12}$$

Thus the scalar potential in the Coulomb gauge is the well known electrostatic potential depending on the charge distribution in all space and evaluated ad the same instant t, as it had an *instantaneous* knowledge of the charge distribution in the whole space. As a consequence, the (5.6) becomes

$$-\nabla^2 \mathbf{A} + \frac{1}{c^2} \frac{\partial^2 \mathbf{A}}{\partial^2 t} = \frac{4\pi}{c} \mathbf{J}_T \tag{5.13}$$

A particular solution of this inhomogeneous differential equation is given by

$$\mathbf{A}(\mathbf{r}, t) = \int d\mathbf{r}' \frac{\mathbf{J}_T(\mathbf{r}', t')}{| \mathbf{r} - \mathbf{r}' |} \tag{5.14}$$

where

$$t' = t - \frac{| \mathbf{r} - \mathbf{r}' |}{c}$$

The dependence on the current density of the vector potential takes account of the *retardation effect* due to the finite value of the velocity of light. This asymmetry between scalar and vector potential is a peculiarity of the Coulomb gauge, where it is the latter to take care of retardation effects.

If we are looking for the classical solutions, in absence of charge or current, for the *free* electromagnetic field, the *radiation field*, we get:

$$\varphi = 0 \quad \nabla^2 \mathbf{A} - \frac{1}{c^2} \frac{\partial^2 \mathbf{A}}{\partial^2 t} = 0 \tag{5.15}$$

The general solution of the homogeneous equation for $\mathbf{A}$ is the superposition of travelling waves. If we choose, as orthonormal basis set, complex plane waves, we obtain

$$\mathbf{A}(\mathbf{r}, t) = \sum_{\mathbf{k},s} \left(\mathscr{A}(\mathbf{k}, s) \hat{\boldsymbol{\varepsilon}}_{s\mathbf{k}} e^{i\mathbf{k}\cdot\mathbf{r} - i\omega_{\mathbf{k}} t} + \mathscr{A}^*(\mathbf{k}, s) \hat{\boldsymbol{\varepsilon}}^*_{s\mathbf{k}} e^{-i\mathbf{k}\cdot\mathbf{r} + i\omega_{\mathbf{k}} t} \right) \tag{5.16}$$

Once the normalization volume $\mathscr{V} = L_x L_y L_z$ is fixed (with the requirement that $\mathscr{V} \to \infty$ will not affect the calculations) the grid of wavevectors $\mathbf{k}$ is given by

$$\mathbf{k} = 2\pi \left(\frac{n_x}{L_x}, \frac{n_y}{L_y}, \frac{n_z}{L_z} \right).$$

We have used the *periodic boundary conditions* on the whole volume $\mathscr{V}$ and n_x, n_y, n_z are relative integers. For each wavevector $\mathbf{k}$, there are two independent polarization vectors, orthogonal to $\mathbf{k}$

$$\hat{\boldsymbol{\varepsilon}}_{1\mathbf{k}} \cdot \mathbf{k} = \mathbf{0} \quad \hat{\boldsymbol{\varepsilon}}_{2\mathbf{k}} \cdot \mathbf{k} = \mathbf{0}$$

and among themselves

$$\hat{\boldsymbol{\varepsilon}}_{1\mathbf{k}} \cdot \hat{\boldsymbol{\varepsilon}}^*_{2\mathbf{k}} = 0$$

If $\hat{\boldsymbol{\varepsilon}}_{1\mathbf{k}}$ and $\hat{\boldsymbol{\varepsilon}}_{2\mathbf{k}}$ are real, they represent the two *linear* polarizations; if we use the complex vectors

$$\hat{\boldsymbol{\varepsilon}}_{(+)\mathbf{k}} = -\frac{1}{\sqrt{2}}(\hat{\boldsymbol{\varepsilon}}_{1\mathbf{k}} + i\hat{\boldsymbol{\varepsilon}}_{2\mathbf{k}}) \quad \text{and} \quad \hat{\boldsymbol{\varepsilon}}_{(-)\mathbf{k}} = \frac{1}{\sqrt{2}}(\hat{\boldsymbol{\varepsilon}}_{1\mathbf{k}} - i\hat{\boldsymbol{\varepsilon}}_{2\mathbf{k}})$$

they will describe *circular* polarizations (*left* and *right*); the angular frequency of each *mode* is given by

$$\omega_{\mathbf{k}} = c \mid \mathbf{k} \mid .$$

The complex amplitudes $\mathscr{A}(\mathbf{k}, s)$ are the new coordinates of the radiation field. Each $\mathscr{A}(\mathbf{k}, s)$ appears in (5.16) with its complex conjugate, to ensure the reality of $\mathbf{A}(\mathbf{r}, t)$. From the same expression one can derive $\mathbf{E}(\mathbf{r}, t)$ by (5.3) and $\mathbf{B}(\mathbf{r}, t)$ by (5.4) and from these the total energy of the field from the expression

$$\mathscr{H}_f = \frac{1}{8\pi} \int_{\mathscr{V}} (\mathbf{E}^2 + \mathbf{B}^2) d\mathbf{r} \tag{5.17}$$

This integral is, in absence of charges and currents, the *Hamiltonian of the free field*.

5.2 The Quantized Free Electromagnetic Field

We write the vector potential (5.16) as a superposition of the different modes (each of them is identified by the wavevector $\mathbf{k}$ and the polarization index s)

$$\mathbf{A}(\mathbf{r}, t) = \sum_{\mathbf{k},s} \left(\frac{4\pi\hbar c^2}{2\mathscr{V}\omega_{\mathbf{k}}} \right)^{\frac{1}{2}} \left(a_{\mathbf{k}s}(t) \hat{\boldsymbol{\varepsilon}}_{s\mathbf{k}} e^{i\mathbf{k}\cdot\mathbf{r}} + a^{\dagger}_{\mathbf{k}s}(t) \hat{\boldsymbol{\varepsilon}}^*_{s\mathbf{k}} e^{-i\mathbf{k}\cdot\mathbf{r}} \right) \tag{5.18}$$

where in each term of the sum a real factor has been put in evidence to multiply a second term made of numerical (adimensional) quantities. The new dynamical variables $a_{\mathbf{k}s}(t)$ and $a^{\dagger}_{\mathbf{k}s}(t)$ are numbers (complex numbers, the latter being the complex conjugate of the former), the new classical dynamical variables of the field. In the

quantum description they will become *quantum operators*: thus $a^{\dagger}_{\mathbf{k}s}(t)$ is not the complex conjugate, but the hermitian conjugate of $a_{\mathbf{k}s}(t)$.

From the second of (5.15) we obtain

$$\frac{\partial^2}{\partial t^2} a_{\mathbf{k}s}(t) = -\omega^2_{\mathbf{k}} a_{\mathbf{k}s}(t) \quad \rightarrow \quad a_{\mathbf{k}s}(t) = a_{\mathbf{k}s} e^{-i\omega_{\mathbf{k}} t}$$

and

$$a^{\dagger}_{\mathbf{k}s}(t) = a^{\dagger}_{\mathbf{k}s} e^{i\omega_{\mathbf{k}} t}$$

We can insert (5.18) into (5.3) and (5.4) and then calculate the total energy of the free field with the use of (5.17). We will obtain, after some calculations, taking into account the orthogonality of two plane waves with different wavevectors in the volume $\mathcal{V}$ and the orthogonality of the two polarizations at the same wavevector, the expression

$$\mathcal{H}_f = \sum_{\mathbf{k},s} \frac{1}{2} \hbar\omega_{\mathbf{k}} (a^{\dagger}_{\mathbf{k}s} a_{\mathbf{k}s} + a_{\mathbf{k}s} a^{\dagger}_{\mathbf{k}s}) \tag{5.19}$$

that is—as expected—independent on time and where we have allowed that $a_{\mathbf{k}s}$ and $a^{\dagger}_{\mathbf{k}s}$ cannot commute. It can be identifyed as the Hamiltonian of an infinite number of independent harmonic oscillators, each labeled by a different wavevector and one of two polarizations. The new variables (quantum operators) are thus written in a way particularly suitable to quantization. If one introduces the commutation rules used in the quantization of a set of independent oscillators

$$[a_{\mathbf{k}s}, a^{\dagger}_{\mathbf{k}'s'}] = \delta_{\mathbf{k}\mathbf{k}'} \delta_{ss'} \tag{5.20}$$

where $[a, b] = ab - ba$, we obtain the familiar expression for the free-field Hamiltonian

$$\mathcal{H}_f = \sum_{\mathbf{k},s} \hbar\omega_{\mathbf{k}} \left(a^{\dagger}_{\mathbf{k}s} a_{\mathbf{k}s} + \frac{1}{2} \right). \tag{5.21}$$

The Hamiltonian $\mathcal{H}_f$ is the sum of *single-mode* terms each (independent of the others) with wavevector $\mathbf{k}$ and polarization s, of the form $\hbar\omega_{\mathbf{k}} \left(\check{n}_{\mathbf{k}s} + \frac{1}{2} \right)$, where

$$\check{n}_{\mathbf{k}s} = a^{\dagger}_{\mathbf{k}s} a_{\mathbf{k}s}$$

is the *number operator*. Each number operators $\check{n}_{\mathbf{k}s}$ is a hermitian operator acting on a quantum state $| \Phi_{\mathbf{k}s} \rangle$ that is a *ket* vector in the Hilbert space of quantum states

associed the $(\mathbf{k}, s)$ mode. The state $\mid \Phi_{\mathbf{k}s}\rangle$ is a superposition of the eigenstates of the number operator

$$\mid \Phi_{\mathbf{k}s}\rangle = \sum_{n_{\mathbf{k}s}} c_{n_{\mathbf{k}s}} \mid n_{\mathbf{k}s}\rangle$$

where

$$\check{n}_{\mathbf{k}s} \mid n_{\mathbf{k}s}\rangle = n_{\mathbf{k}s} \mid n_{\mathbf{k}s}\rangle$$

is the eigenvalue equation for the number operator of the $(\mathbf{k}, s)$ mode. Then $\mathscr{H}_f$ is also a hermitian operator and it acts on different state-spaces corresponding to the different $(\mathbf{k}, s)$ modes.

It is easy to show, from the commutation relation (5.20), that also $a_{\mathbf{k}s} \mid n_{\mathbf{k}s}\rangle$ is an eigenstate of $\check{n}_{\mathbf{k}s}$

$$\check{n}_{\mathbf{k}s}(a_{\mathbf{k}s} \mid n_{\mathbf{k}s}\rangle) = (n_{\mathbf{k}s} - 1)(a_{\mathbf{k}s} \mid n_{\mathbf{k}s}\rangle)$$

with eigenvalue $(n_{\mathbf{k}s} - 1)$. $a^\dagger_{\mathbf{k}s} \mid n_{\mathbf{k}s}\rangle$ is also an eigenstate with eigenvalue $(n_{\mathbf{k}s} + 1)$

$$\check{n}_{\mathbf{k}s}(a^\dagger_{\mathbf{k}s} \mid n_{\mathbf{k}s}\rangle) = (n_{\mathbf{k}s} + 1)(a^\dagger_{\mathbf{k}s} \mid n_{\mathbf{k}s}\rangle)$$

Thus $a_{\mathbf{k}s}$ and $a^\dagger_{\mathbf{k}s}$, acting on an eigenstate of $\check{n}_{\mathbf{k}s}$, transform it into another eigenstate of $\check{n}_{\mathbf{k}s}$, with a difference of ∓ 1 in the number eigenvalue. The spectrum of the eigenvalues of $\check{n}_{\mathbf{k}s}$ must have a minimum value. By multiplying the corresponding eigenstate, $a_{\mathbf{k}s}$ must give 0. Thus $\check{n}_{\mathbf{k}s} = a^\dagger_{\mathbf{k}s} a_{\mathbf{k}s}$, has as lowest eigenvalue 0, the state with no photon in the $(\mathbf{k}, s)$ mode. Putting all these properties together, one obtains that the eigenvalues $n_{\mathbf{k}s}$ of $\check{n}_{\mathbf{k}s}$ can be only non-negative integer numbers 0, 1, 2, 3, ... The operator $\check{n}_{\mathbf{k}s}$ is the operator *number of photons*, while $a_{\mathbf{k}s}$ *destroys* a photon, and $a^\dagger_{\mathbf{k}s}$ *creates* a photon (in the $\mathbf{k}s$ mode). The direct product of quantum states

$$\mid \Phi\rangle = \mid \Phi_{\mathbf{k}_1 s_1}\rangle \otimes \mid \Phi_{\mathbf{k}_2 s_2}\rangle \otimes \ldots \otimes \mid \Phi_{\mathbf{k}_i s_i}\rangle \otimes \ldots$$

is a vector in the Hilbert space of the free electromagnetic field. To construct the eigenstates of $\mathscr{H}_f$ one has to use the eigenstates of $\check{n}_{\mathbf{k}s}$, having a defined number of photons in each mode. With the normalization condition for well-behaving quantum states:

$$\langle n_{\mathbf{k}s} \mid n_{\mathbf{k}s}\rangle = 1 \tag{5.22}$$

we obtain consistently with relations (5.20)

$$a_{\mathbf{k}s} \mid n_{\mathbf{k}s}\rangle = \sqrt{n_{\mathbf{k}s}} \mid n_{\mathbf{k}s} - 1\rangle \tag{5.23}$$

$$a^\dagger_{\mathbf{k}s} \mid n_{\mathbf{k}s}\rangle = \sqrt{n_{\mathbf{k}s} + 1} \mid n_{\mathbf{k}s} + 1\rangle \tag{5.24}$$

$$| n_{\mathbf{k}s}\rangle = \frac{\left(a^{\dagger}_{\mathbf{k}s}\right)^{n_{\mathbf{k}s}}}{\sqrt{n_{\mathbf{k}s}!}} | 0_{\mathbf{k}s}\rangle \tag{5.25}$$

Two states with two different occupation numbers in the same mode are orthogonal

$$\langle m_{\mathbf{k}s} | n_{\mathbf{k}s}\rangle = \delta_{m_{\mathbf{k}s},n_{\mathbf{k}s}}$$

as the states of different modes that correspond to different subspaces of the space of the physical states of the free electromagnetic field

$$\langle m_{\mathbf{k}s} | n_{\mathbf{k}'s'}\rangle = \delta_{m_{\mathbf{k}s},n_{\mathbf{k}'s}}\delta_{\mathbf{k},\mathbf{k}'}\delta_{s,s'}.$$

It is possible to construct a quantum state with defined number of photons for the whole set of modes by the product

$$| \{n_{\mathbf{k}s}\}\rangle = | \ \ldots \ n_{\mathbf{k}s} \ \ldots \rangle = \prod_{\mathbf{k}_i}\prod_{s_i} | n_{\mathbf{k}_i s_i}\rangle \tag{5.26}$$

where each state is labeled by the set of *occupation numbers,* giving the *number of photons* for each mode. This is the basis set for any well defined quantum state of the e.m. field. A *pure* quantum state of the free field is a linear combination of such states, with complex coefficient. Each component of this basis, given by (5.26), has a well defined *total number of photons* and then a well defined energy.

$$N_{\{n_{\mathbf{k}s}\}} = \sum_{k_i\ s_i} n_{\mathbf{k}_i s_i}$$

This is not true for a combination of them with different occupation numbers, as it always happens in quantum physics. Notice that two basis states $| \{n_{\mathbf{k}s}\}\rangle$ and $| \left\{n'_{\mathbf{k}s}\right\}\rangle$ are orthogonal if the occupation numbers (number of photons) are different even in a single mode. Each quantum state indicated by expression (5.26) is an eigenstate of the number operators $\check{n}_{\mathbf{k}s}$ and of the energy, with energy eigenvalue

$$E_{\{n_{\mathbf{k}s}\}} = \sum_{\mathbf{k}_i s_i} \hbar\omega_{\mathbf{k}_i}(n_{\mathbf{k}_i s_i} + \frac{1}{2}).$$

We can construct a linear combination $| \Phi\rangle$ of states (5.26), with number of photons not defined. The resulting vector space is the extended Fock space of the states of the free electromagnetic field.

In the Heisenberg picture the quantum states are fixed (*time-independent*) and the operators evolve with time. In particular the equation of motion of $a_{\mathbf{k}s}(t)$ is

$$i\hbar\frac{da_{\mathbf{k}s}(t)}{dt} = [a_{\mathbf{k}s}(t), \mathscr{H}_f]$$

that means

$$\frac{da_{\mathbf{k}s}(t)}{dt} = -ia_{\mathbf{k}s}(t)$$

The solutions are

$$a_{\mathbf{k}s}(t) = a_{\mathbf{k}s}e^{-i\omega_{\mathbf{k}}t}$$

By hermitian conjugation one gets

$$a^{\dagger}_{\mathbf{k}s}(t) = a^{\dagger}_{\mathbf{k}s}e^{+i\omega_{\mathbf{k}}t}$$

We can now write the vector potential *operator*as

$$\begin{aligned}\mathbf{A}(\mathbf{r},t) &= \sum_{\mathbf{k},s}\left(\frac{4\pi\hbar c^2}{2\mathscr{V}\omega_{\mathbf{k}}}\right)^{\frac{1}{2}}\left(a_{\mathbf{k}s}\hat{\boldsymbol{\varepsilon}}_{s\mathbf{k}}e^{i\mathbf{k}\cdot\mathbf{r}-i\omega_{\mathbf{k}}t} + a^{\dagger}_{\mathbf{k}s}\hat{\boldsymbol{\varepsilon}}^{*}_{s\mathbf{k}}e^{-i\mathbf{k}\cdot\mathbf{r}+i\omega_{\mathbf{k}}t}\right)\\ &= \mathbf{A}^{(+)}(\mathbf{r},t) + \mathbf{A}^{(-)}(\mathbf{r},t)\end{aligned} \tag{5.27}$$

where $\mathbf{A}^{(+)}(\mathbf{r},t)$, also called the positive-frequency part, contains only absorption operators. The negative-frequency part $\mathbf{A}^{(-)}(\mathbf{r},t)$ contains only creation operators. The same separation in two contributions can be done for $\mathbf{E}(\mathbf{r},t)$ and $\mathbf{B}(\mathbf{r},t)$, the *field-operators*

$$\mathbf{E}(\mathbf{r},t) = \sum_{\mathbf{k},s} i\left(\frac{4\pi\hbar\omega_{\mathbf{k}}}{2\mathscr{V}}\right)^{\frac{1}{2}}\left(a_{\mathbf{k}s}\hat{\boldsymbol{\varepsilon}}_{s\mathbf{k}}e^{i\mathbf{k}\cdot\mathbf{r}-i\omega_{\mathbf{k}}t} - a^{\dagger}_{\mathbf{k}s}\hat{\boldsymbol{\varepsilon}}^{*}_{s\mathbf{k}}e^{-i\mathbf{k}\cdot\mathbf{r}+i\omega_{\mathbf{k}}t}\right)$$

$$\mathbf{B}(\mathbf{r},t) = \sum_{\mathbf{k},s} i\left(\frac{4\pi\hbar\omega_{\mathbf{k}}}{2\mathscr{V}}\right)^{\frac{1}{2}}\left(a_{\mathbf{k}s}(\hat{\mathbf{k}}\times\hat{\boldsymbol{\varepsilon}}_{s\mathbf{k}})e^{i\mathbf{k}\cdot\mathbf{r}-i\omega_{\mathbf{k}}t} - a^{\dagger}_{\mathbf{k}s}(\hat{\mathbf{k}}\times\hat{\boldsymbol{\varepsilon}}^{*}_{s\mathbf{k}})e^{-i\mathbf{k}\cdot\mathbf{r}+i\omega_{\mathbf{k}}t}\right)$$

where $\hat{\mathbf{k}} = \mathbf{k}/k$ is the direction of the wavevector $\mathbf{k}$.

As $\mathbf{E}(\mathbf{r},t)$ is now an operator, to reproduce the corresponding classical field, an *observable*, one must take the quantum mean-value on a state of the extendend Fock space. Being $|\,\Phi\rangle$ one of these states, $\langle\Phi\mid\mathbf{E}(\mathbf{r},t)\mid\Phi\rangle$ is the quantum expectation value of the field on this state.

It is easy to observe that, if one calculates the *expectation value* of $\mathbf{E}(\mathbf{r},t)$ on a quantum state with *definite* number of photons, i.e.

$$\langle\{n_{\mathbf{k}s}\}\mid\mathbf{E}(\mathbf{r},t)\mid\{n_{\mathbf{k}s}\}\rangle$$

this is surprisingly always equal to zero. This is a consequence of the presence in the field operator $\mathbf{E}(\mathbf{r},t)$ of the absorption and the creation parts, that are both non-diagonal in the photon-number eigenstates. In order to have non-zero expectation value one must consider states that mix contiguous numbers of photons in the same modes and make a linear combination of them. In order to reproduce the behavior of

a classical wave with a given wavevector $\mathbf{k}$ and polarization $\boldsymbol{\varepsilon}_s$, one has to take the expectation value of $\mathbf{E}(\mathbf{r}, t)$ on a specially built quantum state state $\mid \Phi_c\rangle$, that is a well defined superposition of many (in principle *infinite*) states $\mid n_{\mathbf{k}s}\rangle$ with different numbers of photons in the same mode [2]. Such a quantum state, even in a single mode ($\mathbf{k}$,s), is not an eigenstate of the number operator, but has an *average* number of photons $\overline{n}_{\mathbf{k}s}$ with its quantum *incertitude* $\Delta n_{\mathbf{k}s}$. This is a *coherent state* $\mid \Phi_c\rangle$ and it also has an average value of the initial phase ϕ as an expectation value of a *phase operator*, with its own incertitude.

In the quantum description the *phase* and the *photon-number* in a given mode are complementary variables and they cannot be determined simultaneously on the same quantum state of the field exactly. The product of their incertidudes (or *variances*) has a lower bound due to an inequality of Heisenberg type, in analogy with other pairs of non-compatible dynamical variables or non-commuting operators. It is possible to built states with *phase* completely defined; they will have number or photons totally indetermined. On the other side, the full knowledge of the photon number in a state, destroys any information on the phase, but the energy is completely determined. Coherent states $\mid \Phi_c\rangle$ are the best description of a *classical* wave, with minimum product of incertitudes and in the limit $\overline{n}_{\mathbf{k}s} \to \infty$ the ratio between the amplitude and its uncertainity $\Delta\mathbf{E}$ will diverge, practically recovering the classical shape of a sinusoidal wave; thus the uncertainity effects can be negligible as required by the classical limit. See also the Appendix.

This brief comment has been reported in order to point out the difference between the quantum and the classical language to describe the e.m. field and the interaction with matter. We will discuss in the following sections of absorption and/or emission of photons. The quantum picture is drastically different from the semiclassical approach used in the previous chapter of this volume, where charges were moving in a classical oscillating field. But similar outcomes will be obtained.

5.3 Moving Charges in Interaction with the Electromagnetic Field

Atoms, molecules and solids are systems of N moving particles. Each particle has a mass m_i, a charge q_i, where $i = 1, 2, \ldots, N$. The dynamical variables are the coordinates $\mathbf{r}_i$, and their conjugate momenta $\mathbf{p}_i$. The quantum behavior of the system is described by the commutation relations

$$[r_{i\alpha,}\, p_{j\beta}] = i\hbar\delta_{ij}\delta_{\alpha\beta}, \tag{5.28}$$

the greek letters indicating here the cartesian components of $\mathbf{r}_i$ and $\mathbf{p}_j$ vectors.

In the Coulomb gauge, one has $\nabla \cdot \mathbf{A} = 0$ again, but the electric field in presence of charges contains a further irrotational part $\mathbf{E}_L$. $\mathbf{E} = \mathbf{E}_T + \mathbf{E}_L$, with $\mathbf{E}_L = -\nabla\varphi$. We must add to the total energy of the field the term

$$\frac{1}{8\pi}\int \mathbf{E}_L^2 d\mathbf{r} = \frac{1}{8\pi}\int (\nabla\varphi)^2\, d\mathbf{r} = \frac{1}{8\pi}\int \left(-\varphi\nabla^2\varphi\right) d\mathbf{r} = \frac{1}{2}\int \frac{\rho(\mathbf{r},t)\rho(\mathbf{r}',t)}{\mid \mathbf{r}-\mathbf{r}' \mid} d\mathbf{r}d\mathbf{r}'.$$

This describes the total energy of a charge density distribution and in our case it will be the istantaneous electrostatic interaction between point charges, if we consider the charge distribution as a sum of particle charge distributions and subtract the interaction of each particle with itself. We obtain the well known expression

$$\frac{1}{2}\sum_{i\neq j}\frac{q_i q_j}{\mid \mathbf{r}_i - \mathbf{r}_j \mid}.$$

In absence of the transverse radiation field, by adding to this term the kinetic energy

$$\sum_i \frac{\mathbf{p}_i^2}{2m_i}$$

we get the Hamiltoniam of the free system $\mathscr{H}_s^0$, in non-relativistic approximation. If the charges move in an electromagnetic field one has to make the substitution

$$\mathbf{p}_i \to \mathbf{p}_i - \frac{q_i}{c}\mathbf{A}(\mathbf{r}_i)$$

for each particle momentum. In this way the Hamiltonian of the system of charges becomes

$$\mathscr{H}_s = \sum_i \frac{\mathbf{1}}{2m_i}\left(\mathbf{p}_i - \frac{q_i}{c}\mathbf{A}(\mathbf{r}_i)\right)^2 + \frac{1}{2}\sum_{i\neq j}\frac{q_i q_j}{\mid \mathbf{r}_i - \mathbf{r}_j \mid}$$

The total Hamiltonian (*charged system + free field + interaction*) can be written as

$$\mathscr{H} = \mathscr{H}_s + \mathscr{H}_f^0 = \mathscr{H}_s^0 + \mathscr{H}_f^0 + \mathscr{H}_I = \mathscr{H}_0 + \mathscr{H}_I$$

where $\mathscr{H}_0 = \mathscr{H}_s^0 + \mathscr{H}_f^0$ is the *unperturbed Hamiltonian*

$$\mathscr{H}_0 = \sum_i \frac{\mathbf{p}_i^2}{2m_i} + \frac{1}{2}\sum_{i\neq j}\frac{q_i q_j}{\mid \mathbf{r}_i - \mathbf{r}_j \mid} + \sum_{\mathbf{k},s}\hbar\omega_{\mathbf{k}}\left(a_{\mathbf{k}s}^\dagger a_{\mathbf{k}s} + \frac{1}{2}\right) \tag{5.29}$$

and we can isolate the interaction term $\mathscr{H}_I$ from the unperturbed system (of the charges and the free transverse field)

$$\mathscr{H}_I = \sum_i \left\{ -\frac{q_i}{2m_i c}(\mathbf{p}_i\cdot\mathbf{A}(\mathbf{r}_i) + \mathbf{A}(\mathbf{r}_i)\cdot\mathbf{p}_i) + \frac{q_i^2}{2m_i c^2}\mathbf{A}^2(\mathbf{r}_i)\right\}$$

The Coulomb gauge condition on $\mathbf{A}$, $\nabla \cdot \mathbf{A} = 0$, allows to simplify the interaction term

$$\mathscr{H}_I = \sum_i \left(-\frac{q_i}{m_i c} \mathbf{A}(\mathbf{r}_i) \cdot \mathbf{p}_i + \frac{q_i^2}{2m_i c^2} \mathbf{A}^2(\mathbf{r}_i) \right) = \mathscr{H}_I^{(1)} + \mathscr{H}_I^{(2)} \tag{5.30}$$

which contains a linear and a quadratic term in the radiation field operator. The unperturbed Hamiltonian describes both the system of interacting charges and the free radiation field. Its eigenstates are constructed, neglecting $\mathscr{H}_I$, by the direct product of the Hilbert spaces of eigenstates of $\mathscr{H}_s^0$ and $\mathscr{H}_f^0$.

If we consider an atom, a molecule or a solid, we can separate the coordinates of the nuclei $\mathbf{R}_i$ from the electron variables $\mathbf{r}_i$ and $\mathbf{p}_i$ and treat the former as classical objects. In this way we consider only the dynamics of the electrons which are responsible of the large part of properties of the matter, neglecting the motion of the atomic nuclei and the interaction of the field with them. One has, if $q_i = -e$ and $m_i = m$ for electrons and $q_I = Z_I e$ and $m_I = M_I$ for the nuclei

$$\mathscr{H}_s^0 = \sum_i \frac{\mathbf{p}_i^2}{2m_i} - \sum_I \frac{Z_I e^2}{\mid \mathbf{R}_I - \mathbf{r}_i \mid} + \frac{1}{2} \sum_{i \neq j} \frac{e^2}{\mid \mathbf{r}_i - \mathbf{r}_j \mid} + \frac{1}{2} \sum_{I \neq J} \frac{e^2}{\mid \mathbf{R}_i - \mathbf{R}_j \mid} \tag{5.31}$$

Se the Appendix for a more complete description of the ingredients which also accounts for the spin of the electrons and relativistic corrections [3].

5.4 The Expansion of the Amplitude of Transition

Let us indicate the eigenstates of non-interacting Hamiltonian by

$$\mid \Psi \rangle \; = \mid \psi_\alpha \rangle \otimes \mid \{n_{\mathbf{k}s}\} \rangle \tag{5.32}$$

where $\mid \{n_{\mathbf{k}s}\} \rangle$ is a state for the radiation field with fixed photon numbers in each mode and $\mid \psi_\alpha \rangle$ is a state of the system of N charges with the appropriate set of quantum numbers α and energy E_α. By projecting $\mid \psi_\alpha \rangle$ into the $3N$-coordinate cartesian space one obtains a more familiar object, the $N-$particle wavefunction

$$\psi_\alpha(\mathbf{r}_1, \mathbf{r}_2, \ldots, \mathbf{r}_N) = \langle \mathbf{r}_1, \mathbf{r}_2, \ldots, \mathbf{r}_N \mid \psi_\alpha \rangle.$$

$\mid \Psi \rangle$ is an eigenstate for the Hamiltonianian $\mathscr{H}_0 = \mathscr{H}_s^0 + \mathscr{H}_f$ with energy $E_\alpha + E_{\{n_{\mathbf{k}s}\}}$. In the case where only the electrons are described in a quantum picture, $\mathbf{r}_1, \mathbf{r}_2, \ldots, \mathbf{r}_N$ are the electron coordinates and the state is depending also on ion positions $\{\mathbf{R}_i\}$ treated as classical parameters; if we interchange the coordinates of two electrons, the wavefunction and the state change sign, because the electrons are fermions. We are interested to know the evolution of a state due to the interaction

(5.30) between matter and the radiation field. We imagine that at time t_i the interaction is not yet turned on, while at t_f it has been switched off. We multiply the expression (5.30), the interaction Hamiltonian, by a factor $\lambda(t)$ that is equal to one for a long time interval T when the interaction works, but goes smoothly to zero out of this interval at t_i and t_f. The interaction is not present and at every time, at $t \leq t_i$ and $t \geq t_f$ and we imagine to describe the system in term of the non-interacting states (5.32) before and after the interaction. If $\mid \Psi_a\rangle$ and $\mid \Psi_b\rangle$ are two states of the set (5.32), the quantity

$$\langle \Psi_b \mid U(t_f, t_i) \mid \Psi_a \rangle \tag{5.33}$$

represents the *amplitude of transition* between $\mid \Psi_a\rangle$ and $\mid \Psi_b\rangle$, i.e. a complex value whose square-modulus indicates the probality that the non-interacting system in the state $\mid \Psi_a\rangle$ at the time t_i will be found in the state $\mid \Psi_b\rangle$ at the time t_f as a consequence of the interaction. If we adopt the Heisenberg Picture for the non interacting system, we will work in the so-called Interaction Picture

$$\mid \Psi_a^I\rangle \; = e^{i\mathscr{H}_0 t/\hbar} \mid \Psi_a\rangle$$

When the interaction is switched off, there is no time evolution of the state. The amplitude of transition can be written as

$$S_{ba} = \langle \Psi_b^I \mid \tilde{U}(t_f, t_i) \mid \Psi_a^I \rangle \tag{5.34}$$

where

$$\tilde{U}(t_f, t_i) = e^{i\mathscr{H}_0 t_f/\hbar} U(t_f, t_i) e^{-i\mathscr{H}_0 t_i/\hbar} \tag{5.35}$$

is the *evolution operator* acting on a state in the interaction representation. The link between this operator and the interaction Hamiltonian (5.30) is given by the expansion

$$\tilde{U}(t_f, t_i) = 1 + \sum_{n=1}^{\infty} \tilde{U}^{(n)}(t_f, t_i)$$

where at each order n

$$\tilde{U}^{(n)}(t_f, t_i) = \left(\frac{1}{i\hbar}\right)^n \int\limits_{t_f \geq \tau_n \geq \tau_{n-1}} d\tau_n \ldots \int\limits_{\tau_3 \geq \tau_2 \geq \tau_1} d\tau_2 \int\limits_{\tau_2 \geq \tau_1 \geq t_i} d\tau_1 \widetilde{\mathscr{H}_I}(\tau_n) \ldots \widetilde{\mathscr{H}_I}(\tau_2) \widetilde{\mathscr{H}_I}(\tau_1) \tag{5.36}$$

This expansion at different order n is the basis of the diagrammatic picture (*Feynman diagrams*) of the processes of interaction. In expression (5.36) a time ordered product of $\widetilde{\mathscr{H}_I}(t)$ is present, where

$$\widetilde{\mathscr{H}_I}(t) = e^{i\mathscr{H}_0 t/\hbar}\mathscr{H}_I e^{-i\mathscr{H}_0 t/\hbar}. \tag{5.37}$$

If we need to introduce relativistic corrections and spin we must include in $\mathscr{H}_0$ the terms (5.59) and in $\mathscr{H}_I$ the terms (5.60) as described in the Appendix.

5.5 Elementary Processes

If we consider the first order processes in (5.36), including only the linear term $\mathscr{H}_I^{(1)}$ of (5.30), we can obtain non-zero matrix elements (5.33) between these initial and final states

$$\mid \Psi_a\rangle = \mid \psi_A,\ n_{\mathbf{k}s}\rangle \quad \mid \Psi_b\rangle = \mid \psi_B,\ n_{\mathbf{k}s} \mp 1\rangle.$$

The numbers of photons in the final and initial states have a difference ∓ 1, in the mode $\mathbf{k}s$, because the linear term in (5.30) contains a linear combination of $a_{\mathbf{k}s}$ and $a^\dagger_{\mathbf{k}s}$ and the number of photons must be the same (even zero) for all other modes. In the first case (-1) one has an *absorption* of a photon and in the second case $(+1)$ the *emission* of a photon.

If $\mid \psi_A\rangle$ and $\mid \psi_B\rangle$ are the electron wavefunctions of an atom or a molecule with energy eigenvalues E_A and E_B, in the case of absorption we obtain

$$\begin{aligned} S^{(1a)}_{ab} &= \frac{1}{i\hbar}\frac{e}{m}\left(\frac{4\pi\hbar}{2\mathscr{V}\omega_{\mathbf{k}}}\right)^{\frac{1}{2}} \langle\, n_{\mathbf{k}s} - 1 \mid a_{\mathbf{k}s} \mid n_{\mathbf{k}s}\rangle\langle\psi_B \mid \sum_i e^{i\mathbf{k}\cdot\mathbf{r}_i}\ \hat{\boldsymbol{\varepsilon}}_{s\mathbf{k}}\cdot\mathbf{p}_i \mid \psi_A\rangle \\ &\times \int_{t_f \geq \tau \geq \tau_i} d\tau \exp(+\frac{i}{\hbar}(E_B - E_A - \hbar\omega_{\mathbf{k}})\tau) \\ &= -2\pi i \frac{e}{m}\left(\frac{4\pi\hbar}{2\mathscr{V}\omega_{\mathbf{k}}}\right)^{\frac{1}{2}} (n_{\mathbf{k}s})^{\frac{1}{2}}\ \hat{\boldsymbol{\varepsilon}}_{s\mathbf{k}}\cdot\langle\psi_B \mid \sum_i e^{i\mathbf{k}\cdot\mathbf{r}_i}\ \mathbf{p}_i \mid \psi_A\rangle\delta(E_B - E_A - \hbar\omega_{\mathbf{k}}) \end{aligned} \tag{5.38}$$

where $-e$ and m are the charge and the mass of the electron respectively.

The time integration gives the *conservation of energy*: the charged system is left at an energy E_B equal to E_A plus the energy $\hbar\omega_{\mathbf{k}}$ of the absorbed photon. The amplitude is proportional to the square root of the number of photons present in the mode $\mathbf{k}s$. The matrix element involves the polarization of the mode and the quantum states of the system. If $\mathbf{k}$ can be considered small, i.e. the *wavelength* $\lambda = 2\pi/\mid \mathbf{k} \mid$ is great respect to the atomic dimensions, so that we can write the rapidly convergent series

$$e^{i\mathbf{k}\cdot\mathbf{r}_i} = 1 + i\mathbf{k}\cdot\mathbf{r}_i + \ldots \tag{5.39}$$

We can notice that, also for photons with energy $\simeq$1000 eV, the wavelength is large ($\simeq$12 Å) with respect to the spatial extension of the wavefunction of an electron in a core state of an atom. It is possible to retain *only the first term* of the expansion (5.39), thus the matrix element can be evaluated in the *dipole approximation*.

5.6 The Matrix Element

The dipole matrix element appears in the first-order process and also in the higher order terms. It is

$$\langle \psi_B \mid \mathbf{p}_i \mid \psi_A \rangle \tag{5.40}$$

It can be written in an other form if we consider the identity

$$[\mathbf{r}_i, H_S^0] = \frac{i\hbar}{m}\mathbf{p}_i$$

We can write

$$\begin{aligned}\langle \psi_B \mid \mathbf{p}_i \mid \psi_A \rangle &= \frac{m}{i\hbar}\langle \psi_B \mid \mathbf{r}_i H_S^0 - H_S^0 \mathbf{r}_i \mid \psi_A \rangle \\ &= im\frac{E_B - E_A}{\hbar}\langle \psi_B \mid \mathbf{r}_i \mid \psi_A \rangle = im\omega_{\mathbf{k}}\langle \psi_B \mid \mathbf{r}_i \mid \psi_A \rangle \end{aligned} \tag{5.41}$$

The last form of the matrix element is called *dipole-length* form of the transition $A \to B$, while the original expression (5.41) has the name of *dipole-velocity*.

It is possible to obtain also the *emission transition amplitude* that is associated to the creation part of the field operator: $\mathbf{A}^{(-)}(\mathbf{r}, t)$. The expression is similar to (5.38), but for the emission process one has

$$\begin{aligned} S_{ab}^{(1b)} &= -2\pi i \frac{e}{m}\left(\frac{4\pi\hbar}{2\mathscr{V}\omega_{\mathbf{k}}}\right)^{\frac{1}{2}} (n_{\mathbf{k}s}+1)^{\frac{1}{2}} \\ &\hat{\boldsymbol{\varepsilon}}_{s\mathbf{k}}^* \cdot \langle \psi_B \mid \sum_i e^{-i\mathbf{k}\cdot\mathbf{r}_i}\, \mathbf{p}_i \mid \psi_A \rangle \delta(E_B - E_A + \hbar\omega_{\mathbf{k}}) \end{aligned} \tag{5.42}$$

where it is clear that the emission can take place only if the atomic system is initially in an *excited state* $(E_A \rangle E_B)$. The probabability of emission of a photon increases with the number of photons present in the mode. This process is important in quantum optical devices (*stimulated emission*).

The transition amplitudes of the two processes described in (5.38) and in (5.42) are represented by the first two Feynman diagrams in Fig. 5.1, where only the linear term is included in the interaction (5.30). The incoming arrows indicate the system in state $\mid \psi_A \rangle$ and the outgoing arrows indicate the system in state $\mid \psi_B \rangle$, while the wiggling arrows represent an adsorbed or emitted photon. Feynman diagrams can be easily translated in formulas at all orders of the interaction. The lowest order is the first, with the adsorption or the emission of a single photon, as effect of the interaction term $\mathscr{H}_I^{(1)}$.

We must observe now that the two diagrams representing absorption or emission amplitudes of a photon are exactly zero for a system composed of a single free charge, i.e. a moving electron. A free electron cannot absorb or emit a photon spontaneously

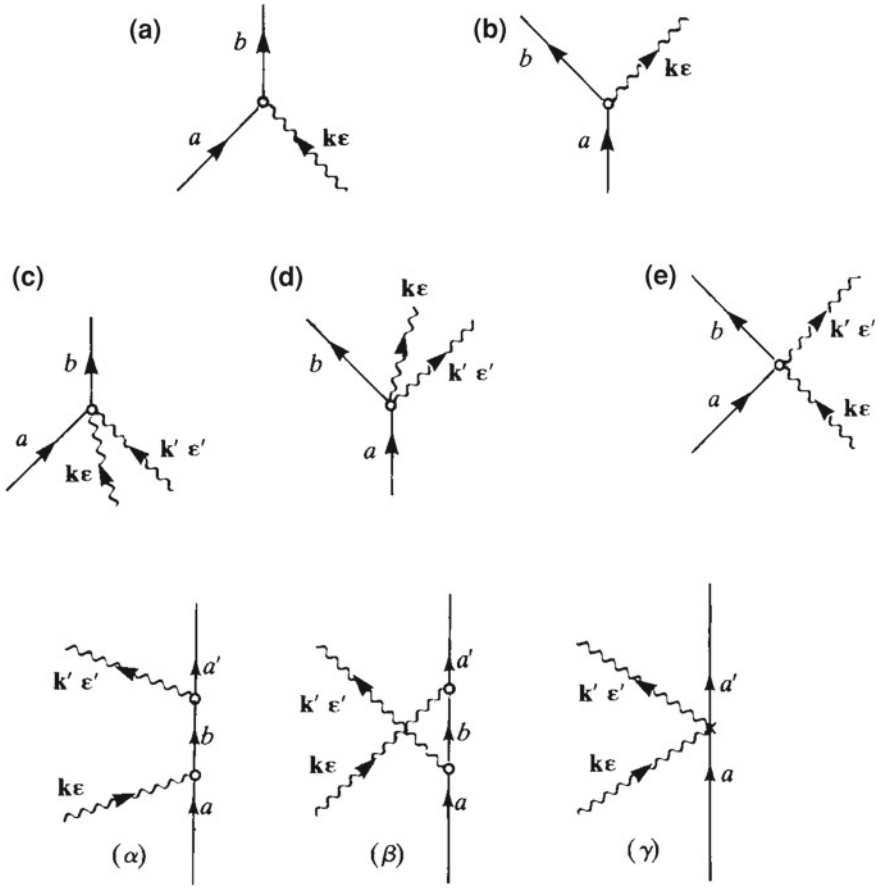


Fig. 5.1 Diagrams of the lowest order process in the interaction $\mathscr{H}_I = \mathscr{H}_I^{(1)} + \mathscr{H}_I^{(2)}$. *1st row* photon absorption, photon emission; *2nd row* absorption of two photons, emission of two photons, diffusion of a photon; *3rd row* contributions at second order of the term lineal in $\mathscr{H}_I^{(1)}$. The diagrams are taken from [4] that gives a wide theoretical overview of these processes

in a first-oder process, but the processes can only take place in a composite system with internal interactions that must be present in (5.29). It is easy to prove this statement directly. This is the same to state that for a single particle the absorption or emission of a photon cannot conserve the total linear momentum and the total energy simultaneously, the equations

$$\frac{(\mathbf{p}')^2}{2m} = \frac{(\mathbf{p})^2}{2m} \pm \hbar\omega_{\mathbf{k}} \qquad \mathbf{p}' = \mathbf{p} \pm \hbar\mathbf{k} \qquad \omega_{\mathbf{k}} = c\,|\mathbf{k}|$$

have no solution. Different is the case when the particle is moving in an external potential $\varphi(\mathbf{r})$, like an electron in a solid or in an atom or a molecule. In this case

the particle state has a continuum distribution of linear momenta and the process can take place. In this case, the absorption or emission of a photon can take place, but the process is first-order in the radiation field and all-orders in the system potential, wich must be considered as an additional interaction acting on a *free* electron through a semiclassical field.

The three diagrams in the second row of Fig. 5.1 are representing the first order contribution coming from the quadratic term $\mathscr{H}_I^{(2)}$ containing $\mathbf{A}^2$ in (5.30). Due to the presence of products $a_{\mathbf{k}'s'}a_{\mathbf{k}s}$, $a^\dagger_{\mathbf{k}'s'}a^\dagger_{\mathbf{k}s}$, and $a^\dagger_{\mathbf{k}'s'}a_{\mathbf{k}s}$, they describe absorption of two photons, emission of two photon and absorption and emission of photons. This last term will be discussed later. As an example two second order terms arising from the linear part in $\mathbf{A}$ are also indicated in the figure: the two vertices correspond to the interactions and the internal line represents the whole set of intermediate states of the unperturbed system that are described by the *propagator* that connects the two interaction *vertices*.

5.7 Beyond the Dipole Approximation

Including the second term in the expansion (5.39) of the plane wave appearing in the matrix element, we obtain, beyond the dipole approximation,

$$\begin{aligned}
&\boldsymbol{\varepsilon}_{s\mathbf{k}} \cdot \langle \psi_B \mid \sum_i (-i\mathbf{k}\cdot\mathbf{r}_i)\,\mathbf{p}_i \mid \psi_A\rangle \\
&\quad = -i \sum_{\alpha,\beta} \boldsymbol{\varepsilon}_{s\mathbf{k}\alpha} k_\beta \langle \psi_B \mid \sum_i r_{i\beta}\, p_{i\alpha} \mid \psi_A\rangle \\
&\quad = -\frac{i}{2} \sum_{\alpha,\beta} \boldsymbol{\varepsilon}_{s\mathbf{k}\alpha} k_\beta \langle \psi_B \mid \sum_i \left(r_{i\beta}\, p_{i\alpha} - r_{i\alpha}\, p_{i\beta}\right) \mid \psi_A\rangle \\
&\qquad - \frac{i}{2} \sum_{\alpha,\beta} \boldsymbol{\varepsilon}_{s\mathbf{k}\alpha} k_\beta \langle \psi_B \mid \sum_i \left(r_{i\beta}\, p_{i\alpha} + r_{i\alpha}\, p_{i\beta}\right) \mid \psi_A\rangle
\end{aligned} \tag{5.43}$$

where the first contribution contains the orbital angular momentum components (*orbital magnetic dipole contribution*), while the second is the *quadrupolar electric contribution* to the matrix element.

These term are relevant in the transition where the dipole matrix element is zero, due to *selection rules* that are based on symmetry properties of the system. If the electric dipole moment (5.41) is nonzero their contribution can be negligible.

For ions and atoms the many-electron states $\mid \psi_A\rangle$ are identified by angular-momentum quantum numers (J, M_j, L, S in $SO(3)$ or $SU(2)$ symmetry). The atomic matrix elements present in the multipole expansion have the appropriate *selection rules*. Similar features appear also when spherical or cylindrical symmetries are broken, in molecules and solids. *Finite-group representation* labels can

identify states in crystals and provide the corresponding selection rules for matrix elements. These effects can be included also in an atomic approach by the use of the *crystal field corrections*. It is possible to rewrite the theory, by a general *multipole expansion* of the matrix element. It can be obtained using *vector spherical harmonics* to expand

$$\boldsymbol{\varepsilon}_{s\mathbf{k}} \exp(-i\mathbf{k} \cdot \mathbf{r}_i)$$

at all orders and by using the irreducible tensor methods to evaluate the matrix elements [5].

5.8 Absorption

We consider the adsorption process with only one photon, $n_{\mathbf{k}s} = 1$, in the initial state. The *matter* initial and final states are many-electron states in the potential of the atomic nucleus (or of the nuclei in the case of a molecule). We are interested in the study of the transitions, generally from the ground state, to various manyfolds of excited states that can be reached by varying the energy and the polarization of the incoming photon. The absorption spectrum obtained as a function of the photon energy is an instrument to investigate the atomic or molecular structure of the material.

We can obtain the cross section of the absorption process in different ranges of the energies of the photon. If we consider only dipole terms, we can obtain the total cross section from the square modulus of the transition amplitude per unit time, divided by the incident flux (for one photon is $(c/\mathcal{V})$) and summing over the final states. We get

$$\sigma(\omega) = 4\pi^2 \alpha \hbar\omega \sum_B |\, \boldsymbol{\varepsilon}_s \cdot \langle \psi_B \,|\, \sum_i \mathbf{r}_i \,|\, \psi_A \rangle \,|^2 \, \delta(E_B - E_A - \hbar\omega). \qquad (5.44)$$

As a function of ω the absorption spectrum presents a number of thresholds, peaks and structures, if the initial and final states have non-zero transition matrix element. An example is the calculated spectrum of absorption for the ion Ni^{2+} for the transition between the ground state of the $3d^8$ configuration and the states of the multiplet of the $2p^5 3d^9$, where an electron of the $2p$ shell is promoted the $3d$ states, a configuration which is reachable in the dipole approximation of the matrix element. For this magnetic ion (where the presence of a magnetic field brakes the degeneracy of a multilplet with a given vector of the total angular momentum **J**) only some transitions are allowed, depending on the polarization of the photon. In Fig. 5.2 the absorption spectra calculated for this transition are presented, in the region between 850 and 880 eV of the photon energy, with different polarizations of the light incoming along the direction of the magnetization or orthogonally to it. We consider two approximations: (a) a single-atom in spherical symmetry broken into a cylindrical symmetry due to magnetization and (b) the same atom with the addition of a crystal field of cubic symmetry and then with magnetization along an axis of the cube. One can

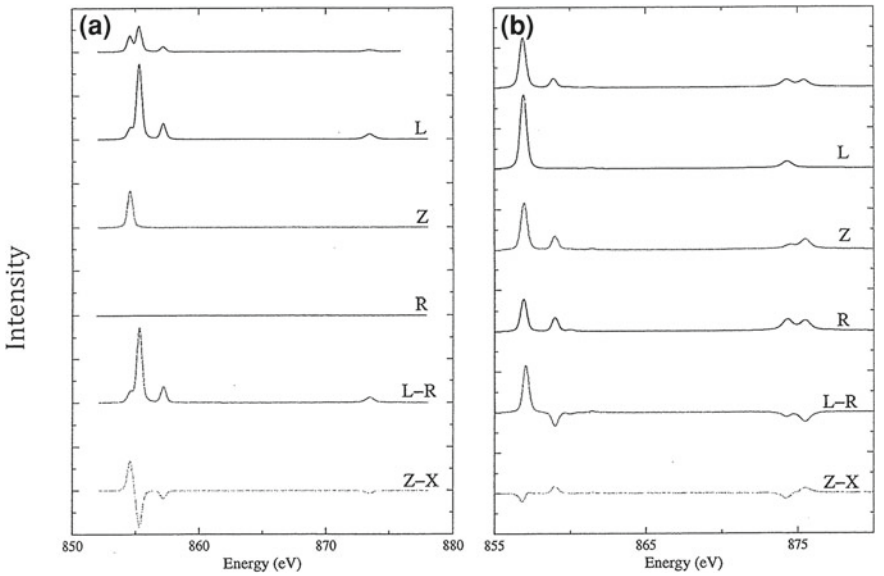


Fig. 5.2 Absorption spectra for the magnetic ion Ni^{2+}, calculated for the transition $(3d^8) \rightarrow (2p^5 3d^9)$ with different polarizations of the light. The spectrum of the *first line* is the average over polarization directions, *L* and *R* indicate respectively *left* and *right* circular polarization, *Z* and *X* indicate linear polarization along the corrisponding axis, being $\hat{z}$ the magnetic axis direction. **a** single ion in cylindrical symmetry; **b** the same ion including crystal-field corrections to account for the symmetry inside the solid. From [7]

see the variations of the spectra calculated for the linear or circular polarizations of the light. The differences (circular and linear dichroism) are shown in the lower two lines of the figure.

This case is a prototype for magnetic systems that can be described with the methods of theoretical atomic physics based on many-electron states [6], with the use of Slater determinants, angular momentum coupling techniques and crystal-field corrections. We see from Fig. 5.2 that the results of theoretical calculations are very sensitive to the ingredients, expecially in the dichroic spectra. If necessary one has also to include configuration interactions [7–9]. The dichroism in absorption spectra associated to the $2p \rightarrow 3d$ transition is used to study the properties of Ni^{2+} and Fe^{3+} ions in oxides and other compounds. The comparison between experimental spectra and theoretical prediction can enlight the magnetic order and the properties of such systems [10, 11].

The absoption spectrum for the excitations from a core level (in this case from $2p$ or more precisely from $2p_{\frac{3}{2}}$ and $2p_{\frac{1}{2}}$ to $3d$) extends well above these L_3 and L_2 thresholds. We can study all the transitions to configurations with an electron in highest energy states and in the continuum. The comparison of theory and experimental data in this case indicates that new structures can be observed above the edge. If we are not dealing with magnetic properties the absorption spectrum at higher energies

must include other electron states and can be treated in a one-electron approach and a simpler model is sufficient.

By choosing a one-electron picture and considering initial and final states as single-electron states described by single-particle wavefunctions, we write respectively $\varphi_c(\mathbf{r})$, as the core localized initial state, and $\psi_k(\mathbf{r})$, as an extended final state in the conduction band. The remaining $N-1$ electrons are not contributing to the process and can be simply neglected; they are considered as passive spectators. Cutting the sum on i, the index running on electron coordinates, a single electron moves in an effective potential due to the nuclei and the other electrons. This one-electron version is useful in the case where we have to describe molecular electronic structure or solid electron bands, where the multiplet splitting or other many-electron effects can be neglected. We can rewrite the cross-section (5.44) as

$$\sigma(\omega) = 4\pi^2 \alpha \hbar\omega \sum_k |\, \boldsymbol{\varepsilon}_s \cdot \langle \psi_k(\mathbf{r}) \mid \mathbf{r} \mid \varphi_c(\mathbf{r}) \rangle \,|^2 \, \delta(\boldsymbol{\varepsilon}_k - \boldsymbol{\varepsilon}_c - \hbar\omega) \tag{5.45}$$

$\varphi_c(\mathbf{r})$ is the electron wave function of a core state, of negative energy $\boldsymbol{\varepsilon}_c$, and $\psi_k(\mathbf{r})$ is the set of the unoccupied final states of energies $\boldsymbol{\varepsilon}_k$ above the Fermi energy of the system, where the excited electron can be promoted. The distribution of these states and the values of the square moduli of the matrix elements determine the shape of the spectrum.

$\psi_k(\mathbf{r})$ can be obtained in different ways. By a band structure calculation for the conduction band of the system, and then evaluating the matrix element as a function of the energy of the final states together with their density of state states to build up the cross section as a function of ω. Alternatively $\psi_k(\mathbf{r})$ is evaluated, through a multiple scattering calculation, at energy $\boldsymbol{\varepsilon}_k$ as an outcoming spherical wave centered on the atomic site of the excitation and scattereded by the neighbouring atoms. Single or multiple scattering events can be included in the description of the final state.

The absorption cross section (5.45) evaluated in one-electron approximation is the starting point to interpret the measurements of the absorption profiles above the treshold in the techniques named XANES (X-ray Absorption Extended Fine Structures) [12, 13] and NEXAFS(Near-Edge X-ray Absorption Fine Structures) [14], where a detailed description of electron wavefunctions is required to obtain structural information from absorption data. These are very useful structural probes for materials that take advantage of the tunability and the intensity of the synchrotron radiation sources.

5.9 Photoemission

The absorption of a photon can drive the system in an highly excited state in the continuum giving rise to the emission of an electron. The understanding of photoelectric effect was one of the basic step in the birth of quantum physics, more than a century ago, but only in the four last decades it has been used as a powerful method to study the electronic structure of atoms, molecules, solids and surfaces, based on

high-resolution measurements of the energy and of the direction of potoemitted electrons. This delay in the use of photoemission in condensed matter studies is linked to the need of technical developments in ultra-high vacuum systems and of the recent advancements of high resolution detectors and analyzers, but the most important advancements have been originated by the availability of the new synchrotron ligth sources. In the meanwhile accurate methods of computation of the electronic structures in solid and surfaces have been developed to interpret the experiments.

In the photoemission process at first-order, a hole is created in a valence or in a core states of the system and an electron is promoted to the continuum above the vacuum level. The excited electron can come out from the sample to be detected. Its kinetic energy, as well as direction of motion and also spin polarization, can be measured. A photoemission spectrum at a given energy of the incoming photon is the distribution of the number of electrons detected as a function of these variables.

The picture in one-electron scheme is simple: if $\boldsymbol{\varepsilon}_f$ is the final energy of the emitted electron and $\boldsymbol{\varepsilon}_i$ is the energy of the hole (both expressed with respect to the Fermi level E_F that we take as the zero of our energy scale, thus $\boldsymbol{\varepsilon}_f \rangle 0$ and $\boldsymbol{\varepsilon}_i \langle 0$), then

$$\hbar\omega = \boldsymbol{\varepsilon}_f - \boldsymbol{\varepsilon}_i .$$

The electron can exit, if no additional (inelastic) process is present, with a kinetic energy

$$\frac{\hbar^2 k^2}{2m} = \boldsymbol{\varepsilon}_f - \Phi = \hbar\omega - \mid \boldsymbol{\varepsilon}_i \mid -\Phi$$

where the work function Φ is the difference between the energy of the vacuum level and the Fermi energy, i.e. the barrier that an electron at the Fermi level has to overcome to move from the system into the vacuum. The measure of the kinetic energy allows to determine the binding energy $\boldsymbol{\varepsilon}_i$. In a photoemission measurement, with the energy of photon fixed, one can measure the number of photoelectrons as a function of their kinetic energy and plot the energy distribution curve as a function of $\mid \boldsymbol{\varepsilon}_i \mid$. This Energy Distribution Curve (EDC) is intuitively interpreted as the distribution of the occupied electronic state before the photoexcitation process, but its shape includes the effects of the matrix element of the photo-excitation process, many-body effects (correlation) and possible inelastic scattering processes of the photoelectron during its travel in the material and across the surface of the sample to the detector. In Fig. 5.3 one has a schematic picture of the photoemission in a solid, limited by a surface, with the EDC of valence and core binding energy. Part of the electrons are scattered inelastically by the other electrons in the solid, to give rise to the so-called *secondary electron distribution*, with a peak at low energies. These electrons have lost information concerning the energies of the primary process, but are moving in the conduction band continuum of states above the vacuum level, and carry information on the states of the conduction band above the vacuum level and on the overall efficiency of the process.

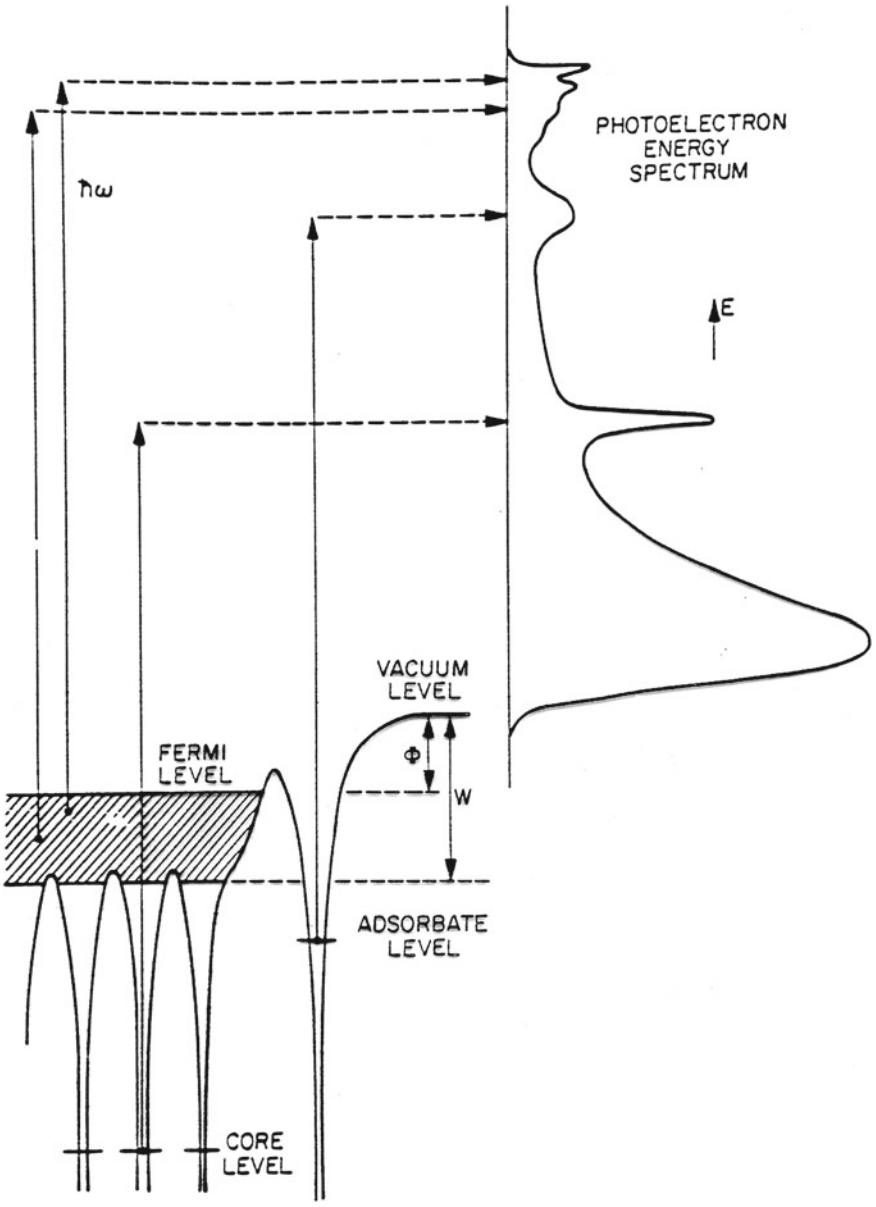


Fig. 5.3 Schematic picture of the photoemission processes at a given frequency of the light with excitation of electrons: the *upper part* of the Energy Distribution Curve (EDC) corresponds to the valence band while the other peaks arise from excitations from core levels of the atoms of the sample or of the atoms adsorbed on the surface. Secondary electrons background is also shown with the typical shape. From [15]

It is clear that in solids photoemission is a technique that is particularly sensitive to a region of the sample involving few atomic layers under the surface. From this very thin region the electrons can escape without inelastic processes and the escape depth, which measures the average path that electrons can travel without loosing energy, will be a function of the material and the kinetic energy itself of the photoexcited electron. By changing the energy of the photon we can choose different relative weights of the contributions of the bulk and of the surface to the photoemission spectrum.

There are different ways to use photoelectron spectroscopy to study the electronic structure of solids: (i) tuning the frequency of the radiation, in order to be more or less sensitive to the surface region; (ii) using the polarization of the light, to explore the symmetry of the electron initial states; (iii) measuring the direction of the outcoming electron, getting information on the initial state wave vector (AREPS = Angular-Resolved Electron Photoemission Spectroscopy); (iv) moving together the energy measured by the detector and the frequency of the light, to obtain Constant Initial State (CIS) spectroscopy, in order to check the properties of the wavefunction of the initial state; (v) selecting the final state to get a Constant Final State (CFS) spectroscopy. All these modes, that can be implemented inside the modern instrumentation by internal software, are used and offer an almost direct interpretation in terms of one-electron states, giving the images of the density of states in case of angle-integretated spectra, or even of the same band dispersion in 2 or 3 dimensions in AREPS.

This picture, based on one-electron approximation, is not satisfactory in a system where correlation among the electrons strongly affects the electron dynamics and modifies or mask the single particle (or *quasi-particle*) nature of the electron excitation. A many-electron point of view would picture the process in a different way: E_i^N is the energy of the N electron initial state, while the final state energy, of the system composed of with $N-1$ electron plus the photoelectron is

$$E_f^{N-1} + \frac{\hbar^2 k^2}{2m}$$

Thus

$$\frac{\hbar^2 k^2}{2m} = \hbar\omega - (E_f^{N-1} - E_i^N)$$

The quantity $(E_f^{N-1} - E_i^N) > 0$ cannot be interpreted as a one-electron energy, but is not too different from an *orbital energy* $\boldsymbol{\varepsilon}_i$ changed in sign, that can be calculated. The value of the orbital energy (now referred to the vacuum level) must be corrected to include the relaxation effect, the change in the particle density of the system induced the presence of the hole and further corrections, that account for electronic correlation. The *effective* binding energy becomes

$$(E_f^{N-1} - E_i^N) = -\boldsymbol{\varepsilon}_i - \triangle E_{rel} - \triangle E_{corr} \tag{5.46}$$

If correlation and relaxation corrections are small, one says that the *K*oopmans theorem is valid, and the ionization energy is almost equal to the energy of the

orbital of the electron removed. In the study of the core-level photoemission in solids one can also find different values of the correlation and relaxation corrections at the surface respect to the bulk.

One has to consider that in the excitation of a core electron more than one energy level E_f^{N-1} can be reached (not only the lowest energy state but also the excited states) with different probability.

From the one-electron picture we can expect a single sharp peak in the core level EDC with kinetic energy slightly larger than expected due to the relaxation of the $N-1$ electrons around the hole. This is true if we are in the *adiabatic approximation*: in this condition, the process of photoemission is sufficiently slow so that the outcoming electron can *see* the relaxation of the ion in the presence of the hole.

On the contrary, if the process is fast, we are in the *sudden approximation* conditions and the EDC contain a number of strucures extending to higher binding energies (lower kinetic energy of the photoelectron). The ion left behind with the hole can reach various excited states and they contribute to the spectrum with different intensities, due to the different transition probabilities.

This is the case of photoemission from inner levels of atoms. In the simple case of $Li(1s^2 2s;^2 S)$ the photoemission from $1s$ atomic level can have as final states $Li^+(1s^1 2s;^1 S)$ plus an outcoming electron of energy $\boldsymbol{\varepsilon}_1$ or the final state $Li^+(1s^1 2s;^3 S)$ plus an electron of energy $\boldsymbol{\varepsilon}_3$. The singlet and triplet states have different energies and different will be the kinetic energies of the outcoming electrons.

This effect can be particularly strong in the photoemission from s levels if there is a d incomplete shell. We consider the EDC spectrum of the $3s$ core level of Mn^{2+}, observed in the ionic crystal MnF_2, where 5 electrons ar present in the $3d$ orbitals of Mn [16]. The spectrum is The initial state $3s^2 3d^5$ is a level ${}^6S$ with ($L=0$ and $S=5/2$). With the emission of an electron from the core shell $3s$, one can obtain, through the coupling of the remaining $3s$ electron with the $3d^5$ electrons, a level ${}^7S$ with ($L=0$ and $S=3$) or a level ${}^5S$ with ($L=0$ and $S=2$). The two states have different energies and would originate two lines in the EDC with intensity ratio that should be equal to the degeneracy ratio $7/5$ and an energy separation extimated in the Hartree-Fock approximation, without mixing other atomic configurations, of about 15 eV. This approximation overestimate the splitting. As indicated by Fig. 5.4 there are two sharp peaks with a lower separation of about 7 eV in the experiment and the intensity ratio is higher than the expected value. This is due to correlation effects that mix the ${}^5S$ state with other states of the same symmetry, arising from more excited configurations. The configuration interaction redistributes the intensity of the ${}^5S$ peak over other structures as seen in the figure and shifts the peak reducing the splitting between the two main structures of about a factor two. This is an extreme case, with many satellites and an extended energy range in the multiplet structure for the photoemission from a $3s$ level. In ionic compounds of other transition metals the $3d$ electrons with filling different with respect to the half-filling of the shell, other multiplet structures can be present with lower peak distances. In general the peak separations are lower than the ones evaluated in Hatree-Fock approximation. A full calculation including correlation in a more stisfactory way gets a screening effect that

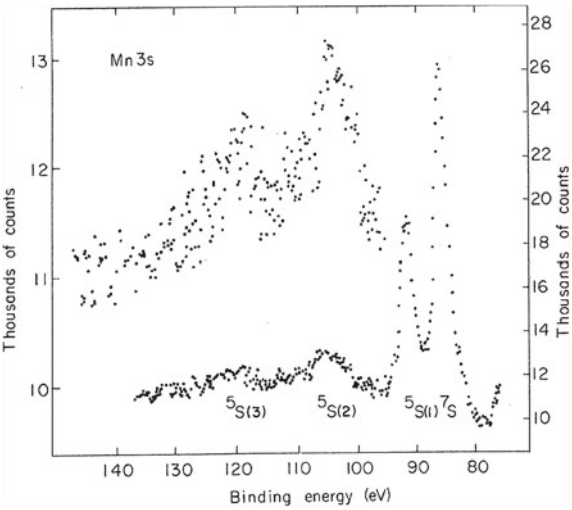


Fig. 5.4 Photoemission spectrum (EDC) with satellite structures from the core level $3s$ of Mn^{2+} in MnF_2. From [16]

reduces the splitting and smooths the structures at higher binding energies. Similar effects can be observed not only in ionic compound but in other compounds less ionic and also in the elemental crystal. The main peak position changes and also the shape and the intensity of the satellites. The d-states are less localized or are delocalized in a wider band and the many-body corrections are still present but are less relevant.

If we are interested in the study of the valence electrons, instead of the core states, the one-electron approach is at first level sufficient. This is the case of Fig. 5.5, where the occupied band states of the metal can be studied by angle-resolved photoemission[17]. The photoemission process is described as a transition between occupied and empty states at a given **k** point of the Brillouin zone of the solid. One has to vary $\hbar\omega$ and analyse the direction and energy of the outcoming electron to identify the transitions and then the final and initial energy. A *band mapping* that can be very accurate allows to have a direct comparison with theoretical calculations of band structures.

In a nearly-free electron metal the process takes place between states that can be very similar to free electron states. We expect that the intensity of the photoemission is low for such a metal. The effect would be absent if the particles were really free. It is the presence of the periodic potential that originates non-zero matrix elements in a transition from a band to another.

The modern applications of photoemission are a variety; we will only mention some of them. In non-correlated systems bulk band mapping of valence and conduction occupied bands can be obtained by angular resolved photoemission at different photon energies, the dispersion of the surface states can be followed both in clean surfaces and in surfaces with ordered adsorbates. Also the symmetry of the electron states, if, for instance, a symmetry plane exists in the sample, can be obtained by the analysis of the selection rules and using polarized light.

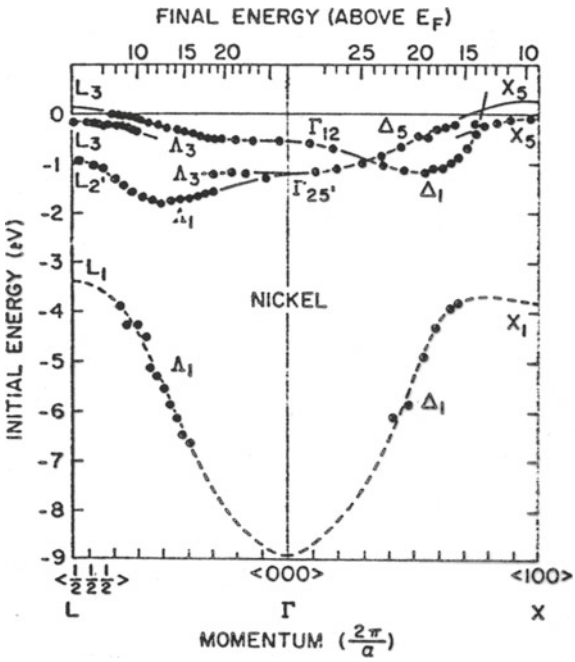


Fig. 5.5 Band mapping of the occupied bands of Ni, by angular resolved photoemission spectroscopy. From [17]

Also the *photoelectron diffraction*, where angular plots of the intensity at different energies can be studied in detail, is a powerful tool to study the structural properties of surfaces. The analysis is based on the same ingredients as EXAFS (the multiple scattering approach to describe the electron final state) but in the case of photoelectron diffraction there is a particular sensitivity to the surface and to the molecules adsorbed on surfaces.

In the systems of atomic type or in general in localized systems many-electron effects, electronic correlation, configurational interactions can be important and can be relevant in the interpretation of the photoelectron spectrum, if we are in the sudden approximation conditions. An additional tool for the analysis is the choice of the energy of the photon, in other to maximize or minimize the effects of matrix element.

The change from one to the other of these regimes can be obtained in the same system passing through a phase transition (metal-insulator for instance) or looking to a series of compound of the same element. In the transition metal series it is easy to perform the band mapping for some elements, if the quasi-particle nature of the excitation spectrum is clearly separable from the background induced by correlation effects. This can be not true for another element, or for the same element in a different compound, were correlation strongly reduce the quasi-particle nature of the electron excitation.

In the recent years a wide literature has grown, dealing with the interpretation of photoemission spectra in correlated systems, expecially after the availability of

instruments providing a direct multidimensional picture of the dispersion relations (binding energy $\boldsymbol{\varepsilon}$ versus $\mathbf{k}$) giving at each value of $\mathbf{k}$ not only a value of the energy of the main observable peak but the *whole spectum* of structures (additional peaks, satellites, background, …) of the *hole* left behind, at higher binding energies [18, 19].

5.10 Thomson Scattering

The diffusion of electromagnetic waves by atomic electrons can be described semiclassically, as seen in the previous chapter. The amplitude of the diffusion can also by obtained as a quantum process by the fifth diagram in Fig. 5.1, which is the main contribution to the elastic scattering in the case $\hbar\omega >> E_I$, where E_I is the set of ionization energy, and $\hbar\omega < mc^2$. The diffusion amplitude is proportional to

$$\frac{1}{i\hbar}\sum_i \langle \mathbf{k}'\boldsymbol{\varepsilon}';\, \psi_B \mid \mathbf{A}^2(\mathbf{r}_i,0) \mid \mathbf{k}\boldsymbol{\varepsilon};\, \psi_A\rangle \int_{t_i}^{t_f} dt\, e^{i(E_B+\hbar\omega_{\mathbf{k}'}-E_A-\hbar\omega_{\mathbf{k}})t}$$

where

$$\mathbf{A}^2(r_i,0) = \sum_{\mathbf{k}_1 s_1}\sum_{\mathbf{k}_2 s_2} \frac{4\pi\hbar c^2}{2\mathcal{V}\omega_{\mathbf{k}_1}\omega_{\mathbf{k}_2}} \left(\boldsymbol{\varepsilon}_{\mathbf{k}_1 s_1}\cdot\boldsymbol{\varepsilon}_{\mathbf{k}_1 s_1}\right)\left(a_{\mathbf{k}_1 s_1} + a^\dagger_{\mathbf{k}_1 s_1}\right)\left(a_{\mathbf{k}_2 s_2} + a^\dagger_{\mathbf{k}_2 s_2}\right)$$

Only mixed terms of the type $a^\dagger a$ or $aa^\dagger$ with $\mathbf{k}_1 s_1$ and $\mathbf{k}_2 s_2$ equal to $\mathbf{k}'\boldsymbol{\varepsilon}'$ and $\mathbf{k}\boldsymbol{\varepsilon}$ will survive. The polarizazion are linear here and we have real polarization vectors. The relevant contribution comes from $\mid \psi_B\rangle \;= \mid \psi_A\rangle$ and the energy of the photon does not depend on the angle of diffusion $\hbar\omega = \hbar\omega'$. One has for the diffusion amplitude

$$\left(\boldsymbol{\varepsilon}'\cdot\boldsymbol{\varepsilon}\right)\frac{e^2}{mc^2}\sum_i \langle \psi_A \mid e^{-i(\mathbf{k}'-\mathbf{k})\cdot\mathbf{r}_i} \mid \psi_A\rangle = \left(\boldsymbol{\varepsilon}'\cdot\boldsymbol{\varepsilon}\right) r_0 n(\mathbf{k}'-\mathbf{k})$$

where one indentifies the Fourier trasform of the electron density, evaluated at the scattering wavevector $\mathbf{k}'-\mathbf{k}$. By calculating the square modulus of the amplitude, summing on the polarizations and on the element of phase volume in the $\mathbf{k}'$ space, dividing by the incident flux, one gets the Thomson-Bragg differential cross section

$$\sigma\,(\omega)\,d\Omega = \mid n(\mathbf{k}'-\mathbf{k})\mid^2 r_0^2(1+\cos^2\theta)d\Omega. \tag{5.47}$$

If we have more than a single diffusion center, as an ordered set of atoms in a crystal lattice, we must sum the various amplitudes and then calculate the square modulus, to get the probability of the process. In this way one gets, for a periodic system, diffraction intensities in the Bragg conditions, when $\mathbf{k}'-\mathbf{k} = \mathbf{G}$, where $\mathbf{G}$ is a reciprocal lattice vector of the crystal; this is the basis of crystallography.

5.11 Second Order Processes

The last three diagrams of Fig. 5.1 describe the diffusion processes. The corresponding scattering amplitudes are, separating in (5.30) the linear and quadratic parts in the vector potential operator and labeling these terms as $\mathscr{H}_I^{(1)}$ and $\mathscr{H}_I^{(2)}$

$$S_{fi}^{1A} = \sum_b \lim_{\eta\to 0_+} \frac{\langle \psi_{a'}; \mathbf{k}'\boldsymbol{\varepsilon}' \mid \mathscr{H}_I^{(1)} \mid \psi_b; 0\rangle\langle \psi_b; 0 \mid \mathscr{H}_I^{(1)} \mid \psi_a; \mathbf{k}\boldsymbol{\varepsilon}\rangle}{E_a + \hbar\omega_{\mathbf{k}} - E_b + i\eta}$$

$$S_{fi}^{1B} = \sum_{b'} \lim_{\eta\to 0_+} \frac{\langle \psi_{a'}; \mathbf{k}'\boldsymbol{\varepsilon}' \mid \mathscr{H}_I^{(1)} \mid \psi_{b'}; \mathbf{k}\boldsymbol{\varepsilon}, \mathbf{k}'\boldsymbol{\varepsilon}'\rangle\langle \psi_{b'}; \mathbf{k}\boldsymbol{\varepsilon}, \mathbf{k}'\boldsymbol{\varepsilon}' \mid \mathscr{H}_I^{(1)} \mid \psi_a; \mathbf{k}\boldsymbol{\varepsilon}\rangle}{E_a - \hbar\omega_{\mathbf{k}'} - E_{b'} + i\eta}$$

$$S_{fi}^{2} = \langle \psi_{a'}; \mathbf{k}'\boldsymbol{\varepsilon}' \mid \mathscr{H}_I^{(2)} \mid \psi_a; \mathbf{k}\boldsymbol{\varepsilon}\rangle$$

$\mid \psi_a; \mathbf{k}\boldsymbol{\varepsilon}\rangle$ is the initial state (the atomic system in ψ_a and a photon in the mode $\mathbf{k}\boldsymbol{\varepsilon}$); $\mid \psi_{a'}; \mathbf{k}'\boldsymbol{\varepsilon}'\rangle$ is the final state with the system in ψ_b and a photon in the $\mathbf{k}'\boldsymbol{\varepsilon}'$ mode. $\mid \psi_b; 0\rangle$ are the intermediate states of the system with energy E_b and zero photon; $\mid \psi_{b'}; \mathbf{k}\boldsymbol{\varepsilon}, \mathbf{k}'\boldsymbol{\varepsilon}'\rangle$ are the same intermediate states for the system by with the presence of two photons in each mode $\mathbf{k}\boldsymbol{\varepsilon}$ and $\mathbf{k}'\boldsymbol{\varepsilon}'$. If our system is a many-particle system we have to distinguish between the low enenergy case ($\hbar\omega_{\mathbf{k}} \ll E_b - E_a$) $\mid$ and the high energy case with $\hbar\omega_{\mathbf{k}} \gg E_b - E_a$. In the first case one has the Rayleigh scattering, leaving the system in the same state or in some excited vibrational state. These terms give a cross-section increasing with $\omega_{\mathbf{k}}^4$. This is linked to the first two contributions. At high energy, ($\hbar\omega_{\mathbf{k}} \gg E_b - E_a$), the dominating term is the last in the elastic scattering (Bragg-Thomson), while the inelastic process correspond to Compton scattering.

It is possible to obtain different contributions to the elastic scattering amplitude including second order terms and the additional contribution (see Appendix) that describe the interaction between the field and the electron spins. We have the *Bragg-Thomson amplitude,* considered before

$$f_{BT} = r_0 \sum_i \langle \psi_0 \mid e^{-i\mathbf{q}\cdot\mathbf{r}_i} \mid \psi_0\rangle(\boldsymbol{\varepsilon}'^*\cdot\boldsymbol{\varepsilon}),$$

the orbital magnetic scattering amplitude

$$f_{M_L} = -ir_0\frac{\hbar\omega_{\mathbf{k}}}{mc^2}\langle \psi_0 \mid \sum_i e^{-i\mathbf{q}\cdot\mathbf{r}_i}\frac{\mathbf{q}\times\mathbf{p}_i}{i\hbar k^2} \mid \psi_0\rangle \cdot (\boldsymbol{\varepsilon}'^*\times\boldsymbol{\varepsilon}).$$

and, including spin, the *spin magnetic scattering* amplitude

$$f_{M_S} = -ir_0\frac{\hbar\omega_{\mathbf{k}}}{mc^2}\langle \psi_0 \mid \sum_i e^{-i\mathbf{q}\cdot\mathbf{r}_i}\mathbf{s}_i \mid \psi_0\rangle \cdot \mathbf{b}$$

where $\mathbf{b} = (\boldsymbol{\varepsilon}'^* \times \boldsymbol{\varepsilon}) + (\mathbf{k}' \times \boldsymbol{\varepsilon}'^*)(\mathbf{k}' \cdot \boldsymbol{\varepsilon}) - (\mathbf{k} \times \boldsymbol{\varepsilon})(\mathbf{k} \cdot \boldsymbol{\varepsilon}'^*) - (\mathbf{k}' \times \boldsymbol{\varepsilon}'^*) \times (\mathbf{k} \times \boldsymbol{\varepsilon})$ and $\mathbf{q} = \mathbf{k} - \mathbf{k}'$. The magnetic scattering terms are significant in the case of incomplete d or f shells and are much smaller than the charge scattering term f_{BT}. For this reason it is convenient to study magnetic diffraction in systems where the periodicity of the magnetic structure is different from the one of the crystal lattice, i.e. of the electron density distribution.

Interesting is the case when the energy of the photon is comparable with the energy of an excitation of the systems. The energy denominators can become very small. One can include, in the second order expansion of the transition amplitude, the effects of higher order terms, [10] putting in the denominators in place of the eigenvalues of the unperturbed Hamiltonian of the system the complex energy values which are the poles of the 1-particle propagator of the interacting systems. As a consequence the energy of the excitation are re-defined and include an imaginary part that account for the finite lifetime of the intermediate states. In this way an expression of the correction of the elastic scattering cross-section, in the neighborood of an absorption edge gives rise to an *anomalous scattering*. The anomalous contribution can be of the type $(\boldsymbol{\varepsilon}'^* \cdot \boldsymbol{\varepsilon})$ as in the *charge* scattering, or of magnetic nature with terms $(\boldsymbol{\varepsilon}'^* \times \boldsymbol{\varepsilon}) \cdot \hat{\mathbf{z}}$ or can be a third contribution of the type $(\boldsymbol{\varepsilon}'^* \cdot \hat{\mathbf{z}})(\hat{\mathbf{z}} \cdot \boldsymbol{\varepsilon})$, where $\hat{\mathbf{z}}$ is the direction of the *magnetic* axis of the system.

5.12 Resonant Raman Scattering

In the last two decades there was a significant growth in the studies on elastic and inelastic scattering of X-rays, in resonant conditions or near-resonant conditions with the excitation of a core hole. The detailed study of the absorption and scattering lineshapes allows to investigate electronic, structural and magnetic properties of elements and compounds. The theoretical approach can be based on *ionic* models to study the different configurations of magnetic ions (with incomplete) d or f shells as many-electron systems. The effect of the symmetry of the crystal can be obtained by adding crystal-field effects. Alternatively, in a single-particle picture, it is possible to use also the wavefunctions of a band-structure calculation for a solid to describe more accurately the presence of the crystal potential, but loosing something in electron-electron correlations. In both descriptions $\mid i\rangle, \mid n\rangle, \mid f\rangle$ are the initial, intermediate and final states. The inelastic scattering cross section in resonant conditions, can be written as

$$\frac{d^2\sigma}{dE_f d\Omega'} \simeq \sum_f \left| \sum_n \frac{\langle f \mid D^L \mid n\rangle\langle n \mid D^{L'} \mid i\rangle}{E_i - E_n + \hbar\omega_{\mathbf{k}} - i\Gamma_n/2} \right|^2 \delta(E_i - E_f + \hbar\omega_{\mathbf{k}} - \hbar\omega_{\mathbf{k}'})$$

where the operators D^L and $D^{L'}$ are the most relevant terms that, in a chosen region of energy, are leading the multipole expansion of the interaction. The selection rules fix the lowest order of the multipole for a possible transition. An example of a

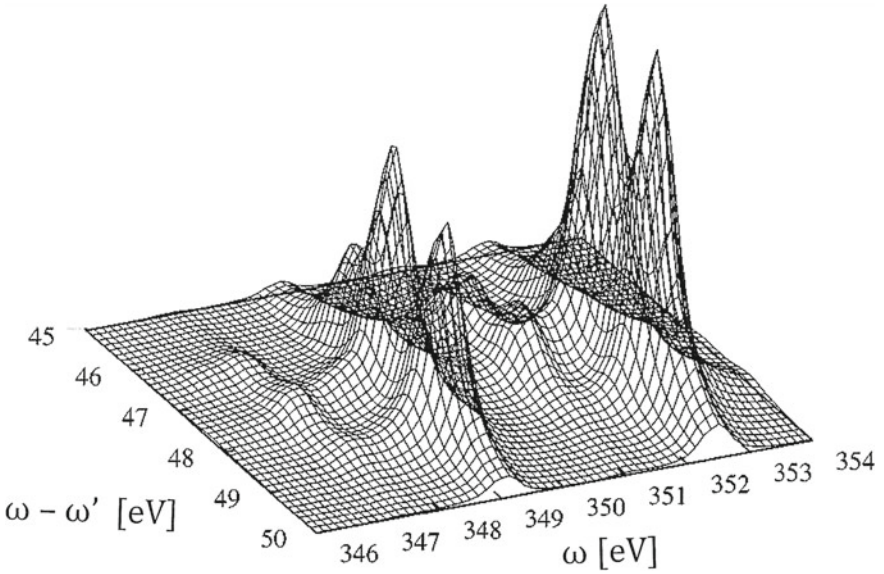


Fig. 5.6 Resonant inelastic scattering of Ca^{2+} corresponding to the transitions $3d^0 \rightarrow 2p^5 3d^1 \rightarrow 3s^1 3d^1$. The intensity og the peaks are reported as a function of the exciting photon frequency and of the frequency difference beween the adsorbed and the emitted photon. The changes of shapes passing through the thresholds of the excitations are visible. From the calculation of [20]

calculation of inelastic cross section by De Groot in 1996 [20] is given in Fig. 5.6. A variety of information can be obtained by looking at the geometry of the scattering experiment using polarized light. Both using ionic localized multi-electron states and one-particle band state calculations (in the case of extended states), the cross section can be described as a function of the geometry of the experiment (direction of the incoming and outcoming light, their polarizations, direction of the magnetic axis). The comparison with the experimental results are powerful ways of investigation, expecially in the case of transition metals and rare earth compounds. This field of research is still in development and a number of papers appeared in the literature on theoretical [21, 22], computational [23–26] and experimental aspects [27, 28] of these techniques.

A simple example of a calculated spectrum for inelastic scattering is shown in Fig. 5.6 where the shape of the inelastic loss spectrum as a function of $\omega - \omega'$, the loss of frequency of the outcoming photon, at different values of incoming photon frequency ω are given. The absorbed photon excites a $2p$ electron to the $3d$ empty shell. The emitted photon is due to a transition of an electron from the $3s$ to the $2p$ state. The intermediate states of the process are the manyfold of states of the system with a $3d$ electron and a $2p$ hole.

5.13 Conclusions

To conclude this brief introduction about the mechanisms of interaction between radiation and matter, offered by quantum theory, we notice that all the effects considered here can be useful to study in detail the property of matter: atoms, molecules, solids, surfaces, chemical reactions, chemisorpion on surface, electronic and magnetic properties. Many of the experimental techiques have been developed recently with a huge degree of sophistication. Often the power of an experimental method is strictly linked to the availability of a theoretical and computational description of the experiment, to improve our understanding from the comparison. The availability of high quality light sources and of more and more refined instrumentation, with high resolution and efficiency of detectors, requires corresponding improvement in the theoretical and simulation methods.

5.14 Appendix

Constants and units. Consistently with the majority of textbooks of theoretical physics, the *cgs* unit systems is used here, in particular the non-razionalized system. In the alternative choice (razionalized system) the factors 4π would disappear in (5.1) and the electronic charge and the values of **B** and **E** would be divided by $\sqrt{4\pi}$.

Here $e = 4.80324\, 10^{-10} e.s.u.$, with $e.s.u. = (\text{erg cm})^{\frac{1}{2}}$. The fields **E** and **B** are measured in the same units.

The fine structure constant is a number whose value is about $(137, 036)^{-1}$ in any system. It is written as

$$\alpha = \frac{e^2}{\hbar c} \tag{5.48}$$

The value of the classical electron radius r_0, which appears in some expressions, is defined by the equality:

$$\frac{e^2}{r_0} = mc^2$$

where m is the electron mass; it is

$$r_0 = \frac{e^2}{mc^2} = 2.81794\ 10^{-13}\,\text{cm} \tag{5.49}$$

This has nothing to do with the *physical size* of the electron. At distance much shorter of this value the electrodynamics is still valid and at length scales much lower the electron is still behaves like a pointlike *elementary particle*.

Mathematical notations. In this chapter from the first section we have used some symbols, whose definitions follow. The gradient operator ∇ in three dimensions is

$$\nabla \equiv (\frac{\partial}{\partial x}, \frac{\partial}{\partial y}, \frac{\partial}{\partial z}) \tag{5.50}$$

We summarize in the following lines its actions on a a function $f(\mathbf{r})$ or on a vector $\mathbf{a}(\mathbf{r})$.

$$\nabla f = (\frac{\partial f}{\partial x}, \frac{\partial f}{\partial y}, \frac{\partial f}{\partial z}) \tag{5.51}$$

is a vector also labeled grad f;

$$\nabla \cdot \mathbf{a} = \frac{\partial a_x}{\partial x} + \frac{\partial a_y}{\partial y} + \frac{\partial a_z}{\partial z} \tag{5.52}$$

is a scalar (a function) also named div $\mathbf{a}$; while

$$\nabla \times \mathbf{a} = (\frac{\partial a_z}{\partial y} - \frac{\partial a_y}{\partial z}, \frac{\partial a_x}{\partial z} - \frac{\partial a_z}{\partial x}, \frac{\partial a_y}{\partial x} - \frac{\partial a_x}{\partial y}) \tag{5.53}$$

is a vector, named rot $\mathbf{a}$.

Coherent states. The coherent states $\mid \Phi_c\rangle$ mentioned at the end of Sect. 5.2, can give expectation value of the field similar to a classical wave. Here some more details on them are given. Restricting to a single mode $(\mathbf{k}, r)$ the state can be expliciltly written as

$$\mid c\rangle = e^{-\frac{1}{2}|c|^2} \sum_{n=0}^{\infty} \frac{c^n}{\sqrt{n!}} \mid n\rangle \quad \text{where} \quad c = \mid c \mid e^{i\delta} \tag{5.54}$$

is a complex number. This state is normalized, being $\langle c \mid c\rangle = 1$ and it is an eigenstate of $a \equiv a_{\mathbf{k},r}$, as can be easily verified.

$$a \mid c\rangle = c \mid c\rangle. \tag{5.55}$$

The eigenvalue c (note that a is non hermitian operator) can be any complex number. The squared modulus and the phase of c are linked to to the *average* number of photons in the state, proportional to the square of the amplitude, and to the phase of the classical wave. By using the (5.22)–(5.24) one obtains evaluating the expectation value of the operator $n = a^\dagger a$ and of $(\Delta n)^2 = n^2 - \langle n\rangle^2$ over the state $\mid c\rangle$,

$$\langle n\rangle = \langle c \mid n \mid c\rangle = \mid c \mid^2 = \overline{n} \qquad (\Delta n)^2 = \mid c \mid^2 \tag{5.56}$$

and then

$$\frac{\Delta n}{\langle n\rangle} = \frac{1}{\langle n\rangle^{\frac{1}{2}}}. \tag{5.57}$$

As a consequence if $\overline{n} = \langle n \rangle = \mid c \mid^2$ increases the standard deviation Δn, its incertitude, becomes smaller than the average number of photons in the state. The expectation value of the field becomes

$$\langle c \mid \mathbf{E} \mid c \rangle = -\boldsymbol{\varepsilon}_{\mathbf{k},s} 2 \left(\frac{\hbar \omega_{\mathbf{k}}}{2V} \right)^{\frac{1}{2}} \mid c \mid \sin\left(\mathbf{k} \cdot \mathbf{r} - \omega_{\mathbf{k}} t + \delta\right) \tag{5.58}$$

If $\overline{n}$ is high the field takes the form of a classical oscillating wave, as the uncertainity $(\triangle \mathbf{E})^2$ rimains limited. See [2].

Further terms in the interaction. The description given by (5.29) or (5.31) and (5.30) are appropriate for a system of scalar non-relativistic particles. In the most cases to describe the electrons in atoms and molecules, we must take into account the spin 1/2 of the electrons and the interactions involving spin. New terms can be obtained starting from the the Dirac equation, with a method (Foldy-Wouthuysen transformation) [3].

The relativistic corrections to $\mathscr{H}_S^0$ for the system of electrons are

$$\frac{1}{2m^2c^2}(-e)\sum_i \mathbf{S}_i \cdot (\nabla\varphi(\mathbf{r}_i) \times \mathbf{p}_i) - \frac{1}{8m^3c^6}\sum_i \mathbf{p}_i^4 - \frac{e\hbar^2}{8m^2c^2}\sum_i \nabla^2\varphi(\mathbf{r}_i) \tag{5.59}$$

where the first term is the spin-orbit term, the second the correction to kinetic energy and the third the Darwin term. $\varphi(\mathbf{r})$ is the electric scalar potential seen by each electron in the system.

The presence of spin introduces two additional terms also in the interaction Hamiltonian $\mathscr{H}_I$: $\mathscr{H}_I^{(3)}$ and $\mathscr{H}_I^{(4)}$ to be added to (5.30)

$$\mathscr{H}_I^{(3)} + \mathscr{H}_I^{(4)} \equiv \frac{e}{mc}\sum_i \mathbf{S}_i \cdot \left(\nabla \times \mathbf{A}(\mathbf{r}_i, t)\right) - \frac{e^2}{2m^2c^4}\sum_i \mathbf{S}_i \cdot ((\frac{\partial}{\partial t}\mathbf{A}(\mathbf{r}_i, t)) \times \mathbf{A}(\mathbf{r}_i, t)) \tag{5.60}$$

The first term describes the interaction of the intrinsic magnetic moments of the electrons with the field. The term $\mathscr{H}_I^{(3)}$ adds, in the matrix element evaluation, the contribution of the intrinsic magnetic moment to the magnetic dipole (5.43) linked to the orbital momentum, that is already included in (5.30).

In (5.60) $\mathbf{S}_i$ is the *intrinsic angular momentum* vector operator for each electron, in $\hbar$ units

$$\mathbf{S}_i = \frac{1}{2}\sigma_i \tag{5.61}$$

where σ is a vector operator represented by the three Pauli matrices

$$\sigma = (\sigma_1, \sigma_2, \sigma_3) = \left[\begin{pmatrix} 0 & 1 \\ 1 & 0 \end{pmatrix}, \begin{pmatrix} 0 & -i \\ i & 0 \end{pmatrix}, \begin{pmatrix} 1 & 0 \\ 0 & -1 \end{pmatrix} \right]. \tag{5.62}$$

References

1. If we are interested to the description of the interaction between high-energy charged particles and e.m. field, the convenient choice of the gauge is the Lorentz gauge. In this approach one defines a 4-vector potential $A^\mu = (\varphi, \mathbf{A})$ where $\mu = 0, 1, 2, 3$ labels the 4-coordinates. Time and space coordinates are grouped into a 4-vector $x^\mu = (ct, \mathbf{r})$. The Lorenz-gauge condition is $(\partial/\partial x^\mu)A^\mu = 0$. See, for instance, the textbook F. Mandl, G. Shaw, *Quantum Field Theory* (Wiley, New york, 1988)
2. R. Loudon, *The Quantum Theory of Light*, Chap. 8, (Clarendon Press, Oxford, 1973)
3. W. Greiner, Theoretical Physics, vol. 3, *Relativistic Quantum Mechanics: Wave Equations*, Chap. 11, (Springer, Berlin, 1990)
4. C. Cohen-Tannoudji, J. Dupont-Roc, G. Grynberg, *Processus d'interation entre photons et atomes* (Editions du CNRS, Paris, 1988)
5. D.A. Varshalovich, A.N. Moskalev, V.K. Kheronskii, *Quantum Theory of Angular Momentum* (World Scientific, Singapore, 1980)
6. R.D. Cowan, *The Theory of Atomic Structure and Spectra* (University of California Press, Berkeley, 1981)
7. P. Ferriani, Thesis, University of Modena, 1999
8. G. van der Laan, B.T. Thole, Phys. Rev. B **42**, 6670 (1990)
9. G. van der Laan, B.T. Thole, Phys. Rev. B **43**, 13401 (1991)
10. C.T. Chen, F. Sette, Y. Ma, S. Modesti, Phys. Rev. B **42**, 7262 (1990)
11. C.T. Chen, Y.U. Idzerda, H.-J. Lin, N.V. Smith, G. Meigs, E. Chaban, G.H. Ho, E. Pellegrin, F. Sette, Phys. Rev. Lett. **75**, 7262 (1995)
12. C.A. Ashley, S. Doniach, Phys. Rev. B **11**, 1279 (1975)
13. A. Filipponi, A. Di Cicco, C.R. Natoli, Phys. Rev. B **52**, 15122 (1995)
14. J. Stöhr, *NEXAFS Spectroscopy* (Springer, Berlin, 1996)
15. D.A. Shirley, *Photoemission in Solids*, Vol. I, eds. by M. Cardona, L. Ley, pp. 165–193 (Springer, Berlin, 1978)
16. S.P. Kowalczyc, L. Lay, R.A. Pollack, F.R. Mc Feely, D.A. Shirley. Phys. Rev. B **7**, 4009 (1973)
17. F.J. Himpsel, K.J.A. Knapp, D.E. Eastman, Phys. Rev. B **19**, 2919 (1979)
18. J. Sanchez-Barriga, J. Fink, V. Boni, I. Di Marco, J. Braun, J. Minár, A. Varykhalov, O. Rader, V. Bellini, F. Manghi, H. Hebert, M.I. Katsnelson, A.I. Lichtenstein, O. Eriksson, W. Eberhardt, A.H. Dürr, Phys. Rev. Lett. **103**, 267203 (2009)
19. J. Sanchez-Barriga, J. Braun, J. Minár, I. Di Marco, A. Varykhalov, O. Rader, V. Boni, V. Bellini, F. Manghi, H. Hebert, M.I. Katsnelson, A.I. Lichtenstein, O. Eriksson, W. Eberhardt, A.H. Dürr, J. Fink, Phys. Rev. B **85**, 205109 (2012)
20. F.M.F. De Groot, Phys. Rev. B **53**, 7099 (1996)
21. P. Carra, M. Di Fabrizio, B.T. Thole, Phys. Rev. Lett. **74**, 3700 (1994)
22. M.A. van veenendaal, P. Carra, B.T. Thole. Phys. Rev. B **54**, 16010 (1996)
23. M. Matsubara, T. Uozumi, A. Kotani, Y. Harada, S. Shin, J. Phys. Soc. Jpn. **69**, 1558 (2001)
24. P. Ferriani, C.M. Bertoni, G. Ferrari, Phys. Rev. B **69**, 104433 (2004)
25. I. Marri, C.M. Bertoni, P. Ferriani, Y. Joly, Phys. Rev. B **74**, 212410 (2006)
26. G. Borgatti, G. Ghiringhelli, P. Ferriani, G. Ferrari, G. van der Laan, C.M. Bertoni, Phys. Rev. B **69**, 1334420 (2004)

27. L. Braicovich, G. van der Laan, G. Ghiringhelli, A. Tagliaferri, M.A. van Veenendaal, N.B. Brookes, M.M. Chervinskii, C. Dallera, B. De Michelis, H.A. Duerr, Phys. Rev. Lett. **82**, 1566 (1999)
28. F. Borgatti, P. Ferriani, G. Ghiringhelli, A. Tagliaferri, B. De Michelis, C.M. Bertoni, N.B. Brooks, L. Braicovich, Phys. Rev. B **65**, 094406 (2002)

Part III
Experimental Methods

Chapter 6
Introduction to X-Ray Absorption Spectroscopy

Paolo Fornasini

Abstract X-ray Absorption Fine Structure (XAFS) contains original information on the local properties of materials. After a general introduction to the X-ray absorption process, the attention is here focussed on the *extended* fine structure (EXAFS). The main approximations that lead to a relatively simple and effective interpretation of EXAFS spectra are reviewed; the peculiar effects of thermal disorder are stressed. The basic instrumentation for EXAFS measurements is described and the most important procedures of data analysis are presented.

6.1 A Phenomenological Introduction to XAFS

Let us consider a collimated X-ray beam, whose flux Φ_0 is the number of photons per unit time and unit cross-section. If the beam traverses a sample of thickness x, the flux is reduced according to the exponential law

$$\Phi = \Phi_0 \exp[-\mu(\omega)x], \tag{6.1}$$

where $\mu(\omega)$ is the *linear attenuation coefficient*, which depends on the energy $\hbar\omega$ of X-ray photons and on the sample composition and density.

X-ray energies for most XAFS applications are between about 1 and 40 keV, corresponding to wavelengths between 0.3 and 12 Å. (The relation between energy $\hbar\omega$, in keV, and wavelength λ, in Ångström, is $\hbar\omega = 12.4/\lambda$). Two different basic mechanisms contribute to the X-ray attenuation in this energy range (Fig. 6.1, left): (a) in *photo-electric absorption*, one photon is absorbed from the beam and an atom is ionized or excited, (b) in *scattering*, one photon is deflected from the original

P. Fornasini (✉)
Department of Physics, University of Trento,
38123 Povo, Trento, Italy
e-mail: paolo.fornasini@unitn.it

S. Mobilio et al. (eds.), *Synchrotron Radiation*,
DOI: 10.1007/978-3-642-55315-8_6, © Springer-Verlag Berlin Heidelberg 2015

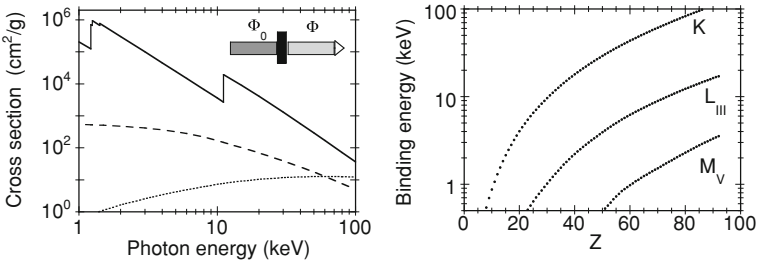


Fig. 6.1 *Left* X-ray absorption cross-sections for Germanium. *Continuous line* photoelectric absorption, with the three L edges (1.217, 1.248 and 1.414 keV) and the K edge (11.103 keV); *dashed line* elastic Thomson scattering; *dotted line* inelastic Compton scattering. *Right* Binding energy of the levels K, L_{III} e M_{V} as a function of the atomic number Z

trajectory by the collision with an electron; scattering from one electron can be elastic (Thomson) or inelastic (Compton). In the energy range from 1 to 40 keV, photo-electric absorption is dominant, and we can approximate the total attenuation coefficient μ of (6.1) with the photo-electric absorption coefficient.

Let us now focus on absorption spectroscopy [1]. When the energy $\hbar\omega$ of X-ray photons increases, the absorption coefficient $\mu(\omega)$ decreases. This smooth behavior is interrupted by sharp discontinuities, the absorption edges (Fig. 6.1, left), which originate when the photons gain high enough energy to extract an electron from a deeper level. The highest-energy absorption edges, the K edges, correspond to the extraction of an electron from the deepest level (1s level). The following table establishes the connection between high energy edges and core electronic levels.

Edge:	M_{V}	M_{IV}	M_{III}	M_{II}	M_{I}	L_{III}	L_{II}	L_{I}	K
Core level:	$3d_{5/2}$	$3d_{3/2}$	$3p_{3/2}$	$3p_{1/2}$	3s	$2p_{3/2}$	$2p_{1/2}$	2s	1s

Since the binding energies of electrons increase monotonically with the atomic number (Fig. 6.1, right), an edge energy corresponds to a well defined atomic species.

After absorption of an X-ray photon, an isolated atom can be either excited, if the photon energy corresponds to the energy difference between an electronic core level and an unoccupied bound level, or ionized, if the photon energy is larger than the binding energy, so that the electron (photo-electron) is ejected from the atom.

In correspondence of an edge, the absorption coefficient exhibits the *X-ray Absorption Fine Structure* (XAFS) [1, 2]. For isolated atoms (noble gases, metallic vapors) the XAFS is limited to a few eV around the edge, and reflects the transitions of the core electron to unoccupied bound levels (Fig. 6.2, left). In molecular gases and condensed systems the XAFS, strongly influenced by the presence of the atoms surrounding the absorber one, can extend up to and beyond one thousand eV above the edge (Fig. 6.2, right). Different regions of XAFS are customarily distinguished:

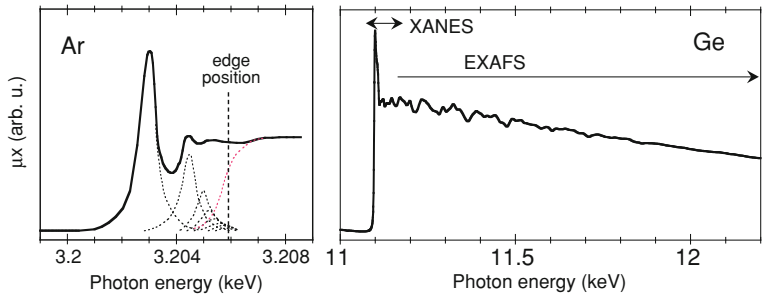


Fig. 6.2 Fine structures at the K edges of Argon (*left*) [derived from L. G. Parratt, Rev. Mod. Phys. 31, 616 (1969)] and Germanium (*right*)

(a) A *pre-edge* and *edge* region, limited to a few eV around the edge (Fig. 6.2, left).

(b) The structure within $30 \div 50\,\text{eV}$ above the edge is called *XANES* (X-ray Absorption Near Edge Structure) or *NEXAFS* (Near Edge X-ray Absorption Fine Structure) [2, 3]. From XANES (including the pre-edge and edge regions), information can be obtained on the local electronic as well as geometric structure.

(c) The fine structure extending from the XANES region up to typically one thousand eV, as in Fig. 6.2, right, is called *EXAFS* (Extended X-ray Absorption Fine Structure). EXAFS contains information on the local geometric structure surrounding a given atomic species. The interpretation of EXAFS is nowadays well established, and easier than the interpretation of XANES [2, 4–9].

The following phenomenological picture can be of help to understand the origin of EXAFS (Fig. 6.3). When an X-ray photon of high enough energy is absorbed by an atom A, a core electron, whose orbital is small with respect to the atomic size, is ejected from the atom. The kinetic energy of the ejected photo-electron is the difference between the photon energy $\hbar\omega$ and the core binding energy E_b. The outgoing photo-electron is described by a wavefunction whose wavelength λ decreases when the photon energy $\hbar\omega$ increases. The absorption coefficient $\mu(\omega)$ of the isolated atom A is proportional to a superposition integral of the localised core wavefunction and the outgoing wavefunction. If the absorber atom A is not isolated, the photo-electron can be scattered by a neighbouring atom B, giving rise to an incoming wavefunction. As a consequence, the total photo-electron wavefunction is now a superposition of the outgoing and the scattered waves. The phase relationship between the outgoing wave and the scattered wave, evaluated at the core site of atom A, depends on the photo-electron wavelength and on the distance R beween atoms A and B. The variation of the phase relationship as a function of photon energy $\hbar\omega$ influences the amplitude of the total wavefunction at the core site, giving rise to a modulation of the absorption coefficient. The frequency of the EXAFS oscillations depends on the distance between absorber and back-scatterer atoms. Their amplitude is proportional to the number of back-scatterer atoms.

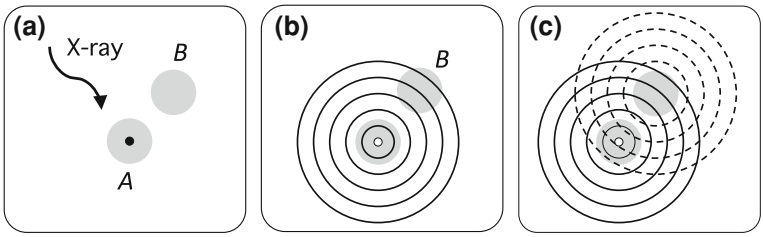


Fig. 6.3 Schematic picture of the EXAFS phenomenon: **a** the X-ray photon impinging on atom *A* (the *black circle* is the orbital of the core electron), **b** the outgoing photo-electron wave function (the *open circle* is the core hole of atom *A*), **c** the final state superposition of the two wavefunctions, outgoing from atom *A* and scattered from atom *B*

To obtain a quantitative interpretation of EXAFS one has to properly describe, within the framework of suitable approximations, the process of photoelectric X-ray absorption (Sect. 6.2) as well as the final state scattering wavefunction (Sect. 6.3).

Two main peculiarities characterize EXAFS: (a) the selectivity of atomic species, which is obtained by tuning the X-ray energy at the corresponding absorption edge; (b) the insensitivity to long-range order, due to the short mean free path of the photo-electron, typically limited to about 10 Å. These peculiarities make EXAFS a very appealing local structural probe. In many-atomic non-crystalline systems, like amorphous alloys or oxide glasses, the atomic selectivity allows one to separately study the environment of each component species. EXAFS is an invaluable tool for systems in which the functional properties are due to individual atoms or small clusters embedded in a matrix of different atomic species, such as heterogeneous catalysts, active sites in biomolecules, impurities in semiconductors, luminescent rare-earth atoms in crystals and glasses. Brilliant applications of EXAFS concern the study of local structural properties of crystalline solids which are different from the average properties detected by diffraction.

6.2 Photoelectric Absorption of X-Rays

In the energy interval between two edges (Fig. 6.1, left), the photo-electric absorption coefficient depends on energy according to an approximate power law, which is generally expressed as a function of the wavelength λ (*Victoreen law*)

$$\mu \propto C\,\lambda^3 \tag{6.2}$$

where C depends on the atomic number Z.

6.2.1 Golden Rule and Further Approximations

The photo-electric absorption process can be described as follows [3, 10, 11]. An atom is initially in its ground state $|\Psi_i\rangle$ of energy E_i. When interacting with the electromagnetic field, the atom can absorb an X-ray photon of energy $\hbar\omega$ and undergo a transition to a final state $|\Psi_f\rangle$ of energy $E_f = E_i + \hbar\omega$. The photon energy is used to promote an electron from a core level to an unoccupied outer level (*excitation*) or to the continuum of free states (*ionization*). The atomic final state is characterized by the presence of a core hole. To account for EXAFS, ionization has to be considered.

The absorption coefficient $\mu(\omega)$ can be expressed (in S.I. units) as

$$\mu(\omega) \;=\; n\,\sigma_a(\hbar\omega) \;=\; (2\hbar/\varepsilon_0\omega A_0^2 c)\; n \sum\nolimits_f w_{fi}\,, \tag{6.3}$$

where n is the number of atoms per unit volume, σ_a is the atomic absorption cross section, $\varepsilon_0\omega A_0^2 c/2\hbar$ is the photon flux (A_0 is the magnitude of the vector potential of the electromagnetic field) and w_{fi} is the probability of transition per unit time (transition rate) from the initial state $|\Psi_i\rangle$ to the final state $|\Psi_f\rangle$.

According to the Golden Rule of the time-dependent perturbation theory, a transition rate w_{fi} can be expressed in terms of a matrix element between the initial and final stationary states $|\Psi_i\rangle$ and $|\Psi_f\rangle$. For a sinusoidal time dependence of the electromagnetic field,

$$w_{fi} \;=\; (\pi e^2 A_0^2/2\hbar m^2) \;\left|\, \langle\, \Psi_f \,|\, \sum\nolimits_j e^{i\mathbf{k}\cdot\mathbf{r}_j}\, \mathbf{p}_j \cdot \hat{\boldsymbol{\eta}}\, |\Psi_i\,\rangle \,\right|^2 \rho(E_f)\,, \tag{6.4}$$

where the sum is over all the electrons inside the atom, $\mathbf{p}_j$ is the conjugate momentum of the j-th electron, $\hat{\boldsymbol{\eta}}$ and $\mathbf{k}$ are the polarization unit vector and the wavevector of the electromagnetic field, respectively ($k = 2\pi/\lambda$), and $\rho(E_f)$ is the density of final continuum states, with $E_f = E_i + \hbar\omega$.

The calculation of the matrix element in (6.4) is simplified by a set of further approximations.

6.2.1.1 One-Electron Approximation

EXAFS is due to the coherent superposition of outgoing and incoming photo-electron wavefunctions. We focus our attention on the so-called *elastic* transitions, in which only one core electron changes its state and the remaining $N - 1$ electrons (passive electrons) simply relax their orbitals around the core hole. In the other possible *inelastic* transitions, the primary core excitation is accompanied by the excitation of outer electrons (*shake-up* and *shake-off* processes), so that the X-ray energy is distributed over all the excited electrons. The measured absorption coefficient is the sum of the elastic and inelastic contributions,

$$\mu(\omega) \;=\; \mu_{\mathrm{el}}(\omega) \;+\; \mu_{\mathrm{inel}}(\omega). \tag{6.5}$$

The elastic contribution is

$$\mu_{\mathrm{el}}(\omega) \;\propto\; \left| \langle\, \Psi_f^{N-1} \psi_f |\; e^{i\mathbf{k}\cdot\mathbf{r}}\, \hat{\boldsymbol{\eta}} \cdot \mathbf{p} \;| \Psi_i^{N-1} \psi_i \,\rangle \right|^2 \rho(\varepsilon_f)\,, \tag{6.6}$$

where Ψ^{N-1} is the Slater determinant of the wavefunctions of the passive electrons. The interaction Hamiltonian operates now only on one electron, of which ψ, $\mathbf{r}$, $\mathbf{p}$ and ε_f are wavefunction, vector position, momentum and final energy, respectively.

6.2.1.2 Electric Dipole Approximation

The calculation of μ_{el} can be simplified by expanding the exponential in (6.6) and truncating the expansion at the first term:

$$e^{i\mathbf{k}\cdot\mathbf{r}} \;=\; 1 \;+\; i\mathbf{k}\cdot\mathbf{r} \;-\; (\mathbf{k}\cdot\mathbf{r})^2/2! \ldots \;\simeq\; 1. \tag{6.7}$$

The electric dipole approximation is reasonable when $|\mathbf{k}\cdot\mathbf{r}|^2 \ll 1$, say when the radiation wavelength is much larger than the size of the system. In the one-electron approximation, the electromagnetic field interacts only with a core orbital, whose extension is smaller than the X-ray wavelength. The electric dipole approximation is generally appropriate for the interpretation of EXAFS.

In the electric dipole approximation, (6.6) can be alternatively expressed in the dipole-velocity form (6.8) or in the dipole-length form (6.9)

$$\mu_{\mathrm{el}}(\omega) \;\propto\; \left| \langle\, \Psi_f^{N-1} \psi_f \;|\; \hat{\boldsymbol{\eta}} \cdot \mathbf{p} \;|\; \psi_i \;\; \Psi_i^{N-1} \,\rangle \right|^2 \rho(\varepsilon_f)\,. \tag{6.8}$$

$$\propto\; \omega^2 \left| \langle\, \Psi_f^{N-1} \psi_f \;|\; \hat{\boldsymbol{\eta}} \cdot \mathbf{r} \;|\; \psi_i \;\; \Psi_i^{N-1} \,\rangle \right|^2 \rho(\varepsilon_f)\,. \tag{6.9}$$

Within the dipole approximation, the angular momentum selection rules hold:

$$\Delta\ell \;=\; \pm 1, \quad \Delta s \;=\; 0, \quad \Delta j \;=\; \pm 1, 0, \quad \Delta m \;=\; 0. \tag{6.10}$$

For one-electron transitions, the selection rule $\Delta\ell = \pm 1$ implies that: (a) if the initial core state has s symmetry ($\ell = 0$, edges K and $\mathrm{L_I}$), the final state has p symmetry ($\ell = 1$); (b) if the initial core state has p symmetry, ($\ell = 1$, edges $\mathrm{L_{II}}$ and $\mathrm{L_{III}}$), the final state can be of both s or d symmetry ($\ell = 0$ or $\ell = 2$, respectively). Dipole-forbidden transitions, due to higher-order terms of the expansion of (6.7), can sometimes give non negligible contributions to the pre-edge and edge fine structure.

6.2.1.3 Sudden Approximation

In the EXAFS region, the photo-electron energy is high enough that its interaction with the passive electrons of the absorbing atom can be neglected. Within the sudden approximation, the atomic wavefunctions can be factorized in the contributions ψ_i and ψ_f of the active electron and Ψ_i^{N-1} and Ψ_f^{N-1} of the passive electrons:

$$\mu_{\rm el}(\omega) \;=\; n\,\sigma_{\rm el} \;=\; n\,(\pi e^2\omega/\varepsilon_0 c)\;\left|\,\langle\,\psi_f|\,\hat{\boldsymbol{\eta}}\cdot\mathbf{r}\,|\psi_i\,\rangle\,\right|^2\;S_0^2\;\rho(\varepsilon_f) \tag{6.11}$$

where the factor

$$S_0^2 \;=\; \left|\,\langle\,\Psi_f^{N-1}|\Psi_i^{N-1}\,\rangle\,\right|^2 \tag{6.12}$$

is the superposition integral of the passive electrons wavefunctions. Generally, $S_0^2 \simeq 0.7$–0.9. In virtue of a sum rule for photo-electric absorption, the total absorption coefficient $\mu(\omega)$ of (6.5) corresponds to the one-electron elastic absorption coefficient of (6.11) in the hypothesis that passive electrons undergo no relaxation, *i.e.* $S_0^2 = 1$. The actual value of the superposition integral $S_0^2 < 1$ thus measures the fraction of total absorption due to the elastic transitions.

6.2.2 De-excitation Mechanisms

An atom with a core hole is unstable, and spontaneously tends to relax, filling the core hole with an electron from an upper level and thereby reducing its energy. Two de-excitation mechanisms are possible: (a) in the *fluorescence* mechanism, the relaxation energy is released to an outgoing X-ray photon; (b) in the *Auger* mechanism, the relaxation energy is used to eject an (Auger) electron from an upper level. The energies of fluorescence photons and Auger electrons depend on the energies of the electron levels and univocally identify the atomic species.

The two de-excitation mechanisms are in competition. Their relative strengths is measured by the *fluorescence yield*

$$\eta_s \;=\; X_s/(X_s + A_s) \tag{6.13}$$

where s labels a given absorption edge (K, $\rm L_I$,…), X_s and A_s are the emission probabilities of a fluorescence photon and an Auger electron, respectively. The fluorescence yield depends on the atomic number (Fig. 6.4, left). The intensity of the fluorescence and Auger emissions depends on the probability of the previous X-rays absorption, and can thus be used to measure the absorption coefficient (Sect. 6.5).

The total de-excitation probability per unit time is inversely proportional to the *core-hole lifetime*. The deeper the core hole and the larger the atomic number Z, the larger is the number of upper levels from which an electron can drop to fill the core hole and consequently the shorter is the core-hole lifetime τ_h (typically

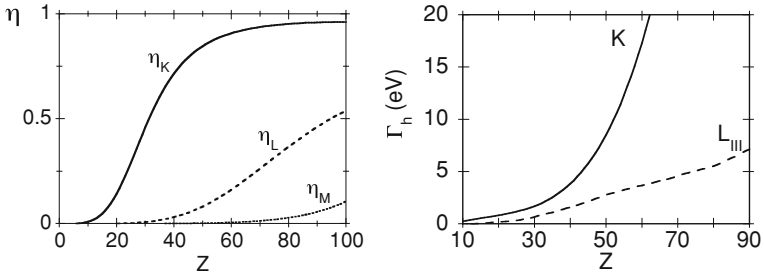


Fig. 6.4 Average fluorescence yield η (6.13) for the K, L and M edges *(left)* and width Γ_h of the K and L_{III} excited states *(right)* as a function of the atomic number Z

$10^{-15} \div 10^{-16}$ s). The core-hole lifetime τ_h represents an upper limit for the time allowed to the photo-electron for probing the local structure surrounding the absorber atom. Because of the time-energy uncertainty relation, the core-hole lifetime is associated with the energy width of the excited state $\Gamma_h \simeq \hbar/\tau_h$. The width Γ_h contributes to the resolution of X-ray absorption experimental spectra. For a given edge, the larger the atomic number Z, the lower is the lifetime τ_h and the larger is the energy width Γ_h (Fig. 6.4, right).

6.3 Basic EXAFS Theory

According to (6.11), the fine structure of the absorption coefficient $\mu_{el}(\omega)$ reflects the variation of the final photo-electron stationary state $|\psi_f\rangle$, evaluated at the core site of the initial state $|\psi_i\rangle$, as a function of the photon energy $\hbar\omega$. It is the final state $|\psi_f\rangle$ that contains structural information. The calculation of the photoelectron final state $|\psi_f\rangle$ in molecules and condensed matter can be made in several different ways. The most effective approach for XAFS is based on the multiple scattering (MS) formalism, which allows a unified interpretation over the entire energy range, from edge to EXAFS. In the EXAFS region, the treatment can be much simplified within the single scattering (SS) approximation, which leads to an effective parametrization in terms of structural and thermal properties [2, 7, 9]. For concreteness, we consider here the contribution of a K edge to the absorption coefficient.

6.3.1 The EXAFS Function

EXAFS oscillations (see for example Fig. 6.2, right) are conveniently represented as a function of the magnitude of the photo-electron wavevector $k = (2\pi/\lambda)$:

$$k = \sqrt{(2m/\hbar^2)\,\varepsilon_f} = \sqrt{(2m/\hbar^2)\,(\hbar\omega - E_b)} \tag{6.14}$$

where ε_f is the photoelectron energy and E_b is the core electron binding energy.

Let us consider the expression (6.11) for the elastic absorption coefficient, and suppose for the moment that $S_0^2 = 1$, say that inelastic transitions are negligible (their contribution will be taken into account later on). In the EXAFS region, the density of final states $\rho(\varepsilon_f)$ varies slowly with energy, so that EXAFS oscillations are entirely described by the matrix element.

If the absorber atom is isolated (as in monatomic gases), the final state $|\psi_f^0\rangle$ is simply an outgoing wave. The corresponding absorption coefficient

$$\mu_0(\omega) \propto \left| \langle \psi_f^0 | \, \hat{\boldsymbol{\eta}} \cdot \mathbf{r} \, | \psi_i \rangle \right|^2 \tag{6.15}$$

is called *atomic absorption coefficient* and decreases monotonically as a function of the photon energy $\hbar\omega$, according to the Victoreen empirical law, (6.2).

If the absorber atom is non-isolated (as in molecular gases and condensed systems) the photo-electron can interact with the surrounding atoms and undergo scattering. In the EXAFS region, the photo-electron energy is much larger than the electron–atom interaction energy, so that the interaction causes a weak perturbation to the final state, $|\psi_f\rangle = |\psi_f^0 + \delta\psi_f\rangle$ and the absorption coefficient becomes

$$\mu(\omega) \propto \left| \langle \psi_f^0 + \delta\psi_f | \, \hat{\eta} \cdot \mathbf{r} \, | \psi_i \rangle \right|^2 . \tag{6.16}$$

The normalised EXAFS function is defined as

$$\chi(k) = (\mu - \mu_0)/\mu_0 \tag{6.17}$$

and is expressed as a function of the wave-number k of (6.14). The amplitude of the EXAFS oscillations typically ranges between 1 and 10 % of the absorption coefficient of a given edge.

We can now insert the absorption coefficients (6.15) and (6.16) in the EXAFS function (6.17) and express the matrix elements in the coordinate representation in terms of superposition integrals of wave-functions. By neglecting the term of second order in $\delta\psi_f$, the EXAFS function becomes

$$\chi(k) = \frac{2\mathrm{Re} \int \left[\psi_i(\mathbf{r}) \, \hat{\boldsymbol{\eta}} \cdot \mathbf{r} \, \psi_f^{0*}(\mathbf{r}) \right] \left[\psi_i^*(\mathbf{r}) \, \hat{\boldsymbol{\eta}} \cdot \mathbf{r} \, \delta\psi_f(\mathbf{r}) \right] d\mathbf{r}}{\int \left| \psi_i^*(\mathbf{r}) \, \hat{\boldsymbol{\eta}} \cdot \mathbf{r} \, \psi_f^0(\mathbf{r}) \right|^2 d\mathbf{r}} . \tag{6.18}$$

The integral in the numerator of (6.18) contains the structural information and is responsible for the EXAFS oscillations. The leading contribution to this integral

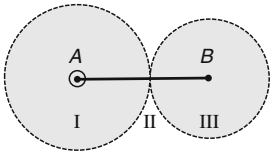


Fig. 6.5 Pair of absorber A and back-scatterer B atoms. The *open circle* represents the core orbital of atom A. The large *grey circles* represent the muffin-tin potential spheres

comes from the limited spatial region of the core orbital, which represents both the source and the detector for the photo-electron that probes the surrounding structure.

6.3.2 Approximate Derivation of EXAFS

A number of equivalent derivations of the EXAFS function have been proposed [6, 7, 12, 13], none of them sufficiently simple for an introductory account. In the following, the basic concepts are highlighted from a phenomenological point of view. Only ideal systems composed of atoms frozen at their equilibrium positions are at first considered; thermal disorder is introduced later on.

6.3.2.1 Two-Atomic System

The simpler system consists of two atoms, an absorber one A and a back-scatterer one B; let R be the distance between the two atoms (Fig. 6.5). We want to interpret the EXAFS function within the single scattering (SS) formalism. For a given photon energy $\hbar\omega$, the photo-electron quantum state is defined by the constant wavevector $k = 2\pi/\lambda$ of (6.14). The interaction of the photo-electron, ejected from the core orbital of atom A, with both atoms A and B is generally approximated in terms of two spherically symmetric potentials of regions I and III joined by an interstitial region II of constant potential (muffin-tin approximation). The effect of the interaction is accounted for in terms of suitable phase-shifts of the constant-k wavefunction.

The wavefunction ψ_i of the initial 1 s core state of angular momentum $\ell = 0$ is confined at the centre of region I. Also the final state wavefunction for the isolated atom ψ_f^0, of angular momentum $\ell = 1$, has to be known only at the centre of region I, in order to evaluate the superposition integrals of (6.15) and (6.18). Actually, the explicit knowledge of ψ_i and ψ_f^0 is not necessary to calculate the EXAFS function. It is sufficient to evaluate the perturbation $\delta\psi_f$ along the scattering path $A \rightarrow B \rightarrow A$.

At the centre of region I, corresponding to the core orbital, the outgoing photo-electron wavefunction is $\psi_f = \psi_f^0$, the same as for an isolated atom. At the border of region I, the radial part of the photo-electron wavefunction can be approximated, for high enough energies ($kr \gg 1$), as

$$\psi_f^0 \, (e^{ikr}/2kr) \, e^{i\delta_1} \tag{6.19}$$

where the phase-shift δ_1 takes into account the effect of the potential of region I.

Let us now consider the interaction between the photo-electron and the atom B in region III. If the photo-electron has high enough energy, only the interaction with the inner electrons of atom B is important. We can then restrict the scattering to a spatial region very small with respect to the interatomic distance R (small atom approximation) and neglect the curvature of the spherical wave impinging on atom B (plane wave approximation). Within these approximations, the process is described in terms of a complex amplitude of back-scattering from atom B in the direction of atom A, $f_B(k,\pi)$, which can be expressed as a function of the partial-wave phase-shifts δ_ℓ [14] as

$$f_B(k,\pi) \;=\; (1/k)\,\sum_{\ell=0}^{\infty}(-1)^\ell\,(2\ell+1)\,e^{i\delta_\ell}\,\sin\delta_\ell\,. \tag{6.20}$$

At the border of region III, the radial part of the back-scattered wave is then

$$\underbrace{\left[\psi_f^0\;(e^{ikR_B}/2kR)\;e^{i\delta_1}\right]}_{\text{wave impinging on B}}\;f_B(k,\pi)\;\;\underbrace{\left[(e^{ikr'}/r')\right]}_{\text{wave scattered by B}} \tag{6.21}$$

where r' is the distance from atom B.

At last, for $r' = R$, say at the absorber core site, the final wave function can be factorized as

$$\psi_f^0\;\;(1/2k)\;\underbrace{e^{i\delta_1}}_{\text{inter.}}\;\underbrace{e^{2ikR}/R}_{\text{propag.}}\;\underbrace{f_B(k,\pi)}_{\text{inter.}}\;\underbrace{e^{2ikR}/R}_{\text{propag.}}\;\underbrace{e^{i\delta_1}}_{\text{inter.}}\,. \tag{6.22}$$

A further phase-shift δ_1 is present in the last factor, to take into account the effect of the potential of region I on the backscattered wavefunction. Equation (6.22) shows that the perturbation $\delta\psi_f$ due to the presence of atom B can be expressed as a sequence of interaction factors and propagators. Such basic structure is shared by alternative, more sophisticated approaches, able to take into account also MS effects.

If the result expressed by (6.22) is properly inserted into (6.18), one gets

$$\chi(k) \;=\; 3(\hat{\boldsymbol{\eta}}\cdot\hat{\mathbf{R}})^2\,(1/kR^2)\;\mathrm{Im}\left\{f_B(k,\pi)\,e^{2i\delta_1}\,e^{2ikR}\right\}. \tag{6.23}$$

By separating magnitude and phase of the complex backscattering amplitude and grouping the phase terms,

$$f_B(k,\pi)\,e^{2i\delta_1} \;=\; |f_B(k,\pi)|\,e^{i\phi}, \tag{6.24}$$

one can write (6.23) in the purely real form:

$$\chi(k) \;=\; 3(\hat{\eta}\cdot\hat{\mathbf{R}})^2\,(1/kR^2)\;|f_B(k,\pi)|\;\sin\left[2kR+\phi(k)\right]. \tag{6.25}$$

Basically, the EXAFS signal has a sinusoidal behaviour in the k space, with frequency $2R$ proportional to the inter-atomic distance. The phase of the sine function is perturbed by the phase-shift $\phi(k)$, while the amplitude is modulated by $|f_B(k,\pi)|$. The k dependence of backscattering amplitudes and phaseshifts is different for different atomic species. For low Z values, the backscattering amplitude decreases fast and monotonously when k increases. When Z increases, the amplitude becomes higher at high k values, and the overall behavior becomes more and more structured. The behavior of the scattering amplitude and phase-shift of the EXAFS signal can give approximate information on the atomic species of the scattering atom. For realistic spherical waves (say if the plane wave approximation is released), phaseshifts and amplitudes weakly depend also on the interatomic distance: $\phi(k,r)$, $|f(k,\pi,r)|$.

6.3.2.2 Many-Atomic Systems

Let us now consider a system composed of more than two atoms. The generalization of (6.25) is immediate, so long as multiple scattering of the photo-electron can be neglected: the EXAFS function can be built up as the sum of many two-atomic contributions, with different interatomic distances R_i from the absorber atom.

The photo-electron emission is more probable in the direction of polarisation of the photon beam. When dealing with macroscopically ordered systems, such as single crystals, the dipole term $\hat{\boldsymbol{\eta}} \cdot \hat{\mathbf{R}}$ can be exploited to get anisotropic structural information. Very often, however, EXAFS measurements are made on isotropic samples, such as polycrystalline powders, amorphous materials, liquids or gases. In the following, we consider only isotropic samples, for which the polarization term can be averaged, $\langle \hat{\boldsymbol{\eta}} \cdot \hat{\mathbf{R}} \rangle = 1/3$, leading to a simplified treatment which neglects the angular part of the wavefunctions. For an isotropic sample, the EXAFS function is

$$\chi(k) = (1/k) \sum_j (1/R_j^2) \,\mathrm{Im}\left\{ f_j(k,\pi)\, e^{2i\delta_1}\, e^{2ikR_j} \right\}, \tag{6.26}$$

where R_j is the distance of the j-th atom from the absorber atom.

6.3.2.3 Inelastic Effects

The simple treatment leading to (6.26) neglects inelastic effects. Two types of inelastic effects are generally distinguished: intrinsic and extrinsic, referring to many-body interactions within the absorber atom and to the photo-electron mean free path, respectively.

Intrinsic inelastic effects are due to the multiple excitations within the absorber atom (Sect. 6.2), which give rise to the inelastic channel μ_{inel} of the absorption coefficient in (6.5). Multiple excitations modify the photo-electron energy and the interference conditions between outgoing and incoming waves. The net effect is a reduction of the coherent EXAFS signal with respect to that expected for purely

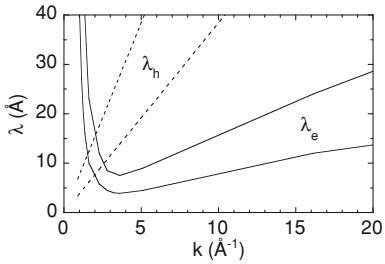


Fig. 6.6 Photo-electron mean free path as a function of wavenumber k. The values λ_e measured for different elements are included between the two continuos lines. The dashed lines include the λ_h values for the K edges of atoms with Z between 30 and 50

elastic excitations. The fraction of total absorption giving rise to elastic excitations is measured by the superposition factor S_0^2 defined in (6.12). Intrinsic inelastic effects are thus taken into account in (6.26) by the factor S_0^2, which typically amounts to 0.7–0.9.

To the *photo-electron mean free path* λ two distinct phenomena contribute: (a) the core-hole lifetime τ_h (Sect. 6.2), depending on the atomic number Z, which establishes the distance $\lambda_h = v\tau_h$ the photo-electron can travel before the de-excitation of the absorber atom takes place (Fig. 6.6, dashed lines); (b) the energy-dependent photo-electron mean-free path $\lambda_e(k)$, caused by the inelastic collisions with other electrons outside the absorber atom (Fig. 6.6, continuous lines).

The actual value of λ is given by

$$1/\lambda \;=\; 1/\lambda_h \;+\; 1/\lambda_e. \tag{6.27}$$

At low energies, in the XANES region, the mean free path is determined by λ_h, while in the EXAFS region the contribution of λ_e is predominant (Fig. 6.6).

The mean free path is generally taken into account in the EXAFS formula by a phenomenological factor $\exp[-2R_j/\lambda(k)]$, with $\lambda \simeq 5 \div 15$ Å. The mean free path factor progressively reduces the amplitude of EXAFS oscillations when R_j increases, contributing to make EXAFS insensitive to long range order.

To summarize, the EXAFS equation taking into account inelastic effects is:

$$\chi(k) \;=\; (S_0^2/k) \sum\nolimits_j \left[e^{-2R_j/\lambda(k)}/R_j^2 \right] \mathrm{Im} \left\{ f_j(k,\pi)\, e^{2i\delta_1}\, e^{2ikR_j} \right\} \tag{6.28}$$

6.3.2.4 Coordination Shells

If the backscattering atoms can be grouped into coordination shells, each one containing N_s atoms of the same species at the same distance R_s from the absorber atom, it is convenient to re-write (6.28) separating the contributions of the different coordination shell:

$$\chi(k) \;=\; (S_0^2/k) \sum\nolimits_s N_s \mathrm{Im} \left\{ f_s(k,\pi)\, e^{2i\delta_1} \left[e^{-2R_s/\lambda(k)}/R_s^2 \right] e^{2ikR_s} \right\}. \tag{6.29}$$

The sum is now over the index s, which labels the coordination shells. The number of atoms N_s is the coordination number of the shell s.

6.3.2.5 Multiple Scattering

Multiple scattering (MS) phenomena, very important in the XANES region, are generally quite weak in the EXAFS region. To take into account MS effects, the absorption coefficient is conveniently written as

$$\mu(k) \;=\; \mu_0(k)\,[1 + \chi_2(k) + \chi_3(k) + \chi_4(k) + \cdots], \tag{6.30}$$

where the terms χ_p of the sum are distinguished by the number p of legs of the scattering paths. The term $\chi_2(k) \equiv \chi(k)$ corresponds to the single scattering contributions up to now considered. In the EXAFS region, the series (6.30) is fast convergent. It has been demontrated [15] that the contribution of MS paths can be expressed, similar to the SS contribution, as the product of an amplitude factor and an oscillating factor:

$$\chi_p(k) \;=\; A_p(k, \{\mathbf{r}\}_p)\, \sin\left[k R_p + \phi_p(k, \{\mathbf{r}\}_p)\right], \tag{6.31}$$

where $\{\mathbf{r}\}_p$ represents the set of all vector distances inside the path, R_p is the total path length, and A_p and ϕ_p are functions depending on the potential acting on the photo-electron.

6.3.3 Disorder Effects on EXAFS

Let us come back to the SS approximation. Equation (6.29) refers to the unphysical situation of a system of atoms frozen at their equilibrium positions. In real systems, atoms are affected by thermal vibrations, whose amplitude increases with temperature but, for quantum reasons, is not negligible even near zero kelvin. The period of atomic vibrations ($\simeq 10^{-12}$ s) is much larger than the photo-electron time of flight ($10^{-16} \div 10^{-15}$ s). An EXAFS spectrum, resulting from the contributions of a very large number of photo-electrons, samples a very large set of instantaneous atomic configurations, corresponding to a distribution of instantaneous interatomic distances for each scattering path.

The distribution of interatomic distances can be further enlarged and modified by the presence of structural disorder. For example, distorted coordination shells are characterized by two or more slightly different interatomic distances. Another example are systems in which the absorber atom has at least two structurally different sites, which cannot be discriminated as different coordination shells. A different kind of disorder is compositional disorder, due to the presence of atoms of different species in the same coordination shell.

6.3.3.1 EXAFS Formula Including Disorder

Let us consider a coordination shell containing only one atomic species (say without compositional disorder). Due to disorder, the distance between absorber and back-scatterer atoms varies according to a probability distribution $\rho(r)$. The EXAFS equation for one coordination shell becomes [2]:

$$\chi_s(k) \;=\; (S_o^2/k)\; N_s \mathrm{Im}\left\{ f_s(k,\pi)\; e^{2i\delta_1} \int_0^\infty P(r,\lambda)\; e^{2ikr}\; dr \right\}, \tag{6.32}$$

where the *effective EXAFS distribution* $P(r,\lambda) = \rho(r)\; (e^{-2r/\lambda}/r^2)$ includes all the r-dependent factors.

The fundamental problem of EXAFS analysis is to recover the *real distribution* $\rho(r)$ from the experimental spectrum $\chi(k)$. No exact solution can be given to this problem, because every experimental spectrum has a finite extension, within the values $k_{\min}$ and $k_{\max}$. In particular, for $k_{\min} \leq 2 \div 3$ Å^{-1} the EXAFS signal cannot generally be utilized, because of: (a) difficulty in determining the atomic absorption coefficient μ_0 in the vicinity of the edge, (b) effects of the core-hole lifetime on the low-energy electrons, (c) influence of multiple scattering processes.

The problem of recovering $\rho(r)$ from $\chi(k)$ is generally solved by hypothesising physically sound structural models and optimising the parameters of their distributions $\rho(r)$ by best fit of (6.32) to the experimental EXAFS spectrum [16].

6.3.3.2 Parametrization of EXAFS Formula

For many applications, the extent of disorder is sufficiently small to allow the expression of the EXAFS formula in terms of a few standard parameters. EXAFS formula (6.32) can then be expressed as

$$\chi_s(k) = \frac{S_o^2}{k}\; N_s\; |f_s(k,\pi)|\; \frac{e^{-2C_1/\lambda}}{C_1^2}\; e^{-2k^2C_2+2k^4C_4/3\cdots}\; \sin\left[2kC_1 - \frac{4k^3C_3}{3} \ldots + \phi(k) \right], \tag{6.33}$$

where the parameters C_i are the cumulants of the *effective* distribution $P(r,\lambda)$ [17, 18]. According to probability theory, the cumulants characterise the position, width and shape of a distribution.The lowest-order cumulants have simple interpretations: C_1 is the mean value, C_2 is the variance and C_3 is a measure of the asymmetry of the distribution.

Actually, one is interested in the cumulants C_i^* of the *real* distribution $\rho(r)$. The first cumulant of the real distribution $\rho(r)$ is significantly larger than the first cumulant of the effective distribution, as a consequence of the spherical nature of the photo-electron wave and its limited mean free path:

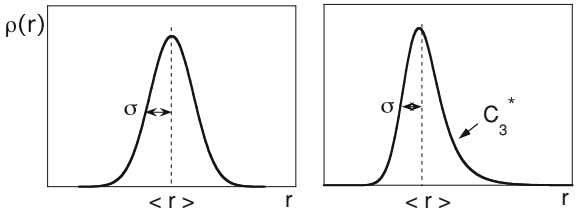


Fig. 6.7 Parametrized models of the real distribution $\rho(r)$ of interatomic distances. *Left* Gaussian distribution, characterized by the average value $\langle r\rangle = C_1^*$ and the standard deviation $\sigma = C_2^*$. *Right* Asymmetric distribution, characterized by one more parameter, the third cumulant C_3^*

$$C_1^* \simeq C_1 + (2C_2/C_1)\,(1 + C_1/\lambda). \tag{6.34}$$

The difference between C_1 and C_1^*, of the order of some 10^{-3} Å, is automatically taken into account by most data analysis packages. The difference between higher-order cumulants of the two distributions is generally negligible.

In some cases, the cumulant expansion can be truncated at the second order term, and (6.33) reduces to the so called standard EXAFS formula

$$\chi_s(k) = \frac{S_o^2}{k}\, N_s\, |f_s(k,\pi)|\, \frac{e^{-2C_1/\lambda}}{C_1^2}\, e^{-2k^2C_2}\, \sin\left[2kC_1 + \phi(k)\right], \tag{6.35}$$

which amounts to consider a gaussian effective distribution $P(r,\lambda)$, which corresponds with good approximation to a gaussian real distribution $\rho(r)$ (Fig. 6.7, left):

$$\rho(r) = (1/\sigma\sqrt{2\pi})\, \exp\left[-(r - \langle r\rangle)^2/2\sigma^2\right], \tag{6.36}$$

where $C_1^* = \langle r\rangle$ is the average distance and $C_2^* = \sigma^2 = \langle (r - \langle r\rangle)^2\rangle$ is the variance. The gaussian approximation, generally reliable for the second and outer coordination shells, is often unfit for the first coordination shell, where the asymmetry of the pair interaction potential is more influent.

For the first coordination shell it is higly recommended to add the third cumulant $C_3^* = \langle (r - \langle r\rangle)^3\rangle$ (mean cubic relative displacement) to account for the distribution asymmetry (Fig. 6.7, right):

$$\chi_s(k) = \frac{S_o^2}{k}\, N_s\, |f_s(k,\pi)|\, \frac{e^{-2C_1/\lambda}}{C_1^2}\, e^{-2k^2C_2}\, \sin\left[2kC_1 - \frac{4k^3C_3}{3} + \phi(k)\right]. \tag{6.37}$$

6.3.4 Summary

For each coordination shell, the following parameters can in principle be obtained from (6.35) or (6.37): (a) the coordination number N, (b) the average inter-atomic distance $C_1^* = \langle r \rangle$, (c) the Debye-Waller factor $\exp[-2k^2\sigma^2]$, where $\sigma^2 = C_2^*$ is the variance of the real distribution of distances and contains information on both thermal and structural disorder, (d) the third cumulant C_3^*, which measures the asymmetry of the real distribution of distances.

To obtain the aforementioned parameters, one has however to know the phase-shifts ϕ_s and the backscattering amplitudes $|f_s(k, \pi)|$ for each coordination shell, as well as the inelastic terms S_0^2 and λ. Such quantities can sometimes be experimentally obtained from reference samples of known structure. More frequently, they are nowadays calculated ab initio [15] by a number of easily available software packages [19–21], with a degree of accuracy sufficient for most applications.

Equations (6.35) and (6.37) are based on the single scattering (SS), plane wave and small disorder approximations. Only the first-shell signal can be safely analysed within the SS approximation, since multiple scattering (MS) paths correspond to longer effective distances. For the outer shells, MS events can be not negligible, in particular when collinear paths are present. The treatment of the outer shells including MS contributions, as well as the calculation of backscattering amplitudes and phase-shifts within the spherical wave formalism, are nowadays available in most data analysis packages. The cumulants parametrisation of (6.33), (6.35) and (6.37) is valid only for relatively small disorder. For large disorder, one should use the general (6.32) and try to build up physically sound models for $\rho(r)$ [16].

6.4 Interpretation of EXAFS Parameters

To better grasp the physical meaning of the structural information obtainable from EXAFS, let us focus the attention on the first coordination shell of a structurally ordered system, such as a crystal, and compare the effects of purely thermal disorder on the EXAFS signal and on the Bragg diffraction patterns (Fig. 6.8, left) [22, 23].

Let $\mathbf{R_0}$ be the equilibrium distance between the absorber and back-scatterer atoms and $\mathbf{u}_a$ and $\mathbf{u}_b$ be their instantaneous thermal displacements. The instantaneous distance between the two atoms is

$$\mathbf{r} = \mathbf{R_0} + \Delta\mathbf{u}, \tag{6.38}$$

where $\Delta\mathbf{u} = \mathbf{u}_b - \mathbf{u}_a$. The projections of the relative displacement $\Delta\mathbf{u}$ parallel and perpendicular to the inter-atomic bond (Fig. 6.8, left) are given by, respectively,

$$\Delta u_{\parallel} = \hat{\mathbf{R}} \cdot \Delta\mathbf{u} \quad \text{and} \quad \Delta u_{\perp}^2 = (\Delta u)^2 - \Delta u_{\parallel}^2 . \tag{6.39}$$

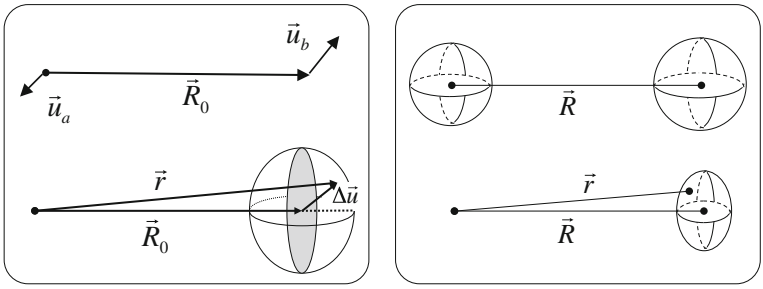


Fig. 6.8 *Left* Instantaneous displacements $\mathbf{u}_a$ and $\mathbf{u}_b$ (*top*) and relative displacement $\Delta\mathbf{u} = \mathbf{u}_b - \mathbf{u}_a$ (*bottom*), whose projections of (6.39) are along the *dotted line* and in the vertical *grey disc*. *Right* Atomic thermal ellipsoids measured by Bragg diffraction (*top*) and relative thermal ellipsoid sampled by EXAFS (*bottom*)

From (6.38) and (6.39), one can express the instantaneous distance r, to first order, as:

$$r \simeq R_0 + \Delta u_\parallel + \Delta u_\perp^2/2R_0\,. \tag{6.40}$$

6.4.1 EXAFS Distance and Crystallographic Distance

The first cumulant of the real distribution $\rho(r)$ is the average value $\langle r\rangle$ of the instantaneous distances:

$$\langle r\rangle = \langle|\mathbf{r}_b - \mathbf{r}_a|\rangle \tag{6.41}$$

According to (6.40),

$$\langle r\rangle \simeq R_0 + \langle\Delta u_\parallel\rangle + \langle\Delta u_\perp^2\rangle/2R = R + \langle\Delta u_\perp^2\rangle/2R \tag{6.42}$$

where $R = R_0 + \langle\Delta u_\parallel\rangle$ is the crystallographic distance, say the distance

$$R = |\langle\mathbf{r}_b\rangle - \langle\mathbf{r}_a\rangle| \tag{6.43}$$

between average atomic positions, measured by Bragg scattering, including the thermal expansion $\langle\Delta u_\parallel\rangle$ (anharmonicity effect). The last term in (6.42) is proportional to the perpendicular Mean Square Relative Displacement (MSRD) $\langle\,\Delta u_\perp^2\,\rangle$, which is always positive. The average distance $\langle r\rangle$ is thus always larger than the crystallographic distance R; EXAFS and Bragg scattering give different and complementary information on the inter-atomic distance in crystals. (In non-crystalline systems, EXAFS and scattering are instead both sensitive to the average distance $\langle r\rangle$).

The temperature dependence of $\langle r\rangle$ for the first coordination shell corresponds to the bond thermal expansion. Since $\langle\Delta u_\perp^2\rangle$ increases when the temperature increases,

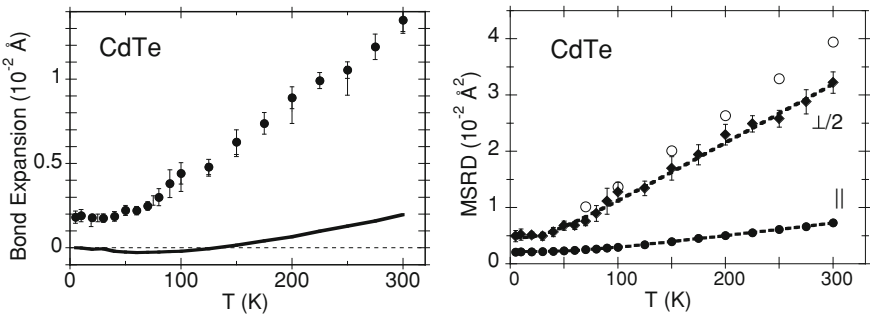


Fig. 6.9 *Left* Expansion of the bond distance Te–Cd in CdTe measured by EXAFS (*full circles*) compared with the crystallographic expansion (*continuous line*). *Right* Parallel MSRD (*full circles*) and half perpendicular MSRD (*diamonds*) for the Te–Cd distance in CdTe compared with the sum of the MSDs from Bragg scattering (*open circles*); the dashed lines are Einstein models

the bond expansion measured by EXAFS is larger than the thermal expansion measured by Bragg diffraction; a quantitative example from [24] is given in Fig. 6.9 (left).

6.4.2 Parallel and Perpendicular MSRDs

The second cumulant is the variance $\sigma^2 = \langle (r - \langle r \rangle)^2 \rangle$ of the real distribution $\rho(r)$, say the parallel Mean Square Relative Displacement (MSRD); to first order

$$\begin{aligned} \sigma^2 \simeq \langle \Delta u_{\parallel}^2 \rangle &= \left\langle [\hat{\mathbf{R}} \cdot (\mathbf{u}_b - \mathbf{u}_a)]^2 \right\rangle \\ &= \langle (\hat{\mathbf{R}} \cdot \mathbf{u}_b)^2 \rangle + \langle (\hat{\mathbf{R}} \cdot \mathbf{u}_a)^2 \rangle - 2 \langle (\hat{\mathbf{R}} \cdot \mathbf{u}_b)(\hat{\mathbf{R}} \cdot \mathbf{u}_a) \rangle . \end{aligned} \quad (6.44)$$

The first two terms on the right of (6.44) are the independent Mean Square Displacements (MSD) of absorber and back-scatterer atoms, which can be obtained from the refinement of Bragg scattering patterns. The third term in (6.44), the Displacement Correlation Function (DCF), depends on the correlation of atomic motions. The stronger is the correlation, the smaller is the parallel MSRD $\langle \Delta u_{\parallel}^2 \rangle$. The correlation term DCF decreases with increasing distance and vanishes for very large distances.

The perpendicular MSRD $\langle \Delta u_{\perp}^2 \rangle$ can be calculated by inverting (6.42) if R is known from Bragg scattering experiments. For isotropic relative atomic displacements, one expects that $\langle \Delta u_{\perp}^2 \rangle / 2 = \langle \Delta u_{\parallel}^2 \rangle$. Actually, one generally finds that the ratio $\langle \Delta u_{\perp}^2 \rangle / 2 \langle \Delta u_{\parallel}^2 \rangle$ is significantly larger than one, corresponding to disc-shaped relative thermal ellipsoids.

The temperature dependence of EXAFS parameters contains original information on the local dynamical behaviour of systems. The comparison of the experimental temperature dependence with theoretical expectations is a good check of the quality of

experimental data and of the soundness of the data analysis procedures. An example of temperature dependence of MSRDs [24] is given in Fig. 6.9 (right).

The parallel MSRD $\sigma^2 = \langle \Delta u_{||}^2 \rangle$ of a given atomic pair in a crystal can be accounted for, in the harmonic approximation, in terms of normal vibrational modes:

$$\sigma^2(T) = \frac{1}{\mathbf{N}} \sum_{\mathbf{q},s} \langle |Q(\mathbf{q},s,t)|^2 \rangle \left| \left(\frac{\mathbf{w}_b(\mathbf{q},s) e^{i\mathbf{q}\cdot\mathbf{R}}}{\sqrt{m_b}} - \frac{\mathbf{w}_a(\mathbf{q},s)}{\sqrt{m_a}} \right) \cdot \hat{R} \right|^2 \tag{6.45}$$

where $\mathbf{N}$ is the number of primitive cells, the sum is over the normal modes (wavevector $\mathbf{q}$, branch index s), the eigenvectors $\mathbf{w}$ give the direction of atomic motion and $Q(\mathbf{q},s,t)$ is the temperature-dependent normal coordinate of mode $(\mathbf{q},s)$:

$$\langle |Q(\mathbf{q},s,t)|^2 \rangle = \frac{\langle E(\mathbf{q},s) \rangle}{\omega^2(\mathbf{q},s)} = \frac{\hbar}{2\omega(\mathbf{q},s)} \coth \frac{\hbar\omega(\mathbf{q},s)}{2kT}. \tag{6.46}$$

Equation (6.46) is of little use in EXAFS applications. The temperature dependence of the parallel MSRD is commonly accounted for by simpler phenomenological models. In the *correlated Debye Model*, only acoustic branches with a linear dispersion relation are considered and the first Brillouin Zone is substituted by a Debye sphere of radius q_D. The maximum frequency $\omega_D = q_D v_s$ is the Debye frequency. The sum over normal modes of (6.45) becomes an integral over the Debye sphere:

$$\sigma^2(q_D,T) = \frac{3\hbar}{q_D^3 m} \int_0^{q_D} dq\, q^2 \frac{1}{\omega} \coth \frac{\hbar\omega}{2kT} \left[1 - \frac{\sin(qR_j^0)}{qR_j^0} \right],$$

where the second term in square parentheses accounts for correlation. The Debye model satisfactorily reproduces the temperature dependence of the parallel MSRD. The Debye temperature is however generally different for different coordination shells, and different from the Debye temperatures obtained by other techniques. Only for monatomic crystals with one atom per primitive cell are the Debye temperatures of different coordination shells very similar and comparable with the Debye temperatures from other techniques.

The alternative *Einstein model* is

$$\sigma^2(\omega_E,T) = \frac{\hbar}{\mu\omega_E} \left[\frac{1}{2} + \frac{1}{e^{\hbar\omega_E/kT} - 1} \right] = \frac{\hbar}{2\mu\omega_E} \coth \left(\frac{\hbar\omega_E}{2kT} \right), \tag{6.47}$$

where μ is the reduced mass of the absorber–backscatterer atomic pair. The Einstein model depends on one parameter, the angular frequency ω_E, which is different for different coordination shells. The Einstein frequency ω_E is connected to a bond-stretching effective force constant $k_0 = \mu\omega_E^2$, which gives a quantitative estimate of the bond strength.

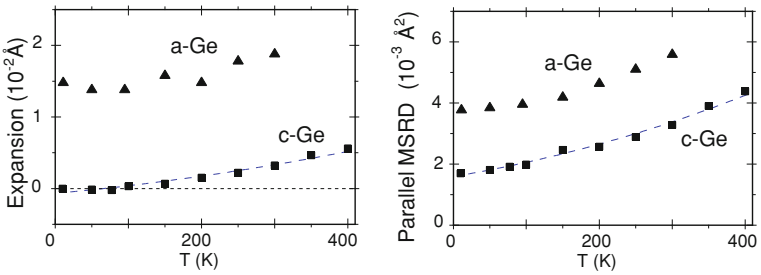


Fig. 6.10 Temperature dependence of the first-shell EXAFS parameters in amorphous (*triangles*) and crystalline (*squares*) germanium. *Left* First cumulants $\langle r \rangle$. *Right* Parallel MSRDs σ^2

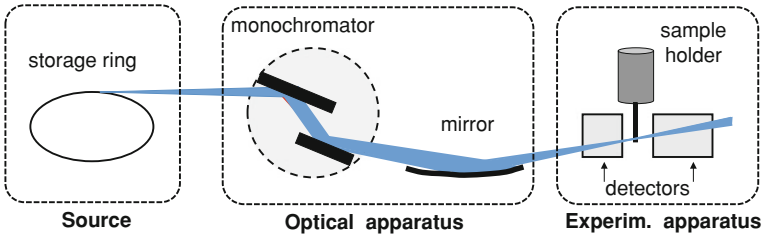


Fig. 6.11 Schematic picture of a Synchrotron Radiation laboratory for XAFS experiments

6.4.3 Structural Disorder

The contributions of thermal and structural disorder to the distribution of interatomic distances can often be disentangled by performing temperature dependent EXAFS measurements. The procedure is exemplified in Fig. 6.10 for the case of amorphous and crystalline germanium. In both cases, the first-shell coordination number is $N = 4$. The nearest-neighbours distance is about 0.015 Å larger in a-Ge than in c-Ge (Fig. 6.10, left); the thermal expansion is however very similar. The effect of structural disorder is evident in the plot of the second cumulants (Fig. 6.10, right) as a positive vertical shift of the a-Ge data with respect to the c-Ge data; the temperature dependence (thermal contribution) is again very similar in a-Ge and in c-Ge.

6.5 Experimental Techniques

The XAFS technique requires the measurement of the X-ray absorption coefficient as a function of photon energy. A laboratory for X-ray absorption spectroscopy with Synchrotron Radiation (Fig. 6.11) is generally composed of: (a) an *optical apparatus*, containing a monochromator and one or more X-ray mirrors; (b) a *measurement apparatus*, containing sample holders and detectors for measuring the absorption coefficient.

6.5.1 Optical Apparatus

Basic tasks of a monochromator are: (a) selecting a beam of energy $E = \hbar\omega$, defined within a width ΔE, from the continuous Synchrotron Radiation spectrum; (b) executing scans over predefined energy ranges. X-ray monochromators are perfect crystals, working according to the Bragg law:

$$2\, d_{\mathrm{hkl}}\ \sin\theta_b\ =\ n\,\lambda, \tag{6.48}$$

where d_{hkl} is the distance between the (hkl) crystallographic planes, θ_b is the incidence (Bragg) angle, n is an integer and λ is the X-ray wavelength. The energy scan is obtained by rotating the crystal around an axis parallel to the crystallographic planes and normal to the beam direction. It is worth remembering some important properties: (a) only crystallographic planes for which the structure factor $F(hkl) \neq 0$ give rise to diffraction; (b) the maximum wavelength selected for a given family of planes (hkl) is $\lambda = 2\, d_{\mathrm{hkl}}$, in correspondence with normal incidence; (c) in addition to the wavelength $\lambda = 2d\ \sin\theta_b$ (fundamental), also wavelengths λ/n (harmonics) are selected. Harmonics are sources of noise in XAFS spectra. For X-ray energies higher than 2 keV, the crystals most frequently utilized are silicon and germanium.

The X-ray beam is diffracted by the monochromator within a finite angular interval around the Bragg angle θ_b. The profile of the diffracted intensity as a function of the angle is called *rocking curve*. The width of the rocking curve (Darwin width) amounts to a few arc-seconds ($1'' = 4.8 \times 10^{-6}$ rad). The Darwin widths are always larger for fundamental reflections than for harmonics. In general, X-ray monochromators for synchrotron radiation are based on consecutive Bragg reflections from two parallel crystals. In this way, the outgoing beam maintains the horizontal direction. By slightly detuning the Bragg angles of the two crystals and exploiting the smaller Darwin width of harmonics with respect to the fundamental wavelength, it is possible to reduce the harmonic content of the outgoing beam. Besides, if one of the two crystals is thin enough to be curved, is can focus the beam in the horizontal plane.

The energy resolution ΔE of the monochromatic beam depends on two factors: (a) the Darwin width of the crystal; (b) the vertical angular divergence Ω of the beam: to a good approximation, $\Omega = (d + s)/\ell$, where s is the vertical size of the source, d is the aperture of the collimating slits and ℓ is the distance between the source and the monochromator. The relative resolution can be easily obtained by differentiating the Bragg law, (6.48):

$$\Delta E/E\ =\ \Delta\lambda/\lambda\ =\ \Delta\Theta\ \mathrm{cotg}\theta_b\,, \tag{6.49}$$

where Θ (in radians) is the convolution between Darwin width and beam divergence. Typically, $\Delta E/E \sim 10^{-4} \div 10^{-5}$.

The monochromator is generally accompanied by one or more X-ray mirrors, whose aims are: (a) to reject the harmonics; (b) to collimate and focalize the beam.

X-ray mirrors are based on total reflection. Basically, the index of refraction can be expressed as

$$n = 1 - \delta - i\beta. \tag{6.50}$$

The imaginary part β is proportional to the absorption coefficient μ. The real part $1 - \delta$ is negative for X-rays. δ, which is proportional to the density ρ of the material and to λ^2, is very small, of the order of $10^{-6} \div 10^{-5}$. For small enough incidence angles, total external reflection occurs. The critical angle depends on the wavelength, $\theta_c \propto \lambda \sqrt{\rho_e}$, and is of the order of milliradians. By properly choosing the incidence angle of the beam on the mirror, it is possible to reflect only the fundamental wavelength, rejecting the harmonics. Besides, by slightly bending the mirror surface it is possible to focalize the beam (typically in the vertical plane). Because of the small values of the critical angle θ_c, the longitudinal size and the bending radius of the X-ray mirrors are very large.

6.5.2 Measurement Apparatus

The physical and chemical environment of the sample can be controlled by properly choosing the sample-holder. Cryostats (liquid N down to 77 K or liquid He down to 4 K) or ovens allow one to vary the sample temperature. Low temperatures are currently used to reduce the thermal damping of EXAFS. By suitable temperature scans, one can study phase transitions, local thermal expansion, lattice dynamics, etc. Different types of high pressure cells are used to perform measurements up to tens of GPa. Chemical reactions, like catalysis, can be studied in suitable reactors.

Different instrumental configurations have been devised to measure the absorption coefficient according to (6.1): $\mu = \ln(\Phi_0/\Phi)/x$. Let us discuss here the most frequently used; further information can be found in [25].

6.5.2.1 Direct Transmission Measurement

The photon fluxes Φ_0 and Φ can be directly measured in front of and behind the sample. In general, the two detectors are *ionization chambers* with plane parallel electrodes, some tens of centimeters long. The efficiency of ionization chambers can be tailored to different X-rays spectral regions by varying the atomic species and the pressure of the filling gas. The output of ionization chambers are two electric currents I_0 and I of low intensity (typically $10^{-10} - 10^{-8}$ A). The absorption coefficient $\mu(\omega)$ is related to the I_0 and I signals by

$$\mu(\omega)x = \ln(\Phi_0/\Phi) = \ln(I_0/I) - \ln C(\omega), \tag{6.51}$$

where $C(\omega)$ is a smoothly varying function, determined by the ionization chambers response, which can be easily subtracted in data analysis.

To optimize the signal to noise ratio, the sample thickness has to be of the order of about $10\,\mu$m. When the sample is a powder, compressed in a pellet or deposited on a thin film, one must carefully avoid holes or inhomogeneities, which could cause spurious variations of the EXAFS amplitude. A rule of thumb is to verify the similarity of EXAFS spectra obtained from samples of different thicknesses.

Transmission measurements are preferred, when possible, in virtue of their easiness and accuracy. In some cases, however, they are not suitable, for example for diluted samples or for surface measurements.

6.5.2.2 Fluorescence Detection

For diluted absorbing species or for very thin samples one resorts to fluorescence measurements, in which the intensity I_f of the fluorescence emitted at the fixed frequency ω_f by the absorbing species A, as a result of radiative de-excitation (Sect. 2.3), is measured as a function of the incident X-rays energy $\hbar\omega$. If both the impinging (I_0) and the fluorescence (I_f) beams make an angle of 45° with the sample surface, the noise due to elastically scattered photons is minimised and fluorescence equations are particularly simple.

In this geometry, for a *thick sample* one can show that [6]

$$I_f(\omega) \;=\; I_0(\omega)\,\frac{\Omega}{4\pi}\,\eta\,\frac{\mu_A(\omega)}{\mu_{\mathrm{tot}}(\omega)\;+\;\mu_{\mathrm{tot}}(\omega_f)}. \tag{6.52}$$

The fluorescence intensity I_f is proportional to the impinging flux I_0, to the solid angle $\Omega/4\pi$ of detector acceptance and to the fluorescence yield η. The fraction in (6.52) shows that the fluorescence intensity I_f allows a direct measurement of μ_A only when $\mu_A \ll \mu_{\mathrm{tot}}$, say for very diluted samples. For thick non diluted samples fluorescence measurements give rise to distortions in the EXAFS amplitude.

For a *thin sample* (for example a thin film) one cas show that

$$I_f(\omega) \;\propto\; \mu_A(\omega). \tag{6.53}$$

Ideal fluorescence detectors should maximise the acceptance angle and minimise the background due to Compton scattering, unwanted fluorescence lines, Bragg peaks, etc. Various alternative solutions, with different performances, are presently available: crystal monochromators, filters and Soller slits with scintillation detectors, solid-state detectors.

6.5.2.3 Electrons Detection

To study surface properties, it is convenient to measure the flux of photoelectrons and/or Auger electrons emitted as a consequence of atomic de-excitation after X-ray absorption. The intensity of both fluxes is proportional to the absorption coefficient.

However, the energy of photoelectrons varies when the photon energy varies, while the energy of Auger electrons is characteristic of the atomic species. Since electrons have a mean free path of the order of 5–10 Å, only Auger and photoelectrons directly generated in the vicinity of the surface can be detected. The inelastic collisions of both Auger and photoelectrons give however rise to secondary electrons, with a large spread of energies, whose escape depth can be of the order of 50–100 Å.

For different requirements one makes use of different detection schemes: (a) The detection of only Auger electrons, by a detector with a narrow energy window (AEY, Auger electrons yield) is particularly suited to study the environment of atoms adsorbed on a surface of different composition (Surface EXAFS, or SEXAFS) [2] (unwanted contributions from photoelectrons can however seriously contaminate the signal). (b) One can detect a large fraction of both Auger electrons and photoelectrons and their secondary, by a large window detector (PEY, partial electrons yield). (c) One can detect all emitted electrons (TEY, total electron yield). The TEY detection is sometimes used to study the surface XAFS of bulk materials: in this case one can show that the full TEY signal is proportional to the absorption coefficient.

6.5.2.4 Energy Dispersive XAFS

In *Energy dispersive XAFS* (EDXAS), a large non-monochromatized beam impinges on a curved crystal "poly-chromator"; different parts of the beam impinge on different regions of the crystal at different Bragg angles, corresponding to different energies, which typically can cover the entire EXAFS interval. The curved crystal focalizes the outgoing monochromatic beams on a single point, where the sample is placed. The sample is thus simultaneously crossed by beams of all the energies within the EXAFS interval. Once the sample has been crossed, the beam is dispersed on a position sensitive detector, where the entire EXAFS spectrum is simultaneously collected. By this method, the beam can be focalised on a very small sample and the acquisition times can be reduced even to a few milliseconds.

6.6 EXAFS Analysis

A number of reliable software packages are available to perform the EXAFS analysis [19–21]. A good understanding of the involved procedures is essential for their sensible use. The most relevant analysis steps are summarised here.

6.6.1 Extraction of the EXAFS signal

The extraction of the normalised EXAFS function $\chi(k)$ from the experimental signal is in principle different for different detection methods (transmission, fluorescence,

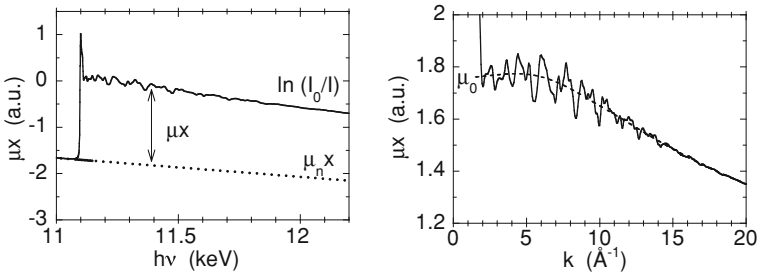


Fig. 6.12 *Left* Experimental absorption signal (*continuous line*) and extrapolation of the pre-edge behavior (*dotted line*). The difference is μx relative to the K edge. *Right* Evaluation of the atomic absorption coefficient (*dashed line*) by a polynomial spline

electron yield, etc.) [4]. Let us consider here the case of transmission measurements (Sect. 4.2) and focus on the absorption spectrum at the K edge of a given element within a compound. According to (6.51), the output of the measurement is

$$\ln(I_0/I) \;=\; \ln(\Phi_0/\Phi) \,+\ln\, C(\omega) \;=\; \mu_{\rm tot}(\omega)x \,+\ln\, C(\omega)\,, \tag{6.54}$$

where $\mu_{\rm tot}(\omega)$ is the total absorption coefficient and x is the thickness of the sample.

The first step of the analysis consists in extracting the contribution $\mu(\omega)x$ of the K edge of the selected element from the experimental signal:

$$\mu(\omega)x \;=\; \ln(I_0/I) \;-\; \mu_n(\omega)x\,, \tag{6.55}$$

where μ_n is the contribution of all the other excitations of the selected element plus the excitations of the other elements of the compound; $\mu_n x$ includes also the contribution of $C(\omega)$ of (6.54). In the pre-edge energy region, $\mu_n x \;=\; \ln(I_0/I)$. Above the edge energy, $\mu_n x$ is estimated by a suitable extrapolation of the pre-edge behavior (Fig. 6.12, left).

The *photo-electron wavenumber* k is defined in (6.14). In general, the core electron binding energy E_b is unknown, and k is experimentally determined as

$$k \;=\; \sqrt{(2m/\hbar^2)\;(\hbar\omega - E_s)} \;=\; 0.51233\,\sqrt{\hbar\omega - E_s}\,, \tag{6.56}$$

where E_s is a threshold energy conventionally chosen in correspondence of some characteristic point of the edge, typically the first inflection point. The last member in (6.56) holds for wavenumbers k measured in Å^{-1} and energies $\hbar\omega$ in eV.

The difference $E_0 = E_b - E_s$ is a priori unknown. If the quantitative analysis is made by comparison with the experimental EXAFS of a reference sample, the same criterion must be used in determining E_s for both samples; E_0 is anyway treated as a free parameter to be optimized by best-fit. If the analysis is made by comparison with theoretical simulations, the E_0 value is a free parameter, again to be optimized by best-fit.

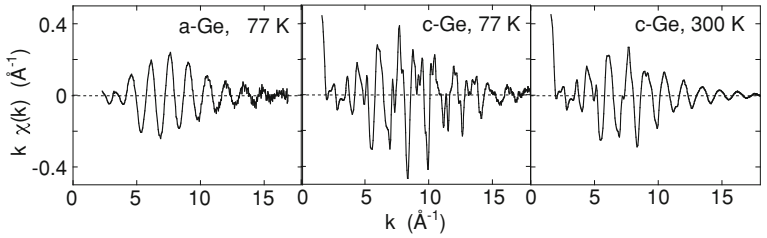


Fig. 6.13 EXAFS of amorphous germanium at 77 K (*left*), and of crystalline germanium at 77 and 300 K (*center* and *right*, respectively)

The *atomic absorption coefficient* μ_0 of the absorber atom embedded into its environment has now to be determined, in order to calculate the EXAFS function $\chi(k) = (\mu - \mu_0)/\mu_0$ (6.17). To evaluate μ_0, one seeks a curve which suitably averages the oscillations of the absorption coefficient. A frequently utilized approach is based on polynomial splines (Fig. 6.12, right).

The visual inspection of the EXAFS signal can directly give qualitative information. For example (Fig. 6.13) the EXAFS of crystalline germanium at 77 K is much more structured than the one of amorphous germanium, since many coordination shells contribute to the former, only one to the latter. When temperature increases, the EXAFS of c-Ge becomes less structured, because thermal disorder more strongly damps the contributions of the outer shells than of the first one.

6.6.2 Fourier Transform and Back-Transform

The direct quantitative analysis of the entire EXAFS signal $\chi(k)$, in principle feasible, is seldom performed. In general, one prefers a different approach, which includes the Fourier transform and back-transform of the EXAFS signal.

The Fourier transform from the space of wavevectors k to the conjugate space of distances r is performed through the integral

$$F(r) = \int_{k_{\min}}^{k_{\max}} \chi(k)\, W(k)\, k^n \exp(2ikr)\, dk\,, \tag{6.57}$$

where $W(k)$ is a window function that reduces the spurious oscillations induced by the finite k range. The factor k^n is used to balance the low-k and high-k regions of the spectrum (typically $n = 1 - 3$). The limits $k_{\min}$ and $k_{\max}$ are chosen so as to exclude both the low-k signal, where the EXAFS formula is unreliable (typically $k_{\min} > 2 - 4$ Å^{-1}), and the high-k signal, where the signal to noise ratio is small. The Fourier transform $F(r)$ of (6.57) is a complex function composed of a real and an imaginary part, $\mathrm{Re}F(r)$ and $\mathrm{Im}F(r)$, respectively (Fig. 6.14). The modulus

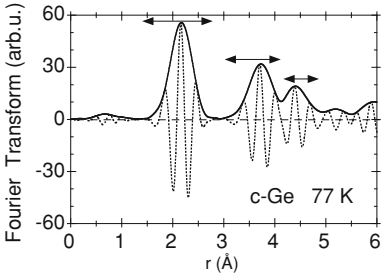


Fig. 6.14 Fourier transform of EXAFS of crystalline germanium at 77 K: imaginary part (*dashed line*) and modulus (*continuous line*). The first three coordination shells are clearly singled out

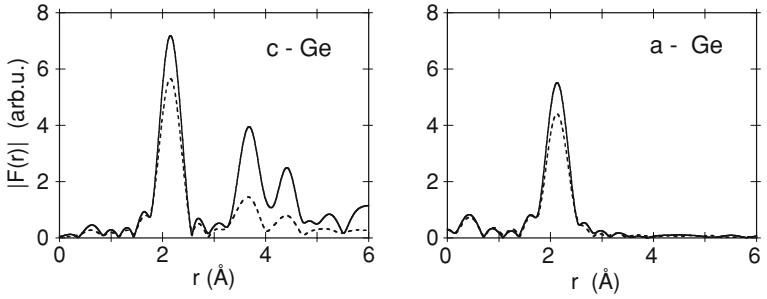


Fig. 6.15 Moduli of Fourier transforms of crystalline (*left*) and amorphous (*right*) germanium at 77 K (*continuous lines*) and 300 K (*dashed lines*)

$$|F(r)| = \sqrt{[\mathrm{Re}F(r)]^2 + [\mathrm{Im}F(r)]^2} \tag{6.58}$$

is characterized by peaks in correspondence of the leading frequencies $2r$ of the $\chi(k)$ signal, say of the most important scattering paths in real space (Fig. 6.14). In general, the most prominent peaks correspond to single scattering paths (coordination shells). The $F(r)$ function is *not* a true radial distribution function: the positions of the peaks are at slightly shorter distances, by about 0.2–0.3 Å, than the real distances, due to the phase-shifts $\phi_s(k)$ present in the total phases $\Phi = 2kR_s + \phi_s$ of each scattering path; besides, the shape of the peaks is strongly influenced by the artefacts of the Fourier transform algorithm.

Important qualitative and sometimes also quantitative information is contained in the Fourier transforms $F(r)$. Let us consider some examples. (1) A non-zero $F(r)$ at shorter distances than the first-shell peak suggests a poor evaluation of the atomic absorption coefficient μ_0, which introduced unphysical low-frequency oscillations. (2) The height of the peaks depends on the coordination number and on the degree of thermal and structural disorder. (3) The Fourier transforms allows a direct visual evaluation of the effects of temperature, pressure, chemical environment on a given sample (Fig. 6.15). (4) The comparison between Fourier transforms of different samples allows one to evaluate differences in distances or disorder effects

(Fig. 6.15). (5) Peaks not corresponding to possible inter-atomic distances can be due to non-negligible multiple scattering effects.

The contribution of a given set of scattering paths can be singled out by an inverse Fourier transform within a distance interval $r_{\min}$ to $r_{\max}$, with window $W'(r)$:

$$\chi'(k) \;=\; (2/\pi) \int_{r_{\min}}^{r_{\max}} F(r)\; W'(r)\; \exp(-2ikr)\; dr. \tag{6.59}$$

The back-transform $\chi'(k)$ is a complex function, whose real part corresponds to the sought filtered signal $\tilde{\chi}(k)$. The filtered signal $\tilde{\chi}(k)$ is significantly different from the original signal $\chi(k)$ owing to the artefacts introduced by the procedure of Fourier transform and back-transform.

6.6.3 Quantitative Determination of Structural Parameters

The final step of EXAFS analysis consists in the quantitative evaluation of the structural parameters: average inter-atomic distances $\langle r \rangle$, coordination numbers N, Debye-Waller exponents σ^2. If the first-shell contribution is well singled out in the Fourier transform $F(r)$, the corresponding back-transformed signal $\tilde{\chi}(k)$ can be safely analysed within the single scattering approximation. The outer shell contributions cannot generally be completely disentangled and are mixed with contributions from multiple scattering paths, which cannot be neglected in refined analyses. In any case, according to (6.33), to obtain the values of the structural parameters from an experimental EXAFS spectrum, one must know the scattering amplitudes $|f(k)|$, phase-shifts $\phi(k)$ and inelastic factors S_0^2 and $\lambda(k)$ of each relevant scattering path.

Most available software packages [19–21] allow a sorting of all the relevant single and multiple scattering paths for a given model structure, as well as the *ab-initio* calculation of scattering amplitudes and phasesihfts for the different scattering paths and an evaluation of the mean free path $\lambda(k)$. It is thus possible to simulate a theoretical EXAFS function $\chi_{\text{sim}}(k)$ for the given model structure. The structural parameters of the studied system can be obtained by building up a suitable starting model structure, calculating $\chi_{\text{sim}}(k)$ for the model structure, comparing with the experimental EXAFS $\chi_{\text{exp}}(k)$ and refining, by a best-fitting procedure, the values of the parameters, including the edge shift $E_0 = E_b - E_s$.

In principle, the fit of theory to experiment could be done over the entire original EXAFS spectrum. More frequently, the fit is limited to a filtered portion of the signal, corresponding for example to the first shell, or to an interval of distances including a number of coordination shells. The comparison of theory with experiment can be done in the r space after Fourier transform or on the k space after back-transform. In any case, since Fourier transforms introduce distortions, it is strictly necessary

that both calculated and experimental EXAFS spectra undergo exactly the same transform procedures before comparison.

The maximum number of independent parameters that can reasonably be obtained from an EXAFS spectrum depends on the quantity and quality of available information. According to a conservative rule of thumb based on information theory, the maximum number of independent parameters obtainable from a Fourier filtered EXAFS signal is

$$n_{\mathrm{ind}} \simeq (2\,\Delta k\,\Delta r)/\pi, \tag{6.60}$$

where $\Delta k = k_{\max} - k_{\min}$ and $\Delta r = r_{\max} - r_{\min}$ are the intervals of the direct and inverse Fourier transforms, respectively.

As for any experimental result, the values of structural parameters obtained from EXAFS analysis are meaningless if not accompanied by a reliable estimate of their uncertainties (error bars). A sound evaluation of error bars is far from trivial [24]. Starting point is in any case the repetition of measurements, at least twice or thrice and possibly in condition of independence.

References

1. B.K. Agarwal, *X-ray Spectroscopy* (Springer, Berlin, 1991)
2. D.C. Koningsberger, R. Prins, *X-ray Absorption: Principles and Application Techniques of EXAFS, SEXAFS and XANES* (Wyley, New York, 1988)
3. J. Stöhr, *NEXAFS Spectroscopy* (Springer, New York, 1996)
4. G. Bunker, *Introduction to XAFS* (Cambridge University Press, Cambridge, 2010)
5. S.J. Gurman, J. Synchrotron Rad. **2**, 56–63 (1995)
6. T.M. Hayes, J.B. Boyce, Solid State Phys. **37**, 173–350 (1982)
7. P.A. Lee, P.H. Citrin, P. Eisenberger, B.M. Kincaid, Rev. Mod. Phys. **53**, 769–806 (1981)
8. D.E. Sayers, E.A. Stern, F.W. Lytle, Phys. Rev. Lett. **27**, 1204–1207 (1971)
9. B.K. Teo, *EXAFS: Basic Principles and Data Analysis* (Springer, Berlin, 1986)
10. G.S. Brown, S. Doniach, The principles of X-ray Absorption Spectroscopy, in *Synchrotron Radiation Research*, ed. by H. Winick, S. Doniach (Plenum, New York, 1980), pp. 353–385
11. E. Merzbacher, *Quantum Mechanics* (Wiley, New York, 1970)
12. I.B. Borovskii, R.V. Vedrinskii, V.L. Kraizman, V.P. Sachenko, Sov. Phys. Usp. **29**, 539–569 (1986)
13. E.A. Stern, Phys. Rev. B **10**, 3027–3037 (1974)
14. G.J. Joachain, *Quantum Collision Theory* (North Holland, Amsterdam, 1975)
15. J.J. Rehr, R.C. Albers, Rev. Mod. Phys. **72**, 621–654 (2000)
16. A. Filipponi, J. Phys, Condens. Matter **13**, 1–38 (2001)
17. G. Bunker, Nucl. Instrum. Methods Phys. Res. **207**, 437–444 (1983)
18. P. Fornasini, F. Monti, A. Sanson, J. Synchrotron Rad. **8**, 1214–1220 (2001)
19. FEFF project home page: http://leonardo.phys.washington.edu/feff/
20. GNXAS home page: http://gnxas.unicam.it/XASLABwww/pag_gnxas.html
21. XAFS software catalog: http://www.esrf.eu/Instrumentation/software/data-analysis/Links/xafs
22. P. Fornasini, J. Phys, Condens. Matter **13**, 7859–7872 (2001)
23. P. Fornasini, e-J. Surf. Sci. Nanotech. **10**, 480–485 (2012)
24. N. Abd el All, B. Thiodjio Sendja, R. Grisenti, F. Rocca, D. Diop, O. Mathon, S. Pascarelli, P. Fornasini, J. Synchrotron Rad. **20**, 603–613 (2013)

25. F. Boscherini, X-ray Absorption Fine Structure in the study of Semiconductor Heterostructures and Nanostructures, in *Characterization of Semiconductor Heterostructures and Nanonstructures*, ed. by C. Lamberti (Elsevier, Amsterdam, 2008), pp. 289–330

Chapter 7
A Close Look into the Low Energy Region of the XAS Spectra: The XANES Region

Maurizio Benfatto and Carlo Meneghini

Abstract The interest in XANES spectroscopy is growing systematically in material sciences as it is a very unique local probe, chemically selective, giving access to fine details of the local atomic structure and electronic state of the photo-absorber, which are hardly reached by other techniques. The recent progresses in theory and computation have extended the application of XANES spectroscopy in many different fields. This chapter aims to be a guide across the different approaches to XANES data analysis, from the phenomenological semi-quantitative methods, to accurate ab-initio modelling and data fitting.

7.1 Introduction

The major advantages of XAFS technique are the relatively easy data collection and the very broad scope in the material science allowing to study materials in every aggregation state (solid, liquid, vapor), crystalline or amorphous, from bulk to the nano-scale and low dimensional systems (thin films, rods, dots), in concentrated as well highly diluted phases. XAFS is specially suited to study materials under extreme conditions such as high temperature, high pressure or high magnetic/electric fields. In addition time resolved XAFS allows probing structural and electronic modifications down to the ps scale. All these features make XAFS a basic probe for material science, widely complementary to common techniques like X-ray diffraction and laboratory spectroscopy (Chap. 6).

M. Benfatto (✉)
Laboratori Nazionali di Frascati, INFN, via E. Fermi, 40, 00044 Frascati, Italy
e-mail: maurizio.benfatto@lnf.infn.it

C. Meneghini
Dipartimento di Scienze, Università Roma Tre, via della Vasca Navale, 84, 00146 Rome, Italy
e-mail: Carlo.meneghini@uniroma3.it

S. Mobilio et al. (eds.), *Synchrotron Radiation*,
DOI: 10.1007/978-3-642-55315-8_7, © Springer-Verlag Berlin Heidelberg 2015

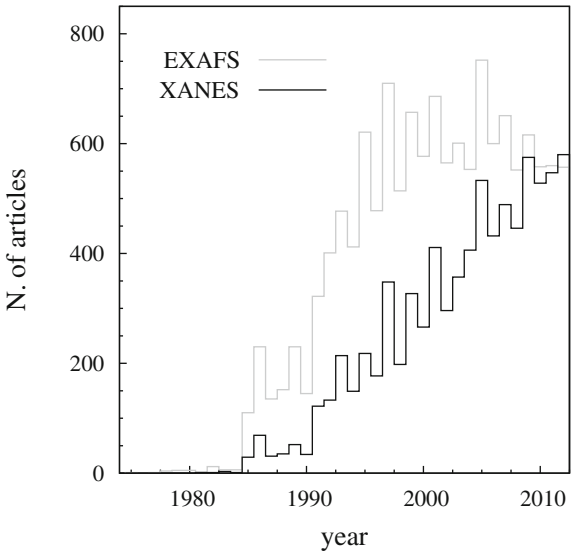


Fig. 7.1 Results of database search on ISI-web of knowledge using "EXAFS" ("XANES") in Topic OR Title fields

Traditionally [1] the XAFS signal is roughly distinguished in near edge and extended regions (Chap. 6). Such a distinction arising from profound differences on the major phenomena involved and data analysis procedures: the EXAFS signal is dominated by single scattering contributions and the theory provides a simple equation (Chaps. 6 and 17) well suited for data fitting and structural refinement. Getting closer to the absorption edge more in-depth theory is required as the progressively longer mean free path of low energy photoelectrons enhances the multiple scattering terms (FMS region) while the finest details characterizing the DoS close to the Fermi level and the interatomic potentials become definitively relevant. All these factors make the theory complex and may hinder the interpretation of the data.

Despite these difficulties, there are several reasons making XANES spectroscopy very suitable in condensed matter and material research, that have raised the interest of the research (Fig. 7.1) and stimulated the recent efforts for ab-initio XANES modeling [2, 3] and data refinement [4] procedures. In fact the spectral features are quite strong close to the edge, making the XANES signal less sensitive to data statistics, sample quality and X-ray beam intensity. These less restrictive requirements on sample quality and concentration makes XANES suitable for studies on natural samples, which are intrinsically inhomogeneous, or biological systems, often extremely diluted in its physiological states. Moreover the effect of structural disorder on XAFS is generally weak close to the edge, therefore the temperature dependence of XANES signal is weak, this allows extremely high temperature measurements preserving the main structural information. XANES data collection is generally fast, therefore is suited for time resolved experiments, especially in experiments aimed to reach the ps scale [5–7]. The near edge spectroscopic features are sensitive to even weak changes of valence state, coordination chemistry, local structure and ligand symmetry around

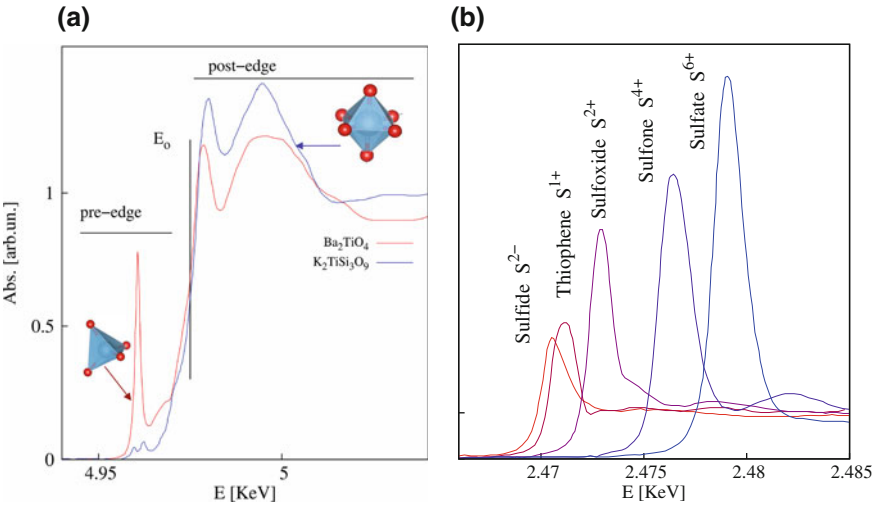


Fig. 7.2 Different Ti^{4+} coordination geometries produce evident differences in Ti K edge XANES (*left panel*). Sulfur K edge chemical shift in different S compounds (*right panel*)

the photoabsorber, and can be used as fingerprints to precisely identify chemical species in mixtures and complex materials. Interestingly is the possibility to probe bindings of light elements hardly visible by XRD and even EXAFS region (i.e. Hydrogen [8]) due to the rapid decrease of the backscattering amplitude functions. XANES can be relatively simply measured at low energies in order to study light elements essential in life sciences (i.e. Carbon or Oxygen). Finally XMCD represents an unique element selective probe for magnetism (see Chaps. 20, 29).

7.2 The Origin of Near Edge Features

Let us start illustrating the structural and electronic information available looking at the XANES region. For sake of clarity we can individuate three main regions in the spectra (Fig. 7.2a) which contains different structural and electronic details and may require different interpretation methods: the edge (E_o), the pre-edge ($E < E_o$) and the post edge ($E > E_o$).

The *edge* energy signals the onset of the continuum state and is related to the oxidation state of the photoabsorber (chemical shift): higher oxidation state raises E_o (Figs. 7.2b and 7.3) even by several eV per oxidation unit. Using the edge position to recognize the valence state of the photoabsorber has been early recognized as valuable method (Fig. 7.3) [9]. Also the shape of the edge is often characteristic of the chemical environment and ligand geometry, then it can be used as a fingerprint of a particular chemical specie. A good example is represented by the L_2 and L_3

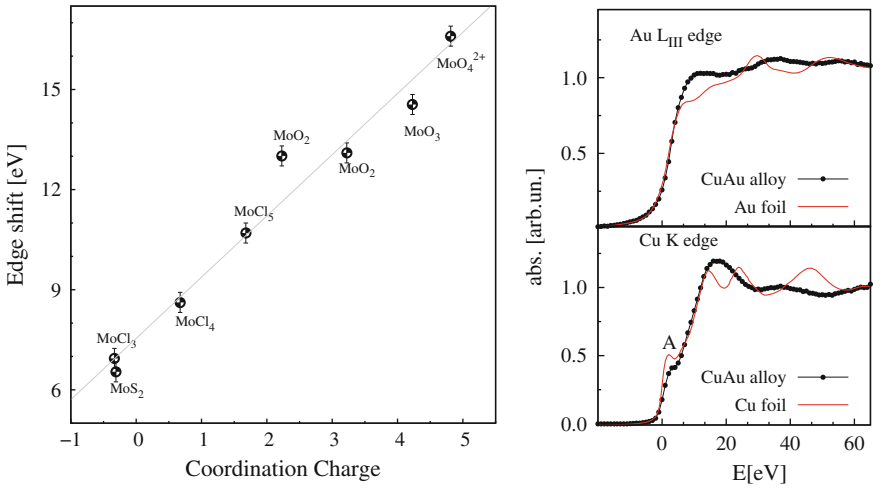


Fig. 7.3 *Left* Mo K edge energy (inflection point) in some Mo compounds measured respect to Mo foil edge, as a function of the absorber coordination charge (adapted from [9] *Copyright* (2013) American Chemical Society). *Right* Au L_{III} and Cu K edge spectra in CuAu thin film compared with metal foils data (*red*): the Au (Cu) XANES intensity at the edge increases (decreases) with respect to Au(Cu) foil due to charge transfer from Au to Cu [19]

edges of *n*d metals [10, 11] signaling $p_{1/2}$-nd and $p_{3/2}$-nd transitions. In each series ($n = 3, 4, 5$) the lower Z elements (Ti ($n = 3$), Zr ($n = 4$), Hf ($n = 5$)) present intense peaks (white line) at the edge signaling the transitions to empty *n*d levels. Raising the atomic number progressively fills the *n*d states, this reduces the white line intensity that disappears for the last elements (Cu ($n = 3$), Ag ($n = 4$), Au ($n = 5$)). This finding is used to reveal the *d*-band filling in oxides, intermetallic compounds and alloys [12, 13].

The *pre-edge* features mainly originate from dipole allowed transition to bound localized states, they are generally weak in metals but particularly evident in oxides. In this energy region the hybridization of the electronic levels is strongly affected by details of the crystalline field caused by the ligand geometry. This gives rise to large differences also for elements in the same valence state but having different local structure. For example Ti^{4+} K edge XANES (Fig. 7.2) depict sharp intense peak in Ba_2TiO_4 (tetrahedral Ti–O_4 units) which is absent in $K_2TiSi_3O_9$ (octahedral Ti–O_6 units) [14, 15]. This effect is due to complex phenomena involving the hybridization of the electronic levels. In this case we must notice that the K pre-edge features are dominated by dipole allowed excitation of s electrons to p-symmetry orbitals, while transitions to d orbitals is definitively scarce (quadrupolar transition) [16]. However hybridization may give *p–d* mixing (hybridization) providing intense dipole allowed transition of 1*s* electrons to the *p*-components of the hybrid orbitals. The group theory can be used to understand hybridization and interpret the pre-edge features in terms of coordination geometry [17, 18]. The character tables show that the regular

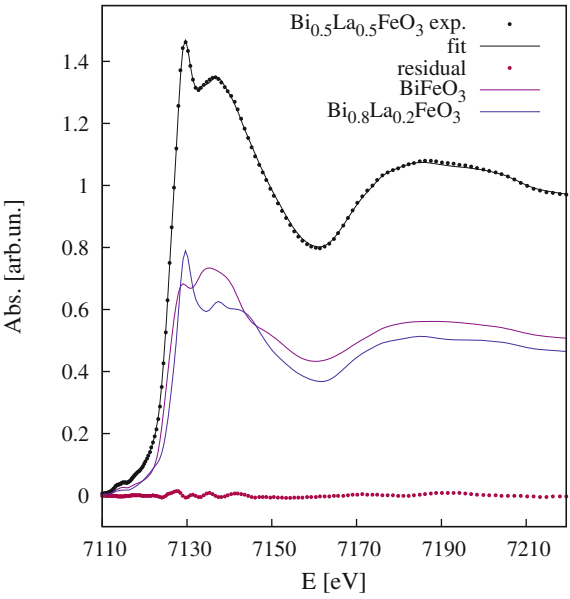


Fig. 7.4 Example of LCA of La doped $Bi_{1-x}La_xFeO_3$: the Fe K edge XANES of x = 0.5 sample is perfectly reproduced as sum of experimental spectra measured on pure $BiFeO_3$ (x = 0 and 0.2) samples. This finding establishes a solution limit around 20 % for La in $BiFeO_3$ [24]

tetrahedron (T_d point group) has the $p_{x,y,z}$ and $d_{xy,xz,yz}$ orbitals belonging to the same irreducible representation (T_2) thus allowing *p–d* hybridization giving rise to the intense pre-edge peak observed at K edge of tetrahedral bonded oxides. On the contrary octahedral bond symmetry (O_h point group representation) does not provide common representation for *p* and *d* orbitals, the absence of *p–d* hybridization generally causes the suppression of pre edge peak at K edge of octahedral coordinated metal oxides (Fig. 7.2a).

The *post-edge* region corresponds to photoelectrons excited in the *continuum* states. Due to the long mean free path of low energy electrons (Fig. 7.6) the absorption signal is dominated by FMS resonances. The recent progresses on ab-initio XANES modeling [2, 3] provide valuable details about local structure and coordination geometry. Moreover strategies have been recently developed [4] to permit structural refinement of XANES data through least square fitting.

It is worth mentioning here that the absorption of linearly polarized photons is an anisotropic process (Chap. 6), this is an interesting property that is exploited (polarized-XAFS) to selectively probe the local atomic structure along specific directions in asymmetric systems (i.e. layered systems, surfaces, interfaces). Polarized-XAFS can also be exploited to specifically discriminate details of the atomic structure along different crystallographic directions in single crystals [20].

Finally we mention here the XMCD effect (Chap. 20), intense in the near edge region, providing unique element specific magnetic information as the signal intensity is related to the magnetic moment of the photoabsorber. It is a valuable magnetic probe under extreme conditions such as high pressure [21, 22, Chap. 29] and high magnetic fields. Noticeably sum rules exist for L edges XMCD signal which in

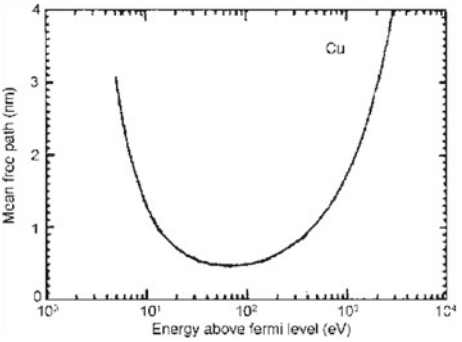


Fig. 7.5 Typical mean free path $\lambda(E)$ behavior in metal

principle would offer a unique possibility to distinguish between spin and orbital contributions to the magnetic moment of the absorbers [23].

7.3 Semi-quantitative Understanding of XANES Features

Ab-initio XANES analysis may result a complex task as it requires specific theoretical skill and in-depth knowledge. Moreover ab-initio XANES calculations can be extremely time consuming in case of complex structures. However the phenomenological interpretation of XANES features is often more intuitive and immediate, then it can provide quick characterization preliminary to more accurate investigation and/or complementary to other experimental probes (XRD, XPS, TEM, etc. …). Several methods have been exploited to achieve specific information about local structure and electronic nature of the photoabsorber. A brief overview of valuable approaches, although qualitative or semi-quantitative, is presented here, organized according the selected features of XANES region (Fig. 7.2a).

Edge shift: The edge position of many elements may depict significant shift as a function of their oxidation state. Therefore, provided a proper energy calibration on reference compounds, the edge position can be used to rapidly assign the oxidation state of the absorber [9, 25]. Checking the oxidation state of the absorber is strongly suggested in metallo-protein crystallography to check the sample integrity. In fact exposure to the intense SR beam may provokes photoreduction of metals worsening the crystallographic information [26].

Linear combination analysis (LCA): The LCA method represents a simple way to quantify the relative amount of chemical species in mixtures and multiphase compounds and it is widely used for quick and reliable XANES interpretation. It exploits the fact that the shape of the XANES reflects the chemical environment of the absorber [25], then it can be interpreted in comparison with the spectra of reference compounds: the normalized experimental spectrum μ_{exp} of unknown samples,

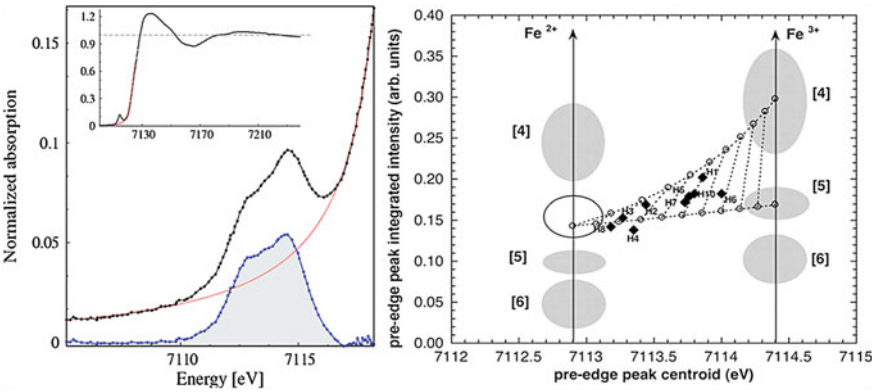


Fig. 7.6 *Left*: example of Fe K edge normalization and extraction of Fe pre-edge contribution. *Right* (reprinted from [33]): pre-edge peak integrated intensity versus the centroid are presented for a set of investigated samples (*dots*), compared with the values measured for reference samples [15, 34] (*grey regions*) in which the Fe oxidation state and coordination numbers (reported in *square brackets*) are known. This allow to understand the average oxidation state and the average coordination number of Fe in samples

is fitted to a theoretical curve μ_{th} calculated as a linear combination of normalized reference compound spectra (Fig. 7.4):

$$\mu_{\exp} = \sum\nolimits_j \alpha_j \mu_{th}$$

the parameters α_j represent the fraction of absorbers in the jth environment/chemical state. Notice that although LCA is a simple method, it requires a proper set of good quality spectra measured on reference compound. Preferably samples and reference spectra must be measured during the same experimental run to avoid artefacts due to different experimental configurations. For example the effect the energy resolution is crucial as it determines the smoothing of the structural features which are sharper near to the absorption edge.

Recent innovative materials, like multiferroic systems, diluted semiconductors (Chap. 17) and so on, depict special physical properties originating from a delicate interplay among structure, composition, magnetic and electronic interactions. In these compounds XAFS play a valuable role, giving the possibility to reveal parasitic phases which may occur during the synthesis, often hidden to standard probes [27]. In particular LCA XANES analysis is quick way to easily recognize structural inhomogeneities [28–30]. LCA approach is also suited in environmental sciences, cultural heritage, biomedical sciences, and so on, because natural samples [31, 32] are intrinsically inhomogeneous, often mixtures and composite materials in which the absorber may be found in different phases, chemical states and local environment.

Principal component analysis (PCA): The PCA method [35] is based on more sophisticated linear algebra techniques and is widely used in pattern recognition: it is

an automatic method in which a set of relevant contributions (principal components) is selected out of a wide ensemble of reference spectra (components). The PCA algorithms automatically reproduce the experimental data as a linear combination of the principal components, selected using only statistical considerations. PCA XANES data analysis is a valuable approach to routinely treat ample data sets as for environmental monitoring [36] but care is required to choose a plausible set of components and carefully check the resulting principal components in order to avoid non-physical answers.

Deconvolution of XANES features: The spectral features close around the edge can be interpreted as relatively sharp peaks, signifying the transitions to localized states, over a smooth background modeling the broad transition to the continuum states. The distribution of the localized states close to the Fermi level are strongly affected by local symmetry and binding geometries, therefore the shape, intensity and position of the XANES peaks as a function of environmental parameters such as temperature, pressure, chemistry, etc. ..., may provide structural and electronic details, specially in comparison with reference systems. A very representative example is the possibility to understand the Fe^{2+}/Fe^{3+} ratio and the average Fe coordination number measuring the centroid and area of Fe pre-edge peak [15, 34] (Fig. 7.5), this method is widely exploited in environmental science to quickly determine average coordination number and valence state of the absorber [33, 37].

7.4 Theoretical Background and the Fit of the XANES Energy Region

XAS spectroscopy concerns the study of the electronic transitions from atomic inner shells to unoccupied states of the system under study. In this spectroscopy the absorption coefficient μ is measured as function of energy and it is proportional to the density n_a of the photoabsorber in the medium and can be written as $\mu(E) = n_a\, \sigma(E)$, where $\sigma(E)$ is the total absorption cross section. This quantity can be calculated on the basis of the so-called Fermi "golden rule", which can be written, within the dipole approximation, as

$$\sigma(\omega) = 4\pi^2 \alpha_0 \hbar\omega \sum_f \left| \left\langle \Psi_f^N \right| \boldsymbol{\varepsilon} \cdot \sum_{i=1}^{N} \mathbf{r}_i \left| \Psi_g^N \right\rangle \right|^2 \delta(\hbar\omega - E_f^N + E_g^N) \tag{7.1}$$

where the initial and final states are in general quite complicated many-body functions. Here $\boldsymbol{\varepsilon}$ is the polarization vector of the incoming photon and $\mathbf{r}_i$ is a generic vector indicating the position of the ith electron. These take into account all the possible excitation processes that occurred during the absorption of a photon and the creation of a hole in the core level $\phi^c_{L_0}$ of angular momentum $L_0 = (l_0, m_0)$. We assume that, to a good approximation [38],

$$\Psi_g^N(\mathbf{r}, \mathbf{r}_1, \ldots, \mathbf{r}_{N-1}) = \sqrt{N!} A \phi_{L_0}^c(\mathbf{r}) \sum_n c_n \Phi_n^{N-1}(\mathbf{r}_1, \ldots, \mathbf{r}_{N-1}) \quad (7.2a)$$
$$= \sqrt{N!} A \phi_{L_0}^c(\mathbf{r}) \Psi_g^{N-1}(\mathbf{r}_1, \ldots, \mathbf{r}_{N-1})$$

where A is the usual anti-symmetrization operator and $\Phi_n^{N-1}(\mathbf{r}_1, \ldots, \mathbf{r}_{N-1})$ are Slater determinants describing the configurations present in the ground state of the system. For simplicity we shall omit spin variables, since we are going to deal with non-magnetic systems. In a similar way we can write without loss of generality

$$\Psi_f^N(\mathbf{r}, \mathbf{r}_1, \ldots, \mathbf{r}_{N-1}) = \sqrt{N!} A \sum_\alpha \phi_\alpha^f(\mathbf{r}) \tilde{\Psi}_n^{N-1}(\mathbf{r}_1, \ldots, \mathbf{r}_{N-1}) \quad (7.2b)$$

where the functions ϕ_α^f, ignoring exchange effects, can be thought to describe the excited photoelectron. The $\tilde{\Psi}_\alpha^{N-1}$ states are eigenstates of the Hamiltonian H^{N-1}describing the remaining $(N-1)$-electron system with eigenvalues E_α^{N-1}:

$$H^{N-1} \tilde{\Psi}_\alpha^{N-1} = E_\alpha^{N-1} \tilde{\Psi}_\alpha^{N-1} \quad (7.3a)$$

The tilde stands as a reminder that in the expansion (7.2b) the relaxed states around the core-hole are dominant. If needed, they can be in turn expanded in terms of Slater determinants describing the intervening configurations in the final state. Borrowing the term from many-particle scattering theory, we can call the states $\tilde{\Psi}_\alpha^{N-1}$ final state channels.

The wave function Ψ_f^N is an eigenstate of the total hamiltonian H^N with eigenvalue $E_f^N = E_g^N + \hbar\omega$, i.e.

$$H^N \Psi_\mathrm{f}^\mathrm{N} = \mathrm{E}_\mathrm{f}^\mathrm{N} \Psi_\mathrm{f}^\mathrm{N} \quad (7.3b)$$

moreover

$$H^N = -\nabla_{\vec{r}}^2 + \sum_i V(\mathbf{r}, \mathbf{r}_i) + H^{N-1} \quad (7.3c)$$

where $V(\mathbf{r}, \mathbf{r}_i)$is the interaction potential of the excited photoelectron with the rest of the system. By inserting (7.2b) into (7.3b), projecting onto the states $\tilde{\Psi}_\alpha^{N-1}$and using (7.3a), one obtains for the amplitude functions ϕ_α^f the set of coupled equations,

$$(\nabla^2 + k_\alpha^2)\phi_\alpha^f(\mathbf{r}) = \sum_\beta \int V_{\alpha\beta}(\mathbf{r}, \mathbf{r}')\phi_\beta^f(\mathbf{r}')d^3r' \quad (7.4a)$$

where

$$k_\alpha^2 = \hbar\omega - (E_g^{N-1} - E_g^N) - (E_\alpha^{N-1} - E_g^{N-1}) = \hbar\omega - I_c - \Delta E_\alpha \quad (7.4b)$$

In (7.4b), I_c is the ionisation potential for the core-state and ΔE_α the excitation energy left behind in the $(N-1)$-particle system. The non-local inter-channel potentials $V_{\alpha\beta}(\mathbf{r}, \mathbf{r}')$ are the matrix elements between states $\tilde{\Psi}_\alpha^{N-1}$ and $\tilde{\Psi}_\beta^{N-1}$ of the interaction potential $V(\mathbf{r}, \mathbf{r}_i)$ and include local terms coming from the Coulomb interaction as well as non-local exchange terms originating from the exchange interaction.

The set of (7.4a) is to be supplemented with the boundary conditions related to the behaviour of the photoelectron at infinity and to the state of the $(N-1)$-electron system according to the partition of the total energy $E_f^N = E_g^N + \hbar\omega$ between them. To each different partition there corresponds a different set of boundary conditions leading to a different solution of the set of equations (7.4a). For more details we refer the reader to [39], where a formal solution of these equations is given in the framework of the multi-channel multiple scattering theory [39]. The set of equations in (7.4a) contains the complete description of all the outcomes of the photoemission process, be it of intrinsic origin (i.e. consequent to the relaxation of the system around the core hole) or extrinsic (excitations created by the photoelectron on its way out of the system). Their complete solution is out of question; however one can analyse their consequences in particular cases. Since we are mainly interested in structural analysis, both in photo-emission and photo-absorption, we need only consider the completely relaxed or elastic channel (i.e. the one for which $\Delta E_\alpha = 0$), since this is the only one capable of carrying structural information. For simplicity we shall attribute to this channel here and in the following, the index $\boldsymbol{\alpha} = 0$.

We can solve the set of coupled Schrödinger equations (7.4a) by eliminating all unwanted channels in favor of the elastic one. The result is a single equation for the channel function $\phi_0(\mathbf{r})$with an effective complex energy dependent non-local optical potential of the kind,

$$(\nabla^2 + k_0^2 - V_c(\vec{r}))\phi_0(\mathbf{r}) = \int \Sigma^{opt}(\mathbf{r}, \mathbf{r}'; \hbar\omega)\phi_0(\mathbf{r}')d^3r' \tag{7.5}$$

where we have isolated its local Coulomb part and indicated the energy dependence coming from the eliminated channels by the argument $\hbar\omega$ in Σ^{opt}. We can solve this equation, with the right asymptotic boundary conditions, using the Multiple Scattering (MS) theory. This can be done by transforming this integro-differential equation into a Lippman-Schwinger equation with non-local potential, following the method illustrated in [39, 40]. In these papers the derivation of the MS equations is given for local potentials, but it is clear that the same derivation is valid for non-local potentials as well.

The MS theory is a method to calculate from first principle the electronic structure of polyatomic molecules and solids. This method [41, 42] avoids many of the difficulties of the standard methods of quantum chemistry and band theory, leading to an accurate description of the wave function in molecules and solids of considerable stereo-chemical complexity. This method works in the real space without the need of any spatial symmetry and translation invariance. This last point is particularly relevant in the calculation of X-ray absorption spectra from core levels because the presence of the core-hole in the final state breaks any translational invariance.

Using this method one can calculate both bound states and the continuum part of molecular wave function. The MS theory normally uses the so-called "muffin-tin" (MT) approximation for the shape of the potential of the cluster of atoms used in the calculation. This means that the space is partitioned into distinct atomic and interatomic regions. Each atom is enclosed in a sphere of a given radius, the so-called MT radius, and an outer sphere envelops the whole molecule. Three regions can be identified: the atomic regions (spheres centered on nuclei), the extra molecular region (the space beyond the outer sphere) and an interstitial region of complicated geometry in which the molecular potential is approximated by a constant position independent potential. The potential within the atomic spheres and outside the outer region is also spherically averaged.

Rather than following the standard MS procedure presented in the above mentioned papers, it is convenient to introduce a Green's function matrix with outgoing boundary conditions

$$G^{+}_{\alpha\alpha'}(\mathbf{r},\mathbf{r}';E)=\sum_{f}\frac{\phi^{f}_{\alpha}(\mathbf{r})[\phi^{f}_{\alpha'}(\mathbf{r}')]^{*}}{E-\Delta E_{f}-k_{f}^{2}+i\eta} \tag{7.6}$$

In this way the photo-absorption cross section is easily seen (using the relation between the delta function and the principal part of the integral) to be

$$\sigma_{abs}(\omega)=-8\pi\alpha\hbar\omega\mathrm{Im}\sum_{m_0}\int\int d^3r\phi^{c}_{L_0}(\mathbf{r})\boldsymbol{\varepsilon}\cdot\mathbf{r}\cdot\sum_{\alpha\alpha'}S^{*}_{\alpha}S_{\alpha'}G^{+}_{\alpha\alpha'}(\mathbf{r},\mathbf{r}';\hbar\omega-I_c)\boldsymbol{\varepsilon}\cdot\mathbf{r}'\phi^{c}_{L_0}(\mathbf{r}')d^3r' \tag{7.7}$$

where the Green's function matrix satisfies the set of coupled equations:

$$(\nabla^2+k^2_{\alpha})G^{+}_{\alpha\beta}(\mathbf{r},\mathbf{r}';E)-\sum_{\gamma}\int V_{\alpha\gamma}(\mathbf{r},\mathbf{r}'')G^{+}_{\gamma\beta}(\mathbf{r}'',\mathbf{r}';E)d^3r''=\delta_{\alpha\beta}\delta(\mathbf{r}-\mathbf{r}') \tag{7.7a}$$

writing E for $\hbar\omega - I_c$ and S_α is the overlap factor $\left\langle\tilde{\Psi}^{N-1}_{\alpha}|\Psi^{N-1}_{G}\right\rangle$.

The $G_{\alpha,\beta}(\mathbf{r},\mathbf{r}';E)$ is the inter-channel matrix representing the amplitude probability of propagation of the excited photoelectron from point $\vec{r}$ to point $\vec{r}'$ while at the same time the excitation energy left in the system changes from ΔE_α to ΔE_β. The Green's function matrix satisfies a set of coupled equations that contains the complete description of all the possible outcomes of a photoemission process, be it of intrinsic origin, i.e. consequent to the relaxation of the system around the core hole, or of extrinsic origin, i.e. created by the photoelectron on its way out of the system. This set is the translation of the (7.4a) set into the language of Green's functions.

Again, the elimination of all channels in favour of the relaxed one ($\boldsymbol{\alpha} = 0$) leads to the following expression

$$(\nabla^2 + k_0^2 - V_c(\mathbf{r}))G_{00}^{+}(\mathbf{r}, \mathbf{r}'; E) - \int \Sigma^{opt}(\mathbf{r}, \mathbf{x}; E)G_{00}^{+}(\mathbf{x}, \mathbf{r}'; E)d^3x = \delta(\mathbf{r} - \mathbf{r}') \tag{7.8}$$

for the elastic part of the Green's function matrix. This respond to an equation that is analogous to (7.5) with the same optical potential. Because of the predominance of such channel we can write

$$\sum_{\alpha\alpha'} S_\alpha^* S_{\alpha'} G_{\alpha\alpha'}^{+}(\mathbf{r}, \mathbf{r}'; E) = |S_0(\omega)|^2 G_{00}^{+}(\mathbf{r}, \mathbf{r}'; E) \tag{7.8a}$$

and the total absorption cross section becomes:

$$\sigma_{abs}(\omega) = -8\pi\alpha\hbar\omega\,|S_0(\omega)|^2 \cdot \mathrm{Im}\sum_{m_0}\int\int d^3r\phi_{L_0}^{c}(\mathbf{r})\;\boldsymbol{\varepsilon}\cdot\mathbf{r}\;G_{00}^{+}(\mathbf{r}, \mathbf{r}'; E)\;\boldsymbol{\varepsilon}\cdot\mathbf{r}'\phi_{L_0}^{c}(\mathbf{r}')d^3r' \tag{7.9}$$

Because we are dealing only with the fully relaxed channel, hereafter the suffix 0 indicates the absorbing site. Due to the localization of the core state we need the solution of (7.8) only for the photo-absorption site 0. The solution within MST for a collection of a muffin-tin type of potential, for $\mathbf{r}$ in cell i and $\mathbf{r}'$ inside the sphere where the absorbing site is located, can be written as [43]:

$$G_{00}^{+}(\mathbf{r}, \mathbf{r}'; E) = -k\sum_{L,L'} R_L^0(\mathbf{r})\tau_{LL'}^{00}R_{L'}^0(\mathbf{r}') + \sum_{L} R_L^0(\mathbf{r})\,S_L^0(\mathbf{r}') \tag{7.10}$$

where $R_L^0(\mathbf{r})$ and $S_L^0(\mathbf{r}')$ are the regular and irregular part of the solution at the origin, $\tau_{LL'}^{00}$ is the scattering path operator of the MS theory defined as $\tau_{LL'}^{00} = [(I - T_aG)^{-1}T_a]_{LL'}^{00}$. The matrix T_a is a diagonal matrix defined through the atomic t-matrix as $T_a = \delta_{ij}\delta_{LL'}t_1^i$ and G are the off-diagonal free electron propagators written using spherical harmonics [44, 45]. This operator contains all the electronic and geometrical information about the atomic cluster. Through this operator it is possible to demonstrate the complete equivalence between the Green function approach, the band structure calculation, and MS theory [44].

At this point we are left with the problem of determining the nature of the optical potential $\Sigma^{opt}(\mathbf{r}, \mathbf{r}'; E)$ in (7.8). This potential contains [46, 47] both the effect of the intrinsic channels (excitations induced in the system by the sudden creation of the core hole) and of the extrinsic channels (excitations created by the photoelectron in its way out of the system). Unfortunately a practical scheme for realistic calculations has not yet been devised. The only optical potentials currently in use are those based on the Dyson self-energy of the photoelectron propagation in the system. This clearly accounts only for the extrinsic losses. Depending on the systems, various reasonable approximations have been devised. It is well known, for example, that for metals one obtains very good agreement with the observed absorption spectra using a one

particle approach with an X-α potential and convoluting the calculated spectrum with a Lorentzian broadening function having an energy dependent width related to the mean-free path of the photoelectron in the system by the relation [48].

$$\Gamma(E) = \frac{\hbar}{\lambda(E)}\sqrt{\frac{2E}{m}} \tag{7.11}$$

where $\boldsymbol{\Gamma(E)}$ is the full width half maximum. In the framework of the above multi-channel approach this finding can be rationalized by observing that in a metal the completely relaxed channel together with the plasmon excitation channels (whether intrinsic or extrinsic) almost completely exhaust the sum rule

$$\sum_{\alpha} |S_{\alpha}|^2 = \sum_{\alpha} \left\langle \Psi_g^{N-1} \middle| \tilde{\Psi}_{\alpha}^{N-1} \right\rangle \left\langle \tilde{\Psi}_{\alpha}^{N-1} \middle| \Psi_g^{N-1} \right\rangle = \left\langle \Psi_g^{N-1} \middle| \Psi_g^{N-1} \right\rangle = 1 \tag{7.12}$$

which holds due to the completeness of the intermediate relaxed states $\tilde{\Psi}_{\alpha}^{N-1}$. Indeed we have already observed that the intensity of the double electron excitation channels is of the order $10^{-2} \div 10^{-3}$ times the main relaxed channel. Therefore an optical potential given by $V_{X-\alpha} + i\Gamma(E)$ is able to give a satisfactory picture of the absorption process for metals. The only discrepancy with experiments lies in the calculated absorption maxima falling short of the observed ones due to the energy independence of the X-α exchange. A better approximation is provided by the Hedin–Lundqvist (HL) potential [49, 50] due to its energy dependent exchange and its imaginary part, which is able to reproduce rather accurately the observed mean-free path in metals (Fig. 7.5) [51].

This is the self-energy, based on the GW approximation, of an electron propagating in an homogeneous interacting electron gas, calculated at the local density of the system under study. Although initially devised to describe exchange and correlation corrections to the Coulomb potential due to the valence charge, Lee and Beni [1] have extended its validity in the atomic core region as well.

By neglecting the effect of the intrinsic processes, one can indeed approximate $\Sigma^{opt}(\mathbf{r}, \mathbf{r}'; E)$ as the Dyson self-energy of the photoelectron in the final state. This approximation is consistent with the physical picture of the photo-absorption process, in which we add an electron to the ground state of the (Z+1)-equivalent atom. From this point of view $G_{00}(\mathbf{r}, \mathbf{r}'; E)$ describes the propagation amplitude of the excited photoelectron from point $\vec{r}$ to point $\vec{r}'$. This is the probability amplitude that the added electron remains in the same original state in which it was added to the system. Its imaginary part gives the total probability amplitude for scattering out of this initial state. In this scheme the self-energy $\Sigma^{opt}(\mathbf{r}, \mathbf{r}'; E)$ acts as a complex optical potential that describes the reduction of the wave-function amplitude of the elastic channel, due to the transitions to all the other channels. The localization of the initial core state has the consequence that the optical paths of the photoelectron in the final state begin and end at the photo-absorbing site. We expect that neglecting the effects of the intrinsic processes on $\boldsymbol{\Sigma}(\mathbf{r}, \mathbf{r}'; E)$ is a reasonably good approximation, since

their main effect is already incorporated in the shape function $|S_0(\omega)|^2$. One can therefore interpret the HL potential as an effective optical potential that controls the propagation and damping of the excited photoelectron everywhere in the system. In this approach it can be viewed as a local density approximation to the self-energy of the photoelectron in real systems. Nowadays it is the potential most widely used with varied success in the calculation of the absorption and photoelectron diffraction cross sections of many systems, ranging from metals and semiconductors to ionic and covalent systems.

Once the optical potential has been specified, one can proceeds to the calculation of $G^{+}_{00}(\mathbf{r}, \mathbf{r}'; E)$ through the scattering path operator $\boldsymbol{\tau}^{00}_{LL'} = [(I - T_a G)^{-1} T_a]^{00}_{LL'}$. The regular and irregular part of the radial part of the solution are easily found by the standard Numerov procedure. The inversion of the MS matrix $(I - T_a G)$becomes time consuming at energies greater than about 50–150 eV, depending on the number of atoms in the cluster. Fortunately in the majority of cases, above ∼50 eV one can invert the MS matrix by series expansion.

In general the total absorption cross section [45] can be written as (in the un-polarized case):

$$\sigma(E) = (l+1)\sigma_0^{l+1}(E)\chi^{l+1}(E) + l\sigma_0^{l-1}(E)\chi^{l-1}(E) \tag{7.13}$$

where $\sigma_0^l(E)$ is the atomic cross section of the absorbing atom at a given edge, and

$$\chi^l(E) = \frac{1}{(2l+1)\sin^2\delta_l^0} \sum_m \mathrm{Im}[(I - T_a G)^{-1} T_a]^{00}_{lm\,lm} \tag{7.14}$$

is a structure factor carrying all the information about the atomic cluster around the absorber. Notice that in the case of isolated atom, i.e. if $G = 0$, this structure factor is equal to one and the total cross section reduces to the atomic one, which is defined as:

$$\sigma_0^l(E) = \frac{8\pi^2}{3}\alpha k(E + I_0)\sin^2\delta_l^0 \int_0^\infty r^3 R_l^0(r)\phi_{l_0}(r)dr \tag{7.15}$$

where $\boldsymbol{\delta}_l^0$ is the l-phase shift of the absorbing atom for a muffin-tin type of potential. The atomic cross section is essentially without structures (in a one-electron approximation) and almost independent of the energy. The final angular momentum l is defined as $l = l_0 \pm 1$according to the dipole selection rules.

The factorization between atomic absorption and structure factor is strictly possible only if the potential is real, but it should be noted that the irregular part gives a negligible contribution to the cross section. For this reason and for sake of simplicity we neglect this part and the above factorization holds. To enlighten the physical meaning of the photoabsorption process, it is convenient to perform the inversion of the MS matrix $(I - T_a G)$by series:

$$(I - T_a G)^{-1} = \sum_{n=0} (T_a G)^n \tag{7.16}$$

provided that the spectral radius $\boldsymbol{\rho}(T_a G)$ (maximum modulus of the eigenvalues) of the matrix $T_a G$ is less than one. In such a case the structural factor $\chi^l(E)$ becomes:

$$\chi^l(E) = 1 + \sum_{n=2} \chi_n^l(E) \tag{7.16a}$$

with

$$\chi_n^l(E) = \frac{1}{(2l+1)\,\sin^2 \delta_l^0} \sum_m \mathrm{Im}[(T_a G)^n T_a]_{lm\,lm}^{00} \tag{7.17}$$

and, $\chi_o^l(E) = 1$, $\chi_1^l(E) = 0$ since G is off-diagonal in the site indices. Each $\chi_n^l(E)$ represents the partial contribution of order n to the photoabsorption coefficient of the cluster under study, coming from all process where the photoelectron emanating from the absorbing site 0 is scattered n$-$1 times by the surrounding atoms before returning to site 0 and later escaping to free space due to the boundary condition. Due to the localization of the initial core state only closed paths beginning and ending at the absorbing atom are possible. It is this peculiarity that entails the site specificity of XAS spectroscopy and makes it a unique tool for studying structural problems and for probing higher order correlation functions in condensed matter. The development in (7.9) is the MS expansion with spherical wave propagators; the $\chi_2^l(E)$ term is the usual EXAFS signal. It is possible to write down complicated expressions for each higher order term $\chi_n^l(E)(n \geq 3)$ using the (3n $-$ 3)$-$j symbols. However their practical usefulness decreases with increasing order. It is much easier to generate them by using a MS program that already calculates the structural signal $\chi^l(E)$by performing the matrix inversion either exactly or via the series expansion. It is also possible to derive recursive relations between consecutive $\chi_n^l(E)$ terms.

For practical application to data analysis the functional form of the quantities $\chi_n^l(E)$is given by the simple expression:

$$\chi_n^l(E) = \sum_{p_n} A_n^l(k, R_{ij}^{p_n}) \sin[k R_{p_n}^{tot} + \varphi_n^l(k, R_{ij}^{p_n})] \tag{7.18}$$

where the sum is over all possible paths $p_n$of order n defined above and $R_{p_n}^{tot}$is the corresponding path length. This form follows from the fact that each spherical wave propagator G carries a factor $e^{ikR_{ij}}$independent of L and L$'$ that can be factorized, and is contained in the Hankel functions of the propagators. It is the form expected on the basis of the interference process between the outgoing and backscattered photoelectron wave at the absorbing site. As a consequence, under the assumption that the MS series converges, one can always fit an experimental spectrum with a series of EXAFS like functions.

To clarify the effect of using the complex potential we observe that the MS series is formed by two building blocks: the propagator $G^{ij}_{LL'}$between site i and j and the l-wave atomic t-matrix t^i_l of the atom at site i. The general term of the MS series is built by several repetitions of the product $t^i_l G^{ij}_{LL'}$ that brings out a factor $e^{-2\delta_2}\, e^{-k_2 R_{ij}}$ when a complex potential is used. Here δ_2 and k_2 are the complex part of the atomic phase shift and wave vector respectively. The complex potential results in the existence of a damping factor that reduces the amplitude of the elastic signal. The interpretation of the XAS spectrum in terms of MS pathways of the photoelectron in the final state is meaningful only if there is numerical equivalence between the two sides of (7.12). This implies that the expansion on the right side of (7.9). must converge to the left site relative to some convergence criterion. From the matrix theory the absolute convergence (relative to some matrix norm) is ensured if $\boldsymbol{\rho}(T_a G) < 1$. This criterion is extremely useful since the absolute convergence entails the property that terms of order n in the series higher than a certain n_0 do not contribute appreciably to the sum. Now $\boldsymbol{\rho}(T_a G)$is a continuous function of the photoelectron wave number k, which goes to zero as k goes to infinity (since $t^i_l \to 0$in this case) and tends to the infinity as k goes to zero because G is singular at $k = 0$ due to the presence of the Hankel function in the definition of the propagators. As a consequence it must cross at least once the value $\rho = 1$; the nearer to 1 is its value the slower is the convergence of the series.

According to the size of the spectral radius $\boldsymbol{\rho}(T_a G)$, one can roughly divide the photoabsorption spectrum into three regions. (1) A full multiple-scattering (FMS) region, characterized by $\rho(T_a G) \geq 1$, where an infinite number of paths (or a great number of them) contribute to the shape of the spectrum. For low Z scattering atoms, this is usually near the edge region, 20–40 eV within the absorption edge. This is the region of the shape resonances where the scattering power of the environment is strong enough that it can scatter the photoelectron many times. Only global information can be extracted from the experimental data such as the point group symmetry and relations of the type $k_r R = \text{const}$. (2) An intermediate multiple-scattering (IMS) region characterized by $0.5 \leq \rho(T_a G) \leq 0.8$, where only a limited number of paths of low order contribute due to the convergence of the MS series. Typically this is in the energy range 30 eV to 200 eV above the absorption edge. It is also the region where information on bond lengths and angles between bonds are contained, since the photoelectron is sensitive to the relative position of two, three or more atoms at the time via the MS paths. (3) A single scattering (SS) region, characterized by $\rho(T_a G) \leq 0.5$, where only paths of order n = 2 contribute significantly. This is the region where the photoelectron is sensitive only to the pair-correlation function, i.e. the relative positions of the central atom and the backscattering atoms. It obviously extends in the IMS and FMS region as well. The corresponding signal is usually referred to as EXAFS in the literature and its energy region extends beyond 200 eV [45].

In Fig. 7.7 (left panel) the experimental evidence of the existence of the three energy regions discussed above is pointed out. The 50 mM aqueous solutions of $MnCl_2$ and $KMnO_4$ salts form an octahedral and tetrahedral cluster of metal-oxygen

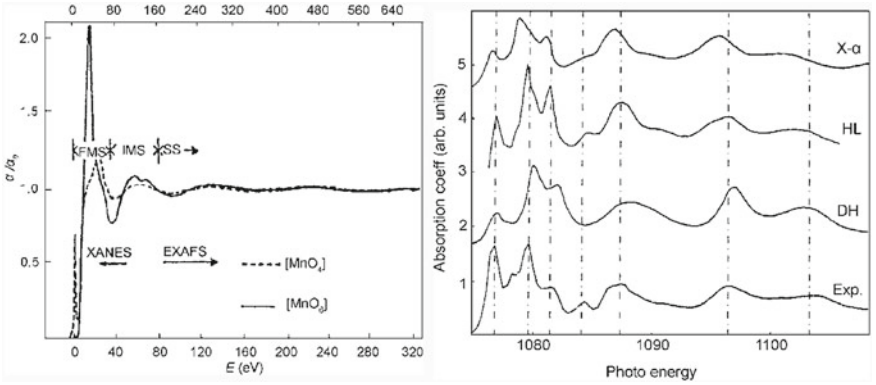


Fig. 7.7 *Left panel*: Comparison between normalized Mn *K*-edge XAS spectra of $(MnO_4)^-$ and $[Mn(OH_2)_6]^{2+}$ ions in water solution. The respective energy scales are given in the *upper* and *lower part* of the figure respectively. The normalization is to a value of the atomic absorption at very high energy. A partition of the spectra in FMS, IMS and SS regions is sketched. *Right panel*: Na K-edge in the NaCl system. Comparison between the experimental data (*lowermost curve*) and three calculations performed with different choices of the exchange and correlation potential

ions respectively. Mn ion is octahedrally coordinated by six H_2O molecules forming a stable $[Mn(OH_2)_6]^{2+}$ cluster with a Mn–O distance $d_1 = 0.217$ nm while the tetrahedral (MnO_4)-cluster is known to have a Mn–O distance $d_2 = 0.163$ nm. In Fig. 7.7 (left panel) the absorption spectra of both compounds are reported. The corresponding energy scales are in the ratio $d_2/d_1 = 0.47$ where d_2 and d_1 are now the Mn–O distances in the two complexes, corrected for the linear term coefficient of the backscattering phase shift according to (7.15). The zero of the energy has been set at the first absorption feature, the $1s$-$3d$ transition, in both spectra. In this way the two spectra, after a further rescaling of the amplitude to take into account of the different number of atoms around the absorber, show a superposed behavior in that energy region that contain information only about the pair correlation function, i.e. the SS energy region. Lower in energy the two spectra are different indicating that information about higher order correlation functions is contained in the XAS spectra.

This is the normal behavior. However a rather unexpected situation may also occur when the spectral radius may stay near unity at some intermediate energies, and then decreases as the energy decreases toward the edge. This situation is encountered in the cupper K-edge spectrum, where in the first 50 eV above the edge the EXAFS signal alone is capable of reproducing the XAS experimental data. Deviations begin to show up in the energy range 50–200 eV due to the peculiarity of the relevant atomic phase shifts $\delta_l^j(E)$ that are small at low energy and cross $\pi/2$ at about 130 eV. Around this energy MS contributions show up in the XAS spectrum.

The general picture of an XAS spectrum that emerges from the preceding discussion is one in which oscillating signals with variable amplitudes are superimposed on a background of a more or less smooth atomic absorption. In the region of con-

vergence of the MS series the SS signal is strongest and acts as a carrier wave that supports all of the other MS waves. Summarizing we can say that in principle any XAS spectrum contains all the three regions mentioned above. Their order with increasing energy and their energy extent are obviously system dependent. The only feature common to all systems is that in the limit of high energy the IMS region should continuously merge into the SS region and finally reduce to pure atomic absorption. This picture is inspiring all the modern methods of analysis of the experimental XAS data.

Typical calculations performed with the method presented above are reported in Fig. 7.7 (right panel). In this figure we report the comparison between the experimental data of the Na K-edge in the NaCl system with three different calculations obtained using X-α exchange potential, a Dirac–Hara (DH) energy dependent exchange potential and HL exchange and correlation complex potential. For these calculations we used a nine-shell cluster formed by 123 atoms. Because both DH and X-α potential are real, the corresponding calculations were convoluted with the imaginary part of the HL potential. The theoretical spectra are further convoluted to account for the experimental resolution and for the core-hole lifetime. The agreement between experimental data and the theoretical calculations is good in the whole energy range both concerning the shape and the energy position of the different features in the spectrum. Moreover it appears clear that the HL potential shows the best agreement with the experiment. This behavior is a general finding for crystalline materials while small problems remain in the first 20–30 eV basically linked to treatment of the inelastic losses in the molecular systems where the HL scheme seems to be inadequate.

In the structural analysis of XAS spectra much attention has been devoted to the inclusion of vibrational effects in the general term of the MS series, but little effort has been put into incorporating such effects directly into the scattering path operator. The reason is both historical and methodological, since on one hand interest was concentrated in analyzing the spectral region where the MS series is converging and the damping effect of the atomic vibrations is sizable. On the other their inclusion in the near edge spectral region was theoretically more difficult and estimated of minor importance. Recently this problem [52, 53] has been solved using the augmented space formalism developed by Mookerjee [54] to calculate the electronic states of binary alloys. It has been shown that thermal vibrations can be included in the calculation using an appropriate effective t-matrix, now dependent on the temperature.

The Fit of the XANES Energy Region

Recently a new method [4, 55] to perform a quantitative analysis of the low energy range, the so called XANES energy region, i.e. from the edge up to 200 eV, has been proposed in the literature and applied to several systems [56, 57]. This method is based on the comparison between experimental data and many theoretical calculations performed by varying selected structural parameters starting from a proposed structure, i.e. from a well-defined initial geometrical configuration around the

absorber. The calculation of XANES spectra related to the hundreds of different geometrical configurations needed to obtain the best fit of the experimental data has been made in the framework of the full MS calculation, i.e. the scattering path operator τ is calculated exactly, and the optimization of parameters is achieved by the minimization of the square residual function in the parameter space. The calculations are performed in the energy space without involving any Fourier transform algorithm; polarized spectra can be easily analyzed because the calculations are performed by the full MS approach. This new method is implemented in a software package called MXAN [4]. This procedure uses the set of programs developed by the Frascati theory group for the full multiple scattering cross section calculation. The optimization in the space of the parameters is achieved using the MINUIT routines of the CERN library. The MINUIT routines minimize the square residual function

$$S^2 = n \frac{\sum_{i=1}^{m} w_i \left[\left(y_i^{th} - y_i^{exp} \right) \varepsilon_i^{-1} \right]^2}{\sum_{i=1}^{m} w_i} \tag{7.19}$$

where n is the number of independent parameters, m the number of data points, y^{th}_i and y^{exp}_i the theoretical and experimental values of absorption, ε_i the individual errors in the experimental data set, and w_i is a statistical weight. For w_i = constant = 1, the square residual function S^2 becomes the statistical χ^2 function. The application of the software package to several test cases shows that the best-fit solution is almost independent from the minimization strategy and to the starting conditions.

The MXAN method is based on the muffin-tin approximation for the shape of the potential and the use of complex optical potential, discussed above. The effects of the non-MT corrections on the XANES calculation are still not well understood, nevertheless evidence exists that their influence, if present, is confined in the very low energy part of the spectrum with a very weak influence on the structural determination. This is not surprising because it is possible to write for potential of any shape a theory having the same formal structure of the usual MS theory but with propagators and scattering matrix modified by adding some suitable quantities [58] we can write:

$$\sigma(E) \approx \mathrm{Im}[(I - TG)^{-1} T] = \mathrm{Im}[T - G]^{-1} \tag{7.20}$$

where now $T = T_a^{-1} + \Delta T$, $G = G_{MT} + \Delta G$. Here T_a^{-1} and G_{MT} are the usual quantities calculated within the MT approximation while the corrections are proportional to the interstitial volume. Writing $\Delta = \Delta T + \Delta G$ we can expand the total cross section in series using Δ as a parameter. In this way

$$\sigma(E) \approx \mathrm{Im}\{\Sigma_{n=0}[(T_a^{-1} - G_{MT})^{-1} \Delta]^n (T_a^{-1} - G_{MT})^{-1}\} \tag{7.21}$$

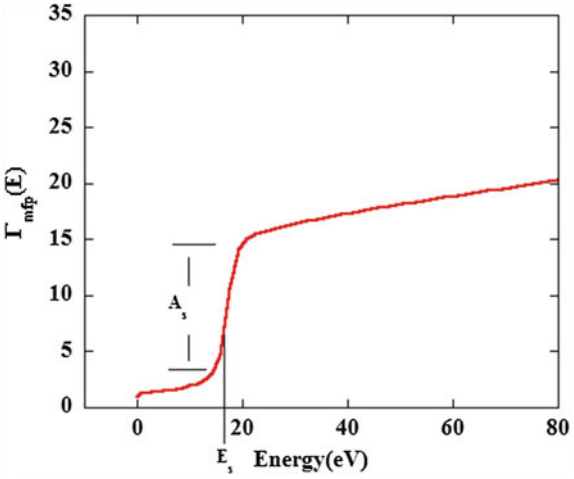


Fig. 7.8 Behaviour of the energy dependent width $\Gamma_{\mathrm{mfp}}(E)$ of the Lorentzian function used in the convolution procedure to account for the inelastic losses

i.e. $\sigma(E) = \sigma_{MT}(E) + corr(E; V_{int})$. In other words the total non-MT cross section can be written as the sum of the cross section calculated in the MT approximation and corrections that decrease with the energy and depend on the potential in the interstitial volume. These corrections depend on the system and go to zero as the energy increases. Their influence is strongly reduced making the fits in the energy range from the edge up to 200 eV. In this way the geometrical arrangements restrains the numerical results of the fitting procedure.

Here we also want to emphasize that this new method needs a phenomenological treatment of the inelastic losses to avoid the over damping at low energies of the complex part of the HL potential in the case of covalent molecular systems. This method accounts for all the inelastic processes by a convolution with a broadening Lorentzian function having an energy dependent width of the form $\Gamma(E) = \Gamma c + \Gamma_{\mathrm{mfp}}(E)$. The constant part Γc includes the core-hole lifetime and the experimental resolution, while the energy dependent term represents all the intrinsic and extrinsic inelastic processes. The $\Gamma_{\mathrm{mfp}}(E)$ function is zero below an onset energy E_s (which in extended systems corresponds to the plasmon excitation energy) and begins to increase from a value A_s following the universal functional form of the mean free path in solids. Both the onset energy E_s and the jump A_s are introduced in the $\Gamma_{\mathrm{mfp}}(E)$ function via an arctangent functional form to avoid discontinuities. Both numbers are derived on the basis of a Monte Carlo search at each step of computation. A typical behavior of the $\Gamma_{\mathrm{mfp}}(E)$ function is reported in Fig. 7.8.

This type of approach is justified on the basis of the multi-channel multiple scattering described above. Considering the sudden limit of the theory, (7.7) becomes diagonal in the α index, i.e., the net absorption is given by a sum over all the possible channels that represent each of the final states allowed in the photo-absorption

process. They include the fully relaxed configuration (index $\alpha = 0$), which gives the main contribution to the spectrum, and all the other possible excited states of the (N −1)-electron system.

By assuming that the channels coming from the excitation of the N −1 electrons are very near in energy, the total absorption is given by a convolution of the one-particle spectrum calculated with the full-relaxed potential with a spectral function representing the weight of the other excited states. Hence the total XAS cross section can be written as

$$\mu = \Sigma_n \mu_n \underset{\Delta E \to 0}{\longrightarrow} \int \mu(\omega - \omega') A(\omega') d\omega' \tag{7.22}$$

make the "ansatz" that the spectral function $A(\omega)$ is well approximated by a Lorentzian function with the energy dependent width $\Gamma(E)$ previously defined. Obviously, in the cases when contributions from one or more of these excited states become relevant, they must be considered explicitly in the calculation.

We show, as test cases, the MXAN analysis of the K-edges of Ni^{2+} and Fe^{2+} ions in aqueous solution. Both ions are often used as test cases due to the well-defined formal valency of the ionic species and the very simple geometry around the absorber. The data at the K-edges have been recorded in transmission mode using a Mylar cell at beam station 7.1 of the Daresbury Laboratory. A double-crystal Si(111) monochromator was used and the storage ring was operated at 2 GeV with an average current of about 150 mA. The samples were prepared as water solutions of 5 and 50 mM of Ni^{2+} and for Fe^{2+} ions respectively. The pH was controlled in order to have the hydrated species. The background contribution from previous edges was fitted with a linear function and subtracted from the raw data. We report in Fig. 7.9 the comparison between the experimental data and the calculations related to the best-fit structures for Ni^{2+} and Fe^{2+} ions in water solution. These best fits [59] correspond to an octahedral symmetry with an oxygen-metal distance of 2.03 ± 0.03 Å and 2.08 ± 0.02 Å for Ni^{2+} and Fe^{2+} solutions respectively. Hydrogen atoms are included in the calculations. The agreement between the experimental data and the best fit theoretical curves are good in the whole energy range, small discrepancies remaining in the intensity of the resonance at 15 eV, perhaps due to the presence of a small contribution of a second shell of water or to the muffin-tin approximation.

The MXAN method has proven to provide reliable structural results confirming the validity of the application of the full MS scheme in the framework of the MT approximation [60]. In this way the low energy part of the XAS spectrum is now fully available for a quantitative analysis and we can benefit from the extreme sensitivity to the structural details of the absorbing site (overall symmetry, distances and bond angles) of this energy region. This is important in the study of many systems like extra-dilute systems, trace element analysis, local investigation of materials under extreme conditions and much more in biological systems where the low S/N ratio and the weak scattering power of the light elements limits the *k*-range of the available experimental data and where the EXAFS can be barely exploited. The structural information on protein metal sites [61] can be obtained with atomic resolution in any state of the protein sample (crystal, solution), allowing either the comparison

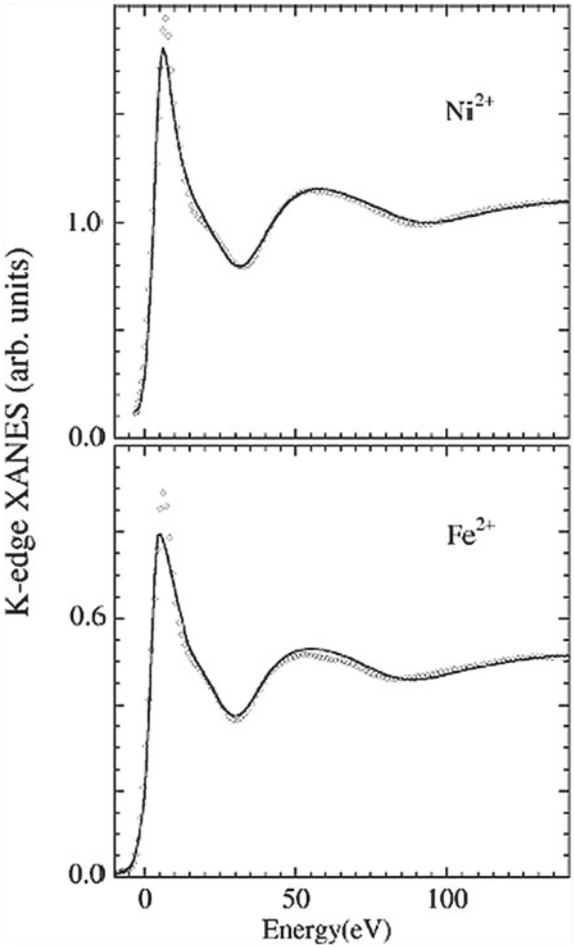


Fig. 7.9 *Upper frame*: comparison between the experimental data (*circles*) and the calculation at the best fit condition of the Ni K-edge of Ni^{2+} in water. *Lower frame*: The same for Fe^{2+} in water

with already known X-ray structures at high resolution or to obtain information on protein that have proven difficult to crystallize.

Recently the MXAN method has been modified to allow fitting difference spectra, i.e. the signal coming from the difference of two XANES spectra [7]. In this way signals coming from differential transient XAS, which consists of the difference between the transmission spectra of a unexcited and a laser excited sample [6] can be analyzed. In these experiments, the system is excited by an ultra-short pump laser pulse, and is probed by a short X-ray probe pulse, whose time delay with respect to the laser pump pulse can be continuously varied. This increases greatly the sensitivity of the experiment while largely reducing systematic errors such as intensity fluctuations or deterioration of the sample during the experiment. At the same time the influence

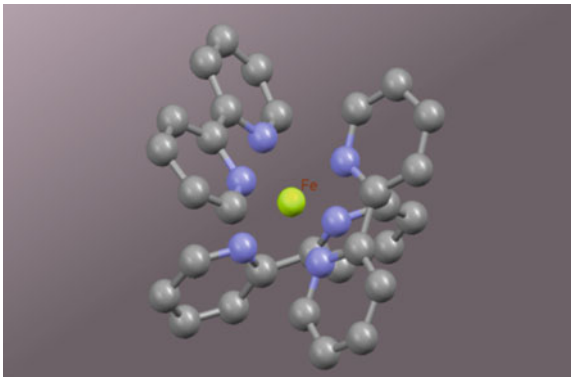


Fig. 7.10 Picture of the geometry of $[Fe^{II}(byp)_3]^{2+}$ complex. In *blue* the nitrogen atoms, in *grey* the carbon atoms and in *yellow-green* the absorbing iron

of possible systematic errors in the calculations is decreased. These come from the approximations used in the theoretical approach.

As an example we want to discuss the case of the iron-(II)-tris bypyridine ($[\ Fe^{II}(byp)_3]^{2+}$) complex where the structural changes induced by ultra-short laser pulse excitation and population of its short-lived (<0.6 ns) quintet high spin state have been detected by pico-second XAS spectroscopy [5]. The molecule is shown in Fig. 7.10.

The characteristic energy level scheme of the $[Fe^{II}(byp)\ _3]^{2+}$ complex is shown in Fig. 7.11 where ΔE^0_{HL} is the energy difference between the low-spin state (LS) and the high-spin state (HS). In this complex this energy is of the order of 6000 cm^{-1}. Photo-excitation of $[Fe^{II}(byp)_3]^{2+}$ by UV-visible light populates the singlet metal-to-ligand-charge-transfer (MLCT) states and is followed by a cascade (in few hundred of fs) of intersystem crossing steps through MLCT and ligand-field (LF) states, which brings the system to its quintet HS state, $^5T_2$, with almost unit quantum yield within <1ps. At room temperature, this state relaxes non-radiatively to the LS ground state in about 0.6 ns.

Through the study of the picosecond Fe K-edge XAS data of the HS state is possible to determine the structural changes occurred going from LS to HS state. These changes are extracted from a fit of the experimental difference XAS spectra without a-priori assumptions.

The laser-pump X-ray-probe experiments were performed at the micro-XAS beam line of the Swiss Light Source. Details of the experimental strategy are described elsewhere [62]. Briefly, an intense 400 nm pulse (100 fs pulse width, repetition rate 1 kHz) excites an aqueous solution of 1–25 mM of $[Fe^{II}(byp)_3]^{2+}$while a 100 ps monochromatic (0.016 % bandwidth) tunable hard X-ray pulse probes the system by X-ray absorption spectroscopy as a function of the adjustable pump-probe time delay. The detected signal is the difference X-ray absorption spectrum between the laser excited and the unexcited sample, recorded on a shot-to-shot basis at 2 kHz.

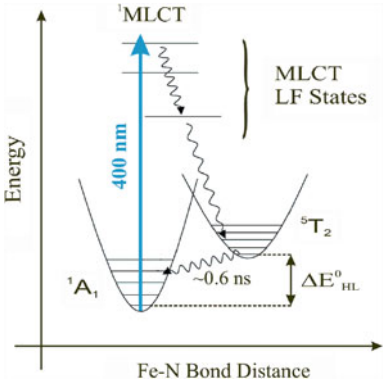


Fig. 7.11 Schematic potential energy curves of $[Fe^{II}(byp)_3]^{2+}$ complex as a function of the Fe–N bond distances, and pathways on non-radiative relaxation leading to the quintet state, upon excitation of the singlet MLCT state in the UV

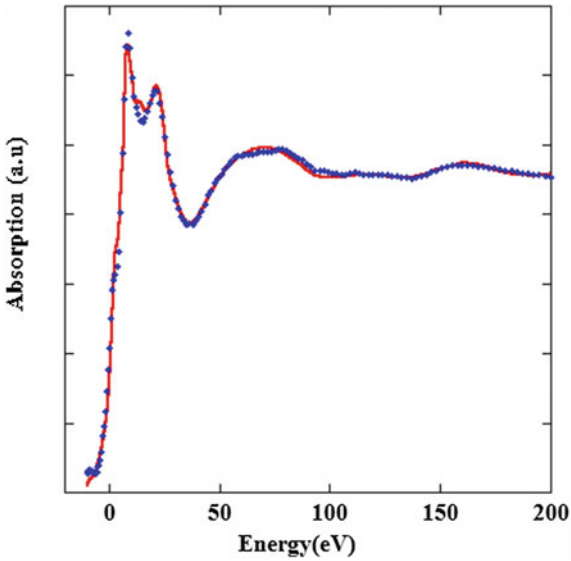


Fig. 7.12 Comparison between the XANES experimental data of $[Fe^{II}(byp)_3]^{2+}$ at the Fe K-edge (*blue points*) and the theoretical calculation (*red line*) at the best fit condition

The XAS of the sample was measured in both transmission and X-ray fluorescence yield modes. The incident X-ray flux was monitored via X-ray fluorescence from a thin Cr foil placed upstream from the sample. The X-ray energy was calibrated via a reference spectrum of an iron foil. Figure 7.12 shows the comparison between the experimental data and the theoretical calculation at the best fit condition of the static spectrum of $[Fe^{II}(byp)_3]^{2+}$ in the LS state.

The fit has been made with MXAN methods using the structure depicted in Fig. 7.10 allowing to change the Fe–N bond length. The best fit condition corresponds to a bond length of $R_{Fe-N} = 2.00 \pm 0.02$ Å. The XRD structural determi-

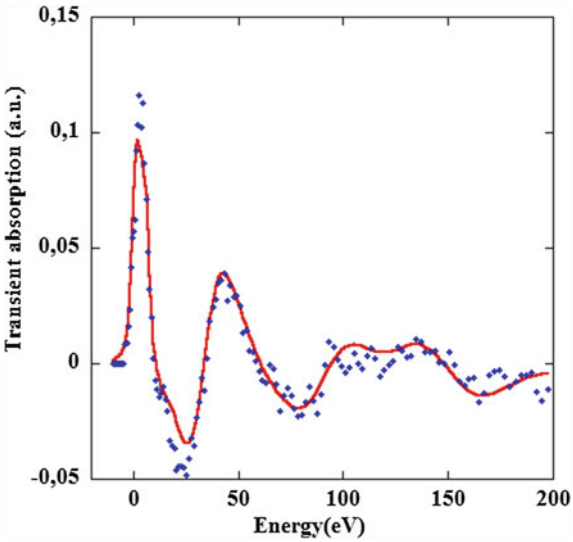


Fig. 7.13 Comparison between the difference XANES experimental spectrum of $[Fe^{II}(byp)_3]^{2+}$ at the Fe K-edge (*blue points*) and the theoretical calculation (*red line*) at the best fit condition

nation reports a distance of $R_{Fe–N} = 1.967 \pm 0.006$ Å. The fit of the LS XAS data is the start point of the structural analysis of the transient XAS data of the HS state. Next, the fit of the difference spectrum, reported in Fig. 7.13 will deliver the Fe-N bond distances in the HS state.

There is a very good agreement in the whole energy range and it corresponds to an increase of the bond Fe–N bond length of $\Delta R_{Fe–N} = 0.20 \pm 0.05$ Å that is in good agreement with density functional theory calculations.

This example shows the strong potentialities of the time-depended XAS data and the MXAN analysis. It should be remarked that this procedure can be made not only in the light-induced or magnetic-field induced time dependent changes, but also when the changes are induced by temperature, pressure, pH changes, etc.

7.5 Conclusions

In this chapter we have presented a review of the understanding of the modern interpretation of XAS spectroscopy coming from the works of several groups in the world. Although very important advances have been made in the last two years in the quantitative use of the XANES spectroscopy, many other items should be addressed to fully exploit the potentialities of XAS spectroscopy. Most of them are linked to a better treatment of the molecular potential. Among these we want to focus attention on overcoming the MT approximation. Several approaches are now available. We want to recall the Finite Difference Method [3] and the non-MT Multiple Scattering Theory [63]. Applications have also shown the practical limitations of the first method,

due the large memory and the long CPU time required by the computer code, especially for low-symmetry systems. In this scheme fitting procedures to experimental data become prohibitive and many applications to interesting systems in biology, earth sciences, chemistry and physics would be out of reach. Computer code using the non-MT MS theory is now available but systematic studies must be done on the effect of the space partitioning on the calculation.

We close this chapter emphasizing that multiple scattering theory is a very general approach to calculating physical quantities from "first principles". To this respect its field of application is not limited to XAS spectroscopy. Many other type of experiments can indeed benefit [64] from this theoretical approach yielding a solid basis for physical interpretation.

Acknowledgments M.B. acknowledges financial support from the SSRL Structural Molecular Biology program for the three months stay as a visiting scientist during which this manuscript has been written. M.B. also thanks Dr. P. Frank of the Department of Chemistry of Stanford University for the friendly discussions, corrections and coffee.

References

1. P.A. Lee, Beni, G. Phys. Rev. B 15, 2862–2883 (1977).
2. J.J. Rehr, J.J. Kas, F.D. Vila, M.P. Prange, K. Jorissen, Phys. Chem. Chem. Phys. **12**, 5503–5513 (2010)
3. Y. Joly, Phys. Rev. B **63**, 125120–1/10 (2001)
4. M. Benfatto, S. Della Longa, J. Synchrotron Rad. **8**, 267–269 (2001)
5. W. Gawelda, V.T. Pham, M. Benfatto, et al., Phys. Rev. Lett. 98, 057401-1–4 (2007)
6. C. Bressler, M. Chergui, Chem. Rev. **104**, 1781–1812 (2004)
7. M. Benfatto, S. Della, Longa, K. Hatada et al. J. Phys. Chem. B **110**, 14035–14039 (2006)
8. E. Bus, J.A. van Bokhoven, Phys. Chem. Chem. Phys. **9**, 2894–2902 (2007)
9. S.P. Cramer, T.K. Eccles, F.W. Kutzler, K.O. Hodgson, L.E. Morteson, J. Am. Chem. Soc. **98**, 1287–1288 (1976)
10. D.H. Pearson, C.C. Ahn, B. Fultz, Phys. Rev. B **74**, 8471–8478 (1993)
11. G. Meitzner, G.H. Via, F.W. Lytle, J.H. Sinfelt, J. Phys. Chem. **96**, 4960–4964 (1992)
12. T.K. Sham, Y.M. Yiu, M. Kuhn, K.H. Tan, Phys. Rev. B **41**, 11881–11886 (1990)
13. M. Kuhn, T.K. Sham, Phys. Rev. B **49**, 1647–1661 (1994)
14. F. Farges, G.E. Brown, J.J. Rehr, Geochim. Cosmochim. Acta **60**, 3023 (1997)
15. M. Wilke, F. Farges, P.E. Petit, G.E. Brown, F. Martin, Am. Mineral. **86**, 714–730 (2001)
16. F. De Groot, G. Vankó, P. Glatzel, J. Phys. C: Condens. Matter **21**, 104207 (2009)
17. T. Yamamoto, X-Ray Spectrom. **37**, 572–584 (2008)
18. R. Sarangi, Coord. Chem. Rev. **257**, 459–472 (2013)
19. C. Meneghini, A. Gupta, J. Zeghenagen, R. Parasmani, Unpublished (2013)
20. C. Meneghini, S. Di Matteo, C. Monesi, T. Neisius, L. Paolasini, S. Mobilio, Phys. Rev. B **72**, 033111 (2005)
21. R. Torchio, S. Pascarelli, O. Mathon, C. Marini, S. Anzellini, P. Centomo, C. Meneghini, S. Mobilio, N.A. Morley, M.R.J. Gibbs, High Press. Rese. **31**, 148–152 (2011)
22. R. Torchio, Y.O. Kvashnin, C. Marini, O. Mathon, G. Garbarino, M. Mezouar, J.P. Wright, P. Bruno, L. Genovese, F. Baudelet, C. Meneghini, S. Mobilio, N.A. Morley, M.R.J. Gibbs, S. Pascarelli, Phys. Rev. B **88**, 184412(1–8) (2013)
23. B.T. Thole, P. Carra, F. Sette, G. van der Laan, Phys. Rev. Lett. **68**, 1943–1946 (1992)

24. D. Kothari, S. Upadhya, C. Meneghini, V.R. Reddy, G. Aquilanti, A. Gupta, AIP Conf. Proc. **1447**, 1319–1320 (2012)
25. A. Vairavamurthy, Spectrochim. Acta A **54**, 2009–2017 (1998)
26. J. Yano, J. Kern, K.D. Irrgang, M.J. Latimer, U. Bergmann, P. Glatzel, Y. Pushkar, J. Biesiadka, B. Loll, K. Kenneth, Sauer, J. Messinger, K.A. Zouni, V.K. Yachandra. Proc. Natl. Acad. Sci. **102**, 12047–12052 (2005)
27. C. Meneghini, S. Ray, F. Liscio, F. Bardelli, S. Mobilio, D.D. Sarma, Phys. Rev. Lett. **103**, 046403 (2009)
28. G. Dezanneau, M. Audier, H. Vincent, C. Meneghini, E. Djurado, Phys. Rev. B 69, 014412-XXXX (2004).
29. S. Middey, C. Meneghini, S. Ray, Appl. Phys. Lett. 101, 042406(4) (2012).
30. T. Chakraborty, C. Meneghini, G. Aquilanti, S. Ray, J. Phys.: Condens. Matter 25, 236002(1–7) (2013).
31. F. Bardelli, M. Benvenuti, P. Costagliola, F. Di Benedetto, P. Lattanzi, C. Meneghini, M. Romanelli, L. Valenzano, Geochim. et Cosmochim. Acta **75**, 3011–3023 (2011)
32. R. Terzano, Z. Al, Chami, B. Vekemans, K. Janssens, T. Miano, P. Ruggiero. J. Agric. Food Chem. **56**, 3222–3231 (2008)
33. G. Giuli, S.G. Eeckhout, E. Paris, C. Koeberl, G. Pratesi, Meteorit. Planet. Sci. **40**, 1575–1580 (2005)
34. F. Farges, Phys. Chem. Miner. **28**, 619–629 (2001)
35. S.R. Wasserman, P.G. Allen, D.K. Shuh, J.J. Bucher, N.M. Edelstein, J. Synchrotron Rad. **6**, 284–286 (1999)
36. F. Bardelli, E. Cattaruzza, F. Gonella, G. Rampazzo, G. Valotto, J. Phys.: Conf. Ser. **190**, 012192 (2009)
37. A.J. Berry, L.V. Danyushevsky, H. St, C. O'Neill, M. Newville, S.R. Sutton. Nature **455**, 960–963 (2008)
38. C.R. Natoli, M. Benfatto, S. Della Longa, K. Hatada, J. Synchrotron Rad. 10, 26–42 (2003).
39. C.R. Natoli, M. Benfatto, C. Brouder, M.F. Ruiz, Lopez, D.L. Foulis. Phys. Rev. B **42**, 1944–1968 (1990)
40. C.R. Natoli, M. Benfatto, S. Doniach, Phys. Rev. A **34**, 4682–4694 (1986)
41. K.H. Johnson, Adv. Quant. Chem. 7, 143-xxxx (1973).
42. F.W. Kutzler, C.R. Natoli, D.K. Misemer et al., J. Chem. Phys. **73**, 3274–3288 (1980)
43. T.A. Tyson, K.O. Hodgson, C.R. Natoli, M. Benfatto, Phys. Rev. B **46**, 5997–6019 (1992)
44. C.R. Natoli, M. Benfatto, J. Phys. (France) Colloq. **47**, C8, 11–23 (1986)
45. M. Benfatto, C.R. Natoli, A. Bianconi, J. Garcia, A. Marcelli, M. Fanfoni, I. Davoli, Phys. Rev. B **34**, 5774–5781 (1986)
46. A.L. Ankudinov, B. Ravel, J.J. Rehr, S.D. Conradson, Phys. Rev. B **58**, 7565–7576 (1998)
47. A.L. Ankudinov, J. Synchrotron Rad. **6**, 236–238 (1999)
48. J.E. Müller, O. Jepsen, JW Wilkins. Solid State Commun. **42**, 4331–4343 (1984)
49. L. Hedin, S. Lundqvist, in *Solid State Physics*, ed. by F. Seitz, D. Turnbull, H. Ehrenreich, vol. 23 (Academic Press, New York, 1969), p. 1.
50. T. Fujikawa, L. Hedin, Phys. Rev. B **40**, 11507–11518 (1989)
51. D.R. Penn, Phys. Rev. B **35**, 482–486 (1987)
52. M. Benfatto, Physica B, B**208 & 209**, 42–44 (1995)
53. M. Benfatto, K. Hatada, K. Hayakawa, Manuscript in preparation (2014)
54. A. Mookerjee, J. Phys. **C6**, 1340–1349 (1973)
55. S. Della Longa, A. Arcovito, M. Girasole, J.L. Hazeman, M. Benfatto, Phys. Rev. Lett. **87**, 155501-1–4 (2001)
56. K. Hayakawa, K. Hatada, P. D'Angelo, S. Della, Longa, C.R. Natoli, M. Benfatto. J. Am. Chem. Soc. **126**, 15618–15623 (2004)
57. P. Frank, M. Benfatto et al., Inorg. Chem. **44**, 1922–1933 (2005)
58. M. Benfatto, S. Della, Longa, P. D'Angelo. Phys. Scr. **T115**, 28–30 (2005)
59. P. D'Angelo, M. Benfatto, S. Della, Longa, N.V. Pavel, Phys. Rev. B **66**, 064209-1–7 (2002)
60. R. Sarangi, P. Frank, et al., J. Chem. Phys. **137**, 205103-1–13 (2012)

61. A. Arcovito, D.C. Lamb, G.U. Nienhaus, J.L. Hazemann, M. Benfatto, S. Della Longa, Biophys. J. **88**, 2954–2964 (2005)
62. M. Saes et al., Rev. Sci. Instrum. **75**, 24–30 (2004)
63. K. Hatada, K. Hayakawa, M. Benfatto, C.R. Natoli, J. Phys. Condens. Matter **21**, 104206-1–12 (2009)
64. M. Benfatto, Y. Joly, C.R. Natoli, Phys. Rev. Lett. **83**, 636–639 (1999)

Chapter 8
X-Ray Diffraction by Crystalline Materials

Davide Viterbo and Giuseppe Zanotti

Abstract Diffraction of X-rays by crystals offers the unique possibility to determine at atomic resolution the three-dimensional structure of solids. This opportunity is exploited by solid state chemists or by mineralogists to study the structure of crystals, by chemists to determine the structure of molecules and by molecular biologists to investigate structure and properties of living organisms molecules, like proteins, nucleic acids etc. In this chapter, after a brief introduction on crystals and crystal symmetries, the general principles of diffraction are introduced, then the reader is made familiar with the mathematical formalism of scattering and diffraction. The physical principles of diffraction by crystals are then introduced, and finally the phase problem in crystallography is presented and the main methods to solve it are shortly outlined. Few notes on the refinement process and on powder diffraction are also reported.

8.1 Introduction

In this chapter we will consider the diffraction of X-rays[1] by crystalline solids. We will first give a very concise description of the main characters of the play: the crystal and the X-rays. For an exhaustive treatment the reader is referred to specific textbooks

[1] The diffraction of other types of radiations, such as neutrons or electrons, may be formally treated in a similar way.

D. Viterbo
Via Saluzzo 88, 10126 Torino, Italy
e-mail: davide.viterbo@mfn.unipmn.it

G. Zanotti (✉)
Dipartimento di Scienze Biomediche, Università di Padova, Viale G. Colombo 3,
35131 Padova, Italy
e-mail: giuseppe.zanotti@unipd.it

S. Mobilio et al. (eds.), *Synchrotron Radiation*,
DOI: 10.1007/978-3-642-55315-8_8, © Springer-Verlag Berlin Heidelberg 2015

[1–6]. The mathematical tools needed for an elegant and concise treatment of X-ray diffraction[2] are then introduced.

Finally we will give a more detailed account of what is the nature of the interaction of X-rays with crystals and on how we can exploit X-ray diffraction in order to obtain structural information at different levels.

The advent of very intense and highly collimated synchrotron X-ray sources has greatly widened the fields of application of diffraction techniques [7].

8.1.1 The Crystal

An ideal crystal (deviations from ideality are outside our scope) is formed by the periodic repeat, in three dimensions, of the same atomic or molecular motif. In Fig. 8.1 an example of the two-dimensional repeat of a motif is illustrated, and we can see that the repeating motif may be represented by a minimal repeating rectangular area, delimited by two vectors **a** and **b**, which is called the *unit cell*. The periodic two-dimensional array formed by the repeat of the unit cell is the **lattice** and an infinite lattice may be represented by the set of vectors

$$\mathbf{r}_{u,v} = u\mathbf{a} + v\mathbf{b} \tag{8.1}$$

where u and v are integers going from $-\infty$ to $+\infty$.

In a similar way we may represent a crystal as a three-dimensional lattice, with a unit cell delimited by three vectors **a**, **b** and **c** (Fig. 8.2). The lattice will be defined by the set of vectors

$$\mathbf{r}_{u,v,w} = u\mathbf{a} + v\mathbf{b} + w\mathbf{c} \tag{8.2}$$

with u, v and w integers going from $-\infty$ to $+\infty$. The vectors **r** define the infinite set of *lattice nodes*. The vectors **a**, **b** and **c** need not be orthogonal and their lengths a, b and c, together with the three angles $\alpha = \mathbf{b} \times \mathbf{c}$, $\beta = \mathbf{a} \times \mathbf{c}$ and $\gamma = \mathbf{a} \times \mathbf{b}$, are the *unit cell parameters*. We may also define the *lattice planes* as those planes passing through the lattice nodes. Each family of planes with the same orientation with respect to the cell vectors is identified by three integers (h, k, l), known as the *Miller indices*.

[2] One of us (DV) had the privilege of attending a course in Parma in 1969 and a meeting in Buffalo in 1974 where Paul Ewald gave memorable lectures on the theory of diffraction by crystals. In these notes the same general approach will be used.

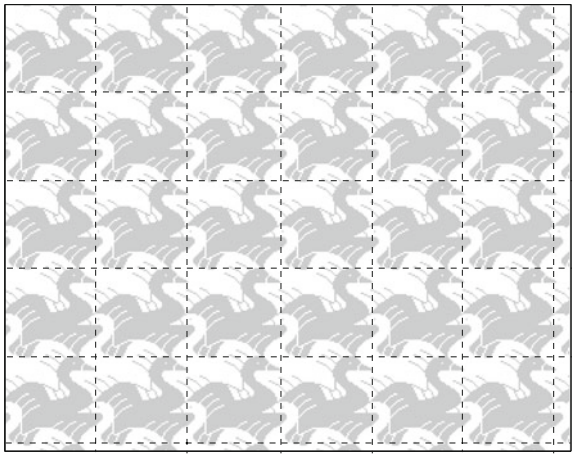


Fig. 8.1 Two-dimensional repeat of a motif and its representation as a lattice

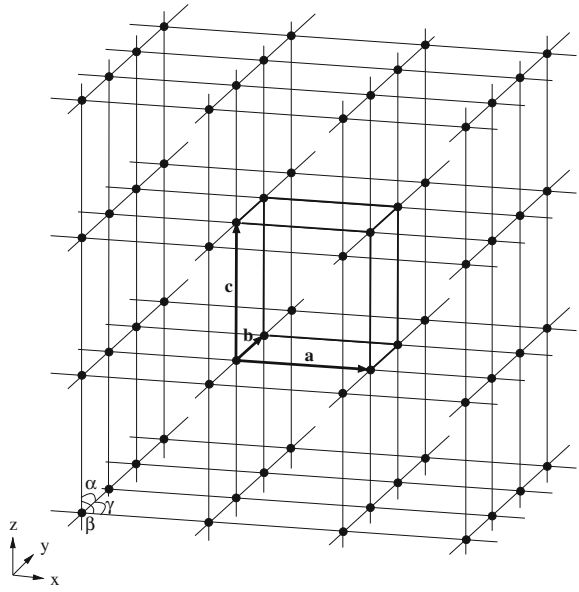


Fig. 8.2 Three-dimensional lattice

8.1.2 Crystal Symmetries

The *unit cell* or *crystal cell* represents the minimum volume of the crystal that repeats itself in all three directions of space simply by translation. In the three-dimensional space only 7 types of cells are possible, and they give rise, according to the different possibilities of the cell of being primitive or centered, to 14 lattices, called *Bravais lattices*:

Crystal system	Cell lengths	Centering
Triclinic	$a \neq b \neq c, \alpha \neq \beta \neq \gamma$	P
Monoclinic	$a \neq b \neq c, \alpha = \gamma (or \beta) = \pi/2$	P, C
Orthorhombic	$a \neq b \neq c, \alpha = \beta = \gamma = \pi/2$	P, C, I, F
Tetragonal	$a = b \neq c, \alpha = \beta = \gamma = \pi/2$	P, I
Trigonal	$a = b \neq c, \alpha = \beta = \pi/2, \gamma = 2\pi/3$	P
Hexagonal	$a = b \neq c, \alpha = \beta = \pi/2, \gamma = 2\pi/3$	P
Cubic	$a = b = c, \alpha = \beta = \gamma = \pi/2$	P, I, F

A crystal cell may contain more than one motif. If these motifs are all identical, they can be superimposed by applying appropriate transformations, called *symmetry operations*. Not all symmetry transformations are compatible with the crystal lattice. Those allowed, along with the symbols used to represent them, are listed below.

Centre of symmetry $(\bar{1})$. It is a point in the unit cell such that, for any point defined by a vector $\mathbf{r}$, there is an equivalent point at position $-\mathbf{r}$.

Mirror plane (m). Also called *plane of symmetry*, is such that everything on one side of the plane is reflected on the other side.

Rotation axes $(1, 2, 3, 4, 6)$. Rotation is necessarily about an axis. The numerical value of the rotation corresponds to $2\pi/n$, where n in a crystal lattice can assume only the values $1, 2, 3, 4, 6$, corresponding to rotations of 2π, π, $2\pi/3$, $\pi/2$, $\pi/3$, respectively.

Inversion axes $(\bar{1}, \bar{2}, \bar{3}, \bar{4}, \bar{6})$. They are combinations of a rotation axis with the centre of symmetry. In practice, after a rotation of order n, the object is reflected through a point located on the axis.

The previous four types of symmetry elements do not include any translation. Their effect, after an integer number of applications, is a return to the starting point. They can be combined and all the combinations compatible with the properties of the lattice give rise to the 32 three-dimensional crystallographic point groups. They are reported, in association with each of the 7 crystal systems, in the Table below.

Crystal system	The 32 crystallographic point groups
Triclinic	$1, \bar{1}$
Monoclinic	$2, m, 2/m$
Orthorhombic	$222, mm2, mmm$
Tetragonal	$4, \bar{4}, 4/m, 422, 4mm, \bar{4}2m, 4/mmm$
Trigonal	$3, \bar{3}, 32, 3m, \bar{3}m$
Hexagonal	$6, \bar{6}, 6/m, 622, 6mm, \bar{6}2m, 6/mmm$
Cubic	$23, m\bar{3}, 432, \bar{4}3m, m\bar{3}m$

In addition to the previous ones, there are symmetry elements for which the periodic nature of the lattice plays a fundamental role. They include:

Glide planes (a, b, c, d, n). They represent a combination of a mirror plane and a translation. Their symbol indicates the direction of the translation: for example, a represents a translation parallel to the unit cell vector $\mathbf{a}$.

Screw axes (n_m : $2_1, 3_1, 3_2, 4_1, 4_2, 4_3, 6_1, 6_2, 6_3, 6_4, 6_5$). A combination of a rotation axis and a translation. The object is first rotated by an angle $2\pi/n$ and then displaced by m/n.

The possible combinations of the 32 point groups with the 14 Bravais lattices are 230 and are called the *230 space groups*. They represent all the possible ways a motif can be arranged in a periodic way in the three-dimensional space.

The basic motif present in the unit cell is called the *asymmetric unit*, defined as the smallest portion of the crystal cell that does not contain crystallographic symmetries. In the case of molecular crystals, the asymmetric unit can correspond to a single molecule, or it can contain more than one molecule, or eventually less than it, if the molecule itself is symmetric.

A final aspect with relevant consequences must be remembered. The symmetry elements described above can be grouped in two classes: those, like rotation axes or screw axes, that keep unaltered the configuration of the object, and those, like mirror planes, centre of symmetry, inversion axes and glide planes, that invert it. Consequently, chiral molecules cannot crystallize in space groups containing second class symmetry elements, unless both enantiomers are present inside the crystal.

8.1.3 The X-Rays

Discovered in 1886 by Röntgen, it was only 10 years later that Sommerfeld measured their very short wavelength (around 0.4 Å) and identified their nature of electromagnetic waves. This was definitely confirmed in 1912 by M. von Laue who, inspired by an intuition of P. Ewald, suggested that crystal lattices could act as diffraction gratings for X-rays. This hypothesis was immediately confirmed by the successful experiment of Friedrich and Knipping.

In the spectrum of electromagnetic waves, X-rays are placed in the region between γ-rays and ultraviolet radiation ($0.1 \leq \lambda \leq 100$ Å), but in X-ray crystallography only high energy radiation with $0.3 \leq \lambda \leq 3.0$ Å is usually employed.

Because of their high energy, the refractive index of X-rays does not deviate significantly from unity in all media. Therefore X-rays can not be focused by lenses as ordinary light or electrons [8]. Only in recent years improvements in X-ray focusing have been realized with the use of suitably shaped crystals acting as focusing mirrors [9].

8.1.4 Some Useful Mathematical Concepts

- **Dirac** δ **function**: In one dimension is defined as

$$\delta(x - x_o) \quad \begin{cases} = 0 & \text{for } x \neq x_o \\ = \infty & \text{for } x = x_o \end{cases} \tag{8.3}$$

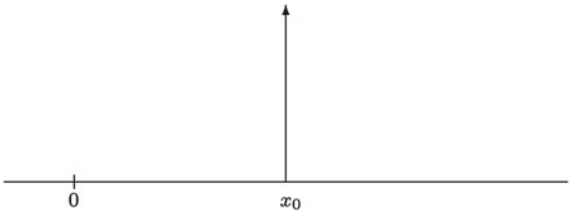


Fig. 8.3 Representation of the Dirac δ function in one dimension

with

$$\int_s \delta(x - x_o)dx = 1 \tag{8.4}$$

It is therefore a normalized, infinitely narrow function (Fig. 8.3), which may be obtained as the limit for zero variance of a Gaussian function

$$\delta(x - x_o) = \lim_{\sigma \to 0} \left[\frac{1}{\sigma\sqrt{2\pi}} e^{-\frac{(x-x_o)^2}{2\sigma^2}} \right] \tag{8.5}$$

In three dimensions a point may be represented by a vector

$$\mathbf{r} = x\mathbf{a} + y\mathbf{b} + z\mathbf{c} \tag{8.6}$$

and the δ function is defined as in one dimension, as

$$\delta(\mathbf{r} - \mathbf{r}_o) = \delta(x - x_o)\delta(y - y_o)\delta(z - z_o) \tag{8.7}$$

We recall the following properties of the δ function

$$* \qquad \delta(\mathbf{r} - \mathbf{r}_o) = \delta(\mathbf{r}_o - \mathbf{r}) \tag{8.8}$$

$$* \qquad f(\mathbf{r})\delta(\mathbf{r} - \mathbf{r}_o) \equiv f(\mathbf{r}_o)\delta(\mathbf{r} - \mathbf{r}_o) \tag{8.9}$$

$$* \qquad \int_s f(\mathbf{r})\delta(\mathbf{r} - \mathbf{r}_o)d\mathbf{r} = f(\mathbf{r}_o) \tag{8.10}$$

$$* \qquad \int_s \delta(\mathbf{r} - \mathbf{r}_2)\delta(\mathbf{r} - \mathbf{r}_1)d\mathbf{r} = \delta(\mathbf{r}_2 - \mathbf{r}_1) \tag{8.11}$$

which are an immediate consequence of its definition.

- **Lattice function**: A one-dimensional lattice is a sequence of equally spaced points, separated by a constant period a. It can be represented by a *lattice function*

$$L(x) = \sum_{n=-\infty}^{\infty} \delta(x - x_n) \tag{8.12}$$

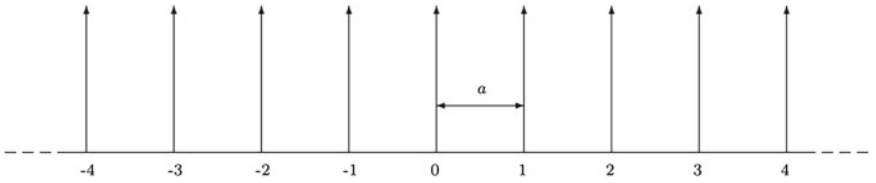


Fig. 8.4 Representation of the one dimensional lattice function defined in (8.12)

where $x_n = na$, n is an integer and a is the constant period; indeed $L(x) \neq 0$ for $x = na$ ($n = -\infty \rightarrow \infty$) (Fig. 8.4).
A three-dimensional lattice defined by the vectors **a**, **b** and **c** can then be represented by the function

$$L(\mathbf{r}) = \sum_{u=-\infty}^{\infty} \sum_{v=-\infty}^{\infty} \sum_{w=-\infty}^{\infty} \delta(\mathbf{r} - \mathbf{r}_{u,v,w}) \tag{8.13}$$

where, as we have seen

$$\mathbf{r}_{u,v,w} = u\mathbf{a} + v\mathbf{b} + w\mathbf{c}$$

with u, v, w integers, are the vectors defining the lattice nodes where $L(\mathbf{r}) \neq 0$.

- **Fourier transform**: Given a function $\rho(\mathbf{r})$, its Fourier transform is

$$\mathbf{F}(\mathbf{S}) = \int_r \rho(\mathbf{r}) e^{2\pi \jmath \mathbf{S}\cdot\mathbf{r}} d\mathbf{r} \tag{8.14}$$

where **S** is a vector in the space in which the transform is defined. It may be shown that the inverse relation applies, i.e.

$$\rho(\mathbf{r}) = \int_s \mathbf{F}(\mathbf{S}) e^{-2\pi \jmath \mathbf{S}\cdot\mathbf{r}} d\mathbf{S} \tag{8.15}$$

In short we can write

$$\mathbf{F}(\mathbf{S}) = T[\rho(\mathbf{r})] \quad \text{and} \quad \rho(\mathbf{r}) = T^{-1}[\mathbf{F}(\mathbf{S})]$$

In general $\mathbf{F}(\mathbf{S})$ is a complex function and may be expressed as

$$\mathbf{F}(\mathbf{S}) = A(\mathbf{S}) + \jmath B(\mathbf{S}) \tag{8.16}$$

with

$$A(\mathbf{S}) = \int_r \rho(\mathbf{r}) \cos(2\pi \mathbf{S}\cdot\mathbf{r}) d\mathbf{r} \tag{8.17}$$

$$B(\mathbf{S}) = \int_r \rho(\mathbf{r}) \sin(2\pi \mathbf{S} \cdot \mathbf{r}) d\mathbf{r} \tag{8.18}$$

Some examples of Fourier transform

1. For a *Gaussian function*

$$\rho(x) = N(\sigma, 0) = \frac{1}{\sigma\sqrt{2\pi}} e^{-\frac{x^2}{2\sigma^2}} \tag{8.19}$$

the transform is given by

$$T[\rho(x)] = F(S) = e^{-\pi^2\sigma^2 S^2} \tag{8.20}$$

which is also a Gaussian type function, but now its width is inversely [and not directly as $N(\sigma, 0)$ in (8.19)] proportional to σ^2 (Fig. 8.5).

2. The Fourier transform of a δ *function* at the origin (Fig. 8.6) is

$$F(S) = \int_{-\infty}^{\infty} \delta(x) e^{2\pi J S x} dx = 1 \tag{8.21}$$

which is infinitely wide.
For a δ function at a distance a from the origin $\rho(x) = \delta(x - a)$ the transform is

$$F(S) = e^{2\pi J a S}$$

3. For a *finite one dimensional lattice* with $N = 2p + 1$ nodes

$$\rho(x) = \sum_{n=-p}^{p} \delta(x - na) \tag{8.22}$$

the Fourier transform is given by

$$F(S) = \frac{\sin N\pi a S}{\sin \pi a S} \tag{8.23}$$

which is a function with principal maxima or minima at $aS = h$ (h integer) of height $\pm N$ and width $2/N$, separated by increasingly smaller ripples as N increases (Fig. 8.7).

4. For a *infinite one dimensional lattice* with $N \to \infty$

$$\rho(x) = L(x) = \sum_{n=-\infty}^{\infty} \delta(x - na) \tag{8.24}$$

the Fourier transform is given by

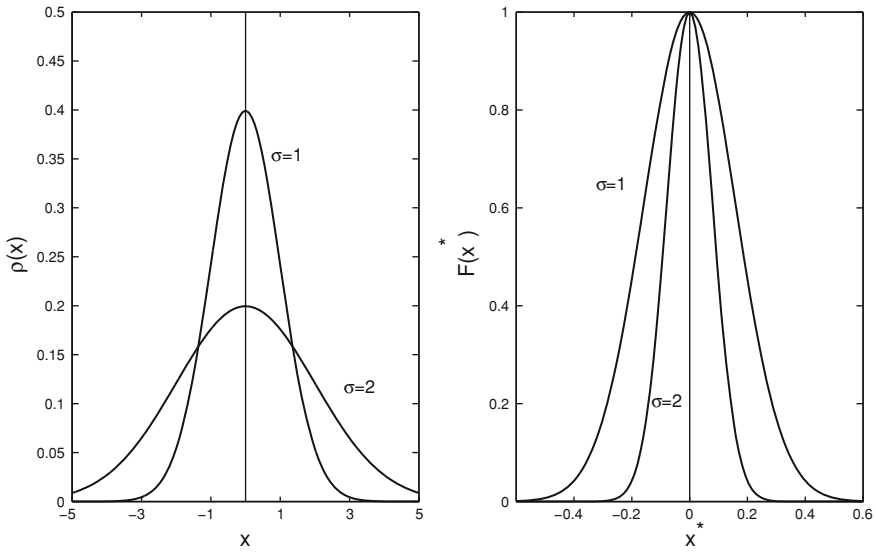


Fig. 8.5 Two Gaussian funtions with $\sigma = 1$ and $\sigma = 2$ and their Fourier transforms

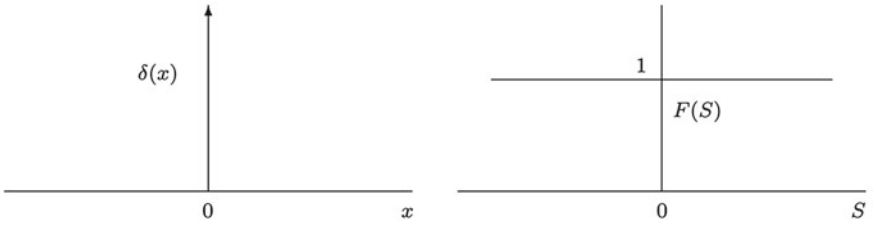


Fig. 8.6 One dimensional δ function at the origin and its Fourier transform

$$F(S) = \lim_{N\to\infty} \frac{\sin N\pi aS}{\sin \pi aS} \tag{8.25}$$

which is a function with infinitely narrow maxima of infinite height at $S = h/a$ and zero value elsewhere; each maximum is a non-normalized δ function and it may be shown that the normalization factor is $1/a$. We can therefore write

$$F(S) = \sum_{h=-\infty}^{\infty} \delta(S - \frac{h}{a}) = \frac{1}{a} \sum_{h=-\infty}^{\infty} \delta(aS - h) \tag{8.26}$$

which is again a lattice function with nodes separated by an inverse period $1/a$.

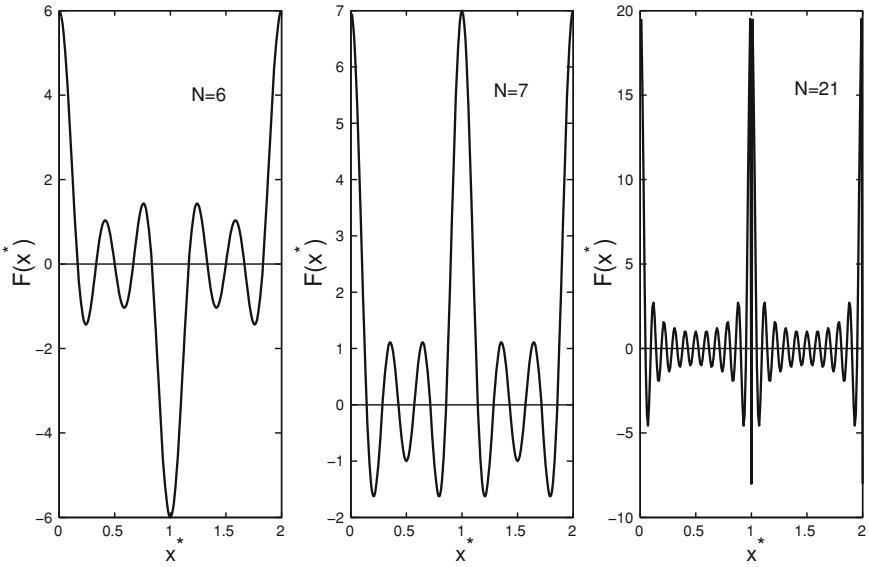


Fig. 8.7 Fourier transforms of three one-dimensional finite lattices with $N = 6$, $N = 7$ and $N = 21$ nodes

5. For a *finite three dimensional lattice* with $N_1 = 2p_1 + 1$ nodes along x, $N_2 = 2p_2 + 1$ nodes along y and $N_3 = 2p_3 + 1$ nodes along z

$$\rho(\mathbf{r}) = \sum_{u=-p_1}^{p_1} \sum_{v=-p_2}^{p_2} \sum_{w=-p_3}^{p_3} \delta(\mathbf{r} - \mathbf{r}_{u,v,w}) \tag{8.27}$$

the Fourier transform is given by

$$\mathbf{F}(\mathbf{S}) = \frac{\sin N_1 \pi \mathbf{a} \cdot \mathbf{S}}{\sin \pi \mathbf{a} \cdot \mathbf{S}} \cdot \frac{\sin N_2 \pi \mathbf{b} \cdot \mathbf{S}}{\sin \pi \mathbf{b} \cdot \mathbf{S}} \cdot \frac{\sin N_3 \pi \mathbf{c} \cdot \mathbf{S}}{\sin \pi \mathbf{c} \cdot \mathbf{S}} \tag{8.28}$$

which, similarly to (8.23), will have maxima and minima at

$$\mathbf{a} \cdot \mathbf{S} = h, \qquad \mathbf{b} \cdot \mathbf{S} = k, \qquad \mathbf{c} \cdot \mathbf{S} = l \tag{8.29}$$

with h, k, l integers.
In order to identify these maxima and minima it is convenient to associate to the lattice defined by the base vectors $\mathbf{a}$, $\mathbf{b}$, $\mathbf{c}$ (*direct lattice*) an other lattice, the *reciprocal lattice*, with base vectors $\mathbf{a}^*$, $\mathbf{b}^*$, $\mathbf{c}^*$, uniquely defined by the relations

$$\begin{array}{lll} \mathbf{a}^* \cdot \mathbf{a} = 1 & \mathbf{a}^* \cdot \mathbf{b} = 0 & \mathbf{a}^* \cdot \mathbf{c} = 0 \\ \mathbf{b}^* \cdot \mathbf{a} = 0 & \mathbf{b}^* \cdot \mathbf{b} = 1 & \mathbf{b}^* \cdot \mathbf{c} = 0 \\ \mathbf{c}^* \cdot \mathbf{a} = 0 & \mathbf{c}^* \cdot \mathbf{b} = 0 & \mathbf{c}^* \cdot \mathbf{c} = 1 \end{array} \tag{8.30}$$

In fact, because of conditions (8.30), the maxima and minima of $\mathbf{F}(\mathbf{S})$ given in (8.29), will be at the end of vectors

$$\mathbf{S}_{hkl} = h\mathbf{a}^* + k\mathbf{b}^* + l\mathbf{c}^* \tag{8.31}$$

which are vectors in the reciprocal space.

6. For a *infinite three dimensional lattice* with $(N_1, N_2, N_3) \to \infty$

$$\rho(\mathbf{r}) = L(\mathbf{r}) = \sum_{u=-\infty}^{\infty} \sum_{v=-\infty}^{\infty} \sum_{w=-\infty}^{\infty} \delta(\mathbf{r} - \mathbf{r}_{u,v,w}) \tag{8.32}$$

Recalling (8.7) and the case of a one dimensional lattice, the Fourier transform will be given by

$$\mathbf{F}(\mathbf{S}) = \frac{1}{V} \sum_{h=-\infty}^{\infty} \sum_{k=-\infty}^{\infty} \sum_{l=-\infty}^{\infty} \delta(\mathbf{S} - \mathbf{S}_{hkl}) \tag{8.33}$$

which is again a three-dimensional lattice defined by the infinite set of reciprocal vectors S given in (8.31) with the integers (h, k, l) going from $-\infty$ to $+\infty$.

- **Convolution**: Given two functions $\rho(\mathbf{r})$ and $g(\mathbf{r})$ their convolution is defined as

$$C(\mathbf{u}) = \rho(\mathbf{r}) \otimes g(\mathbf{r}) = \int_r \rho(\mathbf{r}) g(\mathbf{u} - \mathbf{r}) d\mathbf{r}. \tag{8.34}$$

It is easy to show that for the convolution operation the commutative property

$$\rho(\mathbf{r}) \otimes g(\mathbf{r}) = g(\mathbf{r}) \otimes \rho(\mathbf{r}) \tag{8.35}$$

holds.

An important theorem, relating Fourier transform and convolution, is the *convolution theorem*, stating that

$$T[\rho(\mathbf{r}) \otimes g(\mathbf{r})] = T[\rho(\mathbf{r})] T[g(\mathbf{r})] \tag{8.36}$$

and conversely

$$T[\rho(\mathbf{r}) g(\mathbf{r})] = T[\rho(\mathbf{r})] \otimes T[g(\mathbf{r})] \tag{8.37}$$

Some examples of convolution

1. The convolution of a function $\rho(\mathbf{r})$ with a δ *function*, because of property (8.10), is given by

$$\delta(\mathbf{r} - \mathbf{r}_o) \otimes \rho(\mathbf{r}) = \rho(\mathbf{r} - \mathbf{r}_o) \tag{8.38}$$

   which corresponds to a translation of $\rho(\mathbf{r})$ by a vector $\mathbf{r}_o$ (Fig. 8.8a).
2. The convolution of a function $f(x)$, defined in the range $0 \leq x \leq a$, with a *one dimensional lattice function* is given by

$$L(x) \otimes f(x) = \sum_{n=-\infty}^{\infty} f(x - na) = \rho(x) \tag{8.39}$$

   where $\rho(x)$ is now a periodic one-dimensional function. We obtain in this way the periodic repeat of the function $f(x)$ (Fig. 8.8b)
3. The convolution of a function $f(\mathbf{r}) \equiv f(x, y, z)$, defined in the ranges $0 \leq x \leq a$, $0 \leq y \leq b$, $0 \leq z \leq c$, with a *three dimensional lattice function* is given by

$$L(\mathbf{r}) \otimes f(\mathbf{r}) = \sum_{u,v,w=-\infty}^{\infty} f(\mathbf{r} - \mathbf{r}_{u,v,w}) = \rho(\mathbf{r}) \tag{8.40}$$

   which is a periodic three dimensional function. In Fig. 8.8c a two dimensional example is shown.

8.2 X-Ray Diffraction

When X-rays interact with matter, two types of scattering may occur:

1. *Coherent (Thomson) scattering* with a phase change of $\Delta\phi = \pi$
2. *Incoherent (Compton) scattering*.

Besides, X-rays are absorbed by matter also in two ways:

(a) *without photoemission*
(b) *with photoemission*

We will focus our attention on the *kinematic theory* of diffraction by ideal crystals, while for the more complex *dynamic theory*, capable of handling real crystals (with a finite size and defects in the lattice periodicity), the reader is referred to the textbooks cited in the introduction.

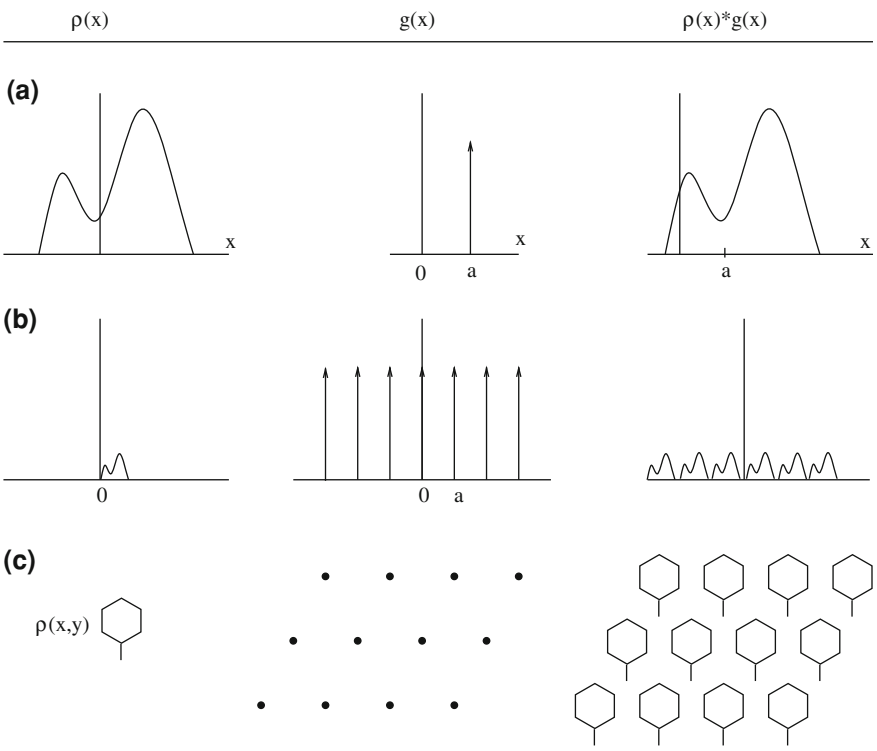


Fig. 8.8 Convolution of a function $f(x)$ with: **a** a δ function; **b** a one dimensional lattice function; **c** convolution of a function $f(x, y)$ with a two dimensional lattice function

8.2.1 X-Ray Scattering

Thomson scattering: The scattering, without loss of energy, of X-rays by a particle was studied by Thomson, who derived that the coherent scattered radiation has an intensity (Fig. 8.9) given by

$$I_{e(Th)} = I_i \left[\frac{e^4}{m^2 r^2 c^4}\right] \frac{1 + \cos^2 2\theta}{2} \tag{8.41}$$

where I_i is the intensity of the incident beam, e is the charge of the particle, m is the mass of the particle, 2θ is the scattering angle and r is the distance from the particle to the point where the intensity is measured. Note that uncharged particles do not give coherent scattering and that, because of the inverse dependence from m^2, in practice only electrons (the smallest nucleus has a mass 1840 times that of electrons) contribute to the scattering in a significant way. The term $P_o = (1 + \cos^2 2\theta)/2$ is the form taken by the *polarization factor* when the incident beam is completely unpolarized, as in the case of the radiation from a conventional X-ray

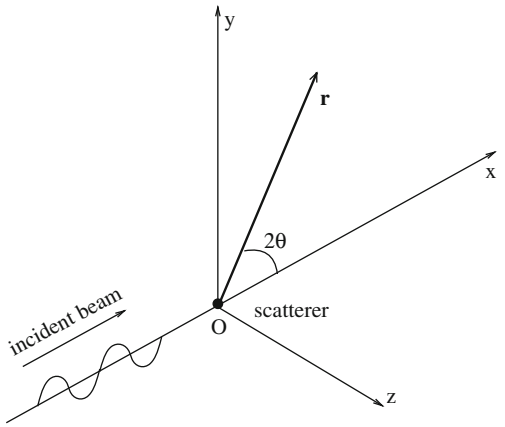


Fig. 8.9 Coherent scattering by a particle in O

tube. Synchrotron sources give partially polarized radiation and the polarization factor changes accordingly.[3]

Compton scattering: Is the incoherent scattering in which the radiation loses part of its energy. The process may be described in terms of an inelastic collision between the X-ray photon and the electron. The difference in wavelength between the incident and the scattered beam is given by

$$\Delta\lambda = 0.024\ (1 - \cos 2\theta)\ \text{Å} \tag{8.46}$$

and is maximum for $2\theta = 180°$ (back-scattering).

---

[3] For partially polarized radiation the polarization factor becomes

$$P = P_o - P' \tag{8.42}$$

where, if ψ is the azimutal angle on the detector,

$$P' = \frac{\tau'}{2}\ \cos 2\psi\ \sin^2 2\theta \tag{8.43}$$

and

$$\tau' = \frac{\alpha(1+\tau) - (1-\tau)}{\alpha(1+\tau) + (1-\tau)} \tag{8.44}$$

where α depends from the monochromator crystal (for a perfect crystal $\alpha = \cos 2\theta_M$, θ_M being the Bragg angle of the monochromator) and

$$\tau = \frac{I_\parallel - I_\perp}{I_\parallel + I_\perp} \tag{8.45}$$

in which $I_\parallel$ is the intensity of the source in a direction parallel to the beam (the electric field vector is along y in Fig. 8.9) and $I_\perp$ is the intensity in a perpendicular direction (electric field vector along z).

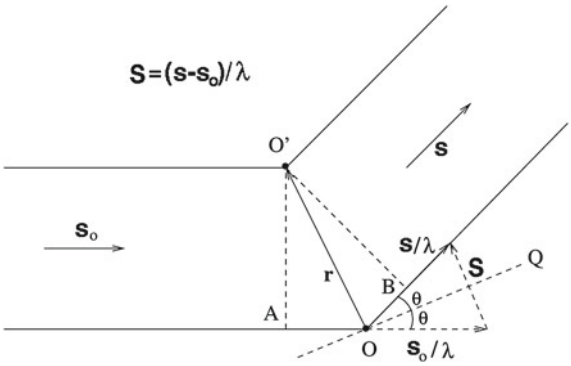


Fig. 8.10 Scattering by two centers in O and O' and their interference

8.2.2 *Interference of Scattered Waves*

Since we are interested in diffraction we have to consider the interference between waves scattered by different scattering particles. In Fig. 8.10, the incident beam, of wavelength λ, hits two point scatterers along a direction defined by the unit vector $\mathbf{s}_o$. Then the phase difference between the wave scattered by the particle in O' in the direction indicated by the unit vector $\mathbf{s}$ and that scattered in the same direction by the particle in O, is given by

$$\delta = \frac{2\pi}{\lambda}(\mathbf{AO} + \mathbf{OB}) = \frac{2\pi}{\lambda}(\mathbf{s} - \mathbf{s}_o) \cdot \mathbf{r} = 2\pi \mathbf{S} \cdot \mathbf{r} \tag{8.47}$$

where

$$\mathbf{S} = \frac{\mathbf{s} - \mathbf{s}_o}{\lambda} \quad \text{with modulus} \quad |\mathbf{S}| = \frac{2\sin\theta}{\lambda} \tag{8.48}$$

where 2θ is the angle between the incident and the scattered waves. If $\lambda \gg r$ then $\delta \to 0$ and interference becomes negligible.

Then, if A_o is the amplitude of the wave scattered by O, the amplitude of the wave scattered by O' will be

$$A'_o e^{J\delta} = A'_o e^{2\pi J \mathbf{S}\cdot\mathbf{r}}. \tag{8.49}$$

As we have seen only electrons contribute to the X-ray scattering and therefore A_o and A'_o will depend on the electron contents of O and O'. Indicating with A_{Th} the amplitude scattered by a free electron, we can define the *scattering factor* as $f = A/A_{Th}$, corresponding to the number of electrons in the scattering point.

If we now have N *scattering points* at the end of the set of vectors $\{\mathbf{r}_i\}$ $(i = 1, N)$, the resulting scattering amplitude, with respect to the amplitude scattered by a free electron at the origin, will be

$$\mathbf{F}(\mathbf{S}) = \sum_{i=1}^{N} \frac{A_i}{A_{Th}} e^{2\pi\jmath \mathbf{S}\cdot\mathbf{r}_i} = \sum_{i=1}^{N} f_i e^{2\pi\jmath \mathbf{S}\cdot\mathbf{r}_i}. \tag{8.50}$$

A *continuous scatterer* may be described by a continuous electron density function $\rho(\mathbf{r})$ and a volume element $d\mathbf{r}$ at $\mathbf{r}$ will contain $\rho(\mathbf{r})d(\mathbf{r})$ electrons, scattering with an amplitude

$$\rho(\mathbf{r})d\mathbf{r}e^{2\pi\jmath \mathbf{S}\cdot\mathbf{r}} \tag{8.51}$$

The total scattered radiation will then be

$$\mathbf{F}(\mathbf{S}) = \int_r \rho(\mathbf{r}) e^{2\pi\jmath \mathbf{S}\cdot\mathbf{r}} d\mathbf{r} = T[\rho(\mathbf{r})] \tag{8.52}$$

which indicates that the scattered amplitude is the Fourier transform of the electron density function. Then $\rho(\mathbf{r})$ will be the inverse Fourier transform of $\mathbf{F}(\mathbf{S})$, i.e.

$$\rho(\mathbf{r}) = \int_S \mathbf{F}(\mathbf{S}) e^{2\pi\jmath \mathbf{S}\cdot\mathbf{r}} d\mathbf{S} = T^{-1}[\mathbf{F}(\mathbf{S})] \tag{8.53}$$

8.2.3 Scattering by Matter

We can now consider an *atomic electron*, for which the electron density may be derived from the wave function

$$\rho_e(\mathbf{r}) = |\psi(\mathbf{r})|^2 \tag{8.54}$$

If we assume that $\rho_e(\mathbf{r})$ has a spherical symmetry,[4] the radiation scattered by an atomic electron will have an amplitude

$$f_e(S) = \int_0^\infty U_e(r) \frac{\sin 2\pi r S}{2\pi r S} dr \tag{8.55}$$

where $r = |\mathbf{r}|$ and $U_e(r) = 4\pi r^2 \rho_e(r)$ is the radial electron density function.

We can then extend the same procedure to the scattering of the whole *atom*. The amplitude scattered by all Z atomic electrons will be

$$f_a(S) = \int_0^\infty U_a(r) \frac{\sin 2\pi r S}{2\pi r S} dr = \sum_{j=1}^{Z} f_{ei} \tag{8.56}$$

[4] This approximation is assumed valid for most applications; only when very accurate diffraction measurements are available the deviations from the spherical symmetry are taken into account for detailed charge density studies.

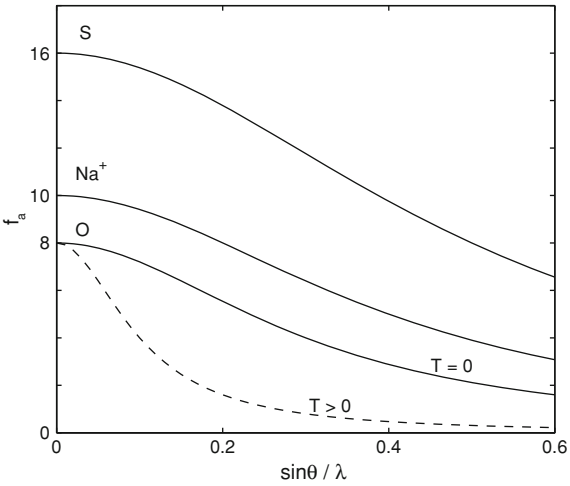


Fig. 8.11 Atomic scattering factors curves for S,Na^+ and O (atoms at rest, $T = 0$). The dotted line shows the O curve for a vibrating atom ($T > 0$)

where $U_a(r) = 4\pi r^2 \rho_a(r)$ is the atomic radial density function and Z the atomic number. The trend of the *atomic scattering factor* $f_a(S)$ as a function of $\sin\theta/\lambda$ is shown in Fig. 8.11 where one can see its decrease as the scattering angle increases.

Atoms, also in the solid state, undergo thermal vibrations and are not fixed at a given position, but oscillate around it. If we assume that this oscillation is equal in all directions (*isotropic displacement*) we can derive that the atomic scattering factor at a temperature T is given by

$$^T f_a(S) = {}^0 f_a(S) e^{-B \sin^2\theta/\lambda^2} \tag{8.57}$$

where ${}^0 f_a(S)$ is the scattering factor for the atom at rest ($T = 0$) and $B = 8\pi^2 U$, U being the mean square displacement of the atom. In Fig. 8.11 the full lines represent the scattering factors for atoms at rest, while the dotted line is the scattering factor for O at room temperature ($T = 298°$). Note that the dotted curve shows a more rapid decrease as $\sin\theta/\lambda$ increases; a vibrating atom will give a negligible contribution at high scattering angles.

8.2.4 Diffraction by a Crystal

We shall first consider the scattering by the *molecules or atoms in the unit cell*. Let us suppose that there are N atoms in the unit cell (they may or may not be connected to form molecules) at positions defined by the set of vectors $\{\mathbf{r}_i\}$ ($i = 1, N$). If we neglect the small fraction of bonding electron density, we can express the electron density of each atom as $\rho_i(\mathbf{r} - \mathbf{r}_i)$, and with this *independent atom* approximation, we can write

$$\rho_M(\mathbf{r}) = \sum_{i=1}^{N} \rho_i(\mathbf{r} - \mathbf{r}_i) \tag{8.58}$$

and the resulting scattered amplitude will be

$$\mathbf{F}_M(\mathbf{S}) = \sum_{i=1}^{N} f_i(\mathbf{S}) e^{2\pi\jmath \mathbf{S}\cdot\mathbf{r}_i} \tag{8.59}$$

An *infinite crystal* may be considered as the infinite periodic repeat of $\rho_M(\mathbf{r})$, i.e.

$$\rho_\infty(\mathbf{r}) = \rho_M(\mathbf{r}) \otimes L(\mathbf{r}) \tag{8.60}$$

Because of the convolution theorem, we can obtain the scattered amplitude as

$$\begin{aligned}\mathbf{F}_\infty(\mathbf{S}) &= T[\rho_M(\mathbf{r})]T[L(\mathbf{r})] = \mathbf{F}_M(\mathbf{S})\frac{1}{V}\sum_{h,k,l=-\infty}^{\infty}\delta(\mathbf{S}-\mathbf{S}_{hkl}) \\ &= \frac{1}{V}\mathbf{F}_M(\mathbf{S})\sum_{h,k,l=-\infty}^{\infty}\delta(\mathbf{S}-\mathbf{S}_{hkl})\end{aligned} \tag{8.61}$$

with

$$\mathbf{S}_{hkl} = h\mathbf{a}^* + k\mathbf{b}^* + l\mathbf{c}^* \tag{8.62}$$

$\mathbf{F}_\infty(\mathbf{S}) \neq 0$ only at the nodes of the reciprocal lattice, where the continuous function $\mathbf{F}_M(\mathbf{S})$ is *sampled*. The sampled values in (8.61) can be indicated by $\mathbf{F}_M(hkl)$, where hkl is a row matrix of the three components of the vector $\mathbf{S}_{hkl}$ in the reciprocal space.

When $\mathbf{S} = (\mathbf{s} - \mathbf{s}_o)/\lambda$ is multiplied by $\mathbf{a}$, $\mathbf{b}$ and $\mathbf{c}$, the so called *Laue diffraction conditions* are obtained

$$\begin{aligned}\mathbf{a}\cdot(\mathbf{s}-\mathbf{s}_o) &= h\lambda \\ \mathbf{b}\cdot(\mathbf{s}-\mathbf{s}_o) &= k\lambda \\ \mathbf{c}\cdot(\mathbf{s}-\mathbf{s}_o) &= l\lambda\end{aligned} \tag{8.63}$$

which, for any given direction $\mathbf{s}_o$ of the incident beam, define the discrete values of $\mathbf{S}$ along which diffraction can occur.

Finally we will consider the case of a *finite crystal* of volume Ω. It is useful to define a *form function*

$$\Phi(\mathbf{r}) \quad \begin{cases} = 1 \text{ within the crystal} \\ = 0 \text{ outside the crystal} \end{cases} \tag{8.64}$$

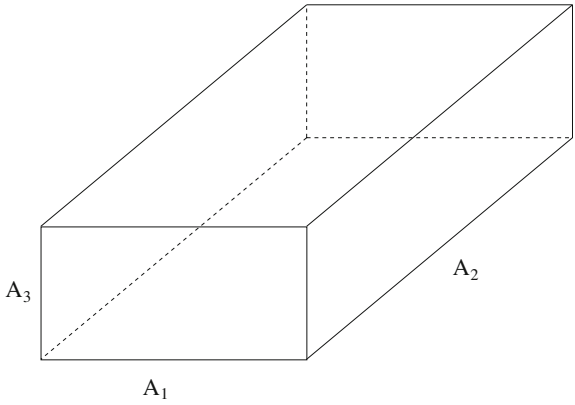


Fig. 8.12 Crystal with the shape of a parallelepiped of edges A_1,A_2,A_3

We can then obtain the finite crystal as

$$\rho_{cry}(\mathbf{r}) = \rho_{\infty}(\mathbf{r})\Phi(\mathbf{r}) \tag{8.65}$$

and, because of the convolution theorem, the scattered amplitude will be

$$\mathbf{F}(\mathbf{S}) = T[\rho_{\infty}(\mathbf{r})] \otimes T[\Phi(\mathbf{r})] = \mathbf{F}_{\infty}(\mathbf{S}) \otimes D(\mathbf{S}) \tag{8.66}$$

where

$$D(\mathbf{S}) = \int_{\Omega} e^{2\pi_J \mathbf{S}\cdot\mathbf{r}} d\mathbf{r} \tag{8.67}$$

is the Fourier transform of the form function, and, recalling (8.61) and the properties of the δ function, we obtain

$$\mathbf{F}(\mathbf{S}) = \frac{1}{V}\mathbf{F}_M(hkl) \sum_{h,k,l=-\infty}^{\infty} D(\mathbf{S} - \mathbf{S}_{hkl}) \tag{8.68}$$

If the crystal is a parallelepiped with edges A_1,A_2,A_3 (Fig. 8.12), it can be shown that

$$D(\mathbf{S}) = \frac{\sin(\pi A_1 S_x)}{\pi S_x} \cdot \frac{\sin(\pi A_2 S_y)}{\pi S_y} \cdot \frac{\sin(\pi A_3 S_z)}{\pi S_z} \tag{8.69}$$

which, similarly to (8.23) and (8.28), has maxima at $A_1 \cdot A_2 \cdot A_3 = \Omega$, with amplitude $(A_1)^{-1} \cdot (A_2)^{-1} \cdot (A_3)^{-1}$. The nodes of the reciprocal lattice become domains of width $(A_i)^{-1}, i = 1, 3$ along the three axes. Similarly for a spherical crystal of radius R the reciprocal lattice nodes will be small spherical domains with radius R^{-1}.

$\mathbf{F}_M(hkl)$ in (8.61) and (8.68) is called *structure factor*. If we now indicate with $\bar{\mathbf{x}}_i \equiv (x_i, y_i, z_i)$ the row matrix with the three components of the position vector $\mathbf{r}_i$ in the direct space, the scalar product of the two vectors $\mathbf{S}_{hkl} \cdot \mathbf{r}_i$ is given by

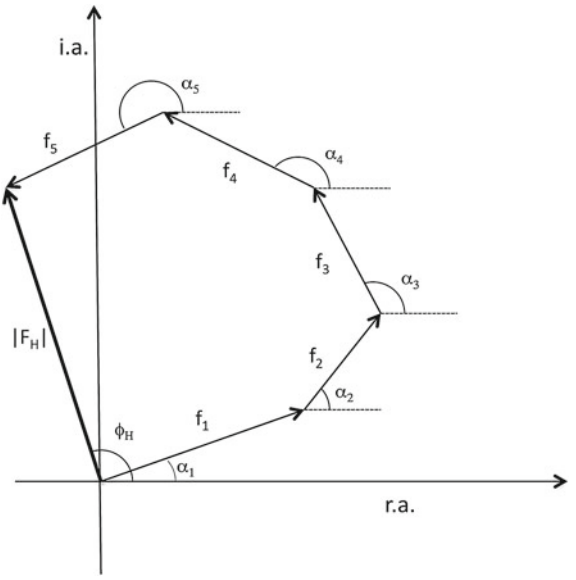


Fig. 8.13 Vector representation in the complex plane of the structure factor of a five atom structure

$$\mathbf{S}_{hkl} \cdot \mathbf{r}_i = hx_i + ky_i + lz_i \tag{8.70}$$

and, substituting in (8.58), the structure factor becomes

$$\mathbf{F}(hkl) = \sum_{i=1}^{N} f_i e^{2\pi \jmath (hx_i + ky_i + lz_i)} = A(hkl) + \jmath B(hkl) \tag{8.71}$$

where

$$A(hkl) = \sum_{j=1}^{N} f_i \cos[2\pi(hx_i + ky_i + lz_i)] \tag{8.72}$$

$$B(hkl) = \sum_{j=1}^{N} f_i \sin[2\pi(hx_i + ky_i + lz_i)] \tag{8.73}$$

With reference to the vector representation of (8.71) in the complex plane, shown in Fig. 8.13, we can express the structure factor in terms of modulus and phase, i.e.

$$\mathbf{F}(hkl) = |\mathbf{F}(hkl)| e^{\jmath \phi(hkl)} \tag{8.74}$$

where

$$|\mathbf{F}(hkl)| = (A(hkl)^2 + B(hkl)^2)^{\frac{1}{2}} \tag{8.75}$$

and

$$\tan\phi(hkl) = \frac{B(hkl)}{A(hkl)} \tag{8.76}$$

Finally, using (8.70), we can write the structure factor as

$$\mathbf{F}_{hkl} \equiv \mathbf{F}(hkl) = \sum_{i=1}^{N} f_i e^{2\pi J(hx_i+ky_i+lz_i)} \tag{8.77}$$

where we can immediately see that the diffracted amplitudes are a function of the coordinates of the atoms in the unit cell, i.e. of *the crystal structure*. We can therefore derive the crystal structure from the diffracted amplitudes, but, as we shall see, this is not a straightforward process. We just note here that relations such as (8.77) are far from being linear and this makes the process of deriving the atomic coordinates directly from these equations impossible in any practical case.

8.2.5 Other Useful Relations and Concepts

The most popular approach to the diffraction by crystals is that proposed in 1912 by W.L. Bragg, who showed that diffraction can be treated in terms of *reflections* by different families of crystal planes. In Fig. 8.14 the horizontal lines represent the traces of two adjacent planes of the family with Miller indices (hkl). The incident $(\mathbf{s}_o)$ and the reflected $(\mathbf{s})$ beams will form the same angle θ with the planes and beams reflected by the two planes will be in phase when their path difference $AB + BC = 2d(hkl)\sin\theta$ is equal to an integer multiple of the wavelength. In this way we can derive *Bragg's law*

$$2d(hkl)\sin\theta = \lambda \tag{8.78}$$

Comparison with (8.48) shows that

$$|\mathbf{S}_{hkl}| = \frac{2\sin\theta}{\lambda} = \frac{1}{d_{hkl}} \tag{8.79}$$

i.e. the reciprocal vector modulus is the inverse of the d-spacing.

Now consider a sphere of radius $1/\lambda$ (Fig. 8.15) and imagine that the incident beam arrives at the origin of the reciprocal lattice in O along the diameter IO. When the node P of the reciprocal lattice, at the end of the vector $OP \equiv |\mathbf{S}_{hkl}|$, is on the surface of the sphere, then

$$OP = |\mathbf{S}_{hkl}| = \frac{1}{d_{hkl}} = IO\ \sin\theta = \frac{2\sin\theta}{\lambda} \tag{8.80}$$

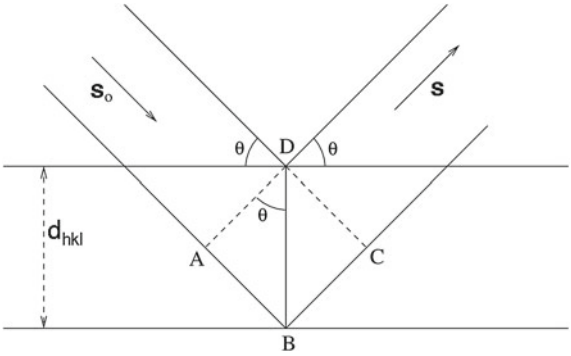


Fig. 8.14 In phase reflection by two adjacent planes of the (*hkl*) family at an inter-planar distance $d(hkl)$

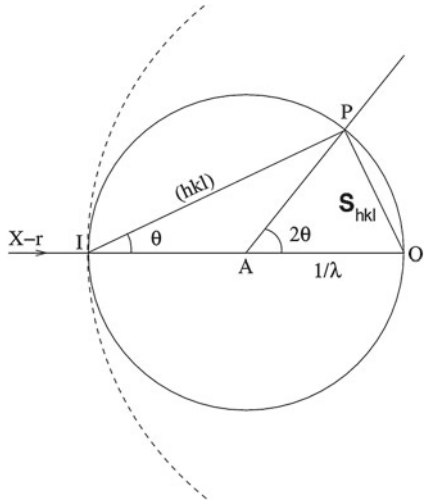


Fig. 8.15 Reflection sphere and limiting sphere

and Bragg's law is fulfilled; the line *IP*, forming an angle θ with the incident beam, will be parallel to the trace of the (*hkl*) planes and the beam will be reflected in the *AP* direction forming an angle 2θ with *IO*. The sphere is known as the *reflection* or *Ewald sphere*. When $OP > 2/\lambda$ the node *P* can never be on the surface of the reflection sphere and we can define a *limiting sphere* of radius $2/\lambda$ delimiting the set of reflections that can be measured with a given wavelength.

With a given wavelength we can therefore only measure a limited number of reflections, but in most cases this may not be an important limiting factor. Indeed, as we have seen the atomic scattering factors are decreasing functions of the scattering angle and the decrease is more pronounced when the thermal vibration increases. When a sufficiently short wavelength (less than 1.0 Å) is used, in most cases the reflections within the limiting sphere became so weak as $\sin\theta/\lambda$ increases, that beyond a certain value they are not detectable. We can then introduce the concept of *resolution*, which is the minimum *d*-spacing corresponding to the maximum useful $\sin\theta/\lambda$, i.e

$$\left(\frac{\sin\theta}{\lambda}\right)_{max} = \frac{1}{2d_{min}} = \frac{1}{2Res} \tag{8.81}$$

For accurate structural determinations it is important to have high angle reflections, which correspond to large (hkl) indices and small d-spacings. Indeed, the exponential terms in the structure factor (8.77), of type $hx_i + ky_i + lz_i$, become more sensitive to errors in the atomic coordinates when h, k and l are large. For instance, with Cu K_α radiation ($\lambda = 1.5418$Å), at the limit imposed by the limiting sphere $\sin\theta_{max} = 1$ and $Res = \lambda/2 = 0.77$ Å. Since the minimum interatomic distance is around 1.0 Å, we shall say that this corresponds to *atomic resolution*. For a poorly diffracting crystal, the maximum angle at which intensities are still detectable may be quite small. Thus for protein crystals it is quite common that, with Cu K_α radiation, $\sin\theta_{max} = 0.3$, and then $Res = 2.6$ Å, and in the electron density map linked atoms will not be resolved as separate maxima.

8.3 The Phase Problem

As indicated by (8.53), the electron density function is related to the scattered amplitude by the relation

$$\rho(\mathbf{r}) = \int_s \mathbf{F}(\mathbf{S}) e^{-2\pi J \mathbf{S}\cdot\mathbf{r}} d\mathbf{S} \tag{8.82}$$

For a crystal we have seen that $\mathbf{F}(\mathbf{S})$ is sampled only at the nodes of the reciprocal lattice; in (8.82) it can be substituted by the discrete values of $F(hkl)$ and the space integral becomes a triple summation over the integer components h,k and l of the reciprocal lattice vectors

$$\rho(\mathbf{r}) = \frac{1}{V} \sum_{h,k,l=-\infty}^{\infty} \mathbf{F}_{hkl} e^{-2\pi J(hx+ky+lz)} \tag{8.83}$$

The electron density is then expressed as a *Fourier series*. It is easy to see that, as expected, it is a real function, which, in terms of the real and imaginary parts of the structure factor [cf. (8.72)], is given by

$$\rho(x,y,z) = \frac{2}{V} \sum_{h=0}^{\infty} \sum_{k=-\infty}^{\infty} \sum_{l=-\infty}^{\infty} [A_{hkl} \cos 2\pi(hx+ky+lz) + B_{hkl} \sin 2\pi(hx+ky+lz)] \tag{8.84}$$

or, in terms of modulus and phase [cf. (8.74)], by

$$\rho(x,y,z) = \frac{2}{V} \sum_{h=0}^{\infty} \sum_{k=-\infty}^{\infty} \sum_{l=-\infty}^{\infty} |F_{hkl}| \cos[2\pi(hx+ky+lz) - \phi_{hkl}] \tag{8.85}$$

We can thus see that it is possible to compute the electron density function within the unit cell, if the structure factors are known in modulus and phase. The positions of the maxima of $\rho(x, y, z)$ would then yield the atomic coordinates defining the crystal structure. Unfortunately the diffraction experiments only give the diffracted intensities, which are proportional to the square of the corresponding amplitude, i.e. $|F_{hkl}| \propto \sqrt{I_{hkl}}$, and the information about the phase ϕ_{hkl} is lost. In order to be able to use (8.85) we will have to overcome the *phase problem*.

8.3.1 Patterson Methods

The oldest method used to solve the phase problem is called the *Patterson method* from the name of its discoverer [10]. It simply consists in calculating the Fourier-transform of the scattered intensities, without phases:

$$P(\mathbf{U}) = \frac{1}{V} \sum_{h,k,l=-\infty}^{\infty} I(hkl) e^{-2\pi_J \mathbf{U}\cdot\mathbf{S}} \tag{8.86}$$

where $\mathbf{U}$ is a vector in the direct space defined as $\mathbf{U} = u\mathbf{a} + v\mathbf{b} + w\mathbf{c}$. The scattered intensity can be written as the product of the structure factor with its conjugate complex number

$$I(hkl) = \mathbf{F}(hkl)\mathbf{F}^*(hkl). \tag{8.87}$$

Remembering the convolution theorem, stating that the Fourier transform of a product of two functions is the convolution of the Fourier transforms of each separated function, it is evident that (8.86) corresponds to the self-convolution of the electron density:

$$P(\mathbf{U}) = \int_V \rho(\mathbf{r})\rho(\mathbf{U} - \mathbf{r}) d\mathbf{r}. \tag{8.88}$$

Application of (8.88) gives us the superposition of the electron density map of the crystal with itself, translated by a vector $\mathbf{U}$. In practice, the Patterson map will present peaks in correspondence to all the interatomic vectors, translated to the origin of the crystal cell. The deconvolution of the map, which is in principle possible, will allow the definition of the original positions of the atoms. The advantage of the Patterson function is that it can be easily calculated from the measured intensities. The disadvantage is that the number of peaks observed for a crystal containing n atoms in the crystal cell is n^2. Since n peaks will be located at the origin, the number of remaining peaks will be $n(n-1)$. We can easily guess that only very small molecules can be solved using this method, since even molecules of 5 or 10 atoms, assuming for example a simple space group with 4 molecules in the unit cell, will give rise to a map containing 380 or 1560 peaks in the crystal cell, respectively. Consider also that even at atomic resolution most of these peaks will, at least partially, overlap,

giving rise to a large, flat background that makes the deconvolution impossible in most cases. Nevertheless, the Patterson method has found several applications in everyday practice. First, it can be used to find the position of one or few heavy-atom(s) in a molecule containing a large number of light atoms: in fact, the map will show large peaks corresponding to inter-atomic vectors between heavy-atoms and this reduces the problem to that of a molecule containing one or few atoms. In addition, Patterson techniques have found widespread use in macromolecular crystallography, in particular in the methods of single- or multiple-isomorphous replacement (SIR or MIR, respectively), described in Chap. 24 of this book.

8.3.2 Direct Methods

Nowadays the structure of *small molecules*, i.e. molecules containing less than about 100-200 atoms, can be routinely solved by the so called *Direct Methods* or, more generally, *ab initio Methods*. The term *Direct Methods* refers to methods that try to derive phases directly from the observed amplitudes through probabilistic relationships. They rely on simple assumptions, like that the electron density is everywhere positive and that crystals are composed of discrete atoms. Based on them, Karle and Hauptman [11], Sayre [12] and many others were able to devise formulas that allow to obtain phases that are approximate, but sufficient to calculate an electron density map that can be interpreted in terms of an atomic or molecular structure. Direct methods are mathematically very complex and they will not be discussed here. A general account of them for the solution of the phase problem may be found in the cited textbooks [13].

8.3.3 Other Methods Used to Solve the Phase Problem

Whilst the structure of small molecule crystals can be solved mainly using the direct methods described in the previous paragraph, the same is not true for macromolecular crystals, with few exceptions. The major reason of their failure is that a very large number of atoms is present in the asymmetric unit (more than 1000 atoms, but in general this number is much larger and can reach values of hundred of thousands in the case of viruses or large macromolecular complexes) and the fact that protein crystals often diffract to a relatively low resolution (generally a resolution better than 1.5 Å is considered quite good, and for very few protein crystals the resolution extends to more than 1 Å). For this reason other methods are used to solve the phase problem: (i) the isomorphous replacement, which can be distinguished in *Single Isomorphous Replacement*, SIR, and *Multiple Isomorphous Replacement*, MIR. They consist in diffusing a compound containing a heavy-atom inside the crystal cell, taking advantage of the presence of the solvent; (ii) *molecular replacement*, where an already known homologous structure already known is properly oriented in the

crystal cell; (iii) *anomalous scattering*, that can assume the form of *Single Anomalous Diffraction*, SAD, and *Multiple Anomalous Dispersion*, MAD. These methods used to solved the phase problem in macromolecular crystallography will be described at length in Chap. 24 of this book.

In this paragraph we want to point out an important aspect of the anomalous scattering. It relies on the fact that, for some atoms and at some wavelength, the atomic scattering factor is not real and its Fourier transform, which is in any case a complex number, does not satisfy the *Friedel law*. As a consequence:

$$F(hkl) \neq F(\bar{h}\bar{k}\bar{l}) \tag{8.89}$$

This inequality not only can be used to determine the position of the anomalous scatterer(s) and consequently to solve the phase problem, but it also represents the only method able to assign the absolute configuration of a molecule. In fact, chiral molecules containing an anomalous scatterer will be able to differentiate between $F(hkl)$ and $F(\bar{h}\bar{k}\bar{l})$.

8.4 Refinement of the Crystal Structure

Once a preliminary or a partial model of the molecule properly positioned in the crystal cell is available, the structure must be *refined*, i.e. atomic coordinates and thermal parameters must be varied in order to improve the agreement between observed and calculated amplitudes. The most widely used method for the refinement of small molecule crystals is the *least-squares method*, where the differences between observed and calculated structure amplitudes are minimized:

$$\Delta = (|\mathbf{F}_{obs}(hkl)| - |\mathbf{F}_{calc}(hkl)|)^2. \tag{8.90}$$

The progress of refinement can be monitored through the calculation of different versions of the so-called *crystallographic R factor*, whose more common version is:

$$R = \frac{\sum |k|\mathbf{F}_{obs}(hkl)| - |\mathbf{F}_{calc}(hkl)||}{\sum k|\mathbf{F}_{obs}(hkl)|} \tag{8.91}$$

where k is the scale factor and the sum is extended over all observed reflections. Another important control parameter is called R_{free}, which is analogous to the R factor, except that it is calculated using a small fraction of reflections, generally 5–10 % of the total, that were excluded from the refinement process. $F_{calc}(hkl)$ is calculated, according to (8.77) :

$$F_{hkl} = \sum_{i=1}^{N} f_i(\mathbf{S}) e^{2\pi\jmath(hx_i+ky_i+lz_i)} e^{-B_i S^2} \tag{8.92}$$

where B_i is the thermal parameter described in Sect. 8.2.3. It represents the isotropic approximation, which is usually not appropriate to describe the thermal motion of atoms. If enough observations are present, it is advisable to introduce an anisotropic description of the atomic thermal displacement using a 3×3 tensor. The latter describes an ellipsoid, centered on the ith atom, in the reference crystal system.

The number of observations is a relevant aspect in the refinement process: their number, i.e. the number of independent reflections, must be at least 5–10 times the number of variables. The latter corresponds to 4–9 times the number of atoms present in the asymmetric unit of the crystal for the isotropic or anisotropic model, respectively. The number of observations, in turn, is strictly related to resolution: when the resolution extends to values close or lower than 1Å, the ratio observations/variables is largely sufficient. If this does not apply, as is generally the case for macromolecules, appropriate tools, based on other available information, must be applied.

The refinement process requires an iterative procedure, where automatic cycles of refinement are alternated with visual inspections of electron density maps. In the latter stage a very useful tool is represented by the Fourier-difference map, calculated with the formula:

$$\rho(\mathbf{r}) = \frac{1}{V} \sum_{h,k,l=-\infty}^{\infty} [k F_{obs}(hkl) - F_{calc}(hkl)] e^{j\phi} e^{-2\pi J(hx+ky+lz)} \tag{8.93}$$

The map calculated with (8.93) will show positive maxima corresponding to atoms absent in the model and negative minima corresponding to atoms misplaced. These errors are hardly corrected by automatic procedures and often require manual intervention.

At the end of the refinement process it is expected that the crystallographic R factor has a value as low as possible: in the case of small molecule crystals it can reach values from 0.02 to 0.06 (higher values, from 0.07 to 0.10 are looked suspiciously and must be justified, for example they can be due to the presence of disorder in some part of the molecule). For macromolecules, higher values are expected, as discussed in Chap. 24.

8.5 Diffraction by Polycrystalline Samples

As we have seen, for an accurate structural analysis, we must achieve the best possible representation of the electron density, $\rho(\mathbf{r})$, by measuring the intensity I_{hkl} of as many reflections as possible. In practical terms we must perform an experiment in which as many as possible reciprocal lattice nodes cross the surface of the reflection sphere. This can be done in three different ways

- Using a single crystal and a monochromatic X-ray beam with a fixed direction $\mathbf{s}_o$, the crystal is moved so that most accessible reciprocal lattice nodes are brought to satisfy Bragg's low. This method will be discussed in other lectures.

- A monochromatic X-ray beam with a fixed direction $\mathbf{s}_o$ hits a large number of randomly oriented crystals. This is the case of the so called *powder diffraction* technique, which we will treat in more details in this section.
- Using a single crystal and a polychromatic radiation each reciprocal lattice node will have a chance of being on the surface of one of the infinite reflection spheres (one for each wavelength of the polychromatic radiation) available. This was the technique used in the first experiment of Friedrich and Knipping and is known as the *Laue method*. In recent years intense white synchrotron radiation sources have been used to obtain Laue diffraction patterns with very short exposure times in order to carry out time resolved experiments on materials and biological molecules [14, 15].

In order to measure their intensity the reflections are collected on a detector, which can be a film, a counter or an area detector (image plate or CCD). The intensities are proportional to the square of the structure factors

$$I_{hkl} = K|F_{hkl}|^2 \tag{8.94}$$

where K includes several terms, among which the Lorentz (taking into account the time needed by the little volume around the reciprocal lattice node to cross the surface of the reflection sphere) and polarization factors, the incident beam intensity I_o, λ^3 and the volume of the sample.

We will now give a brief overview of the *powder diffraction* technique. For a more detailed description the reader is referred to specific publications [16–18].

An ideal crystalline powder is formed by an infinite number of randomly oriented small crystals (*crystallites or grains*). The Fourier transform of this set of randomly oriented lattices will be an infinite number of randomly oriented identical reciprocal lattices all with a common origin. Each reciprocal lattice vector $\mathbf{S}_{hkl}$ will then assume all possible orientations (Fig. 8.16) and the corresponding reciprocal lattice node will becomes the surface of a sphere of radius $|\mathbf{S}_{hkl}|$. This sphere will intersect the reflection sphere on a circle and the reflected beams will be on a cone with vertex in A and aperture 4θ. Of course in a real sample the number of grains will be finite and not necessarily the crystallites will be randomly oriented. In order to approach the ideal case we will have to grind our sample to increase the number of grains and to avoid as much as possible preferred orientations of the crystallites.

8.5.1 Experimental Techniques for Obtaining Powder Diffraction Patterns

The most common setting of powder diffractometers is the so called *Bragg-Brentano* geometry, shown in Fig. 8.17.[5] The X-rays hit the flat sample CP (powder pressed in a flat plate) and with this geometry the reflected beams are focalized on the counter D.

[5] A more detailed description of the experimental techniques is given in Chap. 10.

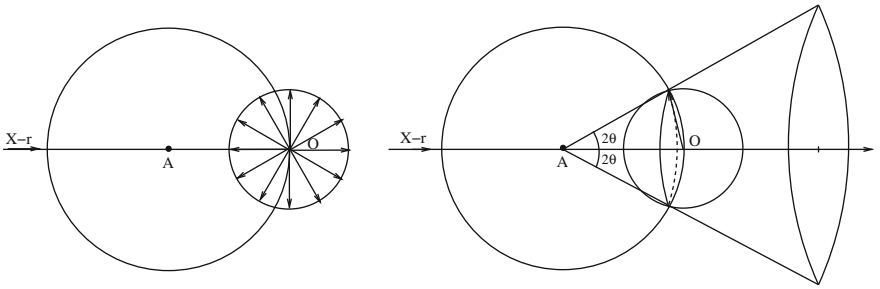
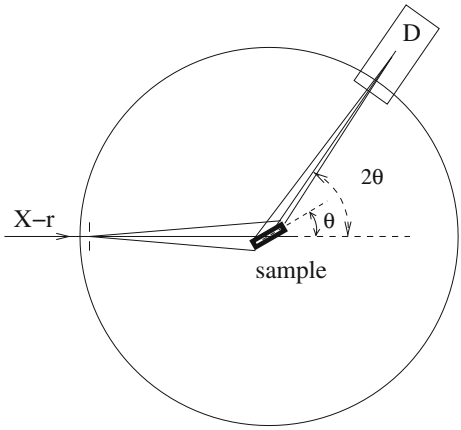


Fig. 8.16 Reflection sphere and sphere generated by a randomly oriented reciprocal lattice vector. Cone of reflected beams

Fig. 8.17 Bragg-Brentano geometry



An other common setting is the so called *Debye-Scherrer* geometry, in which the sample is in a cylindrical capillary and is usually rotated to reduce the effects of preferred orientations. In the early days this geometry was used with film detectors as shown in Fig. 8.18. In modern instruments the film is replaced by a counter or a *position sensitive area detector* (like on a film several reflections are recorded at the same time).

X-rays are monochromatized by a graphite or a silicon monochromator and collimated by different types of slits. Focusing mirrors are always used with synchrotron radiation and often employed with conventional X-ray sources. The recorded diffraction pattern is then digitized and stored in a file with a suitable format. The plot of the pattern of a Silicon sample, used as standard, is shown in Fig. 8.19. From the 2θ value we obtain $\sin\theta$ and for a given wavelength [recalling (8.62)] we have

$$|\mathbf{S_H}| = \frac{2\sin\theta}{\lambda} = |h\mathbf{a}^* + k\mathbf{b}^* + l\mathbf{c}^*| \tag{8.95}$$

Since $d_{\mathbf{H}} = 1/|S_{\mathbf{H}}|$ we can write

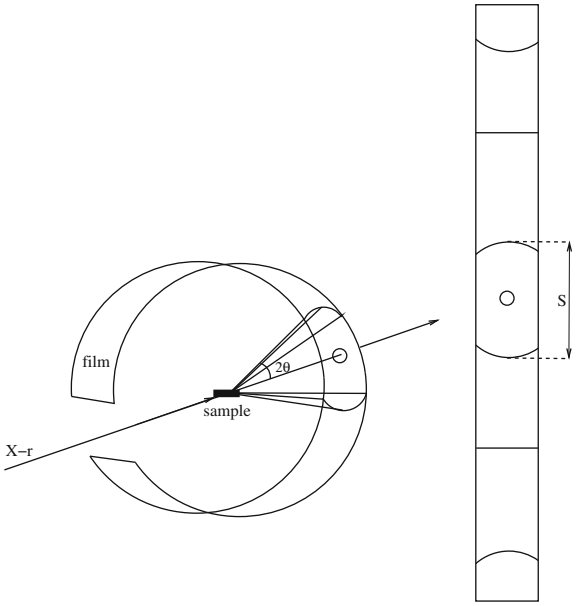


Fig. 8.18 Debye-Scherrer geometry

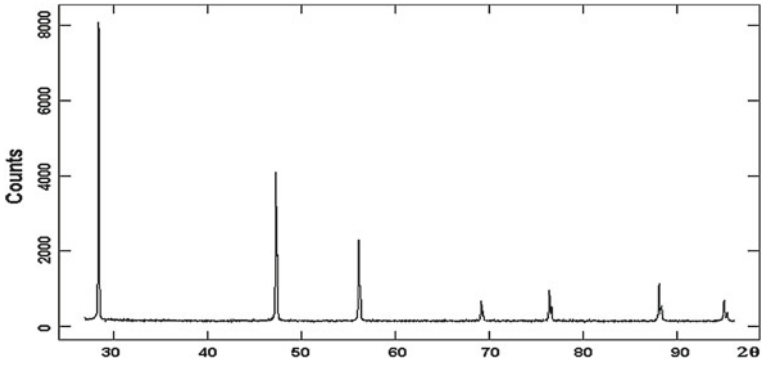


Fig. 8.19 Powder diffraction pattern of Silicon (NBS 640b)

$$\frac{\sin^2\theta}{\lambda^2} = \frac{1}{4d_{\mathbf{H}}^2} = \frac{1}{4}(h^2a^{*2} + k^2b^{*2} + l^2c^{*2} + 2\,h\,k\,a^*b^*\cos\gamma^* + 2\,h\,l\,a^*c^*\cos\beta^* + 2\,k\,l\,b^*c^*\cos\alpha^*) \qquad (8.96)$$

We will have a relation of this type for each reflection and from this set of relations it is possible to derive the reciprocal cell parameters and the indices of the different reflections. This is not a straightforward procedure for low symmetry crystals and becomes usually rather simple for cubic crystals.

The most serious limitation inherent to powder diffraction is *reflection overlap*. In fact, especially at high reflection angles, different families of planes with different (*hkl*) indices (i.e. with different orientations with respect to the reference axes) may have very close $d_{\mathbf{H}}$ values and the orientational averaging arising from the random orientation of the crystallites will cause the overlap of the corresponding reflections. If a peak is the overlap of two or more reflections it will be impossible to decide *a-priori* what fraction of the total intensity should be assigned to the individual reflections. Synchrotron radiation allows a much higher angular resolution and peaks which overlap in an experiment with a conventional source may often be resolved.

8.5.2 Analysis of Powder Diffraction Patterns

We now give a very brief account of the information which can be attained from the analysis of powder diffraction patterns. A more detailed description is reported in Chap. 10.

1. *Phase analysis*: Each crystalline phase has its typical diffraction pattern which is characterized by the d-spacings $d_{\mathbf{H}}$ and the relative intensities $I_{\mathbf{h}}$ of all reflections. If a data base of powder diffraction data of the pure compounds of interest is available (a general database can be purchased [19]), by comparing the set $\{d_{\mathbf{H}}, I_{\mathbf{h}}\}$ of experimental values of an unknown sample with those reported in the database we can identify the crystalline phases present in the sample.
2. *Phase transitions*: When a crystalline compound undergoes a phase transition, its diffraction pattern changes as a consequence of the modification of the lattice. It is possible to record diffraction patterns at continuously increasing temperatures and a transition point can be identified by the sudden change in the pattern.
3. *Quantitative phase analysis*: From the ratios of the intensities of the reflections of the different phases it is possible to obtain an estimate of the relative quantity of each phase. This can be done using the *Internal Standard* method or an extension [17] of the Rietveld refinement technique (see Chap. 10).
4. *Structure determination and refinement*: As we have seen, the determination of a crystal structure requires the knowledge of the structure factors in modulus and phase. The first may be derived from the intensities, but reflection overlap will make this process much more difficult. Patterson and direct methods can be applied to achieve phase information, but the uncertainty on the moduli makes crystal structure solution from powder data more problematic. Recent progresses in the algorithms [20, 21] and the use of high resolution synchrotron diffraction patterns have allowed the solution of increasingly complex structures with up to 30–40 independent atoms. The refinement of the structure is usually performed by the Rietveld method.
5. *Crystallite dimensions and deformations*: (8.68) and (8.69) indicate that finite crystals give wider diffraction maxima. It is therefore possible to derive the average size D of the grains from the analysis of the profiles of the diffraction

maxima. The simplest (but less accurate) relation between D and the *full width at half maximum (FWHM)* $\Delta(2\theta)$ is

$$D = 0.9\frac{\lambda}{\cos\theta\Delta(2\theta)} \tag{8.97}$$

More complex and accurate relations have been derived [22] and a more detailed description is given in Chap. 10.

Deformations of the sample by mechanical, thermal or other treatments cause variations in the lattice cell parameters and consequently the positions of the diffraction maxima will change. It is possible to obtain an estimate of the strain and stress tensors from diffraction experiments [2].

6. *Preferred orientations*: As mentioned before, it may happen that in the powder sample the crystallites are not randomly oriented. Indeed acicular or plate crystals will tend to align or pile in a preferred way and sometimes mechanical and/or thermal treatments can orient the grains. We will then have *textured* samples and in this cases the intensity of the diffracted beams along the cones of Fig. 8.16 will not have a uniform distribution. An analysis of these distributions for some reflections will allow the construction of the so called *polar figures* [22, 23], from which the *orientation distribution functions* (*ODF*) may be derived.

   A very promising method for exploiting preferred orientation to obtain single-crystal-like diffraction data from textured polycrystalline samples has been recently proposed [24].

References

1. B.K. Vainshtein, *Symmetry of Crystals and Methods of Structural Crystallography*, vol I (Springer, Berlin, 1994)
2. C. Giacovazzo, H.L. Monaco, G. Artioli, D. Viterbo, M. Milanesio, G. Ferraris, G. Gilli, P. Gilli, G. Zanotti, M. Catti, *Fundamentals of Crystallography* (Oxford University Press, Oxford, 2011)
3. G.H. Stout, L.H. Jensen, *X-Ray Structure Determination* (Wiley, New York, 1989)
4. E. Zolotoyabko, *Basic Concepts of Crystallography* (Wiley, New York, 2011)
5. M.M. Woolfson, *An Introduction to X-Ray Crystallography* (Cambridge University Press, Cambridge, 1997)
6. C.P. Brook (ed.), *International Tables for Crystallography*, vol 8 (Wiley, New York, 2012)
7. J.R. Helliwell, *Macromolecular Crystallography with Synchrotron Radiation* (Cambridge University Press, Cambridge, 2005)
8. E. Spiller, X-Ray Optics, in Encyclopedia of Optical Engineering (Driggers and Hoffman, eds). (Taylor & Francis, USA, 2003)
9. A.M. Khounsary, A.K. Freund, T. Ishikawa (eds.), in *X-Ray Optics Design, Performance, and Applications, Proceedings of SPIE, Society of Photo-optical Instrumentation Engineers*, Denver, Colorado (1999)
10. M.J. Buerger, *Vector Space and Its Application in Crystal Structure Investigation* (Wiley, New York, 1959)
11. J. Karle, H. Hauptman, Acta Crystallogr. **3**, 181 (1950)
12. D. Sayre, Acta Crystallogr. **5**, 60 (1952)

13. C. Giacovazzo, *Direct Phasing in Crystallography* (Oxford University Press, New York, 1998)
14. D.W.J. Cruickshank, J.R. Helliwell, L.N. Johnson (eds.), *Time-Resolved Macromolecular Crystallography* (Clarendon Press, Oxford, 1992)
15. J.R. Helliwell, P.M. Rentzepis (eds.), *Time-Resolved Diffraction* (Clarendon Press, Oxford, 1997)
16. R.A. Young (ed.), *The Rietveld method* (Oxford University Press, Oxford, 1995)
17. R.E. Dinnebier, S.J. Billinge, *Powder Diffraction—Theory and Practice* (Springer, Berlin, 2008)
18. V. Pecharsky, P. Zavalij, *Fundamentals of Powder Diffraction and Structural Characterization of Materials* (Springer, Berlin, 2009)
19. PDF-2 Powder Diffraction File Database, *The International Centre for Diffraction Data (ICDD)*. Newtown Square, USA
20. A. Altomare, M. Camalli, C. Cuocci, C. Giacovazzo, A. Moliterni, R. Rizzi, J. Appl. Cryst. **42**, 1197–1202 (2009)
21. M. Freeman, A.M. Gorman, J.M Newsam, in *Computer Modeling in Inorganic Crystallography*, ed. by C.R.A. Catlow (Academic Press, London, 1997) pp. 117–150
22. R.L. Snyder, J. Fiala, H.J. Bunge, *Defects and Microstructure Analysis by Diffraction* (Oxford University Press, Oxford, 2000)
23. M. Hatherley, W.B. Hutchinson, *An Introduction to Textures in Metals, Monograph 5* (The Institute of Metallurgists, London, 1980)
24. C. Baerlocher, L.B. McCusker, Science **284**, 487 (1999)

Chapter 9
Photoemission Spectroscopy: Fundamental Aspects

Carlo Mariani and Giovanni Stefani

Abstract Over the past five decades, photoemission has become one of the most popular spectroscopies for investigating matter in its various aggregation states. It finds its application in fields ranging from solid state physics to chemistry, biology and geology, just to mention a few. The number of researchers who need to be introduced to this field is ever increasing, and the spectrum of backgrounds that they possess is very large. Aim of this chapter is to provide for all of them a basic introduction to the models upon which photoemission is based and, by the help of simple examples, to explain what information photoemission can provide.

9.1 Introduction

An electron bound to an atom, a molecule or a solid, is characterized by energy, momentum and spin quantum numbers. Among other spectroscopic techniques, photoemission is the best suited tool to study these physical quantities. It is based upon the photoelectric effect, one of the cornerstones on which quantum mechanics description of matter rests. In essence, the photoelectron effect amounts to shining a monochromatic electromagnetic radiation ($h\nu$) on a sample and producing free electrons with a well-defined energy spectrum. The Einstein equation connects energy of the quantum of the electromagnetic field (photon) with the maximum energy of the ejected free electron (E_e^{MAX}) through a constant characteristic of the sample

C. Mariani
Dipartimento di Fisica, CNISM, Università di Roma "La Sapienza",
Piazzale Aldo Moro 2, 00185 Rome, Italy
e-mail: carlo.mariani@uniroma1.it

G. Stefani (✉)
Dipartimento di Scienze, Università Roma Tre and CNISM Unità Roma 3, Via della Vasca Navale 84, 00146 Rome, Italy
e-mail: stefani@fis.uniroma3.it

S. Mobilio et al. (eds.), *Synchrotron Radiation*,
DOI: 10.1007/978-3-642-55315-8_9, © Springer-Verlag Berlin Heidelberg 2015

(work function Φ) $E_e^{MAX} = h\nu - \Phi$. It establishes a close relationship between sample characteristics and energy spectrum of the ejected electrons and suggests using the photoemission process to build up a wide range of different spectroscopies aimed at studying the electronic structure of matter in its various aggregation states.

Such a spectroscopy allows investigation of the occupied electronic states, it gives information on the dielectric (insulator, semiconductor or metal) and chemical state, on the magnetic properties and on the local structure. Although the photoelectron effect is known since over a century [1–6], spectroscopies based upon this phenomenon [7, 8] have developed over the past fifty years, mostly driven by progresses in development of monochromatic, bright and tunable light sources [9, 10]. Nowadays, photoelectron spectroscopy (PES) has practical applications in many fields of science, such as surface physics and chemistry, material science, nano technologies and still significantly contributes to the understanding of fundamental aspects of physics, chemistry, biology, etc. [11].

The ubiquitous use of photoelectron spectroscopy is testified by the presence of several beam lines devoted to PES in whatever synchrotron radiation source throughout the world. Aim of the present chapter is to establish the fundamental concepts upon which PES relays in order to turn a photoemission experiment into a flexible spectroscopic tool to investigate ground state electronic properties of matter. To this end, we shall make use of the quantum description of the interaction between electromagnetic radiation (EM) and matter outlined in Bertoni's chapter [12]. A selected set of experiments on quantum objects, starting from simple atoms and ending with solids and surfaces, will provide evidences for discussing values and limitations of the approximations needed in order to turn a photionization process into a spectroscopic tool. This brief introduction to photoelectron spectroscopy with synchrotron radiation, will not rigorously and exhaustively treat the process and the scientific results. The reader will be introduced to the fundamentals of photoemission theory and to the various methods of photoelectron spectroscopy with synchrotron radiation, with a few scientific examples. For in depth description of the photoelectron spectroscopy, we refer to review literature [8, 11, 13–15].

9.2 Basic Concepts

The schematics of a modern photoionization spectrometer is shown in Fig. 9.1. In essence, the experiment amounts to measuring the photoelectron current (J_e) as a function of the electron kinetic energy (E_e), the electron ejection angles (θ, ϕ) and the spin (σ) for each given energy ($h\nu$) and polarization vector (ε) of the incident photons.

To this end, it is mandatory to analyse in energy, momentum and (possibly) spin the photoelectrons before detecting them and measuring J_e. This is usually achieved by electrostatic spectrometers in conjunction with electron multipliers that allow for detecting single electrons [16].

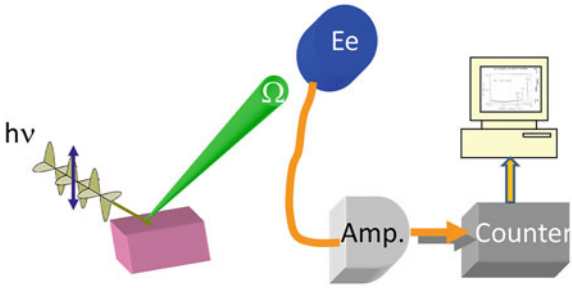


Fig. 9.1 Schematics of a photoionization measurement. A monochromatic photon beam (hν) impinges on the sample; photoelectrons emitted within the solid angle Ω defined by the electron detector (*Ee*) are energy analysed, detected and properly histogrammed as a function of their kinetic energy

The strong interaction of electrons with matter imposes to perform experiments under vacuum (at least 10^{-7} mbar) in order to measure a probability distributions of photoelectrons not altered by interaction with the background atmosphere surrounding the sample. As far as photon source is concerned, there are two different types of quasi monochromatic excitation sources that are available under laboratory conditions, namely VUV line spectra of discharge lamps for energies in the range 10–50 eV (UPS), e.g. with rare gases like helium ($He_{I_\alpha} = 21.218$ eV and $He_{II_\alpha} = 40.814$ eV) and the characteristic lines from the X-ray source (XPS) for which the most commonly used anode materials are aluminium (Al $K\alpha_{1,2} = 1486.6$ eV) and magnesium (Mg $K\alpha_{1,2} = 1253.6$ eV). Although the line width is small enough for many applications, i.e. few meV for discharge lamps and slightly below 1 eV for X-ray anodes, the use of an additional monochromator can be advantageous for the energy resolution and, more importantly, for suppression of background and satellite intensities. More recently, SR sources have allowed for enhancement of several orders of magnitude in resolution, tunability, wavelength span and polarization control in the UV and X-ray sources (see for example [9]).

In the photoemission process, the sample is left in an ionized state when the electron is emitted. Both the sample (atom, molecule or solid) and the emitted electron can be viewed as excited, differing from the fundamental state by the incident photon energy. The photoemitted electron current J_e, as measured by an ideal spectrometer resolving energy, angle, photon and electron polarization states, is a function of 10 variables $J_e = f(h\nu, \varepsilon, \theta, \phi; E_e, \sigma, \theta_e, \phi_e)$, as shown in Fig. 9.2:

In a typical experiment, only a few of these parameters are varied keeping the others either constant or being integrated. For example, in the Energy Distribution Curve (EDC) method, the current J_e is measured as a function of the photoelectron energy E_e, while keeping the other variables fixed. In the angular resolved mode, the θ_e, Φ_e angles are resolved, otherwise the technique is angular integrated. Moreover, if it is possible to analyze the photoelectron spin state σ, the technique gives information on the magnetic state of the sample.

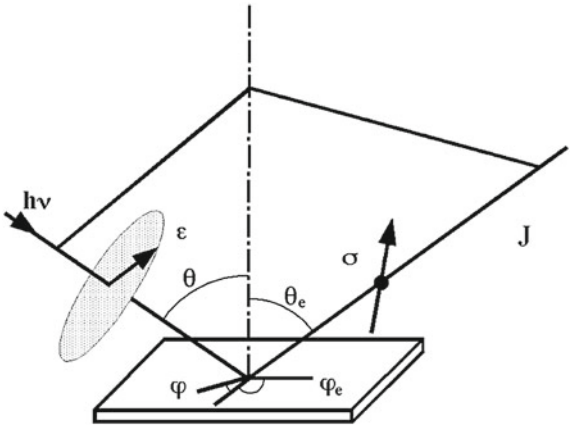


Fig. 9.2 Schematic diagram of the photocurrent J_e and of all the variables

Before entering into the details of the connection between J_e and the photoionization cross section, we stress the high surface sensitivity of this technique. In fact, while photons typically penetrate the solid for tens of nm, obviously depending on the material type and photon wavelength, the typical energy of the photoemitted electrons lies in the 5–1500 eV range and their escape depth is limited to a range from a few to a few tens of Å. The escape depth determines the depth from which photoemitted electrons escape from the solid into vacuum without loosing energy. It can be phenomenologically described as an exponential attenuation of the photoemitted current as a function of the depth from which the photoelectron is emitted. The escape depth value is limited by the electron-electron scattering, mostly the excitation of collective modes (plasmons), while the electrons escape into vacuum from the solid. Thus, a fraction of photoelectrons (primary electrons) escape into vacuum without suffering scattering and energy losses, while a large part of photoexcited electrons (secondary electrons) scatter and suffer various energy losses, giving rise to an unstructured background towards low kinetic energy in the photoelectron spectrum, and essentially loosing information. The escape depth, that is directly proportional to the mean free path λ, is a function of the electron kinetic energy and follows a general behavior, with a minimum value (thus a maximum surface sensitivity) roughly between 10 and 50 eV. There are analytical functions derived for the different materials [17]: As an example the mean free path measured for a series of semiconducting materials [14] is shown in Fig. 9.3.

9.3 Energy Conservation, Binding Energy and Photoelectron Energy

The photoelectric process can be described as the transition of one electron from an initial occupied state to a final empty free-electron level in vacuum. The photoelectron current J_e is a macroscopic quantity directly linked to the photoionization micro-

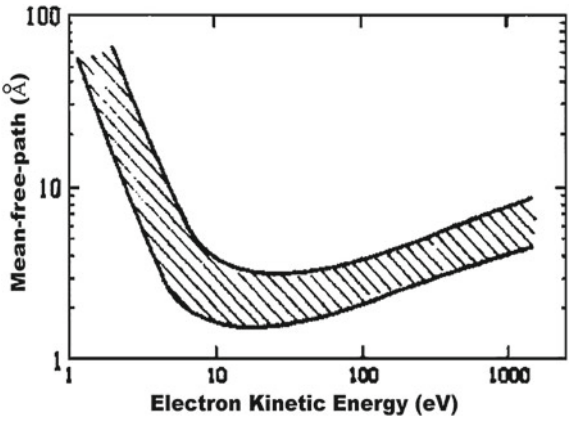


Fig. 9.3 Electron mean-free-path in a solid, as a function of photoelectron energy

scopic cross-section through the relation $J_e = \int_{\Delta\Omega} d\Omega \int_{\Delta E_e} dE_e I \rho_A \left(\frac{d\sigma}{d\Omega\, dE_e}\right) K_s$ where $\Delta\Omega$ and ΔE_e are the electron spectrometer angle and energy acceptances, respectively, I is the incoming photon current, ρ_A is the sample areal density, K_s the spectrometer efficiency and $\left(\frac{d\sigma}{d\Omega\, dE_e}\right)$ the photoionization differential cross section. Hence, to highlight the information contained in the photoelectron current we shall discuss the photoelectric differential cross section. To this end, and for sake of simplicity, let's take the simplest many electron quantum system we can find in nature: i.e. the He atom. In such an atom two electrons are bound to a doubly charged nucleus in a $n = 1, \ell = 0, m = 0, s = \pm 1/2$ quantum state $1s^2$ whose spectroscopic notation is $^1S_0$.

According to treatment of electromagnetic interaction with matter [12] and within the validity of the dipole approximation, the photoabsorption cross-section by a quantum object can be written as:

$$\sigma = 4\pi^2 \alpha h\nu \sum_B \left| \hat{\varepsilon} \cdot \left\langle \Psi_B \left| \sum_i \vec{r}_i \right| \Psi_A \right\rangle \right|^2 \delta(E_B - E_A - h\nu) \tag{9.1}$$

where $\hat{\varepsilon}$ is the light polarization, Ψ_A is the initial state, Ψ_B are the final states of the system and the index i runs over the target electrons. To achieve photoionization of He, one of the two electrons must be promoted to the continuum ($E_e > 0$ with respect to vacuum level), see Fig. 9.4. Hence, in an experiment where a monochromatic photon energy larger than the threshold energy (i.e. the minimum energy needed to ionise the system, see Fig. 9.4) is absorbed by an He atom, the energy conservation δ of (9.1) suggests that electrons are generated with a kinetic energy that satisfies the relation

$$E_B = E_A + h\nu \tag{9.2}$$

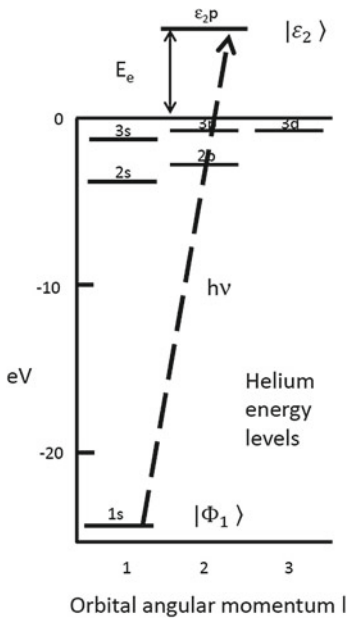


Fig. 9.4 Diagram of the energy levels of the He atom; the *arrow* represents the photon energy required for the photo ionisation process to take place ($h\nu$), $|\Phi_1\rangle$ and $|\varepsilon_2\rangle$ are the single electron initial and final states. The label ε_2p recalls that dipole selection rules imply a continuum state with $\ell = 1$

Let's now assume that initial and final states are correctly described in terms of antisymmetrized product of fully independent particles: i.e. $\Psi_A = \hat{A}\phi_1\phi_2$ and $\Psi_B = \hat{A}\phi_1\varepsilon_2$ where ε_2 is a single particle continuum wavefunction and $\hat{A}$ is an anti-symmetrization operator. Under these conditions (9.2) applied to the case sketched in Fig. 9.4 reads

$$\begin{aligned} E_{1s} + E_e &= E_{1s} + E_{1s} + h\nu \\ E_e &= E_{1s} + h\nu \\ E_e &= h\nu - BE_{1s}(24.6\,\mathrm{eV}) \end{aligned} \tag{9.3}$$

Hence, in the J_e distribution a single peak is to be expected whose kinetic energy is directly linked to the unperturbed initial state single particle binding energy (BE). In other words: photoemission spectra should give direct access to spectroscopy of single particle bound states of a multi electron system such as electronic orbitals for atoms, molecules and clusters. A more elaborate concept is needed for photoemission from solids [11].

Is reality as simple as we think? Let's examine the J_e experimental data for Helium (He). For this atom, the independent particle model is expected to be realistic, and the energy level diagram of Fig. 9.4 can be used to represent both initial and final states. In Fig. 9.5 it is reported the experimental photoemission spectrum of He as measured with a monochromatic beam of energy 89.5 eV, i.e. the $J_e(E_e)$ at a fixed $h\nu$. In case of validity of the fully independent particle model, the observed photoelectron

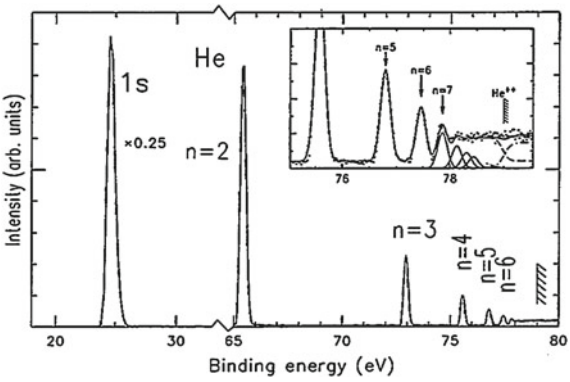


Fig. 9.5 The He photoemission spectrum as measured at $h\nu = 89.5\,eV$. The peak labeled $n = 1$ corresponds to the transition $h\nu + He(1s^2) \rightarrow He^+(1s^1) + \varepsilon_{l=1}$, where the label n refers to the principal quantum number of the excited ionic state. From [18]. Copyright Elsevier, reprinted with permission

spectrum should consist of a single peak, *main peak*, at the photoelectron energy that satisfies (9.3), the one labeled as 1s at a binding energy of 24.6 eV, that corresponds to the transition

$$h\nu + He(1s^2) \rightarrow He^+(1s^1) + \varepsilon_{\ell=1}$$

Further photoemission peaks appearing in the spectrum labeled as $n = 2, 3, \ldots$. and the continuum distribution extending above the He^{++} threshold energy, cannot be interpreted in terms of independent particle model and to explain these so called *satellite structures* many-body properties of the systems should be taken into account. Similar *satellite structures* are observed for all the rare gases [19, 20] and they become more and more relevant as the atomic number increases. We shall see in the following that for targets of increased complexity, such as heavy atoms, molecules, clusters or solids, the photoelectron spectrum is accordingly more complex. To interpret these spectra asks for models more sophisticated than the one outlined in (9.3), and this will be discussed in the following paragraphs.

9.4 Satellite Structures

To understand the origin of the *satellite features* appearing in the photoemission spectra we shall use as a case study the He spectrum. Besides the peak associate with the final state $1s^1$ foreseen by the independent particle approach, a manifold of discrete transitions at larger "apparent" BE followed by a continuum, above the double ionization threshold, is also clearly observed in Fig. 9.5.

In building up the aforementioned energy conservations (9.3), we have implicitly assumed validity of the "frozen core approximation", i.e. relaxation of the sample upon creation of a hole-state and electron-electron correlation is neglected. To overcome these limitations the system is to be described as formed by N interacting

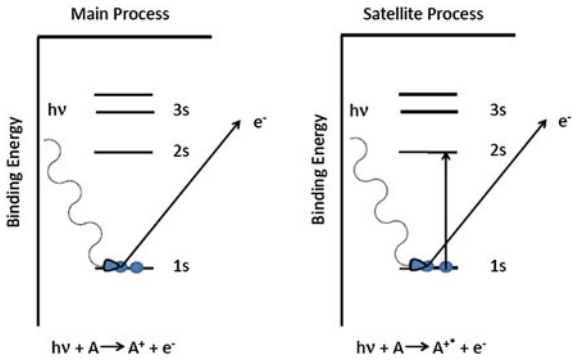


Fig. 9.6 The energy level diagrams are sketches of the mechanism responsible for generation of the main peak (one electron transition) and satellite structures (two electron transitions, see text for details)

electrons, see (Fig. 9.6), the energy eigenvalues of which are defined according to the Schrödinger equation:

$$H_0 \left|\Psi_A^{(N)}\right\rangle = E_A^{(N)} \left|\Psi_A^{(N)}\right\rangle, \tag{9.4}$$

in which the initial state Hamiltonian is

$$\begin{aligned} H_0 &= H_0(kin) + H_0(e-n) + H_0(e-e) + H_0(s-o) \\ &= \sum_1^N \frac{p_i^2}{2m} + \sum_1^N -\frac{Ze^2}{r_i} + \sum_{i>j}^N \frac{e^2}{r_{ij}} + \sum_1^N \zeta(r_j)\vec{\ell}_i \cdot \vec{s}_i \end{aligned} \tag{9.5}$$

and the N-particle wave function is simply described by a Slater determinant of one electron spin-orbitals

$$\left|\Psi_A^{(N)}\right\rangle = \hat{A}(\phi_j(\vec{r}_j, \sigma_j); \Psi_R^{(N-1)}) \tag{9.6}$$

with Â an antisymmetrization operator rendering the N particle state compatible with the Pauli principle, $\Psi_R^{(N-1)}$ as a minor at $N-1$ electrons of the N electrons matrix and is ϕ_j the jth single particle spin orbital of the initial state from which the photoelectron is extracted.

For the final state of the photoionization process

$$H_0' \left|\Psi_B^{(N)}\right\rangle = E_B^{(N)} \left|\Psi_B^{(N)}\right\rangle \tag{9.7}$$

where H_0' is the final state Hamiltonian (note that in general H_0 is not equal to H_0').

Assuming validity of the Sudden Approximation: i.e. the electron in the continuum state $|\varepsilon_l\rangle$, with kinetic energy E_e and momentum $\vec{K}_e$, (photoelectron) is fully decoupled (does not interact) from the residual $(N-1)$ particles ion, the final N-particle state can be expressed as

$$\left|\Psi_B^{(N)}\right\rangle = \hat{A}(\varepsilon_l; \left|\Psi_B^{(N-1)}\right\rangle) \tag{9.8}$$

To appreciate consequences of the many-particle descriptions of the atom on the Je spectrum, let's write down the photoemission cross section at fixed photon energy and differential in the photoelectron energy and emission angle. It derives directly from the absorption cross section (9.1) that, in the case of a discrete-to-continuum transition, represents the total probability of photoemission over the 4π solid angle.

By replacing expressions (9.6) and (9.8) in (9.1) we obtain:

$$\frac{d\sigma}{d\Omega dE_e} \propto \sum_B \left|\hat{\varepsilon}\cdot\left\langle\varepsilon_l\left|\vec{r}_j\right|\phi_j(\vec{r}_j,\sigma_j)\right\rangle\left\langle\Psi_B^{(N-1)}|\Psi_R^{(N-1)}\right\rangle\right|^2 \delta(E_e + E_B^{(N-1)} - E_A^N - h\nu) \tag{9.9}$$

Assuming validity of Koopman's theorem, i.e. the target atom electronic structure stays frozen under creation of the hole state, Hamiltonians of initial and final states are identical ($H_0 = H_0'$) and the monopole matrix element appearing in (9.9), usually termed Fractional Parentage, is 0 unless the ionic state is equal to the frozen residual (N − 1) configuration of the initial state. As a consequence, the photoemission cross section will be different from 0 (J_e different from 0) only for the ionic states that correspond to the frozen residues at N − 1 of the initial N particles ground state. In this way relaxation and correlations are overlooked, energy conservation reduces to the δ function appearing in (9.9) and the Koopman's energy of the photoelectron is directly linked to the binding energy of single particle orbital involved in the photoionization process. Under these circumstances, the only allowed photoemission process for He is: $h\nu + \mathrm{He}(1s^2) \rightarrow \mathrm{He}^+(1s^1) + \varepsilon_{\ell=1}$ that is associated to the most intense peak appearing in Fig. 9.5 (Main line or adiabatic peak). To explain the faint structures highlighted in Fig. 9.5, the condition $H_0 = H_0'$ must be relaxed, thus allowing for a spectrum of possible final ionic states to be associated with removal of an identical single particle spin orbital. There is a manifold of different final states associated to each individual single particle hole state that imply excitation of further electron(s) of the target both to discrete and continuum empty states (shake-up and shake-off satellites respectively). The monopole matrix element of (9.9) determines which final states are allowed (monopole selection rules) and with which probability. In the case of He, for instance, the main allowed transitions present in the spectrum are:

$$\begin{aligned}
h\nu + \mathrm{He}(1s^2) &\rightarrow \mathrm{He}^+(1s^1) + \varepsilon_{\ell=1} \\
h\nu + \mathrm{He}(1s^2) &\rightarrow \mathrm{He}^+(2s^1) + \varepsilon_{\ell=1}, \mathrm{He}^+(3s^1) + \varepsilon_{\ell=1}, \mathrm{He}^+(4s^1) \\
&\quad + \varepsilon_{\ell=1}, \ldots \mathrm{He}^{++} + \varepsilon_\ell + \varepsilon_{\ell'} \\
h\nu + \mathrm{He}(1s^2) &\rightarrow \mathrm{He}^+(2p^1) + \varepsilon_{\ell=0}, \mathrm{He}^+(3p^1) + \varepsilon_{\ell=0}, \mathrm{He}^+(4p^1) \\
&\quad + \varepsilon_{\ell=0}, \ldots \mathrm{He}^{++} + \varepsilon_\ell + \varepsilon_{\ell'}
\end{aligned}$$

These transitions explain most of the satellite structures observed but the next question is: can E_e still be directly connected to single particle binding energies? It can be shown that sum rules applicable to photionization process imply that: (i) the weighted

average of all binding energies (main, shakeup and shake off) yields the Koopman's Theorem binding energy ($BE_{n\ell m}$), (ii) the sum of all intensities is proportional to the frozen orbital cross section $\left(\left|\hat{\varepsilon}\cdot\left\langle\varepsilon_l\left|\vec{r}_j\right|\phi_j(\vec{r}_j,\sigma_j)\right\rangle\right|^2\right)$.

This kind of treatment is very convenient for atoms, molecules and core states of solids, i.e. for all localized electron states. In the case of valence states of solids, i.e. whenever we are dealing with delocalized, continuum electronic state, it is more convenient to formulate the matrix element $\left\langle\varepsilon_l\left|\vec{r}_j\right|\phi_j(\vec{r}_j,\sigma_j)\right\rangle\left\langle\Psi_B^{(N-1)}|\Psi_R^{(N-1)}\right\rangle$ of (9.9) as $\left\langle\varepsilon_l\left|\vec{r}_j\right|\phi_j(\vec{r}_j,\sigma_j)\right\rangle A(\vec{k},E)$ where $A(\vec{k},E)$ is the so called spectral function of the target that can be related to the single particle Green's function. In spite of the formal differences, the conclusions that we have reached on the meaning of main and satellite lines of a photoelectron spectrum are valid independently of the state of aggregation of the target. In particular, the richness of satellite structures is directly linked to the degree of electron correlation that affects the initial bound state involved in the photoionization.

9.4.1 Spin-Orbit Splitting

Besides the aforementioned satellite structures, further splitting of the photoemission peak associated with $\ell \neq 0$ hole states is noticeable. This is particularly evident in the case of the Xe 3d doublet. This is a typical final state effect. In these closed shell atoms the initial state energy does not depend upon spin momentum projections as all orbitals are fully occupied. On the contrary, when a vacancy is created in the orbital identified by *n,l,m* quantum numbers, the energy of the final state depends on the spin projection through the term $H_0(s-o)$ of the Hamiltonian (9.5). Hence, it is to be expected that holes in p ($l=1$) and d ($l=2$) will generate doublets of final states characterized by quantum number $j(j = l + s)$ equal to 1/2, 3/2 and 3/2, 5/2 respectively.

9.4.2 Multiplet Splitting

In moving from closed to open shell systems (i.e. quantum systems in which orbitals are partially occupied) complexity of the photoelectron spectrum increases and splitting of peaks not ascribable to spin-orbit interaction is observed. Such effects, usually termed as "multiplet splitting", were first observed in connection with core photoemission from paramagnetic free molecules and transition metal compounds. An introductory example of multiplet splitting as observed in the photoemission spectra from core O 1s electrons in the paramagnetic free molecules O_2 is given in Fig. 9.7 [21]. The electron configuration of the neutral ground state is:

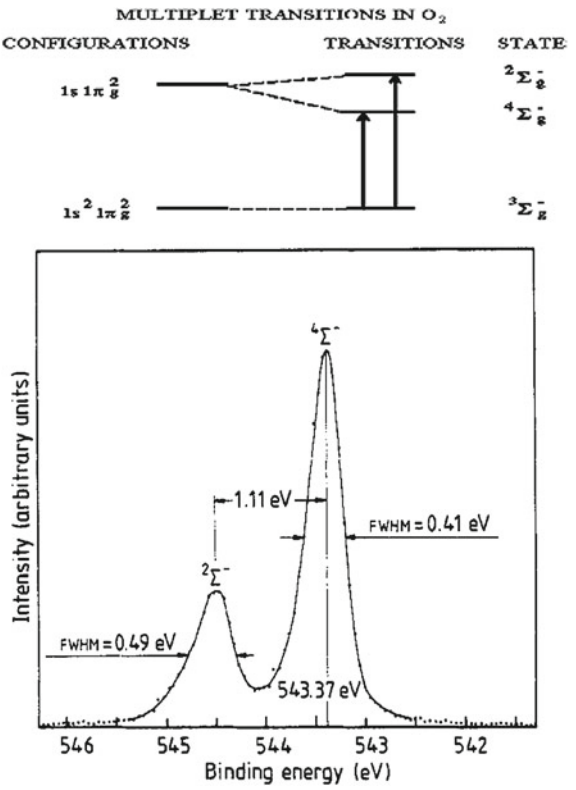


Fig. 9.7 O 1s core photoemission spectrum of molecular oxygen as measured with 1487 eV photons. The observed multiplet splitting of 1.11 eV correspond to the two possible final states outlined in the schematics where energetic of the initial, neutral, and two final ionic states is shown [21]. Copyright Institute of Physics, reprinted with permission

$$KK(\sigma_g 2s)^2(\sigma_u 2s)^2(\sigma_g 2p)^2(\pi_u 2p)^4(\pi_g 2p)^2\,{}^3\Sigma_g$$

As shown in Fig. 9.7, ionization of the K shells leads to two different core hole multiplet states of $O^+{}_2$, one with $^2\Sigma_g$—symmetry, the other of $^4\Sigma_g$—symmetry. Figure 9.7 also shows the XPS spectrum with two separate lines corresponding to these two different final electronic states.

The transitions observed in the photoelectron spectrum can be schematically illustrated as shown in the diagram of Fig. 9.7. The difference in transition energy towards the two different final states, 1.11 eV, arises from spin coupling of the residual 1s core electron with the valence electrons unpaired spins. The relative weight of the two peaks obeys the statistical ratio expected for quartet versus doublet intensity, i.e. 2. It is worth noting that multiplet splittings are observed for both core and valence photoelectron spectra. The valence spectrum of the oxygen molecule, for example, shows very well separated doublet and quartet states. It may also be noted that multiplet splittings are common ingredients in core hole relaxation processes, such as Auger electron spectra, since the final states normally contain two vacancies which may couple in several different ways and give rise to states of different energy.

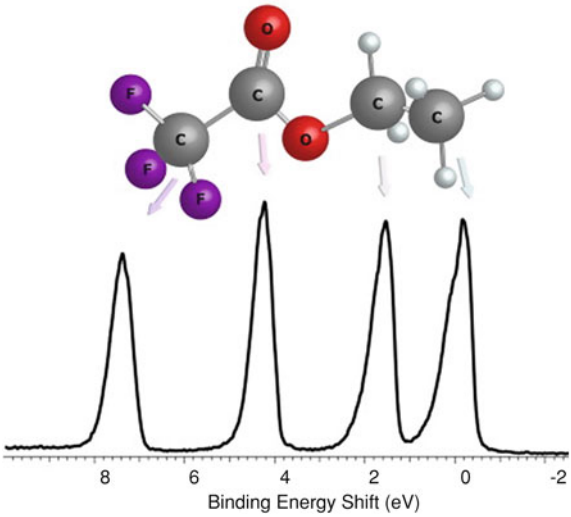


Fig. 9.8 C 1s photoelectron spectrum of ethyltrifluoroacetate showing four different lines due to the chemical shift. The spectrum was excited by monochromatized radiation at 340 eV [22]. Copyright Elsevier, reprinted with permission

9.4.3 Chemical Shift

It is well known that when aggregating atoms to form molecules, clusters or solids, the valence electrons are mostly involved to form bonds while core states remain almost unchanged in their atomic character (i.e. there is a negligible overlap between adjacent atoms core orbitals). Nevertheless, a considerable fraction of photoelectron studies has been primarily involved with the precise measurement of core hole electron binding energies and in particular of what is known as the "chemical shift" suffered by these energies when the chemical environment within which the atom is bound changes. Let's illustrate this effect with an experimental example. In Fig. 9.8 it is shown the photoelectron spectrum of the Ethyl-trifluoroacetate molecule [22]. In this organic molecule four carbon atoms are present in four different chemical environments.

Each individual carbon atom gives rise to a different core photoemission peak, thus allowing for investigating the molecular electronic structure with an atomic scale resolution even though this technique has no spatial resolution. Similar differences are observed for all atoms of the periodic table (C 1s 285–300 eV, O 1s 530–540 eV) and for the same atom bound in different molecules to elements with different electronegativity (C CO_2 298 eV, C CH_4 290.7 eV). The observed difference can be essentially understood in terms of simple electrostatic interactions, when bound to elements with larger electronegativity the binding energy is higher as the screening charge on the atomic site is reduced with respect to the free atom. Vice versa, when bound to elements with smaller electronegativity there is more charge available for screening and e-e-interaction, and the core binding energy accordingly decreases. The chemical shift provides chemically-significant information concerning the initial state electronic structure of the system under study. Both initial (electronegativity)

and final (relaxation of neighboring electrons on the hole) state effects are influenced by chemical environment and contribute to determining the chemical shift.

Empirically, there seems to be a correlation, although exception exists, between chemical shift and electronegativity of neighbor atoms. For small electronegativity differences $\Delta\chi$ the core level shift ΔE is nearly equal to $\Delta\chi$. At larger $\Delta\chi$ the energy shift saturates, probably due to saturation of the charge transfer. From such an empirical behavior, one may predict core level shift for new ligands, or find out from a measured core level shift which ligand (electronegativity of the ligand) is involved.

To accurately calculate chemical shifts, the total "all electron energies" with and without core hole is to be taken into account. In spite of the complexity of this phenomenon, an overall proportionality between binding energy and electronegativity is found in most of the cases.

Core energy shift is also associated to changes in coordination number of the same atom within a given aggregate. Clusters give a clear example where atoms bound to the outermost shell (surface) experience a chemical bond different from those bound to the inner shells (bulk) and the chemical shift is accordingly different.

9.5 Molecular Photoelectron Spectroscopy

The next complex quantum system whose electronic structure is to be investigated by PES is a molecule. It is evident that the extra degree of freedom added to the system by the nuclear motion (i.e. molecular vibrations and rotations) will play a role in the related photoelectron spectra. In this case, energy can be transferred from the electromagnetic field to electronic, vibrational and rotational degrees of freedom of the quantum system. In other words, we ask ourselves how vibrations and rotations will influence molecular photoelectron spectra. Even though we start from a ground state configuration, vibrational and rotational excitations are to be observed besides the electronic ones.

Let's take as an example a simple diatomic molecule, the basic principles laid down in this case remain valid for more complex polyatomic molecules though experimental and theoretical treatments will become accordingly more complex.

9.5.1 Vibrational Overtones

Nitrogen is an archetypal for diatomic molecules and its photoemission spectrum [23] is shown in Fig. 9.9 as a function of the single-particle binding energy, alongside with the molecular orbital assignments. It shows that the three outermost occupied orbitals give rise to three distinct multiplets.

The existence of a fine structure (side bands) for the individual electronic states is ascribable neither to spin-orbit nor to multiplet splitting. This fine structure is due to

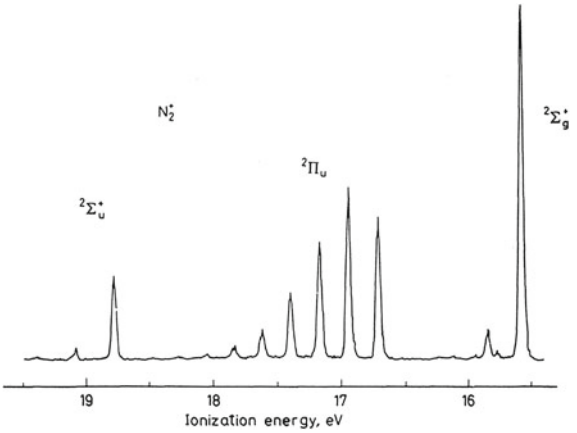


Fig. 9.9 Molecular PES of nitrogen excited by HeI radiation. The molecular orbital assignment is reported alongside the spectrum [23]. Copyright Elsevier, reprinted with permission

an effect that we have neglected so far, namely the generation of the ionized molecule in excited vibrational states.

Vibrational effects are observed in core photoemission spectra as well, as it is demonstrated by the C 1s photoionisation spectrum in CH_4, it displays two overtone peaks displaced by 0.43 and 0.86 eV, respectively, from the carbon main transition [24]. The observed energy splitting is consistent with the vibrational quantum in $CH_4(C1s^{-1})$ while the relative intensities are explained in terms of Frank-Condon factors for transitions to the first and second vibrational states of the molecular ion. Vibrational excitation of the initial ground state is not taken into account as the sample was at room temperature ($kT = 26$ meV) and the nitrogen vibrational quantum is of the order of 400 meV.

Vibrational fine structure is usually clearly visible in UPS (typical energy resolution 0.015 eV) but is obscured in XPS (typical energy resolution 1 eV). Note that a resolution of 0.015 eV corresponds to 120 cm^{-1} (1 eV = 8066 cm^{-1}). This is sufficient to observe a vibrational fine structure but not enough to resolve the rotational fine structure.

To explain the main features of the molecular photoemission spectrum we shall calculate the differential photoemission cross section taking into account that initial and final single particle electronic states are molecular states. For core holes, localization of the electronic state makes atomic like orbitals appropriate for describing both bound and continuum states and an atomic like cross section is appropriate. The situation is more complex for valence delocalised initial states (molecular orbitals) that are described in terms of the usual Born-Oppenhaimer approximation (BO), i.e. as the product of linear combinations of atomic orbitals (LCAO) with independent nuclear motion wavefunctions. Initial and final states should take into account the full geometry of the molecular system and the photoelectron continuum state should account for the interaction with the residual molecular ion, though an atomic continuum model can be assumed valid at high energy and large distance from nuclei. The simplest approximation to continuum wave functions is the Plane Wave (PW) but

several other more elaborate models have been successfully applied (OPW, multiple scattering, etc.).

To calculate the molecular photoemission cross-section we shall follow Gelius approach for XPS where the photoelectron is described as a PW and initial states are described by LCAO. Furthermore, the BO approximation allows to factorise the WFs in a product of electronic and vibrational WFs (we neglect rotational states as they are usually not resolved in PES and XPS).

In other words, the system hamiltonian should now include the nucleus-nucleus interaction

$$\begin{aligned} H_0 &= H_0(kin) + H_0(e-n) + H_0(e-e) + H_0(s-o) + H_0(n-n) \\ &= \sum_1^N \frac{p_i^2}{2m} + \sum_1^N -\frac{Ze^2}{r_i} + \sum_{i>j}^N \frac{e^2}{r_{ij}} + \sum_1^N \zeta(r_j)\vec{l}_i \cdot \vec{s}_i + \sum_{i>j}^M \frac{e^2 Z_i Z_j}{r_{ij}} \end{aligned} \tag{9.10}$$

and the WFs read: $\left|\Psi_{A,B}^{(N)}\right\rangle = \left|\Psi_{A,B}^{(N)^{el}}\right\rangle \left|\Psi_{A,B}^{vib}\right\rangle$. Hence, substituting these initial and final states WFs in the photoemission cross-section (9.9), we obtain the molecular expression of the photocurrent J_e as calculated under the aforementioned approximations and assuming a linear combination of atomic orbitals to represent the initial molecular orbital.

$$\frac{d\sigma}{d\Omega dE_e} \propto \sum_B \frac{\left|\hat{\varepsilon} \cdot \left\langle \varepsilon_l \left|\vec{r}_j\right| \sum_{A\lambda} C_{A\lambda}\phi_{A\lambda}\right\rangle \left\langle \Psi_B^{(N-1)^{el}} \middle| \Psi_R^{(N-1)^{el}} \right\rangle\right|^2}{\left|\left\langle \Psi_B^{vib} \middle| \Psi_A^{vib} \right\rangle\right|^2 \delta(E_e + E_B^{(N-1)} - E_A - h\nu)} \tag{9.11}$$

where $\sum_{A\lambda} C_{A\lambda}\phi_{A\lambda}$ is the LCAO expression of the single particle molecular obital from which the photoelectron is extracted. In the molecular photoelectron spectrum we shall therefore expect as many peaks as many ionic electron-vibrational states are allowed by monopole and vibrational selection rules and with intensities proportional to product of the relevant Frank-Condon (FC) and Fractional-Parentage coefficients. The way FC coefficients will work in a molecular photoionization process is sketched in Fig. 9.10, where the relative probability for exciting final ions in $v = 1, 2, 3, \ldots$ states is depicted as a function of the molecular equilibrium distance of the final ion. As it gets larger and larger with respect to the ground neutral state equilibrium distance (from panel (a) to (d)), increasingly higher v states are accessed in the final ion, till the fragmentation threshold is reached and excitation (discrete vibrational structure in the photoemission spectrum) as well fragmentation (continuum vibrational structure in the photoemission spectrum) are present.

Multiplet splitting is present in molecular spectra as well. A clear example of the experimental vibrational structure observed in the valence photoionization spectrum of molecular oxygen in conjunction with the aforementioned quartet doublet multiplet splitting is given in the PES of O_2 with HeI exciting light [25].

Extensive vibrational structures have been observed also in PES of polyatomic molecules, water is a relevant example. The PES spectrum excited by HeIα radiation at 21.218 eV shows the three outermost valence orbitals whose binding energies

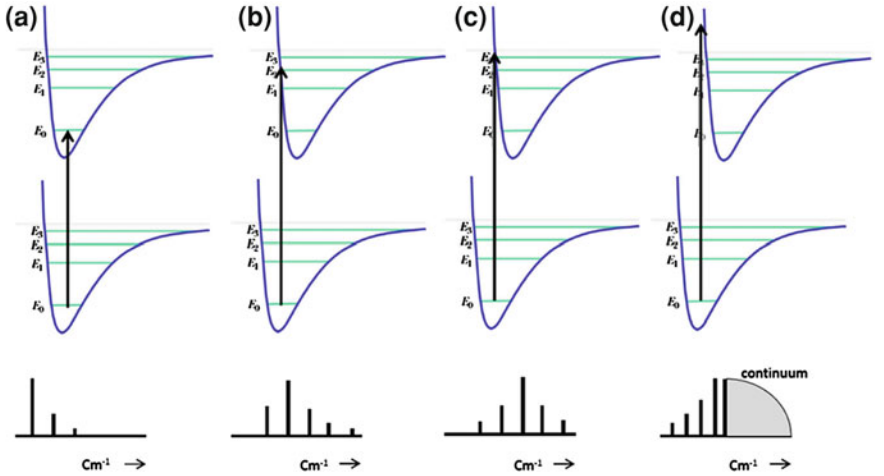


Fig. 9.10 Schematics of the dependence of PES features upon change of the molecular equilibrium distance in the final state molecular ion. Minimum change is the *leftmost* panel, maximum change is the *rightmost* one

have been calculated using a one-electron method (HF) and a many-electron (CI) method. Comparison of the predicted binding energies with the center of mass of the vibrational structure associate to each individual orbital highlights the extreme sensitivity of PES to accurateness of the model adopted in describing the molecular valence orbitals.

Sensitivity of PES vibrational overtones to nuclear masses is demonstrated by the spectra of isotope modified water molecules, ^{18}O instead of ^{16}O and D instead of H [26]. Modern molecular PES studies include spectroscopy of transient states and species as well, but this subject is well beyond the scope of this chapter.

Rotational fine structure is normally not resolved in photoelectron spectra. At a resolution of about 10 meV, the line profiles may be influenced by the rotational excitations, but the individual lines cannot be resolved. At a resolution below about 5 meV, which can be achieved with modern UPS spectrometers, these influences become clearer and can sometimes be used to draw conclusions about the molecular geometry and the intensity of different rotational branches. For diatomic molecules, and larger molecules containing hydrogen, like H_2O or HF, for which the spacing between the individual components of the rotational structure are comparatively large, it may even be possible to observe this fine structure [27].

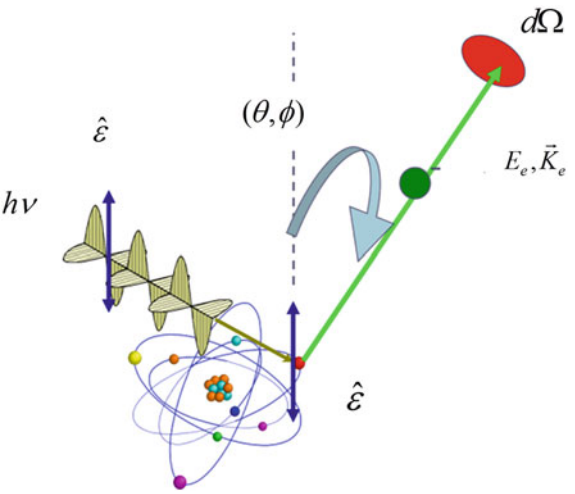


Fig. 9.11 Schematics of an angle resolved photoemission experiment. The linearly polarized light hν photoionises an electron with kinetic energy E_e within the solid angle dΩ in direction (θ, ϕ) with respect to the electric polarization vector ε. θ and ϕ are polar and azimuthal angles, respectively

9.6 Photoelectron Angular Distributions

Up to now we have been dealing only with the energy distribution of the photoelectron probability current, but the cross section (9.9) implies that a distribution in space (ejection angles) exists as well. We shall discuss this aspect of photoemission having in mind that it has a twofold relevance. On the one side angular distribution of photoelectrons is relevant to highlight fine details of photoionization dynamics (hence they are a stringent test for quantum description of radiation-matter interaction). On the other side, accurate description of this phenomenon provides the basis for various spectroscopies based on diffraction of the photoelectron from surrounding atoms that are aimed at studying local geometrical order in molecules, clusters and solids. Let's start from the simple atomic case. Starting from (9.9), it can be shown that, for linearly polarized light and for transition to a well defined ionic state (for fixed photon and photoelectron energies that satisfy the energy conservation δ function), the photoemission cross section reads:

$$\frac{d\sigma}{d\Omega} \propto \sum_B \left| \hat{\varepsilon} \cdot \left\langle \varepsilon_l \left| \vec{r}_j \right| \phi_j(\vec{r}_j, \sigma_j) \right\rangle \left\langle \Psi_B^{(N-1)} | \Psi_R^{(N-1)} \right\rangle \right|^2 \tag{9.12}$$

Hence, we expect the photoelectron current to depend upon direction under which the photoelectron is detected, with respect to polarization vector (see Fig. 9.11), and characteristics of the single particle orbitals involved, both bound and continuum ones.

All molecular and atomic orbitals have a characteristic angular distribution of electrons. This means that the intensity of all final states that we measure in a spectrum will have a certain angular dependence. Upon validity of the approximations

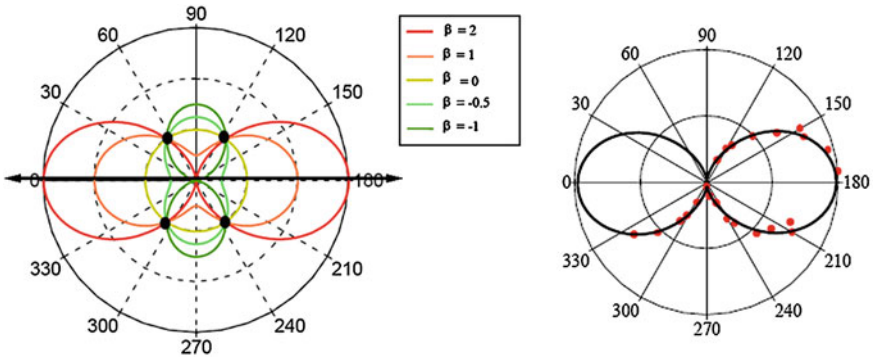


Fig. 9.12 Angular distribution of photoionisation in polar coordinates experimental (*right panel*) and calculated according to (9.13) for different values of β. The polarisation vector ε is reported as a *black bold arrow*. Magic angle has been indicated by a *black point*. Experimental results are relative to He and the best fit to the data is obtained for $\beta = 2$

of expression (9.9), the angular distribution of the emitted photoelectrons can be described using one single parameter, the asymmetry parameter β [28]. In practice it means that the photoelectrons are symmetrically distributed about the polarization direction. Furthermore, upon dipole approximation the photoelectron will be ejected with a continuum wavefunction with $\ell = \pm 1$ with respect to the single particle hole quantum state left behind (this is because the incoming photon carries an unitary angular momentum). This gives an angular distribution of the ejected electron that obeys the relation:

$$\frac{d\sigma}{d\Omega} \propto \frac{\sigma}{4\Pi} [1 + \beta P_2 \cos(\vartheta)] \tag{9.13}$$

where β spans from -1 to 2 and depends on the initial and final state orbitals involved in the ionization process and P_2 is a second order Legendre polynomial. Expected angular dependence of the atomic photoelectron current for selected β values are reported in Fig. 9.12.

By studying this figure it can be seen that there are four directions in which photocurrents are expected to be independent from β values. This occurs at the so called magic angle of 54.74°. At this angle the photocurrent depends only on the total cross section σ and not on the light polarization or the angular momenta of the photoelectron wavefunction or the symmetry of the initial state. That this description is mostly correct in the case of isolated atoms is demonstrated by the good agreement between experimental results on He (dots) and the theoretical prediction for $\beta = 2$ (full line) shown in the right panel of Fig. 9.12.

What happens to photoelectron angular distributions when the atom from which the photoelectron is generated is surrounded by neighboring ones (i.e. in molecules, clusters and solids)? The photoelectron wavefunction gets scattered from each individual atom and the photoelectron analyzer collects a photoelectron current that is

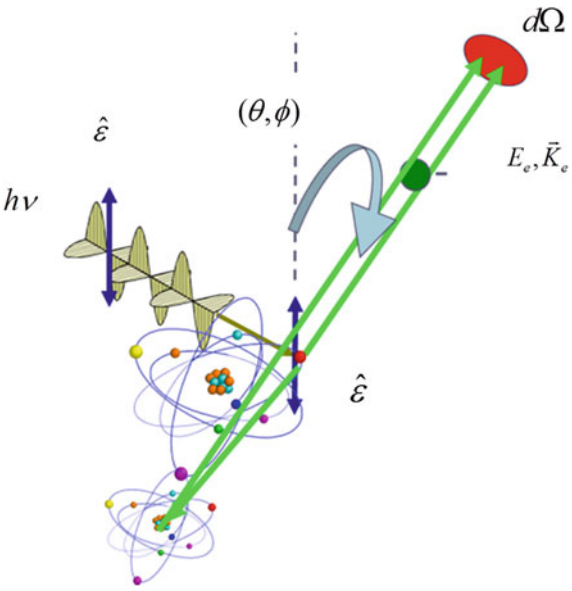


Fig. 9.13 Schematics of an angle resolved photoemission experiment from a dimer oriented in space. The linearly polarized light hν photoionises an electron with kinetic energy *Ee*. The photoelectron current detected within the solid angle dΩ, in direction (θ,ϕ) with respect to the electric polarization vector ε, as determined by coherent superposition of wavefunctions directly generated by the photoemission process and elastically diffused by the neighbor atom

a coherent superposition of source photoelectron wavefunction and point scattered wavefunctions, as schematically shown in Fig. 9.13.

The angular distribution is not any more a smooth distribution determined by β, at will show two main features: A forward intense peak along atom-atom direction, and a diffraction pattern at all other scattering angles. It can be shown that while in the case of an isolated atoms the measured photoelectron current is proportional to the square modulus of the unperturbed photoelectron wave function, i.e. $J_e \propto |\Phi_0|^2$, in the presence of a scatterer it becomes proportional to the square modulus of the coherent sum of the unperturbed and scattered photoelectron wavefunctions, i.e. $J_e \propto |\Phi_0 + \Phi_S|^2$. If we perform measurement of the angular distribution of the photoelectrons ejected from a fixed in space molecule, what is observed is schematically shown in Fig. 9.14 for the case of an aligned in space CO diatomic molecule. Assuming that a core photoelectron is ejected from the carbon atom, the circle represents an hypotetical polar probability distribution determined by the unperturbed wavefunction, while the waving line represents modulation introduced in the photoelectron angular distribution by interference of the direct and scattered wavefunctions.

The intense forward lobe aligned with the molecular axis is to be interpreted as the 0th order peak of the angular diffraction pattern. Intensity maxima appearing at larger angles are higher order diffraction peaks.

It is a crucial issue to establish validity for this simple scheme of interpretation of the photoelectron angular distributions, particularly in the case of core ionization, as it will constitute the cornerstone for applications to solids and surfaces, i.e. for the so-called *photoelectron diffraction*.

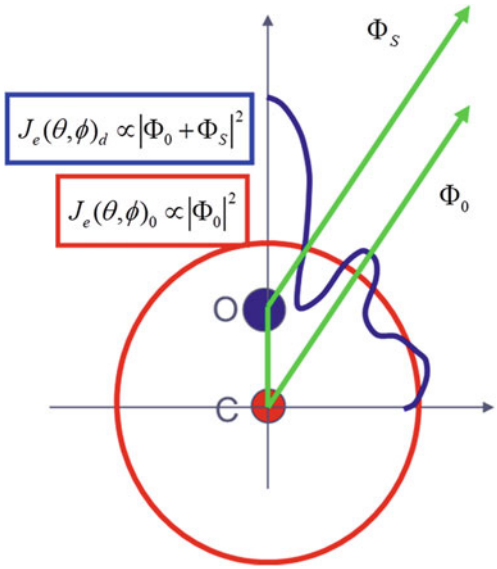


Fig. 9.14 Pictorial view of the photoelectron angular distribution for C ionization of an aligned in space CO molecule

Forward scattering and diffraction features have been clearly seen in an experiment performed on aligned in space CO molecule [29]. The photoelectrons angular distribution was measured in two modes: with the molecular axis parallel or perpendicular to the light polarization vector ε. In the former case the angular distribution is dominated by the forward 0th order diffraction peak as the intensity of the unperturbed wavefunction is low away from the molecular axis. In the latter case the unperturbed wavefunction is weak along the molecular axis while has maxima perpendicular to it, hence the photoelectron angular distribution is dominated by higher order diffraction peaks. These findings have been confirmed by several other independent experiments on similar or different molecular targets, thus providing a sound background for validity of the aforementioned photoelectron diffraction model.

9.7 Core Hole State Relaxation

We have seen that the main peculiarity of photoemission peaks is the linear dispersion of their characteristic kinetic energy with the photon energy (see (9.3)). Inspecting any full energy distribution of photoelectron current, we discover that, besides photoemission peaks, it displays further peaks the energies of which are characteristic of the sample but do not change by changing the photon energy. The origin of these peaks can be explained in an elementary way by the energy diagram shown in Fig. 9.15. The core hole state $|i\rangle$ (i.e. M^+) is created either by direct photoemission (left side panel Fig. 9.15) or by excitation to the excited state $|a\rangle$ (i.e. M*). Obviously, the first process is always possible provided the photon energy exceeds the ionization thresh-

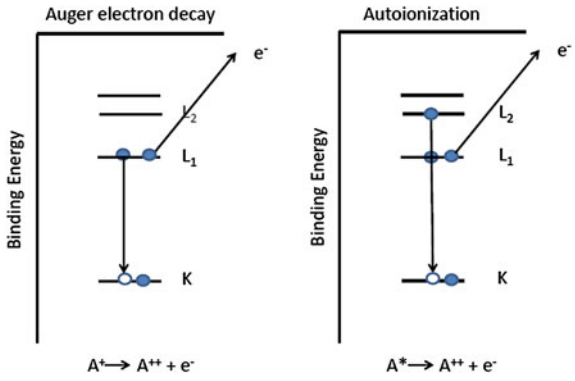


Fig. 9.15 Schematics of the secondary processes leading to electron emission by the decay of a highly excited ionic or neutral system. Usually, the Auger process is associated with the decay of a cation whereas the decay of a neutral system is referred to as autoionization

old, while the second (right side panel) only when the photon matches the difference in energy between the ground state and $|a\rangle$. In both cases, the $|i\rangle$ hole state is part of a singly ionized/neutral excited state whose lifetime is finite. This state will decay through either a radiative way (fluorescence) or a non radiative way i.e. ejecting an electron in the continuum (autoionization). This latter decay channel, originated by electron-electron interaction within the target, is dominant for low Z atoms and is usually termed as autoionization or Auger according to the charge state of the final ion, single or double respectively.

It is evident that the energy spectrum of the autoionizing electrons will reflect the target energy structure through the difference between energy of the final and initial states in as much as the energy of the Auger/autoinozation transition matches the separation energy between $|i\rangle$ and $|a\rangle$.

9.7.1 The Auger Decay

Auger electron emission is usually described within a two-step approximation in which decay incoherently follows the core hole creation $h\upsilon + A \rightarrow A^{+} + e_p \rightarrow A^{++} + e_p + e_A$. The energy distribution of the Auger electrons (e_A) is independent from the photon and photoelectron (e_p) energies, it will be determined by the difference in energy between the intermediate singly ionized state and the final doubly ionized state $E_{Auger} = E_{A^+} - E_{A^{++}}$. Hence, the Auger energy spectrum will be formed by groups of line transitions, one for each core hole state, having as many components as the multiplet configurations allow for the double hole final state. It is therefore spontaneous to indicate each Auger electron emission with a three letter label. The first letter refers to the orbital involved in the intermediate core hole state creation, the other two to the orbitals that generate the doubly ionized final state. Let's take the Ne atom as an example. In its ground state configuration the shells K (n = 1) and L (n = 2) are fully occupied (see leftmost panel in Fig. 9.16).

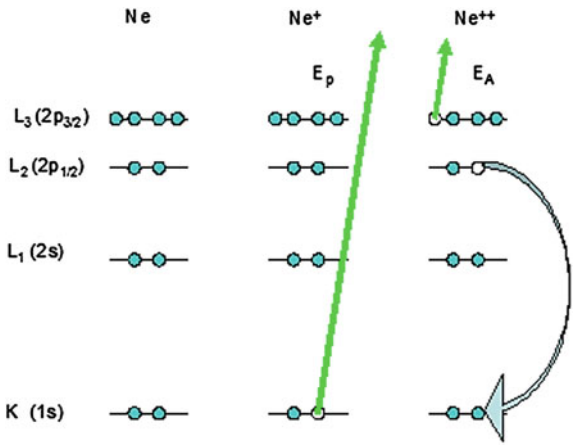


Fig. 9.16 Schematics of the KL_2L_3 Auger process in Ne. E_p and E_A are kinetic energy of the photoelectron and Auger electron, respectively

According to this convention, the Auger transition depicted in the rightmost panel of Fig. 9.16 is KL_2L_3.

This is not the only possible Auger transition for the K core hole to decay, the main groups of transitions with their multiplet structures are listed in the following table.

Auger transition	Double ion valence configuration	Multiplet terms
KL_1L_1	$2s^0\ 2p^6$	$^1S_0$
$KL_1L_{2,3}$	$2s^1\ 2p^5$	$^1P_1, {}^3P_0, {}^3P_2, {}^3P_1$
$KL_{2,3}L_{2,3}$	$2s^2\ 2p^4$	$^1S_0, {}^3P_0, {}^3P_2, {}^1D_2$

The simplest, though coarse, way to calculate individual Auger transition energies is within a simple one-electron model, i.e. ignoring relaxation and final state effects. Within this approximation the multiplet splitting is ignored and the Auger energy can be deduced from the binding energy of the individual orbitals, for instance:

$$E_A(KL_1L_2) = E(K) - E(L_1) - E(L_2, L_1) \tag{9.14}$$

where the latter energy is the binding energy of the L_2 orbital computed in presence of a hole in L_1. There are several methods to calculate more accurately [30], even ab-initio, Auger transition energies but to describe them is beyond the scope of this chapter. The simplified scheme so far outlined is sufficient for interpreting an atomic Auger spectrum such as the one displayed in Fig. 9.17.

Figure 9.17 shows the energy distribution of Auger electrons ($N(E_A)$) from gaseous Krypton as a function of their kinetic energy [31]. The principal transitions can be readily assigned through relation (9.14) and are indexed according to the aforementioned notation. Multiplet splitting of each individual principal transition is

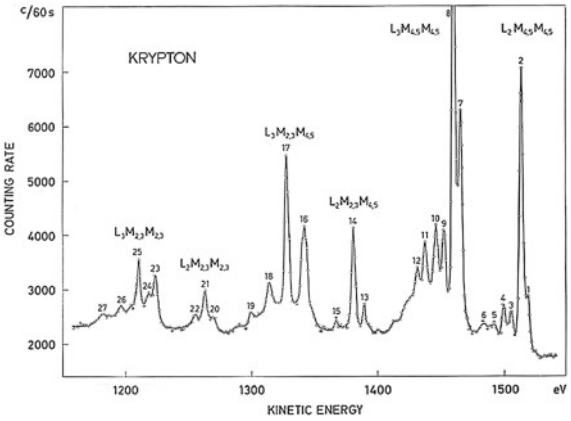


Fig. 9.17 Auger spectrum of gaseous Krypton. The energy distribution is recorded as a function of the Auger kinetic energy. The principal Auger lines are indexed according to the usual notation (see text) [31]. Copyright Elsevier, reprinted with permission

also evident. This effect is better seen, for instance, in the free Zn atom $L_3M_{4,5}M_{4,5}$ spectrum [32]. In Zn, all shells from K to M and the 4s subshell are full, hence a simple two-particles (i.e. two holes in the final doubly ionized state) multiplet structure is appropriate to describe its Auger spectrum. The appropriate spectroscopic terms are: $^1S_0$, $^1G_4$, $^3P_{0,1,2}$, $^1D_2$, $^3F_{2,3,4}$. The overall agreement between theory and experiment is rather good, thus demonstrating that, in spite of the complexity, most features of Auger spectra can be predicted and calculated, thus providing a powerful tool for studying correlated behavior of matter as the final state is always a two interacting particle one. For what concerns intensity of the transitions, the two-step model can be invoked to allow us to compute the probability of an Auger transition as the product of those relative to the core hole creation and decay separately. Hence the probability for an Auger transition initiated by a photon that ionizes a system in state $|0\rangle$ to a core hole state $|i\rangle$ that eventually decays to the doubly ionized state $|f\rangle$ is:

$$P(0,i,f) \propto \left|\left\langle f\varepsilon_p\varepsilon_A\right| C \left|i\varepsilon_p\right\rangle\right|^2 \times \left|\left\langle i\varepsilon_p\right| D \left|0\right\rangle\right|^2 \tag{9.15}$$

in which C and D are coulomb and dipole operators, respectively. The two step model is appropriate as long as the core hole lifetime is much longer than the coulomb interaction time. On the contrary, the single step model is to be adopted. In this frame the core hole state is an intermediate state for the second order transition that leads to the doubly ionized system and the probability reads:

$$P(0,i,f) \propto \left| \int \frac{\left\langle f\varepsilon_p\varepsilon_A\right| C \left|i\tau\right\rangle \times \left\langle i\tau\right| D \left|0\right\rangle}{E_A + E_p - E_\tau - h\nu - i\Gamma/2} d\tau \right|^2 \tag{9.16}$$

In which τ are virtual intermediate states and Γ is the core hole lifetime broadening. It is therefore evident that the main driving force behind Auger transition is the

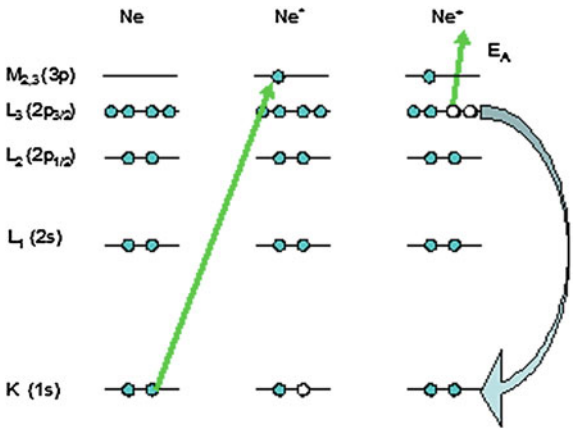


Fig. 9.18 Schematics of the resonant Auger process in Ne. the 1s electron is promoted to the empty 3p level. The core excited Ne* autoionises by filling up the core hole and ejecting a valence electron ($2p_{3/2}$)

coulomb interaction among bound electrons of the system. Furthermore, through the final state $|f\rangle$ correlated properties of the system influence the Auger cross-section.

9.7.2 Resonant Auger and Photoemission

So far we have discussed core hole de-excitations having a singly charged ion as initial state for the Auger decay. Let's now consider the case depicted in the rightmost panel of Fig. 9.18, i.e. the autoionization of a core excited system. In X-ray absorption language we are interested in describing the decay channels of the X-ray absorption near edge spectroscopy (XANES) resonances. This is an autoionization process that ends in a singly ionized state, which is a state identical to the one reached by a direct photoionization. Let's again take Ne as an example. As shown in the schematics of Fig. 9.18, by absorbing a photon of appropriate energy the 1s electron is promoted to the empty 3p level. Afterwards, the core excited Ne* autoionizes filling up the core hole and ejecting a valence (2p in the example) electron. This process is usually termed as a spectator (the 3p state) Auger decay and the final state, which is identical to the final state of a photoionization transition satellite to the $2p_{3/2}$ photoionisation, is termed as a 1 particle 2 hole state.

In other words, the final ionic state depicted in Fig. 9.18 can be created either by a resonant spectator Auger decay or by direct photoianization. What happens when the energies of the resonant Auger and the photoelectron coincide? We shall discuss it by the help of a specific result obtained for an Ar atom [33]. In Fig. 9.19a the lowest ionic states of argon are sketched, that are single hole ($1h$) states, $3p^{-1}$ or $3s^{-1}$. At higher energies a multitude of $2h1p$ states, belonging to the $3p^{-2}nl$, $3p^{-1}3s^{-1}nl$, or $3s^{-2}nl$ manifolds, are found. In direct, nonresonant photoemission, the $1h$ states are strongly dominant, and the $2h1p$ states are observed as weak satellites.

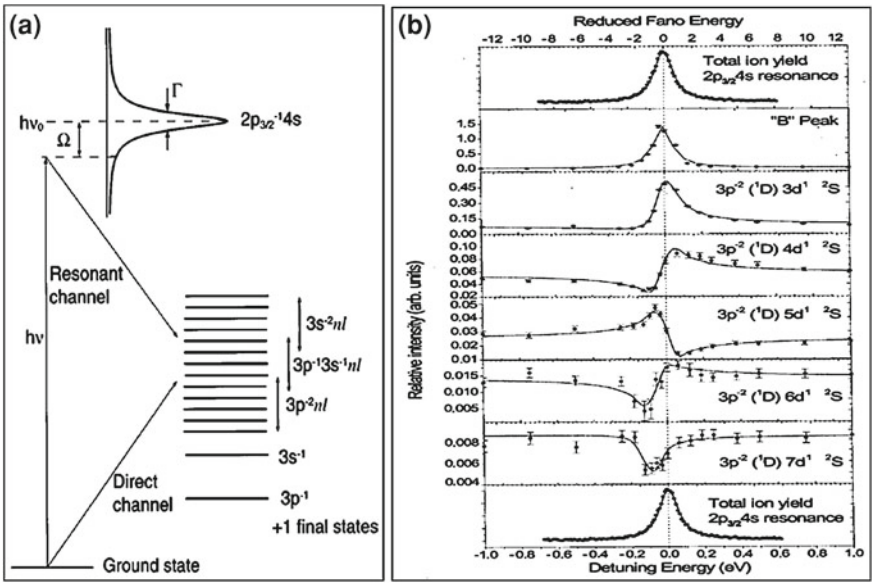


Fig. 9.19 Schematics of the resonant Auger process in Ar. The 2p electron is promoted to the empty 4s level [33]. The core excited Ar* autoionises by filling up the core hole and ejecting a valence electron (3p). See text for details. Copyright American Physical Society, reprinted with permission

The $h\nu + \mathrm{Ar} \rightarrow \mathrm{Ar}^{+}(3s, 3p)^{-2}nl + e^{-}$ photoemission spectrum was recorded for several different photon energies across the resonance $h\nu + \mathrm{Ar} \rightarrow \mathrm{Ar}^{*}(2p_{3/2}^{-1}4s)$ (see Fig. 9.19 panel a). The intensity of the unresolved transitions $h\nu + \mathrm{Ar} \rightarrow \mathrm{Ar}^{+}(3p)^{-2}5s, 4f + e^{-}$is almost zero when the photon is tuned out of resonance ($\Delta\Omega = 7.5\,\mathrm{eV}$) while it becomes dominant when tuning the photon on resonance ($\Delta\Omega = 0\,\mathrm{eV}$). It is therefore evident that for selected photoionization channels the resonant excitation is dominant over the direct ionisation one. Indeed, panel b of Fig. 9.19, where intensity of the individual photolines is reported as a function of $\Delta\Omega$, shows that tuning the photon energy across the core resonance, the photoionisation cross section rises by almost an order of magnitude reaching its maximum for on resonance condition. Observing the behaviour of the transition $h\nu + \mathrm{Ar} \rightarrow \mathrm{Ar}^{+}(3p)^{-2}3d + e^{-}$ as a function of $\Delta\Omega$, we notice that the cross section "on resonance" is larger than "off resonance", but the lineshape is also highly asymmetric with respect to the resonance energy, as it is the case for all the other photoemission investigated and reported in Fig. 9.19b. The origin of this asymmetry is in the double quantum path (see Fig. 9.19 panel a) that, for a given photon energy, can be followed in going from the ground neutral state to the singly ionised 2h 1p states. The final ionic state is created following the resonant or the direct channel with an identical wavefunction but with a different phase. Upon changing the detuning, the phase associate with the direct channel changes slowly and monotonically, while the resonant one changes rapidly. As long as amplitude of one channel is much larger

than the other, the ionisation cross section reduces to the direct photoemission (9.12) or to the non-resonant Auger one (9.16).

When the amplitudes of the matrix elements of the two competing channels become comparable they should be coherently added and the probability of the process becomes:

$$P(0,i,f) = \left| \int \frac{\langle f\varepsilon_A | C | i\tau \rangle \times \langle i\tau | D | 0 \rangle}{E_A + E_p - E_\tau - h\nu - i\Gamma/2} d\tau + \langle f\varepsilon_A | D | 0 \rangle \right|^2 \tag{9.17}$$

The probability of the resonant Auger/photoelectron process is therefore modulated by the interference term resulting from squaring the sum of the two amplitudes. Upon rapid change of the resonant channel phase, interference rapidly switches from constructive to destructive, thus yielding the peculiar lineshapes (Fano profiles) displayed in Fig. 9.19.

In summary, photoemission resonant through an Auger channel provides:

a. an effective spectroscopy of many-electron excited states that are otherwise inaccessible to conventional electron spectroscopies;
b. a unique way to highlight phase changes in the final state wavefunction that are just not detected by other spectroscopies.

9.8 Photoemission from Solids: The Three-Step Model

We have described the basic principles of the photoemission process from atoms and molecules. It can be described as the transition of one electron from an initial occupied state to a final empty free-electron level in vacuum. In the case of an atom or a molecule, the final state corresponds to the final state of an optical excitation, while in a solid the optically excited electrons, whose photoelectron current can be treated through the Fermi golden rule and the transition probability, must travel towards the surface, go through it, and escape into vacuum as a photoelectron to be detected.

In principle, the photoemission process should be treated as a photo-excited electron going into an empty final state in vacuum outside the system as a free electron (*one-step model*). However, if the system is solid, the photoelectron must acquire velocity in the direction normal to the surface, towards the electron analyzer, following energy and momentum conservation rules: the escaping photoelectron energy must be equal to the sum of the initial level energy and of the photon energy. Moreover, the momentum component parallel to the surface ($\mathbf{k}_{//}$) is conserved, while the translation symmetry normal to the surface is lost, so that $\mathbf{k}_\perp$ is not conserved.

A rigorous treatment of these processes in a single coherent step is not straightforward. Furthermore, the photoelectrons can undergo extrinsic scattering processes with the other electrons and intrinsic processes due to the relaxation of the system, once created the photo-hole in the initial state. This is a multi-particle process that

can be treated in an approximate framework, through a *three-step model*, which treats the three processes as independent contributions [34–43].

The three-step model is a better model to interpret the experimental measurements, in particular from the valence band of a solid, which can correlate the measured spectral photoelectron current (Energy Distribution Curve, EDC) to the spectral density of initial valence band states. In this model, the photoemission process can be treated in three sequential independent steps:

(1) excitation of an electron from a Bloch state of energy E_i to a Bloch state of energy $E_i + h\nu$, i.e. electron optical excitation;
(2) electron transport through the solid, including inelastic scattering with the other electrons;
(3) electron escape from the surface, by traveling from the semi-infinite crystal to vacuum.

(i) In the first step, the photon with energy $h\nu$ promotes an electron from an initially occupied Bloch state Φ_i to a final Bloch state Φ_f of free-electron out of the crystal, with energy and momentum conservation (also considering the possible presence of a reciprocal lattice vector **G**). The photoelectron current will be constituted by the sum of the transition probabilities per unit time (w_{if}) weighted by the Fermi-Dirac distribution function f(E) for the initial/final state to be occupied/empty:

$$\begin{aligned} J_e \propto \sum_{if} f(E_i)[1 - f(E_f)]w_{if} &= \sum_{if} f(E_i)[1 - f(E_f)]\,\langle \Phi_i |\, H_{int}\, | \Phi_f \rangle^2 \\ &\times\ \delta\left[E_{kin} - \left(E_f - \Phi\right)\right] \times \delta\left(E_f - E_i - h\upsilon\right) = \sum_{if} f(E_i)[1 - f(E_f)]M_{if}{}^2 \\ &\times\ \delta\left[E_{kin} - \left(E_f - \Phi\right)\right] \times \delta\left(E_f - E_i - h\upsilon\right) \times \delta\left(k_i + G - k_f\right) \end{aligned} \tag{9.18}$$

where H_{int} is the perturbation hamiltonian and M_{if} the matrix element for the transition. The δ functions ensure the following conservation laws: of the energy between the initial Bloch state and the final free-electron level, of the energy in the optical excitation process into the crystal, and of the momentum in the extended Brillouin zone.

(ii) Second step: transmission of the electron through the bulk solid. The traveling photo-electrons can be grouped into two classes, those which reach the solid surface without encountering any scattering and keeping the physical information from within the crystal (primary electrons), and those which undergo multiple inelastic scattering (secondary electrons), mainly due to electron-electron scattering.
The primary electrons are a small fraction of the whole current and can be treated through a coefficient $d(E_f, \mathbf{k})$ representing this fraction of primary electrons with energy E_f and momentum **k** which reach the surface without suffering inelastic processes. The mean free path $\lambda(E_f, \mathbf{k})$ between two collisions can be defined as $\lambda(E_f, \mathbf{k}) = \tau/\hbar|\mathbf{v}_g(E_f, \mathbf{k})| = \tau|(\nabla_k, E)_{E_{f,k}}|$, where τ is the average time lap between two collisions (assumed as isotropic), and $\mathbf{v}_g$ is the electron

group velocity. Thus, assuming α as the optical absorption coefficient of the solid, based on the probability that the electron can reach the surface without scattering, one can assume

$$d\left(E_f, k\right) = \alpha\lambda / \left(1 + \alpha\lambda\right) \tag{9.19}$$

(iii) In the third step, the electrons overcoming the surface and escaping into the vacuum must have the normal component of their momentum different from zero. Since they are free electrons, this component can be defined as $k_{ext}^{\perp} = 1/\hbar\sqrt{(2mE_{kin})}\cos\theta$, there θ is the angle between the emission direction and the normal to the surface. In this third step, we can define a transmission coefficient $T(E_f, \mathbf{k}_{ext})$ as $T(E_f, \mathbf{k}_{ext}) = 0$ if $k_{ext}^{\perp} < 0$ and $T(E_f, \mathbf{k}_{ext}) = x$ if $k_{ext}^{\perp} > 0$, with $x < 1$, since not all the electrons arriving at the surface can overcome it.

The transmission function can be explicitly expressed in terms of Bloch functions as $T(E_f, \mathbf{k}_{ext}) = 0$ if $E_f < E_F + \Phi$ and $T(E_f, \mathbf{k}_{ext}) = 1/2\sqrt{[1 - (E_F + \Phi)/Ef]}$ if $E_f > E_F + \Phi$.

Finally, we can express the photoemission current as the product of these three independent contributions

$$\begin{aligned} J_e \propto \textstyle\sum_{if} f(Ei)[1 - f(E_f)]\, M_{if}{}^2 T\left(E_f, k_{ext}\right) d\left(E_f, k\right) \delta\left[E_{kin} - \left(E_f - \Phi\right)\right] \\ \times\delta\left(E_f - E_i - h\upsilon\right) \times \delta\left(k_i + G - k_f\right) \times \delta\left(k_i^{//} + G^{//} - k_f^{//}\right) \end{aligned} \tag{9.20}$$

where we multiply for a further δ function, ensuring the conservation of the momentum parallel to the surface. In fact, in the definition of the transmission coefficient, we must take into account that for the primary electrons overcoming the surface, only the momentum component parallel to the surface is conserved between the internal and external momentum, because of symmetry considerations. The matrix element of the transition (M_{if}) is assumed as constant. However, it may smoothly vary as a function of energy, and this must be taken into consideration for quantitative purposes. Furthermore, we can consider matrix elements effects when using polarized radiation. If the photo-electron is excited by polarized radiation from an initial state with definite parity, in order to have non-vanishing matrix elements for the transition, there must be overlap between the polarization direction of the vector potential projected onto the final state, and the initial state. As an example, if we consider excitation from an even state for reflection with respect to a mirror plane, with the detector positioned in its mirror plane, also the integrand must be even for reflection with respect to the mirror plane, thus the final state must be even as well [44].

A few considerations on the momentum conservation, concerning angular-resolved photoelectron spectroscopy (ARPES). Symmetry considerations impose the conservation of the parallel component of the electron momentum $\mathbf{k}_{int}^{//} = \mathbf{k}_{ext}^{//}$, while $\mathbf{k}_{norm}$ is not a good quantum number. For a surface or in general for a two-dimensional system, the problem of band mapping is solved, insofar an ARPES experiment does map the electron spectral density of states as a function of the angle θ between the surface normal and the electron emission, thus straightly giving the complete E versus $\mathbf{k}_{//}$

bands:

$$\left|k_{\text{int}}^{//}\right| = \left|k_{ext}^{//}\right| = 2\pi/\text{h}\sqrt{2\text{mE}_{\text{kin}}}\sin\theta \tag{9.21}$$

In order to fully map the band structure in a three-dimensional solid, we should know all the E versus $\mathbf{k}_{\text{int}}$ dispersion curves, however an approximate approach brings to a reasonable solution for the dispersion along k_{norm}. The excited state can be approximated as a quasi-free electron Bloch state

$$E\,(k) = \frac{h^2}{8\pi^2 m}\left(|k_{\text{norm}}|^2 + |k//|^2\right) - |E_0| \tag{9.22}$$

with E_0 the bottom of the valence band with respect to the Fermi level; knowing the $\mathbf{k}_{//}$ component, we can determine the $\mathbf{k}_{\text{norm}}$ component as

$$\left|k_{\text{int}}^{norm}\right| = \frac{2\pi}{h}\sqrt{2mE_{kin}\cos^2\theta + |E_0 + \Phi|} \tag{9.23}$$

Φ is the work function, $\text{E}_\text{o} + \Phi$ is the inner potential which can be estimated [44] either by theoretical methods or it can be inferred by experimentally determining the periodicity of electronic states dispersing along the surface normal, in normal emission, i.e. at emission angle $\theta = 0$, thus $\mathbf{k}_{//} = 0$.

9.9 Spectral Function of Interacting Electrons in a Solid

Let us first consider a model based on interacting particles. The photoexcited electrons in a solid experience extrinsic and intrinsic effects while traveling in the solid. When treating a crystalline solid, we can consider the electronic wave function as extended Bloch functions and we can factorize the wave function of the system with two contributions, the wave function Φ_k of a Bloch state with wavevector $\mathbf{k}$, and the wavefunction $\Psi^{\text{N}-1}$ of an $\text{N}-1$ electron system. This approximation is valid, given the high group velocity of the photo-emitted electron, which almost instantaneously overcomes the surface. In these conditions, the photo-electron does not interact with the remaining system, once excited. The potential of the crystal with $\text{N}-1$ electrons is also considered to change rapidly. Thus, the final state of the system can be written as $\{\Psi_{\text{f}}^{\text{N}}\} = \hat{\text{A}}\,\{\Psi_{\text{f}}^{\text{N}-1}\Phi_{\text{kf}}\}$. We choose $\Psi_{\text{m}}^{\text{N}-1}$ as eigenfunction of the Hamiltonian for the $\text{N}-1$ electrons in the final state, and we can decompose the initial state, so that the photoemission current becomes:

$$J_e \propto \sum_{\text{if}}\left|M_{if}^2\right|\sum_{\text{m}}|m_{im}|^2 \times \delta\left(E_i^N + h\upsilon - E_m^{N-1} - E_{kin}\right) \tag{9.24}$$

where M_{if} is the matrix element between single particle Bloch states, $\text{m}_{im} = \langle\Psi_{\text{m}}^{\text{N}-1}|\Psi_i^{N-1}\rangle$ is the overlap between states of $\text{N}-1$ electrons. If $\Psi_{\text{i}}^{\text{N}-1}$ were an

eigenstate of the Hamiltonian of the $N-1$ electron system, m_{im} would be zero unless $i = m$; in this latter case the resulting spectrum would be a single peak, like in the case of non-interacting electrons. But the $N-1$ particle state associated to Φ_{ki} can be expressed through a destruction operator acting onto the N electron system. Thus, for a correlated system, several elements of the m_{im} overlap will be non-zero. The problem is rather complicated and can be solved within the Green formalism, and one can finally define the single-particle spectral function $\mathbf{A}(\mathbf{k}, \omega)$ as

$$A(k,\varepsilon) = \frac{1}{\pi}\left|\mathrm{Im}\left[G(k,\varepsilon)\right]\right| = \sum_{m}\left|\left\langle \Psi_m^{N-1}\right| c_k \left|\Psi_i^N\right\rangle\right|^2 \delta\left(\varepsilon + E_m^{N-1} - E_i^N\right) \tag{9.25}$$

where $A(k,\varepsilon)$ is the sum of an A^+ and A^- contribution, where c_k is the creation (for A^+) or annihilation (for A^-) operator, respectively. The photoemission current (9.24), multiplied by the Fermi-Dirac distribution function taking care of the occupation of the single-particle states, can be redefined as $J_e(k, \omega) \propto \Sigma_{if}|M_{if}|^2 \mathbf{A}(\mathbf{k}, E_{kin} - h\nu)\, f(E_{kin} - h\nu)$, and the expression of the photoemission current for non-interacting particles can be obtained through the Green approach as

$$\begin{aligned} G(k,\varepsilon) &= \frac{\sum_m \left|\left\langle \Psi_m^{N-1}\right| c_k \left|\Psi_i^N\right\rangle\right|^2}{\varepsilon + E_i^N - E_m^{N-1} - i\eta} = \frac{\sum_m \delta_{im}}{\varepsilon + E_i^N - E_m^{N-1} - i\eta} \\ &= \frac{1}{\varepsilon + E_i^N - E_m^{N-1} - i\eta} = \frac{1}{\varepsilon - E_k - i\eta} \end{aligned} \tag{9.26}$$

where $E_k = E_i^{N-1} - E_i^N$ is the ionization energy of Koopman's theorem, so that we finally obtain $\mathbf{A}(\varepsilon, \mathbf{k}) = \delta(\varepsilon - E_k)$, i.e. the spectral function relative to a single particle, is represented by a single peak.

So far, we have not considered the effects of the multiple interactions on the lineshape. They can be taken into account by introducing a complex quantity, the self-energy $\Sigma(\varepsilon, \mathbf{k})$, containing the effects on the renormalization of the dispersion curves and on the average excitation lifetime. We can re-write the Green function in the E, $\mathbf{k}$ space as

$$G(k,\varepsilon) = \frac{1}{\varepsilon - E_k - \sum(\varepsilon,k)_m} \tag{9.27}$$

with $\Sigma = \Sigma' + i\,\Sigma''$, and the single-particle spectral function becomes:

$$A(\varepsilon,k) = \frac{1}{\pi}\frac{\left|\sum''(k,\varepsilon)\right|}{\left|\varepsilon - E_k - \sum'(k,\varepsilon)\right|^2 + \left|\sum''(k,\varepsilon)\right|^2} \tag{9.28}$$

where the self-energy in general contains contributions due to electron-electron, electron-impurity and electron-phonon scattering.

In the case of Σ function independent on $\mathbf{k}$, the single-particle function has the form of a Lorentzian curve, whose width is proportional to the imaginary part of

the self-energy. Thus, Σ'' can be experimentally directly obtained from the width of the photoemission peaks, once deconvolved from the experimental resolution contribution. Since the Green function is the linear response to the external perturbation due to the incoming electromagnetic field, its real and imaginary parts are in causal relation through the Kramers-Kronig relation, so that experimentally known Σ'', we can easily determine Σ'.

In the following paragraphs, we will present a few examples of studies in which photoemission has given fundamental contributions to the understanding of the physical properties of the investigated systems.

9.10 Energy Distribution Curves

9.10.1 Valence Band Examples (Cross-Section Exploitation and Cooper Minima)

The EDC mode of photoemission essentially gives a representation of the spectral density of the electronic states of the investigated system, valence band or core-levels, also giving information on its chemical state. In this paragraph we will give a few examples of angle-integrated valence band and core-level data, exploiting the excitation cross-section [45] and the surface sensitivity dependence on the energy.

Organic molecules are nowadays attracting scientific and technological attention, due to their potential use for advanced devices at the nano-scale. Metal-Phthalocyanines (MPcs, M-$C_{32}H_{16}N_8$) belong to an exemplary class of organic oligomers constituted by a planar aromatic macrocycle (containing C and N atoms) surrounding a central metal atom [46]. MPcs easily self-assemble as ordered planar nano-chains on surfaces [47, 48], and photoemission EDC data can give indispensable hints for experimentally determine the spectral density of states depending on the different species composing the molecule. In Fig. 9.20, we show the Valence Band (VB) measured at ordered planar thin-films (TF) of FePc and CoPc grown on Au(110). Data are taken with different photon energies, from 21.218 to 150 eV, thus obtaining photo-emitted electrons from the same initial states at different kinetic energies. The VB electronic states in this energy range are expected to be mainly associated either to metal-derived d-symmetry states (b_{2g}/e_g and a_{1g}), or to C and N derived π-states (a_{1u}, highest-occupied molecular-orbital, HOMO) [49], whose relative intensity depends on the photoelectron excitation cross-sections [45]. By combining the calculated excitation cross-section at different energies for the C and N 2p-states (composing the π-orbitals) and for the Fe and Co 3d-states, with the experimental data, a correct attribution to the different contributions in the VB has been given, as indicated in the figure [50].

Another example of cross-section exploitation [51] has been used for disentangling the VB contribution of two different metal species. Cobalt nano-chains have been prepared on the regularly stepped vicinal Pt(997) surface, where the Co atoms

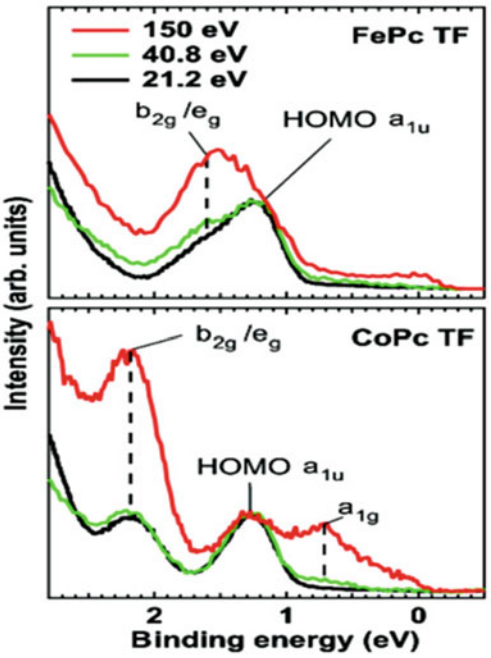


Fig. 9.20 Valence Band EDCs of Fe-Phthalocyanine and Co-Phthalocyanine thin-films grown on Au(110) [50], taken at different photon energies. Data adapted from [50]. Copyright American Physical Society, reprinted with permission

self-assemble as chains at the step edges close to the (111)-oriented terraces [52]. In order to disentangle the d-contribution due to the Co-3d states from that of the substrate Pt-5d states, the authors exploit the differently varying photo-excitation cross-section of the Pt-5d states with respect to the Co-3d levels. Data taken when the Pt-5d states present the Cooper minimum (see inset in the figure) bring to light the VB features associated to the Co nano-wires, as shown in Fig. 9.21. We briefly mention that also resonant photoemission exciting VB electrons with photon energies spanning across the core-level of an atomic species, can help in disentangling the VB attribution [53].

High-luminosity and high-resolution angular-integrated EDC brought to light experimental measurement of the population of the bottom of the conduction band in a narrow gap semiconductor, i.e. highly n-type doped InAs(110). A tiny amount (hundredths of a monolayer) of alkali atoms (Cs) adsorbed on InAs(110) induce a strong bending of the surface bands with respect to the Fermi level, favoring the occupancy of the previously empty InAs conduction band, as shown in Fig. 9.22 (left panel) [54]. The charge accumulation region is hundreds of Å deep, so that electronic charge is confined in the direction normal to the surface and free in the surface plane, generating a quasi-free and spatially confined 2D electron gas with quantized eigenstates (right panel). These occupied quantized energy levels are present in the angular-integrated EDCs shown in Fig. 9.22, in perfect agreement with self-consistent calculations, which results are superimposed to the experimental data [55].

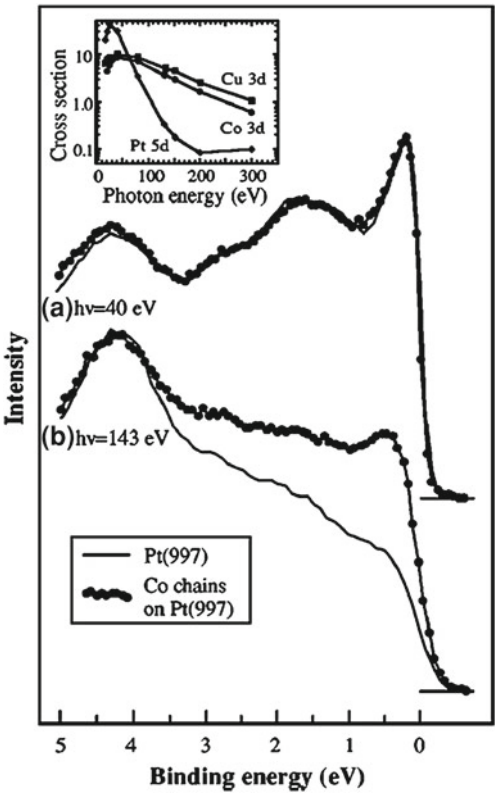


Fig. 9.21 Valence Band EDCs of the clean Pt(997) surface (*thin lines*) and of Co-nanowires grown on Pt(997) (*dots* and *thick lines*), taken at different photon energies. From Fig. 2 of [52]. Copyright American Physical Society, reprinted with permission

9.10.2 Core Level Examples

Use of different photon energies affects the surface sensitivity, as the photoelectron kinetic energy of detection changes for a given excitation (see the "universal" mean free path curve in Fig. 9.3). It is well known that III–V compound semiconductors when cleaved along the (110) surface, present a relaxation of the first atomic plane as minimum energy configuration, due to the bulk symmetry breaking, maintaining the (1×1) symmetry, causing the surface atoms to present a different position with respect to the bulk-like configuration. This reflects into a modification of the VB structure and, as a consequence, the core-levels experience a surface-core level shift (see also [56] in this same book). In Fig. 9.23 (upper panel) we show the In-4d core levels at the freshly cleaved InAs(110) surface, taken at two different photon energies (40.814, $\mathrm{He}_{\mathrm{II}\,\alpha}$, and 48.372, $\mathrm{He}_{\mathrm{II}\beta}$). Data (red dots) have been deconvolved with Voigt peaks (Gaussian-Lorentzian shape), and show surface (S, blue lines) and bulk (B,

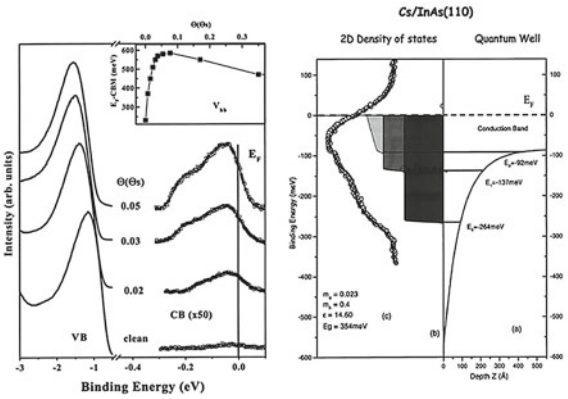


Fig. 9.22 High-resolution Valence Band and Conduction band EDCs of the InAs(110) surface under tiny electron-doping by exposing to Cs (*left panel*); experimental density of states in the CB and results of self-consistent ab-initio calculation of the quantized levels in the confined 2D electron-gas. Reprinted from Fig. 6 (*left*) and 7 (*right*) of [54]. Copyright Elsevier BV, reprinted with permission

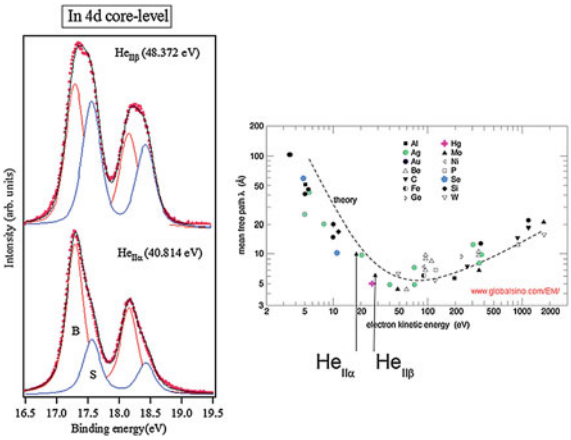


Fig. 9.23 High-resolution In-4d core-levels at freshly cleaved InAs(110), taken with $He_{II\alpha}$ and $He_{II\beta}$ radiation; experimental data (*red dots*), Voigt-profiled fit with surface (*S*, *blue lines*) and bulk (*B*, *red lines*) doublet components (*left panel*); "universal" curve of the electron inelastic mean free path [17] (*right panel*); graph from [57]

red lines) doublets. It is evident that the surface-related In-4d doublet increases its relative intensity upon passing from the $He_{II\,\alpha}$ to the $He_{II\beta}$ radiation, from about 19 to 27 eV kinetic energy, thus increasing the surface sensitivity, as shown in the "universal" curve for the electron inelastic mean free path (lower panel) [17, 57].

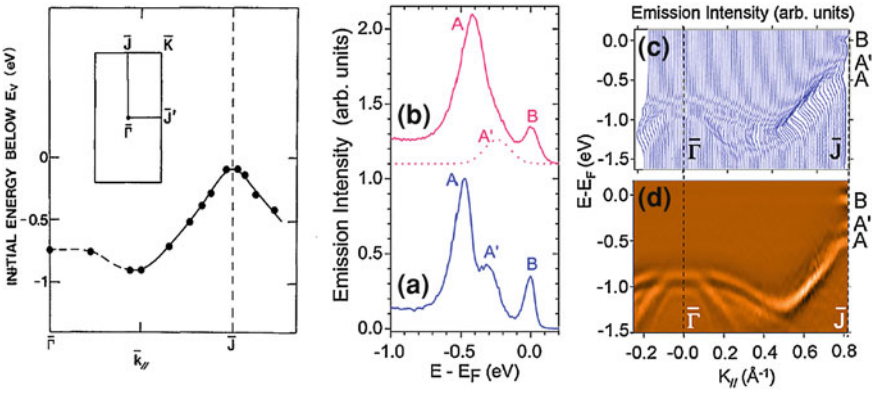


Fig. 9.24 Dangling-bond surface state dispersion at the Si(111)-(2x1) reconstructed surface along the ΓJ direction of the Surface Brillouin Zone (SBZ). One of the first experimental ARPES dangling-bond dispersion (*left panel*). Recent high-resolution ARPES dangling-bond dispersion and selected spectra, with the evidence of isomers-related states (*center* and *right panels*). From Fig. 2 of [60] (*left*) and Fig. 1 of [61] (*center* and *right*). Copyright American Physical Society, reprinted with permission

9.11 Angular Resolved PhotoElectron Spectroscopy

9.11.1 Band Structures

The ARPES technique does not require any assumption for mapping the band structure if the system under investigation is two-dimensional. A valuable example of 2D systems is given by reconstructed surfaces of semiconductors. In particular, at the Si(111) cleaved surface, angular resolved photoemission gave fundamental hints for the understanding of the (2x1) reconstruction mechanisms. Without entering into historical detail on this surface [58], the Si(111)-(2x1) surface is characterized by formation of chains of Si atoms, Pandey's chain reconstruction model [59], one of the pillars of clean semiconductors' reconstruction mechanisms. The dangling bonds associated to the surface Si atoms form surface states which disperse along the ΓJ direction of the Surface Brillouin Zone (SBZ). We present in Fig. 9.24 data from one of the first ARPES experiments showing the dangling-bond dispersing state [60], and one of the most recent, where detail on the formation of isomers on the surface is brought to light thanks to high-resolution ARPES on highly n-doped Si crystal [61].

9.11.2 Adsorbates

A purely 2D system can also be formed by highly-ordered adsorption of atomic or molecular structures. The substrate effects can be neglected when the adsorbate is

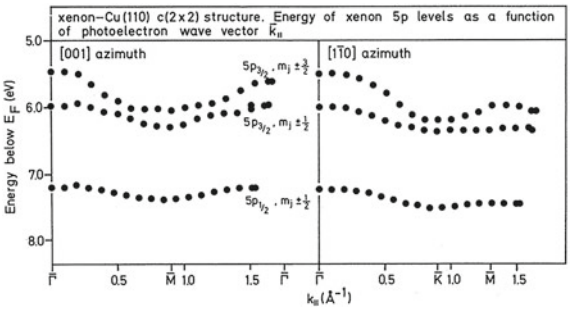


Fig. 9.25 Experimental band structure of the 5p levels of Xe physisorbed in an ordered c(2 × 2) structure onto the Cu(110) surface. ARPES bands. From Fig. 5 of [63]. Copyright American Physical Society, reprinted with permission

weakly bound through van der Waals interactions, like low-temperature physisorbed gases on metals. As first example of highly ordered 2D array, we show the ARPES band structure formed by Xe atoms physisorbed at low temperature on the Cu(110) surface [62], where the noble gas atoms coalesce in an ordered c(2 × 2) structure with respect to the underlying (1 × 1) unit mesh. The lowest binding energy electronic states of Xe are the 5p core-levels, energetically separated from the Cu-3d bands, only slightly interacting with the Cu-4s,p bands. These core-levels associated to a compact ordered 2D structure have been shown to form distinct bands [63], as presented in Fig. 9.25.

Aromatic molecule adsorption on surfaces is encountering a new wave of interest in the recent years, due to their use in advanced opto-electronic and magnetic devices at the nano-scale, and to their ability of self-assembling at the nano-scale, by exploitation of naturally patterned surfaces, thus forming a variety of highly ordered 1D or 2D structures.

Pentacene ($C_{22}H_{14}$) molecules self-assemble as long nano-wires onto the Cu(119) vicinal surface. This surface is a regularly stepped surface with (001)-oriented 1.2 nm-wide terraces and long-ordered step edges, thus favoring planar adsorption of the long pentacene nano-wires [64–67]. Pentacene interacts with copper, due to an orbital mixing between the pentacene molecular orbitals and the Cu states [68], such as occupied interface states form at completion of the first ordered layer [69]. Upon further pentacene deposition on Cu(119), the molecules keep maintaining their ordered structure forming a highly ordered 2 nm-thick molecular film, whose electronic band dispersion of its HOMO has been probed by normal-emission photoemission, changing the photon energy, thus having access to the HOMO band dispersion along the $\mathbf{k}_{\perp}$ direction of the BZ [66], as shown in Fig. 9.26. Several other organic molecules adsorbed on surfaces, like rubrene [70], form planar ordered layers and present $\mathbf{k}_{\perp}$ dispersion of the highest-occupied molecular orbital.

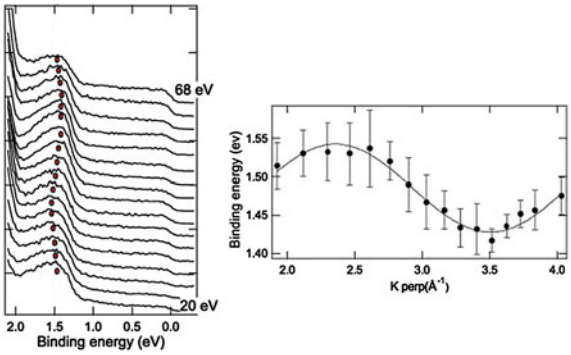


Fig. 9.26 2-nm thick pentacene film grown on Cu(119). ARPES selection of spectra taken at normal emission and varying the photon energy (*left*); highest-occupied molecular-orbital (HOMO) band dispersion along $k_\perp$ (*right*). Reprinted from Figs. 2 and 3 of [66]. Copyright Elsevier BV, reprinted with permission

9.11.3 Graphite and Graphene as Exemplary 2D System

The most classical example by far of two-dimensional band-structure is that of graphite, the sequence of slightly interacting graphene layers. Data taken on highly-oriented pyrolitic graphite (HOPG) along different directions of the BZ and the experimentally determined band structure are shown in Fig. 9.27 [71]: We observe the wide dispersion of the π-bands accompanied by the typical linear behaviour close to the K point and by the higher binding energy σ bands.

Graphene is one of the most exciting exemplary systems in science of the last few years. In fact, Geim and Novoselov were awarded the 2010 Nobel prize [72] for their discovery, which is of great importance in view of its fundamental properties, strictly depending on the topology of the crystal lattice, and for the wealth of potential applications. Graphene is actually at the spotlight of ongoing research on nanoscale systems, due to its unique electronic, mechanical, and transport properties [73–75]. It is the prototype of a 2D system. Without entering into details, we briefly recall in Fig. 9.28 the lattice cell (hexagonal lattice with two C atoms per unit cell), its reciprocal lattice, the π and σ bands as calculated by tight-binding approach along the main symmetry directions of the SBZ, and the well known conical dispersion of the π-bands across the K points of the SBZ [76].

In order to study its electronic band structure, it is necessary to prepare graphene as a highly-ordered sheet, as can be done onto a variety of hexagonally-terminated crystalline substrates [76, 77]. In particular, metal surfaces offer a well-suited support for epitaxial growth [78–86], and the Ir(111) surface has revealed to be an excellent template for minimizing the carbon–substrate interaction [82, 83, 86], while only slightly affecting its proper band structure, leading to a quasi-free standing graphene layer.

The electronic band structure of graphene grown on Ir(111), taken along the main symmetry directions ΓKM of the SBZ, with a zoom on the section of the Dirac cone around the K point, is shown in Fig. 9.29 [87].

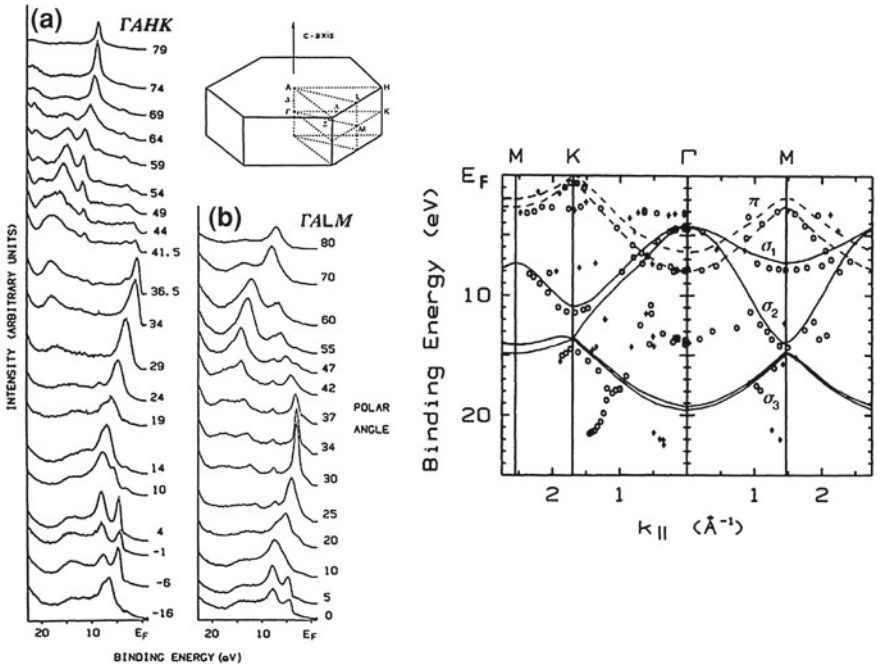


Fig. 9.27 Valence band of graphite (HOPG), stacking of the ARPES spectra as a function of polar angle (*left*) and experimental band structure (*right*). From Figs. 1 and 2 of [71]. Copyright American Physical Society, reprinted with permission

Actual free-standing suspended exfoliated graphene presents a broader spectral trace [88] with respect to graphene supported on Ir, due to the natural corrugation of actual free-standing graphene, which presents intrinsic ripples in its 2D structure [89].

Graphene can be built layer-by-layer in a highly controlled multi-layer sheet on SiC [77]. Furthermore, the evolution of the band structure in a multi-layer sheet (single layer-by-single layer) can also be followed as a function of the number of layers by ARPES, as shown in Fig. 9.30, where we report the emerging of several slightly energy-shifted Dirac cone traces at the point K of the SBZ, each trace corresponding to a single graphene sheet, with the slight energy shift due to the $\pi - \pi$ interlayer interaction. In the lower panel of the figure, the $\mathbf{k}_{\perp}$ versus $\mathbf{k}_{//}$ bands are reported for a binding energy of 1 eV: for 1 layer there is no dispersion in the direction perpendicular to the plane, as expected, while upon increasing the number of layers, there is a clear intensity modulation due to the layer interaction, eventually evolving in the formation of a dispersing π-band of multi-layer (4 layer) graphene towards graphite.

Graphene can be easily doped by alkali metal intercalation, producing electron doping and a shift of the Dirac point towards higher binding energies, basically without modifying the graphene band properties, thus maintaining the linear dispersion. However, the band properties can also be heavily modified by more interacting adsorbates, for example by atomic H-adsorption, which causes a distortion of the C bonds,

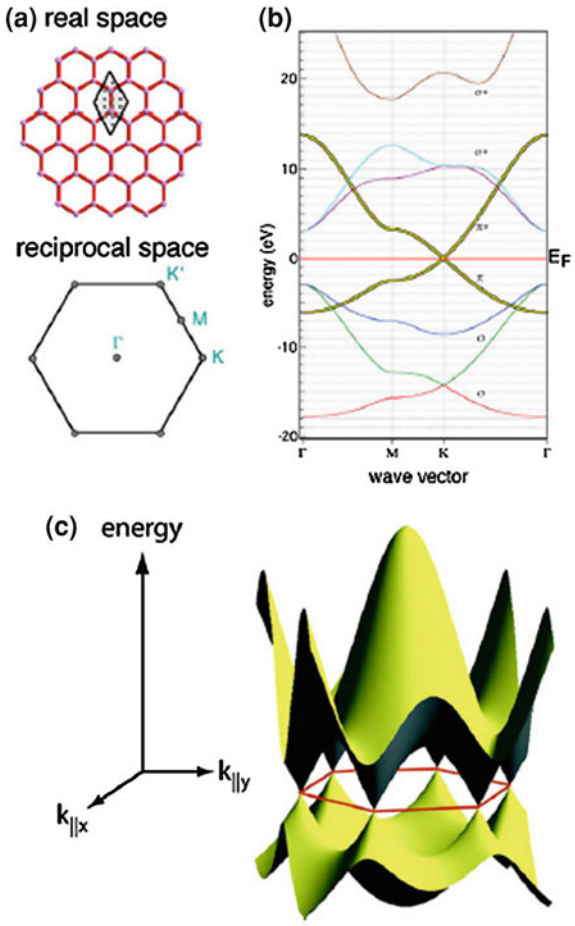


Fig. 9.28 Graphene: real space and reciprocal lattices, tight-binding band-structure along the main symmetry directions, and electronic structure of the π bands, showing the Dirac points where the valence and conduction bands meet at the K points of the Brillouin zone. Reprinted from Fig. 1 of [76]. Copyright Pergamon, reprinted with permission

modifying the sp^2 hybridization towards an sp^3-like condition, with the opening of a band gap [90]. The intriguing properties of graphene are also characterized by many-body interactions slightly affecting the purely linear behaviour of the Dirac cone trace [91]. Finally, deep core-levels are generally expected to be strongly localized and not to present any band dispersion. However, high-resolution ARPES on graphene has recently brought to light the dispersion of the C-1s core-level [92], observed as an emission-angle-dependent binding-energy modulation, thus confirming graphene as one of the best examples of 2D system.

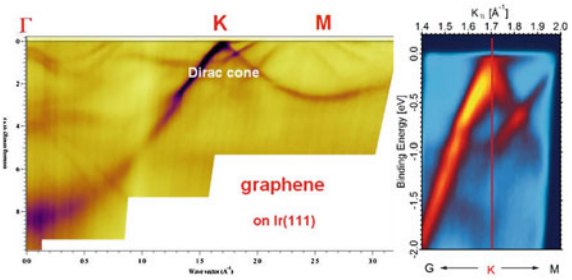


Fig. 9.29 Graphene band structure along ΓKM and zoom of the Dirac cone around the K point of the SBZ. ARPES data taken with high-resolution ARPES and a He discharge source [87]

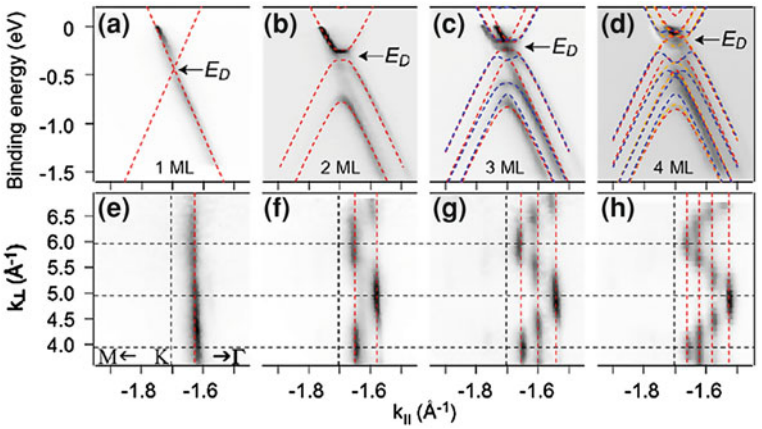


Fig. 9.30 Formation of an electronic band, stepwise: from 1-layer (*extreme left*) to 4-layer (*extreme right*) graphene band structure along across the Dirac point. From Fig. 2 of [77]. Copyright American Physical Society, reprinted with permission

9.12 Final Considerations and Perspectives

In this chapter, we introduced the reader to the photoelectron spectroscopy, briefly recalling the basic theoretical concepts and the experimental aspects of the photoemission technique. We accompanied the discussion with a few exemplary systems, with photoemission applied from atomic and molecular systems to the solid state, with special emphasis on the angular resolved mode. These examples studied by photoemission demonstrate the powerfulness and suitability of photoelectron spectroscopy in studying and completely determining the electronic properties of a variety of physical systems, ranging from atomic, molecular and solid state physics to chemistry, organic chemistry and low-dimensional hybrid organic-inorganic materials.

References

1. H. Hertz, Ann. Physik **31**, 983 (1887)
2. P. Lenard, Ann. Physik **2**, 359 (1900)
3. P. Lenard, Ann. Physik **8**, 149 (1902)
4. P. Lenard, Wien. Berichte **108**, 1649 (1899)
5. J.J. Thompson, Phil. Mag. **48**, 547 (1899)
6. A. Einstein, Ann. Physik **17**, 132–148 (1905)
7. M. Cardona, L. Ley (eds.), *Photoemission in Solids*, vol. 1–2 (Springer, Berlin, 1978)
8. C.S. Fadley, Basic concepts of X-ray photoelectron spectroscopy, in *Electron Spectroscopy, Theory, Techniques and Applications*, vol. 11, ch. 1, ed. by C.R. Brundle, A.D. Baker (Pergamon Press, Oxford, 1978)
9. G. Margaritondo, *Introduction to Synchrotron Radiation* (Oxford University Press, Oxford, 1998)
10. A. Balerna, S. Mobilio, Synchrotron radiation fundamental methodologies and applications, in *SIF Conference Proceedings*, vol. 82, p. 1
11. S. Hűfner, *Photoelectron Spectroscopy, Principle and Applications*, 3rd edn. (Springer, Berlin, 2003)
12. C.M. Bertoni, in *Synchrotron Radiation*, eds. by S. Mobilio et al. (Springer, Heidelberg, 2014)
13. B. Feuerbacher, B. Fitton, R.F. Willis, *Photoemission and Electronic Properties of Surfaces* (Wiley, New York, 1978)
14. P.Y. Yu, M. Cardona, *Fundamental of Semiconductors* (Springer, Berlin, 1996)
15. F.J. Himpsel, Adv. Phys. **32**, 1–51 (1983). doi:10.1080/00018738300101521
16. J.H. Moore, C.C. Davis, M.A. Coplan, *Building Scientific Apparatus*, Chap. 5 (Perseus Books, Reading)
17. M.P. Seah, W.A. Dench, Surf. Interface Anal. **1**, 2–11 (1979). doi:10.1002/sia.740010103
18. U. Becker, J. Electron Spectr. And Rel. Phenomena **75**, 23–34 (1995)
19. K. Siegbahn et al., *ESCA Applied to Free Molecules* (North-Holland, Amsterdam, 1969)
20. R. Wehlitz, F. Heiser, O. Hemmers, B. Langer, A. Menzel, U. Becker, Phys. Rev. Lett. **67**, 3764–3767 (1991). doi:10.1103/PhysRevLett.67.3764
21. M. Larsson, P. Baltzer, S. Svensson, B. Wannberg, N. Mårtensson, A. Naves de Brito, N. Correira, M.P. Keane, M. Carlsson Goethe, I. Karlsson, J. Phys. B At. Mol. Opt. Phys. **23**, 1175–1195 (1990). doi:10.1088/0953-4075/23/7/014
22. O. Travnikova, J.K. Børve, M. Patanen, J. Söderström, L.J. Sæthre, N. Mårtensson, S. Svennson, J. Electron Spectr. Rel. Phenom. **185**, 191–197 (2012)
23. J.H.D. Eland, *Photoemission Spectroscopy* (Butterworths, London, 1974)
24. U. Gelius, J. Electron Spectr. Rel. Phenom. **5**, 985–1057 (1974)
25. O. Edqvist, E. Lidholm, L.E. Selin, L. Åsbrink, Phys. Scr. **1**, 25–30 (1970)
26. R.N. Dixon, G. Duxbury, J.W. Rabalais, L. Åsbrink, Mol. Phys. **31**, 423–435 (1976). doi:10.1080/00268977600100311
27. D. Edvardsson, P. Baltzer, L. Karlsson, M. Lundqvist, B. Wannberg, J. Electron Spectr. Rel. Phenom. **73**, 105–124 (1995)
28. V. Schmidt, *Electron Spectroscopy of Atoms Using Synchrotron Radiation* (Cambridge University Press, Cambridge, 1977)
29. F. Heiser, O. Gressner, J. Viefhaus, K. Wieliczek, R. Hentges, U. Becker, Phys. Rev. Lett. **79**, 2435–2437 (1997). doi:10.1103/PhysRevLett.79.2435
30. M. Thompson, M.D. Baker, A. Christie, J.F. Tyson, *Auger Electron Spectroscopy, Chemical Analysis*, vol. 74 (Wiley, New York, 1984)
31. L.O. Werme, T. Bergmark, K. Siegbahn, Phys. Scr. **6**, 141–150 (1972)
32. S. Aksela, J. Väyrynen, H. Aksela, Phys. Rev. Lett. **33**, 999–1002 (1974)
33. R.R.T. Marinho, O. Björneholm, S.L. Sorensen, I. Hjelte, S. Sundin, M. Bässler, S. Svenson, A. Naves de brito, Phys. Rev. A **63**, 032514 (2001)
34. H.Y. Fan, Phys. Rev. **68**, 43–52 (1945). doi:10.1103/PhysRev.68.43

35. H. Mayer, H. Thomas, Z. Physik **147**, 419 (1957)
36. H. Puff, Phys. Stat. Sol. B **1**, 636–649 (1961)
37. H. Puff, Phys. Stat. Sol. B **1**, 704–705 (1961)
38. C.N. Berglund, W.E. Spicer, Phys. Rev. **136**, A1030–A1044 (1964)
39. W.E. Spicer, C.N. Berglund, Phys. Rev. Lett. **12**, 9–11 (1964)
40. W.E. Spicer, Phys. Rev. **112**, 114–122 (1968). doi:10.1103/PhysRev.112.114
41. G.D. Mahan, Phys. Rev. B **2**, 4334–4350 (1970). doi:10.1103/PhysRevB.2.4334
42. H. Hermeking, J. Phys. C Solid State Phys. **6**, 2898 (1973)
43. P.J. Feibelman, D.E. Eastman, Phys. Rev. B **10**, 4932–4947 (1974)
44. A. Damascelli, Phys. Scr. T. **109**, 61–74 (2004)
45. J.J. Yeh, I. Lindau, At. Data Nucl. Data Tables **32**, 1–155 (1985)
46. S.R. Forrest, Chem. Rev. **97**, 1793–1896 (1997). doi:10.1021/cr941014o
47. M.G. Betti, P. Gargiani, R. Frisenda, R. Biagi, A. Cossaro, A. Verdini, L. Floreano, C. Mariani, J. Phys. Chem. C **114**, 21638–21644 (2010). doi:10.1021/jp108734u
48. S. Fortuna, P. Gargiani, M.G. Betti, C. Mariani, A. Calzolari, S. Modesti, S. Fabris, J. Phys. Chem. C **116**, 6251–6258 (2012). doi:10.1021/jp211036m
49. M.-S. Liao, S. Scheiner, J. Chem. Phys. **114**, 9780 (2001)
50. P. Gargiani, M. Angelucci, C. Mariani, M.G. Betti, Phys. Rev. B **81**, 085412 (2010)
51. http://ulisse.elettra.trieste.it/services/elements/WebElements.html
52. A. Dallmeyer, C. Carbone, W. Eberhardt, C. Pampuch, O. Rader, W. Gudat, P. Gambardella, K. Kern, Phys. Rev. B **61**, R5133–R5136 (2000)
53. P. Vilmercati, D. Cvetko, A. Cossaro, A. Morgante, Surf. Sci. **603**, 1542–1556 (2009)
54. C. Mariani, Surf. Sci. **454–456**, 417–427 (2000)
55. M.G. Betti, V. Corradini, V. De Renzi, C. Mariani, P. Casarini, A. Abramo, Solid State Commun. **110**, 661–666 (1999)
56. A. Baraldi, in *Synchrotron Radiation*, eds. by S. Mobilio et al. (Springer, Heidelberg, 2014)
57. http://www.globalsino.com/EM/page4809.html
58. G.V. Hansson, R.I.G. Uhrberg, Surf. Sci. Rep. **9**, 197–292 (1988)
59. K.C. Pandey, Phys. B+C **117/118**, 761 (1983)
60. R.I.G. Uhrberg, G.V. Hansson, J.M. Nieholls, S.A. Flodström, Phys. Rev. Lett. **48**, 1032–1035 (1982). doi:10.1103/PhysRevLett.48.1032
61. G. Bussetti, B. Bonanni, S. Cirilli, A. Violante, M. Russo, C. Goletti, P. Chiaradia, O. Pulci, M. Palummo, R. Del Sole, P. Gargiani, M.G. Betti, C. Mariani, R.M. Feenstra, G. Meyer, K.H. Rieder, Phys. Rev. Lett. **106**, 067601 (2011)
62. J.W. Gadzuk, S. Holloway, C. Mariani, K. Horn, Phys. Rev. Lett. **48**, 1288–1291 (1982)
63. C. Mariani, K. Horn, A.M. Bradshaw, Phys. Rev. B **25**, 7798–7806 (1982)
64. C. Baldacchini, M.G. Betti, V. Corradini, C. Mariani, Surf. Sci. **566–568**, 613–617 (2004). doi:10.1016/j.susc.2004.05.115
65. L. Gavioli, M. Fanetti, M. Sancrotti, M.G. Betti, Phys. Rev. B **72**, 035458 (2005)
66. E. Annese, C.E. Viol, B. Zhou, J. Fujii, I. Vobornik, C. Baldacchini, M.G. Betti, G. Rossi, Surf. Sci. **601**, 4242–4245 (2007). doi:10.1016/j.susc.2007.04.131
67. M.G. Betti, A. Kanjilal, C. Mariani, J. Phys. Chem. A **111**, 12454–12457 (2007)
68. A. Ferretti, C. Baldacchini, R. Felice, A. Ruini, E. Molinari, M.G. Betti, Phys. Rev. Lett. **99**, 046802 (2007). doi:10.1103/PhysRevLett.99.046802
69. E. Annese, J. Fujii, C. Baldacchini, B. Zhou, C.E. Viol, I. Vobornik, M.G. Betti, G. Rossi, Phys. Rev. B **77**, 205417 (2008). doi:10.1103/PhysRevB.77.205417
70. Y. Nakayama, J. Niederhausen, S. Machida, Y. Uragami, H. Kinjo, A. Vollmer, J.P. Rabe, N. Koch, H. Ishii, Org. Electron. **14**, 1825–1832 (2013)
71. A.R. Law, M.T. Johnson, H.P. Hughes, Phys. Rev. B **34**, 4289–4297 (1986)
72. http://www.nobelprize.org/nobel_prizes/physics/laureates/2010/
73. K.S. Novoselov, A.K. Geim, S.V. Morozov, D. Jiang, Y. Zhang, S.V. Dubonos, I.V. Grigorieva, A.A. Firsov, Science **306**, 666–669 (2004). doi:10.1126/science.1102896
74. A.K. Geim, K.S. Novoselov, Nat. Mater. **6**, 183–191 (2007). doi:10.1038/nmat1849; and references therein

75. A.H. Castro Neto, N.M.R. Peres, K.S. Novoselov, A.K. Geim, Rev. Mod. Phys. **81**, 109–162 (2009). doi:10.1103/RevModPhys.81.109; and references therein
76. A. Bostwick, J. McChesney, T. Ohta, E. Rotenberg, T. Seyller, K. Horn, Prog. Surf. Sci. **84**, 380–413 (2009); and references therein
77. T. Ohta, A. Bostwick, J.L. McChesney, T. Seyller, K. Horn, E. Rotenberg, Phys. Rev. Lett. **98**, 206802 (2007). doi:10.1103/PhysRevLett.98.206802
78. A. Nagashima, N. Tejima, C. Oshima, Phys. Rev. B **50**, 17487–17495 (1994)
79. A.B. Preobrajenski, N.M. Ling, A.S. Vinogradov, N. Mårtensson, Phys. Rev. B **78**, 073401 (2008). doi:10.1103/PhysRevB.78.073401
80. A.T. N'Diaye, J. Coraux, T.N. Plasa, C. Busse, T. Michely, New J. Phys. **10**, 043033 (2008). doi:10.1088/1367-2630/10/4/043033
81. J. Coraux, A.T. N'Diaye, M. Engler, C. Busse, D. Wall, N. Buckanie, F.J. Meyer zu Heringdorf, R. van Gastel, B. Poelsema, T. Michely, New J. Phys. **11**, 023006 (2009)
82. I. Pletikosič, M. Kralj, P. Pervan, R. Brako, J. Coraux, A.T. N'Diaye, C. Busse, T. Michely, Phys. Rev. Lett. **102**, 056808 (2009). doi:10.1103/PhysRevLett.102.056808
83. P. Lacovig, M. Pozzo, D. Alfè, P. Vilmercati, A. Baraldi, S. Lizzit, Phys. Rev. Lett. **103**, 166101 (2009). doi:10.1103/PhysRevLett.103.166101
84. I. Pletikosič, M. Kralj, D. Sokcevič, R. Brako, P. Lazič, P. Pervan, J. Phys. Condens. Matter **22**, 135006 (2010). doi:10.1088/0953-8984/22/13/135006
85. M. Scardamaglia, G. Forte, S. Lizzit, A. Baraldi, P. Lacovig, R. Larciprete, C. Mariani, M.G. Betti, J. Nanopart. Res. **13**, 6013–602 (2011). doi:10.1007/s11051-011-0384-1
86. M. Scardamaglia, S. Lisi, S. Lizzit, A. Baraldi, R. Larciprete, C. Mariani, M.G. Betti, J. Phys. Chem. C **117**, 3019–3027 (2013). doi:10.1021/jp308861b
87. S. Lisi, Ph.D. Thesis, LOTUS laboratory, Università di Roma "La Sapienza", unpublished.
88. K.R. Knox, A. Locatelli, M.B. Yilmaz, D. Cvetko, T.O. Mentes, M.A. Niño, P. Kim, A. Morgante, R.M. Osgood Jr, Phys. Rev. B **84**, 115401 (2011)
89. A. Fasolino, J.H. Los, M.I. Katsnelson, Nat. Mater. **6**, 858–861 (2007)
90. R. Balog, B. Jørgensen, I. Nilsson, M. Andersen, E. Rienks, M. Bianchi, M. Fanetti, E. Lægsgaard, A. Baraldi, S. Lizzit, Z. Sljivancanin, F. Besenbacher, B. Hammer, T.G. Pedersen, P. Hofmann, I. Hornekær, Nat. Mater. **9**, 315–319 (2010)
91. A. Bostwick, T. Ohta, T. Seyller, K. Horn, E. Rotenberg, Nat. Phys. **3**, 36–40 (2007)
92. S. Lizzit, G. Zampieri, L. Petaccia, R. Larciprete, P. Lacovig, E.D.L. Rienks, G. Bihlmayer, A. Baraldi, P. Hofmann, Nat. Phys. **6**, 345–349 (2010). doi:10.1038/nphys1615

Chapter 10
Powder Diffraction and Synchrotron Radiation

Gilberto Artioli

Abstract Powder diffraction is one of the fundamental techniques for the investigation of materials. Its sensitivity to long range order makes it ideal for the identification, quantification and structural characterization of crystalline phases. Powder diffraction experiments performed at synchrotron sources make ample use of the intrinsic characteristics of synchrotron radiation in terms of energy tunability, brilliance, natural divergence, and excellent signal/noise ratio. Synchrotron radiation powder diffraction (SR-PD) enhances and optimizes the traditional applications of laboratory XRPD, such as phase identification, phase quantification, texture analysis, and peak broadening analysis in terms of stress/strain. However, the properties of the synchrotron X-rays also allow a number of experiments not accessible with laboratory sources, especially in terms of time-resolution, the use of non-ambient sample environments, and simultaneous and combined experiments. The mapping of the physical, chemical, and crystallographic properties of the sample in 2D and 3D using smart combinations of diffraction + imaging + spectroscopy is the natural current evolution of many synchrotron instruments, and one that is bound to have a great impact on many aspects of materials studies.

10.1 Powder Diffraction

Diffraction-based techniques and methods are fundamental tools for the characterization and understanding of inorganic and organic crystalline compounds of rather different nature, such as minerals present in Earth and planetary samples (Chaps. 24 and 25), man-made artifacts and industrial materials (Chap. 27), bio-molecules and pharmaceutical compounds (Chap. 23), and cultural heritage materials (Chap. 26).

G. Artioli (✉)
Dipartimento di Geoscienze, Università degli Studi di Padova, Via Gradenigo 6, 35131 Padova, Italy
e-mail: gilberto.artioli@unipd.it

S. Mobilio et al. (eds.), *Synchrotron Radiation*,
DOI: 10.1007/978-3-642-55315-8_10, © Springer-Verlag Berlin Heidelberg 2015

The diffraction effects of X-rays by crystals (Chap. 8) were first observed by Laue and co-workers one hundred years ago, and the recent centennial celebrations of the International Year of Crystallography (IYCr2014 http://www.iycr2014.org) correctly marked the fundamental importance of this discovery [1, 2].

Although single crystal X-ray diffraction (Chap. 8) stands as the primary technique for the investigation of the fine details of the atomic and molecular structures of crystalline phases, in terms of geometric/conformational aspects and displacement parameters [3, 4], diffraction techniques involving polycrystalline samples developed rapidly during last century to become a routine tool for materials analysis in terms of (1) phase identification and quantification of crystalline compounds and complex polyphasic mixtures, (2) the atomic and molecular structure models of the phases involved, (3) the texture and orientation of the crystalline phases in the material, and (4) the physical microstructural state of the material in terms of mean crystallite size and accumulated strain.

A number of excellent textbooks are available describing the general theory and applications of XRPD to natural and synthetic compounds (see for example [5–10]). Historically, XRPD is linked to physics and mineralogy, so that most laboratories in experimental physics and mineralogical crystallography routinely run some kind of instrumentation able to perform powder diffraction. However, because of the importance of XRPD for phase identification, quantification, and microstructural analysis, a number of laboratory instruments are also implemented in many other research and industrial facilities [11], sometimes even running full-time for continuous production control.

Because of the polycrystalline nature of the sample, in powder diffraction we rely on the assumption of ideal *powder averaging*, that is we assume that a large number of crystallites are randomly oriented in space and homogeneously distributed in the probed sample volume, so that the diffracted intensity in different directions for each exchanged vector (or scattering vector $q = 2k \sin\theta$, where $k = 2\pi/\lambda$, and θ is the angle satisfying Bragg's law $2d_{hkl} \sin\theta = n\lambda$) is homogeneous and invariant with respect to any sample rotation. Therefore in the *ideal powder* case the measurement of the diffracted intensities can be equally performed by scanning along any section of the reciprocal space (with point or linear detectors), or by averaging equal-q portions of the reciprocal space measured by area detectors.

However, in the case of non-randomly oriented crystallites, we face orientationally *textured* samples and the assumption of an ideal powder is no more valid. In such a case the correct measurement of the diffraction intensities needs either the experimental randomization of the sample (or of the measured intensities) with special techniques, or a sufficient number of measurements to reconstruct the spatial orientation distribution function (ODF) of the crystallites by crystallographic texture analysis [12, 13].

From the instrumental point of view, all powder diffraction experiments necessarily encompass (1) a **radiation or particle incident beam** having a wavelength comparable with interatomic distances, so that the atomic lattice acts as an interference grating, (2) a **polycrystalline sample**, and (3) some kind of **detector** able to record the scattered intensities in reciprocal space. Powder diffraction can be performed

Table 10.1 XRPD instrumental geometries

Probed sample volume	Geometry	Commonly implemented instruments
Cylindrical	Debye-Scherrer	Laboratory Debye cameras
	or	Parallel- or focusing-beam laboratory goniometers with capillary sample
	Cylindrical geometry	High resolution parallel-beam configurations at synchrotron sources
Flat-plate	Bragg-Brentano	Diverging-beam Bragg-Brentano diffractometers
	or	
	Parafocusing geometry	
Curved	Guinier	Guinier cameras
	or	Seeman-Bohlin cameras
	Focusing geometry	Thin-film focusing-beam goniometers

with X-rays, thermal and pulsed neutrons, and electrons [14–17], though here we will only focus on X-rays and specifically on the comparison and advances in powder diffraction using synchrotron radiation compared to laboratory X-ray sources.

Depending on the nature of the X-ray source (monochromatic, polychromatic) incident on the sample, the shape of the probed sample volume (cylindrical, platy, or curved), and the characteristics of the detector (point, linear or area detector), a number of instrumental configurations are available to explore the reciprocal space and measure the scattering from the sample.

The great majority of powder diffraction experiments are performed with monochromatic incident beams. For historical and practical reasons, XRPD experiments based on monochromatic radiation make use of cylindrical, flat, or curved polycrystalline samples resulting in different instrumental configurations, commonly defined respectively *Debye geometry* (or Debye-Scherrer geometry), *Bragg-Brentano geometry*, and *Guinier geometry*, from the names of the scientists introducing them. Such instrumental configurations are variously compromising the rapid or the precise measurement of diffracted intensities by the use of specific X-ray optics (Table 10.1). Here we are especially concerned with the Bragg-Brentano (flat-plate) geometry, as the most diffused geometry in research and industrial laboratories, and the Debye (or capillary) geometry, as the most used geometry for high-resolution synchrotron applications. The Guinier geometry (or totally focusing geometry) is hardly used for powder instruments, though it is much used in the design and implementation of monochromators and focusing devices.

The use of polychromatic radiation is only possible at synchrotron sources and it is performed by fixed-angle energy-dispersive configurations. It will be discussed in relationship with special applications, such as high pressure diffraction and diffraction micro-tomography.

In terms of practical instrumental performance, the parameters to be optimized for specific applications are:

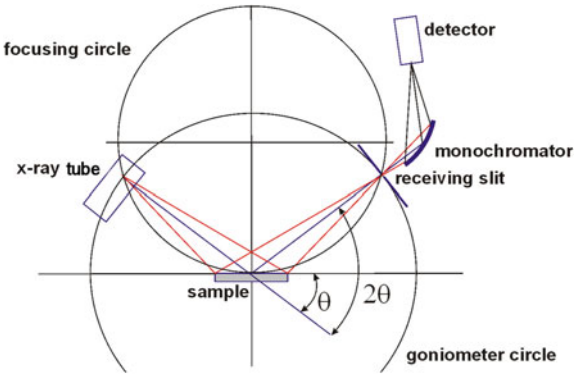


Fig. 10.1 Schematic diagram of the instrumental geometry of a laboratory flat-plate Bragg-Brentano diffractometer

- **$\Delta d/d$ resolution**. That is the ability to separate two contiguous Bragg peaks in reciprocal space. The resolution is generally measured by the Bragg-peak broadening in terms of angular full-width at half maximum (FWHM) as a function of q.
- **Signal/noise ratio**. That is the statistical significance of the Bragg-peak intensity over the instrumental background. The signal to noise ratio is commonly greatly enhanced in synchrotron experiments because of the intrinsic collimation of the source beam.
- **Measurement time**. The total time of the measurement depends on a number of factors including: the scattering power of the sample, the probed volume of sample, the incident flux, the type and efficiency of the detectors, and many more. The high incident photon flux at synchrotron sources normally ensures that XRPD spectra can be measured much more rapidly than on laboratory instruments. Therefore synchrotron XRPD experiments offer additional flexibility to optimize resolution and rapidity of measurement, this is especially important for time-resolved applications.

10.2 Flat Plate Sample (Bragg-Brentano Geometry)

Most laboratory goniometers for powder diffraction employ a conventional X-ray tube source, a diverging incident beam, a flat-plate (often rotating) sample (Fig. 10.1), and various kinds of point or short linear detectors, most recently based on diode arrays or the so-called real time multiple strip detectors (RTMS [18]). The axial or in-plane divergence of the beam is crucially controlled by simple or parallel slit systems (Soller slits) positioned between the source and the sample and the sample and the detector, which are variously employed to reduce the axial aberration and

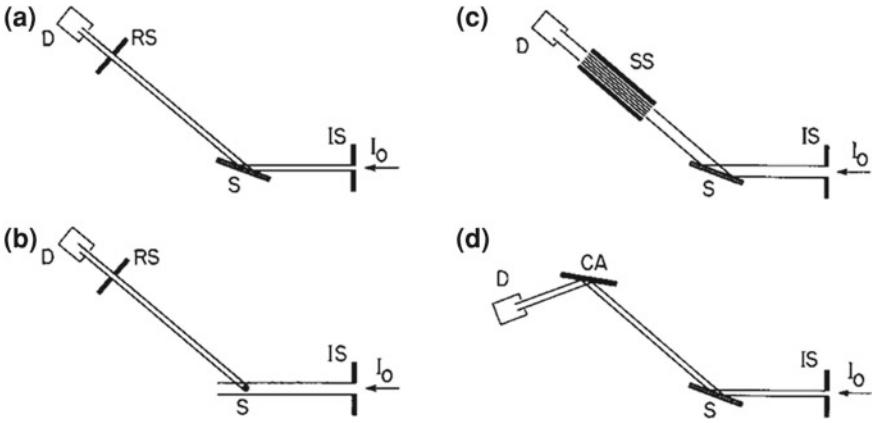


Fig. 10.2 Simplified diagrams of several powder diffraction geometries implemented at synchrotron beamlines: **a** receiving-slit flat-plate geometry, **b** receiving-slit capillary geometry, **c** long Soller slits flat-plate geometry, and **d** analyzer-crystal flat plate geometry. From [21]

to improve the noise rejection. Long Soller slits may also be used in synchrotron flat-plate configurations [19, 20] (Fig. 10.2d).

The universal diffusion of flat-plate diffractometers is related to the simple and fast preparation of the sample, to the rapidity of measurements, and to the relative facility to compromise the signal/noise ratio and the $\Delta d/d$ resolution by adjusting the instrumental parameters (sample to source distance, slits, etc.). However, the resolution is critically related to the instrumental settings, as shown in Fig. 10.3 by the large difference in resolution curves measured on different laboratory flat-plate instruments using a standard specimen, displayed as FWHM of Bragg peaks as a function of the diffraction angle [22]. The high resolution curve obtained by measuring the NAC standard at the old beam line BM16 of ESRF is also shown for comparison and it allows direct perception of the large decrease in Bragg-peak broadening achievable at synchrotron sources.

In laboratory instruments the basic instrumental setup shown in Fig. 10.1 may be variously modified with the insertion of focusing or parallel-beam optics, in order to improve Bragg-peak resolution or to solve sample position problems. However at synchrotron stations using the flat-plate configuration the natural collimation of the beam is often exploited, though it makes the sample rotation mandatory because of the small number of crystallites simultaneously meeting the diffraction conditions. The rotating capillary solution (Debye geometry, Fig. 10.2b) is therefore the most adopted configuration on synchrotron powder beam-lines.

Although not commonly used at synchrotrons, the flat-plate geometry may nonetheless be convenient when analyzing very thin layers of samples, such as fluid-solid interfaces, materials surfaces, and thin films in grazing-incidence mode (Chap. 18) [23, 24].

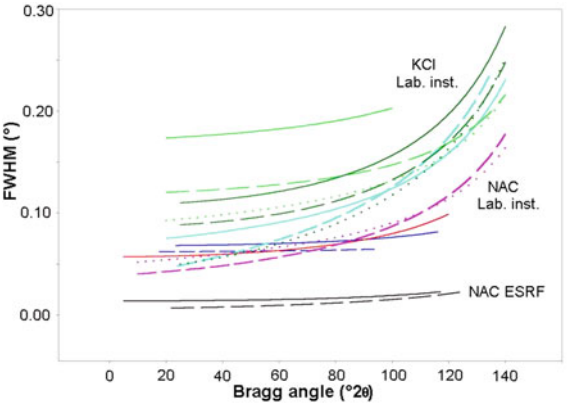


Fig. 10.3 FWHM curves of Bragg peaks of standard KCl measured in different laboratory conditions [22], compared to the resolution curve of NAC measured at the high-resolution BM16 *beam line* at ESRF (now moved to ID31)

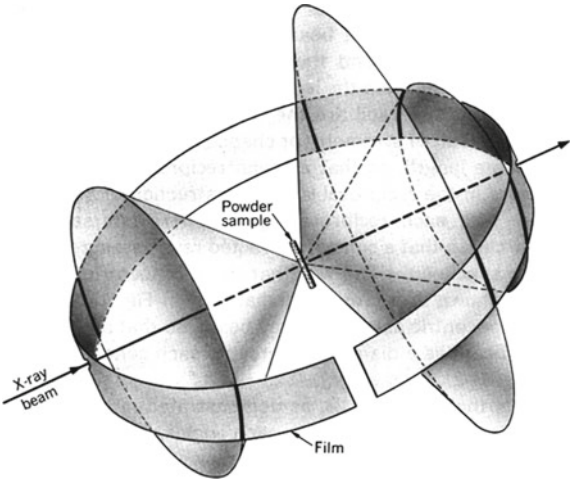


Fig. 10.4 Conventional capillary geometry developed for film-based Debye-Scherrer cameras. The picture shows the film strip intercepting all possible Debye cones in the angular range 0–180 °2θ. In this picture the film is mounted using the technique proposed by Straumanis, which allowed self-calibration of the angle [25, 26]

10.3 Cylindrical Sample (Debye Geometry)

The Debye geometry (Fig. 10.4) using the cylindrical sample is the most simple and effective configuration for a powder experiment. The sample, traditionally prepared in the form of a cylinder by mixing the powdered sample with various kinds of glue, is nowadays invariably enclosed in a glass capillary and rotated in front of the beam. The diffraction cones (Debye cones) are intercepted by various kind of detectors: the old film used in the Debye-Scherrer cameras are now substituted both in the laboratory and at synchrotron powder stations by point detectors (Fig. 10.2b), linear detectors (diode arrays, RTMS, silicon strips, or gas chambers) or area detectors covering different portions of the reciprocal space (pixel detectors [27], image plates).

The use of capillary geometry offers several advantages: it is easy to implement and align, when using a parallel beam the resolution is essentially controlled by



Fig. 10.5 Debye geometry at the ID31 high resolution *beam line* at ESRF (http://www.esrf.eu/UsersAndScience/Experiments/StructMaterials/ID31/). The detector is actually composed of nine crystal multi-analyser stage [28]

the diameter of the capillary, and the environment of the sample can be efficiently controlled and conditioned. This is the reason why most experiments in need of fast measurements (phase transformation, kinetics of reactions, thermal expansion, compressibility, etc.) commonly adopt a Debye geometry with fast detectors.

10.4 The Implementation of Capillary Geometry at Synchrotron Sources, Case Examples

Several of the high resolution beam lines such as ID31at the ESRF, adopt a capillary configuration with multi-analyser crystal detection [28] (Fig. 10.5) in order to have a high throughput diffracted signal while maintaining the highest resolution as possible. The use of perfectly aligned analyser crystals renders the positions of diffraction peaks immune to aberrations, such as specimen transparency and misalignment of the sample with respect to the axis of the diffractometer that affect conventional arrangements with a scanning slit or a PSD. The instrument may actually be used also with flat samples for reflectivity or grazing-incidence measurements (Chap. 18). Similar multi-analyser configurations are implemented on the MS powder diffractometer at the Swiss Light Source (SLS) [29] and at the 11-BM powder diffraction beam line at Advanced Photon Source (APS) [30] to enhance the high-resolution measurement mode.

Many other beam lines compromise the $\Delta d/d$ resolution by using linear or area detectors, thus enhancing the counting statistics and the rapidity of measurement over large angular ranges. The most common instrumental configurations encompass



Fig. 10.6 Various implementations of the Debye capillary geometry at synchrotron powder diffraction stations for time-resolved measurements: *upper left* translating flat image plate at the GILDA beam line at ESRF; *upper right* the MYTHEN II detector at the SLS-MS powder diffraction, the instrument also has a crystal multi-analyser stage; *lower left* the translating cylindrical image plate chamber at the MCX station, Elettra; *lower right* the P2M hybrid pixel detector commissioned on the materials beamline I16 at Diamond [36]

blade gaseous chambers [31], silicon strip detectors [32, 33] and flat or curved image plates [34, 35]. Figure 10.6 shows some of the implemented powder diffraction stations.

Gas-filled detectors have played an important role in experiments at synchrotron sources for many years. Although other X-ray detection technologies are gaining wider use, particularly with the higher flux of new sources, gas-filled detectors are still well suited for specific experiments [31], especially combined SAXS-WAXS experiments.

Most modern instruments actually implement fast area detectors (Mythen, Pilatus) that are able to survey a substantial portion of reciprocal space, ensuring good statistics, very fast data collection, and on-line data transfer. However many experimental stations, especially those focusing on time-resolved studies of solid-state materials that do not require extreme time resolution, mount flat or curved image plates with off-line reading. They offer a very large dynamic range and linearity, thus making time integration possible during the transformation processes.

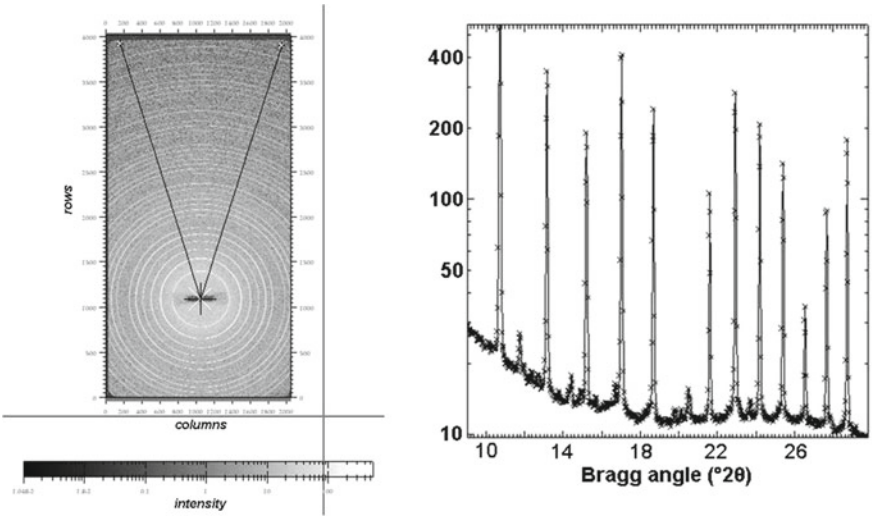


Fig. 10.7 *Left* Debye cones as collected directly on a flat image plate from a cylindrical specimen. Intensities can be integrated over all or part of the Debye ring by appropriate software (such as the excellent ESRF-based Fit2D [40]) to obtain the conventional powder pattern shown in the *right* image

It should be remarked that when point or linear detectors are used the measurement of reliable diffraction intensities depends crucially on the quality and preparation of the sample, since a unique section of the reciprocal space is actually scanned. On the other hand whenever 2D detectors are used, then the ideal or textured character of the sample can be directly gauged and analysed [37]. In the latter case the correct diffraction intensities can be obtained by proper azimuthal integration along the Debye rings (Fig. 10.7), or by hierarchical reciprocal-space modeling of the intensities making use of the appropriate orientation distribution functions [38, 39].

10.5 Basics of Instrumental Strategies

Modern commercial XRPD equipment in general is relatively flexible in the choice of instrumental parameters and configurations, so that the basic identification and quantification work for most materials can be conveniently performed in the laboratory. However, powder diffraction experiments performed at dedicated synchrotron sources offer higher photon flux, energy tunability, better signal/noise ratio, and additional flexibility in the control of the sample environment in non-ambient conditions. It is not uncommon that impurity phases contained in low amounts remain undetected in preliminary laboratory analysis, whereas they readily show up in high quality synchrotron data. Quantification of phases that are present in multiphase mixtures in amounts of the order of 0.1 wt % needs good peak discrimination and superior

peak/background ratio for appropriate assessment. Therefore, although most phase identification and quantification can be performed at home, there may be cases that require synchrotron experiments [41].

Beyond simple extensions of laboratory experiments, of course synchrotron radiation give access to a wide variety of experiments not feasible at home. The two most desirable and useful properties are (1) **high incident flux**, which is fundamental in time resolved studies (Chap. 28), in the investigation of very small samples, such as those required to reach ultra-high pressures (Chaps. 24 and 29), and in the combined studies discussed later; and (2) **high $\Delta d/d$ resolution**, which is mandatory for example in the successful peak indexing and Bragg intensity collection for crystal structure solution and refinement (Chaps. 8 and 18), in the correct assessment of Bragg peak broadening for size-strain studies (Chap. 18), or in the accurate measurement of lattice parameters, such as in thermal expansion and compressibility investigations.

Unfortunately, intensity and resolution are often at variance, and each experiments must be carefully designed in order to enhance one or the other. In general, the use of crystal analyzers gives excellent $\Delta d/d$ resolution, low count rate, slow collection times, and better tolerance to sample displacements (Figs. 10.2d and 10.5). The setting is useable with flat plate or capillary samples. Soller slits give modest resolution, good count rate and insensitivity to sample displacement (Fig. 10.2c). Simple receiving slits and PSD's (Fig. 10.6) give very high count rate, adjustable resolution, and rapid collection times.

It follows that the synchrotron beam lines equipped with crystal multi-analyser stages are most suited for accurate measurement of lattice parameters, assessment of sample broadening, and measurement of intensities for structural investigations. Those equipped with 2D or 3D detectors are most suited for time-resolved experiments, texture studies, and measurements in non-ambient conditions. As we have seen, some beam lines may easily switch between either of the two detecting systems (Fig. 10.6) in order to expand the experimental flexibility and satisfy user's demands. Furthermore, each instrumental configuration may offer a broad range of tunable parameters.

10.6 Time Resolved Experiments, Kinetics, Non-ambient Conditions

The understanding of the transformation processes in the solid state is important in many areas of physics, chemistry, engineering, Earth sciences, materials science, and biology. Traditionally the Earth sciences played a key role in the development of high pressure and high temperature experiments [42–45], because they are the only way to access the extreme conditions present in the Earth and planetary interiors that cannot be directly sampled. The experimental investigations at extreme conditions (Chap. 29) are still much focused on mineral transformations, however in

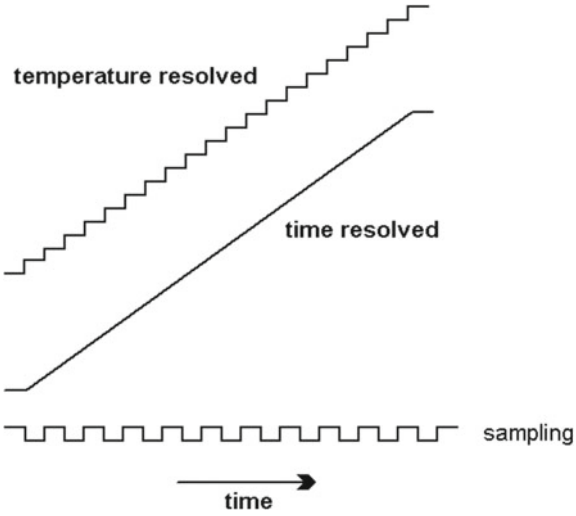


Fig. 10.8 Relationship between the perturbation (in this case temperature) imposed on the sample and the measuring time during in situ experiments

situ studies are now routinely performed in the fields of materials science and the physical chemistry of the solid state. Industrial processes, which are mostly based on the thermal treatment of raw materials, are especially concerned with high temperature experiments, whereas high pressure experiments involve the synthesis of materials with novel properties.

In situ investigations concern the response of solid materials to external perturbations, which can be instantaneous or continuous. It is usually very difficult to perturb the system and maintain it in equilibrium during the measurement, independently of whether the perturbation is maintained or stopped during the measurements. In fact once the system has been perturbed it keeps evolving along the thermodynamic path. It is therefore important that the **measurement time** in the experiment is designed to be short with respect to the whole reaction time to allow multiple snapshot of the evolving system (Fig. 10.8). With respect to time the experiments can be defined as **static** (at the thermodynamic equilibrium), or **dynamic** (during the reaction of the system), and in the latter case we are generally interested in quantifying the **kinetics** of the reaction, that is the reaction rate.

Concerning the reaction kinetics induced by temperature, we may perform **isothermal experiments**, by quickly bringing the sample to different non-ambient temperature and measuring its response in time, or **non-isothermal experiments**, by bringing the sample to the target temperature through different time-temperature paths (i.e. different heating or cooling rates). In any case several experiments performed at different temperatures or heating rates are necessary to determine the kinetic parameters of the reaction.

The same logics of course applies to pressure-dependent experiments or to in situ experiments depending on any other externally imposed parameter.

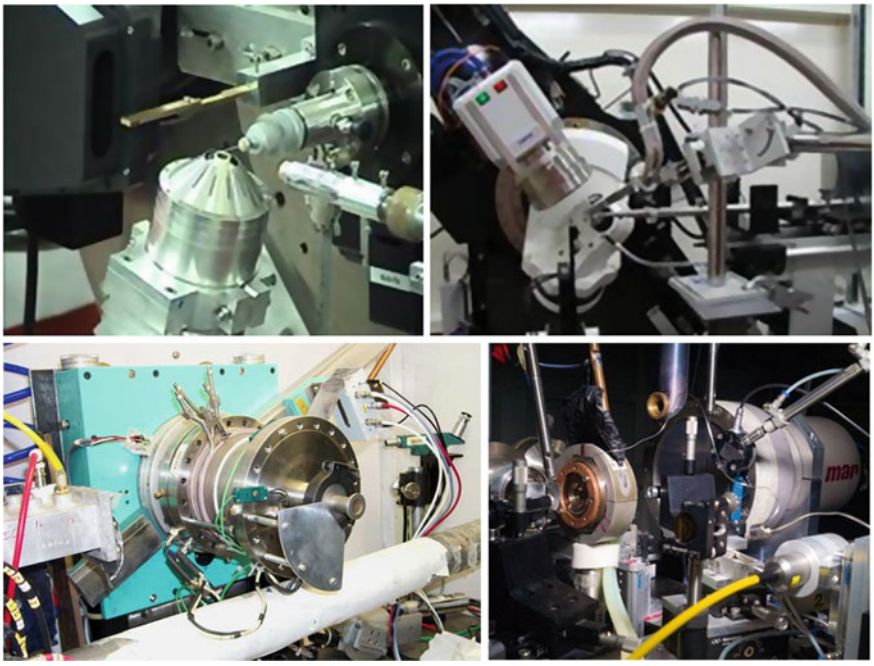


Fig. 10.9 Examples of conditioning apparatuses: *upper left*, hot gas blower usable at Soleil in the temperature range 20–900 °C; *upper right*, gas stream cooler, it can cool to 80 or 30 K depending on the use of liquid N_2 or He; *lower left*, resistance furnace at beam line X3B1 at the NSLS; *lower right*, diamond anvil cell mounted on beam line ID27 at the ESRF

In situ XRPD experiments therefore imply the possibility to perturb the sample while measuring the diffraction signal. This is usually performed by cooling chambers (cold gas streams, Peltier devices), furnaces (hot gas blowers, metal strip chambers, resistance heaters, lasers, etc), reaction chambers (to induce oxidising/reducing conditions, humidity chambers, hydrothermal cells, etc.), and high-pressure devices (diamond anvil cells, piston cylinders, multi-anvil presses, etc.) (Fig. 10.9). The conditioning apparatus must be designed so that (1) the perturbation is applied homogeneously over the probed volume of sample, (2) it allows proper monitoring of the sample conditions, and (3) sufficiently intense diffraction signal can be measured over a sensible portion of reciprocal space.

Details of the experimental designs and technical solutions can be found in the abundant literature on the subject (see for example [43–48]). Here we should just remark that when studying small samples within complex confining apparatuses, it may be rather difficult to access a large portion of q. It may therefore be convenient to exploit the large energy spectrum available at synchrotron sources using energy-dispersive geometries [49–51]. The fixed-angle geometry can in fact be successfully employed to characterize transformation kinetics [52, 53] and it is also increasingly applied to the investigation of materials texture and strain [54].

10.7 Simultaneous and Combined Studies

The high brilliance and collimation of the X-ray source and the great flexibility in experimental design at synchrotron beam lines makes it possible to combine diffraction to other techniques and therefore to obtain complementary information on the investigated system.

First of all we should distinguish between combined techniques and simultaneous measurements. Synchrotron facilities are ideal settings to perform **combined experiments**, that is the sample is measured at different times using different techniques and experimental settings. This is because at each synchrotron facility there are many stations covering a large range of energies and probing methods, some of them even operating at the same beam line, and the environment is therefore favorable to multi-experimental approaches.

However the real advances are due to the possibility of performing **simultaneous measurements**, that is to excite and measure different signals produced by the sample at the same time. There are several kinds of simultaneous experiments:

(1) the measurement of the X-ray scattering signal at low q (SAXS) and at high q (WAXS; that is the XRPD signal). These are commonly called SAXS-WAXS experiments, and they are extremely useful to obtain information on the structural order of the crystalline phases by diffraction, and at the same time on the aggregation state of the system by the small-angle signal (Chap. 11). These investigations are fundamental in interpreting crystallization in inorganic systems and polymerization in soft matter systems [55–57]. The use of even higher q ranges makes it possible to analyse the short range pair distribution function (PDF) of the system: the simultaneous analysis of the SAXS, WAXS, and PDF signal from the sample promise to be an extremely powerful method to extract information over a wide correlation range in the system [58].

(2) the use of spectroscopic techniques that excite the sample using the same X-ray beam and energy range used by diffraction. These are most commonly XAS and XRF, which can be performed using the same incident beam used for diffraction. The simultaneous measurement of the XRD and XAS signal yields complementary information on the crystalline phase and on the local environment of the probed element. The case of crystallization reactions catalyzed by specific elements or heterogeneous catalysis on crystalline media are a very suited topic for these kind of measurements [59, 60]. Combined XRD and XRF measurements are commonly performed using scanning micro-beams to discriminate the elemental and phase composition of complex multiphasic mixtures: the case of pigments in paintings and other cultural heritage materials [61, 62], sub-micron calculi in urolithiasis [63] and that of nanoparticles in environmental pollution [64] are stringent examples. Of course the present trends emphasize the simultaneous measurement and analysis of as much signals as possible: beam lines are therefore planned for the simultaneous micro-mapping of the XRD/XRF/XAS signals [65].



Fig. 10.10 Instrumental setup for simultaneous XRPD and DLS experiments at the GILDA BM8 *beam line* at ESRF

(3) the combination of external spectroscopic techniques that are designed to be synchronized with the diffraction measurements. Most experiments of this kind involve vibrational spectroscopies (FTIR, Raman), in order to combine the crystallographic information obtained by diffraction with the molecular and electronic information obtained by spectroscopy. Full synchronization of the techniques during dynamic measurements can be difficult [66–68], though the successful measurement provides a substantial amount of complementary information on the assembly of molecular systems. Besides vibrational spectroscopies, other techniques can be coupled to diffraction, such as dynamic light scattering (DLS, Fig. 10.10), which allows continuous monitoring of the precursors species to crystallization. UV-Vis optical luminescence excited by X-rays has also been measured in simultaneous mode on semiconductor nanostructures [69].

As mentioned above, the present trend is to simultaneously measure a number of different signals, including diffraction. To exploit the synchrotron micro-beams at best, the aim is to spatially map and quantify in 2D and 3D the crystalline phases using the XRPD signal, and simultaneously combine the information with different kind of spectroscopic information [65].

In two dimensions, the mapping is performed by scanning the surface of the sample with the X-ray micro-beam and by careful space- and time-synchronization of the measured signals into matching maps. Developments into the nano-beam regime are planned [70].

The mapping of the crystalline phases in three dimensions requires the combination of micro-tomographic imaging with diffraction. Several options have recently been developed to this purpose. A 'box beam' (i.e. a rectangular synchrotron X-ray beam, typically a few hundreds microns wide) experimental setup for **diffraction contrast tomography** (DCT) using the absorption signal in conjunction with the diffraction signal of the grains in the analysis, has been successfully used for mapping the position and shape of crystal grains in metal samples [71, 72]. A different setup, usually referred to as **tomographic energy dispersive diffraction imaging** (TEDDI), uses a polychromatic incident X-ray beam and an energy-dispersive detector system to collect a powder-like diffraction signal (scanning and rotating the sample) and uses tomographic reconstruction algorithms to map the distribution of the phases in the sample [73–75]. 'Pencil-beam' **X-ray diffraction computed tomography** (XRD-CT) consists in scanning linear projections of the sample with a microfocused synchrotron X-ray beam, taken at different angular positions during a 180° rotation, as in a first generation tomographic scan. The basic concept is to reconstruct a distribution map, via tomographic inversion algorithms, using results obtained from the X-ray diffraction signal instead of attenuation values [76–79].

At present, the TEDDI technique can be performed in very short times, though it has the limitation in spatial resolution because of the large voxel size. On the other hand, the XRD-CT technique has excellent sub-micron voxel resolution, though the complete tomographic scan requires long collection times because of the pencil beam method. However, there is little doubt that diffraction-enhanced micro-tomography and its instrumental developments will play a major role in the microstructural characterization of materials.

References

1. W.W. Schmahl, W. Steurer, Acta Crystallogr. **A68**, 1–2 (2012)
2. M. Eckert, Acta Crystallogr. **A68**, 30–39 (2012)
3. K.N. Trueblood, H.-B. Burgi, H. Burzlaff, J.D. Dunitz, C.M. Gramaccioli, H.H. Schulz, U. Shmueli, S.C. Abrahams, Acta Cryst. **A52**, 770–781 (1996)
4. G. Artioli, in *Energy Modelling in Minerals*, ed. by C.M. Gramaccioli. EMU Notes in Mineralogy, vol. 42, (Eötvös University Press, Budapest, 2002), Chap. 13, pp. 389–405
5. H.P. Klug, L.E. Alexander, *X-ray Diffraction Procedures for Polycrystalline and Amorphous Materials* (Wiley, New York, 1974)
6. B.E. Warren, *X-ray Diffraction* (Dover Publications, New York, 1990)
7. A. Guinier, *X-ray Diffraction in Crystals, Imperfect crystals, and Amorphous Bodies* (Dover Publications, New York, 1994)
8. R. Jenkins, R.L. Snyder, *X-ray Powder Diffractometry* (Wiley, New York, 1996)
9. R.E. Dinnebier, S.J.L. Billinge (eds.), *Powder Diffraction. Theory and Practice* (RSC Publishing, Cambridge, 2008)

10. V. Pecharsky, P. Zavalij, *Fundamentals of Powder Diffraction and Structural Characterization of Materials*, 2nd edn. (Springer, Heidelberg, 2009)
11. F.H. Chung, D.K. Smith (eds.), *Industrial Applications of X-ray Diffraction* (Marcel Dekker Inc., New York, 2000)
12. H.J. Bunge, *Texture Analysis in Materials Science* (Cuvillier, Göttingen, 1993)
13. U.F. Koch, C.N. Tomé, H.R. Wenk, *Texture and Anisotropy. Preferred Orientations in Polycrystals and Their Effect on Materials Properties* (Cambridge University Press, Cambridge, 1998)
14. C. Giacovazzo (ed.), *Fundamentals of Crystallography*, 3rd edn, IUCr Text on Crystallography, vol. 15 (Oxford Science Publications, Oxford, 2011)
15. R.M. Ibberson, W.I.F. David, in *Structure Determination form Powder Diffraction Data*, ed. by W.I.F. David, K. Shankland, L.B. McCusker, Ch. Baerlocher, IUCr Monographs on Crystallography (Oxford Scientific Publications, Oxford, 2002), Chap. 5
16. X.D. Zou, S. Hovmöller, P. Oleynikov, *Electron Crystallography—Electron Microscopy and Electron Diffraction*, IUCr Text on Crystallography, vol. 16, (Oxford Science Publications, Oxford, 2011)
17. X.D. Zou, S. Hovm öller, Acta Crystallogr. **A64**, 149–160 (2008)
18. C.A. Reiss, IUCr commission on powder diffraction. Newsletter **27**, 21–23 (2002)
19. T. Ida, H. Hibino, H. Toraya, J. Appl. Cryst. **34**, 144–151 (2001)
20. B. Bewer, J. Synch, Rad. **19**, 185–190 (2012)
21. D.E. Cox, in *Synchrotron Radiation Crystallography*, ed. by P. Coppens (Academic Press, London, 1992)
22. N. Masciocchi, G. Artioli, Powder Diffr. **11**, 253–258 (1996)
23. M. Neuschitzer, A. Moser, A. Neuhold, J. Kraxner, B. Stadlober, M. Oehzelt, I. Salzmann, R. Resel, J. Novák, J. Appl. Crystall. **45**, 367 (2012)
24. O.V. Konovalov, A.A. Vorobiev, J. Appl. Crystall. **46**, 270–275 (2013)
25. H. Lipson, *The Study of Metal and Alloys by X-ray Powder Diffraction Methods*, Teaching Pamphlet n. 16, International Union of Crystallography, http://www.mx.iucr.org/iucr-top/comm/cteach/pamphlets/16/index.html
26. L.V. Azároff, M.J. Buerger, *The Powder Method in X-ray Crystallography* (McGraw Hill, New York, 1958)
27. L. Rossi, P. Fischer, T. Rohe, N. Wermes, *Pixel Detectors—from Fundamentals to Applications* (Springer, Berlin, 2006)
28. J.-L. Hodeau, P. Bordet, M. Anne, A. Prat, A.N. Fitch, E. Dooryhee, G. Vaughan, A. Freund, Proc. SPIE **3448**, 353 (1998)
29. F. Gozzo, B. Schmitt, Th. bortolamedi, C. Giannini, A. Guagliardi, M. Lange, D. Meister, D. Maden, P. Willmott, B.D. Patterson, J. Alloys Compd. **362**, 206–217 (2004)
30. P.L. Lee, D. Shu, M. Ramanathan, C. Preissner, J. Wang, M.A. Beno, R.B. Von Dreele, L. Ribaud, C. Kurtz, S.M. Antao, X. Jiao, B.H. Toby, J. Synchrotron Rad. **15**, 427–432 (2008)
31. G.C. Smith, J. Synchrotron Rad. **13**, 172–179 (2006)
32. A. Bergamaschi, A. Cervellino, R. Dinapoli, F. Gozzo, B. Henrich, I. Johnson, P. Kraft, A. Mozzanica, B. Schmitt, X. Shi, J. Synchrotron Rad. **17**, 653–668 (2010)
33. F. Gozzo, A. Cervellino, M. Leoni, P. Scardi, A. Bergamaschi, B. Schmitt, Z. Kristallogr. **225**, 616–624 (2010)
34. C. Meneghini, G. Artioli, A. Balerna, A.F. Gualtieri, P. Norby, S. Mobilio, J. Synchrotron Rad. **8**, 1162–1166 (2001)
35. P. Sarin, R.P. Haggerty, W. Yoon, M. Knapp, A. Berghaeuser, P. Zschack, E. Karapetrova, N. Yang, W.M. Kriven, J. Synchrotron Rad. **16**, 273–282 (2009)
36. J. Marchal, N. Tartoni, C. Nave, Nucl. Instrum. Methods Phys. Res. Sect. A Accelerators Spectrometers Detectors Assoc. Equip. **604**, 123–126 (2009)
37. B.B. He, *Two-Dimensional X-ray Diffraction* (Wiley, Hoboken, 2009)
38. M. Bortolotti, L. Lutterotti, I. Lonardelli, J. Appl. Cryst. **42**, 538–539 (2009)
39. L. Lutterotti, Nuclear Instrum. Methods Phys. Res. Sect. B Beam Interact. Mater. Atoms **268**, 334–340 (2010)

40. A.P. Hammersley, *ESRF Internal Report*, ESRF98HA01T, FIT2D V9.129 Reference Manual V3.1 (1998) http://www.esrf.eu/computing/scientific/FIT2D/
41. B.A. Latella, B.H. O'Connors, J. Amer. Ceram. Soc. **80**, 2941–2944 (1997)
42. G. Artioli, Notiz. Neutroni e Luce di Sincrotrone **2**, 4–13 (1997)
43. R.J. Hemley (ed.), *Ultra-High Pressure Mineralogy*, Rev. Mineral Geochem., vol. 37 (Mineralogical Society of America, Washington, 1998)
44. S.A.T. Redfern, M.A. Carpenter (eds.), *Transformation Processes in Minerals*, Rev. Mineral Geochem., vol. 39 (Mineralogical Society of America, Washington, 2000)
45. R.M. Hazen, R.T. Downs (eds.), *High-Temperature and High-Pressure Crystal Chemistry*, vol. 41 (Mineralogical Society of America, Washington, 2000)
46. D.D.L. Chung, P.W. De Haven, H. Arnold, D. Ghosh, *X-ray Diffraction at Elevated Temperatures* (VCH Publishers, New York, 1993)
47. W.B. Holzapfel, N.S. Isaacs, *High Pressure Techniques in Chemistry and Physics: A Practical Approach* (Oxford University Press, Oxford, 1997)
48. E. Boldyreva, P. Dera (eds.), *High-Pressure Crystallography, NATO Science for Peace and Security Series B: Physics and Biophysics* (Springer, Netherlands, 2010)
49. S.M. Clark, Crystall. Rev. **8**, 57–92 (2002)
50. Ch. Genzel, I.A. Denks, J. Gibmeier, M. Klaus, G. Wagener, Nuclear Instrum. Methods Phys. Res. Sect. A Accelerators Spectrometers, Detectors Assoc. Equip. **578**, 23–33 (2007)
51. L. Gerward, J.Z. Jiang, J. Staun, Olsen, J.M. Recio, A. Waśkowska, J. Alloys Compd. **401**, 11–17 (2005)
52. L.J. McIntyre, T.J. Prior, A.M. Fogg, Chem. Mater. **22**, 2635–2645 (2010)
53. P. Barnes, S. Colston, B. Craster, C. Hall, A. Jupe, S. Jacques, J. Cockcroft, S. Morgan, M. Johnson, D. O'Connor, M. Bellotto, J. Synchrotron Rad. **7**, 167–177 (2000)
54. Ch. Genzel, I.A. Densk, R. Coelho, D. Thomas, R. Mainz, M. Klaus, J. Strain Anal. Eng. Des. **46**, 615–625 (2011)
55. A.M. Beale, A. van der Eerden, S.D.M. Jacques, O. Leynaud, M.G. O'Brien, F. Meneau, S. Nikitenko, W. Bras, B.M. Weckhuysen, J. Am. Chem. Soc. **128**, 12386–12387 (2006)
56. W. Bras, S. Nikitenko, G. Portale, A. Beale, A. van der Eerden, D. Detollenaere, J. Phys. Conf. Ser. **247**, 012047 (2010)
57. T.A. Ezquerra, M.C. Garcia-Gutierrez, A. Nogales, M. Gomez (eds.), *Application of Synchrotron Light to Scattering and Diffraction in Materials and Life Sciences*, Lecture Notes in Physics, vol. 776 (Springer, Berlin, 2009)
58. J. Becker, M. Bremholm, C. Tyrsted, B. Pauw, K.M.O. Jensen, J. Eltzholt, M. Christensen, B.B. Iversen, J. Appl. Cryst. **43**, 729–736 (2010)
59. G. Sankar, J.M. Thomas, C.R.A. Catlow, Top. Catal. **10**, 255–264 (2000)
60. T. Daley, E. Raj, S. Ramos, G. Cibin, A. Dent, T.I. Hyde, G. Sankar, J. Phys. Conf. Ser. **430**, 012080 (2013)
61. M.L. Franquelo, A. Duran, J. Castaing, D. Arquillo, J.L. Perez-Rodriguez, Talanta **89**, 462–469 (2012)
62. D. Creagh, A. Lee, V. Otieno-Alego, M. Kubik, Radiat. Phys. Chem. **78**, 367–374 (2009)
63. S.D. Blaschko, J. Miller, T. Chi, L. Flechner, S. Fakra, A. Kahn, P. Kapahi, M.L. Stoller, J. Urology **189**, 726–734 (2013)
64. K. Janssens, W. De Nolf, G. Van Der Snickt, L. Vincze, B. Vekemans, R. Terzano, F.E. Brenker, TrAC Trends Anal. Chem. **29**, 464–478 (2010)
65. G. Martinez-Criado, R. Tucoulou, P. Cloetens, P. Bleuet, S. Bohic, J. Cauzid, I. Kieffer, E. Kosior, S. Laboure, S. Petitgirard, A. Rack, J.A. Sans, J. Segura-Ruiz, H. Suhonen, J. Susini, J. Villanova, J. Synchrotron Rad. **19**, 10–18 (2012)
66. W. van Beek, O.V. Safonova, G. Wiker, H. Emerich, Phase Transitions **84**, 726–732 (2011)
67. M. Klimakow, J. Leiterer, J. Kneipp, E. Rossler, U. Panne, K. Rademann, F. Emmerling, Langmuir **26**, 11233–11237 (2010)
68. E.V. Boldyreva, Phase Transitions **82**, 303–321 (2009)
69. G. Martínez-Criado, B. Alén, J.A. Sans, A. Homs, I. Kieffer, R. Tucoulou, P. Cloetens, J. Segura-Ruiz, J. Susini, J. Yoo, G. Yi, Nuclear Instrum. Methods Phys. Res. Sect. B Beam Interact. Mater. Atoms **284**, 36–39 (2012)

70. G.E. Ice, J.D. Budai, J.W.L. Pang, Science **334**, 1234–1239 (2011)
71. W. Ludwig, A. King, P. Reischig, M. Herbig, E.M. Lauridsen, S. Schmidt, H. Proudhon, S. Forest, P. Cloetens, S. Rolland du Roscoat, J.Y. Buffière, T.J. Marrow, H.F. Poulsen, Mater. Sci. Eng. A **524**, 69–76 (2009)
72. A. King, M. Herbig, W. Ludwig, P. Reischig, E.M. Lauridsen, T. Marrow, J.Y. Buffière, Nuclear Instrum. Methods Phys. Res. Sect. B Beam Interact. Mater. Atoms **268**, 291–296 (2010)
73. C. Hall, P. Barnes, J.K. Cockcroft, S.L. Colston, D. Hausermann, S.D.M. Jacques, A.C. Jupe, M. Kunz, Nucl. Instrum. Methods Phys. Res. Sect. B **140**, 253–257 (1998)
74. L. Tunna, P. Barclay, R.J. Cernik, K.H. Khor, W. O'Neill, P. Seller, Meas. Sci. Technol. **17**, 1767–1775 (2006)
75. R.J. Cernik, K.H. Khor, C. Hansson, J.R. Soc, Interface **5**, 477–481 (2008)
76. P. Bleuet, E. Welcomme, E. Dooryhée, J. Susini, J.L. Hodeau, P. Walter, Nat. Mater. **7**, 468–472 (2008)
77. G. Artioli, T. Cerulli, G. Cruciani, M.C. Dalconi, G. Ferrari, M. Parisatto, A. Rack, R. Tucoulou, Anal. Bioanal. Chem. **397**, 2131–2136 (2010)
78. H. Palancher, R. Tucoulou, P. Bleuet, A. Bonnin, E. Welcomme, P. Cloetens, J. Appl. Cryst. **44**, 1111–1119 (2011)
79. M. Voltolini, M.C. Dalconi, G. Artioli, M. Parisatto, L. Valentini, V. Russo, A. Bonnin, R. Tucoulou, J. Appl. Cryst. **46**, 142–152 (2013)

Chapter 11
Small Angle X-Ray Scattering (SAXS) with Synchrotron Radiation Sources

Stefano Polizzi and Francesco Spinozzi

Abstract This is not a treatise on small angle scattering; it is a presentation of the application of small angle scattering and the potentialities of synchrotron sources where conventional sources prove limited. A brief introduction describing the technique aims to provide the reader with no more than the qualitative tools necessary to understanding the case studies discussed further on. For a more thorough discussion, the reader is referred to standard texts in the field.

11.1 The Physical Phenomenon

When an X-ray beam passes through matter, the main effect, known as *Thomson scattering* or *elastic scattering* or *elastic scattering*, is the interaction between the electric field of the incident wave and the electrons, which causes the electrons to oscillate at the same frequency as that of the wave. In turn, these oscillating charges give rise to coherent secondary electromagnetic waves with the same wavelength as that of the incident beam. The *scattering vector* $\mathbf{q}$, which represents the *momentum transfer*, is defined as the difference between the wave vectors of the scattered ($\mathbf{k}$) and the incident ($\mathbf{k_0}$) beam. In the case of elastic scattering these vectors have the same modulus. As a consequence the modulus of the scattering vector is $q = 4\pi \sin\theta/\lambda$, λ being the X-rays wavelength and 2θ the scattering angle. The subject of this lesson is the analysis of interferences at small angles among these secondary waves.

S. Polizzi (✉)
Dipartimento di Scienze Molecolari e Nanosistemi, Università Ca' Foscari, Venezia, Italy
e-mail: polizzi@unive.it

F. Spinozzi
Dipartimento di Scienze della Vita e dell'Ambiente, Università Politecnica delle Marche, Ancona, Italy
e-mail: f.spinozzi@univpm.it

S. Mobilio et al. (eds.), *Synchrotron Radiation*,
DOI: 10.1007/978-3-642-55315-8_11, © Springer-Verlag Berlin Heidelberg 2015

Table 11.1 Objects 'seen' by SAXS at different angles and wavelengths

Wavelength	Probed dimension	
[nm]	1°	0.1°
0.15	4.4 nm	44 nm
0.23	6.8 nm	68 nm
…	…	…
400	11 μm	110 μm

11.1.1 Why Small Angles?

All scattering phenomena are ruled by a reciprocal law (through a Fourier transform): the larger the irradiated object, the smaller the scattering angle (if the wavelength of the incident radiation is constant). In other words, as we approach the angle of "zero" (the direction of the incident beam in a transmission experiment), the dimensions we are exploring grow increasingly large.

11.1.2 How Small Is "Small"?

According to Bragg's law, $\lambda = 2d \sin\theta$, the probed dimension d at a given angle 2θ and wavelength λ is of the order of $\lambda/(2\theta)$ ($\sin\theta \approx \theta$ for small angles). Let us refer to Table 11.1 and consider common copper radiation ($\lambda = 0.15$ nm, corresponding to about 8 keV). At one degree (0.017 radian) from the direction of the incident beam, the probed dimension is 4.4 nm. If we can measure the scattering at an angle as small as one tenth of a degree, then we can investigate objects the size of 44 nm. By using the less energetic chromium radiation ($\lambda = 0.23$ nm, about 5.4 keV) at the same angles, we can obtain information on objects of approximately 7 and 70 nm, respectively. Using visible radiation in the hundreds nanometer scale, we can even determine dimensions on a micrometric scale. Therefore, if we can manage to measure the scattered intensity at angles smaller than one degree, then we have a tool that will also cover the intermediate scale ranging between the atomic/molecular resolution of X-ray diffraction and the resolution of an optical microscope. In the 1920s, Wolfgang Ostwald referred to what we now call colloidal dimensions as "the world of neglected dimensions" because of the lack of experimental techniques that would cover it.

The development of small angle scattering started in the early 1930s and it continues to provide essential or, at least, complementary information, despite the large number of different experimental techniques that have since been developed. The most important technique covering the dimensional range investigated by small angle scattering is transmission electron microscopy (TEM), which can provide a direct

and detailed image of the sample. However, the resulting TEM image is so tiny[1] that it is extremely difficult to glean statistically significant average information on the sample. This is where SAXS comes in. The two techniques are complementary: TEM needs SAXS to obtain a significant sampling and make quantitative statements; and SAXS needs TEM for clues about the shape of particles for use in data analysis (see below). SAXS also has a great advantage over TEM: there are no artifacts in sample preparation. SAXS can even investigate wet samples or solutions—an asset when studying biological samples. To cite one example, it has been shown that the protein KLH (Keyhole Limpet Hemocyanin), used in bladder cancer treatment, has a more compact structure in its natural wet state than it does when observed by TEM [2].

11.1.3 What Is an "Object" for SAXS?

Since the incoming electromagnetic radiation interacts with the electrons, what SAXS "sees" as objects are the spatial variations in the electronic density inside the irradiated portion of matter. The electronic density difference is also called contrast, because the greater its value, the higher the scattering intensity. The meaning of electronic density variation is best explained by citing some examples.

The simplest case is that of a homogeneous particle (a portion of matter with a constant electronic density) dispersed in a matrix (a medium with a different electronic density). Consider a macromolecule in a solvent, or a crystal phase-separated in a glass by thermal treatment, or pores in porous material. Yet, what does constant electronic density mean? On an atomic scale, the electronic density continuously varies from higher values in the neighborhood of atomic positions to lower values in the space between atoms. We learned that dimensions explored by small angle scattering are larger than a few nanometers, which implies that *SAXS is not sensitive to electronic density fluctuation on an atomic scale* and that a portion of matter of homogeneous composition is perceived as a homogeneous particle, i.e. a particle with constant electronic density. *This means that both amorphous and crystalline particles and even voids (pores, blisters, cracks or crazes) in an otherwise homogeneous material give rise to an electronic density contrast and are detectable by small angle scattering.*

11.1.3.1 Single Particle Scattering

The scattering of a single particle in a matrix is simply its squared Fourier transform. In other words, it is related to the Fourier transform of a function that describes the particle shape and assumes, inside and outside the particle, two different yet constant electron density values. More formally, we define the *form factor* of a single

[1] Williams and Carter [1] estimated that all TEMs, since they first became available up to the publishing date of their book (1996), have only examined 0.3 mm^3 of material.

particle dispersed in a matrix with constant electron density ρ_0 as the squared Fourier transform of the difference between the electron density of the particle, $\rho_P(\mathbf{r})$, and ρ_0,

$$P(\mathbf{q}) = \left| \mathbf{r_e} \int [\rho_\mathbf{P}(\mathbf{r}) - \rho_\mathbf{0}]\, \mathbf{e}^{\mathbf{iq}\cdot\mathbf{r}}\, \mathbf{dr} \right|^\mathbf{2}, \tag{11.1}$$

r_e being the classical radius of the electron ($r_e = 2.8 \cdot 10^{-13}$ cm). The Fourier transform can be calculated analytically for a large number of homogeneous shapes. For example, the form factor of an ellipsoidal particle with the semi-axes a, b and c oriented along the directions x, y, z and interacting with an X-ray beam propagating along the z axis is

$$P_{\text{ell}}(\mathbf{q}) = (r_e \Delta\rho)^2 \left(\frac{4}{3}\pi abc\right)^2 \left(3\frac{\sin\phi - \phi\cos\phi}{\phi^3}\right)^2 \tag{11.2}$$

where $\phi = \sqrt{a^2 q_x^2 + b^2 q_y^2}$ and q_x, q_y are the components the scattering vector (see Fig. 11.1a). The first factor on the right hand side of this equation contains the contrast, that is, the electronic density difference between particle and matrix; the second factor is the volume of the ellipsoid; and the third factor is a bivariate function, a surface, whose contour lines have an ellipsoidal shape oriented perpendicularly to the particle. This last statement is a consequence of the aforementioned reciprocal law between the scattering object and its scattering pattern, or between a function and its Fourier transform. Notice that since at small angles the component of the scattering vector parallel to the beam, q_z, is negligeable when compared to the other components q_x and q_y, the corresponding semi-axis c does not enter into the equation of the scattering intensity: in other words SAXS experiments on oriented particles cannot "see" characteristic distances along the beam direction. A line section of the scattering pattern (see Fig. 11.2) shows what would be observed with a linear detector: a central peak with a series of rapidly damped peaks of much smaller intensity.

11.1.3.2 Groups of Particles

Dilute Systems

When many particles are present and their reciprocal distances are large in comparison to their average size (called a dilute system), the total scattering intensity is the simple sum of the scattering of each single particle. In the case of N identical and oriented particles in a sample volume V, the result of a SAXS measurement it the so-called *macroscopic differential scattering cross section* (often referred to as *scattering intensity*),

$$I(\mathbf{q}) = nP(\mathbf{q}), \tag{11.3}$$

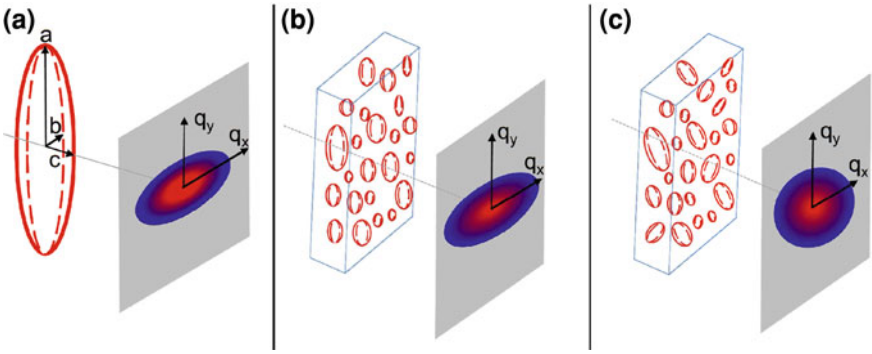


Fig. 11.1 *Panel a* scattering of a single ellipsoidal particle. *Panel b* scattering of a group of ellipsoidal particles all oriented in the same direction. *Panel c* scattering of a group of randomly oriented ellipsoidal particles of different sizes

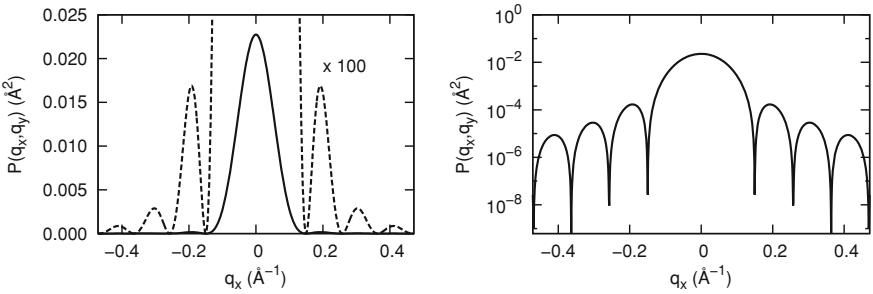


Fig. 11.2 *Left* form factor of an oriented ellipsoidal particles at $q_y = 0$ ((11.2): $r_e \Delta\rho = 3{\cdot}10^{-6}$ Å^{-2}, $a = 30$ Å, $b = c = 20$ Å). *Right* same data in logarithmic scale

where $n = N/V$ is the so-called particle number density. This equation clearly shows that SAXS profiles are proportional to the concentration of particles.

When, however, the oriented particles have the same kind of shape but different sizes (see Fig. 11.1b), in order to describe the resulting scattering intensity, we must multiply the form factor (11.1) by the distribution of sizes (a function that describes the frequency of the sizes of the various particles) and integrate over the whole size dimensional range. For example, the scattering intensity of a group of parallel ellipsoidal particles is given by:

$$I(\mathbf{q}) = n \int D(a, b)\, P_{\text{ell}}(\mathbf{q})\, dadb \tag{11.4}$$

where, in this case, the distribution is expressed as a function of the two semi-axes of the ellipsoid, the two parameters which control the dimensions of the particles. Owing to the presence of particles with different sizes, the secondary peaks found in the case of identical particles (see Fig. 11.2) are dampened, resulting in a monotonous

decreasing curve. This is because particles with different dimensions give rise to secondary peaks at different positions; and unless the size distribution is very narrow, they cancel one another out.

In general, if the orientation of the particles vary, or if their orientation changes over time, a distribution of directions should be also introduced (see Fig. 11.1c). However, in the simplest case of random orientation, the scattering intensity can be simply obtained by averaging the form factor over all the possible orientations of the scattering vector,

$$I(q) = nP(q) = \frac{1}{4\pi} \int_0^{2\pi} d\alpha \int_0^{\pi} \sin\beta \, d\beta \, P(\mathbf{q}) \tag{11.5}$$

α and β being the polar angles of $\mathbf{q}$. Obviously, in this case, the information on particle shapes and dimensions is mixed, and one needs to make assumptions about their shape or size distribution. For example the form factor of an ellipsoidal particle randomly oriented is,

$$P_{\text{ell}}(q) = (r_e \Delta\rho)^2 \left(\frac{4}{3}\pi abc\right)^2 \times \frac{2}{\pi} \int_0^{\frac{\pi}{2}} d\alpha \int_0^{\frac{\pi}{2}} \sin\beta \, d\beta \left(3\frac{\sin\phi - \phi\cos\phi}{\phi^3}\right)^2 \tag{11.6}$$

where $\phi = q\sqrt{(a^2\sin^2\alpha + b^2\cos^2\alpha)\sin^2\beta + c^2\cos^2\beta}$. Notice that, unlike the case of oriented ellipsoids (11.2), ϕ depends on all the three semi-axes. The scattering intensity only depends on the modulus of the scattering vector: the image recorded in the two-dimensional detector will show a circular symmetry around the beam centre position and all the detector counts into the pixels at the same distance from the beam center can be added. This procedure, known as *radial average*, will greatly improve the data statistics. The isotropic orientation of the particles reduces the two-dimensional SAXS intensity to a monotonous decreasing curve that cannot be associated with a unique particle size and shape.

Densely Packed Systems

When particles are close one to another (as in the case of solid state polymers), an additional contribution to the recorded intensity sums up with the single particle intensity; this is due to the combination between scattered beams coming from pairs of distinct particles. In such cases, the form factor should be multiplied by a term called *measured structure factor*,

$$I(\mathbf{q}) = nP(\mathbf{q})\, S_M(\mathbf{q}). \tag{11.7}$$

If the distances between particles have some degree of regularity, they cause a constructive interference similar to the Bragg peaks characteristic of diffraction phenomena (a maximum of intensity also known as a "long period"). The explicit expressions of $S_M(\mathbf{q})$ for monodisperse or polydisperse systems are beyond the scope of this text. However, a deep interpretation of $S_M(\mathbf{q})$ may require a model of interaction among particles that accounts for both short-range and long-range forces. There is a broad range of cases that show the presence of a measured structure factor: starting with the simple case of a single maximum (long period) superposed on a monotonous decreasing trend typical of many synthetic polymers and resulting from the regular folding of long polymeric chains to form so-called micelles; on to the case of natural macromolecules, such as tendons or cellulose, in which a highly ordered, layered structure generates a number of decreasing peaks at regular distances (i.e. with a long period and higher orders); and closing with the case of proper macromolecular crystals having such a large unit cell-edge that their diffraction peaks may only be found in the small angle range.

Concentrated solutions of particles (such as macromolecules or nanoparticles) are typical examples of systems constituted by randomly oriented particles whose positions are, on average, determined by a complex interplay of interactions. The scattering intensity is usually written by taking the isotropic average of (11.7). In the case of a mixture of different kind of particles, it can be shown that the isotropic measured structure factor, $S_M(q)$, is a combination of the structure factors $S_{ij}(q)$ between the particles of kind i and j, which are defined as the Fourier transform of the corresponding radial correlation function,

$$S_{ij}(q) = \delta_{ij} + 4\pi (n_i n_j)^{1/2} \int_0^\infty r^2 [g_{ij}(r) - 1]\, dr \tag{11.8}$$

where r describes radial distances and δ_{ij} is the Kronecker delta function. The reader can refer to the Further Reading section for a detailed description of definitions and properties of $g_{ij}(r)$.

11.2 Data Analysis

To sum up, we have seen that SAXS data contain information on the shapes and sizes of particles, as well as the correlations between them. In general, the information is muddled, making it impossible to separate the three different contributions without the aid of external information, such as a fixed particular shape, a certain distribution, the absence of inter-particle scattering or other detailed assumptions. Data handling procedures of small angle scattering can be roughly divided into two classes: the first includes methods that attempt to retrieve information on particles by processing

the experimental data by means of appropriate mathematical transforms that do not assume specific particle shapes; the second, methods that, on the contrary, start from some assumptions regarding the form factor of the particles and the structure factor of the system, calculate the scattering intensity and try to fit it to the experimental data by optimising several parameters. A large number of mathematical methods have been developed for both strategies, but a detailed description of them is beyond the scope of this lesson. Bear in mind, however, that in many situations, partial information can be obtained without necessarily resorting to complex mathematical transforms by making detailed assumptions and limiting the analysis to a particular angular zone, or by using suitable integral quantities. The most common of these "simplified" approaches are briefly outlined below.

11.2.1 Guinier's Approximation

For a dilute system of randomly oriented particles with similar sizes, Guinier has shown that the smallest angles within the scattering curve can be approximated to a Gaussian function:

$$I(q) = I(0)\, e^{-q^2 R_g^2/3} \tag{11.9}$$

where R_g is the so-called gyration radius and $I(0)$ is scattering intensity extrapolated at zero angle. The gyration radius is defined as analogous to the radius of inertia in mechanics with the difference that here the electrons of the former substitute the mass elements of the latter. Though R_g cannot completely describe the geometry of a particle, its value is precisely known for simple geometrical shapes. For example, the radius of gyration of an ellipsoid particle is a function of the three semi-axis lengths according to $R_g^2 = (a^2 + b^2 + c^2)/5$ (so that for spheres of radius R, it will be simply $R_g = \sqrt{3/5}R$). Thus, (11.9) will readily yield a reckoning of the average particle dimension for groups of particles with a similar shape and size.

The scattering intensity at zero angle is related to concentration, contrast and average particle volume V_P, according to

$$I(0) = nV_P^2(r_e \Delta\rho)^2. \tag{11.10}$$

Such parameters can be derived from $I(0)$ if data have been expressed in so-called absolute units (usually cm^{-1}). More in detail, detector counts C_{ij} in the ij pixel associated to the $\mathbf{q}_{ij}$ scattering vector are transformed in absolute scale by

$$I(\mathbf{q}_{ij}) = \frac{C_{ij}}{\Phi_0 \varepsilon_{ij} A_{ij} t D T \, \Delta\Omega_{ij}} \tag{11.11}$$

where: Φ_0 is the incident flux of photons (photons/s/cm^2), ε_{ij} the pixel efficiency factor, A_{ij} the pixel area (cm^2), t the measurement time (s), D the sample thickness (cm), T the transmission factor of the sample and $\Delta\Omega_{ij}$ (sr) the solid angle seen by the ij pixel in the direction 2θ.

The angular region where the Guinier's approximation applies depends on the particle size through the usual law of reciprocity and is typically determined by the inequality $qR_g \leq 1.3 \div 1.8$ [3]. This region can be easily visualized by checking the linearity of the logarithm of $I(q)$ as a function of q^2, a graph called "Guinier's plot". From the intercept and the slope of this plot the values of $I(0)$ and R_g can be obtained, respectively. Two populations with different particle sizes may give rise to two distinct Guinier's regions. Yet, if the distribution of particle sizes is broad, their different contributions smear out the curve and dimensions are then difficult to determine.

11.2.2 Porod's Law

On the other side of the angular range (high q region), we find that, in most cases, the data follow an asymptotic behaviour with a fourth power-law decay. In this case, the product $q^4 I(q)$ tends to settle on a constant value. Porod showed that this is to be expected for a so-called two-phase systems and demonstrated the following equation:

$$I(q) = (r_e \Delta\rho)^2 \frac{2\pi S}{q^4} \tag{11.12}$$

where S is the total surface of the interface between the two phases divided by the scattering volume. Moreover, possible oscillations shown by the curve when reaching the asymptotic value provide information on the angularity of the interface (be it a smooth or sharp-edged surface) [4, 5]. Situations that deviate from Porod's law have been explained by the presence of a so-called smooth interface, in other words, a gradual change from ρ_P to ρ_0, or by fractality (see below). Porod's approach is particularly important because we need not assume a dilute system, implying that it is appropriate to densely packed particles as well. In fact, scattering due to inter-particles distances (structure factor) is depressed at these angles. The angular range attained by the asymptotic value depends on the particular sample studied and, under certain circumstances, even two distinct Porod's regimes for two distinct particle populations may be identified.

11.2.3 The Scattering Power

Porod also demonstrated that the integral of the scattering intensity (expressed in absolute-scale) over the entire **q**-space depends on the mean square fluctuation of the electron density $\rho(\mathbf{r})$ of the entire system around is average value:

$$\int I(\mathbf{q})\, d\mathbf{q} = (2\pi)^3 r_e^2 < [\rho(\mathbf{r}) - <\rho(\mathbf{r})>]^{\mathbf{2}} > . \tag{11.13}$$

This equation is valid for any system, oriented or disordered, diluted or densely packed and also when it is not possible to recognize a true particle, for example in fractal structures. For a two-phase and isotropic system, (11.13) transforms to the so-called "scattering power" or "Porod's invariant",

$$Q = \int_0^\infty q^2\, I(q)\, dq = 2\pi^2\, \eta(1-\eta)(r_e \Delta\rho)^2 \tag{11.14}$$

where η and $(1-\eta)$ are the volume fractions of the phase with electron density ρ_P and ρ_0, respectively. The quantity may be calculated if the experimental data can be extrapolated to zero and infinity by applying Guinier's approximation and Porod's law, respectively. Thus, if the volumetric fraction is known, the difference in electron densities can be obtained, and vice versa.

For a dilute system of particles $(1-\eta \approx 1)$, the Porod's invariant transforms to

$$Q = 2\pi^2 n V_P (r_e \Delta\rho)^2. \tag{11.15}$$

By combining this equation with (11.10), the average particle volume V_P can be derived even if the contrast is unknown, $V_P = 2\pi^2 I(0)/Q$. However it should be borne in mind that if the particle surface is not sharp-edged, such as for biological macromolecules or for disordered chains, the behaviour of the scattering intensity at high q does not follow the Porod's law and the values of V_P calculated from the Porod's invariant can strongly deviate from the correct value [3, 6]. For porous systems, (11.15) can be combined with (11.12) (Porod law), to obtain the specific surface area $\sigma_P = S/(nV_P)$, a key parameter which is usually measured by adsorption methods, like the Brunauer, Emmett and Teller (BET) method. A comparison with the latter method, however, needs to take into account that, differently from BET, SAXS measures both open and closed pores.

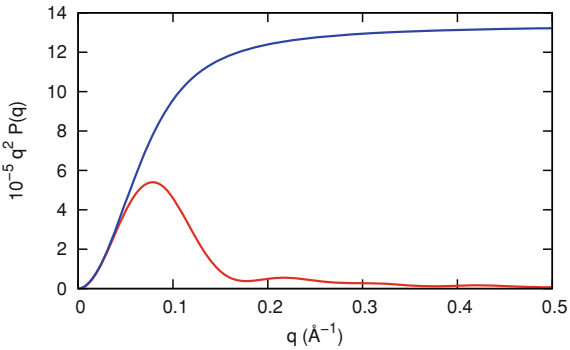


Fig. 11.3 Kratky plots of the form factors of randomly oriented compact and disordered shapes. *Red curve* ellipsoid (11.6): $r_e\Delta\rho = 3 \cdot 10^{-6}$ Å^{-2}, $a = 30$ Å, $b = c = 20$ Å; *blue curve* Gaussian chain with $R_g = 18.4$ Å and the same contrast and volume of the ellipsoid

11.2.4 Debye's Approximation and Kratky Plot

Disordered polymeric chains distributed over many conformations, such as unfolded proteins, can be studied with the SAXS technique. The simplest statistical description of an infinitely thin chain formed by identical monomers separated by a fixed distance b is the "random-walk" or "Gaussian-chain" model: the position of a monomer can be in any point of the space provided the distance form the previous monomer of the chain is b. The form factor of a randomly oriented Gaussian-chain is expressed by the Debye's law,

$$P_{\mathrm{GC}}(q) = (r_e\Delta\rho)^2 V_P^2 \frac{2}{\phi^2}(e^{-\phi} + \phi - 1) \tag{11.16}$$

where $\phi = q^2R_g^2$. The asymptotic behaviour of this equation is q^{-2}. Hence, by reporting experimental scattering intensity in the form of Kratky plot, $q^2I(q)$ versus q, the graph shows a constant value at high q, as shown in Fig. 11.3, blue curve. On the contrary, globular shapes show a Kratky plot with a typical large peak. For the law of reciprocity, the larger the radius of gyration the smaller the value of q where the peak is centered (Fig. 11.3, red curve). It is evident that a simple representation of the scattering intensity in the form of a Kratky's plot can provide at first glance basic information on the compactness of the particles.

11.2.5 Distance Distribution Function

An other relevant information which can be drawn from the data for a two-phase system of randomly oriented particles is the distance distribution function $p(r)$, connected to the scattering intensity by means of an isotropic Fourier transform

$$p(r) = \frac{2r}{\pi} \int_0^\infty dq\, I(q)\, q\, \sin(qr), \tag{11.17}$$

and the scattering intensity is the inverse Fourier transform of $p(r)$,

$$I(q) = \int_0^{D_{\max}} p(r) \frac{\sin(qr)}{qr} dr. \tag{11.18}$$

$p(r)$ represents the probability distribution to find within the particle volume two points at distance r. It is a bell-shaped function, which reaches zero at the maximum particle diameter $D_{\max}$. The "direct" calculation of $p(r)$ via (11.17) requires to extrapolate data at low and high q with Guinier and Porod approximation, respectively. This approach can lead to wrong results, in particular when the experimental q-range is far from the Porod regime q^{-4} or when particles have smooth surfaces. In these circumstances it is preferable to use "indirect" methods, such as GIFT [7] or GNOM [8], where the $p(r)$ is written as a linear combination of elementary functions, such as cubic B splines. The unknown parameters of the linear combination are optimized by fitting the $I(q)$ calculated with (11.18) to the experimental scattering intensity. Regularization procedures can also be applied in order to control the balance between the goodness of fit and the smoothness of the $p(r)$.

11.2.6 Fractality

The fractal dimension of a system is readily assessed through small angle scattering measurement. Scale invariance, the main characteristic of fractal systems, is mirrored in the small angle scattering intensity as a decay in the power-law. In turn, the value of the power-law is directly related to the fractal dimension, and a value of -4 (Porod's law, (11.12)) is expected for a non-fractal system. Therefore, we need only plot the data in bi-logarithmic scales and check for linearity in the curve. The angular region where linearity lies indicates the dimensional range in which the system is fractal; the slope provides its fractal dimension. Slope changes indicate structural level changes. Figure 11.4 is an example of small angle data in a very wide angular range. Measurements taken with different experimental apparatuses have been joined in order to investigate the structure of silica/siloxane, a composite ceramic/polymeric material with a very large range of dimensional scales. The schematic drawings below the curve describe the different fractal objects concerned and their correspondence to angular regions of different slopes. Small angle light scattering (SALS) indicates the presence of globular clusters on a micrometer scale (the change in slope occurs at q with a corresponding value of 0.9 μm). At wider angles, SAXS reveals the fractal nature of the structure down to approximately 15 nm. The linear region with a

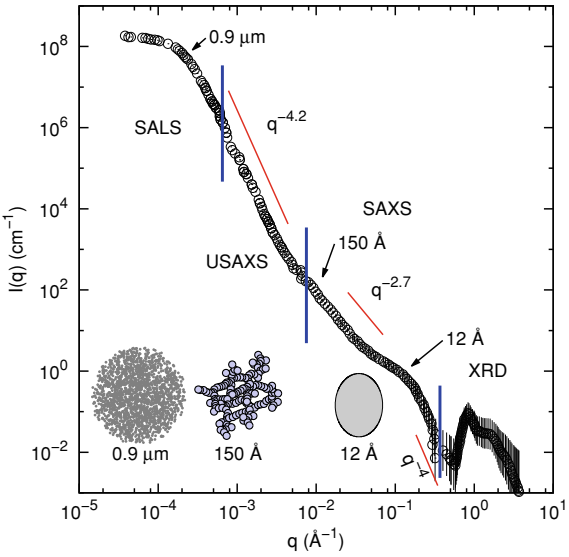


Fig. 11.4 Scattering data of a composite material (silica/siloxane), which shows different fractal regions (adapted from [9], courtesy of G. Beaucage)

slope of −4.2 describes the internal organization of the globular clusters. At sizes of approximately 1.2 nm, the structure is once again fractal, but with a different fractal dimension (slope −2.7), which reveals the basic units of the fractal structure. The last linear part of the data, before the peaks of X-ray diffraction (XRD) come into play, has a −4 slope characteristic of Porod's law.

11.3 Experimental

SAXS is usually measured in transmission geometry: a monochromatic X-ray beam strikes the surface of the sample perpendicularly and the scattering is collected by a detector placed behind the sample. In this experimental configuration, a signal of a significantly lower intensity than that of the transmitted beam must be measured as close as possible to it. The higher the resolution[2] requested, the smaller the incident beam must be. Unfortunately, resolution increases linearly with decreasing the beam size, whereas the corresponding decline of intensity is much more rapid. Thus, special apparatuses must be devised for small angle scattering experiments, in order to reduce the transmitted beam size without compromising its intensity. However the sensitivity and resolution in a SAXS experiment are intrinsically limited by the quantity of photons emitted by the X-ray source.

[2] In the context of SAXS the term 'resolution' is used as a synonym for 'smallest measurable angle' $2\theta_{min}$, which in turn corresponds to the *largest* measurable object D_{max}. Either $2\theta_{min}$ or D_{max} are used to indicate the attainable resolution. Note that the usage made by microscopists or spectroscopists is different. There, resolution stays for the *smallest* detail that can be appreciated.

In 1969, Guinier, one of the inventors of small angle scattering, expressed his concerns by articulating his thought as follows [10]

> From the experimental point of view […], small angle scattering appears to have reached a steady value. The apparatus for small angle scattering will certainly be continuously improved but *no major change can be foreseen, unless the power of X-ray sources is increased by a factor 10 or 100*, which is rather unlikely.

Then synchrotron arrived, and Guinier's pessimistic expectations were proven unwarranted. At the synchrotron source at ESFR (Grenoble, France), X-ray beams with a brilliance 10^{12} higher than those of conventional laboratories were produced! With such intensities devices as monochromators that improve the quality of the incident beam or converging mirrors or microcapillaries that change beam characteristics could now be used despite their absorbing part of the radiation. Sufficient transmitted intensity could be obtained by using soft X-rays. An enormous increase in the distance of the sample-detector was now feasible (12 m at the USAXS line in Hamburg, 56 m from the source!) and two-dimensional detectors could be routinely used.

The dramatic increase in the beam intensity has cleared the way for a series of measurements that were formerly impossible to obtain:

1. *Time-resolved measurements*: Newly developed detectors with greater efficiency also make it possible to collect statistically significant data in seconds and, under certain circumstances, even in milliseconds [11]. Thus the kinetics of such processes as heating, stretching, oxidation, and reduction may be followed in situ.
2. *Space-resolved measurements*: Different devices have been developed to obtain beams with sections in the micron, or even sub-micron range, and thus map samples that are not spatially homogeneous by using small angle scattering.
3. *Reflection measurements*: In order to study the surface of thin layers, measurements may be taken at a grazing incidence that is smaller than the critical angle for total reflection (GISAXS). In this situation, the information stems solely from the surface layer of the sample. With a two-dimensional detector, information on lateral correlation, as well as on the depth profile, can be gathered.
4. *Anomalous scattering* (ASAXS) (also known as resonant or contrast variation): Synchrotron sources have a unique feature that allows the researcher to choose, at will and with continuity, the wavelength to be used in the measurement. ASAXS exploits the very small variation in one part of the atomic scattering factor when the energy of the X-ray is close to the absorption edge of that particular atomic element. By subtracting the scattering obtained at two different energies near the edge, the scattering resulting from that particular element may be isolated, making SAXS an atom-selective technique [12].

11.4 Case Studies

The following describes some exemplary experimental cases that exploit synchrotron light.[3] These measurements could not have been carried out with conventional laboratory equipment.

Polarising Glass

These are types of aluminoborosilicate glass in which well dispersed spherical Ag(Br,Cl) crystallites are allowed to grow inside the glass matrix by means of a thermal treatment. They are then heated above their softening temperature, and drawn. In this way, the softened spherical crystallites lose their shape and transform into needle-shaped crystalline particles that are perfectly parallel to the surface and oriented in the direction of their stretching. A reduction in hydrogen transforms the silver halide into silver and turns the glass into a highly effective polarising material. This material represents a perfect example of the situation previously described under Sect. 11.1.3.2, paragraph "Dilute systems". In Fig. 11.5, a TEM image and a SAXS measurement of such a glass are shown [13, 14]. The two-dimensional analytical Fourier transform of a distribution of ellipsoidal particles can be fitted to the experimental data in order to determine the particle size distribution (the minor and major axes of the ellipsoidal particles). With the two-dimensional fit, data may be extrapolated into the blind zone of the beam-stop in order to obtain information on much larger particles than the resolution of the instrument would otherwise allow. Rough average values for the major and minor axes could be more simply obtained by applying Guinier's approximation to sections of the data along the major and minor axes of the pattern. Yet, the two-dimensional pattern allows us to glean not only the complete distribution, but also information on the drawing process. Its description may be introduced into a mathematical model, where the original distribution of spheres is elongated according to a given function based on fluid-dynamical considerations (see Fig. 11.6). The crystallite size distribution before stretching as well as the value of surface energy of the silver halide phase (from one of the parameters of the elongation function) can be obtained by using this model. By comparing the glasses before and after their chemical reduction, it was found that the loss of Cl and Br atoms during chemical reduction causes a re-arrangement of silver atoms inside the glass cavities containing the elongated particles. The glassy matrix is, in fact, rigid at the temperature at which the chemical reduction occurs, while silver halide approaches its melting point. Silver particles are rearranged inside glass cavities into two or three shorter sub-particles separated by empty regions. Voids constitute approximately two thirds of the total volume of the cavities. However, the polarising optical properties correlate well with dimensions of cavities. This is because the dimensions of voids are much smaller than the wavelength of visible and near-infrared light and represent just a small perturbation to the global effect caused by silver.

[3] For a complete list of SAXS beamlines see under "SAXS" in Wikipedia.

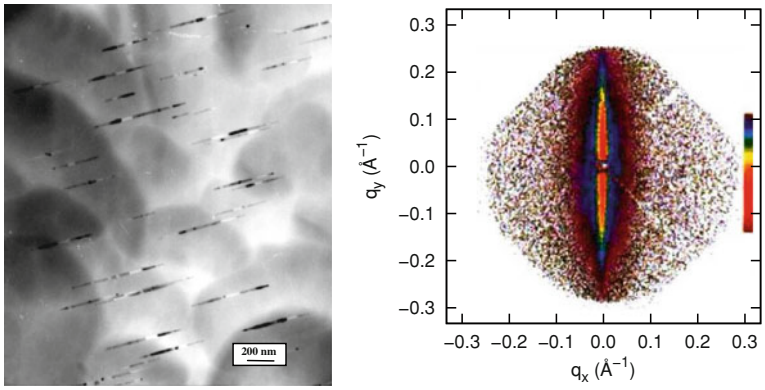


Fig. 11.5 Electron microscopy (*left*) and SAXS two-dimensional pattern (*right*) of a polarising glass containing *needle-like* silver crystals. The *comet-like figure* on the SAXS data is the beam-stop with its support

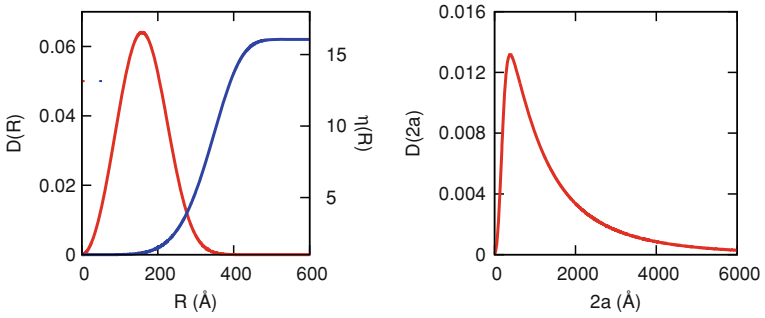


Fig. 11.6 *Left* The distribution of radii $D(R)$ of the crystalline particles before the drawing and the elongation function $\eta(R)$. *Right* The resulting length distribution $D(2a)$ of the elongated particles

Drawn Polymers

During solidification of the styrene-butadiene-styrene (SBS) block co-polymer, a synthetic rubber mainly used for shoe soles, the long, folded polymer chains organize into semi-crystalline domains of one component regularly dispersed in the other amorphous one. The crystalline phase is rigid, whereas the amorphous one is flexible, thus imparting to this material its interesting properties. Which of the two components will crystallize and the shape that the rigid domains assume mainly depend on the composition. SAXS measurements of these samples [15, 16] (Fig. 11.7a) show isotropic patterns with a rather intense ring and two less intense peaks at distances with precise ratios between them: $1:\sqrt{7}$ and $1:\sqrt{3}$. These values are indication of a locally hexagonal structure, while peak positions indicate a mean distance between particles of about 45 nm. This is the case in the Sect. 11.1.3.2, paragraph "Densely packed systems", that is, randomly oriented particles of unknown shape at close regular distances. The presence of peaks at regular distances and with decreasing in-

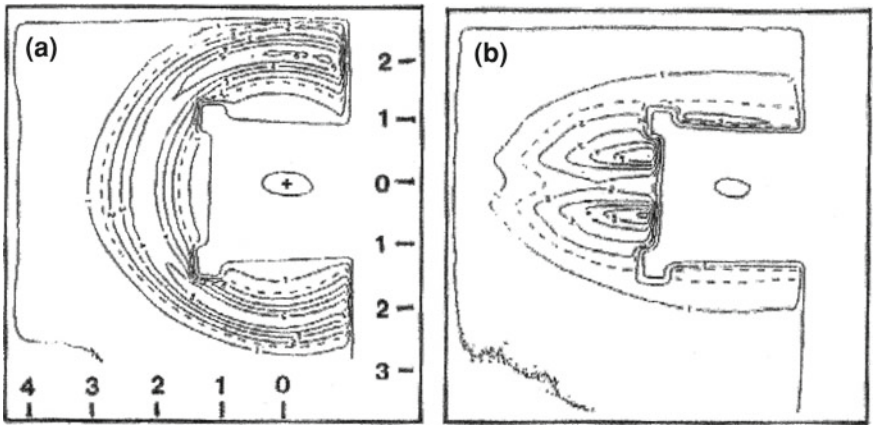


Fig. 11.7 SAXS patterns of an SBS polymer in a time-resolved drawing experiment: before (**a**) and during stretching (**b**). A *rectangular* beam-stop is visible in the *center*

tensities reveal the existence of a structure factor $S_M(\mathbf{q})$, as described in (11.7). Yet, since the material is capable of being deformed, we may obtain further information by looking at changes in the small angle scattering when the material is stretched. In Fig. 11.7b, the pattern drastically changes: an ellipsoidal background is modulated by two "linear" peaks perpendicular to the stretching direction. The distance between these two peaks decreases when the draw ratio increases. Here, the cylindrical domains orient in the direction of the stretching, and the distance between them steadily increases. This situation is similar to that of the polarising glasses discussed above, with the additional factor of a maximum due to the regularity in the distance among the densely packed particles. The shape and dimension of the styrene domains can now be determined from the evaluation of the ellipsoidal background. This information was missed in the unstretched sample because of the average over all randomly oriented domains.

Fibril Crazes

The plastic deformation process of many polymers is accompanied by the formation of fibril crazes, i.e. micron-scale cracks that are bridged by filaments of polymer. Crazes are oriented 90° to the applied stress, while fibrils are parallel to it. Fibrils can absorb up to 90 % of the deformation energy, even though, in some cases, they can develop into pure cracks, a precursor to failure. These structures are often oblate ellipsoids, 50–100 μm long and 0.1–2 μm large, and are grooved by hundreds of different parallel fibrils, 20–30 nm apart and with a diameter of 5–30 nm. The formation of fibrils gives rise to a cross-shaped SAXS pattern that is actually a superposition of the scattering due to the shape of the structure (a void) on the one resulting from the perpendicular fibrils (see Fig. 11.8). Quantitative analysis of these scattering patterns can provide precise information on the dimension of crazes and on their inner structure. Using a synchrotron source, the process of plastic deformation can be followed

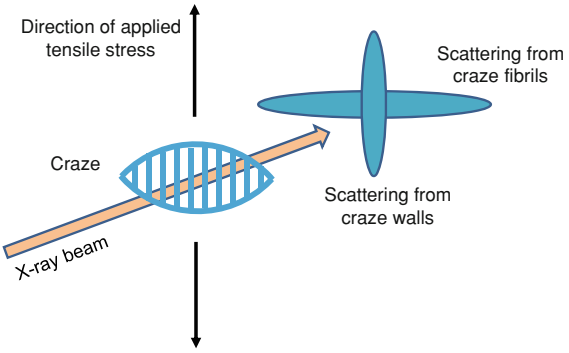


Fig. 11.8 Schematic sketch of the structure of crazes and their SAXS pattern (adapted from [17], courtesy of M.A. Singh)

in situ with a time-resolved measurement, and the formation and growth mechanisms studied.

Metal Supported Catalysts

Most heterogeneous catalysts consist of metal particles well dispersed in a porous matrix. Because these metals are costly, their use must be optimized. The process of catalysis occurs on the surface of metal particles, therefore optimization is obtained by maximizing the surface/volume ratio. Since this ratio increases as the size of the particle decreases, chemical engineers strive to obtain well-dispersed (i.e. not agglomerated) nanoparticles. In principle, SAXS is an ideal technique for determining particle size at this scale; however, pores in the matrix usually cause a very high scattering intensity that hides or interferes with the scattering intensity of the metal phase. Anomalous small angle scattering inherently allows one to remove this unwanted scattering. By using synchrotron radiation, the incident beam energy can be tuned close to the metal absorption edge where the scattering of the metal has a small, but detectable, dependence on energy (see Fig. 11.9) while the scattering of the matrix is constant [18, 19]. By subtracting the scattering of two measurements at different energies, we can isolate the scattering of the metal.

This technique is even more powerful in the case of bi-metallic catalysts, because the two metals can be selectively investigated by tuning the energy to the two absorption edges. In this way, we can determine if the two metals form an alloy, different particles, or two-phase particles (where the core of one metal covers the other with a shell). In the case of Fig. 11.9, ASAXS revealed that the greater part of the metal forms 1–2 nm particles. Diffraction measurements could only detect a second population of larger particles (14 nm) that are significantly less active in the catalytic process.

Spatial Resolution: Micro and Nanofocused Beamlines

The availability of micrometric beams with sufficient intensity at synchrotron laboratories has made the spatial resolution of inhomogeneous materials, such as bones, cartilage, or wood, possible. At the nanometer scale, bone and mineralized cartilage consist of small mineral particles embedded in an organic matrix (collagen). For bone, these particles are known to be needle- or plate-shaped with an average

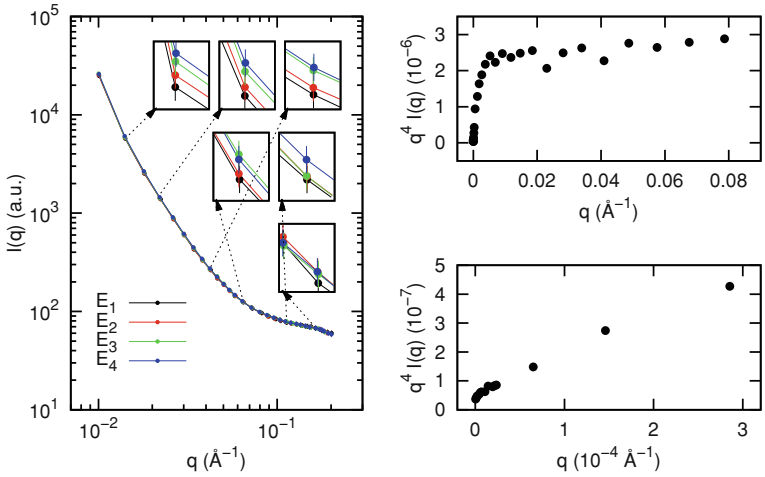


Fig. 11.9 *Left* The scattering of a gold catalyst, dispersed in porous carbon. *Note* in the *insets* the minimal difference in the SAXS signals at different energies. *Right* A Porod's plot of the SAXS signal. Two Porod's regions are found, which indicate the presence of two populations of particles (the innermost Porod's region does not tend towards a constant because of an overlap in the scattering of the two populations of particles)

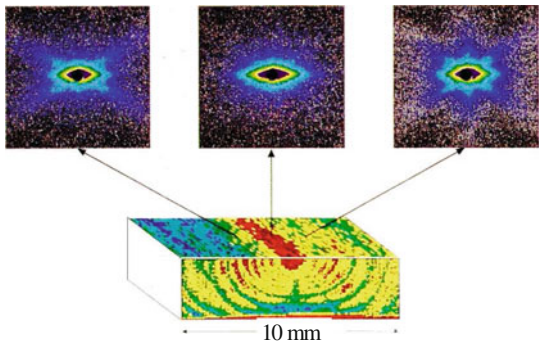


Fig. 11.10 Example of spatially resolved SAXS of a human vertebra specimen [21] (courtesy of P. Fratzl)

thickness of about 3 nm and a length of a few hundred nanometers [20]. One of the first researches using a microbeam [21] showed that it is possible to use SAXS to investigate the different structures of contiguous zones inside a human vertebra and distinguish the different orientations assumed by the mineral particles in different positions of the bone (Fig. 11.10). By using the integrated intensity of each individual SAXS pattern, a sort of orientation-sensitive map of the sample can be composed that is complementary to radiography. The spatial resolution achieved in that experiment at ELETTRA (Trieste, Italy) was 200 μm. Nowadays, dedicated microfocused beamlines can obtain resolution in the microns or even sub-microns range and the new Nanofocused extension of the ID13 beamline at ESRF (Grenoble, France) promits to have a beam size of 50 nm or less.

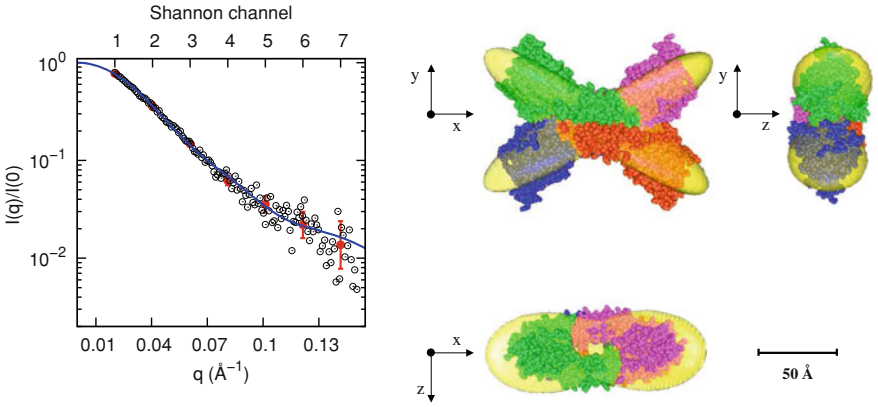


Fig. 11.11 Shape-reconstruction based on MPOLE method [25]. *Left* the *blue solid lines* is the best fit of the experimental SAXS *curve* (*black open points*) related to seven Shannon channels (*red close points*). *Right* reconstructed shape (*yellow envelope*) of the CPSO tetramer superimposed to the computer designed model (*full atoms representation*)

Shape Determination of Solution Proteins: The Proteomics Era

'Proteomics' is a new subject in molecular biology aimed to study structure and function of all the proteins coded in the genome of a cell. Most of those proteins are unknown and only a fraction of them can be crystallized and then investigated by X-ray crystallography. SAXS is one of the most suitable technique to determine the structure of non-crystallizable proteins. In this framework, the actual policy of synchrotrons is to dedicate to biology SAXS beamlines specifically conceived to get an high-throughput of protein structures [22, 23]. Such Bio-SAXS beamlines (such as BM29 at ESRF [24]) equipped with automated data collection aimed to minimize the volume of the biological samples to a few tens of microliters.

The main objective that proteomics demands to synchrotron SAXS is to get the shape of compact proteins in solution. A lot of effort has been put to develop methods and related software able to reconstruct the 3D shape of monodisperse proteins from their 1D SAXS profiles. The first approach was based on the description of the protein envelope as a linear combination of spherical harmonics [26, 27], a method later improved by the implementation of group theory and maximum entropy concepts to deal with protein symmetry [25]. In Fig. 11.11 the shape of the carboxypeptidase enzyme from *Sulfolobus solfataricus* (CPSO) obtained by a SAXS curve recorded at the ELETTRA synchrotron (Trieste, Italy) is shown [28]. Results have confirmed the tetrameric structure provided by a structural alignment of a template. In an other class of shape reconstruction methods (DAMMIN [29], DALAI_GA [30]) the protein structure is obtained by finding the best combination of densely packed identical spheres whose unique diameter is adjusted to mach the experimental resolution. The compactness of the protein is taken into account by introducing penalty terms in the search algorithm. An example of shape reconstruction obtained with DAMMIN is shown in Fig. 11.12 [31].

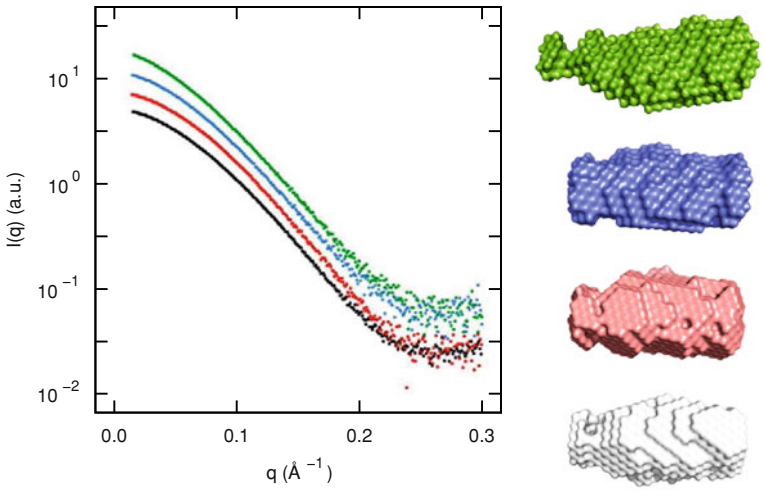


Fig. 11.12 Shape-reconstruction based on DAMMIN method [29]. *Left* experimental SAXS *curves* of four CNPase (2′,3′-cyclic nucleotide 3′-phosphodiesterase) catalytic domain constructs. *Right* best-fit shape reconstructions *colour* coded according to the *left panel* [31] (courtesy of P. Kursula)

The most recent methods, such as GASBOR [32], are based on the best arrangement of connected spheres representing the amino acids sequence of the protein and include constraints for avoiding steric clashes and for promoting compactness.

Time-Resolved Study of Amyloid Fibrils

'Amyloids' are stable, ordered, filamentous aggregates of proteins or peptides that arise from an anomalous folding of the amino acid chain. A broad range of human neuro-degenerative diseases (such as Parkinson's or Alzheimer's diseases) are caused by the deposition of amyloid fibrils. Within the broad field of amyloid research, a key issue is the description of the fibrillogenesis pathway at a molecular level, in particular the study of the early aggregation events. Amyloid research has also shown that any protein, in particular circumstances, can undergo a conformational change that lead to amyloid formation [33]. Time-resolved SAXS is of pivotal importance to gain information on the intermediate structures that form at the beginning of the amyloid fibrillar process, in the millisecond time range. In a recent study, a mutant of apo-myogobin, which forms amyloid fibrils when pH is varied from 4 to 7, has been investigated with time-resolved SAXS [11]. SAXS curves for different times after the pH-jump are shown in Fig. 11.13. The whole set of curves has been analysed by using a unique model that combines four form factors: one unfolded protein monomer ('worm-like' model, code as wlk in Fig. 11.13), two cylinders representing the prefibrillar oligomeric species (cyl,1 and cyl,2) and a very large assembly described by the Porod's law (por). Results indicates that in less than 20 ms after the pH jump the first fibrillar species appear.

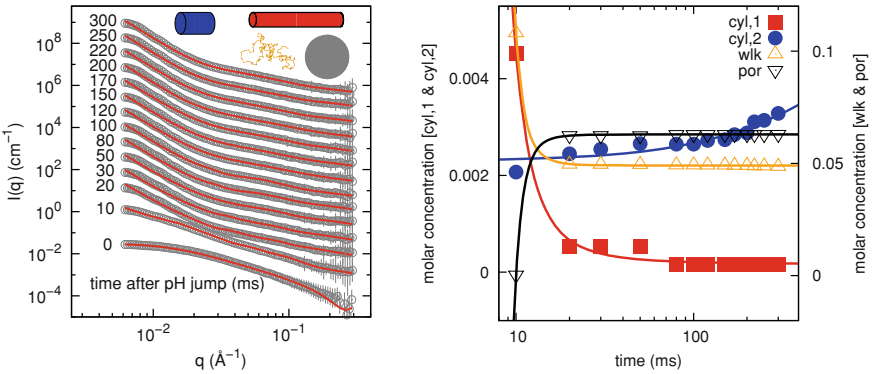


Fig. 11.13 *Left* SAXS *curves* of the apomyoglobin W7FW14F mutant (10 gL^{-1} concentration) measured at different times (reported beside each *curve*) after pH jumps from 4 to 7. *Solid lines* represent the best fits to the data. *Right* Molar concentrations of the four species obtained by fitting SAXS data and expressed as a function of the time after the pH-jump

References

1. D.B. Williams, C.B. Carter, *Transmission Electron Microscopy* (Plenum Press, New York, 1996) NULL
2. H. Hartmann, A. Bongers, H. Decker, T. Nawroth, G. Goerigk, in Hasylab Annual Report 1998 (1998)
3. L.A. Feigin, D.I. Svergun, *Structure analysis by small-angle x-ray, neutron scattering* (Plenum Press, New York, 1987)
4. S. Ciccariello, G. Cocco, A. Benedetti, S. Enzo, Phys. Rev. B **23**, 6474 (1981)
5. S. Ciccariello, A. Benedetti, Phys. Rev. B **26**, 6384 (1982)
6. P.V. Konarev, V.V. Volkov, A.V. Sokolova, M.H.J. Koch, D.I. Svergun, J. Appl. Cryst. **36**, 1277 (2003)
7. A. Bergmann, G. Fritz, O. Glatter, J. Appl. Cryst. **33**, 1212 (2000)
8. D.I. Svergun, J. Appl. Cryst. **25**, 495 (1992)
9. G. Beaucage, T.A. Ulibarri, E.P. Black, D.W. Schaefer, in *Organic Hybrid Materials*, vol. 585, ed. by J.E. Mark, C. Lee, P. Bianconi (ACS Symposium Series, Washington DC, 1995), Chap. 9, pp. 97–111
10. A. Guinier, Phys. Today **22**, 25 (1969)
11. M.G. Ortore, F. Spinozzi, S. Vilasi, I. Sirangelo, G. Irace, A. Shukla, T. Narayanan, R. Sinibaldi, P. Mariani, Phys. Rev. E. **84**, 061904 (2011)
12. S. Polizzi, P. Riello, G. Goerigk, A. Benedetti, J. Synchrotron Radiat. **9**, 65 (2002)
13. S. Polizzi, P. Riello, G. Fagherazzi, M. Bark, N.F. Borrelli, J. Appl. Cryst. **30**, 487 (1997)
14. S. Polizzi, P. Riello, G. Fagherazzi, N.F. Borrelli, J. Non-Cryst, Solids **232–234**, 147 (1998)
15. S. Polizzi, N. Stribeck, H.G. Zachmann, R. Bordeianu, Colloid Polym. Sci. **267**, 281 (1989)
16. S. Polizzi, P. Bösecke, N. Stribeck, H. Zachmann, R. Zietz, R. Bordeianu, Polymer **31**, 638 (1990)
17. G.J. Salomons, M.A. Singh, T. Bardouille, W.A. Foran, M.S. Capel, J. Appl. Cryst. **32**, 71 (1999)
18. A. Benedetti, S. Polizzi, P. Riello, F. Pinna, G. Goerigk, J. Catal. **171**, 345 (1997)
19. A. Benedetti, L. Bertoldo, P. Canton, G. Goerigk, F. Pinna, P. Riello, S. Polizzi, Catal. Today **48**, 485 (1999)
20. P. Fratzl, M. Groschner, G. Vogl, H.J. Plenk, J. Eschberger, N. Fratzl-Zelman, K. Koller, K. Klaushofer, J. Bone Miner. Res. **7**, 329 (1992)

21. P. Fratzl, H. Jakob, S. Rinnerthaler, P. Roschger, K. Klaushofer, J. Appl. Cryst. **30**, 765 (1997)
22. G.L. Hura, A.L. Menon, M. Hammel, R.P. Rambo, F.L. Poole, S.E. Tsutakawa, F.E. Jenney, S. Classen, K.A. Frankel, R.C. Hopkins, S.J. Yang, J.W. Scott, B.D. Dillard, M.W. Adams, J.A. Tainer, Nature Methods **6**, 606 (2009)
23. T.D. Grant, J.R. Luft, J.R. Wolfley, H. Tsuruta, A. Martel, G.T. Montelione, E.H. Snell, Biopolymers **95**, 517 (2011)
24. P. Pernot, A. Round, M. Brennich, Bm29: Biosaxs beamline (2013), http://www.esrf.eu/UsersAndScience/Experiments/MX/About_our_beamlines/BM29
25. F. Spinozzi, F. Carsughi, P. Mariani, J. Chem. Phys. **109**, 10148 (1998)
26. D. Svergun, H. Stuhrmann, Acta Crystallogr. **A47**, 736 (1998)
27. D.I. Svergun, V.V. Volkov, M.B. Kozin, H.B. Stuhrmann, C. Barberato, M.H.J. Koch, J. Appl. Cryst. **30**, 798 (1997)
28. E. Occhipinti, P. Martelli, F. Spinozzi, F. Corsi, C. Formantici, L. Molteni, H. Amenitsch, P. Mariani, P. Tortora, R. Casadio, Biophys. J. **85**, 1165 (2003)
29. D.I. Svergun, Biophys. J. **76**, 2879 (1999)
30. P. Chacón, J.F. Díaz, F. Morán, J.M. Andreu, J. Mol. Biol. **299**, 1289 (1999)
31. M. Myllykoski, A. Raasakka, H. Han, P. Kursula, PLOS one **7**, e31852 (2012)
32. D.I. Svergun, M.V. Petoukhov, M.H.J. Koch, Biophys. J. **80**, 2946 (2001)
33. J. Schnabel, Nature **464**, 828 (2010)

Further Reading

34. O. Glatter, O. Kratky, *Small Angle Scattering X-ray* (Academic Press, London, 1982)
35. A. Guinier, G. Fournet, *Small Angle Scattering of X-ray* (Wiley, New York, 1955)
36. A. Guinier, *X-ray Diffraction* (W.H. Freeman and Co., San Francisco, 1963)
37. R. Hoseman, S.N. Bagchi, *Direct Analysis of Diffraction Methods* (North-Holland, Amsterdam, 1962)
38. C.D. Putnam, M. Hammel, G.L. Hura, J.A. Tainer, Q. Rev. Biophys. **40**, 191 (2007)
39. B.R. Pauw, arXiv:1306.0637v1 submitted (2013)

Chapter 12
Resonant and Magnetic X-Ray Diffraction

Luigi Paolasini

Abstract Hard X-rays magnetic scattering takes advantage of the characteristic properties of X-ray beams at third generation synchrotron radiation facilities: tuneable photon energy, controllable polarization and polarization analysis, excellent stability and brilliance. The aim of this lecture is to review the experimental and theoretical works in the domain of magnetic non-resonant and resonant X-ray diffraction on single crystals and thin films to investigate the electronic and magnetic long range order in strongly correlated electron systems. A general introduction to the theoretical aspects of the interaction between polarized photons and electrons will be given, with special emphasis to the description of the experimental polarized X-ray scattering methods to measure the relevant physical parameters.

12.1 Introduction

The use of X-rays techniques to study the electronic and magnetic properties of materials have received a large impulse with the advent of the so called third generation synchrotron radiation sources. The improvement in brightness, polarization and energy tunability of the X-rays sources delivered by the insertion devices (wigglers and undulators) have been the key ingredients for a wide range of applications of synchrotron radiation in many diverse areas of condensed matter, including physics, chemistry, material science, biology, medicine, geology. The electron-photon coupling interaction was predicted many years ago, starting with the observation of important modifications of the Thomson scattering cross section at high scattering vectors, and this effect is included in the Klein-Nishina formula for Compton scattering [1, 2]. In the 1950s different works on Compton magnetic γ-rays scattering where published, motivated by its use for polarization measurements in nuclear and

L. Paolasini (✉)
European Synchrotron Radiation Facility, BP 220, 38043 Grenoble Cedex, France
e-mail: paolasini@esrf.eu

S. Mobilio et al. (eds.), *Synchrotron Radiation*,
DOI: 10.1007/978-3-642-55315-8_12, © Springer-Verlag Berlin Heidelberg 2015

particle physics [3–5]. In the field of solid state physics seminal and pre-synchrotron magnetic X-ray scattering experiments were carried out in 1970s by de Bergevin and Brunel at CNRS in Grenoble, and they demonstrated the feasibility of magnetic X-ray scattering experiments by using a standard X-ray tube on NiO [6, 7], following the theoretical work of Platzman and Tzoar [8].

The advent of energy-tunable synchrotron sources has open the possibility to adjust the photon energy to different value of absorption edges, living the opportunity to observe resonant effects in many materials [9]. These experiments have open the avenue for the modern synchrotron radiation experiments, allowing the extraction of information from the anisotropic tensors of the atomic structure factor near a resonance of the forbidden lattice reflections, appearing as a consequence of broken lattice symmetries, as for example in the presence of screw-axis or glide plane symmetries [10].

The first resonant magnetic enhancement was reported by Namikawa et al. [11], working at the K-edge of ferromagnetic Ni. In addition to the non-resonant magnetic signal the authors observed at photon energies close to the K-edge, a supplementary signal, which they also assigned to a magnetic origin. Since then X-ray magnetic circular dichroism is widely used to study ferromagnetic systems [12, 13]. Namikawa's results remained unnoticed until 1988, when Gibbs et al. [14] observed the first resonant enhancement at L_3-edge of Ho, attributed to a magnetic resonant exchange scattering, as explained in the theoretical paper of Hannon et al. [15].

This discovery have open the avenue to the synchrotron experiments in which the combination of both the X-ray atomic spectroscopy and diffraction offers the unique perspective to investigate the electronic and magnetic ordering phenomena in condensed matter. The main advantage with respect to the absorption spectroscopies is the possibility to coherently disentangle the electric and the magnetic degree of freedom, and to detail the structure factors for each atom inside the unit cell. This is particularly suitable in the study of strongly correlated electron systems, in which the complex interaction between the charge, orbital and spin degree of freedom can determine peculiar phenomena like superconductivity, colossal magneto-resistance, metal-insulator transition, charge ordering and orbital ordering [16].

12.1.1 Theoretical Aspects of Magnetic and Resonant X-Ray Scattering

In a generic scattering experiment the fundamental quantity determined is the differential cross section ($d\sigma/d\Omega = I_{sc}/(\Phi_0 \Delta\Omega)$), defined as the ratio of number of photons recorded per second in the detector which subtends a solid angle $\Delta\Omega$ and the incident photon flux Φ_0. In the case of the Bragg diffraction, the differential cross section is given by:

$$\left(\frac{d\sigma}{d\Omega}\right)_{\text{Bragg}} = N\frac{(2\pi)^3}{v_0}\sum_{hkl}\delta(\mathbf{Q}-\mathbf{G}_{hkl})\,|F(hkl)|^2 \tag{12.1}$$

where v_0 is the volume of the unit cell and N the number of unit cell in the crystal.

The structure factor F_{hkl} describes the interference between the resultant waves diffused from each atom in the unit cell for any given reciprocal lattice vector $\mathbf{G}_{hkl}$. It is obtained by the sum of f_s over all the atom positions inside the unit cell and determined by the position vectors $\mathbf{d}_s$:

$$F(hkl) = -r_0\sum_s f_s(\mathbf{k},\mathbf{k}',\hat{\varepsilon},\hat{\varepsilon}',\hbar\omega_k)\,e^{i\mathbf{G}_{hkl}\cdot\mathbf{d}_s - W_s} \tag{12.2}$$

where W_s is the Debye-Waller factor, $r_0 = e^2/mc^2 \approx 2.82\times10^{-5}$Å is the classical electron radius, $\mathbf{d}_s = x_1\mathbf{a}_1 + x_2\mathbf{a}_2 + x_3\mathbf{a}_3$ corresponds to the atomic positions inside the unit cell and is expressed in term of fractional coordinates x_i. Depending on the space group of the crystal (systematic conditions), and on the special positions where the atoms lie (accidental conditions), we find the appropriate extra restrictions to the integer values allowed to h, k, l.

Using either single crystals or powders, neutron or X-ray diffraction can be used to measure F^2 (which is proportional to the intensity of a Bragg peak) for various values of (hkl). A direct Fourier inversion of diffraction data to yield crystal structures is not possible because we only measure the magnitude of F, and not its phase.

The structure factor (12.2) contains the information of the distribution of atoms inside the unit cell. If the scattering amplitude f_s associated with a given sample-probe interaction potential is known (for example nuclear, charge, magnetic ...), the comparison of different Bragg peak intensities in the reciprocal space allows the determination of structural arrangement of atoms or the magnetic moment distribution inside the unit cell.

12.1.2 X-Rays Scattering Amplitudes

When we consider the X-ray elastic diffraction of a monochromatic beam on single crystals, at energies $\hbar\omega < 100$ keV, the X-rays interact weakly with bulk samples, and the scattering maybe accurately treated in the lowest Born-Oppenheimer approximation. The scattering amplitude $f = f^0 + f^{magn.} + f^{RXS}$ includes in general three terms: the Thomson contribution $f^0 \propto -Zr_0$ associated to the isotropic charge density distribution, and the only term considered in the simplest "kinematical theory" of X-ray scattering; the non-resonant X-ray magnetic scattering (NRXMS) amplitude $f^{magn.}$ is associated to the orbital and spin magnetic density distribution and gives rise to the magnetic X-ray scattering; the last term $f^{RXS} = f' + if''$ is the anomalous or resonant contribution.

These terms can be calculated separately following the perturbative method developed by Blume [17], which considers an unperturbed system described by the electron $\mathscr{H}_{el}$ and non-interacting photon $\mathscr{H}_{ph}$ Hamiltonians. The scattering amplitudes $f(\mathbf{k}, \mathbf{k}', \hat{\varepsilon}, \hat{\varepsilon}', \hbar\omega_k)$ can be developed in non-resonant and resonant parts, by assuming that the unperturbed radiation is monochromatic, and the vector potential $\mathbf{A}$ which characterizes the radiation field is a linearly polarized plane wave. Photons are defined by the initial state $|\mathbf{k}, \hat{\varepsilon}\rangle$ characterized by wavevector $\mathbf{k}$, polarization $\hat{\varepsilon}$ and energy $\hbar\omega_k$. Initially the electrons are found in the ground state $|g\rangle$, an eigenstate of the unperturbed electron Hamiltonian $\mathscr{H}_{el}$ with energy E_g. The interaction between electrons and photons creates a new final eigenstate $|f\rangle$ for the electrons with an energy E_f and a scattered photon in the state $|\mathbf{k}', \hat{\varepsilon}'\rangle$ with an energy $\hbar\omega'_k = \hbar\omega_k$.

We report here the final expression of scattering amplitudes, in which the non-resonant and the resonant regimes are calculated separately [18]:

$$
\begin{aligned}
f(\mathbf{k}, \mathbf{k}', \hat{\varepsilon}, \hat{\varepsilon}', \hbar\omega_k) &= f^0 + f^{magn.} + f^{RXS} \\
&= -\langle g| \sum_j e^{i\mathbf{Q}\cdot\mathbf{r}_j} |g\rangle \; \hat{\varepsilon}'^* \cdot \hat{\varepsilon} \\
&\quad - i\frac{\hbar\omega_k}{mc^2} \left(\mathbf{L}(\mathbf{Q}) \cdot \mathbf{P}_L + \mathbf{S}(\mathbf{Q}) \cdot \mathbf{P}_S\right) \\
&\quad + \frac{1}{m} \sum_c \frac{E_g - E_c}{\hbar\omega_k} \left(\frac{\hat{\varepsilon}'^* \cdot \langle g|\, \tilde{O}^\dagger(\mathbf{k}')\, |c\rangle\, \langle c|\, \tilde{O}(\mathbf{k})\, |g\rangle \cdot \hat{\varepsilon}}{E_g - E_c + \hbar\omega_k - i\Gamma_c/2} \right. \\
&\quad \left. - \frac{\hat{\varepsilon} \cdot \langle g|\, \tilde{O}(\mathbf{k})\, |c\rangle\, \langle c|\, \tilde{O}^\dagger(\mathbf{k}')\, |g\rangle \cdot \hat{\varepsilon}'^*}{E_g - E_c - \hbar\omega_k} \right)
\end{aligned}
\tag{12.3}
$$

In the Thomson term $f^0 = Zr_0$ all the core and valence electrons interact with the radiation field, and scattering amplitude depends from Fourier transform of the atomic charge density, multiplied for the scalar product of incident and scattered photon polarization $\hat{\varepsilon}'^* \cdot \hat{\varepsilon}$. The Thomson scattering doesn't change the photon polarization state, because the scattering is isotropic, and this property is used analyse the polarisation of scattered beam, as we will seen in Sect. 12.2.1.

The NRXMS amplitude $f^{magn.}$ contains the Fourier transforms of orbital $\mathbf{L}(\mathbf{Q}) = \langle g| \sum_j \mathbf{l}_j e^{i\mathbf{Q}\cdot\mathbf{r}_j} |g\rangle$ and spin $\mathbf{S}(\mathbf{Q}) = \langle g| \sum_j \mathbf{s}_j e^{i\mathbf{Q}\cdot\mathbf{r}_j} |g\rangle$ magnetization densities, multiplied for two distinct vectors describing the polarization and wavevector dependence of orbital $\mathbf{P}_L$ and spin $\mathbf{P}_S$ magnetic scattering process:

$$
\begin{aligned}
\mathbf{P}_L &= -2\, sin^2\theta\, [\mathbf{Q} \times [(\hat{\varepsilon}'^* \times \hat{\varepsilon}) \times \mathbf{Q}]] \\
\mathbf{P}_S &= \hat{\varepsilon}'^* \times \hat{\varepsilon} + (\hat{\mathbf{k}}' \times \hat{\varepsilon}'^*)(\hat{\mathbf{k}}' \cdot \hat{\varepsilon}) - (\hat{\mathbf{k}} \times \hat{\varepsilon})(\hat{\mathbf{k}} \cdot \hat{\varepsilon}'^*) - (\hat{\mathbf{k}}' \times \hat{\varepsilon}'^*) \times (\hat{\mathbf{k}} \times \hat{\varepsilon})
\end{aligned}
\tag{12.4}
$$

It can be seen that by taking advantage of the different geometrical prefactors for spin and orbital moments, X-ray magnetic scattering provides the possibility to separate spin and orbital moment contributions to the total magnetization density.

Table 12.1 Photo-absorption edges for different series of magnetic elements, with the characteristic energy ranges (keV), wavelength λ (Å) and the allowed atomic transitions to the electronic shells

Series	Abs. edge	Energy (keV)	λ (Å)	Shells	Type	Res. ampl. (r_0)
3d	$L_{2,3}$	0.4–1.0	12–30	2p→3d	E1	≈100
	K	4.5–9.5	1.3–2.7	1s→4p	E1	≈0.02
				1s→3d	E2	≈0.01
5d	$L_{2,3}$	5.4–14	0.9–2.2	2p→5d	E1	≈1–10
4f	$L_{2,3}$	5.7–10.3	1.2–2.2	2p→5d	E1	≈0.10
				2p→4f	E2	≈0.05
	$M_{4,5}$	0.9–1.6	7.7–13.8	2d→4f	E1	≈100–300
5f	$L_{2,3}$	17–21	0.6–0.7	2p→6d	E1	≈0.05
				2p→4f	E2	≈0.01
	$M_{4,5}$	3.5–4.5	2.7–6	3d→5f	E1	≈10.0

The *rightmost* column indicates the estimated resonant magnetic scattering amplitudes expressed in r_0 units [19]

More generally, the prefactors can be adjusted by changing either the scattering geometry or the X-ray polarization channels.

When the photon energy is tuned to such a characteristic energy, we are in the resonant regime, where the resonant denominator $\frac{1}{E_g - E_c + \hbar\omega_k - i\Gamma_c/2}$ of (12.3) plays the important role, giving rise to typical enhancement of the magnetic intensities across the absorption edge. The resonant process consists in promoting an electron from core levels into a valence shell (either partially occupied or empty), and the subsequent decay into the same initial state results in an elastically re-emitted photon, were Γ_c is the width of the excited level $|c\rangle$ with energy E_c and $2\pi\hbar/\Gamma_c$ its life time. Notice that the all core-hole spectroscopies like the RXS are "fast" probes, as opposed for example to "slow" probes like Mössbauer spectroscopy, providing an instantaneous "snapshots" of all the fluctuating configuration, the timescale being defined by the core-hole lifetime $2\pi\hbar/\Gamma_c$. The current operator $\tilde{O}(\mathbf{k}) = \sum_j e^{i\mathbf{k}\cdot\mathbf{r}_j}(\mathbf{p}_j - i\hbar\mathbf{k}\times\mathbf{s}_j)$ will be analysed in detail in Sect. 12.4.

Table 12.1 shows the absorption edges exploited for RXS studies and associated to the elements of interest for resonant magnetic diffraction. The lines in italic represent absorption edges in the soft X-ray regime, where the scattering conditions are not fulfilled for most of the ordered magnetic structures, but with a huge enhancement of the resonant magnetic amplitude, as shown in the last column (L-edges of transition metals and M-edges of rare earths). The most important edges for hard RXS cover the energy range 3.5–15 keV, which include K-edges of transition metals, the L-edges of Rare-Earths and both the L-edges and the M-edges of actinides.

12.2 Experimental Methods

In the magnetic and resonant X-ray scattering techniques the choice of the scattering geometry and the sample environment is strictly related to the complex relationships between the photon polarization state and the scattering wavevector **Q** with respect to the sample orientation, as we have seen in previous Sect. 12.1.1.

Typically beamlines for resonant and magnetic X-ray scattering are built on a high-β straight section, thus with a relatively large source size but with a very small divergence, necessary to increase the Q-resolution in diffraction experiments. Due to the low intensity of magnetic X-ray scattering, a high brilliance delivered by undulators is required: typical flux available at the sample ranges from $\approx 10^{13}$ photons/sec at 4 keV up to $\approx 10^{14}$ photons/sec at 10 keV. These conditions represent a challenge for the design of cryogenic equipment, and also a limit for the sample radiation damage. Mirrors are required to provide the harmonic rejection, particularly in experiment performed at low energy (below 6 keV). In order to preserve the good Q-resolution necessary for single crystal diffraction, a moderate demagnification factor is necessary (calculated as the ratio of the source-mirror and mirror-image distances). The main requirements for the optic design of a magnetic diffraction beamline could be summarized in order of importance: UHV optics and high brightness (to reach low absorption edges), beam stability over a long time periods (counting rate of the order of hours), small divergent beam (Q-resolution), fixed exit monochromator (energy scans about 200 eV), an energy resolution $\Delta E/E \approx 10^{-4}$, limited by the Si(111) monochromator [20]. X-ray absorption becomes large at low energy, and then RXS experiments probe a small scattering volume near the surface of the sample. This can be an advantage for single magnetic domain studies, but a severe limitation is introduced in the geometrical scattering condition, due to the reduced Ewald sphere and large scattering angles required to span the available reciprocal lattice space. As a result, most of magnetic and RXS experiments cannot be done in transmission and absorption corrections have to be taken into account.

12.2.1 Polarization Analysis and Azimuthal Scans

The polarization analysis, combined with the rotation $\hat{\psi}$ of the sample about the scattering vector $\mathbf{Q} = \mathbf{k} - \mathbf{k}'$ (the so called azimuthal rotation), are the basic method to separate the magnetic or RXS intensities from the charge scattering. The azimuthal method is also used to discriminate the multiple scattering events (the so called Renninger scans), to establish the magnetic domain populations and to add an extra geometrical degree of freedom in diffraction experiments. In addition, it reduces the fluorescence background near the absorption edges and increases the 2θ angular resolution.

Two scattering geometries can be used for RXS studies: the vertical scattering geometry, adapted for azimuthal studies, and the horizontal scattering geometry for

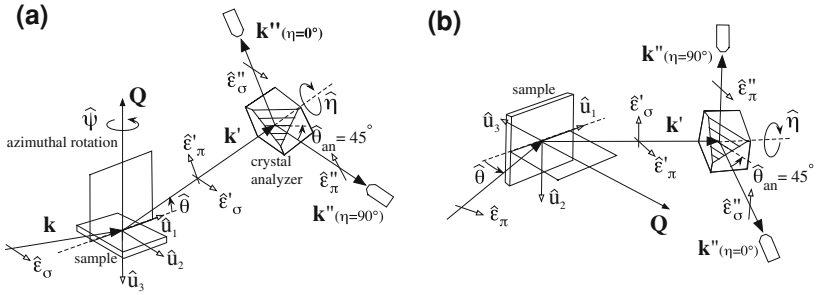


Fig. 12.1 **a** Azimuthal vertical scattering geometry with the polarisation analysis. The incident X-ray polarization $\hat{\varepsilon}_\sigma$ is perpendicular to the scattering plane and the scattered polarization can be analysed in $\sigma - \sigma'$ or $\sigma - \pi'$ polarization channels by rotating the crystal analyser about the scattered vector $\mathbf{k}'$ (angle $\hat{\eta}$). The sample can rotate about the scattering wavevector $\mathbf{Q}$ (angle $\hat{\psi}$) to perform the so called azimuthal scans. The unitary vectors ($\hat{u}_1, \hat{u}_2, \hat{u}_3$) are used as reference for the laboratory system. **b** Horizontal scattering geometry. The incident X-ray polarization $\hat{\varepsilon}_\pi$ is parallel to the scattering plane (from [16])

experiments under extreme conditions, as for example high magnetic fields of heavy cryogenic equipments (see Fig. 12.1).

The polarization analysis of the scattered beam is realised through the elastic Bragg diffraction from a high quality single-crystal, whose the crystal lattice spacing are selected to fulfill the diffraction condition with $\hat{\theta}_{an} = 45°$ for the working energy.

The analyser crystal acts as a polarisation filter for the scattered X-rays because the polarisation term $(\hat{\varepsilon}' \cdot \hat{\varepsilon}'')$ contained in the Thomson scattering amplitude exclude the rotation of the X-ray polarisation [21]. Using the Jones formalism to describe the X-rays polarisation channels [22], we can express the scalar product as:

$$\hat{\varepsilon}'' \cdot \hat{\varepsilon}' = \begin{bmatrix} \hat{\varepsilon}''_\sigma \cdot \hat{\varepsilon}'_\sigma & \hat{\varepsilon}''_\sigma \cdot \hat{\varepsilon}'_\pi \\ \hat{\varepsilon}''_\pi \cdot \hat{\varepsilon}'_\sigma & \hat{\varepsilon}''_\pi \cdot \hat{\varepsilon}'_\pi \end{bmatrix} = \begin{bmatrix} 1 & 0 \\ 0 & \cos 2\theta_{an} \end{bmatrix} = \begin{bmatrix} 1 & 0 \\ 0 & 0 \end{bmatrix} \tag{12.5}$$

We can see that in the case of vertical scattering geometry (see Fig. 12.1a) only the $\sigma - \sigma$ polarisation channel is transmitted. By rotating the analyser about the scattering vector $\hat{\mathbf{k}}'$ (angle η), it is possible to fully characterise the polarisation state of scattered beam.

12.2.2 Circular Polarisation

The incident linear light polarization delivered by the planar undulators can be changed (linear or circular) by using an X-ray phase retarder, and the physical origin of this phenomenon is related to the theory of dynamical diffraction in a perfect crystal [23–25].

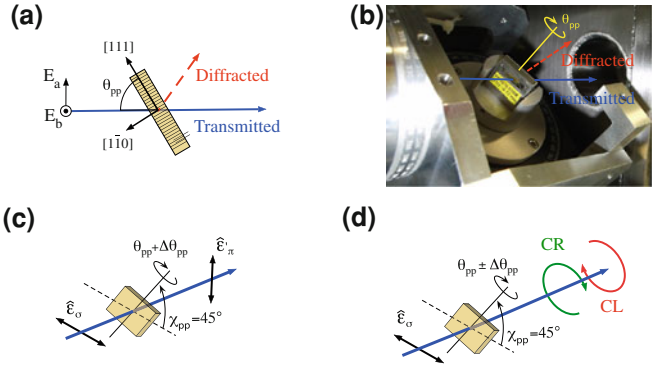


Fig. 12.2 **a** Phase plate retarder are optical elements employed to change the polarization of the X-rays by the phase shift between the transmitted and diffracted beam in the dynamical diffraction limit. The incident beam is partially diffracted by the [111] planes of a diamond single crystal cut in a thin slab perpendicular to the [1$\bar{1}$0] axis. **b** Picture of the diamond phase plate mounted on the rotation stage inside an in-vacuum chamber. **c** Conversions of incident linear X-ray polarization $\hat{\varepsilon}_\sigma$ in $\hat{\varepsilon}_\pi$ linear polarization for a half-wave plate mode ($\Delta\alpha = \pi$). Linear polarization scans can be performed by rotating the the χ_{pp} continuously in half-phase plate mode. **d** Circular polarisations obtained for the quarter wave plate mode ($\Delta\alpha = \pi/2$)

A thin single crystal of diamond is inserted upstream to the sample, and it is set in order to excite a given diamond reflection. Good experimental results are obtained using diamond (111) reflection in symmetric Laue geometry with the diamond slab cut perpendicular to the (1$\bar{1}$0) axis, as shown in Fig. 12.2-a ([1]). Alternative methods could be used, as for example in the case of asymmetric Laue geometry with (1$\bar{1}$1)-cut. In this case, because the 3-fold symmetry of the crystal surface, one has to take care to avoid exciting one of the equivalent reflections ($\bar{1}\bar{1}$1) and (1$\bar{1}\bar{1}$).

The two X-ray polarization components in the diamond reference frame E_{0a} parallel to this scattering plane (σ) and E_{0b} (π) propagate through the diamond crystal with different refraction index ($n_\sigma - n_\pi$) $\neq 0$, and this difference depends on the departure from the Bragg angle of the incident wave $\Delta\theta$.

When the crystal is slightly detuned from the Bragg position (111), the incident and transmitted waves are then phase shifted with respect to each other, as shown in Fig. 12.2-b. The phase plate is oriented in order to form an angle $\chi_{pp} = 45°$ with respect of the laboratory reference frame, where the incident X-ray polarization is $\hat{\varepsilon}_\sigma$ ($E_{0a} = E_{0b}$ in the diamond reference frame), as shown in Fig. 12.2-b. In this conditions, the incident and transmitted polarizations can have a phase difference $\Delta\alpha$ defined as:

[1] Different crystalline materials could be used for phase plate retarders. Diamond crystals fulfill the condition of low absorption at the current working energies.

$$\Delta\alpha = \frac{2\pi}{\lambda}(n_\sigma - n_\pi)d = -\frac{\pi}{2}\left[\frac{r_e^2\lambda^3 Re(F_h F_{\bar{h}})sin2\theta_{pp}}{\pi^2 V^2 \Delta\theta_{pp}}\right]d \tag{12.6}$$

where F_h and $F_{\bar{h}}$ are the complex structure factors for (hkl) and $(\bar{h}\bar{k}\bar{l})$, r_e the classical electron radius, V the unit cell volume, λ the X-rays wavelength, θ_{pp} the phase plate Bragg angle, d the beam path in the crystal and $\Delta\theta_{pp}$ the misalignment relative to the Bragg angle θ_{pp}. Circular polarization is obtained when the phase shift is set to $\pm\lambda/4$ (quarter wave plate), and it is particularly useful for the study of chiral or helical magnetic structures.

12.3 Magnetic Diffraction

A magnetic structure can be described in terms of a **magnetic propagation vector** $\mathbf{q}_m$, characteristic of the eigenfunction of the translational group. The concept of the magnetic propagation vector is very useful in crystal magnetic diffraction because it is directly related to the appearance of magnetic Bragg peaks in the reciprocal space fulfilling the scattering relation $\mathbf{Q} = \mathbf{G}_{hkl} + \mathbf{q}_m$, where $\mathbf{G}_{hkl}$ is a reciprocal scattering vector fulfilling the Bragg scattering conditions. The periodicity of a magnetic structure is defined in the real space by the planes perpendicular to $\mathbf{q}_m$ with the inter-planes distances given by the inverse of its modulus $d = 1/|\mathbf{q}_m|$.

For example, ferromagnetic or ferrimagnetic structures are characterised by a propagation vector $\mathbf{q}_m = (000)$. The magnetic reflections correspond to the nodes of the reciprocal lattice and their intensity are superposed to the structural Bragg reflections (Fig. 12.3-a). Figure 12.3-b shows the antiferromagnetic structure defined by the propagation vector $\mathbf{q}_m = (\frac{1}{2}, \frac{1}{2}, 0)$ in an hexagonal system. The antiferromagnetic structures correspond to integral multiples of the chemical unit cell, i.e. they are commensurate: $\mathbf{q}_m$ in this case corresponds to the symmetry points at the surface of the Brillouin zone. For these structures there is an alternation along the propagation vector of parallel and anti-parallel moments. In the general case the magnetic propagation vector $\mathbf{q}_m$ may be any point inside the first Brillouin zone, and its modulus can be either a fractional number (commensurate structure) or a generic irrational number (incommensurate structures). For the helical magnetic structure represented in Fig. (12.3-c) both the propagation vectors $\mathbf{q}_m = (0, 0, \frac{1}{3}) = \tau^+$ and $\mathbf{q}_m = (0, 0, -\frac{1}{3}) = \tau^-$ are present and they generate a set of satellite covering all the reciprocal space.

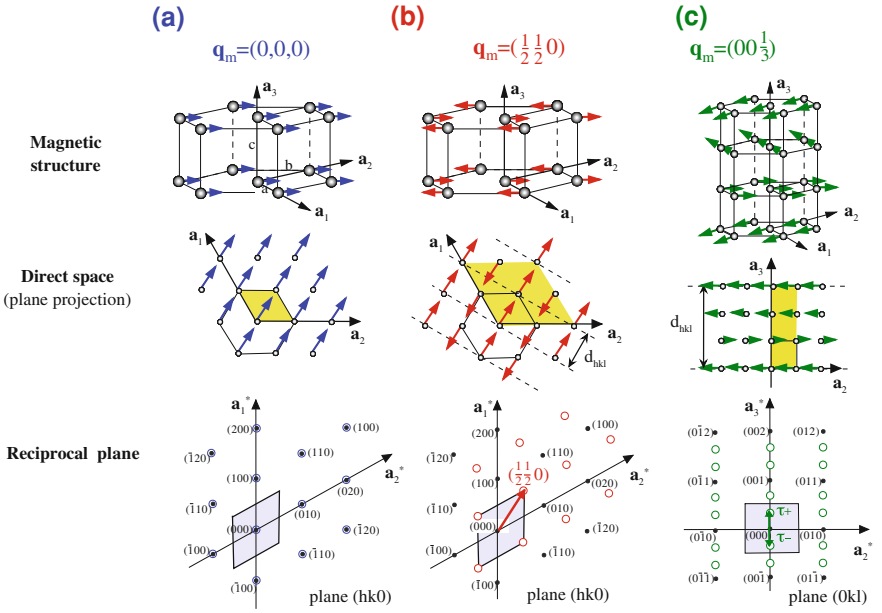


Fig. 12.3 Magnetic structures in an hexagonal system, and relations between the direct and reciprocal lattice vectors. The magnetic structures are classified in term of propagation vectors $\mathbf{q}_m$. *Arrows* in the unit cell (*upper panel*) and in the plane projection (*middle panel*) indicate the magnetic moment directions. Open *circles* (◯) in the reciprocal planes (*lower panel*) correspond to the position of the magnetic reflections, obtained by the translation $\mathbf{q}_m$ of the reciprocal lattice points (•). *Yellow* areas indicate the magnetic unit cell and *blue* areas the corresponding first Brillouin zones. **a** ferromagnetic, $\mathbf{q}_m = (0, 0, 0)$; **b** antiferromagnetic, $\mathbf{q}_m = (\frac{1}{2}, \frac{1}{2}, 0)$; **c** commensurate helical modulated structure, $\mathbf{q}_m = (0, 0, \frac{1}{3})$

12.3.1 Linear Polarisation Analysis of a Simple Antiferromagnetic Structure

Let we consider the linear polarization analysis of a simple antiferromagnetic structure depicted in Fig. 12.4-a. We consider for simplicity a Bravais lattice, with only one magnetic atom per unit cell, and we choose the scattering geometry with the moment μ perpendicular to the magnetic propagation vector $\mathbf{q}_m = (0, 0, 0.5)$.

The magnetic X-rays scattering amplitude $f^{magn.}$ of (12.3) could be decomposed in term of polarisation channels using the Jones matrix, and by projecting the spin $S_i(\mathbf{Q})$ and the orbital $L_i(\mathbf{Q})$ momentum components along the cartesian reference system $\mathbf{u}_i$ (see Fig. 12.1-a) as follows [26]:

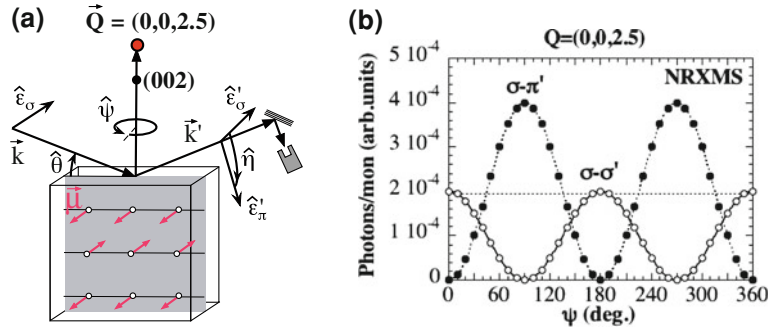


Fig. 12.4 **a** Azimuthal scan and linear polarization analysis of an antiferromagnetic Bragg peak $\mathbf{Q} = (0, 0, 2.5)$. The direction of the magnetic moments μ is perpendicular to the scattering plane when the azimuthal angle $\psi = 0°$. **b** In non resonant magnetic scattering regime (NRXMS) both polarization channels $\sigma - \sigma'$ (*open circles*) and $\sigma - \pi'$ (*black dots*) have a sinusoidal dependence. When $\psi = 90°$ the scattered intensity is detected in the $\sigma - \pi'$ polarization channel

$$f^{magn.} = -i\frac{\hbar\omega}{mc^2}\begin{bmatrix} S_2 \sin 2\theta & -2\sin^2\theta\,[(\cos\theta)(L_1+S_1)-S_3\sin\theta] \\ 2\sin^2\theta\,[\cos\theta\,(L_1+S_1)+S_3\sin\theta] & \sin 2\theta\,[2L_2\sin^2\theta+S_2] \end{bmatrix} \tag{12.7}$$

where the S_i and L_i the components of $\mathbf{S}(\mathbf{Q})$ and $\mathbf{L}$ $(\mathbf{Q})$ defined in the coordinate system $\hat{\mathbf{u}}_i$ (see Fig. 12.1).

We can easy see that, considering the relations between the polarization vectors and the scattering wavevectors in (12.4), the azimuthal rotation $\hat{\psi}$ produce a sinusoidal modulation of scattered intensities in both the polarization channels. In fact, if we consider only the incident polarization σ, the detected intensities in the two polarization channels $\sigma - \sigma'$ and $\sigma - \pi'$ are proportional to the square of the NRMXS amplitudes :

$$\begin{aligned} f^{magn.}_{\sigma-\sigma'} &\propto S_2 \sin 2\theta = S \sin 2\theta \cos\psi \\ f^{magn.}_{\sigma-\pi'} &\propto 2\sin^2\theta\,[\cos\theta\,(L_1+S_1)+S_3\sin\theta] = \cos\theta\,(L+S)\sin\psi \end{aligned} \tag{12.8}$$

where S_i and L_i are the projections of the spin and orbital moment along the reference system u_i. Notice that when $\hat{\psi} = 0°$ we have $S_1 = L_1 = S_3 = 0$, and when $\hat{\psi} = 90°$ $S_2 = S_3 = 0$. In this particular simple case the maximum (minimum) of the $\sigma - \pi'$ $(\sigma - \sigma')$ signal corresponds to the rotation $\psi = 90°$, when the magnetic moments are parallel to the scattering plane. This scattering configuration is particularly useful in the determination of the magnetic moment orientation and the magnetic domain population. By measuring the ratio between the two polarization channels, il is possible to extract the L/S ratio. The separation of L and S presents a distinct difference to neutron scattering, where only the total magnetic moment is

probed. Moreover, the L/S ration can be probed in the ordered state, and in particular in antiferromagnetic systems or in modulated structures.The method of separation of L/S has been applied successfully on simple transition metal oxides [27–29], in actinides [30] and in Jahn-Teller cuprates [31].

12.3.2 Exemple II: Circular Polarisation Analysis in Multiferroics

The study of multiferroics materials is a rapidly expanding field today thanks to the discovery of a strong coupling between spontaneous long-range magnetic order and ferroelectric order. The grand challenge is to find multifunctional materials where multiple physical properties like magnetism, ferroelectricity and ferroelasticity, could be simultaneously exploited in advanced applications in electronics and data storage. Here we present an example of a class of multiferroics of type-II, in which it is the magnetism itself that produces the ferroelectricity by a particular magnetic mechanism [32]. The intrinsic effect is due to the spin frustration, which produces an incommensurate and non-collinear magnetic order (a cycloid), responsible for the breaking of the magnetic inversion symmetry, accompanied by non-centrosymmetric lattice distortions, responsible for the induced net electric polarization [33, 34].

The polarization state of the scattered intensity $I(\eta) = I_0(1 + \bar{P}_1 cos2\eta + \bar{P}_2 sin2\eta)$ could be expressed in terms of Poincaré-Stokes parameters $\bar{P}_i$ as:

$$\bar{P}_1 = \frac{(\varepsilon'_\sigma \varepsilon'^*_\sigma - \varepsilon'_\pi \varepsilon'^*_\pi)}{(\varepsilon'_\sigma \varepsilon'^*_\sigma + \varepsilon'_\pi \varepsilon'^*_\pi)} \quad \bar{P}_2 = \frac{-(\varepsilon'_\sigma \varepsilon'^*_\pi + \varepsilon'_\pi \varepsilon'^*_\sigma)}{(\varepsilon'_\sigma \varepsilon'^*_\sigma + \varepsilon'_\pi \varepsilon'^*_\pi)} \quad \bar{P}_3 = \frac{(\varepsilon'_\sigma \varepsilon'^*_\pi - \varepsilon'_\pi \varepsilon'^*_\sigma)}{(\varepsilon'_\sigma \varepsilon'^*_\sigma + \varepsilon'_\pi \varepsilon'^*_\pi)} \tag{12.9}$$

where $\bar{P}_1$ is the polarization rate parallel and perpendicular to the scattering plane defined by the analyser, $\bar{P}_2$ the degree of oblique polarization and $\bar{P}_3 = \sqrt{1 - (\bar{P}_1^2 + \bar{P}_2^2)}$ the degree of circular polarization, as far as the beam is completely polarized and we can neglect the depolarisation effects.

For example, let us consider the simple cycloidal structure described in Fig. 12.5. The incident circular polarization is described by the complex vectors $\varepsilon_{CR} = \left(\hat{\varepsilon}_\sigma - i\hat{\varepsilon}_\pi\right)$ and $\varepsilon_{CL} = \left(\hat{\varepsilon}_\sigma + i\hat{\varepsilon}_\pi\right)$. In order to calculate the Poincaré-Stokes parameters given in (12.9), we evaluate the final polarization state $\varepsilon' = \left(\hat{\varepsilon}'_\sigma + i\hat{\varepsilon}'_\pi\right)$, exploiting the Jones matrix from the magnetic scattering amplitude (12.7):

$$\begin{aligned} \varepsilon' = \begin{bmatrix} \hat{\varepsilon}'_\sigma \\ \hat{\varepsilon}'_\pi \end{bmatrix} &= 2S \sin^2\theta \begin{bmatrix} 0 & -(\cos\theta - i\sin\theta) \\ (\cos\theta + i\sin\theta) & 0 \end{bmatrix} \begin{bmatrix} 1 \\ \pm i \end{bmatrix} \\ &= 2Ssin^2\theta \begin{bmatrix} \mp(icos\theta + sin\theta) \\ cos\theta + isin\theta \end{bmatrix} \end{aligned} \tag{12.10}$$

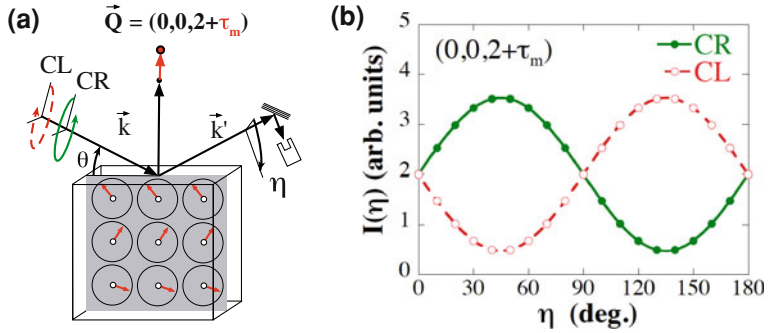


Fig. 12.5 **a** Non-collinear cycloidal magnetic structure investigated with circular *left* (*CL*, *green*) and *right* (*CR*, *red*) X-rays polarisations. The magnetic propagation vector τ_m is parallel to the scattering wave vector **Q**. **b** The scattered magnetic intensity $I(\eta)$ gives distinct scattered intensities as a function of polarization angle η. In this case the Poincaré-Stokes parameters are $\bar{P}_1 = 0$ and $\bar{P}_2 = \pm sin2\theta$, indicating a dominant scattered oblique polarization

where we have supposed that $S_b = S_c$. The Poincaré-Stokes can be calculated easily from (12.9) :

$$\bar{P}_1 = 0 \quad \bar{P}_2 = \pm sin2\theta \quad \bar{P}_3 = \pm cos2\theta \tag{12.11}$$

Now the scattered light have a dominant oblique polarization $\bar{P}_2 = \pm sin2\theta$, with opposite sign for LCP and RCP, as shown in Fig. 12.5-b. When the scattering angle is close to $\theta = 45°$, it became completely linear and oblique ($P_2 = 1$ and $P_3 = 0$).

The circularly polarized XR naturally couple to the handedness of spin cycloids, and through a complete Stokes polarimetry analysis of the scattered beam it is possible to identify information on magnetic structures.

In $Ni_3V_2O_8$ for example there is a low temperature incommensurate (LTI) phase between 2.8 and 6.3 K that is accompanied by the onset of a finite spontaneous electric polarization, as shown in Fig. 12.6-b [36].

Based on neutron diffraction experiments it was proposed that this LTI phase corresponded to a cycloidal order of the spins on two different symmetry nickel sites "spine" and "cross-tie", as shown in Fig. 12.6-c [37]. These two sites could be selectively probed by taking advantage of the magnetic structure factor. Indeed, magnetic reflections can be classified according to their indices (hkl): in type-1 reflections (h = odd, k = odd, l = odd), cross-tie moments cancel such that only the spine site moments contribute; in type-2 reflections (h = even, k = even, l = odd), the reverse is true, such that the cross-tie moments are singled out; in type-3 reflections (h = odd, k = odd, l = even), both moment types contribute to the scattering. The sample was mounted such that the spin cycloid lay in the horizontal scattering plane, which resulted in the polarization state of the scattered beam being strongly sensitive to the domain populations, and cooled down under an electric field, in order to obtain

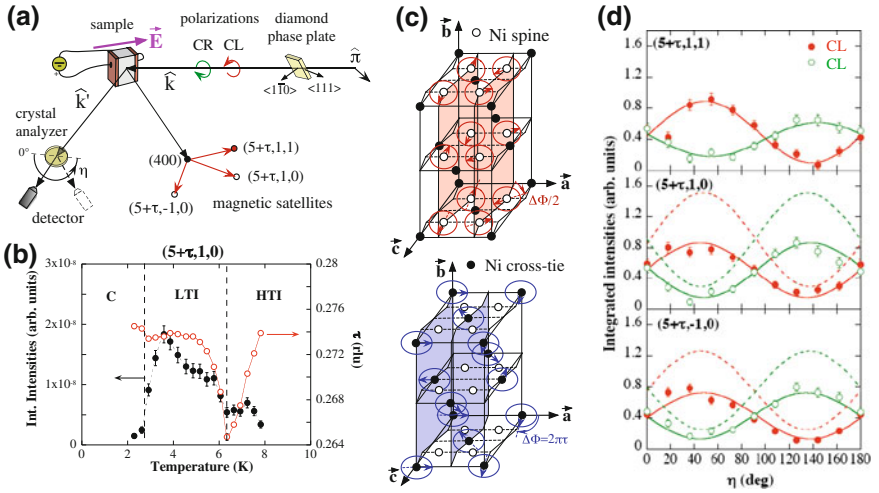


Fig. 12.6 **a** Experimental setup used to measure the magnetic reflections in $Ni_3V_2O_8$. A diamond quarter wave plate is used to convert the incident $\hat{\pi}$ polarization in *circular left* (*CL*, *red*) and *right* (*CR*, *green*) polarizations. A crystal analyser select the final polarization state by rotating around the scattered wavevector **k**' about the angle η. **b** Temperature dependence of the intensity and propagation vector τ of the magnetic reflection $(5+\tau, 1, 0)$ in the low temperature incommensurate (*LTI*) ferroelectric phase. **c** Magnetic structure of $Ni_3V_2O_8$ associated to the Ni magnetic moments in the "spine" (*top panel*) and "cross-tie" sites. **d** Polarization dependence of magnetic satellites as a function of the incident circular polarization. The continuous lines are deduced by the taking into account only the "spine" Ni moments whereas the broken lines are calculated with the neutron scattering model (from [35])

a single magnetic domain. Figure 12.6-d shows the polarization analysis of two class reflections, type-1 $(5 + \tau, 1, 1)$ in which only the spine moment contribute, and type-3 $(5 + \tau, 1, 0)$ which include both spine and cross sites sites. Starting with the pure spine type-1 only reflection $(5 + \tau, 1, 1)$, we have compared our data for both LCP and RCP with a calculation for the magnetic structure proposed in an earlier neutron-diffraction study, which include both the Ni site ordered [37]. These experimental results show unambiguously that the Ni magnetic moment on the cross-tie sites remains disordered. As a results, the onset of ferroelectricity is associated with the cycloidal ordering of the moments on the spine sites only. From Fig. 12.6-d we can also deduce that the scattering process converts quite completely the incident circular polarization state into a linear oblique polarization state inclined at 45° with respect to the scattering plane. By determining the value of P_2 at different points over the sample surface it is then possible to extract the magnetic domain populations.

12.4 Resonant X-Rays Scattering

The theory of RXS includes the general theory of photon-electron interaction in the non-relativistic limit (when NRXMS terms are neglected) which could be applied to both absorption and diffraction regimes, because the signal intensities depend on the matrix elements of the interacting operator between the ground state wave function and the excited one [38].

The RXS amplitude $f^{RXS} = f' + if''$ depends on the intermediate states $|c\rangle$ of the atomic system, and has a specific dependence on the incident photon energy $\hbar\omega$, as shown in (12.3). Notice that usually, in the analysis of the RXS diffraction data, it may be quite accurate to use zero-angle value for f' and f'', which are derived from absorption data or from theoretical calculations in the dipole approximation, because the resonant process arises mostly from inner-shell electrons, which are less sensitive to the atomic size effects.

Different approaches could be used to expand the RXS amplitude in order to evaluate the matrix elements which contains the current operator $\tilde{O}(\mathbf{k}) = \sum_j e^{i\mathbf{k}\cdot\mathbf{r}_j}(\mathbf{p}_j - i\hbar\mathbf{k}\times\mathbf{s}_j)$. A general approach for the the development in multipole expansion could be found in Lovesey et al. [45], and more recently by Di Matteo [40]. Here we restrict the analysis to the most relevant multipole contributions detected by RXS, i.e. electric dipole E1 and electric quadrupole E2 transitions, by omitting the spin and orbital parts in the dispersive term (M1 and M2 matrix elements), which are included in the general expansion of the current operator in the so called **r**-form [40].

Starting from second order terms in (12.3) containing the resonant contribution, and after some approximations, the resonant scattering amplitude became:

$$f^{RXS} \approx -\frac{1}{m}\sum_c \frac{E_g - E_c}{\hbar\omega_k} \cdot \frac{\langle g|\sum_j e^{-i\mathbf{k}'\cdot\mathbf{r}_j}\hat{\varepsilon}'^{*}\cdot\mathbf{p}_j|c\rangle\langle c|\sum_j e^{i\mathbf{k}\cdot\mathbf{r}_j}\hat{\varepsilon}\cdot\mathbf{p}_j|g\rangle}{E_g - E_c + \hbar\omega_k - i\Gamma_c/2} \quad (12.12)$$

The Equation (12.12) was developed by Hannon et al. [15] within the dipole approximation, i.e. by developing $e^{i\mathbf{k}\cdot\mathbf{r}_j} \approx 1 + i\mathbf{k}\cdot\mathbf{r}_j - (\mathbf{k}\cdot\mathbf{r}_j)^2/2 + \ldots$ as a power series and retaining only the two first dominant contributions: the electric dipole (E1) and the electric quadrupole (E2) transitions, which are related to the symmetry of the electronic shell and to type of orbitals probed in the intermediate states, as shown in Table 12.1.

This approximation is valid as far as $\mathrm{kr} \ll 1$, and in general case the multipole expansion on a plane wave is based on the expansion in spherical harmonics (Bessel functions for the radial part and Legendre polynomials for the angular part). The Equation (12.12) can be rewritten in three distinct terms by using the previous relations which include the dipole $\sum_j \mathbf{r}_j$ and the quadrupole $\sum_j \frac{i}{2}\mathbf{r}_j(\mathbf{k}\cdot\mathbf{r}_j)$ operators.

Using a cartesian reference coordinate system for the photon polarization, we can define the following transition matrix elements $D_{\alpha\beta} = \langle g|\sum_j r_j^\alpha|c\rangle\langle c|\sum_i r_i^\beta|g\rangle$, $I_{\alpha\beta\gamma} = \langle g|\sum_j r_j^\alpha|c\rangle\langle c|\sum_i r_i^\beta r_i^\gamma|g\rangle$ and $Q_{\alpha\beta\gamma\delta} = \langle g|\sum_j r_j^\alpha r_j^\delta|c\rangle\langle c|\sum_i r_i^\beta r_i^\gamma|g\rangle$.

These transition matrix elements $D_{\alpha\beta}$, $I_{\alpha\beta\gamma}$ and $Q_{\alpha,\beta,\gamma,\delta}$, are associated to dipole-dipole (E1-E1), dipole-quadrupole (E1-E2) and quadrupole-quadrupole (E2-E2) contributions, characterized by cartesian tensors of second, third and fourth rank, respectively.

The scattering amplitude for RXS can be written in the form:

$$f^{RXS} \approx m \sum_c \frac{(E_c - E_g)^3}{\hbar^3 \omega_k \, (E_g - E_c + \hbar\omega_k - i\Gamma_c/2)} \left[\sum_{\alpha,\beta} \varepsilon'^*_\alpha \, \varepsilon_\beta \, D_{\alpha\beta} + \frac{i}{2} \sum_{\alpha,\beta,\gamma} \varepsilon'^*_\alpha \, \varepsilon_\beta \left(k_\gamma \, I_{\alpha\beta\gamma} - k'_\gamma \, I^*_{\alpha\beta\gamma} \right) + \frac{1}{4} \sum_{\alpha,\beta,\gamma,\delta} \varepsilon'^*_\alpha \, \varepsilon_\beta \, k'_\gamma \, k_\delta \, Q_{\alpha\beta\gamma\delta} \right] \tag{12.13}$$

where α, β, γ, δ are indexes which vary independently over the three cartesian directions x, y, z.

The tensorial nature of resonant X-ray scattering amplitudes has important consequences in the X-ray scattering amplitude (12.13), because forbidden lattice reflections appear at resonance, as demonstrated in seminal experimental works of Templeton [9], with timely analysis of Dimitrienko [10], and the observation of Finkelstein [41], with the theoretical interpretation of Carra [13].

The magnetic atoms in the unit cell are related by symmetry operations and the site symmetry of the individual atoms has important implication on the possible allowed resonant transitions defined by the matrix elements of (12.13).

In general the RXS amplitude can be expressed as a scalar product of two irreducible spherical tensors:

$$f_j^{RXS} = \sum_{p,m} (-1)^q \, X^{(p)}_{-m} \, F^{(p)}_m(j;\omega) \tag{12.14}$$

where $X^{(p)}_m$ depends only on the incident and scattered polarization and wavevector, while $F^{(p)}_{-m}(j;\omega)$ is associated to the tensorial properties of the j-atom, and can be represented in terms of multipole expansion. The rank p defines the order of multipole in the electromagnetic field expansion and the projection q can take $(2p+1)$ values that satisfy $(-p \le m \le p)$. The $p = even$ tensors are time-even, i.e. invariant under time reversal, whereas $p = odd$ tensor are time-odd [42].

For the tensor ranks $p = 0, 1, 2$, (E1-E1) and (E2-E2) tensors represent the same physical quantities, though referred to states with different angular momentum.

Table 12.2 Properties of multiple expansion tensors under time-reversal $\tilde{T}$ and parity $\tilde{P}$ operators (from [43])

Tensor	Rank p	$\tilde{T}$	$\tilde{P}$	Type	Multipole
$F^{(0)}(E1-E1)$	0	+	+	Charge	Monopole
$F^{(0)}(E2-E2)$	0	+	+	Charge	Monopole
$F^{(1)}(E1-E1)$	1	−	+	Magnetic	Dipole
$F^{(1)}(E2-E2)$	1	−	+	Magnetic	Dipole
$F^{(1+)}(E1-E2)$	1	+	−	Electric	Dipole
$F^{(1-)}(E1-E2)$	1	−	−	Polar toroidal	Dipole
$F^{(2)}(E1-E1)$	2	+	+	Electric	Quadrupole
$F^{(2)}(E2-E2)$	2	+	+	Electric	Quadrupole
$F^{(2+)}(E1-E2)$	2	+	−	Axial toroidal	Quadrupole
$F^{(2-)}(E1-E2)$	2	−	−	Magnetic	Quadrupole
$F^{(3)}(E2-E2)$	3	−	+	Magnetic	Octupole
$F^{(3+)}(E1-E2)$	3	+	−	Electric	Octupole
$F^{(3-)}(E1-E2)$	3	−	−	Polar toroidal	Octupole
$F^{(4)}(E2-E2)$	4	+	+	Electric	Hexadecapole

The classification of multipoles illustrated in Table 12.2 is dictated by the unique properties under time-reversal $\tilde{T}$ and parity $\tilde{P}$ transformations of $F^{(p)}$ tensors on one side and multipole terms on the other. In fact, for any given tensor rank $p = 1, 2, 3, 4$, there is just one electromagnetic multipole of the same rank (1→dipole, 2→quadrupole, 3→octupole, 4→hexadecapole) with the same $\tilde{T}$ and $\tilde{P}$ properties. Notice that $\tilde{P}$-odd (E1-E2) tensors have both $\tilde{T}$-odd (-) and $\tilde{T}$-even (+) terms for any p, while $\tilde{P}$-even tensors (both (E1-E1) and (E2-E2)) are $\tilde{T}$-odd if of odd rank and $\tilde{T}$-even if of even rank [43].

Details on the development of RXS in multipole expansion could be found in [40, 43–46], and a classification of the tensors associated to the multipole expansion are summarized in Table 12.2.

All the quantities described in Table 12.2 are accessible and measurable in RXS experiments, where the local transition amplitudes are added with a phase factor that can compensate the possible vanishing effect due to the global symmetry.

RXS is a unique tool to investigate the physics of multipolar ordered parameters and is one of the most exciting research domain of investigation of strongly correlated electron systems. However, it must be remarked that in many cases the possibility to isolate the individual multipole terms remains a hard experimental task, because the difficulty to disentangle the high order magnetic or electric multipole contributions from the dominant resonant terms. In order to single out the individual components of each multipole through the observation of Bragg forbidden lattice reflections, a dedicated experimental tool have been developed in parallel with the development of the theoretical models for the symmetry analysis of resonant phenomena.

12.4.1 Interplay Between Magnetic and Orbital Ordering in $KCuF_3$

The interplay between charge, orbital and spin degrees of freedom is the key ingredient underlying the physics of transition-metal oxides. An ideal tool for studying the consequences of such a correlation is provided by RXS. The tensorial character of the different RXS amplitudes in the (12.14) can lead to a breakdown of the extinction rules valid for the crystal structure, giving rise to a forbidden lattice reflections measurable in Bragg diffraction when the photon energy is tuned to the characteristic energy of the atomic system under investigation. In this landscape, forbidden lattice reflections become permitted due to the a-sphericity of the atomic electron density, giving rise to anomalous tensor susceptibility (ATS) components in the atomic scattering factor.

It is interesting to consider now the magnetic part of the term associated to the E1-E1 transition of (12.13), i.e. the term which include only the magnetic dipole $F^{(1)}(E1-E1)$ in Table 12.2. The polarisation tensor for the magnetic dipole is $X^{(1)} \equiv \hat{\varepsilon}'^{*} \times \hat{\varepsilon}$, and it is quite easy to demonstrate that in this specific example the scattering amplitudes for RMXS are given by the simple expressions ([2]) :

$$\begin{aligned} f_{\sigma-\sigma'}^{RMXS}(E1-E1) &\propto 0 \\ f_{\sigma-\pi'}^{RMXS}(E1-E1) &\propto -z_1 \cos\theta = -z \cos\theta \sin\psi \end{aligned} \tag{12.15}$$

where z_i are the components of the unit vector $\hat{\mathbf{z}}$ parallel to the total magnetic moment projected in the reference frame $\hat{\mathbf{u}}$ (see Fig. 12.1-a). Notice that $\hat{\mathbf{z}}$ is just an axial vector, and don't include the form factor. Notice also that the $\sigma - \pi'$ channel look similar for NRMS and RMXS, but any signal is detected in the $\sigma - \sigma'$ channel. Similar analysis can be done for the polarization and azimuthal dependence of any given RXS amplitudes of Table 12.2, because each multipole have a characteristic polarisation and scattering dependence which can be calculated on the basis of crystallographic symmetries.

We consider now the model system $KCuF_3$, a Mott-Hubbard insulators containing transition metal ions, whose the magnetic behaviour is largely determined by the structural configuration and the presence of nearly degenerate, partially occupied orbitals [48]. The super-exchange Hamiltonian must be generalised to include the orbital degrees of freedom, among the spin one, as described theoretically by Kugel' and Khomskii, who proposed a model able to describe the magnetic structure of substances containing ions with orbital degeneracy [49, 50]. $KCuF_3$ is a quasi-one dimensional spin-$\frac{1}{2}$ magnetic system, which orders antiferromagnetically below $T_N = 38$ K with a simple $(00\frac{1}{2})$ magnetic structure (see Fig. 12.4) [51].

[2] Practical expressions for the RXS amplitudes in this specific cartesian reference system (but valid only for non-parity breaking symmetries, i.e. only for dipole $E1-E1$ and quadrupole $E2-E2$ electric transitions) could be found in [47].

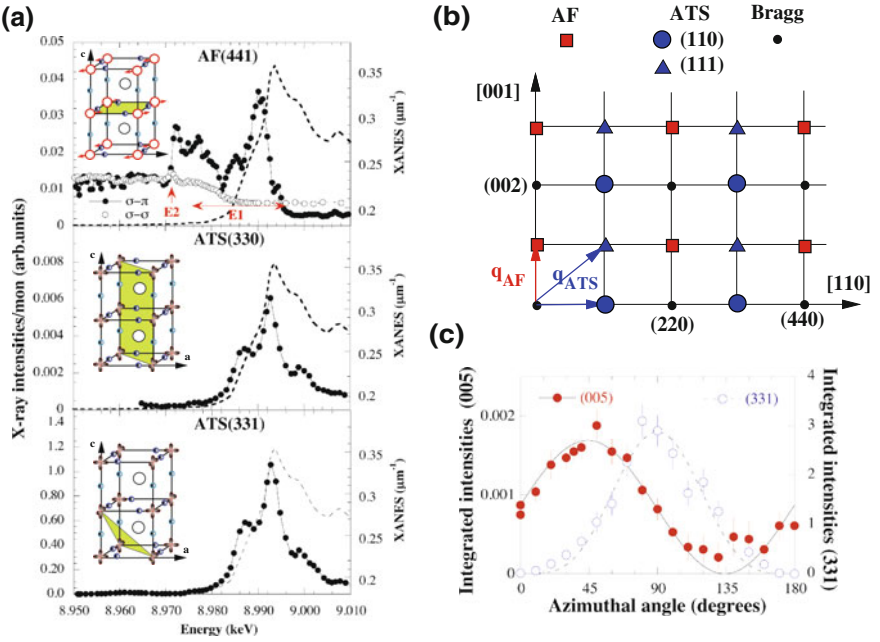


Fig. 12.7 **a** RXS at K-edge of Cu of of the AF reflection (441) (*top panel*) and of the ATS reflections (330) and (331). *Black* (open) symbols refers to $\sigma \rightarrow \pi'$ ($\sigma \rightarrow \sigma'$) polarization channels, and the *dotted line* is the absorption coefficient determined by the fluorescence yield. The insets shows the AF magnetic structure (*top-panel*) and the two orbital structures associated to the twisted and untwisted orbital arrangements. **b** Reciprocal scattering plane with the Bragg (*dots*) AF (*red* symbol) and ATS (*blue* symbols) reflections. **c** Angular dependence of the magnetic (005) and orbital (331) intensities at K-edge E1 resonance and in $\sigma \rightarrow \pi'$ polarisation channel (from [31])

The experiment was performed by tuning the incident energy across the Cu K-absorption edge, and the data were taken at 12 K using LiF(004) analyzer, as shown in Fig. 12.7. Below the absorption edge (i.e. E $\sim$ 8.950 keV), the magnetic reflection (441) show both the $\sigma - \sigma'$ and the $\sigma - \pi'$ contributions, as expected for the the non-resonant X-ray scattering amplitude, discussed in 12.3.1. At the absorption edge, an enhancement of the intensity arise in the polarization channel $\sigma - \pi'$, which is extended over a wide energy region between 8.975 and 9.000 keV. This resonance is attributed to magnetic dipole transitions $F^1(E1 - E1)$, as expected from (12.15), and the polarisation dependence shown in Fig. 12.7-c for the equivalent magnetic reflection (005) confirm this assumption. In contrast, in the pre-edge region (at E = 8.975 keV) a narrow resonance arise in both the polarisation channels, and it is attributed to electric quadrupole transition E2, with a dominant magnetic dipole $F^1(E2 - E2)$ multipole character ([3]). The sensitivity to magnetic order at the quadrupole threshold, $1s - 3d$, has its origin in the spin polarization of the $3d$

[3] The assignment of the correct character is in this case very difficult, because the interference effects with the strong E1 contraibution.

states, whilst at the $1s - 4p$ dipole transition-energy the resonant enhancement for magnetic reflections is due to the $4p - 3d$ intra-atomic Coulomb interaction and to the mixing of the $4p$ with the $3d$ states of neighbouring Cu atoms (see Table 12.1).

New forbidden lattice reflections appears at Cu K-edge at reciprocal lattice position of type (330) and (331), as shown in Fig. 12.7-b. These reflections become permitted due to the a-sphericity of the atomic electron density, giving rise to anomalous tensor susceptibility (ATS) components in the atomic scattering factor. This is due from the difference in $p_{x(y)}$ density of states on the two Cu sublattices, and in an indirect way it indicates an alternate occupation of $3d_{x^2-z^2}$ and $3d_{y^2-z^2}$ Cu^{2+} hole orbitals, attributed to the Jahn–Teller cooperative distortion which remove the orbital (hole) degeneracy. It could be demonstrated from the azimuthal polarisation dependence that they are derived from the electric quadrupole $F^{(2)}(E1 - E1)$. The two propagation vectors $q_{ATS} = [111]$ and $q_{ATS} = [110]$ correspond to an twisted and a untwisted arrangement of orbitals along the c-axis, respectively, as shown in the insets of Fig. 12.7-a. The ratio between the two polytypes vary from different samples, as shown for example for the weak intensity of the (330) in Fig. 12.7-a [51]. Notice that from Fig. 12.7-c the shift of 45° between the two azimuthal curves is a direct proof that the Cu magnetic moments are directed along the [110] direction of the pseudo-cubic cell whilst the main contribution to orbital signal comes from the anisotropy of $p_{x(y)}$ density of states on the two sublattices.

This example shows the basic method applied successful in many strongly correlated electron system to extract information on the magnetic, orbital and charge degree of freedom [52, 53]. However, the correct attribution of the high order multipole to the resonant events could be frustrated by the interference effect between different resonant transitions allowed by symmetry. A special case is reserved to resonant ions lying in a low site symmetry, as shown in the next example.

12.4.2 High Order Multipoles in V_2O_3

V_2O_3 is an archetypical Mott-Hubbard metal insulator [54], whose electronic properties remain elusive despite a large program sustained over several decades of experimental and theoretical studies. In 1978 Castellani et al. [57] proposed a theoretical model that explained the magnetic structure in AFI state from the ordering of V t_{2g} degenerate orbitals. With this example we show the method to extract information from RXS by exploiting all the full polarization analysis and the azimuthal scans, in order to disentangle and characterize the electric and magnetic high order multipoles present in this compound.

At room temperature vanadium sesquioxide crystallises in the α-corundum structure as α-Fe_2O_3 (space group $R\bar{3}c$), which can be described with a pseudo-hexagonal space group (Fig. 12.8-a). The stoichiometric compound V_2O_3 undergoes a strong volume contraction from paramagnetic metal (PM) to antiferromagnetic insulating state (AFI) at $T_N = 150$ K, with a monoclinic first order transition (space group I2/a),

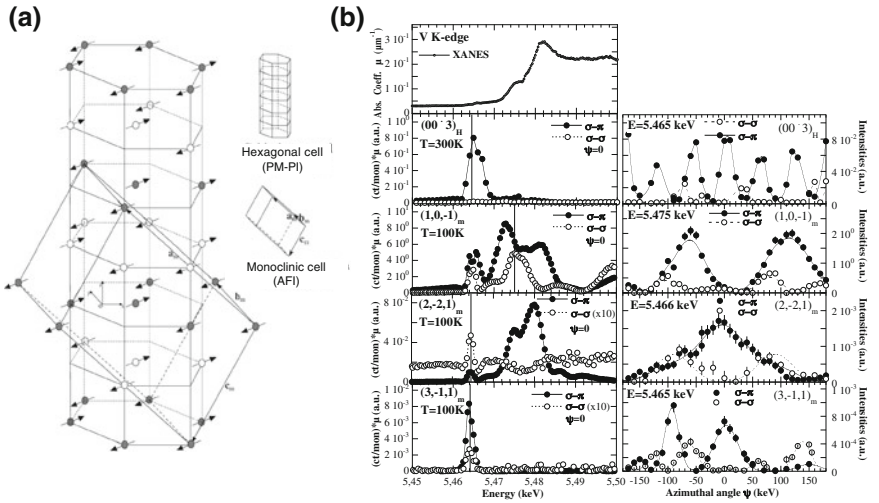


Fig. 12.8 **a** Magnetic structure of V_2O_3 determined by neutron scattering [55]. The pseudo-hexagonal (not primitive) and the monoclinic cells are also indicated. **b** Energy scans of 2.8 % Cr-doped V_2O_3 across the V K-edge (*left*) and the corresponding azimuthal dependence (*right*) of different classes of forbidden lattice reflections found at room temperature (300 K) and in the low-temperature AFI phase (T = 100 K). *Black* (*white*) *dots* refer to the $\sigma \rightarrow \pi'$ ($\sigma \rightarrow \sigma'$) polarization channels. The vertical thin *lines* indicate the photon energy of azimuthal scans (From [63])

and a magnetic structure shown in Fig. 12.8-a [55]. Chromium doping induces a moderate volume contraction from PI to AFI states below $T_N = 180$ K [56].

A general overview of the energy dependence of all the forbidden lattice reflections observed at V K-edge are reported in Fig. 12.8-b as a function of the X-ray polarization and azimuthal dependence. At room temperature forbidden lattice reflections $(00 \cdot l)_H$ with $l = 3(n + 1)$ appear at the V K pre-edge, as shown in Fig. 12.8-b for the reflection $(00 \cdot 3)_H$ (defined in the pseudo-hexagonal setting). These energy scans show well defined resonances in a narrow energy range of about 2 eV around 5.465 keV, with the azimuthal scans showing the 3-fold symmetry. This feature is common to all the Corundum sesquioxides as α-Fe_2O_3 and Cr_2O_3 [41], and these amplitudes have been associated to the $1s \rightarrow 3d$ (electric quadrupole transition E2). the electric dipole E1 transitions $1s \rightarrow 4p$ being forbidden for this class of reflections [13]. A more detailed analysis based on structure factor calculation and multipole expansion showed that they can be attributed to the parity-even and high order multipoles associated to the electric hexadecapole $F^{(4)}$(E2-E2) and to the parity-odd electric octupole $F^{(3+)}$(E1-E2) due to the lack of inversion symmetry at the V-site [65].

In the low-temperature AFI phase, the 3-fold symmetry is lost due to the monoclinic transition and these forbidden reflections split in three monoclinic domains, which could be indexed (in the monoclinic setting) with the Miller indices $(10\bar{1})_m$ [56]. The energy scans show now a dominant contribution due to the electric quadru-

pole $F^{(2+)}$(E1-E1) in a broad energy region of about 20 eV around 5.475 keV, as shown in the second panel of Fig. 12.8-b. The $F^{(4)}$(E2-E2) and $F^{(3+)}$(E1-E2) contribution are also permitted in the pre-edge, but they are strongly affected by the interference effect due to the $F^{(2+)}$(E1-E1) contribution. Notice that in 2.8 % Cr-doped samples weak electric quadrupole contribution exists also at room temperature and increase in intensity by approaching T_N, an indication of a local loss of "corundum" symmetry in favour of a short-range monoclinic precursive symmetry [66]. Open question remain on the role of Cr doping which is responsible for the "moderate" first order transition, destructive in the pure compound, and more in general in the determination of the metal-insulator transition in the paramagnetic phase of V_2O_3.

In the AFI state, two new classes of reflections appear, with the intensities several order of magnitude weaker than the previous one, and associated to the magnetic part of scattering amplitude (i.e. time odd). The first class of reflections are defined by the selection rule $k_m + l_m =$ even and $h_m =$ even, as for example the $(2\bar{2}1)_m$ as shown in Fig. 12.8, and they correspond to the magnetic reflections found also by neutron scattering [55]. In fact the NRXMS intensity is present far from the absorption edge, as we can see from the low energy part of the spectra (i.e. at E = 5.450 keV). The broad resonance observable only in the $\sigma \rightarrow \pi'$ channel is attributed to the magnetic dipole term $F^{(1)}$(E1-E1) and associated to the magnetic polarization of the $4p$ V bands, whereas the pre-edge region contains a resonance centred at E = 5.465 keV which appears in both the polarization channels $\sigma \rightarrow \pi'$ and $\sigma \rightarrow \sigma'$. This last resonance could contains both the time odd and parity even magnetic dipole $F^{(1)}$(E2-E2) and magnetic octupole $F^{(3)}$(E2-E2), but the analysis of the tensorial character of this resonance is complicated by the presence of the strong interference with the dominant magnetic dipole term $F^{(1)}$(E1-E1).

The second class of forbidden lattice reflections, with $k_m + l_m =$ even and $h_m =$ odd are visible only when we tune the incident photon energy around the narrow pre-edge, and shows a particular azimuthal dependence. Because of the selection rules, the (E1-E1) dipole transitions associated to the virtual transitions toward the $4p$ states are forbidden, and only high order multipoles contribute to these class of reflections, as in the case of the $(3\bar{3}1)_m$, where the azimuthal dependence shows a peculiar polarization behaviour on both the polarization channels (Fig. 12.8-b, bottom panel).

The observation of these reflections and their interpretation in term of time-reversal and parity breaking symmetries has opened an intense debate during the last years, acting as a driving force to improve theories and experiments. A set of theoretical models about the AFI ground state of V_2O_3 are based today on a description of a molecular spin state of V ions of spin = 2 [60–62]. Further experiments have been performed to shed light about these RXS forbidden reflections, rising some doubts, based by structure factor calculations, about the possibility that the observed "orbital" reflections could have a magnetic character, i.e. time-odd [63]. Considerations based on the chemical and magnetic space groups, determined previously by neutron diffraction, have lead to a different theoretical interpretations about their physical origin [62, 64, 68]. The advance of calculations and prediction using ab-initio simulations, based on multiple scattering theory and a relativistic extension

of the Schrödinger expansion, combined with new class of experiments, in which more degrees of freedom have been introduced to disentangle the high order multipole resonances, have finally provided a direct evidence of the ordering motif of vanadium magnetoelectric multipoles. From this analysis the expectation values of V magnetoelectric multipoles that are time-odd and parity odd for all the values of their rank could be calculated precisely [69].

The study of these contributions by resonant X-ray diffraction is of fundamental importance in current developments of the electronic structure of materials with complex electronic properties, such as magneto-electricity, piezoelectricity, and ferroelectricity [46]. This work shows the potentialities of RXS to probe directly the multipoles in a crystal with directness of purpose not available with any other experimental method in science of materials.

12.5 Conclusions

The main scientific case for RXS in the hard X-ray regime is focused on measurements of the diffracted intensity of forbidden lattice reflections appearing as a consequence of broken lattice symmetries (magnetic, charge or multipolar), and characterising them in terms of light polarization, angular dependence about the scattering vector (azimuthal dependence), and energy dependence across the absorption edge. The shell and the chemical selectivity of the RXS technique allows to probe directly the 3d and the 4p shells of transition metals (K-edge), the 4f or the 5d shells of lanthanides (L-edges), and the 6d or the 5f shells of actinides (L- and M-edges). The azimuthal dependence is a method which directly probes the symmetries of the tensors involved in resonant scattering amplitudes by measuring the diffracted X-ray linear polarization upon rotating the sample around the scattering vector.

The possibility to control the incident beam polarization by diamond phase plates and to analyze the polarization of the scattered photons as a function of the azimuthal scattering geometry and the incident energy will play an important role in the future development of synchrotron based methods, providing a way to obtain information on the symmetry and the nature of resonances when several multipole excitations close in energy contribute to the same transition.

This technique has been essential in a number of high-profile cases, as for example the orbital and charge ordering in transition metals [71–73, 75, 76], frustrated magnetism in low dimensional magnetic systems [77, 78], multiferroics [79–82], heavy fermion antiferromagnets [83, 84], picnides superconductors [86, 87], magnetic thin films and multilayers [88, 89].

High order multipoles have been detected in actinide compounds [90–93], rare earth compounds [94] and transition metal compounds [67, 95]. The knowledge of the electric and magnetic multipoles of both parities under space-inversion and time-reversal can be of great importance in order to understand the physics of strongly correlated electron systems, and their investigation has been a common theme of research during the last 20 years. In the light of this interpretation, the RXS tech-

nique can be applied to the investigation of many complex materials, such as Mott insulators, colossal magnetoresistive materials, actinides, high-Tc superconductors, multiferroics, heavy fermions and other transition metal oxides, in which orbital or multi-polar hidden order parameters coexist and influence the phase transitions. The separation of the resonant signal in terms of electromagnetic multipoles is, at present, one of the most fashionable ways to classify these experiments and opens new avenues in this research field.

The possibility to exploit the circular polarization for the determination of the non-collinear and incommensurate magnetic structures, is a powerful method which could complement neutron scattering in the determination of complex phase relationship between different magnetic sublattices. Notice that by using the circular polarization the absolute sign of the Dzyaloshinskii-Moriya interaction can be known. Indeed, the possibility to control the helicity of the incident polarization with a polarization rate close to 99 % and to analyse the scattered photon polarization is essential for the determination of the magnetic domain population in chiral systems, and in favorable cases also the absolute phase relationships between different magnetic sublattices. The improvement of X-ray focusing and the high-Q resolution properties of the X-rays could be essential in future developments of this technique to study and to image the magnetic domain evolution under combined external extreme conditions like high magnetic and electric fields, and potentially also high pressure studies.

It is also important to highlight the complementarities of the hard RXS methods with respect to the soft RXS and the absorption spectroscopies, like circular and linear dichroism. The hard X-ray regime, despite the weakness of resonances (for example at K-edges of transition metals), could give access to the investigation of resonant phenomena in different Brillouin zones, exploiting the atomic site selectivity by the structure factor selection rules, a unique way to analyze complex magnetic or electronic long range structures and their evolution through the phase transitions.

References

1. Klein, O., Nishina, Y.: Zeit. Phys. **52**, 853–868 (1929); Nishina, Y., ibid. 869–877
2. Compton, A.H.: Phys. Rev. **50**, 878–881 (1936)
3. M. Gell-Mann, M.J. Goldberger, Phys. Rev. **96**, 1433–1438 (1954)
4. F.E. Low, Phys. Rev. **96**, 1428–1432 (1954)
5. H.A. Tolhoek, Rev. Mod. Phys. **28**, 277–298 (1956)
6. F. de Bergevin, M. Brunel, Phys. Letters **A39**, 141–142 (1972)
7. de Bergevin, F., Brunel, M.: Acta. Cryst. **A37**, 314–331 (1981); ibid. 324–331
8. P.M. Platzman, N. Tzoar, Phys. Rev. B **2**, 3556–3559 (1970)
9. L.K. Templeton, D.H. Templeton, R.P. Phizackerley, K.O. Hodgson, Acta Cryst. **A38**, 74–78 (1982)
10. V.E. Dmitrienko, Acta Cryst. A **39**, 29–35 (1983)
11. K. Namikawa, M. Ando, T. Nakajima, H. Kawata, J. Phys. Soc. Japan **54**, 4099–4102 (1985)
12. B.T. Thole, P. Carra, F. Sette, G. van der Laan, Phys. Rev. Letters **68**, 1943 (1992)
13. P. Carra, B.T. Thole, Rev. Mod. Phys. **66**, 1509–1515 (1994)
14. D. Gibbs, D.R. Harshman, E.D. Isaacs, D.B. McWhan, D. Mills, C. Vettier, Phys. Rev. Letters **61**, 1241–1244 (1988)

15. J.P. Hannon, G.T. Trammel, M. Blume, D. Gibbs, Phys. Rev. Letters **61**, 1245–1248 (1988)
16. L. Paolasini, F. de Bergevin, Compte Rendus Physique **9**, 550–569 (2008)
17. M. Blume, J. Appl. Phys. **57**, 3615–3618 (1985)
18. Blume, M.: Resonant anomalous x-ray scattering. In: Materlik, G., Sparks, J., Fisher, K. (eds.) 495–512. Elsevier Science B.V., Amsterdam (1994)
19. Vettier, C.: J. Elect. Spectr. and Rel. Phen. **117–118**, 113–128 (2001)
20. L. Paolasini, C. Detlefs, C. Mazzoli, S. Wilkins, P. Deen, A. Bombardi, N. Kernavanois, F. de Bergevin, F. Yakhou, J.P. Valade, I. Breslavetz, A. Fondacaro, G. Pepellin, P. Bernard, J. Synchrotron Rad. **14**, 301–312 (2007)
21. D. Gibbs, M. Blume, D.R. Harshman, D.B. McWhan, Rev. Sci. Instrum **60**, 1655 (1989)
22. R.C. Jones, J. Opt. Soc. Am. **31**, 488493 (1941)
23. P. Skalicky, C. Malgrange, Acta Cryst. A **28**, 501 (1972)
24. Giles, C., Malgrange, C., Goulon, J., de Bergevin, F., Vettier, C., Dartyge, E., Fontaine, A., Giogetti, C., Pizzini S.: J. Appl. Cryst. **27**, 232–240 (1994)
25. V. Scagnoli, C. Mazzoli, C. Detlefs, P. Bernard, A. Fondacaro, L. Paolasini, F. Fabrizi, F. de Bergevin, J. Synchrotron Radiat. **16**, 778–787 (2009)
26. M. Blume, D. Gibbs, Phys. Rev. B **37**, 1779–1789 (1988)
27. V. Fernandez, C. Vettier, F. de Bergevin, C. Giles, W. Neubeck, Phys. Rev. B **57**, 7870–7876 (1998)
28. Neubeck, W., Vettier, C., de Bergevin, F., Yakhou, F., Mannix, D., Ranno, L., Chatterji, T.: J. Phys. Chem. Solids **62**, 2173–2180 (2001)
29. L. Paolasini, C. Vettier, F. de Bergevin, F. Yakhou, D. Mannix, A. Stunault, W. Neubeck, M. Altarelli, M. Fabrizio, P.A. Metcalf, J.M. Honig, Phys. Rev. Letters **82**, 4719–4722 (1999)
30. S.L. Langridge, G.H. Lander, N. Bernhoeft, A. Stunault, C. Vettier, G. Grübel, C. Sutter, F. de Bergevin, W.J. Nuttall, W.G. Stirling, K. Mattenberger, O. Vogt, Phys. Rev. B **55**, 6392–6398 (1997)
31. Caciuffo, R., Paolasini, L., Sollier, A., Ghigna, P., Pavarini, E., van der Brink, J., Altarelli, M.: Phys. Rev. B **65**, 174425(1–9) (2002)
32. T. Kimura, T. Goto, H. Shintani, K. Ishizaka, T. Arima, Y. Tokura, Nature **426**, 55 (2003)
33. H. Katsura, N. Nagaosa, A.V. Balatsky, Phys. Rev. Letters **95**, 057205 (2005)
34. M. Mostovoy, Phys. Rev. Letters **96**, 067601 (2006)
35. F. Fabrizi, H.C. Walker, L. Paolasini, F. de Bergevin, T. Fennel, N. Rogado, R.J. Cava, Th Wolf, M. Kenzelmann, D.F. McMorrow, Phys. Rev. B **82**, 024434 (2010)
36. G. Lawes, A.B. Harris, T. Kimura, N. Rogado, R.J. Cava, A. Aharony, O. Entin-Wohlman, T. Yildirim, M. Kenzelmann, C. Broholm, A.P. Ramirez, Phys. Rev. Letters **95**, 087205 (2005)
37. M. Kenzelmann, A.B. Harris, A. Aharony, O. Entin-Wohlman, T. Yildirim, Q. Huang, S. Park, G. Lawes, C. Broholm, N. Rogado, R.J. Cava, K.H. Kim, G. Jorge, A.P. Ramirez, Phys. Rev. B **74**, 014429 (2006)
38. Altarelli, M.: Resonant x-ray scattering: a theoretical introduction. Lect. Notes Phys. Springer **697**, 201 (2006)
39. S. Loversey, E. Balcar, K.S. Knight, J. Fernández-Rodríguez, Phys. Rep. **411**, 233–289 (2005)
40. S. Di Matteo, J. Phys. D: Appl. Phys. **45**, 163001 (2012)
41. K.D. Finkelstein, Q. Shen, S. Shastri, Phys. Rev. Letters **69**, 1612–1615 (1992)
42. Fano, U., Rau, A.R.P.: in "*Symmetry in Quantum Physics*" (Academic press, London, 1996), ISBN 0-12-248455. Phys. Rep. **187** 145-202 (1990)
43. Di Matteo, S., Joly, Y., Natoli, C.R.: Phys. Rev. B **72** 144406(1–6)(2005)
44. Marri, I., Carra P.: Phys. Rev. B **69**, 113101(1–4) (2004)
45. S.W. Lovesey, E. Balcar, K.S. Knight, J. Fernándes-Rodriguez, Phys. Rep. **411**, 233 (2005)
46. Lovesey, S.W., Balcar, E.: J. Phys. Soc. Japan **79**, 104702 (2010)
47. Hill, J., McMorrow, D.: Acta Cryst. A **52** 236–244 (1996)
48. J.B. Goodenough, *Magnetism and Chemical Bond* (Interscience, New York, 1963)
49. Kugel', K.I., Khomskii, D.I.: Zh. Eksp. Teor. Fiz. **64**, 1429 (1973); [Sov. Phys. JEPT **37** 725 (1973)]
50. Kugel', K.I., Khomskii, D.I.: Usp. Fiz. Nauk **136**, 1982 (1982); [Sov. Phys. Usp. **25** 231 (1982)]

51. M.T. Hutchings, E.J. Samuelsen, G. Shirane, K. Hirakawa, Phys. Rev. **188**, 919–923 (1969)
52. Y. Murakami, H. Kawada, H. Kawata, M. Tanaka, T. Arima, Y. Moritomo, Y. Tokura, Phys. Rev. Letters **80**, 1932–1935 (1998)
53. L. Paolasini, R. Caciuffo, A. Sollier, P. Ghigna, M. Altarelli, Phys. Rev. Letters **88**, 106403 (2002)
54. N.F. Mott, *Metal Insulator Transitions* (Taylor and Francis, London, 1974)
55. R.M. Moon, Phys. Rev. Letters **25**, 527–529 (1970)
56. D.B. McWhan, J.P. Remeika, Phys. Rev. B **2**, 3734 (1970)
57. C. Castellani, C.R. Natoli, J. Ranninger, Phys. Rev. B **18**, 4967 (1978)
58. M. Fabrizio, M. Altarelli, M. Benfatto, Phys. Rev. Letters **80**, 3400 (1998)
59. Park, J.-H., Tjeng, L.H., Tanaka, A., Allen, J.W., Chen, C.T., Metcalf, P., Honig, J.M., de Groot, F., Sawatzky, G.A.: Phys. Rev. B **61**, 11506 (2000)
60. Mila, F., Shiina, R., Zhang, F.-C., Joshi, A., Ma, M., Anisimov, V., Rice, T.M.: Phys. Rev. Letters **85**, 1714 (2000)
61. S. Di Matteo, N.B. Perkins, C.R. Natoli, Phys. Rev. B **65**, 054413 (2002)
62. A. Tanaka, J. Phys. Soc. Japan **71**, 1091 (2002)
63. L. Paolasini, S. Di Matteo, C. Vettier, F. de Bergevin, A. Sollier, W. Neubeck, F. Yakhou, P.A. Metcalf, J.M. Honig, J. Elect. Spectr. Rel. Phen. **120**, 1–10 (2001)
64. S.W. Lovesey, K.S. Knight, D.S. Sivia, Phys. Rev. B **65**, 224402 (2002)
65. Di Matteo, S., Joly, Y., Bombardi, A., Paolasini, L., de Bergevin, F., Natoli, C.R.: Phys. Rev. Letters **91** 257402(1–4) (2003)
66. A. Bombardi, F. de Bergevin, S. Di Matteo, L. Paolasini, Phys. B **345**, 40–44 (2004)
67. Mazzoli, C., Wilkins, S. B., Di Matteo, S., Detlefs, B., Detlefs, C., Scagnoli, V., Paolasini, L., Ghigna, P.: Phys. Rev. B **76**, 195118(1–6) (2007)
68. S. Loversey, J. Fernandez-Rodriguez, J.A. Blanco, D.S. Sivia, K.S. Knight, L. Paolasini, Phys. Rev. B **75**, 014409 (2007)
69. Fernández-Rodríguez, J., Scagnoli, V., Mazzoli, C., Fabrizi, F., Lovesey, S. W., Blanco, J.A., Sivia, D.S., Knight, K.S., de Bergevin, F., Paolasini, L.: Phys. Rev. B **81**, 085107(1–7) (2010)
70. Staub, U., Meijer, G.I., Fauth, F., Allenspach, R., Bednorz, G., Karpinski, J., Kazakov, S., Paolasini, L., dAcapito, F.: Phys. Rev. Letters **88**, 126402 (2002)
71. Fagot, S., Foury-Leylekian, P., Ravy, S., Pouget, J.P., Lorenzo, E., Joly, Y., Greenblatt, M., Lobanov, M.V., Popov, G.: Phys. Rev. B **73**, 033102(1–4) (2006)
72. Lorenzo, J.E., Mazzoli, C., Jaouen, N., Detlefs, C., Mannix, D., Grenier, S., Joly, Y., Marin, C.: Phys. Rev. Letters **101**, 226401(1–4) (2008)
73. M. García-Fernández, V. Scagnoli, U. Staub, A.M. Mulders, M. Janousch, Y. Bodenthin, D. Meister, B.D. Patterson, A. Mirone, Y. Tanaka, T. Nakamura, S. Grenier, Y. Huang, K. Conder, Phys. Rev. B **78**, 054424 (2008)
74. García, J., Subías, G., Herrero-Martín, J., Blasco, J., Cuartero, V., Sánchez, M.C., Mazzoli, C., Yakhou F.: Phys. Rev. Letters **102**, 176405(1–4) (2009)
75. A.M. Mulders, S.M. Lawrence, U. Staub, M. García-Fernández, V. Scagnoli, C. Mazzoli, E. Pomjakushina, K. Conder, Y. Wang, Phys. Rev. Letters **103**, 077602 (2009)
76. S.R. Bland, M. Angst, S. Adiga, V. Scagnoli, R.D. Johnson, J. Herrero-Martin, P. Hatton, Phys. Rev. B **82**, 115110 (2010)
77. A. Bombardi, J. Rodriguez-Carvajal, S. Di Matteo, F. De Bergevin, L. Paolasini, P. Carretta, P. Millet, R. Caciuffo, Phys. Rev. Letters **93**, 027202 (2004)
78. Agrestini, S., Mazzoli, C., Bombardi, A., Lees, M.R.: Phys. Rev. B **77**, 140403(1–4) (2008)
79. Fabrizi, F., Walker, H.C., Paolasini, L., de Bergevin, F., Boothroyd, A.T., Prabhakaran, D., McMorrow, D.F.: Phys. Rev. Letters **102**, 237205(1–4) (2009)
80. Mannix, D., McMorrow, D.F., Ewings, R.A., Boothroyd, A.T., Prabhakaran, D., Joly, Y., Janousová, B., Mazzoli, C., Paolasini, L., Wilkins, S.B.: Phys. Rev. B **76**, 184420(1–17) (2007)
81. H.C. Walker, F. Fabrizi, L. Paolasini, F. de Bergevin, J. Herrero-Martin, A.T. Boothroyd, D. Prabhakaran, D.F. McMorrow, Science **333**, 1273–1276 (2011)
82. Johnson, R.D., Bland, S.R., Mazzoli, C., Beale, T.A.W., Du, C.H., Detlefs C., Wilkins, S.B., Hatton, P.D.: Phys. Rev. B **78**, 104407(1–9) (2008)

83. C. Adriano, R. Lora-Serrano, C. Giles, F. de Bergevin, J.C. Lang, G. Srajer, C. Mazzoli, L. Paolasini, P.G. Pagliuso, Phys. Rev. B **76**, 104515 (2007)
84. C. Adriano, C. Giles, E.M. Bittar, L.N. Coelho, F. de Bergevin, C. Mazzoli, L. Paolasini, W. Ratcli, R. Bindel, J.W. Lynn, Z. Fisk, P.G. Pagliuso, Phys. Rev. B **81**, 245115 (2010)
85. Herrero-Martín, J., Scagnoli, V., Mazzoli, C., Su, Y., Mittal, R., Xiao, Y., Brueckel, T., Kumar, N., Dhar, S.K., Thamizhavel, A., Paolasini, L.: Phys. Rev. B **80**, 134411(1–5) (2009)
86. S. Nandi, Y. Su, Y. Xiao, S. Price, X.F. Wang, X.H. Chen, J. Herrero-Martín, C. Mazzoli, H.C. Walker, L. Paolasini, S. Francoual, D.K. Shukla, J. Strempfer, T. Chatterji, C.M.N. Kumar, R. Mittal, H.M. Ronnow, Ch. Ruegg, D.F. McMorrow, Th Bruckel, Phys. Rev. B. **84**, 054419 (2011)
87. J. Herrero-Martín, C. Mazzoli, V. Scagnoli, L. Paolasini, H. Walker, Y. Xiao, T. Brueckel, R. Mittal, N. Kumar, S.K. Dhar, A. Thamizhavel, Y. Su, J. Supercond. Nov. Magn. **24**, 705 (2011)
88. E. Kravtsov, R. Brucas, B. Hjörvarsson, A. Hoser, A. Liebig, G.J. McIntyre, M.A. Miliyaev, A. Nefedov, L. Paolasini, F. Radu, A. Remhof, V.V. Ustinov, F. Yakhou, H. Zabel, Phys. Rev. B **76**, 024421 (2007)
89. P.P. Deen, F. Yokaichiya, L. Paolasini, S. Lee, A. de Santis, F. Bobba, A.M. Cucolo, J. Magn. Magn. Mater. **310**, 2286–2288 (2007)
90. Wilkins, S.B., Caciuffo, R., Detlefs, C., Rebizant, J., Colineau, E., Wastin, F., Lander, G. H.: Phys. Rev. B **73**, 060406(1–10) (2006)
91. Detlefs, B., Wilkins, S.B., Javorsky, P., Blackburn, E., Lander, G.H.: Phys. Rev. B **75**, 174403(1–6) (2007)
92. Detlefs, B., Wilkins, S.B., Caciuffo, R., Paixão, J.A., Kaneko, K., Honda, F., Metoki, N., Bernhoeft, N., Rebizant, J., Lander, G.H.: Phys. Rev. B **77**, 024425(1–10) (2008)
93. P. Santini, S. Carretta, G. Amoretti, R. Caciuffo, N. Magnani, G.H. Lander, Rev. Mod. Phys. **81**, 807–863 (2009)
94. O. Bunáu, R.M. Galéra, Y. Joly, M. Amara, S.E. Luca, C. Detlefs, Phys. Rev. B **81**, 144402 (2010)
95. Bombardi, A., Mazzoli, C., Agrestini, S., Lees, M.R.: Phys. Rev. B **78**, 100406(1–4) (2008)

Chapter 13
Hard X-Ray Synchrotron Imaging Techniques and Applications

Jean-Yves Buffiere and José Baruchel

Abstract The features associated with modern Synchrotron Radiation (SR) machines (intense and coherent beams) result in a substantial extension of X-ray imaging capabilities in terms of spatial and temporal resolution, phase contrast, 3D images and combination of techniques. We describe some of the two and three-dimensional SR based imaging techniques, with emphasis on absorption, phase contrast and Bragg diffraction based imaging. In the last section selected examples illustrate the capabilities of these constantly evolving methods.

13.1 Introduction

A Synchrotron Radiation (SR) study of a sample involves using the adequate X-ray techniques (diffraction, absorption, scattering, ...) to extract the wished information. A very usual additional assumption is that the sample is homogeneous, and that by illuminating the whole volume the result corresponds to the one we could measure locally. This assumption is, of course, not valid when dealing with an inhomogeneous sample: in this case we need to use an "imaging" type approach, i.e. to measure "locally" to produce a map where each of these "local" measurements corresponds to an homogeneous area. The required size of the pixel for the "local" measurement is a function of size of the inhomogeneities. The "image" obtained from the ensemble of local measurements exhibits contrast, defined as the difference in detected signal that makes a feature distinguishable. The maximum *contrast* of an image is the contrast ratio or dynamic range.

J.-Y. Buffiere (✉)
INSA Lyon, 20 avenue Albert Einstein, 69621 Villeurbanne, France
e-mail: Jean-yves.buffiere@insa-lyon.fr

J. Baruchel
European Synchrotron Radiation Facility, BP 220, 38043 Grenoble Cedex, France
e-mail: baruchel@esrf.fr

S. Mobilio et al. (eds.), *Synchrotron Radiation*,
DOI: 10.1007/978-3-642-55315-8_13, © Springer-Verlag Berlin Heidelberg 2015

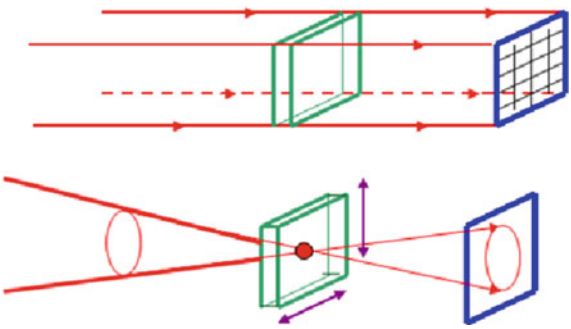


Fig. 13.1 "Parallel" beam and "focussed" beam imaging schemes (*see text*)

Two main experimental schemes, shown on Fig. 13.1, allow these "local" measurements to be performed: (a) a parallel beam is used together with a pixelated detector, in such a way that each pixel corresponds to a given volume in the sample, and the spatial resolution of the image associated with the pixel size (lensless technique).

(b) the beam is focused on a given region of the sample, which is scanned in order to obtain a series of "local" measurements on these regions, the spatial resolution being associated with their size (X-ray lenses are required in this case).

For all imaging techniques, the recorded/observed image results from a convolution of the signal emerging from the sample and the detector characteristics. The observed size feature is a function of its physical size within the X-ray beam exiting the sample and the point spread function of the detector; it also depends on the statistical or instrumental noise, the geometry, …. Whereas X-ray imaging detectors [1] are beyond the scope of the present paper, and will not be mentioned below, we wish to point out that this is a very important aspect, which should not be neglected when extracting information from an image.

X-ray imaging started over a century ago, with the discovery of X-rays, allowing the visualization of the volume of systems opaque to other probes. It was immediately noticed that these radiographs, which exploited the variation of the absorption of the beam when going through the sample, constituted an important tool for medical diagnostic. This led, during the First World War, at the initiative of Marie Curie, to have cars fitted with X-ray generators (their popular name being "petites Curies") to be present in the neighbourhood of the battlefield to provide a quick diagnostic helping saving lives. The applications of radiography to materials were also rapidly developed.

For several decades, absorption radiography remained the only form of X-ray imaging. About 50 years ago, Bragg diffraction imaging developed into practical use. This "diffraction topographic" approach apply to single crystals and basically consist of mapping the intensity and direction of the locally Bragg diffracted beams. It reveals defects in the bulk of single crystals, and helped to develop production of large, practically perfect crystals, for the microelectronics industry. These techniques extended beyond semiconductor crystals, and are useful for investigating induced or

growth defects and distortions. Their range of applications dramatically grew when SR became available to condensed matter scientists.

A major breakthrough was performed when the computing improvements allowed producing three-dimensional (3D) images from a series of radiographs recorded at different angles ("tomography").

All the X-ray imaging methods benefited from the use of SR, the improvements being even more pronounced when considering the new features of modern, "third generation", SR machines. Real time and high spatial resolution experiments are nowadays routinely performed, and the high coherence of the beam allows exploitation of a novel form of radiography, in which contrast arises not only from absorption differences but also from phase variations across the transmitted beam. Several forms of phase contrast imaging developed over the last years. When the detector is located far from the sample (Fraunhofer regime) Coherent Diffraction Imaging (CDI) and, recently, ptychographic CDI, allow, from the recorded patterns, to reconstruct with very high resolution the local phase shift, and, consequently, the local sample density. Microradiography and its three-dimensional companion, phase microtomography, provide useful information on crystal growth-related features (porosities, inclusions, dendritic growth, ...). The spatial resolution of these two or three-dimensional "parallel beam" imaging techniques is now, routinely, in the μm range.

The highly brilliant sources of the modern SR facilities, coupled with new X-ray optics, allowed micro-beams in the μm or sub-μm range to be achieved. This leads to another type of images through the use of X-ray microbeam-based scanning approaches, probing for instance the fluorescence or the absorption near the absorption edges. In addition new devices under constant enhancement, allow nano-imaging to be performed, with a spatial resolution presently around 50 nm.

This brief introduction indicates that nearly all X-ray-matter type of interactions can be exploited within the frame of what we called "imaging approach", i.e. a set of "local" measurements constituting a map or image. In the present paper we focus on images resulting from variations of absorption, phase, or Bragg diffraction, in their two- or three-dimensional ("microtomographic") forms.

13.2 Imaging Techniques

13.2.1 Absorption Radiography

The interaction of X-rays with matter can be expressed through the complex refractive index

$$n = 1 - \delta + i\beta \tag{13.1}$$

that describes both the absorption (β) and the phase change (δ) with respect to a path in vacuum. The absorption of X-rays is usually described by the absorption

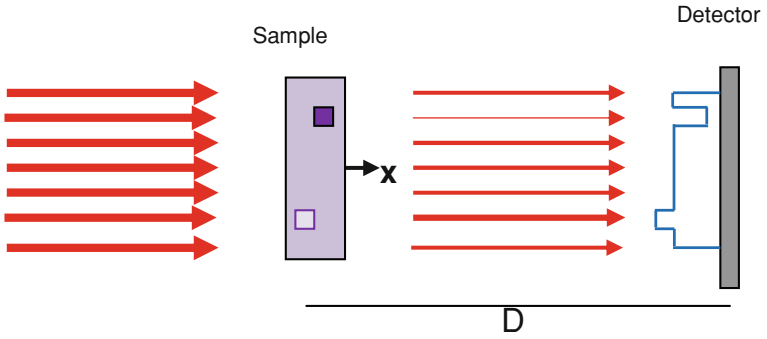


Fig. 13.2 Transmission imaging (radiography): the contrast mechanism can be absorption or, when dealing with a coherent beam, phase

coefficient μ, such that the number of photons N after transmission through the sample, with N_0 being the number of photons in the incident beam, may be written as:

$$\ln(N_0(x,z)/N(x,z)) = \int_{path} \mu(x,y,z)dx \tag{13.2}$$

The absorption coefficient μ is related to β through the simple expression $\beta = \lambda\mu/4\pi$, where λ is the X-ray wavelength.

X-ray absorption imaging consists in detecting the photons transmitted through the investigated sample (Fig. 13.2). The "experimental data" are the **contrast** that results from the inhomogeneous response of the sample. When a two dimensional detector (film, CCD camera) is used, this directly produces a map of the integral of μ(x,y,z), the linear attenuation coefficient, along the X-ray path, as indicated in (13.2).

The behaviour of the linear attenuation coefficient μ is dominated by the photoelectric effect for X-ray energies E below 200 keV. μ is in this case proportional to $\rho\ Z^4\ E^{-3}$ Where ρ is the material density and Z is the atomic number. The separation between Z and ρ implies performing experiments using at least two energies. Above 200 keV, the Compton effect is predominant and the above proportionality is not valid.

The absorption-related coefficient β changes abruptly with the energy of the photons at an absorption edge. The absorption edges are element-specific, and the logarithmic subtraction of images recorded above and below the edge enhances the visibility of the distribution of the element considered. It is also possible, by tuning the energy of the probing photons on the high absorption side of the edge, to take advantage of the oscillations of the absorption curve (XANES). These oscillations reflect the molecular environment of a given atom and provide the basic mechanism for imaging with chemical sensitivity.

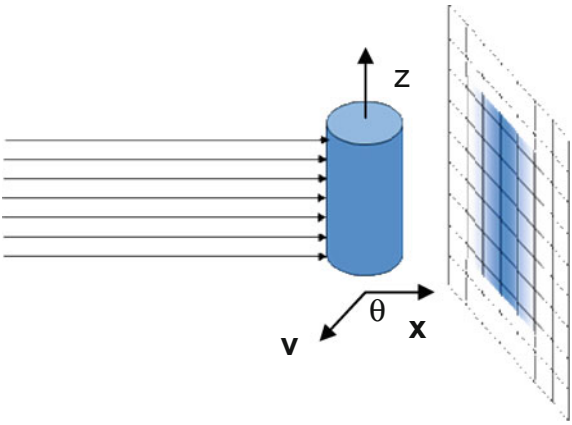


Fig. 13.3 An image of the volume can be obtained by rotating the sample in the beam, around a vertical axis **z**, recording a series of radiographs on a 2D detector, and using a reconstruction software to obtain the 3D image ("tomography")

13.2.2 Microtomography

The radiography of an object displays the resolution associated to the detector in the plane of this detector, but no depth resolution is achieved (Fig. 13.3). To recover the resolution in the depth direction, particularly important for a thick sample, several radiographs can be recorded at different angular positions of the sample with respect to the incoming beam, this sample being rotated, in the case of the figure, around a vertical axis located in its center.

This is the main idea of computer-assisted tomography, which provides the three-dimensional (3D) absorption image of a bulky object from the two-dimensional (2D) images (radiographs) recorded at various angular positions of the object, processed using appropriate algorithms and software. From the reconstructed 3D data any virtual slice, or perspective renditions, of the object can be obtained.

Microtomography, with a spatial resolution better than 20 μm, has been developed over recent years [2]. Several laboratory instruments using micro-sources providing a polychromatic cone beam are now commercially available, and reach spatial resolutions of ≈2–20 μm. However, the best quality images, in terms of signal-to-noise ratio and spatial resolution, are obtained on instruments located in SR facilities. The present text will discuss the SR-based technique.

Figure 13.3 corresponds to the scheme of the most commonly used SR-based tomographic acquisition. As the source is small (∼30 μm) and far away (∼100 m) the beam (monochromatic, with $\Delta E/E \approx 10^{-2}$–$10^{-4}$, or "pink", i.e. filtered white beam) can be considered as parallel. This "parallel beam" approach implies that no magnification is obtained, and the spatial resolution mainly results from the effective pixel size of the detector. But this configuration exhibits the advantage that all the radiographs, recorded on the 2D detector, obtained by rotation of the sample about **z,** are such that each slice, at a given height z, is independent of the other slices. A radiograph (or ≪ projection ≫) corresponds to a given angle θ, formed (Fig. 13.3) by the axes **x** (direction of the X-ray beam) and **v** (in the (**u**,**v**,**z**) sample frame of reference).

Equation (13.2) can be rewritten, in this case, as a series of integrals (the projections $p_\theta(y,z)$), with **y** perpendicular to **x** and **z** and y = 0 on the rotation axis

$$p_\theta(y,z) = \ln\left[N_0(y,z)/N_\theta(y,z)\right] = \int_{path} \mu\left[u(x,y,\theta), v(x,y,\theta), z\right] dx \quad (13.3)$$

In parallel geometry, $p_\theta(y,z) = p_{\theta+\pi}(-y,z)$, meaning that the acquisition of projections over a range $[0,\pi]$ is sufficient. For a given z the ensemble $\{p_\theta(y,z), \theta \in [0,\pi]\}$ constitutes the Radon transform (or "sinogram") of the 2D slice. The inverse transform provides the $\mu(u,v)$ map of the slice. The 3D problem reduces, in parallel geometry, to a sequence of 2D calculations. Let us note that this is not the case for laboratory tomographs, which produce a conical beam.

Several reconstruction algorithms, such as the filtered back-projection (FBP) or the algebraic reconstruction techniques (ART), have been developed. Their mathematical description is beyond the scope of the present paper, but can be found in [3, 4]. The commonly used reconstruction algorithm is FBP, because it provides a better ratio of "image quality/calculation time": the inverse problem can be solved by firstly correcting the projections by a filter $H(f) = f, f$ being the spatial frequency, and then by performing a back-projection procedure.

13.2.3 Phase Imaging

The refractive index of materials (13.1) deviates slightly from unity through a decrement δ, which is in the 10^{-5}–10^{-6} range. δ is proportional to the electronic density in the material, hence to its mass density; it involves a dispersion correction when the photon energy is near an absorption edge. Far from absorption edges, it can be written as:

$$\delta = (\lambda^2 r_0/2\pi V)\sum_j N_j Z_j \quad (13.4)$$

where r_0 is the classical electron radius (=2.82 fm), and N_j is the number of atoms of atomic number Z_j present in the volume V.

The passage of an X-ray beam through a sample entails a phase shift

$$\phi(x,y) = (2\pi/\lambda)\int_{path} \delta(x,y,z)dx \quad (13.5)$$

This phase shift is variable over the cross-section of the beam if the beam has passed through a sample with inhomogeneous thickness and/or density. This can produce an image if this **"local"** variation of the phase shift can be observed through interference

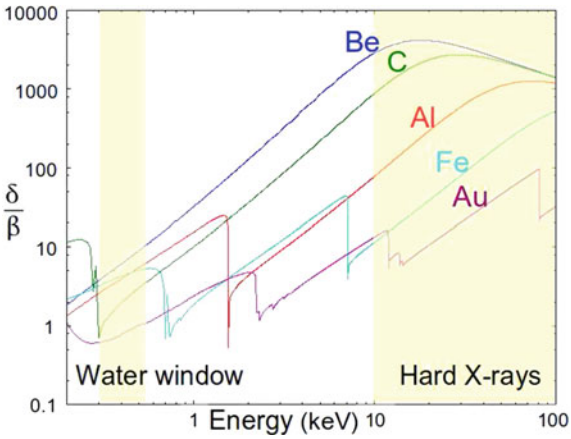


Fig. 13.4 Some ratios δ/β, as a function of the X-ray energy: $\delta/\beta > 10$ (10–100 keV)

phenomena. This requires that the waves scattered by different regions of the sample display well correlated phases, i.e. that the "coherence length" of the incoming beam is large enough. Similarly, the classical "Young's holes" experiment in visible optics only produces interferences if the holes are closer than the lateral coherence length $L_c = \lambda/2\alpha$, where λ is the wavelength and α is the angular size of the source as seen from a point in the specimen. The X-ray beams produced at modern SR facilities exhibit a high degree of coherence, α being in the μ radian range, leading to $L_c \sim 100\,\mu$m ($\lambda = 1$ Å) at long beamlines (100–200 m) like ID19 or ID16 at the ESRF.

Phase images were obtained in the past using rather complex apparatus (systems involving several crystals). The qualitatively new aspect of modern SR beams is that they make it possible to reveal, through the "propagation" technique, with a reasonable instrumental simplicity, the phase variations of hard X-rays. As indicated above, the local phase variations can be changed into intensity variations through the interference of parts of the beam that undergo different phase shifts, but are mutually coherent. It can be described either in terms of Fraunhofer diffraction, when the distance D between sample and detector is large enough to apply the "far field" approximation, or in terms of Fresnel diffraction, when D is smaller. We will briefly describe below the X-ray imaging techniques developed for these configurations.

But let first point out that the great advantage of this new type of imagery is the increased sensitivity it provides. Figure 13.4 shows that δ ($\sim 10^{-5}$–10^{-6}) >> β ($\sim 10^{-9}$–10^{-11}) in the hard X-ray range (E > 6 keV). Indeed a thickness variation of $\sim$1–5 μm, for instance associated with a "cavity" within the material, only involves a very small, usually not detectable, variation of absorption, but can be associated with a phase shift of the order of π, easy to detect. This increased sensitivity allows visualization of tiny objects such as cracks, micro-pipes, μm sized pores, or regions exhibiting even a weak (1 %) density variation with respect to the matrix.

13.2.3.1 Fraunhofer Regime: CDI, Ptychography

Measured in the far field ($D \rightarrow \infty$, Fraunhofer regime), the intensity distribution of coherent light scattered by a specimen is related by a Fourier transform to the wave field directly past the specimen. These wave field variations are related to the local variations of the index of refraction integrated along the X-ray path within the sample. This means that, by selecting a coherent fraction of the incoming monochromatic "partially-coherent" synchrotron beam (for instance by setting slits that reduce the beam to a size smaller than the lateral coherence length), and using it to illuminate a sample, we are able to collect on a detector located in the far field a diffraction pattern allowing, in principle, through a inverse Fourier transform, reaching the electronic density of the sample (Fig. 13.5). However only intensities are measured, and additional analytical means are needed to retrieve the phase-related information. This phase retrieval is performed through iterative feedback algorithms that constitute a crucial ingredient of the technique known as X-ray Coherent Diffraction Imaging (CDI). These algorithms "replace" the objective lens of a typical microscope and allow recovering the local phase introduced by the sample, and, as a consequence, producing a high resolution real space image of this sample [5, 6]. It is clear that the wavefront at the exit side of the sample also incorporates the departures from the plane wave regime of the incident beam: CDI therefore usually requires a well prepared planar wavefront that completely illuminates an isolated sample. Very interesting results have been achieved, in 2D and in 3D, by combining CDI and tomography.

Most of the iterative feedback algorithms are based on the idea of "oversampling", i.e. Shannon's theorem, which states that if the diffraction pattern is sampled at twice the Nyquist frequency (inverse of sample size) or lower, it can yield a unique real space image [7]. This idea, coupled with the dramatic increase in computing power over the last decades, allowed the design of phase retrieval algorithms [8]. Random phases are initially combined with the amplitude information, a Fourier transform being then applied back and forth. During this process constraints (one of them being, in real space, the "support", which restricts the resulting image to a confined space, the volume where the sample stands) are set in such a way that the result evolves into an image, by performing enough (typically hundreds to thousands) iterations. This led to the first demonstration of CDI [5].

The phase retrieval algorithms are under constant evolution, gradually solving the initially encountered problems on the convergence or non-unicity of the resulting image. Different implementations of CDI have been proposed [9–12], which extend the capabilities. Let us note that whereas CDI geometry may appear rather restrictive from a general perspective, it can be naturally implemented in the case of samples illuminated by a X-FEL beam (with specimens investigated by a single pulse per sample in a 'diffract and destroy' manner), and therefore these techniques exhibit a clear potential for the near future.

The combination of CDI with "ptychography", a phase retrieval method proposed in the 1960s for electron microscopy, allowed to substantially enhance the capabilities of these far-field pattern based phase retrieval techniques [13]. Indeed, phases can be determined from far field intensity data when the sample is scanned, with

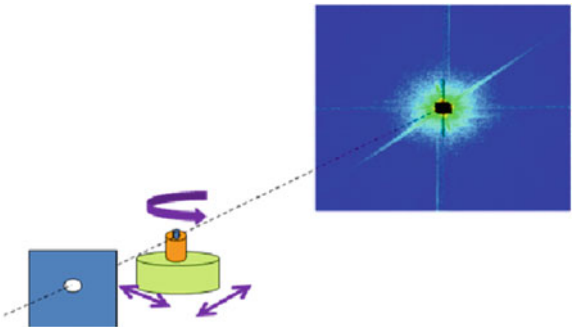


Fig. 13.5 Scheme of Fraunhofer-type phase contrast imaging: the incoming beam is reduced to a size smaller than the coherence length. The sample-to-detector distance is such that the Fraunhofer approximation is fulfilled. The scattered beam allows retrieving, with the help of adapted iterative algorithms, the phase locally introduced by the sample. If the sample is bigger than the beam size, a translation with a step smaller than the beam size is used (ptychography) to produce the phase image. An additional rotation of the sample is necessary when wishing a 3D, tomographic, phase image

a coherent beam and overlapping regions. It has been shown in recent years that this "ptychographic CDI", where the coherent beam is translated laterally in steps smaller than the beam size, and the ensemble of patterns scattered by the sample are recorded in the far field, can greatly improve the convergence rates of iterative reconstruction schemes. This approach which is now usually called "ptychography", allows strongly relaxing the demands and the required pre-knowledge on the illuminating wavefield that were required for the CDI single-image techniques. When applying ptychography the lateral extension of the sample may be much larger than the size of the illumination. In addition the incident wave can substantially depart from an ideal spherical or planar wavefront. As various parts of the sample are illuminated multiple times allows the reconstruction of both illumination and object in parallel [13–16].

13.2.3.2 Fresnel Regime

When the sample is illuminated by a large, parallel, partially coherent beam, and the detector is not set in the far field, but at an intermediate distance D (typically a few 10^{-1} m) from the specimen (Fresnel regime) another type of phase-sensitive image is obtained. An absorption image is obtained if D is small (10^{-3} m range). This corresponds to the fact that the region in the sample that effectively determines the image at a point of the detector, the first Fresnel zone, has a size $r_F = (D\,\lambda)^{1/2}$. When D is in the mm range, the separation of the fringes originating from an area r_F is below the resolution of the detector (μm range), and no interference will be observed, hence the image will be purely due to absorption. For D larger, but such that r_F remains smaller than the size τ of the object to be imaged, the edges of the

image behave independently, and provide the only phase contribution to the image. For D even larger, interference fringes built up. The best sensitivity for an object with size τ is obtained for $D \approx \tau^2/2\lambda$.

Phase variations across the beam exiting the sample lead to variations in intensity, hence to contrast, provided the phase has a two-dimension Laplacian $\nabla^2\phi(y, z) \neq 0$. They show up, for increasing distance D, first through the appearance of a black-white line at the phase discontinuities ("edge enhancement"), then a more and more obtrusive Fresnel fringe system ("holography") which progressively changes towards the Fraunhofer regime [17, 18].

Phase imaging based on the visualization of the edges is very useful to show, qualitatively, relevant features present in the sample like inclusions, holes, or fractures. But it is not a quantitative technique, and its spatial resolution is limited by the occurrence of the fringes used to visualize the borders. Quantitative phase determination implies developing a procedure for the retrieval of the phase maps. Several algorithms were produced [19, 20], and showed to be able, when combined with microtomography, to reconstruct the local phase shift introduced by a volume within the sample. These quantitative phase mapping combined procedures are now routinely used, and provide an invaluable tool for the characterization of condensed matter (from materials science [21] to biological samples) on the μm and sub-μm scale.

13.2.4 Microbeam Based X-Ray Imaging Techniques/Nano Imaging

The absorption or phase-based imaging techniques described above cannot provide information on the local elemental composition and/or local crystallographic structure. This requires combining scattering measurements with scanning of the sample. The X-ray beams produced at modern SR sources can, because they originate from a very small source, be focused into a very fine spot (5.10^{-8}–5.10^{-6} m range) with extremely high intensity. Various focusing elements are currently used to produce small section beams: they include curved crystals, Fresnel zone plates, tapered capillaries, compound refractive lenses, waveguides, and "Kirkpatrick-Baez" focusing mirrors or multilayers ([22] and references therein, and Chap. 3 of the present book). It is then possible to scan the sample and collect quantitative information. This information, displayed in the form of a (y,z) map corresponding to the position of the beam, is the "image" we are concerned with.

X-ray microfluorescence allows mapping of the presence and concentrations of elements on the sample [23]. A beam of energy E_0 is produced ($\Delta E/E \approx 10^{-4}$), a mirror eliminating the hard ($E > E_0$) radiation and focused on a small area of the sample. A solid-state detector is set at 90° with respect to the incident beam. A given element produces fluorescence with a characteristic energy E_f. The spatial resolution is, in the hard X-ray range where the depth of focus is usually large (≈100 μm), mainly determined by the spot size. These experiments, whereas producing unique

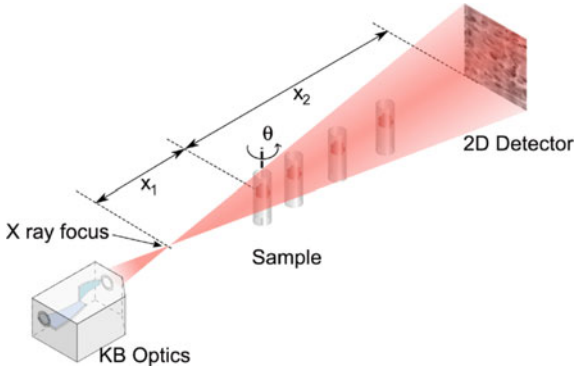


Fig. 13.6 Scheme of the magnified propagation phase contrast imaging tomography: the incoming beam is focused to a few tens of nm sized spot; this spot acts as a secondary source emitting a conical coherent beam. The magnification is obtained (distances x_1 and x_2) by setting the sample at different distances from the source

results, can be time-consuming. The problem is substantially simplified when the element of interest is "heavy" with respect to the matrix (like uranium in soils, or chromium in organic materials).

Fluorescence is not the only quantity that can be mapped: wide angle diffracted X-rays, or small-angle scattered X-rays, absorption, or secondary electrons, provide additional information. Scanning imaging simultaneously exhibits high spatial resolution (μm scale in the hard X-ray range) and elevated chemical selectivity. Local information on different chemical states within systems having the same elemental composition is therefore possible. In addition, combined transmission, fluorescence and Compton microtomography was implemented ("integrated tomographic technique" [24, 25]). It allows a quantitative reconstruction of the internal elemental composition and crystallographic structure of the measured slice.

Synchrotron radiation hard X-ray imaging has a specific and crucial role to play in nano-imaging, both for biology and biomedicine and nano-materials in general because it can combine high spatial resolution and reasonable sample thickness in 3D and, on the same specimen, different imaging modalities such as phase contrast and fluorescence analysis, all this on specimens close to their native state and without sample-modifying, cumbersome preparation procedures. These nano-imaging techniques rest on the continuous progress in source brilliance coupled with long beamlines and improvements of X-ray optics. The Kirkpatrick-Baez mirrors can nowadays, with enhanced mirrors/multilayers, routinely produce focal spots in the 15–25 keV range and the few tens of nm size, while retaining a high enough monochromaticity ($\sim 10^{-2}$) and a high intensity ($>10^{11}$ photons/s). This provides the spatial resolution and elemental sensitivity needed to investigate the presence and metabolism of metals in biological systems, i.e. the growing field of metallomics. When coupled with tomography and phase contrast it allows zooming into the structure of tissues or cells close to their native state, as well as into the nanostructures

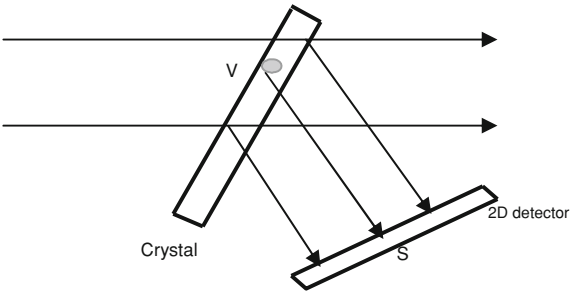


Fig. 13.7 Basic principle of the Bragg diffraction imaging methods (*see text*)

produced for semiconductor devices: projection microscopy (Fig. 13.6) is a magnified version of propagation phase imaging, but can also be considered as Coherent Diffraction Imaging with a curved wavefront [26]. This technique can also be combined with ptychography ("near field ptychography"), obtaining an improved robustness of propagation-based X-ray phase tomography [27].

13.2.5 X-Ray Bragg Diffraction Imaging

Knowing the grain structure in polycrystalline materials, as well as the distortion within a given grain, is often essential to understand their physical properties. A variety of well established techniques give clues on these topics: they include classical light microscopy, as well as transmission, scanning and electron backscatter diffraction. In recent years synchrotron based techniques are of increasing relevance in this field of non-destructive microstructure characterization, through the combination of X-ray imaging (and in particular tomography) and diffraction techniques. In the present section we briefly present Bragg diffractionrelated imaging techniques, which allow characterizing the shapes, orientation and crystalline quality of the grains [28] in polycrystals or, when applied to a single grain, or a single crystal ("X-ray diffraction topography" [29, 30]), investigating inhomogeneous distortion.

Bragg diffraction is associated by many scientists with "reciprocal space". But a Bragg diffracted beam can also be used to form an image in direct space. Figure 13.7 schematically shows, for a platelet shaped single crystal, the basic concept of the diffraction imaging methods. The diffracted beam is recorded on a 2D-detector. Contrast can be observed on S if a volume V (Fig. 13.7) behaves differently from the remaining of the sample from the diffraction point of view (intensity, direction...).

13.2.5.1 Diffraction Contrast Tomography

Several methods, which combine imaging with Bragg diffraction, provide information on the three-dimensional structure (grain shape, orientation, distortion) of

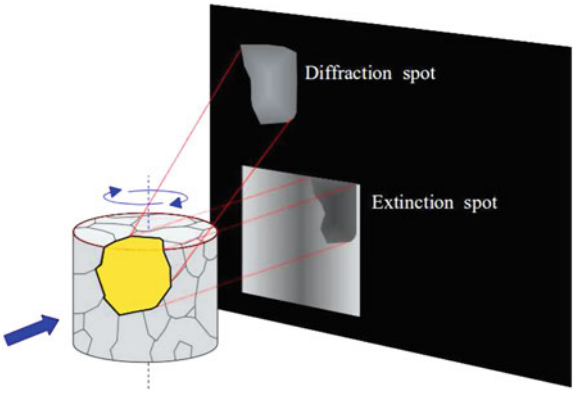


Fig. 13.8 Diffraction contrast tomography setup

polycrystalline materials [31, 32]. We will here briefly describe one of these methods, the ≪ Diffraction Contrast Tomography ≫ (DCT) [28], which recently developed at several synchrotron radiation centres. It combines a microtomographic recording of the radiographic images with the analysis of the Bragg diffracted spots produced by the different grains composing the polycrystal during the rotation of the sample. Indeed during this rotation a given grain goes, for certain angles, through a Bragg position for a particular set of crystallographic planes. Part of the energy is therefore transferred from the incident to the diffracted direction, leading to a simultaneous loss of intensity at the grain location in the transmitted beam, and to a Bragg spot which is recorded, outside the transmitted beam footprint. This procedure is schematically shown on Fig. 13.8 for one selected grain: it allows, with the help of adequate algorithms, which are under constant development, to retrieve the shape and orientation of the grains in the polycrystal [33].

13.2.5.2 Diffraction "Topography" and Rocking Curve Imaging

Bragg imaging ("X-ray diffraction topography") is a well-established method for the visualization and analysis of crystal defects in high quality single crystals [29, 30]. The local variations of the amplitude or direction of the diffracted beam provide information on crystal inhomogeneities. The inhomogeneities are visualized because they can entail a distortion of the crystal lattice (lattice rotation $\delta\theta$ and/or lattice parameter variation $\Delta d/d$); these inhomogeneities include defects such as dislocations, twins, subgrain boundaries, domain walls, inclusions, and macroscopic deformations like bending.

The ≪ Rocking Curve Imaging ≫ (RCI) technique is a fully quantitative counterpart of X-ray topography, which takes advantage of the features of synchrotron radiation beams (flux, weak divergence) and from the substantially increased computer power which is today available [34]. Figure 13.9 shows its principle: the crystal, illuminated by a monochromatic beam, is rotated through the Bragg position for a

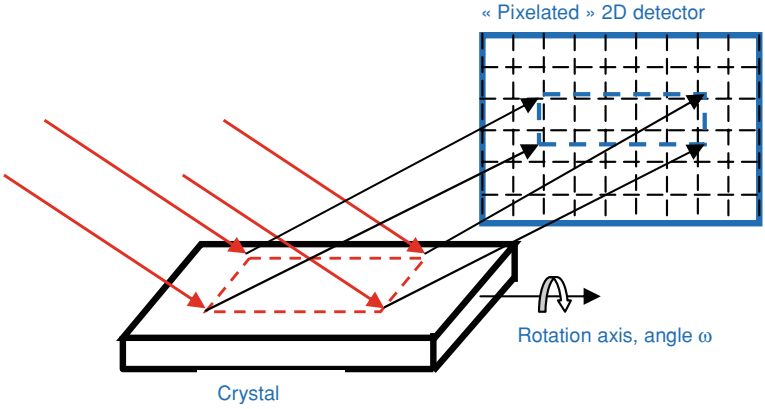


Fig. 13.9 Scheme of Rocking Curve Imaging: the incoming monochromatic beam is Bragg diffracted by the crystal. A small rotation around the Bragg position (angle ω) allows recording the ≪ local ≫ rocking curves for each pixel of the 2D detector

given set of crystallographic planes, and the diffracted beam is recorded, for each angular position along the diffraction rocking curve, on a "pixelated" detector. The "maps / images" are obtained from the data recorded for the ensemble of angular positions. When taking into account that the incoming beam is nearly parallel, we can consider, and this proved to be a very good approximation, that the "local" rocking curves for each of the pixels correspond to a given area in the sample. Three of these "images" are particularly interesting (1) the ≪ integrated intensity ≫ image, i.e. the surface associated to the 'local" rocking curve, which indicates the local crystalline quality (2) the "peak position", which gives access to the variation of lattice parameter, and/or to the respective bending of the various regions of the sample and (3) the full width at half maximum (FWHM), which provides information on the "local mosaic spread" in the sample. Crystalline defects like dislocations are visible on these images, and the distortion they induce is immediately quantified. The spatial resolution of RCI is directly associated with the pixel size, typically in the μm-few μm range.

In the case of projection diffraction imaging in transmission (Figs. 13.7 and 13.8) a 2D image of the 3D actual volume is produced: in other words, a high spatial resolution (μm range) is obtained along the crystal plate surface, whereas the resolution along the crystal depth is poor. Several ways were proposed to solve this problem and obtain depth sensitivity on the images. A "topo-tomography" approach was shown to be able produce a 3D image of defects in some cases [35]. A more general approach consists in restricting the width of the incident beam by an entrance slit of width s, with $s \approx 10$–$20\,\mu$m. In this case ("section" diffraction imaging) a good resolution is also reached along the crystal depth, but at the cost of a drastic reduction of the investigated volume.

The same idea applies for ≪ Rocking Curve Imaging ≫, and leads to a three-dimensional extension (≪ 3D-RCI ≫) of this technique, which allows imaging the whole crystal/grain volume [36]. We will report, in the next section, the unique information provided by this method on the inception of deformation in a tri-crystalline sample.

13.3 Selected Examples of the Application of Synchrotron Radiation Imaging Techniques

With the availability of third generation synchrotron sources the spatial resolution of X-ray imaging techniques has rapidly evolved to reach the micrometer range routinely. This level of resolution, which is comparable to that obtained with optical microscopy, has triggered a wide interest in the scientific community because of the specific aspects of X-rays compared to visible light i.e. the ability to penetrate opaque materials non destructively, the huge number of photons which yields very high signal to noise ratio images very quickly (a fraction of seconds for topographs, milliseconds for radiographs), the possibility to couple imaging with another signal (fluorescence, diffraction …). As a result, the number of papers devoted to X-ray imaging and, more specifically, to tomography has dramatically increased in the literature. The range of studied materials has widened to include all kind of structural materials (polymers, ceramics, metals, composites), cellular solids but also, mainly thanks to phase contrast, biological samples (among which bones), fossils, cultural heritage and extra terrestrial materials. Dedicated symposia are regularly organised in conferences (E-MRS, Euromat and TMS conference series) and, more recently, dedicated conferences on 3D imaging/materials science have appeared. Giving an exhaustive view of the applications of synchrotron imaging is therefore out of the scope of this chapter. In the field of 3D characterisation some reviews have now been published for the interested reader [37]. In what follows we are highlighting a few studies which illustrate some recent developments.

As explained in the previous sections, the images obtained from X-rays can be recorded in situ in two or (indirectly) three dimensions. In the former category, a striking example of the potential of X-rays to capture images of very fast phenomena, is the work from Wang et al. [38], who used radiography at the Advanced Photon Source to monitor in situ pure and aerated liquid jets used to increase combustors efficiency. The key feature of this experiment is the ultrafast imaging capability of the setup which provides an exposure time of 170 ps. The images obtained give an invaluable description of the internal organisation of the gas/liquid mixture within the jet.

Increased recording times are the price to pay for 3D imaging. While this is clearly not an issue for classical 3D observation of a “static” sample like a fossil or a foam, 3D characterisation of dynamical processes has long been restricted by exposure times of the order of ten to twenty minutes. The development of new experimental

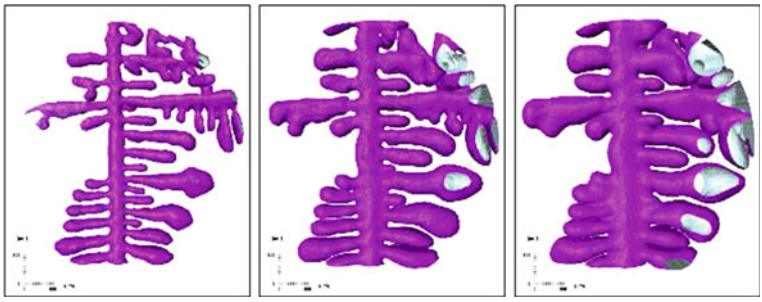


Fig. 13.10 3D rendering of the formation of Al dendrites during the solidification of an Al-10 %wt Cu alloy [40]

set ups has however pushed those limits by several orders of magnitude in the last 10 years. By optimising the number of photons in the beam (pink beams with $\Delta\lambda/\lambda \sim 10^{-2}$–$10^{-3}$ or even white beams), scintillators, camera (CMOS), rotations stages (constant velocity fast air bearing motors) hundreds of images can now be recorded with a spatial resolution close to 1 μm in less than 1 s. Figure 13.10 illustrates the 3D development of dendrites in an Aluminium Copper alloy during cooling rates of the order of 3 °C min^{-1}. Such high acquisition rates have been pioneered at ESRF by a scientific community interested in metal solidification; Nguyen-thi et al. have recently reviewed the work in this field [39] and shown that, besides tomography, in situ fast radiography of solidifying metals also reveal details of the dendrites growth such as dendrite torsion and bending. Such mechanisms can be related, when coupled with topography, to the local crystallographic orientation of the growing crystals.

Fast X-ray imaging is a rapidly evolving field, in particular in the case of tomography, and has already found numerous applications e.g. in the study of damage development in metals under mechanical loading or phase transformation [41]. Developments of phase reconstruction using a single distance have also enabled the fast tomography of weakly attenuating objects allowing, for example, to follow the temporal evolution (coarsening) of a beer foam, and even in vivo monitoring of a fly [42].

For increasing the spatial resolution of 3D images, several possibilities have been explored. In the case of classical absorption tomography a contrast agent can reinforce the visibility of small features as shown for example by Plouraboué et al. [43] for a large micro vascular network in biological tissue samples. Imaging above and below an absorption edge to increase the contrast has been applied first in medical applications [44] and recently this technique has found some application also in materials science: for the 3D characterisation of particle and pores of a sand (imaged at energies below and above the Cs K-edge) [45] as well as the Zn distribution within the cell walls of an Al–Zn–Mg foam [46].

The sensitivity of phase contrast to very small changes in electron density, as explained above, is another very efficient way to increase the spatial resolution of 3D imaging, without focusing optics. Very different sub-voxel features such as cracks

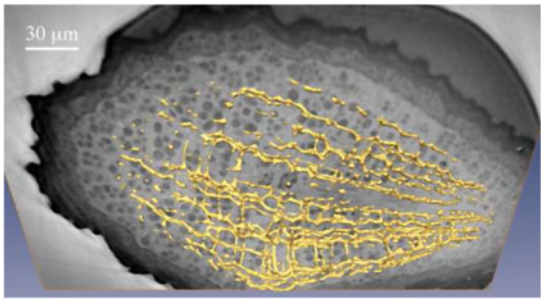


Fig. 13.11 3D rendering of the internal air space network in Arabidopsis seed (300 nm resolution)

in metals [47], or the osteocyte lacunocanalicular network in bones [48], have been imaged in this way with a voxel size down to 0.3 µm (see [37] for a review).

Focusing optics can bring the spatial resolution/voxel size below 100 nm at the expense of a reduced sample size (diameter below a few hundreds micrometers) and strict requirements in terms of mechanical and thermal stability. Up to now this has severely restricted the possibility to perform this kind of observation in situ with a changing sample environment. Nevertheless internal features have been imaged in various kind of samples with unprecedented accuracy. In the case of biological samples, for example, Cloetens et al. have shown the existence of a 3D network of intercellular air space (see Fig. 13.11) in a plant seed (*Arabidopsis*) that can allow exchange for energy supply during germination and/or serve for rapid water uptake and distribution during imbibition [49]. The technique is however not restricted to "soft" material as Tolnai et al. have shown some evolution of the shape of intermetallic phases during (ex situ) solution heat treatment of an Al–Si alloy [50].

The images obtained using far field techniques, usually combined with tomography, are able to produce high quality images. As an example, let us mention the spectacular results that were obtained by [51] on mouse femur bone samples, where osteocyte lacunae and the interconnective canalicular network were imaged with high spatial resolution (100 nm range).

Finally, one important feature of X-ray radiation, as mentioned above, is that it can be coupled with the detection of a complementary signal like diffraction or fluorescence. For example, Kim et al. have visualized the spatial distribution of Iron in *Arabidospsis* using X-ray fluorescence microtomography [52]. Diffraction has been used in combination with tomography to monitor creep induced evolution of a brass alloy: voids initiation and growth, together with dislocations density and texture evolution, have been measured [53]. Other examples include phase transformation accompanying microstructural evolution during annealing of superconducting wires [54], or the coupling between damage evolution and stress distribution in metal matrix composites [55].

As explained above the diffraction signal can be used to reconstruct a 3D image of the spatial distribution of grains in crystalline sample [56]. Further tests can be applied to this sample to study, by tomography, the evolution of the microstructure during, for example, a thermal heat treatment [57], or a mechanical test [58].

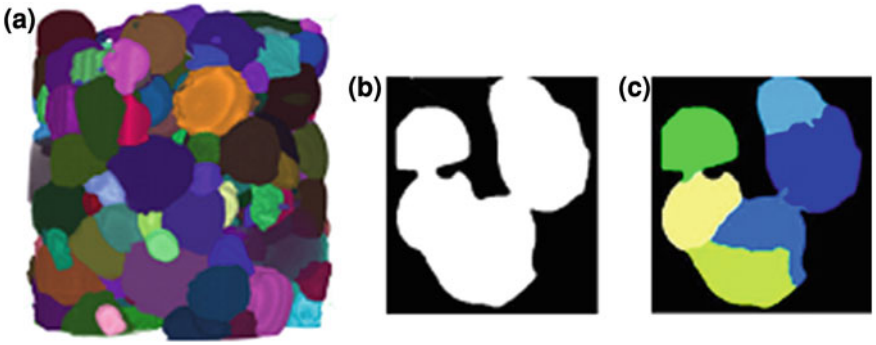


Fig. 13.12 3D rendering of a snow sample, showing (**a**) the ice single-crystalline grains and (**b**–**c**) a cut of a fraction of the previous image in absorption mode (**b**) and diffraction mode (**c**), with colours associated to crystals with different orientation

Figure 13.12 shows an example of the use of diffraction contrast tomography to study snow, which is a conglomerate of ice crystals [59]. On Fig. 13.12a each grain has a colour associated with the orientation of the six-fold axis of the hexagonal structure of ice. Figure 13.12b, c show the difference between an absorption image (b), which suggests the occurrence of 3 grains, and the diffraction image (c), which shows the presence of six crystals in the same area.

The 3D-RCI technique we mentioned above was used to follow the first steps of the deformation of an ice polycrystal. The values of local mosaic spread in the neighbourhood of the defects (initially dislocations, then glide planes and finally the inception of a subgrain boundary) have been measured over two orders of magnitude within the bulk of the crystal [60].

13.4 Conclusion

Synchrotron radiation based X-ray imaging techniques, which exploit most of the photon-matter interactions, exhibit an impressive development over the last years. Imaging techniques are, in this way, one of the key topics for the upgrade programmes of nearly all major synchrotron facilities in the world, because associated with very high level scientific results in very different fields that go from materials science to cultural heritage and biomedical topics. In situ and real-time investigations are increasingly used and allow phenomena such as the growth, fracture or phase transitions to be studied. These techniques are in constant evolution, and spatial resolution improvements, new tools for image processing, and extension to new topics, are constantly observed.

References

1. T. Martin, A. Koch, J. Synchrotron Rad. **13**, 180–194 (2006)
2. B.P. Flannery, H.W. Deckman, W.G. Roberge, K. D'Amico, Science **237**, 1439–1444 (1987)
3. A.C. Kak, M. Slaney, *Principles of Computerized Tomographic Imaging* (IEEE Press, New York, 1988)
4. F. Peyrin, L. Garnero, I. Magnin, Traitement du Signal **13**, 381–413 (1996)
5. J. Miao, P. Charalambous, J. Kirz, D. Sayre, Nature **400**, 342–344 (1999)
6. H.M.L. Faulkner, J.M. Rodenburg, Phys. Rev. Lett. **93**, 023903 (2004)
7. D. Sayre, Acta Cryst. **5**, 843–845 (1952)
8. J.R. Fienup, J. Opt. Soc. Am. A **4**, 118–123 (1987)
9. H.M. Quiney, J. Mod. Opt. **57**, 1–57 (2010)
10. K.A. Nugent, Adv. Phys. **59**, 1–99 (2010)
11. P. Thibault, V. Elser, Ann. Rev. Condens. Matter Phys. **1**, 237–255 (2010)
12. B. Abbey, L.W. Whitehead, H.M. Quiney, D.J. Vine, G.A. Cadenazzi, C.A. Henderson, K.A. Nugent, E. Balaur, C.T. Putkunz, A.G. Peele, G.J. Williams, I. McNulty, Nat. Photonics **5**, 420–424 (2011)
13. J.M. Rodenburg, A.C. Hurst, A.G. Cullis, Ultramicroscopy **107**, 227–231 (2007)
14. P. Thibault, M. Dierolf, A. Menzel, O. Bunk, C. David, F. Pfeiffer, Science **321**, 379–382 (2008)
15. M. Guizar-Sicairos, J.R. Fienup, Opt. Lett. **33**, 2668–2670 (2008)
16. A.M. Maiden, J.M. Rodenburg, Ultramicroscopy **109**, 1256–1262 (2009)
17. A. Snigirev, I. Snigireva, V. Kohn, S. Kuznetsov, I. Schelokov, Rev. Sci. Instrum. **66**, 5486–5492 (1995)
18. P. Cloetens, R. Barrett, J. Baruchel, J.P. Guigay, M. Schlenker, J. Phys. D: Appl. Phys. **29**, 133–146 (1996)
19. P. Cloetens, W. Ludwig, J. Baruchel, D. Van Dyck, J. Van Landuyt, J.P. Guigay, M. Schlenker, Appl. Phys. Lett. **75**, 2912–2914 (1999)
20. D.M. Paganin, *Coherent X-Ray Optics* (Oxford University of Press, Oxford, 2006)
21. J. Baruchel, J.Y. Buffière, E. Maire, P. Merle, G. Peix (eds.), *X-Ray Tomography in Material Science* (Hermes, Paris, 2000)
22. P. Dhez, P. Chevallier, T.B. Lucatorto, C. Tarrio, Rev. Sci. Instrum. **70**, 1907–1920 (1999)
23. F. Adams, K. Janssens, A. Snigirev, J. Anal. At. Spectrom. **13**, 319–331 (1998)
24. B. Golosio, A. Simionovici, A. Somogyi, M. Lemelle, M. Chukalina, A. Brunetti, J. Appl. Phys. **94**, 145–156 (2003)
25. M. Álvarez-Murga, P. Bleuet, G. Garbarino, A. Salamat, M. Mezouar, J.L. Hodeau, Phys. Rev. Lett. **109**, 025502 (2012)
26. K.A. Nugent, J. Opt. Soc. Am. A **24**, 536–547 (2007)
27. M. Stockmar, P. Cloetens, I. Zanette, B. Enders, M. Dierolf, F. Pfeiffer, P. Thibault, Sci. Rep. **3**, 1927 (2013)
28. A. King, G. Johnson, D. Engelberg, W. Ludwig, J. Marrow, Science **321**, 382–385 (2008)
29. J. Baruchel, J. Härtwig, *Encyclopaedia of Condensed Matter Physics*. X-Ray Topography (Elsevier, Amsterdam, 2005), pp. 342–348
30. A. Authier, *Dynamical Theory of X-Ray Diffraction* (Oxford University of Press, Oxford, 2001)
31. B.C. Larson, W. Wang, G.E. Ice, J.D. Budai, J.Z. Tischler, Nature **415**, 887–890 (2002)
32. H.F. Poulsen, *Three Dimensional X-Ray Diffraction Microscopy* (Springer, Berlin, 2004)
33. W. Ludwig, P. Reischig, A. King, M. Herbig, E.M. Lauridsen, G. Johnson, T.J. Marrow, J.Y. Buffière, Rev. Sci. Instrum. **80**, 033905 (2009)
34. D. Lübbert, T. Baumbach, J. Härtwig, E. Boller, E. Pernot, Nucl. Inst. Meth. Phys. Res. B **160**, 521–527 (2000)
35. W. Ludwig, P. Cloetens, J. Härtwig, J. Baruchel, B. Hamelin, P. Bastie, J. Appl. Cryst. **34**, 602–607 (2001)
36. R.T. Kluender, A. Philip, J. Meyssonier, J. Baruchel, Phys. Status Solidi A. **208**, 2505–2510 (2011)

37. S. Stock, *Micro Computed Tomography: Methodology and Applications* (CRC Press, Boca Raton 2009)
38. Y. Wang, X. Liu, K.S. Im, W.K. Lee, J. Wang, K. Fezzaa, D.L.S. Hung, J.R. Winkelman, Nat. Phys. **4**, 305–309 (2008)
39. H. Nguyen-Thi, L. Salvo, R.H. Mathiesen, L. Arnberg, B. Billia, M. Suery, G. Reinhart, C.R. Phys. **13**, 237–245 (2012)
40. N. Limodin, L. Salvo, E. Boller, M. Suery, M. Felberbaum, S. Gailliegue, K. Madi, Acta Mater. **57**, 2300–2310 (2009)
41. E. Gouillart, M.J. Toplis, J. Grynberg, M.H. Chopinet, E. Sondergard, L. Salvo, M. Suery, M. Di Michiel, G. Varoquaux, J. Am. Ceram. Soc. **95**, 1504–1507 (2012)
42. R. Mokso, F. Marone, S. Irvine, M. Nyvlt, D. Schwyn, K. Mader, G.K. Taylor, H.G. Krapp, M. Skeren, M. Stampanoni, J. Appl. Phys. (2013) (In press)
43. F. Plouraboué, P. Cloetens, C. Fonta, A. Steyer, F. Lauwers, J.M. Vergnes, J. Microsc. **215**, 139–148 (2004)
44. F. Esteve, H. Elleaume, B. Bertrand, A.M. Charvet, S. Fiedler, G. Le Duc, S. Corde, C. Nemoz, M. Renier, J.L. Lefaix, J.J. Leplat, P. Suortti, W. Thomlinson, J.F. Le Bas, Acad. Radiol. **9**, S92–S97 (2002)
45. C.S. Willson, N. Lu, W.J. Likos, Geotech. Test. J. **35**, 911–923 (2012)
46. Z. Qiang, H. Toda, Acta Phys. Sin. **60**, 911–923 (2011)
47. P. Cloetens, M. Pateyron-Salomé, J.Y. Buffière, G. Peix, J. Baruchel, F. Peyrin, M. Schlenker, J. Appl. Phys. **81**, 5878–5886 (1997)
48. A. Pacureanu, M. Langer, E. Boller, P. Tafforeau, F. Peyrin, Med. Phys. **39**, 2229–2238 (2012)
49. P. Cloetens, R. Mache, M. Schlenker, S. Lerbs-Mache, PNAS **103**, 14626 (2006)
50. D. Tolnai, G. Requena, P. Cloetens, J. Lendvai, H.P. Degischer, Mat. Sc. Eng. **A550**, 214–221 (2012)
51. M. Dierolf, A. Menzel, P. Thibault, P. Schneider, C.M. Kewish, R. Wepf, O. Bunk, F. Pfeiffer, Nature **467**, 436–440 (2010)
52. S.A. Kim, T. Punshon, A. Lanzirotti, L. Li, J.M. Alonso, J.R. Ecker, J. Kaplan, M.L. Guerinot, Science **314**, 1295–1298 (2006)
53. A. Pyzalla, B. Camin, T. Buslaps, M. Di Michiel, H. Kaminski, A. Kottar, A. Pernack, W. Reimers, Science **308**, 92–95 (2005)
54. C. Scheuerlein, M. Di Michiel, M. Scheel, J. Jiang, F. Kametani, A. Malagoli, E.E. Hellstrom, D.C. Larbalestier, Supercond. Sci. Tech. **24**, 115004 (10 p) (2011)
55. Y.C. Hung, J.A. Bennett, F.A. Garcia-Pastor, M. Di Michiel, J.Y. Buffière, T.J.A. Doel, P. Bowen, P.J. Withers, Acta Mater. **57**, 590–599 (2009)
56. W. Ludwig, A. King, M. Herbig, P. Reischig, J. Marrow, L. Babout, E.M. Lauridsen, H. Proudhon, J.Y. Buffière, JOM **62**, 22–28 (2010)
57. A. Lyckegaard, H.F. Poulsen, W. Ludwig, R.W. Fonda, E.M. Lauridsen, in *Proceedings of Recrystallization and Grain Growth IV*, ed. by E. Palmiere, B. Wynne (2012)
58. M. Herbig, A. King, P. Reischig, H. Proudhon, E.M. Lauridsen, J. Marrow, J.Y. Buffière, W. Ludwig, Acta Mater. **59**, 590–601 (2011)
59. S.R. du Roscoat, A. King, P. Reischig, W. Ludwig, F. Flin, J. Meyssonnier, Adv. Eng. Mater. **13**, 128–135 (2011)
60. A. Philip, J. Meyssonnier, R.T. Kluender, J. Baruchel, J. Appl. Cryst. **46**, 842–848 (2013)

Chapter 14
X-Ray Microscopy

Diane Eichert

Abstract XRM is a versatile and attractive tool, due to the large penetration depth of X-rays in matter, X-rays rich spectral structures and the various contrast mechanisms accessible (absorption, phase contrast, fluorescence) that allow scientific questions in many fields of science to be addressed. This contribution aims to provide an introduction to the physics behind XRM and to describe the current state of the art instrumentation, developments and analytical methodologies. The potential of XRM is illustrated with examples from materials, environment and life science.

14.1 Introduction

Microscopy is appealing: it is a visual technique, the first step of scientific investigation in many cases, and the adage "seeing is believing" contains a fundamental truth. This advantage is fully exploited in elaborated mapping systems that present information in a pictorial manner which is easily understood by the human eyes. Microscopy started 500 years ago with a simple magnifying device: the glass. Soon the microscopist faced the need to overcome initial severe limitations in terms of illumination, resolution, contrast, and image distortions. Such limitations drove the implementation of increasingly ingenious optics, imaging modes, the need to exchange the light source, and to switch from one part of the electromagnetic spectrum for another to reach the current capability to image ultra-structures. Consequently, modern microscopic techniques are important tools in many fields of science, such as physics, materials science, environmental science, biology and medicine. Significant instrumental achievements were realized in light microscopy (LM) with the "super resolution fluorescence microscopies" relying on fluorescence dyes to go

D. Eichert (✉)
Elettra-Sincrotrone Trieste S.C.p.A., Strada Statale 14, km 163.5 in AREA Science Park, 34149 Basovizza, TS, Italy
e-mail: diane.eichert@elettra.eu

S. Mobilio et al. (eds.), *Synchrotron Radiation*,
DOI: 10.1007/978-3-642-55315-8_14, © Springer-Verlag Berlin Heidelberg 2015

Table 14.1 Comparison of various microscopic techniques for bioscience

	Light microscopy	FTIR Raman	X-Ray microscopy	Electron microscopy	AFM NSOM
Resolution	150 nm	3 μm–200 nm*	15 nm	1 nm	0.2–1 nm
Thickness	1–150 μm	1–20 μm	5–100 μm	100 nm	-
Hydrated	Yes	Yes	Yes	No	Yes
Alive	Yes	Yes*	Yes*	No	Yes*
Radiation damage	Low	Low	High	Extreme	High
Contrast -enhancement	Not required	Not required	Not required	Recommended	No
Label	Possible	Not required	Not required	Not required	No
Sample preparation	Easy Medium	Easy Medium	Medium	Elaborated	Medium
Detection method	Absorption Phase contrast Fluorescence Scattering Polarization	Molecular vibrations	Absorption Phase contrast Fluorescence Scattering Diffraction Polarization Spectroscopy Secondary e^-	Absorption Phase contrast Fluorescence X Scattering Diffraction Photon emission	Contact topography
Spectroscopy	Yes	Yes	Yes	No	No
Observation	Partly inside	Partly inside	Inside	Surface	Surface
Focal Depth	Low	Low	High	Extreme	Extreme
3D Imaging	Yes	Yes*	Yes	Limited	-

With: *FTIR* Fourier Transform Infrared; *AFM* Atomic Force Microscopy, *NSOM* Near-Field Scanning Optical Microscopy; * case dependent

beyond the Abbe diffraction limit, Near-field scanning optical microscopy (NSOM), and atomic force microscopy (AFM), providing the ability to resolve membranes, macromolecules and associated conformational changes at sub-nm resolution. Nevertheless, if these techniques indeed overcome the diffraction limited spatial resolution imposed by the wavelength considered, they only deliver information on the object surface or near surface. By using electrons with shorter wavelength, outstanding spatial resolution (sub-nm, even Angström) has been obtained by electron microscopy (EM) allowing, for instance, the identification of macromolecular complexes by their morphology, moreover label-free and in 3D (tomography). But due to the strong scattering of the electrons, EM is limited to the imaging of thin samples and often needs sophisticated sample preparation, prone to change the initial state of a delicate sample.

The main characteristics of various microscopy techniques currently applied in bio-physical sciences are summarized in Table 14.1. XRM evidently bridges the resolution gap between LM and EM, as it combines the strength of both techniques and therefore extends the possibilities for the examination of matter: shorter wavelengths (high spatial resolution), weakly interacting (high penetration depth, less

radiation damage than electrons), and larger depth of focus providing various in-situ experiments possibilities. In addition, the unique interactions of X-rays with matter give access to a wealth of information via the subsequent various contrast modes which provide not only morphological information, but also chemical and physical, and to a certain extent, time resolved and dynamics analysis [1]. Most of these biochemical and physical parameters are unlikely to be readily accessible with other microscopies. Consequently, there is not one XRM, but several XRMs, optimized for the selected X-ray domain (i.e. soft X-rays with energies $E < 2.5\,keV$, middle-range with $2.5 < E < 4\,keV$, or hard X-rays with $E > 4\,keV$), utilizing the different imaging modes (full-field or scanning), and the various contrast mechanisms (absorption, phase contrast, fluorescence, diffraction…).

With the advances of X-ray sources, and especially of 3rd and 4th generation synchrotron sources, XRM is benefiting from the high brilliance, short pulses, energy tunability, low emittance and coherence properties of the source. Together with the breakthroughs in detectors, optics and instrumentation, XRM is now a mature technique tackling the field of the super-resolution microscopies, with remarkable advantages given its unique contrast mechanisms.

14.2 Fundamentals of X-Ray Microscopy

Microscopists can select and optimize the core elements constituting the X-ray microscope to ensure successful imaging: the source of illumination, the optics to efficiently transport and focus the beam on the sample, and the detector.

14.2.1 X-Ray Sources

Several types of source have been employed for the excitation of characteristic X-ray radiation, including those based on electrons, X-rays, γ-rays, plasma, protons, synchrotron radiation and the recent Free Electron Laser (FEL). X-ray radiation is mainly generated via two processes: acceleration of charged particles deflected in a magnetic field (synchrotron, FEL) and de-excitation of atoms striking a target (X-ray tubes). Consequently, the source characteristics differ widely and can be summarized by the following properties: energy (wavelength) and tunability over the X-ray range of the electromagnetic spectrum (soft, middle, hard), collimation, source size and divergence, polarization, intensity and coherence, possible pulsed time, and brilliance. The most suitable parameter to characterize the source is the brilliance, which represents the number of photons per second in a given energy range normalized to the size of the source and to the solid angle under which the radiation is emitted (photons s^{-1} $mrad^{-2}$ mm^{-2} per 0.1 % radiation bandwidth, e.g. 1 eV at 10 keV). While the progresses in laboratory X-ray sources are undeniable, allowing imaging with a resolution down to 50 nm from the soft to the hard

X-rays region, conventional laboratory X-ray sources are still impaired by the lack of energy tunability, an essential condition for X-ray absorption spectroscopy, a limited focused beam size (few micrometers), and especially a limited brilliance (10^8 ph. s^{-1} $mrad^{-2}$ mm^{-2} per 0.1 % BW vs. up to 10^{20} ph. s^{-1} $mrad^{-2}$ mm^{-2} per 0.1 % BW for synchrotrons), the latter points being key for high resolution imaging. A synchrotron source, additionally, allows different electron source conditions, which can be selected according to the specific requirements of the microscope considered. For instance, a full field microscope, needing incoherent illumination with large divergence angle, fits better with a bending magnet source [2] while an undulator source is suited for a scanning microscope, which requires a coherent X-ray spot as brilliant and small as possible. Consequently synchrotron sources still offer the best conditions for spectro-microscopy [3, 4], and their characteristics are described in the books by Attwood [5] for the soft X-ray range and Mills (ed.) [6] for the hard X-ray range.

14.2.2 X-Ray Optics

XRM enclose a variety of optical elements exploiting reflection, diffraction or refraction properties [7] to ensure the delivery of a brilliant, spatially defined and monochromatic beam onto the sample. However, achieving high numerical aperture and efficiency is challenging with X-rays as they have a refractive index very close to unity. Over the years, the improvements in micro- and nano-fabrication methods have fostered the development of several focusing device solutions for covering the entire X-ray range and for complying with the focusing requirements of each particular microscope (Table 14.2).

In particular, Fresnel Zone Plates (FZP) have been successfully used for high resolution XRM, and their versatility allow their employment for the formation of the image in a TXM and for beam focusing in a STXM, from soft to hard X-rays [8]. FZP consist of circular diffraction gratings with alternating absorbing, phase shifting and transparent zones with radially decreasing line spacing such that the path difference of adjacent zones to the first order focus is one wavelength. Therefore the lateral resolution δ is on the same order as the width of the outermost zone Δr and is given by $\delta \approx 1.22\,\Delta r$. The focus, depth of focus and efficiency are consequently limited to a specific bandwidth of the X-ray domains. FZP are currently providing the best resolution for 2D X-ray focusing, and demonstrate their full potential especially in the soft and middle X-ray ranges.

14.2.3 Detectors

Detectors are used for aligning the optics, measuring the photon flux in the focus spot, for acquiring absorption or emission (e.g. fluorescence) spectra and diffraction patterns, and for recording the transmitted image of a sample [9]. In view of the various processes to be measured a number of different detectors is required and

Table 14.2 Characteristics of the main X-ray focusing optics used in XRM

Type	Positive/negative Points	Resolution	X-Ray range	XRM
Refractive	+ on axis focusing, small focus, high aperture, efficiency			
Compound refractive lenses	− chromatic focus	$R_{th} \sim 10$ nm $R_{exp} \sim 50$ nm	Hard	STXM
Reflective	+ achromatic focusing, large aperture, efficiency			
Kirkpatrick-Baez mirror	− aberration	$R_{th} \sim 10$ nm $R_{exp} \sim 30$ nm	Middle, Hard	STXM
Polycapillary		$R_{th} \sim 10$ nm $R_{exp} \sim 10$ μm	Soft, middle Hard	STXM, TXM
Waveguides		$R_{th} \sim 10$ nm $R_{exp} \sim 10$ nm	Hard	STXM
Diffractive	+ on axis focusing, small focus			
Fresnel zone-plate (FZP)	− moderate aperture,efficiency, chromatic focusing	$R_{th} \sim 10$ nm $R_{exp} \sim 15$ nm	Soft, middle, Hard	STXM, TXM
MultiLayerLaue lenses		$R_{th} < 1$ nm $R_{exp} \sim 20$ nm	Hard	STXM

With R_{th} theoretical resolution, R_{exp} experimentally achieved resolution

can be combined in an XRM set-up. All detectors are based on the same concept of conversion of photon energy into an easily measurable and countable electric signal, expected to be proportional to the photon energy. Their properties in terms of energy resolution, sensitivity, proportionality, linearity, imaging capabilities (1D, 2D), dynamic range, spatial resolution, electronic noise, etc. differ significantly, and are linked to the X-ray excitation energy range considered.

14.3 Imaging Modes

14.3.1 Interactions of X-Rays with Matter

When X-rays incident on an object some photons will interact with the particles of the matter and their energy will be absorbed or scattered away from the original path. This attenuation mechanism is described by the Beer-Lambert law: $I_t = I_0 e^{-\mu\rho x}$ with I_t transmitted intensity of the photons, I_0 initial intensity of the photons, μ mass attenuation coefficient [cm^2/g], ρ density related to the specific absorptive properties of the material [g/cm^3] and x the distance travelled (thickness). μ, also called total cross-section for photon absorption is dependent on the atomic number

of the absorbers and of the energy of the incoming photons ($\mu \propto Z^4 \lambda^3$, except at the absorption edge). In addition it also directly measures the penetration depth of X-rays z of specific E through the material: $z = \frac{1}{\mu}$. The behavior of X-rays in matter can also be described with the complex index of refraction $n = 1 - \delta - i\beta$ of which the real part δ (refractive index decrement) describes the refraction of the photons, whereas the imaginary part β (absorption index, related to μ as $\mu = \frac{4\pi\beta}{\lambda}$) is a measure of the photon attenuation in the material. Simplistically, δ constitutes the value measured in phase contrast approaches, and β in absorption contrast methods [5].

The mass attenuation coefficient, in the X-ray domain (1 eV–100 keV), can be expressed as: $\mu(E) = \tau(E) + \sigma_{coh}(E) + \sigma_{inc}(E)$, where τ(E) is the photoelectric mass absorption coefficient; $\sigma_{coh}(E)$ is the coherent mass absorption coefficient and $\sigma_{inc}(E)$ the incoherent mass absorption coefficient. These coefficients account for the three ways X-rays interact with matter: absorption, coherent scattering (i.e. Rayleigh, Thomson) and incoherent scattering (Compton) [10].

14.3.2 Contrast Mechanisms

Due to the variety of processes induced by the interaction of X-rays with matter, several complementary contrast mechanisms apply, which together with the resolution factor, define the level of information that can be extracted from a specific type of X-ray microscope (Fig. 14.1).

14.3.2.1 Absorption Contrast

Absorption is commonly assessed by measuring the total transmitted X-ray intensity; the contrast is therefore generated for a given energy by spatial thickness differences and variations in the mass attenuation coefficient of the material. Radiographs taken in hospital represent one of the applications of this method of contrast in everyday life.

As shown previously, the mass attenuation coefficient depends on the photon energy, and if the photon energy is high enough to exceed the ionization threshold of the atomic core level, a large increase in the absorption occurs as core electrons are ejected and release their energies in the surrounding shells. The energies of the absorption edges is therefore Z dependent, which makes X-ray absorption an element selective technique. A full tabulation of the absorption edges, for elements of $Z < 92$, is available [12, 13]. If the photon energy is tuned below or above the absorption edge of a selected element, the resulting images will display the differences induced in the elemental spatial distribution, local concentration (with subsequent quantitative access to the element mass density), and chemical state.

Case of X-ray absorption spectroscopy: In the vicinity of absorption edges, X-ray absorption spectra show additional fine structures which arise from electronic transitions from the atomic core levels to the continuum. Two domains are typically

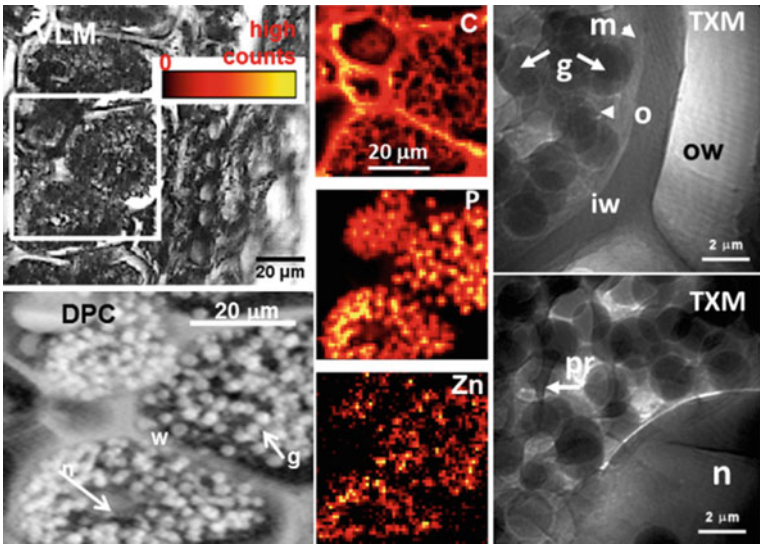


Fig. 14.1 Wheat aleurone layer. VLM and various X-ray contrast mechanisms were used to determine the content of this cellular layer, storing all essential mineral elements. The structures were analysed with STXM in DPC and XRF modes (E_{exc}: 2.1, 1.7 keV, t: 8 s), linking morphology to elemental content. Higher resolution imaging was obtained with TXM (E_{exc}: 720 eV, t: 1 s), highlighting the difference in densities of the globoids (*g*), i.e. of elemental content. With *m* matrix, *ow* outer wall, *iw* inner wall, *o* oleosome, *n* nucleus, *pr* protusion [11]. Courtesy of I. Kreft

differentiated: XANES (X-ray absorption near-edge structure, also called NEXAFS, near-edge X-ray absorption fine spectroscopy; few eV below an absorption edge to about 50 eV above the edge) and EXAFS (extended X-ray absorption fine structure; about 50 eV below to a few hundred of eV above the edge). In the XANES domain the spectral features are determined by electron correlation and density of states, which reveal mainly the electronic properties of the absorbing atom, such as speciation and site symmetry. The EXAFS domain, dominated by scattering events of the ejected electron and the neighboring atoms, gives information about the local atomic structure of the absorbing atom, such as the geometrical arrangements and interatomic distances with the other close atoms.

By tuning the incident energy to the XANES modulations of one specific element present in the material, it is possible to generate contrast variations and thus element specific spectra and cartographies of particular chemical states, moreover, quantitatively. Thanks to its element specificity and its high sensitivity (tens to hundreds of ppm), XAS is a versatile and efficient contrast technique for studying atom specific physical and structural properties in virtually any material state of organization and in chemically complex matrixes [14].

14.3.2.2 Fluorescence Contrast

The energy of the fluorescent lines observed from a given element is defined by the energy states of the atom and the selection rules for allowed transition and tabulation are available [12, 13]. As XRF is the result of a selective photo-electric absorption process, followed by spontaneous atomic emission [15], an efficient excitation for the high sensitivity discrimination of a specific element is obtained by tuning the incoming photon energy just above the edge of this element. In addition, as the excitation energy is sufficient to also excite the elements of a lower Z than the selected element, a series of characteristic X-ray lines from these lower Z elements with lower emission energies will be correspondingly emitted too. Therefore, XRF is a powerful analytical tool for simultaneous spectro-chemical identification of the elements present inside a material and the determination of their concentrations or masses.

14.3.2.3 Phase Contrast

The phase shift term δ of the refraction index describes phenomena like refraction, diffraction, interferences and effects related to the phase of the incoming X-ray waves. δ depends of the wavelength (falls off as λ^2) and produces detectable variations even when the absorption is negligible. However significant contrast and resolution in phase contrast imaging can only be obtained with a source of a high degree of coherence and a detector of sufficient resolution and dynamic range.

Phase contrast imaging, sensitive to density and refraction gradients in object [16], is therefore advantageous for two main reasons: (i) it can image weakly absorbing materials, requires lower X-rays energies, resulting in lower radiation dose and radiation damage [17, 18] and (ii) the sensitivity for probing the sample morphology is higher: even for weakly absorbing materials these imaging modalities can be extended to hard X-rays [19, 20], as the δ of the refractive index decays less than β with respect to the energy. It is also very interesting and valuable to combine phase contrast measurements with fluorescence (especially in the middle and hard X-ray ranges) as the latter is very good at determining low amounts of elements but is not very efficient imaging low-Z elements (C, N, O) due to the low fluorescence yield. It is also possible to obtain quantitative information on the phase shift, providing an assessment of the specimen composition, and the use of theoretical elemental index of refraction to determine the material thickness (crucial in the quantitative analysis of elemental concentration with fluorescence).

Central stops and slits placed in between the sample and the detector(s) (such as quadrant, segmented or slit detector) on the beam path constitute the core of the multiple geometries that can led to phase contrast mechanisms measurements [21], and the main schemes are presented in Fig. 14.2.

Zernike phase contrast: back in 1935 Zernike described how to visualize δ by using a phase shifting disc in the back focal plane of the objective of a microscope (shifting only the un-diffracted beam, the specimen diffracted light remaining undisturbed),

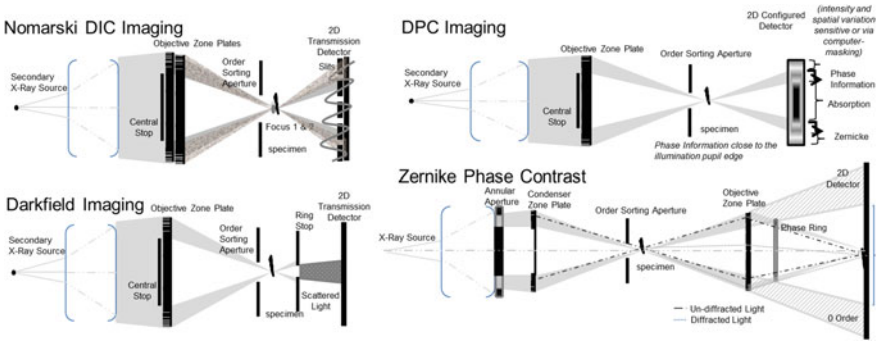


Fig. 14.2 Configurations of the phase contrast modes illustrated for the "scanning mode" (STXM): Nomarski DIC, DPC and Darkfield; and for the full-field mode (TXM): Zernike

the phase modulation refracting the X-ray beam being dependent on the specimen, and imposing a redistribution of the intensity in the detector plane [16, 22] (Fig. 14.3).

DPC: a phase shifting specimen with a linear phase gradient is acting as a prism. The X-ray cone transmitted by the specimen is refracted away from the optical axis towards a split or configured detector, causing an imbalance in the signals where the difference (in signal) is proportional to the phase gradient [24, 25].

DIC (differential interference contrast)—Nomarski: the specimen acting as a prism, some slits in the scattered beam path are used to reveal the difference between detected wavelengths created by two close focal spots [26].

Darkfield: the direct transmitted beam is prevented from entering the image-forming ray paths with a stop. The background of the imaging field is dark, and only light scattered by the specimen discontinuities (i.e. diffracted or refracted according to its physical properties) will appear onto the configured detector [27, 28] as bright dots or lines. Thus, the contrast can become extremely high, and images can be formed even when the dimensions of the scattering object become incredibly small compared to the XRM spatial limits of resolution.

Other mechanisms of contrasts using the δ-induced phase shift exist [29], such as interferometry, coherent diffraction imaging, holography and ptychography.

14.4 Imaging Methods

Imaging with high spatial resolution can be achieved by basically 3 different types of X-ray microscopes differing by their illumination properties, which however are complementary in many aspects: projection microscopes, full-field microscopes (or Transmission X-ray Microscope, TXM) and scanning transmission X-ray microscopes (STXM) (Fig. 14.4). The group of G. Schmahl at Göttingen (Germany) [30, 31] pioneered the TXM mode, and the group of J. Kirz at StonyBrook (USA) [32, 33] established STXM, both in the soft X-ray range. Nowadays, XRMs are

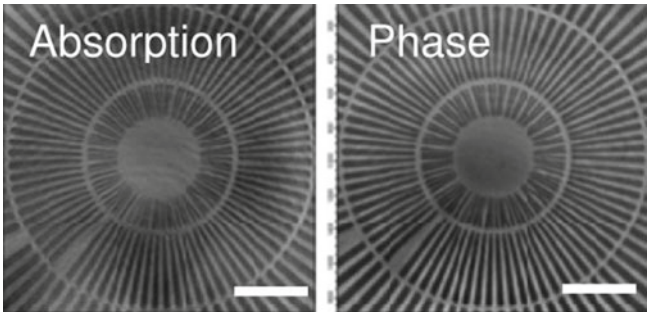


Fig. 14.3 TXM images of a test pattern with innermost Au features of 30 nm pitch, taken with a ZP of 25 nm outermost zone width. Absorption and Zernicke phase contrast signals, bars: 2 μm [23]. Courtesy of I. Kempson

mature tools, with working range from the soft to hard X-rays, and recent reviews give some thorough overviews [1, 8, 21, 34].

The projection microscope does not involve any optics, and relies on the concept of illumination-projection-magnification of the sample onto a detector. In a full-field microscope (similar in concept to that of a visible light brightfield microscope) focusing optics illuminate the sample and other optics provide a magnified projection on a detector, whereas in STXM the image is constructed point by point as the sample is raster scanned in front of a micro-focused beam.

Other types of microscopes exist, probing the diffraction of matter phenomena, with a lensless imaging concept (holography, ptychography, coherent diffraction imaging) [35] and others are making use of the additional processes induced by the interaction of X-rays with matter, such as the photoemission microscopes (PEEM, SPEEM, nano-ARPES) [36].

14.4.1 Projection Microscopy

The principle is extremely simple: to use a source as small as possible to project a magnified shadow on a detector [37]. The obtained magnification factor (M) depends only on the ratio of the distances between the source and the specimen (D_1) and the specimen to the detector (D_2)($M = 1 + D_2/D_1$), and the spatial resolution on the source size and detector resolution. This technique has fallen into disuse over the years, but a few microscopes are still under development [38, 39] for their potential in 3D and phase contrast imaging, considering relevant new technical developments and software treatments. Nevertheless, to overcome the spatial resolution limit of the detector, as well as the difficulty in obtaining sharp images due to diffraction effects, set-ups utilizing optics are largely preferred, as reported below.

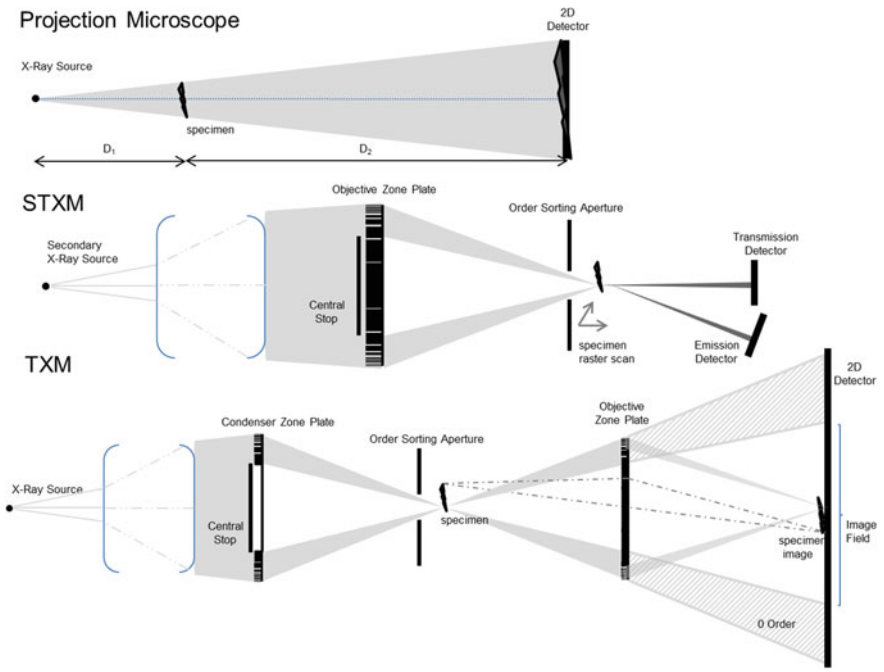


Fig. 14.4 Optical configurations of the projection microscope, STXM and TXM

14.4.2 Transmission X-Ray Microscope

A condenser optic (generally a zone plate [7, 31, 40], but also Kirkpatrick-Baez mirrors [41], or capillary [42]) shapes the X-rays beam in a hollow cone onto the sample, free of the direct focus beam illumination, and an objective lens (a zone plate) magnifies the transmitted light onto the detector, generally a CCD camera. The field of view of these instruments is rather limited, between 10 and 30 μm. The total magnification power is around 1000–2000, with achieved resolutions of 30 nm in the hard X-ray range and 15 nm in the soft X-ray range, and with acquisition time between 1 and 60 s, depending on the specimen itself, the source, and optical properties of the set-up. Within the field of view, the entire specimen is illuminated and re-imaged simultaneously, which enables quick 2D projection imaging. The neighboring areas can be imaged separately and recombined afterwards by software.

This direct mode of imaging has revealed a great potential for tomographic studies and numerous technical developments, as the incorporation of a cryostat [43, 44], were implemented to minimize the radiation dose to the specimen.

Originally developed in the soft X-ray range, especially in the "water window" to take advantage of the natural contrast between proteins and water for high resolution imaging of biological samples [31], full-field microscopy was also pushed towards hard X-ray energies, with significant advantage in terms of depth of focus

and consequently in terms of sample environment (working distance) and image resolution/sharpness [45, 46].

With advances in optics, imaging methods and technologies, and the implementation of complementary (phase) contrast mechanisms, better resolution, enhanced contrast and sensitivity were obtained. Zernike phase contrast especially demonstrated its impressive sensitivity in the water window from the early days of TXM [16, 17, 41], and logically has established its importance at higher energies where phase contrast is the dominant mechanism. More recently, DIC [47, 48] has proven to provide a wealth of complementary information and TXM XRF [49] is at its foundation. In addition, taking advantage of tunable source energy, morphological imaging can be combined (with proper image correction and recalibration software) with XANES, i.e. chemical speciation at the nanoscale [50, 51], and also with tomography [52, 53].

14.4.3 Scanning Transmission X-Ray Microscope

An X-ray beam is focused with a strong demagnification factor into a small spot on a specimen which is raster scanned in 2 dimensions perpendicular to the optical axis, so that the image is formed pixel by pixel [54]. The spatial resolution is defined by the size of the micro- (or nano-) probe, which is dependent on the objective optics, the set-up (distances in between the source, focusing optics, and specimen), and the source properties (spatial coherence is required for diffraction limited resolution, which is best achieved at an undulator source). Nowadays the spatial resolution at a synchrotron source has reached 10 nm for the soft-middle X-ray range with FZP (range of the Δr) [55, 56], and below 80 nm in the hard X-ray range with the use of Kirkpatrick Baez mirrors [57, 58], FZP [46, 59], multi-layer Laue lenses [60] or refractive lenses [61].

One of the major strength of the STXM is the various contrast mechanisms that can be exploited almost simultaneously or at least correlatively to describe the properties of the specimen. For each pixel, during a scan, the specimen transmission from the full thickness can be measured (CCD, pin-diode, ionization chamber), as well as the phase contrast modes by DPC or darkfield (configured CCD), and the fluorescence, elastic (Rayleigh) and inelastic (Compton) scattering signals (EDXRF detector). Traditionally, the soft X-ray range fully exploits the capabilities of absorption imaging, working around an absorption edge, whereas the middle and hard X-ray range mostly make use of the fluorescence contrast. However, phase contrast techniques also reveal their potential in the hard X-ray range, where absorption contrast becomes weak, or for low scattering specimens as measuring the phase delay imposed by the specimen reveals the morphology with higher sensitivity [22, 62, 63]; and fluorescence has been also recently implemented for low Z elements in the soft X-ray range [64, 65]. In addition, by varying the incident energy with a monochromator of sufficient energy resolution ($E/\Delta E \sim 4000$), the XANES contrast can be recorded [50], allowing elemental and chemical speciation of the

specimen to be measured or imaged. Correlatively and successively by exchanging detector, various forms of diffractions can also be assessed.

The area investigated can be large (within the limits of the scanning stage), and the step size can be freely adjusted from coarse to tightly focused analysis. The speed of data acquisition is typically determined by the flux available in the focused spot and the amount of information needed to obtain statistically relevant image signals. Acquisition time can go up to, for a complete fluorescence scans, a few hours, although new detector improvements with large solid angle allowing efficient collection of the XRF signal significantly decrease the acquisition time [66, 67]. Thanks to the versatility of contrast mechanisms accessible with a STXM, easily combining microscopy and spectroscopy, these instruments are also referred to as spectro-microscopes.

14.4.4 Complementary Techniques and Methodological Developments

The complementary and variety of the contrast modes accessible with the different types of XRM was highlighted in the previous sections. However, as specimens are usually complex and defined not only by one but by many properties, other means of investigations need to be considered. These can be linked directly to the end-station of the microscope, as technical developments (stages, detectors, additional excitation sources), and others require completely different sources or set-ups. Combining or correlating micro-analysis and micro-spectroscopy methods and results of different spatial and spectral resolutions is a challenging work, for both technical and scientific reasons, but this multi-modal approach is in constant expansion as it provides a wealth of information, from morphological to chemical and structural points of view [68] (Fig. 14.5).

X-ray tomography: The direct "extension" of the 2D microscopic techniques mentioned above to the third spatial dimension of the specimen, i.e. its volume via tomographic scanning techniques. The advantage is to consider the sample in its whole, without mechanical destruction to obtain thin sections. If the sample is sufficiently transparent with respect to the excitation energy, 2D projections (TXM) or 2D scans (STXM) are acquired for each rotation steps and repeated until a full (or half) rotation of the specimen is completed. The tomographic reconstruction generating the entire volume depends on the contrast mechanism selected. Although absorption or phase contrast are the most common mechanisms probed [44, 69], 3D fluorescence, X-ray absorption spectroscopy or diffraction (small or wide angle X-ray scattering, X-ray diffraction) are now well-established [70–73].

X-ray Scattering: this generic term groups a number of techniques (SAXS, WAXS, XRD) that rely on the same basic principle: the X-rays are deflected by the atoms in matter and produce an interference (or diffraction) pattern. When the atoms have long-range order, the pattern produced is well-defined and X-ray diffraction patterns

are recorded [74]. In case of specimen with no long-range atomic order, scattering will occur. The smaller the scattering angle, the larger the structure causing the scattering is. Small Angle X-ray Scattering is used to study specimens with semi-periodic structures on the order of 1–100 nm, resolving correlations on an inter-molecular level; Wide angle X-ray Scattering resolves structures of about 0.1–1 nm, probing correlations on an intra-molecular, inter-atomic level. Thanks to a tunable X-ray source, the energy can be defined to be close to an absorption edge of an element of interest, highlighting its contribution to the pattern. In a STXM configuration, 2D (even 3D) cartographies of the phases and structural organizations present inside the specimen can be recorded by a high-resolution CCD camera, often however, at the cost of other contrast mechanisms which cannot be acquired simultaneously, such as the transmission signal.

X-ray Excited Optical Luminescence (XEOL): XEOL is a technique that detects the visible emission caused by the absorption of an X-ray photon in order to probe the electronic state, optical properties and the local atomic order at the surface of a specimen [75]. As the visible emission is also modulated by the escape probability of the original photoelectron, as for X-ray fluorescence, the same structural information is encoded in the light. By tuning the excitation energy to a particular absorption edge of an element, the sites responsible for the optical emission can be excited preferentially and identified, and the optical yield obtained can also be used to monitor the absorption (XANES). This signal can be easily extracted by a proper detector (photomultiplier tube) which can be incorporated in a STXM, giving complementary information for each pixel of the map.

Visible Light Microscopy: prior to any investigation under an X-ray microscope, VLM is almost systematically performed for determining the area of interest and resolving the morphology. Incorporating a light microscope with various optical magnifications and contrast modes (bright-field, phase contrasts, filters for fluorescence) into an XRM set-up for positioning, pre-visualization and control is therefore a useful complement. It is technically performed correlatively for space constraint around the sample stage [76] as well as for avoiding interferences (background) from the visible light illumination, deleterious to the X-ray analysis.

Infrared micro-spectroscopy: the FTIR spectroscopy principle relies on the excitation of molecular vibrations and is a common laboratory technique for chemical identification, primarily of organic molecules. Using a synchrotron source has several advantages [78]: its brightness allows dilute samples to be measured on a shorter timescale, the wavenumber range extends over a greater range than with laboratory sources (e.g. globar) due to the tunable nature of synchrotron radiation, and infrared imaging can also be performed, which gives a 2D or even 3D picture of the chemical composition of the material down to few microns resolution. The character of the radiation and the instrumental set-up obviously do not allow the implementation of an infrared probe in a XRM, the analysis having to be conducted separately at a dedicated infrared microscope coupled to a FTIR spectrometer. Nevertheless, the great advantage of infrared is its high molecular sensitivity and its non-destructive nature, which allows performing, on the same specimen and on the same area of interest, consecutive correlative analysis, for instance with XRM in absorption and

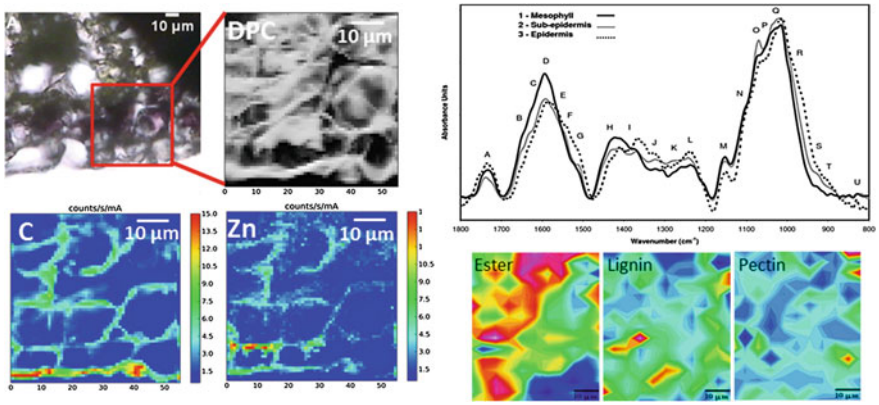


Fig. 14.5 Correlative FTIR-STXM investigations on *Noccaea praecox* hyperaccumulator leave linking metal-binding compounds and plant tolerance. SR-FTIR (*right*) was performed first to reveal the biomolecular make-up of the epidermis, sub-epidermis, mesophyll tissues. Molecular cartographies of key components involved in the stabilization of metals in the plant were generated, and spatially resolved spectra show the differences within the tissues. High proportion of pectin and organic acid were found in the epidermis, whereas mesophyll contains more proteins and carbohydrates. Successively, LEXRF and DPC images were acquired on the same area of interest to unravel the elemental composition (Zn, C) and sub-structures morphology. Pectin compounds were identified as important components of Zn enriched epidermal cell walls. In addition, intense lignification of epidermal cell walls might limit leakage of the trapped metals back to the metabolically active, and thus more sensitive, mesophyll [77]. Courtesy of M. Regvar

fluorescence, thus relating respectively, the morphology and structures, the elemental and the molecular distributions in the specimen, although with different spatial resolutions [68].

14.5 Experimental Conditions

Good experimental conditions are an absolute prerequisite for any kind of microscopy analysis. In principle, the experimentalist would prefer analyzing the sample directly, to avoid any problems arising from sample contamination and artifact that might occur during pre-analysis treatments. In practice major constraints apply: specimen size, state and sensitivity, and the representativeness of the system under study. The quest for the ultimate non-destructive analysis and in-situ observations in controlled environments leads to huge technical developments and efforts. There are two approaches to deal with the frequent incompatibilities that may exist between the properties of the specimen and the optimal operating conditions of the XRM. The instrument can be adapted to minimize the invasive procedures and fulfill experimental in-situ requirements, or the specimen modified to make it more resistant to the analysis, and especially to radiation damage.

14.5.1 Experimental Conditions

Prior to designing any specimen preparation, it is necessary to clearly establish the scientific questions to be answered and whether XRM is the most appropriate technique to use. Gathering as much chemical and structural information as possible about the specimen and its behavior from other laboratory techniques is mandatory. As most specimens are multiphase (chemically complex) it is probably best either to design the preparative procedures to accommodate the most fragile components or set out different procedures for each of the components. This however rules out the possibility of obtaining correlative or combined information on the very same specimen. Sample preparation is THE key to the analysis and is far from being a simple recipe to be applied systematically. On the contrary, it is a complex and delicate procedure, not to say a cornerstone, of which many aspects are still under debate, especially for biological materials [79–81]. Preparation procedures are manifold and comprise: cutting, grinding, polishing, embedding, mounting on support, dehydration, chemical, elemental and structural stabilization or fixation, cleanness, and obviously prevention of sample artifacts and damage. The guiding principle being to stay as close as possible to the natural state, while accommodating the conditions of analysis, basically vacuum conditions for the soft and middle X-ray range, and preventing alteration of the specimen during the time of the analysis (mass loss, radiation dose, distortions). For "sensitive" specimens, this is achieved mainly by two means: low temperatures fixation, impaired by high risks in damage to the morphology; and chemical fixation, with which the chemistry is changed to various degrees, and the morphology is not entirely preserved. But it is now well admitted that high resolution imaging requires cryogenic temperatures (below 100 K) since both the chemistry and the morphology can be better preserved, monitored and controlled [82]. Though huge methodological improvements have been realized in the past years, specimen preparation for X-ray microscopy (especially in biology) is still an immature field. It however benefits from the huge investigations which were undertaken for light and especially electron microscopy [83].

14.5.2 Conditions of Analysis

14.5.2.1 Artifact and Radiation Damage

Damage comprises unexpected or uncontrolled and irreversible change in the specimen before or during the analysis. Artifacts are usually some structural distortions or chemical modifications that arise as a consequence of the specimen preparation or conditions of analysis. Their detection is not obvious and requires a thorough knowledge of the techniques and of the sample.

For instance, fixing chemically or fast freeze-drying cells or tissues can induce some chemical modifications such as removal or displacement of diffusible, labile ionic elements, trace metals contaminations, changes in the elemental speciation, or

changes in the concentration and distribution of light elements (crucial for $Z < 20$), while still maintaining the morphology and the ultra-structures of the specimen. This can eventually be fine for a morphological investigation (transmission, phase contrast), but is deleterious for any elemental and spectroscopy analysis (XRF, XAS). The conservation of the specimen with time and through the time of analysis is another issue.

Case of radiation damage
X-rays are ionizing and this limitation is severe for unfixed fully hydrated specimen, such as biological systems. The level of damage is hard to quantify and is fully specimen dependent (state and composition) [34]. The radiation dose D, on the other hand, is related to the excitation energy applied ($D = \frac{N}{A}\frac{\mu E}{\rho}$ with N number of incident photon, A the irradiated area) and therefore the spatial resolution ($D \propto 1/\delta^4$, Rose criterion) [1], which theoretically implies that for hard X-rays no imaging can be safely considered (radiation dose-wise) below 10 nm and for the soft X-rays below 1 nm [84]. Of notice that consequently and in comparison, the radiation dose required to obtain high resolution imaging is lower in a STXM than in a TXM. Nevertheless, this assumption is not directly related to damages, and specimen preparation procedures (cryo-protectants and radio-protectants) or conditions of analysis (cryogenic temperatures) can help minimizing the dose effects, i.e. increase the specimen tolerance to the radiation dose (typically from 10^4 to 10^8 Gy in the soft X-ray region) [18]. Working, when possible, in the "water region" helps significantly to reduce the radiation dose applied, as the energies required for efficient absorption and phase contrast imaging are lower.

14.5.2.2 Sample Environments

Micro-analysis tends to evolve towards 2D mapping of the morphology, elemental distribution and/or chemical speciation in heterogeneous or dynamic systems under controlled conditions, such as pressure, temperature, or electrical/magnetic gradients. Consequently, sample stages and holders are in constant development for accommodating a variety of samples in different states (frozen, liquid, powder, solid. . .) and under different environmental conditions (sealed, humid cells, compression anvil, cryo, heating stages, oven…). In particular, radiation sensitive samples benefit from being analyzed under cryogenic conditions during the whole time of the analysis [18, 80]. Highly reproducible re-positioning of the sample needs to be ensured, if additional treatments and conditions have to be applied externally, so that the area of interest can be easily followed before and after the treatment. For the soft and middle X-ray ranges, space restriction (focal distance in between optics and specimen) and vacuum conditions (air absorption) can also impose serious limitations for sample environment customizations.

14.5.2.3 Reference Samples and Quantitative Measurements

Imaging is readily answering the question of what is there, and where it is, i.e. providing a qualitative analysis; whether the investigation concerns the distribution of elements with XRF, the chemical speciation with XAS, or the structures with phase contrast or absorption imaging. The answer to the how much is there, i.e. providing a quantitative analysis, is much more difficult and specific requirements must be met. Typically, the observed photon emitted from or transmitted by a specific area of the specimen is a function of many factors including the density, the specimen state or type, the concentration of the element (weight fraction), the matrix, the size (thickness and effective volume probed), the sample preparation, the geometrical set-up, the spectral distribution of the exciting X-rays radiation, and the detection system. In general, probing adequate standards (reference samples), i.e. as similar as possible to the unknown specimen, helps to ensure the accuracy of the analysis. Quantitative determinations are typically considered when 5–10 % accuracy is reached. However, bulk or single standards are not relevant for micro-analysis, where the key aspect to probe is local heterogeneity. For transmission or phase contrast measurements, references of known densities and size are essential to relate to the specimens own signal. Alternatively, comparison and calibration with other techniques such as Rutherford Back Scattering or Scanning Transmission Ion Microscopy can be realized. For XRF, several calibration approaches can be applied: empirical (internal, external standards or scattered line from the X-ray source), and the theoretical approaches. The use of standards is the most accurate approach, since direct calibration curves of peak intensities versus concentration are generated, but also somehow limited since in most cases of analysis little is known about the matrix constituents, which needs to be assessed as precisely as possible and at the micrometer scale. Among the theoretical methods, both considering the various parameters of the set-up and the sample matrix, the Monte-Carlo simulation approach [85] is based on mathematical models describing the relevant photon-matter interactions (relaxation processes, radiation absorption, absorption-enhancement effects), and the fundamental parameter method [86] makes use of influence coefficients for each element detected generated by algorithms correcting for absorption differences between the sample and the standards.

14.6 Applications

X-Ray microscopy is now an established technique in many fields of research ranging from materials science to chemistry, biology to pharmacology, environmental science to archaeometry. This section aims at illustrating, with a few examples, the potential of the technique.

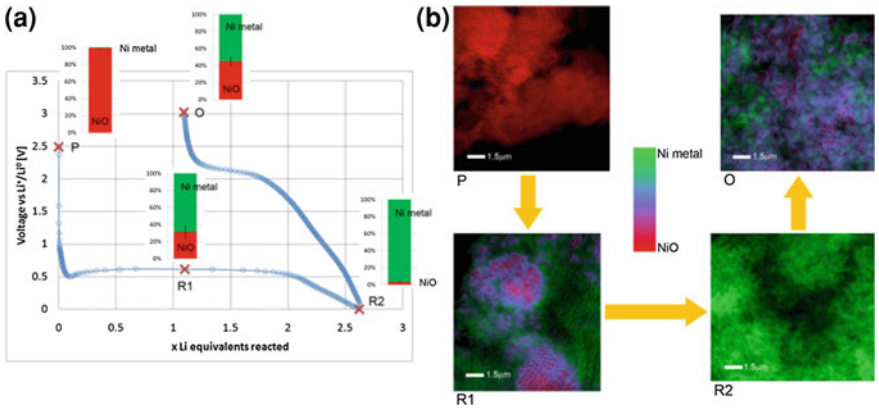


Fig. 14.6 Study of battery electrodes. **a** Trace of the first discharge/charge cycle of a NiO electrode in a Li battery, with *bars* indicating NiO/Ni ratios determined from the chemical phase maps obtained by XANES fitting of several ex-situ samples (Ni K-edge), as in **b** RGB phase maps (red = NiO, $green$ = Ni, $blue$ = mixed stated) for sample *P* (pristine electrode, pure NiO), *R1* (partially reduced), *R2* (pure Ni, fully reduced) and *O* (re-oxidized) [53]. Figure courtesy of F. Meirer, IUCr Copyright

14.6.1 Materials Science

With dozens of new nanomaterials appearing every month and extremely short technological cycles of research and development and renewals, the need of advanced characterization techniques in material science is accute. XRM provides sensitive, selective and spatially resolved analysis in domains such as nanoelectronics, photovoltaics, fuel cells, and polymers where comprehension of the self assembly and material parameters is a prerequisite for determining the stability and the behaviour of these structures, thus contributing to the optimization of the fabrication process and the device performance.

The role of batteries and fuel cells in everyday life is undeniable, and tremendeous efforts are on monitoring the modes of failure and functionalities during operations, and in particular to relate the electrochemical processes to chemical and morphological changes. Electrodes are one of the key points as they condition the charge storage capability of the battery, i.e. the charge-discharge cycle. 2D (Fig. 14.6) and 3D XANES microscopy were used to identify nanoscale chemical and morphological changes that occur during the electrochemical reduction/oxidation of NiO electrodes [53]. Parameters such as porosity, particule aggregation and distribution, and chemical speciation distribution were assessed to quantify the efficiency of this conversion reaction, and to characterize the induced corrosion products. Sample environments allowing these nanoscale reactions and phase transformation to be probed in-situ are under development, and studies are realised both in the hard and soft X-ray ranges [87, 88], making use of all the X-ray contrast mechanisms available.

Other studies have had significant impact on solar cells technologies [89], archaeometry, with the understanding of manufacturing processes for ancient materials [90] and magnetic materials. In the last case, taking advantage of the variable polarization of soft X-rays and using the X-ray dichroism effect (X-ray Magnetic Circular Dichroism), magnetic contrast is achieved revealing and quantifying with high element-, valence-, site-, spatial- and time (ns) sensitivity some of the ferro and antiferro-magnetic properties such as spin and orbitals moment in many complex structured systems [91, 92].

14.6.2 Environmental Science

The environmental field of science embrasses many aspects of our natural and man-made surroundings: soil, plant, food, human health, which are partially conditioned by the human life style, i.e. industries, pollution. Understanding specific and global eco- and bio-spheres require gathering knowledge on environmental factors, plant morpho-physiology, ionome and genetic, but also soil compositions and structure, altogether with their mechanisms of interaction and dynamics. Some interesting articles are giving a more complete overview of the environmental problematics that synchrotron microscopic techniques may help answer [93–97]. Information at the molecular level is therefore of uttermost importance for a better assessment of the chemical and biological processes affecting the speciation, properties and behaviour of contaminants, pollutants and nutrients in the ecosphere.

Soil science has benefited tremendously from spatially resolved spectro-microscopy techniques for revealing hidden but important biogeochemical patterns of the ecosystems. Soil organic matter has received particular attention as a strategic component of carbon cycling in the environment, and the role of elements like sulfur or iron, highly susceptible to redox potential changes, and chemical form (inorganic, organic) are highlighted. As microstructural heterogeneity in soils allows the coexistence of antagonistic reactions (redox reactions, adsorption, precipitation, dissolution, desorption), numerous effects might occur simultaneously (nitrification, microbial production, CO_2 production) and each link of the patterns contributes to the total ecosystem biodiversity and function via specific physico-chemical boundary conditions. This heterogeneity is readily visible in Fig. 14.7,where the specific distribution of the investigated elements on the sub-micron scale allows the identification of organic and inorganic phases mixed together. Evaluating the S K-edge μ-XANES spectra acquired at different microsites reveal a clear heterogeneity of sulfur speciation, with distinct zones enriched in inorganic sulfide and other in organic disulfide, and coexistence of S species (reduced inorganic and organic sulfur) within a few micron [98], while the Fe K-edge μ-XANES remains mainly inorganic. This knowledge contributes to the understanding of the reactivity of soils after ecological or industrial disasters, or under the influence of groundwater, has an impact on agricultural activities and can explain changes in the fauna and flora of the area.

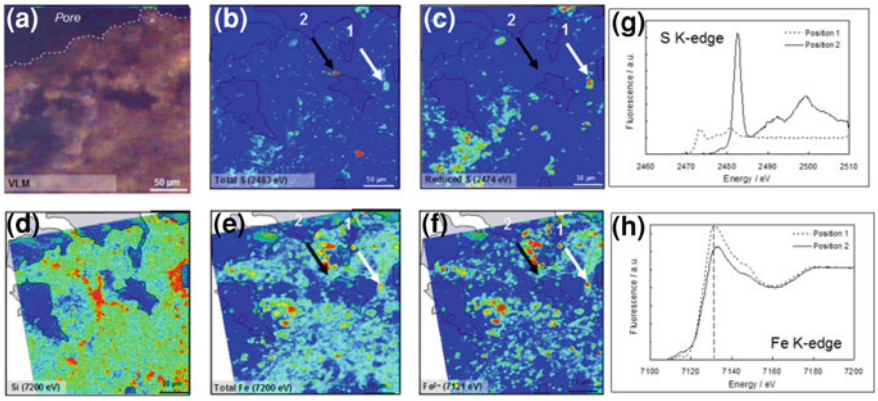


Fig. 14.7 Study of the physico-chemical heterogeneity patterns in soils (soil aggregate). (**a**) VLM of a 300 µm X 300 µm region of the soil forest; Microspatial distribution of (**b**) the total sulfur, (**c**) reduced sulfur, (**d**) silicium and (**e**) total iron and (**f**) divalent iron by µ-XRF. The labels refer to the XANES spectra obtained at (**g**) the S K-edge, and (**h**) Fe K-edge showing the co-existance of organic disulfide with iron bounded to silicate (*1*) and inorganic sulfur with mainly Fe III oxyhydroxide (*2*) [98]. Courtesy of J. Prietzel

Other hot topics among many others concerns characterization of air particulate matter [99], gestion and diffusion of industrial wastes [100], phytoremediation [101, 102], food nutrition and safety [11, 103] and marine biology [104, 105].

14.6.3 Life Science

Knowing at any given time where every atom of every molecule resides in an organism holds the key to answering any research question in the life science. Consequently microscopy is the essential tool for all life-science researchers, and recent technological advances in XRM have led to an exponential increase of the biological applications [106–109] and range of scientific questions addressed [1] by the technique. The entire X-ray range, the various XRM set-ups and plethora of contrast mechanisms contribute significantly to the field, via elemental analysis, chemical state analysis and imaging of elements and substructures within the biological entity. Soft X-ray TXM, for instance, is taking advantage of the water window contrast to reveal the ultra-structures of entire hydrated cells in 2D and 3D, without any use of slicing or staining as it is the case in TEM for high resolution imaging but only with cryo-preservation, and therefore generating a real "atlas" of cellular structures [110, 111].

Overall, the applications are numerous, from resolving sub-structures of various cell lines (Fig. 14.8a–i) [44, 112], determining the effect of specific proteins [113], contrast agents, nanomaterials (Fig. 14.8j, k) [114, 115] and their possible toxicity

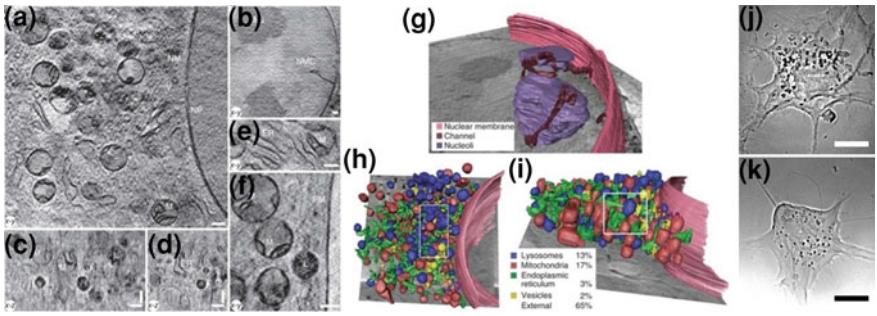


Fig. 14.8 Soft TXM (**a**–**f**) images of a 3134 cell (murine mammary adenocarcinoma cell line), revealing many subcellular organelles including mitochondria (*M*), lysosomes (*L*), endoplasmic reticulum (*ER*), vesicles (*V*), plasma (*PM*) and nuclear membrane (*NM*), nuclear pores (*NP*), nucleoli (*Nu*) and nuclear membrane channels (*NMC*) (E_{exc}: 510 eV, t: 1–4 s, *bars* 0.39 μm). (**g**–**i**) 3D rendering of cell cytoplasm, related to image **b**), and segmented to visualize the association of the nuclear membrane (*pink*) with the various sub-organelles structures as nuclear channels and cytoplasm sub-structures [44]. Courtesy of G. Schneider. Hard TXM images showing different ways of internalization of Au NPs by (**j**) EMT cell and (**k**) CT-26 cell. The picture reveals discrepancies in terms of total amount of internalized Au NPs and NPs cluster morphology, highlighting the importance of means to optimize nanomedicine procedure and conditions to avoid toxicity (E_{exc}: 8 keV, t: 1–4 s, *bars* 5 μm) [114]. Courtesy of I. Kempson

or biotransformation, pharmaceutical treatments, and to study the impact of various physiological conditions and disease on cellular cycle.

Because metals, even as trace elements, are essential and intrinsic components of biological systems, as metal dis-regulation leads to mal-functioning of a biological function and as many drugs and treatments contains metals, XRF investigation efficiently complements pure structural studies [116–118] by giving access to the elemental contents of cells, tissues, and the effect of treatments. Obviously comparison in between controls and affected specimens is a necessity to unknot bio-elemental patterns based on quantitative determination of metals, and of their distribution within the specimen. Clinical studies probing the effect of drugs, for example of neuroprotectants against epileptic seizures (Fig. 14.9) [119, 120], have helped significantly in describing the possible interplays between metals in neurological processes.

However, as metal localizations or co-localizations are obviously not a sufficient parameter to understand the biochemistry of these complex bio-inorganic/organic systems, XAS is logically employed complimentarily to reveal physical states of metals and their chemical environments. In particular, XAS has been particularly proficient in determining the states of metals associated with specific diseases such as neurodegenerative diseases -Parkinson, Alzheimer [121]-, cancer, to probe the integrity of drug delivery agents [122, 123] or bone mineral reactivity [124, 125]. It is of note that some of these studies have been complemented with FTIR micro-spectroscopy [68, 124, 126], stressing the additional complexity of biomolecular changes associated to elemental modifications. The capabilities of XRM were exploited in many

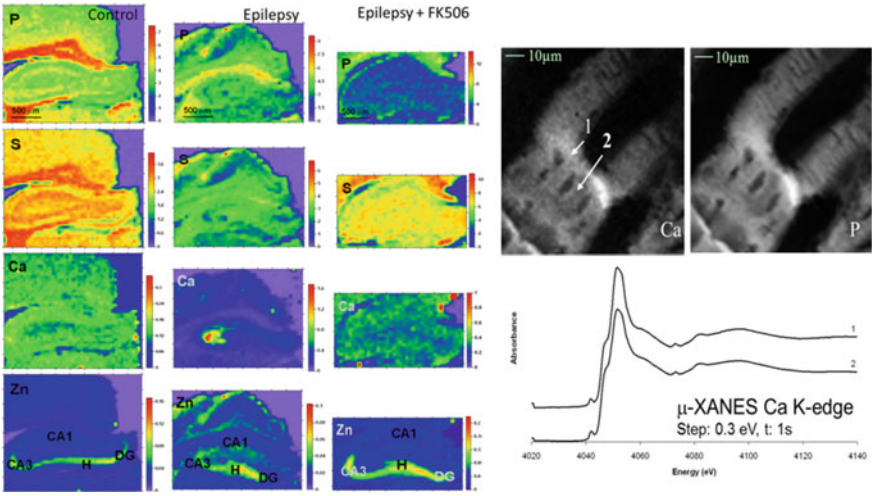


Fig. 14.9 *Left* Effect on drug treatment (FK-506) in epilepsy. Quantitative assessment of the elemental distributions of P, S, Ca and Zn in rat brain, suggesting the inhibition of calcineurin (Ca signal) as drug mode of action and proving the effectiveness of the neuroprotectant for the important metal (Zn) [118]. Courtesy of J. Chwiej. *Right* Study on bone mineralization: XRF maps of Ca and P in a chicken bone embryo (E_{ext}: 4.1 keV, t: 1 s, step: 0.5 µm), revealing the morphology of the bone and the perfect co-localization of the two elements. XANES reveals a spatial heterogeneity in the Ca environment of the apatitic phase, directly connected to the mineral reactivity [124]

other area of research ranging from osteoporosis, biomaterials and bone [127, 128], muscle [129], possible carcinogenic materials [130], etc.

Ultimately, XRM appears as promising and innovative platforms to unravel the mechanisms leading to the development of effective theragnostic nanosystems by probing the specimen for purposes, apart from pure imaging of cells and tissues, such as diagnosis, follow up of the delivery of therapeutics from their introduction to their incorporation in the desired targeted site (or any secondary target or sink), and therapy by monitoring the effects of treatments.

14.7 Conclusions

The versatility and variety of XRM imaging tools are constantly increasing as new scientific questions arisen. Consequently, XRM looks and works beyond the scope of traditional disciplinary boundaries in order to face new challenges in terms of technical developments (sources, optics, detectors), imaging modes (coherent diffraction imaging), analysis (sample environments, data treatment), and to identify new scientific opportunities. The involvement of the various research communities as well as the combination or correlation of XRM with various complementary characterization techniques (VLM, FTIR, Raman, AFM, …) is therefore highly desirable

to push XRM towards new dimensions, in particular to realize its great potential in exploring and understanding the nano-scale world and its dynamics.

Acknowledgments DE wishes to greatly acknowledge Robert Acres, Joanna Chwiej, Ivan Kempson, Ivan Kreft, Florian Meirer, Jörg Prietzel, Marjana Regvar, Gerd Schneider and Giuliana Tromba for their enthusiasm, their support providing comments and/or illustrations, and Werner Jark for many discussions about sources and optics. This chapter couldn't have been written without collaborations with colleagues from many facilities and research institutes.

References

1. J. Kirz, C. Jacobsen, M. Howells, Q. Rev. Biophys. **28**, 33–130 (1995)
2. M. Feser, M.R. Howells, J. Kirz, J. Rudati, W. Yun, J. Synchrotron Radiat. **19**, 751–758 (2012)
3. D. Attwood, J. Phys. D: Appl. Phys. **37**, E01 (2004). doi:10.1088/0022-3727/37/23/E01
4. A. Sakdinawat, D. Attwood, Nat. Photon. **4**, 840–848 (2010)
5. D. Attwood D, in *Soft X-rays and Extreme Ultraviolet Radiation—Principles and Applications* (Cambridge University Press, New York 1999)
6. D.M. Mills (ed.), *Third-Generation Hard X-ray Synchrotron Radiation Sources* (John Wiley & Sons Inc, New York, 2002)
7. A. Erko, M. Idir, T. Krist, A.G. Michette (eds.), *Modern Developments in X-Ray and Neutron Optics* (Springer, New York, 2008)
8. M. Howells, C. Jacobsen, T. Warwick, A. Van den Bos, in *Science of Microscopy*, ed. by P.W.Q. Hawkes, J.C.H. Spence, (Springer, Berlin, 2006), pp. 835–926
9. F. Scholze, A. Longoni, C. Fiorini, L. Strüder, N. Meidinger, R. Hartmann, N. Kawahara, T. Shoji, in *Handbook of Practical X-Ray Fluorescence Analysis*, ed. by B. Beckhoff, B. Kangiesser, N. Langhoff, R. Wedell, H. Wolff (Springer, Berlin, 2006), pp. 199–308
10. R.E. Van Grieken, A. Markowicz (eds.), in *Handbook of X-Ray Spectrometry: Methods and Techniques*, 2nd edn. (Marcel Dekker Inc., New York, 2002)
11. M. Regvar, D. Eichert, B. Kaulich, A. Gianoncelli, P. Pongrac, K. Vogel-Mikuš, I. Kreft, J. Exp. Bot. **62**, 3929–3939 (2011)
12. B.L. Henke, E.M. Gullikson, J.C. Davis, At. Data Nucl. Data Tables **54**, 181–342 (1993)
13. X-ray Data Booklet (Lawrence Berkeley National Laboratory, California, 2009) http://xdb.lbl.gov/. Accessed 28 Jan 2011
14. J.E. Penner-Hahn, in *Comprehensive Coordination Chemistry*, vol. II, ed. by J.A. McCleverty, T.J. Meyer (Elsevier Ltd., Oxford, 2004), pp. 159–186
15. K. Janssens, in *Handbook of Spectroscopy*, ed. by G. Gauglitz, T. Vo-Dinh (Wiley-VCH Verlag GmbH & Co. KGaA, Weinheim, 2003), pp. 363–420
16. G. Schmahl, D. Rudolph, G. Schneider, P. Guttmann, B. Niemann, Optik **97**, 181–182 (1994)
17. G. Schmahl, D. Rudolph, P. Guttmann, G. Schneider, J. Thieme, B. Niemann, Rev. Sci. Inst. **66**, 1282–1286 (1995)
18. G. Schneider, Ultramicroscopy **75**, 85–104 (1998)
19. T.J. Davis, D. Gao, T.E. Gureyev, A.W. Stevenson, S.W. Wilkins, Nature **373**, 595–598 (1995)
20. T.J. Davis, T.E. Gureyev, D. Gao, A.W. Stevenson, S.W. Wilkins, Phys. Rev. Lett. **74**, 3173–3176 (1995)
21. B. Kaulich, P. Thibault, A. Gianoncelli, M. Kiskinova, J. Phys. Condens. Matter **23**, 083002 (2011). doi:10.1088/0953-8984/23/8/083002
22. C. Holzner, M. Feser, S. Vogt, B. Hornberger, S.B. Baines, C. Jacobsen, Nat. Phys. **6**, 883–887 (2010)
23. T.Y. Chen, Y.T. Chen, C.L. Wang, I.M. Kempson, W.K. Lee, Y.S. Chu, Y. Hwu, G. Margaritondo, Opt. Express **19**, 19919–19924 (2011)

24. G.R. Morrison, in *Proceedings of the 4th International Conference*, Chernogolovka, 1994, ed. by V,V. Aristov, A.I. Erko, pp. 478–486
25. G.R. Morrison, B. Niemann, in *X-ray Microscopy and Spectromicroscopy*, ed. by J. Thieme, D. Rudolph, G. Schmahl, E. Umbach (Springer, Berlin, 1996), pp. I85–I94
26. F. Polack, D. Joyeux, in *Proceedings of the* 4th *International Conference*, Chernogolovka, 1994, ed. by V.V. Aristov, A.I. Erko, pp. 432–437
27. G.R. Morrison, M.T. Browne, Rev. Sci. Instr. **63**, 611–614 (1992)
28. G.R. Morrison, in *Soft X-ray Microscopy*, vol. 1741, ed. by C. Jacobsen, J. Trebes (SPIE, Bellingham, 1992), pp. 186–193
29. A. Momose, Jap. J. Appl. Phys. **44**, 6355–6367 (2005)
30. B. Niemann, D. Rudolph, G. Schmahl, Appl. Opt. **15**, 1883–1884 (1976)
31. D. Rudolph, B. Niemann, G. Schmahl, O. Christ, in *X-Ray Microscopy*, ed. by G. Schmahl, D. Rudolph, *International Symposium*, Göttingen, Sept 1983. The Göttingen X-ray microscope and X-ray microscopy experiments at the BESSY storage ring, vol. 43 (Springer, Berlin, 1984), pp. 192–202
32. P. Horowitz, J.A. Howell, Science **178**, 608–611 (1972)
33. J. Kirz, D. Sayre, in *Synchrotron Radiation Research*, ed. by H. Winick, S. Doniach (Plenum Press, New York, 1980) pp. 277–322
34. R. Falcone, J. Kirz, C. Jacobsen, J.C.H. Spence, S. Marchesini, D.A. Shapiro, Contemp. Phys. **52**, 293–318 (2011)
35. K. Nugent, Adv. Phys. **59**, 1–99 (2009)
36. E. Bauer, Rep. Prog. Phys. **57**, 895–938 (1994)
37. V.E. Cosslett, W.C. Nixon, Nature **168**, 24–25 (1951)
38. J. Cazaux, D. Erre, D. Mouze, J.M. Patat, S. Rondot, A. Sasov, P. Trebbia, A. Zolfaghari, In: J. Phys. IV, Colloque C7, ed. by R. Pichoir, P. Costa, 3rd *European Conference on Advanced Materials and Processes*, Paris, June 1993. Recent developments in X-ray projection microscopy and X-ray microtomography applied to materials science, Les Editions de Physique, Paris (1993) pp. 2099–2104
39. S.C. Mayo, P.R. Miller, S.W. Wilkins, T.J. Davis, D. Gao, T.E. Gureyev, D. Paganin, D.J. Parry, A. Pogany, A.W. Stevenson, J. Phys. IV **104**, 543–546 (2003)
40. W. Meyer-Ilse, H. Medecki, L. Jochum, E. Anderson, D. Attwood, C. Magowan, R. Balhorn, M. Moronne, D. Rudolph, G. Schmahl, Synchrotron Radiat. News **8**, 29–33 (1995)
41. A. Sakdinawat, Y. Liu, Opt. Express **16**, 1559–1564 (2008)
42. X. Zeng, Appl. Opt. **47**, 2376–2381 (2008)
43. G. Schneider, E. Anderson, S. Vogt, C. Knoechel, D. Weiss, M. LeGros, C. Larabell, Surf. Rev. Lett. **9**, 177–183 (2002)
44. G. Schneider, P. Guttmann, S. Heim, S. Rehbein, F. Mueller, K. Nagashima, J.B. Hermann, W.G. Müller, J.G. McNally, Nat. Methods **7**, 985–988 (2010)
45. U. Neuhausler, G. Schneider, W. Ludwig, M.A. Meyer, E. Zschech, D. Hambach, J. Phys. D: Appl. Phys. **36**, A79–A82 (2003)
46. Y.S. Chu, J.M. Yi, F. De Carlo, Q. Shen, W.K. Lee, H.J. Wu, C.L. Wang, J.Y. Wang, C.J. Liu, C.H. Wang, S.R. Wu, C.C. Chien, Y. Hwu, A. Tkachuk, W. Yun, M. Feser, K.S. Liang, C.S. Yang, J.H. Je, G. Margaritondo, Appl. Phys. Lett. **92**, 103119 (2008)
47. T. Wilhein, B. Kaulich, E. Di Fabrizio, F. Romanato, S. Cabrini, J. Susini, Appl. Phys. Lett. **78**, 2082–2084 (2001)
48. B. Kaulich, T. Wilhein, E. Di Fabrizio, F. Romanato, M. Altissimo, S. Cabrini, B. Fayard, J. Susini, J. Opt. Soc. Am. A **19**, 797–806 (2002)
49. O. Scharf, S. Ihle, I. Ordavo, V. Arkadiev, A. Bjeoumikhov, S. Bjeoumikhova, G. Buzanich, R. Gubzhokov, A. Günther, R. Hartmann, M. Kühbacher, X.M. Lang, N. Langhoff, A. Liebel, M. Radtke, U. Reinholz, H. Riesemeier, H. Soltau, L. Strüder, A.F. Thünemann, R. Wedell, Anal. Chem. **83**, 2532–2538 (2011)
50. C. Jacobsen, S. Wirick, G. Flynn, C. Zimba, J. Microsc. **197**, 173–184 (2000)
51. P. Guttmann, C. Bittencourt, S. Rehbein, P. Umek, X. Ke, G. Van Tendeloo, C.P. Ewels, G. Schneider, Nat. Photon. **6**, 25–29 (2012)

52. J.D. Grunwaldt, C.G. Schroer, Chem. Soc. Rev. **39**, 4741–4753 (2010)
53. F. Meirer, J. Cabana, Y. Liu, A. Mehta, J.C. Andrews, P. Pianetta, J. Synchrotron Radiat. **18**, 773–781 (2011)
54. J.M. Kenney, J. Kirz, H. Rarback, M.R. Howells, P. Chang, P.J. Coane, R. Feder, P.J. Houzego, D.P. Kern, D. Sayre, Nucl. Instrum. Methods. Phys. Res. A **222**, 37–41 (1984)
55. W. Chao, B.D. Harteneck, J.A. Liddle, E.H. Anderson, D.T. Attwood, Nature **435**, 1210–1213 (2005)
56. W. Chao, P. Fischer, T. Tyliszczak, S. Rekawa, E. Anderson, P. Naulleau, Opt. Express **20**, 9777–9783 (2012)
57. O. Hignette, P. Cloetens, G. Rostaing, P. Bernard, C. Morawe, Rev. Sci. Instrum. **76**, 063709 (2005)
58. H. Mimura, S. Handa, T. Kimura, H. Yumoto, D. Yamakawa, H. Yokoyama, S. Matsuyama, K. Inagaki, K. Yamamura, Y. Sano, K. Tamasaku, Y. Nishino, M. Yabashi, T. Ishikawa, K. Yamauchi, Nat. Phys. **6**, 122–125 (2010)
59. G.C. Yin, Y.F. Song, M.T. Tang, F.R. Chen, K.S. Liang, F.W. Duewer, M. Feser, W. Yun, H.P.D. Shieh, Appl. Phys. Lett. **89**, 221122 (2006)
60. H. Yan, V. Rose, D. Shu, E. Lima, H.C. Kang, R. Conley, C. Liu, N. Jahedi, A.T. Macrander, G.B. Stephenson, M. Holt, Y.S. Chu, M. Lu, J. Maser, Opt. Express **19**, 15069–15076 (2011)
61. C.G. Schroer, O. Kurapova, J. Patommel, P. Boye, J. Fedkamp, B. Lengeler, M. Burghammer, C. Riekel, L. Vincze, A. van der Hart, M. Küchler, Appl. Phys. Lett. **87**, 124103 (2005)
62. A. Menzel, C.M. Kewish, P. Kraft, B. Henrich, K. Jefimovs, J. Vila-Comamala, C. David, M. Dierolf, P. Thibault, F. Pfeiffer, O. Bunk, Ultramicroscopy **110**, 1143–1147 (2010)
63. B. Hornberger, M.D. de Jonge, M. Feser, P. Holl, C. Holzner, C. Jacobsen, D. Legnini, D. Paterson, P. Rebak, L. Strüder, S. Vogt, J. Synchrotron Radiat. **15**, 355–362 (2008)
64. B. Kaulich, A. Gianoncelli, A. Beran, D. Eichert, I. Kreft, P. Pongrac, M. Regvar, K. Vogel-Mikuš, M. Kiskinova, J. R. Soc. Interface **6**, S641–S647 (2009)
65. A.M. Flank, G. Cauchon, P. Lagarde, S. Bac, M. Janousch, R. Wetter, J.M. Dubuisson, M. Idir, F. Langlois, T. Moreno, D. Vantelon, Nucl. Instrum. Methods Phys. Res. B **246**, 269–274 (2006)
66. D.P. Siddons, A. Dragone, G. De Geronimo, A. Kuczewski, J. Kuczewski, P. O'Connor, Z. Li, C.G. Ryan, G. Moorhead, R. Kirkham, P.A. Dunn, in *Nuclear Science Symposium Conference Record 2006 IEEE*, ed. by B. Phlips. IEEE Nuclear Science Symposium Medical Imaging Conference and Room Temperature Detector Workshop, San Diego, Oct-Nov 2006 A high-speed detector system for X-ray fluorescence microprobes, vol. 6 (IEEE, Piscataway, 2006), pp. 725–728
67. C.G. Ryan, R. Kirkham, R.M. Hough, G. Moorhead, D.P. Siddons, M.D. de Jonge, D.J. Paterson, G. De Geronimo, D.L. Howard, J.S. Cleverley, Nucl. Instrum. Methods Phys. Res. A **619**, 37–43 (2010)
68. D. Eichert, L. Gregoratti, B. Kaulich, A. Marcello, P. Melpignano, L. Quaroni, M. Kiskinova, Anal. Bioanal. Chem. **389**, 1121–1132 (2007)
69. M. Stampanoni, A. Groso, A. Isenegger, G. Mikuljan, Q. Chen, A. Bertrand, S. Henein, R. Betemps, U. Frommherz., P. Böhler, D. Meister, M. Lange, R. Abela, in *Developments in X-ray Tomography V*, *Proceedings of SPIE*, vol. 6318, ed. by U. Bonse SPIE (2006), pp. 63180M-1–63180M-14
70. C. Rau, A. Somogyi, A. Simionovici, Nucl. Instrum. Methods Phys. Res. B **200**, 444–450 (2003)
71. B. Golosio, A. Simionovici, A. Somogyi, L. Lemelle, M. Chukalina, A. Brunetti, J. Appl. Phys. Lett. **94**, 145 (2003)
72. C.G. Schroer, M. Kuhlmann, S.V. Roth, R. Gehrke, N. Stribeck, A. Almendarez-Camarillo, B. Lengeler, Appl. Phys. Lett. **88**, 164102 (2006)
73. P. Bleuet, E. Welcomme, E. Dooryhée, J. Susini, J.L. Hodeau, P. Walter, Nat. Mater. **7**, 468–472 (2008)
74. H.F. Poulsen, J. Appl. Cryst. **45**, 1084–1097 (2012)

75. A. Rogalev, J. Goulon, in *Chemical Applications of Synchrotron Radiation, Part II: X-ray Applications*, ed. by T.K. Sham. Advanced Series in Physical Chemistry, vol. 12B, (World Scientific Publishing, River Edge, 2002), pp. 707–760
76. C. Hagen, P. Guttmann, B. Klupp, S. Werner, S. Rehbein, T.C. Mettenleiter, G. Schneider, K. Grunewald, J. Struct. Biol. **177**, 193–201 (2012)
77. M. Regvar, D. Eichert, B. Kaulich, A. Gianoncelli, P. Pongrac, K. Vogel-Mikuš, Plant Soil (2013). doi:10.1007/s11104-013-1768-z
78. L.M. Miller, P. Dumas, Biochim. Biophys. Acta **1758**, 846–857 (2006)
79. S.A. James, D.E. Myers, M.D. de Jonge, S. Vogt, C.G. Ryan, B.A. Sexton, P. Hoobin, D. Paterson, D.L. Howard, S.C. Mayo, M. Altissimo, G.F. Moorhead, S.W. Wilkins, Anal. Bioanal. Chem. **401**, 853–864 (2011)
80. A. Meents, S. Guttmann, A. Wagner, C. Schulze-Briese, Proc. Natl. Acad. Sci. USA **107**, 1094–1099 (2010)
81. J. Chwiej, M. Szczerbowska-Boruchowska, M. Lankosz, S. Wojcik, G. Falkenberg, Z. Stegowski, Z. Setkowicz, Spectrochim. Acta B - At. Spectrosc. **60**, 1531–1537 (2005)
82. J. Goldstein, D.E. Newbury, D.C. Joy, C.E. Lyman, P. Echlin, E. Lifshin, L. Sawyer, J.R. Michael, in *Scanning Electron Microscopy and X-ray Microanalysis*, 3rd edn., (Springer Science + Business Media Inc, New York, 2003), pp. 591–646
83. P. Echlin, *Handbook of Sample Preparation for Scanning Electron Microscopy and X-ray Microanalysis* (Springer Science, New York, 2009)
84. M.R. Howells, T. Beetz, H.N. Chapman, C. Cui, J.M. Holton, C.J. Jacobsen, J. Kirz, E. Lima, S. Marchesini, H. Miao, D. Sayre, D.A. Shapiro, J.C.H. Spence, D. Starodub, Electr. Spectr. Rel. Phen. **170**, 4–12 (2009)
85. L. Vincze, in *X-ray Spectrometry: Recent Technological Advances*, ed. by K. Tsuji, J. Injuk, R. Van Grieken (John Wiley & Sons Ltd, Chichester, 2004), pp. 435–462
86. M. Mantler, in *Handbook of Practical X-ray Fluorescence Analysis*, B. Beckhoff, B. Kanngießer, N. Langhoff, R. Wedell, H. Wolff (Springer, Berlin, 2006), pp. 309–407
87. S.C. Chao, Y.C. Yen, Y.F. Song, Y.M. Chen, H.C. Wu, N.L. Wu, Electrochem. Commun. **12**, 234–237 (2010)
88. B. Bozzini, Kazemian Abyaneh M., Amati M., Gianoncelli A., Gregoratti L., Kaulich B., Kiskinova M. Chem. Eur. J. **18**, 10196–10210 (2012)
89. C.R. McNeill, B. Watts, S. Swaraj, H. Ade, L. Thomsen, W. Belchre, P.C. Dastoor, Nanotechnology **19**, 424015 (2008)
90. A. Guilherme, J. Coroado, J.M.F. dos Santos, L. Lühl, T. Wolff, B. Kanngießer, M.L. Carvalho, Spectrochim. Acta B **66**, 297–307 (2011)
91. P. Fischer, M.Y. Im, C. Baldasseroni, C. Bordel, F. Hellman, J.S. Lee, S.C. Fadley, J. Electron. Spectrosc. Relat. Phenom. (2013), http://dx.doi.org/10.1016/j.elspec.2013.03.012
92. S.S. Kalirai, D.A. Bazylinski, A.P. Hitchcock, PLOS One **8**, e53368 (2013)
93. D.G. Schulze, P.M. Bertsch, Adv. Agron. **55**, 1–66 (1995)
94. J. Thieme, I. McNulty, S. Vogt, D. Paterson, Environ. Sci. Technol. **41**, 6885–6889 (2007)
95. B. Singh, M. Grafe (eds.), in *Synchrotron-Based Techniques in Soils and Sediments* (Elsevier B.V, Oxford, 2010)
96. A. Manceau, M.A. Marcus, N. Tamura, in *Applications of Synchrotron Radiation in Low-Temperature Geochemistry and Environmental Science*, ed. by P.A. Fenter, M.L. Rivers, N.C. Sturchio, S.R. Sutton, Reviews in Mineralogy and Geochemistry, vol 49 (Mineralogical Society of America, Washington DC, 2002), pp. 341–428
97. E. Lombi, J. Susini, Plant Soil **320**, 1–35 (2009)
98. J. Prietzel, J. Thieme, M. Salomé, J. Synchrotron Rad. **17**, 166–172 (2010)
99. K.M. Shakya, S. Liu, S. Takahama, L.M. Russell, F.N. Keutsch, M.M. Galloway, J.E. Shilling, N. Hiranuma, C. Song, H. Kim, S.E. Paulson, L. Pfaffenberger, P. Barmet, J. Slowik, A.S.H. Prévôt, J. Dommen, U. Baltensperger, Aerosol. Sci. Tech. **47**, 543–555 (2013)
100. P.J.M. Monteiro, L. Clodic, F. Battocchio, W. Kanitpanyacharoen, S.R. Chae, J. Ha, H.R. Wenk, Cem. Concr. Compos. **40**, 14–20 (2013)
101. D.H. McNear, R.L. Chaney, D.L. Sparks, Phytochem. **71**, 188–200 (2010)

102. W. Amos, S. Webb, Y. Liu, J.C. Andrews, D.L. Leduc, Anal. Bioanal. Chem. **404**, 1277 (2012)
103. R. Tolrà, K. Vogel-Mikuš, R. Hajiboland, P. Kump, P. Pongrac, B. Kaulich, A. Gianoncelli, V. Babin, J. Barcelo, M. Regvar, C. Poschenrieder, J. Plant Res. **124**, 165–172 (2010)
104. M. Obst, J.J. Dynes, J.R. Lawrence, G.D.W. Swerhone, K. Benzerara, C. Karunakaran, K. Kaznatcheev, T. Tyliszczak, A.P. Hitchcock, Geochim Cosmochim. Ac. **73**, 4180–4198 (2009)
105. J. Diaz, E. Ingall, S. Vogt, M.D. De Jonge, D. Paterson, C. Rau, J.A. Brandes, Limnol. Oceanogr. Methods **7**, 42–51 (2009)
106. A. Ide-Ektessabi (ed.), *Applications of Synchrotron Radiation—Micro Beams in Cell Micro Biology and Medicine* (Springer-Verlag, Berlin Heidelberg, 2007) NULL
107. Z. Qin, J.A. Caruso, B. Lai, A. Matusch, J.S. Becker, Metallomics **3**, 28–37 (2011)
108. C.T. Dillon, Aust. J. Chem. **65**, 204–217 (2012)
109. H. Chen, M.M. Rogalski, J.N. Anker, Phys. Chem. Chem. Phys. **14**, 13469–13486 (2012)
110. W.G. Müller, J.B. Heymann, K. Nagashima, P. Guttmann, S. Werner, S. Rehbein, G. Schneider, J. McNally, J. Struct. Biol. **177**, 179–192 (2012)
111. G. McDermott, M.A. LeGros, C.A. Larabell, Ann. Rev. Phys. Chem. **63**, 225–239 (2012)
112. E. Hanssen, C. Knoechel, M. Dearnley, M.W.A. Dixon, M. Le Gros, C. Larabell, L. Tinney, J. Struct. Biol. **177**, 224–232 (2012)
113. K. Takemotoa, I. Narumi, K. Satoh, T. Ohigashi, H. Namba, H. Kihara, in *The 10th International Conference on X-Ray Microscopy* ed. by I. McNulty, C. Eyberger, B. Lai, 10th *International Conference on X-Ray Microscopy*, Chicago, August 2010. New Approaches for X-ray microimaging of live cells in the water window at subzero temperatures with the use of antifreeze. AIP Conference Proceedings, vol. 1365 (American Institute of Physics, Melville New York (2010), pp. 415–418
114. H.H. Chen, C.C. Chien, C. Petibois, C.L. Wang, Y.S. Chu, S.F. Lai, T.E. Hua, Y.Y. Chen, X. Cai, I.M. Kempson, Y. Hwu, G. Margaritondo, J. Nanobiotechnol. **9**, 14 (2011)
115. S. Ahn, S.Y. Jung, J.P. Lee, H.K. Kim, S.J. Lee, ACS Nano. **4**, 3753–3762 (2010)
116. M. Ralle, S. Lutsenko, Biometals **22**, 197–205 (2009)
117. T. Paunesku, S. Vogt, B. Lai, J. Maser, N. Stojićević, K.T. Thurn, C. Osipo, H. Liu, D. Legnini, Z. Wang, C. Lee, G.E. Woloschak, Nano Lett. **7**, 596–601 (2007)
118. E. Kosior, S. Bohic, H. Suhonen, R. Ortega, G. Devès, A. Carmona, F. Marchi, J.F. Guillet, P. Cloetens, J. Struct. Biol. **177**, 239–247 (2012)
119. J. Chwiej, K. Janeczko, M. Marciszko, M. Czyzycki, K. Rickers, Z. Setkowicz, J. Biol. Inorg. Chem. **15**, 283–289 (2010)
120. R. Ortega, P. Cloetens, G. Devès, A. Carmona, S. Bohic, Plos One **2**, e925 (2007)
121. R. Ortega, J. Anal. At. Spectrom. **26**, 23–29 (2011)
122. E.F. Molina, S.H. Pulcinelli, C.V. Santilli, S. Blanchandin, V. Briois, J. Phys. Chem. B **114**, 3461–3466 (2010)
123. C.M. Weekley, J.B. Aitken, S. Vogt, L.A. Finney, D.J. Paterson, M.D. de Jonge, D.L. Howard, I.F. Musgrave, H.H. Harris, Biochem. **50**, 1641–1650 (2011)
124. D. Eichert, M. Salomé, M. Banu, J. Susini, C. Rey, Spectrochim. Acta B **60**, 850–858 (2005)
125. D. Eichert, M. Salomé, P. Bleuet, S. Bohic, J. Susini, in *X-Ray MicroscopyProceedings of the 8th International Conference on X-ray Microscopy*, Himeji, August 2005 ed. by S. Aoki, Y. Kagoshima, Y. Suzuki. Contribution of X-ray microscopy to bone mineral studies, vol. 7 IPAP Conf. Series 7, Tokyo (2006) pp. 210–212
126. J. Dudala, K. Janeczko, Z. Setkowicz, D. Eichert, J. Chwiej, Nukleonika **57**, 615–619 (2012)
127. M. Gasperini, M.D. Calasans-Maia, R.F.B. Resende, J.M. Granjeiro, A.M. Rossi, R.T. Lopes, I. Lima, X-Ray Spectrom. **41**, 6–11 (2012)
128. J.C. Andrews, E. Almeida, M.C.H. van der Meulen, J.S. Alwood, C. Lee, Y. Liu, J. Chen, F. Meirer, M. Feser, J. Gelb, J. Rudati, A. Tkachuk, W. Yun, P. Pianetta, Microsc. Microana. **16**, 327–336 (2010)
129. B.M. Palmer, S. Vogt, Z. Chen, R.R. Lachapelle, M.M. LeWinter, J. Struct. Biol. **155**, 12–21 (2006)
130. T. Paunesku, S. Vogt, J. Maser, B. Lai, G. Woloschak, J. Cell Biochem. **99**, 1489–1502 (2006)

Chapter 15
Infrared Synchrotron Radiation: From the Production to the Scientific Applications

Andrea Perucchi, Lisa Vaccari and Stefano Lupi

Abstract Today, most of the Synchrotron Radiation (SR) facilities offer a port dedicated to Infrared spectroscopy and microspectroscopy exploiting the high brilliance gain of Infrared Synchrotron Radiation (IRSR) with respect to laboratory-based infrared sources. In this chapter, we review the main figures of merits of IRSR along with its main applications in Condensed Matter Physics, Biology, and Cultural Heritage.

15.1 Introduction

The Infrared (10–10,000 cm^{-1}, 1 meV–1.5 eV, 1000–1 μm) represents one of the most important spectral regions of the electromagnetic spectrum since a multitude of excitations characteristic of Condensed Matter, Chemistry, Biology/Biomedicine, Material and Surface Science, falls in this interval. Infrared (IR) spectroscopy with conventional laboratory sources dates at the end of the eighteenth century [1] but, only in the 1970 it was realized that Synchrotron Radiation (SR) might have a strong potential as an infrared source for spectroscopy and microscopy. Pioneering measurements of Infrared Synchrotron Radiation (IRSR) have been performed on existing UV ports in 1970s at LURE (Orsay, France) by Lagarde et al. and at Tantalus (Stoughton, USA) by Stevenson et al. [2, 3]. The first dedicated IR beamline was

A. Perucchi (✉) · L. Vaccari
Elettra Sincrotrone Trieste, Strada Statale 14, in Area Science Park,
34149 Basovizza, TS, Italy
e-mail: Andrea.perucchi@elettra.eu

L. Vaccari
e-mail: Lisa.vaccari@elettra.eu

S. Lupi
INFN and Department of Physics, Sapienza University of Rome,
P.le A. Moro 2, 00185 Rome, Italy
e-mail: stefano.lupi@roma1.infn.it

S. Mobilio et al. (eds.), *Synchrotron Radiation*,
DOI: 10.1007/978-3-642-55315-8_15, © Springer-Verlag Berlin Heidelberg 2015

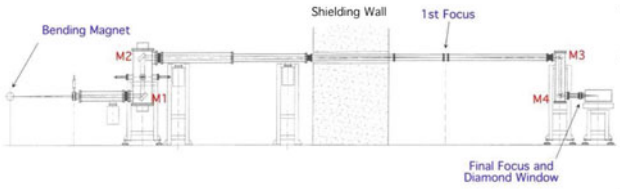


	Figure	Dimension HXV (cm²)
M1	Plane	30X15
M2	Ellipsoidal	35X18
M3	Plane	15X8
M4	Ellipsoidal	16X10

Fig. 15.1 The layout of the IRSR beamline at Elettra, SISSI, is shown on the *left*. On the *right*, the figure and dimension of used mirrors are reported

built in a storage ring in the early 1980s by Yarwood and colleagues [4] at Daresbury in UK. The first published experiment dates from 1985 and it was performed at Bessy in Germany by Schweitzer and collaborators on the vibrational/rotational spectrum of N_2O in the near-IR (around 1 μm) [5]. In the same year, the first research program on IRSR was launched at UVSOR in Japan by Namba [6], followed by an intense IRSR activity at NSLS in USA [7]. Presently, nearly all II and III generation storage rings host one or more IRSR beamlines (see Table 15.1) and new research programs start to be developed also in LINAC-based machines for pump-probe experiments [8]. As an example, the optical layout of the SISSI beamline at Elettra [9] and its mirror characteristics are shown in Fig. 15.1.

IRSR is collected from a bending trajectory arc of 65 ± 5 mrad in the orbit plane and 25 mrad in the vertical direction. The SISSI extraction mirror, M1, is placed in the first vacuum chamber, mounted behind the shielding wall of the synchrotron hall, 350 cm form the source point, assumed as the waist of the particle beam in the bending magnet. The plane mirror M1 deflects upward the IRSR with an angle of 90° to the ellipsoidal focusing mirror M2, 100 cm from M1 and mounted within the same chamber. M2 focuses the IRSR beam at the focal point F1, placed 1150 cm beyond the shielding wall. The source image at F1 is expected to be magnified by a factor 1.8. IRSR radiation is then collected by the plane mirror M3, placed 150 cm from F1, and focused from the ellipsoidal mirror M4 250 cm apart, in F2, where it is demagnified from a factor 4. M3 and M4 mirrors are placed within the second vacuum chamber. At F2, a wedged CVD diamond window separates the low vacuum of the second chamber from the environmental pressure of the experimental end-station.

15.2 IRSR Figures of Merits

15.2.1 Definitions

Synchrotron radiation is emitted when the relativistic velocity of an electron is modified through an external force, for instance, by entering in a dipole magnetic field

Table 15.1 List of IR beamlines worldwide

Synchrotron facility	Country	Beamline name	E (GeV)	I (mA)	Collection angle (H × V mrad)	Source type
ALBA	Spain	MIRAS	3	400	30 × 24	Bending
ALS	USA	1.4.3	1.2	500	40 × 10	Bending
ANKA	Germany	IR1 (MIR)	2.5	300	45 × 15	Bending + Edge
		IR2 (FIR)				Bending
AS	Australia	IR	3	200	58 × 17	Bending + Edge
Bessy II	Germany	IRIS	1.9	100	60 × 30	Bending
CAMD	USA	IR	1.3–1.5	300–150	50 × 50	Bending
CLS	Canada	01B1-1 (MIR)	2.9	300	55 × 38	Bending
		02B1-1 (FIR)			57 × 35	Bending
Daphne	Italy	SINBAD	0.51	5200	17 × 35	Bending
DELTA	Germany	BL-2	1.5	120	9 × 4	Bending
DESY	Germany	TTF2	7.5	30	42 × 35	Bending
Diamond	UK	B22	3	500	55 × 30	Bending + Edge
Elettra	Italy	SISSI	2–2.4	300–140	70 × 25	Bending + Edge
ESRF	France	ID21	6.03	200	8.5 × 16	Edge
INDUS	India	IR-Beam	0.45	100	50 × 30	Bending
MAX-LAB	Sweden	7.3	0.7	280	60 × 100	Bending
MLS	Germany	IR undulator	0.10–0.63	10^{-3}–200	64 × 43	Undulator
		THz				Bending
		IR				Bending
NSLS-I	USA	U2A	0.0808	1000	45 × 45	Bending
		U10B			40 × 40	Bending
		U12IR			90 × 90	Bending
		U2B			45 × 45	Bending
		U4IR			90 × 90	Bending
		U10A			40 × 40	Bending

(continued)

Table 15.1 (continued)

Synchrotron facility	Country	Beamline name	E (GeV)	I (mA)	Collection angle (H × V mrad)	Source type
NSRL	China	U4	0.8	300	75 × 60	Bending
NSRRC	Taiwan	BL14A1	1.5	240	70 × 30	Bending
SESAME	Jordan	EMIRA	2.5	400	39 × 15	Bending
SLS	Switzerland	X01DC	2.4	400	61 × 39	Bending
SRLI	Thailand	BL4.1	1.2	150	92 × 20	Bending
SOLEL	France	SMIS (MIR) AILES (FIR)	2.75	500	78 × 20	Bending + Edge
Spring8	Japan	BL43IR	8	100	36.5 × 12.5	Bending
SRC	USA	IRENI	1	190	320 × 25	Bending
		031			20 × 15	Bending
SSRF	China	ISMI	0.7	300	100 × 18.8	Bending
UVSOR	Japan	BL6A1	0.75–1	100–350	80 × 60	Bending
		BL6B			215 × 80	Bending

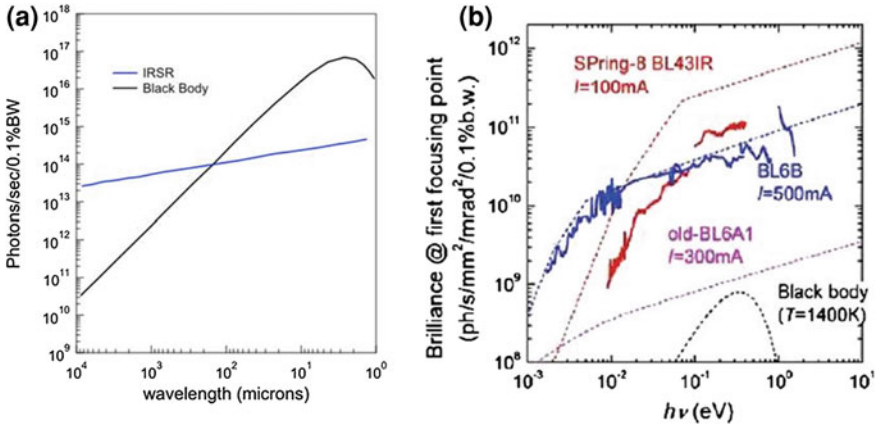


Fig. 15.2 **a** Comparison of the power emitted by a storage ring and a BB source at 2000 K. IRSR is more intense independently of the machine characteristics only in the far-IR (i.e. below 100 μm). **b** Comparison between the experimental brilliance of IRSR and BB sources as measured at different infrared beamlines and for different machine currents (*red curve* BL6A1 beamline at 300 mA; *blue curve* BL6B beamline at 500 mA) of Spring-8. The brilliance gain in the infrared reach about two order of magnitude. Adapted from [11]

of a storage ring. Transverse acceleration is responsible for the standard synchrotron emission, meanwhile the longitudinal velocity change (at the entrance or exit of a magnetic device) generates the so-called "edge radiation". These two types of emission have different spectral and spatial distribution properties (see Sect. 15.3) and they are both collected in the infrared at most of new beamlines in III generation machines. In storage rings, apart super-radiance phenomena (see Sect. 15.3), the total intensity is simply obtained by multiplying the emitted intensity for a single electron by the total number of electrons N, for almost all the emitted spectral range. In other terms, electric fields from each electron incoherently superimpose. The spectrum of emitted radiation is shown in Fig. 15.2a and compared with the one emitted by a Black-Body (BB) laboratory source. Similarly to the other spectral regions, the main figures of merits of IRSR are: (*i*) the emitted power (flux), (*ii*) the brilliance. These figures of merit focused to the infrared will be discussed in the following.[1]

15.2.2 Emitted Power

The infrared emitted power in the horizontal plane obtained as low-frequency limit of the Swinger formula can be expressed as [10]:

$$\mathrm{P}(\lambda) = 4.38 * \ 10^{14} * I * \theta_H * BW * (\rho/\lambda)^{1/3} \ \text{photon/s} \qquad (15.1)$$

[1] All the figures of merit will be discussed.

where I is the current in amperes, $\Delta\Psi_H$(rads) the horizontal collection angle, BW the bandwidth in %, λ the wavelength, and ρ the radius of the ring. λ and ρ are in the same units. The simple dependence on the current I, which is proportional to the number of electrons in a bunch, $I \approx N$, reveals the incoherent nature of the emission. The result of (15.1) is shown in Fig. 15.2a in the energy range 1–10^4 μm (10^4–1 cm^{-1}), for a current of 1 A, a horizontal angle $\Delta\Psi_H = 100$ mrads and $\rho = 5$ m. It is noteworthy that a flux gain can be obtained only in the far-IR below 100 cm^{-1} (corresponding to 100 μm, 12 meV, 3 THz), and this result is practically independent of the machine. The total infrared power cannot be obtained from (15.1), just multiplying P for the vertical collection angle $\Delta\Psi_v$. As a matter of fact, at variance with X-ray, IRSR has a non-uniform wavelength-dependent distribution in the vertical direction. Indeed a given wavelength is emitted at a specific vertical angle that can be approximated as follows [10]:

$$\Delta\Psi_v = 1.66 \cdot \left(\frac{\lambda}{\rho}\right)^{\frac{1}{3}} \tag{15.2}$$

Therefore, the far-IR ($\lambda \sim 100$ μm) is emitted in a larger angle than the mid-IR ($\lambda \sim 100$ μm). For instance at Elettra $\Delta\Psi_v \sim 50$ mrad for $\lambda = 100$ μm. These large vertical emission angles impose severe constraints on the vacuum-chamber vertical size. Indeed in high-energy machines a wide vacuum chamber, needed for collecting the whole flux, would induce instabilities in the electronic beam. Therefore a compromise between the need to maximize the flux and to minimize electronic instabilities should be reached. Collecting angles of operating IR beamlines worldwide are reported in Table 15.1.

15.2.3 Brilliance

The reduced size of an IRSR source in comparison to a laboratory thermal source should provide an important gain in terms of IRSR brilliance. This quantity can be approximated for all storage rings by [10]:

$$B(\lambda) = 3.8 * 10^{20} * I * BW/\lambda^2 \text{ photons/s/mm}^2\text{/sr} \tag{15.3}$$

where again, λ is the wavelength in microns, I the current in amperes, BW the bandwidth in %. The experimental Brilliance gain in the infrared with respect to a BB source as measured at the IRSR beamline at Spring-8 is shown in Fig. 15.2b [11]. The gain in the whole IR region reach nearly two orders of magnitude.

Moreover the brilliance is a very important parameter to obtain a high signal/noise ratio (S/N). Indeed the noise fluctuation (%N) with respect a 100 % baseline of an infrared detector is given by the following expression [10]:

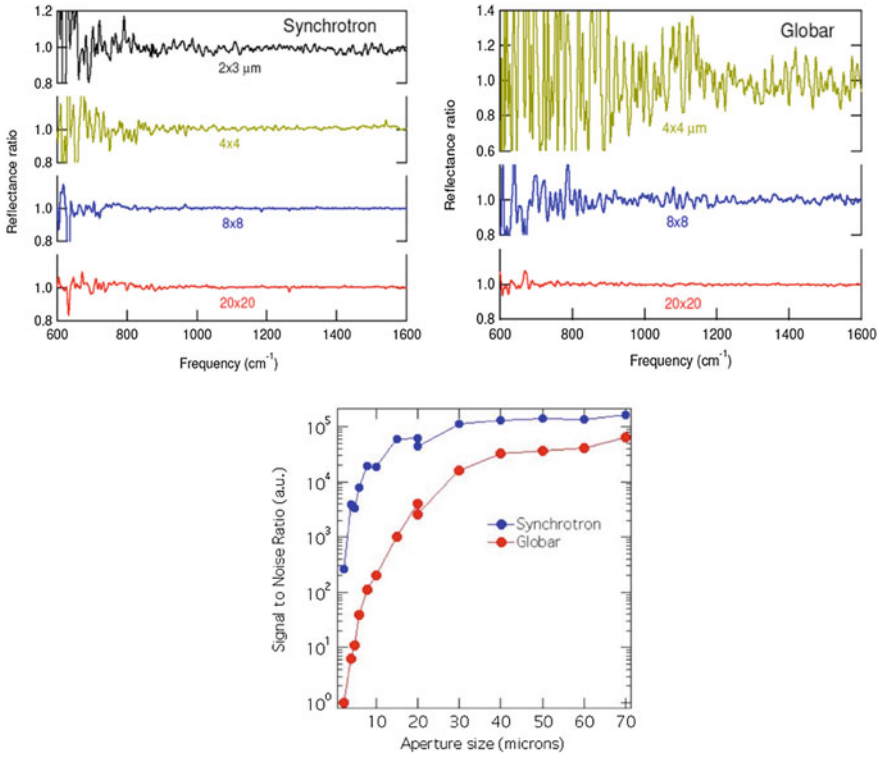


Fig. 15.3 *Upper panels* Reproducibility ratio at different apertures in an infrared microscope as measured at the SISSI beamline at Elettra. A good reproducibility is still achieved with IRSR at 2×3 microns aperture approaching the diffraction limit in the infrared. The reproducibility at the same aperture with a Black-Body source prevents its use for micro-spectroscopy applications. *Lower panel* The Signal to Noise ratio for IRSR and BB sources in the mid-IR as obtained from data in the *upper panels*. Adapted from [12]

$$\%N = \frac{100 * \mathrm{D} * \mathrm{A}^{1/2}}{\mathrm{B}\,(\nu) * \Delta\nu * \varepsilon * \mathrm{t}^{1/2}\xi} \tag{15.4}$$

where A is the detector area, D the detectivity, B(ν) the brilliance, $\Delta\nu$ the frequency bandwidth, ε the experiment's throughput, t the measuring time interval and ξ the optical efficiency. The throughput is the product of the limiting area and angle of the experiment. Multiplying the brilliance by the throughput yields the signal expected at the detector.

The S/N ratio in the mid-IR has been measured at the SISSI beamline at Trieste, Italy [12]. Here, the 100 % baseline (i.e. the ratio between two consecutive acquisitions) for different apertures (which simulate samples of decreasing size) both for IRSR and Black-Body source is shown in Fig. 15.3 (upper panels) while the corresponding S/N ratio (as extracted from statistical fluctuations about the 100 %

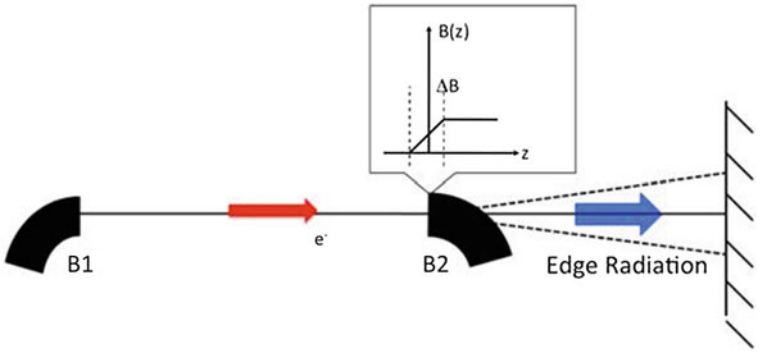


Fig. 15.4 Schematic view of the edge radiation emission. In the cartoon, the finite edge magnetic field is represented

baseline) is represented in the lower panel [12]. A gain of several orders of magnitude for small samples in the S/N ratio can be easily appreciated. This clearly opens the possibility to use infrared microscopy with SR at the diffraction limit.

15.3 Unconventional SR Sources

15.3.1 Edge Radiation

At the entrance or exit of a magnetic device, relativistic electrons experience a longitudinal acceleration due to the non-uniform magnetic field passing from zero to the finite value inside the device (see Fig. 15.4).

This Longitudinal Acceleration (LA) induces the emission of a new type of radiation called "Edge Radiation" (ER). However, it can be demonstrated that the LA in any device is too weak to provide intense radiation above the IR region of the electromagnetic spectrum [13]. Examples of IR edge radiation have been observed in bending magnet as well as in wigglers and undulators [14]. In the far-field, neglecting the spatial extension of the magnetic edge, the emitted power is given by [15]:

$$P(\lambda) = P = \alpha * I * \frac{\gamma^2\Theta^2}{\left(1+\gamma^2\Theta^2\right)^2} \text{ photons/s} \tag{15.5}$$

Thus, the power is zero on the edge axis, it is independent form the wavelength, linearly dependent on the current I (incoherent emission) and concentrated in an emission angle of about $\Theta=1/\gamma \sim 10$ mrads in III generation machines. In the same approximation, the brilliance can be written as:

$$B\,(\lambda) = 2 * 10^{19} * \frac{I\,(\mathrm{A})}{[\lambda\,(\mathrm{microns})]^2} \mathrm{photons/s/mm^2}/sr/0.1\,\%\ BW \tag{15.6}$$

The IRER is strongly collimated in a small (nearly diffraction limited) spot due to (15.6). For this reason, ER became an interesting IRSR source in the last 10 years and most of the III generation beamline present collection optics able to focalize both types of radiation at the entrance of the Michelson interferometer (see Table 15.1). In particular IRER is used for microscopy in the mid-IR while the standard (bending) emission is usually used for spectroscopy applications in the far-IR.

15.3.2 *Superradiance Phenomena and Terahertz Coherent Radiation*

Most of the IRSR radiation collected in II and III generation machines comes from incoherent emission processes in which the flux and brilliance are proportional to the total number of electrons N in a bunch, i.e. to the total current I. In principle it does exist a spectral region where the emitted wavelengths are indeed larger than the longitudinal bunch length. In this case all electrons in the bunch emit in phase and the whole intensity scales with N^2[11]. Practically, this spectral region is located in the microwaves for conventional operating conditions and then it is unsuitable for spectroscopic applications. If the longitudinal length is opportunely squeezed from the millimeter scale (10–100 ps time scale) to hundreds micron (ps time scale), the coherent region is shifted towards higher frequency, in particular in the terahertz (THz) spectral region (1 THz = 33 cm^{-1} = 300 μm), making the coherent emission strongly interesting for several applications. As a general rule, the total power can be written as:

$$P\,(v) = P_0\,(v)\left[(1 - f\,(v))\,N + N^2 f\,(v)\right] \tag{15.7}$$

$$f\,(v) = \left| \int_{-\infty}^{\infty} e^{2\pi i \vec{n}\cdot\vec{z}/c} S\,(z)\,dz \right| \tag{15.8}$$

where P_0 is the power emitted by a single electron (see (15.1)), N is the total number of electrons in a bunch, and $f(v)$ is the form factor which is the Fourier transform of the normalized longitudinal particle distribution within the bunch, $S(z)$, given by (15.8). Several methods have been developped for squeezing the bunches [10], for example the low-α mode, the femto-slicing [16] and the reduction of the machine energy [17]. All these methods, however, do provide coherence in the THz range to the detriment of both machine current and lifetime. Experimentally, a strong enhancement in emission has been observed in LINAC [8] and in storage rings like Bessy-II [10], ALS [16] and Elettra [18]. Data obtained at Elettra are represented in Fig. 15.5, that shows a gain of several order of magnitude with respect to BB source in the THz range.

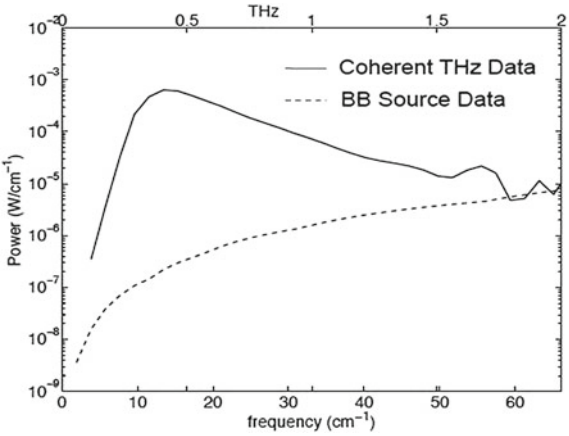


Fig. 15.5 A comparison between the coherent emission at Elettra and the BB intensity in the THz range. Adapted from [18]

15.4 Application of IRSR

15.4.1 Applications of IRSR at High Pressure

Thanks to the use of Diamond Anvil Cells (DAC), pressures in the range from 10^3 to 10^6 bar can be achieved. The basic principle underlying the DAC concept is that the pressure experienced by the sample scales with the ratio between the area of the upper and lower (culet) surfaces of the diamond (see Fig. 15.6). This implies that the space available for the sample in a DAC is rather limited, typically ranging from 100 μm to few micrometers, depending on the maximum pressure to be achieved. The small dimensions of the sample, together with the absorptions (and reflections) from the diamonds, make the throughput of DACs rather low. This is the reason why infrared spectroscopy at High-Pressures (HP) can become rather challenging with conventional sources, and the use of IRSR often becomes mandatory.

The fields of application of infrared spectroscopy at HP are manifold. As a matter of fact, thanks to the use of HP techniques it is possible to probe matter at conditions encountered in the deepest oceans or at the center of the earth (or other planets). This provides a phenomenal tool for the understanding of the mechanisms involved in the transformations of our planet, from seismic activities to volcanic eruptions. It is also very relevant for the study of the origin of life. Several scientists believe that so-called extremophiles, i.e. microorganisms living at extremely high-pressures, and found in the deepest seas or inside rocks, may have been the very first inhabitants of our planet. Also relevant from a geophysical point of view is the study of the various HP phases of water. Several different HP structures of ice (ice VI, ice VII, ice X) are indeed encountered at room temperature [20]. In chemistry, the possibility to monitor reactions occurring at HP allows to optimize the synthesis of new materials

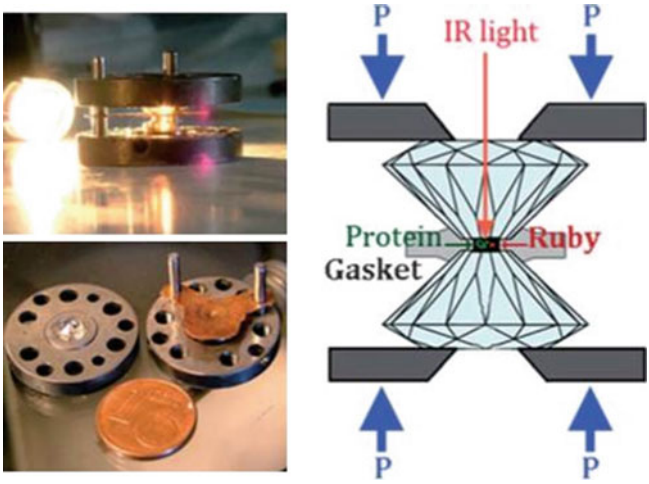


Fig. 15.6 Diamond anvil cell: **a** side view of the closed cell, **b** open cell, and **c** schematic representation and working principle. Adapted from [19]

with peculiar characteristics [21]. The possible occurrence of a metallic phase of Hydrogen [22, 23] is also being addressed through synchrotron infrared spectroscopy [24] at megabar pressures.

On the other hand, the study of pressure-induced Insulator-to-Metal Transitions (IMT) in Strongly Correlated Electron Systems (SCES) can be addressed at much lower pressures. SCES are materials in which the bandwidth (D) is so low as to become comparable with other important energy scales of the system, such as the Coulomb repulsion energy between electrons (U). Because of this, the independent electron approximation breaks down, and a materials with half-filled conduction band may become insulating (Mott insulator), contrary to the predictions of the band theory. By increasing the bandwidth, it is however possible to recover a metallic state, though an anomalous one. This can be experimentally achieved by applying HP. Compared to the previously mentioned case of hydrogen, the pressures involved in the IMT are usually orders of magnitude lower (10^4–10^5 bar). The challenging aspect in the case of Mott IMTs is not only determining the critical pressure at which the IMT takes place, but also extracting physical relevant quantities as plasma frequency, charge density, effective mass, scattering rate, etc. To this aim, one needs to accurately characterize the HP electrodynamics over a broad spectral range extending deeply into the far-infrared and THz range. In the past few years, several studies [25] concentrated on vanadium oxides belonging to the so-called Magnéli phase V_nO_{2n-1}. Due to the competition between different ground states, all the compounds of the Magnéli phase (with the exception of V_7O_{13}) display first-order IMTs as a response to small perturbations of their control parameters (pressure, temperature, filling, etc.). This makes them very attractive as smart materials for technological applications and extremely interesting from a fundamental point of view. As a matter

of fact, since a structural transition usually accompanies the temperature-dependent IMT, it is unclear whether the underlying physics is purely of the Mott–Hubbard type, or if other (Peierls-like) mechanisms are at play. IR spectroscopy at HPs has been extensively used to settle this controversy in different materials. It has been shown indeed that in VO_2, the pressure-dependent IMT decouples the electronic and structural transitions [26]. VO_2 is a monoclinic insulator at room temperature, and above 70 °C it becomes a metal with rutile symmetry. The pressure-dependent IR spectra display clear signatures of metallization above 10 GPa (100 kbar), while Raman measurements indicate that VO_2 remains in a monoclinic structure up to at least 19 GPa (190 kbar). This finding apparently rules out the role of Peierls distortions in driving the IMT, while suggesting the possible occurrence of a new monoclinic metallic phase. On the other hand, V_3O_5 undergoes a room temperature IMT at about 6 GPa (60 kbar), and an ambient pressure one at 428 K, both accompanied by a structural phase transition from P2/c to I2/c. Infrared spectroscopy demonstrates that both transitions involve a redistribution of spectral weight over a frequency range of about 1 eV, thus supporting the key role of the electron-lattice interaction in driving the IMT [27]. Vanadium sesquioxide (V_2O_3) is usually considered as the prototype Mott–Hubbard system. The reconstruction of its Pressure-Temperature phase diagram through Dynamical-Mean-Field-Theory represents one of the key advancements in our theoretical understanding of strongly correlated electron systems. However, from an experimental point of view, Pressure (P) has usually been replaced by Ti or Cr alloying for simulating the effects of positive or negative pressures. A scaling relation corresponding to $x \sim 0.011 \approx P \sim -4$ kbar is normally assumed for $(V_{1-x}Cr_x)_2O_3$. HP infrared spectroscopy [28] demonstrates that such view is oversimplified, since the conductivity of $x = 0.011$ Cr-doped V_2O_3 does not reach that of pure V_2O_3, not even at 15 kbar (see Fig. 15.7). An explanation for this unexpected behavior can be provided in terms of mesoscopic phase-separation in the Cr-doped samples.

Rare earth based intermetallic compounds with f electrons—usually called "heavy-fermion" compounds—constitute another important family within SCES. The f electrons, while being basically localized in the $4f$ orbital, hybridize with the conduction band, thus leading to a partially delocalized state, with an increased effective mass m*. At low temperatures a quantum critical point (QCP) is found in many systems, separating a paramagnetic metallic phase with moderate mass enhancement (intermediate valence state), from an anti-ferromagnetic localized state. Pressure can be used to tune "heavy-fermion" compounds across the QCP, while infrared spectroscopy probes the corresponding electrodynamics. Along with the IMT one expects the surge of a Drude term together with the appearance of a mid-IR band associated to the interband transitions across the so-called hybridization gap. This scenario has been indeed verified on YbS (see Fig. 15.8) [29], while similar results have been reported also for the SmTe, SmS, $CeRu_4Sb_{12}$, and $CeIn_3$ compounds.

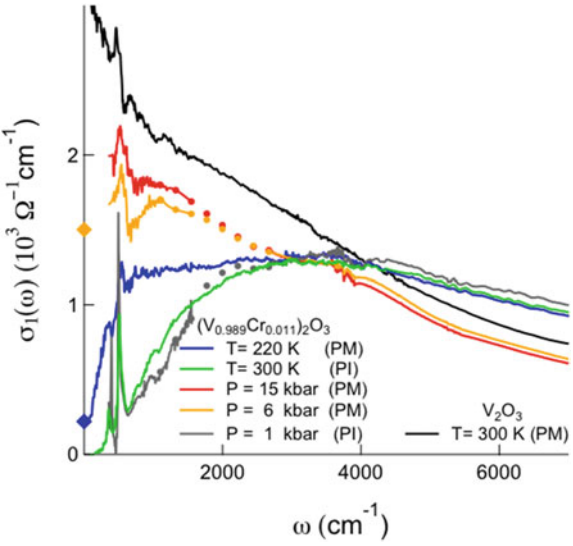


Fig. 15.7 Optical conductivity of $(V_{0.989}Cr_{0.011})_2O_3$ at room temperature versus pressure. Even at 15 kbar the optical conductivity of of $(V_{0.989}Cr_{0.011})_2O_3$ does not reach that of the pure V_2O_3 material. Adapted from [28]

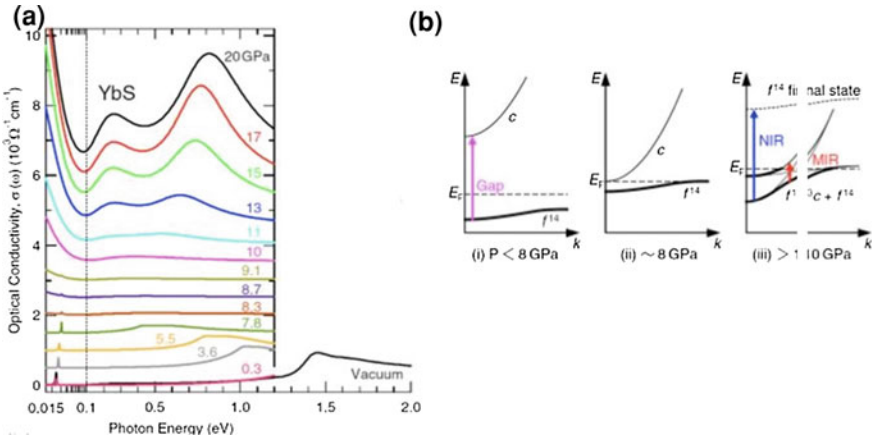


Fig. 15.8 **a** Optical conductivity spectra of YbS under external pressure up to 20 GPa. **b** Proposed model of the microscopic electronic structure of YbS. Adapted from [29]

15.4.2 Terahertz Spectroscopy

During the last two decades the interest in THz spectroscopy has been continuously growing. THz radiation is non-ionizing, highly penetrating, and provides a rather good chemical specificity. This is the reason why this technique is increasingly

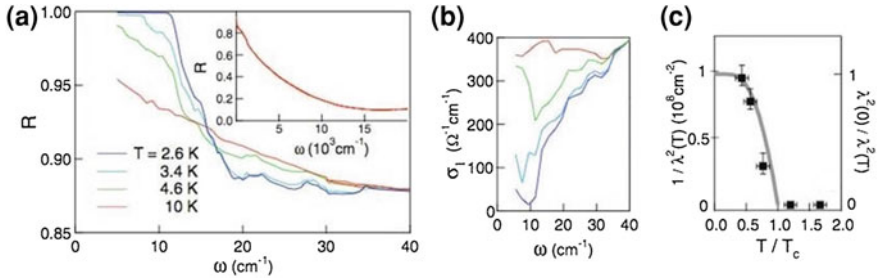


Fig. 15.9 Optical response of superconducting diamond: **a** absolute reactivity in the THz range, at various temperatures. R(ω) at 10 K in the full infrared range is shown in the *inset*; **b** real part of the optical conductivity; **c** inverse square of the penetration depth (*black squares*), compared with its behavior for a dirty BCS superconductor (*gray line*). Adapted from [30]

demanded in several fields of science and technology. A great effort has been undertaken in order to fill the so-called THz gap. Despite the developments of new technologies as THz Time-Domain-Spectroscopy (THz-TDS) and Quantum-Cascade-Lasers (QCL), THz synchrotron light is still highly requested, since it combines high flux with broadband coverage.

One of the driving forces of the development of THz spectroscopy is its capability to couple with the long-wavelength vibrations associated to the tertiary and quaternary structure of biological macromolecules. THz spectroscopy represents a direct probe of the conformational landscapes of proteins, thus providing information on their folding state and aggregation tendencies.

THz spectroscopy directly probes collective modes in solids. THz light can then be employed to investigate vibrational modes, charge ordering and superconducting phenomena. In particular, it has been largely used to characterize superconducting gaps. It is known indeed that superconductors display total reflectance up to a frequency 2Δ (usually falling in the THz range), corresponding to the energy necessary for breaking one Cooper pair. From the point of view of the optical conductivity, following the BCS theory of superconductivity, the electrodynamics is ruled by the universal Mattis–Bardeen equations, predicting the opening of a superconducting gap in the real part of the optical conductivity ($\sigma_1(\omega)$) at 2Δ.

Coherent THz radiation has been employed in 2006, in order to characterize the gap of superconducting diamond [30]. Because of its mechanical properties, excellent thermal conductivity and large gap between valence and conduction bands, diamond is considered as a potentially attractive semiconductor for future applications in electronics. Boron-doped diamond films deposited by chemical vapor deposition (CVD) also become superconductors below 6 K. The first question raised by this discovery was whether diamond has to be considered as a BCS material, or if more exotic mechanisms, as those invoked for high-temperature superconductivity, apply. Since from the SC gap size and its shape one can extract important information on the nature and symmetry of the pairing, THz spectroscopy has been employed to address this crucial issue.

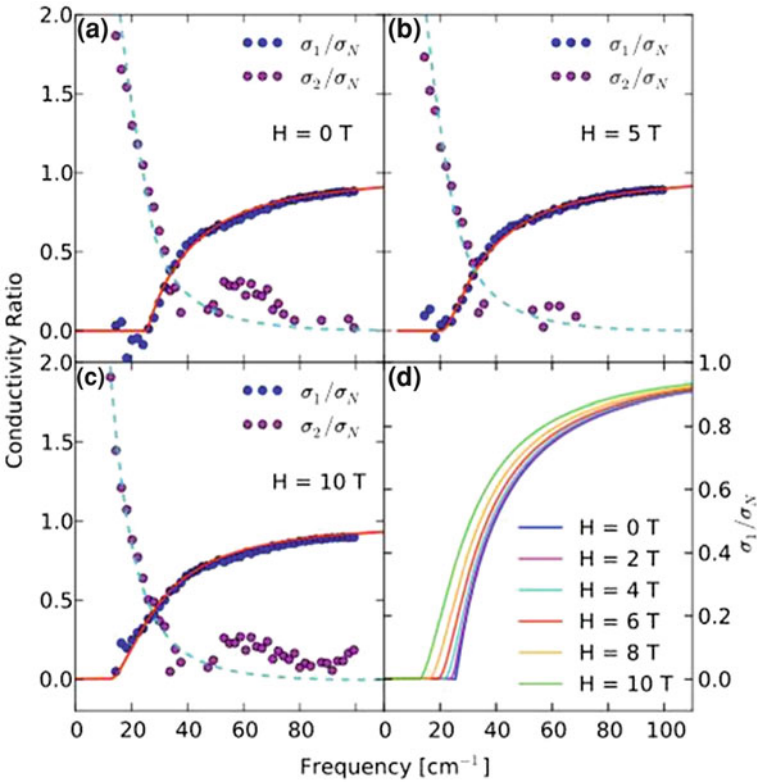


Fig. 15.10 **a–c** The real σ_1 and imaginary σ_2 parts of the T = 3 K superconducting state optical conductivity (normalized to the normal state conductivity) at three different (H = 0, 5 and 10 T) applied magnetic fields. The *red solid lines* are fits to σ_1/σ_N using the pair-breaking theory. The *blue dashed lines* show the corresponding σ_2/σ_N as determined by a Kramers–Kronig transform of the real part. **d** The σ_1/σ_N fitting results are represented at six fields. Adapted from [31]

While entering into the SC state, the reflectivity first depletes (below 35 cm^{-1}), and then steeply increases (below 15 cm^{-1}) (Fig. 15.9a), before reaching total reflection (at about 10 cm^{-1}, at the lowest temperature). Such behavior is consistent with the BCS-like Mattis–Bardeen equations. This is best appreciated when the optical conductivity is calculated through Kramers–Kronig transformations. The resulting $\sigma_1(\omega)$, as shown in Fig. 15.9b, is fully consistent with the universal Mattis–Bardeen curves. The gap value, as determined through fitting provides the value $2\Delta(0)$=12.5 K, thus providing a gap ratio $2\Delta/k_BT_c \sim 3$, slightly lower than the BCS weak coupling limit prediction. This result can be interpreted in terms of a slightly anisotropic s-wave gap. Overall, the THz data indicate that B-doped diamond is a rather conventional BCS superconductor with a nodeless gap.

The high brilliance of IRSR also allows performing THz studies down to very low frequencies under an applied magnetic field. This has enabled in recent years the

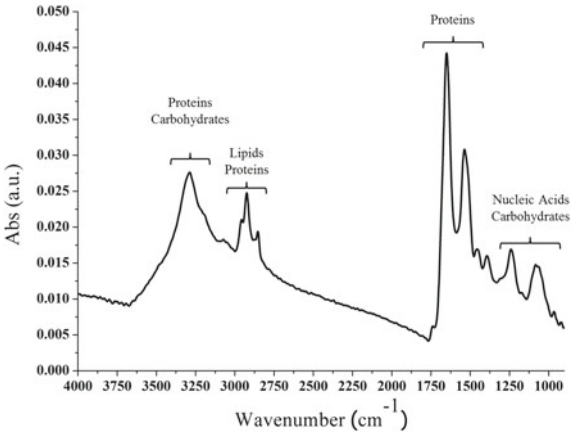


Fig. 15.11 Representative mid-IR absorption spectrum of an eukaryotic single cell

study of the electrodynamics of type II Superconductors in their mixed (Schubnikov) phase. Understanding how the magnetic field penetrates a superconductor is of the primary importance, since the upper critical field H_{c2} is directly connected to the critical current density, i.e. to the maximum current that can be transported in a superconductor.

Xi et al. [31] have addressed the electrodynamics of a thin $Nb_{0.5}Ti_{0.5}N$ film. $Nb_{0.5}Ti_{0.5}N$ can be considered as a model system since it is widely used for the fabrication of superconducting magnets, RF cavities, and photodetectors. The magnetic field is here applied parallel to the thin film surface so that the inter-vortex spacing, comparable to the coherence length ($\xi \sim 20$ nm), is on the same order of magnitude than the film thickness itself. Vortex density is thus expected to be negligible, and one can address the physics of the $Nb_{0.5}Ti_{0.5}N$ superconductor in the presence of the pair-breaking effects induced by the penetration of the field. THz data demonstrate the applicability of the Skalski theory, generalizing the Mattis and Bardeen theory to the case of pair-breaking. The magnetic field dependence of the pair-breaking strength (Γ) is extracted, as well as the excitation energy gap ($2\Omega_G$).

The above-described scenario is different from the case of a magnetic field applied perpendicular to the film surface. In the latter case it has been recently demonstrated that the presence of vortices can be described through an effective medium model as in the Maxwell–Garnett Theory (MGT). The MGT model treats the presence of the normal state vortices as "islands" embedded in a SC background. The MGT model provides a satisfactory agreement with data, by employing Mattis–Bardeen equations to fit the superconducting state. However, the agreement can still be improved by also considering the pair-breaking induced weakening of the SC state due to the penetration of the magnetic field in the remaining SC regions (Fig. 15.10).

Table 15.2 Characteristic spectral bands of a biological sample: band position, assignment and attribution to cellular constituents are given accordingly to Movasaghi et al. [34] and references within it

Band position (cm^{-1})	Assignment	Primary cell constituent
~3500	O–H str. of hydroxyl groups	
~3200	N–H str. (Amide A)	Proteins
~3010	=C–H str.	UFA
3000–2800	Sym. and asym. str. of $–CH_3$, $–CH_2$, and –CH	SFA and proteins
~1730	>C=O str. of ester	Phospholipids
1720–1630	>C=O str. of carbonyl groups	Nucleobases
1700–1600	Amide I: Protein linkage (80 % C=O str., 10 % C–N str., 10 % N–H def.)	
	Amide I components	
	Frequency (cm^{-1})	Secondary structure
	1695–1675	Antiparallel β-sheet/Aggregated strands
	1670–1660	3_{10}-Helix
	1660–1648	α-helix
	1648–1640	Random coil
	1640–1625	Parallel β-sheet
	1628–1610	Aggregated strands
1580–1480	Amide II: Protein linkage (amide linkage mode: 40 % C-N str., 60 % N–H def.)	
1470–1420	Bending modes of $–CH_3$, $–CH_2$	Lipids and proteins
~1380	Def. $-CH_3$	Lipids and proteins
1310–1240	Amide III	Proteins
1250–1220	P=O asym str. of PO_2^- phosphodiester	NAs, phospholipids
1200–900	C–O–C str., C–O str, C–O–P	Ring vibrations of carbohydrates
~1107	C–O str. of C–OH group of ribose	Monosaccharides
~1085	P=O sym str. of PO_2^- phosphodiester	NAs, phospholipids
~1036	CO, C–C, C–C–O str.	Polysaccharides
~970	Str. of PO_4^{2-}	Phosphorylated proteins

List of abbreviations: *str.* Stretching, *def.* Deformation, *sym.* Symmetric, *asym.* Asymmetric, *FA* Fatty acids, *UFA* Unsaturated fatty acids, *SFA* Saturated fatty acids, *NA* Nucleic acids

15.4.3 Synchrotron Radiation Infrared Microspectroscopy for Biology and Medicine

IRSR is a fascinating tool for the study of biological specimens, both isolated single cells and tissue slices, since it is a non-ionizing and non-damaging technique that induces negligible sample heating and does not impact on cell survival and normal cellular progression [32, 33]. Moreover, and possibly more important, it is a label-free technique: position, shape and width of spectral bands are sensitive to concentration, composition, structure and state of order of the fundamental cellular constituents, and to their modification as a function of diseases' related pathways. Figure 15.11 shows the representative spectrum of an entire isolated eukaryotic single cell and the assignment of the most relevant bands is given in Table 15.2.

The diagnostic capabilities of IRSR are largely proven by the increasing number of publications in the biomedical field, where this analytical tool has been extensively used to discriminate pathological states from non-pathological ones and for their biochemical characterization [35]. For example, in the field of neurodegenerative disorders, several papers have been published over the last twenty years. Conventional FTIR spectroscopy has been applied for the structural characterization and folding impairment of several proteins in model systems: PrP^{Sc} (scrapie Prion Protein) in prion disorders [36–38], Aβ in Alzheimer disease (AD) [39, 40], and α-synuclein in Parkinson disease (PD) [41]. Meanwhile, Synchrotron Radiation IR Micro-Spectroscopy (SR-IRMS) has been exploited for highlighting the disease markers on histological samples. As an example, brain amyloid plaques, characterized by accumulation of β-sheet misfolded Aβ protein in AD, have been localized and characterized by SR-IRMS, that has been proven to be a complementary and more informative method with respect to conventional histopathology [42, 43]. As a matter of fact, microcrystalline deposits of creatine, a molecule that plays an important role in maintaining energy balance in the brain, were first detected by SR-IRMS in all animals with advanced plaque pathology and also in hippocampal sections from post-mortem AD human brain [44]. Similarly, chemical composition and morphology of human substantia nigra pars compacta were determined by SR-IRMS. In particular, a higher lipid content has been observed in the case of pathology with respect to the control and in parkinsonian syndrome the Amide I band revealed a peak maximum shifted toward higher frequencies (α-helix: 1656 → 1662 cm^{-1}) and two more peaks centered at 1682 and 1643 cm^{-1}, which were attributed to β-turn and β-sheet structures respectively. These and other findings revealed major changes in biological membranes and dysfunctions in the genetic machinery and proteomic profile related to PDs. With respect to prion disorders, IRMS has revealed molecular alterations in lipids, carbohydrates, and nucleic acids as well, induced by Transmissible Spongiform Encephalopathies (TSE) in neural tissues, even though β-sheet amyloid deposits in neural areas were identified only in terminally ill hamster tissues [45].

Altogether, these studies have been carried out at tissue level; more recently, the possibility to discriminate prion infected cells from healthy ones was demonstrated by Didonna et al. [46]. Hierarchical Cluster Analysis (HCA) on IR microspectra of whole mouse hypothalamic GT1-1 cells, normal (GT1) and chronically infected (ScGT1) with Rocky Mountain Laboratory (RML) prion strain, evidenced a clear differentiation between infected and non-infected cells in the spectral space. This classification is based on the superimposition of multimolecular information, although the most prominent one relates to the ratio between carboxylic and carboxylate groups of glutamic and aspartic aminoacids. This ratio increased upon infection, allowing to deduce an increment of lysosomal bodies within the cytoplasm of infected GT1-1 cells (see Fig. 15.12).

These findings were further confirmed by IRSR at subcellular spatial resolution and supported by fluorescent microscopy (see Fig. 15.13). Overall, the infection related spectral changes occurred without detectable changes in cell volume: by combining infrared on whole-cell spectra and atomic force microscopy (AFM), a

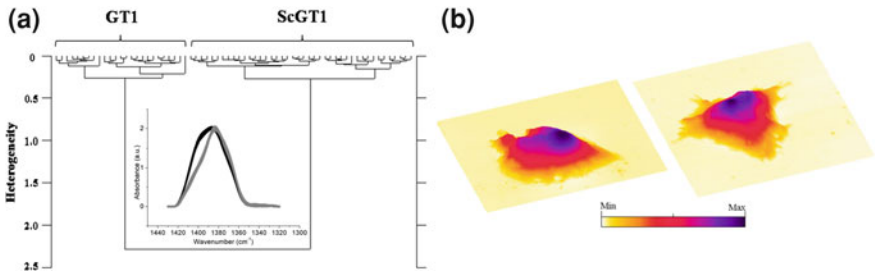


Fig. 15.12 **a** Dendrogram generated by Hierarchial Cluster Analysis (Euclidean distances; Ward's algorithm) of first derivatives of microspectra extended over the spectral range 1800–1150 cm^{-1}. A clear separation of cellular spectra ascribable to prion infection can be inferred by the shown dendrogram. The *inset* shows the average absorbance spectra of GT1 (*black line* with thickness proportional to standard deviation, SD) and ScGT1 (*gray line* with thickness proportional to SD) in the 1425–1325 cm^{-1} range. The decrement of carboxylate groups upon RML infection can be clearly seen by the lowering of the band contribution centered at ∼1400 cm^{-1}. **b** AFM profile of representative GT1 and ScGT1 cells, *left* and *right* respectively. GT1 and ScGT1 cells have similar pyramidal shapes in which the nuclear region is the apex. Adapted from [46]

decrement in total cellular protein content upon prion infection was highlighted and the results have been validated by bicinchoninic acid assay. All together, these results supported the hypothesis of prion disorder to be a lysosomial disorder related to cell spongiosis. Summarizing, in the Didonna's paper, IRMS is proposed as multi-screening analytical platform that, combined with other techniques, can shed new light on diseases.

The new trend of SR-IRMS for cellular analysis is to upgrade this technique to a label-free single cell based assay, that is an analytical methodology able to monitor the biochemical events undergone by live cells in their physiological environment, either those naturally occurring or induced by external stimuli. It is nowadays well established that any probe, both fluorescent markers and radioactive labels, can alter the cellular pathways and bias the experimental results. Moreover, cellular fixation imposes the detection of cellular still frames, and induces relevant morphological and biochemical modifications. It was recently demonstrated [47] that both formalin and ethanol fixatives alter cellular lipidome and proteome profile, affecting protein content and folding as well as lipid composition and cell membrane order. Moreover, they both promote the transition of DNA from the natural B form to A-like helical folding, therefore limiting the technique capability in the diagnosis

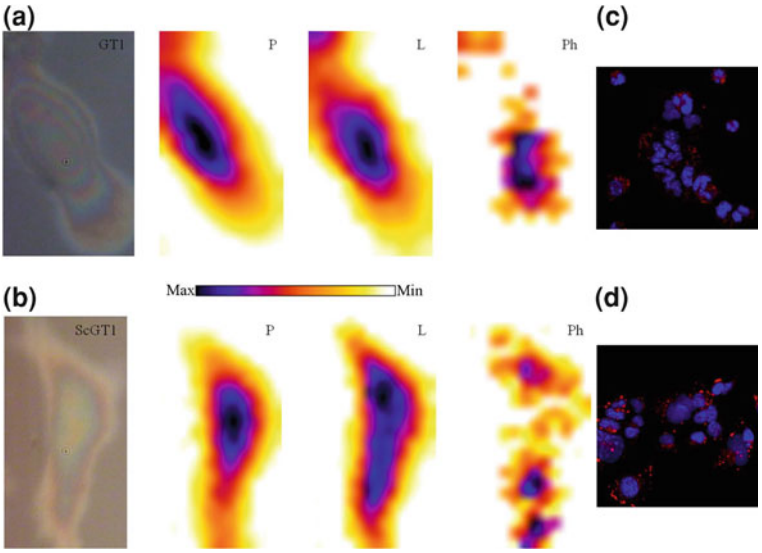


Fig. 15.13 **a** Cell optical image of a single GT1 (30 × 40 μm; scale bar 5 μm) cell and related chemical maps, collected at 6 μm lateral resolution (oversampling 1:2), of total protein content, P, acyl chains of lipids, L, and carbonyl ester of phospholipids. (Min-Max) = P(0–6 au); L (0–2.5 au); Ph (0.01–0.08 au). **b** Cell optical image (23 × 66 μm; scale bar 5 μm) of a single ScGT1 cell and related chemical maps. (Min-Max) = P(0–4 au); L (0–1 au); Ph (0.01–0.04au) **c–d** Fluorescence image of GT1 and ScGT1 cells: blue nuclear staining (DAPI) and red lyso some staining (Lysotracker). ScGT1 cells exhibit larger and more numerous lysosomes compared to GT1. Adapted from [46]

of nucleic acid misfolding. The field of live cell analysis has been pioneered in 1998 by Jamin, Dumas and collaborators [48], that first monitored the mitotic event undergone by live mouse UN2 cells. The cells were simply cytospun onto BaF_2 windows and measured immediately after the preparation. As an example, Protein and lipid distribution of dividing chang liver cells is shown in Fig. 15.14a. Long-term measurements for cellular dynamics requires the fabrication of ad-hoc Vis-IR transparent fluidic devices in order to maintain cells alive and to better control the spectral water contribution, for overcoming the so called "water absorption barrier", that is the strong contribution of water to cellular spectra, able to hide most of the relevant and diagnostic spectroscopic features (see Fig. 15.14b). Several approaches have been recently proposed, based on the exploitation of micro and nanotechnologies capabilities, that resulted in fluidic chips with different design and for different purposes [49–54], spanning from the study of the dynamics of biofilm formation in micro-channels to the investigation of mechanical stress effects on white blood cells [55].

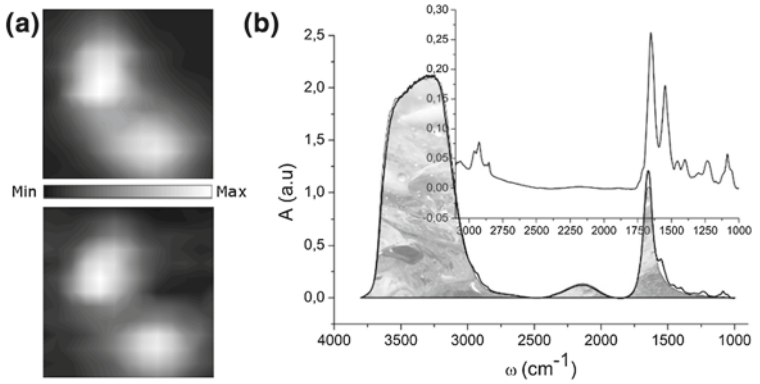


Fig. 15.14 **a** Chemical distribution of proteins and lipids of cells undergoing division (mitotic event). Scale bar = 5 μm. **b** In the foreground, the FTIR microspectrum of a single U937 leukemic monocyte collected in physiological solution is shown and the spectrum of the surrounding cellular medium is watery filled. Upon aqueous buffer spectral subtraction, vibrational features of living cells are disclosed, as shown in the *backward spectrum*

15.4.4 Synchrotron Radiation Infrared Microspectroscopy for Cultural Heritage

Conservation science is a field of paramount importance worldwide: natural aging of artworks, but also their fastened degradation due to human activities (environmental hazards), require advanced characterization tools for setting up proper restoration procedures and in general for improving our knowledge on ancient civilizations. To achieve these goals, a deep understanding of artwork production technology is needed, in other words the identification, chemical characterization and localization of both organic and inorganic materials employed for manufacturing paintings, sculptures, low relieves, statues, ancient books, etc. IRSR has attracted the attention of Cultural Heritage (CH) community due to the ability of the technique to characterize both organic and inorganic materials without sample damaging and thanks to the diffraction limited lateral resolution offered by the technique. Indeed, artworks are made up of a complex mixture of natural and synthetic materials (metal, ceramic, glass, papers, binders, glues, varnish, dyes, pigments), often organized in multilayer structures that reveal both the production technology and the restoration interventions. It is in the analysis of hybrid multilayer micro-fragments, sampled with micro-invasive techniques, that IRSR fully demonstrates its potentialities [56].

Several papers have been published in the last 15 years, where IRSR was complemented with other analytical techniques, either based on SR or conventional sources, for the study of several artworks [57]. Multilayered paintings samples have been extensively studied by IRSR [58–64], but the technique was also employed for the determination of corrosion products [63], for the study of varnish covering of ancient

music instruments [65, 66], for the investigation of bio-deteriorated historical textiles [67], for the study of alteration of silver foils in medieval paintings [68].

Acknowledgments We thank all people partecipating to the IRSR projects in Italy. For the Sinbad project at Dafne in Frascati M. Cestelli Guidi and A. Marcelli. For the SISSI project at Elettra P. Calvani, A. Nucara, and M. Kiskinova.

References

1. E.F. Nichols, Phys. Rev. **1**, 1–3 (1893)
2. P. Lagarde, Infrared Phys. **18**, 395–460 (1978)
3. J.R. Stevenson, H. Ellis, R. Bartlett, Appl. Opt. **12**, 2884–2889 (1973)
4. W.D. Duncan, J. Yarwood, DL/SCI/TM 32E (Daresbury Laboratory, 1982).
5. E. Schweitzer, J. Nagel, W. Braun, E. Lippert, A.M. Bradshaw, Nucl. Intrum. Methods Phys. Res. **A239**, 630–634 (1985)
6. T. Nanba, Rev. Sci. Instrum. **60**, 1680–1685 (1989)
7. G.L. Carr, P. Dumas, C.J. Hirschmugl, G.p. williams, in *Infrared Synchrotron Radiation*, ed. by P. Calvani, P. Roy (Editrice Compositori, Bologna, 1998), pp. 375–395
8. E. Chiadroni, A. Bacci, M. Bellaveglia, M. Boscolo, M. Castellano, L. Cultrera, G. Di Pirro, M. Ferrario, L. Ficcadenti, D. Filippetto, G. Gatti, E. Pace, A.R. Rossi, C. Vaccarezza, L. Catani, A. Cianchi, B. Marchetti, A. Mostacci, L. Palumbo, C. Ronsivalle, A. Di Gaspare, M. Ortolani, A. Perucchi, P. Calvani, O. Limaj, D. Nicoletti, S. Lupi, Appl. Phys. Lett. **102**, 094101–094104 (2013)
9. A. Nucara, S. Lupi, P. Calvani, Rev. Sci. Instrum. **74**, 3934–3942 (2003)
10. G.P. Williams, Rep. Prog. Phys. **69**, 301–306 (2006)
11. S.-I. Kimura, H. Okamura, J. Phys. Soc. Jpn. **82**, 021004–0210031 (2013)
12. S. Lupi, A. Nucara, A. Perucchi, P. Calvani, M. Ortolani, L. Quaroni, M. Kiskinova, J. Opt. Soc. Am. **B24**, 959–964 (2007)
13. R.A. Bosch, in Infrared Synchrotron Radiation, ed. by P. Calvani, P. Roy (Editrice Compositori, Bologna, 1998), pp. 483–494.
14. Y.L. Mathis, P. Roy, B. Tremblay, A. Nucara, S. Lupi, P. Calvani, Phys. Rev. Lett. **80**, 1220–1223 (1998)
15. M. B. Kinkaid, in Infrared Synchrotron Radiation, ed. by P. Calvani, P. Roy (Editrice Compositori, Bologna, 1998), pp. 495–502.
16. M. Abo-Bakr, J. Feikes, K. Holldack, G. Wustefeld, H.W. Hubers, Phys Rev Lett. **88**, 254801–254804 (2002)
17. J.M. Byrd, Z. Hao, M.C. Martin, D.S. Robin, F. Cannibale, R.W. Schoenlein, A.A. Zholents, M.S. Zolotorev, Phys. Rev. Lett. **97**, 074802–074805 (2006)
18. E. Karanzoulis, G. Penco, A. Perucchi, S. Lupi, Inf. Phys. Tech. **53**, 300–303 (2010)
19. F. Piccirilli, S. Mangialardo, P. Postorino, L. Baldassarre, S. Lupi, A. Perucchi, Soft Matter **8**, 11863–11870 (2012)
20. A.F. Goncharov, V.V. Struzhkin, M.S. Somayazulu, R.J. Hemley, H.K. Mao, Science **273**, 218–220 (1996)
21. V. Schettino, R. Bini, Chem. Soc. Rev. **36**, 869–880 (2007)
22. E. Wigner, H.B. Huntington, J. Chem. Phys. **3**, 764–770 (1935)
23. E. Babaev, A. sudbøø n. w. ashcroft. Nature **431**, 666–668 (2004)
24. C.S. Zha, Z. Liu, R.J. Hemley, Phys. Rev. Lett. **108**, 146402–146405 (2012)
25. A. Perucchi, L. Baldassarre, P. Postorino, S. Lupi, J. Phys. Condens. Matter **21**, 323202–323221 (2009)
26. E. Arcangeletti, L. Di Baldassarre, Phys. Rev. Lett. **98**, 196406–196409 (2007)

27. L. Baldassarre, A. Perucchi, E. Arcangeletti, D. Nicoletti, D. Di Castro, P. Postorino, V.A. Sidorov, S. Lupi, Phys. Rev. B **75**, 245108–245112 (2007)
28. S. Lupi, L. Baldassarre, B. Mansart, A. Perucchi, A. Barinov, P. Dudin, E. Papalazarou, F. Rodolakis, J.-P. Rueff, J.-P. Itié, S. Ravy, D. Nicoletti, P. Postorino, P. Hansmann, N. Parragh, A. Toschi, T. Saha-Dasgupta, O.K. Andersen, G. Sangiovanni, K. Held, M. Marsi, Nat. Commun. **1**, 105–109 (2010)
29. M. Matsunami, H. Okamura, A. Ochiai, T. Nanba, Phys. Rev. Lett. **103**, 237202–237205 (2009)
30. M. Ortolani, S. Lupi, L. Baldassarre, U. Schade, P. Calvani, Y. Takano, M. Nagao, T. Takenouchi, H. Kawarada, Phys. Rev. Lett. **97**, 097002–097005 (2006)
31. X. Xi, J. Hwang, C. Martin, D.B. Tanner, G.L. Carr, Phys. Rev. Lett. **105**, 257006–257009 (2010)
32. H.Y. Holman, K.A. Bjornstad, M.P. McNamara, M.C. Martin, W.R. McKinney, E.A. Blakely, J. Biomed. Opt. **77**, 417–424 (2002)
33. H.-Y.N. Holman, M.C. Martin, W.R. McKinney, J. Biol. Phys. **29**, 275–286 (2003)
34. Z. Movasaghi, S. Rehman, D.I. ur Rehman, Appl. Spectr. Rev. **43**, 134–179 (2008)
35. C. Petibois, B. Desbat, Trends Biotechnol. **28**, 495–500 (2010)
36. M. Gasset, M.A. Baldwin, R.J. Fletterick, S.B. Prusiner, Proc. Natl. Acad. Sci. U.S.A. **90**, 1–5 (1993)
37. J. Ollesch, E. Kunnemann, R. Glockshuber, K. Gerwert, Appl. Spectrosc. **61**, 1025–1031 (2007)
38. K. Elfrink, J. Ollesch, J. Stohr, D. Willbold, D. Riesner, K. Gerwert, Proc. Natl. Acad. Sci. U.S.A. **105**, 10815–10819 (2008)
39. M. Griebe, M. Daffertshofer, M. Stroick, M. Syren, P. Ahmad-Nejad, M. Neumaier, J. Backhaus, M.G. Hennerici, M. Fatar, Neurosci. Lett. **420**, 29–33 (2007)
40. P. Juszczyk, A.S. Kolodziejczyk, Z. Grzonka, J. Pept. Sci. **15**, 23–29 (2009)
41. J.C. Rochet, K.A. Conway, P.T. Lansbury, Biochemistry **39**, 10619–10626 (2000)
42. L.P. Choo, D.L. Wetzel, W.C. Halliday, M. Jackson, S.M. LeVine, H. Mantsch, Biophys. J. **71**, 1672–1679 (1996)
43. L.P. Choo, J.R. Mansfield, N. Pizzi, R.L. Somorjai, M. Jackson, W.C. Halliday, H.H. Mantsch, Biospectroscopy **1**, 141–148 (1995)
44. M. Gallant, J. Biol. Chem. **281**, 5–8 (2005)
45. M. Beekes, P. Lasch, D. Naumann, Vet. Microbiol. **123**, 305–319 (2007)
46. A. Didonna, L. Vaccari, A. Bek, G.G. Legname, ACS Chem. Neurosci. **2**, 160–174 (2011)
47. L. Vaccari, G. Birarda, L. Businaro, S. Pacor, G. Grenci, Anal. Chem. **84**, 4768–4775 (2012)
48. N.G. Jamin, P. Dumas, J. Moncuit, W.-H. Fridman, J.-L. Teillaud, G.L. Carr, G.P. Williams, Proc. Natl. Acad. Sci. **95**, 4837–4840 (1998)
49. H.-Y.N. Holman, R. Miles, Z. Hao, E. Wozei, L.M. Anderson, H. Yang, Anal. Chem. **81**, 8564–8570 (2009)
50. H.-Y.N. Holman, H.A. Bechtel, Z. Hao, M.C. Martin, Anal. Chem. **82**, 8757–8765 (2010)
51. E.J. Marcsisin, C.M. Uttero, M. Miljkovic, M. Diem, Analyst **135**, 3227–3232 (2010)
52. J.R. Mourant, Y.R. Yamada, S. Carpenter, L.R. Dominique, J.P. Freyer, Biophys. J. **85**, 1938–1947 (2003)
53. G. Birarda, G. Grenci, L. Businaro, B. Marmiroli, S. Pacor, L. Vaccari, Microelectron. Eng. **87**, 806–809 (2010)
54. L. Vaccari, G. Birarda, G. Grenci, S. Pacor, L. Businaro, J. Phys.: Conf. Ser. **359**, 012007 (2012)
55. G. Birarda, G. Grenci, L. Businaro, B. Marmiroli, S. Pacor, F. Piccirilli, L. Vaccari, Vib. Spectrosc. **53**, 6–11 (2010)
56. M.C. Martin, U. Schade, P. Lerch, P. Dumas, TrAC Trends Anal. Chem. **29**, 453–463 (2010)
57. M. Cotte, E. Checroun, V. Mazel, V.A. Solé, P. Richardin, Y. Taniguchi, P. Walter, J. Susini, e-PreservationSCIENCE **6**, 9 (2009)
58. C.S. Patterson, D. Carson, A. Phenix, H. Khanjian, K. Trentelman, J. Mass, C. Hirschmug, e-PreservationSCIENCE, **9** (2013)
59. N. Salvadó, S. Butí, J. Nicholson, H. Emerich, A. Labrador, T. Pradell, Talanta **79**, 419–428 (2009)

60. M. Cotte, J. Susini, V.A. Sole, Y. Taniguchi, J. Chillida, E. Checroun, P. Walter, J. Anal. At. Spectrom. **23**, 820–828 (2008)
61. N. Salvadó, S. Butí, E. Pantos, F. Bahrami, A. Labrador, T. Pradell, Appl. Phys. A **90**, 67–73 (2008)
62. A. Lluveras, S. Boularand, J. Roqué, M. Cotte, P. Giráldez, M. Vendrell-Saz, Appl. Phys. A **90**, 23–33 (2008)
63. N. Salvadó, S. Butí, M.J. Tobin, E. Pantos, A.J.N.W. Prag, T. Pradell, Anal. Chem. **77**, 3444–3451 (2005)
64. M. Cotte, E. Checroun, J. Susini, P. Walter, Appl. Phys. A **89**, 841–848 (2007)
65. J.P. Echard, M. Cotte, E. Dooryhee, L. Bertrand, Appl. Phys. A **92**, 77–81 (2008)
66. L. Bertrand, L. Robinet, S.X. Cohen, C. Sandt, A.-S. Le Ho, B. Soulier, A. Lattuati-Derieux, J.-P. Echard, 1618–2650 (Electronic)
67. K. Kavkler, Ž. Šmit, D. Jezeršek, D. Eichert, A. Demšar, Polym. Degrad. Stab. **96**, 1081–1086 (2011)
68. N. Salvadó, S. Butí, A. Labrador, G. Cinque, H. Emerich, T. Pradell, Anal. Bioanal. Chem. **399**, 3041–3052 (2011)

Chapter 16
The High-Frequency Atomic Dynamics of Disordered Systems Studied by High-Resolution Inelastic X-Ray Scattering

Giulio Monaco

Abstract The use of momentum-resolved inelastic X-ray scattering with meV energy resolution to study the high-frequency atomic dynamics in disordered systems is here reviewed. The typical realization of this experiment is described and some simple models are presented that are used to interpret the measured spectra and to extract parameters of interest for the investigation of disordered systems. With the help of some selected examples, the present status of the field is discussed, with particular reference to the vibrational dynamics in glasses, and to the high-frequency relaxations in liquids.

16.1 Introduction

The energy spectrum measured in an off-resonance scattering process of X-rays from matter is basically proportional, at least up to energies of some hundreds of meV, to the atomic dynamic structure factor, $S(q, E)$, where q and E are the momentum and the energy exchanged in the scattering process, respectively. The momentum-resolved technique used to measure this spectrum with meV energy-resolution in the 0.1–10 Å^{-1} q-range is often referred to as high-resolution inelastic X-ray scattering (IXS), and this is the definition used hereafter.

An IXS experiment can be readily imagined as an energy-resolved diffraction experiment. In fact, the integral over energy of $S(q, E)$, known as structure factor, $S(q)$, is the observable probed in diffraction experiments.

Formally, $S(q, E)$ is the space and time Fourier transform of the atomic density-density correlation function. This is a key observable in the investigation of the atomic dynamics: it holds, in particular, the information on the phonon dispersion relations in crystals, on the acoustic excitations in disordered systems, and on diffusive processes

G. Monaco (✉)
Dipartimento di Fisica, Università di Trento,Via Sommarive 14, 38123 Povo, TN, Italy
e-mail: giulio.monaco@unitn.it

S. Mobilio et al. (eds.), *Synchrotron Radiation*,
DOI: 10.1007/978-3-642-55315-8_16, © Springer-Verlag Berlin Heidelberg 2015

in gases and liquids. Traditionally, the atomic $S(q, E)$ is measured in inelastic light and neutron scattering experiments. In Brillouin light scattering experiments (BLS), due to the small wavevector of photons in the visible range ($k_0 \sim 10^{-3}$ Å^{-1}), only the $q \rightarrow 0$ limit is basically probed, corresponding to the Γ point in the reciprocal space of a crystal. Inelastic neutron scattering (INS) experiments complement light scattering ones by probing a finite q range, which in particular allows for the measurement of the full phonon dispersion curves in a crystal. This possibility is disclosed to neutron scattering by the fact that the energy of neutrons with wavelengths of the order of the inter-particle distance is ∼100 meV, i.e. quite close to the typical energies of phonons in crystals. Consequently, a neutron spectrometer with a moderate relative energy resolution offers an easy access to the atomic dynamics. Different is the case of X-rays: for example, X-rays with a wavevector of 1 Å^{-1} have an energy of ∼10 keV. Consequently, in order to detect the energy exchanged by an X-ray beam with an acoustic phonon, a resolving power of at least 10^6 is needed. For this technical difficulty, X-rays have been considered not adequate in the study of the atomic dynamics until only recently.

Things have changed considerably since the advent of synchrotron radiation sources, which have provided brilliant X-ray beams amenable for experiments fulfilling such pushed resolving power requests. The first IXS experiment with 55 meV energy resolution was set up during the years 1984–1987 at the second generation synchrotron source of Doris II, Hamburg, and lead to the first IXS measurement of the acoustic phonon dispersion curve in a crystal [1]. Important advances in the technique came few years later with the advent of the third generation synchrotron source of the ESRF, that started to deliver an X-ray beam with an unprecedented brilliance. Exploiting the beam quality, and using new ideas in perfect crystal optics, a new instrument was build up during the years 1992–1996 at the beamline ID16 of the ESRF by F. Sette and co-workers [2–4], capable of achieving a 1.5 meV energy resolution with an intensity still exploitable for experiments. Since then, the IXS technique has seen continuous improvements in terms of flux, flexibility and stability that push further and further its scientific case.

The (q, E) region of interest for the study of the acoustic excitations in disordered systems currently covered by the IXS technique is shown in Fig. 16.1 (black line) together with the regions accessible to Brillouin light and ultra-violet scattering (blue line) and to INS (green line). In Fig. 16.1 the (q, E) region foreseen to be accessible to IXS using improved optical schemes [5] is shown as well (red line).

Nowadays, IXS can be considered as an established tool to measure the atomic $S(q, E)$, in some cases extending and more in general complementing INS techniques. In fact, though IXS and INS probe the same atomic dynamics, the measured spectra are differently modulated by different atomic species, the weight function being the atomic form factor $f(q)$ for IXS and the scattering length for INS. Thus, the study of the atomic dynamics of a polyatomic system profits from the joint use of IXS and INS just in the same way as a structural study profits from a joint use of X-ray and neutron diffraction. Moreover, though IXS presents several disadvantages with respect to INS, it has as well some important advantages which define a class of experiments where IXS really extends the INS capabilities. The most relevant

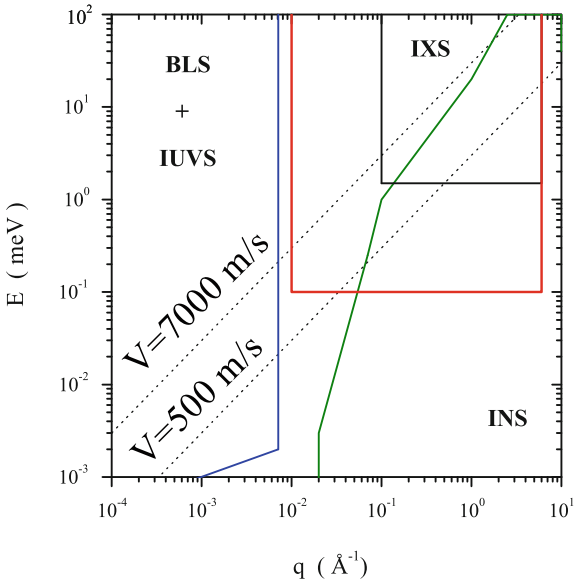


Fig. 16.1 The wavenumber (q) and energy (E) space for the acoustic excitations in first Brillouin zone as covered by different techniques: Brillouin light scattering (*BLS*) together with its extension to the ultraviolet regime (*IUVS*); inelastic neutron scattering (*INS*); inelastic X-ray scattering (*IXS*) in the range that is presently accessible (*black line*) and foreseen to be accessible in the future (*red line*). The *dashed lines* indicate two extreme longitudinal sound velocities for liquids and glasses

disadvantages of IXS with respect to INS are readily listed: (i) The best energy resolution achieved in IXS experiments is ∼1 meV, while INS experiments can easily do much better. Though optical schemes to push the IXS resolution below 1 meV have now been proposed [5], their feasibility for real experiments has not been demonstrated yet. (ii) The rapid decrease of $f(q)$ with q makes IXS experiments very difficult already for q larger than few Å^{-1}, while there is no such stringent limitation in INS experiments. (iii) Neutrons can be scattered both coherently and incoherently, the first channel probing $S(q, E)$ and the second its self part, which gives a direct handle on single atom dynamics; X-rays miss such richness, and only probe $S(q, E)$. In order to understand where IXS extends INS capabilities, it is as well useful to list the main advantages of IXS over INS. (i) In a scattering process, the probe cannot create excitations with an energy larger than its own. This simple fact, together with the energy-wavenumber relation for neutrons, sets kinematic limitations for INS—while IXS does not suffer of this problem. In particular, INS has severe difficulties to probe at low-q collective excitations propagating with a speed larger than ∼1,500 m/s. This is not a problem in single crystal studies, where it is always possible to probe the same excitations at larger q, in some higher order Brillouin zone; it is, however, a severe limitation in the study of the collective excitations of disordered systems where, due to the lack of translational invariance, these excitations only exist at low-q, in the

so-called first pseudo Brillouin zone. This opens a class of scientific problems where IXS significantly extends INS capabilities, with particular reference to the study of the acoustic excitations in liquids and glasses. A similar situation occurs for the study of vibrations in the ∼100 meV range, and in the study of high-energy optic modes in crystals: INS can access these modes only at high-q, where the energy resolution is no longer optimal or, in the case of liquids, where the vibrational spectrum is often already heavily modified as a consequence of the recoil of the atom struck by the neutron. In these cases, IXS has the advantage to be able to easily access high energy vibrations at low-q with high-energy resolution. (ii) X-ray beams, contrary to neutron ones, can easily be focused down to a linear size of ∼10 μm or less. The availability of small beams reduces drastically the problems related to multiple scattering processes, which require sophisticated procedures of data reduction and which are often non negligible in INS experiments. More importantly, small beams disclose the access to samples of small sizes: samples only available in very small quantities, like crystals difficult to grow to large sizes, or very expensive samples, or also materials subjected to extreme thermodynamic conditions. Within this last class of systems, both crystalline and disordered materials under extreme conditions of pressure and/or temperature represent an area of growing interest. (iii) The absence of incoherent scattering, previously listed as a disadvantage, is at the same time an advantage of IXS over INS since it simplifies the cross-section and makes the IXS access to $S(q, E)$ sometimes more direct that the INS one. This is particularly important in line-shape studies of $S(q, E)$ in disordered systems.

It is finally important to underline that IXS with meV energy resolution, due to the above mentioned reasons, has gained an important place among the synchrotron radiation activities worldwide. At the moment, at the ESRF, beamline ID28 [6] is fully dedicated to it; at the Advanced Photon Source in Chicago—the 7 GeV synchrotron radiation source in the USA—two beamlines (ID3 and ID30) are optimized for IXS experiments with meV energy resolution [7]; at SPring-8—the 8 GeV national Japanese synchrotron radiation source—one beamline (BL35XU) is fully dedicated to this activity [8] and a second one is currently in the commissioning phase. Moreover, a new IXS beamline is under study at the new synchrotron radiation source of NSLS-II at Brookhaven, in the USA.

16.2 The High-Resolution Inelastic X-Ray Scattering Experiment

High-resolution inelastic X-ray scattering experiments are presently feasible at the high-energy third generation synchrotron sources ESRF, APS and SPring-8. The way these experiments are realized in these different centers is very similar, and in what follows the experimental setup originally realized at beamline ID16 of the ESRF and there existing until 2011 will be discussed as an example.

The optical layout of beamline ID16 in the high-resolution configuration for atomic dynamics studies is shown in Fig. 16.2. Schematically, the X-ray beam is monochromatized in two steps (premonochromator, monochromator) and then

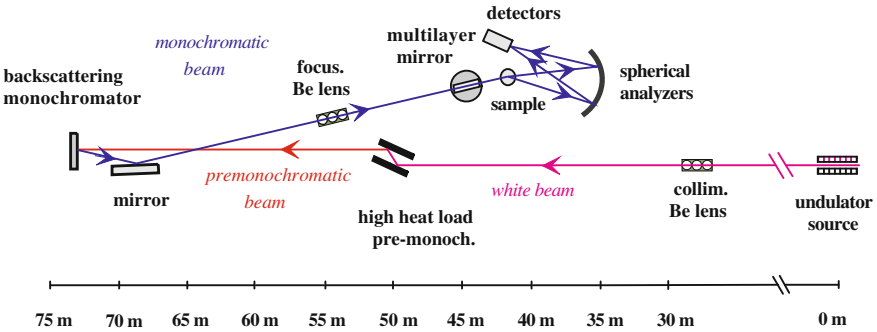


Fig. 16.2 Optical layout of beamline ID16 at the ESRF in the high-resolution configuration for atomic dynamics studies

focused at the sample stage; the radiation scattered by the sample is collected at a chosen scattering angle and analyzed in energy by the spectrometer, basically consisting of a crystal analyzer and a detector. Energy spectra are collected by scanning the energy of the incident beam—this is accomplished by scanning the temperature of the monochromator crystal with respect to that of the analyzer crystal.

The experimental strategy used for IXS measurements with meV energy resolution resembles that of a triple axis neutron spectrometer, where the first axis selects the incident photon energy (backscattering monochromator), the second one selects the scattering angle (sample goniometer), and the third axis selects the scattered photon energy (analyzer crystal).

More in detail, the X-ray beam is provided by three undulators with a magnetic period in the range of 26–35 mm and with a total length of 4.8 m. The X-ray beam from the undulators odd harmonics has a spectral bandwidth $\Delta E/E \sim 10^{-2}$, an angular divergence of approximately $40 \times 20\ \mu\text{rad}^2$ (H × V) FWHM, and an integrated power within this divergence of the order of ∼300 W. A set of cylindrical compound refractive lenses, made out of beryllium, are used to collimate the beam in the vertical direction to better than 2 μrad.

The undulator beam is premonochromatized to a bandwidth $\Delta E/E \sim 10^{-4}$ using a pair of independent Si(1,1,1) crystals cooled using liquid nitrogen to cope with the heat load of the incoming beam. At liquid nitrogen temperatures, in fact, the thermal expansion coefficient of silicon is close to zero, and the effects on the diffracted beam of the heat-load induced thermal bump are thus minimized.

The premonochromatic beam is further monochromatized using a Si crystal operated in near backscattering geometry (Bragg angle $\vartheta_B = 89.98°$, asymmetry angle $\alpha = 85°$ in the dispersive vertical plane) and on a high reflection order. The backscattering geometry is motivated by the requirement that the Darwin width of the reflection of interest should be larger than the natural beam divergence. A high order of reflection is required since the higher is the reflection order the smaller is the corresponding $\Delta E/E$. In fact, for a given Bragg reflection $\Delta E/E$ is basically inversely proportional to the number of reflecting crystalline planes throughout the extinction

length of the X-ray beam, and the extinction length in turn increases with increasing energy or reflection order [5]. At the same time, a higher order of reflection means a lower diffracted intensity, and a compromise has to be found between resolution and intensity. Depending on the experiment, reflection orders between the Si(9,9,9) and the Si(13,13,13) are typically chosen, which correspond to total energy resolutions between 3 and 1 meV. Reflection orders higher than the Si(13,13,13) one provide a beam flux at the sample stage $<10^9$ photons/s, a value that, with current optics and detectors, is too small to perform successful IXS experiments.

The focusing of the beam at the sample position can be provided by different optical schemes which lead to a focal spot typically comprised between $40 \times 60\,\mu m^2$ and $250 \times 100\,\mu m^2$ (H × V) FWHM. The former figures refer to the use of a cylindrical graded multilayer to provide horizontal focusing, while the latter ones refer to the simplest available optical scheme based on the use of a single Pt-coated toroidal mirror located 4 m away from the backscattering monochromator.

The photons scattered by the sample are collected using a 6.5 m long horizontal spectrometer. They are energy-analyzed by five spherical analyzers mounted in the horizontal spectrometer and which operate similarly to the high-resolution monochromator (i.e. in a near-backscattering configuration and at the same reflection order as the backscattering monochromator). These analyzers energy-analyze and focus the scattered photons onto five independent Si-diode detectors installed close to the sample position. The whole spectrometer arm can be rotated around the sample position in order to select the scattering angle $2\theta_s$ and then the exchanged momentum q, being $q = \frac{4\pi}{\lambda} \sin\theta_s$, where λ is the wavelength of the incoming beam. The analyzers are mounted with a constant angular offset of 1.5°, which corresponds to a basically constant q offset at low-q of 0.3 Å^{-1} at 21,747 eV, the energy corresponding to the Si(11,11,11) Bragg reflection. Five spectra at five different exchanged momentum values—one for each analyzer—can then be collected at the same time for each setting of the horizontal spectrometer arm. The q-resolution, Δq, corresponding to each spectrum is selected by slits mounted in front of the analyzer units. Typical figures are $\Delta q/q \approx 10$–$20\,\%$ for q in the 0.1–0.5 Å^{-1} range. Further details on beamline ID16 can be found in [2–4].

16.3 Models to Describe the IXS Spectra

The spectrum $I(q, E)$ measured in a high-resolution IXS experiment on a disordered monatomic system can be readily expressed as:

$$I(q, E) = I_o\,[R(E)] \otimes \left[\frac{E}{k_B T}(n(E) + 1)S(q, E)\right], \tag{16.1}$$

where I_o is an overall intensity factor; $R(E)$ is the resolution (instrument) function; $\otimes$ stands for convolution, $n(E) = [e^{(E/k_B T)} - 1]^{-1}$ is the Bose factor, with T the temperature and k_B the Boltzmann constant; and $S(q, E)$ is the *classical* dynamic

structure factor defined as the Fourier transform of the density fluctuations correlation function, $\Phi_q(t)$. An equation of motion for $\Phi_q(t)$ can be written in the form of a generalized Langevin equation [9], which leads to the following formal expression for $S(q, E)$:

$$S(q, E) = \frac{2\hbar^2 v_o^2 q^2}{E} Im[E^2 - \hbar^2 \omega_o(q)^2 - iEm_q(E)]^{-1}, \tag{16.2}$$

where *Im* denotes the imaginary part. The parameter $\omega_o(q)$ introduced in (16.2) is fixed by the second sum rule for $S(q, E)$ and turns out to be:

$$\omega_o^2(q) = \frac{(qv_o)^2}{S(q)}, \tag{16.3}$$

where $S(q)$ is the static structure factor and v_o is the classical thermal speed defined in terms of the atomic mass, M, being $v_o^2 = k_B T/M$. Moreover, in (16.2) the second memory function, $m_q(E)$, of the so-called Zwanzig-Mori expansion of $S(q, E)$ has been introduced [10, 11]. Alternatively, (16.2) can be simply considered as an equation that defines $m_q(E)$. As a matter of fact, the real advantage in using (16.2) is that the introduction of simple models for $m_q(E)$—instead than directly for $S(q, E)$—guarantees that at least the first two non-zero spectral moments of $S(q, E)$ are always correct.

Different models for $m_q(E)$ are utilized in different portions of the (q, E) space. Two quantities are usually introduced as reference points in such a space: the average interatomic distance, a, and the characteristic relaxation time for the density fluctuations, τ. The conditions $qa \ll 1$ and $E\tau \ll \hbar$ define the region of the (q, E) space where simple hydrodynamics holds, and in this range an analytical, well-known expression for $m_q(E)$ is available [9]. If condition $\omega\tau \ll 1$ fails and $qa \leq 1$, as it occurs for most of the IXS studies, one enters the realm of the so-called molecular hydrodynamics [9]. In this region the atomic dynamics is influenced both by structural and relaxational effects. For what concerns the former ones, their intervention directly comes into play through the structure factor, $S(q)$. For what concerns the latter ones, instead, an appropriate model for $m_q(E)$ has to be introduced. In general, the smooth transition from the simple hydrodynamics regime to the molecular one is the main argument used to extend the hydrodynamics description by retaining its formal structure, but replacing the thermodynamic derivatives and the transport coefficients with functions that can vary both in space (or wavenumber) and time (or energy). Within this formalism, the memory function (in time domain) can be written as:

$$m_q(t) = \omega_o^2(q)[\gamma(q) - 1]e^{-D_T(q)q^2 t} + K_l(q, t), \tag{16.4}$$

where $\gamma(q)$ and $D_T(q)$ are q dependent generalizations of the constant pressure to constant volume specific heat ratio $\gamma = C_P/C_V$ and of the thermal diffusion coefficient $D_T = \kappa/(\rho C_P)$, where κ is the thermal conductivity and ρ the mass density; and where $K_l(q, t)$ is the q and t dependent generalization of the kinematic

longitudinal viscosity ν_l. The strength of the thermal contribution, $\omega_o^2(\gamma - 1)$, is typically one order of magnitude smaller than that corresponding to the longitudinal viscosity contribution [9]. Therefore, the most important and delicate point here is to model $K_l(q,t)$. This is usually accomplished using phenomenological expressions that contain the necessary ingredients to describe the atomic dynamics.

The simplest choice for $K_l(q,t)$ is an exponential decay. This choice, which is usually known as the *viscoelastic* model, allows for a good description of the evolution of $S(q,E)$ with q for $q \simeq q_m$, where q_m denotes the first peak position in the static structure factor $S(q)$. However, for $q \simeq q_m/10$, i.e. in the standard range for IXS studies of disordered systems, the viscoelastic model begins to fail. This is usually explained by saying that, when decreasing q below q_m, the memory function splits into two contributions. The first one is the dominating contribution in glasses, is strongly q-dependent, almost temperature independent, and is related to Rayleigh-scattering of sound waves from elastic heterogeneities [12–15]. The second contribution is often relevant in liquids, describes the relaxation of the density fluctuations at times of the order of τ, and is usually temperature dependent. This second process generally corresponds to the structural relaxation [16].

As a consequence of this conceptual picture, it is customary to represent the function $K_l(q,t)$ as the sum of an exponential to describe the structural relaxation and a simple Markovian term (Dirac's delta) to describe the temperature independent contribution. As a matter of fact, this simple approximation has been shown to be detailed enough to well represent basically all the available experimental data at $q \simeq q_m/10$. In this q-range, then, the minimal expression for $K_l(q,t)$ used in the analysis of the data is the following:

$$K_l(q,t) = 2\Gamma(q)\delta(t) + \frac{q^2}{\rho}\Delta^2(q)e^{-t/\tau(q)}, \tag{16.5}$$

where $\Gamma(q)$ corresponds to the temperature independent contribution to $K_l(q,t)$; $\tau(q)$ is the q-dependent time which characterizes the long time tail of $K_l(q,t)$; and $\Delta^2(q)$ is the relaxation strength which is related to two further important quantities, $c_\infty(q)$ and $c_o(q)$, i.e. the q-dependent generalizations of the usual limiting frequency and adiabatic sound speeds, by the relation [17]:

$$\Delta^2(q) = \rho[c_\infty^2(q) - c_o^2(q)]. \tag{16.6}$$

In fact, the second term on the right hand side of (16.5) is in principle able to describe the classical phenomenology of the dispersion and absorption of sound waves, e.g. the transition of the sound speed from its low-frequency, adiabatic value, $c_o(q)$, to the high frequency, limiting value, $c_\infty(q)$ [18].

The model (16.4) and (16.5) simplifies considerably when applied to IXS studies of glasses. In fact in the limits $\gamma \approx 1$ and $E \cdot \tau(q) \gg \hbar$, which are both appropriate for undercooled liquids and glasses probed at $q \simeq q_m/10$, the dynamic structure factor, (16.2), reads:

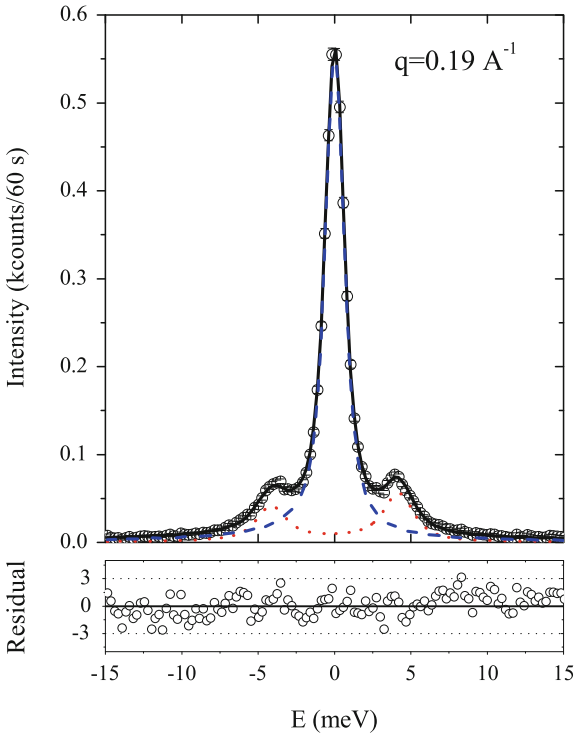


Fig. 16.3 *Upper panel* IXS spectrum of a glass of glycerol at T = 150 K and q = 0.19 Å^{-1} (*open circles*) together with the best fit obtained using the DHO model (*full black line*). The elastic and inelastic contributions derived from this model are shown as well after convolution with the instrument function (*dashed blue line* and *dotted red line*, respectively). *Bottom panel* residual of the fit, in standard deviation units

$$\frac{S(q,E)}{S(q)} = (1-f_q)\frac{2\hbar^3\Omega^2(q)\Gamma(q)}{[E^2-\hbar^2\Omega^2(q)]^2+[E\hbar\Gamma(q)]^2} + f_q\delta(E), \tag{16.7}$$

where $\Omega(q) = qc_\infty(q)$ and $f_q = 1-[\omega_o(q)/\omega_\infty(q)]^2$, the latter being known in the literature of glass-forming systems as the non-ergodicity parameter [16]. The model (16.7) is typically used to analyze IXS spectra of glasses, and is known as *damped harmonic oscillator* (*DHO*) model. Its ability to describe the IXS spectra is demonstrated in Fig. 16.3, where a typical example of an IXS spectrum of a glass is reported (open circles) together with the best fitting (16.7) (full line) and the elastic and inelastic contributions.

At q-values comprised between $q_m/10$ and q_m the situation is more complex and a simple model as the one previously discussed is not necessarily able to describe the IXS spectra. It is in fact well known that on increasing q transverse excitations appear in the spectra of several systems [19]: at q values sufficiently high the pure transverse or longitudinal polarization of the modes cannot be invoked any longer,

and intense modes with a mainly transverse polarization can appear in the $S(q, E)$ spectra. In those cases, the data analysis has been sometimes carried out adding up two DHO contributions for the mainly-longitudinal and the mainly-transverse modes [19–22]. More recently, however, it has been shown that at high-q the IXS spectra for disordered systems, in absence of relaxation effects, simply correspond to a broadened version of the spectra of the corresponding crystals [15, 23, 24], and therefore it has been clarified that no simple fitting model is really adequate to describe them.

16.4 Selected Results

16.4.1 High-Frequency Sound Waves in Glasses

Glasses exhibit universal anomalies in their thermal properties—see [25] for a review and for references to the original papers. (i) The specific heat, C_P, at low temperature is approximately proportional to T and, at $T = 0.1\,\mathrm{K}$, exceeds that of the corresponding crystals by a factor of $\sim$100. Moreover, at temperatures of the order of 10 K a bump appears in C_P/T^3, which corresponds to an excess of low-frequency modes over the Debye density of vibrational states. This excess of low-frequency modes is also directly observed in the vibrational density of states—which can be measured for example using neutron scattering [26]—and in that case is known as boson peak. (ii) The thermal conductivity, κ, is much smaller than in the corresponding crystals and nearly proportional to T^2 below 1 K. Moreover, at the same temperatures where C_P/T^3 shows the bump, κ shows a plateau. These facts contrast with what one would intuitively expect. In a pure dielectric system the low-temperature thermal properties are governed by the behavior of long-wavelength phonons—for example, thermal properties at 1 K are determined by acoustic excitations with wavelengths of $\sim$1,000 Å. On such a scale the regular lattice of a crystal, as well as the irregular network of a glass, should both appear as an elastic continuum. Then, the Debye model which leads to a T^3 dependence for specific heat and thermal conductivity should be applicable in both cases. This, however, is not observed in glasses.

The origin of these thermal anomalies is studied looking at the acoustic properties of glasses, and the overall picture which comes out is quite complex and, to date, still not completely understood [27]. These studies explain the low-temperature anomalies in C_P and κ within the so-called tunneling model [28, 29], i.e. by assuming (i) the existence of almost degenerate configurations for small groups of atoms and (ii) quantum tunneling to permit the atoms to move between these configurations. This model works formally well to describe the low-frequency acoustic behavior and the low-temperature thermal anomalies up to few K. At temperatures higher than that, and in particular in the $\simeq$10 K region where the plateau in the thermal conductivity and the bump in the specific heat appear, additional universal mechanisms have to be

invoked which require to study the acoustic properties in the GHz to THz range. This has triggered a sizable experimental (e.g. [12, 30, 31]), computational (e.g. [32–34]) and theoretical (e.g. [34–36]) research effort which has improved our understanding of the problem but has not fully clarified it yet.

The results obtained by IXS on the acoustic excitations of glasses in the THz and sub-THz frequency range are largely sample-independent and can be summarized as follows. The longitudinal acoustic excitations measured for different values of the exchanged momentum q are characterized, in first approximation, by a sinusoidal dispersion of their frequency $\Omega(q)$, with in particular a linear dependence on q up to q values of a fraction of Å^{-1} and with a slope very close to the limiting longitudinal sound velocity [37].

The maximum q-value up to which it is still possible to observe acoustic excitations is an important information to extract from the experimental spectra. The answer is difficult because, on increasing q, the acoustic excitations become broad and lie on top of the tails of the intense quasi-elastic peak. For this reason, the $S(q, E)$ spectra have been interpreted in quite different, and sometimes contrasting, ways. A typical example of this is represented by the prototypical case of vitreous silica. An interpretation of the IXS spectra of permanently densified vitreous silica is based on a data analysis scheme using a single excitation and shows that around and above the boson peak position the inelastic contribution can be described by a non-propagating excitation quite similar in shape to the boson peak itself [38]. This interpretation is based on the picture that when the acoustic excitation energy reaches the boson peak position the Ioffe-Regel limit is reached beyond which the concept of propagation for the acoustic modes looses its meaning [39]. A similar picture appears as well in models trying to connect the high-frequency acoustic modes to the thermal conductivity and the specific heat in the $\simeq$10 K temperature region [35]. In a different and contrasting view, it has been proposed that the inelastic component at high q is actually the sum of two different excitations. A study of the atomic $S(q, E)$ of vitreous silica—performed on an extended energy range (up to $\simeq$115 meV) and with a high statistical accuracy—has shown that the longitudinal mode disperses up to quite high energies above the boson peak position and that a second excitation becomes more and more evident in the spectra as q is increased [21]. This second excitation—in the q range where it is visible—is almost non dispersing and is assigned to the transverse acoustic branch [21]. Similar results have been reported as well for other glasses [20].

Another relevant information that can be extracted from the analysis of the IXS spectra is the broadening, $\Gamma(q)$, of the acoustic excitations since it gives direct information on the high-frequency acoustic attenuation. In the q region where the acoustic dispersion relation is approximatively linear, the broadening of the acoustic excitations had been found to show a T-independent, q^2 (or Ω^2) behavior up to q values of the order of few tenths of Å^{-1} [40]. It has to be underlined that the Ω^2 behavior found at high frequency does not correspond to the one measured at lower frequencies (for example with Brillouin light scattering) and generally ascribed to anharmonicity. In fact, the origin of the acoustic loss mechanism at high-frequency is surely non-dynamic [40] though its exact nature is still being discussed on. One important observation is based on the fact that also a simulated harmonic glass at

basically zero-temperature shares the same main features for $\Gamma(q)$ as measured in IXS experiments on real glasses [41], thus pointing to the central role of the structural disorder in the high-q acoustic dynamics. In more recent analyses, the Ω^2 dependence of $\Gamma(q)$ has been explained in terms of spatial fluctuations of the local elastic moduli [42], claiming an even quantitative agreement between the model predictions and the measured experimental values.

Recent experimental results which follow the continuous improvement of the technique and the use of better adapted measuring schemes have however evidenced some important additional information. The longitudinal phase velocity actually does not show a smooth decrease on increasing q as one would naively expect in a crystal-like picture. Instead, it shows a small but clear decrease (negative dispersion) of about 5 % over a very small q-range, between 0.1 and 0.2 Å^{-1}, and only at higher q values than that it shows the expected smooth decrease on increasing q. This result, first observed in a glass of glycerol [12], has been then observed in other systems as well [13, 14] and confirmed in numerical simulations [43]. The importance of this observation lies in the fact that, differently from a crystalline system, the breakdown of the Debye approximation does not take place gradually on increasing q and approaching the length-scale fixed by the interatomic spacing, but rather it takes place abruptely and on a length-scale one order of magnitude larger than in crystals, i.e. on the lengthscale of a nanometer.

Moreover, in the same q range where the phase velocity shows the negative dispersion previously discussed, i.e. up to a q value of $\simeq$0.2 Å^{-1}, the broadening of the acoustic excitations shows a quite spectacular increase with q that can be described in terms of a q^4 power law, see Fig. 16.4. This effect, first observed in a densified silica glass [44], has then been observed in several other glasses [12–15, 31] and also in numerical simulations [43]. It is also remarkable that this q^4 dependence is observed up to a q value q_c that, multiplied by the transverse sound velocity, corresponds to the boson peak position, thus clarifying the existence of a strong connection between negative dispersion, q^4 dependence of the acoustic attenuation and boson peak [12, 31].

The q^4 dependence of the acoustic attenuation on q is likely the signature of Rayleigh scattering. However, the nature of this strong scattering regime is debated in the literature. Two main physical mechanisms have been proposed: (i) the Rayleigh scattering from fluctuations in the elastic modulus [45] of the glass; (ii) a resonant interaction between vibrational soft modes and sound waves, as predicted by the soft potential model [35]. The strong scattering law is reproduced also in harmonic models where the atoms vibrate around the sites of a regular lattice with a random distribution of interatomic force constants [32, 34], or in models on the continuum assuming spatially fluctuating elastic moduli [36].

A detailed study of the $S(q, E)$ at q values higher than $\simeq$0.2 Å^{-1} might help to advance our understanding of the high-frequency vibrational dynamics of disordered systems. In fact, the comparison of the $S(q, E)$ spectra of glasses to those of the corresponding crystals in that q range shows that they become very similar and present contributions from both acoustic and optic modes. This is particularly clear when a glass is compared to the corresponding crystal characterized by the same

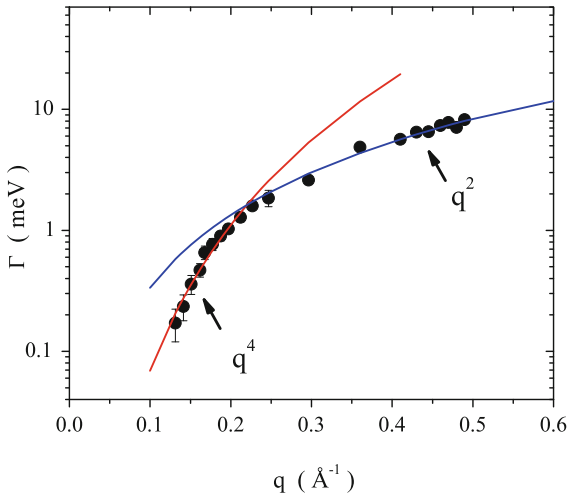


Fig. 16.4 Dependence of the acoustic attenuation Γ of the high-frequency acoustic waves on the exchanged momentum q for a glycerol glass at T = 150 K, from [12]. The *blue line* describes the q^2 dependence at high q, while the *red line* describes the q^4 dependence at low q

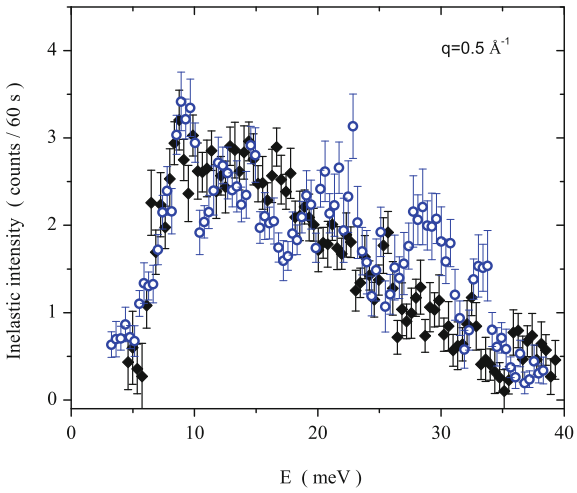


Fig. 16.5 Intensity of the X-rays inelastically scattered at $q = 0.5\,\text{Å}^{-1}$ by an α-quartz powder (*open blue circles*) and by a permanently densified SiO_2 glass (*full black diamonds*), data from [15]. The spectra are normalized taking into account the Bose population factor, with no adjustable parameter

local structure and density, as in the example reported in Fig. 16.5, where spectra for a densified silica glass and for the α-quartz polycrystal are shown [15].

It is then clear at this stage that more precise experimental data are required in order to discriminate among different models, with special reference to experiments

clarifying the connection between the high-frequency vibrational dynamics in glasses and in the corresponding crystals. In particular, this will allow going beyond the existing studies based on the use of one or two excitations to describe the IXS spectra.

16.4.2 Relaxation Processes in Liquids

The susceptibility spectrum of a liquid system in response to an external perturbation is generally smooth and characterized by broad peaks. These peaks correspond to relaxation processes which damp the perturbation applied to the system. Among the various relaxation processes which characterize the dynamical response of a liquid to a given perturbation, there is one which plays a particularly important role since it is universal—it is present in all liquids and dense fluids at basically the same frequency independently of the perturbation which is applied: this is the structural, or α, relaxation process. Its name derives from the fact that it is believed to be related to the collective structural rearrangement of groups of atoms or molecules in response to an external perturbation (or to local fluctuations). The position ω_α of the structural relaxation peak in the loss spectra defines a characteristic time, $\tau = \omega_\alpha^{-1}$. This characteristic time is strongly temperature dependent, being generally proportional to the shear viscosity as $\tau \simeq \eta_s / G_\infty$, where η_s is the shear viscosity and G_∞ is the limiting shear modulus. It follows that $\tau \sim 1$ ps for ordinary liquids with a viscosity of the order of 10^{-3} Pa s and $\sim$1000 s at the glass transition temperature—for those liquids that can reach it—where the viscosity is $\sim 10^{12}$ Pa s.

The intervention of the structural relaxation in the dynamical response of a liquid can be rationalized by viscoelastic models. These models basically describe the obvious kinetic result that if a liquid is studied on a time scale much longer than τ, one probes its equilibrium, or viscous, properties; and if a liquid is studied on a time scale much shorter than τ, one probes its out-of-equilibrium, or elastic, properties. The temperature at which this viscoelastic transition is located obviously depends on the frequency ω used to probe the system and is defined by the condition $\omega\tau(T) = 1$. This clarifies that, while low-frequency techniques are needed to probe the viscoelastic properties of glass-formers close to the glass transition temperature, high-frequency probes are required to perform such studies in liquids at ordinary conditions. This is for example the case of water at room temperature, and of a wide class of other liquids, where techniques exploring the THz frequency range are needed. This, in turn, explains and justifies the success of IXS in this kind of studies. Figure 16.6 reports, as an example, the comparison of τ values as determined in an IXS experiment on liquid water kept at a density of $\simeq$1 g/cm^3 [46] with both ultrasound data [47] and with results recently obtained using inelastic ultraviolet radiation scattering [48]. Figure 16.6 clarifies that while IXS is the only probe that provides reliable τ values in water at high temperature, it becomes less and less sensitive on decreasing the temperature as the structural relaxation leaves the IXS frequency window.

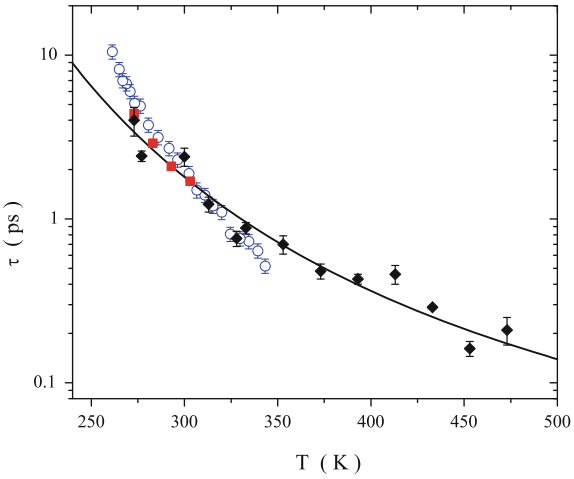


Fig. 16.6 Temperature dependence of the relaxation time τ of liquid water kept at a density of $\simeq$1 g/cm^3: IXS results (*black full diamonds*) [46] are compared to ultrasound data (*red full squares*) [47] and to inelastic ultraviolet radiation scattering data (*open blue circles*) [48]. The *full line* describes an Arrhenius behavior with an activation energy of 3.8 kcal/mol that well represents the data at high temperature but fails at low temperature

IXS studies of the structural relaxation in liquids are interesting for several reasons. One reason is that they give the possibility to probe this relaxation up to the highest possible frequencies where it can be detected. Above the THz frequency range, in fact, the relaxation of an applied perturbation will more likely occur through different paths. Another source of interest for these studies is that they give an idea of the q value up to which it is still possible to make use of the continuum hypothesis inherent in the hydrodynamics description of the density-density correlation function of a liquid. In the case of water, for example, the macroscopic hydrodynamics description is still meaningful up to $q \sim 0.2$ Å^{-1} [46], which is a fairly large value. The same result can be rephrased by saying that the atomic dynamics in water shows a homogeneous character down to a length scale of $\simeq$30 Å. It is important to emphasize that this result is not specific to water but applies in general to simple liquids [49–51].

The structural relaxation is the dominating relaxation mechanism appearing in the $S(q, E)$ spectra of simple enough liquids at low q, as verified in van der Waals liquids [50] as well as in hydrogen-bonded liquids [51] and in liquid metals [49]. However, this is no longer true in liquids that present a more complex phenomenology, since their relaxation pattern will be more complex as well. In these cases, IXS experiments can provide as well a valuable information as they can be used to extend towards high frequencies the traditional acoustic studies performed in the MHz to GHz frequency range.

An example of that is provided by the case of liquid sulfur. In fact, sulfur undergoes, at 432 K and room pressure, a reversible so-called λ-transition between a molecular liquid composed of S_8 rings and a complex solution of polymeric chains in S_8

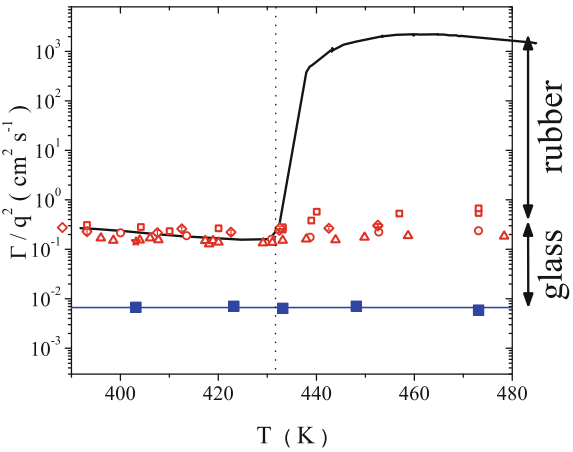


Fig. 16.7 Temperature dependence of the acoustic absorption in liquid sulfur reported as Γ/q^2. The high-frequency IXS results (*blue full squares*) [56] are compared to ultrasound data from [52, 53] (*open circles*), [54] (*open squares*) and [55] (*open diamond*), and to the zero-frequency prediction from [56–58] (*full line*). The *dotted vertical line* marks the λ-transition temperature at 432 K

monomers. In particular, ultrasound studies [52–55] of this liquid-liquid transition had left open the question of whether the high-temperature polymeric liquid form of sulfur could be considered a viscoelastic system at all, and of what would be the relaxation channels that mirror the λ-transition in the dynamic properties. A recent IXS study [56], see Fig. 16.7, has provided high frequency acoustic data that have clarified that viscoelasticity is indeed present in this peculiar liquid phase though it appears under a more complex form than in simple liquids. Specifically, Fig. 16.7 shows the temperature dependence of the acoustic attenuation in liquid sulfur as measured in different frequency ranges. The IXS results refer to the 0.4–1.1 THz frequency range [56], while the ultrasound data cover the 6–155 MHz frequency range [52–55]. The difference between the IXS and ultrasound data corresponds to the glass transition that takes place in the frequency range comprised between 0.1 GHz and 1 THz. Moreover, the full line in Fig. 16.7 corresponds to the zero-frequency, simple hydrodynamics prediction for Γ/q^2 [56–58]. The difference between the ultrasound data and the zero-frequency prediction corresponds to the liquid to rubber transition that takes place at frequencies lower than 6 MHz and only in the high-temperature polymeric phase. Converting these results from the frequency scale to the time scale it can be concluded that the atomic dynamics in liquid sulfur relaxes in two main steps. (i) A first step can be associated to the structural relaxation and is common to both sulfur liquids. In the temperature range around the λ-transition temperature, this relaxation takes place on the $\simeq$10 ps time scale and reflects both the relative motion of the chain segments between entanglement loci and the solvent molecules dynamics. (ii) A second, slower step corresponds to the slippage of the entanglement loci so that the configurational rearrangements of segments separated by entanglements can

then take place. This relaxation characterizes the high-temperature polymeric phase, is strongly temperature dependent and takes place on the $\simeq$10 ms time scale close to the transition temperature. The existence of a rubbery plateau in the polymeric liquid phase of sulfur clarifies that it basically behaves as an uncross-linked solution of high molecular weight polymers.

For a future deeper understanding of the IXS spectra of liquids it is finally important to point out that, as for the case of glasses, for q larger than $\simeq 0.2\,\text{Å}^{-1}$ the $S(q, E)$ spectra of liquids seem to become very similar to those of the corresponding crystals [23, 24]. However, this result requires further confirmations for a larger class of systems than that explored up to now.

16.4.3 The Non-Ergodicity Factor

The quasi-elastic peak present in the atomic $S(q, E)$ spectra of disordered systems holds some very interesting information which complements/extends those which can be obtained from the study of the acoustic excitations. In an undercooled liquid and in a glass, the quasi-elastic peak width—being proportional to the inverse of the structural relaxation time—is very narrow as compared to the typical energy resolution function of an IXS experiment, and cannot be measured. Its area, however, is readily determined and—once normalized to the static structure factor $S(q)$—gives the so-called effective non-ergodicity factor f_q—a central quantity in the mode-coupling description of the liquid-to-glass transition [16]. In its basic version, this theory deals with the dynamics of density fluctuations in the early stage of supercooling, and the glass transition is described as an ergodic to non-ergodic transition occurring at a critical temperature T_c and signaled by a singular behavior of the long-time limit of the normalized density correlator—the non-ergodicity factor. A zero value of the non-ergodicity factor means that a given particle will eventually escape, on a long enough timescale, from the cage of its nearest neighbors, and the system is ergodic. A finite value of the non-ergodicity factor, conversely, corresponds to a frozen structural relaxation which prevents the particles to escape their cages. Thus, the non-ergodicity factor is zero in the liquid phase but positive in the glassy state, and it changes discontinuously as the temperature crosses T_c. The effective non-ergodicity parameter which is measured in scattering experiments corresponds to the normalized density correlator calculated not at $t = \infty$ but at $t = \hbar/\Delta E$, where ΔE is the experimental energy resolution. The effective non-ergodicity factor is expected to show the same discontinuity as the non-ergodicity factor. However, while it equals the non-ergodicity factor in the non-ergodic phase, it is expected to keep a non-zero value in the ergodic phase across T_c. Specifically, the peculiar temperature and wavevector dependences expected for f_q are [16]: (i) A square-root temperature behavior below T_c, $f_q(T) = f_q^c + h_q\sqrt{(T_c - T)/T_c}$, where f_q^c is the critical non-ergodicity parameter and h_q the critical amplitude at a fixed wavevector q. (ii) A dependence on q of f_q^c and of h_q which are in phase and in anti-phase with the static structure factor $S(q)$, respectively. In the last two decades both the peculiar

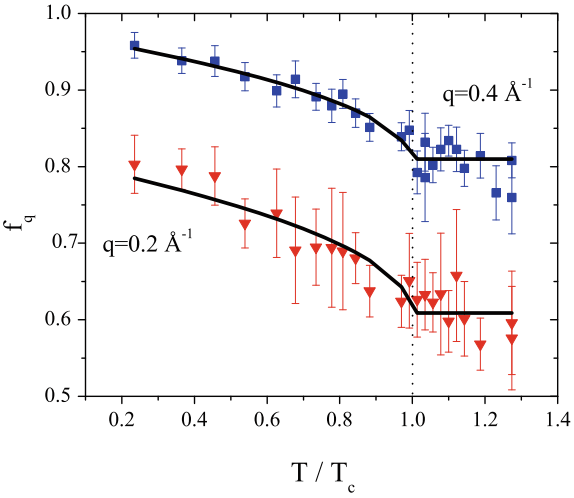


Fig. 16.8 Temperature dependence of the effective non-ergodicity factor f_q of *m*-toluidine for two different values of the exchanged wavevector q, from [59]. The temperature scale has been expressed in terms of the critical temperature $T_c = 230\,\mathrm{K}$. The solid lines are the best fits obtained using the square-root function predicted by the mode-coupling theory [16]

T and q behavior of the non-ergodicity factor predicted by the mode-coupling theory have been tested in van der Waals molecular liquids. The situation is much less clear for associated and covalent liquids, the ubiquitous class of liquids including water and silica. In these liquids the local order extends over several neighboring molecules giving often rise to a non-trivial q behavior of the static structure factor, and the available results of experimental investigations are often mutually contradictory.

A recent IXS experiment [59] has provided experimental evidence that hydrogen bond clustering can coexist with the signature of the ergodic to non-ergodic transition predicted by the mode-coupling theory for simple liquids, see Fig. 16.8. The system investigated, *m*-toluidine, is characterized by a spatial organization of the molecules induced by hydrogen bonds extending over several molecular diameters and giving rise to nanometer size clusters.

The non-ergodicity factor is also related to the glass formation process in an additional subtle way through the concept of *fragility* [60]. Specifically, the kinetic fragility, m, is defined in terms of the shear viscosity η_s as: $m = \lim_{T \to T_g} \frac{d \log(\eta_s)}{d(T_g/T)}$, where T_g is the glass transition temperature. Therefore, m is an index of how fast the shear viscosity increases on approaching the structural arrest at T_g. One interest in this parameter lies in the attempt to relate the temperature behavior of a macroscopic transport property as η_s close to T_g to the microscopic interaction driving the dynamics of the system. In fact, the value of the fragility is empirically related to the kind of interaction potential among the particles constituting the system. Prototypical examples of fragile liquids are those composed by units interacting via isotropic interactions, such as van der Waals-like molecular liquids. The strong glass-forming

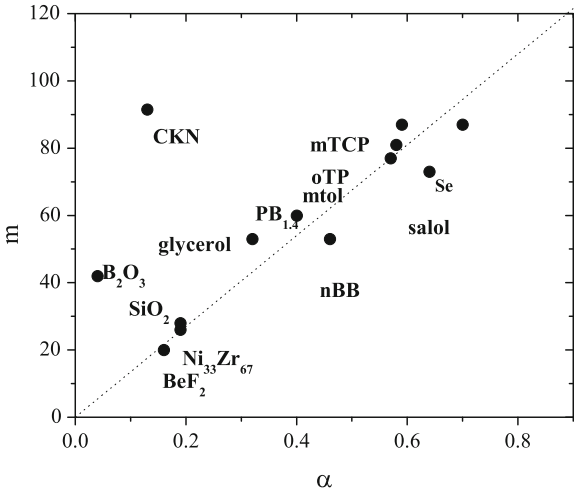


Fig. 16.9 Correlation between the parameter α describing the low-temperature behavior of the non-ergodicity factor and the kinetic fragility m. The original data set from [61] has been completed with data for CKN and B_2O_3 [62, 63] and for $Ni_{33}Zr_{67}$ [64]

liquids, on the other hand, are those characterized by strong covalent directional bonds that form space filling networks. Hydrogen bonded systems are often called "intermediate" between strong and fragile liquids.

A recent IXS study [61], see Fig. 16.9, has shown that, starting from the determination of the non-ergodicity factor in the low temperature glass, it is possible to identify a parameter that controls how fast the non-ergodicity factor decreases on increasing the temperature, and that turns out to be proportional to the fragility m. Specifically, the temperature dependence of f_q at low temperatures can be well described within the harmonic approximation for the vibrational dynamics of the glass; its inverse, f_q^{-1}, depends linearly on temperature and the slope of this line, α, is directly proportional to the fragility index of the glass. At a first glance, this result defines a new way to determine the fragility of a system starting from its glassy phase, microscopic properties. However, its real interest lies in the following observation. If we recall that: (i) the fragility is related to the temperature dependence of the viscosity on approaching T_g, and thus mirrors the diffusive properties of the system, and that (ii) the non-ergodicity factor is only related to the harmonic glassy dynamics, we have to deduce that in a glass the vibrational properties below T_g are related to the diffusive properties above T_g [61]. In the meanwhile a few exceptions to the neat correlation between the low-temperature behavior of the non-ergodicity factor and the fragility index have been found [62], and schemes to make the original proposal even more robust have been reported [65]. In any case, the connection between slow relaxation dynamics close to T_g and fast vibrational properties in the glass proposed in [61] remains very fascinating and will require further studies to be fully explored.

16.5 Conclusions

The inelastic X-ray scattering technique has given an important contribution over the last almost 20 years to our understanding of the high-frequency dynamics in liquids and glasses. It is now clear that acoustic excitations in disordered systems are present up to a relevant fraction of the first pseudo Brillouin zone size and show a crystal-like behavior [15, 23].

For both liquids and glasses, a lot of interesting information lies in the range defined by $q \leq 0.2\,\text{Å}^{-1}$ and $E \leq 5\,\text{meV}$. For liquids, this is the range where simple hydrodynamics still holds, which leaves a reference of fundamental importance for any further interpretation of the IXS spectra [46]. In glasses, this is the relevant range where the acoustic excitations show a clear breakdown of the Debye approximation and show the signature of strong scattering [12, 31], giving rise to some universal properties found in the low-temperature behavior of the specific heat and thermal conductivity of glasses. Unfortunately this most interesting (q, E) range remains difficult for IXS studies mainly due to the present limitations in terms of energy resolution. However, the strong scientific case to push IXS studies of disordered systems towards lower and lower energies and wavenumbers is stimulating the development of new optical schemes to overcome the limitations of the technique. Promising schemes are now available [5], and the near future will hopefully see the advent of advanced IXS spectrometers pushing down the lowest reachable q and E values by as much as one decade.

Acknowledgments G. Baldi, A. Chumakov, V. Giordano, S. Mossa and B. Ruta are gratefully acknowledged for a number of discussions on the issues presented here.

References

1. B. Dorner, E. Burkel, T. Illini, J.Z. Peisl, Phys. B **69**, 179 (1987)
2. R. Verbeni, F. Sette, M.H. Krisch, U. Bergmann, B. Gorges, C. Halcoussis, K. Martel, C. Masciovecchio, J.F. Ribois, G. Ruocco, H.J. Sinn, J. Synchrotron Radiat. **3**, 62 (1996)
3. C. Masciovecchio, U. Bergmann, M. Krisch, G. Ruocco, F. Sette, R. Verbeni, Nucl. Instrum. Meth. B **111**, 181 (1996)
4. C. Masciovecchio, U. Bergmann, M. Krisch, G. Ruocco, F. Sette, R. Verbeni, Nucl. Instrum. Meth. B **117**, 339 (1996)
5. Y. Shvyd'ko, *X-Ray Optics* (Springer, Berlin, 2004)
6. M. Krisch, J. Raman Spectrosc. **34**, 628 (2003)
7. H. Sinn, E.E. Alp, A. Alatas, J. Barraza, G. Bortel, E. Burkel, D. Shu, W. Sturhahn, J.P. Sutter, T.S. Toellner, J. Zhao, Nucl. Instrum. Meth. A **467–468**, 1545 (2001)
8. A.Q.R. Baron, Y. Tanaka, S. Goto, K. Takeshita, T. Matsushita, T. Ishikawa, J. Phys. Chem. Solids **61**, 461 (2000)
9. J.P. Boon, S. Yip, *Molecular Hydrodynamics* (Dover Publications Inc., New York, 1991)
10. R. Zwanzig, in *Lectures in Theoretical Physics*, ed. by W. Brittin (Wiley-Interscience, New-York, 1961), pp. 106–141
11. H. Mori, Prog. Theor. Phys. **33**, 423 (1965)
12. G. Monaco, V.M. Giordano, Proc. Natl. Acad. Sci. U.S.A. **106**, 3659 (2009)

13. B. Ruta, G. Baldi, V.M. Giordano, L. Orsingher, S. Rols, F. Scarponi, G. Monaco, J. Chem. Phys. **133**, 041101 (2010)
14. G. Baldi, V.M. Giordano, G. Monaco, B. Ruta, Phys. Rev. Lett. **104**, 195501 (2010)
15. G. Baldi, M. Zanatta, E. Gilioli, V. Milman, K. Refson, B. Wehinger, B. Winkler, A. Fontana, G. Monaco, Phys. Rev. Lett. **110**, 185503 (2013)
16. W. Götze, in *Liquids, Freezing and the Glass Transition*, ed. by J.P. Hansen, D. Levesque, J. Zinn-Justin (North-Holland, Amsterdam, 1991), pp. 289–503
17. G. Harrison, *The Dynamic Properties of Supercooled Liquids* (Academic Press, New York, 1976)
18. K.F. Herzfeld, T.A. Litovitz, *Absorption and Dispersion of Ultrasonic Waves* (Academic Press, New York, 1959)
19. F. Sette, G. Ruocco, M. Krisch, C. Masciovecchio, R. Verbeni, U. Bergmann, Phys. Rev. Lett. **77**, 83 (1996)
20. T. Scopigno, E. Pontecorvo, R. Di Leonardo, M. Krisch, G. Monaco, G. Ruocco, B. Ruzicka, F. Sette, J. Phys. Condens. Matter **15**, S1269 (2003)
21. B. Ruzicka, T. Scopigno, S. Caponi, A. Fontana, O. Pilla, P. Giura, G. Monaco, E. Pontecorvo, G. Ruocco, F. Sette, Phys. Rev. B **R69**, 100201 (2004)
22. E. Pontecorvo, M. Krisch, A. Cunsolo, G. Monaco, A. Mermet, R. Verbeni, F. Sette, G. Ruocco, Phys. Rev. E **71**, 011501 (2005)
23. V.M. Giordano, G. Monaco, Proc. Natl. Acad. Sci. U.S.A. **107**, 21985 (2010)
24. V.M. Giordano, G. Monaco, Phys. Rev. B **84**, 052201 (2011)
25. W.A. Phillips (ed.), *Amorphous Solids: Low-Temperature Properties* (Springer, Berlin, 1981)
26. U. Buchenau, N. Nücker, A.J. Dianoux, Phys. Rev. Lett. **53**, 2316 (1984)
27. S.R. Elliott, *Physics of Amorphous Materials* (Longmans, New York, 1990)
28. W.A. Phillips, J. Low Temp. Phys. **7**, 351 (1972)
29. P.W. Anderson, B.I. Halperin, C.M. Varma, Philos. Mag. **25**, 1 (1972)
30. F. Sette, M.H. Krisch, C. Masciovecchio, G. Ruocco, G. Monaco, Science **280**, 1550 (1998)
31. B. Rufflé, G. Guimbretière, E. Courtens, R. Vacher, G. Monaco, Phys. Rev. Lett. **96**, 045502 (2006)
32. W. Schirmacher, G. Diezemann, C. Ganter, Phys. Rev. Lett. **81**, 136 (1998)
33. L. Angelani, M. Montagna, G. Ruocco, G. Viliani, Phys. Rev. Lett. **84**, 4874 (2000)
34. S.N. Taraskin, Y.L. Loh, G. Natarajan, S.R. Elliott, Phys. Rev. Lett. **86**, 1255 (2001)
35. V.L. Gurevich, D.A. Parshin, H.R. Schober, Phys. Rev. B **67**, 094203 (2003)
36. W. Schirmacher, Europhys. Lett. **73**, 892 (2006)
37. G. Monaco, C. Masciovecchio, G. Ruocco, F. Sette, Phys. Rev. Lett. **80**, 2161 (1998)
38. M. Foret, R. Vacher, E. Courtens, G. Monaco, Phys. Rev. B **66**, 024204 (2002)
39. A.F. Ioffe, A.R. Regel, Prog. Semicond. **4**, 237 (1960)
40. G. Ruocco, F. Sette, R. Di Leonardo, D. Fioretto, M. Lorentzen, M. Krisch, C. Masciovecchio, G. Monaco, F. Pignon, T. Scopigno, Phys. Rev. Lett. **83**, 5583 (1999)
41. G. Ruocco, F. Sette, R. Di Leonardo, G. Monaco, M. Sampoli, T. Scopigno, G. Viliani, Phys. Rev. Lett. **84**, 5788 (2000)
42. W. Schirmacher, G. Ruocco, T. Scopigno, Phys. Rev. Lett. **98**, 025501 (2007)
43. G. Monaco, S. Mossa, Proc. Natl. Acad. Sci. U.S.A. **106**, 16907 (2009)
44. B. Rufflé, M. Foret, E. Courtens, R. Vacher, G. Monaco, Phys. Rev. Lett. **90**, 095502 (2003)
45. J.E. Graebner, B. Golding, L.C. Allen, Phys. Rev. B **34**, 5696 (1986)
46. G. Monaco, A. Cunsolo, G. Ruocco, F. Sette, Phys. Rev. E **60**, 5505 (1999)
47. W.M. Slie, A.R. Donfor Jr, T.A. Litovitz, J. Chem. Phys. **44**, 3712 (1966)
48. C. Masciovecchio, S.C. Santucci, A. Gessini, S. Di Fonzo, G. Ruocco, F. Sette, Phys. Rev. Lett. **92**, 255507 (2004)
49. T. Scopigno, U. Balucani, G. Ruocco, F. Sette, Phys. Rev. Lett. **85**, 4076 (2000)
50. A. Cunsolo, G. Pratesi, R. Verbeni, D. Colognesi, C. Masciovecchio, G. Monaco, G. Ruocco, F. Sette, J. Chem. Phys. **114**, 2259 (2001)
51. R. Angelini, P. Giura, G. Monaco, G. Ruocco, F. Sette, R. Verbeni, Phys. Rev. Lett. **88**, 255503 (2002)

52. V.F. Kozhevnikov, J.M. Viner, P.C. Taylor, Phys. Rev. B **64**, 214109 (2001)
53. V.F. Kozhevnikov, W.B. Payne, J.K. Olson, C.L. McDonald, C.E. Inglefield, J. Chem. Phys. **121**, 7379 (2004)
54. A.W. Pryor, E.G. Richardson, J. Phys. Chem. **59**, 14 (1955)
55. J.L. Hunter, T.L. Francavilla, J. Acoust. Soc. Am. **35**, 1834 (1963)
56. G. Monaco, L. Crapanzano, R. Bellissent, W. Crichton, D. Fioretto, M. Mezouar, F. Scarponi, R. Verbeni, Phys. Rev. Lett. **95**, 255502 (2005)
57. R.F. Bacon, R. Fanelli, J. Am. Chem. Soc. **65**, 639 (1943)
58. K.M. Zheng, S.C. Greer, J. Chem. Phys. **96**, 2175 (1992)
59. L. Comez, S. Corezzi, G. Monaco, R. Verbeni, D. Fioretto, Phys. Rev. Lett. **94**, 155702 (2005)
60. C.A.J. Angell, J. Non-Cryst. Solids **131–133**, 13 (1991)
61. T. Scopigno, G. Ruocco, F. Sette, G. Monaco, Science **302**, 849 (2003)
62. V.N. Novikov, Y. Ding, A.P. Sokolov, Phys. Rev. E **71**, 061501 (2005)
63. A. Matic, L. Börjesson, G. Ruocco, C. Masciovecchio, A. Mermet, F. Sette, R. Verbeni, Europhys. Lett. **54**, 77 (2001)
64. T. Scopigno, J.-B. Suck, R. Angelini, F. Albergamo, G. Ruocco, Phys. Rev. Lett. **96**, 135501 (2006)
65. T. Scopigno, D. Cangialosi, G. Ruocco, Phys. Rev. B **81**, 100202 (2010)

Part IV
Applications

Chapter 17
Applications of XAFS to Nanostructures and Materials Science

Federico Boscherini

Abstract I will firstly illustrate the role and the characteristics of XAFS as a probe of the local structure in materials and nano science. I will then provide a brief review of the use of the method in these fields, basing the discussion both on results which have stood the test of time and recent papers. Specifically, I will discuss dopants and defect complexes in semiconductors, bulk and heterostructure semiconductor alloys, phase transitions, highly correlated oxides, thin films and interfaces, semiconductor quantum dots and metallic clusters.

17.1 XAFS in Materials and Nanoscience

As illustrated in detail in Chaps. 6 and 7 XAFS can determine the local atomic and electronic structure in condensed matter. According to the spectral region analyzed, the method is conventionally referred to with different acronims: XANES (or NEXAFS) if the region near the absorption edge is analyzed or EXAFS if the spectrum in an extended energy region is used; multiple scattering theory provides a unifying description of XANES and EXAFS, which are intimately related.

Advances in materials and nano science are based on the synergy between:

(i) progress in deposition/synthesis methods;
(ii) refinements in the determination of the atomic, electronic, magnetic and vibrational structure;
(iii) study and application of the physical and chemical properties.

F. Boscherini (✉)
Department of Physics and Astronomy, University of Bologna,
Viale C. Berti Pichat 6/2, 40127 Bologna, Italy
e-mail: federico.boscherini@unibo.it

S. Mobilio et al. (eds.), *Synchrotron Radiation*,
DOI: 10.1007/978-3-642-55315-8_17, © Springer-Verlag Berlin Heidelberg 2015

In this context XAFS is a tool which can be used to obtain refined information on the second aspect and has the following advantages, some of which are shared by other core level electron spectroscopies:

- Atomic selectivity: only the structure around the atomic species chosen via the excited absorption edge is determined.
- Applicability to ordered or disordered matter: the fine structure originates from photoelectron scattering within at most 1 nm from the absorbing atom so that long range ordered crystals, highly structurally disordered clusters or intermediate aggregation states can be studied within the same interpretative framework.
- A very high distance resolution (even 0.001 Å in the first coordination shell), obtainable from high quality EXAFS data.
- Sensitivity to the local site symmetry and three dimensional atomic arrangement (e.g. whether the selected atom is in a tetrahedral, octahedral or other symmetry site), obtainable from analysis of XANES and /or "pre-edge" spectral features.
- Sensitivity to oxidation state and valence, available in many cases from the energy position of the absorption edge and / or a study of the lineshape of "pre-edge" features.
- Sensitivity to electronic structure, available through an interpretation of the XANES lineshape in terms of the site and symmetry projected local density of unoccupied electronic states.
- Applicability to the study of very dilute atomic species (e.g. dopants and impurities) and extremely thin surface layers, possible thanks to specific experimental detection modes and set-ups.
- High resolution in measurement of the relative atomic displacements, which can be used to probe vibrational properties or local disorder effects.
- Possibility of probing structure along given directions thanks to the linear polarization of the x-ray beam and the vectorial character of the dipole matrix element.
- Micron or sub-micron lateral spatial resolution, available on specially designed beamlines [1].
- Time resolutions ranging from 100's of ps (storage ring sources) to 10's of fs (new free electron lasers), available on specialized beamlines [2].
- Last, but not least, a rich and interesting underlying physics.

In this Chap. 1 will briefly review some applications of XAFS to materials and nano science. A more extensive review focused on semiconductors can be found elsewhere [3]. Since these are very broad fields of investigation the selection is inevitably a highly a personal one.

17.2 Dopants

17.2.1 Arsenic Dopants in Silicon Ultra-Shallow Junctions

Ultra shallow junctions (USJ) are 10–20 nm thick surface regions containing a very high (greater than equilibrium) dopant concentration. USJs have been recently

studied by Giubertoni et al. [4]. These authors combined XAFS and *ab-initio* simulations of defect structures with SIMS to measure the As concentration, sheet resistance measurements and Hall effect to measure the carrier concentration and thus the fraction of active As dopants. Samples were obtained by implantation at 2 keV at a dose of 1 and 3×10^{15} atoms/cm^2 followed by laser submelt annealing or rapid thermal annealing; the latter process was followed by etching to remove the disordered topmost layers. The authors were able to fit the EXAFS data with a linear combination of the signal expected for substitutional As in a Si site (As_{Si}) and vacancy—As complexes (v-As_n) and thus obtain relative fractions of these different local As environments. They found a good correspondence between the fraction of active As sites determined from transport measurements and the relative amount of As_{Si} sites determined from EXAFS.

Results are illustrated by Fig. 17.1 in which the Fourier Transforms (FT) of the As K-edge EXAFS for various implanted samples are compared to a reference sample of substitutional As (topmost trace). The trace at the bottom corresponds to an as—implanted and amorphized sample and the intermediate ones to increasing activation levels from bottom to top; it can be noticed that the lineshapes clearly become increasingly similar to the reference with increasing active fraction.

This study clearly shows that As is generally present in a range of local structures: As_{Si} , v-As_n (n = 1 to 4) defects and SiAs precipitates, the fraction of electrically active As. It can be commented that these results could not have been obtained without a significant contribution of ab initio structural simulations; a simple analysis based only on the determination of the average coordination numbers in the first few coordination shells would certainly have failed to describe the details inherent in the distribution of local environments in this rather complex system.

17.2.2 Solar Grade Silicon

In recent years the demand for high purity Si for photovoltaics has increased to the point of exceeding supply; use of "solar grade silicon", which contains concentrations of transition metal impurities much higher than used in microelectronics, has been investigated. Since the impurities decrease the efficiency of solar cells, ways to reduce these detrimental effects have been sought. In this context, micro XAFS investigations performed by Buonassisi et al. [5] have been very important in suggesting a processing recipe which minimizes the adverse effects of metal impurities.

The authors use a highly focussed X-ray beam to perform in combination fluorescence mappin and XANES with a high spatial resolution. Their main result is illustrated in Fig. 17.2, which reports the spatial distribution and XANES spectra of two types of metal defects in commercial solar grade Si: rather small (20–30 nm) and densely packed Fe silicide nanoprecipitates and bigger (several μm) and sparsely distributed Fe oxide precipitates. The relative abundance of these two kinds of defects can be controlled by the cooling rate of the crystal from the melt, a slower cooling rate producing the bigger and sparsely distributed oxide precipitates. Electrical

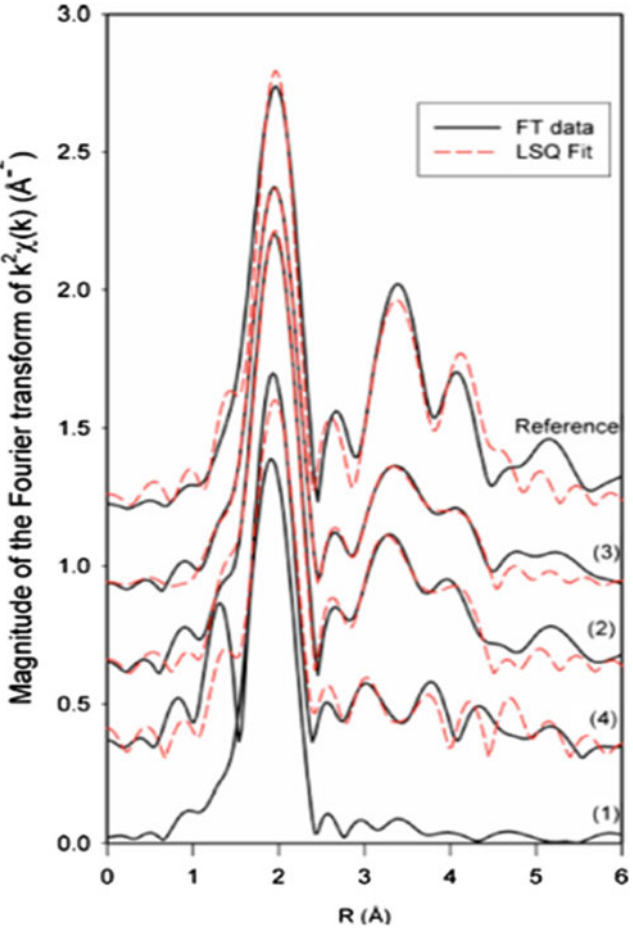


Fig. 17.1 FT of As edge spectra for USJ [4]. Reprinted with permission, © The American Institute of Physics

measurements showed that in this case carrier diffusion lengths are a factor of four higher than for a sample with densely packed, small precipitates, thus indicating the best processing route. These micro–XAFS studies provided a structural and chemical foundation for the processing recipe which leads to the optimization of transport properties, illustrating the power of microbeam X-ray techniques in the characterization of inhomogeneous semiconductor materials. There has been much progress in the field recently [1].

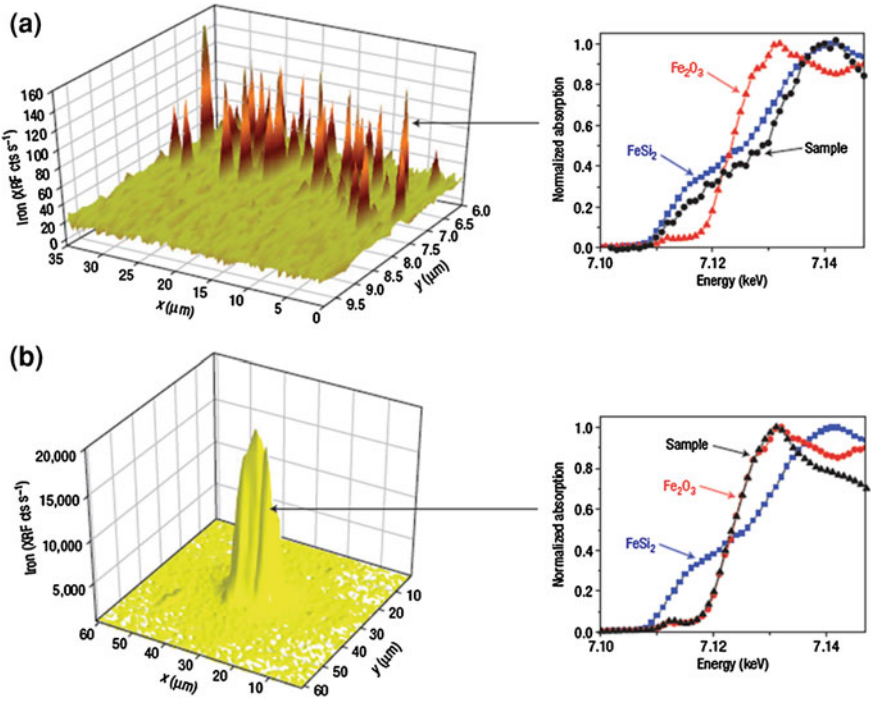


Fig. 17.2 Micro XANES of Fe precipitates in Si. Reprinted with permission from [5]. © Nature publishing group

17.2.3 Silicon in Gallium Arsenide

The site of Si dopants in GaAs has been the subject of thorough investigations published in 1993 and 1995 by Schuppler et al. [6, 7]. At the time, electrical deactivation in GaAs was thought to be due to an "autocompensation" mechanism due to the amphoteric nature of the Si dopant in GaAs; in fact, a substitutional Si on a Ga site acts as a donor while a substitutional Si on an As site acts as an acceptor and both sites are possible. Deactivation was thought to be due to the presence, at high concentrations, of both sites for Si. Schuppler et al. [6, 7], were able to convincingly demonstrate that Si dimers and small clusters are also present and contribute significantly to deactivation.

The papers by Schuppler et al. are an excellent example of application of XAFS to a complex materials science problem. The samples were specifically deposited to solve the issue at hand, the challenging XAFS measurements were made possible by the use of advanced detectors and experimental set-up and the data analysis relied on the comparison with specially designed reference compounds. Nowadays this study would have been aided by (or maybe even relied on) refined structural and

spectral simulations; nevertheless, the direct and empirical approach of these papers published 20 years ago is very convincing.

In the first paper [6] the authors studied a set of eight samples deposited by MBE, half of them on GaAs(001) and the others on GaAs(311)A; at low concentrations the incorporation site is known to be a substitutional Ga site in the former case and a substitutional As site in the latter. For each substrate, four concentrations were investigated: below, at, above and well above the critical concentration of 1×10^{18} atoms/cm^3. The Si K-edge XANES spectra clearly illustrated the changing local environment of Si and, while the spectral evolution is compatible with the presence of both As and Ga substitutional sites, the authors found that it was impossible to fit the highest concentration samples with only these two contributions. The issue was solved in the 1995 paper [7] with the use of EXAFS spectra of the samples and of a set of SiGe random alloy reference compounds. The authors were able to convincingly conclude that Si clustering contributes significantly to deactivation.

17.3 Defect Complexes

Addition to III-V semiconductor alloys of small quantities of an isoelectronic impurity characterized by very different electronegativity and size with respect to host lattice atoms causes dramatic and unexpected changes in physical properties. Incorporation of a low concentration of nitrogen (∼0.1–1 %) in GaAs leads to, among others, a giant (and counterintuitive) band gap reduction. These effects render such "dilute nitrides" attractive for the fabrication of light emitters in the telecommunications wavelength range and of high-efficiency solar cells. XAFS has been used to address the structure of the complexes formed upon irradiation with hydrogen.

An intriguing physical property of dilute nitrides alloys is that the strong changes induced by incorporation of nitrogen can be fully reversed by hydrogen irradiation, which leads to a nearly full reopening of the band gap. The nature of the hydrogen complexes responsible for these alterations of the physical properties has been addressed by a number of techniques and XAFS has played a decisive role. By combining in an original way N K-edge XANES measurements with simulations of their lineshape in the Full Multiple Scattering (FMS) framework performed on the basis of atomic coordinates obtained by *ab-initio* simulations of the structure of the most stable N-H complexes in hydrogenated GaAsN, Ciatto et al. [8] provided convincing evidence that dihydrogen-nitrogen complexes with C_{2v} symmetry are the most abundant. Subsequently, the same group refined the level of structural determination. In order to precisely determine the concentration of passivating defects deuterium, rather than hydrogen, irradiation was used, combined with nuclear reaction analysis for concentration measurement. The results [9] confirmed the local geometry of the complexes and further indicated that: (i) upon deuteration, nitrogen-deuterium complexes form with [D] / [N] = 3, leading to a neutralization of the N electronic effects in GaAs; (ii) a moderate annealing at 250 °C reduces the D concentration to [D] / [N] = 2 while the N-induced electronic properties are still passivated and the

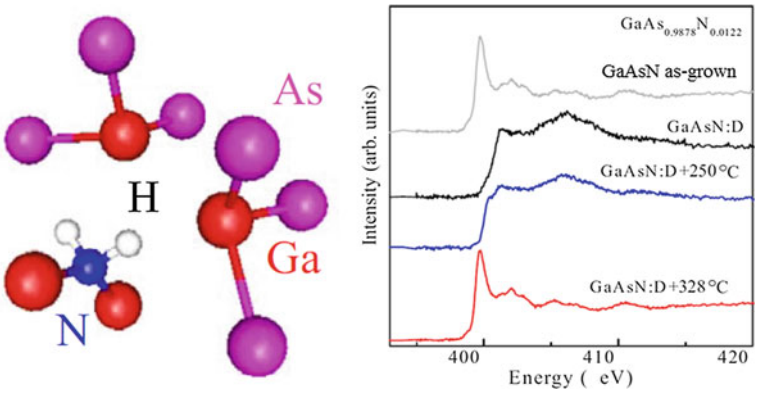


Fig. 17.3 *Left panel* Sketch of the C_{2v} complex in hydrogenated GaAsN; *Right panel* N edge XANES spectra of as grown and treated GaAsN samples. Reprinted with permission from [9]. © The American Physical Society

local structure of the complexes, as indicated by the XANES spectra, is unchanged; (iii) finally, annealing at 330 °C dissolves the deuterium-nitrogen complexes, the XANES spectra returning to that typical of substitutional N in GaAs. In Fig. 17.3 we sketch the structure of the hydrogen complex with C_{2v} symmetry and report N K-edge XANES spectra of GaAsN, as grown, as deuterated, and annealed at various temperatures. These chapter nicely illustrates the high energy resolution in XANES measurements which can be obtained in the soft X-ray range, the three dimensional sensitivity of XANES and the power of combined experimental-simulation studies.

17.4 Bulk and Heterostructure Semiconductor Alloys

The applicability of XAFS to study small bond length variations in bulk semiconductor pseudo-binary alloys was demonstrated in pioneering papers in the 1980's [10]. The main result of these investigations is that bond lengths exhibit a variation with relative concentration which is significantly weaker than that exhibited by the lattice parameter. In fact, the lattice parameter of a pseudobinary semiconductor alloy of composition $A_xB_{1-x}C$ and zincblende structure generally obeys Vegard's law,

$$a(x) = xa_{AC} + (1 - x)a_{BC} \tag{17.1}$$

where a_{AC} and a_{BC} are the lattice parameters of the binary compounds, quite well. It is found experimentally that the bond lengths, R_{AC} and R_{BC}, exhibit a much weaker dependence on x. This can be qualitatively understood as due to the "rigidity" of semiconductor bonds and implies the existence of local distortions, i.e. variations of the bond angles. It should be noted that XAFS is the appropriate tool to study this

problem because of the chemical selectivity and high resolution at the short distance scale.

It is well known that, below a certain critical thickness, when an epilayer with a cubic lattice is deposited on a substrate with a different lattice parameter its unit cell will be subjected to strain due to a tetragonal distortion of the unit cell (pseudomorphic growth). The open issue at the beginning of the 1990's was the effect of this long range strain at the local scale, i.e. on the individual bond lengths. Is there such an effect? If so, in the case of an alloy, is it the same for different bonds and how does it combine with bond length variations induced by alloying itself?

Experiments on strained alloy layers as a function of composition allowed to gain definitive insight on strain-induced bond length changes. Romanato et al. [11] studied tensile and compressively strained $In_xGa_{1-x}As$ epilayers In P(001) in the range $0.25 < x < 0.75$, detecting small but measurable bond length changes as a function of strain, which were found to be independent of the particular bond lengths (In-As or Ga-As); the application of the strain tensor to the local scale was shown to reproduce very well the experimental results.

17.5 Phase Transitions

Structural changes are the most frequent signature of phase transitions. XAFS has provided original information on the variations of the local structure which occur during phase transitions; the difference between the real local structure and that which can be erroneously inferred from a superficial interpretation of diffraction measurements has been highlighted.

Among the first papers to illustrate the peculiar characteristics and advantages of XAFS in this context was a study of the ferroelectric phase transition in $PbTiO_3$ by Sicron et al. [12]. This perovskite undergoes a tetragonal to cubic phase transition at $T_c = 763$ K; the low temperature phase is ferroelectric with a permanent electric dipole moment due to the off center displacement of the Ti ion in its octahedral environment. Based on x-ray diffraction measurements, the phase transition was believed to be purely displacive, that is, implying the disappearance of the local distortions above T_c. Ti and Pb edge XAFS measurements performed by the authors showed, instead, that the local distortions survive well above; this implies that the disappearance of the average electric dipole moment is due to the random isotropic arrangement of locally ordered domains each of which maintains a permanent dipole moment.

A more recent example comes from a completely different context: materials science of optical discs used in DVD-RAMs. Information is stored on DVDs by inducing and detecting changes in the reflectivity of μm sized areas of Ge_2SbTe_5(GST) using laser pulses. In fact, an appropriate laser pulse can cause a change from the amorphous to the crystalline phase of GST; these phases are characterized by different reflectivities which can be probed by a second laser. Kolobov et al. [13] were able to determine the structural change associated to this phase transition. By using

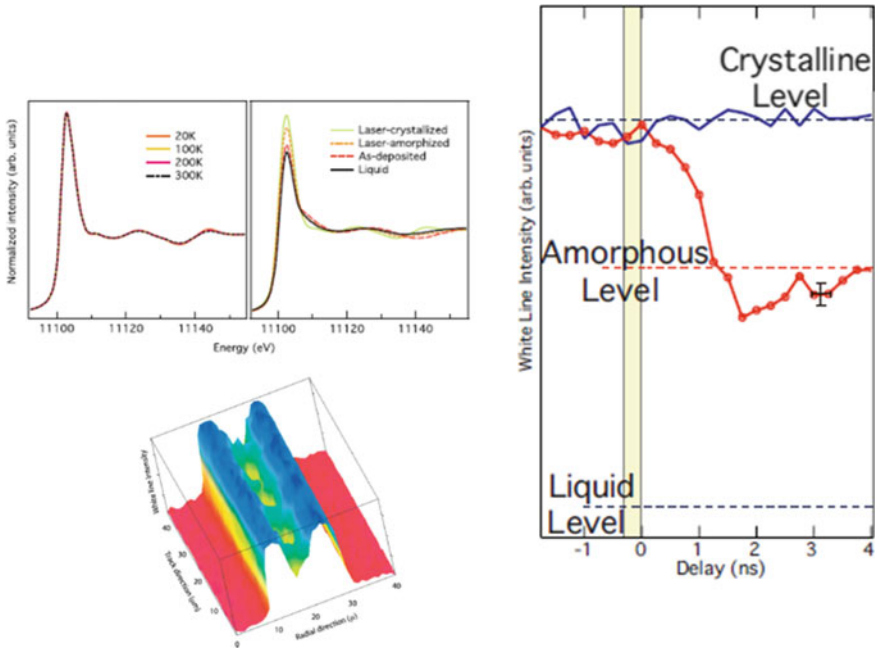


Fig. 17.4 *Top left* Ge K-edge XANES in GST; *bottom left* mapping of the intensity of the Ge edge *white line* in a DVD optical disc; *right* time resolved measurement of the intensity of the Ge edge white line following an amorphization pulse. Reprinted with permission from [14]. © The American Physical Society

XAFS measurements at three absorption edges the authors showed that the phase transition is due to movement of a Ge atom from an octahedral to a tetrahedral site within a face centered cubic Te lattice, accompanied by the breaking of one weak Ge–Te bond while other three stronger ones remain intact. The phase change is thus fast and stable because it does not require the rupture of strong bonds or diffusion.

More recently, the same group [14] reported time resolved sub-ns micro-XAFS measurements of the crystalline—to—amorphous transition. The investigation is based on the fact that it is possible to identify the phase (amorphous or crystalline) using the intensity of the Ge K-edge "white line" (the intense feature just above the edge) as an indicator. This is illustrated in the left panel of Fig. 17.4, where it is also shown that temperature has a negligible effect and that the white line intensity in the liquid phase is significantly smaller than in the other ones; in the center panel of the same figure the intensity of the white line feature is mapped, showing the crystalline band (blue, dark grey), small amorphous mark (yellow, light gray) and as deposited amorphous background (red, intermediate gray). The time resolved measurements were performed by measuring the white line intensity after laser amorphization versus time with a 100 ps time resolution, reported in the right panel. The data clearly show that amorphization proceeds without melting, i.e. that it is a purely photoassisted process due to the rupture of a weak Ge-Te bond.

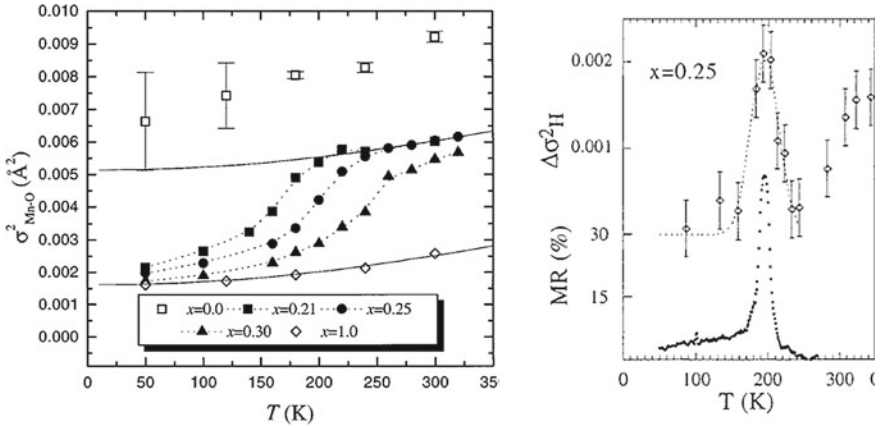


Fig. 17.5 *Left panel* distribution of Mn–O bond lengths σ^2 as a function of temperature for $La_{1-x}Ca_xMnO_3$, reprinted with permission from [15], © The American Physical Society. *Right panel* reduction of σ^2 induced by an applied magnetic field in the same compound (*top traces*) and corresponding magnetoresistance (*bottom traces*); reprinted with permission from [16], © Wiley

17.6 Correlated Oxides

Manganites of the general formula $Ln_{1-x}M_xMnO_3$, in which Ln is a lanthanide atom and M a divalent metal ion have attracted much recent interest due to intriguing physics underlying Colossal Magnetoresistance (CMR); in fact, these materials exhibit a strong coupling of electronic, lattice and spin degrees of freedom which is responsible for CMR.

$La_{1-x}Ca_xMnO_3$has been the object of a number of XAFS investigations which have highlighted this coupling. For $0.2 < x < 0.5$ this oxide, in which Mn is found in both the 3+ and 4+ charge state surrounded by six oxygen atoms in an octahedral environment, has a coincident metal—insulator and ferromagnetic—paramagnetic phase transition at a certain critical temperature T_c. One of the models proposed to explain CMR is Double Exchange, according to which the hopping conductivity between adjacent Mn ions is enhanced if the ions are spin aligned; thus an applied magnetic field can induce a conductivity increase. However, this model underestimates the magnitude of the magnetoresistance effect and it has been proposed that lattice distortions surrounding charge carriers (i.e. polarons) contribute to decrease conductivity above T_c. XAFS measurements at the Mn K edge reported by Booth et al. [15] have detected precisely such an effect. The distribution of the Mn-O bond lengths σ^2 is reported in the left panel of Fig. 17.5. For $x = 1$ and $x = 0$ it exhibits a smooth increase, compatible with the usual thermal contribution to relative atomic motion; instead, for $0.2 < x < 0.5$, at a temperature between 150 and 250 K, an anomalous behavior is apparent, providing support for the presence of polarons surrounding Mn^{3+} ions above T_c.

The influence of the spin alignment on the degree of structural distortion has been highlighted by Meneghini et al. [16]. They found that an applied magnetic field reduces the local structural distortions; in Fig. 17.5 we report the reduction of σ^2induced by the application of a 0.9 T magnetic field (top traces) and the concomitant magnetoresistance (bottom traces), the main features of which clearly occur at the same temperature.

The reported chapter illustrate the capability of XAFS of detecting exquisite details of local disorder in condensed matter, thanks to the high resolution which can be obtained in measuring the mean square relative displacements between absorbing and scattering atoms.

17.7 Thin Films

Structural studies of thin and ultra thin films by XAFS can be aided significantly by the directional dependence of the dipole matrix element and the linear polarization of the synchrotron radiation beam. We briefly review one interesting case in the field of organic thin films.

The possibility of using organic semiconducting molecules as building blocks for a new generation of electronic devices has recently triggered a great amount of interest. Among the advantages of organic semiconductor devices are the possibility of using flexible substrates and the relative low cost of manufacturing.

Since the structure of organic semiconducting molecules is based on five or six membered carbon rings with both σ and π bonds with specific orientation with respect to the substrate, XAFS has found an important application in the determination of the orientation of the molecular structure of organic thin films. Transitions to empty π orbitals give rise to intense peaks at energies lower than the broader features related to transitions to π orbitals [17].

An interesting recent study of an organic field effect thin film transistor (OFET) was performed under actual operational conditions [18]. The OFET is based on DH6T, an oligo-thiophene which easily forms well-ordered thin films. DH6T thin films (17 nm thick) were deposited on SiO_2 (500 nm thick)-precovered Si substrates. A top contact Au electrode (25 nm thick) was deposited on the DH6T thin films in order to apply electrical bias to the device. C K-edge XANES spectra were recorded as a function of the orientation between the sample and the beam. From the orientational dependence of the sharp peak to due transitions to the π^* orbitals the authors were able to demonstrate that the plane of the thiophene rings are perpendicular to the substrate. The same authors were also successful in detecting small changes in the XANES spectra as a function of electrical bias, indicating electric field—induced structural changes.

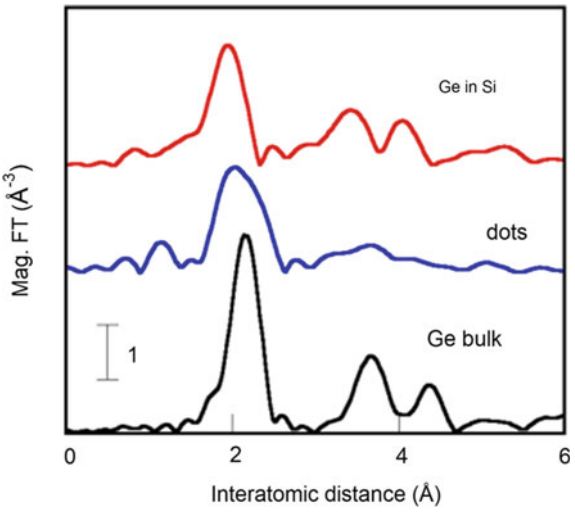


Fig. 17.6 FT of Ge edge XAFS spectra in Ge dots on Si compared to reference samples. Adapted from [19]

17.8 Semiconductor Dots

The possibility of altering the physical properties of semiconductors by exploiting quantum size effects has lead to the strong recent interest in nanostructures. XAFS has provided key results regarding the intermixing in Ge quantum dots and islands on Si. XAFS has the advantage of providing a local view of the atomic environment of the excited atom, thus providing quantitative information on intermixing and bond length strain in a direct fashion.

Ge islands on Si(001) are among the most studied systems. It is known that, due to the 4.2 % lattice misfit, heteroepitaxial growth proceeds with the formation of a two-dimensional wetting layer, followed by the formation of dots which relieve the lattice strain; this is the so-called Stranski-Krastanov growth mode. XAFS experiments [20] on Ge dots formed on Si(001) and Si(111) were among the first to detect the presence of atomic intermixing by any technique, a phenomenon which had been neglected up to that time.

The experimental evidence is rather clear, as can be seen in Fig. 17.6 which compares the FT of Ge K-edge spectra for bulk Ge, for a Ge impurity in crystalline Si and for a representative sample of Ge dots on Si(001). The asymmetrical lineshape of the first peak, which is due to the first coordination shell, indicates the presence of a significant number of Si neighbors to the average Ge atom; this indication has been confirmed by a fitting of the spectra. It is now accepted that diffusion of Si atoms from the substrate reduces the strain energy associated with the heteroepitaxial growth and is a key feature of quantum dot growth. Hence, the appropriate growth mode for quantum dots is a modified Stranski-Krastanow one.

17.9 Metallic Clusters

The study of the variations of local structure in nanometric metallic clusters as a function of size was one of the first applications of XAFS since it was realized very early that the high distance resolution in the first coordination shells make XAFS an ideal probe in this case; a further advantage is that the XAFS signal and interpretative framework do not depend on the morphology (ranging from dimers, trimers, one, two or three dimensional nanostructures).

One of the first important XAFS papers [21] reported, in fact, variations in the first coordination shell interatomic distance as a function of size in Cu and Ni metallic clusters obtained by evaporation on a weakly interacting amorphous carbon substrate; the interatomic distance was measured from the bulk to clusters having an average size of 5 Å. A bond length contraction closely following an inverse proportion with cluster size was clearly detected. This contraction can be interpreted in a macroscopic "liquid drop" model as due to the effect of the surface tension in clusters characterized by a a high surface to volume ratio [22]. From a local point of view it can be related to the inward relaxation of surface atoms due to the reduced coordination number.

The temperature dependent vibrational properties of small Au clusters have been the subject of detailed investigations [23]. These authors detected an increase in the average mean square relative displacement with decreasing cluster size. A model for the phonon density of states of a free sphere well reproduced the results. Again, one can qualitatively interpret the observed effect from a local point of view as due to the increased vibrational amplitude of surface atoms.

More recently [24], extremely high quality XAFS data of small Au clusters have been recorded and analyzed, also taking into account asymmetry of the radial distribution function. These authors found an anomalous thermal expansion behavior in the smallest clusters (40 Å average size); while thermal expansion was detected up to 200 K an unexpected contraction was apparent above this temperature, an effect due to the localization of electronic states induced by reduced dimensions

References

1. G. Martinez-Criado, E. Borfecchia, L. Mino, C. Lamberti, Micro—and nano—X-ray beams, in: *Characterization of Semiconductor Heterostructures and Nanostructures* ed. by C. Lamberti, G. Agostini (Elsevier, Amsterdam, 2013), pp. 361–412
2. M. Chergui, Acta Cryst. A **66**, 229–239 (2010)
3. F. Boscherini, X-ray absorption fine structure in the study of semiconductor heterostructures and nanostructures, in *Characterization of Semiconductor Heterostructures and Nanostructures*, ed. by C. Lamberti, G. Agostini (Elsevier, Amsterdam, 2013), pp. 259–310
4. D. Giubertoni, G. Pepponi, S. Gennaro, M. Bersani, M.A. Sahiner, S.P. Kelty, R. Doherty, M.A. Foad, M. Kah, K.J. Kirby, J.C. Woicik, P. Pianetta, J. Appl. Phys. **104**(8), 103716 (2008)
5. T. Buonassisi, A.A. Istratov, M.A. Marcus, B. Lai, Z. Cai, S. Heald, E.R. Weber, Nat. Mat. **4**, 676–679 (2005)
6. S. Schuppler, D.L. Adler, L.N. Pfeiffer, K.W. West, E.E. Chaban, P.H. Citrin, Appl. Phys. Lett **63**, 2357–2359 (1993)

7. S. Schuppler, D.L. Adler, L.N. Pfeiffer, K.W. West, E.E. Chaban, P.H. Citrin, Phys. Rev. B **51**, 10527–10538 (1995)
8. G. Ciatto, F. Boscherini, A. Amore Bonapasta, F. Filippone, A. Polimeni, M. Capizzi, Rev. B **71**, 201301–1–201301–4 (2005)
9. M. Berti, G. Bisognin, D. de Salvador, E. Napolitani, S. Vangelista, A. Polimeni, M. Capizzi, F. Boscherini, G. Ciatto, S. Rubini, F. Martelli, A. Franciosi, Phys. Rev. B **76**, 205323–1–205323–8 (2007)
10. J.C. Mikkelsen Jr, J.B. Boyce, Phys. Rev. Lett. **49**, 1412–1416 (1982)
11. F. Romanato, D. De Salvador, M. Berti, A. Drigo, M. Natali, M. Tormen, G. Rossetto, S. Pascarelli, F. Boscherini, C. Lamberti, S. Mobilio, Phys Rev. B **57**(14), 619–14622 (1998)
12. N. Sicron, B. Ravel, Y. Yacoby, E.A. Stern, F. Dogan, J.J. Rehr, Phys. Rev. B **50**, 13168–13180 (1994)
13. A.V. Kolobov, P. Fons, A.I. Frenkel, A.L. Ankudinov, J. Tominaga, T. Uruga, Nat. Mat. **3**, 703–708 (2004)
14. P. Fons, H. Osawa, A.V. Kolobov, T. Fukaya, M. Suzuki, T. Uruga, N. Kawamura, H. Tanida, J. Tominaga, Phys. Rev. B **82**, 041203–1–041203–4 (2010)
15. C.H. Booth, F. Bridges, G.H. Kwei, J.M. Lawrence, A.L. Cornelius, J.J. Neumeier, Phys. Rev. Lett. **80**, 853–856 (1998)
16. C. Meneghini, C. Castellano, A. Kumar, S. Ray, D.D. Sarma, S. Mobilio, Phys. Status Solidi B **215**, 647–652 (1999)
17. G. Comelli, J. Stöhr, C.J. Robinson, W. Jark, Phys. Rev. B **38**, 7511–7519 (1988)
18. H.S. Kato, H. Yamane, N. Kosugi, M. Kawai, Phys. Rev. Lett. **107**, 147401–147405 (2011)
19. F. Boscherini, G. Capellini, L. Di Gaspare, M. De Seta, F. Rosei, A. Sgarlata, N. Motta, S. Mobilio, Thin Solid Films **380**, 173–175 (2000)
20. F. Boscherini, G. Capellini, L. DiGaspare, N. Motta, F. Rosei, S. Mobilio, Appl. Phys. Lett. **76**, 682–684 (2000)
21. G. Apai, J.F. Hamilton, J. Stohr, A. Thompson, Phys. Rev. Lett. **43**, 165–169 (1979)
22. A. Balerna, E. Bernieri, P. Picozzi, A. Reale, S. Santucci, E. Burattini, S. Mobilio, Phys. Rev. B **31**, 5058–5065 (1985)
23. A. Balerna, S. Mobilio, Phys. Rev. B **34**, 2293–2298 (1986)
24. T. Comaschi, A. Balerna, S. Mobilio, Phys. Rev. B **77**(10), 075432 (2008)

Chapter 18
Diffraction from Nanocrystalline Materials

Paolo Scardi and Luca Gelisio

Abstract Over the past two decades, advantages of SR in XRPD have been widely exploited in many applications, ranging from basic scientific research to technology. Probably less known is the potentiality of SR-XRPD in studying nanostructured and highly defected materials, which usually present large deviations from the reference "perfect crystal" model. This requires specific methods to correctly analyze the XRPD data and, at the same time, provides an opportunity to investigate lattice defects and nanoscale materials. The present chapter first addresses features and main advantages of SR-XRPD in diffraction Line Profile Analysis (LPA); then, a brief theoretical overview is presented on the two main approaches based, respectively, on reciprocal space (Laue) and direct space (Debye) methods.

18.1 Introduction

Powder diffraction refers to the measurement of scattering phenomena—commonly using X-ray and neutrons or, sometimes, electron beams—from sufficiently numerous and uniform systems of loose particles ("powder") or bulk, nano- or microcrystalline materials. As such, powder diffraction methods strongly rely on the basic diffraction theory presented in Chap. 8 and essential knowledge of crystallography and physics of radiation-matter interactions easily available in textbooks [1–4]. Synchrotron Radiation sources provide unique opportunities to powder diffraction, ranging from basic scientific research to technological applications, exploiting a number of different experimental setups, as shown in Chap. 10.

P. Scardi (✉) · L. Gelisio
Department of Civil, Environmental and Mechanical Engineering, University of Trento,
Via Mesiano 77, 38123 Trento, Italy
e-mail: paolo.scardi@unitn.it

L. Gelisio
e-mail: luca.gelisio@unitn.it

S. Mobilio et al. (eds.), *Synchrotron Radiation*,
DOI: 10.1007/978-3-642-55315-8_18, © Springer-Verlag Berlin Heidelberg 2015

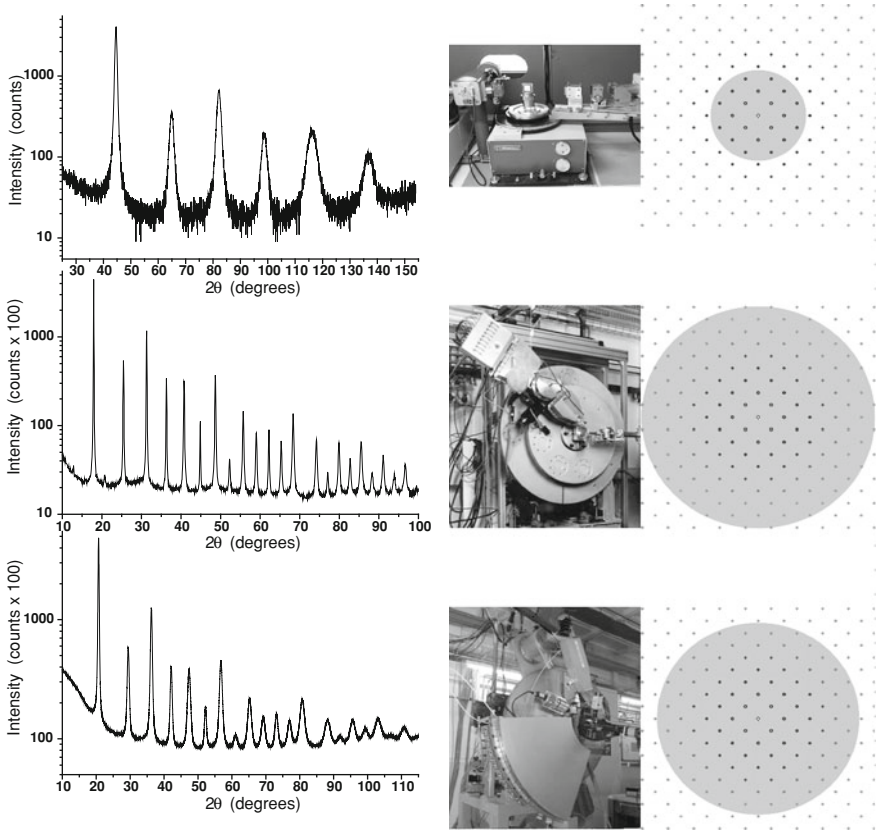


Fig. 18.1 Powder diffraction data from a ball milled Fe1.5 %Mo powder collected **a** on a traditional laboratory instrument (Rigaku PMG-VH, Bragg-Brentano geometry) with CuKα radiation ($\lambda = 0.1540598$ nm) and SR (Debye-Scherrer geometry): **b** ID31 (now ID22) at ESRF, Grenoble (F) ($\lambda = 0.0632$ nm), and MS-X04SA at PSI, Villigen (CH) ($\lambda = 0.072929$ nm). *On the right* schematic of reciprocal space with extension of the limiting sphere (radius $2/\lambda$)

SR-XRPD is primarily used in structural studies, but applications to nanostructured and heavily deformed materials are not just incidental. Main advantages are illustrated in Fig. 18.1. Data were collected on the same specimen, an extensively ball milled iron powder [5, 6], with three different instruments: a common laboratory diffractometer, based on the Bragg-Brentano geometry with a sealed X-ray tube providing CuKα radiation, and two Debye-Scherrer instruments at different SR facilities. The most striking differences are the count rate and amount of information: with the conventional lab measurement, the scintillation detector took ~80,000 s to collect data of 6 broad Bragg reflections with reasonable counting statistics; intensities increased by two orders of magnitude in SR measurements, which encompass many more peaks in as little as 1,500 and 100 s, respectively for the 9-crystal analyser (ID-31) and the Mythen linear detector (MS-X04SA).

To quantify differences, if we set

$$\eta = \frac{counts \times N^{\circ}\, of\ peaks}{data\ coll.\ time}$$

as a figure of merit, given a value of unity for the lab measurement, η raises to 25.000 for ID-31 and to 350.000 for MS-X04SA. This figure, probably, would further increase for dedicated high resolution powder diffraction beamlines with area detectors (e.g., 11-ID-B at APS, Argonne, USA).

Besides brilliance, which provides better counting statistics (or shorter data collection times, useful for in-situ studies, see Chap. 10; for kinetics studies based on LPA, see [7, 8]) and extension of the (powder diffraction) limiting sphere in reciprocal space, further advantages come from the possibility of selecting the beam energy with respect to the absorption edges of the present elements. The usually narrow instrumental peak profile is also of interest: typical values of instrumental FWHM for lab diffractometers are $\approx 0.05^{\circ}$, whereas FWHM of SR XRPD beamlines can easily be one order of magnitude narrower (see Chap. 10). As a direct consequence, the upper limit of detectable crystalline domain size, which is inversely proportional to FWHM according to the Scherrer equation (see Chap. 8 and below), usually estimated as $\sim$200 nm with traditional lab instruments, can be pushed up to several micrometres [9].

18.2 From Single Crystal to Powder Diffraction

The intensity diffracted by a small parallelepiped crystal is proportional to the Laue interference function ($|\mathrm{D}(\mathbf{S})|^2$ in Chap. 8). For the simple case of a cubic domain with N unit cells (a unit cell parameter) along the edge $L = Na$

$$I_{sc} \propto \frac{|F|^2}{V_{uc}^2} \frac{\sin^2(\pi N h')}{\sin^2(\pi h')} \frac{\sin^2(\pi N k')}{\sin^2(\pi k')} \frac{\sin^2(\pi N l')}{\sin^2(\pi l')} \tag{18.1}$$

where the running variables, h', k', l', are real numbers (as in Chap. 8, with $S_x = q_x/2\pi = h/a$, $S_y = q_y/2\pi = k/a$, $S_z = q_z/2\pi = l/a$) equal to the Miller indices (h, k, l) when Laue conditions are fulfilled, F is the structure factor and V_{uc} is the unit cell volume. While (18.1) provides the intensity across the whole reciprocal space (RS), an equivalent expression based on the sum of intensity distributions around each RS point is

$$I_{sc} \propto \frac{|F|^2}{V_{uc}^2} \sum_{h=-\infty}^{\infty} \sum_{k=-\infty}^{\infty} \sum_{l=-\infty}^{\infty} \frac{\sin^2(\pi N h')}{\pi^2 (h-h')^2} \frac{\sin^2(\pi N k')}{\pi^2 (k-k')^2} \frac{\sin^2(\pi N l')}{\pi^2 (l-l')^2} \tag{18.2}$$

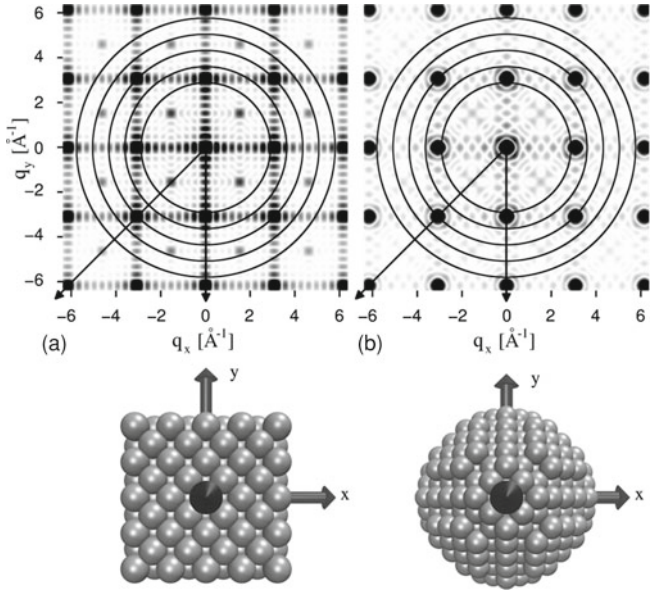


Fig. 18.2 *hk*0 cross-section of intensity distribution in RS for a gold (*fcc*) cubic domain (**a**), and corresponding intensity for a spherical domain with the same number of atoms as the cubic domain (**b**). Thermal effects, polarization and absorption were not considered. Concentric *rings* represent powder integration spheres, and *arrows* the scattering vector along different directions (see text for details)

It is worth noting that the structural information ($|F|^2$) is factorized, so it is relatively simple to write expressions for different crystal shapes, by Fourier transforming the form function $\boldsymbol{\Phi}(\mathbf{r})$ over the desired crystal volume Ω (Chap. 8).

As an example, Fig. 18.2b shows the intensity distribution for a spherical crystal with same volume as the cubic domain of Fig. 18.2a.

The intensity diffracted by a powder can be obtained by summing contributions from all coherent scattering domains. For a system made of identical domains, this corresponds to integrate distributions like those of Fig. 18.2 over all possible orientations, i.e., over a sphere of radius $|\mathbf{q}|=2\pi|\mathbf{s}-\mathbf{s_0}|/\lambda = 4\pi \sin\theta/\lambda$ (or $S = q/2\pi$, or other RS variable consistently used).

The powder integration admits few closed-form analytical solutions. For a powder of spherical domains of diameter D, Patterson has shown that [10]:

$$I_{Sph} \propto \frac{|F|^2}{V_{uc}^2}\left[\frac{1+2\Delta^2-\cos(2\Delta)-2\Delta\sin(2\Delta)}{2\Delta^4}\right. \tag{18.3}$$

$$\left.-\frac{1+2\Xi^2-\cos(2\Xi)-2\Xi\sin(2\Xi)}{2\Xi^4}\right]$$

where $\Delta = \pi D|\mathbf{s}\text{-}\mathbf{s}_0|/\lambda = \pi D\mathrm{S}$ and $\Xi = \pi D|\mathbf{s} + \mathbf{s}_0|/\lambda$ (see [11] for details). The powder integration can otherwise be performed numerically, so that peak profiles can be calculated for crystalline domains of virtually any shape [12].

The structural information in (18.3), as in (18.1) and (18.2), is factorized. More generally, powder diffraction peak profiles can be written in the form $\mathrm{I} = |\mathrm{F}|^2 \cdot \mathbf{\Phi}(\mathrm{S},D)$, where $\mathbf{\Phi}(\mathrm{S},D)$ is the line profile function, which depends on the scattering vector length, S, and on the characteristic length parameter for the given domain shape, D, like the sphere diameter or cube edge. More parameters may be necessary to describe other shapes, like diameter and height of a cylinder.

Before discussing how to determine $\mathbf{\Phi}(\mathrm{S},D)$, it is interesting to discuss interference effects among coherent scattering domains. Figure 18.3 shows a RS cross-section and the corresponding powder pattern for different cubic domains with same total volume. Intensity diffracted by a large cube is confined near points in RS fulfilling the Laue conditions, and the corresponding powder pattern shows narrow peaks (a). If the same volume is broken in smaller cubic domains with different orientations (c) the intensity in RS shows the characteristic powder rings (which look spotty as they refer to $5 \times 5 \times 5$ domains only) and the powder pattern is the same as that of a powder made of the same small cube with random orientations, and is made of broad peaks: different cubes scatter X-rays independently. However, if the orientation of the domains is only slightly different, as in (b), interference effects arise, and the powder pattern, especially at low q values, shows intermediate features between the larger volume and the separate, smaller objects.

These effects have been observed experimentally in materials with small and strongly textured domains [13, 14]; it has also been noted that the relative positions of the domains play an even major role than orientation in determining the interference conditions [15]. Even if rather infrequent in conventional powder diffraction measurements, effects shown in Fig. 18.3b might become of interest with the growing power of X-ray sources and decreasing probe size (at SR and XFEL sources); spatially confined, intense and coherent beams on nanostructured materials might involve relatively few domains and amplify the importance of mutual orientations and positions, such to show interference effects illustrated in Fig. 18.3.

18.3 Powder Diffraction Line Profiles

A significant simplification of the powder integration problem was proposed by Laue in 1926 [16]. Considering that the diffracted intensity is mostly distributed near RS points, a fair approximation to the complex problem of Fig. 18.2 is to integrate the intensity distribution over a plane tangent to the powder diffraction sphere.

The Tangent Plane Approximation (TPA), schematically shown in Fig. 18.4, makes it relatively simple to introduce the powder diffraction condition in RS. For example, in the case of the $\{h00\}$ peak for a powder of cubic domains, the tangent plane is perpendicular to the $[h00]$ direction (i.e., perpendicular to the drawing plane in Fig. 18.4). As a consequence of the TPA, the powder integration over the (k, l)

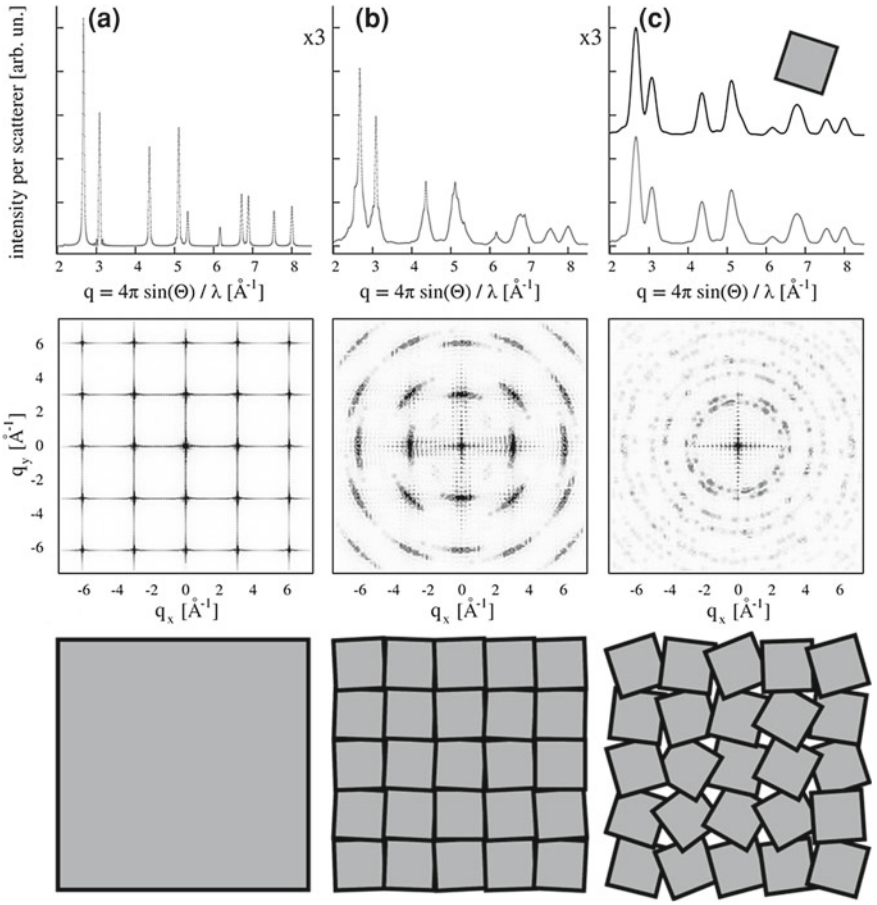


Fig. 18.3 *hk*0 cross-section of the intensity distribution in RS and corresponding powder diffraction pattern for a system of identical Cu domains: *large cube* (**a**), same volume divided in slightly tilted *smaller cubes* (**b**) and *same cubes* strongly misaligned; it is also shown the pattern for a powder of totally *random cubes* (**c**)

plane is straightforward[1]:

$$I_{\{h00\}} \propto |F|^2 \int\int \frac{\sin^2(\pi N h')}{\pi^2 (h-h')^2} \frac{\sin^2(\pi N k')}{(\pi k')^2} \frac{\sin^2(\pi N l')}{(\pi l')^2} \mathrm{d}k' \cdot \mathrm{d}l'$$
$$= N^2 |F|^2 \frac{\sin^2(\pi N h')}{\pi (h-h')^2} \tag{18.4}$$

[1] The result is obtained from: $\int_{-\infty}^{\infty} \sin^2(\pi N x)/(\pi x)^2 \mathrm{d}x = N$

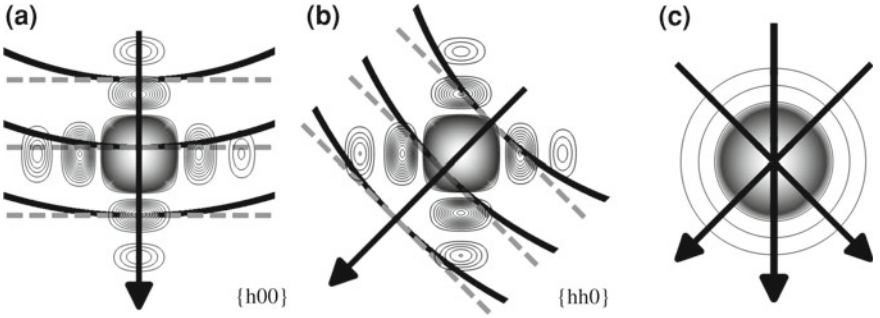


Fig. 18.4 Powder integration (*line*) and Tangent Plane Approximation (*dash*) along two different directions in RS for intensity from a cubic domain (**a**), (**b**). All directions are equivalent for the intensity from a spherical domain (**c**)

It is possible to demonstrate that the peak width, e.g., expressed as integral breadth β (ratio between peak area and peak maximum intensity), is inversely proportional to the domain size along the direction perpendicular to the corresponding (*hkl*) atomic planes [1, 17, 18]. This general result is easily verified in the simple case described by (18.4), which expressed in terms of S variable is:

$$\beta_{\{h00\}}(\mathrm{S}) = \int_{-\infty}^{\infty} \frac{\sin^2(\pi N a \mathrm{S})}{(\pi a \mathrm{S})^2} \mathrm{dS}/I(0) = \frac{Na}{(Na)^2} = \frac{1}{L} \tag{18.5}$$

So the integral breadth along [*h*00] is the inverse of the cubic domain edge, which is a particular case of the equation originally proposed by Paul Scherrer in 1918 [19], written in RS units. The same result written in 2θ space requires a change of variable, $\mathrm{dS} = \mathrm{d}(2\sin\theta/\lambda) = (2\cos\theta/\lambda)\mathrm{d}\theta = (\cos\theta/\lambda)\mathrm{d}2\theta$, so that:

$$\beta_{\{h00\}}(2\theta) = \frac{\lambda}{L\cos\theta} \tag{18.6}$$

Although the case considered by (18.4)–(18.6) is particularly simple, the TPA makes relatively easy to calculate the powder pattern peak profiles for crystalline domains with several simple shapes (e.g., cube, sphere, octahedron, tetrahedron, cylinder, prism [17, 20, 21]). This is the basis of Line Profile Analysis, a traditional application of diffraction to the study of materials microstructure [22, 23].

As an example, Fig. 18.5a shows the diffraction pattern for a powder of identical cubes (10 nm edge) of copper. The simulation refers to a horizontally polarized X-ray beam, as typical of synchrotron radiation, with $\lambda = 0.15406$ nm. Thermal vibrations are accounted for by an isotropic Debye-Waller factor ($2B$=1.13 x10^{-2} nm^2). The simulation also includes the Lorentz factor for the powder geometry [1–4, 11].

Figure 18.5b highlights the anisotropic line broadening effect for the cubic domain shape: secondary maxima are clearly visible near the (200) peak (as well as for any other (h00) peak) as a result of the atomic planes being parallel to the cubic domain

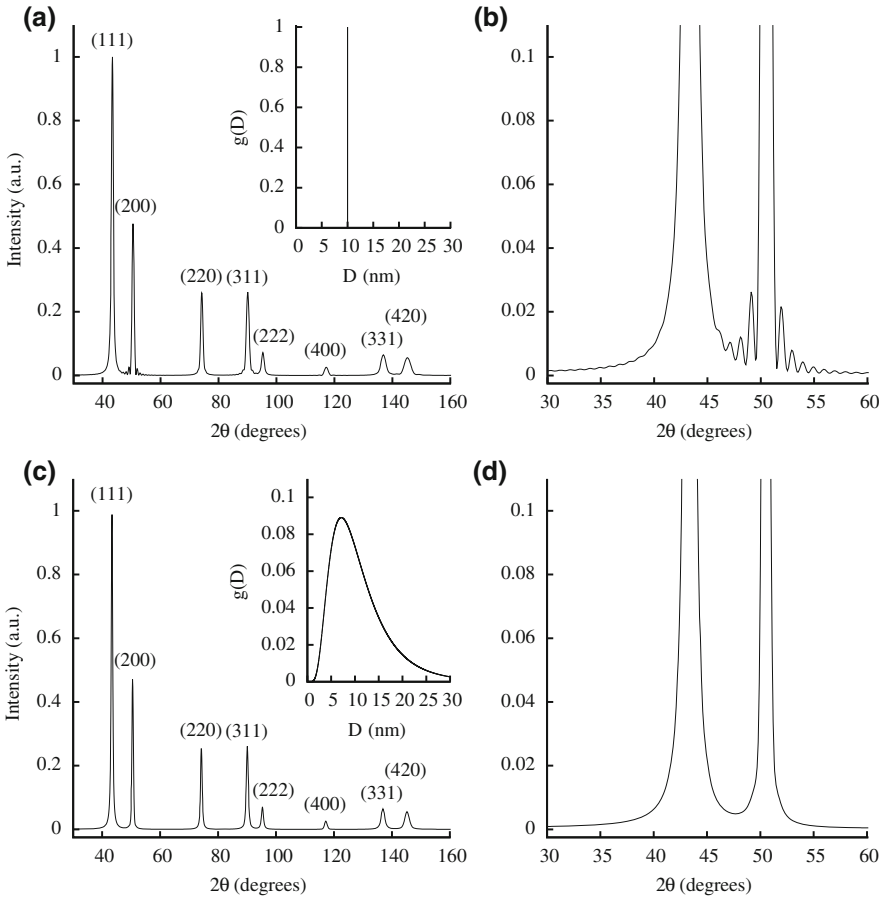


Fig. 18.5 Simulated powder patterns for Cu nanocrystals, $\lambda = 0.15406$ nm: monodisperse system of cubes, 10 nm edge (**a**); detail of (111) and (200) peaks (**b**). Polydisperse system, lognormal distribution of cubes, 10 nm mean edge, 3 nm standard deviation (**c**); detail of (111) and (200) peaks (**d**)

surfaces, whereas peaks from other planes, not parallel to the cube faces (as the (111) peak), have a different, smoother shape.

Cubic nanocrystals are observed in many cases [24], but diffraction peak profiles as in Fig. 18.5b are rarely found. The main reason is the variability of domain shape and polydispersity. Even when the nanocrystals have a given, prevailing shape, some variability is always present (e.g., truncated corners or edges in cubic crystals), resulting in a smoothing of the observed diffraction profiles.

Quite often, even if the shape is the same for all nanocrystals, their size varies. In this case the diffracted intensity is the sum of the intensities from domains with different sizes, weighted on the corresponding volume fraction [25, 26]:

$$I\,(\mathrm{S}) = K(\mathrm{S}) \int_0^\infty I_c\,(\mathrm{S},\,D)\,g(D)V_c(D)\mathrm{d}D \Big/ \int_0^\infty g(D)V_c(D)\mathrm{d}D \tag{18.7}$$

where $g(D)$ is the domain size distribution, $V_c(D)$ is the volume of the crystal of characteristic size D (e.g., sphere diameter) and $K(\mathrm{S})$ groups known constants and trigonometric terms [26]. The averaging effect of (18.7) is clearly seen in the powder pattern. As an example, Fig. 18.5c shows the case of a powder of Cu cubic crystals whose edge sizes are dispersed according to a lognormal distribution with mean $< D >= 10\,\mathrm{nm}$ and standard deviation s.d. $= 3\,\mathrm{nm}$. Peak profiles are narrower than in the pattern of Fig. 18.5a and no secondary maxima are observed in the region of the (h00) peaks (Fig. 18.5d). While the latter effect was already explained above, the former is more subtle, and results from the volume weighting in (18.7). In fact, it can be shown that the Scherrer equation is still valid for polydisperse systems, the peak width being inversely proportional to an effective size, but this length parameter is now a ratio between different moments, $M_i = \int D^i g(D)\mathrm{d}D$, of the size distribution [26]:

$$\beta\,(\mathrm{S}) = \frac{K_\beta}{< D >_V} = K_\beta \frac{M_3}{M_4} \tag{18.8}$$

This expression, a generalization of (18.5), is the Scherrer equation for polydisperse systems of simple, one size parameter domains. The Scherrer constant, K_β, depends on the domain shape, and is generally a function of h,k,l, with the notable exception of spheres, for which $K_\beta = 4/3$ for all peak profiles [26] (Fig. 18.4).

It is worth noting that $< D >_V$ and $< D >_V/K_\beta$ ($= D_{eff}$, aka effective or Scherrer size) are generally different from the arithmetic mean, $< D > = M_1$. This point is frequently source of confusion and data misinterpretation in the literature, although it is just a consequence of the properties of the distribution moments. For example, for a lognormal distribution with lognormal mean $\boldsymbol{\mu}$ and variance $\boldsymbol{\sigma^2}$ [26, 27]:

$$g\,(D) = \frac{1}{D\sigma\sqrt{2\pi}} e^{-\frac{[\log(D)-\mu]^2}{2\sigma^2}} \tag{18.9}$$

$$< D >= e^{\mu+\frac{\sigma^2}{2}} \tag{18.10a}$$

$$< D >_V = \frac{K_\beta}{\beta} = e^{\mu+\frac{7}{2}\sigma^2} \tag{18.10b}$$

$$D_{eff} = \frac{1}{\beta} = \frac{< D >_V}{K_\beta} \tag{18.10c}$$

The difference among the three mean sizes of (18.10a) depends on the skewness of the distribution. For the case shown in Fig. 18.5c, which can be considered as a narrow, little dispersed distribution (s.d. $= 3\,\mathrm{nm}$), differences among $< D >$,

Table 18.1 Mean size values ($< D >_V$ and D_{eff}) for three different atomic planes, in nm) for lognormal distributions with same arithmetic mean size $< D >= 10$ nm and increasing standard deviation (lognormal standard deviation, σ, and distribution standard deviation, s.d.).

σ	μ	s.d.	$< D >_V$	$D_{eff}(111)$	$D_{eff}(200)$	$D_{eff}(220)$
0.3	2.258	3.07	13.1	11.3	13.1	12.3
0.6	2.122	6.58	29.4	25.5	29.4	27.8
0.9	1.898	11.17	113.6	98.4	113.6	107.1

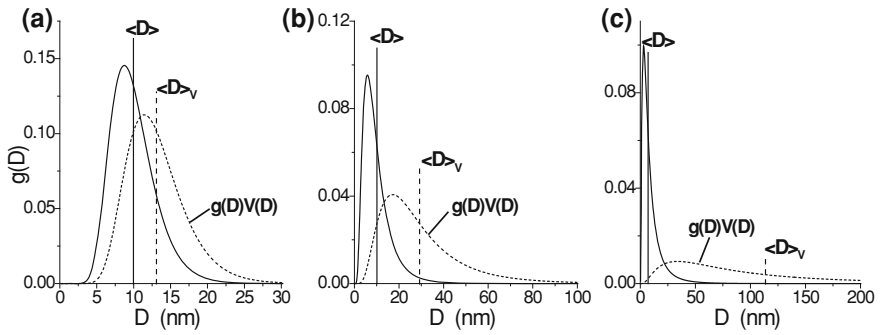


Fig. 18.6 Lognormal distribution *g(D)* (*line*) with same mean value ($< D >= 10$ nm) and increasing standard deviations (cfr. Table 18.1, $\sigma = 0.3$ (**a**), 0.6 (**b**), 0.9 (**c**)). It is also shown the volume weighted distribution, *g(D)V(D)* (*dash*)

$< D >_V$, and D_{eff} (Table 18.1) are within ∼30 %; however, if the s.d. is increased, even with the same mean size, differences can be as high as several 100 s %.

These examples clearly point out that using simple parameters as the peak width to obtain information on the size of nanocrystalline systems can be quite misleading if the studied system is polydisperse. Rather than to a length distribution, the diffraction line profile is related to the volume weighted distribution (Fig. 18.6). Differences between *g(D)* and $g(D)V_c(D)$ grow with an increasing skewness.

Powder diffraction in general—irrespective of the data analysis method employed —tends to be more sensible to larger crystals, which contribute more to the intensity ($\propto V_c(D)$) than the smaller ones.

This means that the quality of the results, i.e., our capability of measuring a size distribution (and other microstructural aspects), tends to decrease with increasing dispersion and skewness of the distribution.

So far nanocrystalline domains were considered as "perfect" domains, so the only source of line broadening was their size and shape. Lattice defects, and in general microstructural features (in broad sense, any deviation from the perfect, long-range crystalline order), also affect the observed diffraction line profile. Dislocations, for example, produce a strain field which displaces atoms and alters, as a consequence, their contribution to the scattered radiation.

The problem may appear rather complex, as the basic crystallographic property of uniform crystal structure is at least locally violated, as most lattice defects tend to modify the symmetry of the local atomic environment. However, as far as effects are relatively small (low defect concentrations) lattice defects can be considered as a perturbation of the otherwise perfect-crystal model; if they can also be considered as non-interacting, the overall diffraction profile can be described by a *convolution* of components for the different microstructural effects [1, 3, 28]:

$$I\,(S) = I^{IP}\,(S) \otimes I^{S}(\mathrm{S}) \otimes I^{D}(\mathrm{S}) \otimes I^{F}(\mathrm{S}) \otimes I^{APB}\,(\mathrm{S}) \otimes I^{C}\,(\mathrm{S}) \otimes I^{GRS}\,(\mathrm{S}) \ldots \tag{18.11}$$

where S stands for domain size/shape, F for planar faulting, APB for AntiPhase Boundaries, C for Compositional (stoichiometry) fluctuations, GRS for Grain Surface Relaxation. If necessary, the convolution in (18.11) can be easily expanded to include further terms. Equation (18.11) is also one of the most simple and rigorous means to include the instrumental contribution (IP), which in turn can be considered as a convolution from the different optical components and features of the specific experimental setup [3, 29].

The convolution of (18.11) can be suitably handled by the Fourier Transform (FT) convolution theorem, so that

$$I\,(\mathrm{S}) = K\,(\mathrm{S})\,|F|^2 \int_{-\infty}^{\infty} C\,(L)\,e^{2\pi i L\mathrm{S}}\mathrm{d}L \tag{18.12}$$

where $C(L)$ is the FT of the observed peak profile, which is the product of the FTs of the various contributing effects:

$$C = \prod_i A_i = T^{IP} \cdot A^{S}_{\{hkl\}} \cdot A^{D}_{\{hkl\}} \cdot (A^{F}_{hkl} + i\,B^{F}_{hkl}) \cdot A^{APB}_{\{hkl\}} \cdot \ldots \tag{18.13}$$

It is worth noting that faulting is not referred to families of equivalent powder reflections as it can affect each RS point differently. In this case the observed $\{hkl\}$ powder peak is obtained as a sum of hkl subcomponents. Fortunately enough, most A_i functions are known in analytical form, as a function of just few parameters, or they can be obtained by suitable numerical techniques, so that the line profile can be modelled by this approach. More details on this aspect can be found in the cited literature on the Whole Powder Pattern Modelling (WPPM), the method based on the ideas around (18.12)–(18.13) [6, 26, 28].

Among the many WPPM applications, e.g., to nanocrystals [30, 31], plastically deformed materials [5, 28, 32], dislocations and faulting in materials [33–35], materials containing anti-phase domains [36], and nanocrystal grain surface relaxation [37], we show here the case of a ball milled metal as in Fig. 18.1. The powder specimen, an iron alloy (Fe1.5Mo) with ferritic (*bcc*) structure, was ground in a planetary ball mill for 128 hours (details in [5, 6]) and the powder pattern was collected at the ID31 (now ID22) beamline of ESRF, Grenoble (F), using the standard capillary

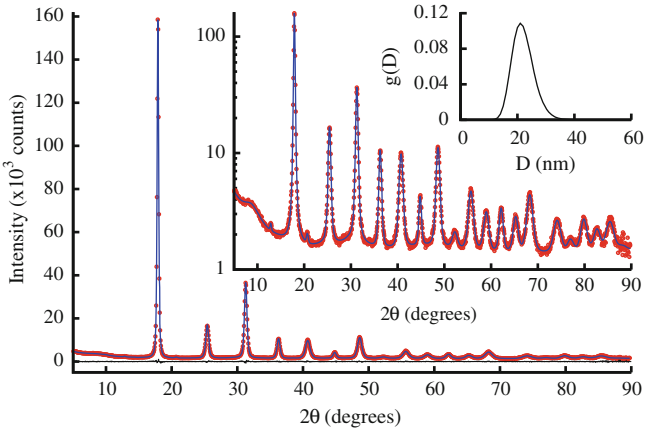


Fig. 18.7 WPPM results for a ball milled iron sample as that of Fig. 18.1. Results are shown in linear and in log scale (expt data (○), model (*line*), and difference (residual, *line* below)), together with the domain diameter distribution, in the inset. See text for more details

geometry. Given the relatively low absorption, the pattern of the empty capillary (ϕ=0.3 mm borosilicate glass capillaries) served as a good starting model for the diffuse background signal, with the optimization of a suitable scaling parameter. The instrumental profile had been previously obtained from a measurement of the NIST LaB_6 standard powder (SRM 660a) and stored in the WPPM software, PM2K [38], in parametric form [39].

Data were modelled assuming a lognormal distribution of equiaxial domains, and dislocations in the primary slip system of ferrite as the main lattice defect. The WPPM analysis, whose graphical result is shown in Fig. 18.7, shows the main effect of high energy grinding: crystalline domains are fragmented down to ca 20 nm, with a relatively narrow distribution of sizes, which is one of the fingerprints of the nanostructure in materials after heavy plastic deformation [5, 6], whereas the dislocation density is as high as $\rho = 2.1(1) \times 10^{16}$ m^{-2}, with an effective outer cut-off radius, $R_e = 12(1)$ nm, somewhat smaller than the mean domain size, and a prevalent (∼60%) edge character.

The high quality of the SR-XRPD data supports a rather stable convergence of the WPPM minimization algorithm. With these unique conditions, additional fine details can be observed, like the small amount of oxide phase (most likely, on the surface of large agglomerates of nano domains), identified by the low signals at ca 12 and 20 degrees, and the so called Wilkens parameter, $R_e\sqrt{\rho}$, providing information on the dislocation arrangement: the value (1.8(5)) is within the validity range of the Wilkens-Krivoglaz theory on dislocation line broadening (see [34] and references therein) but is significantly lower than in the pristine powder (∼5), as an indication of the increase in dislocation correlation caused by the extensive grinding. More details can be found in the cited literature [5, 6].

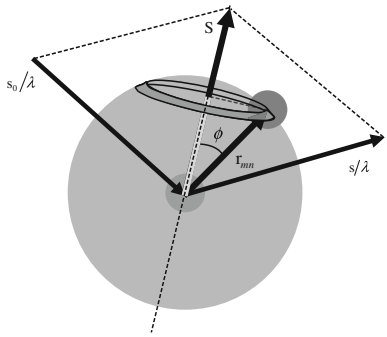


Fig. 18.8 Orientation average in the direct space approach. Representation of the $S \cdot r_{mn}$ scalar product and of the surface element used in the integral of (15)

18.4 Atomistic Modeling of Powder Diffraction from Nanocrystals

So far the basic paradigm of the RS approach was as follows: (i) first calculate the intensity diffracted by a small crystal and then (ii) average the resulting expression over all possible orientations in the powder specimen.

Although this procedure can be made relatively simple and effective by means of reasonable approximations (see Wilson's approach [17]), an inversion between (i) and (ii) can be convenient in some cases. This is the standpoint of the direct (or real) space (DS) approach first proposed by Peter Debye in 1915 [40].

With reference to Fig. 18.8, we consider r_{mn}, the distance vector between any two atoms. It is worth underlying that no reference is made to a specific atomic arrangement: it is always valid (Chap. 8) that the diffracted intensity is proportional to the square modulus of the scattering amplitude, that for N atoms of the same species means:

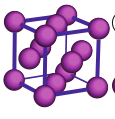
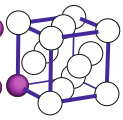
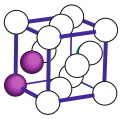
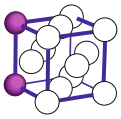
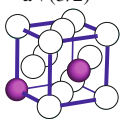
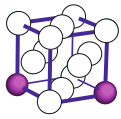
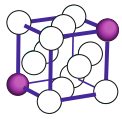
$$I_{sc} \propto \sum_{m=1}^{N} f_m e^{2\pi i (S\cdot r_m)} \sum_{n=1}^{N} f_n^* e^{-2\pi i (S\cdot r_n)}$$
$$= f^2 \sum_{m=1}^{N}\sum_{n=1}^{N} e^{2\pi i [S\cdot (r_m - r_n)]} = f^2 \sum_{m=1}^{N}\sum_{n=1}^{N} e^{2\pi i (S\cdot r_{mn})} \qquad (18.14)$$

irrespective of the phase being crystalline or not.

Figure 18.8 shows the geometrical relation between the generic r_{mn} vector and the scattering vector **S**. The scalar product in the exponent of (18.14) can be written as $S \cdot r_{mn} = \mathrm{S}r_{mn} \cos\phi$. Debye's approach to powder diffraction involves an average ($\langle\ \rangle$) of the phase term in (18.14) over all possible orientations on the sphere of radius r_{mn} shown in Fig. 18.8:

$$\left\langle e^{2\pi i (S\cdot r_{mn})} \right\rangle = \frac{1}{4\pi \mathrm{r}_{mn}^2} \int_0^{\pi} e^{2\pi i \mathrm{S}r_{mn}\cos\varphi} 2\pi \mathrm{r}_{mn}^2 \sin\phi \, \mathrm{d}\phi = \frac{\sin(2\pi \mathrm{S}r_{mn})}{2\pi \mathrm{S}r_{mn}} \qquad (18.15)$$

Table 18.2 Application of the Debye's equation to a powder of *fcc* unit cells of copper ($N = 14$ atoms)

r_{mn}	0	a/√2	a	a√(3/2)	a√2	a√3
						
n	14	72	30	48	24	8

Possible atomic distances are reported together with the corresponding number

As a consequence, the intensity diffracted by a powder specimen can be written as:

$$I\,(\mathrm{q}) \propto f^2 \sum_m \sum_n \frac{\sin\left(\mathrm{q}r_{mn}\right)}{\mathrm{q}r_{mn}} \tag{18.16}$$

Debye's derivation of the powder diffraction intensity is straightforward and leads to an expression intrinsically appropriate to deal with atomic or molecular aggregates, irrespective of their spatial arrangement (crystalline or not). Equation (18.16) can easily be generalized to polyatomic phases but the main limitation is computational, as it requires a number of terms in the double sum that grows with the square of the number of atoms. Several strategies can nowadays be used to make this approach a viable solution in the analysis of nanostructured powders [41–47].

Within the limited scope of this contribution it is interesting to consider some simple applications of (18.16). Table 18.2 shows the application of the Debye's equation to a powder of *fcc* cubes with $N = 14$ Cu atoms. All possible atomic distances (r_{mn}) are reported with the corresponding number (n) of atomic couples. Adding all terms (16) gives:

$$I\,(\mathrm{q}) = f^2\left(14 + \frac{72\sin\left(\mathrm{q}a/\sqrt{2}\right)}{\mathrm{q}a/\sqrt{2}} + \frac{30\sin\mathrm{q}a}{\mathrm{q}a} + \frac{48\sin\left(\mathrm{q}a\sqrt{3/2}\right)}{\mathrm{q}a\sqrt{3/2}} + \frac{24\sin\left(\mathrm{q}a\sqrt{2}\right)}{\mathrm{q}a\sqrt{2}} + \frac{8\sin\left(\mathrm{q}a\sqrt{3}\right)}{\mathrm{q}a\sqrt{3}}\right) \tag{18.17}$$

The corresponding powder pattern for $\lambda = 0.07093\,\mathrm{nm}$ (Mo Kα_1 radiation) is shown in Fig. 18.9: in (a) it is shown $I(2\theta)/f^2$, whereas in (b) (17) is plotted using all necessary terms, i.e., the atomic scattering factor of Cu, a random polarization term (as for a standard laboratory instrument) and an isotropic Debye-Waller factor (same as in Fig. 18.5). Vertical bars mark the expected peak positions for *fcc* Cu: bar length is proportional to peak multiplicity in (a), whereas in (b) it is proportional to the intensity measured in a standard powder pattern from polycrystalline copper.

It is quite remarkable that even such small crystalline domains give the basic features of an *fcc* powder pattern. Even if peak profiles are strongly overlapped, the correspondence with the bar positions is evident. The difference between (a) and

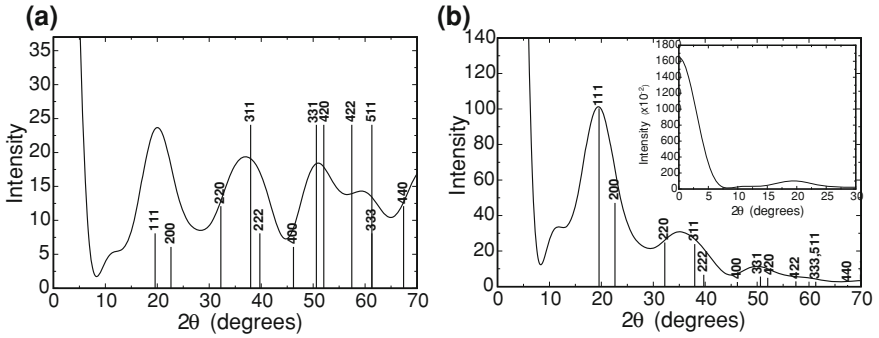


Fig. 18.9 Simulated powder pattern for a system of copper unit cells (Table 18.2). The (18.17) is plotted with $f = 1$ in (**a**) whereas the complete powder diffraction expression is shown in (**b**). The inset shows a detail of the small angle region

(b) underlines the marked 2θ dependence of the atomic scattering factor and of the thermal effects.

It is also worth noting the low angle signal: this portion of the pattern is given by the small angle scattering, which is accounted for by the Debye's equation under the hypotheses of a dilute system of particles.

As shown in the inset of Fig. 18.9b, the intensity value at $2\theta = 0°$ is equal to 164836, which corresponds, as expected [2], to $(Nf)^2$, with N=14 (cfr. Table 18.2) and $f(2\theta = 0°) = 29$ (atomic number of copper).

For the *fcc* cubic domain considered in Fig. 18.5a (10 nm edge) the sum of (18.16) involves more than 7 billion terms. Although the number quickly increases with the crystal size (as N^2), it is possible to recast the (18.16) in more convenient forms for faster calculations. Just as an example, a convenient simplification is to count the number of equal distances, B_m, so to limit the different number of $\mathrm{sinc}(x) = \sin(x)/x$ functions to calculate [41, 42]:

$$I\,(\mathrm{q}) \propto f^2 \sum_{m=1}^{M} B_m \mathrm{sinc}\left(\mathrm{qr}_m\right) \tag{18.18}$$

Figure 18.10a shows the distance histogram (B_m as a function of r_m) for the *sc* cubic crystal of $8 \times 8 \times 8$ unit cells. First bar is at $r_m = 0$ (see the inset in Fig. 18.10a) whereas, for the $N = (8+1)^3 = 729$ atoms, the longest distance (8) is $\mathrm{r}_M = 8\sqrt{3}a$ (5.0 nm). The corresponding powder diffraction pattern (calculated for $f = 1$, no additional trigonometric terms, no thermal factors, Fig. 18.10b) is obtained with a simple calculation involving just 165 $\mathrm{sinc}(x)$ functions, for as many different atomic distances. The small angle part of the pattern (inset of Fig. 18.10b) shows the fringes characteristic of a dilute system of cubes [2, 48].

However, the true advantage in using a DS approach is in the study of complex crystal shapes, as non-crystallographic objects or even non-crystalline particles. As

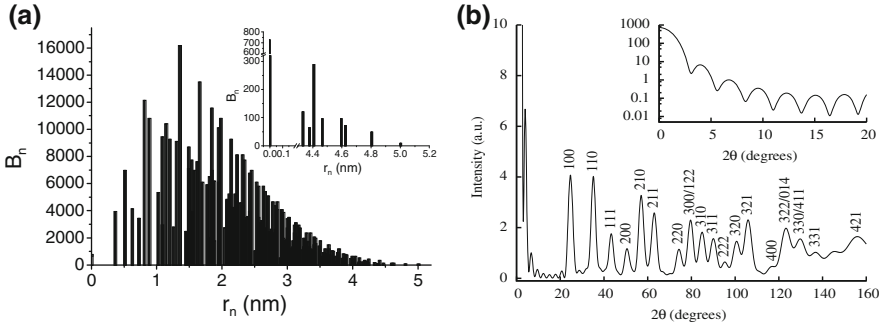


Fig. 18.10 Atomic distance histogram for the cubic crystal with $8 \times 8 \times 8$ *sc* unit cells (**a**) and corresponding powder pattern according to (18.18) ($f = 1$, unit cell parameter, 0.361 nm) (**b**)

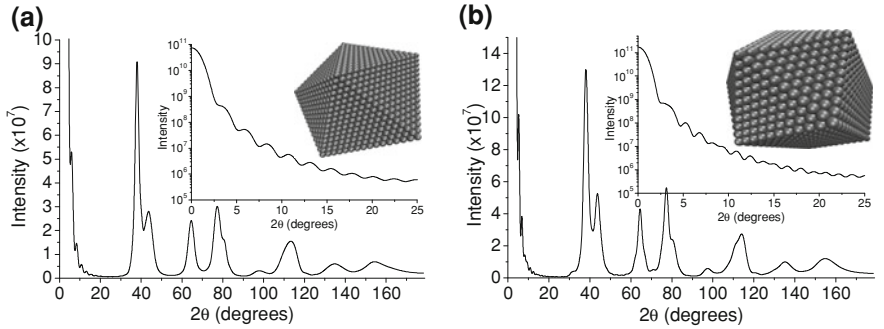


Fig. 18.11 Powder diffraction patterns simulated by (18.16) for gold decahedra: 15 shells, 3416 atoms (**a**) and truncated decahedron, 25 shells, truncation after the 10th, 5251 atoms (**b**). Both simulations refer to horizontally polarized X-rays ($\lambda = 0.15406$ nm), with a Debye-Waller factor $2B = 1.12 \times 10^{-2}$ nm^2. Insets show the small angle region and a sketch of the particle

an example of the former case, Fig. 18.11 shows the powder pattern of a system of copper decahedra: the traditional RS approach would be quite difficult to use in this case.

The DS approach briefly presented in this short contribution is currently the object of extensive research work. On one side it is of interest to understand the difference between RS and DS approaches. If the conventional RS approach is correctly carried out, avoiding the TPA (e.g., for the case of spheres, by using the Patterson expression (18.3), or by numerical powder integration techniques [12]), using the appropriate expressions for the Lorentz factor and Small Angle X-ray Scattering, and following the definitions of Ino and Minami [49], a comparison between RS and DS (Debye) approach leads to nearly identical results, with a small mismatch as expected for the intrinsic differences between the continuous model or RS and the atomistic, discrete model of DS [11, 50].

Until recently the RS approach was limited to simple shapes of convex solids: powder patterns for nanocrystals with complex shapes could only be modelled by

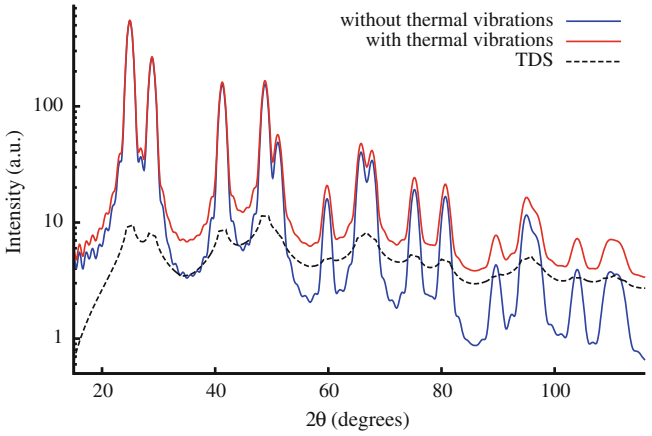


Fig. 18.12 Diffraction pattern for a system of Al spherical clusters (5 nm diameter) simulated by Molecular Dynamics: with or without thermal vibrations [52]. It is also shown (*dash*) the contribution of Temperature Diffuse Scattering

the Debye equation. However, following some recent theoretical developments, peak profiles can now be obtained for crystalline domains of any shape, including "exotic" cases, like hollow nanocrystals and multipods [51].

Recently the RS modelling of nanocrystal has been extended to include the rather peculiar Temperature Diffuse Scattering (TDS). This should increase the reliability in the modelling of experimental data, as the TDS, if not properly accounted for, tends to add to the broadening of the Bragg peaks, thus leading to potentially underestimated domain size values, besides imprecise Debye-Waller factors [52].

As an example, Fig. 18.12 shows the powder pattern for a still and a corresponding thermalized nanoparticle (spherical cluster), as obtained by the Debye equation from a Molecular Dynamics (MD) simulation.

Atomistic models and MD simulations applied to diffraction are also an interesting, novel research area, which should considerably improve the reach and the plausibility of the DS approach [53]. This is nicely shown in Fig. 18.13, where the pattern from a powder of identical Mark decahedra of copper was simulated with the Debye equation for the "standard", purely geometrical model of decahedron, and for the corresponding powder of nanocrystals after energy minimization performed by the means of an iterative Hessian-free truncated Newton scheme. After this physically plausible step, most atoms, especially in the surface region, undergo considerable displacements, so that the relaxed nanoparticles give a powder pattern markedly shifted with respect to the geometrical one, with additional, finer effects on the line profiles caused by the non-uniform atomic displacement produced during the relaxation procedure.

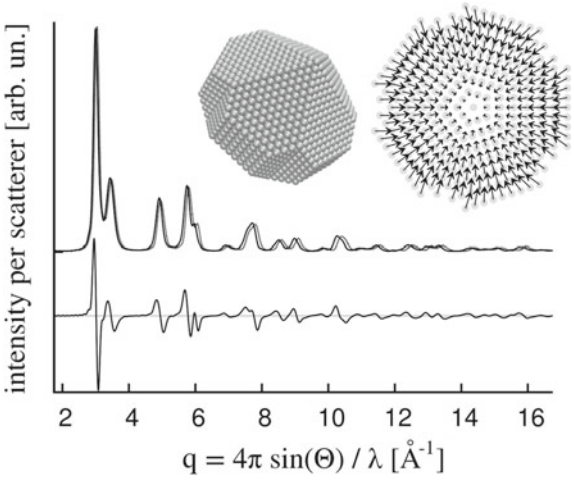


Fig. 18.13 Powder diffraction patterns simulated by (18.16) of an "as-built" copper decahedron (*line*), the same object after energy minimization (*dashed*) and difference (*line* below). Inset shows the decahedron and a sketch of the displacement field on the cross section passing through the centroid of the particle (*arrows*)

18.5 Conclusions

The theory of diffraction from powders of nanocrystalline materials has been presented following two different paradigms, namely the traditional (Laue) reciprocal space approach and the direct space (Debye) approach. While the RS approach—historically developed for bulk phases—requires the evaluation of the intensity for a small crystal in RS, followed by a suitable (usually cumbersome) orientational average for calculating the powder pattern, the DS approach reverses the sequence of these two operations, thus leading to the Debye scattering equation.

The RS approach is certainly more complex, but allows for an evaluation and separate analysis of different contributions to the powder pattern. The latter can be represented as a sum of intensities from different sets of atomic planes, leading to simple expressions to evaluate crystalline domain size and shape. Main limitations concern the capability of correctly representing powders made of fine nanocrystals, on a size level where the intrinsically discrete, atomistic nature cannot be ignored. The DS approach then, is probably more suited to deal with these problems, as it inherently considers atomic clusters (whether they are crystalline or not) as made of discrete entities. Possible limitations, besides those related to the computational requirements, are in the "rigidity" of the DS approach, where no distinction (and no separation) can be made between structural and microstructural features; however, the same "rigidity" can also be seen as a consistency guarantee.

Understanding pros and cons is the best way to exploit the two different approaches outlined in this contribution, so to find the most appropriate solutions for specific conditions.

Acknowledgments Part of this contribution was taken from the booklet made for the 2010 School held at the PSI (Villigen, CH), and published by Insubria University Press. Authors wish to thank the Editors for granting permission to freely use data and figures.

References

1. B.E. Warren, *X-ray Diffraction* (Dover Publications, New York, 1990)
2. A. Guinier, *X-ray Diffraction in Crystals, Imperfect Crystals, and Amorphous Bodies* (Dover Publications, New York, 1994)
3. H.P. Klug, L.E. Alexander, *X-ray Diffraction Procedures for Polycrystalline and Amorphous Materials* (Wiley, New York, 1974)
4. R. Jenkins, R.L. Snyder, *X-ray Powder Diffractometry* (Wiley, New York, 1996)
5. M. D'Incau, M. Leoni, P. Scardi, J. Mater. Res. **22**, 1744–1753 (2007)
6. P. Scardi, in *Powder Diffraction. Theory and practice, Ch. 13*, ed. by R.E. Dinnebier, S.J.L. Billinge (RSC Publishing, Cambridge, 2008), pp. 378–416
7. P. Scardi, M. Leoni, M. Müller, R. Di Maggio, Mat. Sci. Eng. **A528**, 77–82 (2010)
8. M. Leoni, P. Scardi, M. D'Incau, G. Luciani, Metell. Mater. Trans. **43A**, 1522–1527 (2012)
9. O. Masson, E. Dooryhée, A.N. Fitch, J. Appl. Crystallogr. **36**, 286–294 (2003)
10. A.L. Patterson, Phys. Rev. **56**, 972–977 (1939); A.L. Patterson, Phys. Rev. **56**, 978–982
11. P. Scardi, M. Leoni, K.R. Beyerlein, Z. Kristallogr. **226**, 924–933 (2011)
12. K.R. Beyerlein, R.L. Snyder, P. Scardi, J. Appl. Crystallogr. **44**, 945–953 (2011)
13. D. Rafaja, V. Valvoda, J. Kub, K. Temst, M.J. Van Bael, Y. Bruynseraede, Phys. Rev. **B61**, 16144 (2000)
14. D. Rafaja, V. Klemm, G. Schreiber, M. Knapp, R. Kužel, J. Appl. Crystallogr. **37**, 613–620 (2004)
15. L. Gelisio, P. Scardi, J. Nanosci. Nanotechnol. **12**, 8811–8817 (2012)
16. M.V. Laue, Z. Kristallogr. **64**, 115–142 (1926)
17. A.J.C. Wilson, *X-ray Optics* (Methuen, London, 1949)
18. A.R. Stokes, A.J.C. Wilson, Proc. Cambridge Philos. Soc. **38**, 313–322 (1942); A.R. Stokes, A.J.C. Wilson, Proc. Cambridge Philos. Soc. **40**, 197–198 (1944)
19. P. Scherrer, Nach. Göttinger Gesell (1918), p. 98; R. Zsigmondy, Kolloidchemie, 3rd Edn. (Otto Spamer, Leipzig, 1920), p. 394
20. J.I. Langford, D. Louër, J. Appl. Crystallogr. **15**, 20–26 (1982)
21. R. Vargas, D. Louër, J.I. Langford, J. Appl. Crystallogr. **16**, 512–518 (1983)
22. R.L. Snyder, J. Fiala, H.J. Bunge, *Defect and Microstructure Analysis by Diffraction* (Oxford University Press, Oxford, 1999)
23. E.J. Mittemeijer, P. Scardi, *Diffraction Analysis of the Microstructure of Materials* (Springer, Berlin, 2004)
24. Y. Xia, Y. Xiong, B. Lim, S.E. Skrabalak, Angew. Chem. Int. Ed. **48**, 60–103 (2009)
25. J.I. Langford, A.J.C. Wilson, J. Appl. Crystallogr. **11**, 102–113 (1978)
26. P. Scardi, M. Leoni, Acta Crystallogr. **A57**, 604–613 (2001)
27. J.I. Langford, D. Louër, P. Scardi, J. Appl. Crystallogr. **33**, 964–974 (2000)
28. P. Scardi, M. Leoni, Acta Crystallogr. **A58**, 190–200 (2002)
29. R.W. Cheary, A.A. Coelho, J. Appl. Crystallogr. **25**, 109–121 (1992)
30. M. Leoni, R. Di Maggio, S. Polizzi, P. Scardi, J. Am. Ceram. Soc. **87**, 1133–1140 (2004)
31. K.R. Beyerlein, J. Solla-Gullón, E. Herrero, E. Garnier, F. Pailloux, M. Leoni, P. Scardi, R.L. Snyder, A. Aldaz, J.M. Feliu, Mat. Sci. Eng. **A528**, 83–90 (2010)

32. P. Scardi, Z. Metallkd. **96**, 698–702 (2005)
33. M. Leoni, J. Martinez-Garcia, P. Scardi, J. Appl. Crystallogr. **40**, 719–724 (2007)
34. J. Martinez-Garcia, M. Leoni, P. Scardi, Acta Crystallogr. **A65**, 109–119 (2009)
35. A. Fais, P. Scardi, Z. Kristallogr. Suppl. **27**, 37–44 (2008)
36. P. Scardi, M. Leoni, Acta Mater. **53**, 5229–5239 (2005)
37. M. Leoni, P. Scardi, in *Diffraction Analysis of the Microstructure of Materials, Ch. 16*, ed. by E.J. Mittemeijer, P. Scardi, Springer Series in Materials Science (Springer, Berlin, 2004), pp. 413–454
38. M. Leoni, T. Confente, P. Scardi, Z. Kristallogr. Suppl. **23**, 249–254 (2006)
39. P. Scardi, M. Ortolani, M. Leoni, Mat. Sci. Forum **651**, 155–171 (2010)
40. P. Debye, Ann. Phys. **46**, 809–823 (1915)
41. L.H. Germer, A.H. White, Phys. Rev. **60**, 447–454 (1941)
42. O. Glatter, Acta Phys. Austriaca **52**, 243–256 (1980)
43. B.D. Hall, R. Monot, Comput. Phys. **5**, 414–417 (1991)
44. A. Cervellino, C. Giannini, A. Guagliardi, J. Appl. Crystallogr. **36**, 1148–1158 (2003)
45. A. Cervellino, C. Giannini, A. Gaugliardi, J. Comput. Chem. **27**, 995–1008 (2006)
46. A. Longo, A. Martorana, J. Appl. Crystallogr. **41**, 446–455 (2008)
47. L. Gelisio, C.L. Azanza Ricardo, M. Leoni, P. Scardi, J. Appl. Crystallogr. **43**, 647–653 (2010)
48. A. Guinier, G. Fournet, *Small-Angle Scattering of X-rays* (Wiley, New York, 1955)
49. T. Ino, N. Minami, Acta Crystallogr. **A40**, 538–544 (1984)
50. K.R. Beyerlein, A. Cervellino, M. Leoni, R.L. Snyder, P. Scardi, Z. Kristallogr. Suppl. **30**, 85–90 (2009)
51. A. Leonardi, M. Leoni, P. Scardi, Appl. Crystallogr. **46**, 63–75 (2013)
52. K.R. Beyerlein, M. Leoni, P. Scardi, Acta Crystallogr. **A68**, 337–351 (2012)
53. L. Gelisio, K.R. Beyerlein, P. Scardi, Thin Solid Films **530**, 35–39 (2012)

Chapter 19
High-Energy Resolution Core Level Photoelectron Spectroscopy and Diffraction: Powerful Tools to Probe Physical and Chemical Properties of Solid Surfaces

Alessandro Baraldi

Abstract Since the seventies, core level spectroscopy has played a key role in elucidating the geometric and electronic structure of solid surfaces. Due to their high localization, core electrons are extremely sensitive to the chemical state and to the local environment, and for this reason can be used for the identification of local configurations. The high energy resolution now attainable with this technique (below 100 meV) and the reduced data acquisition time (down to few ms per spectrum) has opened the possibility to probe the physical and chemical properties of a large variety of low-dimensional systems and to shed light on complex processes taking place on solid surfaces. The characterization of the properties of mono- and bi-metallic materials, the investigation of the atomic and molecular interactions on solid surfaces and the recent findings on epitaxial graphene outline the potential of high energy resolution core level photoelectron spectroscopy and photoelectron diffraction as precious tools in determining nanoscale electronic, geometrical and chemical properties.

19.1 Introduction

The need to understand the physical and chemical properties of surfaces and interfaces in increasing detail has continuously pushed the scientific community to develop different experimental techniques, test new operating conditions and implement supporting theoretical methods. In this respect, during the last 20 years, core level photoelectron spectroscopy has played a key role in achieving an atomic level

A. Baraldi (✉)
Physics Department, University of Trieste, Via Valerio 2, 34127 Trieste, Italy
e-mail: baraldi@elettra.eu

A. Baraldi
Surface Science Laboratory, Elettra-Sincrotrone Trieste, S.S. 14 km 163.5, 34149 Trieste, Italy

A. Baraldi
Laboratorio TASC, IOM-CNR, Area Science Park, S.S. 14 km 163.5, 34149 Trieste, Italy

S. Mobilio et al. (eds.), *Synchrotron Radiation*,
DOI: 10.1007/978-3-642-55315-8_19, © Springer-Verlag Berlin Heidelberg 2015

understanding of a wide variety of phenomena and processes taking place in the very first few layers of solid surfaces.

The pioneering experiments carried out between the late 50s and the beginning of the 60s by the research group of K. Siegbahn, who was awarded the Nobel Prize for Physics in 1981 for his achievements in this field [1] , represent a milestone in the development of experimental methods based on X-ray photoelectron spectroscopy. Two of the most innovative aspects of the research activity conducted in those years were the capability to distinguish different chemical elements on the basis of the binding energy of the strongly bound core level electrons, and the possibility to isolate the contribution of the atoms from the top layer of the sample in the measured spectra. While the first aspect is intrinsic to the quantum nature of the atoms and to the discretization of the electronic energy levels, the second aspect is linked to the strong interaction between the low energy electrons produced by photon excitation and the solids, which limits the inelastic photoelectron mean free path to few Å.

Besides the large surface and elemental sensitivity of core level photoelectron spectroscopy, the systematic studies performed by Siegbahn's group pointed out the power of this technique in resolving photoelectron lines originating from chemically non-equivalent atoms of the same species [2]. Since then, the analysis of the photoelectrons excited by soft X-ray electromagnetic radiation has helped obtain valuable, quantitative information on the elemental composition and properties of solids and interfaces, and has been increasingly applied to the study of the surfaces of metals, semiconductors, oxides, superconductors and alloys. These efforts have been motivated not only by the goal of extending our basic knowledge of these systems, but also by the appealing perspective of developing new functional materials for potential applications in many fields of modern materials science and nanotechnology. These are certainly the primary reasons why core level photoelectron spectroscopy is at present one of the most widely employed experimental laboratory techniques for both academic and industrial research.

The increase in the use of XPS has been considerably favoured by the advent and diffusion of third generation synchrotron light sources, which allow exploring the properties of materials with increased energy resolution and higher photon flux [3].

Its application has been extended to the detailed and accurate investigation of important phenomena occurring in solids which can be intrinsic or extrinsic to the photoemission process. All these many-body processes (e.g. excitations of phonons, plasmons, e-h pairs) and others (electronic transitions, multiplet splitting, electron-electron correlations, hole-states lifetimes, etc.), can be nowadays probed thanks to the cutting-edge equipment available in most modern soft X-ray beam lines. The main reason is the improved experimental energy resolution, which allows to investigate the lineshape of core level spectra in greater detail.

Besides the electron binding energies and the photoemission lineshape, a very important piece of information is contained in the intensity of the spectroscopic components. While the integrated intensity of the core level components is often used as a direct indicator of the density of the different elements composing the surface and sub-surface of the sample, it is clear that low energy photoelectrons, like those typically employed in soft X-ray core level spectroscopy, can be emitted along

some preferential directions. These effects were observed for the first time in 1970 by Siegbahn and coworkers [4]. Today, the fact that de Broglie electron wavelengths (from ≈0.3 to 2 Å in core electron spectroscopy) is comparable to the interatomic distances in solids is often exploited in photoelectron diffraction to probe the structures of complex surfaces and interfaces [5, 6]. The combination of chemically resolved core-level photoelectron spectroscopy with angular detection capabilities allows collecting the diffraction pattern generated by the coherent interference of the waves directly emitted by same-element surface atoms in non-equivalent configurations with the waves scattered by the surrounding atoms. The advantage of this approach relies on the possibility to independently detect the diffraction pattern originated by identical atoms or molecules at different adsorption sites or layers.

This article is not meant to provide an exhaustive review of this subject, but rather to give, by taking selected examples studied by our research group and others, an overview of the latest progress made by state-of-the-art high-energy resolution core level photoelectron spectroscopy and diffraction. In Sect. 19.2, the results for clean metal surfaces are examined, with a particular emphasis on Surface Core Level Shifts. Section 19.3 focusses on the role of core level spectroscopy in determining the structure and the chemical properties of adsorbate-covered surfaces. The most recent advancements made in the study of graphene are described in Sect. 19.4.

19.2 Single-Element Clean Metal Surfaces

19.2.1 Surface Core Level Shifts

In a typical survey spectrum measured with a conventional Al Kα X-ray source, like the one shown in Fig. 19.1 for Ir(111), it is possible to observe emission lines originating from electronic core and valence band levels and plasmon excitations. Owing to the spin-orbit splitting, the 4*f* level appears as two components separated by 2.97 eV. However, when the same crystal surface is investigated by synchrotron radiation, with enhanced surface sensitivity and energy resolution, the $4f_{7/2}$ component is further split into two peaks (red and blue components in Fig. 19.1). The origin of this doublet is the slight difference in the core level binding energies of top layer atoms with respect to bulk atoms, due to the their different electronic environment: this separation is referred to as Surface Core Level Shift (SCLS) [7].

Since the SCLSs usually range from few meV to several hundreds meV, the energy resolution required for their accurate determination should be very high, and this has prompted the scientific community to a continuous improvement of the experimental set-ups. Despite several attempts performed in the seventies, the first unambiguous observation of a sizeable SCLS is due to Citrin et al. [8], who revealed a surface component at 0.40 eV in the $4f_{7/2}$ spectrum of Au(111), which was interpreted in terms of modified surface density of states. Since then, SCLSs have been measured for a large number of 4*d* and 5*d* transition metal surfaces and have been interpreted

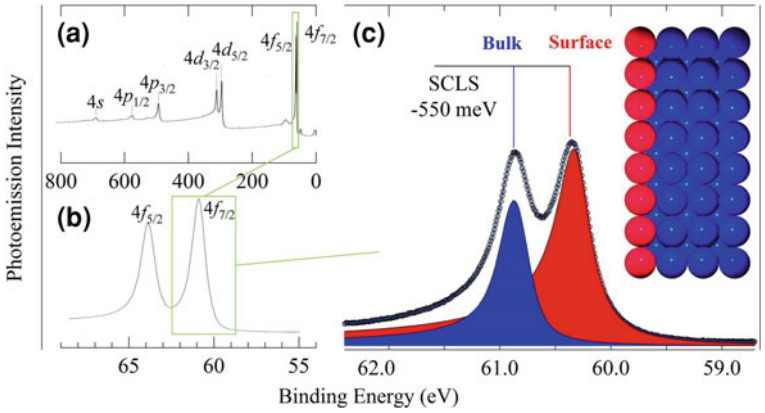


Fig. 19.1 Ir(111) core level spectrum. **a** Survey spectrum in the 800–0 eV binding energy range. **b** Ir 4*f* spectrum, showing the 5/2 and 7/2 spin-orbit split components. **c** Double components Ir $4f_{7/2}$ core level spectrum, corresponding to bulk (*blue peak*) and first-layer (*red peak*) atoms

as mainly due to the reduced coordination of surface atoms with respect to bulk atoms, which results in a narrowing of the surface *d*-band about its centroid. The *d*-band is electrostatically shifted in order to maintain the same chemical potential at the surface and in the bulk, thus causing the surface components to move to lower (higher) binding energy for *d*-bands which are more (less) than half filled.

The tight-binding model has been used to derive the equation for SCLSs in transition metals, which turns out to depend on the coordination numbers of surface (C_s) and bulk atoms (C_b), the number of *d* electrons and the *d*-band width.

This trend is evident in Fig. 19.2, which shows the Rh $3d_{5/2}$ and Pt $4f_{7/2}$ core level spectra of Rh and Pt for different single-crystal surfaces. For the (100) terminations, with $C_s = 8$, the SCLSs are significantly larger than in the case of close-packed (111) crystal planes, where the coordination number is 9. Besides the coordination number, detailed DFT calculations have shown that the SCLS is also affected by surface relaxation, i.e. the first-to-second layer distance [9].

However, the origin of the BE differences between surface and bulk atoms is to be found not solely in the initial state effects, which reflect the changes in the surface band structure of the neutral system prior to excitation, but also in the valence electron screening of the core hole in the final state. In fact, in a metallic system, the measured binding energy is exactly the total energy difference between the final, ionized and the initial, neutral state. Such effects, which for single-element crystal surfaces are typically in the order of up to 100 meV, are especially important in the case of surface alloys, in particular those formed by transition and noble metals, where the calculated deviations from the initial-state trends are explained in terms of the modified inter- as well as intra-atomic screening [10].

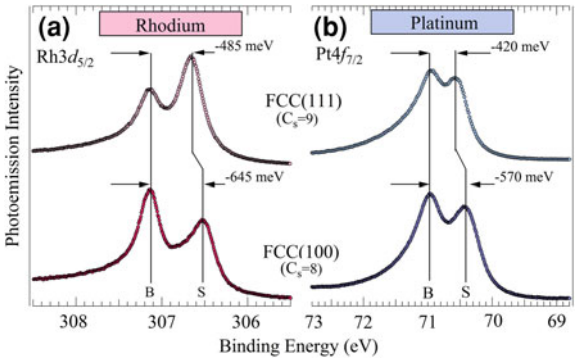


Fig. 19.2 Rh3$d_{5/2}$ (**a**) and Pt4$f_{7/2}$ (**b**) core level spectra corresponding to (100) (*bottom*) and (111) (*top*) surfaces. The corresponding coordination numbers C_S are also reported

19.2.2 Surface Reconstruction

The sensitivity of core level spectroscopy to the structural details of reconstructed surfaces -not only single-element surfaces, but also and especially the surfaces of III-V group compound semiconductors- is well known.

The first pioneering studies were carried out by Easteman and coworkers on GaAs(110) and GaSb(110) [11]. For covalently bond solids, the creation of a surface commonly leads to a significant rearrangement of the atoms, which is reflected in a translational symmetry breaking along the direction normal to the surface. In this case, SCLSs are mainly due to the strong charge redistribution in the first layers. On the contrary, the non-directional character of metallic bonds results in a lower probability of finding a new minimum in the surface free energy upon reconstruction. Nevertheless, some clean, low-Miller index transition metal surfaces experience a major structural rearrangement of the first atomic layer, and many of them have been studied using photoelectron spectroscopy. The main reason can be found in the narrow width of the 3*d* or 4*f* core levels of these elements, which is related to the long core-hole lifetime and makes them especially suited to detect small variations of the electronic structure, provided the energy resolution is sufficiently high.

At present, the surface reconstruction models which are most widely accepted are those of the (100) and (110) terminations of Pt and Ir [12, 13]. The Pt(100) reconstruction [14], involves the rearrangement of first layer atoms into a quasi-hexagonal (HEX) close packed structure. It is known that a HEX reconstruction can be lifted and transformed into the (1 × 1) bulk-like termination upon atomic or molecular adsorption. Using a special procedure [15], it is possible to prepare a clean (1 × 1) unreconstructed Pt(100) surface, which is metastable and can be converted into the HEX phase upon surface annealing.

In Fig. 19.3a the Pt 4$f_{7/2}$ spectrum of the clean (1 × 1) structure is shown [16], which shows two peaks, with a relative shift of 570 meV, due to bulk and surface atoms. Also the spectrum corresponding to the HEX phase (Fig. 19.3d) can be fitted with a bulk and a single surface component. Although this is clearly a crude approximation, a different fitting strategy would require considerably more components,

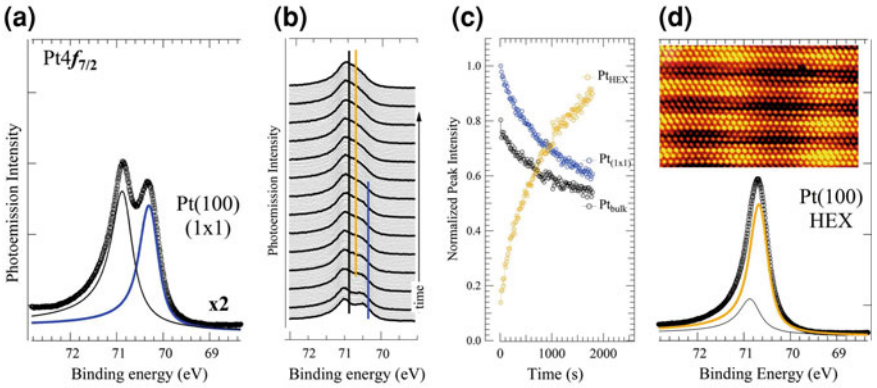


Fig. 19.3 Pt $4f_{7/2}$ core level spectra corresponding to the **a** (1×1) and to the **d** HEX structure. The STM image shows the arrangement of the atoms in the HEX phase (by courtesy of I. Stensgaard). **b**Time evolution of the Pt $4f_{7/2}$ spectra measured at T = 414K. The coloured lines indicate the position of the (1×1) (*blue*) and the HEX-induced (*yellow*) surface peaks. **c** Intensity evolution of bulk, HEX and (1×1) components versus time, obtained by fitting the spectral sequence in (**b**). Adapted from [16]

due to the large number of geometrically non-equivalent first-layer atoms, as shown in the STM image [17]. The intensities of the two spectra are clearly different. In particular, the overall integrated intensity of the HEX peak is 32 % larger than the component associated with the (1×1) structure, a behaviour that can be ascribed to the higher surface atomic density. Using similar arguments, it is possible to explain also the decreased intensity of the bulk component in the HEX spectrum. The investigation of the (1×1) to HEX transition is an important step to interpret the oscillatory behaviour in the chemical reactions on Pt surfaces [18].

The time-lapsed sequence of Pt $4f_{7/2}$ spectra acquired at 414 K and reported in Fig. 19.3b reveals that the higher binding energy surface component, ascribed to surface atoms in the HEX phase (blue), grows with time, while the surface component associated with the (1×1) structure (red) gradually disappears. The results of the data analysis, reported in Fig. 19.3c, show that the intensity of the (1×1) surface component initially decays with an exponential behaviour, while the HEX surface component grows with time. Also the bulk peak intensity diminishes, as expected by comparing the HEX and the (1×1) low temperature spectra. The experiment was repeated at different temperatures, between 393 and 475 K. By fitting the decrease of the (1×1) surface component of the spectrum with an exponential, it was possible to derived an effective barrier of 0.76 ± 0.06 eV for the phase transition.

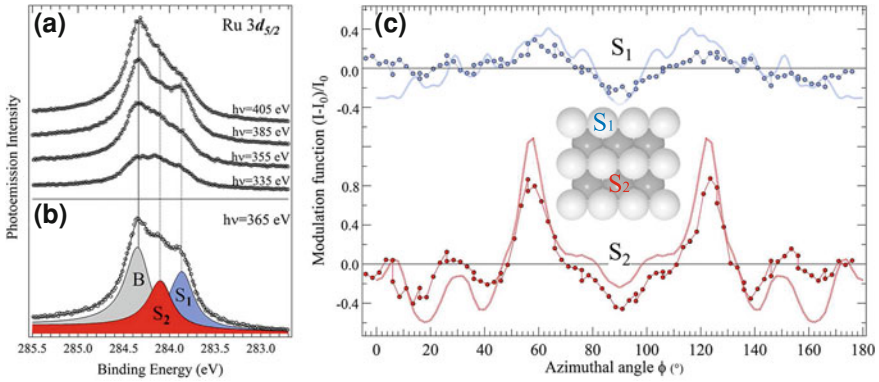


Fig. 19.4 **a** Ru $3d_{5/2}$ core-level spectra from Ru(10$\bar{1}$0) acquired at 120 K using different photon energies in the range 335 ÷ 405 eV. The spectrum in the bottom panel **b** was measured at 365 eV; a fit to three components is shown superimposed. Adapted from [25]. **c** Measured (*dots*) and calculated (*lines*) modulation functions of first (S_1-upper) and second layer (S_2-lower) surface components for an azimuthal scan at a polar emission angle 75 ° off the surface normal

19.2.3 From Surface Structure to Chemical Identity

For most TM surfaces, only the first atomic layer originates an observable SCLS. In fact, second layer atoms are highly coordinated and surrounded by a charge density similar to the one in the bulk. Nevertheless, in some specific situations, a sizeable SCLS can be measured also for atoms in the deeper layers. In 5*d* transition metals, second layer core level shifts have been detected in the very narrow 4*f* core lines [7, 19, 20], but the most interesting example are the 1*s* core-level spectra of Be surfaces, where up to four surface-related components have been observed and assigned to emission from the first four layers [21–24].

Another special case is the Ru(10$\bar{1}$0) surface, because it represents the first case in which a second-layer surface core level shifted component has been clearly observed in 4*d* transition metal surfaces. Figure 19.4 shows Ru $3d_{5/2}$ spectra measured at different photon energies with the emission direction fixed at 40° off the surface-normal. Three distinct components, namely *B*, S_1 and S_2, can be clearly identified in the spectra, with relative intensities that strongly depend on the photoelectron kinetic energy. Upon saturation exposure of the surface to oxygen, only the position of the B peak remains unchanged, hence supporting its assignment to bulk atoms. The identification of the other two components, however, is not straightforward. As previously discussed, the size of the SCLSs is given by the change in coordination of the surface atoms with respect to the bulk configuration. In this picture, one would assign the S_1 component to emission from the first layer and the S_2 component to emission from the second layer, but in some cases this model can dramatically fail [24]. For the Ru(10$\bar{1}$0) surface, shown as an inset in Fig. 19.4, one may expect that, considering the *openness* of the structure, also second layer atoms would exhibit

a sizeable core level shift. An effective method to obtain a reliable assignment of the two components consists of performing a high-energy resolution photoelectron diffraction experiment, exploiting the high atomic forward-scattering factor and the small scattering phase shift of the ion cores for electrons with kinetic energies greater than about 400 eV [25]. In fact, forward scattering features have the great advantage of conveying direct qualitative structural information abou t the system under investigation. In many cases, the position of the intensity maxima allows an immediate determination of the bond angles relative to the crystal lattice directions, and also the symmetry of the sample surface can be directly derived from the diffraction pattern. On the contrary, when the electron kinetic energy is lower than ∼300 eV, backward scattering can become the predominant process. In the specific case of Ru($10\bar{1}0$), when a first-layer atom is placed on the line connecting a second layer atom to the electron energy analyser, the strong forward scattering ensures an enhancement of the subsurface core level component. Figure 19.4c shows the intensities of the S_1 and S_2 components as a function of the azimuthal emission angle ϕ, normalized to the maximum intensity of the S_1 component. It can be clearly seen that S_1, i.e. the peak with the largest core level shift, shows a forward scattering enhancement at the expected angle ($\phi = 57.5°$), whereas S_2 does not change appreciably as a function of ϕ. Furthermore, the lines in Fig. 19.4 represent the result of a multiple-scattering calculation of the diffracted intensity of first and second layer atoms, which agrees remarkably well with the observed modulation.

19.3 Atoms and Molecules on Solid Surfaces

19.3.1 Adsorption and Co-Adsorption: The Adsorbate Core-Levels

Since its early development, high-energy resolution core level photoelectron spectroscopy has played an important role in the study of gas-surface interactions, because of its capability to distinguish different surface chemical species and to quantitatively determine their concentration. With the advent of third generation synchrotron light sources, the new opportunity has opened to apply this experimental technique to investigating the link between adsorption rate, adsorbate coverage, chemical reactivity, ordered structures and bonding configurations during atomic and molecular adsorption, desorption, decomposition and reaction processes.

High-energy resolution core level spectroscopy is widely employed in heterogeneous catalysis studies, usually following two distinct approaches. The first and most often used one makes use of the relevant information derived from the direct measurement of the adsorbates core levels, typically the 1*s* (e.g. for C, N, O atoms) or 2*p* (S atoms) electronic states (Fig. 19.5a). This strategy is especially well suited for the analysis of molecules, because of the high sensitivity of the 1*s* electrons to the adsorption configuration. This is e.g. the case of CO, which is known to occupy high-symmetry adsorption sites on transition metal surfaces.

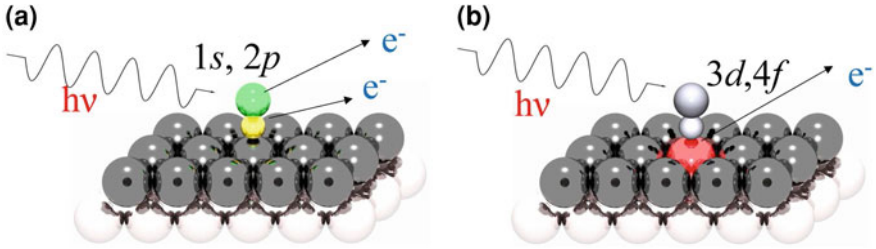


Fig. 19.5 Different approaches to the investigation of the adsorbate-substrate interaction. **a** Exciting the core electrons of the atomic/molecular adsorbates by X-ray radiation. **b** Probing the core electrons of first-layer substrate atoms, which are directly influenced by adsorption

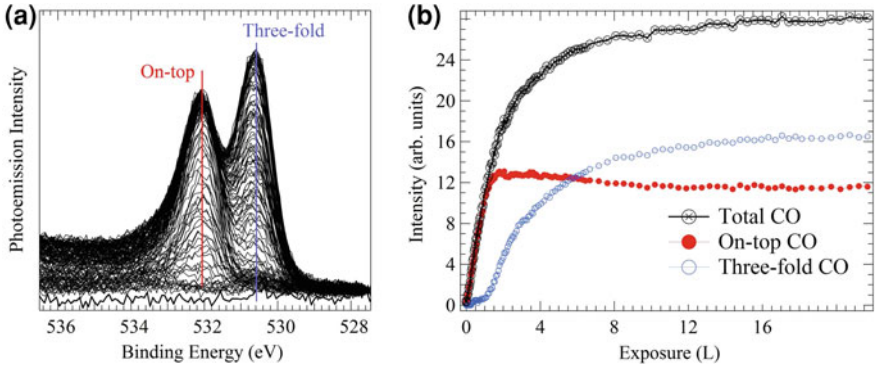


Fig. 19.6 **a** Time-lapsed sequence of O 1*s* core-level spectra acquired during CO uptake on Rh(111). **b** Evolution of the populations of CO molecules in on-top (*red filled markers*) and in threefold hollow sites (*blue empty circles*) obtained from the intensity of the corresponding components in the deconvoluted O 1*s* spectra shown in (**a**)

In the case of chemisorbed molecules, it is generally observed that the core-level binding energy decreases as the coordination with first layer atoms increases. For example, the O 1*s* binding energy varies from 531.5 to 532.6 eV for CO bonded in on-top configuration, and from 530.7 to 531.5 eV for bridge-bonded CO, depending on the specific single crystal surface. Core-level binding energy shifts in adsorbed molecules can be interpreted on the basis of total energy considerations, in which the main contribution comes from the changes in the final state [26].

Figure 19.6a shows a sequence of O 1*s* spectra acquired while dosing carbon monoxide on Rh(111) at 150 K. Two components can be clearly distinguished: the first one, at 532.1 eV, appears at the beginning of the uptake, while the second component, at 530.6 eV, appears at a later stage, a behaviour which reflects the sequential occupation of two non-equivalent adsorption sites. Following the general interpretation, the high binding energy component (532.1 eV) is assigned to CO adsorbed in on-top sites, while the lower binding energy peak (530.6 eV) is associated with CO chemisorbed in threefold hollow sites. The main feature of the uptake curve is

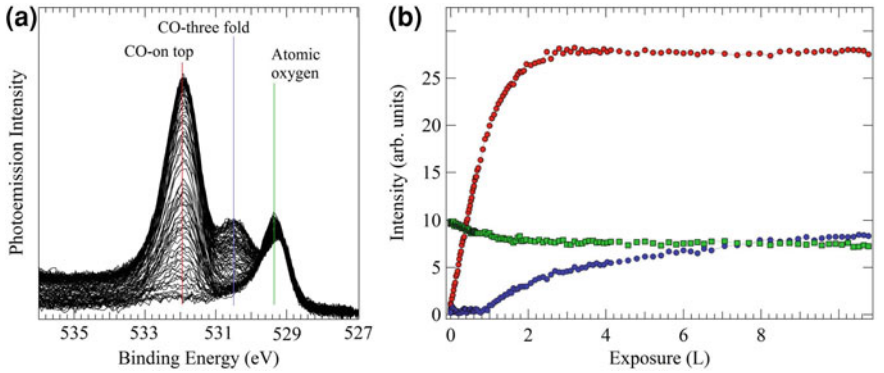


Fig. 19.7 **a** Time-lapsed sequence of O 1*s* core-level spectra acquired during CO uptake on oxygen pre-covered Rh(111). **b** Evolution of the populations of CO molecules in on-top (*red filled markers*) and in threefold hollow sites (*blue empty circles*) obtained from the intensity of the corresponding components in the deconvoluted O 1*s* spectra shown in (**a**)

that the the concentration of on-top CO molecules reaches a maximum in the range $0.25 \div 0.35$ ML and then slightly declines. This is due to the strong repulsive interactions between molecules at short distances. In fact, in the coverage range between 0.25 and 0.33 ML, a $(\sqrt{3} \times \sqrt{3})$ R30° ordered structure, consisting of molecules in next-nearest on-top sites, is formed. The high local compression, characterized by strong dipole-dipole repulsive interactions between molecules, pushes up the potential energy levels of the adsorption system. The CO adlayer rearranges by moving some of the adsorbates from on-top to hollow sites, in order to reach an energetically favourable configuration. This redistribution is a common behaviour in adsorbate system, often observed also in desorption experiments [27].

The capability of distinguishing different chemical species can be particularly appreciated in coadsorption experiments. The relative occupation of different adsorption sites yields information on the influence of molecule-molecule and molecule-atom interactions on the formation of energetically favourite adsorption geometries. These are the interactions which could play a central role in the chemical recombination process. For example, in the case of Rh(111), a large amount of CO can be deposited on a p(2 × 2)-O ordered structure (coverage = 0.25 ML). As shown in Fig. 19.7a, the O 1*s* core level spectrum of atomic oxygen is characterised by a single peak at 529.4 eV. Upon CO exposure at 150 K (see uptake curves in Fig. 19.7b), the O 1*s* spectrum shows the appearance of two new components at 532.0 and 530.6 eV, i.e. at very similar BEs to those found in the case of CO adsorption on Rh(111) (see Fig. 19.6a). They indicate the occupation of top and three-fold sites by CO molecules. The main difference with respect to adsorption on the clean surface is the strongly reduced intensity of the component due to CO in three-fold sites, a clear indication of the competition between atomic oxygen and CO for the same configuration. Since atomic oxygen occupies three-fold fcc sites on Rh(111) [28], the density of available three-fold sites for CO molecules is strongly reduced. On the contrary, CO adsorption in on-top geometries is not influenced by the presence of oxygen atoms sitting in neighbouring sites. This is a clear demonstration that, also in complex systems,

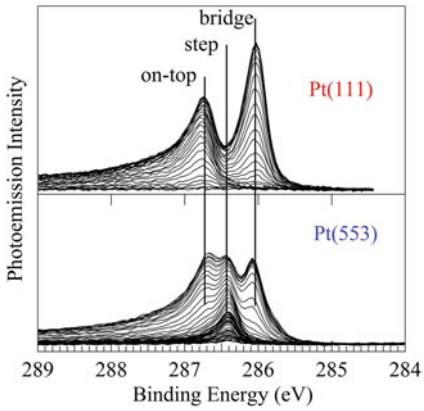


Fig. 19.8 Sequence of time-lapsed C 1*s* spectra of measured during carbon monoxide uptake experiments at on Pt(111) (T = 200 K) and on Pt(355) (T = 130 K). Adapted from [30]

high-energy resolution core level spectral features can be used as fingerprints of non-equivalent adsorption configurations [29].

19.3.2 Adsorption on Stepped Surfaces

The sensibility of high-energy resolution core level spectroscopy is not confined to non-equivalent configuration in low-index Miller surface, but can be used to investigate more complex systems, in particular vicinal surfaces. Near to surface steps, adsorption and activation energies are largely modified. The study of these configurations gives the opportunity to investigate in a controlled way the role of defective adsorption sites, which is essential in determining the overall reaction rate.

Exemplary results are those related to the CO interaction with Pt(355) [30]. This surface is formed by (111) nano-terraces and a single (111) monoatomic step. Sequence of C 1*s* spectra, reported for both Pt(111) and Pt(355) (Fig. 19.8a–b) show that the adsorption behavior on flat and stepped surfaces is very different, especially in the low coverage regime. While at high coverage both on-top and bridge adsorption sites are occupied, for the (355) surface the preferred adsorption site at the beginning of the uptake process is a different one. In fact, the C 1*s* spectrum for the Pt(355) surface shows a single component at 286.43 eV, i.e. at lower and higher binding energy with respect to the components associated to CO in on-top (286.80 eV) and in bridge (286.09 eV) configurations respectively.

Most importantly the quantitative evolution of the different species with overall CO coverage shows that the terrace sites are occupied only when the step sites are almost saturated. This clearly suggests that the adsorption energy on the step sites is larger with respect to the adsorption site on the terraces. This result is quite general, as confirmed by calculations for a wide range of adsorbate-substrate systems.

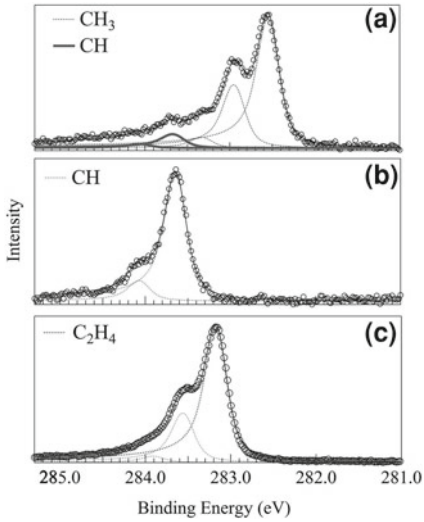


Fig. 19.9 C 1*s* spectra of various adsorbed species on Pt(111) measured with hν = 380 eV, corresponding to **a** Methyl-CH_3, **b** methylidyne-*CH* and **c** ethylene-C_2H_4 adsorbed species. *Dotted lines* show the results of a decomposition into separate contributions from CH_3, *CH*, and C_2H_4, respectively, while the *solid black lines* show the resulting total C 1*s* signal. Adapted from [35]

19.3.3 Vibrational Excitations in Chemisorbed Molecules

When measured with high energy resolution, core level spectra of molecular species can also display vibrational fine structure due to the excitation of vibrations in the final state. The fine structure can be accurately determined, in particular for carbon monoxide and hydrocarbon molecules. It has been firstly measured in gas phase experiments [31, 32] and later on also in the case of chemisorbed molecules [33, 34].

In the hydrocarbon case the C-H vibrations are characterized by a relatively large energy (about 400 meV), thus allowing to separate the contribution of the first vibrational state from the adiabatic peak transition. An elegant experiment in this respect has been performed by using small non-equivalent hydrocarbon species adsorbed on Pt(111) [35]. In Fig. 19.9 the C 1*s* core level spectra of CH_3, CH, and C_2H_4 adsorbed on Pt(111) are shown. The CH_3 layers have been prepared by exposing the surface at T = 120 K using a supersonic molecular beam of CH_4, while methylidyne layers were prepared by heating the methyl layers to 400 K. Adsorbed ethylene was instead obtained by dosing the molecule at 120 K. The CH_3 spectrum in Fig. 19.9a is fitted by three peaks at 282.54, 282.94, and 283.33 eV which keep the same intensity ratio and a constant binding energy separation and for this reason can be interpreted as due to vibrational excitations. A small signal due to *CH* species, due to photon beam induced dissociation is also included. The energetic separation between the adiabatic and the first exited peak in Fig. 19.9a is 400 $\pm$ 4 meV.

In the case of CH species (Fig. 19.9b), the adiabatic peak is found at 283.61 eV and the separation of the first excited peak from the adiabatic peak is 420 $\pm$ 10 meV. Finally the spectrum corresponding to C_2H_4 (see Fig. 19.9c) can be fitted using three components at 283.16, 283.54, and 283.89 eV. In this case the separation of the

adiabatic and the first excited peak is found to be 388 ± 8 meV is slightly larger than the value of 368 meV obtained in gas phase measurements [32]. The appearance of a single adiabatic peak suggests that the two non-equivalent carbon atoms in the C_2H_4 molecule are adsorbed in a locally equivalent geometry. These results clearly indicate that the vibrational energy splitting can be used as fingerprint to identify complex adsorbate species and reaction intermediates.

19.3.4 Adsorbate-Induced Surface Core Level Shifts

Over the last 20 years, high-energy resolution core level spectroscopy has proven a powerful technique to investigate the structural properties of adsorbate systems, not only by directly measuring the core level spectra of the adsorbed atoms or molecules, but also by probing the adsorbate-induced shifts of the substrate core levels at different coverages (see Fig. 19.5b). This approach yields details of the geometrical structure of the atomic and molecular adsorption sites, allows tracking the evolution of the adsorbate populations on the surface and identifying the changes in the local environment of the substrate atoms. Moreover, it also yields insight into the trends in surface chemical reactivity, one of the main goals of surface science.

The first important result is that the time evolution of the intensity of the spectral components during uptake experiments follows simple rules, from which the adsorption sites can be straightforwardly determined.

In Fig. 19.10a the surface components of selected Pt $4f_{7/2}$ core level spectra measured in situ during CO adsorption on Pt(111) are reported. The series of spectra shows large modifications upon CO deposition. The initial state of the experiment is the clean Pt(111) surface, which exhibits, besides the bulk peak, a single first–layer component (Pt_0) with a SCLS of -430 meV. CO adsorption first leads to the appearance of a new core level component with a shift of $+980$ meV, while at increasing coverage also a second peak is detected at $+330$ meV. The integrated intensities of the Pt_0 peak, plotted as a function of the CO coverage in Fig. 19.10b, contain precious information on the CO site occupation during chemisorption. In fact, the initial adsorption site can be directly determined from the low coverage value of the first derivative $\frac{\partial Pt}{\partial \Theta}$, which yields the coordination number of the adsorption site. In the initial stage of the exposure, the Pt_1 component grows linearly with increasing CO coverage, at the expense of the Pt_0 component.

For each new CO molecule adsorbing on the surface, the intensity contribution of several surface Pt atoms moves from Pt_0 to Pt_1. A fit of the data yields $\frac{\partial Pt_0}{\partial \Theta} = -1$ (see Fig. 19.10b), clearly confirming the that CO on Pt(111) adsorbs in on-top sites.

The link between the initial derivative and the adsorption site symmetry generally holds not only for molecular species, but also for atoms chemisorbed on transition metal surfaces. This can be appreciated in Fig. 19.11 where the results of an oxygen uptake experiment on Rh(100) are reported. Figure 19.11a shows, besides the spectrum of the clean surface and its decomposition into bulk and surface components, also the spectra of the O-covered substrate and their deconvolution into surface

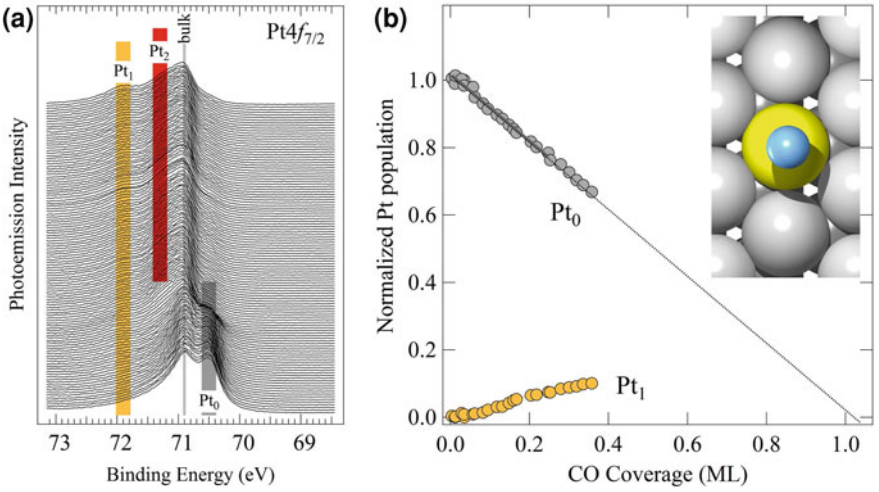


Fig. 19.10 **a** Evolution of the Pt $4f_{7/2}$ core-level spectra during carbon monoxide adsorption on Pt(111). The bulk and surface components (Pt_0, Pt_1 and Pt_2) are indicated. **b** Evolution of the Pt_0 (*grey*) and Pt_1 (*yellow*) surface component versus CO on Pt(111)

peaks originating from first-layer Rh atoms bonded to one (Rh_1, yellow) and two (Rh_2, orange) oxygen atoms, as illustrated in the structural models of Fig. 19.11b. Upon increasing the O coverage, the intensity of the Rh_0 peaks decreases linearly and the first derivative of the Rh_0 signal with respect to the O coverage (blue curve in Fig. 19.11c) is equal to -4, thus showing that the initial adsorption site is four-fold.

An additional, very important application of adsorbate-induced SCLS analysis is related to the possibility of spectroscopically measuring the local surface reactivity.

A number of theoretical studies on gas-surface interaction properties has proven how the reactivity of TMs is directly governed by their surface electronic structure. Hammer and Norskøv demonstrated how it is possible to predict the variation of surface chemical properties on the basis of the $d-$band energy position [36]. However, from the experimental point of view, the measurement of the surface $d-$band center is not straightforward. On the contrary, adsorbate-induced SCLSs are highly correlated with the changes in the surface-projected d-band center of the metal substrate, and for this reasons can be efficiently used to probe the local changes of the surface chemical reactivity [37]. Moreover, in situ measurements during a chemisorption experiment yield details of the geometrical structure of the atomic and molecular adsorption sites, and allow tracking the instantaneous configuration of the adsorbate populations during their evolution on the surface. For this reason, the real-time measurement of the adsorbate-induced SCLSs is considered a valuable tool to interpret the elementary phenomena involved in the kinetics of surface chemical reactions.

Figure 19.12 shows the evolution of the Rh $3d_{5/2}$ core level spectrum of Rh(100) upon deposition of N, O, and S atoms. The slight differences among the three spectra on the bottom, corresponding to the clean Rh(100) surface, in particular the different ratio between the bulk and surface components, are due to non–equivalent experi-

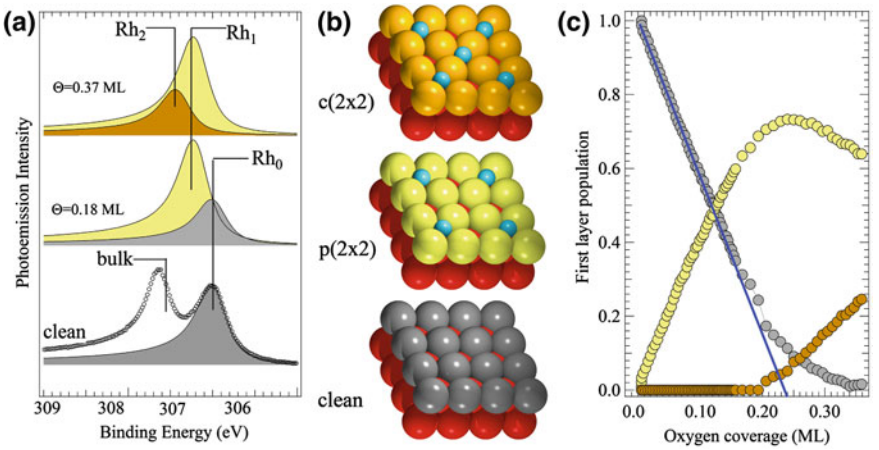


Fig. 19.11 **a** Evolution of the surface components of the Rh3$d_{5/2}$ core level spectra for O adsorption on Rh(100) ad different coverages. The grey component Rh_0 originates from clean surface Rh atoms, while the Rh_1 and Rh_2 peaks originate from surface Rh atoms bonded to one and two oxygen atoms, respectively, as shown in the model structures reported in **b**. **c** Evolution of the intensities of the Rh_0 (*grey*), Rh_1 (*yellow*) and Rh_2 surface component versus oxygen coverage on Rh(111). Adapted from [37]

mental conditions (photon energy, emission angles). Besides these differences, it is also possible to appreciate remarkable similarities among the three systems. The adsorption of these light atoms at low coverages always results in a decreased intensity of the surface core level shifted component corresponding to *clean* first layer atoms, and in the subsequent growth of new peaks associated with the increased population of surface metal atoms bonded to the adsorbates. These new components are always found at higher binding energy with respect to the clean surface component. The shift toward higher binding energies at increasing atomic coverage is expected for the chemisorption of electronegative species on TM surfaces, as a consequence of the charge transfer from the surface to the adsorbates and broadening of the *d*-density of states.

What is especially interesting is the clear trend in the relationship between *d*-band centre evolution and core-level shifts. Figure 19.12d shows the overall experimental shifts as a function of the calculated *d*-band centre displacement ΔB_d in the case of O, N, and S adsorption on Rh(100). The trend is nearly linear both for the oxygen and nitrogen systems, while, in the case of sulphur, final state effects cause a small deviation from the expected linear behaviour. These results prove that adsorbate-induced SCLSs provide a reliable spectroscopic measure of the local surface reactivity.

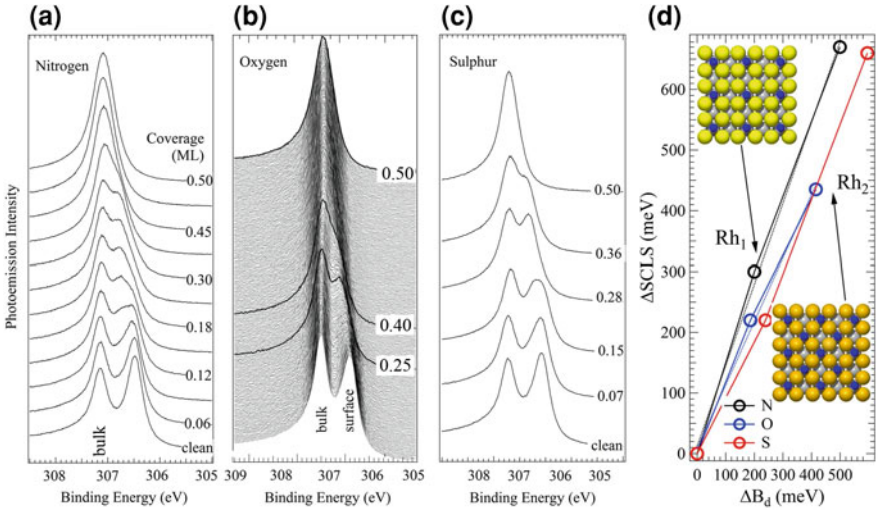


Fig. 19.12 Evolution of Rh3$d_{5/2}$ core level spectra, at increasing **a** N, **b** O and **c** S coverage. **d** Changes of the experimentally determined N-, O- and S-induced core-level shifts for Rh atoms in different configurations, as a function of the calculated atom-projected *d*-band center shift

19.4 New Opportunities for Core Level Photoelectron Spectroscopy from Epitaxial Graphene

The discovery of graphene (GR) in 2004 by Geim and Novoselov has raised a great interest in the scientific community, which is still growing. One of the main goals in this field is to develop new strategies to obtain high-quality GR layers, with the lowest density of defects, thus keeping the transport properties of this extraordinary material unaltered with respect to the ideal, defect-free honeycomb lattice.

One of the most commonly used methods to achieve this target is chemical vapour deposition on solids surfaces. In this respect, the employment of reactive catalytic surfaces, in particular those of transition metals [38], and also in the case of surface alloys [39], has been found extremely promising. The growth of a carbon network on these metal surfaces can result in the formation of commensurate C-substrate structures. More frequently, however, the carbon single-layer is incommensurate or forms a very large unit cell because of the lattice mismatch between GR and the substrate. Apart from the structural differences, these GR layers are highly corrugated, forming periodic 'humps' and 'valleys' on the substrate, where the carbon atoms are alternatively further from or closer to the metal atoms.

In this respect, core level photoelectron spectroscopy has been successfully used to study the structural properties of epitaxial GR. A typical example of the large structural differences that can be found in epitaxial GR grown on different substrates is reported in Fig. 19.13, where the C 1*s* spectra of GR grown on Ir(111) [40] and Re(0001) [41] are reported. In the case of Ir(111), the spectrum shows just a single

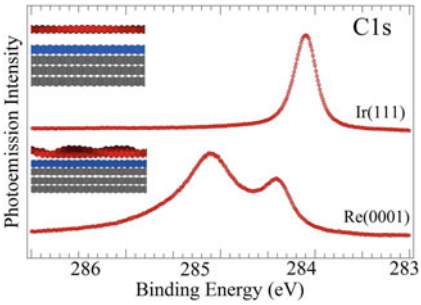


Fig. 19.13 C 1*s* core-level spectra of epitaxial GR grown on Ir(111) and Re(0001), along with their respective structural models, showing that, in the case of Ir, the C layer is quite flat and detached from the substrate, while on Re(0001) is highly corrugated

component, although the C layer forms a large (10 × 10) unit cell on a (9 × 9) substrate unit cell. This result can be explained considering the small corrugation of the carbon layer and, most importantly, the large average C-metal distance (more than 3.2 Å). As a consequence, all the C atoms experience a very similar local environment, and the 1*s* electrons are not affected by the mismatching positions with respect to the first-layer Ir atoms. On the contrary, the C 1*s* core level spectrum of epitaxial GR grown on Re(0001) shows clearly two components, as for the Ru(0001) surface [39]. Graphene on Re is highly corrugated [41], but the origin of exactly two components in the C 1*s* spectrum is not of immediate interpretation. As shown in the case of chemisorbed molecules, an *n*-component spectrum is often associated with the presence of *n* inequivalent species. If one excludes the effect of many-body interactions, it is not straightforward to explain why only two distinct carbon species should be present in the large GR/Re(0001) unit cell. The origin of the two main peaks can be understood only by comparing the experimental line shape with the spectral distribution calculated by DFT [41]. In fact, accurate simulations, including final-state effects, show that the computed C 1*s* core electron binding energies strongly depend on the C-Re separation, in that they are generally larger at smaller C-metal distances. The excellent agreement between experimental and simulated data, clearly proves that the shape of the C 1*s* spectrum arises from an almost continuous, rather than binary, distribution of the C-Re distances.

Measuring the C 1*s* core level spectra of epitaxial GR also allows spotting the dangers of using in a direct way the intensity of the core-level photoelectron signal to determine the concentration of surface atomic species. Figure 19.14 unambiguously shows the role played by photoelectron diffraction effects in the modulation of the photoemission signal from single-layer GR grown on Ir(111) [42]. The intensity modulation (shown in blue scale) at each photon energy appears very large, in particular at $h\nu = 400\,\text{eV}$, where it amounts to more than 50 %. These results deserve special consideration because, for this particular system, the contribution of electron inelastic mean free path effects can be excluded, since all the C atoms are confined to the top layer of the system. The large differences observed in the patterns measured at different photon energies can be therefore be entirely ascribed to photoelectron diffraction effects. The C 1*s* angle-resolved measurements carried

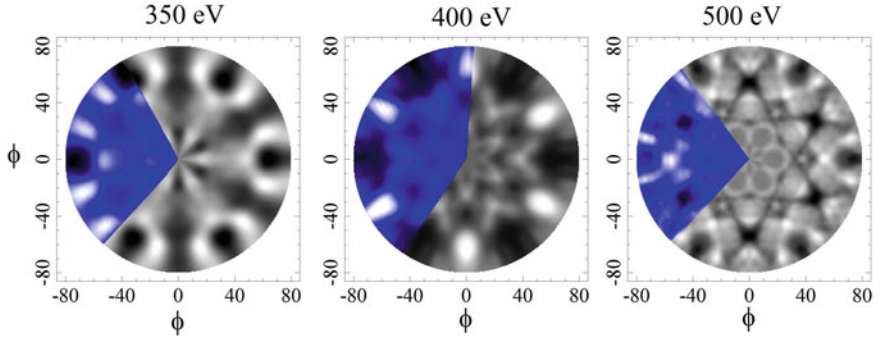


Fig. 19.14 Stereographic projection of the C 1*s* intensity modulation $(I - I_0)/I_0$ from GR/Ir(111) as a function of the emission angle for scans acquired at different photon energies. The *blue slices* represent the experimental data, while the portions in *grey scale* are the calculated intensities. Adapted from [42]

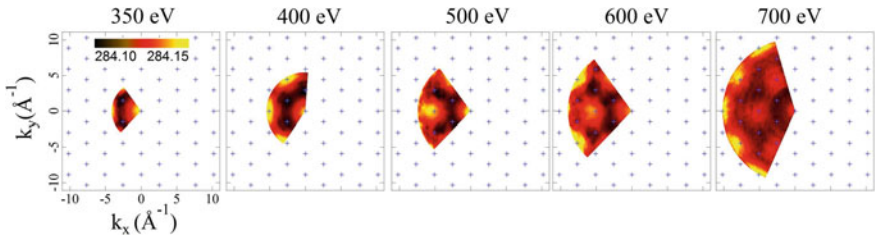


Fig. 19.15 C 1*s* binding energy variation in GR/Ir(111) from angle-resolved photoemission data, whose intensity behaviour is partially shown in Fig. 19.14. The data are plotted as a function of the wave vector component parallel to the surface, blue crosses corresponding to the GR reciprocal lattice points. Adapted from [42]

out at different photon energies are in very good agreement with the photoelectron diffraction simulations for a flat, free-standing layer of GR (reported in grey scale).

A recent discovery in the field of core-level spectroscopy, related to the peculiar properties of GR, is the observation of weak bonding interactions in the deep C 1*s* core levels of epitaxial GR on Ir(111), which result in a *band dispersion* that had previously been found only for valence band electrons [42]. Although the C 1*s* is formally considered a core level and it is not involved in the formation of chemical bonds, there are sufficiently large interactions that induce the formation of bonding and anti-bonding states. Despite its small magnitude (only 60 meV), the C 1*s* energy dispersion can be detected in resolution angle-resolved photoelectron measurements performed at different photon energies. Figure 19.15 shows the binding energy modulation as a function of the wavevector component parallel to the surface. Upon increasing the photon energy (see Fig. 19.15 from left to right), the portion of reciprocal space probed in the experiment increases, but, notably, the periodicity of the pattern does not correspond to the periodicity of the GR reciprocal lattice points. This discrepancy

can be explained only by taking into account an interference effect due to the presence of two non-equivalent atoms in the GR unit cell [42].

Acknowledgments Among all the people I've had the privilege to work with, I would like to thank Silvano Lizzit, with whom I've shared my experimental research activity in the field of core level photoelectron spectroscopy since 1994. I am grateful to many scientists who provided data, figures and images presented in this manuscript. In particular, I would like to thank D. Alfè, H.-P. Steinrück, R. Denecke, C. Papp and I. Stensgaard. Finally, I want to express my gratitude to E. Miniussi for the careful revision of the manuscript.

References

1. Siegbahn, K.: Electron spectroscopy for atoms, molecules and condensed matter. From Nobel Lectures, Physics 1981–1990 World Scientific Publishing Co., Singapore (1993).
2. K. Siegbahn, J. Electron Spectrosc. Relat. Phenom. **5**, 3 (1974)
3. G. Margaritondo, J. Phys. IV **7**, 31 (1997)
4. K. Siegbahn, U. Gelius, H. Siegbahn, E. Olso, Phys. Scr. **1**, 272 (1970)
5. C. Fadley, Surf. Sci. Rep. **19**, 231 (1993)
6. D.P.J. Woodruff, J. Electron. Spectrosc. Relat. Phenom. **178**, 186 (2010)
7. D. Spanjaard, C. Guillot, M.C. Desjonqures, G. Treglia, J. Lecante, Surf. Sci. Rep. **5**(12), 1–85 (1985)
8. P.H. Citrin, G.K. Wertheim, Y. Baer, Phys. Rev. Lett. **41**, 1425 (1978)
9. J.N. Andersen, D. Hennig, E. Lundgren, M. Methfessel, R. Nyholm, M. Scheffler, Phys. Rev. B **50**, 17525 (1994)
10. M.V. Ganduglia-Pirovano, J. Kudrnovský, M. Scheffler, Phys. Rev. Lett. **78**, 1807 (1997)
11. D.E. Eastman, T.C. Chiang, P. Heimann, F.J. Himpsel, Phys. Rev. Lett. **45**, 656 (1980)
12. J. Inglesfield, Progr. Surf. Sci. **20**, 105 (1985)
13. H. Ohtani, C.T. Kao, M.V. Hove, G. Somorjai, Progr. Surf. Sci. **23**, 155 (1986)
14. S. Hagstrom, H.B. Lyon, G.A. Somorjai, Phys. Rev. Lett. **15**, 491 (1965)
15. K. Kuhnke, K. Kern, G. Comsa, Surf. Sci. **343**, 44 (1995)
16. A. Baraldi, E. Vesselli, L. Bianchettin, G. Comelli, S. Lizzit, L. Petaccia, S. de Gironcoli, A. Locatelli, T. Mentes, L. Aballe, J. Weissenrieder, J. N. Andersen, J. Chem. Phys. **127**, 164702 (2007)
17. T.R. Linderoth, J.J. Mortensen, K.W. Jacobsen, E. Lægsgaard, I. Stensgaard, F. Besenbacher, Phys. Rev. Lett. **77**, 87 (1996)
18. R. Imbhil, G. Ertl, Chem. Rev. **95**, 697 (1995)
19. G.K. Wertheim, P.H. Citrin, J.F. van der Veen, Phys. Rev. B **30**, 4343 (1984)
20. G.K. Wertheim, P.H. Citrin, Phys. Rev. B **38**, 7820 (1988)
21. L.I. Johansson, H.I.P. Johansson, J.N. Andersen, E. Lundgren, R. Nyholm, Phys. Rev. Lett. **71**, 2453 (1993)
22. H. Johansson, L. Johansson, E. Lundgren, J. Andersen, R. Nyholm, Phys. Rev. B **49**, 17460 (1994)
23. L.I. Johansson, P.A. Glans, T. Balasubramanian, Phys. Rev. B **58**, 3621 (1998)
24. S. Lizzit, K. Pohl, A. Baraldi, G. Comelli, V. Fritzsche, E.W. Plummer, R. Stumpf, P. Hofmann, Phys. Rev. Lett. **81**, 3271 (1998)
25. A. Baraldi, S. Lizzit, G. Comelli, A. Goldoni, P. Hofmann, G. Paolucci, Phys. Rev. B **61**, 4534 (2000)
26. N. Mårtensson, A.W. Nilsson, in *Application of Synchrotron Radiation*, ed. by E. Eberhardt. Springer Series in Surface Sciences, vol 35 (Springer, Berlin, 1994)
27. A. Baraldi, G. Comelli, S. Lizzit, D. Cocco, G. Paolucci, R. Rosei, Surf. Sci. **367**, L67 (1996)

28. M.V. Ganduglia-Pirovano, M. Scheffler, Phys. Rev. B **59**, 15533 (1999)
29. A. Jaworowski, A. Beutler, F. Strisland, R. Nyholm, B. Setlik, D. Heskett, J. N. Andersen, Surf. Sci. **431**, 33 (1999)
30. B. Tränkenschuh, N. Fritsche, T. Fuhrmann, C. Papp, J. Zhu, R. Denecke, H. Steinrück, J. Chem. Phys. **124**, 074712 (2006)
31. K.J. Randall, A.L.D. Kilcoyne, H.M. Köppe, J. Feldhaus, A.M. Bradshaw, J.E. Rubensson, W. Eberhardt, Z. Xu, P.D. Johnson, Y. Ma, Phys. Rev. Lett. **71**, 1156 (1993)
32. L.J. Sæthre, O. Sværen, S. Svensson, S. Osborne, T.D. Thomas, J. Jauhiainen, S. Aksela, Phys. Rev. A **55**, 2748 (1997)
33. J. N. Andersen, A. Beutler, S. Sorensen, R. Nyholm, B. Setlik, D. Heskett, Chem. Phys. Lett. **269**, 371 (1997)
34. A. Föhlisch, N. Wassdahl, J. Hasselström, O. Karis, D. Menzel, N. Mårtensson, A. Nilsson, Phys. Rev. Lett. **81**, 1730–1733 (1998)
35. H. Steinrück, T. Fuhrmann, C. Papp, B. Tränkenschuh, R. Denecke, J. Chem. Phys. **125**, 204706 (2006)
36. B. Hammer, J. Norskøv, Surf. Sci. **343**, 211 (1995)
37. A. Baraldi, S. Lizzit, G. Comelli, M. Kiskinova, R. Rosei, K. Honkala, J.K. Norskov, Phys. Rev. Lett. **93**, 046101 (2004)
38. M. Batzill, Surf. Sci. Rep. **67**, 83 (2012)
39. D. Alfè, M. Pozzo, E. Miniussi, S. Günther, P. Lacovig, R. Larciprete, S. Lizzit, B. Santos Burgos, T. Mentes, T. Locatelli, A. Baraldi, Sci. Rep. **3**, 2340 (2013)
40. P. Lacovig, M. Pozzo, D. Alfè, P. Vilmercati, A. Baraldi, S. Lizzit, Phys. Rev. Lett. **103**, 166101 (2009)
41. E. Miniussi, M. Pozzo, A. Baraldi, E. Vesselli, R. Zhan, G. Comelli, T. Mentes, M. Nino, A. Locatelli, S. Lizzit, D. Alfè, Phys. Rev. Lett. **106**, 216101 (2011)
42. S. Lizzit, G. Zampieri, L. Petaccia, R. Larciprete, P. Lacovig, E. Rienks, G. Bihlmayer, A. Baraldi, P. Hofmann, Nat. Phys. **6**, 345 (2010)

Chapter 20
Spin Polarization of the Photoelectrons and Photon Polarization of X-Ray Absorption: Spectroscopy and Magnetometry

Giorgio Rossi

Abstract We introduce here how to perform spectroscopies that are sensitive to the spin polarization of the electron states, via the direct measure of the $\boldsymbol{P}$ vector of a (photo)electron beam in a suitable experimental set-up and how to perform photoemission/photoabsorption experiments that, by exploiting the polarization of the exciting photon beam, are directly sensitive to the spin order in the initial state revealing, for example, the magnetization state of solids and surfaces or the effects of spin-orbit interaction in the surface electronic structure.

20.1 Introduction

The energy E, momentum $\boldsymbol{k}$ and spin $\boldsymbol{s}$ structure of solids and surfaces in the reciprocal space reflect the phenomena that we describe as "correlation effects": magnetism, orbital ordering, superconductivity, in short the whole low-energy properties of condensed matter. Angularly Resolved Photo-Electron Spectroscopy (ARPES) [1] can be "completed" by measuring the spin-polarization, $\boldsymbol{P}$, of the photoelectrons; in such case it is called SP-ARPES or S-ARPES meaning "spin-polarized angularly resolved photoelectron spectroscopy" [2–6]. Within the dipole approximation $\Delta S = 0$, robust data analysis methods allow to approximate the initial electron quantum state [1, 2, 7]. The measure of the spin polarization vector $\boldsymbol{P}$ is accomplished by electron scattering experiments [8]: it is performed on photoelectron beams that are pre-selected in energy and in momentum and then accelerated to collide with a heavy-atom solid target. The spin detection is therefore performed "downstream" of

G. Rossi (✉)
Dipartimento di Fisica dell'Università degli studi di Milano, via Celoria 16, 20133 Milano, Italy
e-mail: giorgio.rossi2@unimi.it

Advanced Photoelectric-Effect Experiments (APE) and Nano Foundries and Fine Analysis (NFFA) collaborations, Istituto Officina dei Materiali-CNR, 34149 Basovizza, TS, Italy

S. Mobilio et al. (eds.), *Synchrotron Radiation*,
DOI: 10.1007/978-3-642-55315-8_20, © Springer-Verlag Berlin Heidelberg 2015

the ARPES analyser without loss of information as far as the ARPES selection is done with purely electrostatic fields (no magnetic fields in the photoelectron path) not to perturb the spin of the photoelectron beam. Spin polarization measurements can be accomplished, for example, in the Mott detector where the spin-orbit interaction of a 10–150 keV electron diffused by the central field of a heavy nucleus modifies the purely charge scattering trajectories in such way that a right-left scattering asymmetry is measured in a plane perpendicular to the spin quantization axis [8]. In fact spin-orbit interaction (SOI) is ubiquitous being one of the basic interactions that determines the spin band structure of solids, being dominant in the final state spectroscopy of initially closed core electron shells, being the coupling vehicle between photon polarization and spin structures in the photoexcited matter systems, i.e the mechanism that allows to probe spin ordering with polarized photons, and finally being exploited, under controlled circumstances, for the spin polarization detection. As the angularly resolved photoemission probes the angular structure of the initial state wavefunction [1], the excitation by polarized electromagnetic radiation (linearly or circularly polarized) leads to spin structure sensitivity in photoemission dichroism experiments of extended states, even without performing final state spin detection. The Linear (Circular) Dichroism in the Angular Distribution of photoelectron methods, LDAD and CDAD, are effective in the study of space chirality in adsorbed molecules and time reversal chirality in magnetic surfaces (LMDAD, CMDAD) [9–11]. When performing the complete SP-ARPES experiment the spin-resolved intensities must be understood always in view of the underlying LMDAD or CMDAD effects that are related to the experimental geometry.

The selection rules for absorption of X-rays [7, 12] are also strongly dependent on the experimental geometry because of the SOI so that the presence of a spin quantization axis due to magnetization $\boldsymbol{M}$ is readily detected by measuring absorption dichroism, i.e. by performing "chiral" time reversal experiments. Different experimental geometries define the X-ray natural and magnetic dichroism with linearly polarized (XMLD) and circularly polarized (XMCD) X-rays [13].

The understanding and full control of the geometry of the experiment (relative orientations of all the relevant axes and vectors) are necessary in order to extract reliable information from solids and surfaces, and in particular to analyse spin-sensitive spectroscopies (Fig. 20.1).

In the following we address the implications of spin-analysis on the PES (angularly integrated) and ARPES experiments from core levels, secondary electrons and from extended band states and provide some examples of experiments that lead to unique information on surface states and on surface magnetism. We also discuss the X-ray magnetic dichroism in absorption as the basis for atom-specific magnetometry.

Beyond the articles in this book, and the references contained therein, the important book of Stohr and Siegmann [13] provides a robust reference for a systematic study of magnetic spectroscopies based on X-ray polarization and electron spin-polarization.

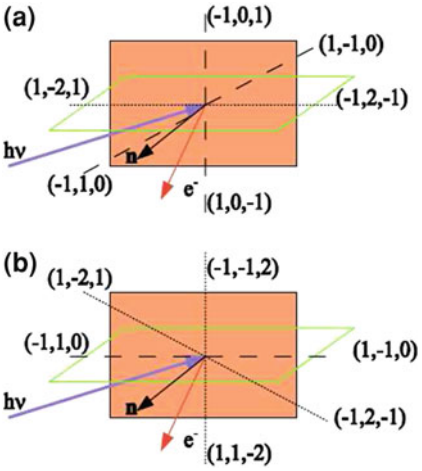


Fig. 20.1 Sketch of two possible experimental geometries for ARPES on a (111) surface of a fcc sample [14]. The photon beam (*violet*), photo-electron momentum (*red*) and surface normal $\boldsymbol{n}$ are contained in the scattering plane (*green contour*). *Dashed lines* are intersections with high symmetry planes of the system (non-mirror planes in fcc(111)), *dotted lines* are intersection with mirror planes. In **a** a mirror plane coincides with the scattering plane (ARPES will measure bands along the Γ-M direction, the dipole selection rules are at work here). In **b** no mirror plane is parallel to the scattering plane and ARPES measures the Γ-K direction. One changes from experiments **a**–**b** by rotating the surface normal by 30°. See further discussion of these specific geometries below. Figure adapted from [10]

20.2 Definition and Measure of the Spin Polarization of the Photoelectrons

The complete determination of the quantum final state of photoelectrons implies measuring $E, \boldsymbol{k}$ and spin polarization $\boldsymbol{P}$ of the photoejected current. $\boldsymbol{P}$ is defined by components Px, Py and Pz that are determined by the number of up and down spins along the x,y,z directions or quantization axes. For a pure spin state $|\boldsymbol{P}| = 1$, for a mixed spin state $|\boldsymbol{P}| < 1$. The degree of spin polarization of a beam of (photo)electrons relative to the quantization direction ξ is defined as:

$$P_\xi = \frac{n^\uparrow - n^\downarrow}{n^\uparrow + n^\downarrow}$$

where the up arrow means parallel to ξ and the down arrow means parallel to -ξ [9]. If a magnetization $\boldsymbol{M}$ is present, then one defines the spin-polarization with respect to $\boldsymbol{M}$ of the sample, i.e. with respect to the direction of the minority spins. When an electron beam of intensity I and polarization $\boldsymbol{P}$ propagates through a magnetized solid film, we can measure the transmitted intensities (through the film) for the cases of $\boldsymbol{P}$ and $\boldsymbol{M}$ being parallel or antiparallel yielding an asymmetry:

$$A = \frac{I^{\text{maj}} - I^{\text{min}}}{I^{\text{maj}} + I^{\text{min}}}$$

where I^{maj} and I^{min} identify the intensity measured with $\boldsymbol{P}$ and $\boldsymbol{M}$ antiparallel (i.e. direction of the majority electrons of the magnetized film) or parallel (i.e. direction of the minority electrons in the magnetized film) [9]. When measuring the spin polarization of E and $\boldsymbol{k}$ selected photoelectrons in the SP-ARPES experiment one "filters" the photoelectron intensity by a scattering experiment yielding [4, 9]

$$P_I(E, \boldsymbol{k}) = \frac{I_\uparrow(E, \boldsymbol{k}) - I_\downarrow(E, \boldsymbol{k})}{I_\uparrow(E, \boldsymbol{k}) + I_\downarrow(E, \boldsymbol{k})}$$

$I_{\uparrow,\downarrow}(E, \boldsymbol{k})$ are the spin resolved spectra referred to a chosen quantization axis that is determined by the scattering geometry. In a practical spin resolved photoemission experiment one measures a) the unpolarized (spin-integrated) spectrum $I_M(E,\boldsymbol{k})$ (identically as in a standard ARPES experiment) *and* the $P_I(E,\boldsymbol{k})$ that, togheter, allow to derive the two spin-resolved spectra:

$$I_{\uparrow,\downarrow}(E, \boldsymbol{k}) = I_M(E, \boldsymbol{k}) \frac{[1 \pm P_I(E, \boldsymbol{k})]}{2}$$

Summing the spin resolved spectra for opposite spin reproduces the unpolarized spectrum [2]. The measured $\boldsymbol{P}$ is non zero if there exist a spin-quantization axis that is efficiently probed in the chosen experimental geometry, and if spins are unbalanced with respect to it. The quantitative interpretation of $\boldsymbol{P}$ requires a deep understanding of the spectral function [1, 2], that is generally difficult. Low energy many-body excitations (plasmons, phonons, magnons) occur on the relevant scale for spin scattering and therefore influence $\boldsymbol{P}$ of the final state electrons blurring the information on the initial state bands. A thorough understanding of the experiment geometry, the chirality with respect to the scattering plane (containing photon beam and photoelectron momentum $\boldsymbol{k}$), including photon-polarization, sample magnetization, sample surface normal $\boldsymbol{n}$, is a prerequisite to understand the spin-resolved photoemission and its exploitation for determining bands and Fermi surfaces.

In ferromagnets the exchange interaction (spin-spin) dominates the energy splitting of minority and majority bands throughout the Brillouin zone, with special changes occurring at the surface. In non-magnetic surfaces it is the spin-orbit (LS) coupling or SOI of 2D surface states that can lead to spin polarization of $E,\boldsymbol{k}_{//}$ states perpendicularly to the surface plane [2].

20.2.1 Detecting the Electron Spin

The total photoelectron current ejected from a solid surface as a consequence of photo-excitation by monochromatic radiation is composed of primary photoelectrons that carry information on the spin polarization of the initial states owing to the

dipole selection rule $\Delta \boldsymbol{S} = 0$, either extended or localized according to energy and electronic structure, and the so called secondary electrons ejected in vacuum by scattering mechanisms and by auto-ionization decays of the inner core holes [1, 2, 9]. At photoemission threshold energy $\boldsymbol{P}$ is directly related to the electron states at the Fermi level [9, 11]. At higher photo-excitation energies both itinerant and localized states are photo-emitted and can be inelastically scattered before emerging in vacuum. Also the spin polarization $\boldsymbol{P}$ of the inelastically scattered electrons that emerge with low energies in the secondary peak turns out to be related to the spin polarization $\boldsymbol{P}$ of the occupied bands due to multiple scattering with band electrons and electron-hole pair production across the Fermi level [9, 11]. The E and $\boldsymbol{k}$ resolved photoelectron beams selected by a state-of-the-art ARPES apparatus yield typically 10–100 femto-Ampere currents with an energy spread of 1–10 meV with an angular resolution of 0.1–0.3° [1, 2]. In both cases (total photo-ejected yield and $E,\boldsymbol{k}$ selected current) one can form *periaxial electron beams* with the photo-ejected electrons by means of electrostatic fields (electron lenses), accelerate or just transport those to spin detection experiments that are all based on SOI scattering mechanisms, at different energies. The non-classical nature of the electron spin does not allow to separate spatially the two spin states of a free electron in an external magnetic field [4]. To measure $\boldsymbol{P}$ one *must* exploit spin-dependent scattering which yields a geometric asymmetry A that one relates to $\boldsymbol{P}$ by $P = A/S$ where S is the so-called Sherman function [4] representing the spin-resolving power of the experimental set-up that depends on the energy of the elastically scattered electrons and on the scattering angle $\boldsymbol{\theta}$. The measured asymmetry is related to the degree of spin-polarization of the beam, and can be inferred as the spin-polarization of the initial or scattering states in the sample [9, 11].

20.2.2 LS Mott Scattering

At high enough energy, so that the De Broglie wavelength of the electron is small with respect to the interatomic distances of the target material, one can think of the electron as being scattered by the positive charge of the target atom that is approached, with an effective magnetic field experienced in the reference frame of the electron that has concentric circular field lines, weaker as the distance from the scattering nucleus increases (the electron "sees" the nucleus moving towards it as a positive electric current) [4, 9]. The force exerted by this graded field onto the spin of the electron combines with the Coulomb force that dominates the scattering process. Consider a scattering plane as sketched in Fig. 20.2 [9] with the electron beam contained in the plane and perpendicular to the target surface, and the relevant spin quantization axis perpendicular to the plane along which the $\boldsymbol{P} = \boldsymbol{m}$ of the electron beam is defined. The effect of the LS coupling is that if the "up" spin electron scatters on the target atom passing on the right side of it, then the magnetic field lines and the electron own spin are parallel and deviate the electron trajectory towards the increasing field, i.e. towards the center of the atom, i.e. towards the *left*. If the electron passes on

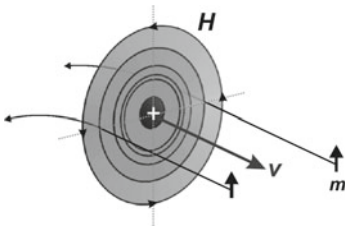


Fig. 20.2 Sketch of spin-orbit coupling in elastic Coulomb scattering. The electrons with magnetic moment ***m*** "up" is diffused by an atom whose field projection perpendicular to the electron momentum ***k*** is shown as shaded area. The electron is impinging on the atom and "sees" in its reference-frame the atomic nucleus as a counter-propagating current with velocity ***V*** and circular magnetic field lines. The force on the magnetic moment **m** is applied towards increasing field when **m** and the field are parallel and towards decreasing field when they are anti-parallel: in both cases towards the *left* in the scattering plane. Electrons with ***m*** "down" will be scattered to the right. If **m** and **H** are perpendicular to each other no LS (SOI) scattering occurs. In this way a *left-right* asymmetry A is determined in the scattering plane for a spin-polarized beam, and can be measured by a suitable arrangement of electron counters [13]. (© *Springer, reprinted with permission*)

the left of the atom the magnetic field and the spin are opposite (antiparallel) and the force will push towards weaker fields, i.e. away from the nucleus, i.e. again to the *left* in the scattering plane. All "up" electrons do scatter to the *left* in the scattering plane perpendicular to the quantization axis of ***m***: the scattering plane does contain the linear momentum ***k*** of the incoming electron beam and the ***k***' after scattering by the angle **θ**. The ***k*** × ***k***' product gives an axial vector perpendicular to the scattering plane that coincides with the axial **m**: one therefore retrieves the direction of the axial **m** by scattering on a polar field (*E-field* of the target) assuming that **m** has a projection along the normal to the scattering plane (along which we define "up" and "down" orientations).

One measures therefore the degree of spin polarization as

$$P_{\perp} = \frac{n^{\uparrow} - n^{\downarrow}}{n^{\uparrow} + n^{\downarrow}}$$

where $n^{\uparrow}$ and $n^{\downarrow}$ are the number of electrons in the primary beam that carry spin up and down with respect to the chosen scattering plane (the one where we have installed the *right* and *left* detectors. The measured P is perpendicular to this plane). The set-up will simultaneously collect signals from a "left" and a "right" detector placed symmetrically with respect to the impinging beam and containing the target surface normal; such plane is therefore perpendicular to the quantization axis of the detected spins. The asymmetry

$$A = (I^{\text{right}} - I^{\text{left}})/(I^{\text{right}} + I^{\text{left}})$$

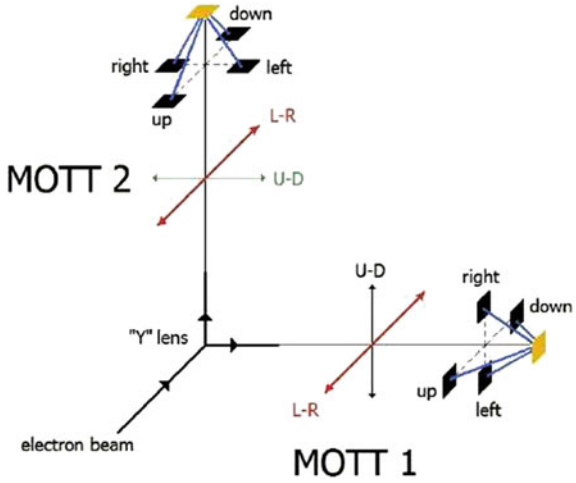


Fig. 20.3 Mott scattering in a vectorial arrangement of detectors. A "γ shaped" electrostatic lens rotates $\boldsymbol{k}$ (but not $\boldsymbol{m}$) by 90° between two subsequent measures each of which probes simultaneously two perpendicular components of $\boldsymbol{P}$. The component along the red direction is measured in both experiments and serves also as an internal calibration of the apparatus. Adapted from [15]

is obtained from the electron beam, *and is suitable for performing time resolved experiments even with ultrashort electron pulses like those excited by HHG fs lasers or by Free Electron Lasers in the UV and X-ray regime*. The Sherman function S(θ,E) contains information on the target Z number, the electron beam energy E, the scattering angle θ and relates the asymmetry A to the degree of spin polarization $A = P_{\perp}$. It can be calculated for kinematic single scattering [4], but it is generally determined experimentally, allowing for the effective finite thickness of the target (usually a thin film of high Z atoms allowing for high transmission of the primary beam at energies of 10–150 KV) that implies some energy losses and multiple scattering, and for angular integration on the solid angle defined by the active area of the detectors. The overall efficiency of the spin-dependent scattering experiment is defined by $\varepsilon = S^2 I/I_0$ that can be called "figure of merit" (FOM) of the detector. This determines the accuracy of a $\boldsymbol{P}$ measurement, i.e. the statistical error $\Delta P_{\perp} = 1/(\varepsilon I_0)^{1/2}$ [4, 9]. If two perpendicular Mott scattering experiments are performed in quick time sequence, like in the geometry sketched in Fig. 20.3, the three perpendicular components of $\boldsymbol{P}$ can be measured.

At most two $\boldsymbol{P}$ components can be measured simultaneously, the third one requires an independent measure i.e the measure of a different electron beam, e.g. rotated in $\boldsymbol{k}$ by 90° (not in spin) by means of a suitable electrostatic field, as shown in Fig. 20.3. The scattering probability I/I_0 (I_0 is the impinging electron beam intensity on target and I is the intensity of the (back)scattered electron current) is typically 10^{-2} because in order to optimize the ratio of spin-orbit scattering over the charge scattering special angles (like $\pm 120°$) are chosen that do correspond to minima in the scattering probability; under these circumstances the effective S function for an optimized Mott detector is 0.1–0.2 [8]. The FOM of the Mott detector is consequently of order 10^{-4}. Using Au as target in UHV, and given the penetration length of 10–150 keV electrons that exceeds some nm, one does not suffer of aging phenomena of the detector from surface contamination: the FOM of the detector remains stable in

time and allows for quantitative comparison between $\boldsymbol{P}$ values obtained from different experiments [8, 13, 16, 17]. At lower electron energies the left-right asymmetry is still measureable and practical detectors have been made [18]. In fact a beam of electrons of 100-150 eV directed perpendicularly to a polycrystalline Au surface gives a measureable left-right asymmetry that is strongly dependent on θ and has a Sherman function value that depends sensitively upon the structure and effective composition of the target surface due to the reduced mean free path of the primary electrons in the detector. The detector FOM in this case is less well defined and may be less reproducible. Reliable $\boldsymbol{P}$ measurements can be obtained by Mott scattering and much surface physics has been explored by SP-ARPES data collected with such apparatuses [2–6]. The low efficiency of Mott scattering penalizes nevertheless the method and E and $\boldsymbol{k}$ resolutions need to be lowered in order to have enough intensity for the spin analysis.

20.2.3 Exchange Scattering

Low-energy electron diffraction of polarized electrons from a magnetically ordered target single crystal surface is an alternative scheme of spin polarization measurement, with potentially much higher efficiency than Mott scattering [19]. At low energy (few eV-few tens of eV) the interaction is limited to the surface and a few subsurface layers of the target. Spin dependence in LEED has been demonstrated and used in surface science studies, and can be exploited as a spin detector [20]. Exchange scattering determines the band structure of the ferromagnets: it depends on the exchange integral J that in turn depends on (surface) structure, bond distances, coordination number and effective composition of the surface (oxides, contaminations). The spin polarization of the electrons in the magnetic target surface depends on the magnetization $M(T)$. In a reflectivity experiment the magnetic contribution will be proportional to $M(T)$ [13]. If the spin polarization $\boldsymbol{P}$ of an electron beam impinging on a target is known then reflectivity experiments can be performed as a function of E and reflection angle θ yielding data on the $M(T)$ of the scattering surface. This is applied in fact in the SPLEEM microscope [21]. The spin asymmetry A of the elastic reflected electrons is obtained and is referred to $\mathrm{I}^{\mathrm{maj}}$ and $\mathrm{I}^{\mathrm{min}}$ of the target. A depends on E and momentum transferred $\boldsymbol{q}$. It can be of the order of 0.1–0.2 at low energies and decreases by one order of magnitude at 100 eV or more [13]. In fact at low enough energies, the De Broglie wavelength of the electrons is large with respect to interatomic distances and one avoids diffraction so that most of the intensity is specularly reflected. As a relevant example the reflectivity of Fe(100), in a single magnetic domain, for 10 eV electrons at near-normal incidence gives an asymmetry A of 20 % and a total reflected fraction of 10 % [13]. If we now invert the problem and use a well known single crystal target surface (e.g. Fe(100)), fully magnetized at the remnant $M(T)$ value as a detector we can develop an efficient spin detector as far as we control the aging and effective $M = (M(T)/M(0))$ of the target during the time of the experiment.

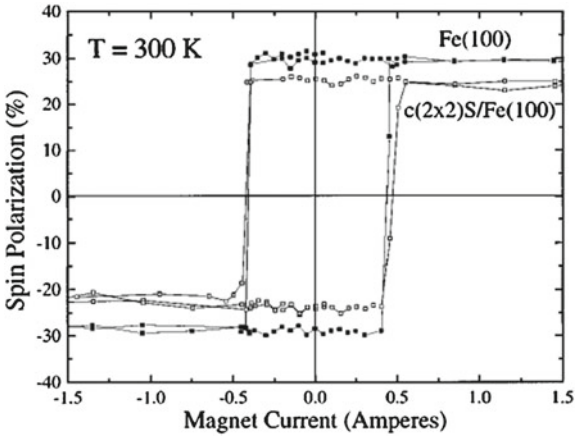


Fig. 20.4 Ferromagnetic hysteresis curves obtained by measuring the spin polarization of the total electron yield photoemission with a 100 KV Mott detector from Fe(100) (full symbols) and for the c(2x2) S/Fe(100) (open symbols) surfaces [23]. (© *American Physical Society. Reprinted with permission*)

One such application is the VLEED (very low-energy-electron-diffraction) detector where the spin-dependent reflectivity of electrons of a few eV at a magnetized ferromagnetic Fe(001)-p(1x1)-O target surface is measured [22]. The spin-split band structure of (surface oxidized) Fe(001) determines a different energy and momentum (i.e. angular) dependence of the reflectivity (R) of spin-polarized electron beams: optimum scattering geometry and energy conditions can be found for obtaining maximum asymmetry A of the reflected electrons. FOM is here defined as A^2R. The high reflectivity in the very low energy range, gives a FOM for the VLEED detector of the order 10^{-2} [22]. The advantage of simultaneous asymmetry measurement (2 P components like in Mott detectors) is that main spurious asymmetries due to non linearity in the left and right counters or non perfectly periaxial beam in the accelerator are normalized by repeating the experiments on ferromagnetic samples with reversed remnant magnetization. A well known ferromagnetic surface can therefore "calibrate" the Mott detector for new experiments on magnetic and non magnetic samples, provided careful alignment protocols are adopted. If a carefully closed magnetic circuit is built that contains the ferromagnetic sample and a horse shoe electromagnet, or if a single crystal sample of "picture-frame" shape, then the magnetic field does not emerge from the sample surface and truly surface sensitive hysteresis loops can be measured for low coercivity surfaces (Fig. 20.4).

20.3 Towards the Complete Electron Spectroscopy

20.3.1 Spin Polarized ARPES

The electric dipole operator that determines the photoemission transition does not act on either spin $\boldsymbol{s}$ or momentum $\boldsymbol{k}$, so these quantities are conserved. With this understanding the careful measures of the electron kinetic energy in the final state,

the emission direction and of the spin polarization ***P***, provide information that can be used for describing the initial states [2, 13]. Mapping the spin-resolved band structure in the Brillouin zone is feasible if one measures multiple angles and/or multiple kinetic energies for the same initial state. The approximation of the free electron like final state with parabolic dispersion folds back the measured intensities and energies to initial state properties. By adopting any of the advanced description of the full manybody photoemission problem, accounting for the complete response of the system to the photoexcitation (photohole state single particle spectral function) and extending to the spin-polarization analysis of the signal one can retrieve the full band and spin structure in the reciprocal space [1, 2].

Ferromagnets are stabilized by the exchange splitting of majority and minority bands that are split by correlation and exchange energies quantized along the magnetization direction [13]. Regions of the Brillouin zone where majority and minority bands do not overlap sustain therefore fully spin-polarized states. Assuming single domain magnetized samples to saturation *M(T)* and high ***E,k,s*** resolution, the SP-ARPES photoemission experiment leads to the full description of the ferromagnetic surface. The SOI can determine spin-split bands reflecting the coupling of spin and ligand field of the sample, and its changes at the surface or other internal boundaries, also in absence of ferromagnetic exchange. These phenomena are relevant both in magnetic materials, reflecting the surface magnetism of relaxed/reconstructed surfaces or spin-orbit vs. exchange coupled interfaces, as well as in systems that do not display magnetization but present well-defined spin structures. All these cases can be studied by ***k***-dependent spin polarization photoemission measurements [2–6].

20.3.2 Spin Polarization of the Quantum Yield

The low kinetic energy "secondary peak" of the photoelectron spectrum is determined mainly by multiply-scattered electrons from higher energy excited states. The lifetime of photo-excited electron states of 10–100 eV in condensed matter is of the order of 10^{-15} s, representing a very short free-travel through the solid, usually described as a short probing (or escape) depth. In ferromagnets the formation of the electron cascade occur via multiple scattering of the excited electron with the spin-polarized extended states near the Fermi level, i.e. mostly with the d-states [13, 24, 25]. One can therefore define and measure both a spin-averaged electron probing depth λ_e and two spin resolved probing depths $\lambda+$ and $\lambda-$ by performing ***P*** measurement on the secondary electrons. Different $\lambda+$ and $\lambda-$ simply arise from the difference in number of holes in the majority or minority bands (mostly d-character in 3d transition metals) so that the free travel of minority spin excited electrons in the ferromagnet is always shorter than that of majority electrons and the ferromagnet consequently acts as a spin-filter of the (photo)electron current. Values of $\lambda+ = 6.5$ Å and $\lambda- = 5.2$ Å in iron were determined by total yield ***P*** in overlayer experiments with selective excitation of the layered material [26] (Fig. 20.5).

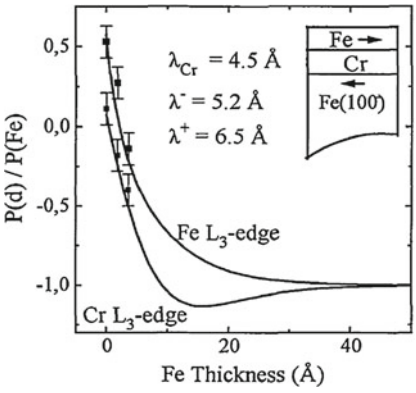


Fig. 20.5 Spin dependent mean free path in iron from overlayer experiments by measuring the SP of the total electron yield as excited at the Cr L_3 edge and at the Fe L_3 edge [26]. (© *Journal de Physique. Reprinted with permission*)

As a consequence the measure of ***P*** of the total quantum yield, that is dominated by secondary electrons even in absence of final state energy selection, bears a direct proportionality to the average ***P*** of the initial state bands of the photoexcited material. The accelerator lens forming the periaxial beam for Mott scattering can be tuned for optimal transmission of initially low energy photoelectrons acting as a bandpass filter. Alternatively an angle integrating analyser or ARPES apparatus can be tuned to the secondary peak, or an imaging electron optics can be used for lateral resolution obtaining a SEMPA: scanning electron microscope with polarization analysis [24]. A relative magnetometry can be performed therefore in such photoemission experiments, with intrinsic high surface sensitivity. Surface magnetism has been studied by measuring *M(T)* curves by spin-polarized photoemission yield, obtaining the typical 2D behaviour as contrasted to the bulk *M(T)* behaviour that can be simultaneously measured on the same samples e.g. by the magneto-optic Kerr effect with 100–1000 Å probing depth [23, 25, 27, 28]. The spin character of the electron states of a ferromagnet near the Fermi level can be directly probed by threshold photoemission spin-polarized experiments [13]. Strong ferromagnetism implies that only minority states extend up to the Fermi level (E_F) since the fully occupied majority band has binding energies larger than the Stoner gap. The minority spin photoemission current is strongly scattered by the large DOS of minority spin d-states and the measurement of ***P*** in threshold photoemission is determined by both initial state spin structure and spin-filtering effect [13]. Threshold photoemission of Ni shows negative ***P*** "as expected" whilst Co, also a strong ferromagnet, shows positive ***P*** at threshold due to very effective filtering of minority photoelectrons [13]. The spin filtering effect has been long considered as a suitable mechanism for efficient spin polarization detection, although no practical detectors based on filters have been engineered yet. The fast response and high secondary yield in photoemission make such experiments promising also to explore the ultra-short time domain by exploiting HHG laser sources and Free Electron Lasers pulses of 10-100 fs duration to excite the photoemission: the measure of ***P*** from the total ejected electron yield after a single light flash gives a measure of the magnetization state and pump-probe experiments in surface magnetism can be designed.

20.3.3 Matrix Element Effects

In photoemission, energy and momentum conservation allow to trace energy bands, but tell nothing about peak intensities and widths. The transition matrix elements in ARPES include only the spatial part of the wavefunction so that the orbital degrees of freedom of the electronic states of the sample are probed. Changes of photoemission intensity as a function of experimental geometry and light polarization are ubiquitous and carry precious information [1]. Large intensity modulations are observed in ferromagnets upon magnetization reversal in well understood chiral geometries indicating that the orbital degrees of freedom are coupled to the magnetization direction, i.e. to the spin degrees of freedom of the electronic system [9, 29]. SOI manifests in photoemission in several ways, including band structure effects and Rashba-type effects that show up directly in the SP-ARPES data [2–6]. With reference to the experimental geometry of Fig. 20.1 one can further distinguish experiments in which: the sample surface normal lie in the scattering plane or not, the linearly polarized light polarization lies *in-plane* (*p* polarization) or *perpendicular* (*s* polarization), or *oblique*, the circularly polarized light spin $\boldsymbol{L}_{ph}$ is oriented parallel, antiparallel, or perpendicular to a relevant spin-quantization axis. It is easy to see from Fig. 20.1 that if there is magnetic order in the surface, for example directed perpendicularly to the scattering plane, the geometry is chiral and a reversal of $\boldsymbol{M}$ due to a suitable applied external $\boldsymbol{H}$-field produces a specular geometry. In such experiments both measured $\boldsymbol{P}$ and photoelectron intensities are different.

All spin-resolved photoemission measurements are to some degree angularly resolved, unless the energy integrated total yield is collected and then formed in a periaxial beam for spin analysis. Matrix element effects and experimental geometry lead one to observe spin polarization also from closed shells that are intrinsically non polarised, but whose radial distribution of photoelectrons is only partially sampled by the apparatus. It is important to distinguish the case of core levels (sphero-symmetric in the initial state) and of extended states (reflecting the symmetry of the crystal).

20.3.4 Core Levels

One of the most striking final state effects in photoemission spectroscopy is the spin-orbit splitting. A core level, or a completely filled valence band, have a total spin equal to zero because the number of spin-up and spin-down electrons is the same as described by the Pauli principle.

The photoemission experiment probing such systems always reveals a spin-orbit splitting of the photohole final state, as shown in the classical example of *Cu 3p* core level photoemission reported in Fig. 20.7 [31].

In these core level studies all the intensity and polarization effects are understood in terms of final state effects with the meaning that only by considering the final states there is a possible description, and this includes spin-orbit and exchange energy splitting as well as spin-dependent transport of the individual m_j photoelectrons in the

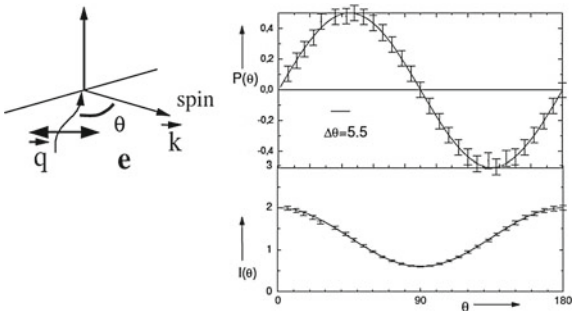


Fig. 20.6 Linearly polarized angular distribution of photoemission intensity and spin-polarization as measured from Ar 3p with hν=21.2 eV. The inset shows the light propagation q and linear polarization. Spin analysis was accomplished by Mott scattering [30], (© *American Physical Society. Reprinted with permission*)

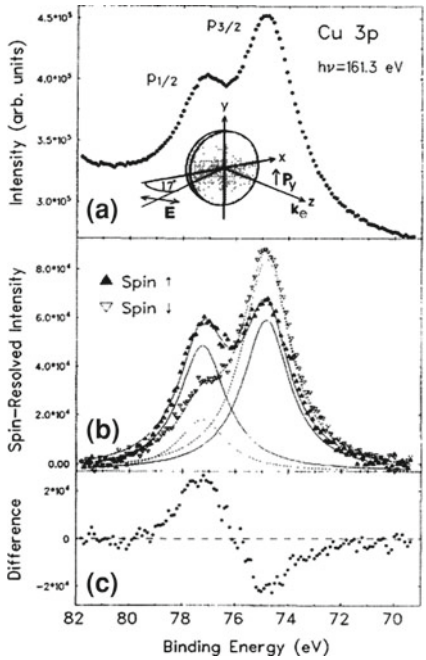


Fig. 20.7 Cu 3p angularly resolved PES: the final state doublet is due to SOI of the photo-hole and its spin-polarization shows the values, in the selected direction of photoemission, of the J = 1/2 and J = 3/2 multiplets, If full angular integration was performed the SP would average to zero [31]. (© *American Physical Society. Reprinted with permission*)

given direction that is probed by the experiment. In the case of non-magnetic surfaces, like Cu(001), the final state energy splitting is measured both in spin integrated mode as in spin-resolved mode. The total spin of the *Cu 3p* ground state is zero being the $6\ m_j$ sublevels degenerate. The photoemission spectrum shows a splitting of about *2eV* because the photo-hole left behind by the photoelectron transforms the core level in a non-zero spin level that is subject to spin-orbit interaction. This is the reason of the observed double peak of the *Cu* core level photoemission spectrum (in fact of any core level spectrum for initial states with $l = 1$ or higher). Furthermore one experimentally measures a non-zero spin polarisation, i.e. the sum of the spin-up and spin-down measured intensities is non-zero: this is a consequence of the finite angular acceptance of the detector. The partial angular integration that is intrinsic to

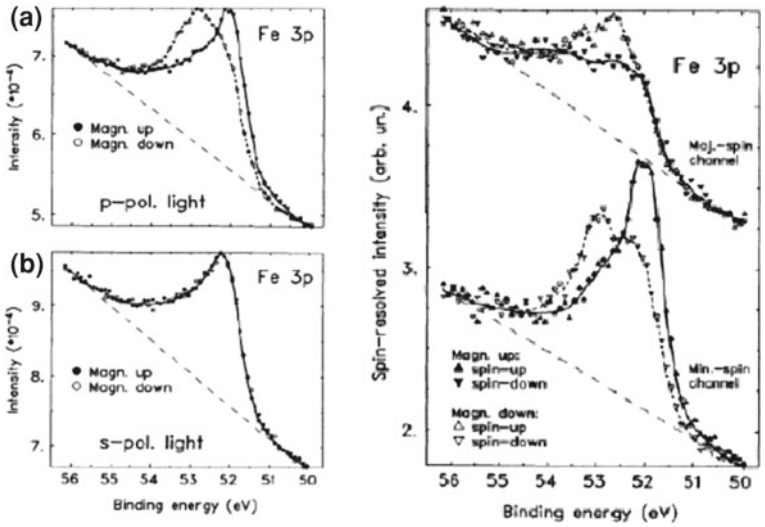


Fig. 20.8 Fe 3p angularly resolved PES in chiral (p-polarization and M reversal) and non chiral (s-polarization). *Left* spin-integrated photoemission intensities. *Right* spin resolved photoemission intensities [32]. (© *American Physical Society. Reprinted with permission*)

a SP-PES experiment, gives a net spin-polarization in the experiment, but $\boldsymbol{P}$ would certainly sum to zero if the data were integrated over the whole 2π srad. There are no magnetic interactions between the *6* m_j sublevels and the valence band in copper and the two *Cu 3p* final states are two-fold ($3p_{1/2}$) and four-fold ($3p_{3/2}$) degenerate respectively. The measured angular dependent spin-polarization values are similar to what can be measured from atomic *Ar 2p* or Xe 5p levels in the gas-phase as shown in Fig. 20.6 [30].

Similar chiral experiments on *Fe 3p* or *Co 3p* from magnetically ordered surfaces define the *LMDAD (or MLDAD)* and *CMDAD* (*linear/circular magnetic dichroism in angular distribution*) type of measurements that very directly probe the exchange-split m_j sublevels by measuring the angular dependent intensities of each m_j contribution, that are also directly identified if spin resolved data are collected [9, 32]. In these cases the degeneracy of the spin-orbit final states is further removed by the exchange interaction between each individual m_j sublevel and the spin-polarized valence band, so that each sublevel contributes intensity and spin polarization at a different energy in the final state directional photoemission spectrum, the energy spread of the sublevels being proportional to the magnetic moment of the photo-excited atom. These facts were shown by both spin resolved and spin integrated *LMDAD* measurements in chiral geometry on $l = 1$ core levels of the *3d* ferromagnets, and reported in Figs. 20.8 and 20.9.

A basic atomic model could provide the relevant understanding of the angular resolved intensities from each of the non-degenerate m_j sublevels in the final state [13]. The exchange interaction with the spin-polarized valence (3d) electrons completely removes the degeneracy of the *3p* final states into sublevels with a given

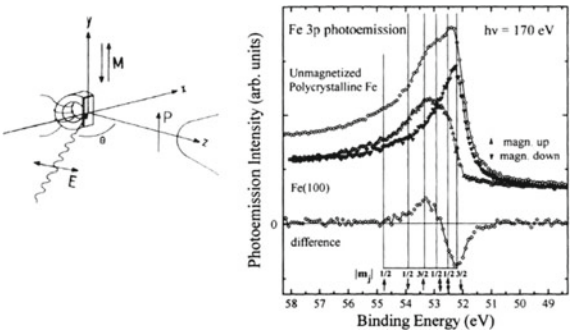


Fig. 20.9 Centre dark *triangles*: Fe 3p angularly resolved PES in chiral geometry (*p*-polarization and ***M*** reversal), *top* integral spectrum, *bottom* difference LMDAD spectrum. The grid of energy levels identifies the characteristic components that change in sign and intensity in the LMDAD [9, 33]. (© *American Physical Society. Reprinted with permission*)

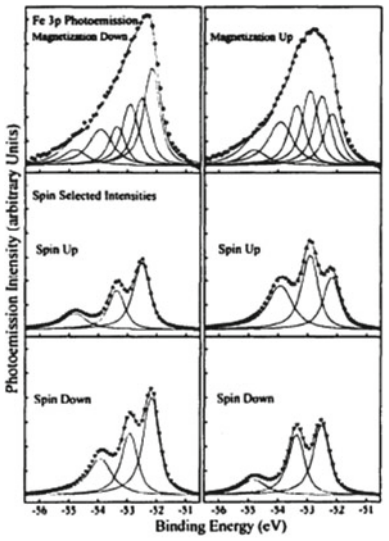
projection m_j on the magnetic quantization axis. Each sublevel in the photoemission final state is therefore at a characteristic energy and it is polarized. The *LMDAD* experiment is defined by the difference of two photoemission spectra when measured in mirror geometries, as obtained by reversing the sample magnetization along the perpendicular to the scattering plane with an external ***H***-field pulse. If the core-valence exchange splitting is large enough with respect to the lifetime broadening of the core hole the overall shape of the core level photoemission spectrum is very different in the two specular measures. The lineshape differences, i.e. the different *I(E)* across the spectrum, identify the m_j fine structure of the core spectrum that can be modelled by a simple sextuplet model in the case of $l = 1$. From the relative intensity changes of each m_j component the splitting level ordering is obtained and, accordingly the spin character of each energy resolved intensity. These findings have been further exploited for establishing a surface magnetometry [28] (Figs. 20.10, 20.11).

As photoelectrons undergo diffraction from near neighbours [34] with large forward focussing modulations of the measured intensity as a function of electron ***k*** and crystal orientation, one expects and indeed observes structure-related modulations of the magnitude of the *LMDAD* and similar dichroism in the photoemission [35]. Under particular circumstances it was shown how the *bulk* and *surface* photoemission contributions of *Fe(100)* could be clearly disentangled and how, through the *LMDAD* spectra, the energy splitting of the *Fe 3p bulk* and *surface* final state $J_{3/2}$ multiplets could be measured as 0.95(2) eV and 1.29(5) eV respectively showing that the *spin magnetic moment at the surface* of *Fe(100)* is 36 % larger than in the bulk (under the assumption that the $J_{3/2}$ splitting is linear in the exchange field) [36].

Today, with increased detection performances, these results could be refined and provide reference data to the spectroscopy of band states of highly correlated systems that show ***P*** or *Zeeman-like* splittings [37].

20.3.5 Band States

Extended states reflecting the symmetry of the crystal are probed in ARPES; then the symmetry of the initial bands enters directly in the determination of the measured



	Fe − 3p		Co − 3p	
m_j	B.E.(eV)	Lor.	B.E.(eV)	Lor.
+3/2	52.2	0.42	59.6	0.7
+1/2	52.5	0.42	60.0	0.7
−1/2	52.9	0.42	60.5	0.7
−3/2	53.3	0.42	61.2	0.7
−1/2	53.9	0.85	61.8	1.0
+1/2	54.8	0.85	63.0	1.0

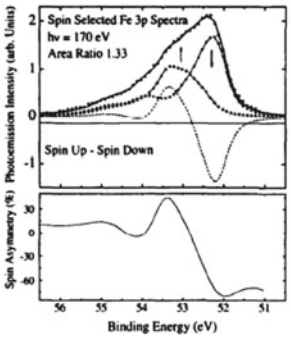


Fig. 20.10 Fe 3p LMDAD data and analysis with a simple atomic m_j multiplet that allows to identify the spin character of the components from the non-spin polarized photoemission intensity variations [9, 33]. (© *Elsevier. Reprinted with permission*)

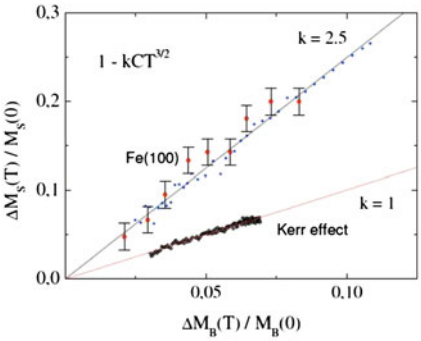


Fig. 20.11 Thermal decrease of surface magnetization versus bulk magnetization as measured by Spin.polarization of the total yield (*blue dots*), Fe 3p LMDAD (*red dots* with error bars) and bulk-sensitive magneto-optic Kerr effect from iron [28]. (© *American Physical Society. Reprinted with permission*)

intensities. In the relativistic analysis of photoemission, accounting for spin-orbit coupling, the selection rules are $\Delta j = 0, \pm 1$ and $\Delta m_j = \pm 1$ with j and m_j referred to the total angular momentum. In the simplified non-relativistic analysis $\sigma_l = \pm 1$ and $\Delta m_j = 0, \pm 1$ according to light polarization being linear or circular with opposite handedness. The manybody response of the electron system to the photoexcitation is described by the spectral function of the hole state A($\boldsymbol{k}$,ω)

$$A_i(\boldsymbol{k}, \omega) = \frac{1}{\Sigma''(\boldsymbol{k}, \omega)} \frac{1}{1 + \left[\frac{(\omega - \varepsilon_0(\boldsymbol{k},\omega) - \Sigma'(\boldsymbol{k},\omega))}{\Sigma''(\boldsymbol{k},\omega)}\right]^2}$$

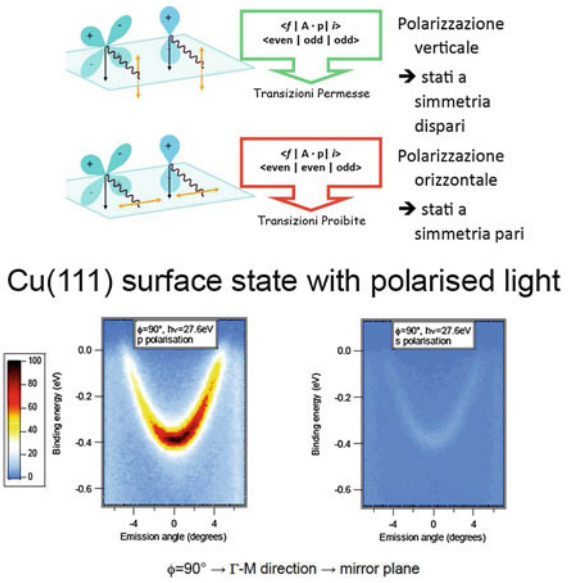


Fig. 20.12 Symmetry rules for photoemission with linearly polarized light at crystal mirror planes: L-gap surface state of Cu(111) as measured in p and s polarization along Γ-M direction. Adapted from M. Mulazzi, PhD thesis, Università di Modena, 2006

where the real part of the self-energy $\Sigma(\boldsymbol{k}, \omega)$ identifies the energy and mass and the imaginary part gives the peak width (that would be zero if A is reduced to a simple δ function) [1, 2]. The measured intensity at a well defined $\boldsymbol{k}_{//}$ is related to a transition between bands of same spin. The measured E_{kin} of the final state is then $\mathbf{k}_{//} = \sin\theta \sqrt{(2m/\hbar^2)E_{\text{kin}}}$. $\mathbf{k}_{//}$ is conserved whilst $\mathbf{k}_{\perp}$ is affected by the break of translational symmetry perpendicular to the surface and is well defined only for normal photoemission, when $\mathbf{k}_{//} = 0$ is conserved upon change of photon energy. With these basic ingredients the *E versus k* description of occupied states can be based upon angularly resolved, energy resolved and spin resolved photoemission spectroscopy (SP-ARPES) [1, 2].

Energy distribution curves (EDC), momentum distribution curves (MDC), and constant energy maps all with spin-polarization, can be measured and understood in well designed experimental geometries. Symmetry rules for extended states determine greatly final state intensities when measuring in proximity of crystal mirror planes: matrix elements are non-zero only if the state generated by the application of the interaction operator on the initial state overlaps with the final state (Fig. 20.12). It is an important aspect of the measure because the experimentalist has ways to select which states will appear in the spectrum since the wavefunction is invariant under reflection or rotation about some planes and axes. The reflection properties of the wavefunction are measured by ARPES using polarized light [1, 14, 38]. The matrix element has the overall effect of modulating the peak intensities according to photon energy and experimental geometry. On the other hand if nothing is known about the final state, the peak intensities will receive contributions from every state resulting in very complicated intensity patterns and no simple on/off rules are defined.

20.4 Symmetry Breaking Mechanisms

Below the Curie temperature (T_C) of a ferromagnet the magnetization vector acquires a non-zero magnitude and a specific direction [13]. The rotational symmetries that leave the orientation of this vector invariant remain unbroken but the other rotations become spontaneously broken. The surface by definition breaks the three-dimensional translational invariance of the bulk crystal, introducing by itself a reduction of the symmetry. In a ferromagnetic solid, the local magnetic moments attached to each lattice site typically lower the symmetry (with respect to the nonmagnetic lattice), depending on their direction $\boldsymbol{M}$. Hence the observables in the photoemission experiment can depend on the orientation of the magnetization ($\pm\boldsymbol{M}$). The above discussed magnetic dichroism in photoemission in which the photocurrent I changes upon reversal of $\mathbf{M}$, i.e. $I(+\boldsymbol{M}) \neq I(-\boldsymbol{M})$, is an example. At magnetic surfaces also the band structure can depend on the magnetization direction, i.e. $E(\boldsymbol{k}_{//},+\boldsymbol{M}) \neq E(\boldsymbol{k}_{//},-\boldsymbol{M})$, whereas the bulk electronic structure is not affected. ARPES data of the *Ni(111)* surface gave evidence of such effect on the dispersion of the *sp* states [38]. The effect shows up as shifts of intensity maxima in both energy and wave vector upon reversal of $\boldsymbol{M}$, thereby indicating band structure changes, and is accompanied by changes of the photocurrent, as expected for magnetic dichroism (Fig. 20.13).

This ARPES observation is phenomenologically understood by symmetry considerations involving the point group of the *fcc(111)* surface and is different from dichroism that is mainly related to hybridization regions in the band structure, i.e. band gaps induced by spin-orbit coupling [38] and leads to intensity variations different as well from the Rashba-Bychkov effect on surface states (see below). Spin resolved momentum distribution curves for majority and minority spins were directly measured for the *sp* states of *Ni(111)* in a reference experiment by Osterwalder et al. with the *COPHEE* apparatus using a vectorial arrangement of two Mott detectors after the momentum and energy selection by a dispersive hemispherical apparatus [2, 39] (Fig. 20.14).

The broken inversion symmetry at the surface creates the condition to observe spin-splitting of surface states due to the spin-orbit interaction also in non-magnetic systems. The Fermi surface of *Au(111)* for example includes surface states that bear analogies with 2D-electron gases as found at semiconductor heterostructures. In those systems the Rashba effect is described as due to the motion of an electron in the plane of the 2DEG (characterized by its Bloch vector $\mathbf{kk}$) through a perpendicular electric field, $\mathbf{E}_{\perp}$, resulting in a magnetic field in the rest frame of the electron, that couples to the spin, $\mathbf{s}$,of the particle therefore lifting the spin degeneracy $\mathrm{Eup}(\mathbf{k}) = \mathrm{Edown}(\mathbf{k})$. The details of the electric field gradients in the neighbourhood of the surface atoms, i.e. the details of the asymmetric wavefunction, namely the lack of inversion symmetry of the surface state, that determines the decay into the bulk, do actually determine the size of the Rashba splitting effect. A surface state with predominantly *p*-character decays into the bulk by acquiring hybrid states with orbitals *s* and *d* character. The admixture of *d*-character to a *p*-type surface state creates a decaying state and consequently a $\boldsymbol{k}$-dependent splitting of this state (Fig. 20.15).

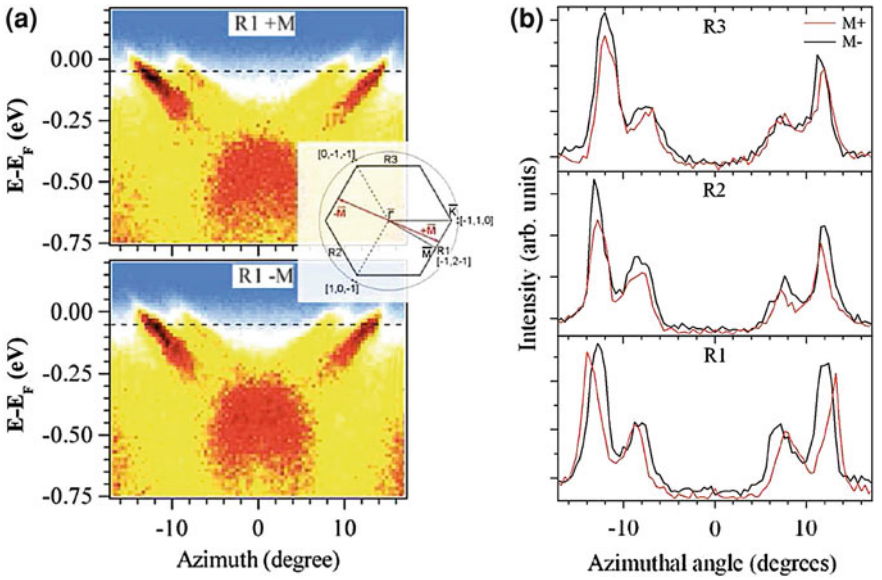


Fig. 20.13 **a** Maps of the photoemission intensity of the sp-states at 30 eV photon energy on Ni(111) surface, p-polarized light, and 56° polar angle (i.e. k// / = 1.14 a0–1) for region R1 with "positive (+M) and negative (−M) magnetization orientation. The zero of the azimuthal angle coincides with the [211] axis. The R1 and R2 regions are drawn in the inset. The red arrows indicate (+M) and (−M) orientations of the magnetization magnetization which is tilted by 7° off the [−1, 2, 1−1] axis [38]. (© *IOP. Reprinted with permission*). **b** Momentum distributed curves obtained by cutting through the *dashed line* of Fig. 20.13a, i.e. binding energy 50 meV, for the three regions R1, R2 and R3 indicated in the geometry inset. *Black curves* are for +M and *red curves* are for −M; i.e. three different experimental geometries are probed by photoemission in this case, R2 being in-plane perpendicular to the magnetization direction is unaffected by magnetization reversal. The peaks on R1 and R3 are shifted by −1, 2° and ì1.6° by the sign of M indicating the band-structure effects due to symmetry breaking [38]. (© *IOP. Reprinted with permission*)

This is by the way consistent with the matrix element analysis of the *Cu(111) L-gap SS* performed by light-polarization dependent *ARPES* that displays large energy-dependent asymmetries of the photoemission intensity with respect to dispersion [14]. Qualitatively one has a perpendicular net field gradient with respect to the surface plane, so that the interaction will orient the spin in plane, perpendicularly to the electron velocity vector (also contained in the surface plane). The energy splitting of *Au(111) L-gap* surface states and their Fermi surface contours have been measured by many, the spin direction has been directly measured by *COPHEE* as tangential to the Fermi surface, as expected [40, 41]. SOI splits two Fermi surface contours, a larger one for the state of lower energy, and a smaller one. The in-plane tangential spins will therefore appear as describing an anticlockwise circuit and a clockwise circuit respectively. Vectorial *SP-ARPES* has given full experimental evidence of the Rashba effect in Au(111) therefore establishing the sensitivity to systems where the loss of spin degeneracy is not imposed by an order parameter (like

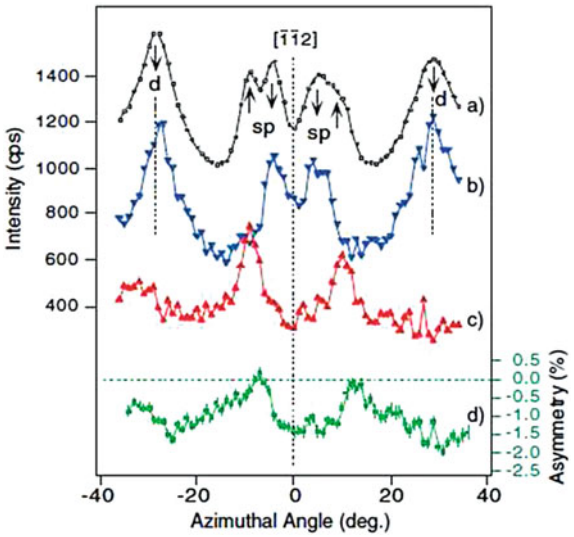


Fig. 20.14 Momentum distributed curves of the sp-states Ni(111) obtained by spin integrated (*black*) and spin resolved cutting (*blue curve* for minority and red curve for majority spins) as measured by the COPHEE spin polarized experiment (*green curve*) by the Osterwalder group [2, 5, 39]. (© *Elsevier. Reprinted with permission*)

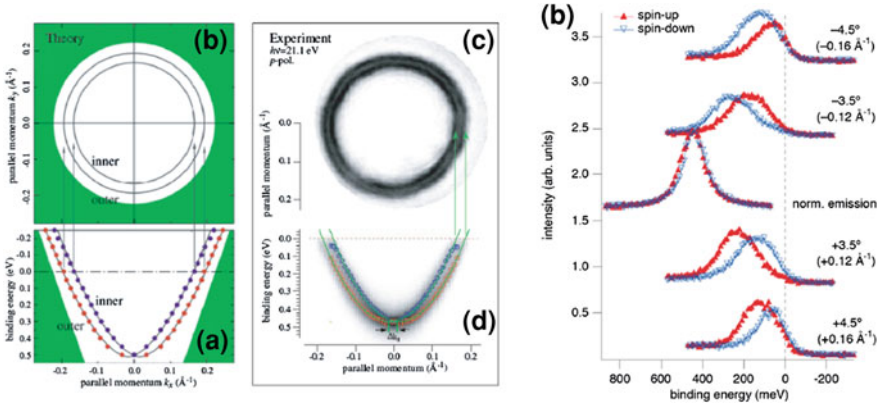


Fig. 20.15 *Left* SOI splitting of the Au(111) Shockley surface state of Au(111). **a** The calculated dispersion along k_x of the inner and outer surface state in the L-gap where no bulk states (*green areas*) exist. **b** MDC. *Center* **c** Fermi surface experimental map measured by spin integrated ARPES. **d** Experimental dispersion. *Right* SP-ARPES measured by COPHEE on Au(111) with $h\nu = 21.2$ eV [40, 41]. (© *American Physical Society. Reprinted with permission*)

magnetization) but by an intrinsic combination of spin-orbit splitting and reduced symmetry, yielding fully spin-polarized states. The case of *Au(111) L-gap* Schokley surface state is favourable due to the large energy and momentum splitting compared with experimental resolving power. In the related cases of *Ag(111)* and *Cu(111)* the

smaller size of the effect make the photoemission intensities of the opposite spin states to overlap largely, but a very narrow continuum Laser-source at 6.05 eV energy, focussed on a micrometric spot, has allowed to clearly resolve in momentum the Rashba splitting of surface state also in the case of *Cu(111)* [37]. The "spin-texture" of low symmetry systems is a key to understand the special topological properties of solids and surfaces, the spin-resolved conductivity of topological insulator surfaces. Topological superconductivity, and other correlation effects are likely to be clarified by high resolution *SP-ARPES* experiments [37].

20.5 Time Resolved Experiments and High Excitation Density

Laser sources with harmonics extending to the UV and far UV ranges and FEL sources and ultrashort pulses in the 1–100 fs range have opened the field of non-equilibrium electronic structure relaxation studies either by multi-photon photoexcitation or by the pump-and-probe method where an infrared pulse "prepares" the sample in an excited state of the electron system further probed by ARPES at chosen time delays aiming to monitor the decay mechanism of collective excitations. The time resolution and the high density of excitation regimes that Laser and FEL photoemission experiments start exploring are likely to give evidence of fundamental correlations in solids and surfaces, but prompt the need of new interpretation schemes since the initial states in these photoemission experiments are themselves excited states of matter.

20.6 X-Ray Absorption Dichroism

Magneto-Optical dichroism, like the Faraday and Kerr effects can be described in semiclassical terms by assuming the sequence of absorption of polarized light, oscillatory motion of the electrons along the ***E****-field*, rotation of the motion of the electrons due to the Lorentz force and re-emission of photons with rotated polarization (elliptical) or changed phase shift between circularly polarized light of opposite handedness. The geometry of the experiments, in the laboratory frame, is determined by the magnetization axis of the sample, the relative orientation of the linear photon polarization and the sample surface normal. Different geometries probe differently the matrix elements for the absorption (or reflectivity) yielding intensities that reflect interband transitions i.e. probing the joint density of states [13]. X-ray absorption is localized on atoms and is characteristic of the absorbing specie so that the initial state is described by an atomic-like wavefunction even in condensed matter (core level) and the final states span all the empty band in the Brillouin zone, as selected principally by the dipolar selection rules and by the symmetries of the system accessible in the chosen experimental geometry. Averaging on the band states means yielding X-ray absorption intensities that are proportional to occupation numbers of the

valence shells and, through the spin-orbit coupling, to the spin and orbital moments. Magnetic X-ray dichroism was measured first in 1986 at the LURE synchrotron laboratory, with linearly polarized light and later with circularly polarized light [42]. In 1992 the "Sum Rules" were derived providing a very effective way to understand experimental intensities in XMCD (X-ray magnetic circular dichroism) in terms of ground state orbital and spin moments [43, 44] and in 1995 quantitatively tested on a transmission experiment on iron [45]. The orbital moment in solids is reduced by the crystal symmetry that "quenches" the orbits in the ligand field, so it represents only a small fraction of the total magnetic moment. The high sensitivity of XMCD nevertheless gives direct access to this quantity that is fundamentally related to the coupling of magnetization and lattice. The study of surface magnetism, interface magnetism and nano-particle magnetism has therefore strongly developed as any lowering of the ligand field symmetry is reflected in large changes of orbital magnetic moment describing magnetocrystalline anisotropy, surface/interface anisotropy and nano-scale magnetic phenomena [13]. X-rays from high-brilliant sources are suitable for nanometer-scale resolution and therefore can be also exploited in microscopy, and magnetic microscopy (Scanning X-ray Microscopy), at the relevant length scale for surfaces, interfaces and nano-structured objects [46]. The X-ray absorption process is extremely fast and X-ray photon pulses of fs duration or shorter can be exploited for time resolution of fundamental physical processes in condensed matter, like demagnetization/magnetization reversal, chemical reactions, catalysis, phase transitions in correlated systems [13]. The first "Sum Rule" at work in X-ray absorption concerns the total intensity of the absorption at threshold, integrated on the energy span of the unoccupied density of states. By considering the "white line" intensity of the strong 2p-3d absorption in the transition metals one can state that it is directly related to the total number of holes in the valence electronic ground state. This can be written as $< I > = CN_h$ where $C = AR^2\ L/3(2L+1)$ with $A = 4\pi^2\alpha\hbar\omega$ and R is the radial $nc \rightarrow n'L$ matrix element and α is the fine structure constant.

By "orientation averaged" it is meant that the rule applies on intensities measured in such a way to integrate any anisotropy in the experimental geometry and sample orientation. If the sample has cubic or higher symmetry this means averaging the results of three measurements in orthogonal geometries. This is automatically accomplished by a single measurement in the case of polycrystalline samples. If polarized X-rays are employed the single measurement may depend on the orientation of the sample so that the intensities do not represent integration on the atomic volume, but are modified by anisotropy. The orientation-averaged intensity for L_3 and L_2 resonances is directly proportional to the *total* number of d holes above the Fermi level, i.e. to the total occupancy of the d-band of the metal, as summarized in Fig. 20.16 (from [13]). Experimental correlation of the white line intensity defined as peak areas of the L_3 and L_2 resonances and the number of d-band holes from calculation gives a linear relationship for the ferromagnetic 3d metals. As we can measure the total number of holes, it becomes appealing to exploit the selection rules in order to measure the number of holes of *majority* and *minority* spin character in a ferromagnet because such determination would represent directly the magnetic moment of the sample. Such experiment is the XMCD experiment that requires

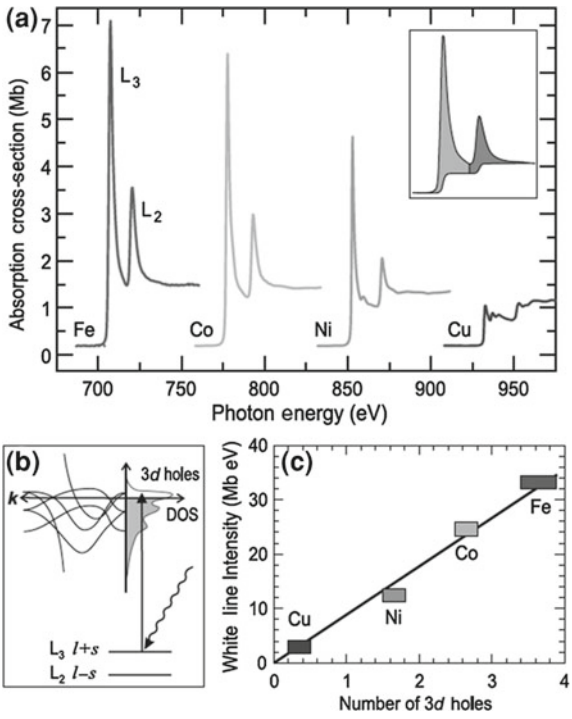


Fig. 20.16 L-edge XAS for 3d metals. The sum of L3 and L2 intensities (**a**), as defined in the inset, is plotted against the number of 3d holes, as obtained by integrating the density of states sketched in (**b**) in the plot (**c**) a linear relationship is obtained giving evidence of the total intensity sum-rule [13]. (©*Springer. Reprinted with permission*)

circularly polarized X-rays and an experimental geometry in which the photon spin or angular momentum $\boldsymbol{L}_{ph}$ and the magnetization $\boldsymbol{M}$ of the sample are collinear (or do have a large projection one on the other). Four measurements can be performed: two measurements with $\boldsymbol{L}_{ph}$ and $\boldsymbol{M}$ parallel, and two measurements with $\boldsymbol{L}_{ph}$ and $\boldsymbol{M}$ antiparallel. It is in fact possible to invert $\boldsymbol{L}_{ph}$ by changing handedness of the incident radiation and to reverse the sign of $\boldsymbol{M}$ by applying an external antiparallel $\boldsymbol{H}$ field that exceedes the sample coercivity.

A set of relative orientations of $\boldsymbol{M}$ and $\boldsymbol{L}_{ph}$ in the XMCD measurement is sketched in Fig. 20.17. The case of perpendicular orientation gives no difference as a function of $\boldsymbol{M}$ or $\boldsymbol{L}_{ph}$ reversal and yields a spectral intensity that is equivalent to the average of the two opposite geometries in the collinear case. The dichroism intensity is usually plotted according to $\Delta I = (I_{\text{antiparallel}} - I_{\text{parallel}})$ which corresponds to assuming the minority spin direction (of the magnetic electrons) as parallel with $\boldsymbol{M}$. The XMCD spectral difference, as defined in the figure and above, for a given degree of circular polarization of the light P_{circ} is directly proportional to the degree of magnetization of the sample and to the magnetic moment carried by excited atom.

$$I_{XMCD} \propto P_{circ} m \cdot L_{ph} \propto P_{circ} \langle m \rangle \cos\theta$$

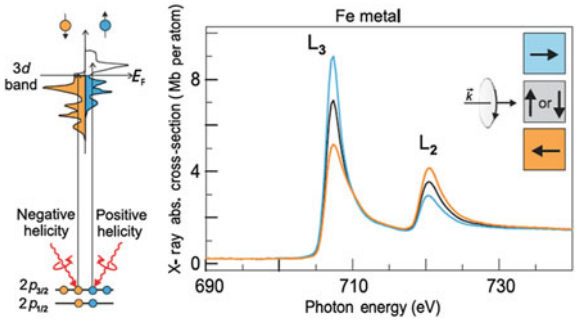


Fig. 20.17 Illustration of the XMCD phenomenon for Fe 2p core thresholds ($L_{2,3}$-edges) [13]. The inset mimics the Stoner model of ferromagnetism in iron and shows the different spin-polarized DOS. The coloured curves are actual data from Chen et al. [45] obtained in a transmission experiment with circularly polarized light of the handedness shown in the inset and the four orientations of sample magnetization. (© *Springer. Reprinted with permission*)

20.6.1 The XMCD as Diagnostic of Magnetization

The measure of I_{XMCD} is an extremely powerful diagnostic of magnetic order and magnetization direction. Even in absence of an absolute calibration of P_{circ} (the photon source degree of circular polarization) the very appearance of I_{XMCD} indicates that at an angle different from $\pi/2$ with respect to the propagation of the photon beam there is a quantization axis of the magnetic moments with a net M. By adapting the experiment geometry one can find the orientation of **M** with respect to, say, the sample surface or to specific crystallographic directions. I_{XMCD} can be exploited for performing ferromagnetic hysteresis cycles by scanning the applied $\boldsymbol{H}$ field while measuring the X-ray absorption intensity at the maximum of the L_3 or L_2 edges (or measuring full spectra). In this way the presence of parallel/antiparallel coupling at an interface between materials containing different *3d* atoms gives direct evidence of the saturation and coercive fields of complex heterostructures or to sublattices of impurities in a matrix.

The study of the interface between a thin Fe layer and a bulk ferromagnetic semiconductor like FeMn(5 %)As with Curie temperature $<$50 K is a typical materials science problem that could be attacked by XMCD giving evidence of a proximity-effect that orders, even at temperatures $>$ 300 K, the Mn magnetic moments in a thin (few nm from the interface) ferromagnetic phase exchange coupled (antiparallel) to the surface iron film magnetization (Fig. 20.18). The atom-selected XMCD hysteresis curves are a powerful diagnostic based on the intrinsic combination of magnetometry and chemical specificity [47]. The high sensitivity of I_{XMCD} on *L-edges* in *3d* atoms allows even to study paramagnetic molecular submonolayer systems weakly coupled to ferromagnetic substrates, and derive the orbital order that characterizes the interface electronic states [48].

The *M(T)* curves for bulk and surface overlayer systems can be measured by atom specific I_{XMCD} data and compared to intrinsically surface sensitive *S-ARPES*

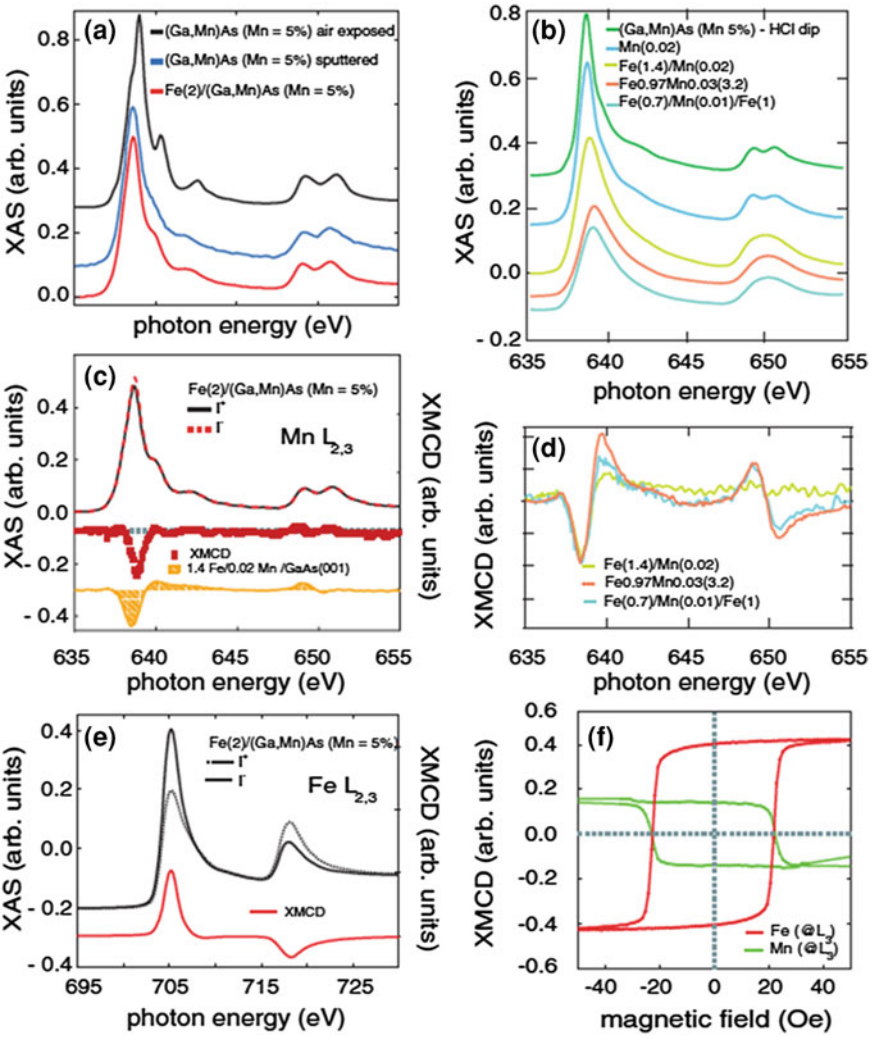


Fig. 20.18 XAS and XMCD spectra for Mn L2,3 edges in as grown GaMn(5 %)As samples and surface cleaning treatments (**a**); **b** various surface decorations with Mn and Fe overlayer growth; **c** XMCD of Mn for 2 nm Fe overlayer on GaMnAs (*red*) and for 1.4 nm Fe overlayer (*yellow*); **d** XMCD lineshapes of samples of (**b**); **e** Fe L2,3 XMCD for 2nmFe/GaMnAs(Mn5 %); **f** hysteresis curves from XMCD of Fe (*red*) and Mn (*Green*): one observes the full antiparallel coupling and identical coercive fields. All the data were measured at T = 300 K [47]. (© *American Physical Society. Reprinted with permission*)

data on core levels or extended states. The use of I_{XMCD} has proven extremely fruitful also to study in detail the atomic level ordering in coupled molecular systems where the lineshapes of X-ray absorption with linear and circular polarization at cryogenic temperatures and under intense external $\boldsymbol{H}$ fields of several Tesla allow to

distinguish and recognize the symmetries of the relevant HOMO–LUMO final states involved in the X-absorption resonances [48]. Remanent magnetization was also found in metal-organic systems adsorbed in ferromagnetic surfaces giving evidence of exchange coupling at the hybrid interface, limited to the contact molecules [49].

20.6.2 The XMCD as a Magnetometer

Assuming $P_{circ} = 1$ (that means knowing the correction factor to be applied to the actual photon beam) and assuming saturation of the magnetization at the temperature T of the experiment, then the I_{XMCD} can be interpreted as an absolute magnetometry within some approximation [13]. The charge sum rule indicated above in the case of $p \rightarrow d$ transitions can be written as

$$\langle I_{L_3} + I_{L_2} \rangle = C N_h$$

where the dimensions of C are area times energy, or [Mb eV]. The above value is understood as the result of orientational averaged measurements. Provided analogous averaging is performed in XMCD experiments, i.e. saturation of M is forced by an applied field along three orthogonal k directions, then the averaged A and B intensities as defined in the drawings (from 13, p. 398) can be used as experimental input in the "spin sum rule" that connects such intensities with the spin moment per atom in the following way:

$$\langle -A + 2B \rangle = \frac{C}{\mu_B} m_s$$

The same experimental intensities can be combined in a different "orbital sum rule" that relates the dichroism with the average size of the orbital moment per atom in the following way:

$$-\langle A + B \rangle = \frac{3C}{2\mu_B} m_o$$

With this formulation the sum rules require careful orientation averaged data [13]. If the experimental information is limited to a given geometry other terms enter to account for the anisotropies that complicate the analysis but may give insight to quadrupolar charge distributions.

A sketch of the "sum rules" on the experimental intensities is presented in Fig. 20.19 (also from Stohr and Siegmann, [13]).

Although the m_s and m_o determinations are in principle quite powerful their values are affected by the incertitude on the actual saturation of the *M(T)* value. This is more easily obtained in ferromagnets displaying rectangular hysteresis although saturating along hard magnetization directions (to do the orientation average) may be challenging for the experimental set-up. In the case of paramagnetic molecular layers on surfaces again the degree of magnetic alignment versus $\boldsymbol{H}$ and versus

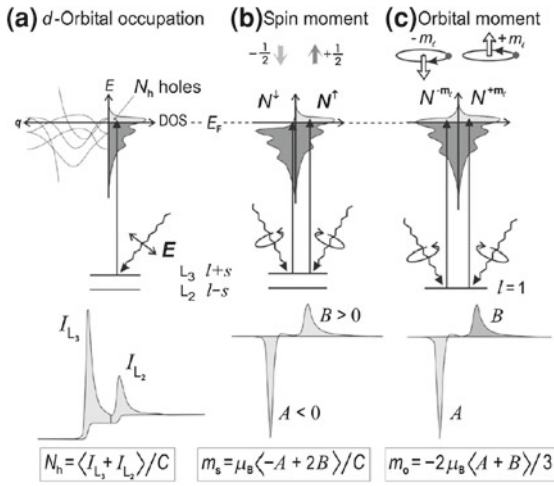


Fig. 20.19 XMCD spectra for monolayers of metal-phtalocyanines (FePc, CoPc, CuPc) lying "flat" on Au(110) surfaces at T = 8 *K* and under 5T applied field. In the case of a single layer of CoPc/Au(110) the interface bonding modifies the molecular orbital occupation and quenches completely the magnetic moment (no dichroim, central panel) [48]. (© *American Phyiscal Society. Reprinted with permission*)

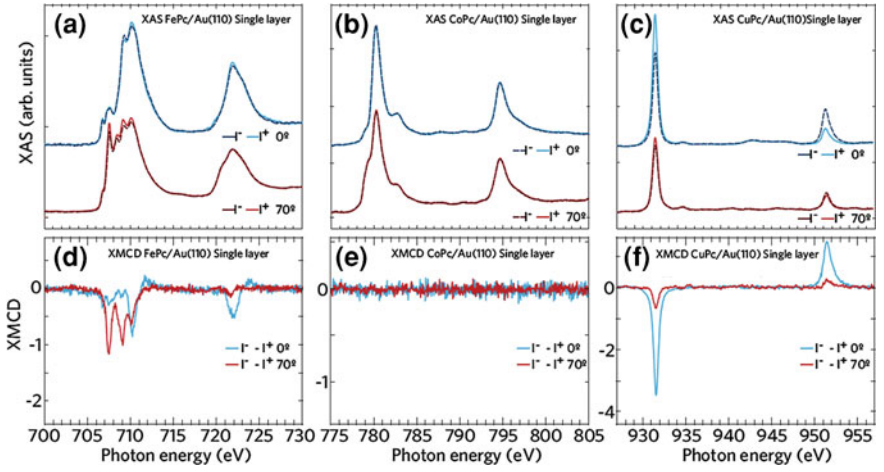


Fig. 20.20 Illustration of the XAS intensities and XMCD intensity-differences between dichroic spectra (as seen in Fig. 20.17). The sum rule on the total number of holes is shown under the XAS spectra, and the sum rules on the spin and orbital magnetic moments are shown under the dichroism spectra [13, 43, 44]. (© *Springer. Reprinted with permission*)

T must be explored and even several Tesla and few degrees Kelvin may not suffice to align all the moments preventing for a true absolute magnetometry unless a fitting to the Langevin function can be done reliably [48] (Fig. 20.20). The high sensitivity of XMCD and the quantitative analysis of moments allow to study the

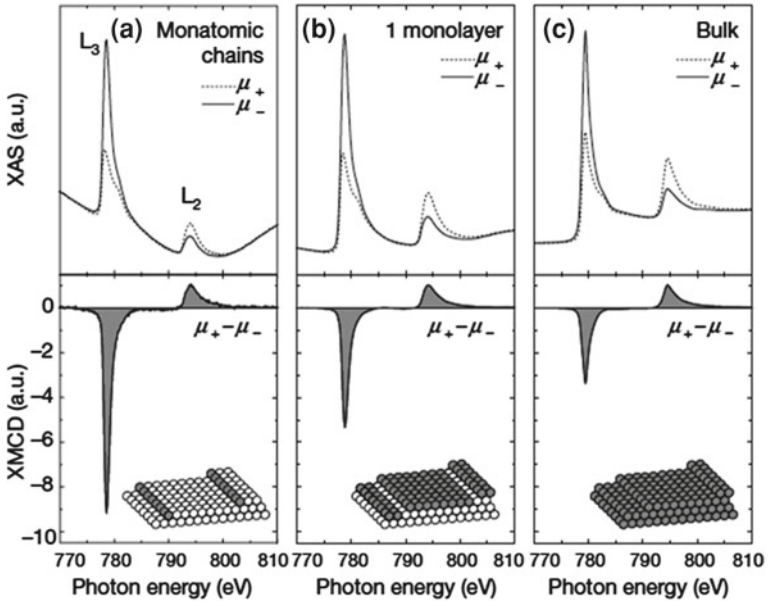


Fig. 20.21 Co XMCD spectra and dichroism (difference curves) for monoatomic chains at step edges (*left*) for one monolayer coverage of terraces (*center*) and for a thick film all grown on a Pt(997) vicinal (i.e. stepped) surface. The very large change in dichroism, through Sum-Rule analysis, indicates the increase of orbital magnetic moment in going from solid (film) to 2D layer (surface monolayer) 1D array (step decoration chains) [50]. Even larger increase of m_{orb} was measured for isolated Co impurities at the surface [51]. (© *Springer. Reprinted with permission*)

magnetic properties of low dimensional systems supported on surfaces. Evidence of large enhancements of magnetic anisotropy through the series 3D-2D-1D-0D for supported ferromagnetic atomic arrangements have been obtained providing novel insight in magnetism [50, 51] (Fig. 20.21).

XMCD is a powerful diagnostic and relative changes in I_{XMCD} are easily measured in studies where the sample environment is controlled (*T,* $\boldsymbol{H}$, $\boldsymbol{E}$, strain/stress, idrostatic pressure, electrochemical potential). Several beamlines at synchrotron sources are fully equipped to perform such experiments, allowing to switch *Lph* and to scan highly monochromatic photon beam energies in a fast manner. Fewer beamlines do offer cryogenic conditions and high magnetic fields sufficient for saturating *M(T)* so that the actual exploitation of the sum-rules for absolute spin and orbital moments and for magnetocrystalline anisotropy determination (see *XMLD*) are limited to ferromagnets and only some paramagnetic systems.

The exploitation of *XMCD* in the ultrashort time domain, as an obvious extension of the early fast magnetization studies based on the magneto-optical Kerr effect, is undergoing with new experimental set ups being implemented at Free Electron lasers (FLASH, LCLS, Fermi@Elettra) and will allow to follow time evolution of magnetic order parameters with pump-probe experiments at 10–100 fs resolution.

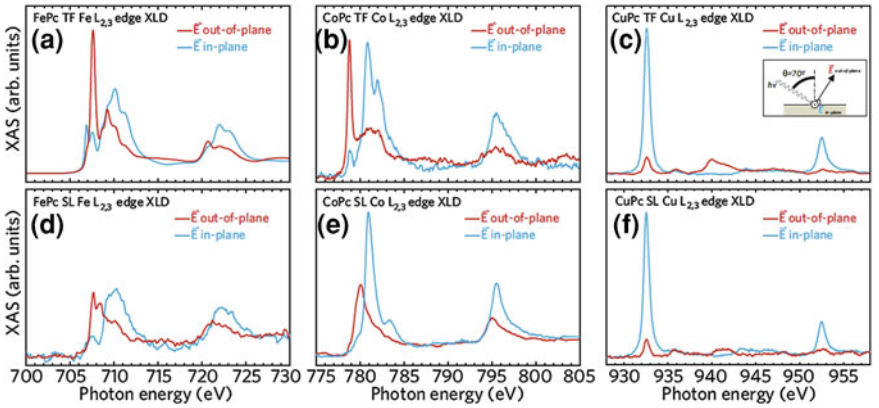


Fig. 20.22 XNLD spectra for the same systems as in Fig. 20.19: upper panels thin films on Au(110), lower panels Single Layer (monolayer films) on Au(110) [48]. (© *American Physical Society. Reprinted with permission*)

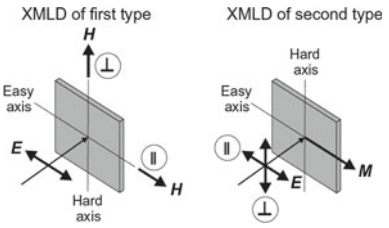


Fig. 20.23 XMLD spectra in the first and second kind of geometries. The first kind is a purely magnetic effect [13]. (© *Springer. Reprinted with permission*)

20.6.3 The XLD

By performing experiments in which the linearly polarized radiation of **E** vector is oriented with different angles with respect to anisotropic samples, one can exploit the linear dichroism that is consequent to the nonspherosymmetric charge distribution of the excited atom due to a low symmetry ligand field (Fig. 20.22), or to magnetization (magnetostriction). Natural LD (*XNLD*) refers to purely ligand field effects whilst magnetic *XMLD* refers to cases where magnetostriction is at work [13].

XNLD has a very broad application in intrinsically low symmetry systems like *2D* interfaces and monolayer at surfaces. In that case the anisotropy of the empty states parallel versus perpendicular to the surface (interface) is directly probed by impinging the linearly polarized light at normal incidence in one experiment and at glancing incidence in a second experiment, or exploring also intermediate incidence angles. When ***E*** is aligned along an orbital it gives maximum absorption, when it is otherwise oriented in a nodal plane it gives zero intensity. There is a simple formulation and definition of *XNLD* as "search light" effect of ***E*** with respect to the empty orbitals in the *low-D* system, equivalently one can describe the effect as probing the angular part of the matrix elements.

If one measures the X-absorption intensity as a function of angle between $\boldsymbol{E}$ and a symmetry axis, e.g. the surface/interface normal, then

$$\mathrm{I}(\Theta) = \mathrm{I}_{//}\cos 2\Theta + \mathrm{I}_{\perp}\sin 2\Theta$$

If the charge distribution has a node perpendicular to the symmetry axis then $\mathrm{I}_{\perp} = 0$ and the XNLD depends only on the $\cos 2\Theta$. This is the case for a uniaxial system.*XMLD* also probes the anisotropy of the atomic charge by a uniaxial field since the spins are axially aligned along $\boldsymbol{M}$ by exchange and consequently the spin-orbit interactions deforms the charge to become non spherical. A phenomenon that is measured also by magnetostriction. The appearance of *XMLD* requires unequal population of the m_j sublevels and an energy splitting that can be resolved by the experiment.

The I_{XMLD} is defined as a difference between measurements in two geometries: one in which the $\boldsymbol{E}$-vector is parallel to $\boldsymbol{M}$ and the other in which it is perpendicular.

$$\mathrm{I}_{XLMD} = \mathrm{I}_{//} - \mathrm{I}_{\perp}$$

By assuming the spin-spin splitting of the initial core hole level (similarly to the model for *LMDAD*) the I_{XLMD} is then the difference for all the individual transition intensities, that only partially overlap in the spectrum. The complete discussion is found in [13]. In systems of lower than cubic symmetry both *XNLD* and *XMLD* are present and need to be disentangled by experiment. Again proper geometries allow to do that by defining experiments of *XMLD* of first type where the light scattering geometry with respect to the surface normal and crystallographic axes is fixed and it is the magnetization that is rotated by 90° from the easy to the hard magnetization direction. Assuming that the applied $\boldsymbol{H}$ field is sufficient to saturate $\boldsymbol{M}$ in the hard direction the only net effect will be magnetic, i.e. *XMLD*, since the *XNLD* will be canceled by the spectral difference. The second possible geometry keeps $\boldsymbol{M}$ fixed in the easy axis and rotates $\boldsymbol{E}$ parallel and perpendicular (Fig. 20.23).

Both experiments become equivalent for negligible magnetocrystalline anisotropy or cubic or higher symmetry. A sum rule has been proposed by Carra et al. [52] and verified by Dhesi et al., [53] concerning the XMLD (first type) and the magnetocrystalline anisotropy energy ΔE_{SO} via the I_{XMLD} on L_3 and L_2 edges and the spin-orbit parameter.

20.6.4 The X-Ray Measurement of Ferromagnetic Resonance

Adding time resolution to XMCD allows to design pump-probe experiments and also to exploit ferromagnetic resonance (FMR) [54]. The oscillation of moments under resonance conditions can be probed by XMCD. The experiment consist in setting the frequency of oscillation of an applied magnetic field in phase with the X-ray pulses of the synchrotron source. The precession of the moments determines a periodic

alignment with the XMCD probing direction so that the XFMR can be probed and the dynamics properties of the sample explored in the frequency domain [54, 55].

20.7 Conclusions

Complete photoemission experiments and X-ray absorption dichroism experiments can be performed under different conditions at various synchrotron radiation measurement stations [56]. Advances and extreme sample environment will make many more experiments possible and will also develop in the directions of in-operando measurements (i.e. data acquisition while changing the sample environment, or while undergoing sample phase changes) and high-throughput, also thanks to submicrometric X-ray beams and scanning devices. A novel frontier is that of ultrashort-pulsed X-rays from free electron lasers where femtosecond time scale under high excitation-density conditions set the stage for exploring new physics.

References

1. C. Mariani, G. Stefani, in *Synchrotron Radiation: Basics, Methods and Applications*, ed. by F. Boscherini, C. Meneghini S. Mobilio (Springer, Heidelberg, 2014, this volume), pp. 275–317
2. J. Osterwalder, Lect. Notes Phys. 697, 95–120 (2006) Springer Verlag Berlin Heidelberg (2006), and references quoted therein
3. J. Osterwalder, J. Phys.: Condens. Matter **24**, 171001 (2012)
4. U. Heinzmann, J.H. Dil, J. Phys.: Condens. Matter **24**, 173001 (2012)
5. F. Meier, J.H. Dil, J. Osterwalder, New J. Phys. **11**, 125008 (2009)
6. J.H. Dil, J. Phys.: Condens. Matter **21**, 403001 (2009)
7. C.M. Bertoni, in *Synchrotron Radiation: Basics, Methods and Applications*, ed. by F. Boscherini, C. Meneghini S. Mobilio (Springer, Heidelberg, 2014, this volume), pp. 145–178
8. J. Kessler, *Polarized Electrons* (Springer, Berlin, 1976)
9. G. Rossi, F. Sirotti, N.A. Cherepkov, F. Combet-Farnoux, G. Panaccione, Solid State Commun. **90**, 557–562 (1994)
10. L. Baumgarten, C.M. Schneider, H. Petersen, F. Schafers, J. Kirshner, Phys. Rev. Lett. **65**, 492 (1990)
11. G. van der Laan, M.A. Hoyland, M. Surman, C.F.J. Flipse, B.T. Thole, Phys. Rev. Lett. **69**, 3827 (1993)
12. P. Fornasini, in *Synchrotron Radiation: Basics, Methods and Applications*, ed. by F. Boscherini, C. Meneghini S. Mobilio (Springer, Heidelberg, 2014, this volume), pp. 181–211
13. J. Stohr, H.C. Siegmann, Magnetism From Fundamentals to Nanoscale Dynamics (Springer, 2006). ISSN 0171–1873.
14. M. Mulazzi, G. Rossi, J. Brown, J. Minar, H. Ebert, G. Panaccione, I. Vobornik, J. Fujii, Phys. Rev. **B79**, 165421 (2009)
15. G. Panaccione et al., Rev. Sci. Instrum. **80**, 043105 (2009)
16. V.N. Petrov, M.S. Galaktionov, A.S. Kamochkin, Rev. Sci. Instrum. **72**, 3728 (2001)
17. R. Clauberg, W. Gudat, E. Kisker, E. Kuhlmann, Z. Phys. B: Condens. Matter **43**, 47–54 (1981)
18. L. Moreschini, G. Ghiringhelli, K. Larsson, U. Veit, N.B. Brookes, Rev. Sci. Instrum. **79**, 033905 (2008)
19. M. Kolbe et al., Phys. Rev. Lett. **107**, 207601 (2011)
20. B. Krömker, J. Kirschner et al., Rev. Sci. Instrum. **79**, 053702 (2008)

21. C. Jozwiak et al., Rev. Sci. Instrum. **81**, 053904 (2010)
22. T. Okuda, Y. Takeichi, Y. Maeda, A. Harasawa, I. Matsuda, T. Kinoshita, A. Kakizaki, Rev. Sci. Instr. **79**, 123117 (2008)
23. G. Rossi, G. Panaccione, F. Sirotti, Phys. Rev. **B54**, 4080 (1996)
24. M.R. Scheinfein et al., Rev. Sci. Instrum. **61**, 2501 (1990)
25. H.C. Siegmann, J. Phys.: Condens. Matter **4**, 8395 (1992)
26. F. Sirotti, G. Panaccione, G. Rossi, Journal de Physique IV, Colloque C9, 175–178, supplement, Journal de Physique III, vol 4 (1994).
27. H.C. Siegmann, in Core Level Spectroscopies for Magnetic Phenomena: Theory and Experiment, ed. by P.S. Bagus, G. Pacchioni, F. Parmigiani. NATO ASI Series B: Physics, vol 345 (Plenum, New York, 1995).
28. F. Sirotti, G. Panaccione, G. Rossi, Phys. Rev. **B52**, R17063–R17072 (1995)
29. E. Kisker, W. Gudat, E. Kuhlmann, R. Clauberg, M. Campagna, Phys. Rev. Lett. **45**, 2053 (1980)
30. G. Schonhense, Phys. Rev. Lett. **44**, 640–643 (1980)
31. Ch. Roth, F.U. Hillebrecht, W.G. Park, H.B. Rose, E. Kisker, Phys. Rev. Lett. **73**, 1964 (1994)
32. Ch. Roth, F.U. Hillebrecht, H.B. Rose, E. Kisker, Phys. Rev. Lett. **70**, 3479 (1993)
33. F. Sirotti, G. Rossi, Phys. Rev. **B49**, 15682 (1994)
34. A. Baraldi, in *Synchrotron Radiation: Basics, Methods and Applications*, ed. by F. Boscherini, C. Meneghini S. Mobilio (Springer, Heidelberg, 2014, this volume), pp. 519–538
35. F. Bruno, G. Panaccione, A. Verdini, R. Gotter, L. Floreano, P. Torelli, M. Sacchi, F. Sirotti, A. Morgante, G. Rossi, Phys. Rev. **B66**, 024417 (2002)
36. G. Panaccione, F. Sirotti, G. Rossi, Solid. State Comm. **113**, 373–377 (2000)
37. C. Jozwiak, P. Cheol-Hwan, K. Gotlieb, C. Hwang, L. Dung-Hai, S.G. Louie, D. Denlinger, C.R. Rotundu, R.J. Birgeneau, Z. Hussain, A. Lanzara, Nat. Phys. **9**, 293–298 (2013)
38. M. Mulazzi, M. Hochstrasser, J. Fujii, I. Vobornik, G. Rossi, J. Henk, Europhys. Lett. **82**, 57001 (2008)
39. M. Hoesch et al., J. Electron Spectrosc. Relat. Phenom. **124**, 263 (2002)
40. M. Muntwiler, M. Hoesch, V.N. Petrov, M. Hengsberger, L. Patthey, M. Shi, M. Falub, T. Greber, J. Osterwalder, J. Electron. Spec. Rel. Phen. **137–140**, 119–123 (2004)
41. M. Hoesch, M. Muntwiler, V.N. Petrov, M. Hengsberger, L. Patthey, M. Shi, M. Falub, T. Greber, J. Osterwalder, Phys. Rev. **B69**, 241401 (2004)
42. G. van der Laan et al., Phys. Rev. **B34**, 6529 (1986)
43. B.T. Thole et al., Phys. Rev. Lett. **68**, 1943 (1992)
44. P. Carra et al., Phys. Rev. Lett. **70**, 694 (1993)
45. C.T. Chen, Y.U. Idzerda, H.-J. Lin, N.V. Smith, G. Meigs, E. Chaban, G.H. Ho, E. Pellegrin, F. Sette, Phys. Rev. Lett. **75**, 152 (1995)
46. A. Locatelli, S. Cherifi, S. Heun, M. Marsi, K. Ono, A. Pavlovska, E. Bauer, Surf. Rev. Lett. **09**, 171 (2002)
47. M. Maccherozzi, M. Sperl, G. Panaccione, J. Minar, S. Polesya, H. Ebert, U. Wurstbauer, M. Hochstrasser, G. Rossi, G. Woltersdorf, W. Wegschneider, Ch. Back, Phys. Rev. Lett. **101**, 267201 (2008)
48. P. Gargiani, G. Rossi, R. Biagi, V. Corradini, M. Pedio, S. Fortuna, A. Calzolari, S. Fabris, J.C. Cezar, N.B. Brookes, M.G. Betti, Phys. Rev. **B87**, 165407 (2013)
49. E. Annese, F. Casolari, J. Fujii, G. Rossi, Phys. Rev. **B87**, 054420–6 (2013)
50. P. Gambardella, A. Dallmayer, K. Maiti, M.C. Malagoli, W. Eberhardt, K. Kern, C. Carbone, Nature **416**, 302 (2002)
51. P. Gambardella et al., Science **300**, 1130 (2003)
52. P. Carra, H. Koenig, B.T. Thole, M. Altarelli, Physica B **192**, 182 (1993)
53. S.S. Dhesi, G. van der Laan, E. Dudzik, A.B. Shick, Phys. Rev. Lett. **87**, 067201 (2001)
54. J. Goulon et al., JETP Lett. **82**, 696 (2005)
55. G. Boero, S. Rusponi, P. Bencock, R.S. Popovic, H. Brune, P. Gambardella, Appl. Phys. Lett. **87**, 152503 (2005)
56. F. Wilhelm, Synchrotron Radiat. News **26**(6), 2–5 (2013)

Chapter 21
Chemical and Magnetic Imaging with X-Ray Photoemission Electron Microscopy

Andrea Locatelli and Tevfik Onur Menteş

Abstract X-ray photoemission electron microscopy (XPEEM) is a full-field imaging technique giving access to the chemical state and magnetic order of laterally inhomogeneous surfaces, interfaces and thin films. In its simplest variant, synchrotron-based PEEM uses secondary emission to map local differences in the oxidation state, valence, and bond orientation around the emitter. The combination with X-ray circular and linear dichroism techniques represents the most frequent application, and has found extensive use in imaging ferromagnetic and antiferromagnetic domains. XPEEM instruments with energy filter can implement laterally resolved X-ray photoelectron spectroscopy (XPS) and angle resolved photoelectron spectroscopy (ARPES), reaching high chemical and electronic structure sensitivity. Here, we describe the basic aspects and methods of synchrotron-based spectromicroscopy with the PEEM, and its combination with low energy electron microscopy (LEEM). The present state of the art of the technique will be illustrated by applications in diverse fields, spanning from surface and materials sciences to biology and magnetism.

21.1 Introduction

The investigation of nanostructured materials and composite interfaces necessitates analytical characterization methods that combine the capabilities of X-ray photoemission spectroscopy with those of microscopy at the nanometer scale. The high brilliance of third generation synchrotron radiation sources has promoted the rapid

A. Locatelli (✉) · T. O. Menteş
Elettra-Sincrotrone Trieste S.C.p.A., Strada Statale 14, km 163.5 Area Science Park,
34149 Basovizza, Trieste, Italy
e-mail: andrea.locatelli@elettra.eu

T. O. Menteş
e-mail: tevfik.mentes@elettra.eu

S. Mobilio et al. (eds.), *Synchrotron Radiation*,
DOI: 10.1007/978-3-642-55315-8_21, © Springer-Verlag Berlin Heidelberg 2015

development of a variety of spectromicroscopic investigation tools, either implementing the scanning or the full-field approach [1]. They enable laterally resolved versions of the most popular X-ray spectroscopies, providing chemical, magnetic and electronic structure sensitivity. Among them, one of the most prominent is photoemission electron microscopy (PEEM), often used in combination with X-ray absorption spectroscopy and its close derivatives, circular and linear magnetic dichroism [2, 3]. Energy filtering capability and combination with low energy electron microscopy (LEEM) have further widened the application field of synchrotron radiation photoemission electron microscopy, paving the way to the use of electron spectroscopy for the chemical characterization of nanomaterials at high lateral resolution [4]. The last decade has witnessed a rebirth of the early interest in geology and biology, with several new developments in the study of biominerals [5].

PEEM has a long and exciting history [6], whose beginning dates in 1933, when the German physicist Brüche demonstrated that photoelectrons produced by UV light could be used for imaging when accelerated to high energy. Modern instruments still use the same operating principle but have evolved tremendously, due to parallel progress in electron optics, UHV technology, and electron detection. The simultaneous development of third generation synchrotron radiation sources has enabled spectroscopic imaging, taking advantage of the high brilliance and tuneability of undulator sources. For this reason, photoemission electron microscopy beamlines are frequently found in modern synchrotron radiation laboratories. Thanks to the versatility of PEEM, application fields are manifold, and mirror the heterogeneity of the synchrotron user community.

This work aims at providing a broad overview on XPEEM spectromicroscopy. We follow a practical approach to the technique, placing the emphasis on method and applications, offering also a quick guide to the vast and rapidly growing literature, which can be accessed through numerous topical reviews [7–11]. In Sect. 21.2 we summarize the basic concepts of PEEM; its operation principle and methods are then detailed; Sect. 21.3 illustrates the PEEM methodology through a variety of applications, highlighting the most recent developments and the state-of-the-art of the technique.

21.2 Photoemission Electron Microscopy

PEEM is a full-field, *direct* imaging technique. The microscope images a restricted portion of the specimen area illuminated by the photon beam. Photoemitted electrons are collected at the same time by the optics setup, which produces a magnified image of the surface. The key element of the microscope is the objective lens, also known as cathode or immersion lens, of which the sample is part. The aberrations introduced by the objective dominate over those of the other optical components, and usually determine the ultimate resolution of the microscope. Even without aberration correction, the PEEM can routinely reach a lateral resolution approaching few tens nm.

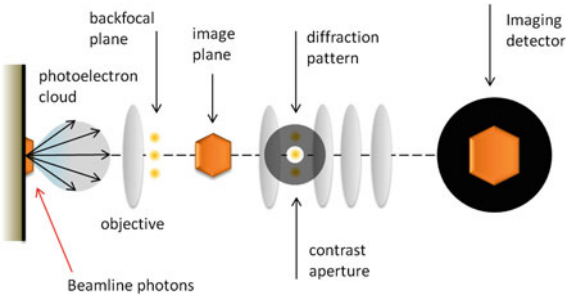


Fig. 21.1 Basic setup of a PEEM. The *red arrow* represents the focused X-ray beam, stimulating the emission of a photoelectron cloud. The photoelectron beam is accelerated by the strong electric field of the objective lens, which produces a magnified image of the sample, eventually projected onto the imaging detector

21.2.1 Instrumental Aspects

21.2.1.1 Operating Principle

The photons illuminate the sample, typically at grazing incidence (see Fig. 21.1). The photoelectrons emitted from the surface are collected in normal emission geometry, strongly accelerated by the intense electric field (few kV/mm) that is applied between the sample (cathode) and the outer electrode of the objective lens (anode). The objective lens produces a magnified image of the specimen and, for crystalline surfaces, creates an image of the diffraction pattern which is located in the lens back-focal plane (BFP). Many instruments can image the objective BFP, enabling access to such diffraction pattern. The objective lens is typically followed by other electron optical elements, which form the imaging column of the microscope. A complex optical system comprising transfer and projector lenses allows changing the magnification or choosing a different operation mode. Some instruments are equipped with energy filter, which may implement either the high-pass or band-pass design. At the end of the imaging column, the magnified image of the sample is projected onto an imaging detector. Typically, the detector consists of a double stage micro channel plate (MCP) image intensifier coupled to a phosphorous screen. Sensitive cameras with CCD or sCMOS pixel detectors are used to acquire the image produced on the phosphorous screen. Computer controlled data acquisition enables video frame rate. Novel, in vacuo operated CMOS detectors are currently being developed as an alternative to MCPs [12]. Their performance, both in terms of lateral resolution and speed, is expected to soon surpass that of the MCP-CCD combination.

21.2.1.2 Lateral Resolution

In practice, the objective lens is far more complex than the simple electrostatic lens consisting of two parallel planes kept at different potential. Its front electrode is shaped as a truncated cone, with a small hole allowing electrons to continue their

path through the optical system. Purely electrostatic and electromagnetic variants of the objective lens are available, namely the electrostatic triode and tetrode, and the electromagnetic triode, to mention the most common. The calculated lateral resolution can approach few nm, depending on the exact geometry chosen [13].

An indispensable part of the PEEM is the contrast aperture, an iris that is inserted in the objective back-focal plane, or in any other crossover along the optical path. The opening size of this aperture defines the angular acceptance of the microscope. Diminishing the angular acceptance suppresses spherical and chromatic aberrations, thus improving the lateral resolution. In the homogeneous field approximation, the resolution loss can be treated analytically [14]. Chromatic and spherical aberrations determine a smearing that increases with the first and third power of the acceptance angle respectively, while the diffraction limit dominates at small acceptance angles. It can be seen that the improvement of lateral resolution is accompanied by the decrease of microscope transmission; a compromise has to be found case by case depending on experimental conditions.

The correction of the spherical and chromatic aberrations by an electron mirror has nowadays become a reality, de facto improving the resolution limit of PEEM. Instruments with different optical design have been proposed and several prototypes have already been built [15–17]; notably, commercial versions of these microscopes are already available. Aberration corrected (AC) instruments have already demonstrated 15 nm lateral resolution in PEEM [18] and about 2 nm in LEEM [18, 19]. As far as PEEM is concerned, space charge phenomena might impede reaching the calculated performance of AC instruments [20]. Interestingly, the correction of the aberrations not only improves the lateral resolution, but also the transmission, as larger contrast apertures can be used while keeping the contribution of spherical and chromatic aberrations low [15].

21.2.1.3 Practical Issues

Samples must exhibit a smooth and flat morphology. Rough surfaces and sharp objects like nanotubes should be avoided. Fresnel diffraction from asperities can in fact create an artificial modulation of the illumination intensity, making compositional analysis complex. Further, the intense electric field applied between sample and objective might induce high voltage leakage or discharges, which can lead to lateral resolution loss and surface contamination. Other techniques, such as scanning photoemission microscopy (SPEM) and scanning transmission X-ray microscopy (STXM), are much more versatile in this regard, because no high voltage is applied to the sample. In order to avoid discharges between sample and objective, the PEEM must be operated in the pressure range below 10^{-4} mbar. High pressure decreases also the electron mean free path in vacuum, diminishing notably the collection efficiency. Other techniques can be more fruitfully employed in such conditions. High pressure variants of SPEM and STXM microscopes have been successfully built, based on a special design of the electron energy analyzer which includes a multistage differential pumping system [21].

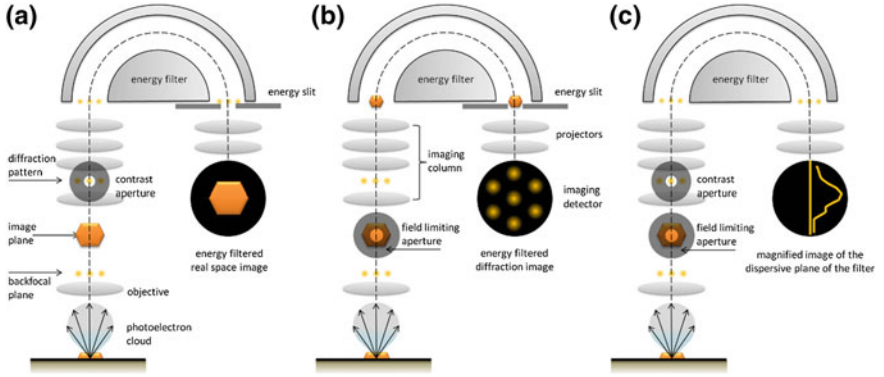


Fig. 21.2 Electron optics configuration of the SPELEEM microscope in three different operation modes: **a** imaging mode, used in XPEEM spectroscopic imaging; **b** spectroscopic diffraction imaging; the area of interest is selected by inserting an aperture in the image plane after the objective lens; **c** microprobe-spectroscopy operation. The last projectors of the microscope are set to image the dispersive plane of the energy filter. This appears as a line, and its intensity profile represents the photoemission spectrum. Reprinted from [23]. Copyright (2012), with permission from Elsevier

21.2.2 Combination with Low Energy Electron Microscopy

PEEM is often employed in combination with low energy electron microscopy (LEEM) [13, 22]. LEEM is a cathode lens microscopy technique which probes surfaces and interfaces with elastic backscattering of low energy electrons. Owing to the large electron backscattering cross section of most materials, LEEM warrants acquisition at video frame rate. Therefore, it is particularly well suited to monitor dynamic processes, such as surface reconstructions, epitaxial growth, step dynamics, self-organization, etc. LEEM adds structure sensitivity to the capabilities of synchrotron based PEEM, providing several complementary methods for structural characterization, of which the most important is low energy micro-probe diffraction (μ-LEED). In addition, dark-field operation (using secondary diffracted beam for imaging) may be used to assess the lateral extent of well-defined surface phases and their rotational domains. Mirror electron microscopy is another technique available in a LEEM microscope, which is particularly useful to image the morphology of non-crystalline samples exploiting work function contrast.

The electron optics layout of a LEEM generally exhibits a high complexity, due to the need of switching between different operation modes. LEEM offers PEEM as a byproduct, provided a UV or X-ray source can illuminate the sample. A special case is that of the spectroscopic photoemission and low energy electron microscope (SPELEEM), a hybrid LEEM-XPEEM microscope that is equipped with band-pass energy filter [24]. The SPELEEM is a unique multi-method instrument offering imaging, microprobe-diffraction, and microprobe-spectroscopy capability. Depending whether electrons or photons are used as probe, one can carry out LEEM,

electron energy loss spectroscopy (EELS), or PEEM imaging. By choosing diffraction operation, microprobe LEED, microprobe X-ray photoelectron diffraction (XPD) and ARPES are available, all requiring the use of the energy filter. The region of interest is selected by means of a field limiting aperture inserted in one of the image planes of the instrument. Microprobe spectroscopy, or micro-XPS, is yet another operation mode, which allows spectroscopic acquisition based on imaging the dispersive plane of the energy filter. The three different electron optics configurations of the SPELEEM are illustrated by the diagram in Fig. 21.2. Chromatic and spherical aberration have been shown to affect microprobe operation, causing the contamination of the signal emitted from the area of interest with the signal from the neighboring areas [25].

21.2.3 PEEM Methods

Work function contrast In its simplest form, PEEM can be used to measure the lateral variations of the surface work function. In laboratory instruments using UV sources, higher work function results in a lower photoelectron yield, thus giving a direct contrast mechanism. The addition of the energy filter, together with the higher photon energies of the X-ray beam, allows to quantitatively measure relative work function changes across the surface. This is achieved by measuring the onset of photoemission on the secondary photoelectron yield.

XAS Relevant for most XPEEM studies, the soft X-ray regime below 1 keV is particularly important in near-edge spectroscopy, due to transitions which include the K edges of carbon and oxygen, L, M and N edges of transition metals. The former ones open possibilities on organic and carbon related materials, whereas the latter is crucial in chemical and magnetic studies regarding metal and metal-oxide materials. In an XPEEM instrument X-ray absorption spectroscopy can be performed in a laterally-resolved manner by measuring the intensity of the secondary emission yield as a function of photon energy. The energy resolution is determined by the X-ray monochromator, and no energy analyzer is required. Moreover, the large inelastic mean free path of the low secondary photoelectron energies (typically less than 10 eV) allows probing buried layers and interfaces down to a depth of more than 5 nm. Tonner and Harp initiated the use of PEEM at synchrotron radiation sources; their electrostatic instrument first demonstrated spectroscopic imaging in combination with near edge absorption spectroscopy (XANES) [26].

XMC(L)D PEEM From the microscopy standpoint, X-ray dichroism can be used to image magnetic surfaces in a straightforward manner, as a natural extension of X-ray absorption spectroscopy using a synchrotron-based XPEEM setup [27]. X-ray magnetic linear dichroism (XMLD) and circular dichroism (XMCD) are implemented by imaging the secondary photoelectrons emitted upon absorption of X-rays with given polarization. In XMCD-PEEM, the grazing incident angle of the photons determines a preferential sensitivity to the in-plane component of the

magnetization vector in magnetic materials. The magnetic contribution to the image contrast is extracted by taking the difference of two images with different photon polarization (circular left/right in the case of XMCD-PEEM, linear vertical/horizontal for XMLD-PEEM) and normalizing the result with the sum of the two images. The circularly polarized case results in an image of the ferromagnetic domains, with the domains oriented parallel or antiparallel to the X-ray direction giving opposite contrast. The image algebra used to obtain the dichroic image cancels out all other contrast mechanisms except the magnetic one. In the case of XMLD-PEEM, the magnetic signal is proportional to the square of the dot product between the X-ray polarization vector and the local magnetization vector. For antiferromagnetic surfaces, a comparison between images taken with mutually orthogonal polarization states (e.g. linear horizontal and linear vertical) results in a spatially-resolved map of antiferromagnetic domains of different spin axis.

XPS, UPS and ARPES Energy-filtered PEEM can be carried out in imaging, diffraction or spectroscopy modes, collecting electrons photoemitted from atomic core levels or the valence band. The binding energy of a core level electron, E_b, can be determined from the well known relation $E_k = \hbar\omega - E_b - \phi$, where $\hbar\omega$ is the energy of the X-ray or UV beam, kept fixed, and ϕ the work function of the analyzer [28]. In practice, E_k is unknown and can be replaced by V_{start}, the bias voltage which is applied to the sample. In this way, $V_{start} = \hbar\omega - E_b - \delta\phi$, where $\delta\phi$ is the work function difference between sample and analyzer. Spectral imaging is carried out by acquiring images for different values of E_k, which is done by varying V_{start}. Local spectra are extracted from the resulting image-stack by calculating the (average) intensity in well-defined regions of interest for each image. Since the core-level photoemission intensity is directly proportional to the number of surface emitters, XPEEM is primarily used to determine quantitatively the local coverage of a certain adsorbate. In addition to the intensity, differences in the binding energy may cause further contrast variations, permitting a visual identification of chemically nonequivalent atoms of a given species. Normal emission favors sensitivity to bulk. Exacerbating this concept, hard X-rays spectroscopic-imaging of buried layers has been recently demonstrated (HAXPES-PEEM) [29]. Valence band photoemission PEEM may be used to map variations in the local electronic structure. These quantitative measurements, for instance, give a direct measure of the density of states at the Fermi level. Some energy-filtered microscopes can also be operated in microprobe-XPS or microprobe-diffraction modes. Microprobe-XPS mode allows much faster acquisition times as well as optimal energy resolution, at the price of a limited lateral resolution (defined by the size of the field limiting aperture). Microprobe-diffraction mode is typically used to image the full angle-resolved photoemission pattern, thus enabling to probe the electronic structure of the surface.

21.3 Applications and Examples

21.3.1 Chemical Imaging of Nano-Structured Surfaces and Interfaces

The exploitation of energy-filtered PEEM as analytic investigation method began in the mid-90s, using the first prototype of Bauer's SPELEEM. This instrument reached 22 nm lateral resolution in imaging mode, demonstrating also microprobe ARPES and microspectroscopy operations [24]. Among early applications, we recall the study of Au-induced faceting of vicinal Si(100), where LEEM and XPEEM were used to image in situ and real-time the giant restructuring of the surface [30]. By monitoring Au $4f$ and Si $2p$ core levels, the experiments could quantify the critical Au coverage needed for (001) terrace expansion, and subsequent adsorption on step bunches for creation of the (119) facets [30]. LEEM and LEED provided here useful complementary information, which have led to a better understanding of the structural transformation dynamics. Since then, the SPELEEM has been routinely used in applications in materials and surface sciences. For instance, the high lateral resolution of PEEM was key to assess the surface stoichiometry of a wide variety of semiconductor quantum dots [31], nano-structures [32, 33], and even single wall carbon carbon nanotubes [34]. XPEEM was also employed for the characterization of metallic nanoparticles on oxide substrates, and in particular Au [35, 36] and Pd [37] on the (110) surface of rutile titania. Oxide surfaces, however, are often hampered by charging, beam-induced damage and substrate reduction effects [38].

Following the experiments on chemical waves by G. Ertl, synchrotron radiation spectromicroscopy was successfully employed in the study of spatio-temporal patterns during surface catalytic reactions. Contrary to laboratory based UV-PEEM, synchrotron based PEEM provides the advantage of true elemental sensitivity [39]. This approach is mandatory for complex reactions involving the co-adsorption of more than one species, where simple work function contrast would not unambiguously disentangle the adlayer composition. SPEM was initially applied to study the NO reduction reaction by hydrogen on Rh(110), where alternating oxidation and reduction fronts propagate producing target or spiral spatio-temporal patterns [40]. Spectromicroscopy was here crucial to quantify the coverage of the various adspecies, enabling theorists to develop a mathematical model for the reaction. Similar experiments, carried out with the microprobe-LEED operation mode of the SPELEEM, could precisely identify the related changes in surface structure [41]. Following this experiment, a few XPEEM investigations focused on the reaction induced mass transport of alkali [42, 43], and noble metals [44]. XPEEM was also successfully employed to investigate reactive phase separation phenomena, i.e. processes where the reaction inhibits a phase separation of the adlayer favoring the formation of regular compositional stationary patterns. Such phenomena were first observed in K adlayers during the water formation reaction on Rh(110) [45]; reaction-induced organization processes were also observed in Au + Pd submonolayers, for the same reaction system [46]. By using LEEM, the pattern wavelength was found to obey a

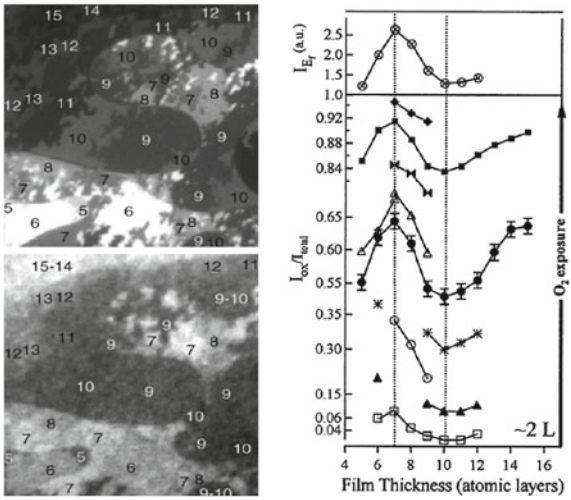


Fig. 21.3 (*Top left*) 5 × 5 μm LEEM image of Mg/W(110) showing reflectivity changes due to quantum well states in the film. Film thickness is indicated by labels (*Bottom left*) XPEEM image of the same film after exposure to 9 L of O_2 at 320 K. The image intensity corresponds to the extent of local Mg oxidation. (*Right*) Correlation between DOS at E_F and film reactivity as a function of Mg thickness. Reprinted with permission from [49]. Copyright (2004) by the American Physical Society

power-law dependence on the reaction rate [46], verifying previous theoretical predictions. Comprehensive reviews on these works can be found in [39, 47]. Recently, XPEEM experiments were extended to more complex systems such as vanadium oxide layers on a Rh(111) [48].

The SPELEEM methodology is well illustrated by experiments making full use of its multi-technique ability. An exemplary case is provided by the study on the reactivity of Mg thin films by Aballe et al. [49], which addressed the important subject of the size-dependent chemical activity. For this purpose, Mg was deposited at such temperature to obtain quasi layer-by-layer growth mode, resulting in the development of multi-thickness regions. Quantum size contrast in LEEM [50] was exploited to precisely determine the local thickness. Subsequently, the same film was exposed to molecular oxygen and XPEEM was used to locally evaluate the film oxidation, which was ascertained by fitting the Mg 2*p* spectrum. The correlation between film thickness and oxidation rate can be appreciated in Fig. 21.3. Microprobe-XPS experiments could successfully link the oscillations in reactivity to periodic variations in the density of states at the Fermi level, originated by thickness dependent quantum resonances crossing the Fermi surface. The decay length in vacuum of such electronic states was later invoked to explain the observed variations in reactivity [51]. A subsequent study of the oxidation rate in ultra-thin Al films grown on W(110) confirmed the above interpretation, although the analysis could not exclude other effects, such as of O_2 ionization, spin, and molecular rotations [52].

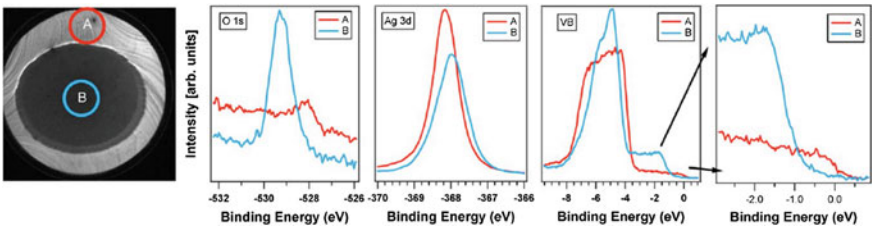


Fig. 21.4 From *left* to *right*. Mirror electron microscopy image of an oxide patch formed by dosing 70 L NO_2 at 300 K under irradiation with 40 eV electrons (flux = 2 pA/μm^2, fluence = 1.5×10^{10} electrons/μm^2. Spectra obtained outside (*A*) and inside (*B*) the irradiated zones, identified by the labels. Reprinted with permission from [53]. Copyright 2009, "American Institute of Physics"

In another class of experiments, initiated by Bauer and co-workers [36], the LEEM e-beam is exploited to promote surface modifications. The study of the e-beam assisted oxidation of Ag(111) demonstrates chemical patterning of the surface without the use of any resist, providing an elegant demonstration of the capabilities of this technique [53]. The oxidation of the Ag surface was here obtained by irradiating the surface while dosing NO_2 at 300 K. Under normal conditions, NO_2 adsorbs dissociatively, with NO_{ad} inhibiting surface oxidation. Irradiation with low energy electrons, however, induces the desorption of NO_{ad}, causing the accumulation of atomic oxygen. Microprobe spectroscopy could determine the surface chemical state of the e-beam irradiated area. Figure 21.4 shows local spectra taken outside (A) and inside (B) the oxide patch formed after dosing 70 L NO_2 at 300 K under irradiation with 40 eV electrons. The higher oxygen concentration in B becomes evident after comparison with the spectrum of the surrounding area, characterized by the 4×4 reconstruction. The energy of the Ag 3*d* spectrum in A indicates that silver is metallic, whereas the shift observed in B suggests the formation of Ag_2O; this interpretation is confirmed by the valence band spectra, which does not show a Fermi level within the oxide patch B.

21.3.2 Graphene

The extraordinary scientific interest in graphene has recently motivated a large number of experimental studies on this intriguing material. Cathode lens microscopy have been widely employed, providing a wealth of information about the morphology and crystal structure of few layer graphene (FLG) grown on transition metals as well as supported on a variety of Si substrates [54, 55]. LEEM had a prominent role in these studies, addressing the nucleation and growth of several graphene epilayers [56, 57]; these analyses were often complemented by microprobe diffraction, which enabled precise understanding of the lattice periodicity in moiré patterns [58]. Compared to other techniques, LEEM offers the advantage of thickness determination by quantum

size contrast. The low energy electron reflectivity of FLG was incorrectly interpreted in a few cases [59, 60] and eventually clarified by ab initio calculations by Feenstra et al. [61].

A few XPEEM studies are reported in the literature. The XANES K-edge absorption spectrum of exfoliated FLG on SiO_2 was characterized using both SPEM [62] and PEEM [63]. One of these studies identified spectral features reflecting the properties of the unoccupied states of a single layer [63]. A splitting of the π^* resonance in FLG was ascribed to interlayer states, but these results were later questioned [64]. Recently, the dark-field (df) PEEM method has been demonstrated, [23, 65] paving the way to laterally-resolved measurements of the local density of states of the π band. Such experimental approach was successfully used to characterize graphene on Ir(100) [66]. Here, distinct graphene phases characterized by flat and buckled morphology coexist at room temperature. They form stripe-shaped domains which relieve the strain accumulated during cooling from growth temperature. By imaging emission from graphene's π-band at the reciprocal space K point, df-PEEM enabled a direct comparison of the film local electronic structure. The low image intensity observed in buckled graphene points to the disruption of the Dirac cones (see Fig. 21.5). The hybridization with Ir states was found to be determined by the chemisorption of a surprisingly small fraction of C atoms to the Ir substrate.

Microprobe-APRES operation available was also used to study the electronic structure of epitaxial [67–69] and exfoliated graphene [70, 71]. The method applicability is however limited by the modest energy resolution of XPEEM microscopes, of the order of few hundred meV. Fine details in graphene band structure, e.g. phonon induced broadening and band-splitting in graphene bilayers, cannot be resolved, making conventional ARPES more appealing. In practice, LEEM has been often employed as a preparation method for optimizing growth conditions, in view of subsequent ARPES analysis, to be carried out with dedicated instruments. As a further limitation, experiments on SiO_2-supported graphene are hampered by substrate-induced corrugations, which determine severe broadening effects in ARPES due to the lack of coherence of the photoelectron wave [70]. A method was devised to extract energy-dependent band-structure information from corrugated layers, based on independent ARPES and LEED measurements [71].

21.3.3 Biominerals

PEEM was applied to biology and medical sciences already starting from the mid 60s [6]. Later, Griffith and Rempfer performed extensive work in these fields [73], before Tonner and Harp introduced PEEM at synchrotron radiation sources [26]. Using their instrument, de Stasio et al. could image neurons using XANES [74]. Since then, XANES-PEEM has became an established method, counting up an increasing number of applications in various related research fields and also geology. More recently, Gilbert et al. have investigated several biominerals [5], motivated by the interest in biological control on crystal nucleation, growth, self-assembly and templation.

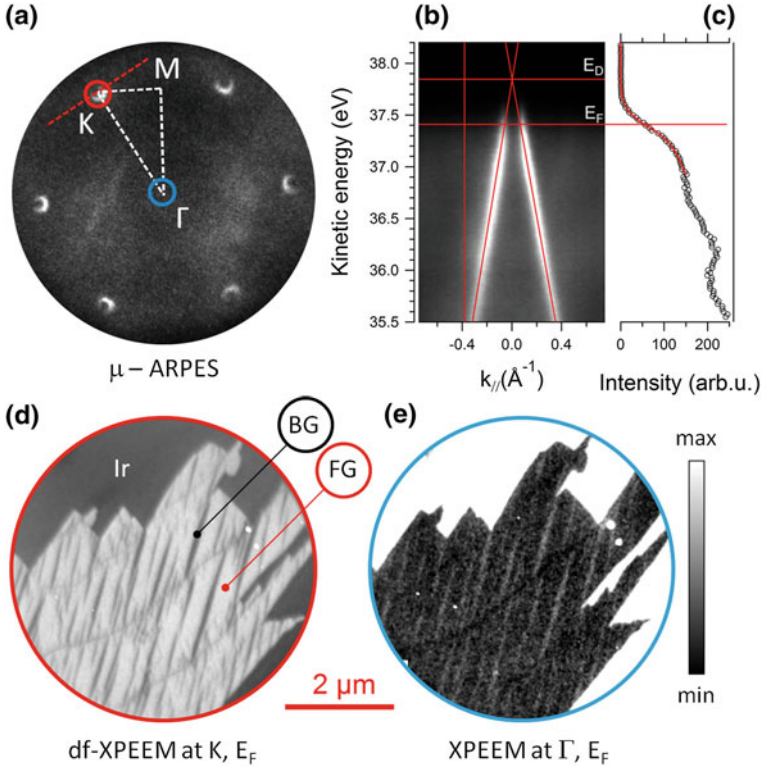


Fig. 21.5 **a** Microprobe ARPES map of flat graphene (*FG*) on Ir(100) and **b**, **c** cross section through one of the Dirac cones. **d** Dark-field PEEM image, obtained positioning the contrast aperture at the *K* point, demonstrating that flat graphene has a much higher DOS then buckled graphene (*BG*); **e** inversion of contrast in the PEEM image at the Γ reveals hybridization with Ir states in BG. Reprinted with permission from [66]. Copyright (2013) American Chemical Society

Mineralized fibrils produced by bacterial activity were among the first biomineral systems investigated using the PEEM II/III setups at ALS [75]. In these studies, features in the fibrils' local Fe L-edge XANES spectrum were used as fingerprints to determine the material's chemical composition and unambiguously identify the crystalline order by comparison with iron oxyhydroxide standards. Other studies focused on carbonate biominerals, and aragonite in particular [76]; these compounds have fundamental importance since they are the building blocks for skeleton support, protection of inner organs, and tools for mastication. Their outstanding properties originate from the intricate architecture that they exhibit at the nano- and micro-scale. The great structural complexity of biominerals can be appreciated when looking at the cross section of the tooth of see urchins, illustrated by the PEEM images in Fig. 21.6. XANES-PEEM was here employed to obtain Mg composition maps of the tooth, which consists of plates and rounded fibers (dark, elongated structures) embedded in

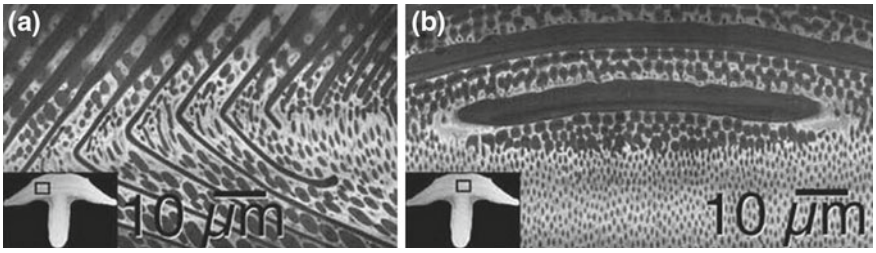


Fig. 21.6 XPEEM magnesium maps of urchin tooth cross section. Mg rich parts are rendered in lighter gray level, plates and fibers in dark. **a** Detail of a region away from the tooth center (see inset), which is shown in (**b**). Adapted with permission from [72]. Copyright (2011) WILEY-VCH Verlag GmbH & Co. KGaA, Weinheim

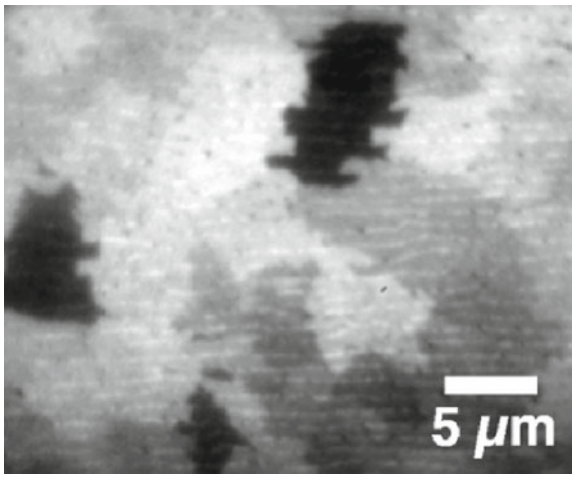


Fig. 21.7 X-PEEM O π^* map of a polished cross section of red abalone nacre, obtained by ratio of 534 and 518 eV images. The angle between the growth direction and the polarization vector was 61°. The growth direction in this sample was 60° from the normal to the polished nacre surface, so the layer thickness appears to be greater than 500 nm. Reprinted with permission from [76]. Copyright (2007) by the American Physical Society

a Mg-rich polycrystalline calcite cement giving the material exceptional resistance and hardness [72].

The high lateral resolution of XANES-PEEM, in conjunction with exploitation of linear dichroism, has become one of the most powerful tools to image individual single-crystalline tablets in biominerals. Red abalone nacre provided the first reported example of linear dichroism in a biomineral [76]. Figure 21.7 shows an XPEEM image of a cross section of this shell, where thin layers of an organic matrix alternate with thicker aragonite tablets. As can be seen, adjacent tablets show different intensity in the XANES-PEEM image (polarization image contrast, PIC), which has been interpreted as due to disorder in the tablet stacking. The observed intensity variations are due linear dichroism (observed for both the O and C π^* transition), resulting in a cos^2 dependence of the absorption intensity on the polar angle θ between the electronic charge and the X-ray polarization vector. In calcite crystals, the π-bonded orbitals of C atoms are perpendicular to the carbonate planes and normal to the c-axis. By recording variations in the image intensity as a function of the orientation of the X-ray polarization vector, one can measure the precise angular orientation of

the c-axis. Protocols have been developed in order to perform this type of analysis quantitatively [77]. Interestingly, XANES-PEEM experiments have shown that the tablet structure in nacre is species-specific and varies in mollusk species, which has been interpreted as a result of adaptation to diverging environments [78]. In the same study, a strong correlation between nacre crystal misorientations and environmental temperature was established. We underline that these experiments present numerous challenges. Since biominerals are in general non conductive, special sample preparation procedures need to be carried out, which allow to embed, polish, and coat samples in such a manner that spectroscopic analysis by XANES becomes possible and, at the same time, sample charging is inhibited [79].

21.3.4 Magnetic Imaging

The first experimental demonstration of X-ray magnetic circular dichroism was given at the end of 1980s [80]. The first significant demonstration of magnetic contrast via X-ray dichroism in an XPEEM instrument was the leading work of Stöhr et al. [81]. Very shortly after, a similar demonstration was published by Schneider et al. at higher photoelectron energies using an instrument with an energy filter [82]. In the following years, examples were given using XPEEM with X-ray linear dichroism in imaging ferromagnetic [83] and antiferromagnetic [84] domain structures.

Sensitivity to both antiferromagnetic (AFM) and ferromagnetic (FM) order, and the ability to probe buried layers due to the relatively large inelastic mean free path at the secondary photoelectron energies, make XPEEM an excellent tool to study exchange-coupled layered magnetic systems. The work of Nolting et al. [85] on a $Co/LaFeO_3$ interface is a good illustration in this respect. A 2.5 nm polycrystalline Co film was grown on top of a $LaFeO_3$ film. The FM domains in the Co layer were imaged in remanence using XMCD-PEEM at the Co L-edge, whereas the AFM texture in the $LaFeO_3$ underlayer was visualized by XMLD-PEEM at the Fe L-edge. As can be seen in Fig. 21.8, the correlation between the AFM and FM domains resulted in a direct measure of the exchange-coupling. On the technical side, the dichroism images showed a lateral resolution comparable to normal XPEEM operation, far below the micron-resolution reported in the proof-of-principle experiments of the previous decade.

Domain structures and transformations in patterned magnetic *bits* constitute another line of research that found great application using XMCD-PEEM. A significant example in this field has been the effect of a current through a magnetic nanowire on the domain walls within the wire itself. XMCD-PEEM imaging showed that this *spin-torque* effect, not only causes a domain-wall motion, but also induces transformations of the domain wall type [86]. In this and similar measurements, the lithographically patterned samples are prepared ex-situ, and capped by protective films to prevent oxidation during air exposure. The probing depth at the secondary electron energies provides the flexibility to access the buried structures in these studies.

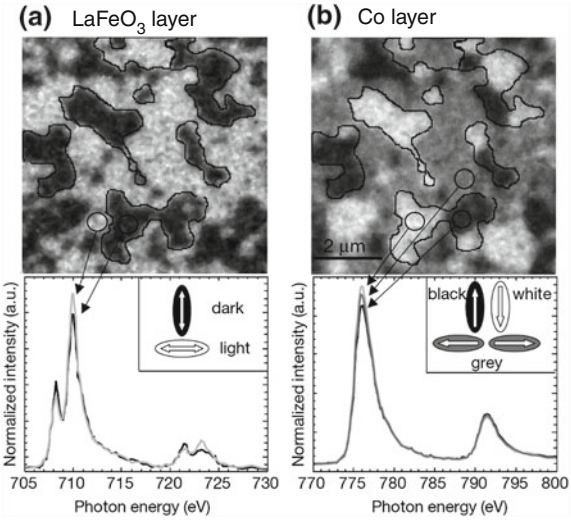


Fig. 21.8 1.2 nm Co on $LaFeO_3/SrTiO_3$, **a** XMLD image at the Fe L-edge, **b** XMCD image at the Co L-edge. The corresponding XAS spectra are shown in the bottom panels. Reprinted with permission from [85]. Copyright (2000) by Nature Publishing Group

In terms of fabricating magnetic bits, self-organization is an important alternative to lithography. XPEEM have proven to be a great resource in studies of self-organized magnetic nanostructures. A significant example was given on the strain-induced elongated Fe islands on the W(110) surface [87]. Combined XMCD imaging and micromagnetic simulations have revealed that the flux-closure domains at the surface and interface can be manipulated independently, introducing another degree-of-freedom in the amount of information stored in such a magnetic unit. From another perspective, self-organization studies usually involve in-situ growth, which requires sample characterization beyond magnetic imaging. The spectroscopic techniques available in a synchrotron-based XPEEM instrument prove to be valuable in this respect. This is illustrated in studies of epitaxial Fe-oxide island formation on Ru(0001). By tuning Fe coverage, temperature, and oxygen partial pressure, 1-nm thick highly-regular triangular Fe_3O_4 islands were obtained [88]. The distinction of various Fe-oxide phases is a considerable challenge, which was accomplished by XAS and XPS spectromicroscopy measurements, complemented with LEEM and micro-LEED characterization available in the same setup.

Arguably, the most important development in XMCD-PEEM has been time-resolved magnetic imaging. The first realizations were published almost simultaneously in 2003, by Vogel et al. [90] and then by Krasyuk et al. [91]. The idea is based on the pulsed nature of synchrotron sources. In a storage ring synchrotron, electrons circulate in short bunches, and the corresponding photon bursts produced by each electron bunch typically have pulse lengths of tens of picoseconds (in the new generation free electron laser sources, the typical pulse length is considerably below one picosecond). Each photon pulse gives a precisely-timed snapshot of the system under study. On the other hand, an XPEEM image usually requires millions of photon pulses at a 3rd generation synchrotron source in order to collect sufficient

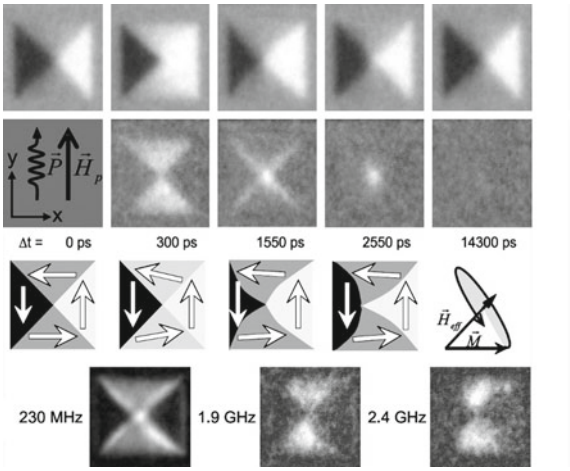


Fig. 21.9 XMCD imaged sequence showing the time evolution of magnetization after a field pulse of 60 Oe. *Second row* highlights the difference from the equilibrium state, *third row* gives a sketch of the magnetic configuration in each frame, and the *last row* feature the images of Fourier amplitudes obtained by transforming the image sequence. Reproduced with permission from [89]. Copyright (2005) by the American Physical Society

statistics. Therefore, the time-resolved measurements are done in a *stroboscopic* manner. The magnetic system is excited periodically by a (magnetic field, current, laser etc) pulse which precedes the photon pulse by a precise time difference. The photon pulse provides a snapshot of the magnetization during its evolution towards the steady-state. The final image is obtained by repeating this *pump-probe* cycle many times to accumulate statistics. The assumption is that the magnetic system will follow the exact same pathway towards steady-state every time it is kicked out of equilibrium. In practice, magnetic structures with strong shape anisotropy satisfy this assumption, and the deviations from reproducibility are averaged out in the stroboscopic measurement.

The pump-probe XMCD-PEEM imaging found significant application in the precessional magnetization dynamics in micron-sized magnetic structures. It was shown that, when placed out of equilibrium, the flux-closure magnetization patterns seen in such structures follow oscillatory dynamics as it returns to the equilibrium state [89, 92]. An example is provided in Fig. 21.9. The typical time scale involved is somewhat below one nanosecond, therefore, the synchrotron pulses are sufficiently short in order to probe the details of the magnetization dynamics. On the technical side, the excitation pulse (pump) usually has a frequency considerably below the synchrotron pulses operated at RF rates. Therefore, the pump-probe experiments either require a lower synchrotron repetition rate, or the possibility to filter out synchrotron pulses in order to effectively lower the measurement frequency. The latter has been accomplished by *gating* the detector of the XPEEM setup, i.e. activating the detector only for short times at a frequency matching that of the pump signal. Deflecting the photoelectron beam within the electron-optical path of the XPEEM instrument provides an alternative gating method which was demonstrated only recently [93].

21.4 Conclusions and Outlook

The last twenty years of PEEM have witnessed significant instrumental progress, helped by the great development of third generation light sources. On the one hand, PEEM applications based on absorption spectroscopy, e.g. XANES and XMC/LD, have reached full maturity. XANES-PEEM has approached with great success fields such as geology and biology, favored by the development of methodologies for the preparation of non-conductive samples. In parallel, magnetic imaging at synchrotron radiation beamlines has developed so much to become a standard. By exploiting the pulsed nature of synchrotron radiation in stroboscopic experiments, PEEM endeavored the investigation of the temporal domain, giving access to dynamic processes such as spin precession, reorientation and magnetization reversal. Further, the availability by instruments with electron energy analyzer made PEEM one of the most powerful methods for characterizing surfaces and interfaces. By imaging photoelectrons emitted from core levels (or the valence band), XPEEM can currently provide quantitative information on the local chemistry (electronic structure), with few tens nm lateral resolution. Nevertheless, the scientific community awaits for further technical progress. The energy resolution of the filters awaits to be meliorated, so that XPEEM can close the wide gap separating it from dedicated ARPES facilities. Other important improvements are needed on the cryogenic capabilities, in order to attain temperatures nearing that of liquid He. In this way, PEEM will be hopefully able to tackle issues of great scientific relevance such as superconductors, and metal-insulators transitions. Presumably, the progress in synchrotron radiation, especially concerning source intensity, will not be an important issue. Several materials, such as oxides, organic material and the soft matter, are in fact sensitive to radiation damage. Such applications would instead benefit by higher transmission and increased detection efficiency. Detectors based on sCMOS technology may soon replace the combination of MCP and phosphorous screen. They are already faster, but yet more work is needed for their adaptation to UHV conditions. More importantly, the second generation of PEEM is coming, opening the era of aberration-corrected microscopes. As previously underlined, these instruments will bring two important benefits: a significant improvement of the lateral resolution, and enhanced transmission. In this way, PEEM will take a further, important step towards atomic resolution, almost certainly disclosing a closer view on a wealth of new exciting phenomena.

References

1. S. Günther, B. Kaulich, L. Gregoratti, M. Kiskinova, Progr. Surf. Sci. **70**(48), 187 (2002). doi:10.1016/S0079-6816(02)00007-2
2. J. Feng, A. Scholl, *Science of Microscopy*, Photoemission Electron Microscopy (PEEM) (Springer, New York, 2007)
3. J. Stöhr, H. Siegmann, *Magnetism: From Fundamentals to Nanoscale Dynamics*, vol. 152, Springer Series in Solid-State Sciences (Springer, Berlin, 2007)
4. E. Bauer, J. Phys.: Condens. Matter **13**(49), 11391 (2001). doi:10.1088/0953-8984/13/49/316
5. P. Gilbert, J. Electron Spectrosc. Relat. Phenom. **185**(10), 395 (2012). doi:10.1016/j.elspec.2012.06.001
6. E. Bauer, J. Electron Spectrosc. Relat. Phenom. **185**(10), 314 (2012). doi:10.1016/j.elspec.2012.08.001
7. E. Bauer, Ultramicroscopy **119**, 18 (2012). doi:10.1016/j.ultramic.2011.09.006
8. A. Locatelli, E. Bauer, J. Phys.: Condens. Matter **20**(9), 093002 (2008). doi:10.1088/0953-8984/20/9/093002
9. G. Margaritondo, J. Electron Spectrosc. Relat. Phenom. **178–179**, 273 (2010). doi:10.1016/j.elspec.2009.05.007
10. C.M. Schneider, A. Krasyuk, S. Nepijko, A. Oelsner, G. Schönhense, J. Magn. Magn. Mater. **304**(1), 6 (2006). doi:10.1016/j.jmmm.2006.02.013
11. G. Schönhense, J.Electron Spectrosc. Relat. Phenom. **137–140**, 769 (2004). doi:10.1016/j.elspec.2004.02.161
12. R. van Gastel, I. Sikharulidze, S. Schramm, J. Abrahams, B. Poelsema, Ultramicroscopy **110**(1), 33 (2009). doi:10.1016/j.ultramic.2009.09.002
13. E. Bauer, Rep. Prog. Phys. **57**(9), 895 (1994). doi:10.1088/0034-4885/57/9/002
14. J. Chmelik, L. Veneklasen, G. Marx, Optik **83**, 155 (1989)
15. T. Schmidt, U. Groh, R. Fink, E. Umbach, O. Schaff, W. Engel, B. Richter, H. Kuhlenbeck, R. Schlogl, H.J. Freund, A.M. Bradshaw, D. Preikszas, P. Hartel, R. Spehr, H. Rose, G. Llilienkamp, E. Bauer, G. Benner, Surf. Rev. Lett. **09**(01), 223 (2002). doi:10.1142/S0218625X02001811
16. W. Wan, J. Feng, H. Padmore, D. Robin, Nucl. Instrum. Methods Phys. Res. Sect. A **519**(12), 222 (2004). doi:10.1016/j.nima.2003.11.159
17. R. Tromp, J. Hannon, A. Ellis, W. Wan, A. Berghaus, O. Schaff, Ultramicroscopy **110**(7), 852 (2010). doi:10.1016/j.ultramic.2010.03.005
18. T. Schmidt, A. Sala, H. Marchetto, E. Umbach, H.J. Freund, Ultramicroscopy **126**, 23 (2013). doi:10.1016/j.ultramic.2012.11.004
19. R. Tromp, J. Hannon, W. Wan, A. Berghaus, O. Schaff, Ultramicroscopy **127**, 25 (2013). doi:10.1016/j.ultramic.2012.07.016
20. A. Locatelli, T.O. Menteş, M.Á. Niño, E. Bauer, Ultramicroscopy **111**(8), 1447 (2011). doi:10.1016/j.ultramic.2010.12.020
21. T. Warwick, K. Franck, J.B. Kortright, G. Meigs, M. Moronne, S. Myneni, E. Rotenberg, S. Seal, W.F. Steele, H. Ade, A. Garcia, S. Cerasari, J. Denlinger, S. Hayakawa, A.P. Hitchcock, T. Tyliszczak, J. Kikuma, E.G. Rightor, H.J. Shin, B.P. Tonner, Rev. Sci. Instrum. **69**(8), 2964 (1998). doi:10.1063/1.1149041
22. E. Bauer, *Science of Microscopy*, LEEM and SPLEEM (Springer, New York, 2007)
23. T.O. Menteş, A. Locatelli, J. Electron Spectrosc. Relat. Phenom. **185**(10), 323 (2012). doi:10.1016/j.elspec.2012.07.007
24. T. Schmidt, S. Heun, J. Slezak, J. Diaz, K.C. Prince, G. Lilienkamp, E. Bauer, Surf. Rev. Lett. **5**(6), 1287 (1998). doi:10.1142/S0218625X98001626
25. R. Tromp, Ultramicroscopy **120**, 73 (2012). doi:10.1016/j.ultramic.2012.06.003
26. B.P. Tonner, G.R. Harp, Rev. Sci. Instrum. **59**(6), 853 (1988). doi:10.1063/1.1139792
27. C.M. Schneider, G. Schönhense, Rep. Progr. Phys. **65**(12), 1785 (2002)
28. S. Hüfner, *Photoelectron Spectroscopy: Principles and Applications*. Advanced Texts in Physics (Springer, Berlin, 2003)

29. C. Wiemann, M. Patt, S. Cramm, M. Escher, M. Merkel, A. Gloskovskii, S. Thiess, W. Drube, C.M. Schneider, Appl. Phys. Lett. **100**(22), 223106 (2012). doi:10.1063/1.4722940
30. F.J. Meyer zu Heringdorf, T. Schmidt, S. Heun, R. Hild, P. Zahl, B. Ressel, E. Bauer, M. Horn-von Hoegen, Phys. Rev. Lett. **86**, 5088 (2001). doi:10.1103/PhysRevLett.86.5088
31. G. Biasiol, S. Heun, L. Sorba, J. Nanoelectronics and Optoelectron. **6**(1), 20–23 (2011). doi:10.1166/jno.2011.1130
32. T. Schmidt, J.I. Flege, S. Gangopadhyay, T. Clausen, A. Locatelli, S. Heun, J. Falta, Phys. Rev. Lett. **98**, 066104 (2007). doi:10.1103/PhysRevLett.98.066104
33. J.T. Robinson, F. Ratto, O. Moutanabbir, S. Heun, A. Locatelli, T.O. Menteş, L. Aballe, O.D. Dubon, Nano Lett. **7**(9), 2655 (2007). doi:10.1021/nl071051y
34. S. Suzuki, Y. Watanabe, Y. Homma, S. ya Fukuba, S. Heun, A. Locatelli, Appl. Phys. Lett. **85**(1), 127 (2004). doi:10.1063/1.1768304
35. A. Locatelli, T. Pabisiak, A. Pavlovska, T.O. Menteş, L. Aballe, A. Kiejna, E. Bauer, J. Phys.: Condens. Matter **19**(8), 082202 (2007). doi:10.1088/0953-8984/19/8/082202
36. T.O. Menteş, A. Locatelli, L. Aballe, A. Pavlovska, E. Bauer, T. Pabisiak, A. Kiejna, Phys. Rev. B **76**, 155413 (2007). doi:10.1103/PhysRevB.76.155413
37. D.S. Humphrey, G. Cabailh, C.L. Pang, C.A. Muryn, S.A. Cavill, H. Marchetto, A. Potenza, S.S. Dhesi, G. Thornton, Nano Lett. **9**(1), 155 (2009). doi:10.1021/nl802703e
38. S. Günther, A. Kolmakov, J. Kovac, M. Kiskinova, Ultramicroscopy **75**(1), 35 (1998). doi:10.1016/S0304-3991(98)00047-3
39. A. Locatelli, M. Kiskinova, Chemistry A Eur. J. **12**(35), 8890 (2006). doi:10.1002/chem.200601189
40. A. Schaak, S. Günther, F. Esch, E. Schütz, M. Hinz, M. Marsi, M. Kiskinova, R. Imbihl, Phys. Rev. Lett. **83**, 1882 (1999). doi:10.1103/PhysRevLett.83.1882
41. T. Schmidt, A. Schaak, S. Günther, B. Ressel, E. Bauer, R. Imbihl, Chem. Phys. Lett. **318**(6), 549 (2000). doi:10.1016/S0009-2614(00)00061-0
42. L. Hong, H. Uecker, M. Hinz, L. Qiao, I.G. Kevrekidis, S. Günther, T.O. Menteş, A. Locatelli, R. Imbihl, Phys. Rev. E **78**, 055203 (2008). doi:10.1103/PhysRevE.78.055203
43. S. Günther, H. Liu, T.O. Mentes, A. Locatelli, R. Imbihl, Phys. Chem. Chem. Phys. **15**, 8752 (2013). doi:10.1039/C3CP44478C
44. A. Locatelli, C. Sbraccia, S. Heun, S. Baroni, M. Kiskinova, J. Am. Chem. Soc. **127**(7), 2351 (2005). doi:10.1021/ja045285k
45. Y.D. Decker, H. Marbach, M. Hinz, S. Günther, M. Kiskinova, A.S. Mikhailov, R. Imbihl, Phys. Rev. Lett. **92**, 198305 (2004). doi:10.1103/PhysRevLett.92.198305
46. A. Locatelli, T.O. Menteş, L. Aballe, A. Mikhailov, M. Kiskinova, J. Phys. Chem. B **110**(39), 19108 (2006). doi:10.1021/jp065090u
47. R. Imbihl, J. Electron Spectrosc. Relat. Phenom. **185**(10), 347 (2012). doi:10.1016/j.elspec.2012.05.001
48. F. Lovis, M. Hesse, A. Locatelli, T.O. Menteş, M.A. Niño, G. Lilienkamp, B. Borkenhagen, R. Imbihl, J. Phys. Chem. C **115**(39), 19149 (2011). doi:10.1021/jp206600q
49. L. Aballe, A. Barinov, A. Locatelli, S. Heun, M. Kiskinova, Phys. Rev. Lett. **93**, 196103 (2004). doi:10.1103/PhysRevLett.93.196103
50. M. Altman, W. Chung, Z. He, H. Poon, S. Tong, Appl. Surf. Sci. **169–170**, 82 (2001). doi:10.1016/S0169-4332(00)00644-9
51. N. Binggeli, M. Altarelli, Phys. Rev. Lett. **96**, 036805 (2006). doi:10.1103/PhysRevLett.96.036805
52. L. Aballe, A. Barinov, N. Stojić, N. Binggeli, T.O. Menteş, A. Locatelli, M. Kiskinova, J. Phys.: Condens. Matter **22**(1), 015001 (2010). doi:10.1088/0953-8984/22/1/015001
53. S. Günther, R. Reichelt, J. Wintterlin, A. Barinov, T.O. Menteş, M.Á. Niño, A. Locatelli, Appl. Phys. Lett. **93**(23), 233117 (2008). doi:10.1063/1.3040685
54. M. Batzill, Surf. Sci. Rep. **67**(34), 83 (2012). doi:10.1016/j.surfrep.2011.12.001
55. K.L. Man, M.S. Altman, J. Phys.: Condens. Matter **24**(31), 314209 (2012). doi:10.1088/0953-8984/24/31/314209
56. E. Loginova, N.C. Bartelt, P.J. Feibelman, K.F. McCarty, New J. Phys. **10**(9), 093026 (2008)

57. P. Sutter, J.I. Flege, E.A. Sutter, Nat. Mater. **7**, 406 (2008). doi:10.1038/nmat2166
58. E. Miniussi, M. Pozzo, A. Baraldi, E. Vesselli, R.R. Zhan, G. Comelli, T.O. Menteş, M.A. Niño, A. Locatelli, S. Lizzit, D. Alfè, Phys. Rev. Lett. **106**, 216101 (2011). doi:10.1103/PhysRevLett.106.216101
59. H. Hibino, H. Kageshima, F. Maeda, M. Nagase, Y. Kobayashi, H. Yamaguchi, Phys. Rev. B **77**, 075413 (2008). doi:10.1103/PhysRevB.77.075413
60. A. Locatelli, K.R. Knox, D. Cvetko, T.O. Menteş, M.Á. Niño, S. Wang, M.B. Yilmaz, P. Kim, R.M. Osgood, A. Morgante, ACS Nano **4**(8), 4879 (2010). doi:10.1021/nn101116n
61. R.M. Feenstra, N. Srivastava, Q. Gao, M. Widom, B. Diaconescu, T. Ohta, G.L. Kellogg, J.T. Robinson, I.V. Vlassiouk, Phys. Rev. B **87**, 041406 (2013). doi:10.1103/PhysRevB.87.041406
62. K.J. Kim, H. Lee, J.H. Choi, Y.S. Youn, J. Choi, H. Lee, T.H. Kang, M.C. Jung, H.J. Shin, H.J. Lee, S. Kim, B. Kim, Adv. Mater. **20**(19), 3589 (2008). doi:10.1002/adma.200800742
63. D. Pacilé, M. Papagno, A.F. Rodríguez, M. Grioni, L. Papagno, Ç.O. Girit, J.C. Meyer, G.E. Begtrup, A. Zettl, Phys. Rev. Lett. **101**, 066806 (2008). doi:10.1103/PhysRevLett.101.066806
64. H.K. Jeong, H.J. Noh, J.Y. Kim, L. Colakerol, P.A. Glans, M.H. Jin, K.E. Smith, Y.H. Lee, Phys. Rev. Lett. **102**, 099701 (2009). doi:10.1103/PhysRevLett.102.099701
65. N. Barrett, E. Conrad, K. Winkler, B. Kromker, Rev. Sci. Instrum. **83**(8), 083706 (2012). doi:10.1063/1.4746279
66. A. Locatelli, C. Wang, C. Africh, N. Stojić, T.O. Menteş, G. Comelli, N. Binggeli, ACS Nano **7**(8), 6955 (2013). doi:10.1021/nn402178u
67. P. Sutter, M.S. Hybertsen, J.T. Sadowski, E. Sutter, Nano Lett. **9**(7), 2654 (2009). doi:10.1021/nl901040v
68. P. Sutter, J.T. Sadowski, E. Sutter, Phys. Rev. B **80**, 245411 (2009). doi:10.1103/PhysRevB.80.245411
69. C. Mathieu, B. Lalmi, T.O. Menteş, E. Pallecchi, A. Locatelli, S. Latil, R. Belkhou, A. Ouerghi, Phys. Rev. B **86**, 035435 (2012). doi:10.1103/PhysRevB.86.035435
70. K.R. Knox, S. Wang, A. Morgante, D. Cvetko, A. Locatelli, T.O. Menteş, M.Á. Niño, P. Kim, R.M. Osgood, Phys. Rev. B **78**, 201408 (2008). doi:10.1103/PhysRevB.78.201408
71. K.R. Knox, A. Locatelli, M.B. Yilmaz, D. Cvetko, T.O. Menteş, M.Á. Niño, P. Kim, A. Morgante, R.M. Osgood, Phys. Rev. B **84**, 115401 (2011). doi:10.1103/PhysRevB.84.115401
72. C.E. Killian, R.A. Metzler, Y. Gong, T.H. Churchill, I.C. Olson, V. Trubetskoy, M.B. Christensen, J.H. Fournelle, F. De Carlo, S. Cohen, J. Mahamid, A. Scholl, A. Young, A. Doran, F.H. Wilt, S.N. Coppersmith, P.U.P.A. Gilbert, Adv. Funct. Mater. **21**(4), 682 (2011). doi:10.1002/adfm.201001546
73. O.H. Griffith, G.F. Rempfer, Annu. Rev. Biophys. Biophys. Chem. **14**(1), 113 (1985). doi:10.1146/annurev.bb.14.060185.000553
74. G. de Stasio, S.F. Koranda, B.P. Tonner, G.R. Harp, D. Mercanti, M.T. Ciotti, G. Margaritondo, EPL (Europhysics Letters) **19**(7), 655 (1992). doi:10.1209/0295-5075/19/7/015
75. C.S. Chan, G. De Stasio, S.A. Welch, M. Girasole, B.H. Frazer, M.V. Nesterova, S. Fakra, J.F. Banfield, Science **303**(5664), 1656 (2004). doi:10.1126/science.1092098
76. R.A. Metzler, M. Abrecht, R.M. Olabisi, D. Ariosa, C.J. Johnson, B.H. Frazer, S.N. Coppersmith, P.U.P.A. Gilbert, Phys. Rev. Lett. **98**, 268102 (2007). doi:10.1103/PhysRevLett.98.268102
77. P.U.P.A. Gilbert, A. Young, S.N. Coppersmith, Proc. Nat. Acad. Sci. **108**(28), 11350 (2011). doi:10.1073/pnas.1107917108
78. I.C. Olson, R. Kozdon, J.W. Valley, P.U.P.A. Gilbert, J. Am. Chem. Soc. **134**(17), 7351 (2012). doi:10.1021/ja210808s
79. G.D. Stasio, B.H. Frazer, B. Gilbert, K.L. Richter, J.W. Valley, Ultramicroscopy **98**(1), 57 (2003). doi:10.1016/S0304-3991(03)00088-3
80. G. Schütz, W. Wagner, W. Wilhelm, P. Kienle, R. Zeller, R. Frahm, G. Materlik, Phys. Rev. Lett. **58**, 737 (1987). doi:10.1103/PhysRevLett.58.737
81. J. Stöhr, Y. Wu, B. Hermsmeier, M. Samant, G. Harp, S. Koranda, D. Dunham, B. Tonner, Science **259**, 658 (1993)

82. C.M. Schneider, K. Holldack, M. Kinzler, M. Grunze, H.P. Oepen, F. Schafers, H. Petersen, K. Meinel, J. Kirschner, Appl. Phys. Lett. **63**(17), 2432 (1993). doi:10.1063/1.110498
83. F.U. Hillebrecht, T. Kinoshita, D. Spanke, J. Dresselhaus, C. Roth, H.B. Rose, E. Kisker, Phys. Rev. Lett. **75**, 2224 (1995). doi:10.1103/PhysRevLett.75.2224
84. J. Stöhr, A. Scholl, T.J. Regan, S. Anders, J. Lüning, M.R. Scheinfein, H.A. Padmore, R.L. White, Phys. Rev. Lett. **83**, 1862 (1999). doi:10.1103/PhysRevLett.83.1862
85. F. Nolting, A. Scholl, J. Stöhr, J.W. Seo, J. Fompeyrine, H. Siegwart, J.P. Locquet, S. Anders, J. Lüning, E.E. Fullerton, M.F. Toney, M.R. Scheinfein, H.A. Padmore, Nature **405**, 767 (2000). doi:10.1038/35015515
86. M. Klaui, M. Laufenberg, L. Heyne, D. Backes, U. Rudiger, C.A.F. Vaz, J.A.C. Bland, L.J. Heyderman, S. Cherifi, A. Locatelli, T.O. Mentes, L. Aballe, Appl. Phys. Lett. **88**(23), 232507 (2006). doi:10.1063/1.2209177
87. F. Cheynis, A. Masseboeuf, O. Fruchart, N. Rougemaille, J.C. Toussaint, R. Belkhou, P. Bayle-Guillemaud, A. Marty, Phys. Rev. Lett. **102**, 107201 (2009). doi:10.1103/PhysRevLett.102.107201
88. M. Monti, B. Santos, A. Mascaraque, O. Rodriguez de la Fuente, M.A. Niño, T.O. Menteş, A. Locatelli, K.F. McCarty, J.F. Marco, J. de la Figuera, Phys. Rev. B **85**, 020404 (2012). doi:10.1103/PhysRevB.85.020404
89. J. Raabe, C. Quitmann, C.H. Back, F. Nolting, S. Johnson, C. Buehler, Phys. Rev. Lett. **94**, 217204 (2005). doi:10.1103/PhysRevLett.94.217204
90. J. Vogel, W. Kuch, M. Bonfim, J. Camarero, Y. Pennec, F. Offi, K. Fukumoto, J. Kirschner, A. Fontaine, S. Pizzini, Appl. Phys. Lett. **82**(14), 2299 (2003). doi:10.1063/1.1564876
91. A. Krasyuk, A. Oelsner, S.A. Nepijko, A. Kuksov, C.M. Schneider, G. Schönhense, Appl. Phys. A: Mater. Sci. Process. **76**, 863 (2003). doi:10.1007/s00339-002-1965-8
92. S.B. Choe, Y. Acremann, A. Scholl, A. Bauer, A. Doran, J. Stöhr, H.A. Padmore, Science **304**(5669), 420 (2004). doi:10.1126/science.1095068
93. F. Nickel, D. Gottlob, I. Krug, H. Doganay, S. Cramm, A. Kaiser, G. Lin, D. Makarov, O. Schmidt, C. Schneider, Ultramicroscopy **130**, 54 (2013). doi:10.1016/j.ultramic.2013.03.005

Chapter 22
Medical Imaging with Synchrotron Radiation

Giuliana Tromba

Abstract The use of Synchrotron Radiation for medical imaging has seen impressive growth in the last decades. The availability of highly coherent, tunable monochromatic X-ray beams, over a wide energy range, makes Synchrotron Radiation an incomparable tool of research for a variety of purposes. This chapter highlights the main achievements and the perspectives of medical imaging research carried out at various Synchrotron Light laboratories.

22.1 Introduction

Since the discovery of X-rays, for over a century, the principle of image formation in medical radiology has been virtually unchanged. The contrast was determined by the properties of the sample under study to differently attenuate X-rays. The advent of Synchrotron Radiation (SR), with its unique features, opened the way for the implementation of innovative imaging techniques and their rapid application to a variety of fields.

Medical imaging research with SR started in the 80s with the first studies on coronary angiography. Contrast agents, generally Iodine-based, opaque to X-rays, were used to visualize the blood arteries of the heart. The main SR feature exploited for this application was the monochromaticity of the beam. Indeed, the use of contrast agents takes advantage in the application of the so-called K-Edge Subtraction (KES) imaging. This technique requires two images taken at two monochromatic X-ray energies, one just below, the other just above, the K-absorption edge of the contrast agent. From the logarithmic subtraction of these images, the visibility of structures

G. Tromba (✉)
Elettra-Sincrotrone Trieste S.C.p.A., Strada Statale 14 - km 163,5 in Area Science Park, 34149 Basovizza, Trieste, Italy
e-mail: giuliana.tromba@elettra.trieste.it

S. Mobilio et al. (eds.), *Synchrotron Radiation*,
DOI: 10.1007/978-3-642-55315-8_22, © Springer-Verlag Berlin Heidelberg 2015

perfused by the contrast agent is greatly enhanced and the signals due to other tissues are practically suppressed.

The use of KES imaging has also been explored in pre-clinical studies of lung and brain developed on animal models.

The development of new third generation SR facilities along with the availability of sources with high spatial coherence brought to the second revolution in the hard X-ray imaging (after the discovery of Computed Tomography (CT)), i.e. the Phase Contrast Imaging (PCI).

In conventional radiology the image contrast, originated by a variation in density, composition or thickness of the sample, is based exclusively on the detection of amplitude variations of the transmitted X-rays. The main limitation of this technique is the poor enhancement of weakly absorbing details in soft tissue.

PCI techniques are based on the observation of phase-shifts produced by the sample on the incoming X-ray wavefield. In general, the phase part becomes important if the source has a high spatial coherence, as it occurs with SR sources.

Since mid 80s SR techniques have been successfully applied to many biomedical research programs such as angiography, mammography, bronchography and imaging of soft tissues, study of tendons and cartilages, brain, etc.

This chapter gives an overview of the medical research carried out at different SR facilities. General reviews reporting research progress in this area have been published since 2003 [1–4].

Considering the vastness of the research and the number of successful ongoing applications, this chapter cannot be complete or exhaustive. As a matter of brevity it will be focused mainly on research with direct or indirect clinical implications, giving a glimpse in particular to studies that may lead to in-vivo imaging procedures on patients or animals. Furthermore, this chapter does not include researches carried out on bones, teeth, scaffolds, biomaterials and engineered tissues, although they are also very promising for medical purposes.

22.2 Advantages of Synchrotron Radiation for Medical Imaging

When compared with conventional generators, SR offers several advantages for medical imaging. The natural collimation of SR makes it possible to select monochromatic radiation by using crystals. Monochromatic X-rays have been always considered as a '*dream*' for medical radiologists since they enable the tuning of the X-ray energy as a function of the specific sample's characteristics and the examination needs. Consequently, the delivered radiation dose can be reduced, with benefits to the patient's health or to the preservation of the sample.

Monochromaticity also reduces the problems of the beam hardening in CT, a common effect that introduces artefacts in the reconstructed images.

Moreover, monochromaticity facilitates the quantitative characterization of different tissue components (in both absorption and phase contrast imaging) and takes

particular advantage of the use of contrast agents in the visualization of specific anatomical features, like blood vessels or lungs alveolar trees.

The collimation of the beam has also the advantage of producing images with spatial resolution limited only by the detector. The detector can be placed far from the object, to eliminate the scattering contribution from the detected beam.

As already mentioned, for imaging applications the high spatial coherence of the X-ray source is by far the main issue, being essential for the application of PCI.

A variety of techniques have been developed to exploit the phase information of the sample. These can be classified in five main categories.

(i) Propagation-Based Imaging (PBI) methods [5–7].
(ii) Analyzer-Based Imaging (ABI) implemented, for the first time with different names as "refraction-contrast radiography", "phase dispersion introscopy" [8, 9]. Its first physics interpretation was given by [10, 11].
(iii) Interferometric methods with crystals [12, 13].
(iv) Grating interferometric imaging (GI) [14].
(v) Grating non-interferometric methods [15].

These methods differ not only in the experimental set-up but also for the requirements of the source's spatial and temporal coherence. They provide a variety of information producing different kind of images at different delivered X-ray doses.

A detailed description of these techniques is reported in Chap. 8. The most recent review of their characteristics and use for medical imaging can be found in [4].

22.3 Current Research Status at SR Beamlines

In the last decades the number of imaging beamlines operating at third generation SR sources has consistently increased.

Research in medical imaging is extensively carried out at almost all the SR facilities operating at energies of at least 2 GeV. For many years, the most active in this field have been ESRF (Grenoble, F), Elettra (Trieste, I), DESY (Hamburg, G), NSLS (Upton, NY, USA), SSRL (Stanford, USA), Spring-8 (Hyogo, J), Photon Phactory (Tsukuba, J), PSI (Zurich, CH) and APS (Chicago, USA). To the above ones more recently new beamlines developed at the newest SR Centers have been added, such as SSRF (Shangai, Cina), CLS (Saskatoon, Canada) and Australian Synchrotron (Melburne, A).
The main research topics, along with the corresponding techniques, are described in the following sections.

22.3.1 Angiography

Coronary angiography is an important diagnostic exam used to image the coronary arteries. A Iodine-based contrast agent is injected into the arteries through a catheter which is inserted into the iliac artery and guided up to the aorta, at the beginning of

a coronary artery. After injection of the contrast agent, a sequence of radiographs is taken at short intervals (cine-angiography). The method is well-developed and quite effective but is very invasive and often presents complications and even mortality (0.1–0.2 %). These problems prevent its widespread application for screening and follow-up studies.

The coronary angiography programs launched since the 1980s at some SR laboratories addressed this problem and aimed at developing a procedure with less risks and the capability of reducing the patient's discomfort and frequent required hospitalizations.

KES angiography with SR provided images of clinical quality even when the iodinated contrast agent was injected into a peripheral vein. In this way the risks associated with arterial catheterization are avoided. Historically coronary angiography was the medical application of SR, and the only one, to have been extensively applied in clinical research.

Thanks to its low invasiveness KES SR coronary angiography became a method suitable for follow-up and basic research on coronary disease. Consequently, clinical protocols were carried out at SSRL (Stanford, USA), Hasylab (Hamburg, Germany), NSLS (Brookhaven, USA), ESRF (Grenoble, France), and KEK (Tsukuba, Japan) [16–24] and over 500 patients have been examined with this technique.

22.3.2 Microangiography

Microangiography is used to access information about microcirculation and cardiovascular function. A recent work reviews the advantages offered by the combination of SR absorption microangiography and SAXS of cardiac muscle for real-time, in vivo vascular imaging in small animals, showing the dynamic motion of the heart and lungs [25].

SR microangiography is the ideal tool to study changes in cerebral blood flow and vascular morphology in real time in the rodent brain. A study conducted at SSRF on animals with an artificially produced occlusion on the median cerebral artery showed the advantage of the SR technique in contrast with MR angiography [26]. The same technique was also used for monitoring angiogenesis in mice brains after the transient of a middle cerebral artery occlusion [27].

Intravascular contrast agents can be used with micro-CT modality to visualize in 3D the vascular structure of mouse heart specimens.

However, for mouse coronary artery disease models, it is desirable to image coronary artery walls and visualize atherosclerotic plaques. For this purpose, an ex-vivo contrast-enhanced micro-CT protocol, based on tissue staining with Osmium tetroxide (OsO_4) solution has been proved at APS [28]. As a tissue-staining contrast agent, OsO_4 is retained in the vessel wall and surrounding tissue and cleared from the vessel lumens. Its high X-ray attenuation makes the artery wall visible in CT. Additionally, since OsO_4 preferentially binds to lipids, it highlights lipid deposition in the artery wall, enhancing the visualization of early formation plaques.

22.3.3 Bronchography

For the diagnosis of lung obstructive diseases, the need for an imaging technique capable of providing simultaneous information about airways structure and function is very well known. Among the diagnostic tools commonly used in clinical practice, PET and MRI do not present enough spatial resolution while spirometry provides soley information about global function.

Following the experience of coronary angiography, the KES technique has been applied also to lungs studies using Xenon gas as a contrast agent [29, 30].

At the ESRF, the bronchography programme is focused on studies of animal models. The aim is to develop protocols for quantitative imaging of ventilation in asthma and chronic obstructive pulmonary disease. KES technique is well suited for these purposes as it allows simultaneous imaging of central conducting airway dimensions and quantitative measurement of regional ventilation in experimental models of induced airway obstruction [31].

CT studies are performed on anaesthetized animals connected to a respiration apparatus, where the inhaled gas mixture and the breathing cycle are controlled by a computer. Mechanical ventilation and image acquisition are synchronized to reduce motion artefacts.

This method is used to study the effects on lungs ventilation induced by different treatments on healthy or asthmatic animals.

As an example studies have been carried out to evaluate allergic reactions on rabbits sensitized by ovalbumine and compare them to the asthma reactions caused by non-specific drug provocation such as Methacholine (Mch) (Fig. 22.1).

Reconstructed slices from CT scans showed that Mch caused airway narrowing mainly on the large airways, while allergen like ovalbumine provoked heterogeneous changes in the peripheral ventilation, leaving unchanged the airways sections [32].

22.3.4 Breast Imaging

Mammography is the standard method for the diagnosis of breast cancer at an early pre-clinical stage. Recognition of breast cancer is based on the detection of characteristic features such as nodules or structures with density close to that of the normal tissue, micro-calcifications, parenchimal distortions, skin thickening, asymmetries between the two breasts, etc. The small differences in the attenuation of X-rays between normal and malignant tissue result in low contrast and make cancer detection difficult with conventional absorption based technique.

Due to its high clinical relevance, breast imaging has been one of the first medical applications of SR [33, 34]. The main studies were based on the use of PBI and ABI. Recently PCI applications in mammography has been extensively reviewed [35, 36].

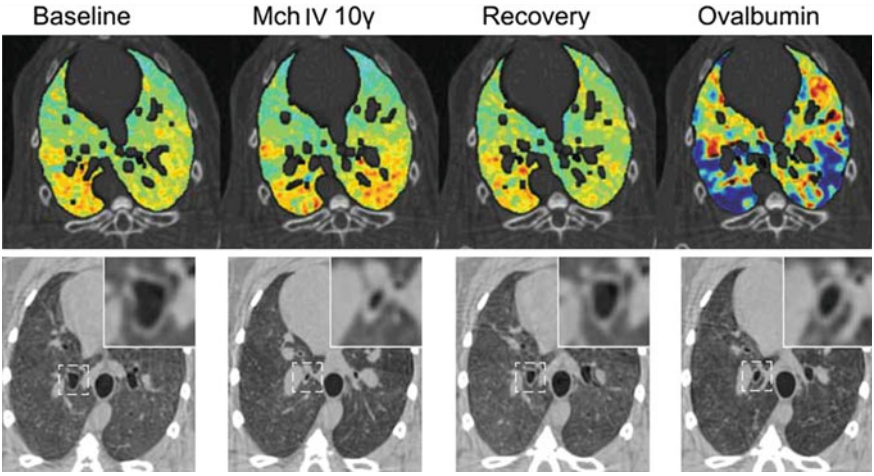


Fig. 22.1 *Upper part* images of specific ventilation in one representative sensitized rabbit at baseline, during methacholine (Mch) infusion, upon recovery and after ovalbumine allergen provocation. *Lower part* Absorption CT slices showing changes in the central airway cross-sectional area at the different experimental stages in one representative animal. Magnifications of the indicated *square* areas are shown in the *right-upper corners*. (Image from http://www.esrf.eu/UsersAndScience/Experiments/Imaging/ID17/)

22.3.4.1 The Mammography Program @ Elettra

PBI was firstly used in planar modality for a direct comparison with respect to clinical mammography. Feasibility studies pioneered at Elettra on test objects and excised breast tissue samples showed the effectiveness of the technique with an increased image contrast and an improved visibility of tissue structures and lesions [34, 37] in comparison with standard diagnostic images. This research launched the preparation of the clinical trial, performed since 2006, at the SYnchrotron Radiation for MEdical Physics (SYRMEP) beamline of Elettra.

The facility for clinical mammography equipped with the needed safety, dosimetric, and control systems has been realized downstream from the pre-existing experimental hutch of the SYRMEP beamline, used for the feasibility studies [38].

In the initial research phase, conventional screen film systems were used as detectors [39], the choice being motivated by its high intrinsic spatial resolution.

In the second phase commercial storage phosphor detectors (Imaging Plates) are implemented [40]. The third phase, presently under evaluation, will combine the planar image with a tomographic scan performed on a selected portion of the breast.

The first clinical trial aimed at evaluating the contribution of PBI in the diagnosis of patients with suspicious breast abnormalities as they were identified by the combination of conventional mammography and ultrasonography (US) studies [39] and classified according to the BI-RADS categories [41].

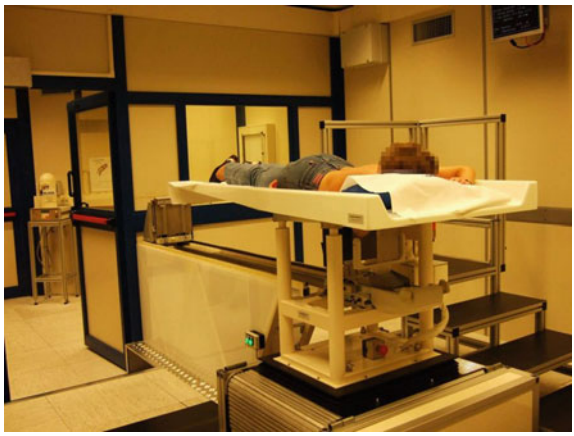


Fig. 22.2 Patient and detector supports. Reprinted from [40], Copyright (2013), with kind permission from Springer-Verlag Italia

The mammographic examination was performed with the patient lying prone on a custom designed support, with the breast hanging outside of an ergonomically designed aperture, as shown in Fig. 22.2.

A mild compression system was used for stretching and equalizing the breast thickness. The film or the IP detector accommodated in a special holder, mounted on a 2 m long rail, to optimize the distance for edge enhancing effects of PBI. Planar breast projections were obtained by simultaneously scanning patient and detector [38].

In the first clinical protocol, 71 patients were examined [39]. SR images were evaluated by two radiologists and compared with conventional studies. The SR images showed a higher specificity, and a reduced number of false positives.

As an example, the SR mammography and the corresponding conventional image, obtained for one of the studied patients, is shown in Fig. 22.3a and b [38].

In both views an opacity is clearly visible in the dense background tissue.

SR exams have an important reduction of the delivered doses, particularly for thicker breasts, due to the X-ray energy tunability and optimization.

The edge enhancement effects typical of PBI help in highlighting the visibility of microcalcifications and spiculae. Furthermore, the energy optimization and the rejection of scattered radiation, further contribute to improve the quality of SR images.

In comparison with conventional mammography, examinations with SR showed a higher specificity, reducing in particular the number of false positives. More in general, the diagnoses based on the SR studies present a larger agreement with final diagnosis (determined by the biopsy results, considered as 'the golden standard') than those performed with conventional exams. These results suggest that mammography with SR can be used to clarify cases of questionable or suspicious breast abnormalities identified by conventional mammography.

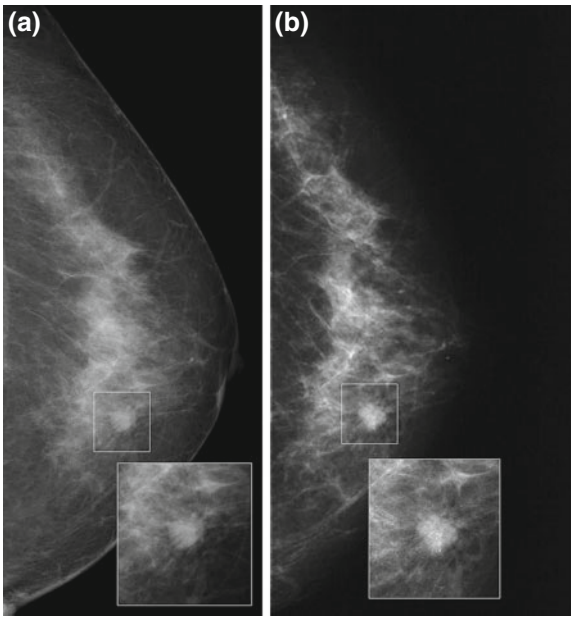


Fig. 22.3 Cranio-caudal mammograms obtained at the conventional unit (**a**) and a at the SYRMEP station at Elettra (**b**). Reprinted from [38], Copyright (2008), with kind permission from Elsevier

22.3.4.2 Breast Imaging Research at Other Synchrotron Sources

ABI was firstly successfully used for pilot experiments on test objects and small tissue samples performed at the NSLS [42]. ABI apparent absorption and refraction images obtained on tissue specimens containing embedded lesions, confirmed the enormous potential of the technique for breast imaging [43].

The latest research in mammography with SR is now focused on the development of low dose tomographic phase-based methods which make possible the 3D imaging of the breast with an improved sensitivity over conventional mammography.

Most of this work has been performed in vitro on breast tissues excised after clinical mastectomy procedures. High resolution CT studies (∼20 lp/mm) showed that the ABI technique may provide highly detailed images, comparable to the histopathology slices, both for partial [44] and full size tissues [45].

The application of ABI with a thin Laue-type crystal set-up, for the selection of the non-deviated and refracted (+ scattered) X-rays, has also been successfully applied to image a small breast tissue specimen with ductal carcinoma in situ [46].

Recently it was demonstrated that the use of PCI CT scans at X-ray energies higher than 50 keV, with a innovative reconstruction algorithm, known as "equally sloped tomography" [47, 48], is very effective in producing 3D views of a whole human breast, identifying a malignant lesion at a radiation dose comparable with dual-projection mammography [49]. Figure 22.4 shows an ABI-CT slice reconstructed by this method with the segmentation of the lesion (A) and the 3D volume rendering of the lesion embedded in the breast tissue (B). These results confirm the potential

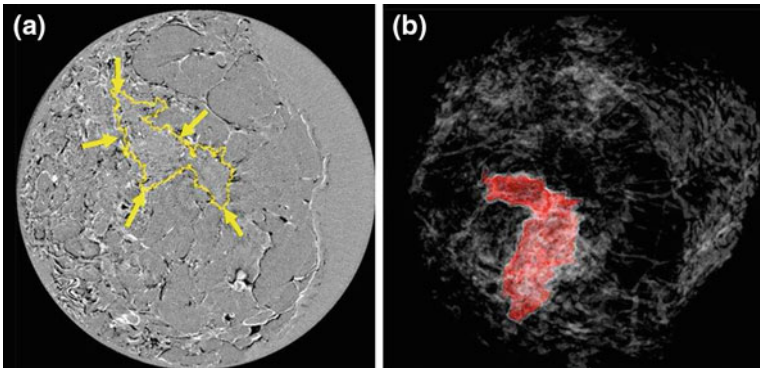


Fig. 22.4 Three-dimensional visualization of a tumour bearing breast tissue from the PCI-CT reconstruction performed with the Equally Sloped Tomography algorithm. **a** A segmented tumour in an axial slice, in which the *yellow contour line* and *arrows* indicate the lesion boundary. **b** Volume renderings of the sample showing the lesion in *red* (modified image from [49], kind permission of A. Bravin)

of the technique in producing high resolution 3D images of the breast at clinically compatible doses.

Application of GI to breast imaging is more recent. Main studies of breast tissue samples with GI have been conducted on conventional X-ray generators [50]. At ESRF a small portion ($2 \times 2 \times 2\,\mathrm{cm}^3$) of a breast sample containing a tumour was investigated using the GI in CT mode with SR [51]. The aim was to assess the technical feasibility of grating-based PC-CT imaging of the breast for the characterisation of ductal carcinoma in situ. The results demonstrated the high capability of this technique in the differentiation of soft-tissue components.

22.3.5 Imaging of Cartilages

Osteoarthrosis (OA) is a disease characterized by the progressive degeneration of articular cartilage and the development of altered joint congruency. It has a high incidence in the adult population. Affecting mainly the elderly population, it is one of the main causes of disability worldwide. Conventional radiography detects only important osseous changes, at advanced OA or RA stages, when therapeutic strategies are less effective. Early changes in the cartilage and other articular tissues are not directly visible. MRI imaging works better but the maximum achievable spatial resolution is not always adequate.

The limitations of the conventional diagnostic techniques brought to investigate the use of PCI approaches. In order to anticipate diagnosis, there is a need to use a technique able to non-invasively monitoring soft articular tissues, cartilages, and early changes in the adjoining subchondral and trabecular bone.

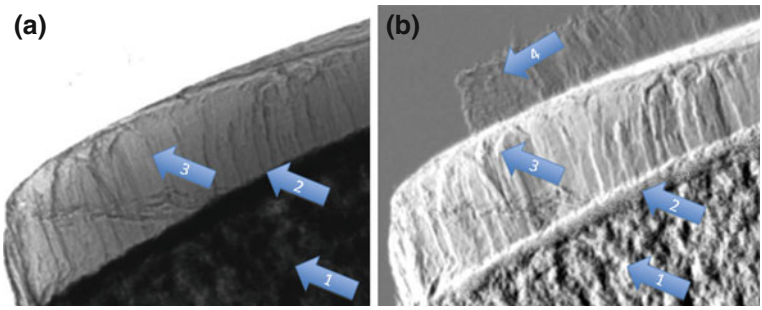


Fig. 22.5 ABI images of a specimen of human head femur. **a** Refraction image, **b** apparent absorption image (modified image from [53], *1* trabecular bone; *2* subchondral bone; *3* vertical striations; *4* tape/parafilm kind permission of R.-H. Menk)

First studies demonstrated that the ABI technique can be a powerful tool for this purpose [52–54]. The detection of cartilage abnormalities, especially in the initial stages of degenerative joint disease (or early in its progression) was shown with ABI on specimens of human ankle and hip and on excised human femoral heads.

ABI images of a specimen of human femur head obtained at 25 keV at Elettra are shown in Fig. 22.5. Vertical striations indicating the cartilage organization are easily visible, particularly in the apparent absorption image. In the refraction image, the structure of the subchondral bone, trabecular bone, and cartilage are simultaneously visible.

In Fig. 22.6 comparative ABI and MRI data are shown utilizing a human hip specimen [54]. The ABI image was acquired at DESY at the X-ray energy of 50 keV, working at 15 % rocking curve. The superior capability of the ABI technique in the detection of cartilage defect, as well as in the evaluation of the cartilage thickness, is clearly shown.

In the figure, the correct height of the cartilage (blu diamond arrow) is detected only in the ABI images. In (a) the height is only half of the actual tissue expansion. The defect is not visible in (a) or (b) because of its high content of water.

More recently the capability of ABI in the differentiation between OA and healthy cartilage was successfully shown, showing an excellent match with histological results [55, 56], as shown in Fig. 22.7.

Specimens of intact cadaveric human knee joints were imaged, using ABI in the CT mode at NSLS [57] at the energy of 51 keV. The images simultaneously show soft tissue and bone contrast at a level never achieved previously. Identifiable structures include articular cartilage, cruciate ligaments, loose connective tissue, menisci, and chondrocalcinosis.

ABI (in both planar and CT modalities) was used for in-vivo studies of guinea pigs knees at ESRF [58]. Results demonstrated the capability of this application that visualizes, simultaneously, soft and hard tissues. This becomes particularly important in the diagnosis of OA, a pathology affecting not only the cartilage tissue, but also the organization of the bone and the joint covering soft tissues.

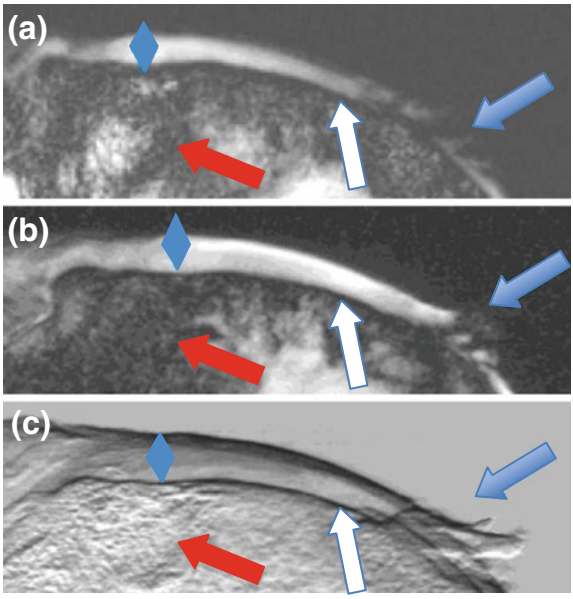


Fig. 22.6 Hip head in water: a comparison of MRI (**a**, **b**) (T1 and T2 w, 20 min exposure) and ABI (**c**) with respect to the apparent cartilage thickness (*red diamond arrow*). Two MRI images in the area of the structural cartilage defect (indicated by the *blue arrow*) seen in (**c**) are presented. *Red arrows* show trabecular bone, *white arrows* indicate subcontral bone (modified image from [54], with kind permission of R.-H. Menk)

22.3.6 Lungs Imaging

PCI tecniques are ideal for studying weakly absorbing tissues such as the air-filled lungs. Since late nineties, PBI and ABI have been employed for in-vivo and in-vitro studies of small animal lungs [59, 60].

One of the most promising research line developed in the last years concerns the dynamical imaging of lung clearance at birth [60–62].

PBI planar images were taken in rapid succession to study lung aeration at birth in spontaneously breathing neonatal rabbits. As the liquid-filled fetal lungs have low absorption contrast, they are not visible. They become visible with PCI techniuqs only as they aerate, allowing a detailed examination of this process. Pups were imaged live from birth to determine the timing and spatial pattern of lung aeration and the relative levels of lung aeration were measured. The effect of sample-to-detector propagation distance on images of a newborn rabbit pup, showing the edge enhancing properties of PBI, is shown in Fig. 22.8.

PBI has been used for studying lung and airspace structures and function in animal models [63].

In the same framework, it was shown that the application of an interface-specific phase retrieval algorithm, developed by Beltran et al. [64], is particularly effective in the imaging of lungs structure, bringing a considerable improvement to the image contrast with respect to conventional reconstruction algorithms.

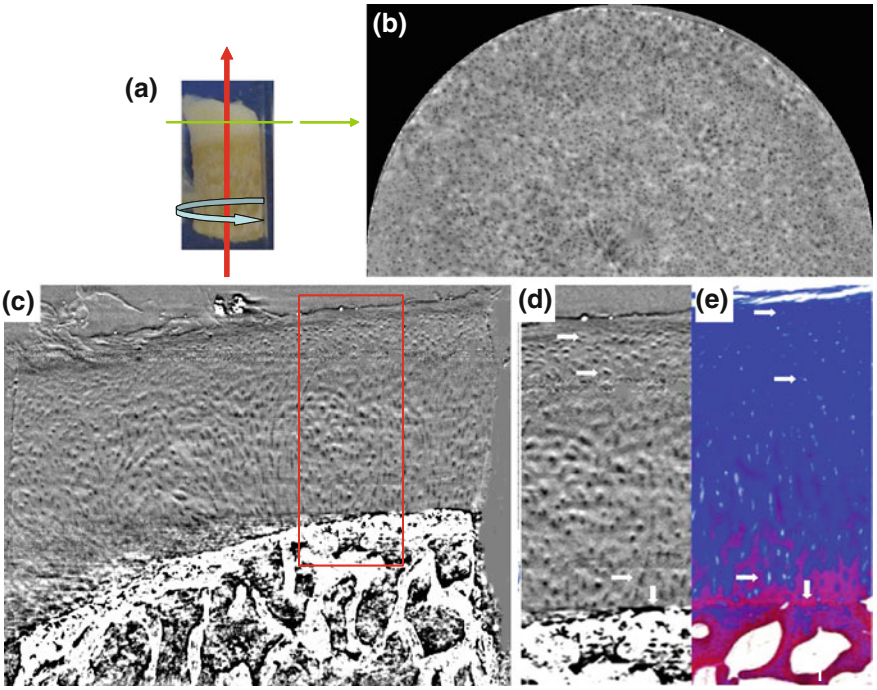


Fig. 22.7 Specimen of normal cartilage (**a**), Axial ABI-CT slice acquired at the 50 % slope position of the crystal (**b**), Coronal plane extracted from the reconstructed CT volume (**c**), Magnified portion identified by the ROI (**d**), Corresponding section from histologic preparation (**e**). ABI CT was taken at 26 keV with a detector pixel size of $8 \times 8\,\mu m^2$ (modified image from [55], with kind permission of A. Bravin)

Figure 22.9 shows a reconstructed slice of a preterm rabbit pup thorax, obtained after the application of the above cited algorithm. X-ray energy is 24 keV, sample-to-detector distance was 50 cm.

Studies on airway distension at different conditions of lung inflation were performed with healthy and allergic-sensitised mice at Spring-8, showing again the effectiveness of PBI for in-vivo imaging of lung disease. CT scans of healthy and ovalbumine-treated mice were acquired and the morphometric airways segments (in terms of diameter, length, and volume) were calculated [65, 66]. The same technique was used to visualize the movement of fluid in airways and to reveal the bolus fluid dosing dynamics for gene transfer into mouse airways [67].

Another application regarded the reduction of the airway surface liquid associated with cystic fibrosis, performed using GI method in a mouse model [68].

At CLS, ABI has been also used to image injured lungs [69]. It was shown that, for a rat model of gastric acid aspiration, ABI is capable of distinguishing between a healthy and an injured lung. The full extent of the lung and the lung damage

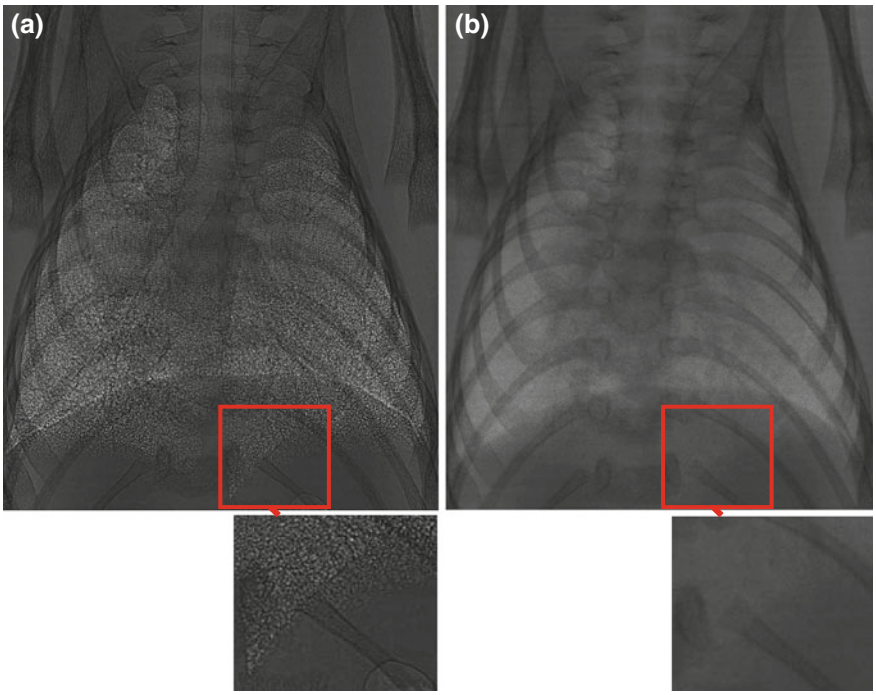


Fig. 22.8 The effect of sample-to-detector propagation distance on images of a newborn rabbit pup. Images are recorded at SPring-8 at the energy of 25 keV. *Left image* **a** is taken in FPI modality at a distance of 3 m, *right image* **b** is in absorption (distance = 7 cm). Enlarged areas marked by *rectangle* in (**a**) and (**b**) are shown below (modified image from [61], kind permission of M. Kitchen)

features were visualized with improved image quality with respect to clinical chest radiograph.

The capability of ABI in the quantitative characterization of the mouse lung has been demonstrated with recent experiments carried out at SSRF [70]. The three-dimensional model of the lung was established, and an excellent view of lung airways was provided. Important morphological parameters, such as diameter and alveolar surface area were also measured. These results offer a new perspective in the diagnosis of respiratory disease and may guide future work in the study of respiratory mechanism at the alveoli level [70].

Studies on individual alveolar movements during respiration, performed at Spring-8, have recently been published [71]. This technique (called Tracking X-ray microscopy (TrXM)) monitors the movements of upper right lung apices alveoli in live mice during respiration and identifies the natural alveolar dynamics. TrXM analysis in alveolar dynamics could be significant for better understanding of alveolar-based diseases such as ventilator induced lung injury in acute respiratory distress syndrome.

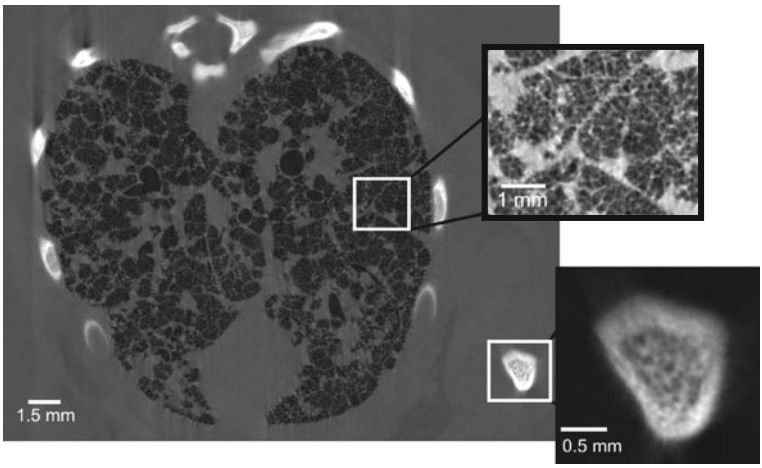


Fig. 22.9 Interface-specific tomographic reconstruction of a preterm rabbit pup thorax, focusing on the air/lung tissue interface. Magnified section highlights the visibility of the terminal airways (*upper box*). Magnified section in which the bone/lung tissue interface appears blurred as a result of the chosen phase retrieval filter (*lower box*) (modified image from [64] with kind permission of M. Kitchen)

Two new phase-retrieval algorithms for ABI providing information about the sample's X-ray absorption, refraction and scattering properties, have been developed by Kitchen et al. [72, 73] and successfully implemented for lungs imaging at Spring-8.

22.3.7 Microvascularization and Imaging of Soft Tissues

22.3.7.1 Micro-Bubbles as Contrast Agents for PCI

As reported above, imaging blood vessels and circulation takes benefit of the use of contrast agent, like Iodine or Gd and the application of KES techniques.

Also in PCI the contrast agents can be helpful. Gas-filled micro-bubbles, a standard contrast agent in ultra-sonography, determine contrast in ABI and PBI because of the multiple-refraction produced by micrometer-size bubbles [74].

Indeed, the introduction of micro-bubbles into tissue produces a significant change in the refractive index and highlights the visibility of the vessels lumen, acting as a positive contrast medium.

At SSRF micro-bubble based contrast agent was applied with PBI in an ex-vivo experiment, to visualize micro-vessels in a mouse [75] and to study in-vivo angiogenesis in subcutaneous tumors [76].

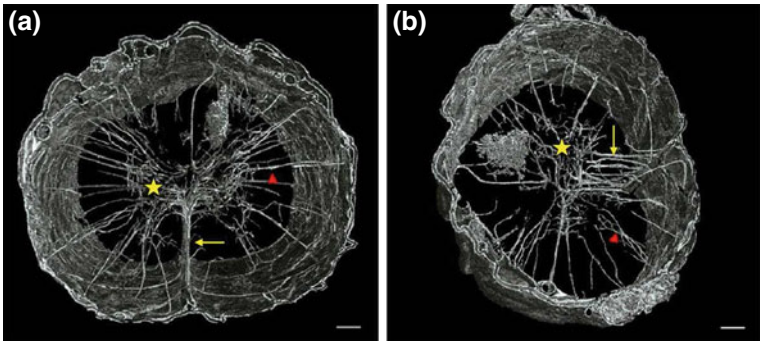


Fig. 22.10 View of 3D angio-architectural map in rat normal thoracic cord. **a** *Top view* of the vasculature. **b** *Oblique view* of vasculature. Both (**a**) and (**b**) showed the main blood supply system in common, including the spinal anterior vessels, the spinal posterolateral vessels, the central sulcal vessels (*arrow*) and the rami perforating branches (*triangle*) and the micro-vessel networks formed to feed the blood supply in gray matter (*star*). *Bar* = 100 μm. (Modified image from [79] with kind permission of T. Xiao)

Gaseous contrast agents have been employed in other PCI micro-CT applications: ambient air was employed to study the vascular tree of mice livers [77] and CO_2 was used to image micro-vasculature in rat kidneys [78].

22.3.7.2 Other Studies

Micro-vasculature of the spinal cord has been successfully imaged without a contrast medium in a rat model by Hu et al. at the SSRF medical imaging beamline [79].

PBI micro-CT was used to obtain 3D micro-vessel structure without angiography, simply using a saline solution as staining solution for the sample. As an example, Fig. 22.10 shows a 3D view of microvessels structure in a rat thoracic cord. The images were consistent with data obtained from histomorphology sections.

GI is a high sensitivity technique particularly suited for imaging soft tissues. Compared with FPI, it enables to achieve a higher contrast resolution with a better differentiation of the different phases without the need of staining or contrast agents.

At Spring-8 GI was applied to the study of mouse fetus. The CT reconstructed slices clearly depict the various organs, without any staining, at a pixel size of 5 μm [80].

Figure 22.11 shows approximately the sagittal tomographic sections of mouse fetuses at gestational days of 11, 13 and 15.

These data show how the technique can be particularly useful to examine anomalies that take place during development.

The same method was used to visualize atherosclerotic plaques in mice that had been fed on high-cholesterol diet [81].

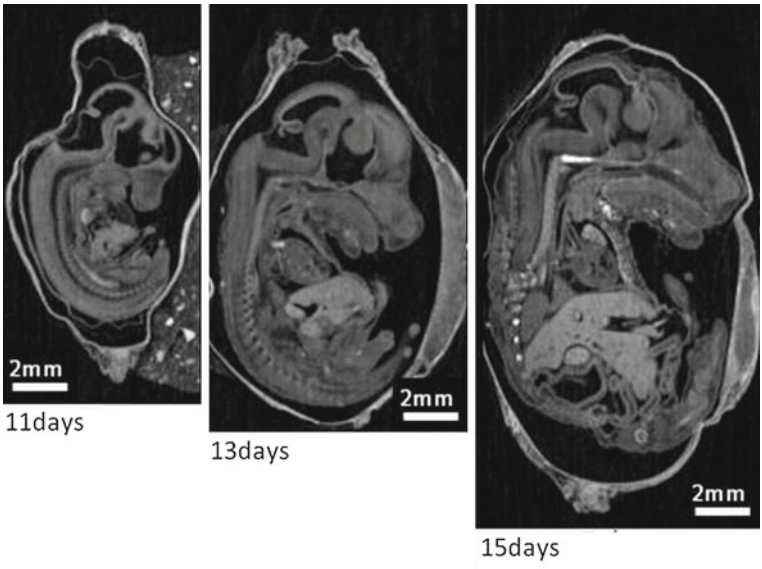


Fig. 22.11 Sagittal tomographic sections of mouse fetuses at gestational days of 11, 13 and 15 (data from [79], kind permission of N. Yagi)

Furthermore, GI was also used in studies of the hepatic circulation in rats [82]. The portal vein, the capillary vessel area and the hepatic vein of live rats were revealed sequentially by injecting physiological saline into the portal vein. Vessels greater than 0.06 mm in diameter were clearly shown with low radiation dose. This demonstrates that in-vivo vessel imaging in small animals can be performed, as conventional angiography, without the side effects of the presently used iodinated contrast agents [82].

SR PBI was applied to detect the 3-D structure of dermal tissues at SSRF [83]. The study shows the mesoscopic difference between normal dermal tissue and scar tissue and demonstrates that the high level of interweaving capability of collagen is compromised when dermal tissue is injured, providing a basis for future studies with this technique [83].

22.3.8 Brain Imaging

Brain studies with SR based PCI have been addressed for several purposes mainly on small animal models. GI is the most commonly used technique as it intrinsically provides a superior contrast resolution to visualize the different tissue structures without use of contrast agents. The brain tumour and the white and gray brain matter structure in a rat's cerebellum were clearly resolved [84–86]. The results have potentially a

high clinical relevance, as a similar approach using a system of three transmission gratings can be implemented with conventional X-ray sources.

Another important application of GI regards the detection of core pathological features of Alzheimer's disease (AD). Diagnosis of AD aims at detecting amyloid beta (Aβ) plaques, constituted by small ($\sim$50 μm) details resulting in low radiological contrast not visible with conventional methods.

SR microCT feasibility studies have been conducted on the brains of AD-model mice with ABI at NSLS and using GI at PSI [87]. They demonstrated the capability of both techniques to visualize these features as small nodules in the cortex and hippocampus of the brain. These results have an extreme relevance and open the way for developing new research protocols in mouse models of AD.

SR micro-CT studies can be applied for cell tracking purposes. An imaging protocol that permits 3D visualisation of a small number of glioma cells, implanted in a rat brain, has been developed at Elettra. The glioma cells, marked with nanoparticles of colloidal Au, were implanted into the brains of adult male Wistar rats during general anaesthesia. After tumours had been allowed to develop for up to 2 weeks, the animals were sacrificed and micro-CT scans of the intact cranium were acquired.

In the resulting volume datasets the tumour bulk is clearly visible, well differentiated from the background, and the infiltrating nature of the malignant growth is well demonstrated [88, 89].

More recent studies showed the protocol applicability for in-vivo studies [90] demonstrating that the cluster of 100,000 Au implanted cells into the brain mouse were well visible also in the scan carried out at low doses (see Fig. 22.12).

22.4 Conclusions

Imaging with SR has greatly developed in the last years thanks to the progress achieved in the applications of novel techniques exploiting the features of SR.

Studies conducted at several laboratories, in a wide research area of medicine, including cardiology, bronchography, mammography, imaging of cartilages, joints, brain, etc., demonstrated the high diagnostic significance of SR techniques.

Initially, SR imaging showed its clinical diagnostic relevance for studies with patients in coronary angiography where the beam monochromaticity was exploited with the application of KES technique.

More recently, with the development of PCI techniques, successful results have been obtained in the first protocol of clinical mammography with SR. In the same area, new interesting perspectives have been raised from the implementation of low dose tomo-mammography protocols.

Several groups showed that ABI is the ideal technique for the study of cartilages and joints. Images of human cartilages and joints acquired with this technique at very low radiation doses, have higher clinical quality than the conventional diagnostic method, opening possibilities for new clinical application of SR.

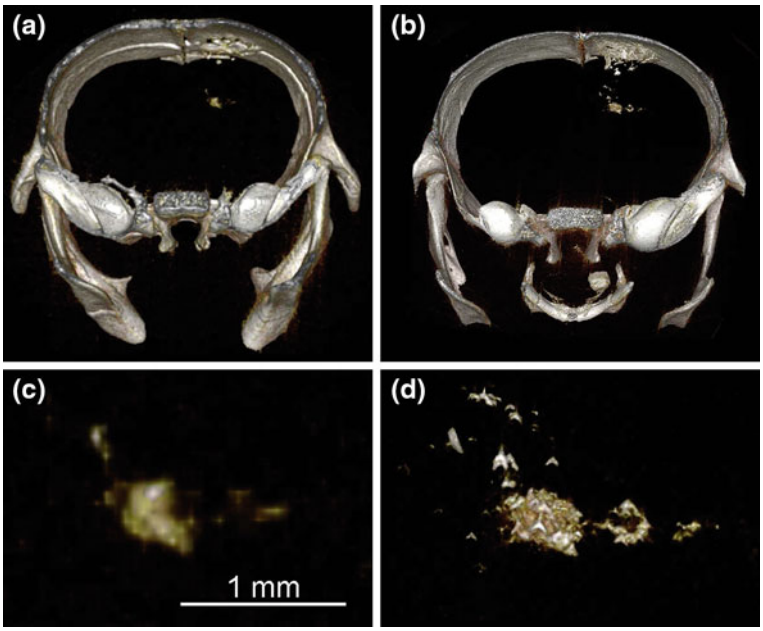


Fig. 22.12 Comparison of two 3D renderings of a CT of a mouse injected with 100,000 GNP-loaded F98 cells depicts (**a**–**c**) the low dose in-vivo data and (**b**–**d**) the high dose (and high resolution) ex-vivo image. The images in *panels c* and *d* are enlargements at full system resolution of the developed tumour depicted in *panels a* and *b*, respectively. Reprinted from [90], Copyright (2013), with kind permission from Elsevier

GI is very promising for brain studies, an example is represented by the excellent visualization of early pathological features obtained in a animal model of Alzheimer's disease.

In general SR imaging is very well suited for in-vivo studies on small animals, as widely shown in the research carried out with PBI on lungs, providing simultaneous information about structure and function.

On the other side SR cannot become a diagnostic tool for routine investigations as its use requires the implementation of great infrastructures, like SR facilities, not compatible with a clinical environment. Therefore SR, with its features, is likely to remain a *golden standard* for medical diagnosis.

The dissemination of SR research to the clinical practice must go through the developments of new and more compact X-ray sources. These machines are designed to deliver X-rays with characteristics as much as possible similar to SR ones, in terms of monochromaticity, intensity and spatial coherence, but with the advantage of compactness that makes them locatable in a hospital.

Acknowledgments I am grateful to A. Bravin (ESRF), F. de Carlo (APS), M. Kitchen (Melbourne Univ.), R.-H. Menk (Elettra), T. Xiao (SSRF), N. Yagi (Spring-8) for their support in the preparation of the manuscript.

References

1. P. Suortti, W. Thomlinson, Phys. Med. Biol. **48**, R1–R35 (2003)
2. R.A. Lewis, Phys. Med. Biol. **49**, 3573–3583 (2004)
3. S.-A. Zhou, A. Brahme, Phys. Med. **24**, 129–148 (2008)
4. A. Bravin, P. Coan, P. Suortti, Phys. Med. Biol. **58**, R1–R35 (2013)
5. A. Snigirev, I. Snigireva, V. Kohn, S. Kuznetsov, I. Schelokov, Rev. Sci. Instrum. **66**, 5486–5492 (1995)
6. S.W. Wilkins, T.E. Gureyev, D. Gao, A. Pogany, A.W. Stevenson, Nature **384**, 335–338 (1996)
7. P. Cloetens, R. Barratt, J. Baruchel, J.P. Guigay, M.J. Schlenker, Phys. D. Appl. Phys. **29**, 133–146 (1996)
8. K.M. Podurets, V.A. Somenkov, S.S. Shil'shtein, Sov. Phys. Tech. Phys. **654**, 34–36 (1989)
9. V.N. Ingal, E.A. Beliaevskaya, J. Phys. D: Appl. Phys. **28**, 2134 (1995)
10. D. Chapman, W. Thomlinson, R.E. Johnston, D. Washburn, E. Pisano, N. Gmür, Z. Zhong, R. Menk, F. Arfelli, D. Sayers, Phys. Med. Biol. **42**, 2015–2025 (1997)
11. E. Forster, K. Goetz, P. Zaumseil, Krist. Tech. **15**, 937–945 (1980)
12. U. Bonse, M. Hart, Appl. Phys. Lett. **6**, 155–161 (1965)
13. A. Momose, T. Takeda, Y. Itai, K. Hirano, Nat. Med. **2**(4), 473–475 (1996)
14. T. Weitkamp, A. Diaz, C. David, F. Pfeiffer, M. Stampanoni, P. Cloetens, E. Ziegler, Opt. Express **13**(16), 6296–6304 (2005)
15. A. Olivo, R.A. Speller, Appl. Phys. Lett. 074106(1–3) (2007)
16. W. R. Dix, K. Engelke, W. Graeff, C. Hamm, J. Heuer, B. Kaempf, W. Kupper, M. Lohmann, B. Reime, R. Reumann, Nucl. Instrum. Methods Phys. Res. Section A, **314**(2), 307–315 (1992)
17. T. Dill, W.R. Dix, C.W. Hamm, M. Jung, W. Kupper, M. Lohmann, B. Reine, R. Ventura, Eur. J. Phy. **19**(6), 499–511 (1998)
18. W.R. Dix, W. Kupper, T. Dill, C.W. Hamm, H. Job, M. Lohmann, B. Reine, R. Ventura, J. Synchrotron Radiat. **10**(3), 219–227 (2003)
19. E. Rubenstein, R. Hofstadter, H.D. Zeman, A.C. Thompson, J.N. Otis, G.S. Brown, J.C. Giacomini, H.J. Gordon, R.S. Kernoff, D.C. Harrison, Proc. Nat. Acad. Sci. **83**(24), 9724–9728 (1986)
20. E. Rubenstein, in *Synchrotron Radiation in the Biosciences*, ed. by B. Chance et al. (Oxford University Press, New York, 1994), pp. 639–645
21. W. Thomlinson, N. Gmur, D. Chapman, R. Garrett, N. Lazarz, H. Moulin, A.C. Thompson, H.D. Zeman, G.S. Brown, J. Morrison, P. Reiser, V. Padmanabahn, L. Ong, S. Green, J. Giacomini, H. Gordon, E. Rubenstein, Rev. Sci. Instr. **63**(1), 625–628 (1992)
22. H. Elleaume, S. Fiedler, F. Esteve, B. Bertrand, A.M. Charvet, P. Berkvens, G. Berruyer, T. Brochard, G. Le Duc, C. Nemoz, M. Renier, P. Suortti, W. Thomlinson, J.F. Le Bas, Phys. Med. Biol. **45**(9), L39–45 (2000)
23. T. Takeda, K. Umetani, T. Doi, J. Echigo, H. Ueki, K. Ueda, Y. Itai, Acad. Radiol. **4**(6), 438–445 (1997)
24. S. Ohtsuka, Y. Sugishita, T. Takeda, Y. Itai, J. Tada, K. Hyodo, M. Ando, Brit. J. Radiol. **72**(853), 24–28 (1999)
25. M. Shirai, D.O. Schwenke, H. Tsuchimochi, K. Umetani, N. Yagi, J.T. Pearson, Circ. Res. **112**(1), 209–221 (2013)
26. Y. Guan, Y. Wang, F. Yuan, H. Lu, Y. Ren, T. Xiao, K. Chen, D.A. Greenberg, K. Jin, G.-Y. Yang, Stroke **43**(3), 888–891 (2012)
27. H. Lu, Y. Wang, X. He, F. Yuan, X. Lin, B. Xie, G. Tang, J. Huang, Y. Tang, K. Jin, S. Chen, G.Y. Yang, Stroke **43**(3), 838–843 (2012)
28. V.M. Pai, M. Kozlowski, D. Donahue, E. Miller, X. Xiao, M.Y. Chen, Z.-X. Yu, P. Connelly, K. Jeffries, H. Wen, J. Anat. **220**(5), 514–524 (2012)
29. J.C. Giacomini, H. Gordon, R. O'Neil, A. Van Kessel, B. Cason, D. Chapman, W. Lavendar, N. Gmur, R. Menk, W. Thomlinson, Z. Zhong, E. Rubenstein, Nucl. Instrum. Methods Phys. Res. Section A, **406**(3), 473–478 (1998)

30. S. Bayat, G. Le Duc, L. Porra, G. Berruyer, C. Nemoz, S. Monfraix, S. Fiedler, W. Thomlinson, P. Suortti, C.G. Standertskjöld-Nordenstam, A.R. Sovijärvi, Phys. Med. Biol. **46**(12), 3287 (2001)
31. S. Bayat, L. Porra, H. Suhonen, C. Nemoz, P. Suortti, A.R.J. Sovijärvi, Appl. Physiol. **100**(6), 1964–1973 (2006)
32. S. Bayat, S. Strengell, L. Porra, T.Z. Janosi, F. Petak, H. Suhonen, P. Pekka Suortti, Z. Hantos, A.R.A. Sovijärvi, W. Habre, Am. J. Respir. Crit. Care Med. **180**(4), 296–303 (2009)
33. E.D. Pisano, R.E. Johnston, D. Chapman, J. Geradts, M.V. Iacocca, C.A. Livasy, D.B. Washburn, D.E. Sayers, Z. Zhong, M.Z. Kiss, W.C. Thomlinson, Radiology **214**(3), 895–901 (2000)
34. F. Arfelli, M. Assante, V. Bonvicini, A. Bravin, G. Cantatore, E. Castelli, L. Dalla Palma, M. Di Michiel, R. Longo, A. Olivo, S. Pani, D. Pontoni, P. Poropat, M. Prest, A. Rashevsky, G. Tromba, A. Vacchi, E. Vallazza, F. Zanconati, Phys. Med. Biol. **43**(10), 2845–2852 (1998)
35. J. Keyriläinen, A. Bravin, M. Fernández, M. Tenhunen, P. Virkkunen, P. Suortti, Acta Radiologica **51**(8), 866–884 (2010)
36. P. Coan, A. Bravin, G. Tromba, Accepted for publication in J. Phys. D (2013)
37. F. Arfelli, V. Bonvicini, A. Bravin, G. Cantatore, E. Castelli, L. Dalla Palma, M. Di Michiel, M. Fabrizioli, R. Longo, R. Menk, A. Olivo, S. Pani, D. Pontoni, P. Poropat, M. Prest, A. Rashevsky, M. Ratti, L. Rigon, G. Tromba, A. Vacchi, E. Vallazza, F. Zanconati, Radiology **215**(1), 286–293 (2000)
38. D. Dreossi, A. Abrami, F. Arfelli, P. Bregant, K. Casarin, V. Chenda, M.A. Cova, R. Longo, R.-H. Menk, E. Quaia, E. Quai, L. Rigon, T. Rokvic, D. Sanabor, M. Tonutti, G. Tromba, A. Vascotto, F. Zanconati, E. Castelli, Eur. J. Radiol. **68**(3), S58–S62 (2008)
39. E. Castelli, M. Tonutti, F. Arfelli, R. Longo, E. Quaia, L. Rigon, D. Sanabor, F. Zanconati, D. Dreossi, A. Abrami, E. Quai, P. Bregant, K. Casarin, V. Chenda, R.H. Menk, T. Rokvic, A. Vascotto, G. Tromba, M.A. Cova, Radiology **259**(3), 684–694 (2011)
40. E. Quai, R. Longo, F. Zanconati, G. Jaconelli, M. Tonutti, A. Abrami, F. Arfelli, D. Dreossi, G. Tromba, M.A. Cova, La, Radiologia Medica **118**(1), 89–100 (2013)
41. BIRADS, American College of Radiology Illustrated Breast Imaging Reporting and Data System 2003, 4th edn. Reston (VA), ACR (2003)
42. R.E. Johnston, D. Washburn, E. Pisano, C. Burns, W.C. Thomlinson, L.D. Chapman, F. Arfelli, N.F. Gmur, Z. Zhong, D. Sayers, Mammographic phantom studies with synchrotron radiation. Radiology **200**(3), 659–663 (1996)
43. W. Thomlinson, D. Chapman, Z. Zhong, R.E. Johnston, D. Sayers, in *Medical Applications of Synchrotron Radiation*, ed. by M. Ando, C. Uyama (Springer, Tokyo, 1998), pp. 72–76
44. J. Keyriläinen, M. Fernández, M.L. Karjalainen-Lindsberg, P. Virkkunen, M. Leidenius, K. von Smitten, P. Sipilä, S. Fiedler, H. Suhonen, P. Suortti, A. Bravin, Radiology **249**(1), 321–327 (2008)
45. A. Sztrókay, P.C. Diemoz, T. Schlossbauer, E. Brun, F. Bamberg, D. Mayr, A. Bravin, P. Coan, Phys. Med. Biol. **57**(10), 2931–42 (2012)
46. M. Ando, H. Bando, S. Ichihara, E. Hashimoto, K. Hyodo, T. Kunisada, G. Li, A. Maksimenko, K. Mori, D. Shimao, H. Sugiyama, T. Yuasa, E. Ueno, Eur. J. Radiol. **68**(3), S32–S36 (2008)
47. J. Miao, F. Förster, O. Levi, Phys. Rev. B **72**(5), 052103 (2005)
48. B.P. Fahimian, Y. Mao, P. Cloetens, J. Miao, Phys. Med. Biol. **55**(18), 5383–5400 (2010)
49. Y. Zhao, E. Brun, P. Coan, Z. Huang, A. Sztrókay, P.C. Diemoz, S. Liebhardtd, A. Mittone, S. Gasilov, J. Miao, A. Bravin, Proc. Natl Acad. Sci. USA **109**(45), 18290–18294 (2012)
50. M. Stampanoni, Z. Wang, T. Thüring, C. David, E. Roessl, M. Trippel, R.A. Kubik-Huch, G. Singer, M.K. Hohl, N. Hauser, Invest. Radiol. **46**(12), 801–806 (2011)
51. A. Sztrókay, J. Herzen, S.D. Auweter, S. Liebhardt, D. Mayr, M. Willner, D. Hahn, I. Zanette, T. Weitkamp, K. Hellerhoff, F. Pfeiffer, M.F. Reiser, F. Bamberg, Eur. Radiol. **23**(2), 381–387 (2013)
52. J. Mollenhauer, M.E. Aurich, Z. Zhong, C. Muehleman, A.A. Cole, M. Hasnah, O. Oltulue, K.E. Kuettnera, A. Margulis, L.D. Chapman, Osteoarthr. Cartil. **10**(3), 163–171 (2002)
53. C. Muehleman et al., X-ray detection of structural orientation in human articular cartilage. Osteoarthr. Cartil. **12**, 97–105 (2004)

54. A. Wagner, M. Aurich, N. Sieber, M. Stoessel, W.D. Wetzel, K. Schmuck, M. Lohmann, B. Reimec, J. Metge, P. Coan, A. Bravin, F. Arfelli, L. Rigon, R.-H. Menk, G. Heitner, T.Irvingi, Z. Zhong, C. Muehleman, J.A. Mollenhauer, Nucl. Instrum. Methods Phys. Res. Section A, **548**(1), 47–53 (2005)
55. P. Coan, F. Bamberg, P.C. Diemoz, A. Bravin, K. Timpert, E. Mützel, J.G. Raya, S. Adam-Neumair, M.F. Reiser, C. Glaser, Invest. Radiol. **45**(7), 437–444 (2010)
56. E.C. Ismail, W. Kaabar, D. Garrity, O. Gundogdu, O. Bunk, F. Pfeiffer, M.J. Farquharson, D.A. Bradley, Appl. Rad. Isot. **68**(4), 767–771 (2010)
57. J. Li, Z. Zhong, D. Connor, J. Mollenhauer, C. Muehleman, Osteoarthr. Cartil. **17**(9), 1193–1196 (2009)
58. P. Coan, A. Wagner, A. Bravin, P.C. Diemoz, J. Keyriläinen, J. Mollenhauer, Phys. Med. Biol. **55**(24), 7649–7662 (2010)
59. N. Yagi, Y. Suzuki, K. Umetani, Y. Kohmura, K. Yamasaki, Med. Phys. **26**, 2190–2193 (1999)
60. R.A. Lewis, C.J. Hall, A.P. Hufton, S. Evans, R.H. Menk, F. Arfelli, L. Rigon, G. Tromba, D. Dance, I.O. Ellis, A. Evans, E. Jacobs, S.E. Pinder, K.D. Rogers, J. Brit. Rad. **76**(905), 301–308 (2003)
61. M.J. Kitchen, R.A. Lewis, M.J. Morgan, M.J. Wallace, M.L. Siew, K.K.W. Siu, A. Habib, A. Fouras, N. Yagi, K. Uesugi, S.B. Hooper, Phys. Med. Biol. **53**(21), 6065–6077 (2008)
62. S.B. Hooper, M.J. Kitchen, M.L. Siew, R.A. Lewis, A. Fouras, A.B. te Pas, K.K. Siu, N. Yagi, K. Uesugi, M.J. Wallace, Clin. Exp. Pharm. Phys. **36**, 117–125 (2009)
63. D.W. Parsons, K. Morgan, M. Donnelley, A. Fouras, J. Crosbie, I. Williams, R.C. Boucher, K. Uesugi, N. Yagi, K.K.W. Siu, J. Anat. **213**, 217–227 (2008)
64. M.A. Beltran, D.M. Paganin, K.K.W. Siu, A. Fouras, S.B. Hooper, D.H. Reser, M.J. Kitchen, Phys. Med. Biol. **56**(23), 7353–7369 (2011)
65. K.K. Siu, K.S. Morgan, D.M. Paganin, R. Boucher, K. Uesugi, N. Yagi, D.W. Parsons, Eur. J. Radiol. **68**(3), S22–S26 (2008)
66. T. Sera, H. Yokota, K. Uesugi, N. Yagi, Respir. Phys. Neurobiol. **185**, 639–646 (2013)
67. M. Donnelley, K.K. Siu, R.A. Jamison, D.W. Parsons, Gene Therapy **19**(1), 8–14 (2011)
68. K.S. Morgan, M. Donnelley, D.M. Paganin, A. Fouras, N. Yagi, Y. Suzuki, A. Takeuchi, K. Uesugi, R.C. Boucher, D.W. Parsons, K.K.W. Siu, PLoS ONE **8**(1) (2013)
69. D.M. Connor, Z. Zhong, H.D. Foda, S. Wiebe, C.A. Parham, F.A. Dilmanian, E.B. Cole, E.D. Pisano, Acad. Radiol. **18**(12), 1515–1521 (2011)
70. L. Zhang, S. Luo, Open Med. Inform. J. **5**(Suppl. 1), 19–25 (2011)
71. S. Chang, N. Kwon, B.M. Weon, J. Kim, C.K. Rhee, H.S. Choi, Y. Kohmura, M. Yamamoto, T. Ishikawa, J.H. Je, Scientific Reports 3, (2013)
72. M.J. Kitchen, D.M. Paganin, K. Uesugi, B.J. Allison, R.A. Lewis, S.B. Hooper, K.M. Pavlov, Opt. Express **18**(19), 19994–20012 (2010)
73. M.J. Kitchen, D.M. Paganin, K. Uesugi, B.J. Allison, R.A. Lewis, S.B. Hooper, K.M. Pavlov, Phys. Med. Biol. **56**(3), 515–534 (2011)
74. F. Arfelli, L. Rigon, R.H. Menk, Phys. Med. Biol. **55**(6), 1643–1658 (2000)
75. Y. Xi et al., Microbubbles as contrast agent for in-line x-ray phase-contrast imaging. Appl. Phys. Lett. **99**, 011101 (2011)
76. R. Tang, Y. Xi, W.M. Chai, Y. Wang, Y. Guan, G.Y. Yang, H. Xie, K.M. Chen, Phys. Med. Biol. **56**(12), 3503–3512 (2011)
77. C.M. Laperle, T.J. Hamilton, P. Wintermeyer, E.J. Walker, D. Shi, M.A. Anastasio, Z. Derdak, J.R. Wands, G. Diebold, C. Rose-Petruck, Phys. Med. Biol. **53**(23), 6911–6923 (2008)
78. U. Lundström, D.H. Larsson, A. Burvall, P.A. Takman, L. Scott, H. Brismar, H.M. Hertz, Phys. Med. Biol. **57**(9), 2603–2617 (2012)
79. J.Z. Hu, T.D. Wu, L. Zeng, H.Q. Liu, Y. He, G.H. Du, H.B. Lu, Phys. Med. Biol **57**(5), N55–63 (2012)
80. M. Hoshino, K. Uesugi, N. Yagi, Biol. Open **1**(3), 269–274 (2012)
81. M. Takeda, T. Yamashita, M. Shinohara, N. Sasaki, H. Tawa, K. Nakajima, A. Momose, K.I. Hirata, Int. J. Cardiovasc. Imaging **28**(5), 1181–1191 (2012)

82. T. Takeda, A. Yoneyama, J. Wu, F.A. Momose, K. Hyodo, J. Synchrotron Radiat. **19**(2), 252–256 (2012)
83. Y. Jiang, Y. Tong, T. Xiao, S. Lu, Dermatology **225**(1), 75–80 (2012)
84. F. Pfeiffer, O. Bunk, C. David, M. Bech, G. Le Duc, A. Bravin, P. Cloetens, Phys. Med. Biol. **52**(23), 6923–6930 (2007)
85. S.A. McDonald, F. Marone, C. Hintermuller, G. Mikuljan, C. David, F. Pfeiffer, M.J. Stampanoni, Synchrotron Radiat. **16**(4), 562–572 (2009)
86. G. Schulz, T. Weitkamp, I. Zanette, F. Pfeiffer, F. Beckmann, C. David, S. Rutishauser, E. Reznikova, B. Müller, J. Royal Soc. Interface **7**(53), 1665–1676 (2010)
87. B.R. Pinzer, M. Cacquevel, P. Modregger, S.A. McDonald, J.C. Bensadoun, T. Thuering, P. Aebischer, M. Stampanoni, Neuroimage **61**(4), 1336–1346 (2012)
88. C.J. Hall, E. Schültke, L. Rigon, K. Ataelmannan, S. Rigley, R. Menk, F. Arfelli, G. Tromba, S. Pearson, S. Wilkinson, A. Round, S. Crittell, R. Griebel, B.H.J. Juurlink, Eur. J. Radiol. **68**(3), S156–S159 (2008)
89. R.H. Menk, E. Schültke, C. Hall, F. Arfelli, A. Astolfo, L. Rigon, A. Round, K. Ataelmannan, S. Rigley MacDonald, B.H. Juurlink, Nanotech. Biol. Med. **7**(5), 647–654 (2011)
90. A. Astolfo, E. Schültke, R.H. Menk, R.D. Kirch, B.H. Juurlink, C. Hall, L.-A. Harsan, M. Stebel, D. Barbetta, G. Tromba, F. Arfelli, Nanomed.: Nanotech. Biol. Med. **9**(2), 284–292 (2013)

Chapter 23
Synchrotron Radiation and Bio-crystallography

Marco Nardini and Martino Bolognesi

Abstract The last decade has witnessed the development of new methodologies in molecular biology and biochemistry which, together with the widespread availability of computing power for fast calculation and graphics, have supported the striking growth of crystallographic studies of biological relevance. This surge in new methodologies experienced by macromolecular crystallography has been largely fuelled by developments in structural genomics and by the needs of the pharmaceutical industry. A key contribution to such rapid growth was certainly provided by the increased access to synchrotron sources, which resulted in new ways of collecting X-ray diffraction data and allowed novel structure determination techniques, otherwise not possible on conventional X-ray sources. Open access to synchrotron sources, together with the use of efficient X-ray detectors, is probably the fundamental reason of the exponential growth of structural biology studies during the last 15 years. The next paragraphs cover some general aspects and select recent advances in macromolecular crystallography, focussing especially on synchrotron radiation applications.

23.1 Macromolecular Crystals

Almost every week new three-dimensional structures of proteins, nucleic acids, and their complexes appear in the most important scientific journals. The complexity of such structures is steadily growing, and their experimental resolution is often at atomic level. These results provide one of the most exciting and accurate tools for innovation in life sciences, particularly for applications in drug-design, immunol-

M. Nardini (✉) · M. Bolognesi
Department of Biosciences, University of Milano, Via Celoria 26, 20131 Milano, Italy
e-mail: marco.nardini@unimi.it

M. Bolognesi
e-mail: martino.bolognesi@unimi.it

S. Mobilio et al. (eds.), *Synchrotron Radiation*,
DOI: 10.1007/978-3-642-55315-8_23, © Springer-Verlag Berlin Heidelberg 2015

ogy, virology, and in enzymology [1–5]. Protein crystallography, which has a growing role in the human genome project, is one of the most powerful techniques in modern biology for three-dimensional structure determination. However, it can only be applied providing that suitable crystals can be obtained. The ability to produce suitable crystals is currently the major bottleneck to structure determination.

23.1.1 Physical and Chemical Properties

A crystal of organic material (such as proteins, DNA fragments, tRNA molecules, viruses, etc) is a three-dimensional periodic array of macromolecules. In terms of crystal size bio-macromolecular crystals are rather small, with volumes rarely exceeding $0.1\,mm^3$ and crystal lattice periodicity often >100 Å. Macromolecular crystals show unique physical and chemical properties, among other crystals in Nature. In particular, they display poor mechanical stability and a high solvent content. Both the fragility of these crystals and their sensitivity to external conditions are related to the weak interactions between macromolecules in the crystal lattice, which are based mainly on hydrogen bonds and van der Waals interactions. The energy responsible for crystal lattice stabilization is very low (<10 kcal/mol), typically lower than the energy required for protein folding. Therefore, the lattice forces usually do not disrupt the overall conformation of the crystallized macromolecules. This is a critical point since it ensures that the three-dimensional structure of a macromolecule in a crystalline environment is identical to the structure of the same molecule in solution.

The fragility of macromolecular crystals is also related to their high solvent content (from 30 % to more than 80 % v/v). In fact, to prevent crystal cracking or collapse due to dehydration, the crystals must be kept in a solvent saturated environment. The high solvent content of the crystals has two important and useful implications. Firstly, the macromolecule concentration in the crystal is of the same order of magnitude of that typical of cytoplasmic compartments in vivo (about 10^{-2} M). Secondly, extended solvent channels (completely crossing the crystal volume and touching each crystallized protein molecule) allow the efficient diffusion of small molecules within the crystals. The diffused molecules can be either heavy atoms or other ligands (substrates, inhibitors, cofactors, etc), thus providing key information for structure determination purposes and for the mechanicistic description of enzymatic reactions.

23.1.2 Crystal Growth

Despite dramatic progress in macromolecular crystallography research, crystallization remains a major bottleneck in the structural characterization of macromolecules. In fact, the methods used to produce crystals have also evolved over the years as a result of increased understanding and advancing technology, but crystallization

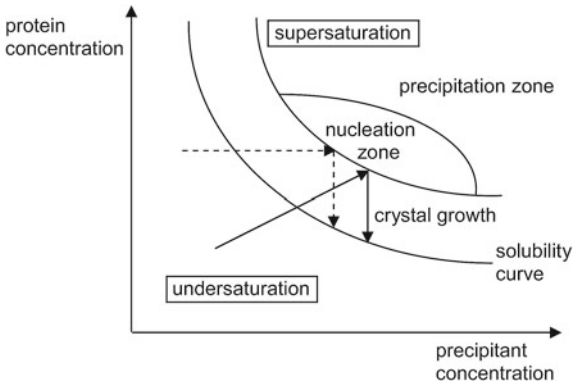


Fig. 23.1 Solubility curve for a protein versus precipitant concentration (salt or another chemical parameter affecting protein molecule aggregation) in a typical vapour diffusion (*continuous line*) or dialysis (*dashed line*) crystallization experiment

strategies continue to be rooted in massive trial-and-error approaches [6–8]. In general, it is common belief that insufficient purity of the sample is the most probable cause of unsuccessful crystallization. The sample quality requirements for protein crystallography are more stringent than the requirements for most biochemical tests. To grow macromolecular crystals of good quality the protein sample must be highly homogeneous: other compounds should be absent, all protein molecules should have the same surface properties (particularly for what concerns surface charge distribution), and the same oligomerization state.

The fundamental task in protein crystallization is to create a solution supersaturated with protein that will produce single, well-ordered crystals. More often than not, supersaturated solutions produce precipitate or phase separation instead. There is no a priori theory for discerning which solutions will produce crystals and which will produce precipitate. So the crystallization process is separated into two stages: screening and optimizing. Each stage is conducted with a largely empirical approach. The screening process discovers lead crystallization conditions ('hits'), which typically produce microcrystals, thin rods or plates. The optimization process is devoted to grow crystals of size and regularity adequate for a successful X-ray diffraction data collection.

Crystal growth is a multiparametric process involving three basic steps: nucleation, growth, and cessation of growth (Fig. 23.1). To achieve the spontaneous formation of the first ordered aggregates (nuclei) the sample solution is brought to supersaturation. Supersaturation can be achieved by varying intrinsic physical and chemical parameters, such as ionic strength, dielectric constant of the solvent, pH, temperature, macromolecule concentration, concentration of chemicals (precipitant, buffer, additives). Once nuclei have formed, crystal growth can begin and proceed while the degree of supersaturation is reduced. Maintaining high supersaturation would result in the formation of too many crystallization nuclei, which will develop into too many small crystals. Furthermore, crystals should grow slowly to reach the maximum degree of intrinsic order. Cessation of growth can be triggered by different causes, such as growth defects, poisoning of the crystal faces, "ageing" (chemical reaction) of the macromolecules, or simply depletion of the macromolecules from

the crystallization media. From a practical point of view, precipitation of the macromolecules to form crystals is mostly achieved using techniques known as "vapour diffusion" (increase of protein concentration by evaporation of water in a sealed environment), or by dialysis (Fig. 23.1). A great number of experiments (100–500) are usually necessary to determine the best crystallization conditions. Therefore, crystallization experiments are run on a very small scale (μl samples). Macromolecular crystals suitable for X-ray diffraction experiments have a typical linear size of 10–100 μm, and grow in a time period varying from few hours, to weeks or even months. In case of limited crystal growth, not related to biochemical problems, crystallization experiments carried out in space, under "microgravity" conditions, might improve the quality of the crystals [9].

When screening methods for protein crystallization fail, the modification of target proteins is often necessary to increase the susceptibility of the proteins to crystallization. Each change to the sequence of the protein (amino acid mutation) or its ligation state generates a new crystallization target for screening. This approach includes the crystallization of single domains in multi-domain proteins, of truncated forms at the N- and C-terminus, of truncated forms generated by limited proteolysis, and of single/multiple site-specific mutants. Site-directed mutagenesis is a common method to alter the surface properties of the target, or to stabilize the target. In addition, one can also attempt to engineer crystal contacts when the crystal structure of a homologous protein or a low-resolution structure of the target is available.

23.1.3 Crystal Handling and Radiation Damage

Macromolecular crystals are usually very fragile, and need special handling care. This unique property reflects the fact that the macromolecules are loosely packed in the crystal, with large solvent-filled channels crossing the crystal volume. Removal of the solvent destabilizes the crystal, which can easily dissolve or shatter. Protein crystals must, therefore, always be kept in their mother liquor or in its saturated vapour, even when exposed to X-rays.

For data collection purpose, the crystal can be hosted in a thin-walled capillary, containing a small amount of mother liquor. Water vapour will guarantee proper hydration of the crystal when the capillary is sealed on both sides by resin (Fig. 23.2a). Then, the capillary is easily mounted on a goniometer head and properly oriented for X-ray exposure. Unfortunately, the energy released by absorption of X-rays in a crystal inevitably damages it by causing the formation of free radicals in the crystal (especially OH· due to water radiolysis) which react with the protein molecules and irreversibly damage their crystal packing. The most common symptoms of radiation damage are a decrease of diffraction intensity and resolution limits (ultimately resulting in the X-ray pattern dying away), a variation of the unit cell volume with consequent non-isomorphism within a data series (thus hampering traditional phasing methods), and site-specific damage. The latter occurs in a well-defined order, starting with the breakage of disulphide bonds, followed by decarboxylation of aspartates,

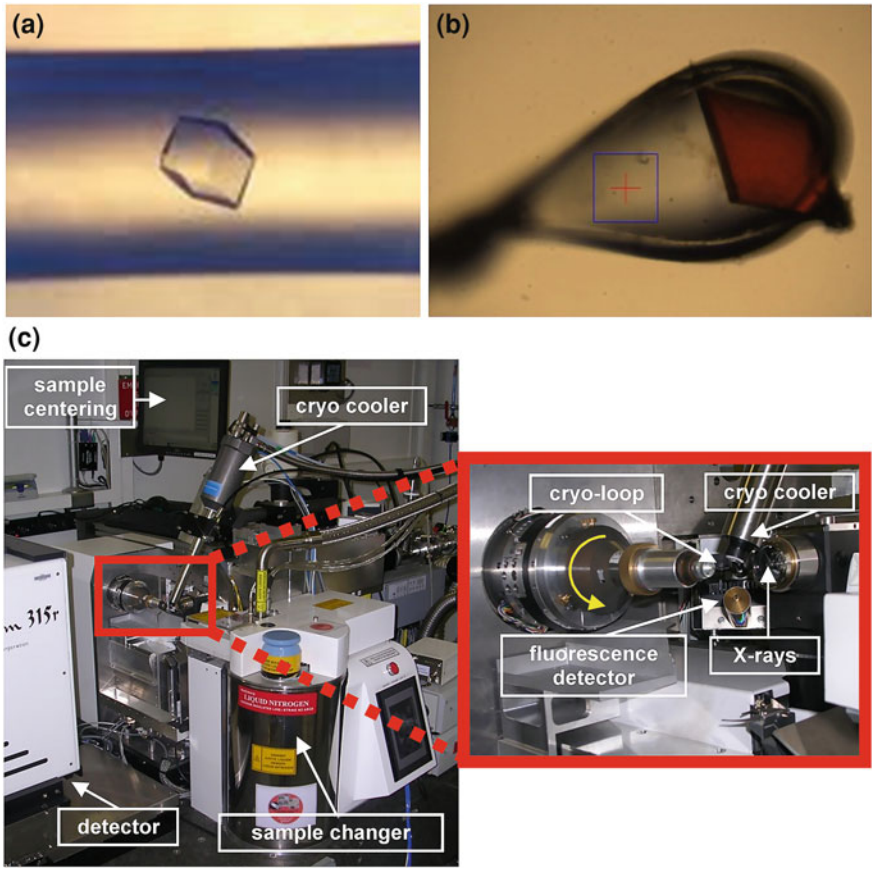


Fig. 23.2 Crystal mounting. **a** Protein crystal in equilibrium with mother liquor in a thin-walled capillary. **b** Crystal on a fiber loop at 100 K. The size and position of the X-ray beam is shown as a *blue square*. **c** Typical set-up for recording data from a slowly rotated crystal at a MAD synchrotron beamline (ESRF, Grenoble, France). Crystal rotation around an axis orthogonal to the X-ray beam is indicated by the *yellow arrow*

glutamates and the C-terminus, and then loss of the hydroxyl group from tyrosines [10]. The extent of radiation damage depends on the applied radiation dose, on the photon energy (it is lower for energy higher than 12.4 keV, or $\lambda = 1.0$ Å), on the type of proteins and on the chemical composition of the solvent. The damage continues even after X-ray exposure, due to the long half-life time of the free radicals.

Nowadays, the extensive use of synchrotron radiation has made almost obligatory the cooling of the crystal samples to cryogenic temperature. In liquid nitrogen at 100 K, the radiation damage effects are so much reduced that they are often negligible. Most protein crystals can be cooled to cryogenic temperatures (with appropriate care for the solvent properties) using the so called "flash-freezing" technique. The crystal is "fished" by using a nylon fibre loop, where it remains suspended in a thin film of

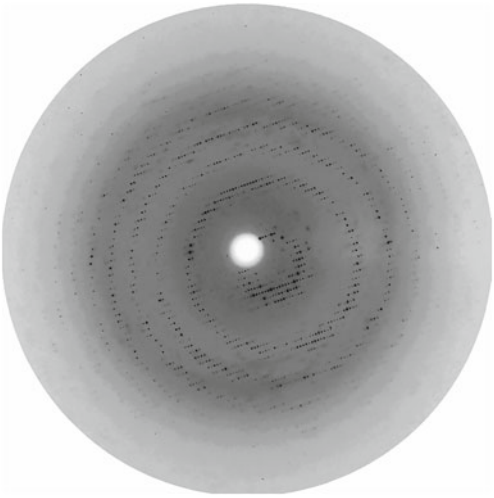


Fig. 23.3 Diffraction pattern of a protein crystal subjected to small-angle oscillation data collection

solvent (Fig. 23.2b). The loop is then cooled very rapidly by immersion into liquid nitrogen through the temperature where ice crystals may grow, to below 190 K where water forms a stable glassy state. If flash-freezing is successful, the liquid film in the loop freezes into a glass and remains clear. For data collection, the loop is mounted onto a goniometer head, where it is held in a stream of cold nitrogen gas (Fig. 23.2c). Crystallographers can take or ship loop-mounted flash-frozen crystals to synchrotron, minimizing handling of crystals at the data collection site.

23.2 X-Ray Diffraction and Phasing Problem

23.2.1 Fundamentals of Crystallography

Let's now consider a crystal ideally schematised by a mosaic of crystalline blocks. At fixed wavelength, a Bragg reflection only occurs if the incident beam makes the correct angle with the reflecting planes. Because of the slight disorder in a real crystal, the reflection can be fully excited if the crystal is rotated through its reflecting position. In fact, all fixed-wavelength observing techniques use a rotating crystal system. Usually, the crystal is rotated around an axis orthogonal to the X-ray beam (Fig. 23.2c). For a protein crystal, a very large number of diffracted beams (called 'reflections' to remind the Bragg's law) may be recorded, and it is necessary to avoid them overlapping. By rotating the crystal through a small angle (0.5–1°), they can easily be observed separately (Fig. 23.3). For macromolecules in a crystal to be observed at atomic resolution, very many reflections must be recorded. At the modest resolution of 2 Å a moderate-sized protein unit cell edge of 50 Å will give 25 orders of diffraction along this direction. Therefore, in three dimensions the *hkl* all vary

between −25 and +25, assuming that the three cell dimensions are similar. Very roughly 125,000 different Bragg reflections exist to this resolution and should be collected. In fact, the number of independent reflection is reduced by a factor of two if the Friedel's law applies and the number is further reduced depending on crystal symmetry.

If the crystal is rotated with an angular velocity ω through the reflection position, then the total energy of a diffracted X-ray along the direction defined by the Bragg reflection associated to the lattice planes *hkl* is expressed by the Darwin equation:

$$E_{hkl} = \frac{e^4}{m^2 c^4 \omega} I_0 \lambda^3 A L P \frac{V_X}{V_0^2} |\mathbf{F}_{hkl}|^2 \tag{23.1}$$

where I_0 is the incident beam intensity, λ is the wavelength, A is the correction due to the absorption of the sample, L and P are the Lorentz and the polarization factors, V_x is the volume of the crystal and V_0 the volume of the unit cell. Each structure factor $\mathbf{F}_{hkl}$ is a complete description of a diffracted X-ray recorded as reflection *hkl* and, therefore, is characterized by an amplitude and a phase and it can be represented in the imaginary plane as a vector (Fig. 23.4a).

The Darwin equation shows that many different factors contribute to weaken the intensities of the waves diffracted by macromolecular crystals: the amplitude of the structure factors $|\mathbf{F}_{hkl}|$ are small, due to the low atomic number of the component elements (H, C, N, O, etc.) of the biological macromolecule, the crystal volume is always small, while the unit cell is normally quite large. Therefore, significant diffracted intensities can be measured if high intensity incident radiation is applied, and if the sample X-ray absorption (by varying λ) as well as the diffused background radiation (by using a highly collimated beam) is minimized. All these experimental adjustments can be achieved using synchrotron radiation, while they are more difficult (or impossible) to achieve on a normal rotating anode X-ray source [11, 12].

A unique application of the synchrotron radiation in bio-crystallography is the so called Laue technique [13]. In this method the sample is hit by "white" radiation (λ ranging from 0.5 to 3.0 Å). As a consequence, many families of lattice planes are simultaneously "excited", thus producing a complex pattern of diffraction that can, however, be deconvoluted. The advantage of this technique is that very short X-ray pulses ($<<1$ s) can be used, due to the high intensity of the white radiation. In some cases (high symmetry of the crystal) one single pulse of radiation is sufficient to record the full diffraction diagram. This technique is at the basis of time-resolved crystallography experiments, which have found their major applications in the study of biological photoactivated protein reactions. The development of time-resolved multiwavelength Laue crystallography allows following the time course of biochemical processes (i.e. the catalytic cycle of an enzyme) through analysis of the related high resolution three-dimensional structure(s), with a time resolution in the (sub)nanosecond-millisecond range. In the past few years, this technique has evolved considerably due to the improvement of synchrotron sources, of beamline optics, charge-coupled detectors and of the optimized reaction triggering strategies based

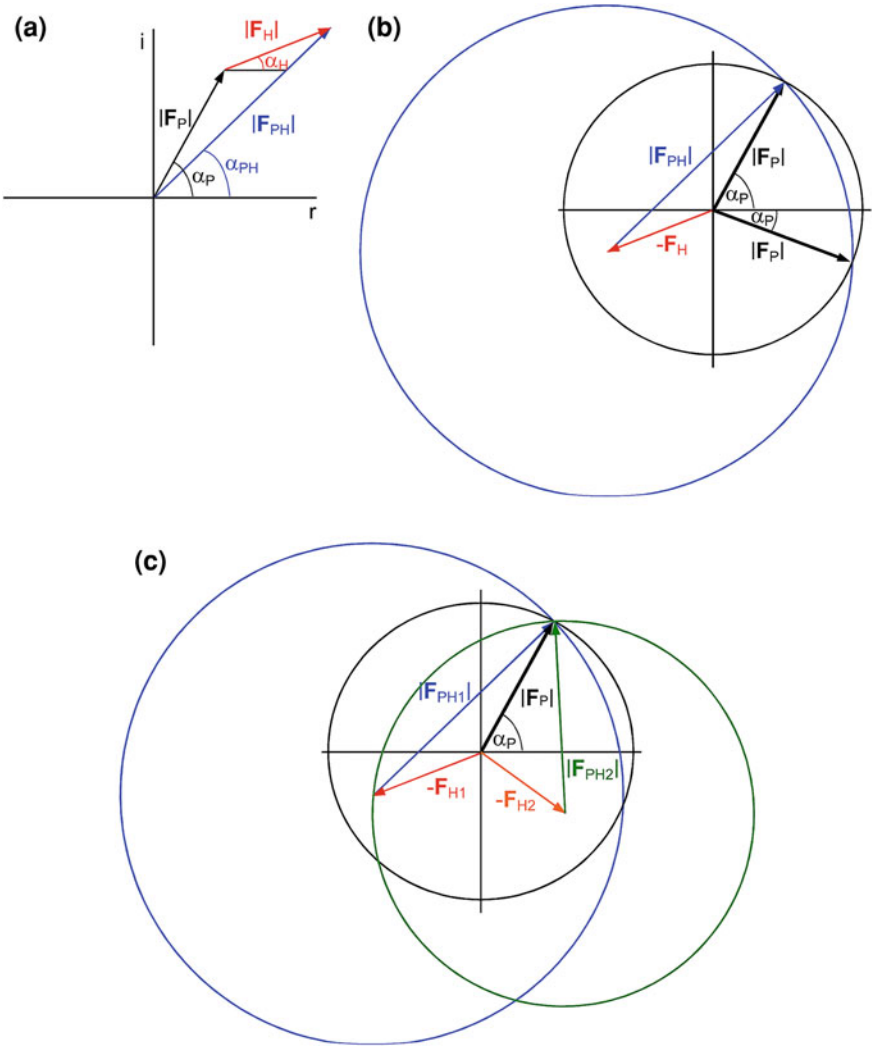


Fig. 23.4 **a** Argand diagram for a single isomorphous replacement. Amplitude moduli and phases are indicated on the corresponding vectors for a native reflection ($\mathbf{F}_P$), a derivative reflection ($\mathbf{F}_{PH}$), and for the contribution of the bound heavy atom ($\mathbf{F}_H$). **b** Harker diagram for one heavy atom derivative. **c** Harker diagram for two heavy atom derivatives in a MIR experiment

on femtosecond-picosecond laser pulses. In fact, the dynamical processes investigated with Laue diffraction require an accurate triggering event (initiated usually by a laser pulse) to achieve the correct timing between protein structural transitions and X-ray beam exposure [14–16].

23.2.2 Solution of the Phase Problem

In the diffraction experiment we measure the intensity of the diffracted beam I_{hkl}, which is proportional to the square of the amplitude of the structure factor $\mathbf{F}_{hkl}$. The structure factor is a function of the scattering due to the electrons of individual atoms comprising the unit cell electron density, f_i, known as the atomic scattering factor:

$$\mathbf{F}_{hkl} = \sum_{i=1}^{N} f_i e^{2\pi j(hx_i+ky_i+lz_i)} \tag{23.2}$$

Instead of summing over all N separate atoms in the unit cell, we can integrate over all electrons in the unit cell volume V:

$$\mathbf{F}_{hkl} = \int_V \rho(x, y, z) e^{2\pi j(hx+ky+lz)} dV \tag{23.3}$$

The reverse of this Fourier transform provides an expression of the electron density as a function of all structure factors:

$$\rho(x, y, z) = \frac{1}{V} \sum_{hkl} \mathbf{F}_{hkl} e^{-2\pi j(hx+ky+lz)} \quad \text{where} \quad \mathbf{F}_{hkl} = |\mathbf{F}_{hkl}| e^{j\alpha_{hkl}} \tag{23.4}$$

So, to calculate the electron density at the position (x, y, z) in the unit cell of a crystal requires us to perform the summation over all the *hkl* planes of the contributions to the point (x, y, z) of waves scattered from plane *hkl* whose amplitudes must be added with the correct phase relationship (α_{hkl}). Structure factor amplitudes can be measured, but the phases are lost in the experiment. This is "the phase problem" [17].

A similar equation can be calculated using the diffraction intensities as coefficients and with all phase angles equal to zero:

$$\overset{P}{\rho}(u, v, w) = \frac{1}{V} \sum_{hkl} |\mathbf{F}_{hkl}|^2 \cos[2\pi(hu + kv + lw)] \tag{23.5}$$

This equation is the Patterson function. It can be always calculated from the diffraction data since it depends on the squared structure factor amplitudes and it can be demonstrated to be a self-convolution of the electron density. The Patterson function is particularly useful both for the localization of "heavy atoms" (meaning atoms with atomic number higher than typical protein atoms), when heavy atom methods are applied for phasing, and for the correct orientation and translation positioning of a model in the crystal unit cell when the molecular replacement phasing method can be applied [13].

23.2.3 The MIR Method

The Multiple Isomorphous Replacement (MIR) method is the most successful and general experimental approach for the determination of phase angles and their assignment to the corresponding structure factors. The method is based on the possibility of modifying structure factors and phases of the "native" protein crystal by specific binding of heavy atoms ("derivative" crystal). When the positions of the heavy atoms bound to the protein have been found by a Patterson map calculation, then it is possible to calculate the phase of each observed structure factor by proper consideration of the variation of the structure factor moduli in the native protein and in the derivative crystals [13].

Practical application of the MIR method requires the comparison of X-ray diffraction patterns of the native protein crystal and of the crystals of at least two independent heavy atom derivatives. In case of perfect isomorphism (the conformation of the protein molecules, their position and orientation relative to the crystallographic axes, as well as the unit cell parameters must be exactly the same in the native and derivative crystals) the structure factor differences between the native protein crystal ($\mathbf{F}_P$) and the derivatives ($\mathbf{F}_{PH}$) are exclusively due to the contribution of the bound heavy atoms ($\mathbf{F}_H$). The contribution of the heavy atom replacement to the structure factor amplitude and phases is best illustrated on the Argand diagram (Fig. 23.4a).
The structure factor of the heavy atom derivative is then expressed by the vectorial summation:

$$\mathbf{F}_{PH} = \mathbf{F}_P + \mathbf{F}_H \tag{23.6}$$

The amplitudes $|\mathbf{F}_{PH}|$ and $|\mathbf{F}_P|$ are experimentally measured from the diffraction pattern of the native and derivative crystals, respectively. $\mathbf{F}_H$ (module and phase) is calculated from the position of the heavy atoms, which can be obtained from the Patterson synthesis of the isomorphous differences $(|\mathbf{F}_{PH}| - |\mathbf{F}_P|)^2$. The native phase angle α_P (assigned to the structure factor $\mathbf{F}_P$) can be calculated by using the cosine rule:

$$\alpha_P = \alpha_H + \cos^{-1}\left[\frac{|\mathbf{F}_{PH}|^2 - \left(|\mathbf{F}_P|^2 + |\mathbf{F}_H|^2\right)}{2\,|\mathbf{F}_P|\,|\mathbf{F}_H|}\right] \tag{23.7}$$

leading to two possible solutions symmetrically distributed around the heavy atom phase ($\alpha_P = \alpha_H \pm \alpha_0$). This two-fold ambiguity is better illustrated in the Harker construction (Fig. 23.4b). In this representation the possible structure factors $\mathbf{F}_P$ and $\mathbf{F}_{PH}$ are drawn by circles in the complex plane, having radius $|\mathbf{F}_P|$ and $|\mathbf{F}_{PH}|$, respectively. The two possible phase values occur at the circle intersections. The phase ambiguity can be removed by measuring at least two different heavy atom derivatives. The comparison of the two heavy atom contributions identifies the common correct value of α_P (Fig. 23.4c).

In real experimental cases, one heavy atom makes little difference to the structure factor amplitudes of the native protein. Furthermore, the calculation of $\mathbf{F}_{\mathrm{H}}$ is often not precise, due to an approximate deconvolution of the isomorphous difference Patterson, and due to the fact that binding of heavy atoms can introduce non-isomophism between native and derivative crystals. As a result of several sources of experimental noise, the Harker circles do not intersect at a single point and uncertainty is present in the assignment of the correct phase angle α_{P}.

A method recognising these difficulties has been therefore proposed, based on the consideration of a probability function for the phase angle α_{P}, as a function of the observed experimental parameters. These phase probability distributions can be used to estimate "best phases", with appropriate weighting, yielding the protein electron density map with the least error. If ε is the "lack of closure" of the phase triangle $\mathbf{F}_{\mathrm{PH}} = \mathbf{F}_{\mathrm{P}} + \mathbf{F}_{\mathrm{H}}$ (between observed and calculated data) for the phase angle α:

$$\varepsilon = |\mathbf{F}_{\mathrm{PH}}|^{\mathrm{obs}} - |\mathbf{F}_{\mathrm{PH}}|^{\mathrm{calc}} = |\mathbf{F}_{\mathrm{PH}}|^{\mathrm{obs}} - \left| |\mathbf{F}_{\mathrm{P}}|\, \mathrm{e}^{j\alpha_{\mathrm{P}}} + |\mathbf{F}_{\mathrm{PH}}|\, \mathrm{e}^{j\alpha_{\mathrm{H}}} \right| \tag{23.8}$$

then for each heavy atom derivative "i", and for each Bragg reflection *hkl*, a phase probability $\mathrm{P_i}(\alpha_{\mathrm{P}})_{hkl}$ can be defined, making the assumption that all the errors reside in $|\mathbf{F}_{\mathrm{PH}}|^{\mathrm{calc}}$ and that errors follow a Gaussian distribution:

$$\mathrm{P_i}\,(\alpha_{\mathrm{P}})_{hkl} = \mathrm{N}\mathrm{e}^{\left(-\frac{\varepsilon_{\mathrm{i}}\alpha_{\mathrm{P}}^2}{2\mathrm{E}_{\mathrm{i}}^2}\right)_{hkl}} \tag{23.9}$$

where N is a normalization factor of the probability over 2π, and E_i is the error associated to the structure factor measurements. As expected, the distribution is bimodal if only one derivative is considered, the two peaks corresponding to the intersection points of the circles with radii $|\mathbf{F}_{\mathrm{P}}|$ and $|\mathbf{F}_{\mathrm{PH}}|$ (Figs. 23.4b and 23.5a). The total probability for each (*hkl*) reflection is obtained by multiplying the separate probabilities of each derivative "i":

$$\mathrm{P}\,(\alpha_{\mathrm{P}})_{hkl} = \prod_{\mathrm{i}=1}^{\mathrm{n}} \mathrm{P_i}\,(\alpha_{\mathrm{P}})_{hkl} \tag{23.10}$$

The composed $\mathrm{P}(\alpha_{\mathrm{P}})_{hkl}$ distribution normally shows a unimodal shape (Fig. 23.5b). An electron density map calculated with a weighted amplitude representing the centroid of the phase distribution yields the least error. The polar coordinates of the centroid define the phase angle ${\alpha_{\mathrm{P}}}^{(best)}{}_{hkl}$ and a number m_{hkl} (varying between 0 and 1) called "figure of merit", used as a weight associated to the corresponding native structure factor moduli $|\mathbf{F}_{hkl}|$:

$$\mathbf{F}_{hkl}^{(best)} = \mathrm{m}_{hkl}\, |\mathbf{F}_{hkl}|\, \mathrm{e}^{\left[j\alpha_{\mathrm{P}}^{(best)}\right]_{hkl}} \tag{23.11}$$

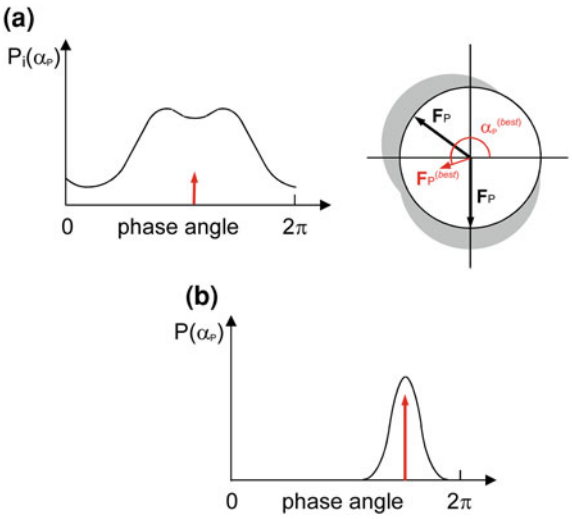


Fig. 23.5 **a** Bimodal distribution, for the *hkl* reflection, of the probability $P_i(\alpha_P)$ for a phase angle α_P derived from derivative "i". $\mathbf{F}_P^{(best)}$ is the centroid of the distribution. **b** Unimodal distribution of the total probability $P(\alpha_P)$ for a phase angle α_P derived from more than one derivative. (Adapted from [17])

The figure of merit corresponds to the cosine of the mean error in phase angle, providing an estimate of the quality of the phasing process. Reflections not properly phased have a bimodal distribution $P(\alpha_P)_{hkl}$, and a figure of merit close to 0. On the contrary, if the phasing has been accurate, then the probability distribution for each reflection $P(\alpha_P)_{hkl}$ is unimodal and m_{hkl} is close to 1. After the computation of the phase angles using the MIR method, it is possible to calculate an electron density map using native protein data and the phase angles derived from isomorphous replacement.

$$\rho(x, y, z) = \frac{1}{V} \sum_{hkl} m_{hkl} \, |\mathbf{F}_{hkl}| \, e^{\left[j\alpha_P^{(best)}\right]_{hkl}} e^{-2\pi j(hx+ky+lz)} \tag{23.12}$$

Inspection of such electron density map allows to detect structural features typical of proteins (i.e. α-helices, β-strands, amino acid residues, etc), and to build an atomic model of the macromolecule. The knowledge of the atomic coordinates allows to calculate new phases that are usually more accurate of the "best" MIR phases. Then, the phase improvement will continue by the iteration of electron density map calculation, model rebuilding, and crystallographic refinement.

23.2.4 The SIRAS Method

All elements, particularly those of high atomic number, display "anomalous scattering" when exposed to X-rays. The effect depends on the wavelength of the X-rays, being relevant when the energy of the incoming radiation is close to the element

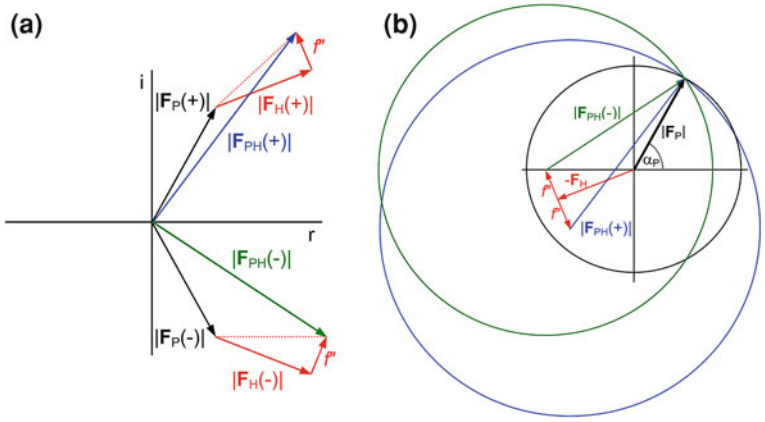


Fig. 23.6 **a** Breakdown of Friedel's law if an anomalous scatterer is present: $\mathbf{F}_{hkl} \neq \mathbf{F}_{-h-k-l}$ or $\mathbf{F}_{\mathrm{PH}}(+) \neq \mathbf{F}_{\mathrm{PH}}(-)$. **b** Harker construction for SIRAS

X-ray absorption edge. At such wavelength the energy of the X-ray photon is sufficient either to excite an electron of the strongly absorbing atom to a higher quantum state, or to eject the electron completely from the atom. As a consequence, the scattering factor *f* for the atomic species "i" (which is normally a real number for low atomic number elements) becomes "complex", having three components:

$$f(\theta, \lambda)_{\mathrm{i}} = f_0(\theta)_{\mathrm{i}} + f'(\lambda)_{\mathrm{i}} + jf''(\lambda)_{\mathrm{i}} \tag{23.13}$$

where $f_0(\theta)_{\mathrm{i}}$ is the normal scattering term that is dependent on the Bragg angle θ, while $f'(\lambda)_{\mathrm{i}}$ and $f''(\lambda)_{\mathrm{i}}$ are the anomalous scattering dispersive and absorption terms which depend on the wavelength λ.

The dispersive term (negative) decreases the normal scattering factor amplitude, whereas the absorption term is 90° advanced in phase and results in giving a complex nature to $f(\theta, \lambda)_{\mathrm{i}}$. This leads to a breakdown in Friedel's law, giving rise to small but significant anomalous differences between the absolute values and phases of $\mathbf{F}_{hkl}$ and its Bijvoet mate $\mathbf{F}_{-h-k-l}$. The anomalous or Bijvoet difference ($\Delta F^{\pm} = |\mathbf{F}_{\mathrm{PH}}(+)| - |\mathbf{F}_{\mathrm{PH}}(-)|$ in Fig. 23.6) can be used in the same way as the isomorphous difference in Patterson method to locate the anomalous scatterers and can profitably be exploited for the determination of the protein phase angles. Figure 23.6a shows the origin of the differences between $\mathbf{F}_{hkl}$ and $\mathbf{F}_{-h-k-l}$ (Bijvoet pair).

The use of anomalous scattering in determining protein structures has increased recently in relation to the use of synchrotrons as X-ray sources [11, 12]. Synchrotron radiation is tunable, and its wavelength may, within certain limits, be tuned at will. This provides the opportunity of measuring the X-ray diffraction data pattern of a protein crystal at wavelengths selected near (but also far) from the absorption edges of any anomalous scatterer present (even as light as a sulfur atom). Phases for the native structure factors can then be derived in a similar way to the MIR case.

Anomalous scattering can be used to break the phase ambiguity in a single isomorphous replacement experiment, leading to SIRAS (single isomorphous replacement with anomalous scattering) or MIRAS in case of multiple isomorphous replacement using anomalous scattering. Note that because of the 90° phase advance of the f'' term, anomalous scattering provides orthogonal phase information to the isomorphous term.

23.2.5 The MAD Method

A different application of the anomalous scattering for macromolecular structure determination is the so called "Multiple wavelength Anomalous Dispersion" method (MAD). This method provides an extremely handy tool for the determination of protein phases, directly from just one crystal containing a good anomalous scatterer. The great advantage of using one crystal is that the lack of isomorphism problems are totally abolished. The anomalous scatterer may be provided by a conventional isomorphous derivative, by a selenium atom substituted to a sulfur atom in methionine and cysteine residues [18], or by an ion already present in native metalloproteins. In the case of engineered Se-substituted proteins the presence of one Se atom in a protein of approximately 150 amino acids is sufficient for a successful application of the MAD method [19].

MAD data are collected at several wavelengths, typically three, in order to maximize the absorption and dispersive effects. Typically, wavelengths are chosen at the absorption f'' peak (λ_1), at the point of inflection on the absorption curve (λ_2), where the dispersive term (which is the derivative of the f'' curve) has its minimum, and at a remote wavelength (λ_3). Figure 23.7 shows a typical absorption curve for an anomalous scatterer, together with the phase and Harker diagrams.

The changes in structure factor amplitudes arising from anomalous scattering are generally small and require accurate measurement of intensities. The signal increases with resolution owing to the fall-off of normal scattering with resolution. The actual shape of the absorption curve must be determined experimentally by a fluorescence scan on the crystal at the synchrotron (Fig. 23.2c), as the environment of the anomalous scatterers can affect the details of the absorption. There is a need for excellent optics for accurate wavelength setting with minimum wavelength dispersion. Generally, all data are collected from a single frozen crystal to ensure the surviving of the same crystal to three data collections (Fig. 23.7), with high redundancy in order to increase the statistical significance of the measurements and data are collected with as a high completeness as possible.

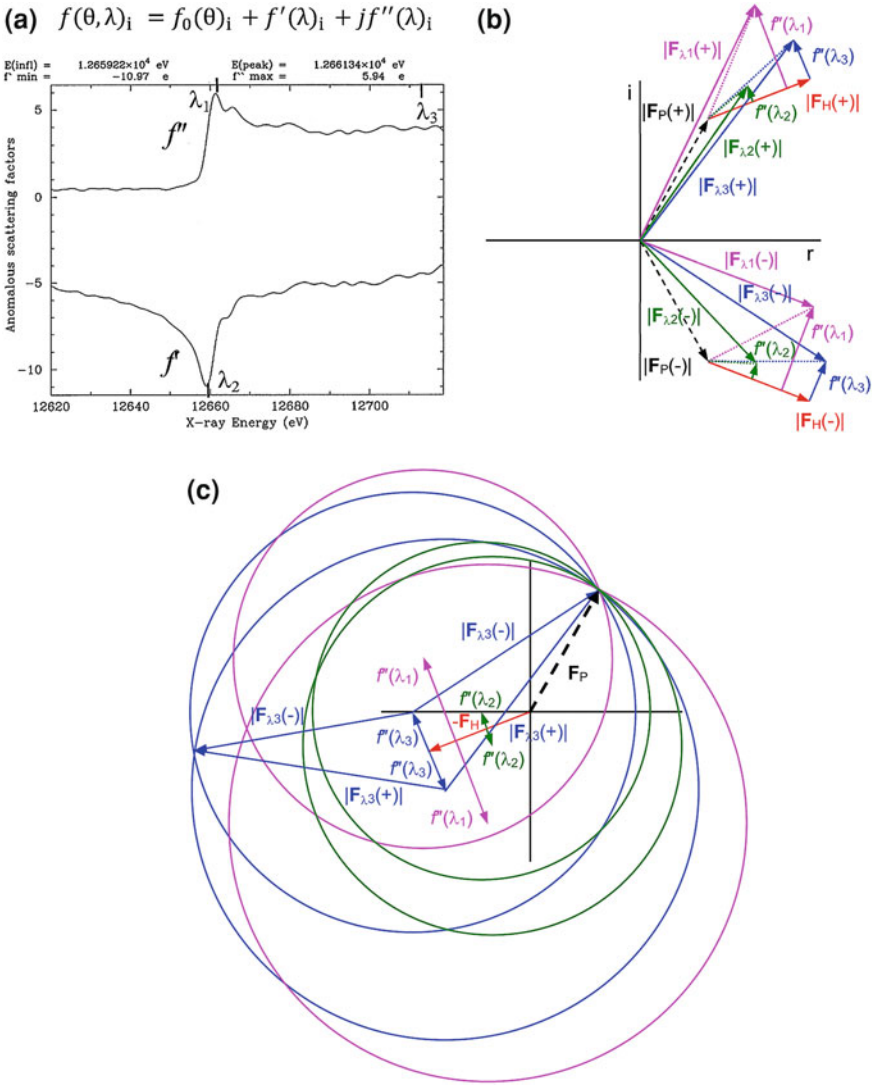


Fig. 23.7 MAD phasing. **a** Typical absorption curve for an anomalous scatterer (in this example Se). **b** Phase diagram. $|\mathbf{F}_P|$ is not measured (*dashed line*), so usually the remote λ_3 is chosen as the "native". **c** Harker construction. (Adapted from [17])

23.2.6 The Molecular Replacement Method

The molecular replacement method is a phasing procedure of a native protein, that does not require specifically the use of synchrotron radiation. Here it is mentioned for completeness, since it represents one of the most common methods of protein

phase determination in X-ray crystallography. The method is based on the observation that proteins which are homologous in their amino acid sequences have often a very similar three-dimensional fold. As a rule of thumb, a sequence identity >25 % and an r.m.s. deviation <2.0 Å between the Cα atoms of the model and the final new structure are normally required, although there are exception to this. Therefore, if one parent protein structure is available, it can be used to solve the 3D structure of homologous proteins, without the use of heavy atom derivatives. Conceptually, one has to transfer the known protein structure (search model) from its crystalline arrangement to the crystal of the protein of unknown structure (target protein). Such a procedure allows the calculation of approximated phases ($\alpha_{hkl}{}^{\mathrm{calc}}$); these are combined with the observed structure factors ($|\mathbf{F}_{hkl}|^{\mathrm{obs}}$) of the target protein, yielding a hybrid electron density map

$$\rho(\mathrm{x},\mathrm{y},\mathrm{z}) = \frac{1}{\mathrm{V}} \sum_{hkl} |\mathbf{F}_{hkl}|^{\mathrm{obs}} e^{j\alpha_{\mathrm{hkl}}^{\mathrm{calc}}} e^{-2\,\pi\, j\,(hx+ky+lz)} \tag{23.14}$$

which allows the iterative building of the target protein molecular model [13].

The correct positioning (orientation and translation) of the search model in the target unit cell is the key step for calculating starting phases sufficiently accurate to be able to model the target protein structure in the hybrid electron density map. Usually, the positioning of the search model in the target unit cell takes place in the Patterson space. If the model and the target protein are indeed similar and if they are oriented in the same way in unit cells of the same dimensions and symmetry, they should have very similar Patterson maps. We might image a trial-and error method in which we compute Patterson maps for several model orientations and compare them with the Patterson map of the target protein. In this manner, we could find the best orientation of the model, and then use that single orientation in the search for the best translational position of the model. In this approach, the rotational and translational searches are defined by the functions:

$$\mathrm{C}(\mathbf{R}) = \int\limits_{\substack{self\\ vectors}} \mathrm{P}_{\mathrm{cryst}}(\mathbf{u})\mathrm{P}_{\mathrm{mod}}(\mathbf{R},\mathbf{u})\mathrm{d}\mathbf{u} \tag{23.15}$$

$$\mathrm{D}(\mathbf{t}) = \int\limits_{\substack{cross\\ vectors}} \mathrm{P}_{\mathrm{cryst}}(\mathbf{u})\mathrm{P}_{1,2}(\mathbf{u},\mathbf{t})\mathrm{d}\mathbf{u} \tag{23.16}$$

where $\mathrm{P}_{\mathrm{cryst}}(\mathbf{u})$ and $\mathrm{P}_{\mathrm{mod}}(\mathbf{R},\mathbf{u})$ are the Patterson functions of the target protein crystal and of the search model rotated by matrix $\mathbf{R}$, respectively, and $\mathrm{P}_{1,2}(\mathbf{u},\mathbf{t})$ is the cross-Patterson function of the model structure, properly translated by the vector $\mathbf{t}$ within the unit cell. The rotational function $\mathrm{C}(\mathbf{R})$ operates in a volume around the origin

with a radius equal to the molecular diameter expected for the target protein. This region hosts all the intramolecular Patterson vectors (self-vectors set), which define the orientation of the search model with respect to the unit cell axes of the target crystal. The next step after the correct orientation of the search model is its proper translational positioning within the unit cell of the target crystal. The translational function D(**t**) is calculated in the Patterson space, in the region external to the sphere used for the rotational search. This is because in that region lie the intermolecular vectors (cross-vectors set) which define the position of the macromolecule relative to the unit cell symmetry elements.

If **X** is the set of atomic coordinates (x,y,z) of the search model, **R** is the rotational matrix obtained from the first step, and **t** is the translational vector from the second step of the molecular replacement method, then

$$\mathbf{X}' = \mathbf{XR} + \mathbf{t} \tag{23.17}$$

provides the atomic coordinates $\mathbf{X}'$ of the search model in the target crystal [20]. It is from these coordinates that a set of preliminary phases can be calculated. These phases, combined with the structure factor amplitudes experimentally measured from the target crystal, produce the hybrid electron density map. Usually, more similar the structures of the search and target proteins are, less approximated is the calculated electron density map. The analysis of this map, using computer graphics, allows the building of a starting molecular model for the target macromolecule. Such model will be subjected to several cycles of crystallographic refinement and modelling until the best model fitting the observed data is reached (see Sect. 23.4).

23.3 Density Modification

If the quality of the first electron density map is not good enough to allow a complete and unambiguous tracing of the polypeptide chain, improvement of the protein phase angles may be required prior to model building and refinement. Phase improvement can be based on two different techniques of "density modification" [13]. The first technique (known as "solvent flattening") is based on the assumption that the protein molecules are characterised by regions of relatively high electron density whose boundaries can be located. On the contrary, the electron density map in the solvent regions, between protein molecules packed in the crystal lattice, is rather low. This is related to the dynamic nature of the solvent molecules in these regions of the unit cell, and results in the presence of noise peaks in the corresponding electron density. Such a noise can be removed by setting the electron density for the disordered solvent regions to a low constant value, related to its chemical composition. Then, new phases are calculated by back-transforming the modified electron density map. In the next step a new electron density map is calculated with experimentally observed structure factor amplitudes and with phase angles either from the solvent flattening alone or by combining them with phase angles obtained from isomorphous or

molecular replacement method. The iteration of this procedure, along with the continuous updating of the envelope which separates the protein from the solvent region, and the addition (in small steps) of the data at higher resolution, is able to transform an initial hardly interpretable electron density map to a map where an atomic model can be easily built.

A similarly successful result can be achieved with the density modification technique known as "non-crystallographic symmetry averaging". This technique is applied when more than one protein molecule is present in the crystal asymmetric unit. The assumption is that the electron density in molecules related by non-crystallographic symmetry (NCS) is essentially equal. If the NCS operators present in the asymmetric unit are known, then the electron density is averaged at each (x,y,z) point of NCS-related protein molecules, the solvent region flattened and the asymmetric unit is reconstituted. Phase angles from this new model are calculated by back-transforming the averaged electron density map. A new and improved density map is calculated with experimentally observed structure factor amplitudes and phase angles obtained from the NCS procedure [21]. If necessary, this phase information can be combined with previously known phases. The result is an improved signal-to-noise ratio and, in the end, a clearer image of the molecules. The NCS averaging method is spectacularly successful in systems with high symmetry, such as virus.

23.4 Crystallographic Refinement

23.4.1 Least Squares Refinement

The native protein phases, obtained by one of the methods discussed previously, allow the calculation of a preliminary electron density map, whose interpretation results in an approximated model of the protein structure showing the main features of the macromolecular architecture (Fig. 23.8). The partial model can be improved using the information present in the observed structure factor amplitudes. Such a process, known as crystallographic refinement, consists of iterative corrections of the model, to reach the best possible agreement between the calculated and observed structure factors. This procedure is essential to achieve the maximum reliability for the molecular model, as well as to provide the atomic resolution structural details needed for an effective biological research.

During crystallographic refinement the molecular model is allowed to vary by changing the positional parameters **p**, which are for each non-hydrogen atom "i" of the structure the coordinates (x_i,y_i,z_i) and the temperature factors (B_i). The temperature factors B_i are generally assumed to be isotropic, being related to the thermal oscillation (μ_i) of each atom "i" around its equilibrium position by the relation: $B_i = 8\pi^2 <\mu_i^2>$. The adjustment of the parameters (x_i,y_i,z_i,B_i) for all atoms within the initial approximated model is obtained by minimization of the function:

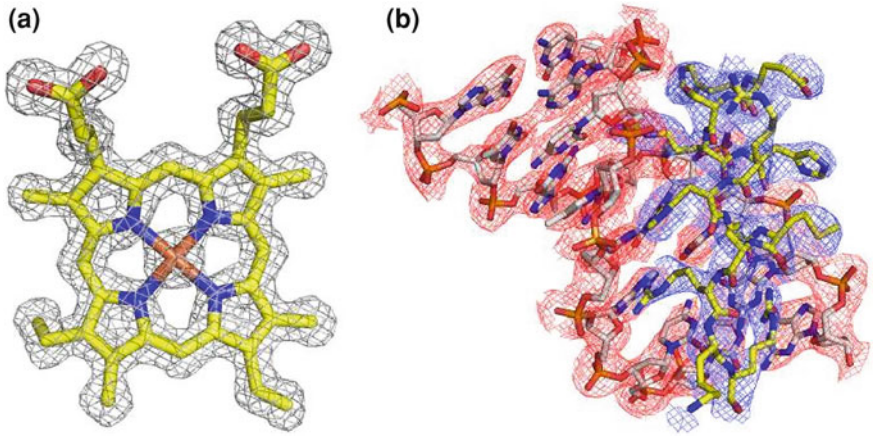


Fig. 23.8 A small section of the electron density map (mesh representation) contoured at 1 σ, with the final structure superimposed (ball and stick representation) for (**a**) the haem of *Methanosarcina acetivorans* protoglobin (*gray mesh*; 1.5 Å resolution) [22], and for (**b**) the transcription factor NF-Y in complex with DNA (*blue* and *red mesh*, respectively; 3.1 Å resolution) [23]

$$Q(\mathbf{p}) = \sum_{hkl} w_{hkl} \left(|\mathbf{F}_{hkl}|_{obs} - \left|\mathbf{F}(\mathbf{p})_{hkl}\right|_{calc} \right)^2 \tag{23.18}$$

The summation is calculated over all crystallographically independent reflections and w_{hkl} is the weight given to each observation ($w_{hkl} = 1/\sigma_{hkl}{}^2$, where σ_{hkl} is the standard deviation for the *hkl* observation).

Least squares is the simplest statistical method used in macromolecular refinement. The least squares refinement of atomic coordinates and temperature factors is an iterative process. In each step the parameters to be refined shift only partially in the direction of their final values; usually, several refinement cycles are carried out before convergence is reached. The larger is the difference between the observation and the model's prediction, the worse the model. The more precise is an observation, the more important that observation becomes in the overall sum. One varies the parameters of the model to find a set that gives the lowest sum of deviants.

Whereas for small molecules the ratio between observations ($|\mathbf{F}_{hkl}|$) and parameters to be refined is about 10:1, for macromolecules such a ratio is often close to 1. Such poor over-determination is generally compensated by the introduction of additional "observations", mostly related to the known stereochemical properties of the proteins (bond lengths, bond angles, van der Waals contacts, etc). The function which is then minimized is:

$$C = Q + kU \tag{23.19}$$

where Q is the crystallographic term previously introduced, U is the potential energy associated to a particular conformation of the macromolecule, and k is a scaling factor

which controls the relative contribution of the energy and X-ray terms. U consists of several contributions based on the deviations of the stereochemical parameters of the protein model from ideal values, mainly derived from small molecule structures:

$$U = \sum_i \frac{1}{2} k_{b,i} \left(b_{i,calc} - b_{i,obs}\right)^2 + \sum_i \frac{1}{2} k_{\tau,i} \left(\tau_{i,calc} - \tau_{i,obs}\right)^2 + \sum_i k_\phi \left(n\phi_i - \delta\right) + \sum_{ij} \left[\left(Ar^{-12}\right)_{ij} + \left(Br^{-6}\right)_{ij}\right] \quad (23.20)$$

The potential energy function includes terms for bond stretching (b terms), bond angle bending (τ terms), torsion potentials, and van der Waals interactions, respectively. Electrostatic interactions are usually ignored, because they act over rather long distances and they are not particularly sensitive to small changes in atomic positions. When the crystallographic residual Q is minimized together with the potential energy term U, the refinement process is defined as "restrained" since the stereochemical parameters (treated as new "observations") are allowed to vary in a narrow range around their standard values. The atomic coordinates of the protein model vary within a sort of harmonic potential, driven by minimization of the crystallographic term. If the deviation of the model atoms from those of the real structure is large, the refinement may be trapped in a local minimum instead of converging to the correct solution. This situation can be avoided by correcting manually the model *via* computer graphics analysis, or by applying a more sophisticated refinement technique, which includes the contribution of molecular dynamics. This technique, which takes into account the kinetic energy associated to each atom of the macromolecule during the refinement, has rapidly gained popularity because of its wider radius of convergence which allows a faster refinement of the initial model [24].

23.4.2 Maximum-Likelihood Refinement

In general, the assumptions of the least squares method are that errors in the observations obey a normal distribution with completely known ("observed") variances and that, given perfect observations and the best parameters, the model would predict the observations perfectly. In many refinement problems, however, these assumptions are not completely correct. The simplest example occurs when the model is incomplete, say missing a protein domain. In this case it is impossible for any set of parameters to reproduce all the observations. The refinement function must account for the unknown contribution of the unmodelled part of the molecule and least squares cannot do that. Recently a more general approach has been introduced in the refinement procedure, by using the so called "maximum-likelihood" approach.

Maximum-likelihood is a general statistical framework for estimating the parameters of a model on the basis of observations [25]. This approach differs from least squares in that maximum-likelihood can accommodate observations with

uncertainties of arbitrary character and model parameters whose values are also expected to have such uncertainties. While maximum likelihood is completely general, macromolecular refinement is such a difficult problem that no computer can perform a likelihood refinement in complete generality. Therefore the maximum likelihood method depends critically on the assumptions made about the nature of the uncertainties in the observations and the parameters of the final model [26]. The maximum-likelihood method begins with the assumption that the current structural model itself contains errors (Fig. 23.9a). Instead of a single location, as assumed by the least squares method, there is a cloud of locations that each atom could occupy (usually, the distributions of positions are assumed to be normal and have equal standard deviations). This distribution of structures results in a distribution of values for the complex structure factors calculated from that model. Because of the nonlinear relationship between real and reciprocal space, the value of the structure factor calculated from the most probable model (labelled $\mathbf{F}_{\text{calc}}$ in Fig. 23.9b) is, however, not the most probable value for the structure factor distribution. This is the key difference between least squares and maximum likelihood methods. The most probable value for the calculated structure factors has the same phase of $\mathbf{F}_{\text{calc}}$ but a smaller amplitude which equalize $\mathbf{F}_{\text{calc}}$ only when the model is infinitely precise. The width of the distribution, named σ_{calc}, also arises from the coordinate uncertainty and is large when the difference between $\mathbf{F}_{\text{calc}}$ and the most probable value of the structure factor distribution is high.

In refinement without experimental phase information, the probability distribution of the calculated values of the structure factors are converted to a probability distribution of the amplitude of this structure factor by integrating the two-dimensional distribution over all phase angles at each amplitude.
This integral is represented by a series of concentric dashed circles in Fig. 23.9b. As expected, the most probable amplitude is smaller than $|\mathbf{F}|_{\text{calc}}$ (Fig. 23.9c). With this distribution the likelihood of any value for $|\mathbf{F}|_{\text{obs}}$ can be evaluated, and one can calculate how to modify the model to increase the likelihood of $|\mathbf{F}|_{\text{obs}}$. For instance, in the case shown in Fig. 23.9c the likelihood of $|\mathbf{F}|_{\text{obs}}$ can be improved by either increasing $|\mathbf{F}|_{\text{obs}}$ or increasing the precision of the model.

In general, compared to the least squares method, the basic maximum-likelihood residual function is:

$$Q(\mathbf{p}) = \sum_{hkl} \frac{\left(|\mathbf{F}_{hkl}|_{\text{obs}} - \left\langle \left|\mathbf{F}(\mathbf{p})_{hkl}\right|_{\text{calc}} \right\rangle\right)^2}{\sigma_{\text{obs}}^2 + \sigma(\mathbf{p})_{\text{calc}}^2} \tag{23.21}$$

where $< |\mathbf{F}(\mathbf{p})_{hkl}|_{\text{calc}} >$ is the expectation value of the amplitude of a structure factor calculated from all plausible model similar to $\mathbf{p}$, and $\sigma(\mathbf{p})_{\text{calc}}$ is the width of the distribution of values for $|\mathbf{F}(\mathbf{p})_{hkl}|_{\text{calc}}$.

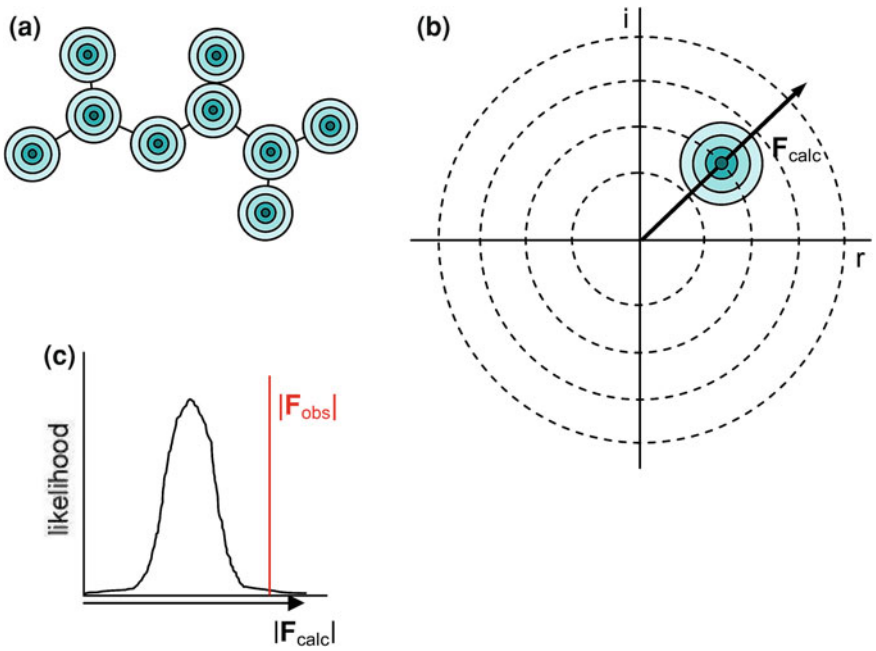


Fig. 23.9 Probability distributions for one reflection in the maximum-likelihood approach. **a** Probability distributions of the atoms in the model. **b** The distribution of structures results in a distribution of values for the structure factors calculated from that model. $|\mathbf{F}|_{calc}$ indicates the value of the structure factor calculated from the most probable model. A series of concentric *dashed circles* represent the integral over all phase angles at each amplitude needed to convert the probability distribution of the calculated value of the structure factor to a probability distribution of the amplitude of this structure factor. **c** The probability distribution for the amplitude of the structure factor. The *arrow below* the horizontal axis represents the amplitude of $|\mathbf{F}|_{calc}$, calculated from the most probable model. The corresponding $|\mathbf{F}|_{obs}$ is also indicated. (Adapted from [26])

23.4.3 Quality of the Model

The progress of the crystallographic refinement is monitored by comparing the measured structure factor amplitudes ($|\mathbf{F}_{hkl}|_{obs}$) with those calculated from the current atomic model ($|\mathbf{F}_{hkl}|_{calc}$). As the model converges to the correct structure, the calculated structure factor amplitudes should also converge to the corresponding measured values. The most widely used measure of convergence is the so called "residual index", or *R*-factor:

$$R = \frac{\sum_{hkl} ||\mathbf{F}_{hkl}|_{obs} - |\mathbf{F}_{hkl}|_{calc}|}{\sum_{hkl} |\mathbf{F}_{hkl}|_{obs}} \tag{23.22}$$

Values of the *R*-factor range from zero, for perfect agreement of calculated and observed structure factors, to about 0.6, when the measured structure factors are

compared to a set of random amplitudes. An early model with *R*-factor near 0.4 is promising and is likely to improve during the refinement procedure. A desirable target *R*-factor for a refined protein model with data to 2.5 Å is about 0.2.

A more revealing criterion of model quality and improvement is the so called "free *R*-factor", or R_{free}. The R_{free} is calculated exactly as the *R*-factor but the summations are on a small set of randomly chosen reflections (5–10 % of the total measured reflections), the so called "test set", which are set aside from the beginning and never used during the refinement procedure. Therefore, at any stage in refinement, R_{free} measures how well the current atomic model predicts a subset of measured amplitudes that were not included in the refinement of the model. For this reason, R_{free} provides a less biased measure of the overall model quality, correlating very well with phase accuracy of the atomic model. In general, during intermediate stages of refinement, R_{free} values are higher than the *R*-factor, but in the final stages, the two often become more similar (the final R_{free} value is generally higher than the *R*-factor by 2–7 %).

In addition to *R*-factors as indicators of convergence, other structural parameters can be monitored to check whether the model is chemically, stereochemically, and conformationally reasonable. During the progress of refinement, all of these structural parameters should improve.

23.5 The Protein Data Bank

The macromolecular structures solved by means of X-ray crystallography or NMR techniques are usually submitted to the Protein Data Bank (www.rcsb.org/pdb) as text files (PDB files) [27]. The head of each PDB file contains specific information about the macromolecule, whereas the body of the file consists of a list of PDB coordinates for each single atom of the structure (expressed in Å and referred to orthogonal axes), with their temperature factors and occupancies. Additionally, the atomic coordinates of a variable number of experimentally located solvent molecules (usually water molecules) are also present in the PDB files. These solvent molecules are localized on the surface of the macromolecule as well as in internal cavities. A substantial revision of the PDB is currently in progress with the aim of improving the quality and the completeness of the deposited structural and biological information. For instance, the PDB provides several links to correlated data bases and access to structural analysis software for the study of protein folds, general research in various fields of structural biology, and for the validation of each new deposition. As a rule of thumb, the basic data that an occasional user should check to evaluate the quality of a deposited structure are:

(a) agreement index between calculated and observed structure factors (*R*-factor and R_{free})
(b) maximum resolution of the data used during the refinement procedure

(c) global stereochemistry of the macromolecule (as evaluated by estimates of the deviation from the ideal values for bond length, bond angles, etc.)
(d) atomic temperature factors (average and local values) of the macromolecule and of the localized solvent molecules.

The amount of data provided by bio-crystallographic analysis is continuously increasing. This flood of information, however, does not necessarily correspond to novel structural information, since many protein folds are well conserved through the different evolutionary *phyla*. Statistics and biological considerations suggest that the all proteins present in Nature (about 10^5 different types in humans) are compatible with the existence of a limited number of folds, probably less than 10^4.

23.6 Structural Genomics

Macromolecular crystallography is experiencing a surge in new methodologies, largely fuelled by developments in structural genomics and by the needs of the pharmaceutical industry. While most structural biologists pursue structures of individual proteins or protein groups, specialists in structural genomics pursue structures of proteins on a genome wide scale, in particular human proteins implicated in disease states, as well as proteins from a set of pathogens. The Human Genome Project has produced an enormous body of information about the sequence of the human genome and in addition genome sequences of a large number of human pathogens, from tuberculosis to malaria, are also known. However, detailed information on the structure, function and interaction of the tens of thousands of proteins encoded by these genomes is required in order to fully exploit this new panoply of data. The rapidly increasing numbers of known protein atomic structures will provide strategic benefits for medical research, basic and applied. In particular, knowledge of the three-dimensional structures of key human proteins or human pathogenic proteins is vital for speeding up the difficult task of discovering new antibiotics or anti-cancer drugs (The Center for Structural Genomics of Infectious Diseases: http://csgid.org). X-ray crystallography at latest generation synchrotron sources is the key technique that will build the database of three-dimensional information on protein structure and by generating large amounts of systematic crystallization data that may lead to more prediction-based crystallization methods. Nuclear magnetic resonance techniques and neutron scattering constitute further important and complementary structure determination tools.

As opposed to traditional structural biology, the determination of a protein structure through a structural genomics effort often (but not always) comes before anything is known regarding protein function. This implies new challenges in structural bioinformatics, i.e. determining protein function from its three-dimensional structure and the need to speed up the structure determination process by optimising each step for high throughput, including target selection, protein production, purification, crystallization and structure analysis by X-ray crystallography and/or NMR spectroscopy.

As an example, several synchrotron beamlines normally provide the so called "remote data collection system" for macromolecular crystallography, which allows users to work on their samples, shipped and mounted on the beamline goniometer, through the use of extensive robotics that allow for comprehensive crystal manipulation, screening, selection of best samples, and data collection, all done from their home laboratory. The users can also conduct data processing and phasing calculations during the actual data collection experiment (i.e. "on the fly"). This service not only minimizes the cost of data collection, but also simplifies the operation of the beamline, thereby reducing human traffic and security issues.

References

1. C. Branden, J. Tooze, *Introduction to Protein Structure*, 2nd edn. (Garland Publishing Inc, New York, 1999)
2. B.W. Matthews, Methods Enzymol. **276**, 3–10 (1997)
3. P.G. Gane, P.M. Dean, Curr. Opin. Struct. Biol. **10**, 401–404 (2000)
4. H. Erlandsen, E.E. Abola, R.C. Stevens, Curr. Opin. Struct. Biol. **10**, 719–730 (2000)
5. N. Ban, P. Nissen, J. Hansen, P.B. Moore, T.A. Steitz, Science **289**, 905–920 (2000)
6. A. Ducruix, R. Giegé, *Crystallization of Nucleic Acids and Proteins: A Practical Approach* (Oxford University Press, Oxford, 1992)
7. A. McPherson, *Crystallization of Biological Macromolecules* (Cold Spring Harbor Laboratory Press, New York, 1999)
8. P.C. Weber, Methods Enzymol. **276**, 13–22 (1997)
9. N.E. Chayen, J.R. Helliwell, N.Y. Ann, Acad. Sci. **974**, 591–597 (2002)
10. R.B.G. Ravelli, E.F. Garman, Curr. Opin. Struct. Biol. **16**, 624–629 (2006)
11. J.R. Helliwell, *Macromolecular Crystallography with Synchrotron Radiation* (Cambridge University Press, Cambridge, 1992)
12. J.R. Helliwell, Methods Enzymol. **276**, 203–217 (1997)
13. J. Drenth, *Principles of Protein Crystallography*, 2nd edn. (Springer, Berlin, 1999)
14. D. Bourgeois, U. Wagner, M. Wulff, Acta. Crystallogr. D **56**, 973–985 (2000)
15. F. Schotte, J. Soman, J.S. Olson, M. Wulff, P.A. Anfinrud, J. Struct. Biol. **147**, 235–246 (2004)
16. M. Milani, M. Nardini, A. Pesce, E. Mastrangelo, M. Bolognesi, IUBMB Life **60**, 154–158 (2008)
17. G. Taylor, Acta Crystallogr. D **59**, 1881–1890 (2003)
18. S. Doublié, Methods Enzymol. **276**, 523–530 (1997)
19. W.A. Hendrickson, C.M. Ogata, Methods Enzymol. **276**, 494–523 (1997)
20. J. Navaza, P. Saludjian, Methods Enzymol. **276**, 581–594 (1997)
21. F.M.D. Vellieux, R.J. Read, Methods Enzymol. **277**, 18–53 (1997)
22. M. Nardini, A. Pesce, L. Thijs, J.A. Saito, S. Dewilde, M. Alam, P. Ascenzi, M. Coletta, C. Ciaccio, L. Moens, M. Bolognesi, EMBO Rep. **9**, 157–163 (2008)
23. M. Nardini, N. Gnesutta, G. Donati, R. Gatta, C. Forni, A. Fossati, C. Vonrhein, D. Moras, C. Romier, M. Bolognesi, R. Mantovani, Cell **152**, 132–143 (2013)
24. A.T. Brünger, L.M. Rice, Methods Enzymol. **277**, 243–269 (1997)
25. N.S. Pannu, R.J. Read, Acta. Crystallogr. A **52**, 659–668 (1996)
26. D. Tronrud, Acta. Crystallogr. D **60**, 2156–2168 (2004)
27. H.M. Berman, J. Westbrook, Z. Feng, G. Gilliland, T.N. Bhat, H. Weissig, I.N. Shindyalov, P.E. Bourne, Nucleic Acids Res. **28**, 235–242 (2000)

Chapter 24
Synchrotron Radiation in the Earth Sciences

Simona Quartieri

Abstract The enormous advantages that synchrotron radiation offers over conventional X-ray sources—among which brilliance, tunability and intrinsic collimation—strongly contribute to improve our knowledge on the physical, chemical and structural properties of Earth materials and on planetary processes. This chapter will review some applications and developments in the fields of synchrotron radiation-based Earth Sciences research. Some of the main problems of modern mineralogy, petrology and geochemistry will be discussed and recent case studies will be presented to show to what extent synchrotron radiation can contribute to their solution.

24.1 Introduction

Currently, most research in the fields of the Earth, Environmental and Planetary Sciences takes advantage of synchrotron radiation (SR) sources and of the unique characteristics of emitted radiation to investigate at an atomic level the chemical, physical and crystallographic properties of geological materials [1, 2].

Most of these mineralogical, petrological and geochemical studies are performed in the energetic range corresponding to hard X-rays, even if the use of soft X-rays and UV and IR radiation is also potentially extremely useful, for example to study the structural environment of light elements and for the characterization of mineral-fluid interfaces.

In the Earth Sciences, SR can be used with two main different approaches:

- for applications of conventional techniques, already widely used in mineralogical investigations, but with which one intends, for instance, to study extremely small

S. Quartieri (✉)
Dipartimento di Fisica e di Scienze della Terra, Università di Messina, Viale Ferdinando Stagno d'Alcontres 31, 98166 Messina, Italy
e-mail: simona.quartieri@unime.it

S. Mobilio et al. (eds.), *Synchrotron Radiation*,
DOI: 10.1007/978-3-642-55315-8_24, © Springer-Verlag Berlin Heidelberg 2015

volumes, or to obtain better resolution, signal-to-noise ratio and detectability limits with respect to conventional sources;
- as a unique radiation source, necessary for more innovative techniques such as XAFS spectroscopy on trace elements, XAFS and X-ray diffraction under extreme P and T conditions, anomalous scattering, in-situ kinetic studies of phase transitions and synthesis reactions, X-ray fluorescence microanalysis with high spatial resolution and low detectability limits, X-ray topography and tomography.

Since Earth materials are often heterogeneous, X-ray micro-beam studies are valuable in unraveling this complexity. Spatial resolutions down to 100 nm are achievable using zone plates, mirrors, and refractive optics. Most X-ray based methods can be applied with high spatial resolution, including X-ray fluorescence, X-ray absorption fine structure, X-ray diffraction, and computer microtomography. Moreover, by applying these techniques in a nearly simultaneous fashion, it is possible to produce elemental maps with sub-part-per-million sensitivity and determine the speciation and mineralogy at selected locations in the material.

The SR-based methods most frequently used in studying geological materials are the following:

(1) Single-crystal X-ray diffraction [3–6]:

- structural studies on micro-volumetric crystals;
- investigations under extreme conditions.

(2) X-ray powder diffraction [7–11]:

- high-resolution static investigations on structural, crystallochemical and textural problems and qualitative analyses;
- in-situ dynamical studies on synthesis reaction and phase-transition kinetics;
- in-situ high pressure and/or temperature experiments.

(3) Small Angle and Wide Angle Synchrotron X-ray Scattering (SAXS/WAXS) [12–15]. This technique is particularly useful for:

- studies of paracrystalline and amorphous systems**;**
- in situ studies of crystallization reactions;
- studies of the interaction between minerals and organic substances on a nanometer scale.

(4) X-ray absorption spectroscopy [16–19]:

- determination of the local structural environment, of the oxidation state and of the short-range ordering of a particular chemical species (major, minor or trace) in minerals, glasses, silicatic melts, metamictic minerals, fluid inclusions, polymers and gels;
- in-situ high-pressure and/or temperature investigations and time-resolved studies of transient phenomena by means of dispersive EXAFS;
- studies of static and dynamic disorder in geological materials.

(5) X-ray fluorescence microanalysis [20, 21]:

- trace element analysis on small-volume samples, such as microparticles, micrometeorites and fluid inclusions;
- studies of the spatial element distribution on a micrometric scale (i.e. diffusion profiles in crystals, chemical zoning and impurity distributions).

(6) Infrared and Raman spectroscopy [22–24]:

- determination of trace hydroxyls in nominally anhydrous phases;
- determination of the hydroxyl content in fluid micro-inclusions in ultra-high pressure minerals;
- in situ studies of mineral phase transitions, also present in micro-inclusions;
- studies of deep mantle and core mineral phases under extreme conditions.

(7) Synchrotron Mössbauer Spectroscopy [25, 26]

- studies of iron in mantle materials;
- investigations of spin cross-over transitions in the iron component of lower mantle phases;
- studies of P-dependence of magnetism in geological materials.

(8) X-ray topography and microtomography [27–31]:

- studies of dislocations, planar defects, stacking faults, anti-phase domain walls, incommensurate phases and growth defects;
- non-destructive imaging;
- qualitative and quantitative analysis of the internal features of rocks, minerals, meteorites and fossils.

The Earth Sciences research fields which mostly benefit from third-generation SR sources are those relative to: (a) *elements in extremely low concentrations*; (b) *microcrystals and microvolumes*; (c) *samples under extreme conditions*; (d) *kinetic studies of transformations involving fast reactions*; (e) *micro- and non-destructive techniques.*

In the literature, several excellent reviews on the main applications of SR to the Earth Sciences can be found [32–37]. This contribution—which is a revised and updated version of a previous one [35]—will by no means attempt to review all the applications and the developments in the fields of SR-based mineralogical research, rather, it will attempt to discuss some of the main problems of modern mineralogy, such as those previously cited, and to show, describing case studies, to what extent SR can contribute to their solution. For the same reasons the reference list is not to be considered exhaustive, but rather, representative of the most recent results from SR-based Earth Science research.

24.2 X-Ray Diffraction

24.2.1 X-Ray Powder Diffraction

X-ray powder diffraction (XRPD) underwent rapid development at the beginning of the 80s. Two major factors underlie the transformation of polycrystalline diffraction from the status of a routine identification method to that of a powerful characterization technique: the widespread use of profile-fitting methods, essentially based on full-profile and Rietveld techniques and access to intense high-resolution sources such as dedicated synchrotron rings and neutron time-of-flight sources. SR allows the recording of diffraction patterns with an excellent signal to noise ratio and a very high resolution of the diffraction peaks. These features, together with experimental flexibility (in terms of intensity/resolution ratio, sample volume, non-environmental conditions) impose XRPD as one of the most versatile methods for structural and crystal-chemical investigations in Material and Earth Sciences.

Earth scientists greatly benefit from intense synchrotron sources especially in the fields of high pressure and high temperature research, (discussed in a special following section), since diffraction studies of phase transitions and of mineral stability under conditioned environments take full advantage of the brilliance and tunability of SR—and in crystallographic studies of complex systems with low symmetry. The angular resolution resulting from SR experiments is, in fact, at least an order of magnitude better than that usually obtained with a conventional source and it thus makes the study of compounds characterized by low symmetry and high overlap of the diffraction peaks possible.

SR-XRPD is, for instance, commonly used for structural and kinetic studies as a function of T and/or P of the ion-exchange, dehydration and compression of natural and synthetic porous and clay materials (for instance, [38–45]) for the study of HT and HP-induced cation ordering and phase transitions in rock-forming minerals (e.g. [46–48]), of crystallization processes [49], of the dehydroxylation and phase transformations of asbestos materials [50] (Fig. 24.1), and of microscopic strain in pyrope-grossular solid solutions [51]. Moreover, numerous studies, performed by high-resolution SR-XRPD, have been devoted to the determination of the crystal structure of minerals (e.g. [10, 11, 49, 52, 53]. SR-XRPD has also been used for the analysis of meteorites [54, 55].

24.2.2 Single-Crystal X-Ray Diffraction

The special properties of SR—in particular the low divergence and high brilliance of the beam—has provided new opportunities also in single-crystal X-ray crystallography, especially in investigations at extreme conditions (see the specific paragraph in the following) and in studies of natural microcrystals with dimensions around 10 μm.

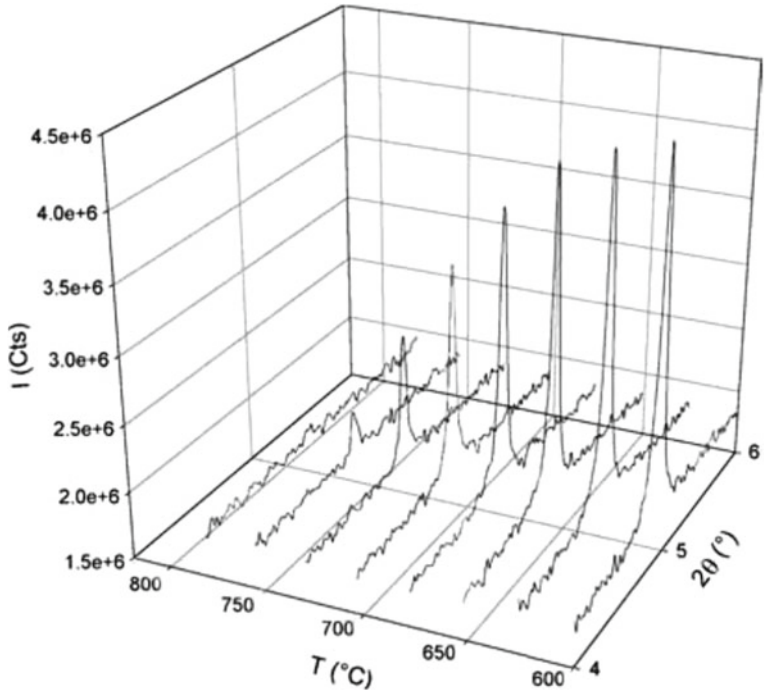


Fig. 24.1 Selected 2θ range of the three-dimensional real-time synchrotron powder diffraction sequence to follow the evolution of the (002) chrysotile peak in the temperature range 600–800 °C [50]. © Springer

Such experiments have led to great progress in several fields of solid state research for the following reasons:

(a) Diffraction intensities which obey the kinematical diffraction theory are excellently suited to the study of details of atomic arrangements. Such details are, for example, the density of bonding electrons or anharmonic thermal vibrations. Under normal laboratory conditions diffraction data are very frequently strongly influenced by absorption and extinction. Diffraction experiments on very small crystals allow the reduction of these systematic errors to a great extent.
(b) Frequently, crystals cannot be grown—or cannot be found in nature—to sizes which allow single-crystal diffraction with conventional X-ray sources.
(c) Crystals in special environments may be limited in size by experimental conditions; this holds especially for single-crystals in high-pressure cells and compressed in the pressure range above 10 GPa (these particular cases are discussed in the dedicated section in the following).

Some examples of studies based on SR single-crystal XRD are the following:

- Structural resolution of the new natural zeolite mutinaite, from Mt. Adamson, Antarctica [$(Na_{2.76}\,K_{0.11}\,Mg_{0.21}\,Ca_{3.78})\,(Al_{11.20}\,Si_{84.91})\,\cdot 60\,H_2O$]. The structure

of the natural counter-part of the synthetic zeolite ZSM-5 has been determined by a single-crystal XRD experiment performed at ESRF (ID11), working on a microcrystal of $30 \times 30 \times 15\,\mu m^3$ and using a CCD area detector [56].
- Structural study of two hydrous wadsleyite (β-Mg_2SiO_4) crystals with different hydroxide content. From comparison with hydrous and anhydrous wadsleyite structures, the Mg-vacant structural modules were found to be the building units for the structure of hydrous wadsleyite [57].
- Study of the crystal structure of a second antigorite polysome ($m = 16$) [58].
- Determination of the real crystal structure of fukalite, $Ca_4Si_2O_6(OH)_2(CO_3)$, an example of an OD structure with two-dimensional disorder [59].
- Description of the modular crystal structure, OD-character, polytypism, and twinning, of vurroite, $Pb_{20}Sn_2(Bi, As)_{22}S_{54}Cl_6$) [60].
- Study of the internal structure of natural regular and irregular diamonds, using the Laue synchrotron method [61].

24.3 X-Ray Absorption Spectroscopy

X-ray Absorption Fine Structure Spectroscopy (XAFS: EXAFS + XANES) is a widely used technique for the determination of local atomic structure in Materials Science, even on very small volumes and on extremely dilute elements; these conditions are often present in geological samples.

EXAFS and XANES are often used to characterize crystalline solids with a complementary approach with respect to the diffractometric methods, so as to obtain detailed structural information about a particular chemical species. XAFS has in fact the advantage of being element selective and very sensitive to low concentrations of trace species (<1000 ppm). It can provide direct information on the local structural environment of a specific element in the presence of other species sharing the same crystallographic site and is a tool for understanding the geometrical structure modifications involved in the substitution.

In particular, the problem of direct structural characterization of trace elements is of great geochemical and petrogenetic interest since the distribution of these elements among the various minerals co-existing in the sample is used to interpret the crystallization and metamorphic history of the rock. However, this is usually done without a precise crystal-chemical characterization of the trace element, due to the difficulties in obtaining diffractometric information on such highly dilute species. In several cases, little is known about the distribution of these elements in mineral structures (crystallographic sites versus defect sites) or about their crystal chemical behavior (bonding, site partitioning, short-range ordering, diffusion mechanisms, etc.) On the contrary, XAFS is particularly efficient in structural investigations on intra-crystalline distribution of trace elements and in the study of those minerals which are complex mixtures of different end-members.

Some examples of crystal chemical problems which can be successfully solved by XAFS, are the following:

- the structural relaxation associated with element substitution, which affects the stability of solid solutions;
- the location of minor and trace elements, which can explain element partitioning between coexisting phases. Among mineral solid solutions, those containing very dilute species are studied in the fluorescence mode. Over the last few years substantial improvements in fluorescence detectors have allowed XAFS measurements at concentrations of some hundreds of ppm.
- the relationship between local structural deformation and deviations from ideal behavior of solid solutions;
- the detection of order versus random distribution of specific elements or clustering effects.

Since XAFS is a non-destructive technique, it can be applied to the study of all the aggregation states of matter, and hence to a large variety of compounds of geological interest (crystals, disordered and amorphous solids, liquids, gels, silicate melts, metamict materials) and also to the mineral/solution interfaces, which are of great interest for the alteration, precipitation and crystallization phenomena involved in geochemical processes. Moreover, being a non-destructive method, XAFS spectroscopy is a potentially very useful technique for application in archaeological studies, on samples which are precious cultural heritages and are made of many different materials (see Chap. 26 of this volume, specifically dedicated to the applications of SR to cultural heritage).

As discussed in the Introduction, most of the mineralogical, petrological and geochemical studies are performed in the hard X-ray range, while soft X-rays and UV radiation is much less used. This is essentially due to the following technical problems: (a) in the low energy region absorption by air has an important effect, hence ultrahigh vacuum conditions are necessary; (b) the required detection modes are fluorescence or total electron yield; (c) in the range between 100 and 1500 eV the number of available beamlines which allow good XAFS measurements is relatively limited (see the list of the available beamlines at www.iucr.org/resources/commissions/xafs). However, if we consider that, as far as the major elements are concerned, most minerals are alumino-silicates containing alkaline, alkaline-earth and a few transition elements, we immediately understand the importance of the local structural characterization of the light elements in minerals. Actually, in the last few years, these problems have been widely addressed by means of the XANES technique, as documented by the abundant literature cited later.

Finally, there has been a recent remarkable development in micro-XAFS spectroscopy, based on the use of a strongly collimated beam capable of monitoring a signal from micro-volumes. This technique has been used in combination with SR-X-ray fluorescence microanalysis to obtain not only the two-dimensional distribution of chemical elements, but to perform an oxidation state-specific mapping. The combined approach is particularly useful for the study of fluid and micro-glass inclusions, micrometeorites, zoned or altered samples, calcareous biominerals etc.

In conclusion, the main mineralogical applications of XAFS can be briefly summarized as:

(a) determination of cation local environment, oxidation state, site distribution and short range order (among the recent literature see for instance [62–75];
(b) study of the distribution of major and minor elements in glasses, silicate melts and other disordered systems, such as polymers and gels [76–81];
(c) micro-XANES investigations by synchrotron X-ray microprobe of minerals, fluid inclusions, and biominerals and biomineralizing processes [82–90];
(d) structural studies of metamict materials [91, 92];
(e) time-resolved studies of transient phenomena and investigations under extreme P and/or T conditions [93–95];
(f) study of the static and dynamic disorder in geological materials [96, 97].

Recently, the ability of XANES in determining the oxidation state distribution of multi-valence elements present in minerals (specifically sulfur [75]) has been critically compared to that of X-ray emission spectroscopy (XES). The authors point out some advantages of XES to disentangle contributions due to different oxidation states; applications of XES are relatively few in the Earth Sciences but there is great potential for more widespread use.

24.4 X-Ray Fluorescence Microanalysis

The application of micro-beam methods to in-situ trace element analysis of geological materials can strongly contribute to a better understanding of the geological processes in the Earth and in extraterrestrial bodies.

The SR-X-ray microprobe technique allows the synergy of the common fluorescence analysis, one of the most widespread quantitative chemical analysis methods in Earth Sciences, and a high spatial resolution in the analyzed sample volume, which is typical of electron microprobe analysis (EMPA). Due to the heterogeneous nature of geological materials, a lateral resolution of the order of a few micrometers is important for any micro-analytical method. This requirement is fulfilled by a number of methods including ion probe (SIMS: secondary-ion mass spectroscopy), PIXE: (particle/proton-induced X-ray emission), laser-ablation mass-spectrometric techniques (e.g. laser-ablation ICP-MS) and SR-XRF (synchrotron radiation X-ray fluorescence).

XRF is based on the emission of characteristic X-rays after excitation with hard X-rays. SR emission is very intense, highly collimated and linearly polarized, leading—even for very small sample volumes—to good counting statistics and very good peak to background ratios. The yield of characteristic X-rays in relation to the impinging energy for XRF is two orders of magnitude higher than for electron-microprobe analysis and more than three orders of magnitude higher than for PIXE. Due to the limited interaction between inorganic substances and hard X-rays, SR-XRF is completely non-destructive for geological materials. Being a method for the

simultaneous analysis of multiple elements, SR-XRF microprobe provides a fast method well-suited for many geological problems, such as:

- analysis of trace elements and impurity distributions, and of multi-element profiles in geological samples (see Fig. 24.2) [98–101];
- in-situ analysis of trace elements in fluid inclusions in minerals and glasses [102–108];
- detailed study of micrometeorites and eolian and cosmic dust [109–111].

24.5 Materials Under Extreme Conditions

The study of the effects of pressure and temperature on materials deserves a section on its own since it is fundamental to a range of problems spanning condensed-matter physics and chemistry, Earth and planetary sciences and material science and technology [112]). In particular, high-pressure/high-temperature research is vitally important for studying the composition, thermal state and processes in the Earth and other planets [9, 23, 113–118]. Measurements of physical and chemical properties of rocks and plausible mantle and core mineral phases under appropriate conditions of pressure and temperature, together with the interrelationship of such data with geophysical and geochemical observations, are indispensable for the understanding and the modelling of planetary interiors. SR provides a powerful high-energy beam for penetrating the highly absorbing walls of the pressure vessels. Moreover, high-brilliance beams are ideal to obtain micron-sized focii needed to probe the very small samples required for high-P studies.

Study of the structure, composition, and history of the Earth and planetary interiors is an extremely challenging task because the deep interior is inaccessible. Among the most exciting geophysical problems to be resolved are the dynamics, rheology, compositional stratification and heterogeneity of the Earth's mantle and core and the nature of the lithosphere-astenosphere coupling. In particular, the composition, structure, formation, evolution and current dynamic state of the Earth's core is a hot research topic and in this case the keys to understanding the available geophysical data are the material properties of liquid and crystalline iron under core conditions. With the development of ultra-high pressure diamond anvil cell (DAC) techniques and with the possibility of performing experiments under high P and T, the behavior of materials under ultra-high pressure (i.e. to above 300 GPa) can now be explored. Since these conditions encompass the pressure range prevailing within the Earth, such experiments are essential for probing the nature of our planet's deep interior.

The acquisition of definitive high P-T data depends on the following prerequisites: (i) reaching P-T conditions to study the stable phases; (ii) measuring material properties in situ at high P and T; (iii) achieving the necessary accuracy. With the application of SR to the study of minerals under extreme conditions these prerequisites can be met and problems which were previously considered completely unapproachable can now be addressed. For example, it is now possible to interpret the discontinuities

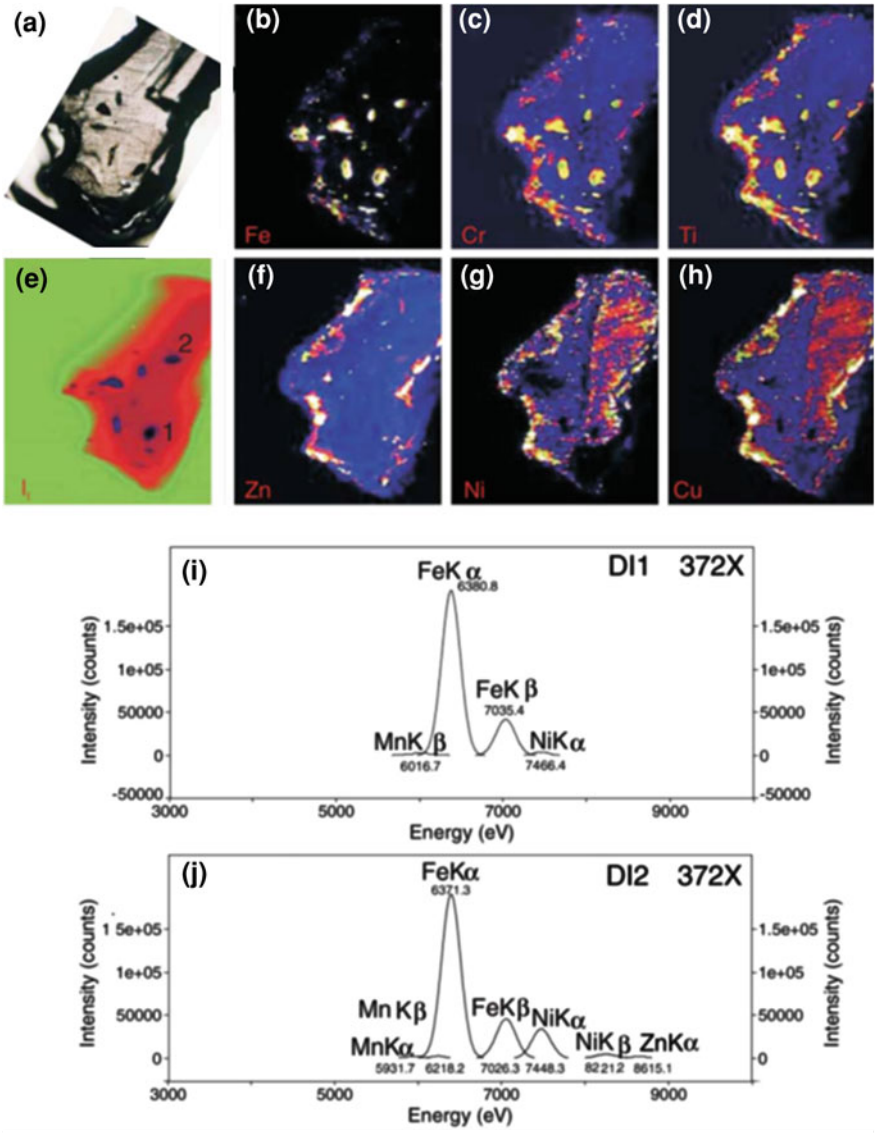


Fig. 24.2 Optical image, μXRF maps, and chemistry of a mineral inclusion in diamond. **a** Optical image; specimen is 3.05 mm in maximum dimension. Images (**b**–**d**) and (**f**–**h**) are false color maps for Fe, Cr, Ti, Zn, Ni, and Cu. On all X-ray maps, the brightness of the colors is proportional to element concentration. Location of spectra is shown on the *I*t density map (**e**). **i** Results of the deconvolution of μXRF spectra for inclusions DI1 and DI2 [99]. Reprinted with permission. © The Mineralogical Society of America

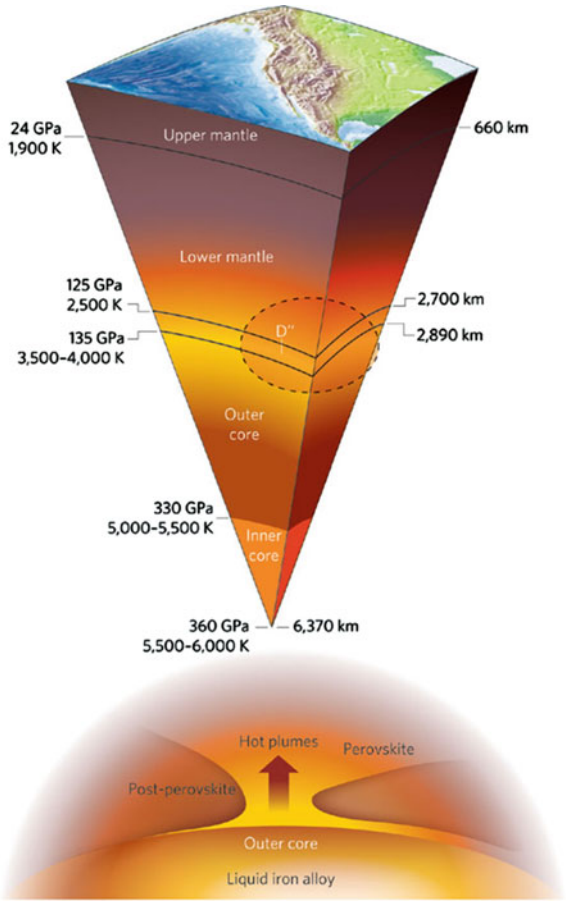


Fig. 24.3 Cross-section of the Earth's interior showing. **a** The lower mantle extends from a depth of 660 km to a depth of 2,890 km, with the D″ region extending about 200 km above the core. **b** A simplified diagram of possible structures of the D″ region near the core–mantle boundary (the region indicated by dashed lines in (**a**) [116]. Reprinted with permission. © Nature publishing group

observed by ultrasonic measurements during earthquakes in the deep earth on the basis of the phase transformations of the major components of the Earth.

A recent flurry of DAC research activity has focused on the discovery of a post-perovskite phase transition in $MgSiO_3$ near 125 GPa [119, 120]. This discovery is of great relevance to improving our understanding of the structure and dynamics of the lowermost portion of the mantle (<300 km from the core–mantle boundary). The Core-Mantle-Boundary (CMB) at a depth of 2,900 km separates the liquid outer core from the silicate lower mantle (Fig. 24.3). The change in physical properties across this boundary is as great as that between the solid Earth and the atmosphere at Earth's surface. The CMB region is highly anomalous, and holds the key to a number

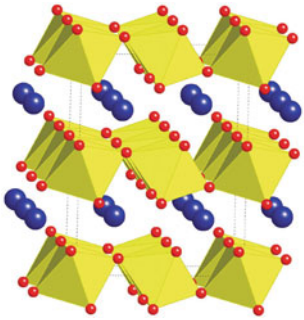


Fig. 24.4 Crystal structure of $CaIrO_3$-type (post-perovskite) phase of $(Mg, Fe)SiO_3$ [116]. Reprinted with permission. © Nature publishing group

of fundamental geophysical questions including: thermal structure of the deep Earth, origin of geochemical heterogeneity, ultimate repository of subduction slab material, and chemical interactions between the mantle and core. Just above the CMB at 2,700 km a discontinuity in seismic wave velocities is observed, commonly referred to as D″. Recent advances in HP science make it now possible to routinely generate pressure and temperature conditions of the CMB in the laboratory. The discovery of the structural phase transition from perovskite to a $CaIrO_3$-type phase (post-perovskite) at pressure and temperature conditions close to the D″ discontinuity has revolutionized our understanding of the CMB. (Fig. 24.4). However, the interaction of the molten outer core with the silicate mantle is still largely unknown. Knowledge of exchange reactions at HP and HT between a metal from one side and refractory oxides and silicates from another side is important for understanding the early Earth differentiation. The temperature of the liquid outer core and the temperature profile over the CMB are still unknown. Measurements of the melting temperature, elastic properties and crystal structures of iron alloys, metal oxides and lower mantle silicates (e.g. perovskite and post-perovskite) at high pressure and temperature will allow further insight into the composition, temperature, and structure of the CMB.

The current emphasis for studies of the Earth's interior rests on the following main points: (a) definition of the thermodynamic stability fields of the minerals constituting the mantle and the core; (b) determination of the equation of state (EOS: in P-V-T space) of these phases; (c) study of phase structure, transitions and order/disorder reactions under extreme conditions; (d) study of the rheological properties of the relevant mantle minerals.

Among the most important and studied mineralogical phases of the Earth's interior are the iron alloys, the iron polymorphs, the polymorphs of the systems FeO, MgO and SiO_2, and the main phases present in the mantle: $(Mg, Fe)_2\ SiO_4$ olivine-spinel, β phase, dense hydrous magnesium silicate phases, majorite, $(Mg, Fe)SiO_3$ ilmenite, perovskite and post-perovskite.

In the following, the main techniques used in deep-Earth mineralogy which take advantage of SR are discussed.

24.5.1 Single-Crystal and Powder X-Ray Diffraction

The ability to focus the intense SR beam and the use of energy dispersion detection are especially useful for high-P/high-T studies since they allow very small crystals [6, 121], or powdered samples [122] to be studied by rapid collection of diffraction data, obtaining in this way kinetic information. Moreover, the low beam divergence and the ability to tune the beam to give highly monochromatic radiation provides narrow peak widths in the powder diffraction spectra, with excellent signal-to-noise ratio and the possibility of determining structures of powder samples using the Rietveld method. Very recently, melting processes in the deep mantle have been reproduced and investigated by SR XRPD experiments under ultra high P and T [123] to obtain information on the melt production mechanisms near the core-mantle boundary. The results show that the iron partition coefficient between aluminium-bearing (Mg, Fe)SiO perovskite and the liquid is significantly higher than that previously estimated and hence iron is not so incompatible with deep-mantle minerals.

24.5.2 Single-Crystal and Powder IR Spectroscopy

SR-IR spectroscopy has become an important technique for HP studies. In fact, the high brilliance of synchrotron sources at IR wavelengths results in major improvements in the ability to probe microscopic samples [22, 23, 113]. In general, as an infrared source, synchrotron radiation has the following major advantages compared to conventional laboratory sources: (i) *higher brilliance*: as it is almost a point source, one can focus the light to a diffraction limited size (gain up to 1000×); (ii) *broader spectral range*: continuous from FIR to the visible; (iii) *higher photon flux in the FIR*; (iv) *intense coherent emission* in the lower energy part of the FIR: gain up to 10^5 compared to incoherent SR; (v) *pulsed source* in the ns range: the light is emitted from electron bunches which allows fast timing measurements.

HP vibrational IR spectra elucidate changes in the bonding properties of compressed crystals, glasses and melts, allow identification of phase transitions, provide information on crystal symmetry and reveal directly lattice dynamic variables which are important for calculating thermodynamic properties [124]. Moreover, this technique is able to identify, both under room conditions and in-situ at high pressure, the presence of trace hydrogen in nominally anhydrous mantle phases, a problem of great importance in mantle mineralogy. For instance, the uptake of hydrogen in $MgSiO_3$ perovskite, the magnesium end-member phase of the most abundant mineral in the planet, was examined by Meade et al. [125]. Although nominally anhydrous, the synchrotron measurements revealed that the material can accommodate a surprising amount of hydrogen so that a significant fraction of the water in the current ocean might be stored in the lower mantle. The technique has also been used to study multiphase assemblages such as microscopic inclusions in diamond. Measurements of the OH content in a suite of silicate inclusions in diamond were not possible with

conventional IR methods but were readily measured by SR-IR, and the presence of OH was clearly demonstrated in kyanite inclusions. Measurements of OH bands as a function of pressure were also performed on amphiboles and phyllosilicates (e.g. [126]).

24.5.3 X-Ray Absorption Spectroscopy

XAS is a powerful tool for the determination of bond length variations (local compressibility) and coordination and oxidation state changes under high pressure conditions, since it allows experimental following of phase transformation processes in diamond cells (e.g. [93–95, 127–130]). Moreover, the energy-dispersive geometry allows for the fast collection of spectra as a function of temperature and pressure. XAS can also be successfully used to study temperature and pressure-induced short range ordering in minerals and silicatic melts. In fact, the cation ordering or clustering phenomena in crystalline phases and local environments in the amorphous phases are particularly sensitive to cooling, crystallization or amorphization rate of the material. These phenomena are undetectable by X-ray diffraction and this confirms the importance of combined approaches based on the complementary use of both techniques.

Among the recent results we note that several iron-containing oxides and silicates including $(Mg_{0.88}\,Fe_{0.12})\,SiO_3$, $(Mg_{0.86},\ Fe_{0.14})\,(Si_{0.98}, Al_{0.02})O_3$ perovskites, and $(Mg_{0.80}, Fe_{0.20})O$ ferropericlase were studied using Fe K-edge XANES under pressure up to 85 GPa at ambient temperature [93]. First-principles calculations of Fe K-edges of $(Mg_{0.88}\,Fe_{0.12})\,SiO_3$ perovskite and $(Mg_{0.80},\ Fe_{0.20})O$ ferropericlase were performed using a spin-dependent method. The amount and quality of the data collected allowed performance of a systematic study of the absorption edge features as a function of pressure in these geophysically important systems, providing direct experimental validation for band-structure calculations. The comparison between experiment and theory allowed analyzing in detail the effect of Fe valence and spin state modifications on the spectra, allowing to confirm qualitatively the presence of a pressure induced spin pairing transition in (Mg, Fe)O ferropericlase and a high-spin intermediate spin crossover in (Mg, Fe)(Si, Al)O_3 perovskite.

Another recent study has investigated the oxidation state of iron in $FeTiO_3$ under high pressure by combining X-ray diffraction, Mössbauer spectroscopy, X-ray-absorption spectroscopy, and density-functional theory based calculations [94]. The results demonstrated that the ilmenite-to-perovskite phase transition occurs above 20 GPa at room temperature and on compression two phases coexist to 40 GPa. The Fe^{3+}/Σ Fe ratio increases up to 16 GPa, probably due to the *d*-electron drifting of cations via the oxygen bridge in the adjacent octahedral site, then decreases at higher pressure due to the ilmenite-to-perovskite phase transition accompanied by a slight decrease in iron valence state.

24.5.4 HP Synchrotron Mössbauer

Most of the minerals and polymorphs expected in Earth's interior are believed to incorporate low concentrations of Fe^{2+} and/or Fe^{3+} of about 10 at% or less. They are not expected to be magnetically ordered in Earth's lower mantle because of the low Fe content and the elevated temperature. However, as previously discussed, valence and spin state of the Fe in minerals may still be relevant with respect to density, iron partitioning, partial melting, radiative thermal conductivity, and compositional layering. SR Mössbauer spectroscopy (SMS) [26] can measure quadrupole splittings and isomer shifts similarly to traditional Mössbauer spectroscopy but the high brilliance of SR greatly reduces the data collection times and allows easier access for HP studies. Recently, SMS has been applied to silicates, oxides and metals in studies of geophysical interest [131].

24.6 X-Ray Tomography and Topography

In the last decade the number of applications of X-ray micro-tomography techniques to Earth Science problems has been increased, since these techniques have been found to be extremely useful in the non-destructive internal imaging of samples which cannot be prepared as thin sections for conventional microscopy investigations. Examples of these are: imaging of the internal structure of rare or brittle fossils [132]; imaging of the internal distribution of minerals and chondrules in unique or rare meteorites, such as the lunar and martian ones; characterization and imaging of the porous structure and the mineralogical texture of soils.

Of great interest is the possibility of tomographically detecting (a) the signal of a specific chemical species (chemical tomography), or (b) the signal diffracted by a phase of interest (compositional tomography). In this way it is possible to obtain the specific three-dimensional distribution of the element or phase in the sample bulk. Very recently, nanoscale X-ray fluorescence tomography has been applied to the 3D elemental imaging of cometary matter [133] and to the study of mineral inclusions in chromite from ordinary chondrites [134]. Moreover, apparata have been developed for microtomographic studies under high pressure [31].

X-ray topography techniques (with a white or monochromatic beam) are used for the study of crystal defects and growth structures, thanks to the extreme sensitivity of the method to small variations in the orientation or dimension of the lattice vectors. The technique is particularly suitable for the study of the relationship between the occurrence of a phase transition, the density of lattice defects and the formation of twinning or anti-phase boundaries in the crystal. Examples of applications are: the study of the $\alpha - \beta$ transition in quartz and associated lattice defects and the study of an incommensurate phase intermediate between the α and β phases of quartz and berlinite [28, 135].

24.7 Future Prospects

The application of SR to Earth Sciences is in a phase of rapid and continuous development and one can foresee that in the near future a much larger number of Earth scientists will benefit from new-generation SR sources, in particular for problems involving:

- extremely low elemental concentrations;
- very small sample volumes;
- integrated ultra-high pressure and temperature experiments, to reproduce conditions equivalent to those of the lowest region of the lower mantle and core;
- transient phenomena, during which very rapid data acquisition is required,
- high spatial resolution levels;
- non-destructive nano-scale imaging;
- simultaneous measurements combining diffractometric and spectroscopic techniques (like X-ray diffraction + XAS or X-ray fluorescence + XAS, X-ray diffraction + X-ray fluorescence).

References

1. P. Fenter, M. Rivers, N. Sturchio, S. Sutton (eds.) Applications of Synchrotron Radiation in Low-Temperature Geochemistry and Environmental Science. Rev. Mineral. Geochem. 49, MSA Series, Washington, DC (2002)
2. S.R. Sutton, M.W. Caffee, M.T. Dove, ELEMENTS **2**, 15–21 (2006)
3. C.T. Prewitt, R.T. Downs, in *Ultrahigh Pressure Mineralogy*, ed. by R. J. Hemley, Rev. Mineral. Geochem. 37, 283–317, MSA Series, Washington, DC (1998)
4. Å. Kvick, Nato ASI series C-221, 187–203 (1998)
5. S.D. Jacobsen, J.-F. Lin, R.J. Angel, G. Shen, V.B. Prakapenka, P. Dera, H. Mao, R.J. Hemley, Jour. Synchrotron Rad. **12**, 577–583 (2005)
6. P. Dera, in *High-Pressure Crystallography: From Fundamental Phenomena to Technological Applications*, ed. by E.Boldyreva, P. Dera (Springer Sciences, 2010), pp. 11–22
7. L.W. Finger, in *Modern Powder Diffraction*. Rev. Mineral. Geochem. 20, 309–331 MSA Series, Washington, DC (1989)
8. D.E. Cox, in Synchrotron Radiation Crystallography, ed. by P. Coppens (Academic Press, London, 1992)
9. J.B. Parise, C.L. Cahill, Y. Lee, Can. Mineral. **38**, 777–800 (2000)
10. S.M. Antao, I. Hassan, J. Wang, P.L. Lee, B.H. Toby, Can. Mineral. **46**, 1501–1509 (2008)
11. Á.G. de la Torre, M.C. Martín-Sedeño, L. León-Reina, J.M. Compaña, M.A.G. Aranda, in *Synchrotron Radiation in Mineralogy. Seminarios de la Sociedad Española de Mineralogía*, vol. 6, ed. by M. Suárez, E.Y. Ayuso, E.M. Manchado (2009), pp. 29–59
12. C. Meneghini, A.F. Gualtieri, C. Siligardi, J. Appl. Cryst. **32**, 1090–1099 (1999)
13. D. Pontoni, J. Bolze, N. Dingenouts, T. Narayanan, M.J. Ballauff, J. Phys. Chem. B **107**, 5123–5125 (2003)
14. G. Sankar, T. Okubo, W. Fanc, F. Meneaud, Faraday Discuss. **136**, 157–166 (2007)
15. C. Gilow, E. Zolotoyabko, O. Paris, P. Fratzl, B. Aichmayer, Growth Des. **11**, 2054–2058 (2011)
16. G.E. Jr. Brown, G. Calas, G.A. Waychunas, J. Petiau, in Spectroscopic Methods in Mineralogy and Geology. Rev. Mineral. Geochem. 18, 431–512, MSA Series, Washington, DC (1988).

17. E.D. Crozier, Nucl. Instrum. Methods Phys. Res. Sect. B-Beam Interact. Mater. Atoms **133**, 134–144 (1997)
18. G. Calas, A. Manceau, J.M. Combes, F. Farges, in *Absorption spectroscopy in Mineralogy*, ed. by A. Mottana, F. Burragato (Elsevier, Amsterdam, 2002)
19. J. Chaboy Nalda, in *Instrumental Techniques Applied to Mineralogy and Geochemistry. Seminarios de la Sociedad Española de Mineralogía*, vol. 6, ed. by I. Subias, B. Bauluz (2008), pp. 43–56
20. L. Vincze, G. Silversmit, B. Vekemans, R. Terzano, F. Brenker, in *Nanoscopic Approaches in Earth and Planetary Sciences*, ed. by F. Brenker, G. Jordan. EMU Notes in Mineralogy, vol. 8 (2010), pp. 169–237
21. F. Adam, EPJ Web Conf. **9**, 165–180 (2010)
22. R.J. Hemley (ed.), Ultrahigh-pressure Mineralogy. Physics and chemistry of the Earth's deep interior. Rev. Mineral. Geochem. 37, MSA Series, Washington, DC (1998)
23. R.J. Hemley, H. Mao, V.V. Struzhkin, J. Synch, Rad. **12**, 135–154 (2005)
24. B. Gasharova, in Raman, Conventional Infrared and Synchrotron Infrared Spectroscopy in Mineralogy and Geochemistry: Basics and Applications. Seminarios de la Sociedad Española de Mineralogía. Madrid, vol. 5, ISSN 1698–5478 (2008), pp. 59–81
25. J.M. Jackson, E.A. Hamecher, W. Sturhahn, Eur. J. Mineral. **21**, 551–560 (2009)
26. J. Jackson, in *High-Pressure Crystallography: From Fundamental Phenomena to Technological Applications*. ed. by E. Boldyreva, P. Dera, Nato Sciences for Peace and Security Series-B: Physics and Biophysics (Springer Sciences, 2010), pp. 43–50
27. V. Cnudde, M.N. Boone, Earth Sci. Rev. **123**, 1–17 (2013)
28. A. Zarka, B. Capelle, E. Philippot, J.C. Jumas, J. Appl. Crystallogr. **19**, 477–481 (1986)
29. R.A. Ketcham, W.D. Carlson, Comput. Geosci. **27**, 381–400 (2001)
30. F. Mees, R. Swennen, M. Van Geet, P. Jacobs (eds), Applications of X-ray Computed Tomography in the Geosciences. Geol. Soc. London Spec. Publ. 215, 1–6 (2003)
31. Y. Wang, T. Uchida, F. Westferro, M.L. Rivers, N. Nishiyama, J. Gebhardt, C.E. Lesher, S.R. Sutton, Rev. Sci. Instr. **76**, 073709 (2005)
32. W.A. Bassett, G.E. Brown, Annu. Rev. Earth Plan. Sci. **18**, 387–447 (1990)
33. C.M.B. Henderson, G. Cressey, S.A.T. Redfern, Radiat. Phys. Chem. **45**, 459–481 (1995)
34. J.B. Parise, in *Transformation Processes in Minerals*, vol. 39, ed. by S.A.T. Redfern, M.A. Carpenter. Rev. Min. Geochem. MSA Series (2000).
35. S. Quartieri, in *Synchrotron Radiation: Fundamentals, Methodologies and Applications*, ed. by S. Mobilio, G. Vlaic (Società Italiana di Fisica, Bologna, 2003)
36. I. Subias, B. Bauluz (eds.), in Instrumental Techniques Applied to Mineralogy and Geochemistry. Seminarios de la Sociedad Española de Mineralogía. vol. 5, SEM, Madrid, ISSN 1698–5478 (2008), p. 154
37. M. Suárez, E. Ayuso, E.M. Manchado (eds.), Synchrotron Radiation in Mineralogy. Seminarios de la Sociedad Española de Mineralogía. 6, SEM, Salamanca, ISSN 1698–5478 (2009) p. 141
38. Y. Lee, J.A. Hriljac, T. Vogt, J.B. Parise, G. Artioli, J. Am. Chem. Soc. **123**, 12732–12733 (2009)
39. Y. Lee, J.A. Hriljac, A. Studer, T. Vogt, Phys. Chem. Minerals **31**, 22–27 (2004)
40. G. Cruciani, J. Phys. Chem. Solids **67**, 1973–1994 (2006)
41. J.E. Post, D.L. Bish, P.J. Heaney, Am. Mineral. **92**, 91–97 (2007)
42. J.E. Post, P.J. Heaney, Am. Mineral. **93**, 667–675 (2008)
43. S. Ori, S. Quartieri, G. Vezzalini, V. Dmitriev, Am. Mineral. **93**, 53–62 (2008)
44. D. Gatta, in *High-Pressure Crystallography: From Fundamental Phenomena to Technological Applications*, ed. by E. Boldyreva, P. Dera (Springer Sciences, 2010) pp. 481–491
45. S. Quartieri, G. Montagna, R. Arletti, G. Vezzalini, J. Solid State Chem. **184**, 1505–1516 (2011)
46. G. Iezzi, M. Tribaudino, G. Della Ventura, F. Nestola, F. Bellatreccia, Phys. Chem. Minerals 7, 515–523 (2005)
47. S.M. Antao, I. Hassan, W.A. Crichton, J.B. Parise, Am. Mineral. **90**, 1500–1505 (2005)

48. T. Ballaran, J. Liu, L.S. Dubrovinsky, R. Caracas, W.A. Crichton, Phys. Rev. B **80**, 214104–214111 (2009)
49. E. Mazzucato, A.F. Gualtieri, Phys. Chem. Minerals **27**, 565–574 (2000)
50. A. Cattaneo, A.F. Gualtieri, G. Artioli, Phys Chem Minerals **30**, 177–183 (2003)
51. M. Dapiaggi, C.A. Geiger, G. Artioli, Am. Mineral. **90**, 506–509 (2005)
52. J.E. Post, P.J. Heaney, J. Hanson, Powder Diffr. **17**, 218–221 (2002)
53. S. Nazzareni, P. Comodi, L. Bindi, L. Dubrovinsky, Am. Mineral. **95**, 655–658 (2010)
54. A.H. Treiman, A. Lanzirotti, D. Xirouchakis, *Lunar Planet* (Sci , XXXV, 2004)
55. J.K. Hong, C.D.K. Herd, R.G. Cavell, in 42nd Lunar and Planetary Science Conference (2011), pp. 96–97.
56. G. Vezzalini, S. Quartieri, E. Galli, A. Alberti, G. Cruciani, A. Kvick, Zeolites **19**, 323–325 (1997)
57. Y. Kudoh, T. Inoue, Phys. Chem. Minerals **26**, 382–388 (1999)
58. G. Capitani, M. Mellini, Am. Mineral. **91**, 394–399 (2006)
59. S. Merlino, E. Bonaccorsi, A.I. Grabezhev, A.E. Zadov, N.N. Pertsev, N.V. Chukanov, Am. Mineral. **94**, 323–333 (2009)
60. D. Pinto, E. Bonaccorsi, T. Balić-Žunić, E. Makovicky, Am. Mineral. **93**, 713–727 (2008)
61. E.N. Fedorova, V.P. Afanasyev, N.P. Pokhilenk, J. Surf. Invest. **5**(6), 1032–1037 (2011)
62. S. Quartieri, M.C. Dalconi, F. Boscherini, R. Oberti, F. D'Acapito, Phys. Chem. Minerals **31**, 162–167 (2004)
63. S. Quartieri, R. Oberti, M. Boiocchi, M.C. Dalconi, F. Boscherini, O. Safonova, B.A. Woodland, Am. Mineral. **91**, 1240–1248 (2006)
64. R. Oberti, S. Quartieri, M.C. Dalconi, F. Boscherini, G. Iezzi, M. Boiocchi, S. Eeckhout, Am. Mineral. **91**, 1230–1239 (2006)
65. C.M.B. Henderson, A.M.T. Bell, J.M. Charnock, K.S. Knight, R.F. Wendlandt, D.A. Plant, W.J. Harrison, Mineral. Mag. **73**(3), 433–455 (2009)
66. A. Bordage, C. Brouder, E. Balan, D. Cabaret, A. Juhin, M.-A. Arrio, Ph Sainctavit, G. Calas, P. Glatzel. Am. Mineral. **95**, 1161–1171 (2010)
67. G. Cibin, A. Mottana, A. Marcelli, G. Cinque, W. Xu, Z. Wu, M.F. Brigatti, Am. Mineral. **95**, 1084–1094 (2010)
68. K.H. Hattori, Y. Takahashi, T. Auge, Am. Mineral. **95**, 622–630 (2010)
69. E.D. Ingall, J.A. Brandes, J.M. Diaz, M.D. de Jonge, D. Paterson, I. McNulty, W.C. Elliott, P. Northrup, J. Synch, Rad. **18**, 189–197 (2011)
70. N.D. Tailby, A.M. Walker, A.J. Berry, J. Hermann, K.A. Evans, J.A. Mavrogenes, H. St.C. O'Neill, I.S. Rodina, A.V. Soldatov, D. Rubatto. Geochim. Cosmochim. Acta **75**, 905–921 (2011)
71. D. Li, M. Peng, T. Murata, Can. Mineral. **37**, 199–206 (1999)
72. G. Giuli, G. Pratesi, M. Corazza, C. Cipriani, Am. Mineral. **85**, 1172–1174 (2000)
73. C. Romano, E. Paris, B.T. Poe, G. Giuli, D.B. Dingwell, A. Mottana, Am. Mineral. **85**, 108–117 (2000)
74. S. Quartieri, F. Boscherini, C. Dalconi, G. Iezzi, C. Meneghini, R. Oberti, Am. Mineral. **93**, 495–498 (2008)
75. R. Alonso Mori, E. Paris, G. Giuli, S.G. Eeckhout, M. Kavcic, M. Zitnik, K. Bucar, L.G.M. Pettersson, P. Glatzel, Analytical Chem. **81**, 6516–6525 (2009)
76. M. Wilke, F. Farges, G.M. Partzsch, C. Schmidt, H. Behrens, Am. Mineral. **92**, 44–56 (2007)
77. G. Giuli, S.G. Eeckhout, C. Koeberl, G. Pratesi, E. Paris, Yellow impact glass from the K/T boundary at Beloc (Haiti): Meteoritics & Planetary Sci. 43, 981–986 (2008)
78. G. Giuli, E. Paris, K. Hess, D.B. Dingwell, M.R. Cicconi, S.G. Eeckhout, K.T. Fehr, P. Valenti, Am. Mineral. **96**, 631–636 (2011)
79. F. Farges, Chromium speciation in oxide-type compounds: application to minerals, gems, aqueous solutions and silicate glasses. Phys. Chem. Minerals **36**, 463–481 (2009)
80. E. Chalmin, F. Farges, G.E. Brown Jr, Contrib. Mineral. Petrol. **157**, 111–126 (2009)
81. N. Trcera, D. Cabaret, S. Rossano, F. Farges, A.-M. Flank, P. Lagarde, Phys. Chem. Minerals **36**, 241–257 (2009)

82. M. Mosbah, J.P. Duraud, N. Metrich, Z. Wu, J.S. Delaney, A. San Miguel, Nucl. Instrum. Methods Phys. Res. Sect. B **158**, 214–220 (1999)
83. D.M. Dyar, J.S. Delaney, S.R. Sutton, M.W. Schaefer, Am. Mineral. **83**, 1361–1365 (1998)
84. D.M. Dyar, E.W. Lowe, C.V. Guidotti, J.S. Delaney, Am. Mineral. **87**, 514–522 (2002)
85. R. Schmid, M. Wilke, R. Oberhansli, K. Janssens, G. Falkenberg, L. Franz, A. Gaab, Lithos **70**, 381–392 (2003)
86. S.R. Walker, H.E. Jamieson, A. Lanzirotti, C.F. Andrade, G.E.M. Hall, Can. Mineral. **43**, 1205–1224 (2005)
87. F. Scordari, M.D. Dyar, E. Schingaro, M. Lacalamita, L. Ottolini, Am. Mineral. **95**, 1657–1670 (2010)
88. J. James-Smith, J. Cauzid, D. Testemale, W. Liu, J.-L. Hazemann, O. Proux, B. Etschmann, P. Philippot, D. Banks, P. Williams, Am. Mineral. **95**, 921–932 (2010)
89. J. Thieme, C. Schmidt, ESRF Exp. Rep. ME-53 (2000).
90. F. Farges, A. Meibom, A.-M. Flank, P. Lagarde, M. Janousch, J. Stolarski, J. Phys. Conf. Ser. **190**, 012074 (2009)
91. F. Farges, Am. Mineral. **82**, 44–50 (1997)
92. J. Dubrail, F. Farges, L. Gautron, M. Harfouche, C. Borca, D. Grolimund, J. Phys.: Conf. Ser. **190**, 012152 (2009)
93. O. Narygina, M. Mattesini, I. Kantor, S. Pascarelli, X. Wu, G. Aquilanti, C. McCammon, L. Dubrovinsky, Phys. Rev. B **79**, 174115–174124 (2009)
94. X. Wu, G. Steinle-Neumann, O. Narygina, I. Kantor, C. McCammon, S. Pascarelli, G. Aquilanti, V. Prakapenka, L. Dubrovinsky, Phys. Rev. B **79**, 094106–094112 (2009)
95. J-P. Itie, A-M. Flank, P. Lagarde, S. Ravy, A. Polian, in *High-Pressure Crystallography: From Fundamental Phenomena to Technological Applications*, ed. by E. Boldyreva, P. Dera. Nato Sciences for Peace and Security Series-B: Physics and Biophysics, (Springer Sciences, 2010), pp. 51–67
96. S. Quartieri, G. Antonioli, G. Artioli, C.A. Geiger, P.P. Lottici, Phys. Chem. Minerals **24**, 200–205 (1997)
97. P.E. Petit, F. Guyot, F. Farges, J. Phys, IV FRANCE 7. Colloque **C2**, 1065–1067 (1997)
98. T.H. Hansteen, P.M. Sachs, F. Lechtenberg, Eur. J. Mineral. **12**, 25–31 (2000)
99. H. Sitepu, M.G. Kopylova, D.H. Quirt, J.N. Cutler, Th.G. Kotzer, Am. Mineral. **90**, 1740–1747 (2005)
100. L. Core, P. Daniel, S.E. Kesler, E.J. Essene, E.B. Dufresne, R. Clarke, D.A. Arms, D. Walko, M.L. Rivers, Can. Mineral. **43**, 1781–1796 (2005)
101. C. Schmidt, K. Rickers, D.H. Bilderback, R. Huang, Lithos **95**, 87–102 (2007)
102. A.J. Anderson, R.A. Mayanovic, S. Bajt, Can. Mineral. **33**, 499–508 (1995)
103. A.J. Anderson, R.A. Mayanovic, S. Bajt, Can. Mineral. **36**, 511–524 (1998)
104. C. Romano, D.B. Dingwell, F. Lechtenberg, Phys. Chem. Glasses **39**, 181–183 (1998)
105. B. Bühn, A.H. Rankin, M. Radtke, M. Haller, A. Knöchel, Am. Mineral. **84**, 1117–1125 (1999)
106. Y.H. Tang, C.M. Han, Z.K. Bao, Y.Y. Huang, W. He, W. Hua, Analysis of apatite crystals and their fluid inclusions by synchrotron radiation X-ray fluorescence microprobe. Spectrochim. Acta, Part B **60**, 439–446 (2005)
107. H. Nagaseki, K. Hayashi, A. Iida, Eur. J. Mineral. **18**, 309–318 (2006)
108. J. Cauzid, P. Philippot, A. Somogyi, B. Ménez, A. Simionovici, P. Bleuet, Chem. Geology **227**, 165–183 (2006)
109. G.J. Flynn, S.R. Sutton, F. Horz, *Lunar Planet* (Lunar and Planetary Institute, Houston, TX, Sci. XXVII, 1996), pp. 369–370
110. S.R. Sutton, M.L. Rivers, S. Bajt, K. Jones, J.V. Smith, Nucl. Instr. Meth. Phys. Rev. **A347**, 412–416 (1994)
111. G. Cibin, A. Marcelli, V. Maggi, M. Sala, F. Marino, B. Delmonte, S. Albani, S. Pignotti, Spectrochim. Acta, Part B **63B**(12), 1503–1510 (2008)
112. E. Boldyreva, P. Dera (eds.), *High-Pressure Crystallography: from Fundamental Phenomena to Technological Applications*. Nato Science for Peace and Security Series - B: Physics and Biophysics. Springer Sciences (2010)

113. R.J. Hemley, A.F. Goncharov, R. Lu, V.V. Struzhkin, M. Li, H.K. Mao, Nuovo Cimento **20D**, 539–551 (1998)
114. R.J. Hemley, H.K. Mao, S.A. Gramsh, Mineral. Mag. **64**, 157–184 (2000)
115. T.S. Duffy, Rep. Prog. Phys. **68**, 1811–1859 (2005)
116. T.S. Duffy, Nature **451**(7176), 269–270 (2008)
117. M. Mezouar, in High-Pressure Crystallography: From Fundamental Phenomena to Technological Applications, ed. by E. Boldyreva, P. Dera. Nato Science for Peace and Security Series-B: Physics and Biophysics (Springer Sciences, 2010), pp. 23–33.
118. L. Dubrovinsky, J-F. Lin, N. Dubrovinskaia in High-Pressure Crystallography: From Fundamental Phenomena to Technological Applications ed. by E. Boldyreva, P. Dera. Nato Science for Peace and Security Series-B: Physics and Biophysics (Springer Sciences, 2010), pp. 35–41.
119. M. Murakami, K. Hirose, K. Kawamura, N. Sata, Y. Ohishi, Science **304**, 855–858 (2004)
120. A.R. Oganov, S. Ono, Nature **430**, 445–448 (2004)
121. H.K. Mao, R.J. Hemley, High-Pressure Res. **14**, 257–267 (1996)
122. G. Fiquet, D. Andrault, J. Synch, Rad. **6**, 81–86 (1999)
123. D. Andrault, S. Petitgirard, G. Lo Nigro, J.-L. Devidal, G. Veronesi, G. Garbarino, M. Mezouar, Nature **487**, 354–357 (2012)
124. P.F. Mc Millan, A.M. Hofmeister, vol. 18, ed. by F.C. Hawthorne F.C. (ed.), Rev. Mineral. Geochem, MSA, Washington D.C (1988), p. 99
125. C. Meade, J.A. Effner, E. Ito, Science **264**, 1558–1560 (1994)
126. G. Iezzi, Z. Liu, Phys. Chem. Minerals **36**, 343–354 (2009)
127. J.P. Itié, Phase Trans. **39**, 81–98 (1992)
128. D. Andrault, M. Madon, J.P. Itie, A. Fontaine, Phys. Chem. Minerals **18**, 506–513 (1992)
129. J. Badro, P. Gillet, P.F. Mc Millan, A. Polian, J.-P. Itié, Europhysics Lett. **40**, 533–538 (1997)
130. J. Badro, J.P. Itié, A. Polian, P. Gillet, J. Phys, IV FRANCE 7. Colloque **C2**, 987–989 (1997)
131. W. Sturhahn, J.M. Jackson, in Advances in High-Pressure Mineralogy: GSA Special Paper, vol. 421 ed. by E. Ohtani (2007), pp. 157–174.
132. P. Tafforeau, R. Boistel, E. Boller, A. Bravin, M. Brunet, Y. Chaimanee, P. Cloetens, M. Feist, J. Hoszowska, J.-J. Jaeger, R.F. Kay, V. Lazzari, L. Marivauw, A. Nel, C. Nemoz, X. Thibault, P. Vignaud, S. Zabler, Applied Physics A **83**, 195–202 (2006)
133. G. Silversmit, B. Vekemans, F.E. Brenker, S. Schmidz, M. Burghammer, C. Riekel, L. Vincze, Anal. Chem. 81, 6107–6112 (2009) and ESRF Highlights 2009, 114–115 (2009).
134. C. Alwmark, B. Schmitz, S. Holm, F. Marone, M. Stampanoni, Meteorit. Planet. Sci. **46**, 1071–1081 (2011)
135. A. Zarka, B. Capelle, in *Synchrotron radiation applications in mineralogy and petrology*, ed. by S.S. Augustithis (Theophrastus Publications, Athens, 1988), pp. 191–203

Chapter 25
Synchrotron Radiation and Environmental Sciences

Giovanni De Giudici, Piero Lattanzi and Daniela Medas

Abstract Synchrotron-based techniques have been one of the most powerful tools for the development of molecular environmental science (MES), that is, understanding at the molecular scale the phenomena controlling environmentally relevant processes. The most commonly applied techniques include X-ray absorption spectroscopy, X-ray diffraction, X-ray imaging, and other microbeam or surface techniques.

25.1 Introduction: What Is Environmental Science?

Environmental science, or, perhaps more appropriately, environmental sciences, is a complex, comparatively young, field of study that encompasses all aspects pertaining to the natural and human environment. Inasmuch as the latter is an intersection of nature, culture, and society, it follows that environmental sciences include not only natural (in turn comprised of life, Earth, and atmospheric sciences) and physical (physics and chemistry) sciences, and engineering, but also social sciences, politics, and economy. All these aspects have extremely complex interconnections, a quantitative description of which is a truly challenging task. There is obviously no single individual that can claim to be an expert in all these fields, although anybody seriously approaching environmental sciences should be aware of at least the basic concepts. In practice, most researchers and research groups, and therefore most studies, are focused either on the scientific and technical aspects *stricto sensu*, or on social, economic, and political issues. This chapter, being addressed to an audience of "hard" scientists, deals only with the first aspects. Even with this specification, the complexity of the investigated systems remains enormous, and requires a truly

G. De Giudici · P. Lattanzi (✉) · D. Medas
Department of Chemical and Geological Science, University of Cagliari, Via Trentino 51, 09127 Cagliari, Italy
e-mail: lattanzp@unica.it

S. Mobilio et al. (eds.), *Synchrotron Radiation*,
DOI: 10.1007/978-3-642-55315-8_25, © Springer-Verlag Berlin Heidelberg 2015

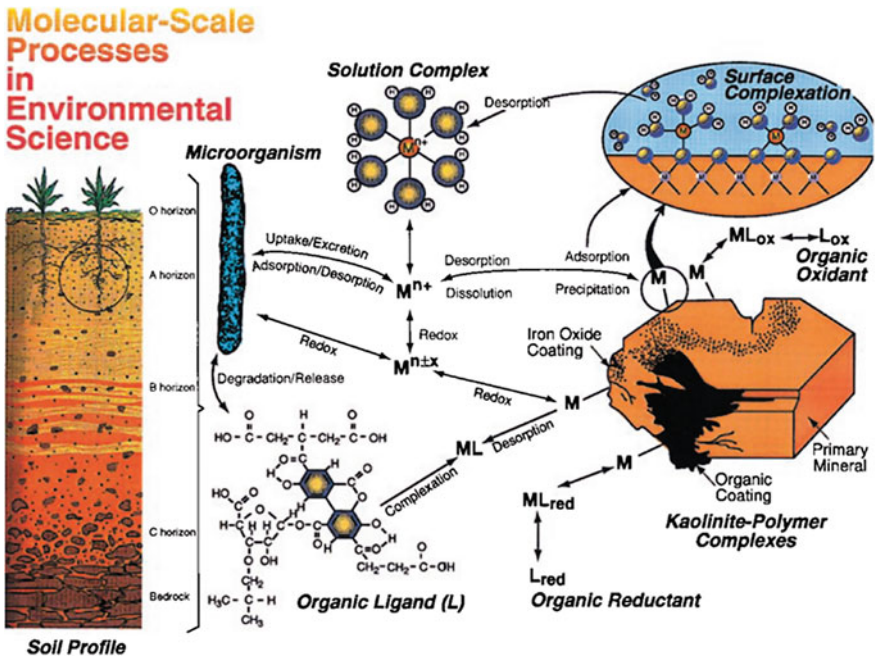


Fig. 25.1 A scheme of some important micro- to nano-scale processes of environmental interest occurring in a soil. Reproduced with permission from [4] (Copyright 1999 National Academy of Sciences, U.S.A)

interdisciplinary approach, being characterized by many parameters of very different nature, and by nonlinear, often chaotic, phenomena, well exemplified by the butterfly paradox, whereby a flap of butterfly wings in Amazonia sets off a tornado in Texas (cf. [1]). The extreme interconnection of all phenomena pertaining to the environment led to the concept that the whole planet should be regarded as a single organism (the Gaia hypothesis; [2]).

In this context, it is no surprise that many environmental studies, especially in the early stages, were of mainly descriptive, empirical nature, and that mechanistic interpretations were seldom attempted. However, in the last two decades there has been the growing awareness that even global scale phenomena find their ultimate origin in something that happens at the atomic scale, and therefore environmental investigation must be pushed to that limit, if we want to move beyond empirical evidence toward understanding. This awareness prompted the quest for what is now known as molecular environmental science (MES; e.g., [3], and references therein). Figure 25.1 aptly summarizes many micro- to nano-scale processes of interest for MES.

The development in the 1990s of 3rd generation synchrotron facilities has been instrumental in the birth, growth, and booming of MES. Today, synchrotron sources are the most valuable items in the MES toolbox, to the extent that at several facilities

(e.g., SSRL, ALS, NSLS) there are beamlines dedicated to, or mainly focused on, MES, and that collective actions were undertaken to foster synchrotron applications to environmental sciences (e.g., Envirosync in Northern America, and Envirosynch in UK; [5, 6]). There are several excellent reviews of synchrotron techniques in environmental sciences. The most comprehensive coverage, as seen mainly from an Earth science perspective, remains Vol. 49 of Reviews in Mineralogy and Geochemistry [7]. More recent reviews are focused on a specific technique, or a specific field (e.g., [8–14]); they include a good coverage of plant and soil sciences. The scope of the present contribution is to offer just an overview of the topic, and cannot replace those references, to which the reader is referred for a more detailed treatment.

25.2 Overview of the Most Common Techniques

A very large variety of synchrotron-based techniques have been applied for environmental studies, the most common being X-ray Absorption Spectroscopy, X-ray microscopies, and X-ray diffraction. Other SR methods of interest include soft X-ray photoemission spectroscopy [15], X-ray standing waves [16], X-ray reflectivity measurements [17], small angle X-ray scattering [18], X-ray microtomography, X-ray microscopy measurements, photoelectron diffraction, and synchrotron infrared spectroscopy. Each of these provide useful, and in many cases, unique information about Earth and environmental materials and their interactions with aqueous fluids, atmospheric gases, organic matter, microbial organisms, plant roots, and environmental contaminant ions (e.g., [4, 19, 20]). The basic theory of most of these techniques is presented elsewhere in this book. Moreover, synchrotron beamlines carry on a continuous update of techniques, and can be thought as factories of new synchrotron applications. Mapping at the nanometer scale is now one of the pioneered frontiers (see [21]).

Synchrotron techniques are generally non destructive, and offer the capability of applying many different complementary characterization methods. As previously mentioned, most environmental studies involve extremely complex and heterogeneous materials, where the phase(s) and element(s) of interest may be quite dispersed and diluted. This fact represents an obvious limitation to the application of bulk techniques that, nevertheless, were instrumental in the early stages in showing the potentialities of synchrotron sources in environmental sciences. These techniques are still of wide use, but clearly, with the advent of microbeam facilities, there has been a dramatic increase of demand for those beamlines. In addition, also surface techniques have been of great interest, inasmuch as many critical MES phenomena occur at surfaces and interfaces. A typical study of environmental samples often involves the combined use of one or more synchrotron-based techniques (see e.g. [22]), and of other analytical methods (see the case history of Sect. 25.3). In this section, we offer an overview of some widely used synchrotron-based methods, with no claim of exhaustive coverage.

25.2.1 Synchrotron-Based X-Ray Diffraction

SR-XRD brought tremendous advances in solving crystal structures. The most impressive progresses are registered in the field of macromolecular crystallography (see Chap. 23), a major fundament of modern molecular biology. Important contributions were also provided to mineralogy and material sciences (see Chaps. 18, 24 and 26). By comparison, bulk SR-XRD application to environmental studies is more limited, because the phases of environmental interest are often non-crystalline, or occur in very tiny amounts with respect to the bulk matrix. Micro- and surface-diffraction are indeed becoming of more common use (see Sects. 25.2.3 and 25.2.4). However, there are several examples of how bulk SR-XRD contributed to understanding environmental processes. The superior high resolution that can be achieved in synchrotron-based diffraction patterns proved to be essential for solving or refining the structures of environmentally important phases such as ferrihydrite [23], pyromorphite-mimetite [24], and schwertmannite [25, 26]. Moreover, the high resolution allows an easier detection of minor phases in a mixture, and therefore makes possible the (semi) quantitative characterization of complex multiphase samples through Rietveld analysis of powder diffraction patterns. Another important application is represented by time-resolved experiments, whereby the progress of a specific reaction is monitored through the appearance/disappearance of diagnostic reflections of one or more phases (e.g., [27]). A quite peculiar technique that is only possible with synchrotron radiation is anomalous diffraction (Chap. 8). With this technique, one can assign a given element to a specific structure in a mixture of phases. For instance, Lattanzi and coworkers [28], using anomalous diffraction at the Cd K-edge, could demonstrate that in the biomineralization at Rio Naracauli, Sardinia, Cd is not bound to a crystalline phase, in agreement with its higher mobility with respect to Zn (see Sect. 25.3 for more details).

25.2.2 X-Ray Absorption Spectroscopy

XAS has been traditionally one of the most widespread and powerful synchrotron-based techniques for applications in environmental sciences (e.g., [29]). The reason for this success is (a) XAS is in practice only possible at synchrotron sources, (b) it is very useful to address a key issue in many environmental studies, i.e. the chemical state (the so called speciation) of contaminants, (c) element-specific information can be obtained independent on the physical state of the sample (crystalline, amorphous, or liquid and even gaseous). All components of the absorption spectrum, XANES, EXAFS, and NEXAFS, have been used, the last one being however of less common use. Here and again, the development of microbeam techniques (μ-XAS) resulted in a major breakthrough (see Sect. 25.2.3). However, bulk XAS was, and still is, a very useful tool.

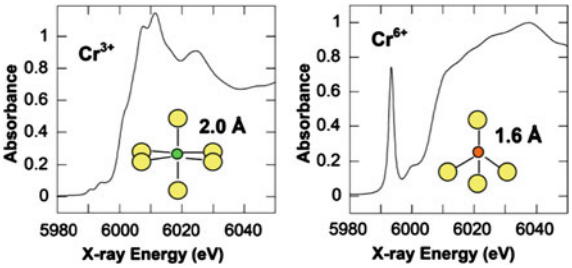


Fig. 25.2 XANES spectra of Cr(III) (*left*) and Cr(VI) (*right*) in coordination with oxygen. From [29], modified

As hinted above, the importance of speciation in many environmental studies cannot be overemphasized, as it strongly controls the mobility, bioavailability, and in several cases also toxicity, of contaminants. In the simplest case, the empirical comparison of the XANES portion of the absorption spectrum of a contaminated matrix with reference spectra of an adequate set of standard compounds may give a major clue to solve a specific environmental problem. Well known examples concern elements such as As and Cr, whose toxicity is strongly dependent on the oxidation state, Cr(VI) and As(III) being more toxic than Cr(III) and As(V), respectively. In the case of Cr, the key difference lies in the pre-edge region, where the tetrahedral Cr-O geometry of the chromate ion gives rise to a distinct peak, corresponding to the 1s $\rightarrow$ 3d transition, that is nearly absent in the octahedral coordination of the trivalent ion (Fig. 25.2).

By an adequate calibration of the pre-edge peak with standard Cr(III)-Cr(VI) mixtures, it is possible to estimate quantitatively the relative proportion of the two forms in a contaminated soil (e.g., [30, 31]).

In the case of As, the difference is less obvious, being mainly expressed by a shift in the edge position, but with proper energy calibration it allows easy recognition of As(III) from As(V). For instance, Gault et al. [32] could demonstrate that As in nails and hair of humans exposed to As-contaminated water in Cambodia is mainly in the trivalent state (Fig. 25.3). By comparison with reference spectra of arsenite, arsenate, and arsenic glutathione, they further suggested that in those biologic samples an important fraction of arsenic is bound to sulphur species.

Another important situation, where the oxidation state is critical for environmental purposes, occurs when the different oxidation states shows a marked difference in mobility. A typical case is represented by U and other elements of the actinide group (e.g., Pu), that in the tetravalent state tend to occur as quite insoluble oxides MeO_2, whereas in the hexavalent states are fairly mobile in the form of MeO_2^{2+} ions. An example of this approach is the study for remediation of Pu in soils and concrete at Rock Flats Environmental Technology Site (RFETS), Colorado [33]. Pu L_{II}-edge EXAFS studies indicated that Pu in soils was predominantly present as the highly insoluble species PuO_2(s), backing up the concept that soluble transport models are not applicable to Pu migration in RFETS soils, and that particulate transport is the dominant transport mechanism for Pu migration at the site. According to [3], "This prediction translates directly into very substantial cost savings…Pu XAFS

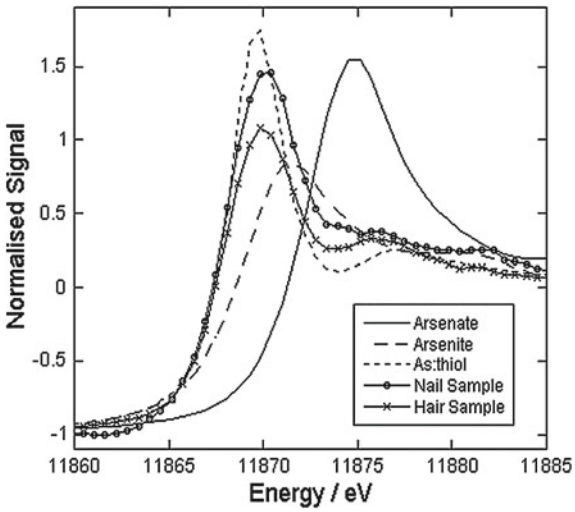


Fig. 25.3 XANES spectra of As in nail and hair from humans living in an As-contaminated area in Cambodia, compared with spectra of standard compounds. Reproduced with permission from [34] (Copyright 2007 American Institute of Physics)—see also [32]

measurements have developed into a decision-making tool [that] saved the company millions of dollars by focusing site-directed efforts in the correct areas".

More specific structural information on the local atomic environment of an element can be obtained from interpretation of the EXAFS spectrum (cf. Chaps. 6 and 17). This information indicates in which way the element is bound to the surrounding environment, and constrains the processes that control its uptake and mobility. A typical application is to understand the mode of occurrence of a trace element in soils or other relevant environmental matrices, e.g. adsorbed onto a mineral phase (and, in this case, whether as an inner sphere or an outer sphere complex), or as a surface precipitate, or else incorporated as substitute ion in a mineral structure (see many examples in [22, 29] and the case history of Sect. 25.3).

25.2.3 Microbeam Techniques

As previously emphasized, many environmental materials have heterogeneous nature, often show a large variability in both chemical composition and crystal domains, and comprise biological tissues and organic molecules. Whenever molecular scale processes depend on local conditions or investigation size, microbeam techniques should be applied. This situation commonly occurs when two distinct phases react via an interface, e.g. when plant roots interact with soil minerals, pollutant diffuses through a geochemical barrier, nanoparticles diffuse through biological tissues, and so on.

In the 1990s, scanning probe microscopy began to prompt tremendous advances in molecular studies [35] concomitantly with spectroscopic and computational methods

[36, 37]. At the same time, synchrotron microbeam techniques started to be available. Currently, several synchrotron sources comprise beam stations allowing for beam micro-focusing and scanning over discrete surface areas.

Due to high directionality of synchrotron radiation, an X-ray microbeam can be obtained from SR by cutting the beam with a precise slit system. Microbeam allows in situ mapping at nanometer to submicrometer scale. The minimum spot size of the beam depends upon the synchrotron source and the specific characteristic of the beamline. Spot size varies in order of magnitude between about $0.065 \times 0.05\,\mu m$ and $200 \times 200\,\mu m$ [13]. By placing the sample onto an X-Y piezo stage, it can be scanned under the focused beam with submicron step size.

An obvious application of microbeam facilities is X-ray microscopy, usually accomplished by soft X-rays. In its simplest form, the obtained image is in practice a microradiography of the studied area. This use of soft X-ray microscopy is now quite widespread in medicine, biology, and environmental sciences. Other imaging techniques are in fact microscale maps of a specific signal arising from interaction of SR with the sample.

Scanning transmission X-ray microscopy (STXM) is an emerging technique that provides imaging of the structure at the local scale. Samples are taken as thin films cut by microtome or deposited onto ultrathin membranes. The STXM techniques itself provides information that can be coupled to any other kind of complementary information, ranging from nano-scale secondary ion mass spectrometry (nanoSIMS, [38]) to a number of techniques, some of which are cited in this chapter. Recently, coupling STXM and μXRF became popular also because it is state of the art in diffusion of nanoparticles and chemical elements through biological cells (e.g. [39–41] see also Fig. 25.4 and related text).

Another effective microbeam technique for environmental studies is micro-XAS, especially when combined with μXRD and/or μXRF. For practical reasons, it is at present mostly limited to the XANES component, but even with this limitation it provides important information. For instance, by combining μXRF and μXAS, Costagliola et al. [42] could demonstrate that in a travertine rock of southern Tuscany, Italy, arsenic is distributed among iron oxyhydroxides and calcite, and occurs mostly in the pentavalent state with a minor trivalent component.

The principles of conventional computed axial tomography have been transferred to synchrotron based computed microtomography [43]. The latter usually achieves higher spatial resolution because of the high collimation and intensity of the X-ray beam. Four basic types of microtomography can be identified: transmission, edge, fluorescence, and diffraction. In all cases, the approach is to measure projections of some parameter through the object, collect these projections viewed from different angles, and then reconstruct the dataset to obtain the internal distribution of the parameter. Microtomography is extensively used also because of the nearly complete lack of need for sample preparation. The main concerns are optimizing the sample size (attenuation/absorption), incident energy and detector for the particular application. Once defined the optimum experimental set-up, this technique allows to investigate also precious samples [44], and has recently been used for in vivo investigation of cell evolution [45].

The availability of high brilliance synchrotron sources together with continuous progress in focusing optics (e.g achromatic) allows us to reach submicron spatial resolution for the conventional, century-old XRD technique. The new capabilities include the possibility to map in situ grain orientations, crystalline phase distribution, and full strain/stress tensors at a very local level, by combining white and monochromatic X-ray microbeam diffraction. The combination of synchrotron-based μXRD techniques with μXRF provides just the tool needed to make the key identification of most reactive constituents in complex, heterogeneous matrixes such as soils, and the uptake mechanism of associated trace elements.

μXRF techniques, also known as X-ray microprobe, are very similar to Energy Dispersive X-ray analysis (EDX) available in common Electron Microscopy (EM) systems. Even if the X-Y scanning systems usually adopted in synchrotron beamlines is generally less precise than the scanning coils used in EM, the brilliance of third generation synchrotron sources is orders of magnitude superior to the highest brilliance obtained by using field emission guns in EM. For this reason, μXRF chemical mapping allows one to detect elements at lower concentrations and better lateral homogeneity than conventional EDX systems. However, synchrotron beamlines operate in a restricted energy window. Particularly, low-energy XRF is a state-of-the-art technique to map biologically important elements; it can be applied to plants, soils, microbes, and particulate matter samples. XRF can be coupled with other synchrotron techniques to study chemical speciation [13, 46].

Most techniques based on synchrotron light allow collection of signals that are much more intense than in conventional techniques. As a difference, synchrotron Fourier transform infrared spectroscopy (FTIR) does not benefit of a strong gain in the intensity of the signal, but benefits of a lower background. Specifically, μFTIR has also the advantage of a better lateral homogeneity of the absorbing volume of the sample, and allows measurements to be made rapidly at a few microns dimension (microscope), and/or at low concentration (and high spectral resolution; [47]).

Figure 25.4 represents an instance of how SR-based microbeam techniques provide unique insights into the complexity of environmental matrices. Figure 25.4a shows a SEM-FEG (Field Emission Gun) image of *Euphorbia pythiusa* root growing in Zn-rich mine residues comprising quartz, illite, sphalerite and carbonates as soil minerals. The *Euphorbia pythiusa* specimen was grown on the polluted substrate during a bioremediation experiment (see [48]). Zooming in Fig. 25.4a shows evidences for the activity of microbes especially inoculated at the root-soil mineral interface. EDX analysis based on the FEG microbeam indicated a surface composition made of Al, Si, Na, C, O and Fe. Au signal is due to gold coating of the studied sample for better morphological study. Figure 25.4b illustrates the thin section of the root deposited onto the grid for STXM (Fig. 25.4c) and μXRF analysis. Figure 25.4d shows an enrichment in Al and Si in an external rim. However, Fig. 25.4e illustrates that the enrichment in Zn (and Na) is much deeper, as these elements can diffuse through the Al-Si external cortex. To definitely solve the MES problem of how Zn can be translocated through the external mineral cortex of the *Euphorbia pythiusa* roots, complementary XAS, or better, μXAS analysis is needed.

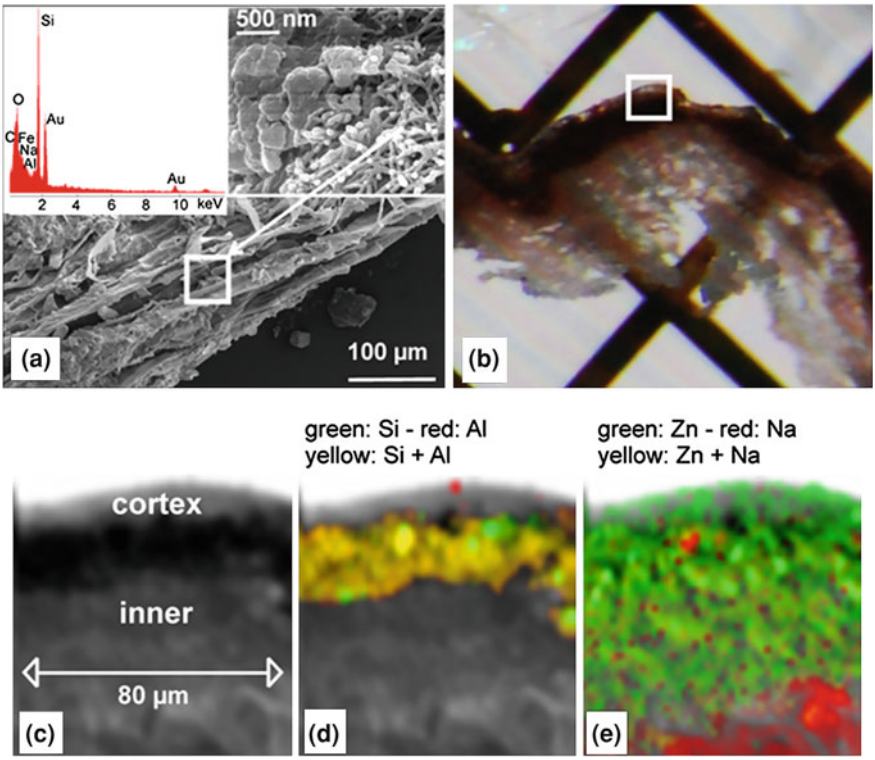


Fig. 25.4 *Euphorbia pithyusa* root growing in Zn-rich mine residues. **a** SEM-FEG image and EDX analysis. It is evident the activity of microbes especially inoculated at the root-soil mineral interface. **b** Thin section of the root deposited onto the grid photographed under light stereo-microscope with the indicated scanned region. **c**, **d** and **e** Scan of the root section (size $80 \times 80\,\mu m^2$, scan 80×80 pixels). *Bright* field (absorption) image (**c**). Si-Al μXRF map (**d**) and Zn-Na μXRF map (**e**). *Images* **c** to **e** were collected at the TwinMic beamline, ELETTRA

25.2.4 Surface Techniques

Surfaces structures are the place where most of the chemical reactions relevant to the environment occur. This concept especially applies to the interaction between minerals and organic/biologic substances. Common examples of natural organic materials are extracellular polymeric matrices generated by bacteria, biofilms, hydrocarbons from industrial effluents and fossil fuel products, and numerous humic substances. Because of their hydrophobicity, many natural organic materials have low solubility in water, and tend to accumulate at solid surfaces. As a result, in groundwater and soils mineral surfaces are commonly coated with organic films. Thus, surface properties are crucial to understand MES reactions. As surface properties significantly differ from bulk properties, MES offers specific surface tools. These allow to investigate a range of materials from minerals to biological tissues, and their interfaces.

GIXD [49] uses small incident angles for the incoming X-ray, so that diffraction can be made surface sensitive. It is used to study surfaces and layers because wave penetration is limited. Additionally, if polarization of the X-ray is parallel to the studied surface, scattering takes place in the surface layer allowing to apply complementary surface techniques. More information on GI techniques can be found in [17].

The use of X-ray scattering is described in details elsewhere in this book (Chap. 11). Its application to probe the structure of mineral-water interfaces was pioneered by Chiarello, Sturchio, and colleagues in the early 1990s with measurements of small angle X-ray reflectivity at the calcite-water interface [50], heteroepitaxial film growth on calcite [51], and high-resolution crystal truncation rod measurements [52]. Studies continuing to the present have applied these techniques to solid solution formation at the calcite-water interface [53]; ion adsorption [54]; molecular-scale structure and speciation measurements of calcite, orthoclase and barite interfaces [55–57]; measurements of real-time dissolution processes [58] and dissolution kinetics [7]; the three-dimensional structure of the calcite-water interface [59]. In the above studies, specifically, scattering from the crystal surfaces is used in the crystal truncation rod (CTR) technique. Measurement of the scattering intensity for a semi-infinite lattice, and calculation of the structure factor for the semi-infinite lattice, i.e. the tools of CTR, can be applied to any two-dimensional interface [7].

One of the current MES challenges that can be addressed by SAXS is to improve our understanding of heterogeneous nucleation processes. Ray et al. [18] used GISAXS/SAXS to investigate the nucleation of iron oxyhydroxides on quartz surfaces coated by different polymeric substances. Fernandez-Martinez et al. [60] used that technique to determine in situ the interfacial energies between heterogeneously nucleated $CaCO_3$ and quartz substrates; this study provides important data on the thermodynamics of CO_2 trapping.

Using highly collimated X-ray sources, it is now possible to place the entire output of a synchrotron insertion device onto the surface of a flat crystal or analogous sample with minimal angular divergence at the critical angle for total external reflection. The intensity of the beam allows for measurement of the X-ray absorption and emission spectrum with sufficient counting statistics so that extremely small surface coverages of impurities, precipitates or sorbed species can be structurally probed. These techniques best apply on substrates having extremely perfect surfaces, and can sometimes allow detection of surface XAS [17].

The principle advantages of Total Reflection XRF (TR-XRF) are its sensitivity, which rivals any other technique, the ease of sample preparation, and the resistance to various types of interferences and matrix effects. TRXRF (mainly laboratory based) has been applied to the measurement of trace contaminants in river and spring waters, coastal sediments, oceanic waters, groundwaters, airborne particulates, aerosols, geological microsamples, tobacco smoke, wine, biofilms, humic substances, and cancerous tissue.

XSW technique has been used in the past decades to investigate a wide range of surface, interface, and thin film structures. For a comprehensive illustration of the technique see [16]. XSW has been applied also in geochemistry and environmentalscience

for surface structure investigations of phenomena such as aqueous ion adsorption and incorporation at mineral surfaces, metal distribution in organic membranes and organic matter at solid surfaces, and the electrical double-layer structure at water-solid interfaces. Moreover, XSW has been applied in MES to solve problems of impurity structures in minerals. A well known example of XSW investigation is the ion adsorption at the calcite-water interface [57, 61–65].

XPS is a powerful tool for surface and interface analysis, providing the elemental composition of surfaces and the local chemical environment of adsorbed species. Surface analysis techniques and surface microspectroscopy such as photoelectron emission microscopy (PEEM) or scanning photoelectron microscopy (SPEM) are available in most modern synchrotron laboratories. These techniques make possible the XPS analysis of areas as small as few tens of nanometers suitable for characterizing single nanostructures or nanodevices [15, 66]. Conventional XPS experiments have been limited to ultrahigh vacuum (UHV) conditions due to the short mean free path of electrons in a gas phase. The recent advances in instrumentation coupled with third-generation synchrotron radiation sources enables in situ XPS measurements at pressures above 5 Torr (see [67], and references therein). These authors provide examples of in situ XPS studies at the MES beamline at the Advanced Light Source, Berkeley, on water adsorption on two different Cu surfaces, and the TiO_2 (110) surface.

25.3 Case History: Zinc Biomineralization at Naracauli, Sardinia

We present here a case history drawn from our own experience, that we believe can illustrate how environmental sciences can take profit from molecular studies, including synchrotron-based techniques.

The Rio Naracauli stream in southwestern Sardinia, Italy, is a seat of a peculiar, and, to our knowledge, unique phenomenon of Zn biomineralization. The stream drains the abandoned Pb-Zn mining district of Montevecchio-Ingurtosu, and is contaminated by several heavy metals released from mine tailings. At two distinct locations along the stream, the biologically induced precipitation of Zn minerals results in a significant abatement of Zn and other heavy metals in waters [68, 69]. The phenomena have obvious potential implications for remediation, and have been the subject of several studies (see references in [68, 69]). Key aspects for practical applications include (a) what is (are) the control mechanism(s) for biomineralization, and (b) how strongly are heavy metals bound to the biominerals. At one location, bioprecipitation results in the formation of hydrozincite (Zn hydroxycarbonate, $Zn_5(CO_3)_2(OH)_6$), in association with a photosynthetic community composed of a cyanobacterium (*Scytonema* sp), and a microalga (*Chlorella* sp). Scanning electron microscopy clearly shows the association of the mineral with biological structures such as sheaths, filaments, and extracellular polymeric substances (Fig. 25.5a). The conventional source X-ray diffraction pattern is compatible with the reference pattern of hydrozincite, although peak broadening suggests a certain degree of structural

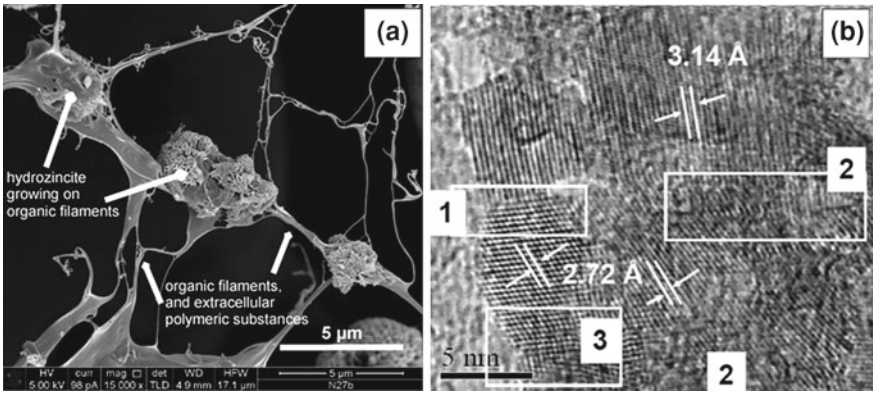


Fig. 25.5 **a** SEM-FEG image (secondary electrons, SE) of the biomineral hydrozincite showing as hydrozincite precipitates on organic filaments; **b** HR-TEM image of Naracauli hydrozincite biomineralization. Different lattice defects in the nanometric crystallites are outlined. *1* is a grain boundary between two crystallites; *2* and *3* are line dislocation and plane defects, respectively. After [70]

disorder. This suggestion is well substantiated by high resolution TEM (Transmission Electron Microscopy) images (Fig. 25.5b), and by high precision powder diffraction patterns collected with synchrotron radiation. With respect to abiotic hydrozincite, the biomineral shows higher content in lattice defects such as grain boundary, line defects, and likely stacking fault defects in the sequence of octahedral ZnO_6 sheets occurring in the structure, corresponding to large differences in the lattice constants. In addition of Zn, the Naracauli hydrozincite contains small, but environmentally significant, amounts of other heavy metals, such as Pb and Cd. EXAFS spectra were essential to demonstrate how these metals are bound to hydrozincite, information that is critical to predict their mobility from the biomineral. For Cd, the results of EXAFS analysis, backed by anomalous X-ray diffraction, suggest a disordered mode of occurrence, presumably as an amorphous surface precipitate. For Pb, a more complex model is suggested: this metal is supposed to occur partly as an amorphous surface carbonate, partly either as a substituting ion in the tetrahedral Zn site of the hydrozincite structure, or as an inner-sphere surface complex.

At the other location, biomineralization (Fig. 25.6) is associated with the bacterium *Leptolyngbya frigida*, and results in an entirely amorphous phase. This difference is presumably due to differences either in the associated microbiological consortia, and/or in local physicochemical parameters [69–71]. Also in this case, the biological character of the mineral is demonstrated by its association with biological structures such as bacterial sheaths, and extracellular polymeric substances. Because of the amorphous nature of this biomineral, information on its structure entirely relies on XAS (both XANES and EXAFS) spectra. It was shown that the local atomic environment of Zn is similar to the silicate mineral hemimorphite. Similar to other biomineralization process, this amorphous phase might be a precursor of

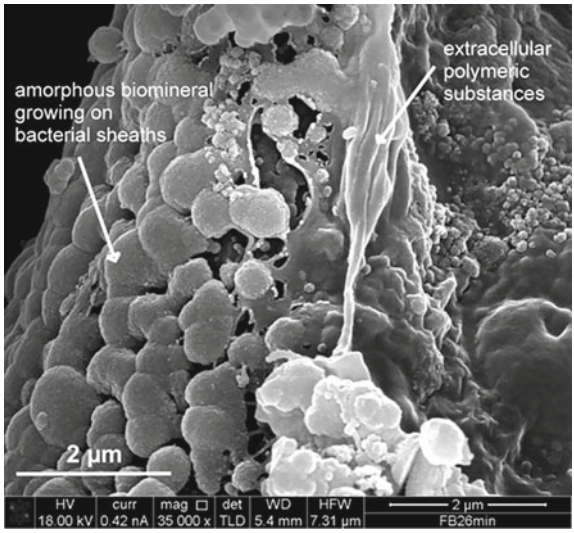


Fig. 25.6 SEM-FEG image (secondary electrons, SE) of the amorphous biomineral. This is made up of nanometric globules that precipitates on bacterial sheaths

a more stable, crystalline phase. In summary, synchrotron-based techniques applied to Zn biominerals at Naracauli provided unique information that may prove very useful for application of these phenomena for remediation of heavy metal contaminated waters.

25.4 Concluding Remarks

Synchrotron radiation techniques are nowadays one of the most powerful tools for molecular environmental science, providing information to solve many of the MES chemical speciation and local scale problems. Thus, synchrotron radiation was instrumental in the evolution of environmental sciences from a largely empirical, descriptive approach to a more quantitative understanding of underlying processes. From a conceptual standpoint, this evolution follows the line of the thermodynamic concepts laid in the 1950s for describing the physicochemical activity of elements in solids and at their surfaces, well exemplified by milestone books such as Prigogine and Defay's "Chemical Thermodynamics" and Garrels and Christ's "Solutions Minerals and Equilibria", that has been for decades the reference approach to calculate mineral stability and ionic speciation in waters. The further evolution step was to incorporate the key role of kinetics for non-equilibrium conditions typical of most environmental systems.

In this chapter, several examples are provided on the successful use of such a mechanistic approach to molecular environmental problems. The consequences of this approach go well beyond the purely academic sphere, and touch upon important societal challenges such as preservation of the environment, public health, and waste

management. The use of MES toolbox is necessary to properly address problems such as the chemical speciation of low concentration pollutants, that is critical for managing environmental and health hazards. MES and related synchrotron techniques are likely to grow further, inasmuch as science, laws and regulations will be demanding for small scale understanding of environmental phenomena.

Acknowledgments The environmental mineralogy and geochemistry group at Università di Cagliari was established by Luca Fanfani. It has been a pleasure to share our studies with Rosa Cidu, Franco Frau, Francesca Podda, and many Ph.D. and post-doc coworkers. Over the years our research was funded by many institutions; we mention here MIUR (PRIN 2010-2011 to P.L.), Regione Sardegna (L.R. 7/2007 grants to G. D.G. and P.L.), and European Union (UMBRELLA project, G. D.G.). Our experience and results with synchrotron sources would have been impossible without the help of all those persons who patiently introduced us beginners to at least the elementary practice and basic concepts. We wish to thank Giuliana Aquilanti, Gilberto Artioli, Fabrizio Bardelli, Francesco D'Acapito, Alessandra Gianoncelli, Antonella Iadecola, Chiara Maurizio, Settimio Mobilio, Angela Trapananti, and above all Carlo Meneghini.

References

1. R.C. Hilborn, Amer. J. Phys. **72**, 425–427 (2004)
2. J.E. Lovelock, L. Margulis, Tellus **26**, 2–10 (1974)
3. G.E. Brown et al., SLAC-Report-704 (2004)
4. G.E. Brown Jr, A.L. Foster, J.D. Ostergren, Proc. Nat. Acad. Sci. USA **96**, 3388–3395 (1999)
5. EnviroSync, http://www.cems.stonybrook.edu/envirosync/
6. S. Shaw, C.M.B. Henderson, NERC, Report (2007)
7. P.A. Fenter, M.L. Rivers, N.C. Sturchio, S.R. Sutton (eds.), Rev. Mineral. Geochem. **49**, 579 (2002)
8. H. Bluhm et al., J. Electr. Spectr. Relat. Phenom. **150**, 86–104 (2006)
9. E. Lombi, J. Susini, J. Plant Soil **320**, 1–35 (2009)
10. T. Punshon, M.L. Guerinot, A. Lanzirotti, Ann. Bot. **103**, 665–672 (2009)
11. B. Singh, M. Gräfe, (eds.), Dev. Soil Sci. **34** (Amsterdam, Elsevier) (2010)
12. J. Thieme, J. Sedlmair, S.C. Gleber, J. Prietzel, J. Coates, K. Eusterhues, G. Abbt-Braun, M. Salome, J. Synchrotron Rad. **17**, 149–157 (2010)
13. S. Majumdar, J.R. Peralta-Videa, H. Castillo-Michel, J. Hong, C.M. Ricoa, J.L. Gardea-Torresdey, Anal. Chim. Acta **755**, 1–16 (2012)
14. G. Sarret, E.A.H. Pilon Smits, H. Castillo Michel, M.P. Isaure, F.J. Zhao, R. Tappero, Adv. Agron. **119**, 1–82 (2013)
15. H. Ade (ed.), Spectromicroscopy, special issue of J. Electr. Spectr. Rel. Phenom. **84** (1–5) (1997)
16. M.J. Bedzyk, L. Cheng, in: P.A. Fenter, et al. (eds.), Applications of synchrotron radiation in low-temperature geochemistry and environmental sciences, pp. 221–266, Rev. Mineral. Geochem. **49**, Geochemical Society, Washington, DC. (2002)
17. G.A. Waychunas, Rev. Mineral. Geochem. **49**, 267–315 (2002)
18. J.R. Ray, B. Lee, J. Baltrusaitis, Y.S. Jun, Environ. Sci. Technol. **46**, 13167–13175 (2012)
19. P.M. Bertsch, J.C. Seaman, Proc. Natl. Acad. Sci. USA **96**, 3350–3357 (1999)
20. P.M. Bertsch, D.B. Hunter, Chem. Rev. **101**, 1809–1842 (2001)
21. F. Bourdelle, K. Benzerara, O. Beyssac, J. Cosmidis, D.R. Neuville, G.E. Brown Jr, E. Paineau, Contrib. Mineral. Petrol. **166**, 423–434 (2013)
22. A. Manceau, M.A. Marcus, N. Tamura, in: P.A. Fenter et al. (eds.), Applications of synchrotron radiation in low-temperature geochemistry and environmental sciences, pp. 341–428, Rev. Mineral. Geochem. **49**, Geochemical Society, Washington, DC. (2002)

23. F.M. Michel, L. Ehm, S.M. Antao, P.L. Lee, P.J. Chupas, G. Liu, D.R. Strongin, M.A.A. Schoonen, B.L. Phillips, J.B. Parise, Science **316**, 1726–1729 (2007)
24. J. Flis, O. Borkiewicz, T. Bajda, M. Manecki, J. Klasa, Synchrotron Rad. **17**, 207–214 (2010)
25. A. Fernandez-Martinez, V. Timon, G. Roman-Ross, G.J. Cuello, J.E. Daniels, C. Ayora, Am. Mineral. **95**, 1312–1322 (2010)
26. R.A. French, M.A. Caraballo, B. Kim, J.D. Rimstidt, M. Murayama, M.F. Hochella Jr, Am. Mineral. **97**, 1469–1482 (2012)
27. P.J. Heaney, J.E. Post, T.B. Fischer, D.R. Hummer, C.L. Lopano, A.J. Wall, Mineral. Mag. **72**, 179–184 (2008)
28. P. Lattanzi, C. Maurizio, C. Meneghini, G. De Giudici, F. Podda, Eur. J. Mineral. **22**, 557–564 (2010)
29. G.E. Brown Jr, N.C. Sturchio, Rev. Mineral. Geochem. **49**, 1–115 (2002)
30. M.L. Peterson, G.E. Brown, G.A. Parks, C.L. Stein, Geochim. Cosmochim. Acta **61**, 3399–3412 (1997)
31. J.M. Zachara, C.C. Ainsworth, G.E. Brown, J.G. Catalano, J.P. McKinley, O. Qafoku, S.C. Smith, J.E. Szecsody, S.J. Traina, J.A. Warner, Geochim. Cosmochim. Acta **68**, 13–30 (2004)
32. A.G. Gault, H.A.L. Rowland, J.M. Charnock, R.A. Wogelius, I. Gomez-Morilla, S. Vong, M. Leng, S. Samreth, M.L. Sampson, D.A. Polya, Sci. Total Environm. **393**, 168–176 (2008)
33. V. LoPresti, S.D. Conradson, D.L. Clark, J. Alloy. Compd. **444–445**, 540–543 (2007)
34. J. Charnock, D.A. Polya, A.G. Gault, A.J. Morgan, AIP Conf. Proc. **882**, 211–213 (2007)
35. C.M. Eggleston, M.F. Hochella Jr, Geochim. Cosmochim. Acta **54**, 1511–1517 (1990)
36. R.T. Cygan, Rev. Mineral. Geochem. **42**, 1–35 (2001)
37. J.D. Kubicki, Rev. Mineral. Geochem. **42**, 459–483 (2001)
38. X. Liu, J. Eusterhues, K. Thieme, V. Ciobota, C. Höschen, C.W. Mueller, K. Küsel, I. Kögel-Knabner, P. Rösch, J. Popp, K.U. Totsche, Environ. Sci. **47**, 3158–3166 (2013)
39. P. Marmorato, G. Ceccone, A. Gianoncelli, L. Pascolo, J. Ponti, F. Rossi, M. Salomé, B. Kaulich, M. Kiskinova, Toxicol. Lett. **207**, 128–136 (2011)
40. B. Bozzini, A. Gianoncelli, B. Kaulich, M. Kiskinova, M. Prasciolu, I. Sgura, ChemSusChem **3**, 846–850 (2011)
41. A. Gianoncelli, P. Marmorato, J. Ponti, L. Pascolo, B. Kaulich, C. Uboldi, F. Rossi, D. Makovec, M. Kiskinova, G. Ceccone, X Ray Spectrom. **42**, 316–320 (2013)
42. P. Costagliola, F. Bardelli, M. Benvenuti, F. Di Benedetto, P. Lattanzi, M. Romanelli, M. Paolieri, V. Rimondi, G. Vaggelli, Environm.Sci. Technol. **47**, 6231–6238 (2013)
43. R.S. Sutton, P.M. Bertsch, M. Newville, M. Rivers, A. Lanzirotti, Eng, P. Rev. Mineral. Geochem. Cygan and Kubichi (Eds.) **42**, **42** 9–483 (2001)
44. X. Ni, D.L. Gebo, M. Dagosto, J. Meng, P. Tafforeau, J.J. Flynn, K.C. Beard, Nature **498**, 60–64 (2013)
45. J. Moosmann, A. Ershov, V. Altapova, T. Baumbach, M.S. Prasad, C. LaBonne, X. Xiao, J. Kashef, R. Hofmann, Nature **497**, 374–377 (2013)
46. J.L. Torresday, J.R.P. Videa, G.D. Rosa, J. Parsons, Coord. Chem. Rev. **249**, 1797–1810 (2005)
47. L. Vaccari, G. Birarda, L. Businaro, S. Pacor, G. Grenci, Anal. Chem. **84**, 4768–4775 (2012)
48. E. Kothe, G. Büchel (guest eds.), Umbrella: Using microbes for the regulation of heavy metals mobility at ecosystem and landscape scale. Environm. Sci. Pollution Res. special issue (2014). doi:10.1007/s11356-014-2689-y
49. Y. Yoneda, T. Horiuchi, Rev. Sci. Inst. **42**, 1069–1070 (1971)
50. R.P. Chiarello, R.A. Wogelius, N.C. Sturchio, Geochim. Cosmochim. Acta **57**, 4103–4110 (1993)
51. R.P. Chiarello, N.C. Sturchio, Geochim. Cosmochim. Acta **58**, 5633–5638 (1994)
52. R.P. Chiarello, N.C. Sturchio, Geochim. Cosmochim. Acta **59**, 4557–4561 (1995)
53. R.P. Chiarello, N.C. Sturchio, J. Grace, P. Geissbühler, L.B. Sorensen, L. Cheng, S. Xu, Geochim. Cosmochim. Acta **61**, 1467–1473 (1997)
54. N.C. Sturchio, R.P. Chiarello, L. Cheng, P.F. Lyman, M.J. Bedzyk, Y. Qian, H. You, D. Yee, P. Geissbühler, L.B. Sorensen, Y. Liang, D.R. Baer, Geochem. Cosmochem. Acta **61**, 251–263 (1997)

55. P. Fenter, P. Geissbühler, E. DiMasi, G. Srajer, L. Sorensen, N.C. Sturchio, Geochim. Cosmochim. Acta **64**, 1221–1228 (2000)
56. P. Fenter, H. Teng, P. Geissbühler, J.M. Hanchar, K.L. Nagy, N.C. Sturchio, Geochim.Cosmochim. Acta **64**, 3663–3673 (2000)
57. P. Fenter, M.T. McBride, G. Srajer, N.C. Sturchio, D. Bosbach, J. Phys. Chem. B. **105**, 8112–8119 (2001)
58. H.H. Teng, P. Fenter, L. Cheng, N.C. Sturchio, Geochim. Cosmochim. Acta **65**, 3459–3474 (2001)
59. P. Geissbühler, P. Fenter, E. DiMasi, G. Srajer, L.B. Sorensen, N.C. Sturchio, Surf. Sci. **573**, 191–203 (2000)
60. A. Fernandez-Martinez, Y. Hu, B. Lee, Y.S. Jun, G.A. Waychunas, Sci. Technol. **47**, 102–109 (2013)
61. L. Cheng, P.F. Lyman, N.C. Sturchio, M.J. Bedzyk, Surf. Sci. **382**, L690–L695 (1997)
62. L. Cheng, N.C. Sturchio, J.C. Woicik, K.M. Kemner, P.F. Lyman, M.J. Bedzyk, Surf. Sci. **415**, L976–L982 (1998)
63. L. Cheng, P. Fenter, N.C. Sturchio, M.J. Bedzyk, Geochim. Cosmochim. Acta **63**, 3153–3157 (1999)
64. L. Cheng, N.C. Sturchio, M.J. Bedzyk, Re. B **61**, 4877–4883 (2000)
65. S. Rihs, N.C. Sturchio, K. Orlandini, L. Cheng, H. Teng, P. Fenter, M.J. Bedzyk, Environ. Sci. Technol. **38**, 5078–5086 (2004)
66. M. Amati, M. Dalmiglio, M. Kazemian Abyaneh, L. Gregoratti, J. Electron. Spectrosc. Relat. Phenom. 189, 30–34 (2013)
67. S. Yamamoto, H. Bluhm, K. Andersson, G. Ketteler, H. Ogasawara, M. Salmeron, A. Nilsson, J. Phys. Condens. Matter **20**, 184025 (2008)
68. D. Medas, R. Cidu, P. Lattanzi, F. Podda, G. De Giudici, Natural biomineralization in the contaminated sediment-water system at the ingurtosu abandoned mine, in *Bio-Geo-Interactions in Metal Contaminated Soils, Soil Biology*, ed. by E. Kothe, A. Varma (Springer, Heidelberg, 2012), pp. 113–130
69. D. Medas, P. Lattanzi, F. Podda, C. Meneghini, A. Trapananti, A. Sprocati, M.A. Casu, E. Musu, G. De Giudici, Environ. Sci. Poll. Res. (2014). doi:10.1007/s11356-013-1886-4
70. G. De Giudici, F. Podda, R. Sanna, E. Musu, R. Tombolini, C. Cannas, A. Musinu, M. Casu, Am. Mineral. **94**, 1698–1706 (2009)
71. F. Podda, D. Medas, G. De Giudici, P. Ryszka, K. Wolowski, K. Turnau, Environm. Sci. Pollut. Res. (2014). doi:10.1007/s11356-013-1886-4

Chapter 26
Synchrotron Radiation in Art, Archaelogy and Cultural Heritage

Simona Quartieri

Abstract Scientific investigations aimed to archaeometric analyses, characterization and conservation of archaeological and artistic finds are in general based on a strong interdisciplinary approach, which implies the collaboration among scientists and archaeologists expert in many different fields. In particular, knowledge transfer among research groups is required by the number of different conventional and advanced techniques which can be applied to ancient materials. One of the main requirements imposed by the archaeologists in the studies of ancient and precious materials is that the selected techniques must be non-destructive (or at most micro-destructive). In this scenario, synchrotron radiation-based methods can play a central role, being specifically suitable for micro-non-destructive analyses. This chapter is intended to show how synchrotron radiation-based experiments, employing highly brilliant and collimated micro-beams of X-rays, can be exploited in diffractometric, spectroscopic and imaging investigations of archaeological and artistic objects, obtaining results with unprecedented space and energy resolution.

26.1 Introduction

The application of synchrotron radiation (SR) in the archaeological and cultural heritage (CH) sciences is relatively recent, dating to the end of the '80s, and has become really widespread only recently, thanks to a close dialog between archaeologists and experts of the physical and chemical techniques based on the use of SR. This strong development is mainly due to the fact that, for many reasons, SR is a very suitable and powerful tool in the investigations of very rare and fragile objects, on which no damage can be done and only non-destructive analyses are allowed.

S. Quartieri (✉)
Dipartimento di Fisica e di Scienze della Terra, Università di Messina, Viale Ferdinando Stagno d'Alcontres, 98166 Messina, S. Agata, Italy
e-mail: simona.quartieri@unime.it

S. Mobilio et al. (eds.), *Synchrotron Radiation*,
DOI: 10.1007/978-3-642-55315-8_26, © Springer-Verlag Berlin Heidelberg 2015

Moreover, a peculiar characteristic of the archaeological finds is that they are often heterogeneous and complex in shape and composition (pottery, glass, metals, paper, pigments, wood, cloths, etc.) and are often covered by alteration layers. The use of SR micro-beams and methods for analysis of micro-volumes are particularly suited to study such materials.

The questions that archaeologists ask more often regarding an ancient object are:

(1) what material is it made of (composition)?
(2) when was it made (dating)?
(3) where was it made (provenance)?
(4) how was it made (art technology)?
(5) how can we avoid its destruction (conservation)?

To answer these questions, a thorough knowledge of the nature of the original material and of the ancient production techniques is mandatory. Using SR, experiments based on very brilliant and collimated micro-beams of X-rays are employed to obtain diffraction, spectroscopic and imaging data with unprecedented space and energy resolution.

Among the SR-based investigations more widely performed in archaeometric studies we may point out the following:

(i) Elemental microanalysis down to the sub-ppm level by means of X-ray fluorescence analysis (μ-XRF).
(ii) Local chemical state determinations of selected (trace) constituents using XAS and μ-XAS (X-ray absorption spectroscopy)
(iii) Information on the presence and nature of crystalline phases via X-ray diffraction (XRD), which usually employs X-ray photons with energies in the 0.5–30 keV range.
(iv) Imaging of entire objects using high energy SR to allow high quality radiographic or tomographic measurements, revealing the internal structure of these artifacts.

In this chapter, some of the most frequently applied techniques will be discussed, with the aim to illustrate the essential role that SR has assumed in the resolution of several important archaeological problems.

26.2 Examples of SR-X-Ray Diffraction Studies of Cultural Heritage

X-ray diffraction, and in particular X-ray powder diffraction (XRPD) is an extremely frequently applied technique in material science, even with conventional sources. XRD is the main experimental technique for probing the long range order of atoms in samples and is the most straightforward method for identifying crystalline phases. When it is supported by the use of SR, it can provide excellent signal/noise ratio and

strong peak resolution and allows performing micro-diffractometric non-invasive investigations. Moreover, diffraction patterns contain information on the dimensions and arrangement of the microscopic grains, which is related to the artifact making technique.

The basic assumption for quantitative XRPD is that the material consists of a homogeneous population of randomly oriented crystallites. In reality, many archaeological polycrystalline products are inhomogeneous: they exhibit non-uniformities, such as large variations in the grain size, large absorption contrasts, presence of many phases, differences in chemical composition, anisotropic orientation of the grains, presence of a substrate and poor crystallinity. The specific features of synchrotron radiation (energy tunability, high photon flux, and high collimation) help to solve part of these problems. These characteristics make SR-XRPD a really powerful method for the study of CH.

Due to the very high number of applications of XRD to archaeometric and conservation problems, it is impossible to offer an exhaustive review and hence only some particularly representative case studies will be discussed here.

One of the most famous examples which illustrate the possible applications of non-destructive synchrotron-XRPD—complementing other standard analytical tools—in the study of CH, is the investigation performed by Doorhyee and co-workers [1–3] of ancient Egyptian cosmetic recipes and of the manufacturing process of make-up. In this project, synchrotron micro-beam techniques—like μ-XRF, μ-XRD and μ-XANES—were combined in order to identify selectively the phases and the trace elements present in different populations of grains representative of the powders and to perform a quantitative determination of the different phases forming the cosmetics.

A large number of cosmetics, used in Ancient Egypt and conserved in the Louvre Museum, was analyzed. The study revealed a great variety of compositions based on lead compounds and an advanced know-how in chemical synthesis. Moreover, it shows that 4000 years ago, people already wanted more from their cosmetics than simply highlighting the eyes. The study includes the analysis of the Bragg line profiles in relation to the microstructure (size and distortions of the grains) of some minerals. In particular, among the compounds found in the studied mixtures, two natural phases were identified: black galena (PbS) and white cerrusite ($PbCO_3$). Galena is a component still used in North Africa as a base for many traditional cosmetics (like khols); white cerrusite, is part of the composition of white-to-grey powder make up. Both galena and cerrusite are rather common minerals which can be found in the Red Sea region. More surprisingly, the analyses revealed the presence of two other white components: laurionite (PbOHCl) and phosgenite ($Pb_2Cl_2CO_3$) (Fig. 26.1). These phases are very rare in nature and could not have been extracted from the mines in sufficient quantities for the preparation of the cosmetics. In fact, one must consider that, in the ancient Egypt, cosmetics were extensively used by both women and men over a period of at least eight centuries. These compounds could, in principle, have been formed by alteration of the basic components by chlorine but no foreign cations or chlorinated phases were detected in the more than 50 analyzed samples. Therefore the alteration of natural lead minerals within the make-up is unlikely. Hence, the conclusion was that laurionite and phosgenite were

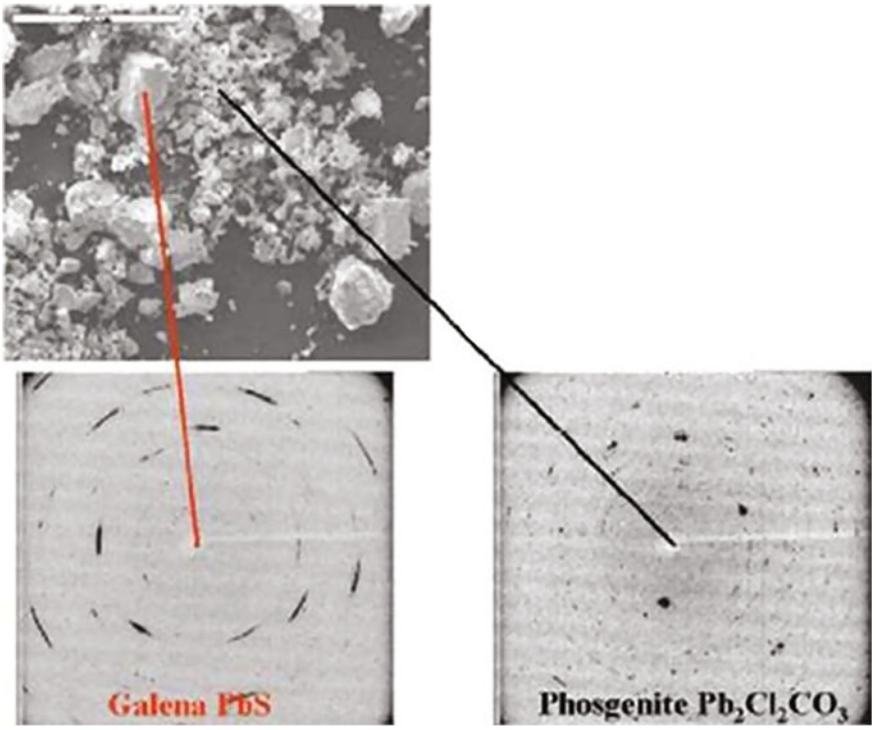


Fig. 26.1 *Top left* SEM picture of the archaeological sample probed by the X-ray micro-beam (ESRF, ID22). *Bottom left* 2D transmission X-ray micro-diffraction pattern showing the presence of galena powder in the sample. *Bottom right* 2D transmission X-ray micro-diffraction pattern showing the presence of phosgenite powder in the sample (modified after [3])

synthesized artificially. The synthetic origin of PbOHCl e $Pb_2Cl_2CO_3$ was confirmed by the analysis of the diffraction peak profiles, comparing the effects due to strains and to the crystallite dimensions with those present in the natural phases. It resulted that galena present in the cosmetics was crushed, probably to confer to the make-up the desired texture and brightness. On the contrary, the peak profiles of laurionite and phosgenite were lacking of strain effects, suggesting that the crystallites were produced by direct synthesis.

Now the question is: why produce white components to be added to galena when cerrusite was available? The answer can be found in the historical hieroglyphics. In the ancient Egypt, cosmetics were not only used for aesthetic purposes but also for their purported therapeutic and magic properties. The Greco-Roman texts mention that the white precipitates synthesized from PbO are good for eye and skin care. These lead compounds could be used as bactericides and as a protection for the eye against exposure to the sun.

A second very interesting example of the application of synchrotron XRPD to CH is the study of the Maya Blue pigment [4–8]. The composition of Maya Blue



Fig. 26.2 Examples of mural paintings and of pottery objects decorated with Maya *blue*. The image on the *right* represents Tlàloc, the Maya god of rain

has confounded researchers for decades. How could the bright turquoise hue and extreme stability of this hybrid organic/inorganic pigment be explained? How did Mayas combine skills in organic chemistry and mineralogy to create an important technology—the first permanent organic pigment—by binding indigo dye to a clay mineral substrate? Maya blue was first produced by the Mayas about the 8th century AD and extended well into the Spanish colonial era, before its production technology was lost. Due to its attractive turquoise color and light fastness, Maya blue was widely used in mural paintings, ceramics and codices (Fig. 26.2). Maya blue is extremely stable: it can resist the attack of concentrated nitric acid, alkali and organic solvents without losing its color.

It has been demonstrated that Maya blue is a complex formed between a fibrous microporous clay mineral (namely palygorskite or seldom sepiolite, whose crystal structures are permeated by nano-tunnels parallel to the length of the fibres and filled by weakly-bound H_2O molecules) and the indigo dye (which the ancient Mayas extracted from the leaves of the Indigofera Suffruticosa tree).

Although the pieces of the puzzle—indigo and palygorskite/sepiolite clay—had been identified, researchers have struggled since to explain how they fit together to create a material with such remarkable properties. A simple mixture of palygorskite and indigo, in fact, lacks resistance to chemical attacks and needs to be heated above 100 °C in order to produce stable Maya Blue. This is due to the fact that in Maya Blue the indigo molecule can diffuse within the palygorskite (or sepiolite) tunnels once zeolitic H_2O is lost during heating (Fig. 26.3). Incorporation inside the tunnels shelters the dye molecule from the external environment; consequent formation of specific interactions between the guest indigo and the hosting clay framework stabilizes the resulting hybrid composite, conferring to Maya Blue its exceptional stability.

Encapsulation of indigo inside the hosting clay mineral was first observed while refining the crystal structure of the pigment on synchrotron collected diffraction patterns by means of the Rietveld method [4, 7]. These studies, supported also by molecular mechanics and spectroscopic investigations, proved that fixation of the guest indigo in palygorskite is more stable with respect to sepiolite. Indigo is, in fact, perfectly juxtaposed inside the narrower tunnels of palygorskite (6.4 × 3.7 Å),

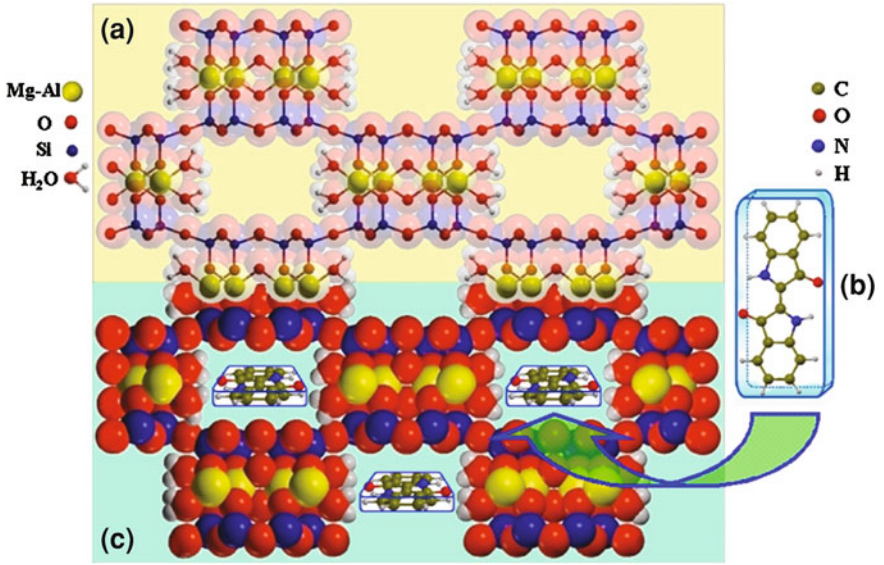


Fig. 26.3 **a** The structure of palygorskite projected on the (001) plane; **b** the indigo molecule; **c** encapsulation of indigo inside the nano-tunnels of palygorskite forms the Maya *Blue* pigment (zeolitic H_2O not shown for sake of clarity)

forming interactions on both sides of the molecule. Conversely, in the wider sepiolite channels (10.6 × 3.7 Å) indigo can bind only on one side of the molecule, causing the related hybrid composite to show a decreased resistance to chemical attacks. Besides being incorporated in the channels, indigo can also be adsorbed in the superficial grooves which cover the surface of these clay minerals fibers [8]. Similarly to what happens within the tunnels, the weakly-bound H_2O usually filling these grooves at room temperature is removed while heating the clay/dye mixture (>100 °C), thus leaving room for indigo. The amount of dye filling both the tunnels and the grooves is in agreement with the thermogravimetric measurements and occupancy factors estimated by synchrotron data.

26.3 Archaeometric Applications of X-Ray Absorption Spectroscopy

X-ray Absorption Spectroscopy (XAS) offers a combination of features particularly well-suited for the study of rare, ancient materials and works of art. XAS techniques are noninvasive, have low detection limits, afford high lateral resolution, and provide exceptional chemical sensitivity. They can be applied in air and virtually do not require any restriction on the type and size of the sample, which can be metal, ceramic, glass, cloth etc. and, finally, it is applicable to most of the elements of interest, even

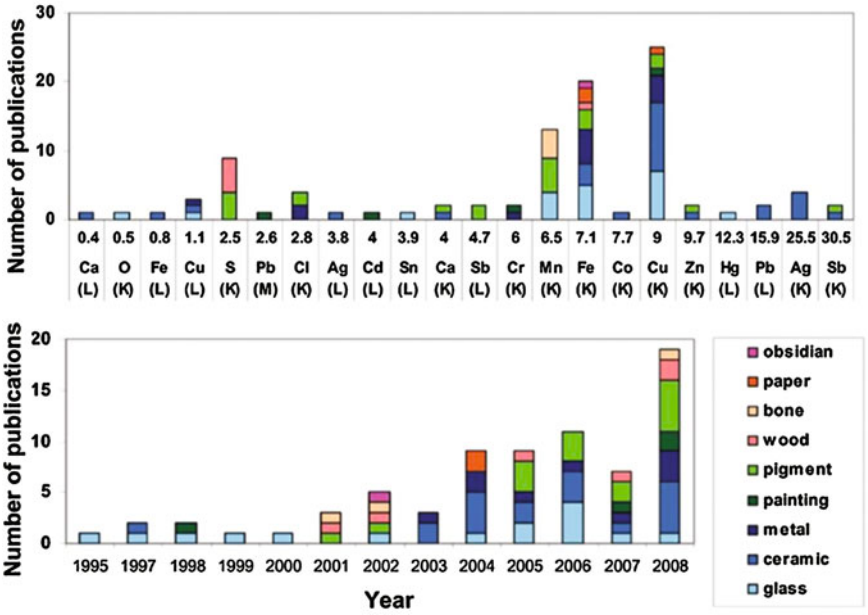


Fig. 26.4 Evolution of the publications reporting XAS analyses on CH items over the past decade. Statistics are sorted by type of material versus elements and absorption edges and versus time (modified after [9])

in very low concentration. These characteristics are highly desirable for the chemical characterization of precious, heterogeneous, and complex materials. In particular, the chemical mapping capability, with high spatial resolution that provides information about local composition and chemical states, even for trace elements, is a unique asset [9, 10].

As shown in Fig. 26.4 the applications of XAS cover a wide range of materials, ranging from hard matter such as glass, ceramics and metals to softer materials such as paintings, bone, wood and paper. The main objective for the first group of materials is to understand their original fabrication process. This mostly concerns the craftsman's control over synthetic reactions at high temperature resulting in various optical effects in glasses, glazes, lusters, ceramics, and pigments. Studies on the second group of materials focus on unintentional degradation reactions. In general, these occur over longer time scales and are either due to past conservation treatments or due to passive external circumstances or may even be inherent to the chemical composition of the artwork itself.

XAS techniques were first applied to the study of **ancient glass** [11, 12] More recently, glazes and ceramics, based on similar vitreous matrices, have also benefited from an increasing interest. Indeed, XAS techniques are particularly adapted for the study of these types of materials. The good match between method capabilities (short-range probe, sensitive) and material properties (amorphous and diluted state), allows XANES and EXAFS providing unique chemical information.

Modification of color are usually obtained in glass by modulating the oxidation states of transition elements such as Mn, Fe, Co, and Cu; these elements have characteristic absorption frequencies in the visible region as a result of d–d electronic transitions. This explains the high number of XAS studies at the K-edge of these elements (Fig. 26.4). For instance, XANES analyses at the Fe and Mn K-edges of ancient glasses from Sicilian archaeological sites in the Messina Province (Patti Roman villa [13] and Ganzirri site [14]) and of Medieval glass from Val Gargassa glasswork [15], supported the hypothesis that pyrolusite (MnO_2) could have been added intentionally as a decolorant during the melting procedure.

Many of the above-mentioned optical effects (such as color and transparency) can also be affected by long-term corrosion. For instance, the oxidation of Mn^{2+} into Mn^{4+} has been observed in medieval glass windows exposed to progressive weathering in Cathedral du Bosc, Normandy, France, (14th century) [16]. This oxidation results in the precipitation of manganese oxi-hydroxides, which in turn leads to opacification and a change in color (brown) of the glass panes.

XAS can also be exploited, together with SR-based X-ray fluorescence and XRPD, to study the **opacifiers** used to confer different colors to opaque glass, as was done in Roman glass mosaic tesserae [17, 18, and references therein] or on Etruscan glass vessels and beads [19]. The first work was devoted to the characterization of a suite of very rare, highly decorated and colored glass vessels and beads from the VII to the IV century BC. The most serious difficulty in developing this study was that any sampling—even micro-sampling—was absolutely forbidden. As a consequence, the mineralogical and chemical nature of chromophores and opacifiers present in these Iron Age finds were identified by means of the following SR-based, strictly non-destructive, techniques: μ-XRF, Fe K-μ-XANES and XRPD. The μ-XRF mapping (Fig. 26.5) evidenced high levels of Pb and Sb in the yellow decorations and the presence of only Sb in the white and light-blue ones. Purple and black glass exhibit high amounts of Mn and Fe, respectively. The XRPD analyses confirmed the presence of lead and calcium antimonates in yellow, turquoise and white decorations. Fe K-edge μ-XANES spectra (Fig. 26.6) were collected in different colored parts of the finds, thus enabling the mapping of the oxidation state of these elements across the samples. In most of the samples, iron is present in the reduced form Fe^{2+} in the bulk glass of the vessels, and in the oxidized form Fe^{3+} in the decorations, indicating that these glass artifacts were produced in at least two distinct processing steps under different furnace conditions.

XAS has also been applied to the study of **luster** [20, 21], a decoration typical of the Medieval and Renaissance pottery of the Mediterranean basin, consisting of a metal-glass nanocomposite thin layer embedded in a glass matrix (Fig. 26.7). TEM measurements showed that luster consists of a thin film composed by a heterogeneous distribution of silver and copper nanoparticles of sizes ranging from 5–100 nm. These decorations show peculiar optical properties, producing brilliant reflections of different colors, cangiant effects and iridescences. The origin of luster decoration technique is one of most complex and fascinating issues of the history of ceramics. Its preparation, described by Cipriano Piccolpasso in 1557, is one of the most complex to realize, and, surprisingly, the formation of the nano-particles is strongly

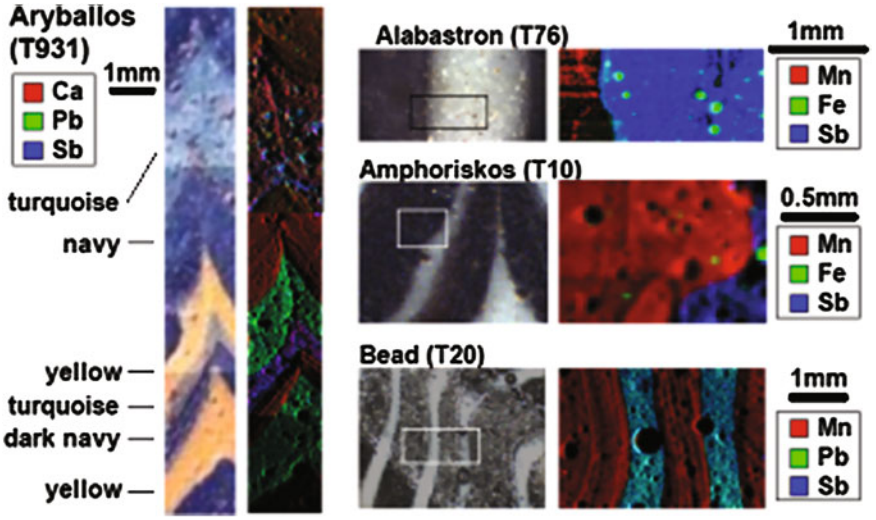


Fig. 26.5 Visible images and elemental mapping obtained by μ-XRF and represented with RGB visualization. Samples from [19]: Aryballos T931; Alabastron T76; Amphoriskos T10; bead T20. A logarithmic scale was used for the Alabastron sample. Legend scales are given for fluorescence maps (modified after [19])

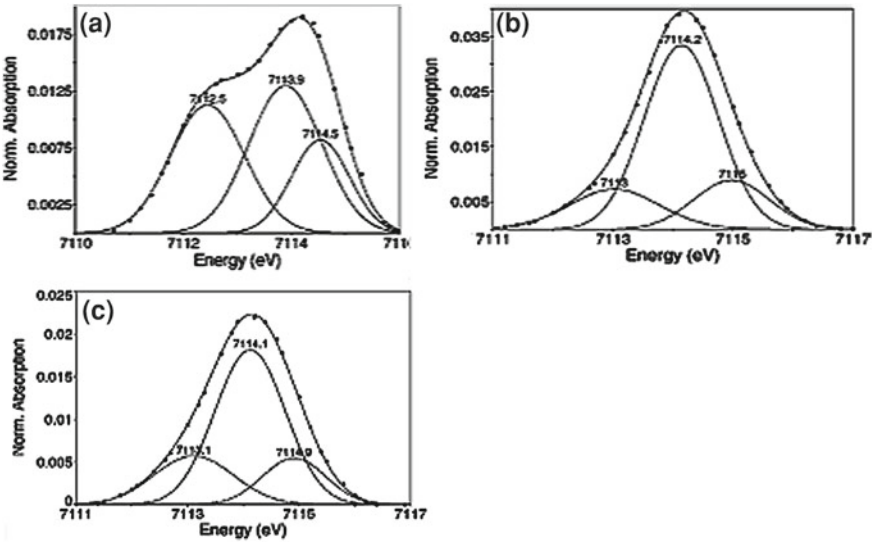


Fig. 26.6 Normalized Fe K pre-edge spectra (*dots*) and the best fit calculated for: **a** bulk dark-navy glass, **b** *yellow* decoration, **c** turquoise decoration of Aryballos T931 (modified after [19])



Fig. 26.7 Luster decorations on Italian Renaissance ceramics from Deruta (1530)

analogous to that found in Roman red mosaic tesserae [17] and in the modern synthetic metal-glass nanocomposites.

Following the pioneering transmission electron microscopy studies, a number of projects dedicated to luster characterization by EXAFS and XANES were performed aiming mainly at establishing a correlation between color (red, gold, or green), chemical composition, and copper or silver oxidation states.

The main results of the spectroscopic investigations of luster are the following:

1. In gold luster, elemental silver and copper are present at concentrations of about 20 and 1–3 wt. %, respectively, distributed within a thin layer 60–120 nm in depth. Metal nanoparticles are virtually made up of silver only, being copper mostly or exclusively found as Cu^{+} and Cu^{2+} ions.
2. In the case of red luster, elemental copper is present at about 8 wt. % distributed within a thicker layer (60–180 nm), with no silver. Nanoparticles of copper are present. However, only a minor fraction of copper is in the reduced metallic form (∼20 %), most of it being found in the form of Cu^{+} ions surrounded by the nonbonding oxygen of the glaze matrix.
3. The gold and red colors can be attributed mainly to the silver and copper nanoparticles, respectively. The fact that in both gold and red luster, copper is significantly present in oxidized forms explains the failure of previous attempts, carried out by XRF or inductively coupled plasma atomic emission spectroscopy, to relate the elemental copper/silver ratio to the luster color. The chromatic effects are determined only by the fraction of metal ions reduced to nanoparticles.



Fig. 26.8 Paleolithic paintings from caves in Spain

4. In red luster, characterized by a large quantity of Cu^{+}, the higher polarizability and the smaller ionic radii of the exchanged Cu^{+} ions compared to that of the substituted alkali ions are responsible for a local structural rearrangement of the glaze matrix. The local modification changes the index of refraction of the glassy host, therefore influencing the optical properties of the luster.

XAS techniques can also be exploited to track possible heat-induced color transformations in various **pigments**. This has proven to be particularly relevant for manganese-based pigments. For instance, Mn K-edge XANES and EXAFS were used to understand the thermal effect on the structural environment of Mn in fossilized mastodon ivory or bone [22] or for the characterization of black pigments found in Spanish and French prehistoric caves [16, 23, 24] (Fig. 26.8).

Several atypical manganese oxide minerals such as manganite, groutite, todorokite, and birnessite were identified in this last study. TEM and XANES analyses revealed that, instead of synthesizing these compounds through heat-induced reactions, natural pigments were favored. Thus, these raw pigments, rare in nature, are likely to originate from non-local geological sites and may have had to be imported from a distant location.

XAS techniques are also increasingly used to study chemical reactions involved during **pigment alteration** processes. As an example, sulfur-based pigments, such as HgS (cinnabar when natural, vermilion when synthetic), as well as CdS, may suffer from discolorations. While red HgS tends toward shades of gray or black, bright yellow CdS may evolve into a white transparent matter. XANES at the sulfur K-edge revealed that both HgS, in Pompeian paintings [25] and CdS, in paintings by the 19th Century artist James Ensor [26] are subject to oxidation.

Another interesting application of XAS to the study of alteration phenomena concerns the blackening of copper resinate in a XV century Italian painting [27]. The study was aimed at providing structural information of the oxidation states and the local chemical of copper in the unaltered and blackened pigments, in order to elucidate the discoloration mechanism. EXAFS revealed that the local chemical environment of Cu in copper resinate can be described using neutral copper acetate as a model. It consists, essentially, of bimetal Cu^{2+} carboxylate complexes with a

distorted octahedral coordination. Such a structure is retained, with some differences, in the blackened pigment. The alteration takes place without change of the valence state of Cu(II) ions and the formation of the copper oxides CuO and Cu_2O responsible for the embrownment is excluded. Discoloration of copper resinate may be related to the local modification of the copper coordination structure, evidenced by the increase of the Cu-Cu and Cu-C distances in the EXAFS spectra.

26.4 SR-Based FT-Infrared Micro-Spectroscopy Applied to Cultural Heritage

Synchrotron-based Fourier transform infrared micro-spectroscopy (SR-FTIR) is one of the emerging techniques increasingly employed for CH analytical science [28]. This technique combines the assets of FTIR spectroscopy (namely, the identification of molecular groups in various environments: organic/inorganic, crystallized/amorphous, solid/liquid/gas), with the extra potential of chemical imaging (localization of components) and the properties of the synchrotron source (namely, high brightness, offering high data quality even with reduced dwell time and reduced spot size).

This method can be applied to nearly all kinds of materials found in museum objects, from hard materials, like metals, to soft ones, like paper, and passing through hybrid ones such as paintings and bones. The purpose is usually the identification of complex compositions in tiny, heterogeneous samples, and hence, a good example is the application of SR-FTIR to the analysis of ancient cosmetics [29], which are heterogeneous at micron scale and may be composed of a mixture of organic and inorganic phases. Their study requires non-destructive techniques, with high detectivity, high lateral resolution, and high chemical sensitivity (atomic, molecular and structural probes). The studied samples originated from a 33 centuries old Egyptian cosmetic remain. New insights into the composition and spatial location of both organic and mineral components were obtained. Five different particles were analyzed and similar findings were obtained: the core is fat rich, and surrounded with a mineral phase. In two particles, lead palmitate was clearly identified as a major component. Phosgenite ($Pb_2CO_3Cl_2$), a lead salt synthesized in aqueous solution, was also located in region near the surface of the particles.

26.5 SR-Based Techniques for Non-Destructive Sub-surface Analysis of Painted Cultural Heritage Artifacts

High energy SR X-rays are particularly suited for analysis of **paintings** [30]. Studies can be performed directly on the entire painting such as, for example, by K-edge subtraction imaging (radiography with X-rays of energy below and above the absorption edge), which offers a direct visualization of the elemental distributions at the paint-

ing scale. But, analyses are generally carried out on micro-samples taken from the art work.

The success of synchrotron techniques for such studies is linked to the intrinsic characteristics of the paintings that make classical analyses very hard. First, the amount of matter is usually tiny (less than 1mm thickness), hence requiring sensitive techniques. Second, paintings always exhibit multi-layered structures, with layer thicknesses $\sim$10 μm; this leads to the preference for the use of micro-imaging techniques, with a good lateral resolution (about one micrometer). Third, painting fragments are very complex in their chemistry, as they are made of mineral and organic matters, amorphous and crystallized phases, major and minor elements. Accordingly, a multi-modal approach is usually essential to solve the chemical complexity of such hybrid materials. In particular, the combination of micro X-ray fluorescence, micro X-ray absorption near edge spectroscopy, micro X-ray diffraction and micro-FTIR (infrared) spectroscopy is a key tool for the complete elucidation of painting compositions in order to derive information on its history (painter techniques, pigment synthesis, authentication…) and on its preservation for the future (mechanisms of degradation, processes of restoration and related issues).

As an example, the combination of μ-X-ray fluorescence and μ-X-ray spectroscopy was successfully employed for the visualization of a lost painting by Vincent van Gogh [31]. Vincent van Gogh (1853–1890), one of the founding fathers of modern painting, is best known for his vivid colors, his vibrant painting style, and his short but highly productive career. His productivity is even higher than generally realized, as many of his known paintings cover a previous composition. This is thought to be the case in one-third of his early period paintings. van Gogh would often reuse the canvas of an abandoned painting and paint a new or modified composition on top. These hidden paintings offer a unique and intimate insight into the genesis of his works. Yet, current museum-based imaging tools are unable to properly visualize many of these hidden images. Synchrotron radiation based X-ray fluorescence mapping was applied to visualize a woman's head hidden under the work Patch of Grass by van Gogh. The scientists recorded decimeter-scale, X-ray fluorescence intensity maps, reflecting the distribution of specific elements in the paint layers. In doing so they succeeded in visualizing the hidden face with unprecedented detail. In particular, the distribution of Hg and Sb in the red and light tones, respectively, enabled an approximate color reconstruction of the flesh tones. This reconstruction proved to be the missing link for the comparison of the hidden face with van Gogh's known paintings (Fig. 26.9).

26.6 X-Ray Computed Tomography in Cultural Heritage Studies

Born in the early Seventies for medical applications, X-ray Computed Tomography is currently playing an increasingly important role in the field of Cultural Heritage diagnostics. In fact it represents a powerful non-destructive investigation technique,

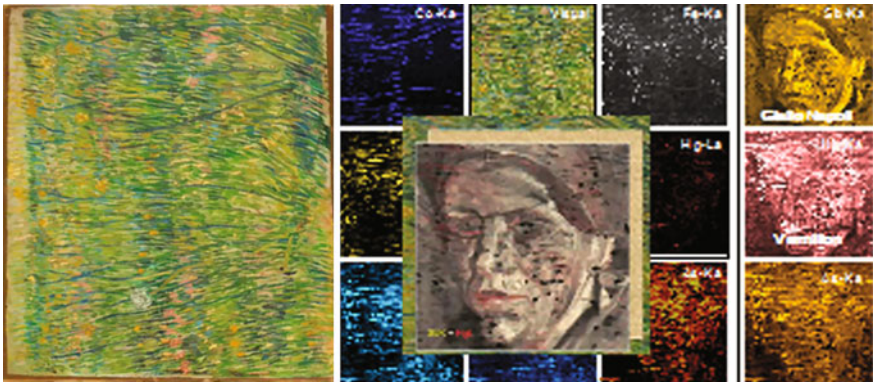


Fig. 26.9 *Left* Vincent van Gogh: Patch of Grass (Paris, 1887). *Right* Synchrotron radiation X-ray fluorescence maps, and reconstruction of the hidden image by combination of the Sb and Hg maps (modified after [31])

capable of displaying in a three-dimensional way the volume and the internal structure of the investigated objects, also thanks to modern 3D rendering techniques. This kind of information is very important for determining adequate conservation and restoration procedures [32, 33]. The last generation synchrotron sources have increased the interest in this technique [34–36].

An example of application is the study of an early 16th century prayer nut, one of the most fascinating objects in the Rijksmuseum (Amsterdam, The Netherlands) [37]. This spherical wooden object measures 4 cm in diameter and consists of two hemispheres connected with a small hinge so that it can be opened (Fig. 26.10). The interior of the nut holds wood carvings with scenes from the life of Christ. These miniature reliefs show an incredible degree of finish with carving details well beyond the millimeter scale. Synchrotron-based computer X-ray tomography revealed the structure and fabrication method of the bead. The central part of the relief was cut from a single piece of wood, rather than assembled from multiple components, underlining the extraordinary manual dexterity of its maker. In addition, a piece of fibrous material contained in the inner structure of the bead is revealed. This may have served as a carrier for an odorous compound, which would be in line with the religious function of the prayer nut.

SR computed tomography can also be exploited for studying old precious stringed instruments, as shown by recent experiments performed at Elettra [34]. For the restoration and conservation of these instruments, the most crucial stage regards how to analyse the composition of the object fully, cleanly and without the slightest hint of damage. These requirements were fulfilled applying SR-microtomography to a 1753 violin by Giovanni Battista Guadagnini, with the aim to obtain detailed information on the instrument interior. Much of the restoration works were clearly visible. In addition, some small holes produced by insects were revealed. In general, it has been demonstrated that these studies on stringed instruments can allow to measure arching distorsions and to check the internal situation of the instruments (neck sets, cracks, damage by insects).

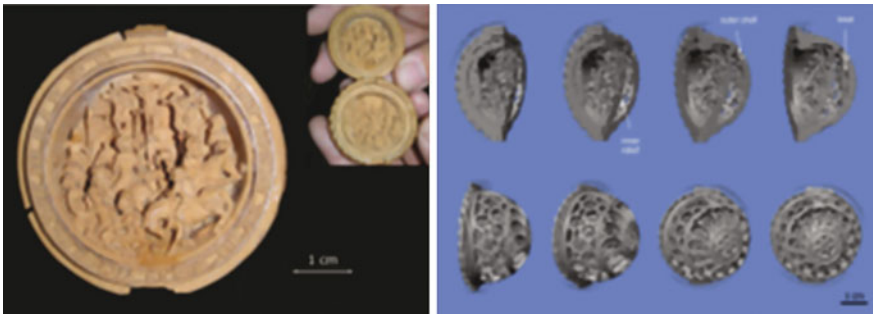


Fig. 26.10 *Left* Boxwood prayer nut with Christ carrying the cross and the crucifixion, c. 1515, Rijksmuseum, Amsterdam, The Netherlands. *Right Upper row* volume reconstructions with a vertical cut through the middle of the nut, revealing the shell structure as well as the knot sandwiched between the outer and inner shells. Note the openings in the outer shell. *Lower row* volume reconstruction of the outer shell with Gothic motif

26.7 Application of SR-Based Techniques to the Study of Paleontological Findings

The study of fossil remains and ancient human artifacts provides a wealth of information on ancient cultures or cultural events and, more generally, can explain how systems or organisms adapted and evolved over time. Moreover, such work may help in predicting how current systems will evolve in the future, and to understand how extinct organisms and the worlds they once inhabited may have functioned. Fundamental scientific questions may be unequivocally answered by chemical or imaging analysis of physical remnants. Piecing together various strands of chemical evidence with other sources of information, such as structural data or knowledge of a specimen's precise age, history, and provenance, can then yield critical insights about a specific event, environment, person, or species.

One of the major problems that is encountered during the analysis of rare and ancient paleontological specimens derives from the fact that many analytical tools destroy at least part of the object under study. In this concern, SR can be a very powerful tool for non-destructive investigations, to be performed by X-ray diffraction, X-ray spectroscopy or imaging experiments, or, sometimes, with combinations with these techniques.

A recent study [38, 39] shows that synchrotron X-ray techniques can provide powerful new data for understanding the biochemistry of extinct organisms. In particular, several methods have been applied to the study of fossils and extant organisms, including *Confuciusornis sanctus*, in order to map and characterize possible chemical residues of melanin pigments. Actually, color is an elusive but critically important feature of extinct organisms, and until recently, it was nearly impossible to make robust conclusions about animal color with traditional methods. Feather color in birds stems mostly from chemical pigments, of which the most common are melanins. Resolving color patterns in extinct species may hold the key to under-

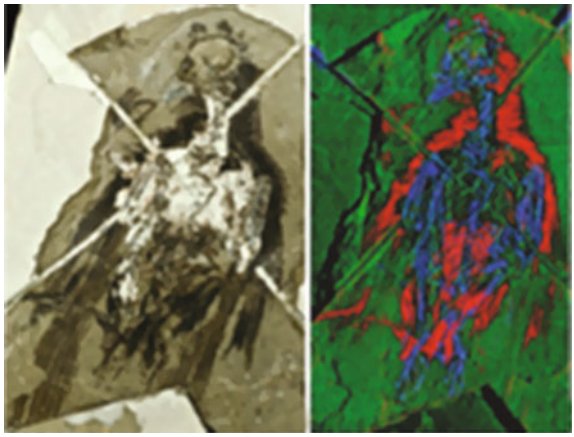


Fig. 26.11 **a** An optical image of *Confuciusornis sanctus* (MGSF315). **b** Synchrotron rapid scanning X-ray fluorescence *false-color* images of the MGSF315 main slab. *Red*, Cu; *blue*, Ca. *green*, Zn

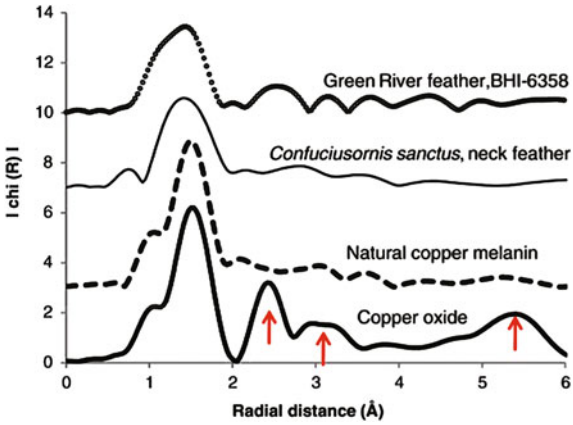


Fig. 26.12 Radial distribution functions (RDFs) from EXAFS analysis at the Cu K edge of two standards compared with fossil feathers. The *arrows* in the copper oxide standard spectrum indicate features that are not present in the eumelanin standard

standing the selection processes in crucial evolutionary periods, and may help discern non-flight functions such as camouflage, communication, and sexual selection.

Figure 26.11a shows a visible light image of one of the *C. sanctus* specimens analyzed. Figure 26.11b presents the distribution of the key trace metals Cu, Ca, and Zn within this specimen as a false-color intensity map. The detail revealed in the distribution of Cu is striking and strongly implies that the Cu zoning is endogenous. Moreover, full EXAFS analysis of the Cu in the *C. sanctus* feather regions indicates that the element is organically bound, closely resembling the coordination environment found for Cu in natural melanin pigment (Fig. 26.12).

The advent of a new technology in a certain field can often dramatically alter the state of knowledge, and such is the case with the application of synchroton X-ray microtomography to fossil imaging [40–43]. This technique is becoming more and more widely used in paleontology. The first works of this kind—related to Weng'an microfossils—were only very recently reported [42, 44]. Microtomography permits

non-destructive computational examination of the specimen from any vantage point, visualization of internal characters in virtual sections in any plane, as well as 3D virtual extractions of internal structures. A third generation synchrotron can produce nearly parallel, high flux, partially coherent monochromatized X-ray beams. Thanks to the partial coherence, it is possible to use propagation phase contrast based imaging techniques (PPC-SR-μCT), that can reveal many structures that are invisible, or hardly visible using classical absorption contrast based microtomography [43, 45, 46].

26.8 Recent and Future Trends

The application of SR-based methods to cultural heritage has very much matured since the first case studies, especially due to the evolution of instrumentation, radiation sources and experimental approaches.

The recent trends which are sensitive to evolution of the SR-based techniques can be summarized in the following:

1. there is a general and strong tendency towards the use of microbeams, in particular devoted to μ-IR, μ-XRD, μ-XAS, μ-XRF, to produce 2D mapping. In these fields SR has and will maintain a leading position due to its intrinsic characteristics.
2. Three-dimensional imaging will undergo strong developments.
3. Another general trend concerns the use of multi-technique approaches, again based on microbeams. Indeed, the possibility of simultaneously obtaining high quality data by several techniques on μg-quantities of material is considerably extending the information that we can obtain on micro-samples. The flexibility of the instrumental configurations at synchrotron sources is also a bonus parameter that makes large-scale facilities invaluable for almost any experiment that one may think of in this field.

Acknowledgments The section on Maya Blue has been greatly improved by Roberto Giustetto (University of Turin).

References

1. Ph. Walter, P. Martinetto, G. Tsoucaris, R. Brniaux, M.A. Lefebvre, G. Richard, Talabot J., Dooryhee E. Nature **397**, 483–484 (1999)
2. P. Martinetto, Ph. Walter, E. Dooryhee, M. Anne, in *Radiation in Art and Archeometry*, ed. by D.C. Creagh (Elsevier Science, Amsterdam, 2000), pp. 297–316
3. E. Dooryhee, P. Martinetto, Ph. Walter, M. Anne, Radiat. Phys. Chem. **71**, 863–868 (2004)
4. G. Chiari, R. Giustetto, G. Ricchiardi, Eur. J. Mineral. **15**, 21–33 (2003)
5. M. Sanchez del Rio, A. Gutierrez-Leon, G.R. Castro, J. Rubio-Zuazo, C. Solis, R. Sanchez-Hernandez, J. Robles-Camacho, J. Rojas-Gaytan, Appl. Phys. A **90**, 55–60 (2008)

6. M. Sánchez del Rio, P. Martinetto, C. Reyes-Valerio, E. Dooryhée, M. Suárez, Archaeometry **48**, 115–130 (2006)
7. R. Giustetto, D. Levy, O. Wahyudi, G. Ricchiardi, J.G. Vitillo, Eur. J. Mineral. **23**, 449–466 (2011)
8. G. Chiari, R. Giustetto, J. Druzik, E. Doehne, G. Ricchiardi, App. Phys. A **90**, 3–7 (2008)
9. M.S.J. Cotte, J. Dirk, K. Janssens, Acc. Chem. Res. **43**, 705–714 (2010)
10. J. Roque-Rosell, J. Proenza, N. Estaugh, M. Vendrell-Saz, F. Mosselmans, in *Synchrotron Radiation in Mineralogy. Seminarios SEM*, ed. by M. Suárez, E.Y. Ayuso, E.M. Manchado, vol. 6, (2009), pp. 61–88
11. I. Nakai, M. Matsunaga, M. Adachi, K.I. Hidaka, J. Phys. IV **7**, 1033–1034 (1997)
12. P.F. Schofield, G. Cressey, W. Wren, Howard, C.M.B. Henderson, Wren Howard W., C.M.B. Henderson, Glass Technol. **36**, 89–94 (1995)
13. S. Quartieri, M. Triscari, G. Sabatino, F. Boscherini, A. Sani, Eur. J. Mineral. **14**, 749–756 (2002)
14. R. Arletti, C. Giacobbe, S. Quartieri, G. Sabatino, G. Tigano, M. Triscari, G. Vezzalini, Archaeometry **52**, 99–114 (2010)
15. S. Quartieri, M.P. Riccardi, B. Messiga, F. Boscherini, J. Non-Cryst. Solids. **351**, 3013–3022 (2005)
16. F. Farges, E. Chalmin, C. Vignaud, I. Pallot-Frossard, J. Susini, J. Bargar, G.E. Brown Jr, M. Menu, Phys. Scr. **T115**, 885–887 (2005)
17. R. Arletti, C. Dalconi, S. Quartieri, M. Triscari, G. Vezzalini, App. Phys. A Mater. Sci. Processing. **83**, 239–245 (2006)
18. S. Quartieri, R. Arletti, in *Modern Methods for Analysing Archaeological and Historical Glass*, ed. by K. Janssens (Wiley, USA, 2013), pp. 299–307
19. R. Arletti, G. Vezzalini, S. Quartieri, D. Ferrari, M. Merlini, M. Cotte, Appl. Phys. A **92**, 127–135 (2008)
20. S. Padovani, C. Sada, P. Mazzoldi, B. Brunetti, I. Borgia, A. Sgamellotti, A. Giulivi, F. D'Acapito, G. Battaglin, J. Appl. Phys. **93**, 10058–10063 (2003)
21. A.D. Smith, T. Pradell, J. Roque', J. Molera, M. Vendrell-Saz, A.J. Dent, E. Pantos, J. Non-Cryst, Solids **352**, 5353–5361 (2006)
22. I. Reiche, G. Morin, C. Brouder, V.A. Sole', P.E. Petit, C. Vignaud, T. Calligaro, M. Menu, Eur. J. Mineral. **14**, 1069–1073 (2002)
23. E. Chalmin, C. Vignaud, H. Salomon, F. Farges, J. Susini, M. Menu, Appl. Phys. A **83**, 213–21 (2006)
24. E. Chalmin, C. Vignaud, F. Farges, M. Menu, Phase Transitions **81**, 179–203 (2008)
25. M. Cotte, J. Susini, N. Metrich, A. Moscato, C. Gratziu, A. Bertagnini, M. Pagano, Anal. Chem. **78**, 7484–7492 (2006)
26. G. Van der Snickt, J. Dik, M. Cotte, K. Janssens, J. Jaroszewicz, W. De Nolf, J. Groenewegen, L. Van der Loeff, Anal. Chem. **81**, 2600–2610 (2009)
27. L. Cartechini, C. Miliani, B.G. Brunetti, A. Sgamellotti, C. Altavilla, E. Ciliberto, F. D'Acapito, Appl. Phys. A **92**, 243–250 (2008)
28. M. Cotte, P. Dumas, Y. Taniguchi, E. Checroun, Ph. Walter, J. Susini, C. R. Phys. **10**, 590–600 (2009)
29. M. Cotte, P. Dumas, G. Richard, R. Breniaux, Ph. Walter, Anal. Chim. Acta **553**, 105–110 (2005)
30. K. Janssens, J. Dik, M. Cotte, J. Susini, Acc. Chem. Res. **43**, 814–825 (2010)
31. J. Dik, K. Janssens, G. Van Der Snickt, L. van der Loeff, K. Rickers, M. Cotte, Anal. Chem. **80**, 6436–6442 (2008)
32. F. Casali, in *Physical Techniques in the Study of Art, Archaeology and Cultural Heritage*, ed. by D. Bradley, D. Creagh (Elsevier, 2006), pp. 41–123
33. M.P. Morigi, F. Casali, M. Bettuzzi, R. Brancaccio, V. D'Errico, Appl. Phys. A Mater. Sci. Process. **100**, 653–661 (2010)
34. L. Rigon, E. Vallazza, F. Arfelli, R. Longo, D. Dreossi, A. Bergamaschi, B. Schmitt, R. Chen, M.A. Cova, R. Perabò, M. Fioravanti, L. Mancini, R.H. Menk, N. Sodini, G. Tromba, F. Zanini, Preserv. Sci. **7**, 71–77 (2010)

35. L. Mancini, G. Tromba, F. Zanini, J. Neutron Res. **14**, 75–79 (2006)
36. H. Roemich, F. Zanini, K. Wittstadt, C. Mueller-Weinitschke, N. Sodini, Nondestr. Test. J. **13**, 30–39 (2008)
37. P. Reischig, J. Blaas, C. Botha, A. Bravin, L. Porra, C. Nemoz, A. Wallert, J. Dik, J. Synchrotron Rad. **16**, 310–313 (2009)
38. U. Bergmann, P.H.L. Manning, R.A. Wogelius, Annu. Rev. Anal. Chem. **5**, 361–389 (2012)
39. R.A. Wogelius, P.L. Manning, H.E. Barden, N.P. Edwards, S.M. Webb, W.I. Sellers, K.G. Taylor, P.L. Larson, P. Dodson, H. You, L. Da-qing, U. Bergmann, Science **333**, 1622–1626 (2011)
40. Y. Chaimanee, D. Jolly, M. Benammi, P. Tafforeau, D. Duzer, I. Moussa, J.-J. Jaeger, Nature **422**, 61–65 (2003)
41. M. Feist, J. Liu, P. Tafforeau, Amer. J. Botany **92**, 1152–1160 (2005)
42. P.C.J. Donoghue, S. Bengtson, X.-P. Dong, N. Gostling, T. Huldtgren, J.A. Cuningham, C. Yin, Z. Yue, F. Peng, J. Stampanoni, Nature **442**, 680–683 (2006)
43. P. Tafforeau, R. Boistel, E. Boller, A. Bravin, M. Brunet, Y. Chaimanee, P. Cloetens, M. Feist, J. Hoszowska, J.-J. Jaeger, R.F. Kay, R.F. X Lazzari, L. Marivaux, A. Nel, C. Nemoz, X. Thibault, P. Vignaud, S. Zabler, Appl. Phys. A Mater. Sci. Process. **83**, 195–202 (2006)
44. J.-Y. Chen, D.J. Bottjer, E.H. Davidson, S.Q. Dornbos, X. Gao, Y.-H. Yang, C.-W. Li, G. Li, X.-Q. Wang, D.-C. Xian, H.-H. Wu, Y.-K. Hwu, P. Tafforeau, Science **312**, 1644–1646 (2006)
45. E.M. Friis, P.R. Crane, K.R. Pedersen, S. Bengtson, P.C.J. Donoghue, G.W. Grimm, M. Stampanoni, Nature **450**, 549–553 (2007)
46. M. Lak, D. Néraudeau, A. Nel, P. Cloetens, V. Perrichot, P. Tafforeau, Microsc. Microanal. **14**, 251–259 (2008)

Chapter 27
Synchrotron Radiation and Chemistry: Studies of Materials for Renewable Energy Sources

Antonino Martorana, Francesco Giannici and Alessandro Longo

Abstract We present an overview of selected applications of synchrotron radiation methods to topical chemical research. The analysis is limited to the studies on materials for renewable energy sources, focussing on topics peculiar to chemical research, such as reactivity and synthesis routes; in particular, the paper takes into account subjects having some relevance for the production and storage of energy based on hydrogen. Hydrogen production and storage are taken into account in the sections concerning: (i) Dye-sensitized solar cells, (ii) Metal-organic frameworks and (iii) Hydrides for hydrogen storage; production of energy by fuel cell devices is treated in (iv) Oxide ion and proton conductors and in (v) Electrodes for fuel cells. These arguments allowed to give a coherent outline of the involvement of synchrotron radiation techniques in traditional branches of chemistry such as inorganic and organic chemistry, catalysis and electrochemistry.

27.1 Introduction

This paper deals with applications of synchrotron radiation (SR) in chemistry. The focussed topics concern the atomic and electronic structure in relation to desired properties and reactivity, with particular attention to the modifications occurring in operative conditions, but excluding issues peculiar of chemistry such as catalysis and reactions evolving in the time scales of pico to femtoseconds, that are treated in specific papers of this textbook. When necessary, peculiar experimental arrangements and, as far as possible, an essential bibliography is given to outline SR applications encompassing the classical fields of physical and inorganic chemistry, while

A. Martorana (✉) · F. Giannici
Dipartimento di Fisica e Chimica, Università di Palermo,
viale delle Scienze, 90128 Palermo, Italy
e-mail: antonino.martorana@unipa.it

A. Longo
ISMN-CNR, via Ugo La Malfa, 153, 90135 Palermo, Italy

S. Mobilio et al. (eds.), *Synchrotron Radiation*,
DOI: 10.1007/978-3-642-55315-8_27, © Springer-Verlag Berlin Heidelberg 2015

also bordering organic chemistry. However, the matter is so vast that an exhaustive overview is almost impossible and, moreover, the overlapping with physics, biology, materials science, geochemistry, environmental and cultural heritage studies is so extensive that a sharp delimitation of the field can be a very hard task.

An effort to arrange the arguments in a unitary thread lead us to privilege the description of SR studies on materials for renewable energy sources, focussing on topics that can be clearly ascribed to the field of chemical research, either because reactivity plays a relevant role in the functional properties, or due to peculiar design and synthesis routes; in particular, the paper takes into account subjects having some relevance for the production and storage of energy based on hydrogen.

Metal-organic frameworks (MOFs, treated in the Sect. 27.2) are materials typically falling in the field of chemical research, due to their inorganic-organic composition and to the almost endless possibilities of design and synthesis of tailored compounds, mostly depending on chemists' creativity. The applications as materials for energetics rely mainly on the largest known surface area among crystalline solids, and consequently, in view of the hopefully soon advent of the hydrogen-based society, on the potentalities as hydrogen-storage materials. The easy modification of the organic bridges by insertion of proton-bearing organic species between the metal cornerstones opens also interesting perspectives for the exploitation of MOFs as proton conducting hybrid materials, even if at present MOFs are far from the performances of the best solid state proton conductors. As hydrogen-storage materials, MOFs are to date overcome by metal hydrides (see Sect. 27.3), even if MOFs, hosting the unreacted hydrogen molecule, ensure more straighforward hydrogen supply. Both classes of materials involve challenging use of synchrotron techniques, in particular exploiting the beam brigthness for in-situ structural studies during hydrogen absorption and desorption and detailed structural analysis necessary for tailoring design and synthesis routes of new materials. With this respect, taking into account that light atoms are often involved, the use of SR made viable, in some cases, a detailed analysis of host-guest interaction.

Among the devices for environment-friendly energy production, this paper focusses on Sect. 27.4 and fuel cells (treated in the Sects. 27.5 and 27.6). For both types of devices the research on the involved materials concern typical chemical themes, such as the performances of catalysts and electrocatalysts, the tailoring of reactivity and electronic structure by suitable modification of materials by doping or insertion of specific functionalities, the correlation between atomic and electronic structure and specific properties, such as solid state ionic conduction. Beside, obviously, fuel cells, also solar cells can be involved in the hydrogen technology development, and in particular in the production of hydrogen by water electrolysis. SR techniques are exploited in the research about solar and fuel cells in different ways: while, for fuel cells, in-situ and in-operando experiments are very useful for the study of the structure and oxidation state of electrode materials, for both electrodes and electrolytes one of the key problem is the dopant-host matrix interaction, which strongly affects conductivity and reactivity; on the other hand, for dye sensitized solar cell, the alignement of electronic levels of the component materials can be effectively investigated by SR electron spectroscopy techniques.

27.2 Metal-Organic Frameworks

Metal-organic frameworks (MOFs) are crystalline materials constituted of metal ions or clusters linked by organic bridges. The intrinsic order of these materials allows to establish well-defined structure-properties correlations and to design and synthesize new materials with desired functionalities. The key factors giving MOFs exciting perspectives of development in many fields are the largest known surface area originated by the ordered pore structure and the possibility of fine-tuning the size and chemical properties of the bridging organic links [1]. Actually, MOFs attracted the interest of researchers due to their versatility in different fields, such as sorption of pollutants, hydrogen storage, catalysis and electrocatalysis, magnetism and proton conduction [2]. Examples of MOFs for hydrogen storage are given in Fig. 27.1.

Synchrotron studies on MOFs are mainly focussed on the detailed structural analysis, where X-ray diffraction is effectively complemented by X-ray absorption. A critical review by Bordiga et al. [3] features an extensive discussion about the complementarity of the two techniques in MOFs investigations, outlining in particular the influence of adsorbates on the local structure of metal clusters. This topic is especially relevant for the research on MOFs, as the high microporosity makes these compounds particularly suited for various sorption applications such as gas separation, environmental remediation and drug delivery. The paper by Millange et al. [4] reports a typical SR structural study on MOFs, addressing the issue of the interaction of MOFs with different guest molecules. The authors focus on the metal(III) carboxylate family MIL-*n*, that shows a peculiar "breathing" effect leading to large and reversible structural displacements of the MOF network as a consequence of the insertion of adsorbates. The effect is investigated by in-situ EDXRD (energy-dispersive XRD): the use of the intense synchrotron white beam allowed very fast data acquisition during the introduction of different molecules (pyridine, lutidine, m-xylene) into the hydrated iron(III) 1,4-benzene dicarboxylate $Fe^{III}(OH,F)\{O_2C\text{-}C_6H_4\text{-}CO_2\} \cdot H_2O$(MIL-53(Fe),$H_2O$). The guest molecules enter into lozenge-shaped channels formed by carboxylate-linked iron octahedra and produce the typical breathing effect monitored in real time by the EDXRD experiment.

In general, the research on MOFs in the field of renewable energy sources addresses the issues of hydrogen storage [5–7] and proton conducting solid electrolytes [8–11].

Effective on-board hydrogen storage in automotive transport is crucial for the development of a hydrogen economy. The chemical storage of hydrogen with dissociation of the H_2molecule and incorporation in metal hydrides have drawbacks concerning the facile release of hydrogen and the sensitivity to impurities of the host material. The strategy of storage leaving intact the molecular identity of hydrogen seems, in this concern, a promising alternative. Among the recipes to reach optimal gravimetric and volumetric hydrogen uptake in MOFs, the review by Rowsell and Yaghi [5] cites the relevance of a pore size similar to that of the adsorbate hydrogen molecule and reports, as tools for tuning the pore size and improving the H_2 attraction, the insertion of adsorbates in the MOF pores and the intergrowth of two or

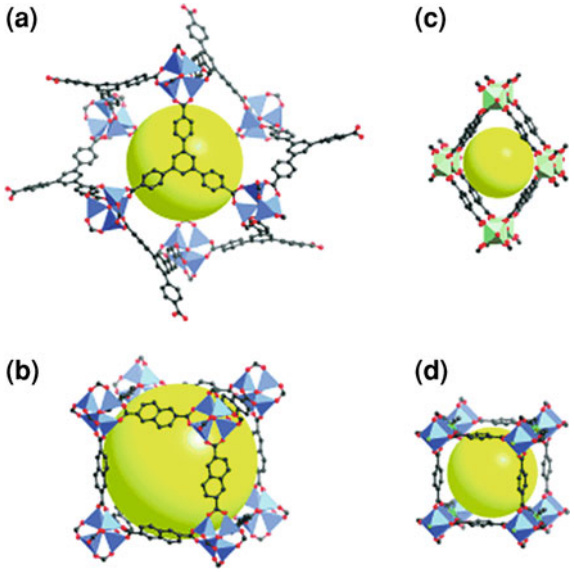


Fig. 27.1 Examples of metal-organic frameworks (MOFs) studied for hydrogen adsorption: **a** MOF-177, $Zn_4O(btb)_2$ (btb = benzene-1,3,5-tribenzoate); **b** IRMOF-8, $Zn_4O(ndc)_3$ (ndc = naphthalene-2,6-dicarboxylate); **c** MIL-53, M(OH)(bdc) ($M = Al^{3+}$ or Cr^{3+}), and **d** $Zn_2(bdc)_2(dabco)$ (dabco = 1,4-diazabicyclo[2.2.2]octane). Reprinted from [5]. Copyright 2005 Wiley-VCH Verlag GmbH & Co. KGaA, Weinheim

more MOF lattices. Other strategies point to suitable functionalization of the organic linkers or of the metal clusters. Then, an important part of the research on hydrogen storage in MOFs concerns the structural characterization, usually carried out by XRD. This analysis takes great advantage from the high resolution and optimal signal-to-noise ratio that can be obtained by SR. To this respect, it is remarkable that a Maximum Entropy Method (MEM) analysis, carried out on SR XRD data and, of course, favoured by the predominance of light elements, allowed to determine the location of adsorbed H_2 and the related occupancy within the pores of the CLP-1 MOF $[Cu_2(pzdc)_2(pyz)]_n$ (pzdc = pyrazine-2,3-dicarboxylate, pyz = pyrazine) [6]. The charge density maps obtained by the MEM algorithm evidenced that the hydrogen adsorption site is close to the O1 oxygen of the carboxylate group and the H1 hydrogen of the pyrazine (as referred to the $P2_1/c$ space group). The paper by Chavan et al. reports EXAFS experiments on UiO-66 and UiO-67. These MOFs consist of $Zr_6O_4(OH)_4$ cornerstones linked by 1,4-benzene-dicarboxylate and by the longer 4,4′-biphenyl-dicarboxylate, respectively. The latter ligand causes lower density and higher microporosity, while the structure of the cornerstones, as demonstrated by EXAFS, undergo only minor modifications in the two compounds. The EXAFS analysis was complemented by XRD, IR, FTIR, UV-vis and TGA data, so obtaining a full understanding of the structural, vibrational, electronic and thermal properties of these MOFs. The results of H_2 absorption revealed that the better

performance of UiO-67 in molecular hydrogen uptake (2.4 vs. 4.6 wt %) is related to porosity, that is one of the largest for this class of materials [7].

State of the art proton conducting materials are today sulfonated polymers like Nafion, with a conductivity around 0.1 S/cm at 80 °C. The low working temperature, necessary to keep the membrane hydrated, is at the origin of drawbacks concerning low tolerance to pollutants, unfeasible use of hydrocarbon fuels and complicated water management, that stimulate the research on anhydrous or low-hydrated proton conducting materials. Possible strategies to obtain proton conducting MOFs are the inclusion of suitable functionalities in the organic linkers and the insertion of proton-bearing molecules or inorganic clusters in the pores [9, 10]. In both approaches the crystalline structure of MOFs allows to establish a well-defined correlation between structural features and proton conduction, so that MOFs can be very interesting also as model systems for computational analysis and design of new materials. Actually, synchrotron experiments on proton conducting MOFs are usually addressed to atomic structure investigation: in the paper by Sadakiyo et al. powder X-ray diffraction measurements were carried out on $\{NR_3(CH_2COOH)\}[MCr(ox)_3] \cdot nH_2O$, (R = methyl, ethyl or n-butyl, M = Mn or Fe). These MOFs have a cationic component composed of carboxylic acid groups that act as proton carriers. The hydrophilicity of the cationic ions depends on the NR_3 residue, in the order $[NMe_3(CH_2COOH)]^+ > [NEt_3(CH_2COOH)]^+ > [NBu_3(CH_2COOH)]^+$. The MOFs structure, as determined by laboratory single crystal data and powder SR XRD, is constituted by 2D atomic layers able to host water molecules in the interlayer gaps and the amount of adsorbed H_2O molecules is determined by the hydrophilicity of the $[NR_3(CH_2COOH)]^+$ cations. It was proposed that, while the carboxylic acids provide the proton-bearing groups, the water molecules act as ion-conducting medium through the formation of a network of hydrogen bonds with the carboxylic groups. The most hydrophilic Me-FeCr compound show the higher proton conductivity (10^{-4} S/cm) [11].

In conclusion, MOFs are very flexible materials for a wide spectrum of different applications. In the field of materials for energy, the development of MOFs for hydrogen storage has so far obtained interesting results. Proton-conducting MOFs are far from reaching performances suitable for technological exploitation. However, they can have also an important role, due to their crystalline order, as model compounds for a deeper knowledge of the proton transfer mechanism and, consequently, for the design of innovative materials. The SR studies are mainly devoted to a detailed structural analysis, both local and long-range, allowing to establish precise structure-properties correlations enhanced by the crystalline order of these materials.

27.3 Hydrides for Hydrogen Storage

The lack of safe and efficient ways to store hydrogen has hindered so far the development of a hydrogen economy more than any other cause. This is especially true for vehicles and mobile applications. Metal hydrides, such as MgH_2 or $LiAlH_4$, can store efficiently the hydrogen atoms, stabilizing them by means of covalent bonding.

Due to the low atomic number of the other elements, the resulting hydrogen density in the solid state is very high (up to 18 % in weight) [12].

Metal hydrides release H_2 with temperature: the release and uptake is fully reversible in most cases, and it happens through the conversion of the hydride to the corresponding metal (in the case of simple hydrides), or to other compounds (in the case of complex borohydrides or alanates, e.g. $Mg(BH_4)_2$ to MgB_2). The high temperature needed to release H_2, and the slow desorption kinetics, remain the major challenges to overcome in order to develop a mature technology. The research efforts in the areas of solid-state and materials chemistry have been devoted to understand the structural mechanisms governing hydrogen storage, and the chemical interactions between the hydrides and the additives that may improve their performance.

Light metals hydrides are a showcase for the extreme capabilities of SR-XRD in terms of accuracy and sensitivity. The X-ray scattering factors of light elements are very low, and an extremely bright X-ray source is needed for structure resolution. On the other hand, if all elements are lightweight, hydrogen atoms become non-negligible scatterers, and XRD is suitable to resolve their position. For these reasons, powder XRD with SR has been used extensively for the study of hydride structures: in most cases, XRD is more suited than neutron diffraction because of the fast data acquisition, so that hydrogen absorption and release reactions can be followed in situ at different temperatures and at different hydrogen pressures.

Studies with SR allowed the resolution of many unknown structures ab initio, locating up to 55 independent atoms using powder XRD. Another important application involves the structure resolution by "decomposition indexing". In this method, the Bragg peaks are assigned to one or more phases thanks to their appearance and disappearance during a temperature ramp, so that the chemical knowledge of the species involved in the reaction ultimately allows the resolution of unknown structures. Such methods have been used for many alkali metal borohydrides and their derivatives, and they were reviewed recently by Ravnsbaek et al. [13], and by Cerny et al. [14].

The basic $LiBH_4$ crystal structure was solved rather recently: in their study, Soulié et al. first demonstrated the possibility of locating an hydrogen atom with powder XRD [15]. $LiBH_4$ has the highest H_2 mass density achieved to date, but favorable storage features are shown only by the high temperature polymorph, that has defied DFT computational predictions regarding its structure and stability. Single-crystal and powder XRD from 80 to 500 K showed that at low temperatures $LiBH_4$ is orthorhombic, while the high temperature polymorph is hexagonal. Both structures are formed by regular $[BH_4]^-$ tetrahedra; The *Pnma-P6*$_3$*mc* first order phase transition at 381 K is characterized by highly anisotropic and anharmonic atomic displacement, causing also an anisotropic thermal expansion [16]. Comparison of the two polymorphs' structure is provided in Fig. 27.2.

An interesting case of polymorphism is represented by $Mg(BH_4)_2$. Powder XRD identified a new nanoporous phase, only obtained by solvent evaporation. Its structure features pores of about 4 nm, with a high accessible surface area: when exposed to H_2, it forms $Mg(BH_4)_2 \cdot 0.8\ H_2$. The ability to store molecular hydrogen, the nanoporosity, and the volume collapse and amorphization under pressure, are all

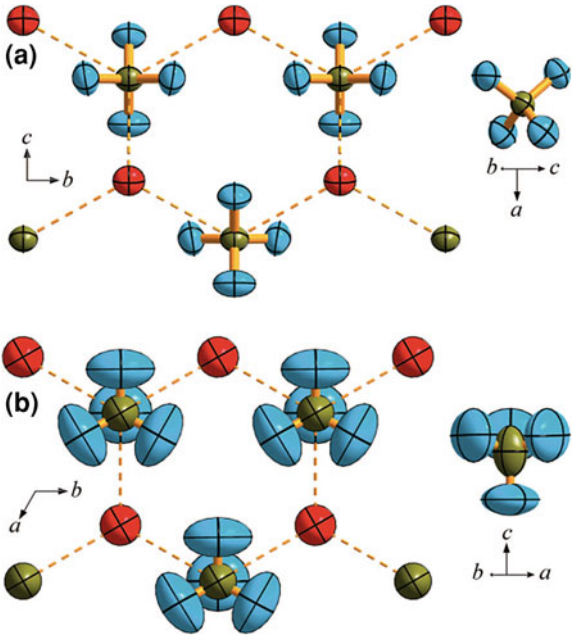


Fig. 27.2 **a** The low temperature .5 $LiBH_4$ *Pnma* polymorph. **b** The high temperature $P6_3mc$ structure. The thermal ellipsoids are shown, showing the anisotropic thermal displacement of the BH_4^- units. Reprinted from [16]. Copyright 2008 American Chemical Society

structural and chemical features very similar to MOFs. Chemically, they have been explained with the onset of a partially covalent linear Mg. . .BH_4. . .Mg bond [17]. Borohydrides of transition metals, and complex hydrides containing complex anions (such as $[Sc(BH_4)_4]^-$, or $[Zn(BH_4)_3]^-$), were discovered more recently, showing a rich structural chemistry. Only hydrides based on cations with a d^0, d^5 or d^{10} electron configuration have been prepared so far, showing that the chemical properties play a significant role in the lattice stability of the hydrides [18].

The thermodynamic and kinetic parameters of hydrogen storage in pure hydrides are often unfavorable, since they must be heated at several hundred K before significant hydrogen release. For this reason, an inorganic additive (usually a metal chloride or oxide) is ball-milled together with the hydride particles to promote mechanochemical reactions at the interphase that improve the hydrogen release performance.

A complete time-resolved XRD screening of the reaction between $CdCl_2$ and alkali borohydrides, using the decomposition indexing approach, appeared recently [19]. Undesirable reactions have also been observed with the same approach: molten $LiBH_4$ reacts even with the most stable materials, like SiO_2 (forming lithium silicates) or Au (forming a Li-Au alloy) [20].

X-ray absorption techniques have also been used alongside XRD to investigate the role of additives. As an example, simultaneous energy-dispersive time-resolved XAS and XRD were used to monitor the thermal evolution of a MgH_2/Nb_2O_5 mixture. After ball-milling, mixed oxides $Mg_{1-x}Nb_xO_y$, and metastable Nb hydrides were shown to improve the hydrogen desorption [21].

These two complementary techniques were also used to study the role of Ti compounds as additives in a variety of systems. In $LiBH_4/MgH_2$, the addition of Ti isopropoxide improves the desorption kinetics: EXAFS/XANES on the Ti K-edge showed a transition from anatase TiO_2 to a mixture of Ti_2O_3 and TiB_2 upon the first desorption cycle: this mixture is stable upon further cycling, and it is thought to improve desorption from $LiBH_4$ after MgH_2 is first decomposed [22]. The addition of Ti chlorides to $NaAlH_4$ does not lead to any crystalline phase, but after repeated cycling a Ti–Al alloy is formed [23, 24]. A detailed EXAFS analysis, corroborated by ab initio molecular dynamics, located the Ti atoms within the first monolayer of the alloy, favoring the formation of mobile AlH_3 clusters on the surface and to the facile desorption of H_2 [25].

27.4 Dye-Sensitized Solar Cells

The layout of a dye-sensitized solar cell is drawn in Fig. 27.3. The photoanode is constituted of a mesoporous dye-sensitized semiconductor: the dye eletrons are photoexcited to the LUMO level and injected into the semiconductor condution band, so producing dye oxidation that in turn induces oxidation of the electrolyte; conduction electrons are brought to the cathode through an external load and the overall system is restored by reduction of the electrolyte.

After the breakthrough paper by O'Regan and Grätzel [26], the number of papers dealing with the various aspects of photoelectrochemical cells has exponentially grown, due to the perspective of achieving low-cost efficient devices able to introduce in the society widespread sources of renewable energy [27]: however, at the moment silicon-based photovoltaic devices are still more reliable and by far more efficient. By inspection of Fig. 27.3, it is clear that a crucial role is played by the interface alignement of the energy levels. In particular, the dye LUMO must lie higher in energy with respect to the semiconductor conduction band, while the HOMO should be lower than the hole level of the electrolyte. In view of this mutual arrangement, most of the SR studies are addressed to the investigation of the electronic strucure by photoemission and soft X-ray absorption techniques [28–30].

Aiming at investigating the possibilitiy of fine-tuning the dye electronic structure, Ti-phtalocyanines (TiPc) dyes where investigated by Pickup and coworkers by the complementary use of computational simulations, laboratory XPS and NEXAFS at the Ti 2*p* edge and at the N 1*s* edge [28]. The dyes were modified by axial (monodentate oxo vs bidentate catechol) and peripheral (t-butyl vs t-butylphenoxy) ligands. NEXAFS experiments allowed to demonstrate that the modification of the Ti site symmetry by the two different axial ligands had a significant effect on the Ti 2*p* edge. In particular, the authors observed that the substitution of the monodentate ligand with the bidentate produced a significative modification of the Ti 2*p*-3*d* transitions, specifically involving a new transition to the $3d_{xy}$ level that was attributed to a decreased symmetry of the Ti site from 4-fold to 2-fold. On the other hand, the axial and peripheral ligands only marginally modified the Pc ring, as demonstrated by

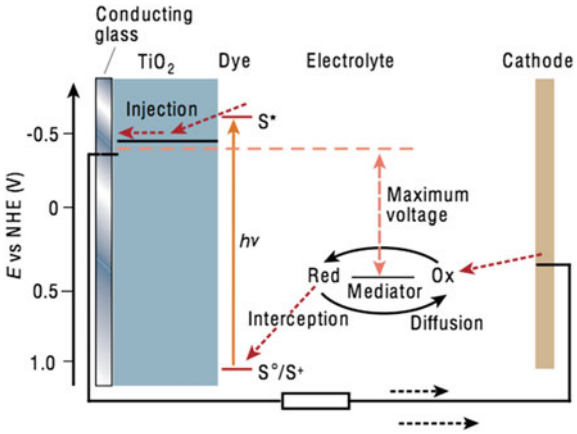


Fig. 27.3 Layout of dye-sensitized cell operation. Reprinted from [26]. Copyright 2001 by Macmillan Magazines Ltd

the minor modifications of the nitrogen 1s band. The complementary computational simulations carried out at the DFT level showed that, shifting from monodentate to bidentate ligand, the dye LUMO turns from the Pc inner ring to the $3d_{xy}$ orbital, while the d_{x2-y2} and d_{z2} levels are reversed. The fine tuning of the dye HOMO-LUMO gap demonstrated by this combined absorption, photoemission and computational study can clearly be exploited, for example, for improving the light harvesting properties of dye-sensitized solar cells.

While the above cited paper deals exclusively with the electronic structure of dye molecules, the alignement of the dye-semiconductor electronic levels is clearly another crucial issue for DSSC efficiency. The interface FePc-TiO_2 was studied by SR photoemission and X-ray absorption by Palmgren et al. [29]. The dye-TiO_2 (110) interface is probed at different coverages (0.7, 1.4, 3, 5 monolayers) showing that a strong interaction takes place. C1s core level photoelectron spectroscopy reveals that the first-layer dyes are strongly bound to the semiconductor surface, as results from a shift of about 2 eV towards larger binding energies and from the absence of shakeup shoulders with respect to the spectral features characteristic of the second-layer adsorbed molecules. These observations are substantially confirmed by the N1s spectra, so pointing to an oxidation of the FePc molecules in direct contact with the TiO_2 surface. From the analysis of the N K-edge X-ray absorption spectra taken with the electric vector parallel and, respectively, perpendicular to the TiO_2 surface, the authors conclude that the dye molecules are adsorbed with the Pc ring parallel to the rutile (110) surface; as concerns the electronic levels alignement, the dye LUMO is always higher in energy with respect to the TiO_2 conduction band minimum, even if the distortion of the electronic structure of the dye first monolayer and the possible interactions between FePc molecules at high coverages could hinder electron injection.

Today, the research in dye-sensitized solar cells is focussed to the elimination of liquid electrolytes [30], involving cumbersome management and leakage-related performance decay. Actually, solid hole conducting polymers like spiro-OMeTAD

(2,2′,7,7′-tetrakis(N,N′-di-p-methoxyphenylamine)-9,9′-spirobifluorene ensure better efficiency, durability, thermal and electrochemical stability with respect to liquid electrolytes. In the paper by Schölin et al. [31] the energy levels of spiro-OMeTAD and of lithium bistrifluoromethylsulfonylamine (Li-TFSI)-added spiro-OMeTAD were compared by hard X-ray photoemission spectroscopy. It was showed that a shift of the Fermi level is induced by Li-TFSI, so demonstrating the possibility of tailoring the energy levels of spiro-OMeTAD. In a study also dealing with the enhancement of hole conductivity [32], spiro-OMeTAD was doped with WO_3, and the electronic levels at the (p-dopant)-polymer interface studied by photoemission spectroscopy.

In conclusion, SR radiation studies on dye-sensitized solar cells are mainly addressed to the analysis of the electronic structure of components and interfaces. These investigations are mostly carried out by photoemission and X-ray absorption experiments. Among the most interesting issues concerning the chemical research, the fine tuning of the electronic structure by means of suitable materials modifications involve the creativity and the capacity of chemists to design and synthesize new compounds. This activity is often supported by complementary experimental techniques, while the exploitation of computational approaches is becoming more and more important [33].

27.5 Oxide-Ion and Proton Conductors

Electrochemical devices based on solid oxides, such as fuel cells (SOFC), work at medium to high temperatures (500–900 °C). This provides several technological advantages: (a) interfacial reactions with the gas phase are fast, and do not require expensive noble metal catalysts; (b) excess heat can be recirculated, increasing the overall thermodynamic efficiency [34].

In these devices, the electrolyte material is an oxide that conducts either oxide-ion defects (through vacancies or interstitials), or protons (through hopping between oxygen sites). These compounds usually crystallize in the fluorite (e.g. ZrO_2) or perovskite structure (e.g. $LaGaO_3$), with more complicated structures like apatites (e.g. $La_{9.33}Si_6O_{26}$) appearing occasionally. The charge carriers are introduced into the lattice either by doping with aliovalent cations, or by stabilization of intrinsic defects.

The oxide-ion conductivity properties have been directly correlated with lattice size, and mechanistic simulations of the anion diffusion rely on precise crystal structure determination: SR diffraction has provided in many cases the necessary peak resolution to clarify the unit cell size and contents, usually complementing neutron diffraction to locate the oxygen atoms. In fact, thanks to the maximum entropy methods, Ali et al. successfully used high-resolution XRD alone to locate the excess interstitial oxide ions that move in linear hexagonal tunnels along the c axis of the doped apatite $La_{9.71}(Si_{5.81}Mg_{0.18})O_{26.37}$, while the atomic displacement analysis

clarified the localized motion of the other oxide ions surrounding the Si/Mg cations [35, 36].

The most prominent examples of intrinsically defective fluorite is Bi_2O_3, that displays a $BiO_{1.5}$ structure at high temperatures with 0.5 oxygen vacancies per unit formula. Different dopant cations stabilize the defect fluorite structure of Bi_2O_3, giving rise to a variety of fluorite-related polymorphs and superstructures: for this reason, X-ray diffraction has long been employed for the study of binary and ternary Bi_2O_3 phase diagrams. Among others, very recent contributions concerned the study of new polymorphs with formulas $Bi_{26}Mo_{10}O_{69}$ and $Bi_{46}V_8O_{89}$. While V^{5+} adopts a fixed tetrahedral coordination due to its small ionic size, both MoO_4 and MoO_5 distorted pyramids are present in $Bi_{26}Mo_{10}O_{69}$ (a tetrahedral only model would result in a $Bi_{26}Mo_{10}O_{68}$ stoichiometry), whose structure was investigated with a combination of singe-crystal and powder SR-XRD [37, 38]. At 310 °C, $Bi_{26}Mo_{10}O_{69}$ undergoes a triclinic to monoclinic transition, above which the MoO_x units are rotationally disordered, which is fundamental for achieveving a high conductivity.

A similar disordered cubic fluorite phase has been detected also for some Ln_6WO_{12} oxides, with 2/7 oxygen vacancies per unit formula (Ln = lanthanide or Y^{3+}): in fact, at high temperatures the most stable phase is rhombohedral, which poses practical problems for solid-state synthesis. Low-temperature synthesis proved successful in preparing disordered cubic fluorite phases for a variety of Ln^{3+}cations. Variable-temperature time-resolved XRD was then used to monitor the irreversible conversion of disordered cubic to ordered rhombohedral [39].

Another mechanism of rotational disorder between isolated polyhedra governs the properties of $La_{0.8}Ba_{1.2}GaO_{4-x}$ proton conductors, where the GaO_4 units are separated by larger La/Ba cations. In a combined static and time-resolved XRD study, the accurate determination of lattice size variations upon hydration and dehydration allowed to formulate a mechanism of proton stabilization along one axis, in which an O-H bond pulls together two neighboring GaO_4 tetrahedra [40]. Most solid oxide proton conductors have a perovskite structure: despite being reported as an ideal cubic perovskite, the $BaZrO_3$ proton conductor doped with small amounts of trivalent dopants has been reported as either cubic or tetragonal by different authors, also due to the difficulty in preparing single-phase and homogeneous powders: recently, high-resolution XRD allowed to detect a very slight tetragonal distortion upon Y^{3+} doping in the otherwise cubic $BaZrO_3$ perovskite. Site-selective EXAFS on the Y edge also pointed out to significant local symmetry reduction in the dopant environment, that likely induces long-range distortion [41].

The $La_{1+x}Sr_{1-x}Ga_3O_{7+x/2}$ oxide-ion conductor shows a related structure, named after the melilite silicate minerals. It is formed by layers of corner-sharing GaO_4 tetrahedra, forming five-fold channels, and La/Sr cations aligned with the channels along the c axis. Trivalent-ion excess introduces oxide ion interstitials which diffuse along the channels. High-temperature XRD allowed to exclude any phase transition, and pointed out the anomalous anisotropic change of the thermal expansion along the c axis around 400 °C that coincides with an ionic conductivity increase [42].

The mechanical stability during heating and cooling is of the utmost importance, since cracks and other mechanical wear is an important cause of failure in

high-temperature devices. For this reason, the study of phase stability and phase transitions has been of central interest in SOFC materials research. SR-XRD has been used to monitor the phase transitions in situ during temperature changes. Low-symmetry perovskites, such as $BaCeO_3$, are especially prone to mechanical stress, since they undergo phase transitions to higher symmetry on increasing the temperature. Mixed cerate-zirconate oxides with formula $BaCe_{0.85-x}Zr_xY_{0.15}O_3$ were evaluated to raise the overall lattice symmetry, and the phase diagram was studied with combined neutron and X-ray diffraction, the latter providing the necessary high-resolution determination of lattice parameters. As expected, the Zr^{4+} insertion over $x = 0.3$ drives the lattice towards a higher symmetry, with a single rhombohedral to cubic transition around 600 °C. For comparison, the parent $BaCe_{0.85}Y_{0.15}O_3$ shows a series of transitions in the same tmperature range, monoclinic to orthorhombic to rhombohedral, and eventually to cubic [43].

While the as-collected diffraction contains information on the average long-range structure, data analysis techniques have been developed to derive the pair distribution function (PDF) from XRD scans over a broad Q-range, thereby allowing to probe directly the interatomic distances on a local scale.

The local structures of fluorite, apatite and brownmillerite oxide-ion conductors have been investigated very recently with X-ray total scattering PDF analysis. CeO_2 shows complete miscibility with Gd_2O_3, resulting in a single fluorite phase, and the charge difference between Gd^{3+} and Ce^{4+} is compensated by the formation of mobile oxygen vacancies: the conductivity, however, does not always increase with increasing Gd^{3+} content, hinting at some kind of interaction between defects. In fact, the average fluorite structure correctly models the diffraction only for distances larger than 10 Å: on the local scale, the structure is better represented as a mixture of fluorite and Gd_2O_3-like phases, each extending in domains about 6–10 Å in diameter [44].

$Ba_2In_2O_5$ crystallizes in the brownmillerite structure, with an alternating array of InO_4 tetrahedra and InO_6 octahedra. At high temperatures, barium indate becomes a disordered cubic perovskite with formula $BaInO_{2.5}$, and 0.5 oxygen vacancies per unit cell. The substitution of 10–15 % of total In^{3+} ions with phosphorus or sulfur has been shown to stabilize the high-temperature conducting phase so that high oxide-ion mobility is achieved also at lower temperatures. The local structure of doped $Ba_2In_2O_5$ can still be described as orthorhombic as in the undoped case, while the average global structure (at distances larger than about 10 Å) is cubic [45].

The local structure determination with site selectivity, from X-ray absorption spectroscopy, has been extensively applied for the study of many doped oxides used as SOFC electrolytes. These studies were mainly focused on the role of the dopant atoms and its relation with the transport properties. Most studied materials fall into one of the following categories: fluorites, perovskites, structures based on tetrahedral units.

As an electrolyte, ceria (CeO_2) is doped with trivalent ions (usually Ln^{3+} lanthanides) to introduce mobile oxygen vacancies. Their mobility is the reason why ceria is one of the most studied fluorites also in catalysis. The local structural effects induced by different Ln^{3+} loadings up to 30 % were investigated with EXAFS: the Ce-O disorder increased significantly more than Ln-O upon increasing the Ln^{3+}

content. Most importantly, the Ln-O distance and Ce-O distance were used to derive the average coordination numbers around each species, and then used to differentiate between different statistical models of defect association [46]. In a recent study, the EXAFS analysis was used to determine the dopant distribution inside the grains of cerium oxide. Yb^{3+}, Y^{3+} and Bi^{3+} dopants either segregate at the grain boundaries or diffuse completely into the grain cores, depending on the different preparation routes and on the grain size. This in turn affects deeply the conduction properties of ceria electrolytes, as preferential paths for oxygen vacancies can be formed along the grain boundaries if the dopant concentration is very high, bypassing the grain cores altogether [47].

Another important example of the dopant-vacancy interaction in fluorites is the case of Ti^{4+} insertion into yttria-stabilized zirconia $Zr_{0.85}Y_{0.15}O_2$: here the EXAFS analysis determined that vacancies associate around Ti^{4+}, which on average is five-coordinated in a square-pyramidal geometry [48].

A number of studies were recently devoted to the systematic investigation of trivalent dopants in $BaCeO_3$ and $BaZrO_3$ proton conducting perovskites. The evidence that different dopants affect conductivity in seemingly unpredictable ways, unrelated to ionic size, has been known for more than 10 years [49]. In fact, the structural studies on the average crystal structure using diffraction techniques have not settled the issue, due to their poor sensitivity to local structural effects. The XAS investigations highlighted the peculiar role of each dopant in controlling the local atomic structure and dynamics, and in turn how these influence the ion conduction properties. Some general trends have been highlighted, linking lattice disorder and proton mobility, but the actual proton conductivity seems to be determined by specific chemical and structural matching between the dopant and the host cations [50].

When inserted in a perovskite lattice, In^{3+} causes lattice deformation due to its size mismatch, being smaller than Ce^{4+} and larger than Zr^{4+}. This bond length strain affects a large volume around the dopant, comprising several coordination shells. There is no solubility limit of In^{3+} in both systems, which form a continuous solid solution between $BaCeO_3$/$BaZrO_3$ and $Ba_2In_2O_5$. Even in the low concentration limit, the In^{3+} doping affects the whole lattice, raising the activation energy for proton transfer [51, 52].

On the contrary, the perturbation of lattice shape and symmetry is fairly limited in the case of Y^{3+} doping, which affects a very limited volume. This has been explained in terms of dopant polarizability, and its matching between dopant and host cations [51]. Figure 27.4 reports the photoelectron paths and the fitting of the model to the data for yttrium-doped barium cerate proton conductors.

The comparison of EXAFS spectra on the dopant and host cation absorption edges between protonated and deprotonated electrolytes allowed to investigate the interaction between M^{3+} and protonic defects. The defect association depends on the particular dopant/host pair, and is generally not easily related to overall electrolyte performance, with Y:$BaCeO_3$ and Gd:$BaCeO_3$ displaying significant association, while Y:$BaZrO_3$ and In:$BaCeO_3$ do not [54–56].

EXAFS spectroscopy has also be used to assess the solubility of niobium inside Y:$BaCeO_3$, to increase its chemical stability. Up to 6 % co-doping, niobium in the +5

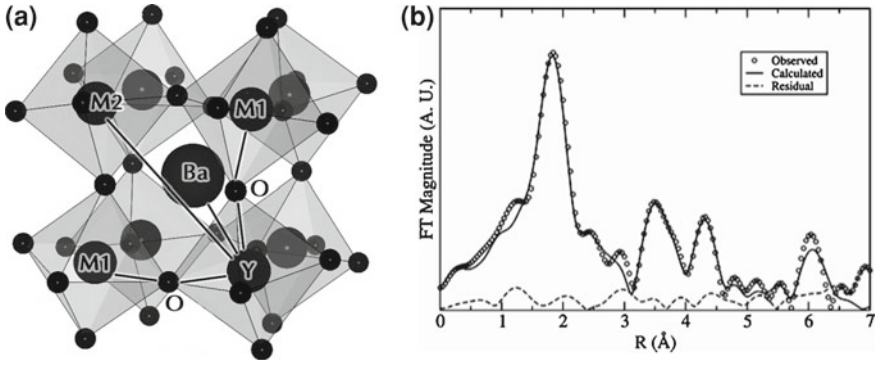


Fig. 27.4 XAS analysis at the Y K-edge of Y-doped barium cerate. **a** Photoelectron paths. **b** Radial distribution around yttrium. Reprinted from [53]. Copyright 2006 American Chemical Society

state substitutes cerium in the perovskite B-site. The reduction of protonic defects due to Nb^{5+} higher charge is compensated by a significant chemical resistance to CO_2-containing atmospheres [57].

27.6 Electrodes for Fuel Cells

Fuel cells based on polymer electrolyte membranes (PEM) work at low temperature ($<100\,°C$). The oxidation of fuel at the anode and the reduction of oxygen at the cathode are catalyzed by finely dispersed noble metal particles (usually Pt/C) also acting as electrodes. The recent research efforts on PEM catalysts are focused on nanoparticle structural characterization, and their inactivation through carbon deposition (coking), or through poisoning by different chemical species [58].

The lower operating temperature of the cell and the negligible X-ray absorption of the polymer electrolyte ease the measurement of XAS on the noble metal absorption edge in operating conditions, and the development of dedicated electrochemical cells for experiments with SR in operating conditions and during potentiostatic/galvanostatic conditioning of the device [59]: a conceptually similar setup was also used to measure XAS on the anode PtRu catalyst in a direct methanol fuel cell [60]. More recently, Lewis et al. described a cell for simultaneous X-ray and infrared spectroscopy, to follow the metal particle restructuring, its inactivation, and the electrochemical performance are followed during H_2 and CO conditioning [61].

A comprehensive review of XAS experiments on PEM catalysts appeared in 2004 [62]. Relevant recent XANES studies on PEM anodes focussed on the fast time resolution (500 ms) of the surface events on Pt_3Co during operation, and the change in charge density on Pt due to the adsorption of H_2 [63]. An important point in the XANES analysis of such systems is the detection of very subtle charge density

changes on Pt due to the adsorption of H_2 and –OH species, as was shown by Friebel et al. for Pt/Rh bimetallic catalysts [64].

Solid oxide fuel cells (SOFC) work at high temperatures (>700 °C), and may employ cheaper transition-metal oxides as electrodes. A good SOFC electrode must be a mixed electronic and ionic conductor (MIEC), with high surface area, and chemical and structural stability at the interface with the supporting electrolyte [65]. Most applications of SR in SOFC electrode chemistry involved the chemical and structural characterization at high temperatures and in different atmospheres. Such studies were devoted to both assessing the feasibility of new compositions, and to elucidate the finer structural details of well-characterized materials.

Thanks to the higher working temperatures, SOFC electrodes suffer less from poisoning, so SR studies on this topic have been mainly devoted to addressing two points: (a) the chemical state of the transition metal cations in operating conditions, and the overall electronic state of the band structure, employing X-ray absorption and photoemission; (b) the phase stability and chemical compatibility between electrodes and electrolyte materials, also making use of a microfocused beam to allow for spatial resolution at different distances from the interphase.

Typical anode materials are ceramic-metal composites, like Ni/YSZ, where the metal is partially oxidized in operating conditons. Microfocused beam XANES was employed to quantify the Ni/NiO ratio at different distance from the anode/electrolyte interface [66].

BSCF ($Ba_{1-x}Sr_xCo_{1-y}Fe_yO_{3-z}$) adopts the perovskite structure common to many MIEC, and it was proposed in 2004 as a high-performance cathode: in situ XANES has shown that Fe and Co reduce to different extents in low oxygen environment, and also that the total cation charge reduction is not consistent with the oxygen nonstoichiometry measured via thermogravimetry [67]. Oxides based on the brownmillerite structure, which is related to perovskite, have been proposed as cathodes. The oxygen conduction mechanism in the $Sr_2Fe_2O_5$ brownmillerite was investigated by resolving the local structure of Fe in situ during the electrochemical insertion of oxygen [68]. Other prospected candidates for SOFC cathodes also include Ruddlesden-Popper phases like La_2NiO_{4+x}. The oxidation state of Ni was determined in situ using XANES in different environments and for different La/Ni ratios [69]. The compatibility of La_2NiO_{4+x} cathodes with GDC was assessed with in situ powder XRD: at high temperatures the phase stability of the cathode material depends highly on the oxygen partial pressure when in contact with the electrolyte [70].

The diffusion of chromium from the interconnect to electrolytes and electrodes ("Cr poisoning") is the foremost mechanism of SOFC degradation, and a major factor in device durability. Microbeam XRD was proposed as an effective method to monitor the phase stability after Cr poisoning as a function of depth in a planar SOFC stack [71].

Bozzini et al. recently reported on a series of experiments performed with soft X-ray spectromicroscopy to investigate the chemical changes occurring between components in SOFC (Ni/YSZ) and in PEM (Pt/C/Nafion) after prolonged operation. These included the cathode deactivation due to carbon deposition, the migration

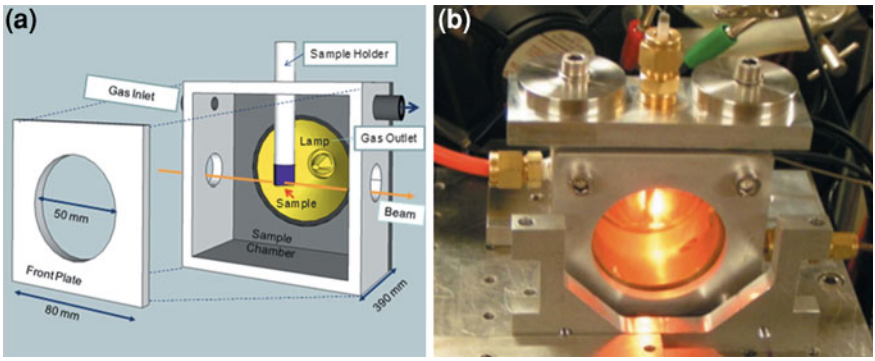


Fig. 27.5 Setup for in situ XAS analysis of fuel cell electrodes. **a** Layout of the device. **b** Photograph of the apparatus in operation. Reprinted from [72]. Copyright 2012 International Union of Crystallography

of cations at the interconnects, the role of overpotential inhomogeneities, and the corrosion of metals in contact with PEM electrolytes [73].

SR was also employed to study the performance degradation of single components: for instance, soft X-ray XANES experiments on Mn L- and O K-edges determined that in $La_{1-x}Sr_xMnO_3$ the high operating temperatures induce long-term changes in the Sr/La and Mn^{4+}/Mn^{3+} ratios in the first surface layers [74].

Compared to PEM, SOFC have a rather more complex design, and they show a more diverse range of compounds used as components: therefore a wide range of dedicated experimental setups have been developed recently to perform in situ experiments with SR during the electrochemical conditioning of the devices.

As what concerns XAS, the setup resembling most closely a high-temperature working SOFC under an SR beam was described by Hagen et al. although the possibility of feeding hydrogen gas to the anode side was not included [72]. Figure 27.5 shows the details of the device.

SR opens the possibility to perform XPS in an environment that is very near to ambient pressure, as opposed to the high vacuum of laboratory instruments. This is extremely beneficial for the study of the gas-solid interactions in SOFC electrodes. McDaniel et al. described an XPS experiment on Ni/CeO_2 anodes during the polarization of a working $Ni/CeO_2/YSZ/Pt$ cell at 700 °C. This allowed to follow the Ce 3d states as a function of polarization [75].

An experimental setup for depth-resolved XAS was also recently presented, in which a 2-dimensional detector collects the grazing-exit fluorescence signal, whose angular distribution is correlated to depth in a similar fashion as what happens with grazing-incidence techniques: this setup was tested on $La_{1-x}Sr_xMnO_3$ cathodes at 700 °C under an external applied voltage [76].

27.7 Conclusions

Our task in the assembly of this book was to outline how the research in chemistry can take advantage from the exploitation of synchrotron light. The obvious approach of gathering together some representative studies soon appeared unfeasible, due to the huge variety of issues concerning chemistry and, on the other hand, to the difficulty of disentangling, in the medley of SR applications, case studies peculiar to chemical research. The attempt to avoid an excessive scattering of subjects led us to focus the paper on materials for renewable energy sources. Even if the field is shared with other disciplines, for instance physics and engeneering, this choice gave us the opportunity to outline the involvement of SR techniques in traditional branches of chemistry: in electrochemistry (for both fuel cells and solar cells), in catalysis (fuel cell electrodes), in electronic structure investigations and, last but not the least, in the design and synthesis of new compounds, concerning both organic and inorganic chemistry.

References

1. J.R.. Long, O.M. Yaghi (eds.), The pervasive chemistry of metal organic frameworks. Chem. Soc. Rev. **38**(5), 1201–1508 (2009)
2. J.R. Long, O.M. Yaghi, Chem. Soc. Rev. **38**, 1213–1214 (2009)
3. S. Bordiga, F. Bonino, K.P. Lillerud, C. Lamberti, Chem. Soc. Rev. **39**, 4885–4927 (2010)
4. F. Millange, C. Serre, N. Guillou, G. Férey, R.I. Walton, Angew. Chem. Int. Ed. **47**, 4100–4105 (2008)
5. J.L.C. Rowsell, O.M. Yaghi, Angew. Chem. Int. Ed. **44**, 4670–4679 (2005)
6. Y. Kubota, M. Takata, R. Matsuda, R. Kitaura, S. Kitagawa, K. Kato, M. Sakata, T.C. Kobayashi, Angew. Chem. Int. Ed. **44**, 920–923 (2005)
7. S. Chavan, J.G. Vitillo, D. Gianolio, O. Zavorotynska, B. Civalleri, S. Jakobsen, M.H. Nilsen, L. Valenzano, C. Lamberti, K.P. Lillerud, S. Bordiga, Phys. Chem. Chem. Phys. **14**, 1614–1626 (2012)
8. R.M.P. Colodrero, K.E. Papathanasiou, N. Stavgianoudaki, P. Olivera-Pastor, E.R. Losilla, M.A.G. Aranda, L. León-Reina, J. Sanz, I. Sobrados, D. Choquesillo-Lazarte, J.M. García-Ruiz, P. Atienzar, F. Rey, K.D. Demadis, A. Cabeza, Chem. Mater. **24**, 3780–3792 (2012)
9. A. Morozan, F. Jaouen, Energy Environ. Sci. **5**, 9269–9290 (2012)
10. V.G. Ponomareva, K.A. Kovalenko, A.P. Chupakhin, D.N. Dybtsev, E.S. Shutova, V.P. Fedin, J. Am. Chem. Soc. **134**, 15640–15643 (2012)
11. M. Sadakiyo, H. Okawa, A. Shigematsu, M. Ohba, T. Yamada, H. Kitagawa, J. Am. Chem. Soc. **134**, 5472–5475 (2012)
12. S. Orimo, Y. Nakamori, J.R. Eliseo, A. Züttel, C.M. Jensen, Chem. Rev. **107**, 4111–4132 (2007)
13. D.B. Ravnsbæk, Y. Filinchuk, R. Cerný, T.R. Jensen, Z. Kristallogr. **225**, 557–569 (2010)
14. R. Černý, Y. Filinchuk, Z. Kristallogr. **226**, 882–891 (2011)
15. J. Soulie, G. Renaudin, R. Cerny, K. Yvon, J. Alloys Compd. **346**, 200–205 (2002)
16. Y. Filinchuk, D. Chernyshov, R. Cerny, J. Phys. Chem. **112**, 10579–10584 (2008)
17. Y. Filinchuk, B. Richter, T.R. Jensen, V. Dmitriev, D. Chernyshov, H. Hagemann, Angew. Chem. Int. Ed. **50**, 11162–11166 (2011)
18. L.H. Rude, T.K. Nielsen, D.B. Ravnsbæk, U. Bösenberg, M.B. Ley, B. Richter, L.M. Arnbjerg, M. Dornheim, Y. Filinchuk, F. Besenbacher, T.R. Jensen, Phys. Status Solidi A **208**, 1754–1773 (2011)

19. D.B. Ravnsbæk, L.H. Sørensen, Y. Filinchuk, F. Besenbacher, T.R. Jensen, Angew. Chem. Int. Ed. **51**, 3582–3586 (2012)
20. L. Mosegaard, B. Moller, J. Jorgensen, Y. Filinchuk, Y. Cerenius, J.C. Hanson, E. Dimasi, F. Besenbacher, T.R. Jensen, J. Phys. Chem. C **112**, 1299–1303 (2008)
21. O. Friedrichs, D. Martínez-Martínez, G. Guilera, J.C. Sánchez López, A. Fernández, J. Phys. Chem. C **111**, 10700–10706 (2007)
22. E. Deprez, M.A. Muñoz-Màrquez, M.A. Roldàn, C. Prestipino, F.J. Palomares, C. Bonatto minella, U. Bösenberg, M. Dornheim, R. Bormann, A.J. Fernàndez, J. Phys. Chem. C **114**, 3309–3317 (2010)
23. H.W. Brinks, C.M. Jensen, S.S. Srinivasan, B.C. Hauback, D. Blanchard, K. Murphy, J. Alloys Compd. **376**, 215–221 (2004)
24. H.W. Brinks, B.C. Hauback, S.S. Srinivasan, C.M. Jensen, J. Phys. Chem. B **109**, 15780–15785 (2005)
25. S. Chaudhuri, J. Graetz, A. Ignatov, J.J. Reilly, J.T. Muckerman, J. Am. Chem. Soc. **128**, 11404–11415 (2006)
26. B. O'Regan, M. Grätzel, Nature **353**, 737–740 (1991)
27. A. Hagfeldt, G. Boschloo, L. Sun, L. Kloo, H. Pettersson, Chem. Rev. **110**, 6595–6663 (2010)
28. D.F. Pickup, I. Zegkinoglou, B. Ballesteros, C.R. Ganivet, J.M. García-lastra, P.L. Cook, P.S. Johnson, C. Rogero, de F. Groot, A. Rubio, de la G. Torre, J.E. Ortega, F.J. Himpsel, J. Phys. Chem. C **117**, 4410–4420 (2013)
29. P. Palmgren, K. Nilson, S. Yu, F. Hennies, T. Angot, C.I. Nlebedim, J.-M. Layet, G. Le Lay, M. Göthelid, J. Phys. Chem. C **112**, 5972–5977 (2008)
30. J.M. Pringle, Phys. Chem. Chem. Phys. **15**, 1339–1351 (2013)
31. R. Schölin, M.H. Karlsson, S.K. Eriksson, H. Siegbahn, E.M.J. Johansson, H. Rensmo, J. Phys. Chem. C **116**, 26300–26305 (2012)
32. R. Hock, T. Mayer, W. Jaegermann, J. Phys. Chem. C **116**, 18146–18154 (2012)
33. F. Labat, T. Le Bahers, I. Ciofini, C. Adamo, Acc. Chem. Res. **45**, 1268–1277 (2012)
34. J. Larminie, A. Dicks, *Fuel Cell Systems Explained* (Wiley, Chichester, 2003), pp. 163–226
35. R. Ali, M. Yashima, Y. Matsushita, H. Yoshioka, K. Ohoyama, F. Izumi, Chem. Mater. **20**, 5203–5208 (2008)
36. R. Ali, M. Yashima, Y. Matsushita, H. Yoshioka, F. Izumi, J. Solid State Chem. **182**, 2846–2851 (2009)
37. C.D. Ling, W. Miller, M.R. Johnson, D. Richard, S. Rols, J. Madge, I.R. Evans, Chem. Mater. **24**, 4607–4614 (2012)
38. X. Kuang, J.L. Payne, J.D. Farrell, M.R. Johnson, I.R. Evans, Chem. Mater. **24**, 2162–2167 (2012)
39. Z.D. Apostolov, P. Sarin, R.P. Haggerty, W.M. Kriven, J. Am. Ceram. Soc. **96**, 987–994 (2013)
40. F. Giannici, D. Messana, A. Longo, A. Martorana, J. Phys. Chem. C **115**, 298–304 (2011)
41. F. Giannici, M. Shirpour, A. Longo, A. Martorana, R. Merkle, J. Maier, Chem. Mater. **23**, 2994–3002 (2011)
42. X. Kuang, M.A. Green, H. Niu, P. Zajdel, C. Dickinson, J.B. Claridge, L. Jantsky, M.J. Rosseinsky, Nat. Mat. **7**, 498–504 (2008)
43. L. Malavasi, C. Tealdi, C. Ritter, V. Pomjakushin, F. Gozzo, Y. Diaz-Fernandez, Chem. Mater. **23**, 1323–1330 (2011)
44. M. Scavini, M. Coduri, M. Allieta, M. Brunelli, C. Ferrero, Chem. Mater. **24**, 1338–1345 (2012)
45. A. Mancini, J.F. Shin, A. Orera, P.R. Slater, C. Tealdi, Y. Ren, K.L. Page, L. Malavasi, Dalton Trans. **41**, 50–53 (2012)
46. S. Yamazaki, T. Matsui, T. Ohashi, Y. Arita, Solid State Ionics **136–137**, 913–920 (2000)
47. P. Lupetin, F. Giannici, G. Gregori, A. Martorana, J. Maier, J. Electrochem. Soc. **159**, B417–B425 (2012)
48. P. Duran, F. Capel, C. Moure, A.R. Gonzalez-Elipe, A. Caballero, M.A. Bañares, J. Electrochem. Soc. **146**, 2425–2434 (1999)
49. K.D. Kreuer, S. Adams, W. Münch, A. Fuchs, U. Klock, J. Maier, Solid State Ionics **145**, 295–306 (2001)

50. F. Giannici, A. Longo, K.D. Kreuer, A. Balerna, A. Martorana, Solid State Ionics **181**, 122–125 (2010)
51. F. Giannici, A. Longo, A. Balerna, K.D. Kreuer, A. Martorana, Chem. Mater. **19**, 5714–5720 (2007)
52. F. Giannici, A. Longo, A. Balerna, K.D. Kreuer, A. Martorana, Chem. Mater. **21**, 2641–2649 (2009)
53. A. Longo, F. Giannici, A. Balerna, C. Ingrao, F. Deganello, A. Martorana, Chem. Mater. **18**, 5782–5788 (2006)
54. F. Giannici, A. Longo, F. Deganello, A. Balerna, A.S. Arico', A. Martorana, Solid State Ionics **178**, 587–591 (2007)
55. F. Giannici, A. Longo, A. Balerna, A. Martorana, Chem. Mater. **21**, 597–603 (2009)
56. F. Giannici, M. Shirpour, A. Longo, A. Martorana, R. Merkle, J. Maier, Chem. Mater. **23**, 2994–3002 (2011)
57. E. Di Bartolomeo, A. D'Epifanio, C. Pugnalini, F. Giannici, A. Longo, A. Martorana, S. Licoccia, J. Power Sources **199**, 201–206 (2012)
58. J. Larminie, A. Dicks, *Fuel Cell Systems Explained* (Wiley, Chichester, 2003)
59. R. Viswanathan, R. Liu, E.S. Smotkin, Rev. Sci. Instrum. **73**, 2124–2127 (2002)
60. S. Stoupin, E.-H. Chung, S. Chattopadhyay, C.U. Segre, E.S. Smotkin, J. Phys. Chem. B **110**, 9932–9938 (2006)
61. E.A. Lewis, I. Kendrick, Q. Jia, C. Grice, C.U. Segre, E.S. Smotkin, Electrochim. Acta **56**, 8827–8832 (2011)
62. A.E. Russell, A. Rose, Chem. Rev. **104**, 4613–4636 (2004)
63. N. Ishiguro, T. Saida, T. Uruga, S. Nagamatsu, O. Sekizawa, K. Nitta, T. Yamamoto, S. Ohkoshi, Y. Iwasawa, T. Yokoyama, M. Tada, ACS Catal. **2**, 1319–1330 (2012)
64. D. Friebel, V. Viswanathan, D.J. Miller, T. Anniyev, H. Ogasawara, A.H. Larsen, C.P. O'Grady, J.K. Nørskov, A. Nilsson, J. Am. Chem. Soc. **134**, 9664–9671 (2012)
65. E.V. Tsipis, V.V. Kharton, J. Solid State Electrochem. **12**, 1367–1391 (2008)
66. K. Hamamoto, T. Suzuki, B. Liang, T. Yamaguchi, H. Sumi, Y. Fujishiro, B. Ingram, A.J. Kropf, J.D. Carter, J. Power Sources **222**, 15–20 (2013)
67. D.N. Mueller, R.A. De Souza, J. Brendt, D. Samuelis, M. Martin, J. Mater. Chem. **19**, 1960–1963 (2009)
68. A. Piovano, G. Agostini, A.I. Frenkel, T. Bertier, C. Prestipino, M. Ceretti, W. Paulus, C. Lamberti, J. Phys. Chem. C **115**, 1311–1322 (2011)
69. R.J. Woolley, B.N. Illy, M.P. Ryan, S.J. Skinner, J. Mater. Chem. **21**, 18592–18596 (2011)
70. R. Sayers, J.E. Parker, C.C. Tang, S.J. Skinner, J. Mater. Chem. **22**, 3536–3543 (2012)
71. D. Liu, J. Almer, Appl. Phys. Lett. **94**, 224106 (2009)
72. A. Hagen, M.L. Traulsen, W. Kiebach, B.S. Johansen, J. Synchrotron Rad **19**, 400–407 (2012)
73. B. Bozzini, M.K. Abyaneh, M. Amati, A. Gianoncelli, L. Gregoratti, B. Kaulich, M. Kiskinova, Chem. Eur. J. **18**, 10196–10210 (2012)
74. L.F.J. Piper, A.R.H. Preston, S.W. Cho, A. De Masi, B. Chen, J. Laverock, K.E. Smith, L.J. Miara, J.N. Davis, S.N. Basu, U. Pal, S. Gopalan, L. Saraf, T. Kaspar, A.Y. Matsuura, P.A. Glans, J.H. Guo, J. Electrochem. Soc. **158**, B99–B105 (2011)
75. A. McDaniel, F. El Gabaly, E. Akhadov, R.L. Farrow, K.F. McCarty, M.A. Linne, S.C. Decaluwe, C. Zhang, B. Eichhorn, G.S. Jackson, Z. Liu, M. Grass, Z. Hussain, H. Bluhm, ECS Trans. **25**, 335–343 (2009)
76. K. Shinoda, S. Suzuki, K. Yashiro, J. Mizusaki, T. Uruga, H. Tanida, H. Toyokawa, Y. Terada, M. Takagaki, Surf. Interface Anal. **42**, 1650–1654 (2010)

Chapter 28
Catalyst Characterization by XAS and XES Spectroscopies: In Situ and Operando Experiments

Francesca Bonino, Elena Groppo, Carmelo Prestipino, Giovanni Agostini, Andrea Piovano, Diego Gianolio, Lorenzo Mino, Erik Gallo and Carlo Lamberti

Abstract The role of a catalyst in improving the activity and the selectivity of a given chemical reaction is provided, together with a discussion on the reasons why XAS and XES are so important techniques in the understanding, at the molecular level, of the structure and of the electronic configuration of a working catalyst. Two industrially relevant catalysts are described as key studies: (i) the combined XAS/XES in situ study on TS-1 catalyst provided the structure of the Ti active center in selective oxidation with H_2O_2, and its evolution upon molecular coordination; (ii) the combined in situ/*operando* XAS study revealed the red-ox catalytic cycle of $CuCl_2/Al_2O_3$ during the ethylene oxychlorination reaction.

F. Bonino · E. Groppo · G. Agostini · L. Mino
Department of Chemistry, NIS Centre of Excellence and INSTM Reference Center, University of Turin, Via Giuria 7, 10125 Torino, Italy

C. Lamberti (✉)
Department of Chemistry, CrisDi Interedepartmental Centre for Crystallography and INSTM Reference Center, University of Turin, Via Giuria 7, 10125 Torino, Italy
e-mail: carlo.lamberti@unito.it

C. Lamberti
Southern Federal University, Zorge Street 5, 344090 Rostov-on-Don, Russia

C. Prestipino
Institut des Sciences Chimiques de Rennes, Université de Rennes 1, UMR CNRS-UR1 6226, Campus de Beaulieu, Bât 10B, 35042 Rennes Cedex, France

A. Piovano
Institut Laue-Langevin (ILL), BP 156 X, 38042 Grenoble Cedex, France

D. Gianolio
Diamond Light Source Ltd, Harwell Science and Innovation Campus, Didcot OX11 0DE, UK

G. Agostini · E. Gallo
European Synchrotron Radiation Facility (ESRF), 6 Rue Jules Horowitz, 38043 Grenoble, France

S. Mobilio et al. (eds.), *Synchrotron Radiation*,
DOI: 10.1007/978-3-642-55315-8_28, © Springer-Verlag Berlin Heidelberg 2015

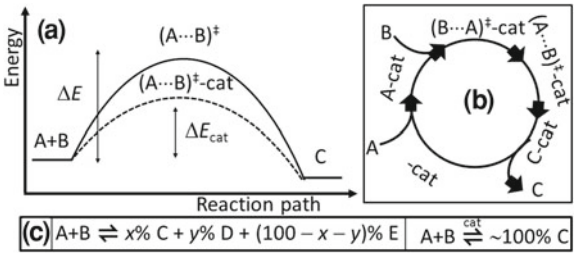


Fig. 28.1 **Part a** Schematic representation of a catalyzed (*dotted curve*) and un-catalyzed (*solid line*) path of the general chemical reaction $A + B \leftrightarrow (A \cdots B)^{\ddagger} \leftrightarrow C$. The catalyst allows to lower the activation energy from ΔE to ΔE_{cat}. **Part b** Example of a possible catalytic cycle for the reaction reported in **a**. **Part c** ideal example of catalyzed increased selectivity towards C

28.1 Introduction

This chapter provides a brief description of the basic concepts of catalysis and discusses the role of XAS and XES to elucidate the catalytic activity. The understanding of the structural (EXAFS) and electronic (XANES and XES) properties of the catalytic active site is of prime significance to obtain a rational catalyst design that points towards the improvement of already established reaction and to develop catalyst for new reactions. Consider a given chemical reactions, where reactants A and B yield the product C. In the simplified scheme reported in Fig. 28.1a, the reaction proceeds through an intermediate state $(A \cdots B)^{\ddagger}$ that has an activation energy ΔE. In the example reported in Fig. 28.1a, once the intermediate state $(A \cdots B)^{\ddagger}$ is reached, the evolution to the final state C is energetically favorable [1]. Hence, the overall reaction rate depends on the fraction of A + B molecules that can reach the intermediate state $(A \cdots B)^{\ddagger}$, which is proportional to $\exp(-\Delta E/k_B T)$, where k_B is the Boltzmann constant and T is temperature (in Kelvin) at which the reaction is run. Consequently, the reaction rate, i.e. the number of C molecules that are produced per unit time (at a given A and B concentration) can be increased either by increasing T or by reducing ΔE. An increase of T is the easiest option, but it has significant economic and environmental drawbacks in terms of energy consumption. Indeed, it rises the costs, it implies higher technological problems in the construction of the industrial plants and it causes safety concerns. Consequently, the most suitable solution is to lower ΔE. This action is performed using a catalyst in the reaction (cat in Fig. 28.1).

Catalysis is the branch of science aimed in increasing (i) the rate of a chemical reaction and (ii) the selectivity towards the desired product C (usually A + B may yields different C, D, E, ... products, with different branching ratios, Fig. 28.1c) [2–4]. This goal is achieved inserting in the reacting medium a substance called "catalyst". Usually the catalyst undergoes multiple chemical transformations, but at the end of the cycle, unlike other reactants (A, B in Fig. 28.1) it remains unchanged, so that it is not consumed and can start the conversion of a new couple of molecules A+B into C, and so on, indefinitely. Figure 28.1b reports a model catalytic cycle, where first

molecule A is adsorbed on the catalytic site "−cat", then the successive adsorption of a B molecule results to the adduct $(B \cdots A)^{\ddagger}$-cat , that undergoes a rearrangement into the $(A \cdots B)^{\ddagger}$-cat adduct, which reacts to yield the product molecule adsorbed on the site C-cat, which is finally desorbed leaving –cat unchanged and ready to start a new cycle.

The main goal of the present chapter is the description of the methodologies allowing to understand, at the molecular level, the structure of the catalytic site "-cat" and its modification along the whole cycle schematized in Fig. 28.1b. The activity and selectivity of a catalyst may be tuned to the desired performances of a specific reaction by the presence of other substances known as additives, dopants or promoters (when they are aimed at increasing the rate) or as inhibitors or poisons (when they are aimed at reducing it). In such cases, the study is also aimed at understanding the effect of promoters on the structure and reactivity of the active catalytic site; examples will be given in Sect. 28.4.

In the vast majority of the cases catalysts do not exhibit long range order. This is obviously the case for homogeneous catalysis, where reactants, products and catalysts are in the liquid phase. For heterogeneous catalysis, in which the reaction is confined to the interface between the catalyst (a solid phase) and the reactants that are either in the liquid or in the gaseous phases, the lack of long range order still holds in most of the cases. In fact, in order to maximize such interface, most of the solid supports are high surface area materials (10^2–10^3 $m^2\,g^{-1}$) with a very poor crystallinity (e.g. $\gamma-Al_2O_3$, active carbons [5, 6] or polymers [7]) or amorphous (e.g. silica [8]). This implies that usually XRD [9, 10] cannot be used to determine the structure of the catalytic active centers. This makes EXAFS the most suited characterization technique to understand the structure of the catalytic sites [11–20], while XANES [18–22] and XES [18–20, 23–25] are informative for its electronic structure. Exception to this statement is made for two main classes of crystalline microporous catalysts, where XRD has played a role: we are speaking about zeolites (that are industrially widely used) and metal-organic frameworks (MOFs, which are of potential interest in the near future [26]). However, also for zeolites and MOFs, when XRD data have been complemented by a XAS study, a better understanding of the material was achieved [13, 14, 18, 21, 27].

The great benefit of XAS and XES spectroscopies applied to catalyst investigation is related to the high penetration depth of hard X-rays, allowing to measure catalysts under operation conditions, i.e. in presence of reactants and products from the gas or liquid phases. This is a mandatory step to understand all the intermediate steps foreseen in Fig. 28.1b.

28.2 Methods and Instrumentation

The instrumentation needed to perform XAS and XES data collection on a working catalyst is the same needed for standard experiments [18, 28]. The specific instrumentation requirements are related to the sample environment. In most of the cases, the

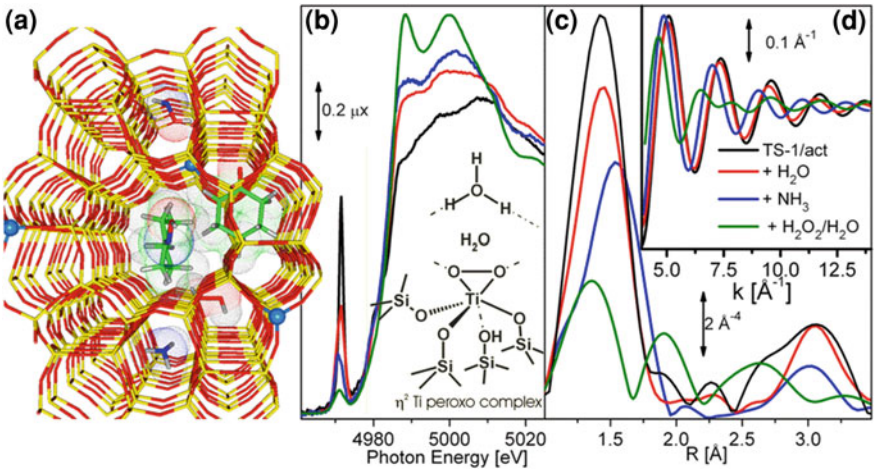


Fig. 28.2 **Part a** sticks representation of the TS-1 molecular sieve (O *red*, Si *yellow*), Ti atoms, isomorphically substituting Si, are represented as blue spheres. Ammonia, cyclohexanone and hydroxylamine molecules are shown in the channel. **Parts b–d** effect of interaction with molecules of increasing interaction strength with Ti(IV) sites: H_2O (*red*), NH_3 (*blue*) and H_2O_2/H_2O solution (*green*). For comparison also the spectrum of the TS-1 activated at 400 K is reported (*black*). **Part b** XANES region. **Part c** moduli of the corresponding k^3-weighted FT. **Part d** corresponding first shell filtered Fourier back-transformed spectra. The scheme in **b** reports the structure of the Ti site upon interaction with H_2O_2/H_2O solution

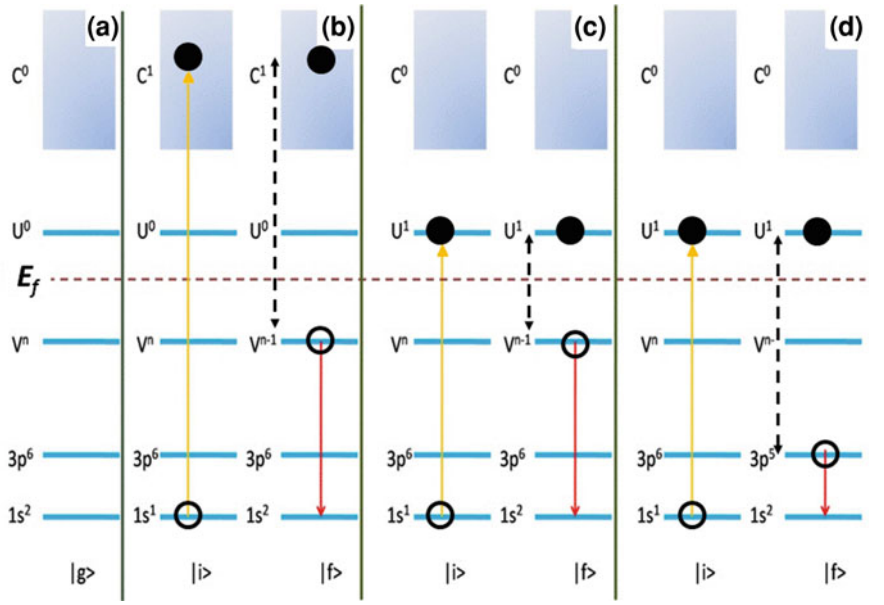
active sites cannot be in contact with the ambient atmosphere because they will react with O_2, H_2O, traces of hydrocarbons etc… with consequent change of their oxidation and coordination state and possibly their irreversible deactivation. Each catalyst must undergo a specific activation treatment at a given temperature under either (i) *vacuum* conditions or (ii) inert atmosphere (e.g. N_2, He, Ar) or (iii) oxidative conditions (e.g. O_2, N_2O, O_3) or reductive conditions (H_2, CO, C_2H_4). We discriminate between in situ and *operando* experiments [29]. In in situ experiments the activated catalyst is measured before and after the dosage of probe or reactant molecules. The experiments are performed with a closed cell that prevents the contamination of the catalyst atmosphere with the ambient atmosphere. The step-scan acquisition mode is used in these cases. Figures 28.2, 28.4 and 28.5 report examples of in situ experiments. *Operando* experiments need quick-EXAFS or dispersive EXAFS set-ups; they are performed in flux conditions, where inert gases and/or reactants are fluxed through the catalyst while XAS/XES data are collected; the gas output is analyzed by a mass spectrometer in order to correlate the changes in the catalyst activity with changes observed in the spectroscopic data. Coming to the theory needed to analyze the XAS and XES data, the reader should refer to the authoritative chapters on EXAFS [30], on XANES [31] and on inelastic X-ray scattering [32] that are available in this book. In the following we shall just report a brief and simplified, one electron, description of the XAS and XES processes allowing a first level understanding of the XANES and XES results reported in Sects. 28.3 and 28.4.

XAS and XES are two complementary synchrotron-based techniques for the characterization of the electronic and geometric structure of selected elements inside materials. *A priori*, the interaction of electromagnetic radiation with matter should be treated in the framework of the quantum electron dynamic theory [33]. However, a simplified one electron picture can be used to describe the basic physical aspect of XES and XAS features. Referring to an element of the third row of the periodic table we can define the radiative transitions of a metal 3p electron to the 1s hole as K_β main lines (core-to-core XES lines) historically referred to as $K_{\beta_{1,3}}$ and $K_{\beta'}$ that are sensitive to the metal oxidation- and spin-states [34]. The transition of a valence electron to the metal 1s hole give rise to the valence-to-core (vtc) X-ray emission spectroscopy (XES) that is responsive to the type, distance and number of ligands around the metal center as well as to the metal oxidation and spin-state [23, 24, 34, 35].

The vtc-XES can be divided in two regions: $K_{\beta''}$ and $K_{\beta_{2,5}}$. The first is mainly linked to transitions involving s type atomic orbital of the metal ligands while the second is primarily due to valence 3d, 3p, 4p metal and ligand p orbital mixing [36]. It has been shown that a theoretical interpretation using ground state density functional theory (DFT) calculation adopting the one-electron approximation is effective [37]. In the one electron approximation, the basic steps of vtc-XES can be described using Scheme 28.1b: (1) a core electron is excited above the Fermi energy E_f by an incident photon (of energy $\hbar\Omega$) producing an intermediate state $|i\rangle$ with a core hole that subsequently decays into a final state $|f\rangle$ with the emission of a photon of energy $\hbar\,\omega$ [23, 35]. If the intermediate state $|i\rangle$ imply the filling of an unoccupied states just above E_f (lowest unoccupied molecular orbitals, MOs, see Scheme 28.1c and d.) the excitations are referred as resonant (r). Resonant excitation present the advantage to shows distinct features as this region is dominated by bound states in respect to higher excitation energies where the features become broad reflecting a continuous distribution. We distinguish furthermore between decays of the intermediate state where the 1s hole is filled by a valence electron (rvtc-XES) or by another core (c) electron (rctc-XES), see Scheme 28.1b and c. In case of resonant excitation it is helpful to define the energy transfer as the difference between incident and emitted energy: $\hbar(\Omega - \omega)$. This energy that remains in the sample can be interpreted as a net transition of the system. For rvtc-XES the net excitation can be as low as few eV corresponding to the range of optical spectroscopy, with the remarkable difference that rvtc-XES is element selective [38, 39].

28.3 Understanding the Structure of the Ti Active Site in TS-1 Catalyst: A XAS/XES Study

Silicalite-1 is a pure siliceous (chemical formula SiO_2) crystalline microporous material with internal channels exhibiting a pore opening of about 5 Å in diameter that allows small molecules to enter and diffuse inside the solid [40], see Fig. 28.2a.

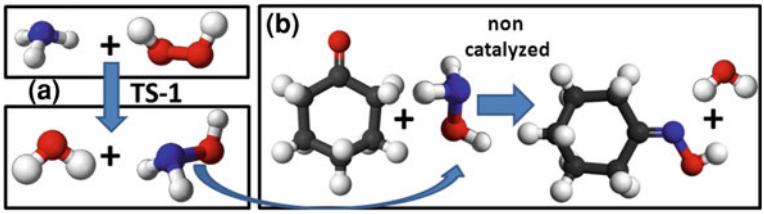


Scheme 28.1 One electron representation of: **a** the ground state $|g\rangle$; **b** vtc-XES; **c** rvtc-XES; and **d** rctc-XES processes. V^n indicates the number (n) of electrons in the valence MOs (V) just below E_f. U indicates the unoccupied MOs just above E_f and C the continuum excitations. The *yellow arrows* represent the transition of the 1s electron due to the adsorption of an incoming photon of energy $\hbar.\Omega$ to reach the intermediate state $|i\rangle$. The *red arrows* indicate the decay of an electron from a higher level to the core hole with final state $|f\rangle$, accompanied by the emission of a photon of energy $\hbar\,\omega$. The energy transfer $\hbar(\Omega - \omega)$ is indicated with *dashed black arrows*. Adapted with permission from [36], copyright Wiley VCH (2013)

Coming back to the general A + B reaction discussed in the Introduction, see Fig. 28.1c, among all possible C, D, E, ... products only a fraction can be obtained inside the pores: this is the key of the so called shape-selectivity of molecular sieves catalysts. Defect-free silicalite-1 can be used as a molecular sieve, but is inactive as catalyst, owing to the absence of reactive catalytic sites.

In the early eighties, ENI researchers, adding few wt.% of pure Ti precursor to the silicalite-1 synthesis obtained the Ti-silicalite-1 (TS-1) material [41] that has shown to be an active and selective catalyst in an impressive number of low-temperature partial oxidation reactions with aqueous H_2O_2 as oxidant [42, 43]. Among them we mention the catalytic oxidation of ammonia to hydroxylamine (Scheme 28.2a) and the cyclohexanone ammoximation to cyclohexanone oxime (Scheme 28.2b) [44], which are intermediate steps for the nylon-6 production.

It was immediately clear that the active site contains Ti, but its true nature remained unknown for a decade. In the whole eighties and at the beginning of the nineties, several local structures were proposed by different authors, ranging from tetrahedral, square pyramidal, up to octahedral symmetries were hypothesized, for a review see [18, 45]. As a consequence a multitude of hypothesis were inferred for active species:



Scheme 28.2 Example of two industrially relevant reactions occurring inside TS-1: the catalyzed oxidation of ammonia to hydroxylamine, **part a**, which in turns react with cyclohexanone to give cyclohexanone oxime, **part b** [44]

titanyl groups, extraframework defect sites, monomeric and dimeric Ti species, Ti species incorporated in edge sharing type structures forming bridges across the zeolite channels and many other. In 1994 EXAFS and XANES results on activated TS-1 [46], represented the first direct prove that the active Ti centers in the TS-1 catalyst are isolated Ti(IV) atoms substituting Si atoms, forming tetrahedral $[Ti(O-Si)_4]$ units. These data definitively closed the lively debate present in the specialized literature about the structural nature of the Ti centers in TS-1.

The XANES spectra of TS-1 activated at high temperature (see black spectrum in Fig. 28.2b) show a narrow and intense pre-edge peak at 4967 eV, due to the $1s \rightarrow 3pd$ electronic transition involving Ti(IV) atoms in tetrahedral coordination [45, 46]. The same electronic transition for Ti(IV) species in TiO_2 (anatase or rutile) or in ETS-10 titanosilicate, where Ti(IV) species are in octahedral environment, is characterized by a very low intensity due to the small *pd* hybridization which occurs in octahedral-like symmetry [47, 48]. Indeed, the transitions $A_{1g} \rightarrow T_{2g}$ are symmetrically forbidden in the case of perfect octahedral coordination while the transition $A_1 \rightarrow T_2$ is allowed in the case of tetrahedral coordination, as in the case of $[TiO_4]$ units hosted in the activated MFI framework. The analysis of the EXAFS spectrum (see black curves in Fig. 28.2c and d) was compatible with 4 O atoms at 1.79 Å, representing an important expansion of the $[TiO_4]$ unit with respect to the $[SiO_4]$ one, which exhibits an average Si-O distance of 1.60 Å [49]. This local observation explains the unit cell expansion observed by XRPD when moving from silicalite-1 to TS-1 [50, 51].

Interaction with ligands of increasing coordination strength (H_2O and NH_3) modifies the XANES features causing a progressive reduction of the pre-edge peak and a progressive increase in the white-line intensity, testifying the distortion from the T_d-like geometry and the coordination of additional ligand(s) to the Ti site. Ligand insertion caused a progressive elongation of the first shell Ti-O bond from 1.79 to 1.82 and 1.84 Å for H_2O and NH_3, respectively [52]. No cleavage of framework Ti-O-Si bonds was observed, as the coordination number was still compatible with $N = 4$ O atoms. The location of one or two (H_2O or NH_3) molecules was inferred from the XAS data reported in Fig. 28.2c and d, but it was not possible to extract the backscattering signal from the molecule(s), because it was of much lower intensity than the perturbation that the molecular adsorption induced on the Ti local environment.

Adsorption of H_2O or NH_3 simply caused a progressive shrinking of the oscillations of the first shell-filtered $k\chi(k)$ signal. This was not the case of the interaction

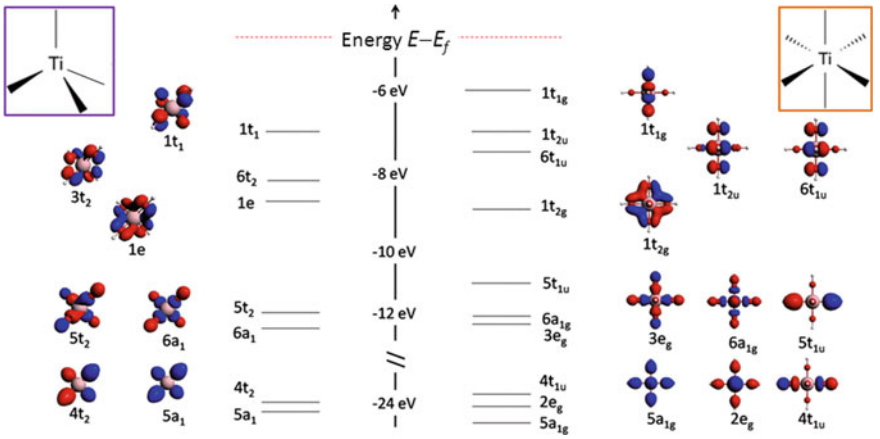


Fig. 28.3 Occupied valence MOs for $Ti(OH)_4$ and $Ti(OH)_6$ clusters in perfect T_d and O_h symmetry. Reproduced with permission from [36], copyright Wiley VCH (2013)

with H_2O_2/H_2O solution (see Fig. 28.2d). In this case a strong beat is observed around 7 $Å^{-1}$, indicating the presence of two first shell contributions whose bond distance differs by about $\Delta r \sim \pi/2k_{beat} \sim 0.2$ Å. Indeed, the data analysis revealed the cleavage of one Ti-O-Si bond out of 4, resulting in 2.8 ± 0.3 framework O atoms at 1.83 ± 0.02 Å plus 2 oxygens of the deprotonated $[O = O]^{2-}$ molecule at 2.01 ± 0.02 Å adsorbed with a side-on geometry [53, 54], as depicted in the inset of Fig. 28.2b. DFT calculations and resonant Raman studies supported the model obtained by EXAFS [45, 55]. This result, obtained after 20 years from the catalyst first synthesis and 10 years after the first XAS experiments, was of primary importance, because it highlighted the structure of the active site precursor that allows the reactions of Scheme 28.2 to occur inside TS-1.

More recently the XES experiments allowed to shed new light on this system [36, 56]. In particular, the experiment of Gallo et al. [36] can be used as key study due to its highly didactic character. Upon molecular adsorption, the Ti local environment moves form T_d–like to O_h–like symmetry, such argument could be used to gain insight into the experimental vtc-XES data, because the intensities of the vtc-XES spectral features are related to the matrix elements $\langle \psi_{Ti(1s)} | \mathbf{e_j} \cdot \mathbf{r} | \psi_{v-MO} \rangle$ [57], where $\mathbf{e}_j$ is a set of three orthogonal unit vectors and $\psi_{v-MO}/\psi_{Ti(1s)}$ are the valence and Ti(1s) based MOs, respectively. The former are reported in Fig. 28.3 as computed for a perfect T_d (left part) and O_h (right part) symmetries.

The Ti(1s) orbital is totally symmetric and hence the intensity of a vtc transition can be examined using the symmetry of the v-MOs. Two simple models with octahedral ($Ti(OH)_6$) and tetrahedral ($Ti(OH)_4$) symmetry (Fig. 28.4a) were employed to exemplify this point. The vtc-XES of $Ti(OH)_6$ consists of two main peaks that involve MOs with t_{1u}-symmetry: $4t_{1u}$ and $5t_{1u}$ (Fig. 28.3 and top of Fig. 28.4b). The $4t_{1u}$- and the $5t_{1u}$-MOs have strong O(2s) and O(2p) atomic character, respectively. MOs that have ungerade symmetry, i.e. that give rise to Laporte allowed transitions,

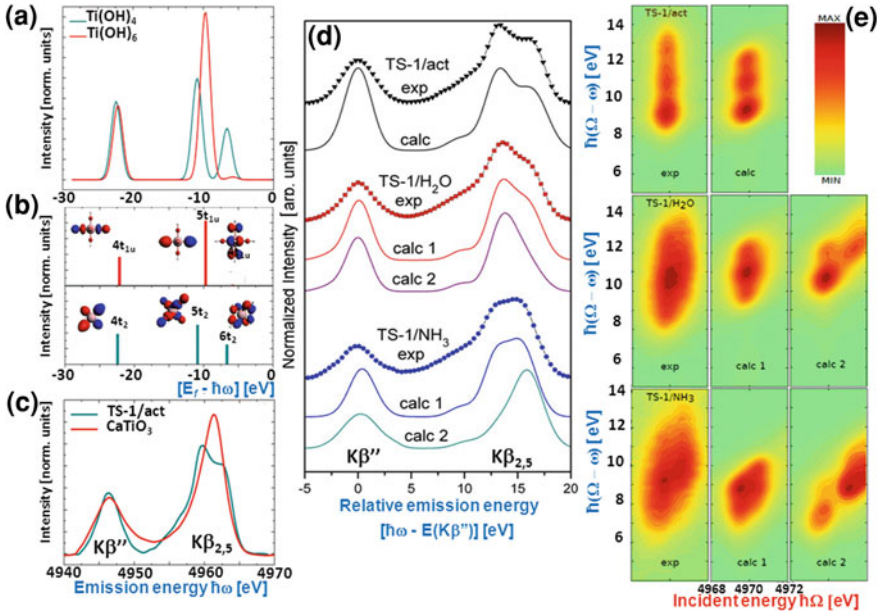


Fig. 28.4 **Part a** Calculated vtc-XES spectra of $Ti(OH)_4$ (*green line*) and $Ti(OH)_6$ (*red line*). **Part b**: intensities for the vtc transitions and significant MOs. **Part c** vtc-XES of TS-1/act (*green line*) and $CaTiO_3$ (*red line*) model compounds. **Part d** Experimental (exp) and calculated (calc) vtc-XES spectra of TS-1/act, TS-1/H_2O and TS-1/NH_3. (calc 1) and (calc 2) are obtained using model structures containing one and two adsorbed molecules per Ti site respectively. **Part e** comparison between the experimental (exp) and calculated (two models) rvtc-XES maps of TS-1/act (*top*), TS-1/H_2O (*middle*) and TS-1/NH_3 *bottom*. Adapted with permission from [36], copyright Wiley VCH (2013)

but with small (e.g. $6t_{1u}$) or zero (e.g. $1t_{2u}$) Ti p-character (i.e. orbital moment $l = 1$ with respect to Ti centre) do not significantly contribute to the spectra. The vtc-XES of $Ti(OH)_4$ is composed of three peaks (Fig. 28.4a and b). Each peak is associated with MOs with t_2-symmetry and thus Ti p-character. The absence of inversion symmetry and thus possibility for *pd*-mixing in T_d symmetry increases the number of observed transitions in the $K_{\beta_{2,5}}$ region of vtc-XES. Orbitals with Ti 3d-character can contribute to the vtc-XES in T_d symmetry while they are absent in O_h symmetry.

It is interesting to note that the observations are different at the K absorption pre-edge where the spectral feature becomes sharper (and more intense) in T_d as compared to O_h symmetry (see Fig. 28.2b). The reason is that the absorption pre-edge in perfect O_h symmetry draws its spectral intensity from weak electric quadrupole transitions and removing inversion symmetry allows strong dipole contributions only for t_2 symmetry. Figure 28.4c reports the experimental spectra of activated TS-1 (TS-1/act) and of $CaTiO_3$, considered as model compounds for Ti in local T_d and O_h symmetry, respectively. The vtc-XES of $CaTiO_3$ presents a sharp $K_{\beta_{2,5}}$ line in contrast to the double feature in TS-1/act. This is in good qualitative agreement with the computed

spectra reported in Fig. 28.4a. It is worth noticing that the sensitivity of vtc-XES extends beyond the first coordination sphere [56] and the simple theoretical model adopted excludes many additional effects. Considering a larger cluster and small deviations from the perfect O_h local symmetry will reduce some degeneracy and result in broader spectral features.

However XES experiments not only help a better interpretation of past experiments but could be a valuable asset for a deeper understanding. Effectively Gallo et al. [36] investigated the adsorption on activated TS-1 observing that Ti centers are able to adsorb only one ligand molecule of H_2O and NH_3 molecules, contrarily to what previously thought [45, 51, 52]. Figure 28.4d (top) shows a comparison of the experimental and calculated vtc-XES of TS-1/act. In contrast to Fig. 28.3a, the cluster that is used for the calculations now contains atoms including the 3rd coordination sphere of Ti [56]. The MOs involved in the vtc-XES transitions have strong ligand character while the spectral intensity arises from the Ti(p) contribution. An analysis of the MOs reveals that the main contributions to the Kβ'' feature are due to almost degenerate MOs with strong O(2s) atomic character, while MOs with O(2p) atomic character mostly contribute to the $\mathbf{K}_{\beta_{2,5}}$ [36].

The $\mathbf{K}_{\beta_{2,5}}$ region of TS-1/H_2O(NH_3) has a double feature in contrast to $Ti(OH)_6$ or $CaTiO_3$ (see Fig. 28.4a, c). The middle and bottom parts of Fig. 28.4d report the comparison between experimental and computed vtc-XES spectra of TS-1/H_2O and TS-1/NH_3 assuming one (calc 1) and two (calc 2) adsorbed molecules. The resulting geometries have been optimized at the DFT level [36]. The $\mathbf{K}_{\beta_{2,5}}$ region exhibits a double feature in case of one adsorbed molecule in agreement with experiment. It becomes sharper when the Ti center is assumed to be six-coordinated, i.e. when two molecules are adsorbed. This is in agreement with the simplified model discussed, see Fig. 28.4a–c. The theoretical vtc-XES of TS-1/act, TS-1/H_2O (calc 1) and TS-1/NH_3 (calc 1) present similar relative changes in intensity as the experimental vtc-XES spectra. When one molecule is adsorbed on the Ti centers the degeneracy of the MOs linked to the main features of the vtc-XES is removed and new transitions involving MOs with O^{water}(2p) and $N^{ammonia}$(2p) atomic character arise in the $K_{\beta_{2,5}}$ region [36]. The calculation reproduces the shift of the Kβ'' region, which is consequently attributed to the presence of transitions involving MOs with O^{water}(2s) and $N^{ammonia}$(2s) atomic character [36].

It is worth recalling that the non-resonant XES data probe occupied orbitals. Conversely, previous work that proposed six-coordinated Ti in TS-1 upon H_2O or NH_3 adsorption [45, 51, 52] used only XAS that relates to the unoccupied electronic levels. It is possible to combine XAS with XES by resonantly exciting a Ti 1s electron into low lying unoccupied MO [24]. In this way it is possible to simultaneously probe both occupied and unoccupied orbitals and thus considerably increase the sensitivity to the local coordination. The energy that is transferred to the sample is measured, similarly to optical resonance Raman spectroscopy [58, 59]. Resonant vtc-XES (rvtc-XES, see Scheme 28.1) allows to record electronic excitations covering and extending the range of UV-visible measurements [38, 39, 60], that is limited to ~6 eV by the emission spectrum of UV lamps. The technique is element-selective and is thus particularly sensitive to ligand-to-metal charge transfer excitations. The

measured and calculated rvtc-XES maps of TS-1/act TS-1/H_2O and TS-1/NH_3 are reported in Fig. 28.4e. A good agreement between calculation and experiment is found for TS-1/act. The features are mainly due to transitions between MOs with Ti(p)-character having strong O or/and SiO_4 character to MOs with strong Ti(3d–4p) character. Additional spectral intensity at higher incident energy is observed upon adsorption of H_2O or NH_3. This intensity is significantly overestimated when two adsorbed molecules are assumed in the calculations. The agreement between experiment and theory is notably better when only one adsorbed molecule on the Ti-center is considered in the calculations. Summarizing, the study of Gallo et al. [36] provided strong experimental evidence, based on element-selective XAS/XES spectroscopies, that only one molecule is adsorbed on the Ti centers in TS-1. This evidence is relevant, as both H_2O and NH_3 molecules are present in the reaction ambient of the working catalyst, see Scheme 28.2.

28.4 Understanding the Chemistry of the Oxychlorination Catalysis by In Situ and *Operando* Experiments

Nowadays, almost all the world production of polyvinyl chloride (PVC) is based on the polymerization of vinyl chloride, which is produced by cracking of 1, 2-dichloroethane (EDC), according to the following reaction:

$$C_2H_4Cl_2 \rightarrow C_2H_3Cl + HCl \tag{28.1}$$

$C_2H_4Cl_2$ is in turn obtained by two parallel processes, direct chlorination (28.2) and oxychlorination (28.3):

$$C_2H_4 + Cl_2 \rightarrow C_2H_4Cl_2 \tag{28.2}$$

$$C_2H_4 + 2HCl + 1/2O_2 \rightarrow C_2H_4Cl_2 + H_2O \tag{28.3}$$

The latter reaction, recycling HCl produced by the cracking of EDC, is particularly important in industrial applications because it was specifically developed to reduce the consumption of Cl_2 and the release of useless and noxious products (HCl), in agreement with the modern requests of chemical industry that needs more environmentally friendly reactions. Oxychlorination of ethylene offers a significant economic benefit in two ways: firstly, it uses cheap and abundant feedstock and, secondly, it recycles waste HCl produced in the EDC cracking (28.1).

Oxychlorination reaction (28.3) is performed at 490–530 K and 5–6 atm using both air and oxygen in fluid or fixed bed reactors. Commercial catalysts are produced by impregnation of γ-Al_2O_3 with $CuCl_2$ (4–8 wt% Cu). Other metal-chlorides (mainly alkaline or alkaline earth chlorides) in a variable concentration are also added in order to improve the catalytic performances, making the catalyst more suitable for use in industrial reactors. In particular, KCl is always present in the catalysts used in fixed

bed technologies, sometimes together with other alkali-metal chlorides, such as CsCl, NaCl or LiCl. Rare earth metal chlorides, such as $LaCl_3$, added to $CuCl_2$ and KCl, are also claimed in the patent literature. $MgCl_2$ is the base additive in the catalysts used in fluid bed processes, where alkali-metal (such as LiCl) or rare-earth-metal chlorides (such as $LaCl_3$) can also be added.

The high dispersion of this catalyst avoid the formation of crystalline supported phases as a consequence EXAFS was a fundamental tool to investigate the structure of the undoped catalyst in the pristine condition, Leofanti et al. [61–65] demonstrated that in the catalyst two Cu phases coexist: Cu-aluminate and supported $CuCl_2$, being the latter the only active one [62]. It was also shown that the active phase in ethylene oxychlorination reaction (28.3) is the highly dispersed $CuCl_2$, following the three steps redox mechanism reported below [63, 64]:

$$2CuCl_2 + C_2H_4 \rightarrow C_2H_4Cl_2 + 2CuCl, \tag{28.4}$$

$$2CuCl + 1/2O_2 \rightarrow Cu_2OCl_2, \tag{28.5}$$

$$Cu_2OCl_2 + 2HCl \rightarrow 2CuCl_2 + H_2O \tag{28.6}$$

This redox cycle was experimentally demonstrated by means of an in situ Cu K-edge XANES and EXAFS study, where the three reagents (C_2H_4, O_2 and HCl) have been separately dosed on the activated $CuCl_2/\gamma$-Al_2O_3 at 500 K in the given order (see Fig. 28.5). In particular, the chlorination of ethylene, (28.4), occurs by reduction of $CuCl_2$ to CuCl, as testified by the red-shift of the Cu K-edge, see Fig. 28.5a top curves. The oxidation of CuCl to an oxychloride, (28.5), is proved by both the opposite blue-shift of the Cu K-edge and the appearance of a low-distance contribution in the |FT| of the EXAFS spectra, due to the insertion of oxygen in the first coordination sphere of Cu, see middle curves in Fig. 28.5a and b, respectively. Finally, the catalytic cycle is closed by the re-chlorination of the oxychloride phase with HCl, (28.6), as demonstrated by the disappearance of the above mentioned oxygen contribution in the FT of the EXAFS spectrum, see red curve in the bottom of Fig. 28.5b.

The spectra shown in Fig. 28.5a demonstrate that the oxidized and the reduced form of the catalyst are easily recognizable by XANES spectroscopy. In particular, XANES spectrum of the oxidized catalyst is characterized by an intense white line at 8995 eV, while that of the reduced catalyst shows a less intense white line at 8993 eV and exhibits a red shift of the edge of 5 eV. Even more informative are the derivative spectra (see insets), where the oxidized catalyst exhibits a strong maximum at 8988 eV and a negative peak at 8998 eV, while the reduced catalyst shows a maximum at 8982 eV.

More recently Muddada et al. [66–69] extended the works of Leofanti et al. [61–65] from bare to LiCl-, KCl-, CsCl-, $MgCl_2$- and $LaCl_3$-doped $CuCl_2/Al_2O_3$ catalysts. Combining in situ XANES/EXAFS, IR spectroscopy of adsorbed CO, CO chemisorption and catalytic tests performed using a pulse reactor in depletive mode, the authors succeeded in understanding the role of dopants (LiCl, KCl, CsCl, $MgCl_2$

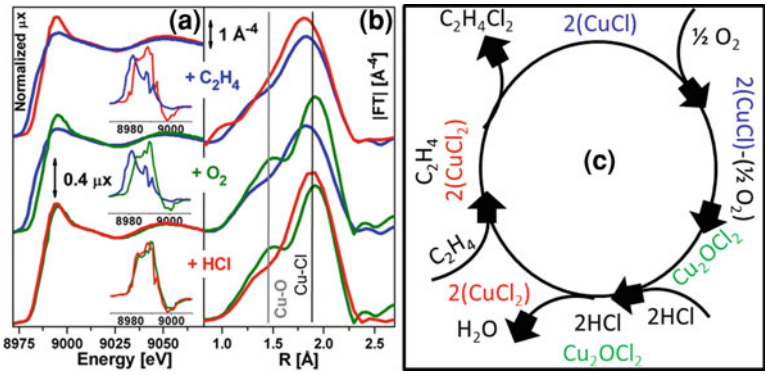


Fig. 28.5 Three steps redox mechanism of the ethylene oxychlorination reaction, (28.4)–(28.6), followed by in situ XANES and EXAFS, **parts a** and **b**, respectively. From *top* to *bottom* the effect of the separate and successive dosage of the three reagents is reported: activated catalyst before (*red line*) and after (*blue line*) ethylene interaction; reduced catalyst before (*blue line*) and after (*green line*) interaction with O_2; oxidized catalyst before (*green line*) and after (*red line*) interaction with HCl. In all cases the interaction temperature was 500 K. Insets in **part a** report the derivative of the spectra reported in the main part. **Part c** catalytic cycle. Unpublished figure reporting data collected at LURE DCI (EXAFS13 beam line) from [63, 64]

$LaCl_3$) in determining the nature, relative fraction, reducibility and dispersion of Cu-phases on $CuCl_2/\gamma-Al_2O_3$ catalysts for oxychlorination reaction (*vide infra* the main parts of Fig. 28.7 for the reduction by ethylene at 500 K, (28.4)). It was shown that in the undoped catalyst two Cu phases coexist: Cu-aluminate and supported $CuCl_2$, the latter being the only active one [62]. EXAFS and XANES data demonstrated the following trend in the ability of the dopant cation to compete with Cu^{2+} in the aluminate phase formation: $K^+ \leq Cs^+ \leq Li^+ \ll Mg^{2+} < La^{3+}$ [67]. In particular, a fraction close to 100 % of copper in the active phase was obtained by adding $MgCl_2$ or $LaCl_3$ dopants. Moreover, EXAFS directly, and IR indirectly, proved that the addition of KCl or CsCl (and less efficiently of LiCl) promotes the formation of mixed CuK_xCl_{2+x} or $CuCs_xCl_{2+x}$ phases, thus altering the chemical nature of the active phase. XANES spectroscopy indicated that addition of $MgCl_2$ or $LaCl_3$ does not affect the reducibility by ethylene of the active $CuCl_2$ phase and that the reducibility of the new copper-dopant mixed chloride are in the order $CuCl_2 > CuLi_xCl_{2+x} > CuK_xCl_{2+x} > CuCs_xCl_{2+x}$ [67], (*vide infra* the main parts of Fig. 28.7).

The determination of the rate determining step among reactions (28.4)–(28.6) was successively achieved by a time resolved XANES *operando* study [70, 71]. The experiment was performed by feeding a cell containing a self-supported thin pellet of the catalyst with a diluted mixture of the three reagents (C_2H_4 : HCl : O_2 : N_2 = 100 : 36.1 : 7.6 : 180), representative of the fixed-bed process. In the course of the experiment the temperature was increased from 373 to 623 K and then decreased again to 373 K. Time resolved XANES spectra were collected in dispersive geometry and the catalyst activity was simultaneously analyzed with a quadrupole

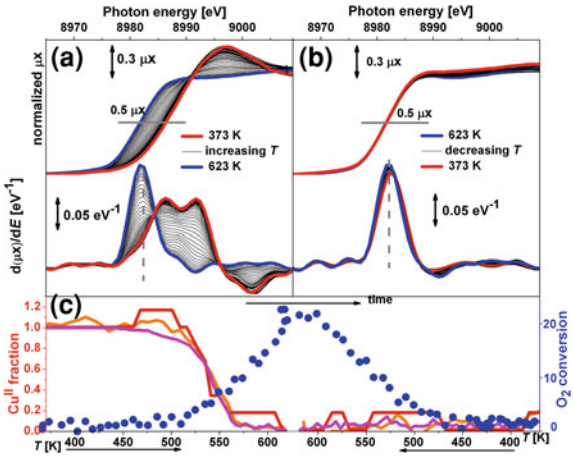


Fig. 28.6 **Part a** XANES spectra (*top*) and corresponding derivatives (*bottom*) of $CuCl_2/Al_2O_3$ system in ethylene oxychlorination environment, during the heating step of the experiment (from 373, *blue curve*, to 623 K, *red curve*, by 12 K min^{-1}). **Part b** as **part a** for the cooling step of the experiment (from 623, red curve, to 373 K, blue curve, by 12 K min^{-1}). XANES spectra have been collected each 30 s, corresponding to a ΔT of 6 K. **Part c** summary of the results of the *operando* experiment (both heating and cooling steps, *left* and *right* parts, respectively), by correlating the catalyst activity, monitored as O_2 consumption (*dotted scattered blue points*, *right ordinate axis*) with the fraction of Cu^{2+} (*left ordinate axis*) *red*, *orange* and *magenta lines*, evaluated according to three different methods. Figure reporting data collected at ESRF ID24 beam line and published in [70, 71]; reproduced with permission from [18], copyright American Chemical Society 2013

mass spectrometer. The results of the experiment are summarized in Fig. 28.6, part (a) for the heating step and part (b) for the cooling step of the experiment. The top curves in parts (a, b) report the evolution of the XANES spectra, while the bottom curves correspond to their first derivatives. Figure 28.6c summarizes the evolution of the Cu^{2+} fraction (red, orange and magenta curves) estimated from the XANES analysis and compared with the catalyst activity reported in terms of oxygen consumption (scattered blue dots).

The XANES spectra reported in Fig. 28.6a and b indicate a progressive reduction of Cu^{2+} into Cu^{+} during the heating step, whereas almost no changes are observed in the XANES spectra collected in the cooling step. As described elsewhere [18, 66, 71], three independent methods were used to quantify the fraction of Cu^{2+} belonging to the active phase on the catalyst in the i-th spectrum, x_i. They are based on: (i) the determination of the edge energy position; (ii) the intensity of the first maximum of the derivative XANES spectra; (iii) the linear combination of the two reference spectra. Comparing, in Fig. 28.6c (left axis), the fraction of Cu^{2+} species (x_i) evaluated according to the different methods for the series of spectra reported in Fig. 28.6a and b we can conclude that in all cases the agreement among the three methods is rather good, as they provide values in relative agreement within $\pm 5\,\%$.

From the whole set of data summarized in Fig. 28.6c the following observations can be drawn. At the starting point (373 K) only Cu^{2+} is present and the catalyst is inactive. Both O_2 conversion and Cu^{2+} reduction start at the same temperature range (470–490 K) and progressively increase upon increasing the temperature because $k_B T$ increases and starts to be comparable with the reaction activation energy ΔE, see Fig. 28.1a. Cu^{2+} reduction is completed at 600 K, see Fig. 28.6c. During the cooling step, O_2 conversion progressively declines becoming negligible in the 490–470 K range, while the oxidation state of Cu does not change anymore. These results provide evidence that at the typical oxychlorination temperature, Cu^{+} is the dominant phase and the rate determining step is the oxidation of CuCl, according to (28.5).

The key role of KCl dopant, present in the industrial catalysts used in fixed bed technologies, was highlighted in a similar experiment [70]. It has been shown that the $KCl/CuCl_2/\gamma-Al_2O_3$ catalyst behaves differently from the base one, working in a prevailing oxidized state (Fig. 28.7b). Combining *operando* XANES experiments with catalytic tests of ethylene conversion in pulse reactors and with IR experiments of adsorbed CO, it was concluded that the active phase of the $KCl/CuCl_2/\gamma-Al_2O_3$ is a mixed chloride (K_xCuCl_{2+x}) phase [70], which reduces the ability of the active surface to adsorb ethylene and/or transfer two Cl atoms to each ethylene molecule. Although not detectable by XRD, because of the too small crystal size [62], the formation of the mixed-chloride double compound, was suggested by IR spectroscopy of adsorbed CO [70] and successively confirmed by EXAFS [67].

More recently, Muddada et al. [66–69] extended the works of Lamberti et al. [70, 71] to the LiCl-, CsCl-, $MgCl_2$-, $CeCl_4$- and $LaCl_3$-doped $CuCl_2/Al_2O_3$ catalyst. Some of these results are summarized in Fig. 28.7. The authors succeeded in understanding, at the atomic level, the role played by additives in the chemistry of the industrial catalyst used in the ethylene oxychlorination. Both KCl (Fig. 28.7b) and CsCl (Fig. 28.7c) form in reaction conditions a mixed phase with $CuCl_2$, which strongly modify the catalyst behavior [66]. In particular, these additives were able to reverse the rate determining step, from the CuCl oxidation (typical of the undoped catalyst) to the $CuCl_2$ reduction, i.e. from (28.5) to (28.4). The change in the rate determining step is a consequence of the decrease of the rate of the latter reaction, thus of the overall activity of the system. For all remaining additives (Fig. 28.7d–f) the rate determining step remains the CuCl oxidation, as for the undoped catalyst [66], because the chloride additives do not mix with $CuCl_2$, that remains the active phase.

28.5 Conclusions and Perspectives

In this chapter we have provided the bases needed to understand the relevant role that XAS (and more recently XES) have played in disclosing, at the molecular level, the structural changes undergone by the active site of a working catalyst. Two relevant examples (TS-1 and $CuCl_2/Al_2O_3$) have been used as case studies to show the potentialities of the techniques.

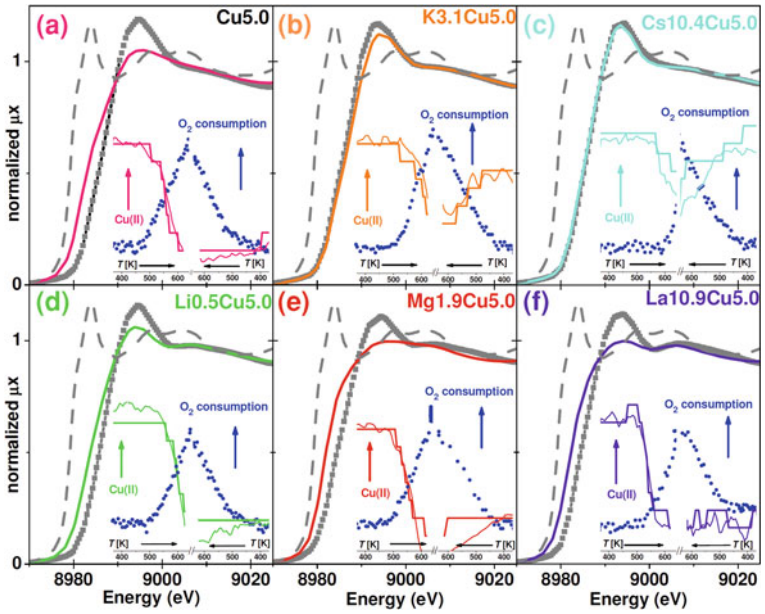


Fig. 28.7 Main parts: XANES spectra (in situ experiments at LURE DCI, EXAFS13 beam line) of doped samples before (*grey scattered curves*) and after (*colored solid lines*) reduction by ethylene at 500 K compared with a spectrum of pure Cu^{I} chloride (*dashed grey line*; same curve in all frames). The insets show the results of *operando* experiments (ESRF ID24 beam line) reporting the evolution of the Cu^{II} fraction along the heating and cooling runs, estimated from the edge shift (*bold colored line*) and from the intensity of the maximum of the first derivative (*full colored line*) together with the catalyst activity (*scattered blue dots*). Unpublished figure reporting data published in [66, 67, 69]

We foresee that remarkable advances in the use of XAS techniques in catalysis will be available in the future; the principal are listed hereinafter. (i) The further improvement and more extended application of modulation excitation spectroscopy, which potentially will allow to selectively detect minority species that are sensitive to an external stimulus [72]. (ii) Experimental setups allowing parallel IR, UV-Vis, Raman data to be collected simultaneously with the XAS/XES data [14–16, 18] are expected to be a key area of technical development. (iii) Space resolved (tomographic) techniques will allow to have a precise three-dimensional insight into the whole catalytic bed (hosted inside a capillary) and the individual catalyst grains, to investigate effects such as the change in the reactants/products ratio occurring along the catalytic bed [18, 73–75]. (iv) The realization of new and improved secondary emission spectrometers at various beam lines will allow oxidation state-specific EXAFS (to obtain separate EXAFS signals in samples containing the same element in different oxidation states [23, 76]) and spin-selective EXAFS spectra collection [77]. (v) Hard X-ray Raman scattering [32] will allow to collect XAS-like signal from relevant light atoms as e.g. C, O, N under catalytically working conditions. (vi) Laser pump/x-rays

probe experiments, applied up to now mainly in studies related to the photoinduced structural dynamics, may in the next future be employed to investigate photocatalysts, clarifying the structural and electronic rearrangements of the photocatalytic site just after (visible) photon absorption or other external stimulus [78–80]. Furthermore, in the immediate future, the incoming new X-ray free electron lasers (XFEL) sources will revolutionize the physics and the chemistry of time resolved experiments [81]. (vii) The simulation of the XANES and XES spectra will be used more and more frequently to confirm or discard local structures hypothesized from the refinement of EXAFS or diffraction data or obtained from DFT calculations [36, 82, 83]. (viii) Joint EXAFS/DAFS studies will allows to explore bi-phasic systems and e.g. to disentangle the contribution coming from two co-existing crystalline phases or from co-existing amorphous and crystalline phases [84]. (ix) As far as metal nanoparticles are concerned, total scattering (PDF) experiments [85] will be able to bridge the gap between EXAFS, dominating the 0–30 Å diameter interval, and XRPD, informative in the 80 Å-bulk range [86]. (x) X-ray magnetic circular dichroism (XMCD), coupled with more conventional visible light MCD and EPR, will bring new insight in the investigation of transition metal supported catalysts [87] and in bio-catalysis [88].

Acknowledgments We are particularly grateful to our colleagues G. Berlier, S. Bordiga, E. Borfecchia, who greatly contributed to the realization of this Chapter. Moreover our gratitude is for the colleagues who spend a fraction of their time in high level education activities. We are indebted to G. Vlaic and S. Mobilio who organized in 1990 the first national synchrotron radiation school in Pula. SB and CL attended that school as PhD students; from that event a group able to use synchrotron radiation was born and grew up in Torino. Several of the other authors of this chapter attended the successive editions of the school. Results reported in Fig. 28.4 have been obtained in collaboration with P. Glatzel (ESRF ID26). This work has been supported by "Progetti di Ricerca di Ateneo-Compagnia di San Paolo-2011- Linea 1", ORTO11RRT5 project. C.L. thanks the support from the Mega-grant of the Russian Federation Government to support scientific research at Southern Federal University, No.14.Y26.31.0001.

References

1. Actually, the chemical equilibria are driven by the variation of the Gibbs free energy G between the final and the initial states: $\Delta G = \Delta H - T\Delta S$, being ΔH and ΔS the enthalpy and entropy variation respectively. In this simplified discussion we neglect the entropic therm.
2. M. Baerns, *Basic Principles in Applied Catalysis* (Springer, Berlin, 2004)
3. I. Chorkendorff, J.W. Niemantsverdriet, *Concepts of Modern Catalysis and Kinetics*, 2nd edn. (Wiley, Berlin, 2007)
4. A. Zecchina, S. Bordiga, E. Groppo, *Selective Nanocatalysts and Nanoscience. Concepts for Heterogeneous and Homogeneous Catalysiss* (Wiley, Weinheim, 2011)
5. P. Serp, L.J. Figueiredo, *Carbon Materials for Catalysis* (Wiley, Hoboken, 2009)
6. E. Furimsky, *Carbons and Carbon Supported Catalysts in Hydroprocessing* (RSC, Cambridge, 2008)
7. E.A. Bekturov, S.E. Kudaibergenov, *Catalysis by Polymers* (Wiley, Weinheim, 2002)
8. E. Groppo, C. Lamberti, S. Bordiga, G. Spoto, A. Zecchina, Chem. Rev. **105**, 115–183 (2005)
9. G. Zanotti, in *Synchrotron Radiation: Basics, Methods and Applications*, ed. by F. Boscherini, C. Meneghini, S. Mobilio (Springer, Berlin, 2014, this volume), pp. 241–273

10. G. Artioli, in *Synchrotron Radiation: Basics, Methods and Applications*, ed. by F. Boscherini, C. Meneghini, S. Mobilio (Springer, Berlin, 2014, this volume), pp. 319–336
11. J.H. Sinfelt, G.D. Meitzner, Acc. Chem. Res. **26**, 1–6 (1993)
12. J. Evans, Chem. Soc. Rev. **26**, 11–19 (1997)
13. B.S. Clausen, H. Topsoe, R. Frahm, Adv. Catal. **42**, 315–344 (1998)
14. M.A. Newton, A.J. Dent, J. Evans, Chem. Soc. Rev. **31**, 83–95 (2002)
15. M.A. Newton, Chem. Soc. Rev. **37**, 2644–2657 (2008)
16. M.A. Newton, W. van Beek, Chem. Soc. Rev. **39**, 4845–4863 (2010)
17. A.I. Frenkel, Chem. Soc. Rev. **41**, 8163–8178 (2012)
18. S. Bordiga, E. Groppo, G. Agostini, J.A. van Bokhoven, C. Lamberti, Chem. Rev. **113**, 1736–1850 (2013)
19. A.L. Mino, G. Agostini, E. Borfecchia, D. Gianolio, A. Piovano, E. Gallo, C. Lamberti, J. Phys. D-Appl. Phys. **46**, 423001 (2013)
20. B.C. Garino, E. Borfecchia, R. Gobetto, J.A. van Bokhoven, C. Lamberti, Coord. Chem. Rev. (2014). doi:10.1016/j.ccr.2014.03.027
21. J.M. Thomas, G. Sankar, Acc. Chem. Res. **34**, 571–581 (2001)
22. M. Fernandez-Garcia, Catal. Rev.-Sci. Eng. **44**, 59–121 (2002)
23. F. de Groot, Chem. Rev. **101**, 1779–1808 (2001)
24. P. Glatzel, U. Bergmann, Coord. Chem. Rev. **249**, 65–95 (2005)
25. J. Singh, C. Lamberti, J.A. van Bokhoven, Chem. Soc. Rev. **39**, 4754–4766 (2010)
26. A. Corma, H. Garcia, F. Xamena, Chem. Rev. **110**, 4606–4655 (2010)
27. S. Bordiga, F. Bonino, K.P. Lillerud, C. Lamberti, Chem. Soc. Rev. **39**, 4885–4927 (2010)
28. G. Aquilanti, L. Vaccari, J. Plaisier, A. Goldoni, in *Synchrotron Radiation: Basics, Methods and Applications*, ed. by F. Boscherini, C. Meneghini, S. Mobilio (Springer, Berlin, 2014, this volume), pp. 65–104
29. G. Berlier, C. Lamberti, M. Rivallan, G. Mul, Phys. Chem. Chem. Phys. **12**, 358–364 (2010)
30. P. Fornasini, in *Synchrotron Radiation: Basics, Methods and Applications*, ed. by F. Boscherini, C. Meneghini, S. Mobilio (Springer, Berlin, 2014, this volume), pp. 181–211
31. M. Benfatto, C. Meneghini, in *Synchrotron Radiation: Basics, Methods and Applications*, ed. by F. Boscherini, C. Meneghini, S. Mobilio (Springer, Berlin, 2014, this volume), pp. 213–240
32. G. Monaco, in *Synchrotron Radiation: Basics, Methods and Applications*, ed. by F. Boscherini, C. Meneghini, S. Mobilio (Springer, Berlin, 2014, this volume), pp. 461–482
33. C.M Bertoni, in *Synchrotron Radiation: Basics, Methods and Applications*, ed. by F. Boscherini, C. Meneghini, S. Mobilio (Springer, Berlin, 2014, this volume), pp. 145–178
34. G. Peng, F.M.F. de Groot, K. Hamalainen, J.A. Moore, X. Wang, M.M. Grush, J.B. Hastings, D.P. Siddons, W.H. Armstrong, O.C. Mullins, S.P. Cramer, J. Am. Chem. Soc. **116**, 2914–2920 (1994)
35. F. de Groot, A. Kotani, *Core Level Spectroscopy of Solids* (CRC Press, London, 2008)
36. E. Gallo, F. Bonino, J.C. Swarbrick, T. Petrenko, A. Piovano, S. Bordiga, D. Gianolio, E. Groppo, F. Neese, C. Lamberti, P. Glatzel, ChemPhysChem **14**, 79–83 (2013)
37. J.C. Swarbrick, Y. Kvashnin, K. Schulte, K. Seenivasan, C. Lamberti, P. Glatzel, Inorg. Chem. **49**, 8323–8332 (2010)
38. L. Mino, V. Colombo, J.G. Vitillo, C. Lamberti, S. Bordiga, E. Gallo, P. Glatzel, A. Maspero, S. Galli, Dalton Trans. **41**, 4012–4019 (2012)
39. E. Gallo, C. Lamberti, P. Glatzel, Inorg. Chem. **52**, 5633–5635 (2013)
40. E.M. Flaningen, J.M. Bennett, R.W. Grose, J.P. Cohen, R.L. Patton, R.M. Kirchner, J.V. Smith, Nature **271**, 512–516 (1978)
41. M. Taramasso, G. Perego, B. Notari, US Patent No. 4410501 (1983)
42. B. Notari, Adv. Catal. **41**, 253–334 (1996)
43. M.G. Clerici, in *Metal Oxide Catalysis*, ed. by S.D. Jackson, J.S.J. Hargreaves (Wiley, Weinheim, 2009), pp. 705–754
44. Scheme 2 reports a possible reaction path for the overall reaction $NH_3 + H_2O_2 + C_6H_{10}O \rightarrow C_6H_{10}NOH + 2H_2O$ that occur inside TS-1. The path consists in the catalytic oxidation of ammonia to NH_2OH, followed by the non-catalyzed condensation of NH_2OH with the ketone. Actually, a second path (not shown) is also possible, consisting in the preliminary condensation of the ketone with ammonia, followed by the catalyzed oxidation of the imine to the oxime

45. S. Bordiga, F. Bonino, A. Damin, C. Lamberti, Phys. Chem. Chem. Phys. **9**, 4854–4878 (2007)
46. S. Bordiga, S. Coluccia, C. Lamberti, L. Marchese, A. Zecchina, F. Boscherini, F. Buffa, F. Genoni, G. Leofanti, G. Petrini, G. Vlaic, J. Phys. Chem. **98**, 4125–4132 (1994)
47. Z.Y. Wu, G. Ouvrard, P. Gressier, C.R. Natoli, Phys. Rev. B **55**, 10382–10391 (1997)
48. C. Prestipino, P.L. Solari, C. Lamberti, J. Phys. Chem. B **109**, 13132–13137 (2005)
49. G. Artioli, C. Lamberti, G.L. Marra, Acta Cryst. B **56**, 2–10 (2000)
50. C. Lamberti, S. Bordiga, A. Zecchina, A. Carati, A.N. Fitch, G. Artioli, G. Petrini, M. Salvalaggio, G.L. Marra, J. Catal. **183**, 222–231 (1999)
51. S. Bordiga, A. Damin, F. Bonino, C. Lamberti, in *Surface and Interfacial Organometallic Chemistry and Catalysis*, ed. by C. Copéret, B. Chaudret (Springer, Heidelberg, 2005), pp. 37–68
52. S. Bordiga, A. Damin, F. Bonino, A. Zecchina, G. Spanò, F. Rivetti, V. Bolis, C. Lamberti, J. Phys. Chem. B **106**, 9892–9905 (2002)
53. F. Bonino, A. Damin, G. Ricchiardi, M. Ricci, G. Spanò, R. D'Aloisio, A. Zecchina, C. Lamberti, C. Prestipino, S. Bordiga, J. Phys. Chem. B **108**, 3573–3583 (2004)
54. C. Prestipino, F. Bonino, A. Usseglio Nanot, A. Damin, A. Tasso, M.G. Clerici, S. Bordiga, F. D'Acapito, A. Zecchina, C. Lamberti, ChemPhysChem **5**, 1799–1804 (2004)
55. S. Bordiga, A. Damin, F. Bonino, G. Ricchiardi, C. Lamberti, A. Zecchina, Angew. Chem. Int. Ed. **41**, 4734–4737 (2002)
56. E. Gallo, C. Lamberti, P. Glatzel, Phys. Chem. Chem. Phys. **13**, 19409–19419 (2011)
57. G. Smolentsev, A.V. Soldatov, J. Messinger, K. Merz, T. Weyhermuller, U. Bergmann, Y. Pushkar, J. Yano, V.K. Yachandra, P. Glatzel, J. Am. Chem. Soc. **131**, 13161–13167 (2009)
58. G. Ricchiardi, A. Damin, S. Bordiga, C. Lamberti, G. Spanò, F. Rivetti, A. Zecchina, J. Am. Chem. Soc. **123**, 11409–11419 (2001)
59. S. Bordiga, A. Damin, F. Bonino, G. Ricchiardi, A. Zecchina, R. Tagliapietra, C. Lamberti, Phys. Chem. Chem. Phys. **5**, 4390–4393 (2003)
60. C. Garino, E. Gallo, N. Smolentsev, P. Glatzel, R. Gobetto, C. Lamberti, P.J. Sadlerd, L. Salassa, Phys. Chem. Chem. Phys. **14**, 15278–15281 (2012)
61. G. Leofanti, M. Padovan, M. Garilli, D. Carmello, A. Zecchina, G. Spoto, S. Bordiga, G.T. Palomino, C. Lamberti, J. Catal. **189**, 91–104 (2000)
62. G. Leofanti, M. Padovan, M. Garilli, D. Carmello, G.L. Marra, A. Zecchina, G. Spoto, S. Bordiga, C. Lamberti, J. Catal. **189**, 105–116 (2000)
63. G. Leofanti, A. Marsella, B. Cremaschi, M. Garilli, A. Zecchina, G. Spoto, S. Bordiga, P. Fisicaro, G. Berlier, C. Prestipino, G. Casali, C. Lamberti, J. Catal. **202**, 279–295 (2001)
64. G. Leofanti, A. Marsella, B. Cremaschi, M. Garilli, A. Zecchina, G. Spoto, S. Bordiga, P. Fisicaro, C. Prestipino, F. Villain, C. Lamberti, J. Catal. **205**, 375–381 (2002)
65. C. Prestipino, S. Bordiga, C. Lamberti, S. Vidotto, M. Garilli, B. Cremaschi, A. Marsella, G. Leofanti, P. Fisicaro, G. Spoto, A. Zecchina, J. Phys. Chem. B **107**, 5022–5030 (2003)
66. N.B. Muddada, U. Olsbye, L. Caccialupi, F. Cavani, G. Leofanti, D. Gianolio, S. Bordiga, C. Lamberti, Phys. Chem. Chem. Phys. **12**, 5605–5618 (2010)
67. N.B. Muddada, U. Olsbye, G. Leofanti, D. Gianolio, F. Bonino, S. Bordiga, T. Fuglerud, S. Vidotto, A. Marsella, C. Lamberti, Dalton Trans. **39**, 8437–8449 (2010)
68. N.B. Muddada, U. Olsbye, T. Fuglerud, S. Vidotto, A. Marsella, S. Bordiga, D. Gianolio, G. Leofanti, C. Lamberti, J. Catal. **284**, 236–246 (2012)
69. D. Gianolio, N.B. Muddada, U. Olsbye, C. Lamberti, Nucl. Instrum. Met. Phys. Res. B **284**, 53–57 (2012)
70. C. Lamberti, C. Prestipino, F. Bonino, L. Capello, S. Bordiga, G. Spoto, A. Zecchina, S.D. Moreno, B. Cremaschi, M. Garilli, A. Marsella, D. Carmello, S. Vidotto, G. Leofanti, Angew. Chem. Int. Edit. **41**, 2341–2344 (2002)
71. C. Lamberti, S. Bordiga, F. Bonino, C. Prestipino, G. Berlier, L. Capello, F. D'Acapito, F.X.L.I. Xamena, A. Zecchina, Phys. Chem. Chem. Phys. **5**, 4502–4509 (2003)
72. D. Ferri, M.S. Kumar, R. Wirz, A. Eyssler, O. Korsak, P. Hug, A. Weidenkaff, M.A. Newton, Phys. Chem. Chem. Phys. **12**, 5634–5646 (2010)
73. J.D. Grunwaldt, C.G. Schroer, Chem. Soc. Rev. **39**, 4741–4753 (2010)

74. A.M. Beale, S.D.M. Jacques, B.M. Weckhuysen, Chem. Soc. Rev. **39**, 4656–4672 (2010)
75. L. Mino, E. Borfecchia, C. Groppo, D. Castelli, G. Martinez-Criado, R. Spiess, C. Lamberti, Catal. Today (229), 72-79 (2014)
76. F.M.F. de Groot, Top. Catal. **10**, 179–186 (2000)
77. P. Glatzel, L. Jacquamet, U. Bergmann, F.M.F. de Groot, S.P. Cramer, Inorg. Chem. **41**, 3121–3127 (2002)
78. C. Bressler, M. Chergui, Chem. Rev. **104**, 1781–1812 (2004)
79. L.X. Chen, D.-J. Liu, Synchrotr. Rad. News **22**, 17–22 (2009)
80. E. Borfecchia, C. Garino, L. Salassa, C. Lamberti, Philos. Trans. R. Soc. A-Math. Phys. Eng. Sci. **371**, Art. n. 20120132 (2013)
81. F. Parmigiani, in *Synchrotron Radiation: Basics, Methods and Applications*, ed. by F. Boscherini, C. Meneghini, S. Mobilio (Springer, Berlin, 2014, this volume), pp. 761–785
82. E. Borfecchia, S. Maurelli, D. Gianolio, E. Groppo, M. Chiesa, F. Bonino, C. Lamberti, J. Phys. Chem. C **116**, 19839–19850 (2012)
83. D.F. Giordanino, E. Borfecchia, K.A. Lomachenko, A. Lazzarini, G. Agostini, E. Gallo, A. V. Soldatov, P. Beato, S. Bordiga, C. Lamberti, J. Phys. Chem. Lett (5), 1552-1559 (2014)
84. A.I. Frenkel, A.V. Kolobov, I.K. Robinson, J.O. Cross, Y. Maeda, C.E. Bouldin, Phys. Rev. Lett. **89**, Art. n. 285503 (2002)
85. E.S. Bozin, P. Juhás, S.J.L. Billinge, in *Characterization of Semiconductor Heterostructures and Nanostructures II*, ed. by C. Lamberti, G. Agostini (Elsevier, Amsterdam, 2013), pp. 229–257
86. M.A. Newton, K.W. Chapman, D. Thompsett, P.J. Chupas, J. Am. Chem. Soc. **134**, 5036–5039 (2012)
87. D.B. Roa, I.D. Barcelos, A. de Siervo, K.R. Pirota, R.G. Lacerda, R. Magalhaes-Paniago, Appl. Phys. Lett. **96**, Art. n. 253114 (2010)
88. S. Staniland, B. Ward, A. Harrison, G. van der Laan, N. Telling, Proc. Natl. Acad. Sci. USA **104**, 19524–19528 (2007)

Chapter 29
Studies of Matter at Extreme Conditions

Sakura Pascarelli

Abstract The striking advances in high pressure techniques and in theoretical methods have boosted synchrotron radiation research at extreme conditions. This chapter introduces the basic tools and methods used and illustrates a few examples of applications in the fields of Physics, Geochemistry and Environmental Science.

29.1 High Pressure Research

This aim of this chapter is to give a brief introduction to high pressure studies as they are performed at modern synchrotron radiation facilities today. Section 29.1 gives a very general introduction to high pressure research, with focus on the motivation and importance of understanding the behaviour of matter under so called "extreme conditions". It also gives a brief introduction to the basic high pressure tools and methods. The remaining sections illustrate examples of high pressure research, chosen from the huge variety of areas of application, that span from physics to chemistry, from biology to materials science, from mineralogy to planetary science, from to environmental science to new energy resources. In Sect. 29.2 high pressure methods combined to modern SR techniques are used to investigate one of the many physical phenomena induced by compression: the collapse of ferromagnetism. Section 29.3 gives a flavour of how high pressure studies help reveal Earth's interior, understand our planet's formation and how it is likely to evolve, while Sect. 29.4 is devoted to illustrating how they can help explore potential new sources of energy and understand climate change.

S. Pascarelli (✉)
European Synchrotron Radiation Facility, BP 220, 38043 Grenoble Cedex, France
e-mail: sakura@esrf.fr

S. Mobilio et al. (eds.), *Synchrotron Radiation*,
DOI: 10.1007/978-3-642-55315-8_29, © Springer-Verlag Berlin Heidelberg 2015

29.1.1 Introduction

Of the common thermodynamic variables pressure and temperature, it is temperature that has played by far the most prominent role in probing condensed matter and in our fundamental understanding of it. High pressure (HP) studies have been considered in the past by scientists as a marginal field of investigation. HP conditions were often described as "exotic" or "extreme", and a very small scientific community explored them, more for the technological performances than for the physical information. Indeed, this lack of interest in the thermodynamic parameter pressure might seem strange, as one of the main goals in science is understanding the properties of matter as it exists actually in the universe. Most condensed matter is found inside planets at pressures of several hundreds of gigapascals (100 GPa = 1 Mbar) and "ambient" conditions are not at all ordinary. Furthermore, of all physical variables, pressure possesses one of the greatest ranges: over 60 orders of magnitude. At the high end, the pressures are those of the interiors of neutron stars; at the other, they gauge conditions of the remotest vacua of outer space.

HP studies are a relatively new field. Up until the end of the 60s, HP generation devices were heavy, difficult to use and expensive. The quality of results of early experiments and the difficulty in monitoring pressure conditions further hindered the development of HP science. Finally, the poor agreement between theoretical calculations and experimental results did not favour cross-interaction between experimentalists and theoreticians. Nowadays, thanks to development of different HP generation devices such as diamond anvil cells (DACs) and large volume cells (LVCs) in combination with the availability of international facilities such as synchrotron and neutron sources, it is possible to perform high quality HP experiments exploiting different techniques. Theoretical methods as well have experienced a remarkable improvement: ab initio calculations are able now to describe fairly well a system without experimental input, allowing a closer interaction between theory and experiment.

29.1.2 Matter Under "Extreme Conditions"

It is through pressure, which is a special case of generalized stress, that one can change the volume of a system or the average particle density. The changes may be brought about in a quasi-static way, typically nowadays by the use of DACs, or they may be brought about dynamically, through the use of shock methods [1]. In either case, atoms in condensed forms of matter are driven closer together. As observed by Percy Williams Bridgman (Nobel Prize in Physics in 1946) of Harvard University in 1926, this compression offers a route to "breaking down" the electronic structure of the atoms themselves and to the possibility of creating entirely different bulk properties. Through application of pressure, we can bring about one of the most basic of all changes, the crossing of the "great divide" from insulators to metals (i.e. [2]). Pressure-induced insulator-to-metal transitions have been documented in a

long list of materials and over a broad range of pressures. One of the most well studied of these materials is Silicon, which transforms from the diamond-type semiconductor phase to the metallic β-Sn structure at 12 GPa [3].

If we hold macroscopic quantities of a pure element, for example, in a volume V, a consequence of this confinement boundary condition is that the stationary states of the fundamental Schrödinger equation

$$H\,\psi(V) = E(V)\,\psi(V)$$

are functions of volume V and hence alterable by pressure. In solids, described by the energy-band picture, pressure can alter both bandwidths and bandgaps, and offers a way to refine both—that is, pressure acts as a probe of band structure. The stationary states of the Schrödinger equation can also be electronically ordered, exhibiting magnetic or superconducting states, for example. So application of pressure can induce major modification of electronic and magnetic states, including the formation of conductors or superconductors from materials originally possessing substantial bandgaps [4–6]. In ferromagnets, as will be shown in Sect. 29.2 of this chapter, electronic band broadening induced by compression eventually leads to a suppression of ferromagnetic order. Typically compression causes a tendency toward closer packing of atoms, ions and molecules, often assumed to mean a corresponding tendency toward simpler structures, but sometimes quite the opposite is true. Indeed, pressure may induce order, but can also bring out disorder [7] or higher complexity [8]. Generally, compression is followed by an increase of local coordination; this increase in turn is intimately linked to changes in electron hybridization. In various ways such changes all affect chemical behaviour: pressure can induce chemical reactions that do not occur under more familiar conditions [9], and it can speed up or slow down known chemical reactions.

Although many of these effects of pressure have been known for years, it is only recently that the full potential of the pressure variable in condensed matter sciences has begun to be realized. This is mainly due to the striking advances that have occurred in parallel in experimental high pressure techniques and in theoretical methods respectively.

29.1.3 High Pressure to Study Earth's Interior, Understand Climate Change, Explore New Sources of Energy

Earth's interior continues to affect society in very direct and profound ways [10, 11]. Earthquakes and volcanic eruptions result from chemical reactions and motions in Earth's mantle, the stony region from a few tens of km depth beneath the continents to almost 3,000 km in depth. Buried at shallow levels beneath the ocean floor and preserved by high pressures in the sediments are the greatest known deposits of hydrocarbon energy resources. We know that Earth's mantle likely contains far more

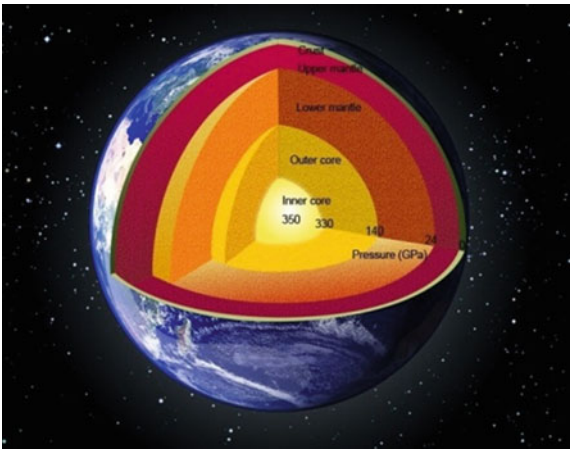


Fig. 29.1 James Wong Wing-On: Knowledge of earth's interior in 21st century. http://jameswongwingon-online.blogspot.fr/2012/07/interior.html

water and carbon dioxide than is present in all the world's oceans and atmosphere combined. Direct evidence of carbon reservoirs in the mantle can be seen in diamonds. Thus, mantle processes have probably had a strong influence on the quantity of carbon dioxide—a major greenhouse gas—present in the atmosphere.

The interiors of Earth and other planets cannot be directly observed. No borehole has ever pierced Earth's thin crust due to the high temperatures and pressures existing at depth. Yet we know a great deal about Earth's interior. The last two decades have brought unprecedented advances in understanding Earth's interior as well as other planetary bodies in our solar system and beyond. The simple layered models depicted in textbook diagrams (Fig. 29.1) are being replaced with more sophisticated models that show the complexity and dynamics of Earth's interior (Fig. 29.2). The features of this internal system give us clues as to how the interior works–for example how material moves, how heat is transported and what it is made of—and how Earth developed to this state. We now know that motions in Earth's metallic core are responsible for the magnetic field at the surface, which is the basis for navigation. Computer simulations show liquid metal flow in the outer core can generate a magnetic field like Earth's.

One of the greatest achievements of high pressure science has been the ability to reach pressures and temperatures of Earth's core in the laboratory. This pressure regime is from 130 GPa at the boundary between the rocky mantle and the liquid core (or Core Mantle Boundary—CMB) to 350 GPa at Earth's center (Fig. 29.1).

Not only is it today possible to reach these pressures, but samples can be heated to core temperatures (~6,000 K) using focused laser beams, while probing the atomic, electronic and magnetic structures using XRD, XAS and other SR-based techniques. Sophisticated quantum mechanical calculations can be performed to simulate the behavior of minerals and iron at the relevant P and T conditions.

Any realistic interpretation of the geophysical observations requires accurate knowledge of the material properties of candidate materials under extremely high

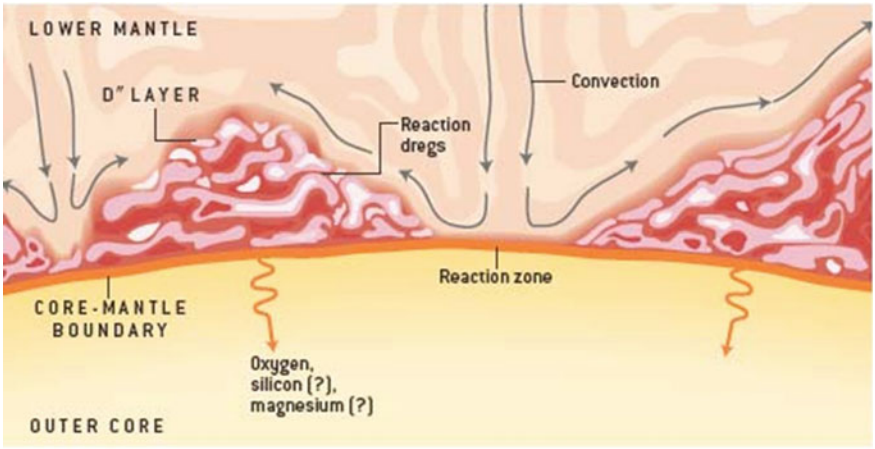


Fig. 29.2 The Core-Mantle Boundary. Ian Worpole, nature.com

pressures and temperatures. For example, to understand the cause of seismic anisotropy of the inner core and how core material deforms in response to various forces, we need to know the elastic constants of iron under inner core conditions. These have been measured and calculated (see for example [12, 13]). At the CMB where the core and mantle are in contact, the structure is suggestive of large scale chemical reactions and the presence of iron-rich silicate liquids. The CMB region may be as complicated as the interface between the solid Earth and the atmosphere. To understand the origin of material exchanges at the CMB, and the exchange of oxygen between deep mantle and globe surface we need to know the oxidation state of metals found in natural rocks under the actual conditions of the Earth's interior, as well as the chemical reactions that occur between them. Examples of research in this area are illustrated in the last two sections of this chapter.

29.1.4 Tools and Experimental Methods

Among the numerous HP cells now available, such as large volume cells, multi anvil cells, etc. (for an exhaustive review see [14]), the DAC allows to reach the highest static pressures. The great number of results in the field of HP research is strictly related to the development of the DAC technique; see for example [15] for a review of early developments. This device, that can fit into the palm of the hand, can generate pressures of the order of magnitude of 500 GPa [16]. The DAC is very simple in principle. It consists of two gem-quality single crystal diamonds with flat surfaces to serve as anvil faces (Fig. 29.3). The diamonds are mounted so that a sample can be squeezed between the anvil faces (Fig. 29.4). The smaller the area A of the anvil faces, the higher the pressure P reached by the DAC for an equivalent value of applied

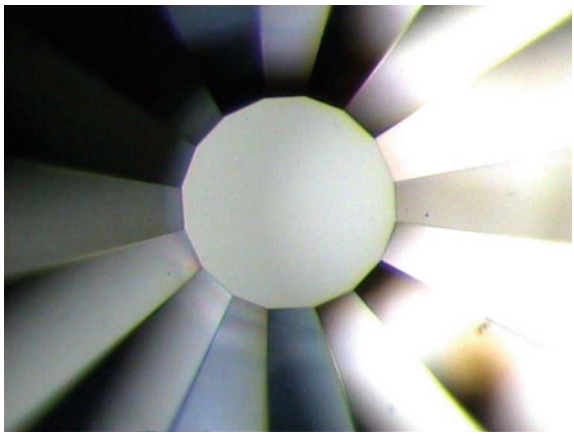


Fig. 29.3 Diamond anvil seen from *top* (Challenges for energy dispersive X-ray absorption spectroscopy at the ESRF: microsecond time-resolution and Megabar pressures, Giuliana Aquilanti PhD Thesis, http://tel.archives-ouvertes.fr/tel-00828730.)

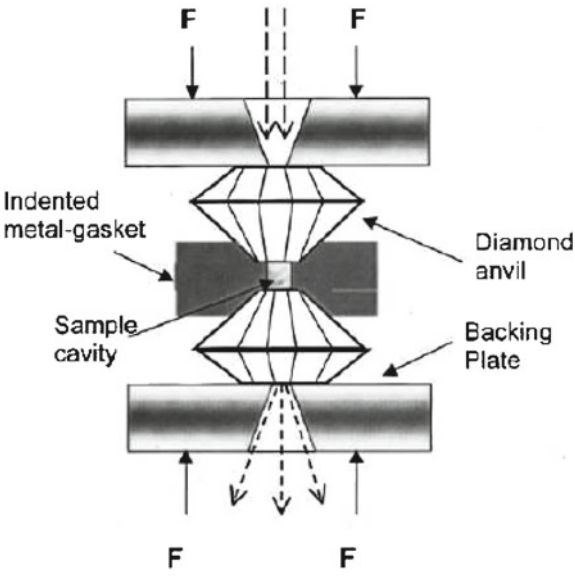


Fig. 29.4 Principle of DAC (Challenges for energy dispersive X-ray absorption spectroscopy at the ESRF: microsecond time-resolution and Megabar pressures, Giuliana Aquilanti PhD Thesis, http://tel.archives-ouvertes.fr/tel-00828730. Magnetism structure and chemical order in the 3d metals and their alloys at extreme pressures, Raffaella Torchio PhD Thesis, http://tel.archivesouvertes.fr/docs/00/69/78/78/PDF/34066_TORCHIO_2012_archivage.pdf)

force F, according to the well known relationship P = F/A. To apply pressure to the sample, the anvil faces must have a high degree of parallelism. One of the diamond anvils is usually mounted on the end of a sliding piston, while the other is stationary. A cylinder guides the piston so that the anvil faces meet very precisely. The piston is pushed by a mechanical device such as a screw or a small hydraulic or pneumatic ram, thus driving the two anvils together.

When the sample is placed between the anvil faces, as the anvils are forced together, the sample is trapped and develops a uniaxial pressure, whose distribution ranges from a maximum at the center to essentially zero pressure at the edge of the sample area. In order to have an isotropic pressure distribution the sample

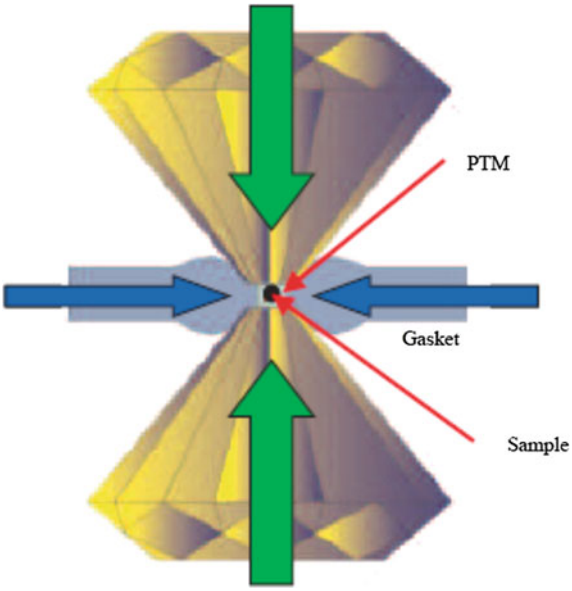


Fig. 29.5 The use of a PTM and of a gasket to encapsulate sample and PTM allows to overcome the uniaxial pressure generated by the diamonds and to have isotropic pressure (Challenges for energy dispersive X-ray absorption spectroscopy at the ESRF: microsecond time-resolution and Megabar pressures, Giuliana Aquilanti PhD Thesis, http://tel.archives-ouvertes.fr/tel-00828730.)

Table 29.1 Dimensions of anvil flat, gasket indentation thickness and maximum P achievable

Flat diameter (μ)	Indentation thickness (μ)	P max (GPa)
>500	50–60	<20
300	40–45	50–70
150	25–30	100–150
<100	20–25	>150

must be embedded and confined in a pressure transmitting medium (PTM) softer than the sample. To encapsulate the sample and the hydrostatic medium, both are placed in a small hole drilled in a metallic gasket (Fig. 29.5). The gasket consists of a metallic foil of typically 200 μm of thickness. To increase the hardness of the metal, the foil is placed between the two diamonds and is pre-indented to about 30–60 μm. The higher the pressure that has to be achieved during the experiment, the higher the pre-indentation pressure and the smaller the final gasket thickness (and sample volume). A hole in the pre-indented gasket is then drilled by electro-erosion or by a laser. The diameter of the hole depends critically on the diameter of the diamonds, and it is typically one third the diameter of the flat of the diamond.

Table 29.1 shows typical values of maximum pressures to reach and corresponding values of diameters of anvils flats and indentation thicknesses to use. Several methods for measuring pressure have been developed. If the experimental technique is in situ XRD, then the diffraction pattern of an internal standard such as NaCl or Au, can be obtained along with that of the sample. The pressure is then determined from the lattice parameters calculated from the diffraction pattern. Another means of measuring the pressure is the ruby fluorescence method. This method is particularly

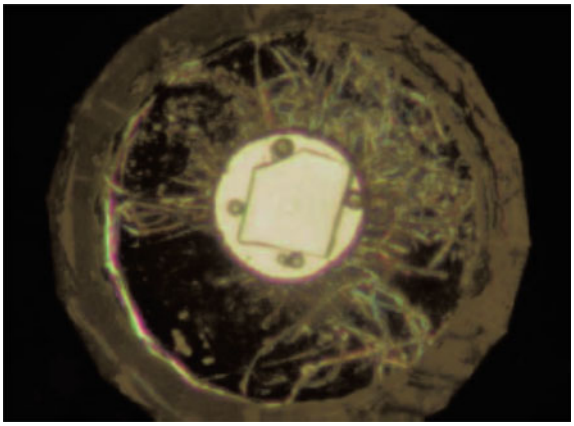


Fig. 29.6 Photo of a typical loading: the sample is inserted in the middle of the gasket hole, and 4 ruby spheres are placed around it (Magnetism structure and chemical order in the 3d metals and their alloys at extreme pressures, Raffaella Torchio PhD Thesis, http://tel.archivesouvertes.fr/docs/00/69/78/78/PDF/34066_TORCHIO_2012_archivage.pdf.)

well adapted to DAC technology since it exploits the high transparency of diamonds to visible light. Forman et al. [17] in 1972 first showed that the luminescence doublet of peaks R_1 and R_2 of Cr^{3+}-doped Al_2O_3 (ruby lines) shift linearly with hydrostatic pressure in the range of 1–2.2 GPa, and that the two lines broaden if the ruby experiences nonhydrostatic stresses. In this method a tiny chip of ruby (5–10 μm in dimensions) is placed in the pressure medium along with the sample (Fig. 29.6), and its luminescence is excited by a laser. The shift in wavelength is followed as a function of pressure.

To achieve simultaneous HP and HT conditions, resistive heating of the DAC allows to reach temperatures up to ∼1,000 K [18] whereas laser heating is required for higher temperatures [19].

29.2 Physics

29.2.1 Collapse of Ferromagnetism in the 3d Metals

The compression of interatomic distances in the *3d* metals (Fe, Co, Ni…) leads to variations in the elementary magnetic moment and in the Curie temperature. The former effect is generally interpreted, in the framework of the Stoner model, as a consequence of the decreased DOS at the Fermi level which follows from the pressure induced band broadening associated to the interatomic distance squeezing. As an example, high pressure (zero temperature) DOS calculations for pure Ni are

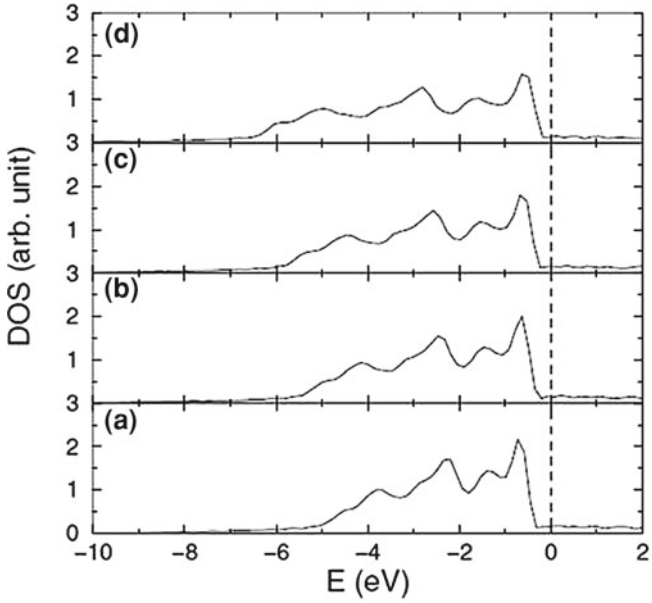


Fig. 29.7 Pressure dependence of the spin-up density of states in Ni. **a** P = 0 GPa, **b** P = 20 GPa, **c** P = 40 GPa, **d** P = 80 GPa From [20]

shown from Xie and co-workers up to 80 GPa [20] in Fig. 29.7. As the pressure is increased, the DOS spread out and the height of the DOS at the Fermi level decreases.

The latter effect, the Curie temperature shift with pressure, is related to the variation in the exchange interactions. Experimental observations of the Curie temperature shift with pressure only reach 2, 15 and 25 GPa for Fe, Ni and Co respectively. In this low pressure range, T_c is seen to remain constant (Fe) or to increase (Co and Ni).

In the *3d* metals the loss of ferromagnetism is generally concomitant to a structural transition. Several zero temperature high pressure calculations have been carried out, and there is a general agreement on the expected pressure induced magnetic/structural transitions. Fe is predicted to transform from the bcc ferromagnetic to hcp non-magnetic phase around 10–15 GPa [21, and refs. therein]; ferromagnetic Co would transform into a non magnetic fcc phase around 100 GPa [22], while Ni is expected to remain in a stable fcc ferromagnetic structure up to the 10^2 GPa range [21, 22]. In the *3d* metals compression thus favors closed packed arrangements and a higher resistance of magnetism can be associated to a stronger ferromagnetism, following from the progressive filling of the minority *d*-band when going from Fe to Ni. However, a large debate is still open on whether structural instabilities are driven by magnetic instabilities or viceversa.

The advantage of high pressure studies with respect to high temperature ones, is that high pressure can bring to real non-magnetic states (characterized by zero local moment), to be distinguished from the T-induced paramagnetic states where the

magnetic order has been disrupted but an elementary moment still exists. However, as mentioned above, also the Curie temperature is expected to vary with pressure and the disentanglement of the two effects—i.e. suppression of elementary moment and thermal disorder—may not be trivial.

From the experimental point of view, the loss of ferromagnetism in Fe, Co and Ni upon compression has been probed by K-edge X-ray magnetic circular dichroism (XMCD) by a number of groups. Polarized X-ray absorption spectroscopy contains intrinsic structural, electronic, and magnetic probes through the combination of the XANES and the XMCD signals. Thus, for each pressure point, simultaneous information on both the magnetic and the structural properties of the system can be provided without any relative pressure incertitude, which is very important in the high pressure domain where the reproducibility of high-pressure hydrostatic conditions is difficult to obtain.

These are challenging experiments due to the very small amplitude of the K-edge XMCD signal (of the order of 10^{-3}) and to the strong absorption of X-rays by the diamond anvils. At 7.1 keV—the Fe K-edge energy—the transmission of two 2 mm thick diamond anvils is $\sim 10^{-4}$. Early work using XMCD was carried out on pure Fe [23]. Subsequent important systematic studies on the *3d* metals were then published by Iota and co-workers [24] and Ishimatsu and co-workers [25, 26] and more recently by Torchio [27, 28].

The theoretical interpretation of the signal is also complex. Contrary to $L_{2,3}$ edge spectroscopies which directly probe the final 3d states, K-edge absorption spectroscopy probes 4p final states: information on the 3d magnetic moment arises indirectly through spin-orbit coupling (3d spin moment $\rightarrow$ 3d orbital moment) and p-d hybridization (3d $\rightarrow$ 4p). In recent years, much progress has been made in the theoretical understanding of this spectroscopic tool, mainly thanks to the possibility to measure very small signals with high precision and in a large pressure range [28]. Figure 29.8 summarizes the results of recent experimental and theoretical work in this field. The top panel reports the integral of the measured XMCD signal, whereas the bottom panel reports the theoretical calculation of the total spin moment. As can be seen, the ordered magnetic moment decreases for the three metals upon compression, but the evolution and the pressure limit for total suppression differ for Fe, Co and Ni.

29.2.2 Examples of Recent Work on Fe, Co and Ni

29.2.2.1 Iron

Thanks to the lower pressure range, the iron case has been widely investigated. At room temperature and atmospheric pressure, pure iron is stable in the bcc (α) ferromagnetic phase. This phase is believed to be stabilized by magnetism [29]. Under the application of an external pressure at ambient T, iron undergoes a transition at 13 GPa from the bcc α-phase to the hcp ϵ-phase structure, with the loss of its

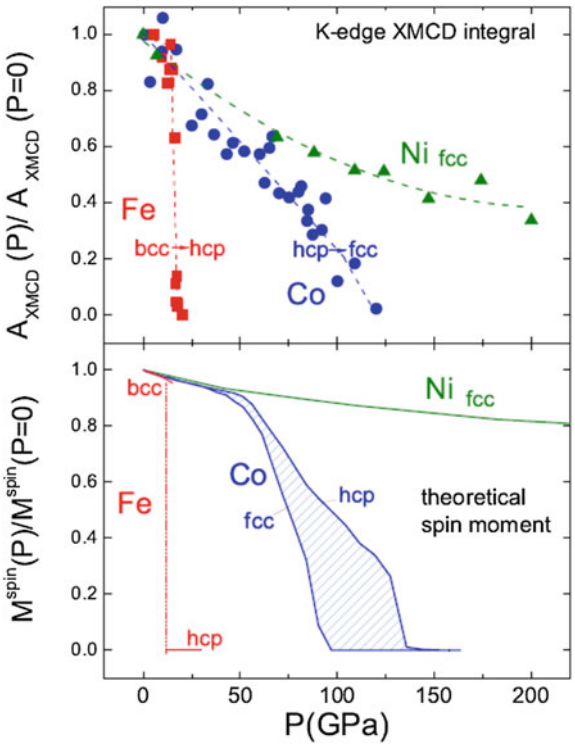


Fig. 29.8 Recent results on Fe, Co and Ni. *Top* integral of the measured XMCD signal; *Bottom* theoretical calculation of total spin moment (Magnetism structure and chemical order in the 3d metals and their alloys at extreme pressures, Raffaella Torchio PhD Thesis, http://tel.archivesouvertes.fr/docs/00/69/78/78/PDF/34066_TORCHIO_2012_archivage.pdf)

ferromagnetic long range order [30, 31]. The evolution with pressure of the magnetic and structural state across this transition is still a subject of active theoretical and experimental research. Moreover, a large debate is still open on which, between the structural and magnetic degrees of freedom, plays a driving role. Many ab initio theoretical studies of this transition have been carried out (see [2] and references therein). The first order nature of the structural and magnetic transitions is well established as well as the non ferromagnetic state of the hcp phase. Some theoretical works support that the phase transition is primarily due to the effect of pressure on the magnetism, rather than induced by phonon softening.

Structural investigations have been reported using X-ray diffraction [25, 30, 32, among others] and extended X-ray absorption fine structure (EXAFS) [33]. The iron bcc-hcp phase transition is described as a martensitic transition with a slow variation of the relative bcc and hcp phases abundance. Distorted bcc and hcp phases with anomalously large lattice constant (bcc) and c/a ratio (hcp) when the relative amounts become small are reported and attributed to interfacial strain between the bcc and the hcp phases. Magnetic measurements based on Mossbauer techniques [31] and on inelastic X-ray scattering [34] showed that the magnetic moment of iron decreases over the same pressure range as the bcc to hcp transition, i.e., 8 GPa.

Nevertheless, the lack of reproducibility of high-pressure conditions does not allow a precise correlation between the structural and the magnetic transition when measured separately. An accurate combined XMCD/XANES study [23] suggests that the magnetic transition slightly anticipates the structural one supporting a magnetism driven process in agreement with phonon dispersion measurements.

29.2.2.2 Cobalt

Under ambient conditions cobalt crystallizes into a ferromagnetic hcp structure [32], often coexisting with a metastable cubic close-packed fcc phase. This is in contrast to the *4d* and *5d* counterparts Rh and Ir, which show nonmagnetic fcc structure. The fact that the hcp structure is more stable than the fcc structure in Co is due to the presence of magnetism [29]. The equation of state (EOS) of hcp Co has been widely investigated both experimentally and theoretically [32]. In 2000 Yoo and co-workers [35] reported the first evidence of a pressure induced hcp-fcc transition in cobalt characterized by no change in volume and a broad coexistence range (about 100–150 GPa). Such a big interval of co-existence was attributed to the small energy difference between the two phases and to a possible non hydrostaticity of the sample. The high-pressure fcc phase of cobalt is generally thought to be non magnetic and favoured with respect to the hcp-ferromagnetic phase starting from 80 to 100 GPa [29]. The hcp and fcc structures differ only in their stacking sequence of the planes, so the transition requires relatively small atomic displacements and thus occurs martensitically [22].

Results of recent XMCD and XANES measurements (shown in Fig. 29.9 left panel) coupled to FEFF and DFT calculations give a complete description of the structural and magnetic Co phase transition [27], highlighting major differences with the Fe case. A continuous reduction of the XMCD intensity is observed until complete suppression at 120 ± 10 GPa. A progressive change in the arrangement of the first atomic shells from an hcp- to an fcc-like local structure starting from P $\approx$ 80 GPa can be detected from the XANES, providing a coherent scenario which correlates well with elastic and structural anomalies reported in the same pressure range. The magnetic response in Co, as seen from K-edge XMCD, seems to be uniquely affected by compression and not by structural modifications.

The combination of experimental and theoretical results support the total disappearance of spin magnetization (local magnetic moment) in the mixed hcp/fcc phase around 120 ± 10 GPa. Nevertheless a similar study by Ishimatsu and co-workers [26] did not observe the total extinction of the signal. This finding was interpreted as the occurrence of a paramagnetic phase in Co above 150 GPa. These disagreements claim for further experimental work aimed at the coupling of HP and LT conditions.

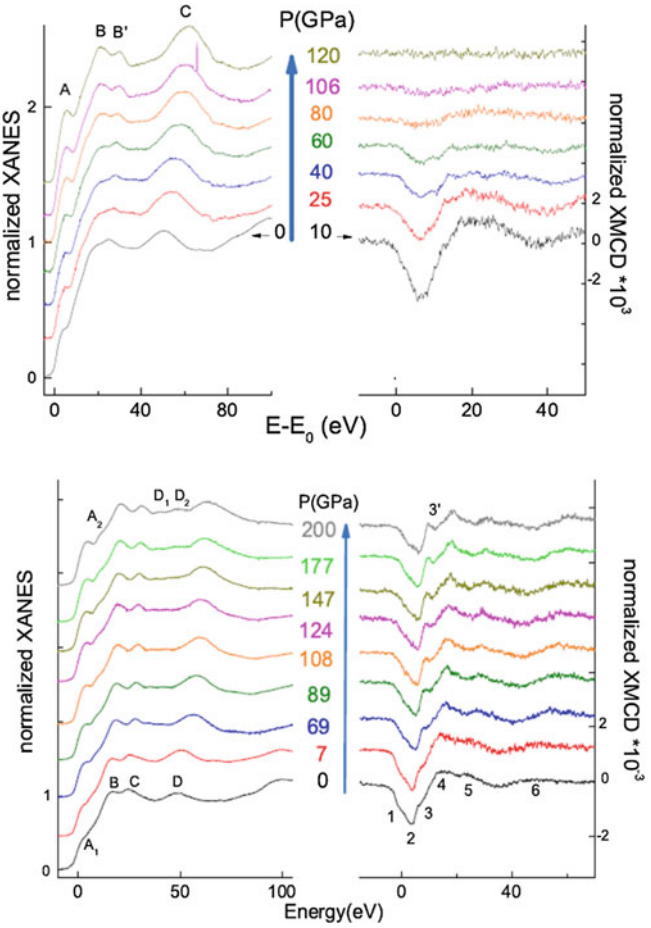


Fig. 29.9 *Top* Co K-edge XANES and XMCD from ambient up to total extinction of the XMCD signal at ∼120 GPa. From [27] *Bottom* Ni K-edge XANES and XMCD as a function of pressure. The XMCD signal is strongly attenuated with pressure but ferromagnetism persists up to 200 GPa, the maximum pressure reached before anvils failure. From [28]

29.2.2.3 Nickel

The fundamental interest in nickel stems from its simplicity. As seen previously, in iron and cobalt the collapse of ferromagnetism with pressure is related to a structural phase transition. The pressure limit of ferromagnetism in Ni is still not established, and the fcc structure is stable in a very large P-T interval. In fact, neither pressure nor temperature induced structural transitions have been ever reported in the so far explored P-T range: up to 150 GPa at RT and up to melting temperatures in the 0–110 GPa range. Such a high structural stability offers a unique opportunity to

investigate how the simple compression of the interatomic distance influences the magnetic properties.

At ambient conditions Ni crystallizes into a ferromagnetic fcc structure. At room temperature the fcc symmetry is retained up to at least 150 GPa as seen by diffraction [32]. Theoretical calculations agree on the high pressure stability of the fcc phase in the 10^2 GPa range and above [20, 21, 36]. The Curie temperature (T_{rmc}) of Ni is 631 K at ambient pressure and it increases up to 15 GPa with some tendency to saturation. Recent work based on first-principles calculations and partition function approach [20] predicts T_c to start decreasing sharply around 120 GPa and reaching ambient temperature around 160 GPa. But, recent XRD combined to XMCD measurements on pure Ni up to 200 GPa [28] show that fcc Ni is structurally stable and ferromagnetic up to 200 GPa (Fig. 29.9 right panel) in contrast to the prediction of an abrupt transition to a paramagnetic state at 160 GPa. Moreover, novel DFT calculations allow to get an insight into the different behavior of orbital and spin moments in compressed Ni, pointing out that the pressure evolution of the Ni K-edge XMCD closely follows that of the p projected orbital moment rather than that of the total spin moment. According to these calculations, the disappearance of magnetism in Ni is predicted to occur above 400 GPa.

29.3 Earth Science

29.3.1 Fe Partitioning in the Earth Mantle

Because of its abundance and possible changes in oxidation state, iron is one of the major elements governing past and present of Earth (see for example a recent review in [37]), and knowledge of its oxidation state and its partitioning between different co-existing minerals is fundamental. By combining synchrotron radiation XRD and Fe K-edge XANES in a laser-heated DAC it is now possible to investigate iron valence and partitioning at conditions of Earth's mantle as well as at and beyond the CMB.

The upper mantle is essentially constituted of olivine $(Mg_{1-x}Fe_x)_2SiO_4$ and its high-pressure and high-temperature polymorphs, whereas the lower mantle mainly contains silicate perovskite $(Mg,Fe)SiO_3$ and ferropericlase (Mg,Fe)O minerals, as well as post-perovskite $(Mg,Fe)SiO_3$, most likely located close to the CMB (in the so-called D" layer region—see also Fig. 29.2). Olivine is known to transform to a modified spinel (wadsleyite) and γ-spinel (ringwoodite) structures respectively, at ~13.5 GPa/1,100 K and ~18 GPa/1,200 K. At 660 km in depth (~24 GPa/1,600 K)—at the border between the upper and lower mantle—in correspondence to an important seismic discontinuity, ringwoodite (Rw) decomposes into Fe perovskite (Pv) and ferropericlase (Fp). The reaction of geophysical interest in the following:

$$(Fe_{0.12}Mg_{0.88})_2SiO_4 \rightarrow (Fe_x, Mg_{1-x})SiO_3 + (Fe_y, Mg_{1-y})O \qquad (29.1)$$

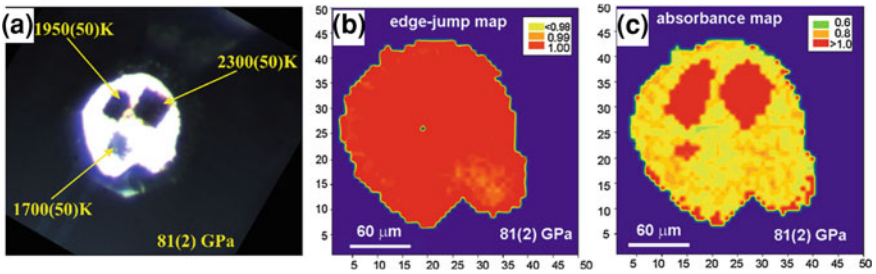


Fig. 29.10 **a** Optical image of the starting $(Mg_{0.88}\ Fe_{0.12})_2SiO_4$ Rw compressed in a LiF pressure medium in a DAC, where different parts of the sample were laser heated at 1,700(50) K, 1,950(50) K and 2,300(50) K at 81(2) GPa. Pre-normalised-XANES edge-jump map (**b**) and normalised absorbance map (**c**), plotted at 7,132 eV, collected after laser heating at 81(2) GPa. From [39]

As shown by their structural formula, each of the crystalline phases of the Earth's mantle allows iron–magnesium substitutions. The partitioning of Fe and Mg between co-existing Pv and Fp, can be calculated from the following ion exchange reaction:

$$FeSiO_3(Pv) + MgO(Fp) \Leftrightarrow MgSiO_3(Pv) + FeO(Fp)$$

characterised by the apparent partition coefficient, K_D:

$$K_D = \frac{\left(X_{Fe}/X_{Mg}\right)^{Pv}}{\left(X_{Fe}/X_{Mg}\right)^{Fp}} \tag{29.2}$$

where X is the molar fraction of Fe (Fe^{2+} and Fe^{3+}) or Mg in Pv or Fp. Although Fe–Mg partitioning between Pv and Fp as a function of pressure, temperature, and composition has been extensively studied, neither the absolute values, nor even the pressure–temperature trend of K_D are well defined [38]. The reasons for the discrepancies relate to the difficulty in performing high quality chemical analyses of the samples treated in DACs in the megabar pressure range and the lack of in situ partitioning experiments.

Fe K-edge XANES on a $(Fe_{0.12}\ Mg_{0.88})_2\ SiO_4$ ringwoodite sample in a DAC were measured at different pressures, up to ~115 GPa, before and after laser heating [39]. In order to track temperature gradients and absorber inhomogeneities (that can occur under strong thermal gradients), two dimensional information over the whole surface of the sample is acquired [40]. 2D maps are obtained, where each pixel contains full XANES information [41]. Figure 29.10 reports the optical image (panel a), the edge-jump map (panel b) and the absorbance map—value of absorption at fixed energy—(panel c) of a Rw sample compressed up to 81 GPa and then laser heated to increasing temperatures (1700, 1950 and 2300 K) in three different regions. Absorber homogeneity is maintained upon laser heating, as testified by the constant value of the jump in panel b (the little dot in the center is a small ruby sphere).

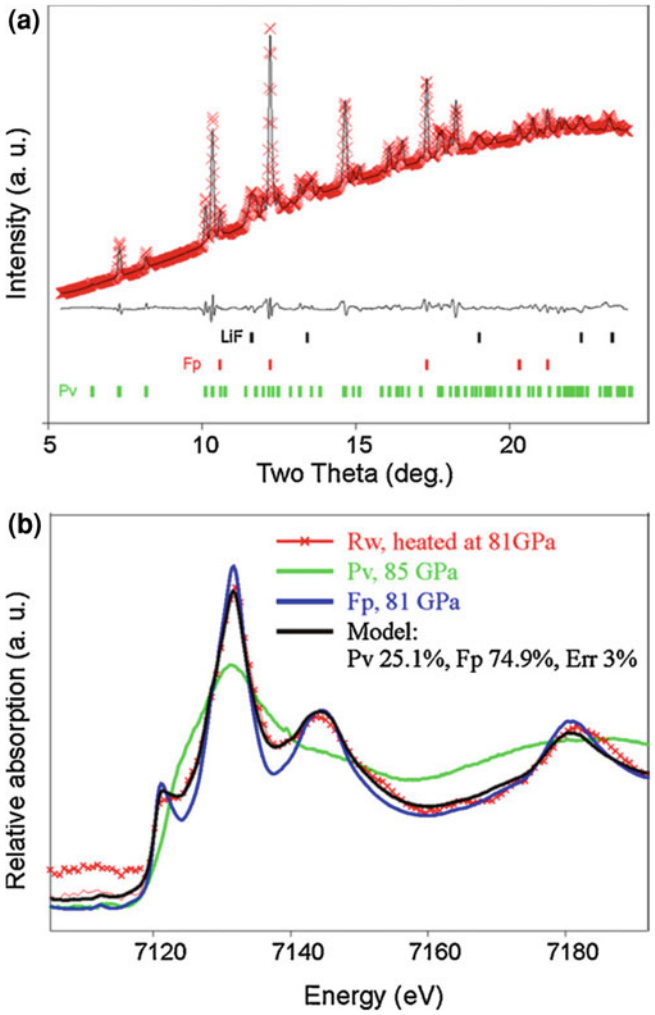


Fig. 29.11 **a** X-ray diffraction pattern from Rw laser heated at 2,300(50) K and 81(2) GPa. **b** Deconvolution of the XANES spectrum, collected from the area that was laser-heated at 81(2) GPa and 2,300(50) K. From [39]

Chemical decomposition in the three laser heated regions is clearly visible in the optical image (panel a) and in the absorbance map (panel c). Figure 29.11 reports an XRD pattern and XANES collected on the sample at 81 GPa and heated to 2,300 K. Apart from LiF (used as pressure transmitting medium) only diffraction peaks from Pv and Fp are observed, confirming the complete decomposition of Rw to Pv and Fp in the proportion 1:1 via the breakdown reaction (29.1).

The deconvolution of the XANES yields a 1:3 ratio between the Pv and Fp components: Fe has a preference for a Fp environment. Using the combined informa-

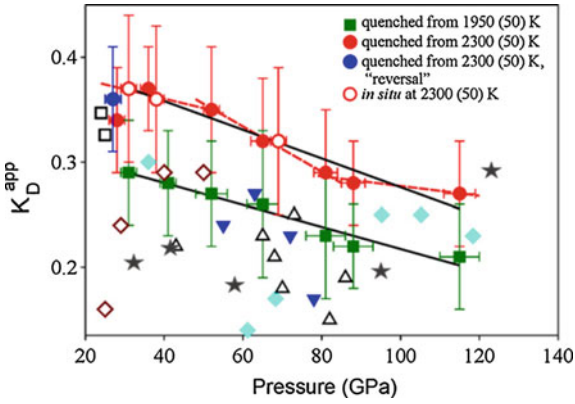


Fig. 29.12 Apparent Fe–Mg partition coefficient between (Mg,Fe)SiO_3 Pv and (Mg,Fe)O Fp as a function of pressure and temperature. From [39]

tion from the XRD and XANES, it was possible to extract the partitioning coefficients. Figure 29.12 illustrates the apparent Fe–Mg partition coefficient between (Mg,Fe)SiO_3 Pv and (Mg,Fe)O Fp as a function of pressure and temperature up to 120 GPa and 2,300 K. The combined results show that temperature promotes iron partitioning into Pv, while pressure acts oppositely.

29.3.2 Fe Partitioning at and Beyond the Core-Mantle Boundary

At P,T conditions of the CMB, the phase diagram for (Fe,Al)-bearing $MgSiO_3$ remains ambiguous. The sharp phase transition in $MgSiO_3$ from perovskite (Pv) to post-perovskite (PPv) has been often invoked in order to explain seismic observations of the D" layer [42]. On the other hand, actual seismic evidences correspond to local phenomena in specific mantle regions, rather than to geographically extended mantle features, in sharp contrast with what is observed at 410 and 660 km depth discontinuities. A number of models have been proposed to explain the regional character of the D" features [43]. In most of these the effects of Fe^{2+} or Fe^{3+}, and Al^{3+} major elements on the Pv to PPv phase transition are neglected due to lack of in-situ data. Their presence and distribution can modify severely the transition depth as well as the depth over which the two phases coexist in the D" layer. This issue remains very controversial, based on the three sources of information available to date (i) in-situ XRD in the laser-heated DAC (LH-DAC), (ii) post-mortem examination of LH-DAC samples using transmission electron microscope and (iii) ab initio structure simulations. Large uncertainties concern both the Pv and PPv phase fractions as a function of P, T and composition and the Fe and Al partitioning coefficients between the two phases.

Combined XRD and Fe K-edge XANES were used to investigate the partitioning of iron between Pv and PPv up to more than 150 GPa after annealing at about 3,300 K [44].

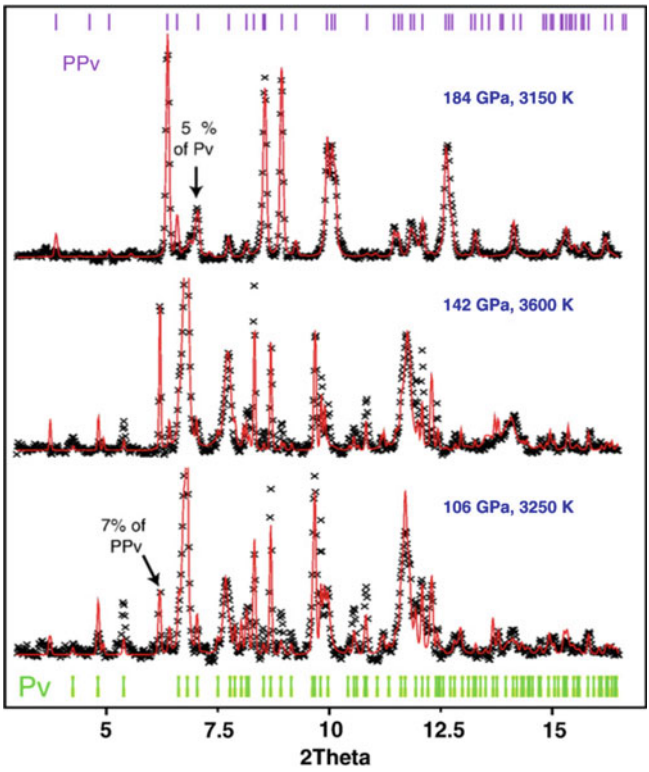


Fig. 29.13 Integrated diffraction patterns recorded for Al-bearing $(Mg,Fe_{0.19})SiO_3$ Codera samples after laser heating at pressures of 106, 142 and 184 GPa. From [44]

XRD patterns recorded on Al-bearing $(Mg,Fe_{0.19})SiO_3$ Codera samples after laser heating at pressures of 106, 142 and 184 GPa are shown in Fig. 29.13. Pv and PPv phases are found to co-exist throughout the full pressure range. The PPv content increases from 7 to 36 and 95 % with increase pressure. Fe K-edge XANES, illustrated in Fig. 29.14, show important changes in the Fe local structure when the Fe environment changes progressively from Pv to PPv. By using an iterative calculation and the measured Pv/PPv phase fractions obtained by XRD, it was possible to extract XANES corresponding to the "pure" Pv and PPv phases. The spectrum at 142 GPa could then be reproduced using a linear combination of these. A unique solution for the Fe partitioning coefficient Pv/PPv of 4.2 ± 0.5 is found. The main results evidence that the two silicates should coexist over the whole D" region, with the main post-perovskite phase being largely depleted in Fe compared to the perovskite.

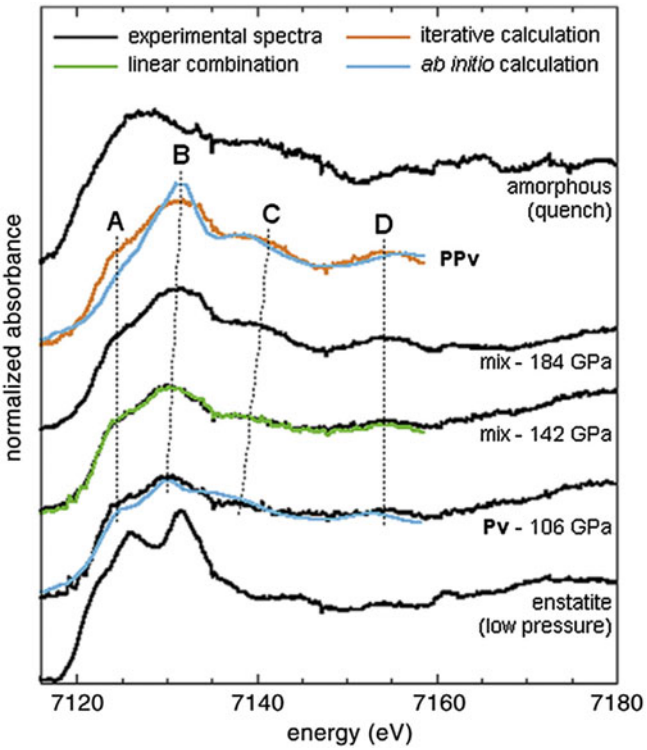


Fig. 29.14 XANES as a function of pressure (*black lines*) or calculated (*color lines*) at the Fe K-edge for the Codera sample. Spectra of the enstatite starting material and amorphous quenched material are shown for comparison. From [44]

29.4 Energy, Environment, Climate

29.4.1 The Deep Carbon Cycle

Carbon-based fuels supply most of our energy, while small carbon-containing molecules in Earth's atmosphere play a major role in our variable and uncertain climate. The nature and extent of carbon reservoirs and fluxes in Earth's deep interior are not well known. The primitive chondritic meteorites that formed our planet average ~3.2 % carbon, yet estimates of Earth's total carbon inventory are much lower, ranging from 0.07 to 1.5 wt% (an uncertainty of more than 20-fold). Earth appears to be significantly depleted in highly volatile elements compared to chondrites, but we do not know for sure because large reservoirs of carbon may be hidden in the mantle and core. Likewise, we know that the subduction of tectonic plates and volcanic outgassing are primary vehicles for carbon fluxes to and from deep in Earth, but the

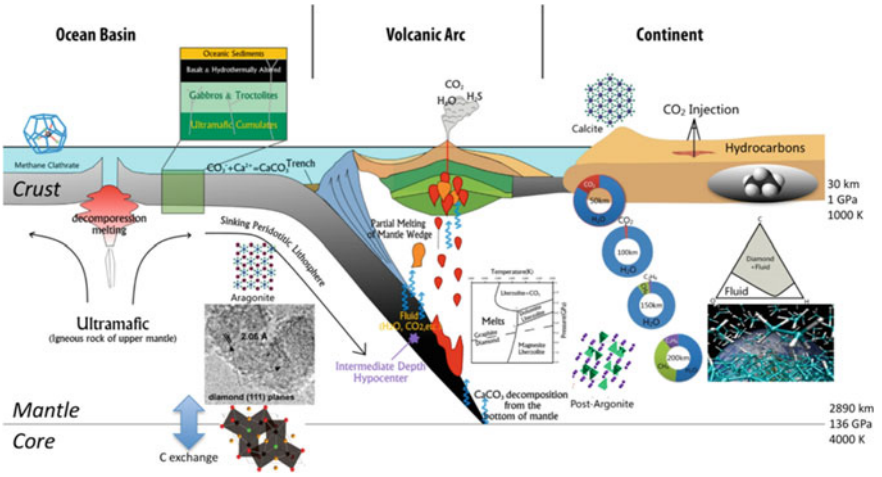


Fig. 29.15 The deep carbon cycle. http://www.lens.unifi.it/images/news/deep_carbon_cycle.png

processes and rates of these fluxes—as well as their variation throughout Earth's history—remain poorly understood.

The deep carbon cycle (see Fig. 29.15) has unknown and potentially profound connections to societal concerns related to energy, environment and climate. Anecdotal, and often contradictory, evidence has pointed to possible abiotic organic synthesis in some deep crustal and mantle environments. Deep organic synthesis may contribute to hydrocarbon energy resources and may have played a role in life's origins as well. Below, two examples of recent high pressure research directions are illustrated: understanding formation processes and stability of hydrocarbons (Sect. 29.4.2) , and exploring new chemical forms of carbon in the deep Earth (Sect. 29.4.3).

29.4.2 Stability of Hydrocarbons in the Deep Earth

Determining the thermochemical properties of hydrocarbons (HCs) at high pressure and temperature is a key step toward understanding carbon reservoirs and fluxes in the deep Earth. The stability of carbon-hydrogen systems at depths greater than a few thousand meters is poorly understood and the extent of abiogenic HCs in the Earth mantle remains controversial. Much effort is therefore today being devoted today to understand the chemistry and biochemistry of HC formation (for example [45]). In the case of methane, many open questions remain concerning its dissociation and possible polymerization under pressure, in spite of the increasing number of experiments carried out in recent years. Laboratory experiments indicate that methane can form under P-T conditions of the Earth's upper mantle through carbonate reduction

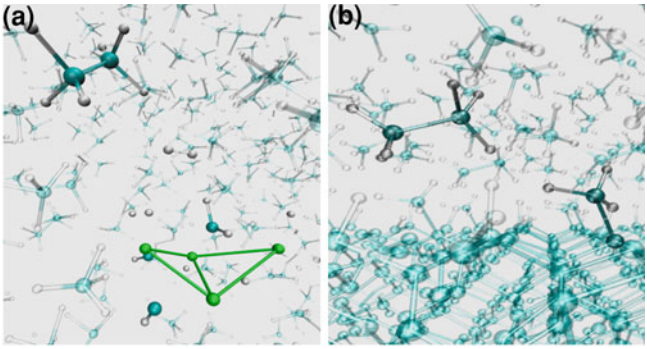


Fig. 29.16 Snapshots from ab-initio simulations. From [45]

processes [46]. Early laser-heated DAC experiments [47] indicated the formation of both HCs and diamond at 19 GPa and 2,000–3,000 K. Raman measurements support the formation of ethane, propane, and butane upon methane compression, in a range of pressure and temperature compatible with upper mantle conditions, i.e., P $\sim$ 2–5 GPa and T $\sim$1,000–1,500 K. Ethane was also found as a reaction product in a DAC experiment at T $>$1100 K and P $>$10 GPa. Substantial experimental evidence indicates that heavier hydrocarbons form upon compression of methane. This stimulates theoretical efforts to investigate the relative stability of methane and higher HCs. Recent ab-initio calculations [45] show that for T $\sim$ 2,000 K and P $\sim$ 4 GPa HCs higher than methane are energetically favoured. Moreover, the interaction of methane with a transition metal facilitates the formation of these HCs in a range of temperature where otherwise pure methane would be metastable. Such theoretical approaches help both in the interpretation of experiments but also provide detailed microscopic models of methane dissociation and polymerization at high pressure and temperature.

For example, Fig. 29.16 shows snapshots from ab initio simulations. The left panel illustrates methane in contact with an Ir_4 cluster at 2,500 K and 4 GPa: the Ir_4 cluster acquires a butterfly shape and several fragments—CH_3 and CH_2—are observed during the simulation together with molecular hydrogen and ethane. The right panel shows liquid methane in contact with a partially H-terminated diamond surface [100] at 2,500 K and P $\sim$4 GPa. A CH_3 group attached to the surface and a newly formed ethane molecule are highlighted.

29.4.3 Exploring the Nature of C-bearing Minerals

The global geochemical carbon cycle involves exchanges between the Earth's interior and surface (see Fig. 29.15). Carbon is recycled into the mantle via subduction mainly as carbonates and is released to the atmosphere via volcanism mostly as CO_2.

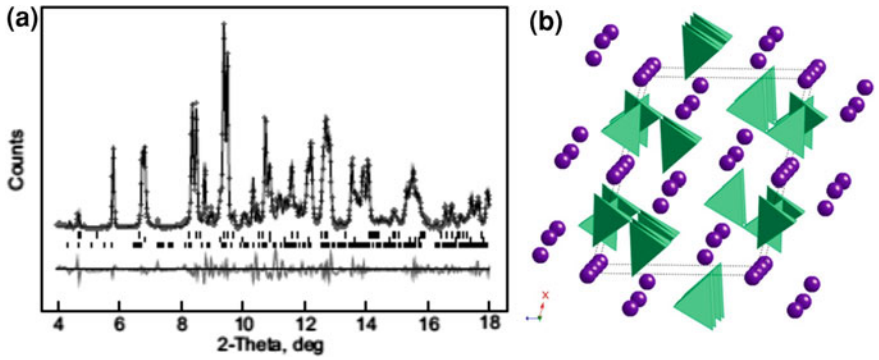


Fig. 29.17 *Left* XRD pattern collected at 80 GPa and room temperature of siderite transformed at 1,850–2,300 K. *Right* Structure of the new high-pressure phase. $(CO_4)^{4-}$ tetrahedra appear in green and magnesium atoms are shown as *violet spheres*. From [48]

Together with primordial C, this subducted component is considered to contribute significantly to the lower mantle carbon reservoir. Because of its very low solubility in deep Earth's minerals, C is likely to be present as a separate phase, either as carbonates or as diamonds. Much experimental and theoretical research effort is devoted to trying to identify the most important hosts of C at depth. Several studies have suggested that magnesium carbonate (magnesite—$MgCO_3$) could become the main host for C at depth at the expense of other minerals.

Recent X-ray diffraction (XRD) patterns collected at P and T of about 80 GPa—2,400 K on $MgCO_3$ and on the assemblage $MgO + CO_2$ [48], show several new peaks that cannot be attributed to the known structures of MgO and CO_2 oxides nor to magnesite. Rather, they indicate that a new structure is stabilized in this pressure range. Upon quenching to room temperature, the high-pressure phase is back-transformed to the low-pressure magnesite structure. In contrast with the $MgCo_3$ end member, a similar treatment on Fe-bearing (FeMg) CO_3 (siderite) produces a new high pressure structure that is quenchable (see Fig. 29.17).

This new Mg–Fe carbon-bearing compound could therefore be found at conditions corresponding to depths greater than 1,800 km. Its structure, based on three-membered rings of corner-sharing $(CO_4)^{4-}$ tetrahedra, closely agrees with predictions by first principles quantum calculations [49].

This high-pressure polymorph of carbonates concentrates a large amount of Fe^{3+} as a result of intracrystalline reaction between Fe^{2+} and $CO_3{}^{2-}$ groups schematically written as $4FeO + CO_2 \rightarrow 2Fe_2O_3 + C$. This results in an assemblage consisting of the new high-pressure phase, magnetite and nanodiamond.

References

1. R.A. Graham, (Springer, New York 1993)
2. M. Ekman, B. Sadigh, K. Einarsdotter, P. Blaha, Phys. Rev. B **58**, 5296 (1998)
3. S. Minomura, H.G. Drickamer, J. Phys. Chem. Solids **23**, 451–456 (1962)
4. V.V. Struzhkin, H.K. Mao, J. Hu, M. Schwoerer-Bohning, J. Shu, R.J. Hemley, W. Sturhahn, M.Y. Hu, E.E. Alp, P. Eng, G. Shen, Phys. Rev. Lett. **87**, 255501(4) (2001)
5. E. Gregorianz, V.V. Struzhkin, R.J. Hemley, M.I. Eremets, H.K. Mao, Y.A. Timofeev, Phys. Rev. B **65**, 64504(6) (2002)
6. A.G. Gavriliuk, I.A. Trojan, V.V. Struzhkin, Insulator-Metal Transition in Highly Compressed NiO. Phys. Rev. Lett **109**, 086402 (2012)
7. J.-W.G. Bos, B.B. Van Aken, T.T.M. Palstra, Chem. Mater. **13**, 4804–4807 (2001)
8. C.J. Pickard, R.J. Needs, Nat. Mater. **9**(8), 624–627 (2010)
9. M. Citroni, M. Ceppatelli, R. Bini, V. Schettino, High Press. Res. **22**, 507–510 (2002)
10. J. Bass (ed.), *Current and Future Research Directions in High Pressure Mineral Physics* (COMPRES, New York, 2004)
11. Deep Carbon Observatory. http://www.deepcarbon.net/
12. D. Antonangeli, J. Siebert, J. Badro, D.L. Farber, G. Fiquet, G. Morard, F.J. Ryerson, Earth Planet. Sci. Lett. **295**, 292–296 (2010)
13. G. Steinle-Neumann, L. Stixrude, R.E. Cohen, O. Gulseren, Nature **413**, 57–60 (2001)
14. M.I. Eremets, (Oxford University Press, Oxford, 1996)
15. A. Jayaraman, Rev. Mod. Phys. **55**, 65–108 (1983)
16. J.A. Xu, H.K. Mao, P.M. Bell, Science **232**, 1404–1406 (1996)
17. R.A. Forman, G.J. Piermarini, J.D. Barnett, S. Block, Science **176**, 284–285 (1972)
18. S. Pasternak, G. Aquilanti, S.A. Pascarelli, R. Poloni, B. Canny, M.V. Coulet, L. Zhang, Rev. Sci. Instrum. **79**, 085103(5) (2008)
19. E. Schultz, M. Mezouar, W. Crichton, S. Bauchau, G. Blattmann, D. Andrault, G. Fiquet, R. Boehler, N. Rambert, B. Sitaud, P. Loubeyre, High Press. Res. **25**, 71–83 (2005)
20. J. Xie, S.P. Chen, H.V. Brand, R.L. Rabie, J. Phys. Condens. Matter **12**, 8953–8962 (2000)
21. Y.S. Mohammed, Y. Yan, H. Wang, K. Li, X. Du, J. Magn. Magn. Mater. **322**, 653–657 (2010)
22. J.E. Saal, S. Shang, Y. Wang, Z. Liu, J. Phys. Condens. Matter **22**, 096006(6) (2010)
23. O. Mathon, F. Baudelet, J.P. Itié, A. Polian, M. d'Astuto, J.C. Chervin, S. Pascarelli, Phys. Rev. Lett. **93**, 255503(4) (2004)
24. V. Iota, J.P. Klepeis, C. Yoo, J. Lang, D. Haskel, G. Srajer, Appl. Phys. Lett. **90**, 042505(3) (2007)
25. N. Ishimatsu, H. Maruyama, N. Kawamura, M. Suzuki, Y. Ohishi, O. Shimomura, J. Phys. Soc. Jpn **76**, 064703(7) (2007)
26. N. Ishimatsu, N. Kawamura, H. Maruyama, M. Mizumaki, T. Matsuoka, H. Yumoto, H. Oashi, M. Suzuki, Phys. Rev. B **83**, 180409(4)(R) (2011)
27. R. Torchio, A. Monza, F. Baudelet, S. Pascarelli, O. Mathon, E. Pugh, D. Antonangeli, J.P. Itie, Phys. Rev. B **84**, 060403(4)(R) (2011)
28. R. Torchio, Y.O. Kvashnin, S. Pascarelli, O. Mathon, C. Marini, L. Genovese, P. Bruno, G. Garbarino, A. Dewaele, F. Occelli, P. Loubeyre, Phys. Rev. Lett. **107**, 237202(5) (2011)
29. P. Söderlind, R. Ahuja, O. Eriksson, J.M. Wills, B. Johansson, Phys. Rev. B **50**, 5918–5927 (1994)
30. J.C. Jamieson, A.W. Lawson, J. Appl. Phys. **33**, 776–780 (1962)
31. M. Nicol, G. Jura, Science **141**, 1035–1038 (1963)
32. A. Dewaele, M. Torrent, P. Loubeyre, M. Mezouar, Phys. Rev. B **78**, 104102(13) (2008)
33. F.M. Wang, R. Ingalls, Phys. Rev. B **57**, 5647–5634 (1998)
34. J.P. Rueff, M. Krisch, Y.W. Cai, A. Kaprolat, M. Hanfland, M. Lorenzen, C. Maschiovecchio, R. Verbeni, F. Sette, Phys. Rev. B **60**, 14510–14512 (1999)
35. C.S. Yoo, H. Cynn, P. Sonderlind, V. Iota, Phys. Rev. Lett. **84**, 4132–4135 (2000)
36. A.K. McMahan, R.C. Alberts, Phys. Rev. Lett. **49**, 1198–1201 (1982)

37. B.J. Wood, M.J. Walter, J. Wade, Nature **441**, 825–833 (2006)
38. A.L. Auzende, J. Badro, F.J. Ryerson, P.K. Weber, S.J. Fallon, A. Addad, J. Siebert, G. Fiquet, Earth Planet. Sci. Lett. **269**, 164–174 (2008)
39. O. Narygina, L. Dubrovinsky, H. Samuel, C.A. McCammon, I.Y. Kantor, K. Glazyrin, S. Pascarelli, G. Aquilanti, V.B. Prakapenka, Phys. Earth Planet. Inter. **185**, 107–111 (2011)
40. G. Aquilanti, S. Pascarelli, O. Mathon et al., J. Synchrotron Radiat. **16**, 376–379 (2009)
41. M. Munoz et al., High Press. Res. **28**, 665–673 (2008)
42. M. Murakami, K. Hirose, K. Kawamura, N. Sata, Y. Ohishi, Science **304**, 855–858 (2004)
43. J. Wookey, S. Stackhouse, J.M. Kendall, J.P. Brodholt, G.D. Price, Nature **438**, 1004–1007 (2005)
44. D. Andrault, M. Munoz, N. Bolfan-Casanova, N. Guignot, J.-P. Perrillat, G. Aquilanti, S. Pascarelli, Earth Planet. Sci. Lett. **293**, 90–96 (2010)
45. L. Spanu, D. Donadio, D. Hohl, E. Schwegler, G. Galli, P. Natl. Acad. Sci. USA **108**, 6843–6846 (2011)
46. H.P. Scott et al., P. Natl. Acad. Sci. USA **101**, 14023–14026 (2004)
47. L.R. Benedetti, J.H. Nguyen, W.A. Caldwell, H. Liu, M. Kruger, R. Jeanloz, Science **286**, 100–102 (1999)
48. E. Boulard, A. Gloter, A. Corgne, D. Antonangeli, A. Auzende, J. Perrillat, F. Fuyot, G. Fiquet, Proc. Natl. Acad. Sci. USA **108**, 5184–5187 (2011)
49. A. Oganov, S. Ono, Y. Ma, C.W. Glass, A. Garcia, Earth Planet. Sci. Lett. **272**, 38–47 (2008)

Chapter 30
Science Frontiers with X-Ray Free Electron Laser Sources

Flavio Capotondi, Martina Dell'Angela, Marco Malvestuto and Fulvio Parmigiani

Abstract The advent of X-rays can represent a groundbreaking advancement for innovative studies of the non-equilibrium physics, time-resolved spectroscopies and radiation scattering, unlocking the gate for a transformative X-ray tool for science. However, only the advent of fully spatial and temporal coherent X-ray sources, delivering ultrashort pulses and having the control on the light polarization and the photon frequency tunability will make the free electron lasers a revolutionary observational tool capable of bridging the critical gaps in our understanding of radiation-matter interactions. Such a light source will expand, by far beyond, our present days capability to use X-rays for imaging, structure determination, and spectroscopy, while piercing the frontier of the actual X-ray technology, detection systems and devices. In the following some preliminary examples, along with the future perspectives and applications to the study of the structure and properties of novel and exotic materials are reported.

F. Capotondi · M. Dell'Angela (✉) · M. Malvestuto · F. Parmigiani
Elettra-Sincrotrone Trieste S.C.p.A., Strada Statale 14-km 163,5 in AREA Science Park, 34149 Basovizza, Trieste, Italy
e-mail: maritna.dellangela@elettra.trieste.it

F. Capotondi
e-mail: flavio.capotondi@elettra.trieste.it

M. Malvestuto
e-mail: marco.malvestuto@elettra.trieste.it

F. Parmigiani
Department of Physics, University of Trieste, Via A.Valerio 2, 34127 Trieste, Italy
e-mail: fulvio.parmigiani@elettra.eu

S. Mobilio et al. (eds.), *Synchrotron Radiation*,
DOI: 10.1007/978-3-642-55315-8_30, © Springer-Verlag Berlin Heidelberg 2015

30.1 Introduction

Nowadays, the fundamental and urgent needs of our society require the science to address these needs by transforming practical problems into basic knowledge. Some examples are given by the capability of understanding and promoting natural and artificial photosynthesis, catalysis, advanced combustion science, quantum materials, fundamental charge dynamics in molecules, nano-spin and nano-magnetization, nano-scale materials nucleation, bio-imaging from structure-to-function. For these studies the possibility of extending the conventional laser spectroscopy and light scattering, either in the frequency and time domain, to the X-ray spectral region would be revolutionary for understanding the basic structure and functions of novel and complex materials that constitute the cornerstone of the near and future humankind progress and sustainability.

A particular attention must be given to fully coherent high repetition rate free electron lasers (FELs) operating in the soft-X-ray spectral region having the full control on the spectral brightness, polarization, transversal and longitudinal coherence and tunability. For achieving the control on the polarization helical undulators must be used for the radiation section of the FEL, whereas the full spatial and temporal coherence can be achieved by external seeding, as for example in the case of the FERMI FEL operating at Elettra Sincrotrone Trieste or self-seeding as for the LCLS FEL operating at SLAC-Stanford. Beside the control on the polarization and tunability the possibility of generating transform limited pulses with time structure ranging from hundred of attoseconds (10^{-18} s) to femtoseconds (10^{-15} s) will be desirable. For such a source ideal parameters are 10^6 pulses per second, average X-ray power up to 100 W continuously powered superconducting accelerator, and photon energy range from 0.1 to 2.5 keV. The photon flux must be controlled from moderate to high flux with 10^8–10^{12} photons/pulse, along with a multiple pump pulse across the spectrum from THz to X-ray.

The control of the polarization and the photon energy tunability are essential for spectroscopy and scattering studies. Such a radiation source will unlock the gate for ultrafast dynamics studies of functional materials, since non-equilibrium processes such as molecular chemical reactions and many phase transition phenomena are determined on a femtosecond timescale. The femtosecond phenomena targeted should be relevant to the development of materials via the understanding of structural transitions (order-disorder and/or amorphous-crystalline), transitions between conducting (metal)-semiconducting-insulator phases or multiferroic transitions (ferroelectric, ferro-elastic, magneto-optic, magneto-electric, opto-electric), as well as transitions and phenomena induced and altered by symmetry-breaking (magneto-electric, magneto-chiral) within these states.

30.2 Coherent Free Electron Laser Sources

The quest for ultra-bright Fourier transform-limited (fully coherent) femtosecond X-ray pulses with tunable photon energy and variable polarization has unlocked the gate for novel and extremely bright X-ray sources, capable of delivering ultrashort pulses with peak and average brightness several orders of magnitude larger than those generated with the most advanced accumulation rings. This is the main reason for the impressive development of FEL sources we have witnessed in this last decade. FEL sources can operate in several ways. To date, most of the existing and planned very-short wavelength FELs [e.g. FLASH and XFEL (DESY), Swiss-FEL, LCLS I and LCLS II (SLAC-USA) and SACLA-Spring-8 (Japan)] have employed the self amplification of spontaneous emission (SASE) mode of operation. In detail, as shown in Fig. 30.1a, the electrons propagating through a long, periodic magnetic dipole array (undulator) spontaneously emit radiation. This radiation interacts itself with the travelling cloud of electrons causing an exponential growth of the radiation finally emitted. While it is possible to get extremely high brilliance by this operation mode, the temporal structure of a SASE output pulse is normally composed of a series of micro-pulses that individually have random phase and highly fluctuating peak intensity and time duration (Fig. 30.1a). For SASE devices, synchronization to external sources for pump probe experiments is normally limited by the temporal jitter of the accelerator. This jitter can be tens of femtoseconds or greater, especially for accelerators based upon non-superconducting cavities. As an alternative, short-wavelength FEL sources based upon seeding techniques, in which the FEL pulse is initiated by a coherent radiation pulse generated by a conventional laser (see Fig. 30.1b) have been developed.

For the first time the FERMI@Elettra source has proved that seeded FELs can obtain output radiation bandwidths close to the Fourier transform limit up to the soft X-ray regime, see Fig. 30.2a, b) [2, 3].

The FERMI@Elettra FEL facility, operates on the base of a combined coherent laser seeding and harmonic upshifting to provide coherent emission over a photon energy range of 12–300 eV in the fundamental emission and up to ∼900 eV at the third harmonic. Such photon energy range allows covering, with ultra-short, ultra-bright and variable polarization radiation pulses, the $M_{4,5}$ and $L_{2,3}$ absorption thresholds of the 3d-transition metals based materials (see Fig. 30.3). The intensity of such a source will be about 5-order of magnitude larger than synchrotrons available today.

In this last year the FERMI FEL has faced a smashing success, first producing fully coherent 100 fs pulses up to ∼60 eV in the fundamental and up to ∼300 eV in the higher harmonic orders. Then piercing the frontier of the FEL physics and technology by generating the first High Gain Harmonic Generation (HGHG) FEL EUV-light.

A further general question, which might be tackled by the new class of X-ray sources, relates to the very interpretation of quantum mechanics. According to the Dirac postulate of projection of states, any attempt to measure the state of a quantum

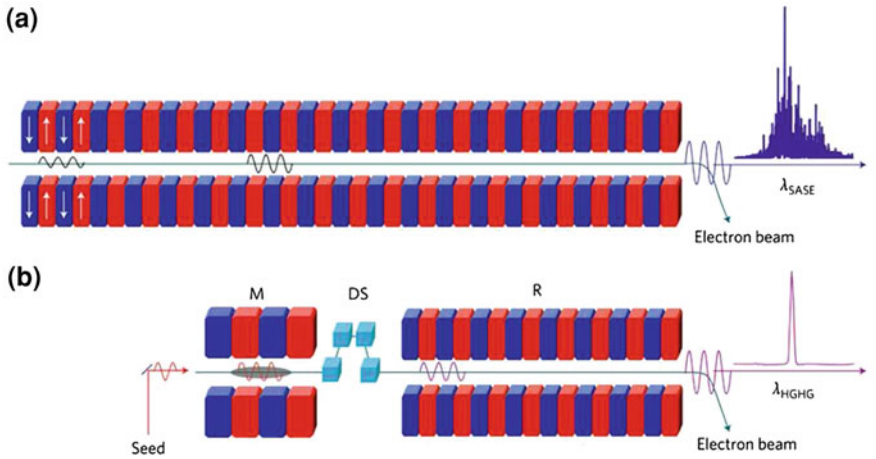


Fig. 30.1 **a** SASE FEL scheme and typical output pulse. **b** Seeded FEL scheme. Output pulses with a well-defined temporal shape and intensity stability that permits relatively straightforward synchronization with external lasers. Adapted by permission from Macmillan Publishers Ltd: Nature Photonics [1], copyright 2012

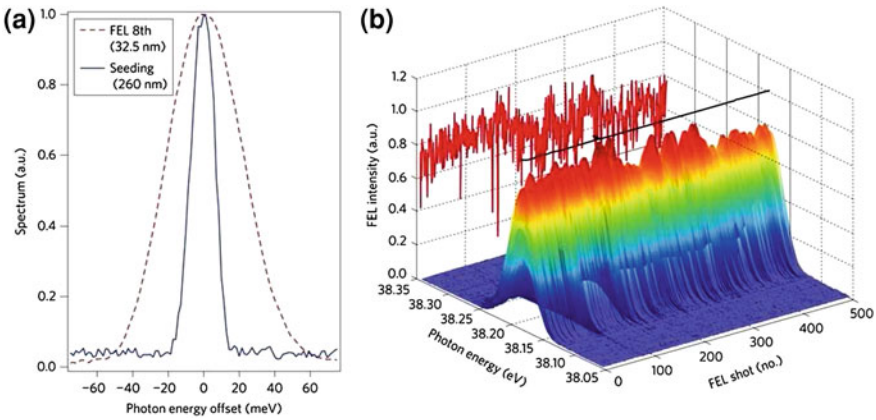


Fig. 30.2 Single shot and multi-shot spectra at 32.5 nm **a** Measured FEL and seed laser spectrum (*dashed red* and continuous *blue lines* respectively). **b** Acquisition of five hundreds consecutive FEL spectra. Reprinted by permission from Macmillan Publishers Ltd: Nature Photonics [3], copyright 2012

mechanical system projects its state into one of the possible eigenstates of the relevant Hamiltonian. If very short times are available, one might start asking questions like how long is the time required for this projection process and how does it evolve in time (see e.g. [4]) Because of the intrinsic non-deterministic nature of this process, one would rely on single shot experiments. In this respects the new generations of X-ray sources offers the real perspective for entering this realm of physics which

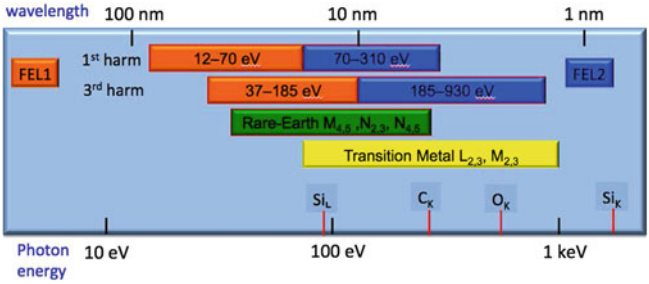


Fig. 30.3 Absorption thresholds covered by the FERMI@Elettra fully coherent variable polarization pulses. 1st harm refers to the fundamental emission, whereas 3rd harm refers to the third harmonic emission

has been established as postulates during the birth of quantum mechanics but still awaiting for unambiguous experiments to be validated.

30.3 Coherent Diffraction Imaging with Free Electron Lasers

The advent of high brilliant X-ray sources has opened the unique opportunities to explore material properties with nanometric spatial resolution. The longer X-ray penetration length allows the study of samples too thick for electron microscopy. Moreover chemical sensitivity is provided by tuning the photon energy to one of the X-ray absorption edges of the sample under investigation. Conventional X-ray microscopy is based on the "classical" scheme of an optical microscope: the source radiation is focalized on the sample plane by an optical element, i.e. a lens, and the scattered photons from the sample are collected by a second lens to reconstruct a magnified image [5, 6]. Today lens-based X-ray microscopes have almost reached the resolution limit of few tens of nm, mostly limited by the fabrication of the high quality optical elements. To push further the lateral resolution to the diffraction limit of the impinging radiation an "unconventional" form of microscopy based on X-ray scattering has been developed, namely Coherent Diffraction Imaging (CDI), also known as lensless X-ray microscopy. The principle of CDI is based on the interference effects in X-ray scattering. Coherent X-ray scattering produces a characteristic "speckle pattern" on a detector placed far from the sample. This pattern reflects the Fourier amplitudes of the real-space charge distribution, from nanometer to micron length scales. The real-space image is reconstructed from the "speckle pattern" by recovering the missing Fourier phases, commonly via recursive phase-retrieval algorithms. After the first demonstration of CDI as a powerful microscopy method on synchrotron radiation source [7], the advent of ultra-intense, ultra-short FELs pulses has opened the opportunities to acquire snapshots so fast to envision that even single atoms in the photographed object remain frozen at their positions paving the way to combine high spatial image resolution to ultrafast dynamic processes.

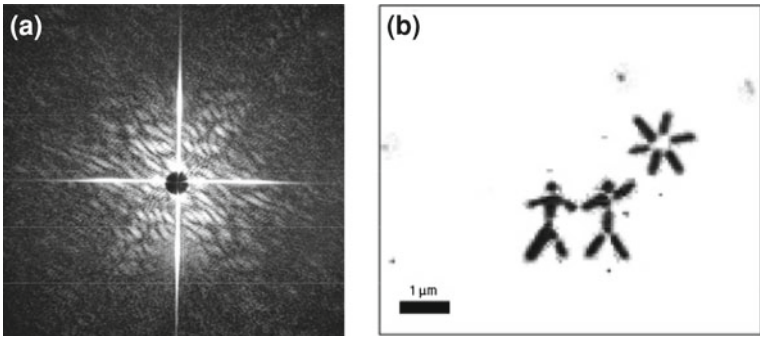


Fig. 30.4 **a** Coherent diffraction patterns recorded for a single FEL pulse (log scale). **b** Image reconstructed, from the ultrafast coherent diffraction pattern in (**a**), by phase retrieval algorithm. Adapted by permission from Macmillan Publishers Ltd: Nature Physics [8], copyright 2006

The first proof of principle single-shot CDI imaging experiment from a non-periodic object was performed at the FLASH by H.N. Chapman and co-workers [8]. In this experiment an artificial structure on a Si_3N_4 window has been illuminated by a single 25 fs FEL pulse at 32 nm wavelength. During this ultra-short pulse, the power deposited by the radiation was so huge (about 4×10^{13} W/cm^2) that the sample exploded into a plasma with a temperature of 60000 K. Due to different timescales between the pulse duration and the plasma formation the diffraction pattern collected on a CCD detector (see Fig. 30.4a) contains the morphological information of the deposited structure before its explosion. The real space image of the illuminated object has been obtained using a phase retrieval reconstruction of the acquired speckle pattern (see Fig. 30.4b) showing an almost diffraction limited resolution of 62 nm, determined by the geometry of the experimental set-up.

One of the great opportunities opened by this first ultrafast imaging experiment with FEL is the possibilities to monitor with nanometric resolution the transient state of mater in several research fields going from condensed matter, biology and magnetism, using pump and probe schemes. As an example, A. Barty and co-workers [9] were able to acquire a real space sequence of images of the sample ablation after the illumination with an intense laser pulse with ps time resolution. In their experiment an external laser was synchronized with the FEL radiation and several replica of the same structure were used to acquire single shot images at different time delay. The reconstructed images (Fig. 30.5) show that the structure disintegrates in tens of ps, in according to hydrodynamic expansion of the sample at the sound speed.

Those pioneering experiments in the soft-X ray regime have demonstrated the possibility for diffraction technique to overpass the radiation damage problem thanks to the combination of high photon flux and the short duration of the FEL pulse. This makes hard X-ray FEL based on the "diffraction before destruction" technique extremely appealing for radiation sensitive, weakly scattering biological sample [10, 11] and for structural biology [12]. A major bottleneck in structural biology today is the necessity of isolating, purifying and crystallizing sufficiently large

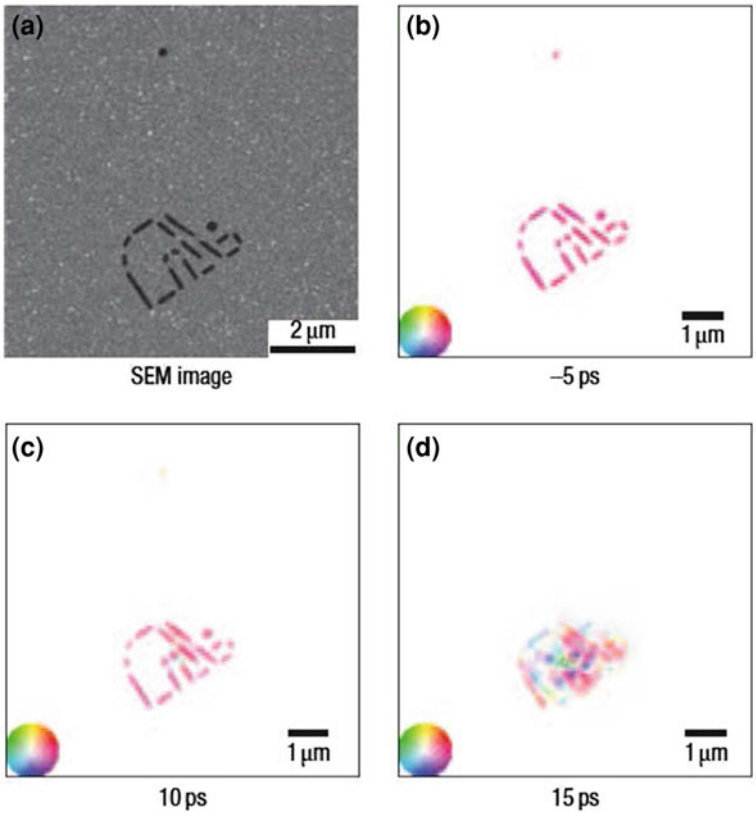


Fig. 30.5 **a** Scanning electron microscopy image of the nanofabricated reference object. **b–d** Phase retrieved images at various delay time after the excitation of a laser pulse: **b** 5 ps before the laser excitation, **c** 10 ps and **d** 15 ps after laser excitation. Reprinted by permission from Macmillan Publishers Ltd: Nature Photonics [9], copyright 2008

($>10\ \mu m^3$) samples for a synchrotron-based experiment. As demonstrated at LCLS by H.N. Chapman and co-workers [12] this problem can be circumvented by continuously injecting nanometric size crystals in the tight focused FEL beam, using a liquid jet (see Fig. 30.6). When the FEL pulse hits the nanocrystal the Bragg diffraction pattern is collected on a CCD detector. A single LCLS X-ray pulse vaporized the sample, but the liquid stream replenishes it before the arriving of the next pulse. Each collected diffraction pattern represents a particular "slice" of the Ewald sphere depending on the random crystallographic orientation of the nanocrystal with respect to the beam.

By indexing the individual Bragg peaks in more than 15000 diffraction patterns a complete 3D dataset of the Ewald sphere has been constructed, allowing the reconstruction of the electron density of a large membrane protein complex (Photosystem I) with a resolution of about 80 A.

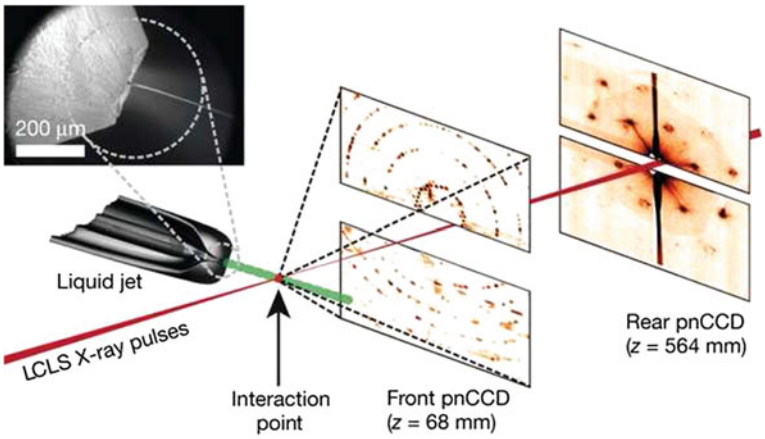


Fig. 30.6 Scheme of the experimental set-up for femtosecond serial crystallography. Reprinted by permission from Macmillan Publishers Ltd: Nature Photonics [12], copyright 2011

All the above reported experiments have been performed with SASE-based FELs. Undesired properties of the SASE radiation are the poor shot to shot intensity and photon energy stabilities due to the stochastic nature of the amplification process. For instance the SASE radiation has not sufficient spectral stability for performing time-resolved resonant CDI experiments and usage of a monochromator at expense of the incoming flux is needed. Fine control of the emitted radiation wavelength and its polarization is particularly important to selectively excite atomic resonances, increasing their scattering power above and below the absorption edge. The advent of new seeded source like FERMI, in the soft X-ray, or the development of self-seeding scheme at LCLS in the hard X-ray regime open the possibility to explore multicomponent nanostructures, in order to access the spatial aspects of the dynamic processes: as for example the spatial evolution of the magnetic domains during the fast demagnetization process [13, 14] or the functional properties of soft matter and biological objects in their native state [11].

30.4 Spectroscopy on Solids at FELs

In the last decades, several techniques employing synchrotron radiation delivered by storage rings have been ideated and developed to perform spectroscopic studies of matter, leading to a deeper understanding of the materials under investigation. Thanks to these achievements, new compounds have been designed and produced that are used in the devices of our everyday life. In the free electron laser (FEL) "era" there has been right from the beginning an attempt to extend the same well studied and developed spectroscopic techniques to the time domain. The final dream of the

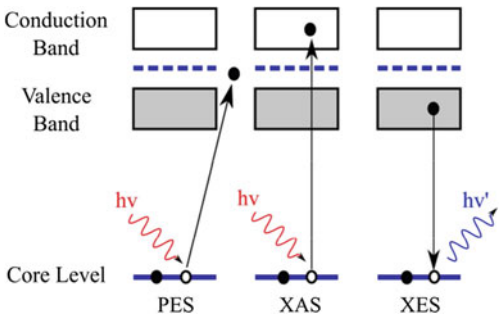


Fig. 30.7 Scheme of electronic transitions in PES, XAS and XES

FEL science in this field is to be able to access transiently excited states of matter and their dynamics by taking electronic structure movies during a reaction path. This vision is absolutely equivalent with respect to taking snapshots of the crystallographic structure of a protein crystal during its activity, i.e. performing therefore the so called molecular movie.

In the following we will limit our discussion to three examples of core level spectroscopies that have been employed at FELs, i.e. photoelectron spectroscopy (PES), X-ray absorption spectroscopy (XAS) and resonant X-ray emission spectroscopy (RXES), all of them applied to solid samples. As shown in the simplified scheme in Fig. 30.7, in all three techniques a photon removes one electron from a core level. In PES the energy of the incoming photon is such that the same electron is detected after being emitted from the sample, giving therefore direct information of the core level binding energy. In XAS the electron is promoted by the photon into an empty state in the material. If the photon energy is tuned across the absorption edge (i.e. the energy of the transition between the core level and the empty state) and the total number of electrons (electron yield) or photons (fluorescent yield) emitted at each photon energy after the excited material relaxes is collected, it is possible to obtain information about the empty states in the material. Finally if the de-excitation paths are singled out by sorting as a function of energy the photons emitted from the sample (RXES), it is possible to obtain information on the occupied electronic states projected onto the core level, i.e. the states in the valence band from where the electrons decay to fill the core hole. The three techniques allow therefore a complete study of occupied and unoccupied electronic states in the materials.

The common feature and main advantage of the three "core" techniques is determined by their sensitivity to the site-specific electronic state, determined by the initial core level on which the X-ray act. In contrast optical methods probe integral properties of the sample and diffraction methods are mainly sensitive to the long range order in the material. If we consider for example a chemical reaction or a phase transformation in a material, the challenge is, as mentioned above, to be able to take snapshots of the electronic structure during the process takes place. To this aim the first step is to understand what are the relevant time scales. It has been shown already with synchrotron techniques that by using the intrinsic duration of the scattering

process, dynamical evolutions during the core hole lifetime contribute to the signal and processes on the femtosecond time scale are studied (core hole clock technique). By means of those techniques for example several charge transfer processes from the adsorbed molecules to the bottom electrodes have been studied [15]. However to have a complete picture of a chemical reaction, we are interested in dynamics that take place slower than the core hole relaxation time, i.e. in the picosecond time scale. To this aim FELs are the perfect tool: they deliver photon pulses about few fs to 100 fs long. By using this photon pulses it is possible to perform experiments in a pump probe detection scheme: a first pulse (that can be an optical pulse or a FEL pulse itself) triggers the reaction and a second FEL pulse measures the system during evolution at fixed delays. The high brilliance of FELs can then be an advantage or a disadvantage, depending on the experiment. The high X-ray fluences in fact can lead to permanent damage of the samples, therefore often it is necessary to attenuate the FEL radiation to make use of the temporal structure of the pulse in the experiments. On the other side the high brilliance is an advantage for XES experiments, because of the low fluorescent yield. Therefore a delicate balance between the possibility of performing a measurement in few hours and the sample damage has always to be established. A final point has to be kept in mind: in all the discussion we always described the X-ray/sample interactions as one photon at a time impinging on the sample and causing a transition. But the high fluences available at FELs, open the way to regimes with more then one photon at a time on the sample, opening therefore a complete research field of spectroscopy of matter under extreme conditions.

Experiments at FELs are still at an infant stage. In the following we will review some key spectroscopic experiments that have been performed at the SASE FELs FLASH and LCLS. As for the CDI measurements (see Sect. 30.3), SASE sources introduce several issues in the experiments due to the properties of the photon beam. The major one, making them difficult and time consuming, is its natural instability in particular the pulse to pulse energy and intensity fluctuations of the delivered photon pulses. Therefore most of the time and efforts of the scientists up to now have been invested in developing and implementing new instrumentation that can perform single shot acquisitions and in writing analysis routines that can sort appropriately the acquired data. The stability and tunability of the new seeded FELs (like FERMI) eliminate or reduce this problem, therefore several experiments are now and will soon be feasible in a more efficient way opening the field to a stronger application of core level spectroscopies at FELs.

30.4.1 Photoelectron Spectroscopy

Time and angle resolved photoelectron spectroscopy (trARPES) is a widely employed laser based technique in the study of the femtosecond evolution of conduction and valence bands in solids. Experiments are usually performed in a pump probe scheme, where the pump is tipically 800 or 400 nm femtosecond laser pulses from a Ti:Sa source, while the probe pulses are obtained by high harmonic generation (HHG)

from the Ti:Sa and usually the available photon energies are in the range 3–100 eV. The possibility to access the information carried out by deeper core levels on chemical state and composition of the materials in a time resolved manner represents an important step forward. Nowadays the soft X-ray photon energy range can be achieved only at FELs. In fact the generation of femtosecond soft X-rays from lab sources has recently been reported [16], however the photon densities in this set-up is at the moment not enough to perform photoemission experiments.

Before describing optical pump-X-ray (FEL) probe schemes, we have to take several steps starting from the question about feasibility of photoemission experiments at FELs. The first photoemission measurement has been performed at the monochromator beam line PG2 at FLASH by Pietzsch et al. [17]. The authors have measured W 4f core levels of a W(100) surface. Modifications of the measured W4f core levels as a function of X-ray intensity impinging on the sample have been observed (see Fig. 30.8a). SASE sources like FLASH present a strong pulse to pulse energy and intensity fluctuations of the beam. To make it clear each pulse from the FEL contains several modes (photon energies) and the next pulse can contain different modes, therefore at the experimental endstation it is possible to have a variable photon outcome from the beamline. Moreover the X-ray pulses are also varying in intensity. The pulse intensity is directly correlated to the space charge: this is a very simple effect. In few words the higher the X-ray intensity, the more electrons in the same time window will be emitted from the sample. This highly dense cloud of electrons will be deformed while travelling in vacuum from the sample towards the analyzer due to electrostatic repulsion. This deformation is translated into spectral deformations of the energy distribution measured by the analyzer. Therefore as seen in Fig. 30.8a the higher the photon density impinging on the sample, the more the W 4f core levels are shifted and broadened.

Hellmann et al. [19] have established a data analysis approach that allows the elimination of the space charge. In particular by considering in the dataset only shots originating the same number of counts per pulse detected in the hemispherical analyzer, similar space charge conditions can be analyzed and the shift and broadening of the core levels could therefore be eliminated. As shown in Fig. 30.8b and c they have been able to perform a 800 nm pump-X ray probe experiment on the 1T-TaS_2 and observe the evolution as a function of pump-probe delay of the energy splitting of the Ta 4f due to nonequivalent sites in the material. This has been related to changes in charge-order dynamics of the charge-density wave in the Mott insulator [18].

Some important limitations have to be considered in optical pump-FEL probe photoemission experiments. As shown in Fig. 30.9 the infrared pump itself is causing strong space charge effects in the measured core levels, therefore if a reaction needs a strong pump to be initiated, as for example typical femptochemistry catalytic reactions as we will see later for CO/Ru, the measured photoemission spectra will suffer strong modifications, making extremely difficult a data analysis. The second important limitation in this kind of experiments is represented by the low detection efficiency of the existing analyzers. Most of the times the measurements are limited to 1 detected electron per photon pulse. It is clear that high repetition rates of the FELs are needed to reduce the measurement time. To this aim the only photon sources

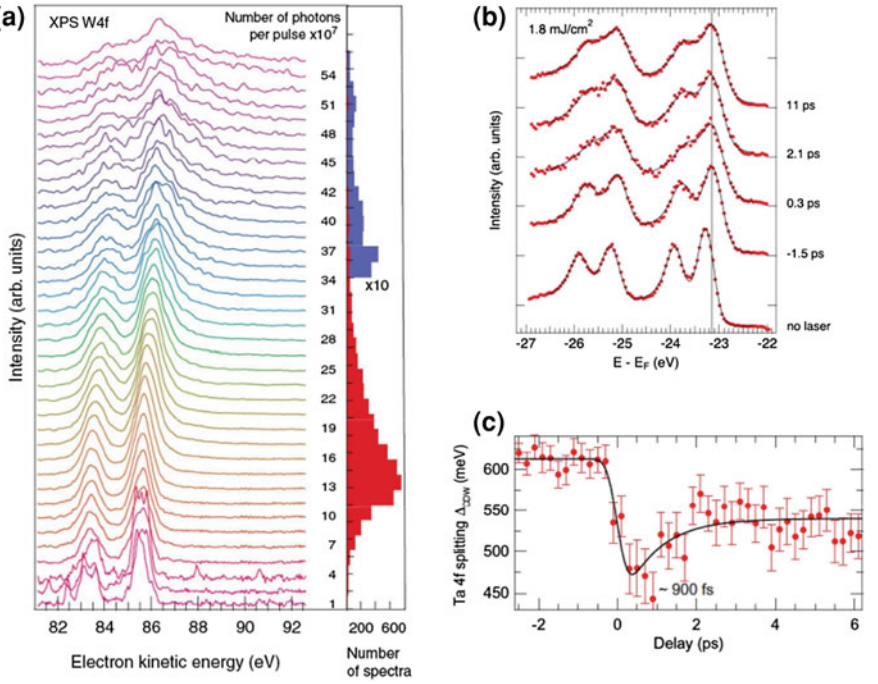


Fig. 30.8 **a** W 4f core levels as a function of intensity in the photon pulse. Reproduced from [17] © IOP Publishing & Deutsche Physikalische Gesellschaft. CC BY-NC-SA. **b** Ta 4f core levels in 1T-TaS2 at several time delays between the 800 nm optical pump and the X-ray probe [18]. **c** Splitting of the Ta 4f 7/2 core levels as a function of pump probe delay. Reproduced from [19] © IOP Publishing & Deutsche Physikalische Gesellschaft. CC BY-NC-SA

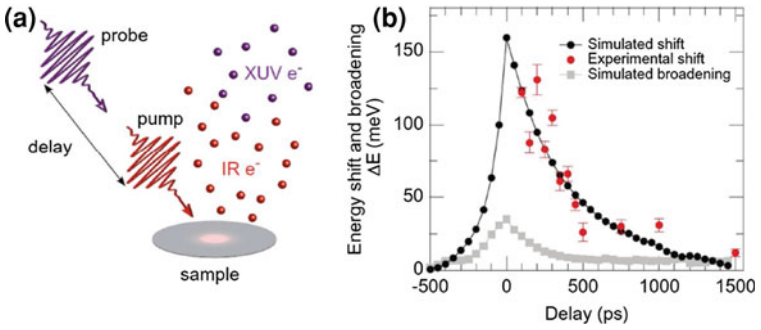


Fig. 30.9 **a** Schematics of the electron emission from the sample due to the pump and probe beams. **b** Measured and simulated energy shift and broadening of the Ta 4f core levels due to the effect of the IR pump. Reproduced from [19] © IOP Publishing & Deutsche Physikalische Gesellschaft. CC BY-NC-SA

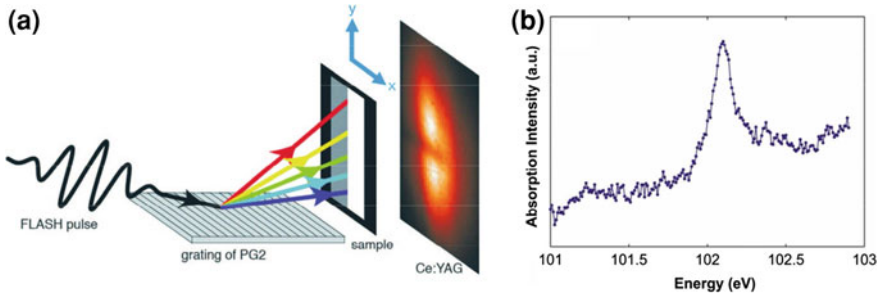


Fig. 30.10 **a** Experimental set up for single shot XAS **b** $^3D_1$ absorption resonance at the $N_{4,5}$ edge of the La^{3+} ions in $LaMnO_3$. Reproduced with permission from [21]. Copyright 2009, AIP Publishing LLC

competitive for photoelectron spectroscopy measurements are FLASH and XFEL due to the possibility of microbunching allowing at FLASH pulse trains spaced by 10 Hz with up to 800 X-ray pulses at 1 MHz rep rate.

30.4.2 X-Ray Absorption Spectroscopy

XAS experiments at SASE FELs are extremely challenging. The main ingredient necessary to perform such experiments is the tunability of the incoming photon energy across an absorption edge of the material under investigation. Due to the fact that the existing SASE FELs have fixed undulators, it can be realized only by fine tuning the electron beam energy in the machine, that is quite difficult. This difficulty is completely solved in seeded FELs like FERMI, where the variable gap undulators can easily be varied [20].

However up to now preliminary XAS experiments have been performed at SASE sources being the only ones available till few years ago. The trick has been to exploit the bandwidth of the SASE beam (that is of the order of few % of the incoming photon energy). In Fig. 30.10a the experimental set up adopted for performing such measurement at FLASH by Bernstein et al. [21] is reported. The FEL beam dispersed in the vertical direction by the monochromator of the PG2 beamline is transmitted through a $LaMnO_3$ film deposited on a Si_3N_4 membrane. The sample has been manufactured such that half of the beam does not cross the thin film and is used for normalization. The transmitted photons are then converted in optical photons by a Ce:YAG screen and imaged by means of a CCD detector. In Fig. 30.10b the measured $_3D^1$ absorption resonance of the La^{3+} ions in $LaMnO_3$ is reported. It is important to observe that it has been obtained by integrating over several FEL shots and normalizing shot by shot by the reference beam.

30.4.3 Resonant X-Ray Emission Spectroscopy

RXES, often called Resonant Inelastic X-ray Scattering (RIXS), is a valuable tool to probe electronic, orbital, magnetic and lattice excitations in an element specific and chemical selective manner. The main disadvantage of RXES experiments at synchrotron sources are the long acquisition times required to create statistically relevant spectra. The reason is that after XAS takes place in a material, most of the de-excitation paths proceed via Auger processes (98 % electron yield) and the probability of having a fluorescent decay is only of the order of 2 %. Thanks to the high brilliance of FELs, RXES can easily be employed at this sources.

The first RXES experiment performed at FLASH has been the study of the ultrafast non thermal melting of silicon after laser excitation [22]. Silicon is a prototypical water-like system that undergoes in equilibrium a phase transformation between from solid to a high density liquid phase, just as from ice to water. The novelty in this experiment is that for the first time the predicted low density phase was measured during the phase transformation. As described in Fig. 30.11a a silicon sample was excited by a ultrashort 400 nm optical laser pulse, and the RXES was probed across the silicon L-edge. In Fig. 30.11b the calculated DOS and measured RXES as a function of pump probe delay are reported. At time zero spectral changes in the conduction and valence band are clearly visible. After comparison with theoretical calculations, the authors concluded that the first instantaneous changes in the spectra are due to the heating of the electrons via the pump pulse. They are responsible to a first phase transformation into the LDL phase. Later on, at 6 ps, the electrons transfer the latent heat for the first order phase transition into the lattice system going into the HDL phase, which then proceeds quickly and becomes apparent in the second shift of the valence band edge.

RXES is often used in literature to probe the electronic structure of adsorbed molecules. A natural extention of this technique will be the study of chemical dynamics on surfaces, i.e. the study of how bonds in molecules are formed or broken. The final dream is to understand the driving forces of heterogenueus catalysis in order to be able to improve the yield of some catalytically relevant reactions in our life. A preliminary study has been performed at LCLS on the femtosecond desorption of carbon monoxide molecules adsorbed on a Ru(0001) surface [23]. The desorption was activated by 400 nm femtosecond optical pulses. In Fig. 30.12a the RXES and XAS measured before and 12 ps after the pump impinges on the sample are reported. By comparing the measured changes with the spectra of the gas phase molecules (peak positions are reported in the upper axis), a clear change of the CO molecules in the direction of gas phase can be inferred. In [23] a comparison between experiment and simulations has been performed to explain the measured spectral differences. The conclusion is that the 400 nm optical pulses trigger the desorption from the surface. After initial electronic excitation, they induce in the picosecond time scale heating of the coupled adsorbate and lattice system. The CO molecules are then excited and remain trapped in the so called precursor state. Once there, they can relax back or desorb in longer timescales. For more clarity in Fig. 30.12b the calculated potential

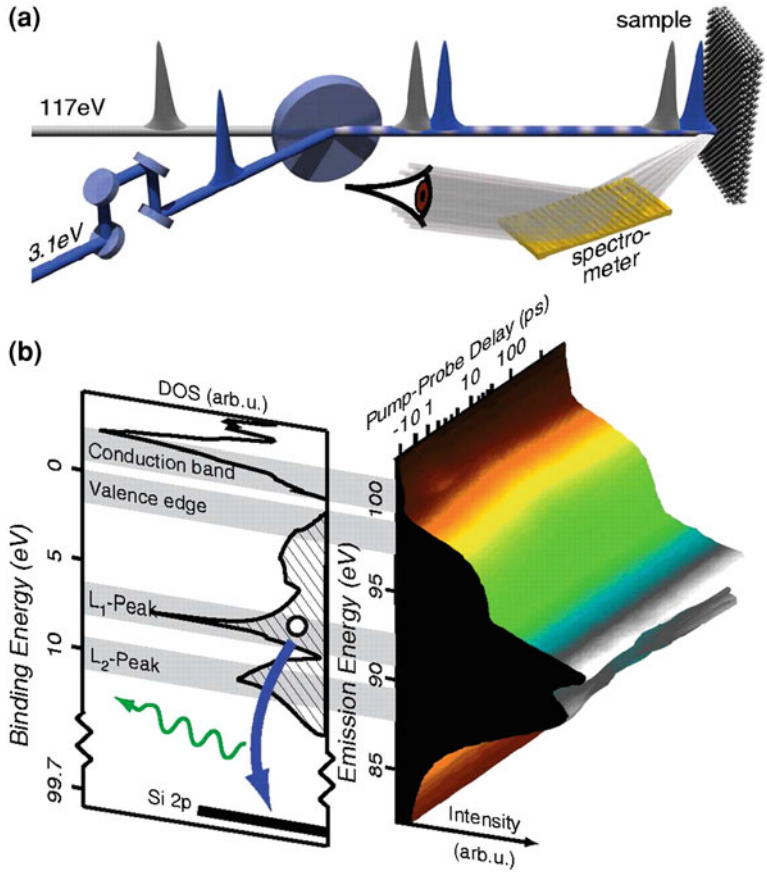


Fig. 30.11 Pump-probe resonant X-ray emission on silicon. **a** 400 nm Pump-X-ray Probe RXES experimental set up. The soft X-ray photons with energies above the silicon L-edge impinged with a well-defined pump-probe delay time on the same spot of the sample. The induced X-ray emission spectra have been recorded with a Rowland-type spectrometer. **b** Calculated (on the *left*) and measured RXES as a function of pump probe delay. Shortly after time zero, a population of the conduction band is visible, whereas also an energetic shift appears in thevalence band edge. Reproduced with permission from [22]

of mean free force is reported for different system temperatures. It presents a clear minimum at 2.5 Å that corresponds to the chemisorbed CO molecules. When increasing the temperature a shallow minimum at longer distance from the surface is present, that is the precursor state. By increasing the temperature with the 400 nm pulse the barrier to populate the precursor state can eventually be overcome. The CO bond to the surface is then weakened in the picosecond time scale. It is important to observe that in this experiment that the 400 nm pump fluence necessary to trigger this reaction is of the order of 150 J/m^2. Photoemission measurements performed at this

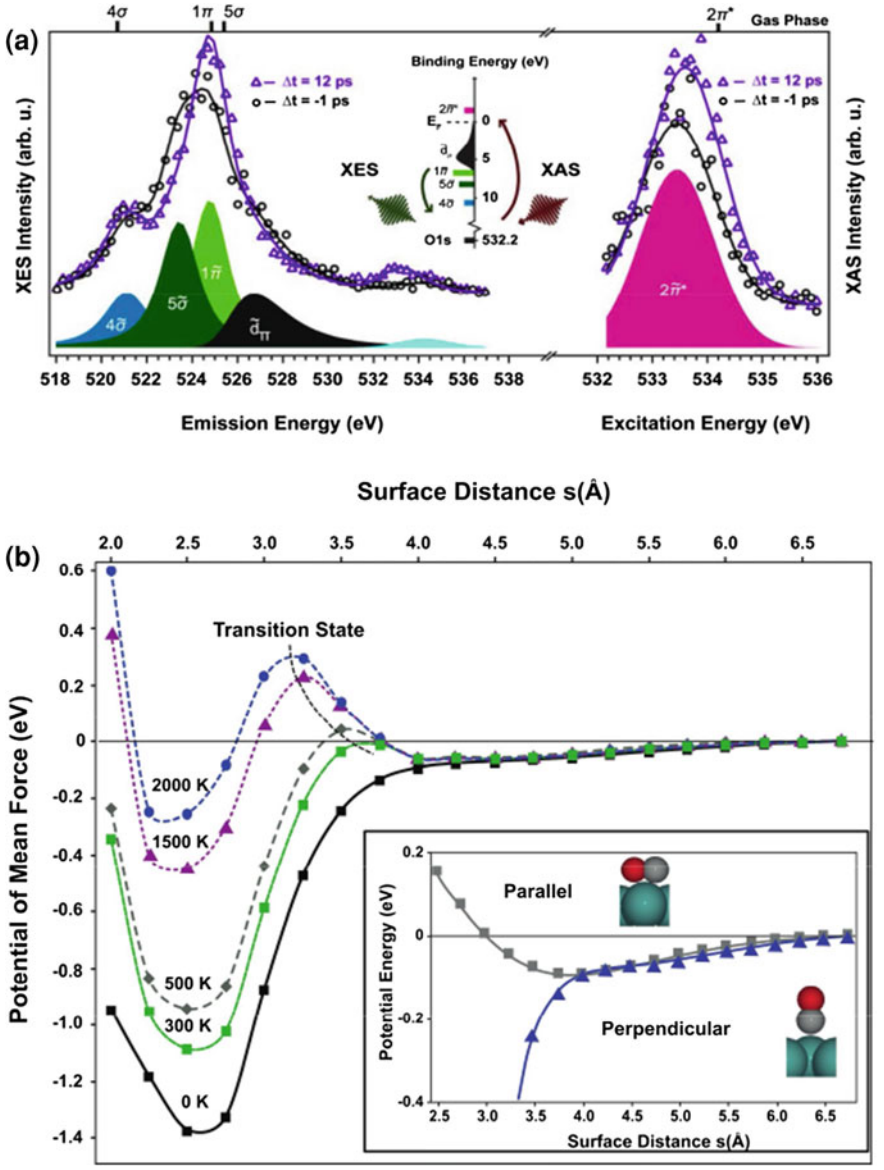


Fig. 30.12 **a** Measured XES and XAS spectra from CO on Ru(0001) before and 12 ps after a 400 nm pump impinges on the sample causing CO desorption. **b** Calculated potential of mean free force at different sample temperatures experienced by the CO molecules. Adapted from [23]. Reprinted with permission from AAAS

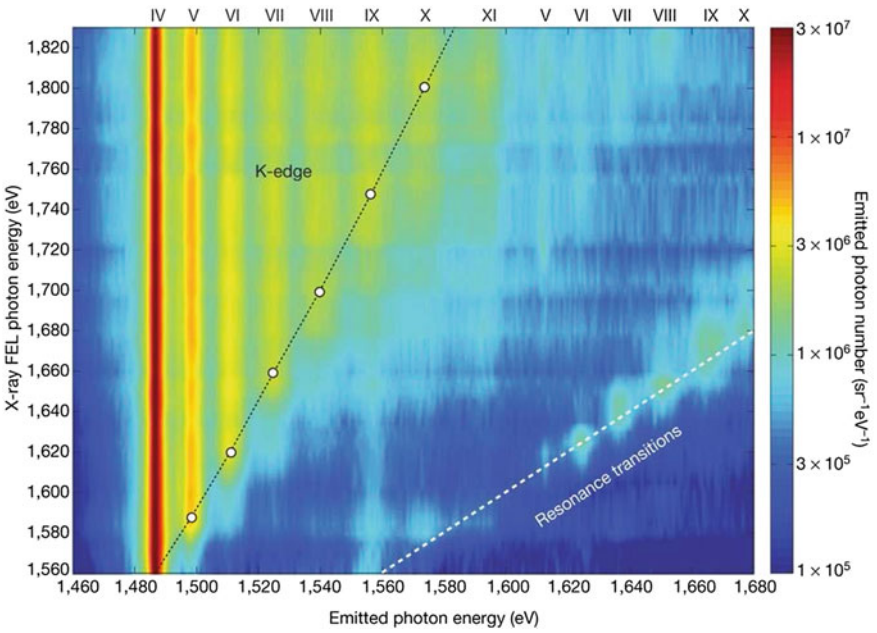


Fig. 30.13 Spectrally resolved Ka emission as a function of the X-ray FEL excitation photon energy. Roman numerals (*top*) indicate the charge state of the emission peak: *red*, for states with a single K-shell hole; *blue*, for states with a double K-shell hole. Reprinted by permission from Macmillan Publishers Ltd: Nature [24], copyright 2012

fluence will correspond to strong shifts and broadening of the core levels and data interpretation will be extremely difficult. The power of RXES is that the measurements are instead feasible by looking at the fluorescent yield and space charge free.

In the two experiments presented in this paragraph the FEL probe beam was appropriately attenuated to avoid sample damage. The high brilliance of the FELs however can be used to study new states of matter, the so called field of matter under extreme conditions. At LCLS, for example, up to 10^{17} W/cm^2 X-ray pulses can be created and an interesting question is how single atoms interact with such intense X-rays. A pioneering RXES experiment at such high fluences has been performed for Aluminum samples at the K-edge [24]. The results are reported in Fig. 30.13. The absorption process in the Al foil is dominated by K-shell photoabsorption at 1,487 eV, ejecting a core electron into the continuum, because the cross-section for L-shell and valance-band photoionization is over a factor 10 smaller. After photoionization, the filling of the K-shell hole proceeds mainly by KLL Auger decay, producing an ion with two holes in the L shell. At the high fluences higher charge states due to a growing number of L-shell holes can be produced and they are labeled with the red roman numbers in the figure. Moreover the black roman numbers represent stages with two holes in on atom. These experiments open new questions in the description of light matter interaction that require further studies.

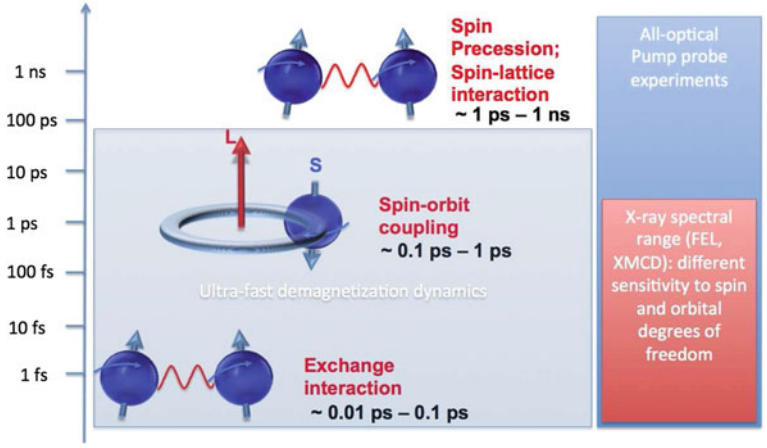


Fig. 30.14 Time scales in magnetism as compared to pump probe experiments with different spectral sensitivities. The short duration of the laser pulses makes them an attractive alternative to manipulate the magnetization. The element and orbital selectivity of femtosecond soft X-ray probes makes them suitable to separate the spin and orbital components during ultrafast magnetization dynamics

30.5 Magneto-Dynamical Studies

The overarching topic in the realm of spintronics deals with the exploitation of the spin as the major degree of freedom. Research on spintronic combines the scientific beauty, arising from the quantum mechanical nature of the spin, with the opportunity to reduce, in magnetic devices the power consumption and heat dissipation by exploiting both the spin and charge degrees of freedom of the individual electrons. Concomitantly, there is an ongoing quest to discover advanced magnetic materials with enhanced performances.

Nowadays a central problem arises from a deep understanding of the out-of-equilibrium magnetism in excited electronic and spin states. Such states, typically initiated by changes in temperature, optical excitations, fields (charge currents) or spin currents, define the operational processes and timescales in magnetic devices.

Their understanding is therefore of interest from both a scientific and a technological perspective. The archetypal experiment is a pump–probe configuration in which a first laser pump pulse abruptly modifies the fundamental magnetic ground state of the material and a second probe pulse, delayed by a short period of time, yields information on the transient magnetization at the moment it is probed. Such experiments now have a time resolution below 1 ps (10^{-12}s), well into the fs (10^{-15}s) range. The timescales in the picosecond and femtosecond range are of great interest because they naturally correspond to important magnetic energies (see Fig. 30.14).

Ultrafast techniques have been applied to look for an answer to many fundamental aspects of magnetism. For more than two decades we tried to address the

question concerning the interplay among magnetic moment, phonons and spin when a ferromagnet is excited by an ultrashort laser pulse that suddenly heats up the electron gas. In the early 1990s, Vaterlaus and co-workers [25] carried out time- and spin-resolved photoemission (TSPE) experiments on gadolinium, yielding a rough estimate of the demagnetisation time, $\tau_M \sim 100 \pm 80$ ps.

In this timescale, around 100 ps, the excitation of faster magnetic response is limited by the spin-orbit coupling. The spin-orbit interaction is the responsible of the coupling between the orbital angular momentum L and the spin S (LS coupling). The LS coupling mediates the spin-lattice interaction, i.e. the angular momentum transfer between them. Thus, promoting the transfer of angular momentum from the spin to orbital degree of freedom a faster magnetization loss could be achieved. Unfortunately, the spin-orbit coupling time scale ranges from tens of picosecond to hundreds of picoseconds.

In fact, in this regime, the magnetization dynamics is still controlled by the Landau-Lifshitz-Gilbert equation, which restricts the switching time scale to sub-nanosecond regime.

$$\frac{dM}{dt} = -\gamma(M \times H_{eff} - \eta M \times \frac{dM}{dt}) \tag{30.1}$$

where η is the damping parameter, which is characteristic of the material.

In view of the above, new results in 1996 by Beaurepaire et al. [26] exploiting time-resolved magneto-optical Kerr effect (TRMOKE) studies on nickel thin films came as quite a surprise. It was found that demagnetisation after sub-100 fs pulsed-laser excitation proceeds well within a picosecond (see Fig. 30.15). i.e. beyond the timescale of the spin-orbit interaction. Since then, manipulating and controlling magnetization with ultrafast laser pulses have become a new field in modern magnetism that is referred to as femtosecond magnetism.

This ultrafast dynamics (of the order of 200 fs) opens promising ways for the magnetization control. In particular it demonstrates that the fundamental limit of the magnetization dynamics time scale is not restricted by the conventional LLG equation.

Beaurepaire and co-workers explained the observed loss of the magnetic order caused by the interaction of a laser pulse with Ni thin films on the basis of a so-called phenomenological three temperature model (3TM). The 3TM assumes that the energy from the laser pump pulse is mainly absorbed by the electron system which is described by a temperature T_e. This is a reasonable assumptions: first, in the spectral range where the laser pulse works the direct deposition of photon energy is only efficient in electron system [27] direct ex-citation of phonons would require far infrared spectral range [28], and second, femtosecond pump-probe photo-emission experiments have showed that the hot electrons follow a quasi equilibrium Fermi distribution [29]. The excess of energy in the electron system is then redistributed into the phonon and spin systems also described in terms of temperatures. Within this model the magnetization reduction is considered in terms of an increase of the

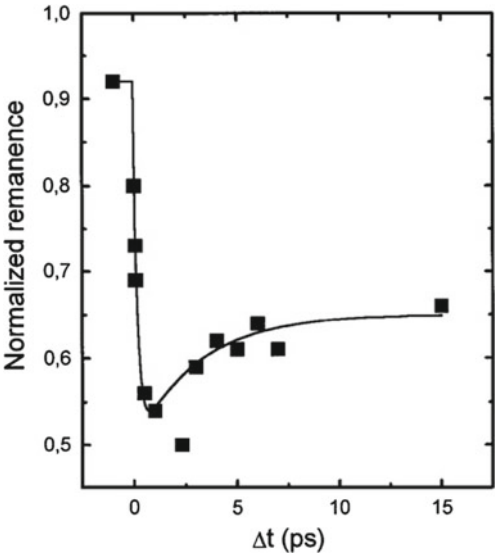


Fig. 30.15 Ultrafast demagnetization in ferromagnetic Nickel induced by a 60 fs laser pulse. Figure taken from seminal work of Beaurepaire et al. [26]

spin temperature due to energy transfer to the spin system via electron-spin or/and phonon-spin interactions.

These models are also based on the energy flow picture and leave unidentified the angular momentum transfer mechanism and the underlying quantum mechanism responsible for the spin flip. However, the thermal excitations, which disorder the spin system, have to arise from a microscopic spin-flip process, acting on a femtosecond timescale. Depending on the characteristics of the system the demagnetization can occur via electron-spin, lattice-spin or electron-lattice-spin coupling. In transition metals, the elementary scattering events in a quantum description can be divided into two processes, sketched in Fig. 30.17, that are seen to be the most relevant.

The first candidate is the Elliott-Yafet [31] process. It makes use of the fact that due to spin-orbit interaction the spin of the electron is not a good quantum number anymore and, as a consequence, intermixes the spin channels at some high symmetry points of the band structure. If the electrons, heavily ex-cited by the energy input of the intense femtosecond laser pulse, are scattered into these spin hot spots in the Fermi surface (by defects, phonon scattering events etc.), the final state has a certain probability to be of opposite spin direction. The second process is the electron-electron scattering mediated by exchange interaction.

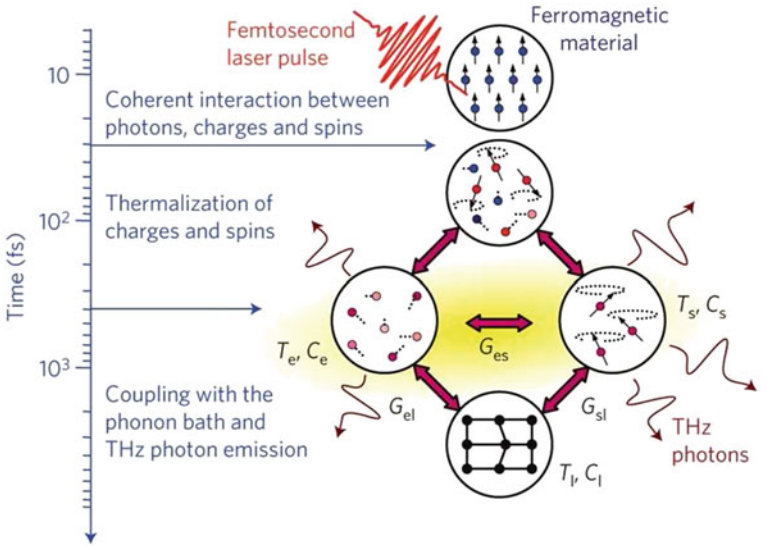


Fig. 30.16 Schematic representation of mechanisms taking place in ultrafast magnetization dynamics. Reprinted by permission from Macmillan Publishers Ltd: Nature Physics [30], copyright 2009

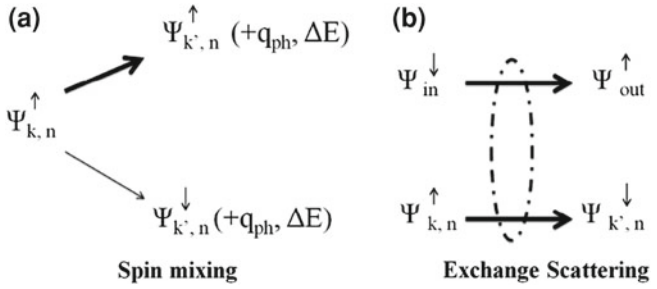


Fig. 30.17 Schematics of the spin-flip processes. **a** Elliott-Yafet process of an electron-scattering event with a phonon to an unoccupied intra-band band state is depicted. The spin-orbit interaction intermixes the spin channels in some points of the band structure. In the final state a certain probability of a reversed spin is given. The phonon takes energy and momentum from the electron system. **b** Exchange scattering of a hot electron which in effect exchanges the spin orientation of the hot electron and the locally remaining electron at lower energy

30.5.1 Ultra Fast X-Ray Experiments

While lasers and pump probe magneto-optics have paved the way for the studies of the ultra fast dynamics, the ultimate goal relies on the understanding of the intimate nature of the magnetization, i.e. the angular momentum (J).

The key questions concern the physics of the angular momentum when the system is in an excited state and how and why the different components (spin (S) and orbital (L) momenta) of the total angular momentum, are competing, see (30.2),

$$J = S_{electron} + L_{electron} + L_{phonons} - L_{excitingphoton} \tag{30.2}$$

To uncover the dynamics of the transient magnetization requires sensitivity to the angular momentum associated with the spins, the low-energy valence excitations, the phonons and the spin-excitations. This can be achieved by replacing, for example, the femtosecond optical laser probe pulse with ultrashort soft X-ray probe pulses with control on the polarization, such those generated by properly designed FEL source. In this case the probe will be element-specific allowing to carry out core level resonant measurements, such as X-ray magnetic circular dichroism (XMCD) and resonant inelastic X-ray scattering (RIXS). More specifically, time-dependent XMCD [32] spectroscopy in an ultrafast optical pump X-ray probe scheme would reveal the separate evolution of the spin and orbital components of the magnetization (time resolved $S_{electron}$ and $L_{electron}$, see (30.2)), providing key information on the transfer of angular momentum out of the spin system that has to accompany any magnetization change.

30.5.2 Ferromagnetism and Superconductivity: A Background Starting Point

Ferromagnetism (FM) and superconductivity (SC) are phenomena in modern solid-state physics that have been separately investigated for several decades. Since 1957, the antagonistic characters of the superconducting and the FM order parameters have been known. The attention increased considerably when a non-linear behavior of the superconducting transition temperature in dependence of the FM layer thickness had been reported [33]. This was the motivation for several experimental and theoretical studies on conventional SC/FM hetero-structures. Coupling phenomena have been reported like a phase shift of the order parameter in one superconducting layer to the order parameter in next superconducting layer or an oscillation of the superconducting phase transition temperature in dependence of the FM layer thickness [34–36]. In the late 1990s, the first studies on non-conventional SC/FM hetero-structures have been reported [37, 38]. The use of high temperature SCs and FM manganese-oxides promised a possible application in devices due to the high transition temperatures and the spin-injection into the SC enabled by the half-metallic properties of the manganese-oxides. Soon, novel proximity-induced effects were discovered that have a much larger length scale than the ones observed in conventional hetero-structures [39, 40]. Subsequently, more and more studies indicated a strong mutual interaction between the superconducting and the FM order parameters [41–43] and motivated researchers to further investigate such hetero-structures.

30.5.3 Physics of FM/SC Heterostructures

In combining a SC (SC) with a ferromagnet (FM) rather than with a normal metal, various effects have been predicted to occur. One is spin selectivity in the conductance of an SF junction, with strong implications for devices at mesoscopic length scales. Another is the possibility of a phase difference in the SC state over an S/F/S junction, resulting in an oscillatory behavior of the superconducting transition temperature Tc. Finally, giant magnetoresistance and proximity-induced triplet-singlet SC transitions. Of particular interest are recent experiments on FM/SC junctions with high TC in which a decrease of the super-current by non-equilibrium spin density was demonstrated. Furthermore, theoretical studies also indicate that spin imbalance in a SC can lead to suppression of SC. In a double tunnel junction containing a normal metal or a SC sandwiched between two FMs, both injection of polarized current and spin accumulation are possible, and thus provide an ideal test ground for the theory. When the magnetic moments of the two FM leads are in opposite orientations (referred to as the anti FM (AF) alignment), the difference in the number of majority and minority spins in the central electrode brings in a chemical potential difference. In a SC, this difference gives rise to pair breaking, same as the Zeeman effect does to SC in the paramagnetic limit. The effect can be turned on and off by manipulating the mutual orientations of the magnetic moment of the two FM layer.

All such effects concern the behavior of the superconducting order parameter near the SC/FM interface, and in that sense they form part of the general issue of the proximity effect, well known for the SC/N case, but hardly investigated for the SC/FM case. The microscopic mechanism underlying these phenomena are almost entirely unexplored, and, for example, very little is known about the interfacial magnetization profile, the interplay/competition between FM and superconductive order, the dynamical processes of magnetization dynamics and superconducting condensate formation. The first step towards an effective comprehension of all the electronic mechanisms responsible for these effects requires the knowledge of the behaviour the electronic and magnetic structure and behavior of the interface.

The coexistence of the SC-FM state occurs naturally only in few exotic materials (the Chevrel phase alloys and the Rutheno-Cuprates), but now we aim to produce it artificially in nano-structured composite materials, such as S-F, S-F-S and F-S-F multi-layers. A few observations, including the induced triplet-pairing models and a Fulde-Ferrell-Larkin-Ovchinikov state in an FM-SC junction, have already attracted attention and diverse interpretations. For SC-FM and SC-FM-SC multi-layers and SC films, even the nature of the ground state is an open issue, not to mention charge transport properties and magnetization dynamics.

30.5.4 New and Promising Fields of Research and Innovation

Pump-probe time-resolved spectroscopy gives the possibility to explore the interplay among all degrees of freedom (charge, spin, orbital and lattice), heavily entangled

in functional materials, by unveiling the mutual relaxation processes as functions of time and in the out-of-equilibrium regime. Such knowledge will allow achieving optical control on the switching (on:emergence/off:suppression) of unconventional states of matter, usually driven by mechanisms for breaking symmetries or strong correlations, and on the tunability of their functional properties. This extremely high-degree of optical manipulation ability will in turn lead at designing optical devices (e.g. ultrafast photoconductive switches for THz production and application, time-resolved SQUIDs triggered by ultrashort pulses, FET based on the optically-induced melting of the superconducting phase in cuprates) with enormous capabilities and huge impact on our daily life.

References

1. Z.T. Zhao et al., First lasing of an echo-enabled harmonic generation free-electron laser. Nat. Photonics **6**(6), 360–363 (2012)
2. E. Allaria, C. Callegari, D. Cocco, W.M. Fawley, M. Kiskinova, C. Masciovecchio, F. Parmigiani, The FERMI@Elettra free-electron-laser source for coherent x-ray physic: photon properties, beam transport systemand applications. New J. Phys. **12**, 075002 (2012)
3. E. Allaria et al., Highly coherent and stable pulses from the FERMI seeded free-electron laser in the extreme ultravioler. Nat. Photonics **6**, 699–704 (2012)
4. E.J. Squires, How long does it take to male a measurement? Phys. Lett. A **148**(8–9), 381–383 (1990)
5. W. Chao, B.D. Harteneck, J.A. Liddle, E.H. Anderson, D.T. Attwood, Soft X-ray microscopy at a spatial resolution better than 15 nm. Nature **435**(7046), 1210–1213 (2005)
6. B. Kaulich, P. Thibault, A. Gianoncelli, M. Kiskinova, Transmission and emission x-ray microscopy: operation modes, contrast mechanisms and applications. J. Phys. Condens. Matter **23**(8), 083002 (2011)
7. J. Miao, P. Charalambous, J. Kirz, D. Sayre, Extending the methodology, of X-ray crystallography to allow imaging of micrometre-sized non-crystalline specimens. Nature **400**(6742), 342–344 (1999)
8. H.N. Chapman et al., Femtosecond Diffractive Imaging with a Soft-X-ray Free-Electron Laser. Nat. Phys. **2**(12), 839–843 (2006)
9. A. Barty et al., Ultrafast single-shot diffraction imaging of nanoscale dynamics. Nat. Photonics **2**, 415 (2008)
10. R. Neutze, R. Wouts, D. Van der Spoel, E. Weckert, J. Hajdu, Potential for biomolecular imaging with femtosecond X-ray pulses. Nature **406**, 752–757 (2000)
11. M.M. Seibert et al., Single mimivirus particles intercepted and imaged with an x-ray laser. Nature **470**, 78–81 (2011)
12. H.N. Chapman et al., Femtosecond x-ray protein nanocrystallography. Nature **470**, 73–77 (2011)
13. T. Wang et al., Femtosecond single-shot imaging of nanoscale ferromagnetic order in Co/Pd multilayers using resonant X-ray holography. Phys. Rev. Lett. **108**, 267403 (2012)
14. B. Pfau et al., Ultrafast optical demagnetization manipulates nanoscale spin structure in domain walls. Nat. Commun. **3**, 1100 (2012)
15. P.A. Brühwiler, O. Karis, N. Mårtensson, Charge-transfer dynamics studied using resonant core spectroscopies. Rev. Mod. Phys. **74**, 703 (2002)
16. T. Popmintchev et al., Bright coherent ultrahigh harmonics in the keV X-ray regime from mid-infrared femtosecond lasers. Science **336**, 1287 (2012)

17. A. Pietzsch et al., Towards time resolve core level photoelectron spectroscopy with femtosecond x-ray free-electron lasers. New J. Phys. **10**, 033004 (2008)
18. S. Hellmann et al., Ultrafast Melting of a Charge-Density Wave in the Mott Insulator 1T-TaS_2. PRL **105**, 187401 (2010)
19. S. Hellmann et al., Time-resolved x-ray photoelectron spectroscopy at FLASH. New J. Phys. **14**, 013062 (2012)
20. E. Allaria et al., Tunability experiments at the FERMI@Elettra free-electron laser. New J. Phys. **14**, 113009 (2012)
21. D.P. Bernstein et al., Near edge x-ray absorption fine structure spectroscopy with x-ray free-electron lasers. Appl. Phys. Lett. **95**, 134102 (2009)
22. M. Beye et al., The liquid-liquid phase transition in silicon revealed by snapshots of valence electrons. PNAS **107**(39), 16772–16776 (2010)
23. M. Dell'Angela et al., Real-time observation of surface bond breaking with an X-ray laser. Science **339**(6125), 1302–1305 (2013)
24. S.M. Vinko, Creation and diagnosis of a solid-density plasma with an X-ray free-electron laser. Nature **482**, 59 (2012)
25. A. Vaterlaus, M. Aeschlimann, M. Lutz, M. Stampanoni, F. Meier, Magnetization reversal in a-GdTbFe investigated by time-resolved, spin-polarized photoemission. J. Magn. Magn. Mat. **83**, 85–86 (1990)
26. E. Baurepaire, J.-C. Merle, A. Daunois, J.-Y. Bigot, Ultrafast spin dynamics in ferromagnetic Nickel. PRL **76**(22), 4250–4253 (1996)
27. J. Stohr, H.C. Siegmann, *Magnetism* (Springer, Berlin, 2006)
28. K. Nakamoto, *Infrared and Raman Spectra of Inorganic and Coordination Compounds* (Wiley, New York, 1986)
29. U. Bovensiepen, Coherent and incoherent excitations of the Gd(0001) surface on ultrafast timescales. J. Phys. Condens. Mat. **19**, 083201 (2007)
30. J.-Y. Bigot, V. Mircea, E. Beaurepaire, Coherent ultrafast magnetism induced by femtosecond laser pulses. Nat. Phys. **5**, 515–520 (2009)
31. R.J. Elliott, Theory of the effect of spin-orbit coupling on magnetic resonance in some semiconductors. Phys. Rev. **96**(2), 266–279 (1954)
32. C. Boeglin et al., Distinguishing the ultrafast dynamics of spin and orbital moments in solids. Nature **465**, 458–461 (2010)
33. H.K. Wong et al., Superconducting properties of V/Fe superlattices. J. Low Temp. Phys. **63**, 307 (1986)
34. C. Strunk et al., Superconductivity in layered Nb/Gd films. PRB **49**, 4053 (1994)
35. Th Muhge et al., Possible origin for oscillatory superconducting transition temperature in superconductor/ferromagneti multilayers. PRL **77**, 1857–1860 (1996)
36. Z. Radovic et al., Transition temperatures of superconductor-ferromagnet superlattices. PRB **44**, 759–764 (1991)
37. G. Jakob et al., Superconductivity and gaint negative magnetoresistance in $YBa_2Cu_3O_7/La_{0.67}Ba_{0.33}MnO_3$ superlattices. Appl. Phys. Lett. **66**, 2564 (1995)
38. A.M. Goldman et al., Cuprate/manganite heterostructures. J. Magn. Magn. Mater. **200**, 69 (1999)
39. Z. Sefrioui et al., Ferromagnetic/superconducting proximity effect in $La_{0.7}Ca_{0.3}MnO_3/YBa_2C_3O_{7-\delta}$ superlattices. RB **67**, 214511 (2003)
40. T. Holden et al., Proximity induced metal insulator transition in $YBa_2C_3O_7/La_{2/3}Ca_{1/3}MnO_3$ superlattices. PRB **69**, 064505 (2004)
41. N. Haberkorn et al., Antiferromagnetism at the $YBa_2C_3O_7/La_{2/3}Ca_{1/3}MnO_3$ interface. Appl. Phys. Lett. **84**, 3927 (2004)
42. V. Pena et al., Giant magnetoresistance in ferromagnet/superconductor superlattices. PRL **94**, 057002 (2005)
43. J. Stahn et al., Magnetic proximity effect in perovskite superconductor/ferromagnet multilayers. PRB **71**, 140509(R) (2005)

Index

A

Ab-initio structural simulation, 487
Abalone, 583
Ablation, 648, 766
Absorption beamlines, 80
Absorption coefficient μ, 81, 108, 109, 112, 115, 125–127, 183–189, 194, 201–208, 227, 302, 379, 392, 414
Absorption edges, 71, 117, 219, 228, 350, 354, 362, 365, 379, 391–394, 404, 414, 415, 420, 422, 485, 486, 493, 501, 593, 501, 593, 627, 683, 710, 765, 768–773
Absorption Fine Structure (XAFS/EXAFS/XANES), 646
Absorption spectroscopy, 70, 127, 182, 201, 412, 414, 421, 539, 576, 587, 642, 646, 654, 663, 664, 678, 682, 742, 743, 746, 769, 773
Adsorbate, 168, 309, 521, 526–533, 577, 669, 774
Adsorbed molecules, 540, 705, 725–727, 770
Adsorption, 526
Advanced photon source, 25, 325, 403, 464
Air particulate, 429
Algebraic reconstruction techniques (ART), 394
Alzheimer, 357, 430, 610
Analyzer-based imaging (ABI), 595, 600, 602
Ancient glasses, 683–684
Angiography, 593–597, 683, 684
Angular aperture of synchrotron radiation, 22
Angular collimation, 8, 20, 22, 23, 32
Angular momentum selection rules, 186
Angular resolved photoemission/photoelectron spectroscopy (ARPES), 87, 92, 168, 302, 309, 539, 576, 577
Anomalous or Bijvoet difference, 627
Anomalous scattering/diffraction, 109, 122, 172, 350, 354, 664
Anomalous small angle scattering, 354
Anomalous thermal expansion, 497
Antiferromagnetic structure/state, 369–372, 378, 571, 577, 584
AntiPhase boundaries, 509
Arabidospsis, 405
Archaeological heritage, 677
Area detectors, 268, 269, 320, 321, 324, 326, 646
Argand diagram, 624
Arsenic, 486
Asymmetric unit, 245
Asymmetry parameter, 292
Atomic cross section, 123, 226
Atomic force microscopy, 410
Au clusters, 497
Auger, 83, 108, 187, 204, 205, 285, 295–300, 774, 777
Autoionization, 91, 92, 295, 298

B

$Ba_2In_2O_5$, 708
$BaCeO_3$, 709
Band mapping, 168, 169
$BaZrO_3$, 709
Beads, 684
Beam micro-focusing, 667
Beamline, 8, 30, 34–38, 59, 60, 65–102, 276, 323, 236, 351, 354–359,

S. Mobilio et al. (eds.), *Synchrotron Radiation*,
DOI: 10.1007/978-3-642-55315-8, © Springer-Verlag Berlin Heidelberg 2015

366, 395, 399, 437–445, 462–466, 486, 501, 509, 520, 566, 572, 587, 595, 598, 607, 619–621, 639, 647, 663, 667, 669, 671, 771, 773
Beer-Lambert law, 78, 112, 413
Bending magnet, 5–9, 12, 15, 17, 20–22, 25, 30–37, 40, 42, 44, 45, 61, 80, 412, 438
Berlinite, 655
Bi_2O_3, 707
Bijvoet, 627
Bioavailability, 665
Biochemistry, 430
Bio-crystallography, 617–639
Biofilms, 669, 670
Biological specimens, 405, 419, 453, 454
Biomineral/biomineralization, 581, 648, 664, 671–673
Bio-molecules, 319
Bio-SAXS, 356
Blaze, 82, 84, 89, 90
Bone, 354, 355, 358, 403, 405, 430, 431, 594, 601–603, 606
Booster, 5, 66, 69
Born-Oppenheimer, 124, 288, 363
Boson peak, 470
Bragg-Brentano geometry, 268, 321
Bragg law/diffraction, 72–74, 77, 82, 170, 171, 197–199, 202, 204, 205, 254, 261, 262, 267–269, 320–324, 328, 338, 343, 362, 363, 367–369, 371, 377–379, 389–391, 400, 401, 465, 466, 500, 515, 620, 621, 625, 627, 679, 702, 767
Brain, 431, 453, 594–596, 608–610
Bravais lattices, 243, 370
Breast, 597–601
Brightness/Brilliance, 6–8, 19–21, 25, 26, 29, 32, 34–36, 40, 41, 44, 50, 54, 60, 66, 83, 93, 95, 96, 108, 319, 331, 350, 361, 366, 399, 411, 412, 422, 441, 445, 451, 462, 501, 571, 572, 641–644, 649, 650, 653, 668, 680, 762, 673, 770, 774, 777
Brillouin zone, 168, 200, 301, 309, 313, 369, 370, 384, 462, 464, 471, 480, 542, 548, 559
Bronchography, 594, 597
Bunch, 10–12, 34, 36, 38, 50–56, 442, 445, 578, 585, 653, 773

C
Capillary, 269, 321–328, 350, 413, 419, 509–510, 608, 618–619, 732
Capillary geometry, 324
Carbon cycle, 756
Cartilage, 354, 594, 601–604, 609
Catalyst, 80, 184, 354–355, 698, 706, 710, 711, 717–733
CCD, 93, 268, 392, 419–422, 573, 646, 766–767, 773
Cell (biology), 356, 415, 423–431, 452–457, 609–610, 667
Centre of symmetry, 244
CeO_2, 708
Cerrusite, 679
cgs unit systems, 174
CH_3, 530
C_2H_4, 530
CH (Cultural Heritage), 530
Chemical bonds, 58
Chemical dynamics, 774
Chemical reaction, 770
Chemical shift, 286
Chondritic meteorites, 755
Chromite, 655
Circular polarisation, 17, 148, 367
Cobalt, 748
Coherence, 38, 41, 412, 445, 761, 762
Coherence length, 40, 395
Coherent diffraction, 391, 396, 417–418, 765–766
Coherent Diffraction Imaging, 391, 765
Coherent states, 175
Co nano-wires, 306
Combined experiments, 331
Combined XMCD/XANES, 748
Complex refractive index, 391
Compton scattering, 129, 252
Computed tomography (CT), 393, 594, 597
Constant Final State, 166
Constant Initial State, 166
Continuous scatterer, 256
Contrast, 389, 392, 399, 411, 414, 420, 606
Convolution, 251
Cooper minima, 305
Coordination shells, 193–200, 208–209, 486–487, 709
Copper resinate, 687
Core-hole lifetime, 187
Core level spectroscopies, 519–522, 526, 529, 531, 536, 769–770
Core mantle boundary (CMB), 651, 653, 740
Coronary angiography, 593, 595

Correlated Debye Model, 200
Correlated electron systems, 377
Correlation function, 227–229, 343, 460, 467, 475
Cosmetic, 679, 688
Coulomb gauge, 146, 147, 153
Crab Nebula, 3
Critical angle, 71, 98, 116, 203, 350, 670
Critical energy, 16, 18–20, 22, 27, 34, 43
Cross-section, 163
Cross section of the elastic and inelastic scattering, 134
Cryogenic cooling, 94
Crystal, 325–328, 372–374, 500, 520, 540, 549
Crystal growth, 616, 617
Crystal lattice, 72, 172, 244–245, 311, 367, 401, 526, 616, 631
Crystallite dimensions, 271
Crystallites, 268
Crystallite size distribution, 351
Crystallographic refinement, 632
Crystals, 549
$CuCl_2/\gamma$-Al_2O_3, 728
Cultural heritage, 66, 219, 319, 331, 406, 457, 647, 677–693, 698
Cumulants, 195–202
Curie temperature, 556, 562, 744–750
Current operator, 375
Curved trajectories, 3
Cutoff wavelength, 15
Cyanobacterium, 671
Cicloidal, 372–374
Cystic fibrosis, 604

D
Darkfield, 417
Darwin equation, 621
Darwin term, 176
Darwin width, 73, 74, 202, 465
d-band, 522
Debye cones, 324
Debye geometry, 321
Debye ring, 327
Debye's equation, 512
Debye's law, 347
Deconvolution of XANES, 220, 752
Defects, 509
Dendrites, 404
Density of states (DoS), 6, 50, 53, 127, 214, 411, 545, 549, 566, 744
Detective quantum efficiency, 77
Detector, 14–15, 32–33, 44, 76–81, 93, 96, 164, 166, 174, 190, 201, 203–205, 254, 268–269, 277, 302, 320–328, 333, 340, 342, 344, 349, 362, 374, 390–402, 411–413, 416–422, 431, 442–443, 451, 465, 489, 500, 501, 540, 544–549, 551, 556, 573, 586, 587, 595, 598, 599, 603–605, 615, 621, 646–647, 667, 712, 765–767, 773
Diagnostic capabilities, 454
Diamond anvil cells, 330, 425, 446, 447, 649, 738, 741–743, 746, 749, 757
Dichroism, 572
Dielectric constant, 111, 113, 617
Differential interference contrast, 417
Differential scattering cross section, 118, 340
Diffraction, 74, 361, 389, 492, 670, 672
Diffraction (photons), 38–42, 66, 70, 72–75, 79, 80, 84, 89, 91, 96, 99–102, 108, 122–123, 170, 172, 184, 197–199, 202, 213, 241–271, 319–333, 338, 343, 349, 354, 361–384, 389–391, 395-396, 400–406, 410–412, 416–421, 443-445, 457, 461–462, 492, 499–517, 617–624, 642, 644–645, 653–654, 661–664, 667–668, 670–672, 678–681, 689, 691, 699, 702, 706–709, 733, 743, 747, 750, 752, 754, 758, 765–767, 769, 784
Diffraction beamlines, 79, 366, 501
Diffraction contrast tomography, 333, 400
Diffraction imaging, 333, 390, 391, 396, 400, 402, 406, 417, 575, 765
Diffraction limit, 26, 42, 60, 96, 100, 368, 410, 420, 443–445, 457, 501, 574, 653, 765–766
Diffraction peak profile, 501, 503, 505–507, 509, 512, 515
Dilute nitrides, 490
Dipole approximation, 127, 157, 170
Dipole matrix element, 158
Dirac equation, 125
Dirac–Hara potential, 230
Direct lattice, 250
Direct methods, 265, 271, 348, 710
Diseases, 357, 430, 452, 453, 455, 596, 597, 601, 602, 604–605, 609–610, 638
Dispersion relation, 110, 112, 170, 200, 461, 471

Dispersive EXAFS, 77, 205, 642, 720
Dispersive optics, 76
Displacement Correlation Function, 199
Dopant, 485–489, 698, 706–709, 719, 728–729, 731
Doppler shift, 29, 33, 46, 47, 60, 61
Double crystal monochromator, 73, 74, 80
DPC, 417
Dye-sensitized solar cell, 697, 704–706
Dynamic light scattering, 332
Dynamic range, 78, 326, 389, 413, 416
Dynamic theory, 252, 721

E

Earth, 238, 319, 328, 365, 446, 448, 641, 649, 641–656, 661, 663, 727–728, 739, 740, 747–741, 750–751, 755–758
Edge radiation, 398, 441, 444
Edge shift, 209, 216, 218, 732
Effective EXAFS distribution, 195
Einstein model, 200
Elastic scattering cross section, 108, 112, 118–119, 122, 128–129, 134, 137, 170–173, 301, 337
Electron diffraction, 226, 293–294, 519–521, 535, 546–547, 576, 663
Electric dipole operator, 126
Electric dipole transitions, 186, 375
Electron classical radius, 120, 174, 363, 369, 394
Electron density map, 631
Electron detector, 277
Electron microscopy, 410, 424
Electron orbit, 17
Electrons detector, 277
ELETTRA, 66, 67, 70–74, 79–81, 85, 88–89, 326, 355–356, 438–439, 442–443, 445–446, 566, 595, 598, 600, 602, 609, 669, 762–763, 765
Elliptically polarized, 37
Elliptical mirrors, 84
Emittance, 19, 20, 25, 26, 67–69, 74, 96, 411
Energy dispersive X-ray diffraction, 668
Energy distribution curve, 164, 165, 277, 301, 305, 555
Energy recovery LINAC, 60
Energy resolution, 72–73, 79–80, 83–84, 87, 91–94, 202, 219, 277, 288, 366, 413, 420, 461–462, 464–466, 477, 491, 519–537, 576–577, 581, 587, 677–678
Environmental Science/studies, 59, 66, 219–220, 331, 409, 426, 428, 641, 661–674 , 698–699, 718, 727, 737
Equation of state, 652, 748
Escape depth, 166, 205, 278, 548
ESRF, 5, 11–12, 20, 66–67, 77, 97, 323–327, 330, 332, 355–356, 395, 404, 439, 462, 464–465, 500, 509, 595–598, 601–602, 610, 619, 646, 680, 730, 732, 737, 743
Ethylene, 530, 717, 727–732
Euphorbia pythiusa, 668–669
Ewald, 242, 245, 262, 366, 767
EXAFS, 74, 77, 83, 163, 169, 181–210, 213–215, 227–230, 233, 415, 485–497, 642, 646, 664–666, 672, 683, 686–688, 692, 700, 704, 707–709, 718–720, 723–724, 728–733, 748
EXAFS function, 188–192, 205, 207, 209
Exchanged wavevector, 121, 478
Exchange scattering, 546–547, 781
Excitation, 185
Extreme conditions, 217, 233, 328, 367, 384, 464, 642–644, 649, 652, 737–758, 770, 777
Extreme P and/or T conditions, 648, 742, 747
Extremophiles, 446

F

Femtosecond, 66, 569, 622, 697, 762, 763, 768, 770, 774, 778–780, 782
FERMI, 566, 762, 763, 765, 768, 770, ,773, 779
Fermi-dirac, 93, 304
Fermi Golden Rule, 125, 126, 131, 133, 135, 220, 300
Fermi Golden rule, 185
Fermi level, 164, 214, 220, 303, 306, 543, 548–549, 560, 577–580, 706, 744–745
Ferromagnetism, 549, 562, 737, 744–746, 749, 782
Ferropericlase, 654, 750
Feynman diagrams, 156–158
Filtered back-projection (FBP), 394
Fine structure constant, 126, 174, 560
First order (relativistic) scattering, 132, 138, 140
FLASH, 566, 763, 766, 770–771, 773-774
Flat-plate diffractometers, 323
Fluorescence, 79, 108, 187–188, 295, 456

Fluorescence contrast, 416, 420
Fluorescence detection mode, 81, 204–205, 236, 421–422, 647, 684
Fluorescence detection method, 421, 422
Fluorescence map, 423, 487, 685, 689, 690
Fluorescence micro-analysis, 391, 398–399, 642–643, 647–648, 689
Fluorescence microscopy, 409–411
Fluorescence tomography, 405, 655, 667
Fluorescence yield, 187, 236, 379, 416, 647
Focusing, 5, 6
Focusing (electron beam), 5–6
Focusing optics/mirrors, 35–36, 70–71, 83–90, 95–102, 245, 269, 321, 384, 398, 404–405, 412–413, 418–420, 438, 466, 606, 666–668
Focusing (sagittal), 7, 75, 80, 466
Folded polymer, 352
Folding, 343, 357, 450, 455, 543–546, 616
Forbidden lattice reflections, 362, 377–378, 380–383
Form factor, 339–344, 347, 357, 378, 445, 462
Fossils, 403, 643, 655, 691–692
Fourier transform, 57, 121–122, 129, 134, 137, 141–142, 207–210, 231, 247–251, 256, 259, 264, 266, 268, 338–340, 343, 347–348, 351, 364, 396, 410, 461, 467, 487, 502, 509, 623, 668, 688, 763
Fourier transform infrared spectroscopy (FTIR), 410, 668, 688
Fourth-generation sources, 3, 6, 66
Fractional parentage, 283, 289
Fraunhofer diffraction/regime, 391, 395, 397–398
Free electron lasers (FEL), 3, 6–7, 29, 50, 53–55, 58–61, 66, 411, 486, 545, 549, 566, 569, 585, 733, 761–784
Fresnel diffraction/fringe, 395, 397–398, 574
Friedel's law, 266, 621, 627
Fresnel zone plate, 99–101, 412–413, 419, 642
Fuel cells, 427, 697–699, 706, 710–713
Fukalite, 646
Full multiple scattering (FMS), 214, 217, 228, 490

G

GaAs, 489, 490, 523
GaAsN, 490
Galena, 679–680
GaSb(110), 523
Gas-filled detectors, 326
Gauge (transformation), 111, 146–147, 153, 155
Gaussian function, 248
GIXAXS, 350, 670
GIXD, 670
Glass transition, 474–478
Glide planes, 244–245, 362, 406
Glioma, 609
Golden Rule, 185
Graphene, 311–314, 519, 521, 534–535, 580–582
Grating interferometric imaging (GI), 595
Gratings, 46, 82–92, 99, 245, 320, 412, 595, 601, 609
Grazing incidence, 85, 98, 116, 118, 323, 325, 350, 573, 712
Green function, 223–224, 235, 284, 304–305, 373–374
Guinier, 321, 344–351
Gyration radius, 344, 347

H

Hankel function, 227–228
Harker construction, 622, 624, 627–629
Harmonic generation, 763, 770
Harmonic oscillator, 149, 469
Harmonic rejection, 80, 366
Hartree-Fock approximation, 124, 167
HCl, 727–729
Hcp phase, 745–748
Heat load, 66, 90, 94–95, 98–99, 465
Heavy-fermion, 383–384, 448
Hedin–Lundqvist (HL) potential, 225
Heterostructure, 485, 491, 556, 562, 783
High energy inelastic scattering, 134
High pressure, 203, 213, 217, 321, 328–330, 384, 446, 574, 642, 644–645, 649, 652–656, 737–740, 744–750, 756–758
High-spin, 235, 654
High temperature, 213–214, 328–329, 474–477, 644, 649, 653, 683, 702–703, 706–708, 711–712, 723, 740, 744–745, 750, 782
High-temperature superconductivity, 450
Holography, 82, 398, 417–418
HOMO-LUMO gap, 564, 705
Human Genome Project, 616, 638
Hydrogen storage, 697–703
Hydrozincite, 671, 672

I
III-V semiconductor alloys, 490
Ice crystals, 6, 95–96, 98, 101, 108, 116, 319, 333, 389–406, 409–432, 549, 571–587, 593–610, 643, 655–656, 661, 667, 677–678, 688–693, 761–762, 765–766
Imaging beamlines, 595, 607
Impurity phases, 327
In situ (studies), 329–330, 354, 403–406, 411, 423, 427, 501, 531–532, 578, 585, 600–601, 642–643, 648–649, 653, 667–671, 698–699, 702, 708, 711, 712, 717–733, 743, 751, 753
In vivo, 404, 594, 602–610, 616, 667
InAs(110), 306
Index of refraction, 70, 97, 109, 100, 111–117, 203, 245, 368, 391, 394, 396, 414, 416, 606
Inelastic (X-ray) scattering, 83, 108, 112, 128–129, 134, 164, 172–173, 301, 461–480, 720, 747, 774, 782
Infrared micro-spectroscopy, 422, 443–444, 452, 457, 688
Infrared spectroscopy, 437, 446–448, 668, 689, 710, 779
Insertion devices (ID), 6, 20–23, 26, 30, 66, 69, 83, 85, 95, 361, 670
Instrumental FWHM, 501
Insulator-to-metal transitions, 169, 362, 380, 382, 494
Interaction Hamiltonian, 125, 131, 133, 135, 137–138, 156, 186
Interface, 112, 117–118, 217, 310, 323, 345, 485, 520–521, 548, 560, 562, 564–565, 567–568, 571, 575–576, 578, 584–585, 587, 603, 606, 641, 647, 663, 666, 668–671, 704–706, 711, 719, 741, 783
Intrinsic angular momentum, 176
Inverse compton scattering, 60
Inversion axes, 244
Inversion symmetry, 372, 381, 383, 556, 725
Ionization, 166, 170, 304
Ionization chambers, 8–81, 203, 420
Infrared (IR) beamlines, 87, 437, 439, 441–442
Iron, 26, 235–236, 286, 405, 428–429, 500, 509–510, 548–549, 554, 560, 562, 582, 643, 649, 652–655, 667, 670, 684, 699, 740–741, 746–753
IRSR (Infrared synchrotron radiation), 437–458
IRSR brilliance, 442
Isomorphous replacement, 265, 622, 624–628, 631

J
Jones formalism/matrix, 367, 370, 372

K
K edges, 182–183, 188, 193, 206, 215–219, 229–230, 233–237, 362, 365, 379–384, 404, 427–429, 487, 490–496, 576, 581, 593, 654, 664, 864, 687–692, 704–705, 710, 712, 728, 746, 748–755, 777
K-edge XMCD, 746, 748, 750
K-Edge subtraction, 593
$KCuF_3$, 378
Kerr effect, 549, 554, 559, 566, 779
Kinematic theory (difraction), 252, 363, 645
Kirkpatrick Baez mirrors (KB), 84, 87, 98–99, 102, 398–399, 413, 419–420
Koopman's theorem, 166, 283, 304
Kramers Kronig transformations, 113, 305, 450, 452
Kratky plot, 347

L
L/S ratio, 371
Lambert equation, 78, 112, 413
Laser-heated DAC, 750, 753
Lateral coherence, 39, 41–42, 395–396
Lateral resolution, 95–96, 101, 456–457, 572–74, 578, 58–84, 587, 648, 682, 688–689, 765
Lattice (crystal), 72, 172, 244–245, 311, 367, 401, 526, 616, 631
Lattice function, 246–253
Lattice reflection, 362, 377–778, 380–83
Laue, 101, 245, 258, 268, 320, 368, 413, 420, 499–503, 516, 600, 621–622, 646
LCLS, 566, 762–763, 767–768, 770, 774, 777
$LiBH_4$, 702–704
Life science, 215, 409, 429, 615
Light scattering, 348, 462–463, 471, 568
LINAC, 5, 60, 66, 438, 445
Line broadening, 15, 505, 508, 510
Line profile analysis, 499, 505

Line profile (diffraction and spectroscopy), 250, 503, 508–509, 515
Linear attenuation coefficient, 392
Linear combination analysis, 218
Linear detectors, 320, 322, 324, 327, 340, 500,
Linear polarization, 17–18, 37, 134, 148, 162, 368, 370–371, 383, 486, 495, 551
Lippman-Schwinger equation, 222
Lorentian function/curve, 232–233, 304, 307
Lorentz, 31, 33, 45, 52, 114, 119, 621
Lorentz contraction, 29, 45–47
Lorentz factor, 268, 505, 514, 621
Lorentz force, 9, 30, 44, 50–52, 54–55, 111
Lorentzian broadening, 225
Lorentz model, 107, 114, 119
Lotentz transformation, 31, 33
Low energy electron diffraction, 546–547, 575–576, 578, 581, 585,
Low energy electron microscopy, 96, 338, 352, 396, 424, 575, 658, 696, 765
Low-frequency modes, 470
Low-spin, 235
LS coupling, 543
Lungs, 594–97, 603–06, 610
Luster, 683–687

M

Macromolecular crystallography, 265, 410, 615–618, 621
Macromolecular crystallography, 265–266, 616, 638–639, 664
Magic angle, 292
Magnetic (Bragg) diffraction/scattering, 135, 141–142, 171–172, 361–366, 369, 371–372
Magnetic domain, 366, 371, 374, 384, 546, 577, 768
Magnetization, 364, 539–542, 546–550, 553–563, 564, 566–568, 577, 586–587, 748, 762, 768, 778–783
Magnetoresistance, 494–495, 783
Magnetostriction, 567–568
Mammography, 594, 597–600, 609
Manganites, 494
Material science, 213, 276, 361, 427, 649, 664, 678
Maxwell equations, 109, 145
Maya blue, 680–683
MCX beamline, 75, 79, 326
Mean field approximation, 124
Mean free path, 93, 184, 192–195, 205, 209, 214, 217–218, 225, 232, 278, 301, 308, 520, 535, 546, 549, 574, 576, 584
Mean square (relative) displacement (MSRD), 119, 198–199, 257, 495, 497
Medical imaging, 593–609
Metal hydrides, 698–702
Metal impurities, 487
Metal insulator transition, 494
Metal oxidation and spin-state, 721
Metal solidification, 404
Metal(III) carboxylate, 700
Metal insulator transition, 169, 362, 380, 382, 494
Metallic clusters, 485, 497, 699–700
Metalloproteins, 628
Metal-organic frameworks, 769–700, 719
Metal-phthalocyanines, 305
Metamict materials, 642, 647–48
$Mg(BH_4)_2$, 702
Michelson interferometer, 445
Micro-analysis, 421, 425, 426
Micro channel plate (MCP), 573, 587
Microalga, 671
Microangiography, 596
Microbeam, 331–333, 354, 391, 642, 648, 677, 678–680
Microbunching, 50, 51, 54, 56, 773
Microfocus, 333, 355, 711
Micrometric beams, 354
Microradiography, 391, 667
Microscopy, 6, 87, 95–96, 100–101, 338, 352, 358, 396, 400, 403, 409–432, 437, 444, 455, 560, 571–587, 605, 655, 663, 666–672, 686, 711, 765, 767
Microspectroscopy, 437, 452, 457, 578, 671
Microstructure characterization, 400
Microtomography, 391, 393, 398–399, 405, 642–643, 663, 667, 690, 692–693
Micro-XAS, 235, 488–489, 493, 647–648, 667
Miller indices, 242, 261, 381, 501, 523
Mineralogy, 320, 663, 664
MINUIT, 231
Mirrors, 20, 39–99, 69–72, 75, 81–87, 90, 95, 98–99, 102, 118, 201–203, 245, 269, 350, 366, 419, 438, 642
Mixed electronic and ionic conductor, 711
Molecular environmental science, 661, 662, 673

Molecular movie, 769
Molecular replacement method, 265, 623, 629, 631
Molecular sieve, 720–722
Momentum transfer, 337, 546, 780
Monochromators, 40, 42, 57, 69–76, 80,82–85, 87–90, 92–95, 201–202, 204, 233, 254, 269, 277, 321, 350, 464–466,576
Mosaic crystal, 402, 406, 620
Mosaic tessera, 684, 686
Mössbauer spectroscopy, 365, 643, 654, 655, 747
Mott detector, 540, 545, 547, 556
Mott insulator, 447, 771
Mott scattering, 543–546, 549, 551
Mott Hubbard insulators, 378, 380, 448
MS expansion, 227
MS theory, 222–224, 231, 238
Muffin-tin, 190, 223–224, 226, 231, 233
Multiferroics materials, 219, 372, 383–384, 762
Multilayer, 98–99, 383, 398–399, 413, 457, 465–466
Multiple Anomalous Dispersion, 266
Multiple Isomorphous Replacement (MIR), 265, 624, 626
Multiple scattering, 163, 188, 192, 194–197, 209, 222, 228, 231, 237–238, 366, 382, 485, 490, 526, 543, 545, 548
Multiple splitting, 163
Multiple wavelength Anomalous Dispersion, 628
Multiplet splitting, 163, 284–287, 289, 296, 520
Multipole magnet, 21
Multiwavelength Laue crystallography, 621
MXAN, 231–237

N

Nafion, 701, 711
Nanocrystal/nanocrystalline, 499–516, 767
Nano-imaging, 391, 399
Nanoparticles, 515, 578, 666
Nanotube, 574, 578
Naracauli, 664, 671–673
$Nb_{0.5}Ti_{0.5}$, 452
Near-Edge X-ray Absorption Fine Structures NEXAFS, 163
Neurons, 581
Neutron scattering, 371, 374, 381, 382, 384, 462, 463, 470, 638
Ni, 749—750,779–780
Non-crystallographic symmetry (NCS), 632
Non-ergodicity factor, 477–479
Non-resonant x-ray magnetic scattering, 363—364, 371
Normal incidence monochromator, 87–88
Numerov procedure, 226

O

One electron approach/ approximation/model/picture/, 124, 127, 163–168, 185–187, 226, 278, 282, 296, 300, 720–722
One-dimensional lattice, 246–248, 251, 253
Opacifiers, 684
Operando experiments/measurements, 569, 698, 720, 727–731
Optical amplification, 50–54, 56, 58
Optical constants, 109,113–114
Orbital magnetic dipole moment, 135,137,160,565–566
Orbital magnetic scattering, 171
Orbital angular momentum, 142, 176, 560, 564, 566, 725, 746, 750
Orientation distribution function, 272, 320, 327
Osteoarthrosis, 601
Oversampling, 396
Oxide-ion and proton conductors, 706

P

Paintings, 331, 457–458, 681–683, 687–689
Paleontological findings/specimens, 691–692
Palygorskite, 681–682
Parkinson disease/syndrome, 357, 430, 454
Passive electrons, 127, 185–187
Patterson function/map/method, 264–265, 271, 514, 623—627, 630–633
Pentacene, 310
Perovskites, 492, 651–654,706, 753–754
Phase analysis, 271
Phase contrast imaging, 116, 389, 391, 395, 397, 399, 403, 409–414, 416–426,594,693
Phase plate, 368
Phase problem, 122, 263–266,620
Phase retrieval algorithims/reconstruction, 396, 603, 606, 765–766
Phase transitions, 169, 203, 271, 384, 406, 448, 492, 494, 524, 560, 642–644,

651–655, 702, 707–708, 747–748, 753, 762, 774, 782
Phaseshifts, 191, 192, 197
Phonons, 461–462, 470, 497, 520, 542, 581, 748, 779–782
Phosgenite, 679, 688
Photoelectric absorption/effect, 163, 182, 184, 275, 278, 392, 414
Photo-electron mean free path, 193
Photoelectron/Electron inelastic mean free path, 278, 671
Photoelectron/photoemission spectroscopy, 275–298
Photoelectron diffraction, 169, 226, 293, 294, 519, 526, 535–536, 576, 663
Photoelectron spectroscopy/photoemission spectroscopy, 87, 163–169, 275–318, 519–538, 541–555, 571–588, 705, 770–773
Photoemission electron microscopy, 571–592
Photovoltaics, 427, 487
Pigments, 331, 457, 678, 683, 687, 691
Pixel/pixel detector, 79, 324, 326, 342, 344, 345, 389, 390, 393, 402, 420, 422, 573, 604, 607, 669, 751
Plain grating monochromators, 84–85
Planetary processes/samples/sciences, 319, 328, 641, 649, 737, 740
Plasmons, 225, 232, 278, 520, 521, 542
Poincaré-Stokes, 372
Polarization (of the EM field/of x-rays), 130, 148, 153, 157, 161, 185, 276, 279, 291–294, 368–369, 428, 486, 561, 576, 577, 595
Polarization (factor/dependence), 137, 140, 141, 173, 192, 220, 253, 254, 268, 378, 381, 512, 621
Polarization (of matter), 113–114, 368
Polarization (of synchrotron radiation), 17–19, 26, 37–38, 83, 361, 372
Polarization (of scattered radiation), 366–368, 371, 373, 374, 376, 379, 381, 382
Polarization (of synchrotron radiation), 17, 26
Polarization vector, 140, 148–149, 170, 302, 364, 583
Polarons, 494
Polychromator, 76
Polycrystalline samples (diffraction patterns), 267–272, 320–321, 512, 644
Polycrystalline samples (imaging), 400–401, 406
Polycrystalline samples (photoemission spectra), 93
Polycrystalline samples (X-ray absorption spectra), 192, 560
Polymer electrolyte membranes, 710
Polyvinyl chloride, 727
Porod's law, 345—-346, 348—-349, 355, 357
Porous and materials, 339, 346, 354, 644, 655, 681, 702, 704, 719, 721
Position sensitive area detector, 269
Position sensitive detectors, 79
Powder diffraction, *see* Polycrystalline materials (diffraction patterns)
Powder diffraction geometries, 323
Preferred orientations, 268–269, 272
Pressure-induced transitions, 447, 654, 738
Principal component analysis, 219
Prion, 454, 455
Projection Microscopy, 418
Propagation-based imaging (PBI), 595, 604
Protein crystallography, 616, 617
Protein Data Bank, 637
Proteins, 218, 233, 263, 265, 339, 347, 356–357, 419, 423, 429, 450–457, 615–639, 767, 769
Proton conducting materials, 698—701, 709
Pseudomorphic growth, 492
Pt, 305, 307, 522, 523, 529–532, 566, 710–712
Ptychography, 396–397, 400, 417–418
Pulsed time structure, 8, 38
Pump and probe experiments, 234–235, 438, 549, 559, 566, 568, 586, 732, 762–763, 766, 770–776, 778–781
Pyrolusite, 684

Q

QEXAFS, 74
Quadrupolar transitions, 160, 216
Quadrupole magnets, 6
Quadrupole splitting, 655
Quantum dots, 496, 578
Quartz, 473, 655, 668

R

Radiation damage, 71, 366, 410, 416, 423–425, 587, 618–620, 766
Radio frequency, 5, 30

Radiography, 390–393, 403–404, 595, 601, 667, 688
Radon transform, 394
Rare earth elements and compounds, 173, 184, 365, 383, 448, 728
Re, 535
Refractive lenses, 97, 398, 413, 420, 465
Relativistic effects, 3, 8–9, 12–13, 30–34, 45–56, 137–142, 154–157, 176, 382, 554
Relaxation (of electronic states), 166–167, 187, 222–223, 236, 281, 287, 294–300, 770, 784
Relaxation (of atomic structure), 307, 467, 468, 470, 474–477, 479, 497, 509, 515, 522, 559, 647
Resolution, 262, 322
Resonant, 361, 366
Resonant contribution, 363
Resonant magnetic enhancement, 362
Resonant Raman Scattering, 172
Resonant Scattering, 109, 135–137, 140, 375–383
Resonant X-ray diffraction, 383
Resonant X-rays scattering, 375
Rh, 522, 527–533, 578–579, 711, 748
Rietveld method, 271, 644, 653, 664, 681
RIXS, 83, 774, 782
Rocking curve, 202, 401
Röntgen, 245
Root-soil mineral interface, 668, 669
Rotational matrix, 631
Rotation axes, 244
Roughness, 71, 98
Rowland circle, 87
Ru, 535, 585, 771, 774
Ru($10\bar{1}0$), 525
RXES, 769, 774, 777
Rydberg states, 92

S

Sagittal focusing, 71, 75, 80
SASE, 57, 763, 768, 770, 771, 773
Satellite structures, 281–284
Saturation length, 56
SAXS, 75, 326, 331, 337–359, 421, 642, 670
Scalar potential, 146, 147, 176
Scattering, 107, 108, 181
Scattering amplitude, 171, 192, 255, 362, 364, 367, 370, 372, 375, 376, 379, 382, 511
Scattering function, 122
Scattering intensity, 338, 340
Scanning optical microscopy, 410
Scanning transmission X-ray microscope (STXM), 96, 412, 417–423, 425, 574, 667, 668
Scattering vector, 320, 337, 340, 342, 344, 366, 367, 369, 383, 501, 503, 511
Scherrer, 269, 270, 321, 324, 500, 501, 505, 507
Schwinger's formula, 9
Screening, 522
Screw axes, 245, 361
Secondary electron distribution, 164, 166
Secondary peak, 542, 548, 549
Second order processes, 171
Second order relativistic scattering, 139, 140
Seeded FEL, 763, 768, 770, 773
Seeding, 57, 60, 761, 763, 768
Seismic anisotropy, 741
Self energy, 304, 305, 555
Semi-classical, 106, 109, 124, 125, 127, 128, 135, 153, 160, 559
Semi-classical approach, 124
Semi-classical approximation, 109
Semi conductor, 491
Sepiolite, 681
Shake-off, 283
Shake-up, 283
Shannon's theorem, 396
Shape errors, 98
Sherman function, 543, 545, 546
Si, 309
Signal/noise, 319, 322, 323, 327, 442, 443
Silica, 471, 473
Silicate melts, 648, 654
Silicon drift detector, 79
Simultaneous HP and HT, 744
Single Anomalous Diffraction, 266
Single Isomorphous replacement, 265, 622, 627
Single isomorphous replacement with anomalous scattering (SIRAS), 628
Single scattering, 188, 190, 194, 197, 208, 209, 214, 228, 544
Single scattering (SS) formalism, 190
Single scattering (SS) region, 228
Single-crystal X-ray diffraction, 644
S.I. units, 146
SIRAS, 626–628
SISSI beamline, 438, 443, 458
Slater determinants, 221, 124, 127, 161, 186, 221, 282
Slope errors, 71, 86, 95

Small angle light scattering, 348
Soft tissues, 594, 601, 602, 606, 607
Soft X-ray, 66, 81–87, 91–94, 98–101, 365, 412, 417, 419, 420, 425, 427, 429, 491, 520, 576, 663, 667, 704, 711, 712, 762, 763, 768, 771, 782
Soft X-ray energy optics, 83
Soil, 428, 663, 665, 666, 668
Solar cells, 428, 487, 490, 696, 698, 703
Solar grade silicon, 487
SOLEIL, 77
Solid oxide fuel cells, 711
Solid solutions, 647, 670, 709
Soller slits, 322, 323, 328
Solvent flattening, 631
Sources, 361
Source size, 36
Space coherence, 38
Space groups, 245, 264, 363, 380, 382, 700
Space-resolved measurements, 350
Spatial resolution, 78, 79, 100, 108, 286, 333, 354, 390, 391, 393, 398–405, 410, 413, 417–420, 425, 454, 486, 487, 595, 597, 601, 642, 648, 656, 667, 683, 711, 765
Speciation, 415, 420, 424–428, 642, 664, 665, 668, 670, 673, 674
Speckle, 765, 766
Spectral distribution, 12–16, 29, 32, 34, 42, 44, 46, 426, 535
Spectral function, 284, 303, 304, 542, 548, 554
Spectro-microscopy, 412, 428
Spectroscopy, 437
Spherical harmonics, 161, 224, 356, 375
Spin, 364, 539
Spin density, 141, 783
Spinel, 652, 750
Spin-flip, 780
Spin magnetic scattering, 171
Spin of the electrons, 138
Spin-orbit, 91, 138, 176, 284, 287, 521, 539, 540, 542, 544, 545, 548, 550–552, 554, 556, 558, 560, 568, 746, 779–781
Spin-polarization, 541
Spintronics, 778
SPring-8, 67, 99, 441, 442, 464, 595, 604–607, 610, 763
SR-XRD(Synchrotron radiation x-ray diffraction), 664, 702, 707, 708
SR-XRPD(Synchrotron radiation x-ray powder Diffraction), 498, 500, 510, 644, 679
Stereochemical parameters, 634
Stochastic cooling, 60
Storage ring, 8, 29, 32
Straight sections, 20
Strain, 272, 319, 320, 328, 330, 454, 492, 496, 508, 581, 585, 644, 668, 680, 709, 747
Stranski-Krastanov growth, 496
Structure determination, 271
Structure factor, 202, 226, 259–264, 342–345, 353, 362, 363, 373, 381–384, 461, 467, 468, 477, 478, 501, 621, 623–628, 631, 632, 635, 636, 670
Sub-ns, 493
Substitutional, 487, 489–491
Sudden approximation, 167, 169, 187, 282
Sudden limit, 232
Sulfur, 475, 476
Sum rule, 187, 217, 225, 283, 467, 560, 564, 566, 568
Superconducting, 782
Superconducting gaps, 450
Superconductivity, 362, 450, 539, 559, 782
Supernova, 3
Supersaturation, 617
Surface core level shifts, 521, 531
Surface magnetometry, 553
Surface reconstruction, 523, 575
Surface roughness, 98
Surfaces, 519
Switching mirror, 89
Synchronous electron, 9

T

Tangent plane approximation, 503, 505
Temperature diffuse scattering, 515
Temporal resolution, 78, 389
Terahertz, 58, 87, 445, 450
Terahertz spectroscopy, 87, 449
Texture and strain, 330
Textured, 272, 320, 327, 503
Textured domains, 503
Thermal vibrations, 194, 230, 257, 505, 645
Thin films, 79, 213, 305, 323, 361, 383, 452, 485, 495, 571, 579, 667, 670, 779
Third generation sources, 361, 391, 594, 66, 87
Third generation synchrotron, 6, 26, 61, 65, 94, 141, 361, 391, 403, 462, 464, 520, 526, 571, 572, 668, 671, 693

Thomson, 364
Thomson-Bragg differential cross section, 170
Thomson cross section, 120, 135
Thomson scattering, 170, 252, 253, 337, 361, 364, 367
Three dimensional lattice, 242, 247, 250–252
Three-step model, 300, 301
Three temperature model, 779
Time coherence, 29, 38, 57
Time structure, 8, 9, 29, 38, 45, 57, 762
Time-resolved, 213, 214, 268, 322, 328, 350, 354, 357, 411, 493, 545, 559, 585, 586, 621, 642, 648, 664, 703, 707, 729, 733, 761, 768, 771, 779, 782–784
Time-resolved magnetic imaging, 585
Time-resolved SAXS, 357
Time-resolved spectroscopies, 761
Ti-phtalocyanines, 704
Tissues, 431
Tomographic energy dispersive diffraction imaging, 333
Tomography, 391, 399, 600
Top-up mode, 66, 69
Toroidal mirror, 71, 84, 85, 466
Total absorption cross section, 220, 224, 226
Total absorption cross section, 220, 224, 226
Total cross section, 120, 142, 161, 226, 231, 292, 413
Total emitted power, 34, 35, 94
Total power, 22, 94
Total reflection XRF (TR-XRF), 670
Trace elements, 424, 430, 642, 646, 647, 649, 668, 679, 683
Transformation kinetics, 325, 330
Transient magnetization, 778, 782
Transition, 746
Transmission measurement, 203, 204, 206
Translational searches, 630
Transmission X-ray microscope (TXM), 96, 417, 419, 420
Two-dimensional mapping, 425
Type II superconductors, 452

U

Ultrafast dynamics, 762, 779, 781
Ultrafast techniques, 778
Ultrashort pulses, 559, 761, 763, 784
Undulator, 5, 6, 13, 21–26, 29, 30, 34, 37, 40, 44–50, 53, 54, 56, 61, 66, 69, 86, 89, 94, 361, 366, 367, 412, 420, 444, 465, 572, 762, 763, 773
Undulator emission, 50
Unit cell, 242–245, 257, 261, 264, 311, 343, 362, 363, 369, 370, 376, 492, 501, 513, 534, 535, 537, 618, 620, 621, 623, 630, 631, 706, 708, 723
Unit cell parameters, 242
Universal synchrotron radiation function, 15
UPS, 577

V

V_2O_3, 380
Vacuum level, 279
Vacuum ultraviolet, 81
Vanadium oxides, 447
Vector potential, 110, 111, 124, 125, 131, 146–148, 152, 171, 185, 302, 364
Vegard's law, 491
Vertical angular distribution, 19
Very low-energy-electron-diffraction, 547
Vibrational density of states, 470
Vibrational fine structure, 288, 530
Victoreen law, 184
Vincent van Gogh, 690
Viscoelastic model, 468, 474
Visible light microscopy, 422
Von Laue, 245
Vortex, 452

W

Wadsleyite, 646
Water, 474
Water window, 419, 420, 429
White line, 493, 560, 723, 728
Whole powder pattern modelling, 509
Wigglers, 5, 21–25, 30, 34, 37, 40, 44, 66, 69, 72, 75, 361, 444
Wilkens-Krivoglaz, 510
Wilkens-Krivoglaz theory, 510
Wilkens parameter, 510
Work function, 164, 276, 303, 575–578

X

X-α potential, 225, 230
X-FEL, 3, 6–7, 29, 50, 53–55, 58–6166, 411, 486, 545, 549, 566, 569, 585, 733, 761–784
X-ray absorption fine structure (XAFS), 73–83, 163, 169, 181–210, 213–238, 415, 485–497, 642, 646–

648, 683, 686–692, 700, 704, 707–709, 718–733, 747
X-ray absorption spectroscopy, 70, 127, 181–210, 213–238, 412, 414, 421, 539, 576, 587, 642, 646, 654, 663–664, 678, 682, 742–743, 746, 769, 773
X-ray Coherent Diffraction Imaging, 391, 396, 417–418, 765–766
X-ray computed tomography, 421, 655, 689–690
X-ray crystallography, 77, 615
X-ray detectors, 77
X-ray diffraction, 66, 70–72, , 241–271, 320, 333, 338, 349, 361–384, 401, 421, 492, 617–622, 627, 642–644, 653–656, 663–664, 670–672, 677–678, 689, 691, 699, 707–708, 747, 752, 758
X-ray emission spectroscopy (XES), 648, 717–722, 724–726, 728–733, 769, 770, 774–777
X-ray excited optical luminescence (XEOL), 422
X-ray free electron lasers (XFEL), 733, 761–784
X-ray imaging, 96, 101, 390–406, 594
X-ray magnetic circular dichroism (XMCD), 83, 215, 217, 362, 540, 560–568, 576–577, 584–586, 733, 746–750, 782
X-ray magnetic linear dichroism (XMLD), 540, 566–568, 584, 585, 576,
X-ray magnetic scattering, 135, 141–143, 171–172, 361–384
X-ray microscopy, 96, 100–101, 409–432, 560, 574, 667, 765
X-ray mirrors, 70–72, 75, 201–203
X-ray optics, 95–97, 101, 321, 391, 399, 412
X-ray photoelectron diffraction (XPD), 226, 293–294, 519, 521, 535, 576, 663
X-ray photoelectron spectroscopy, 83, 218, 277, 288–289, 520, 571, 585, 576–579, 671, 704, 712
X-ray powder diffraction (XRPD), 241, 268–271, 319–333, 499–517, 642–644 653, 656, 664, 672, 678
X-ray X-ray detectors, 615
XAFS, 74–83, 163, 169, 181–210, 213–238, 415, 485–497, 642, 646–648, 664-—665, 672, 683, 686–692, 700, 704, 707–709, 718–733, 747
XANES/NEXAFS, 83, 163, 183, 381, 392, 415, 420–422, 427–431, 485–495, 576, 581–587, 646–648, 654, 664–667, 672, 679, 683–687, 704, 710–714, 718–720, 723, 728–733, 746–755
XAS, 70, 127, 181–210, 213–238, 412, 414, 421, 539, 576, 587 642, 646, 654, 663–664, 678, 682, 742–743, 746, 769, 773
XPS, 576, 83, 218, 277, 285, 288–289, 570, 571, 576–579, 585, 671, 704, 712
XSW (X-ray standing wave), 670–671

Z

Zeolite, 645, 646, 719, 723
Zernike phase contrast, 416
ZP (Zone plate), 99–101, 418
ZP efficiency, 101
ZP spatial resolution, 100